Arya Uthaman
Sabu Thomas
Tianduo Li
Hanna Maria   *Editors*

Advanced Functional Porous Materials

From Macro to Nano Scale Lengths

Springer

Engineering Materials

This series provides topical information on innovative, structural and functional materials and composites with applications in optical, electrical, mechanical, civil, aeronautical, medical, bio- and nano-engineering. The individual volumes are complete, comprehensive monographs covering the structure, properties, manufacturing process and applications of these materials. This multidisciplinary series is devoted to professionals, students and all those interested in the latest developments in the Materials Science field, that look for a carefully selected collection of high quality review articles on their respective field of expertise.

Indexed at Compendex (2021)

More information about this series at https://link.springer.com/bookseries/4288

Arya Uthaman · Sabu Thomas · Tianduo Li · Hanna Maria

Editors

Advanced Functional Porous Materials

From Macro to Nano Scale Lengths

Springer

Editors
Arya Uthaman
Laboratory of FRP Composites
and Structures
School of Civil Engineering
Harbin Institute of Technology
Harbin, China

Tianduo Li
School of Chemistry and Pharmaceutical
Engineering
Qilu University of Technology
Jinan, China

Sabu Thomas
School of Energy Materials
Mahatma Gandhi University
Kottayam, Kerala, India

Hanna Maria
School of Energy Materials
Mahatma Gandhi University
Kottayam, Kerala, India

Contents

Contributors

Hani Nasser Abdelhamid Advanced Multifunctional Materials Laboratory, Department of Chemistry, Assiut University, Assiut, Egypt;
Proteomics Laboratory for Clinical Research and Materials Science, Department of Chemistry, Assiut University, Assiut, Egypt

Mohd Fareezuan Abdul Aziz Fakulti Kejuruteraan Pembuatan, Universiti Teknikal Malaysia Melaka, Melaka, Malaysia

S. Anitha Department of Nanoscience and Technology, Sri Ramakrishna Engineering College, Coimbatore, Tamil Nadu, India

K. F. Anna Dilfi School of Civil Engineering, Harbin Institute of Technology, Harbin, China

Mohd Asyadi Azam Fakulti Kejuruteraan Pembuatan, Universiti Teknikal Malaysia Melaka, Melaka, Malaysia

M. A. Azmah Hanim Department of Mechanical and Manufacturing Engineering, Faculty of Engineering, Research Center Advance Engineering Materials and Composites (AEMC), Universiti Putra Malaysia, Seri Kembangan, Malaysia

Raquel V. Barrulas Department of Materials Science (DCM), NOVA School of Science and Technology (FCT NOVA), i3N|Cenimat, NOVA University Lisbon, Caparica, Portugal

Marta C. Corvo Department of Materials Science (DCM), NOVA School of Science and Technology (FCT NOVA), i3N|Cenimat, NOVA University Lisbon, Caparica, Portugal

Niall J. English School of Chemical and Bioprocess Engineering, University College Dublin, Belfield, Dublin, Ireland

A. T. N. Fajar Department of Applied Chemistry, Graduate School of Engineering, Kyushu University, Fukuoka, Japan

Hong-Xia Fan State Key Laboratory of Clean and Efficient Coal Utilization, Taiyuan University of Technology, Taiyuan, China

Li Feng Co-Innovation Center of Efficient Processing and Utilization of Forest Resources, International Innovation Center for Forest Chemicals and Materials, College of Materials Science and Engineering, Nanjing Forestry University, Nanjing, China

Jella Gangadhar Mechanical Engineering Department, Birla Institute of Technology and Science, Pilani-Hyderabad Campus, Telangana, India

Drashya Gautam Acharya Narendra Dev College, University of Delhi, New Delhi, India

Mohammad Reza Ghaani School of Chemical and Bioprocess Engineering, University College Dublin, Belfield, Dublin, Ireland

Mpitloane J. Hato Nanotechnology Research Lab, Department of Chemistry, School of Physical and Mineral Sciences, University of Limpopo (Turfloop), Polokwane, South Africa

Shuijian He Co-Innovation Center of Efficient Processing and Utilization of Forest Resources, International Innovation Center for Forest Chemicals and Materials, College of Materials Science and Engineering, Nanjing Forestry University, Nanjing, China

Sunita Hooda Acharya Narendra Dev College, University of Delhi, New Delhi, India

Shaohua Jiang Co-Innovation Center of Efficient Processing and Utilization of Forest Resources, International Innovation Center for Forest Chemicals and Materials, College of Materials Science and Engineering, Nanjing Forestry University, Nanjing, China

G. T. M. Kadja Division of Inorganic and Physical Chemistry, Institut Teknologi Bandung, Bandung, Indonesia;
Research Center for Nanosciences and Nanotechnology, Institut Teknologi Bandung, Bandung, Indonesia;
Center for Catalysis and Reaction Engineering, Institut Teknologi Bandung, Bandung, Indonesia

Leila Keshavarz School of Chemical and Bioprocess Engineering, University College Dublin, Belfield, Dublin, Ireland

Y. K. Krisnandi Solid Inorganic Framework Laboratory, Department of Chemistry, Faculty of Mathematics and Natural Science, Universitas Indonesia, Depok, Indonesia;
Inorganic Chemistry Division, Department of Chemistry, Faculty of Mathematics and Natural Science, Universitas Indonesia, Depok, Indonesia

Sarita Kumar Acharya Narendra Dev College, University of Delhi, New Delhi, India

Hiran Mayookh Lal School of Civil Engineering, Harbin Institute of Technology, Harbin, China

L. Larasati Division of Inorganic Chemistry, Universitas Sebelas Maret, Kentingan, Jebres, Surakarta, Indonesia

W. W. Lestari Division of Inorganic Chemistry, Universitas Sebelas Maret, Kentingan, Jebres, Surakarta, Indonesia

Wen-Ying Li State Key Laboratory of Clean and Efficient Coal Utilization, Taiyuan University of Technology, Taiyuan, China

Mohit Mahajan Pharmacy Department, The M. S. University of Baroda, Vadodara, Gujarat, India

Emine Hilal Mert Faculty of Engineering, Department of Polymer Materials Engineering, Yalova University, Yalova, Turkey

Hatice Hande Mert Faculty of Engineering, Chemical Engineering Department, Yalova University, Yalova, Turkey

Kwena D. Modibane Nanotechnology Research Lab, Department of Chemistry, School of Physical and Mineral Sciences, University of Limpopo (Turfloop), Polokwane, South Africa

N. Nurdini Division of Inorganic and Physical Chemistry, Institut Teknologi Bandung, Bandung, Indonesia

A. Pangestu Division of Inorganic Chemistry, Universitas Sebelas Maret, Kentingan, Jebres, Surakarta, Indonesia

Fatma Nur Parin Polymer Materials Engineering Department, Faculty of Engineering and Natural Sciences, Bursa Technical University, Bursa, Turkey

Moorthi Pichumani Department of Nanoscience and Technology, Sri Ramakrishna Engineering College, Coimbatore, Tamil Nadu, India

Antony Rajendran State Key Laboratory of Clean and Efficient Coal Utilization, Taiyuan University of Technology, Taiyuan, China

Sadhana Rajput Pharmacy Department, The M. S. University of Baroda, Vadodara, Gujarat, India

Nur Ezyanie Safie Fakulti Kejuruteraan Pembuatan, Universiti Teknikal Malaysia Melaka, Melaka, Malaysia

O. A. Saputra Division of Inorganic Chemistry, Universitas Sebelas Maret, Kentingan, Jebres, Surakarta, Indonesia

I. R. Saragi Solid Inorganic Framework Laboratory, Department of Chemistry, Faculty of Mathematics and Natural Science, Universitas Indonesia, Depok, Indonesia;

Department of Chemistry, Faculty of Mathematics and Natural Science, Universitas Sumatera Utara, Medan, Indonesia

Omid Saremi School of Chemical and Bioprocess Engineering, University College Dublin, Belfield, Dublin, Ireland

Amir Servati Department of Electrical and Computer Engineering, University of British Columbia, Vancouver, BC, Canada;
Department of Materials Engineering, University of British Colombia, Vancouver, BC, Canada

Peyman Servati Department of Electrical and Computer Engineering, University of British Columbia, Vancouver, BC, Canada

Aarti Sharma Acharya Narendra Dev College, University of Delhi, New Delhi, India

Thabang R. Somo Nanotechnology Research Lab, Department of Chemistry, School of Physical and Mineral Sciences, University of Limpopo (Turfloop), Polokwane, South Africa

Ravindran Sujith Mechanical Engineering Department, Birla Institute of Technology and Science, Pilani-Hyderabad Campus, Telangana, India

Neha Suvindran School of Biomedical Engineering, University of British Columbia, Vancouver, BC, Canada

Pınar Terzioğlu Polymer Materials Engineering Department, Faculty of Engineering and Natural Sciences, Bursa Technical University, Bursa, Turkey

Sabu Thomas School of Energy Materials, Mahatma Gandhi University, Kottayam, Kerala, India

Tiju Thomas Department of Metallurgical and Materials Engineering, Indian Institute of Technology, Chennai, Tamil Nadu, India

Barath Tirumuruhan Mechanical Engineering Department, Birla Institute of Technology and Science, Pilani-Hyderabad Campus, Telangana, India

Arya Uthaman School of Civil Engineering, Harbin Institute of Technology, Harbin, China

Nasir Vadia Department of Pharmaceutical Sciences, Saurashtra University, Rajkot, Gujarat, India

S. Venkatachalapathy Department of Mechanical Engineering, National Institute of Technology, Tiruchirappalli, Tamil Nadu, India

S. Vijayan Department of Mechanical Engineering, National Institute of Technology, Tiruchirappalli, Tamil Nadu, India

Changshui Wang Co-Innovation Center of Efficient Processing and Utilization of Forest Resources, International Innovation Center for Forest Chemicals and Materials, College of Materials Science and Engineering, Nanjing Forestry University, Nanjing, China

Bing Yan Co-Innovation Center of Efficient Processing and Utilization of Forest Resources, International Innovation Center for Forest Chemicals and Materials, College of Materials Science and Engineering, Nanjing Forestry University, Nanjing, China

Y. Yasmine Solid Inorganic Framework Laboratory, Department of Chemistry, Faculty of Mathematics and Natural Science, Universitas Indonesia, Depok, Indonesia

Marcileia Zanatta Department of Materials Science (DCM), NOVA School of Science and Technology (FCT NOVA), i3N|Cenimat, NOVA University Lisbon, Caparica, Portugal

Qian Zhang College of Science, Nanjing Forestry University, Nanjing, China

Fundamentals of Porous Materials

Hiran Mayookh Lal, Arya Uthaman, and Sabu Thomas

Abstract The necessities of porous materials in society make huge developments from past centuries. The application of porous materials like adsorption, catalysis, nanotechnology, biomedical could tend the scientific world. This chapter briefly emphasizes the fundamentals of porous materials, properties, types, and classification of porous materials.

Keywords Porous materials · Mesoporous · Microporous · Nanoporous · Classification of porous materials · Applications of porous materials

1 Introduction

For many years, the astonishing properties of porous materials results make great attention by the scientists and chemists. The most promising characteristics of porous materials are molecules or atoms are able to interact all over the material. From past centuries, there are different types of porous materials are designed and synthesized. The main historical stages of porous materials investigation was in 1976 by Swedish mineralogist A. F. Cronstedt, with natural zeolites, the zeolite's synthesis subjected to hydrothermal conditions, and in 1992, the ordered mesoporous materials like MCM-41, MCM-48, etc. (Kresge et al. 1992; Monnier et al. 1993). Another great discovery was in 1990, the MOFs by assembling the inorganic and organic units (Eddaoudi et al. 2001; Kitagawa et al. 2004). Then the invention of porous organic frameworks (POFs) by light elements through covalent bonds (Wu et al. 2012; McKeown 2012).

The potential performances of porous materials in the applications depend on the volumes, shape, and size distribution of voids. Moreover, the uniformity of the shape, volume, and size distribution of voids in the porous materials needs to be considered for enhancement in applications (Davis 2002). In addition, the tremendous increase in usage of porous materials in application of porous materials especially

H. M. Lal (✉) · A. Uthaman (✉)
School of Civil Engineering, Harbin Institute of Technology, Harbin 150090, China

S. Thomas
School of Energy Materials, Mahatma Gandhi University, Kerala, Kottayam, India

1
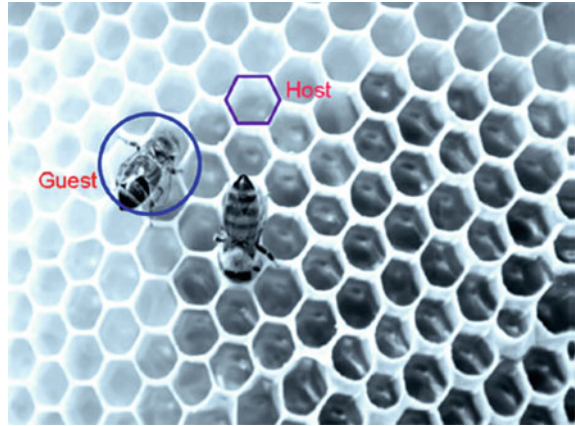
in heterogeneous catalysis, and chemical separation (Barton et al. 1999). Generally, the porous mediums occurred as solid skeleton with a free space that filled with liquid or gas (Bear and Bachmat 2012; Coutelieris and Delgado 2012; Qiu et al. 2016). Porous solids can be considered as two types; natural and artificial (Gibson and Ashby 1997). The naturally occurring porous structured materials can see in our day-to-day life, for instance; honeycomb, hollow bamboo, etc. (Chowdhury et al. 2019). The hexagonal cells in the honeycomb can assume as a building and the bees could stay inside and outside of this building. Here, the bee can consider as guest and the honeycomb as the host (Zhu and Ren 2015) is shown in Fig. 1. The artificial porous materials can be divided as porous metals, porous ceramics, and polymer foams (Liu and Chen 2014).

2   Pores

Pores are of two kinds, such as open pores and closed pores. This type of classification is through the approachability of materials surroundings. Open pores are connected in the outer layer or surface of materials and the pores which are in fluid form, those isolated from the outer layer are called closed pores. Open pores are commonly used in industrial applications. Closed pores can affect the mechanical properties of the solid materials and moreover, these are products of insufficient evolution of gaseous substances. The application of closed pores is usually in low specific gravity structural parts or in sonic and thermal insulators. Open pores are accessible and can be interconnected, dead end or passing but closed pores are inaccessible (Boucher 1976; Kaneko 1994; Ishizaki et al. 1998; Zdravkov et al. 2007). The schematic representation of open and closed pores is shown in Fig. 2.
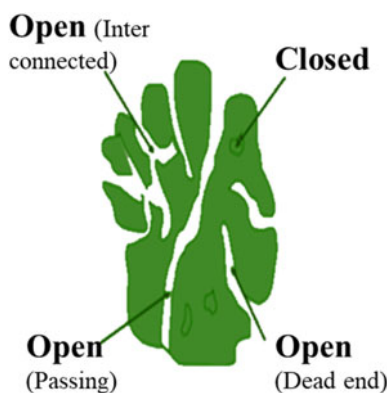
2.1 Porosity

The porosity is a vast area of concept, can be defined by many terms such as different pore morphologies, pores materials incorporated, pore size, and furthermore, considered on application (Betke and Lieb 2018). From Porosity, we can perceive nature of a material and produce advanced structures (Jiang et al. 2009). The major structural factors of a porous material or polymers are pore size, topology, pore surface functionality, and building framework structure (Chowdhury et al. 2019; Wu et al. 2012). The schematic demonstration of pore geometry, pore surface, pore size, and framework structure of porous materials or polymers are shown in Fig. 3. In the case of application purposes, the main benefits of the porous materials are its great surface
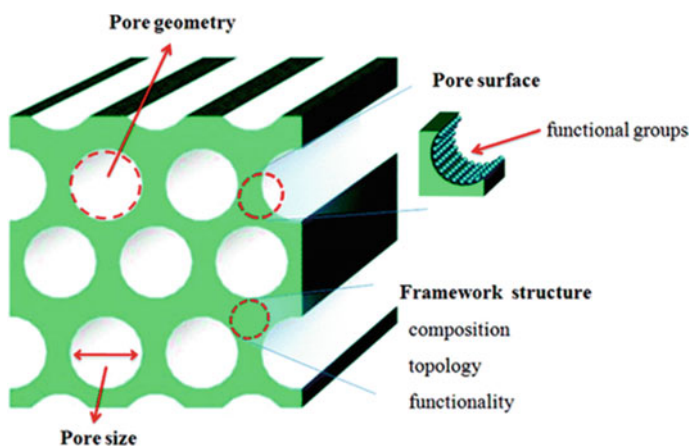
Fig. 3 Schematic demonstration of pore geometry, pore surface, pore size, and framework structure of porous polymers. Republished from Wu et al. (2012) with permission of American Chemical Society

area and well-defined porosity (Jiang et al. 2009; Ben et al. 2009). Furthermore, the easy processibility of porous materials, increases the usage in applications (Beiler et al. 2007; Olson et al. 2007).

3 Classification of Porous Materials

The porous materials are classified into different types, depending upon pores size (porosity), building framework, pore shapes, etc., and are shown in Fig. 4.

3.1 Based on Pores Size

The International Union of Pure and Applied Chemistry (IUPAC) has been proposed mainly three types of porous materials as micropores, macropores, and mesopores, The porosity of materials is less than 2 nm are defined as Micropores, the porosity in between 2 and 50 nm are called Mesopores and the porosity range is more than 50 nm is Macropores (Boucher 1976; Davis 2002; Rouquerol et al. 1994; Thommes et al. 2015). The classification based on pore size of porous materials is shown in Fig. 5.

Fig. 4 Classification of Porous materials
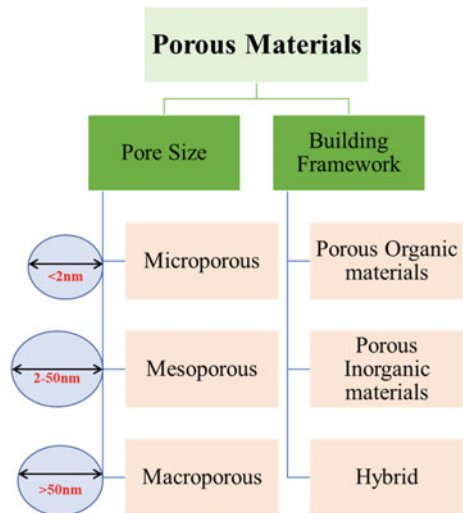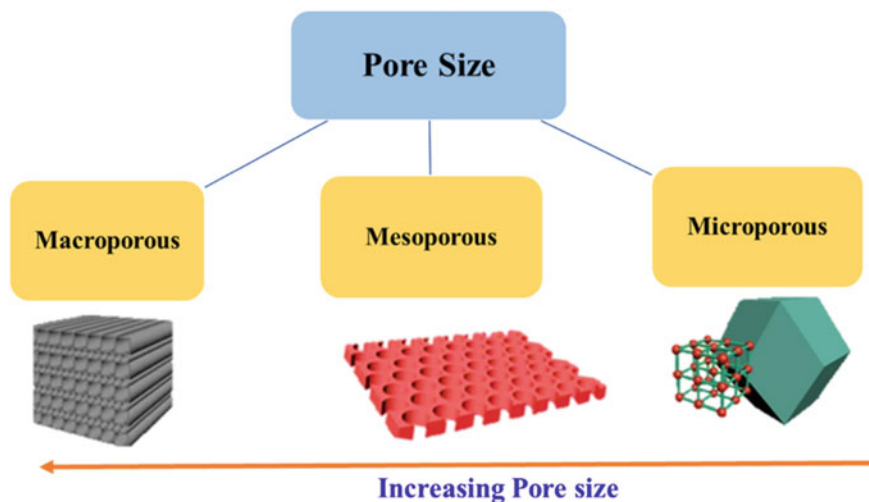
Fig. 5 Classifications based on pore size of porous materials

3.1.1 Microporous Materials

Microporous materials are materials that the pore size ranges less than 2 nm and having large surface area of about 300–2000 m^2/g (Schüth et al. 2002). The common microporous crystalline compounds are metal organic frameworks (MOFs), AlPO$_4$, and Zeolites (Thommes et al. 2015). The structure of microporous material is shown in Fig. 6. Zeolites are most generally considering and are aluminosilicates or molecular sieves. There are natural and synthetic zeolites however, usually synthetic zeolites are known. In 1950s, zeolite Y was first synthesized by Barrer (Alexander

Fig. 6 Structure of microporous material
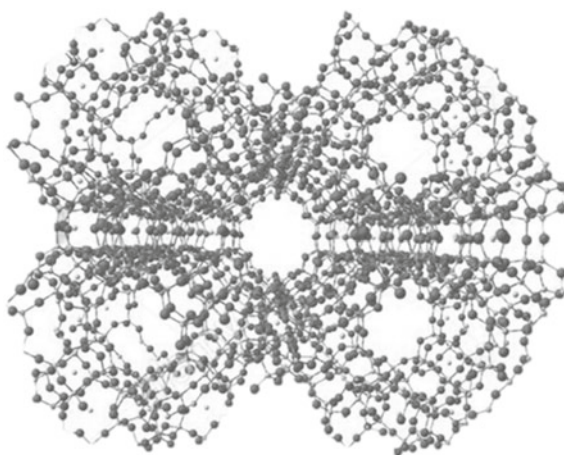
et al. 1944; Barrer 1985). More details of Zeolites are describing in Chap. 9 of this book.

3.1.2 Mesoporous Materials

Mesoporous materials are the materials pore size ranges between 2–50 nm and arranged as ordered array. The common examples of mesoporous materials are MgO, ZnO, SiO_2, TiO_2, etc. There are lots of benefits are found for mesoporous materials such as high surface area, tunable pore size, periodically arranged mesopore space, large open active sites. Hence, these materials are widely considering in catalysis, drug delivery, adsorption, etc. The invention of M41S family of ordered mesoporous materials having pore size 2–10 nm, by the template as quaternary alkyl ammonium surfactants (e.g., cetyltrimethylammonium bromide) is a great discovery in the history of porous materials world (Clark and Macquarrie 1997). The synthesis of mesoporous materials in different methods is depicted in Fig. 7. The synthesis, characterization, and applications of mesoporous materials are profoundly explained in Chaps. 5 to 8 of this book.

3.1.3 Macroporous Materials

Macroporous materials have pore size of more than 50 nm and these are the greatest porosity in the porous materials family (Kanamori and Nakanishi 2011). The most popularly fabricating method is the colloidal templating route. Figure 8 shows the comparison of various types of fabrication processes of macroporous particles (Wang et al. 2017). The readers can get a deep view of synthesis and characterization of macroporous materials from Chaps. 2 to 4 of this book (Fig. 8).

3.1.4 Hierarchical Porous Materials

The "hierarchy" is primarily featured as a certain ordering of solely materials relative to each other. Hierarchical materials consist of different pore size distribution of micro porous, mesoporous, and macroporous and hence, exhibit great surface by electrochemically, small diffusion distance and eminent mass transfer rate while considering as electrode materials in energy storage devices. The different pore levels intersect to provide the splitting of reagent or product flow as hierarchical (Eisenberg et al. 2016) is shown in Fig. 9.
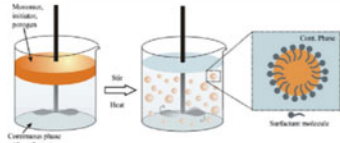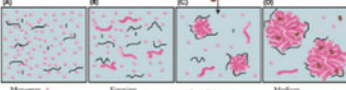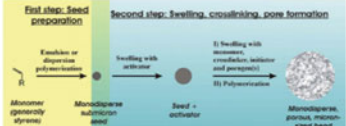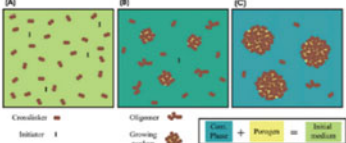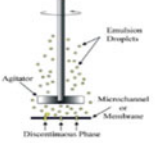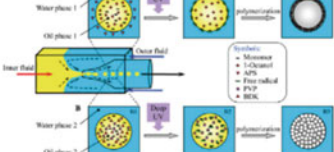
In a single system, the organization of materials hierarchically through the combination of entities, components, and geometrical structures having diverse properties (for instance densities and viscosities) form a path of compartments or matters. Furthermore, hierarchical systems could be arranged in a discontinuous/ continuous and homogenous/heterogeneous way and are much comprised of elements with
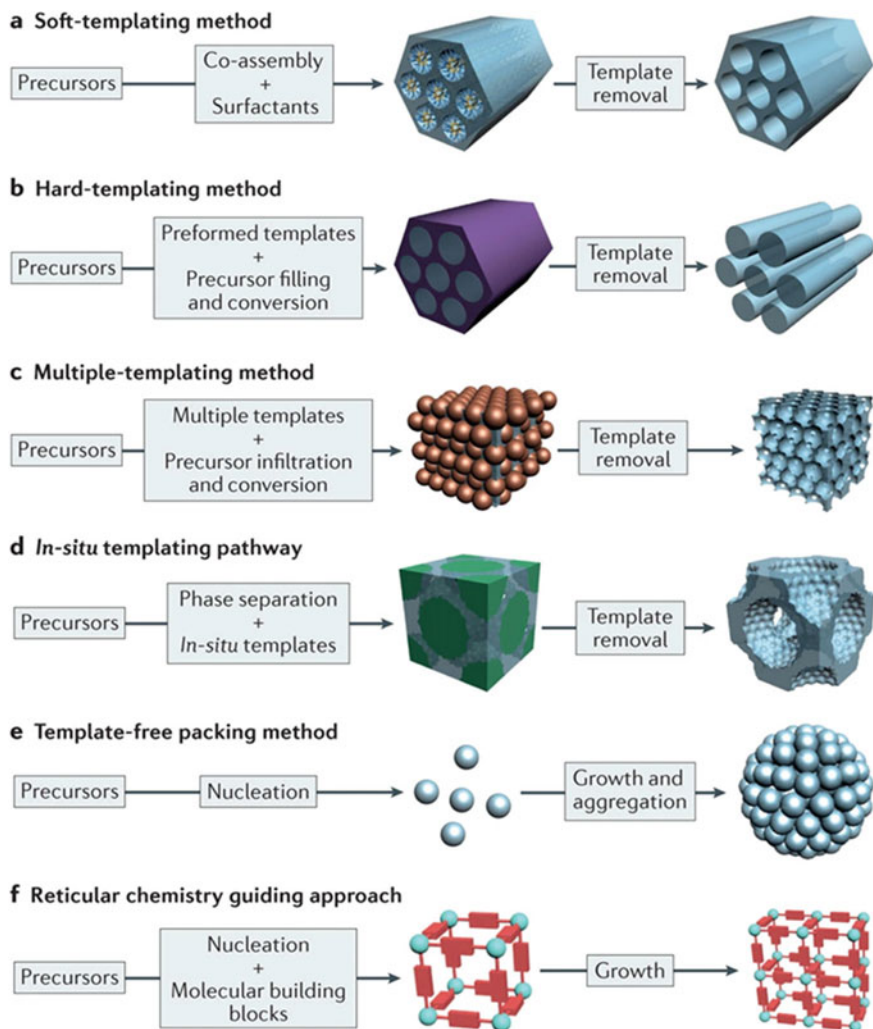
Fig. 7 Different types of synthesis methods of mesoporous materials. Republished from Li et al. (2016) with permission of Springer Nature

various sizes crossing many orders of magnitude. Hence, this is stated as 'hierarchical'; and these materials have to satisfy two fundamental standards such as the structural elements could be characterized by more than one scale length and each element have a different but complementary function (Jeffrey Brinker 1996; Lakes 1993; Schwieger et al. 2016). The fundamentals and applications of hierarchically porous materials are deeply explained in Chap. 12.

Method (discovery)	Diameter of beads (µm)	Minimum CV of beads	Fabrication easiness/cost	Schematic illustration	Ref.
Suspension polymerization (1920s)	5–2000	Very high	Easy/cheap		55, 58, 59, 97 and 109–112
Dispersion polymerization (1970s)	0.1–20	2–3%	Easy/cheap		55, 58, 59, 110, 111, 113 and 114
Seeded suspension polymerization (1980s)	0.5–200	2–3%	Cheap/time consuming		55, 58, 97 and 110
Precipitation polymerization (1990s)	0.1–8	2–3%	Easy/costly		55, 58, 110, 111, 115 and 116
Membrane/ microchannel emulsification (1990s)	10–1000	10% (membrane) or 2–3% (channel)	Difficult/ costly		58, 117 and 118
Microfluidics (2000s)	10–1000	<1%	Costly device		18, 69, 70, 76, 119 and 120

Fig. 8 Comparison of various fabrication processes of macroporous particles. Republished from Wang et al. (2017) with permission of Royal Society of Chemistry

3.2   Based on Building Framework

Porous materials are classified as porous organic, porous inorganic, and hybrid materials based on building framework.
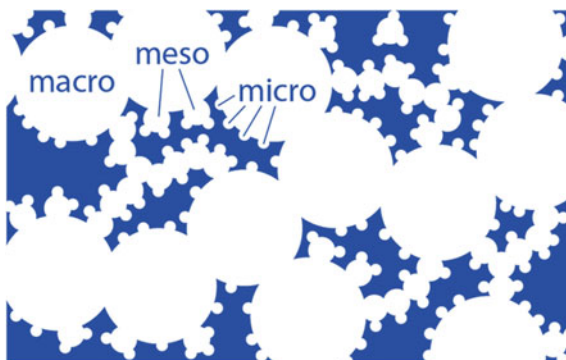
3.2.1 Porous Organic Materials

These are porous organic polymers (POPs). In case of organic porous materials, POPs are the highly considering research area equated with molecular counterparts. The synthesis of POPs contains different polycondensation processes from elimination of water to metal catalyzed C–C couplings with respect to various organic building blocks (Baldwin et al. 2016; Ben et al. 2009). Basically, POPs are formed as amorphous (porous aromatic frameworks (PAFs), hypercrosslinked polymers (HCPs), and conjugated microporous polymers (CMPs)) or crystalline (covalent organic frameworks (COFs)) (Bildirir et al. 2017). These are not soluble in common organic solvents, however, except in few polymers that contains intrinsic microporosity (PIMs), and also the fabricating process greatly influences the porosity (Weber and Thomas 2013; McKeown 2012).
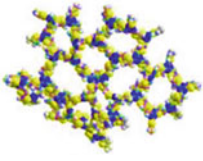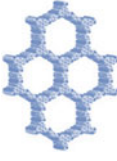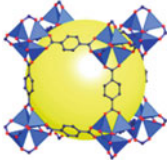
3.2.2 Porous Inorganic Materials

These are derivatives of porous carbon and porous metal oxides. The emerging use of porous inorganic materials in elevated temperature applications is because of the materials abundant, great stability, and have cheap building blocks such as zeolites (Bildirir et al. 2017; Cheetham et al. 1999).

3.2.3 Hybrid

In this type, the combination of organic porous and inorganic porous materials. These hybrid materials mostly consist of silica-based materials. Some alumino phosphates are also synthesized by using surfactant templating route. These hybrid materials could be developed by using sol gel process, self-assembly, dispersion of nano building blocks, hierarchical structure, and or interpenetrating networks (Chowdhury et al. 2019). For instance, Metal Organic Frameworks (MOFs) and (POPs). In

Table 1 The porosity, designability, crystallinity, stability of POPs, COFs, and MOFs (Slater and Cooper 2015)

Features	POPs	COFs	MOFs
Stability	Good to excellent peculiarly hydrothermal	Imines good and Boronates poor	Poor to good
Porosity	Mostly microporous; broader pore sizes	Micro/mesoporous; narrow PSDs	Micro/mesoporous; narrow PSDs
Crystallinity	Amorphous	Modest to high	Typically high
Designing	Good; controlled composition; porous structure challenging	Good; isoreticular approach possible	Excellent; isoreticular synthesis
Summary	Rapidly growing in number; various chemistry applications: use of cocatalyst	Much less developed than MOFs; efficient without use of cocatalyst	Highly developed; can be efficient with or without cocatalyst

the application of inorganic porous materials were endure insufficient functionalization even though, the basic synthesis structures are not complex (Yu and Xu 2010). Hence, the consideration of hybrid MOFs is enhanced in applications. In addition, these MOFs provide great surface area of about 7000 m^2/g and is easy to incorporate the functional groups into their backbone through organic materials (Lu et al. 2014). The porosity, designability, crystallinity, stability of POPs, COFs, and MOFs (Slater and Cooper 2015) are illustrated in Table 1.

3.3 Artificial Porous Materials

These are classified as porous metals, porous ceramics, and polymer foams (Liu and Chen 2014).

3.3.1 Porous Metals

Porous metals are popularly considering as engineering materials that can process structural and functional purposes (Nakajima et al. 2001; Zhu 1999). Porous metals have various features like high specific surface area, penetrability, low bulk density, low thermal conductivity, mechanical damping electromagnetic shielding, etc. There are different characteristics of porous metals are powder sintering type, fiber sintering

type, melt casting type, metal deposition type, directional solidification type, and composite type (Liu and Chen 2014). The detailed descriptions of porous metals are written in Chap. 15 of this book.

3.3.2 Porous Ceramics

In 1970s, porous ceramics or cellular ceramics starts developing. Porous ceramics consist of a heat resistant porous material having several gaseous pores. The porosity of porous ceramics mostly spans from 20 to 95%, pore size ranges as angstrom to millimeter levels and temperature difference as room temperature to 1600 ˚C (Scheffler and Colombo 2005; Wang et al. 1998). The porous ceramics are classified as two types such as honey comb ceramics and ceramic foam. The good chemical stability, strength, rigidity, and thermal stability are some of the major characteristics of porous ceramics. Porous ceramics and its applications are intensely described in Chaps. 16 and 17 of this book.

3.3.3 Polymer Foams

Polymer foams are porous plastics composed of bubble-like pores hence, polymer foams are also known as plastic foams. In addition, polymer foams contain several gaseous pores. The density of these materials is measured by the volume ratio of gaseous pores to solid polymer. In low density plastic foams, the ratio range is 9:1 and in case of high-density polymer foams, the ratio is around 1.5:1. Based on pore structure, the polymer foams are divided as open and closed cell polymer foams. Based on density, the polymer foams are of three types such as low foaming, moderate foaming, and high foaming. Based on rigidity, polymer foams are classified into three kinds such as rigid, semi rigid, and flexible. Moreover, the common characteristics of polymer foams are low relative density, great performance of heat insulation, impact energy absorption, sound insulation, specific strength, etc.

4 Applications of Porous Materials

The application of porous materials varies depending on the pore size, structure, building framework, etc. The common applications of porous materials are shown in Fig. 10. The most important applications of porous materials are in catalysis, biomedical, adsorption, sensors, supercapacitors, waste water treatment, photonics, electronics, gas separation, and storage, etc. Here we described briefly, the detailed discussions were found in the coming chapters.

In Lithium-ion batteries, the polymer monoliths can act as a significant role as an effective separator. Since the polymer monoliths are comprised of bicontinuous skeletal structures having macroporous sizes (submicrons to micrometers).
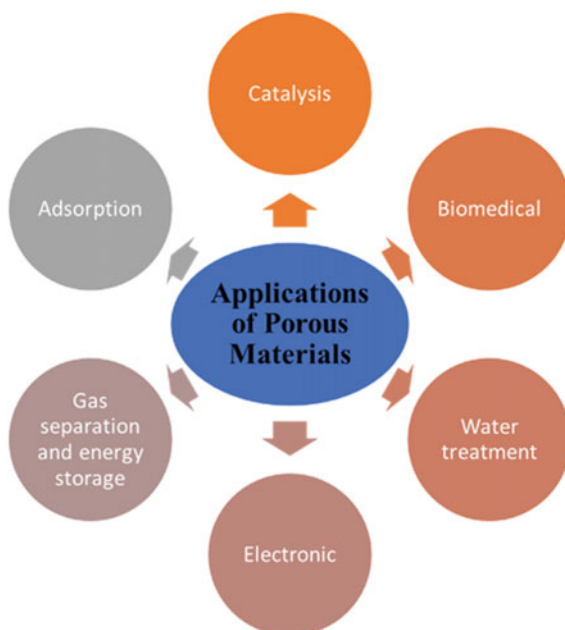
The epoxy-amine systems (Uthaman et al. 2021a) can produce unique bicontinuous monoliths (Sakakibara et al. 2017). This is due to the thermosetting nature of epoxy resin and its great processability. In addition, in the case of electronic applications, epoxy resins are broadly considered due to its good chemical resistance, moisture resistance, low cost, etc. (Lal et al. 2020; Uthaman et al. 2020) and the affinity of epoxy resin to electrolytes having great dielectric constants. In Lithium-ion batteries, the separators need to fulfill these properties. These epoxy reinforced separators can be used in lithium-ion batteries, fuel cells, etc. (Sakakibara et al. 2017).

Another important application of porous materials belongs to biomedical field. Porous ceramics like hydroxyapatite are considered in prostheses. The open pores are needed, in order to boost the ingrowth of tissue and fixation of prosthesis. This can create a great convoluted interface (Ishizaki et al. 1998). The porous materials are highly being used in controlled drug delivery applications. The silver nano particles have great antiviral properties (Lal et al. 2021b) so they are widely considered for biomedical applications (Lal et al. 2021a; Uthaman et al. 2021b, c). The pore size, porosity is significant for the controlled release of drug.

Furthermore, an important application of porous materials belongs to the adsorption, separation, and catalytic conversion of CO_2. The emission of CO_2 from industries causes global warming. For avoiding the emission of CO_2, need careful solutions in the utilization techniques, storage, etc. The porous materials have great surface area and pore volume so this can be applied as solid adsorbents for CO_2 (Chowdhury et al. 2019). Zeolites are mainly considered for the adsorbent of CO_2. And also, carbon nanotubes, mesoporous silica, COFs, etc. can also be considered as adsorbents.

5 Conclusion

In this chapter, the fundamentals of porous materials and its classification, different types of porous materials, and their applications are briefly described. After evaluating all the prospects, we can summarize that there is a wide opportunities are open for future research on finding an environmentally friendly, facile, and green synthetic route to synthesize porous materials. The green synthesis routes avoid the route of utilizing harmful chemicals reagents, for the preparation of porous materials which would be potentially useful in commercial fields. In the following chapters of this book mainly discusses different types of porous materials from macro to nano scale lengths; synthesis, characterization, and applications. In addition, physical modeling of porous materials.

References

Alexander, A.E., Barrer, R.M., Hinshelwood, C.N., MacArthur, I., Preston, G.D., Robertson, J.M.: General and physical chemistry. Annu. Reports Prog. Chem. **41**, 5–86 (1944)

Baldwin, L.A., Crowe, J.W., Pyles, D.A., McGrier, P.L.: Metalation of a mesoporous three-dimensional covalent organic framework. J. Am. Chem. Soc. **138**, 15134–15137 (2016). https://doi.org/10.1021/jacs.6b10316

Barrer, R.M.: Synthesis of zeolites. Stud. Surf. Sci. Catal. **24**, 1–26 (1985). https://doi.org/10.1016/S0167-2991(08)65264-7

Barton, T.J., Bull, L.M., Klemperer, W.G., Loy, D.A., McEnaney, B., Misono, M., Monson, P.A., Pez, G., Schere, G.W., Vartuli, J.C., Yaghi, O.M.: Tailored porous materials. Chem. Mater. **11**, 2633–2656 (1999). https://doi.org/10.1021/cm9805929

Bear, J., Bachmat, Y.: Introduction to Modeling of Transport Phenomena in Porous Media. Springer Science+Business Media, vol. 4 (2012)

Beiler, B., Vincze, Á., Svec, F., Sáfrány, Á.: Poly(2-hydroxyethyl acrylate-co-ethyleneglycol dimethacrylate) monoliths synthesized by radiation polymerization in a mold. Polymer (guildf). **48**, 3033–3040 (2007)

Ben, T., Ren, H., Ma, S., Cao, D., Lan, J., Jing, X.: Targeted synthesis of a porous aromatic framework with high stability and exceptionally high surface area. Angew. Chemie. **121**, 9621–9624 (2009). https://doi.org/10.1002/ange.200904637

Betke, U., Lieb, A.: Micro-macroporous composite materials—preparation techniques and selected applications: a review. Adv. Eng. Mater. **20**, 1–28 (2018). https://doi.org/10.1002/adem.201800252

Bildirir, H., Gregoriou, V.G., Avgeropoulos, A., Scherf, U., Chochos, C.L.: Materials Horizons Porous organic polymers as emerging new materials for organic photovoltaic applications: current status and future challenges. Mater. Horizons. **4**, 546–556 (2017). https://doi.org/10.1039/C6MH00570E

Boucher, E.A.: Porous materials: structure, properties and capillary phenomena. J. Mater. Sci. **11**, 1734–1750 (1976). https://doi.org/10.1007/BF00737529

Cheetham, A.K., Férey, G., Loiseau, T.: Open-framework inorganic materials. Angew. Chemie. **111**, 3466–3492 (1999). https://doi.org/10.1002/(SICI)1521-3757(19991115)111:22<3466::AID-ANGE3466>3.0.CO;2-M

Chowdhury, A.H., Salam, N., Debnath, R.: Design and fabrication of porous nanostructures and their applications. In: Nanomaterials Synthesis, pp. 265–294. Elsevier Inc. (2019)

Clark, J.H., Macquarrie, D.J.: Heterogeneous catalysis in liquid phase transformations of importance in the industrial preparation of fine chemicals. ACS Org. Process Res. Dev. **1**, 149–162 (1997). https://doi.org/10.1021/op960008m

Coutelieris, F.A., Delgado, J.M.P.Q.: Transport processes in porous media. Adv. Struct. Mater. **20** (2012)

Davis, M.E.: Ordered porous materials for emerging applications. Nature **417**, 813–821 (2002)

Eddaoudi, M., Moler, D., Li, H.: Modular chemistry: secondary building units as a basis for the design of highly porous and robust metal-organic carboxylate frameworks. Acc Chem Res. **34**, 319–330 (2001)

Eisenberg, D., Prinsen, P., Geels, N.J., Stroek, W., Yan, N., Hua, B., Luo, J.-L., Rothenberg, G.: The evolution of hierarchical porosity in self-templated nitrogen-doped carbons and its effect on oxygen reduction electrocatalysis. RSC Adv. **6**, 80398–80407 (2016). https://doi.org/10.1039/C6RA16606G

Gibson, L.J., Ashby, M.F.: Cellular Solids: Structure and Properties. Cambridge University Press, Cambridge (1997)

Ishizaki, K., Komarneni, S., Nanko, M. (eds.): Porous Materials: Process technology and applications. Springer Science+Business Media, Dordrecht (1998)

Jeffrey Brinker, C.: Porous inorganic materials. Curr. Opin. Solid State Mater. Sci. **1**, 798–805 (1996). https://doi.org/10.1016/S1359-0286(96)80104-5

Jiang, J.X., Trewin, A., Su, F., Wood, C.D., Niu, H., Jones, J.T.A.: Microporous poly(tri(4-ethynylphenyl)amine) networks: synthesis, properties, and atomistic simulation. ACS Macromol. **42**, 2658–2666 (2009). https://doi.org/10.1021/ma802625d

Kanamori, K., Nakanishi, K.: Controlled pore formation in organotrialkoxysilane-derived hybrids: from aerogels to hierarchically porous monoliths. Chem. Soc. Rev. **40**, 754–770 (2011). https://doi.org/10.1039/C0CS00068J

Kaneko, K.: Determination of pore size and pore size distribution 1. Adsorbents and catalysts. Rev. J. Memb. Sci. **96**, 50–89 (1994)

Kitagawa, S., Kitaura, R., Noro, S.: Functional porous coordination polymers. Angew. Chemie - Int. Ed. **43**, 2334–2375 (2004)

Kresge, C., Leonowicz, M., Roth, W.: Ordered mesoporous molecular-sieve synthesized by a liquid-crystal template mechanism. Nature **359**, 710–712 (1992)

Lakes, R.: Materials with structural hierarchy. Nature **361**, 511–515 (1993). https://doi.org/10.1038/361511a0

Lal, H.M., Xian, G., Thomas, S., Zhang, L., Zhang, Z., Wang, H.: Experimental study on the flexural creep behaviors of pultruded unidirectional carbon/glass fiber-reinforced hybrid bars. Materials. **13**, 11–13 (2020). https://doi.org/10.3390/ma13040976

Lal, H.M., Thomas, S., Li, T., Maria, H.J.: Polymer Nanocomposites Based on Silver Nanoparticles: Synthesis, Characterization and Applications. Springer Nature Switzerland AG (2021a)

Lal, H.M., Uthaman, A., Thomas, S.: Silver Nanoparticle as an Effective Antiviral Agent, pp. 247–265 (2021b). https://doi.org/10.1007/978-3-030-44259-0_10

Li, W., Liu, J., Zhao, D.: Mesoporous materials for energy conversion and storage devices. Nat. Rev. Mater. (2016). https://doi.org/10.1038/natrevmats.2016.23

Liu, P.S., Chen, G.F. (ed.): General introduction to porous materials. In: Porous Materials: Processing and Applications. Elsevier (2014)

Lu, W., Wei, Z., Gu, Z.-Y., Liu, T.-F., Park, J., Park, J., Tian, J., Zhang, M., Zhang, Q., Gentle III, T., Bosch, M., Zhou, H.-C.: Tuning the structure and function of metal–organic frameworks via linker design. Chem. Soc. Rev. **43**, 5561–5593 (2014). https://doi.org/10.1039/C4CS00003J

McKeown, N.B.: Polymers of intrinsic microporosity. Int. Sch. Res. Netw. (2012). https://doi.org/10.5402/2012/513986

Monnier, A., Schüth, F., Huo, Q.: Coopperative formation of inoraganic-organic interfaces in the synthis of silicate mesostructures. Science **80**(261), 1299–1303 (1993)

Nakajima, H., Hyun, S.K., Ohashi, K., Ota, K., Murakami, K.: Fabrication of porous copper by unidirectional solidification under hydrogen and its properties. Coll Surf. **14**, 179–209 (2001)

Olson, D.A., Chen, L., Hillmyer, M.A.: Templating nanoporous polymers with ordered block copolymers. ACS Chem. Mater. **20**, 869–890 (2007). https://doi.org/10.1021/cm702239k

Qiu, G., Xiao, J., Zhu, J.: Research history, classification and applications of metal porous material. Metal. Int. **18**, 1–11 (2016)

Rouquerol, J., Avnir, D., Fairbridge, C.W., Everett, D.H., Haynes, J.M., Pernicone, N., Ramsay, J.D.F., Sing, K.S.W., Unger, K.K.: No Title. Pure Appl. Chem. **66**, 1739 (1994)

Sakakibara, K., Kagata, H., Ishizuka, N., Sato, T., Tsujii, Y.: Fabrication of surface skinless membranes of epoxy resin-based mesoporous monoliths toward advanced separators for lithium ion batteries. J. Mater. Chem. **5**, 6866–6873 (2017). https://doi.org/10.1039/C6TA09005B

Scheffler, M., Colombo, P.: Cellular ceramics. Wiley-VCH, Weinheim (2005)

Schüth, F., Sing, K., Weitkamp, J. (eds.): Handbook of Porous Solids. Wiley, Weinheim (2002)

Schwieger, W., Machoke, A.G., Weissenberger, T., Inayat, A., Selvam, T., Klumpp, M., Inayat, A.: Hierarchy concepts: Classification and preparation strategies for zeolite containing materials with hierarchical porosity. Chem. Soc. Rev. **45**, 3353–3376 (2016). https://doi.org/10.1039/c5cs00599j

Slater, A.G., Cooper, A.I.: Function-led design of new porous materials. Science **80**, 348, aaa8075 (2015). https://doi.org/10.1126/science.aaa8075

Thommes, M., Kaneko, K., Neimark, A.V., Olivier, J.P., Rodriguez Reinoso, F., Rouquerol, J., Sing, K.S.W.: Pure Appl. Chem. **87**, 1051 (2015)

Uthaman, A., Xian, G., Thomas, S., Wang, Y., Zheng, Q., Liu, X.: Durability of an epoxy resin and its carbon fiber-reinforced polymer composite upon immersion in water, acidic, and alkaline solutions. Polymers **12** (2020). https://doi.org/10.3390/polym12030614

Uthaman, A., Lal, H.M., Li, C., Xian, G.: Mechanical and water uptake properties of epoxy nanocomposites with surfactant-modified functionalized multiwalled carbon nanotubes. Nanomaterials **11**, 1–15 (2021a). https://doi.org/10.3390/nano11051234

Uthaman, A., Lal, H.M., Thomas, S.: Silver Nanoparticle on Various Synthetic Polymer Matrices: Preparative Techniques, Characterizations, and Applications. Springer, Berlin (2021b)

Uthaman, A., Lal, H.M., Thomas, S.: Fundamentals of silver nanoparticles and their toxicological aspects. In: H.M. Lal et al. (ed.) Polymer Nanocomposites Based on Silver Nanoparticles, pp. 1–24. Springer Nature Switzerland AG (2021c)

Yu, J., Xu, R.: Rational approaches toward the design and synthesis of zeolitic inorganic open-framework materials. Am. Chem. Soc. **43**, 1195–1204 (2010). https://doi.org/10.1021/ar900293m

Wang, L.X., Ning, Q.J., Yao, Z.C.: Development of porous ceramics material. Bull Chin Ceram. Soc. **1**, 41–45 (1998)

Wang, B., Prinsen, P., Wang, H., Bai, Z., Wang, H., Luque, R., Xuan, J.: Macroporous materials: Microfluidic fabrication, functionalization and applications. Chem. Soc. Rev. **46**, 855–914 (2017). https://doi.org/10.1039/c5cs00065c

Weber, J., Thomas, A.: Nanoporous polymers. In: Xu, Q. (ed.) Nanoporous Materials Synthesis and Applications, pp. 1–34. CRC Press, Taylor & Francis (2013)

Wu, J., Xu, F., Li, S., Ma, P., Zhang, X., Liu, Q., Fu, R., Wu, D.: Porous polymers as multifunctional material platforms toward task-specific applications. Adv. Mater. **31**, 1–45 (2019). https://doi.org/10.1002/adma.201802922

Wu, D., Xu, F., Sun, B.: Design and preparation of porous polymers. ACS Chem. Rev. (2012)

Zdravkov, B.D., Čermák, J.J., Šefara, M., Janků, J.: Pore classification in the characterization of porous materials: a perspective. Cent. Eur. J. Chem. **5**, 385–395 (2007). https://doi.org/10.2478/s11532-007-0017-9

Zhu, G., Ren, H.: Introduction to porous materials. In: Porous Organic Frameworks, pp. 1–11. SpringerBriefs in Molecular Science, Berlin, Heidelberg (2015)

Zhu, Z.G.: Metallic foam materials. Physics (College. Park. Md). **28**, 84–88 (1999)

Synthesis of Macro Porous Ceramic Materials

M. A. Azmah Hanim

Abstract This chapter explored the synthesis method of macro porous ceramic by using the partial sintering, direct foaming, replica template and sacrificial template technique. The focus is to produce macro porosity in the ceramic for specific application purposes that required this porosity range. At first, fundamentals in each technique were discussed and the advancement in the topic for the recent five years was presented. This is followed by advantages and limitations existing with the current technology for each synthesizing technique. Finally, the chapter covers the possible future trends that can be explored in making the process of synthesizing macro porous ceramic to be more repeatable, stable and sustainable in the near future.

Keywords Macro porosity · Ceramic · Partial sintering · Direct foaming · Replica template · Sacrificial template

1 Introduction

Ceramic material is unique compared to other material categories due to its compression strength, resistance against wear by having high hardness value, great resistance against corrosion and oxidation, low thermal expansion hence great dimensional stability, post sintering and it can withstand very high temperature exposure for a long time (Chen et al. 2021). These characteristics outperform other material categories such as polymer, metal and its composites. Especially where the need for the material to operate in harsh conditions such as at the sea side, or exposure to working conditions at extreme temperatures such as furnaces. However, the properties of the ceramic is previously haunted by the pores property such as its distribution, its shape and size. Porosity is a big part of ceramic characteristics. It influences the level of brittleness and other mechanical properties of the ceramic material, especially its durability to perform without cracking.

M. A. Azmah Hanim (✉)
Department of Mechanical and Manufacturing Engineering, Faculty of Engineering,
Research Center Advance Engineering Materials and Composites (AEMC), Universiti Putra
Malaysia, Seri Kembangan, Malaysia
e-mail: azmah@upm.edu.my

However, with the advancement in technology, what is considered to be the ceramic weakness previously is now one of the major characteristics that contributes to the advancement of ceramic material application. As an example, porous scaffolds for bone regeneration in bioengineering application where the material must contain interconnected macro porosity with sizes of pores in a range of 100–1000 μm to induce angiogenesis and promotes bone growth (Karageorgio and Kaplan 2005). In such application, it has been established that bio ceramic is the best material candidate to promote tissue and bone growth (Natividad et al. 2021). Hence it is important to control porosity in ceramic in terms of its shape, distribution and size. Because of this and application in other fields as well, it opens up multiple new features of the ceramic that covers large specific surface area, low density, high toughness, large specific surface area, high resistance against thermal shock, low dielectric constant, good thermal insulator and other amazing features that were not available in its dense counterpart (Chen et al. 2021). Listed below are some of the examples for ceramic application with tailored porosity (Chen et al. 2021; Karageorgio and Kaplan 2005; Hedayat et al. 2017):

I.   Filtration components application to filter and collect particulate matter in hot gas exhaust from diesel engine and industrial processes.
II.   As catalyst support for pollutants degradation, environmental remediation, phenol mineralisation and hydrogen production.
III.   Filtration parts for purification of water to filter and remove contaminants, heavy metal and virus.
IV.   Components to store energy in batteries and concentrated solar power configurations.
V.   Porous scaffolds in bio engineering technology for bone tissue and cells regeneration implants
VI.   It has efficient electromagnetic interference (EMI) shielding effect which opens up application in automobile applications, modern aircraft and commercial wireless communication devices.
VII.   Provide heat insulation and sound absorption capability, ideal for construction material.
VIII. Ferroelectric ceramics can be incorporated with pores for the development of advanced micromechanical systems (MEMS), which can be exploited to power small scale electronic devices by taking energy from the surrounding environment so that it will not depend fully/ to eliminate batteries. Batteries have a finite lifetime and the maintenance cost is high.

Hence the opportunity listed above for application of ceramic with tailored porosity opens up endless possibilities for its use as advanced engineered material to further evolve and drive our technology forward. However, since the application relies heavily on the porosity characteristic in the ceramic, sustainability and repeatability is important for all methods of producing the components. It is imperative to understand each and every stage of the process. The subsequent topic will discuss the different types of porosity in porous ceramic material.

2 Structural Characters of Porous Ceramic Materials

Porous ceramic can be classified into three categories based on the size of pores, as stated by the International Union of Pure and Applied Chemistry (IUPAC) (Chen et al. 2021; Sing 1985):

i.   Macro porosity ($d > 50$ nm)
ii.   Meso porosity (2 nm $< d <$ 50 nm)
iii. Micro porosity ($d < 2$ nm)

A single monolithic matrix typically consists of combinations of pore size. However, it can be categorized as macro, meso or micro porosity based on the majority pore size in the matrix. Other than size, it can also be categorized based on the structure such as open cell or closed cell (Chen et al. 2021). Open-cell means that the pores are interconnected to each other hence allowing liquid or gas to pass through from one end of the ceramic to the other end. Closed cell means that the pores are individually isolated from each other. This is great for insulation purposes since the flow of fluid, heat and gas is restricted through the material. In order to determine the best material choice for each application, other than size of the pores, connectivity between the pores are also important (Chen et al. 2021). Shape of the pores can be categorized into spherical, elongated or random (Hedayat et al. 2017). All of these pore parameters will influence the characteristic of the ceramic material such as the mechanical strength, ability to absorb or isolate sound, corrosion resistance, thermal conductivity and others.

3 Synthesizing Method

The prized characteristic of porous ceramics comes from the personalized feature of the pores. To achieve the characteristic needed, it is desired to control the pores created in the ceramic matrix. Without taking into account the additive manufacturing (AM) process, there are four main conventional synthesis methods for porous ceramics (Chen et al. 2021):

i.   Partial sintering
ii.   Direct foaming
iii. Sacrificial template
iv.   Replica template

The latter three processes are then followed by the setting or the drying stage to set the mixture followed by pyrolysis or sintering stage to remove the template and for densification of the ceramic components. Figure 1 shows the relationship between porosity percentage and the pore size in ceramic in terms of its application, synthesis process and properties.
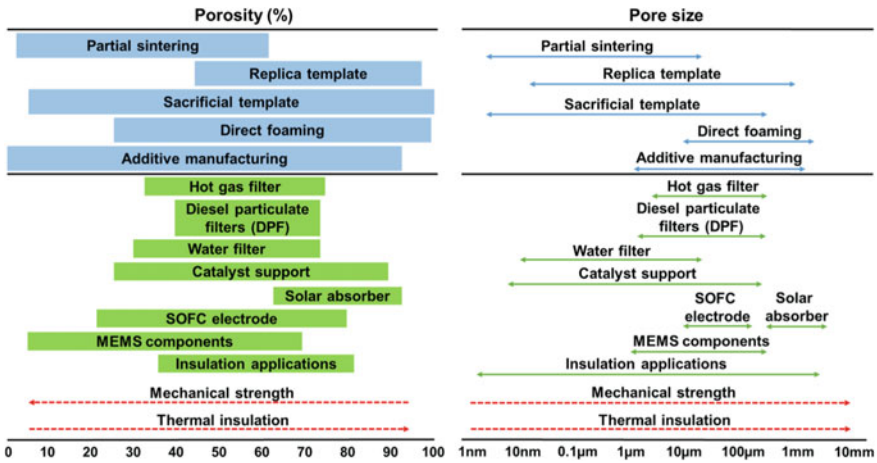
Fig. 1 Pore size distribution and porosity percentage can be created through partial sintering, direct foaming, sacrificial template and replica template and its effect on some of the ceramic properties. Reprinted from Chen et al. (2021), Copyright (2021), with permission from Elsevier

3.1 Partial Sintering

Partial sintering is a simple technique for porous ceramic synthesis. The temperature range is lower while the time of sintering is shorter compared to the usual process to produce dense ceramic (Jean et al. 2014). The microstructure (pore morphology and density) of the ceramic is highly dependent on the powder size of the starting material, the percentage of the components and its drying and sintering parameters (temperature, heating rates, atmosphere, pressure, others). Porosity decreases with increasing temperature, pressure and time (Jean et al. 2014). As an example, bigger pore size and higher porosity percentage are achievable when sintered at low temperature, however, it reduces many mechanical properties, such as fracture, fatigue behaviours and strength. Denser ceramics have improved version of the mechanical properties (Mouiya et al. 2019). During partial sintering, the powder particles are bonded by recrystallization, surface diffusion, solution reprecipitation or evaporation–condensation process. The full densification potential is retarded when the sintering temperature or time is reduced and this is the reason that the pores are bigger and more in partial sintered specimen (Chen et al. 2021). In a study by Mouiya et al. 2019, ceramics made of clay and banana peels were sintered at different temperatures of 900, 1000 and 1100 °C for 2 h. Samples with 900 °C showed larger pores and as the temperature increases, the density increase and the porosity size reduce. This can also be contributed by limited amount of vitreous phase available to fill in the pores at lower sintering temperatures. Samples sintered at 1100 °C showed existence of alkaline-rich phases such as K_2O and Na_2O and it is believed that these oxide phases have the fluxing effect to accelerate vitrification process in the ceramic. Other than that, when the metakaolin decomposes, it released amorphous silica that

also promotes the formation of vitreous phase. The function of the vitreous phase is to bind the particles and fill in the small pores and the effect is much more prominent as the temperature increase (Mouiya et al. 2019). Mechanical strength of ceramic is also limited by the contact points formed (solid necks formation) between the powder particles. We can summarize that the mechanical properties depend on the pore size, pore amount, pore shape and degree of neck formation or bond between powder particles.

However, for ceramic with low sinterability, the density of the ceramic were not highly influenced by the sintering temperature. Sintering additives were used instead to increase or slow down the grain growth which ultimately determines the density and porosity formed in the ceramic (Xu et al. 2003). The use of sintering additives have been documented for SiC and Si_3N_4 ceramics, but, its use in other partially sintering ceramic types is limited (Chen et al. 2021).

In a study by Lao et al. (2021), the research studied on effect of several sintering additives on the properties of β-SiAlON–SiC ceramics. β-SiAlON ($Si_{6-z}Al_zO_zN_{8-z}$, $z = 0–4.2$), is a solid solution from β-Si_3N_4, AlN and Al_2O_3. It has similar mechanical properties to Si_3N_4, however, the high temperature strength is superior, higher creep resistance and oxidation resistance. SiC is the secondary phase added to increase the mechanical strength of β-SiAlON in this study. But, the sintering temperature needed is higher due to the strong covalent bonding of β-SiAlON and SiC, the materials have low self-diffusion coefficients. In order to improve the sinterability of β-SiAlON–SiC composites at lower temperatures, liquid-phase sintering with different sintering additives were added. The function of the sintering additives is to increase liquid content in the mix by forming liquid together with other components and thus assist densification. But, if the amount added is equal, or more than 10 wt%, excessive glassy phase could form and this will soften the ceramic when exposed to high temperature. It would be a negative effect on the strength of the ceramic at high temperature applications.

Few methods have also been explored for partial sintering process, such as spark plasma sintering (SPS), partial hot-press technique and it can also be combined with other processes to improve porosity formation such as in-situ chemical reaction and sacrificial template or pore former (Chen et al. 2021). Partial hot-press method is a conventional process that is convenient and utilizes simple tools. However, when the sintering process was terminated before the ceramic mix is fully densify, the bond formed between the particles were also incomplete and this reduces the strength, hardness and durability of the final ceramic formed. To solve this issue, compaction pressure was applied to the green body prior to sintering which reduces agglomeration and increases interfacial bonding strength. Hence the name, hot-press technique. Other limitation to this method is the low heating rate, long time of process and non-uniform heating that resulted in its inability to really control the pore shape and size (Chen et al. 2021).

Another method is spark plasma sintering (SPS), which is also known as pulsed electric current sintering (PECS) which can accelerate the process with better control of the pore formation (Chen et al. 2021). In SPS, the current flows through the sample and die, ionizing the gas around the powder particles heating it to higher

temperature. Rapidly heated powders are then consolidated at constant pressure. The speed of the process helps to retain fine pores and gives better control for densification and pore formation. When the current is applied uniaxially, it could produce oriented controlled grains in one direction hence producing anisotropic mechanical and thermal properties for the composite material (Honda et al. 2016). The disadvantage of this method is that the method does not rely on a template, hence there is no porosity template morphology to copy as in the other pore synthesizing methods such as replica or sacrificial template (Ferraro et al. 2018). This reduces the repeatability aspect of the technique. Other than that, it also depends highly on the material's electrical property and the power supply capability which limits its application. "Hot spots", is also a concern with this method. The phenomena happen due to preferential current flow in the material that causes microstructural heterogeneity in the produced ceramic (Guo et al. 2021). Extensive studies on the relationship of parameters, e.g. current, plasma and particle size are also needed to manipulate the porosity formation in the final ceramic (Ferraro et al. 2018).

In order to improve the efficiency of the method, partial sintering method can be combined with other processes such as in-situ chemical reaction in order to produce ceramics with more than 50% porosity. The gas produced from the chemical reaction was trapped and used as pore-forming agent. Other methods that can be combined with partial sintering to escalate formation of pores is sacrificial pore former or also known as sacrificial template method (Chen et al. 2021; Jean et al. 2014).

3.2 Replica Template

This process is also called polymer foam replication technique (Marsh et al. 2021). As the name implies, the method works by impregnating sponge or foam made of polymer that has certain porosity structure with ceramic slurry (liquid mix that contains ceramic) (Marsh et al. 2021). It is suitable to produce interconnected open-cell with large surface area porous ceramic. Thermal treatments were used to remove the polymeric sponge or foam. The temperature used during thermal treatment must be high enough to decompose the polymeric substances. Final product is the porous ceramic that duplicates the shape and structures of the foam (Himoto et al. 2016). Examples of template materials that can be used is polyurethane, wood, cellulose and marine sponge to achieve more than 70% open-celled porosity. The template determines the porosity characteristic while the ceramic slurry used influenced the mechanical properties of the final product (Chen et al. 2021; Vakifahmetoglu 2016). For artificial foam like polyurethane (PU), there is a certain code to the PU foam template, example: M-type means partially closed cell foam, while P-type structure is completely open-cell (Santhosh et al. 2021). Figure 2 shows the synthesis method of replica template.

The process of coating the foam were conducted by dipping it into the slurry and the excess slurry were squeezed out from the foam. This process is repeated few times in order to increase the solid loading and to fully penetrate inside the void area with the
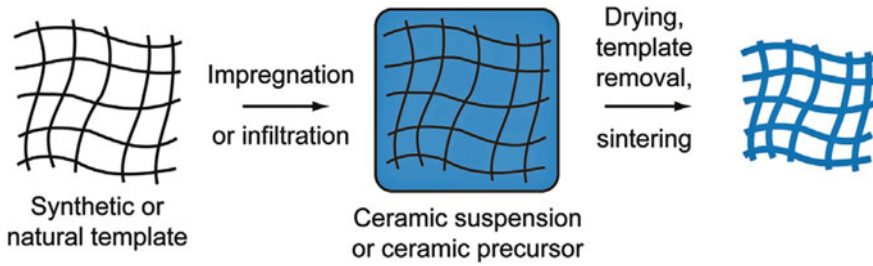
Fig. 2 Replica template synthesis method to make porous ceramic structure. Reprinted from Hammel et al. (2014), Copyright (2021), with permission from Elsevier

slurries. Viscosity of the slurry must be optimized to produced even coating, correct coating thickness and does not clog the pores. The foam is then left to dry prior to the sintering process, or it will go through the first heat treatment to remove the organic binders (Marsh et al. 2021; Liang et al. 2016; Bowenn and Thomas 2015). Since this method can be categorized under wet forming method which means that the ceramic is in slurry form (high binder and liquid content), thus the dry shrinkage percentage is higher for this method (Otitoju et al. 2020). Dry cracking due to high shrinkage, drying time and energy cost for drying are some of the concerns related to this part of the process (Otitoju et al. 2020). The next process stage is sintering, which will burn out the template, leaving just the ceramic material and for densification purposes. However, the gas generated from the decomposition process of the foam produces ceramic hollow struts with triangular shaped voids (Liang et al. 2016) as shown in Fig. 3 (Marsh et al. 2021) and the degassing stage can also create cracks at the struts for the gas to escape (Bowenn and Thomas 2015). Dwell and slower heating rate of the foam pyrolysis stage may produce gradual outgassing of the polymeric foam during degradation and consequently reduce cracking formation (Bowenn and Thomas 2015).

The pyrolysis temperature also determines the crystallinity of the ceramic (Santhosh et al. 2021). for example, for SiC ceramics formed through replica template, at lower pyrolysis temperature (<1000 °C) amorphous ceramic formed, but, with increase in the pyrolysis temperature (1000–1400 °C), it will eventually change into crystalline due to the arrangement of the C_{free} phase (Santhosh et al. 2021).

Another common issue with components synthesized from this method is low mechanical strength. This is because of the high porosity component that is usually produced from this technique. Several methods have been used to enhance the mechanical properties such as surface pre-treatment, extra coating and re-infiltration (Chen et al. 2021). However, some of the side effects from these processes involve reduction in porosity size and amount. Study by Bowen and Thomas (2015) evaluate the recoating process of Ti_2AlC Max-phase before and after sintering. Recoating before sintering gives better compression strength but, with more clogged pores while recoating after sintering improve the stability of the structure.
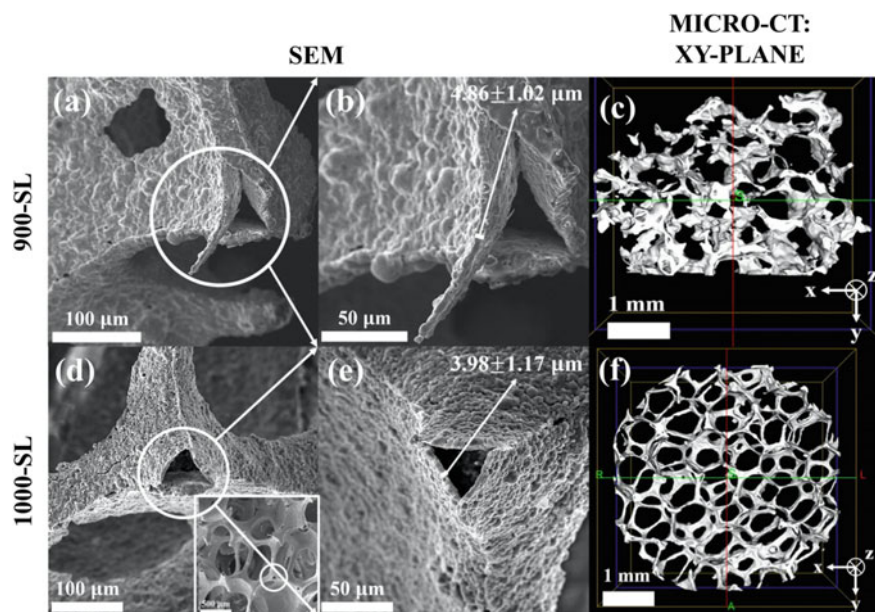
Fig. 3 Triangular shaped void in the struts from decomposition of foams in replica template. Reprinted from Marsh et al. (2021), Copyright (2021), with permission from Elsevier

In a study by Marsh et al. (2021), the authors used polyurethane foam (United States Plastic Corporation) with average pore diameter of $569 \pm 63.6 \, \mu m$ (45 pores per inch (PPI)) to produced Ag-doped sol-gel derived bioactive glass (BG)-ceramic [$58.6SiO_2$–$26.4CaO$–$7.2P_2O_5$–$4.2Al_2O_3$–$2.1Ag_2O$–$1.5Na_2O$ (wt%)]. The foam was cut into $12.5 \times 12.5 \times 12.5$ mm cubes and ultrasonically cleaned with ethanol. This is then followed by soaking in slurry (mix of water, poly(vinyl) alcohol (PVA) and Ag-BG particles ($< 38 \, \mu m$) at a ratio of 1.67:0.167:1 respectively) for 60 s. The excess slurry was removed from the foam by applying 50% manual compression along the principal axes of the foam cube. First step, heat treatment at 400 °C at 2 °C min^{-1} for 1 h was to remove organics. Followed by sintering using two maximum temperatures (T_{max}); either 900 °C or 1000 °C, with heating rate of 10 °C min^{-1} for 5 h. At this stage, Ag-BG particles coalesce and densify. After that, the ceramic is left to cool down to ambient temperature at a rate of 5 °C min^{-1}. For the pore features, the as-received polyurethane foam structure contains porosity of more than 98% and after sintering, the porosity of the ceramic produced using 900 and 1000 °C is approximately 90%. Open porous networks of the polymeric foam was successfully retained. Pore diameter 1000 °C, ~ 700 μm > foam, ~ 570 μm > 900 °C, ~ 490 μm. The aimed application for the produced ceramic would be to produced scaffolds for bone regeneration.

Another study on replica templates by Santhosh et al. (2021) used Polycarbosilane which is a pre-ceramic resin to produce SiC. Polyurethane (PU) foams type MTP-55

(M-type, $\rho b1 = 0.055 \pm 5\%$ g cm^{-3}, consist of partially closed cells) and PPI-60 (P-type, $\rho b = 0.025 \pm 8\%$ g cm^{-3}, completely open with larger cells) were used. In this processing method, the PU foams were impregnated with the precursor, solvent and catalyst solution mix. The foams were then dried overnight at room temperature. Pyrolysis was then conducted at 600 °C with ramp rate of 5 °C min^{-1} and were stagnant at that temperature for 30 min to ensure complete PU template removal. This is followed by heating to maximum temperature (1200, 1500 °C or 1800 °C) with heating rate of 5 °C min^{-1} and dwelled for 2 h at the peak temperature. The bulk density of the ceramic foam decreases at the pyrolysis temperature increase. This is because the struts become porous as the pyrolysis temperature increase due to the carbothermal reduction of silica that produces gas. Image as in Fig. 4. Microcracks start to form at pyrolysis temperature 1500 °C above and at 1800 °C, mesoporous structure starts to form on the struts surfaces producing rough patterns. Pore volume reduced at higher pyrolysis temperature due to partial closure of the pores previously formed. For the P-type foam, the pore diameter at 1800 °C was maintained at ~ 3.7 nm,
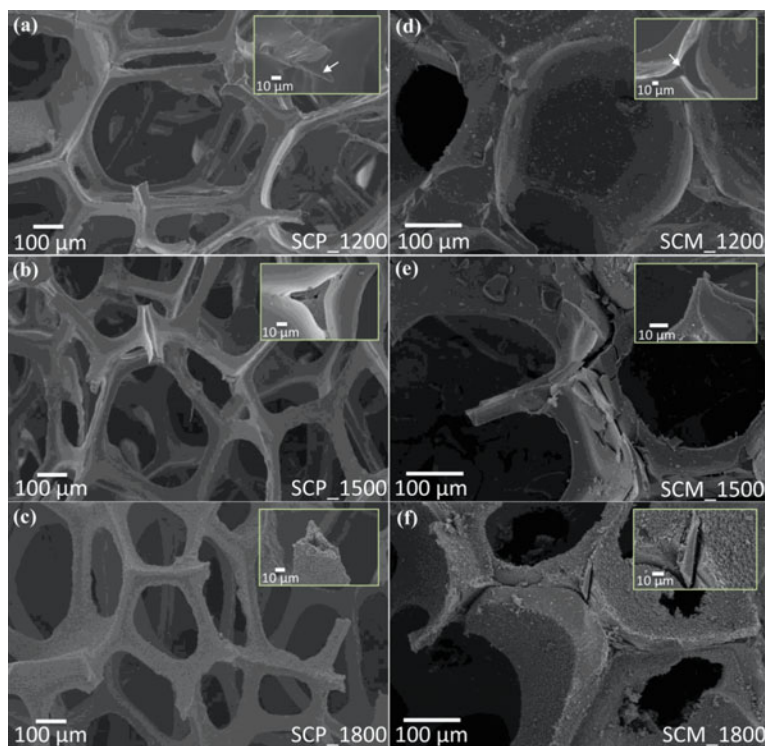
Fig. 4 SEM micrographs of the ceramic foams, pyrolyzed at 1200, 1500 and, 1800 °C, from **a–c** P-type (PPI) and **d–f** M-type (MTP) templates. Reprinted from Santhosh et al. (2021), Copyright (2021), with permission from Elsevier

while for the M-type at 1800 °C, the pore diameter reduced to ~ 2.9 nm. This is one way to produce SiC porous ceramics from foam method.

3.3 Sacrificial Template

Sacrificial template method controlled the porosity parameter like pore shape, pore size, structure of the pores and percentage of porosity by selecting the sacrificial template or fugitive materials as pore-forming agents that will be mixed with the ceramic material (Hedayat et al. 2017; Vakifahmetoglu et al. 2016). This method is different from replica template because this process copies the negative replica of the original pore feature. Once the template is removed, it usually produces thick and dense struts compared to replica template, hence higher mechanical strength when the two methods were compared (Vakifahmetoglu et al. 2016). It can be used to create both open and close-cell. In the first step, the sacrificial pore former was mixed together with the matrix materials which is the ceramic powders. After forming the component, the pore former was removed through evaporation, burn-off, thermal decomposition, etching or leaching. It is imperative that the pore former does not react with matrix material at elevated temperatures. The sacrificial template was categorized into four categories; natural sources like silk, synthetic organics like polyethylene (PE) beads, inorganic matters like graphene sheets and frozen liquids like water. The first three categories comprise solid pore former material while the fourth method used liquid pore former material (Chen et al. 2021).

While according to another source by Hedayat et al. (2017), the sacrificial template method was divided into pore-forming agent template (pore former), polymerization template (gel-casting), phase-inversion template, colloidal crystal template and ice template or also known as freeze casting. Under the branch of pore-forming template, it is divided into oxide and pyrolizable pore formers. The pyrolizable pore formers can then be categorized into organic and inorganic pore formers.

Figure 5 show the sacrificial method for solid pore former. The type, fraction and dimensional features of the pore former determine the size, shape, structures and
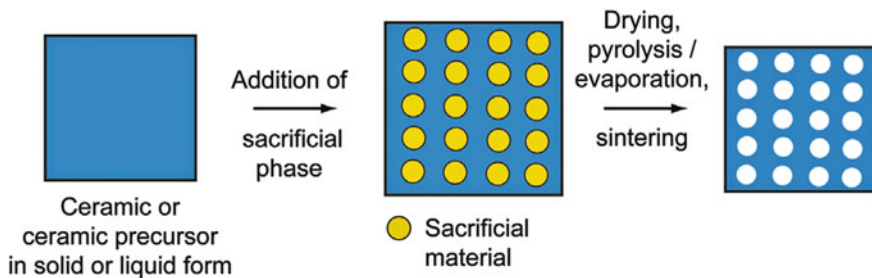
Fig. 5 Sacrificial method using solid pore former. Reprinted from Hammel et al. (2014), Copyright (2021), with permission from Elsevier

amount of porosity in the synthesized porous ceramic. Some of the recent trends focus on using food, agricultural and industrial waste as pore former (Salleh et al. 2021; Dele-Afolabi et al. 2017). The pore former candidates from this category is lucrative to be used in the process of producing porous ceramics because its use in this industry reduces the possibility of it ending in the landfill and thus polluting water, air and land. This will assist in stabilizing the current economic growth pattern to be more sustainable.

In a study by Di et al. (2021), they synthesized coral-like porous Si–C from diatomite that acts as a self-template and precursor. At first, diatomite powder, magnesium and NaCl powders were mixed together with agate mortar for 20 min. The mix were then placed in the quartz tube furnace, in argon gas environment and were exposed to 700 °C, ramp rate of 5 °C min^{-1} and held for 4 h at the peak temperature. The sample were then cooled down to room temperature and then rinsed with deionized water (DI) to clean the sample from NaCl. Next step, is to remove MgO byproduct by soaking in 6 wt% HCl for 10 h. Proceed to wash with DI water and dried under vacuum at 80 °C. The powdered sample were placed in the ceramic boat and then dried in a horizontal furnace with argon gas flow rate of 80 sccm. The furnace temperature were increased to 800 °C, ramp rate 25 °C min^{-1}. Acetylene then flowed into the furnace with flow rate 20 sccm for 30 min. Once the furnace cooled down to room temperature, the powder sample were taken out and immersed in 5 wt% HF for 10 h to remove the residual SiO$_2$ at room temperature. Finally, porous Si/C materials with diatomite as the precursor and also template were produced. Figure 6 shows the synthesis route of the process. This is an example procedure for chemical etching to remove the pore former or also known as the template.

Liquid template uses freeze casting method. This method is used to solve the issue with mismatched thermal cracking during burning process of different material phases by using solid pore former. Freeze casting uses frozen liquid as pore former (Deville 2008; Yanhai et al. 2018). In freeze casting, physical interaction and no chemical reaction is the main reaction that forms the pores hence, the material
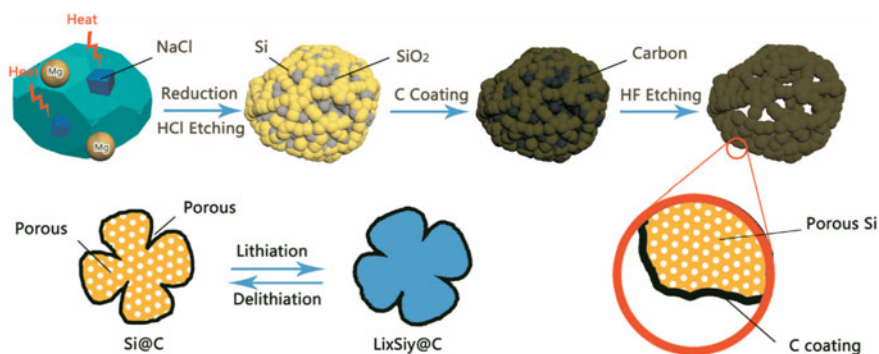
Fig. 6 Schematic diagram for the preparation of coral-like porous Si/C. Reprinted from Di et al. (2021), Copyright (2021), with permission from Elsevier

chemical component can be neglected. During solidification of a solution or suspension, walls are templated due to the particle's rejection or/and solute by a solidifying fluid. The volume fraction, size, shape, size and orientation of the porosity template can be changed by changing the suspension characteristics (parameters such as fluid type, particle fraction and additives) and also solidification parameters (mould design, freezing components material, solidification technique and freezing component temperature). However, since any changes in the parameters will influence the porosity templated, this adds certain complexity in understanding the effect each and every parameter have on the process (Yanhai et al. 2018; Scotti and Dunand 2018; Chang and Chen 2020).

The steps involved are; slurry preparation (aqueous or nonaqueous colloidal suspension mix that are stable), the mix were then poured into the mould, let the slurry solidify, sublimation of fugitive second phase and the final step is sintering to consolidate the porous ceramic structure (Otitoju et al. 2020; Deville 2008). The pores formed would be unidirectionally aligned pores at macro size (Deville 2008). In the solidification process, the particles in the slurry are rejected from the solidification front and accumulated between the frozen channel prior to removal of the generated ice crystals by vacuum sublimation, leaving highly permeable porous structure behind for sintering (Otitoju et al. 2020). The slurry contains ceramic powder, solvent and additives. In some cases, the green body may collapse during the sublimation stage since the binder is removed. Hence, suitable amount of binder additives will maintain the structural integrity during the sublimation process while waiting to go through sintering process (Deville 2008). The porosity characteristics of the component depend on the slurry content, the solidification parameters like cooling rate and additives or solvent used (Chen et al. 2021; Deville 2008; Yang et al. 2020; Huh and Kwark 2020).

Typical freeze casting synthesis method using low temperature and pressure during sublimation stage, followed by sintering above 1000 °C to consolidate the powders. This limits the available suitable material to be use and more time and energy is consumed in the process for all the stages to be completed. To overcome these limitations, sol-gel/freeze casting hybrid method can be used. The gel synthesized by sol-gel method replaced the ceramic slurry, followed by freeze casting process to form porous structure. This approach changed the precursor of synthetic sol-gel into colloidal solution, which then reacts to form inorganic gel. The advantage of this hybrid process is that it does not require sintering at high temperatures and does not require drying under low temperatures and pressure to sublime the binder. The ice will slowly melt using mould assisted melting at room temperature. Hence inorganic ceramic and organic polymer can be combined and synthesized in one stage process during slurry preparation and it helps to maintain structural integrity during sublimation for highly porous structures. All of these advantages help to widen the material selection options and opens up potential applications for porous structure ceramics (Chang and Chen 2020).

In a study by Yang et al. (2020), the freeze casting method was used together with liquid infiltration to produce a hybrid structure consisting of Al/Al$_2$O$_3$ with horn-mimetic tubular/lamellar hybrid structure. Freeze casting was used to produce the

connected macro porosity in tubular or lamellar form. Figure 7 show the schematic preparation of the metal ceramic composite and Fig. 8 show the microstructure of the porous Al_2O_3 structure prior to Al infiltration using different cyclohexane to water ratios.

Example of steps for dense metal/ceramic composite synthesized through emulsion-ice-templating (Yang et al. 2020): (a) Mix the water-based ceramic slurry using Al_2O_3 powders (5 μm, 99.5% purity); (b) Cyclohexane and Span 80 (20 mg/ml) are the solution and emulsifier for the oil phase (solidifying point ≈ 6.5 °C); (c) Mix the water-based ceramic slurry with the oil phase to form the emulsion-water Al_2O_3 slurry. Adjust the amount of each phase so that the emulsion-water Al_2O_3 slurries would be having constant solid loading of 10 vol.% and the volume ratio of cyclohexane: water; 0:100, 25:75, 50:50 and 75:25; (d) De-aired the mix and then using
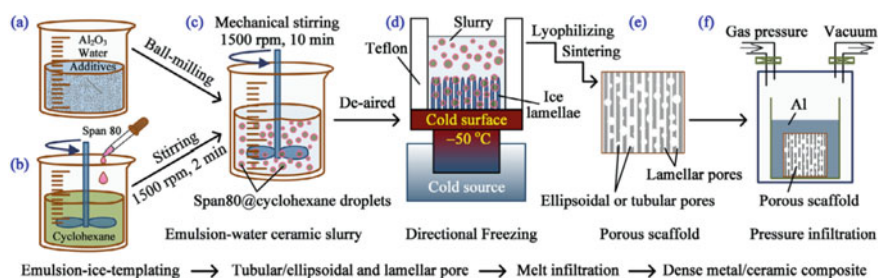
Fig. 7 Schematic of the biomimetic tubular/lamellar hybrid structures preparation process for metal/ceramic composites. Reprinted from Yang et al. (2020), Copyright (2021), with permission from Elsevier
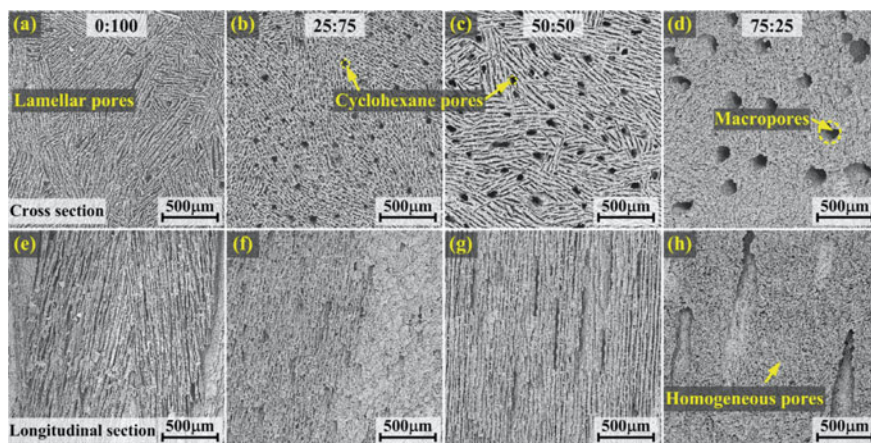
Fig. 8 Microstructures of the porous Al_2O_3 porous structure prepared with different cyclohexane to water ratios: **a, e** 0:100, **b, f** 25:75, **c, g** 50:50 and **d, h** 75:25. Reprinted from Yang et al. (2020), Copyright (2021), with permission from Elsevier

cold Cu surface, directionally freeze the mix at $-50\,°C$; (e) De-moulded the frozen samples and transferred it to a freeze dryer for sublimation process (removal of both ice and cyclohexane) at $-50\,°C$ for 48 h in a 10 Pa vacuum chamber. After that, sintering process was conducted at 1400 °C for 2 h; (f) Once the porous structure is ready, infiltrate the porosity with liquid Al (99.9% purity) using gas aided pressure infiltration (850 °C, 2 MPa) to produce dense metal/ceramic composites (Yang et al. 2020).

Figure 8 show the structural changes from lamellae to homogeneous porosity due to the slurry viscosity increase value when the cyclohexane concentration increase. Based on the principle of freeze casting, when the freezing front velocity of the slurry (v) is smaller than the threshold solidification velocity (v_c), the lamellar structure will appear. If that is not the case, then, a homogeneous structure will form instead (Naglieri et al. 2013). In this study (Yang et al. 2020), the freezing front velocity of the 75:25 slurry is presumably larger than the threshold solidification velocity, eventually resulting in the disappearance of the lamellar structure.

3.4 Direct Foaming

In direct foaming, gaseous phases were added/formed into a ceramic suspension by either injection of gas stream, foaming by mechanical agitation, chemical frothing, or gas releasing chemical reactions. This is followed by stabilization of the wet foam, drying and sintering process (Chen et al. 2021; Otitoju et al. 2020). Using this synthesized method, closed and open pore structures can be obtained from simple, low-cost and fast processing approaches (Chen et al. 2021). Figure 9 shows the direct foaming method.

The key item in this process is the consolidation and stabilization mechanism of the foam. The wet foams are thermodynamically unstable where gas bubble coarsening and drainage of the liquid phase can degrade the foam and burst it. Gravity is prone to pull the flow of the liquid phase downwards hence the drainage is inevitable. Reducing the liquid-phase content will result in the bubble's coalescence (Barg et al.
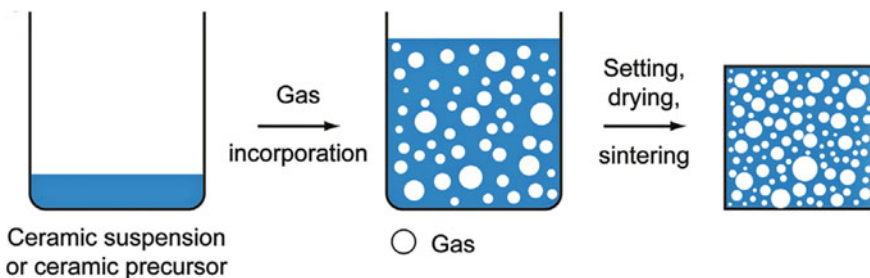
Fig. 9 Direct foaming method for synthesizing porous ceramic. Reprinted from (Hammel et al. 2014), Copyright (2021), with permission from Elsevier

2008). Gas diffusion will occur between bubbles of different sizes and consequently resulting in different gas concentrations due to the difference in Laplace pressure between them (Studart et al. 2006). These mechanisms of foam degradation are driven by the reduction of the Gibbs free energy of the system. Therefore, it is imperative to activate other stabilization methods to control the natural evolution of the foamed powder suspensions as well as to provide adjustment to the cellular ceramic microstructure (Barg et al. 2008).

Porosity of the resulting ceramic is proportionate to the air content in the suspension after foaming (Bhaskar et al. 2015):

$$\text{Air content} = \frac{\left(V_{\text{wet foam}} - V_{\text{suspension}}\right) \times 100}{V_{\text{wet foam}}}$$

$V_{\text{wet foam}}$ and $V_{\text{suspension}}$ are the suspension before and after the foaming process. For stability of the foam, it requires partially hydrophobic particles to be attached on the surface of bubbles with contact angle $\theta < 90°$ (readily occurs when θ is between 50 and 90°). Stability of the wet foam can be evaluated by volume change subjected to drying in a cylindrical mould (Bhaskar et al. 2015):

$$\text{Foam stability} = \frac{V_{\text{Final}}}{V_{\text{Initial}}} \times 100$$

V_{Final} is the volume of the foam after the drying procedure and V_{Initial} is the volume of the wet foam when it is filled into the mould. Foam stability can be measured by the free energy (ΔG) for the absorption of a particle at the interface (Bhaskar et al. 2015):

$$\Delta G = \pi r^2 \gamma_{\alpha\beta} (1 - \cos\theta)^2, \theta < 90°$$

In the above equation, r is the radius of the particle, γ is the surface tension of the suspension and θ is the contact angle. High adsorption free energy leads to irreversible adsorption of particles at the air-liquid interface resulting in outstanding stability of the bubbles. Other than that, there are also investigation on the Laplace pressure (ΔP) that indicates the pressure difference between the inside and outside of a gas bubble (Bhaskar et al. 2015):

$$\Delta P = \gamma \left(\frac{1}{R_1} + \frac{1}{R_2} \right) = \frac{2\gamma}{R}$$

In the above equation, γ is the surface tension of the suspension and R_1 and R_2 are the radii of two interfacing bubbles (Bhaskar et al. 2015).

One way to achieve ultra-stable wet foam is by adding long chain or short chain surfactants and biomacromolecules (proteins, carbohydrates and nucleic acid) in the fabrication process (Du et al. 2020). Generally, hydrophobicity of the ceramic particles could be improved by absorption of surfactants onto the ceramic particles.

Rheological properties of the slurries also impact the foamability of the mix (Du et al. 2020). In a study by Du et al. (2020), they fabricate highly porous silica foam using direct foaming with surfactants as stabilizing agents. The material mix is silica powder (2.0 μm mean particle size), α-Si$_3$N$_4$ powder as sintering additives (0.42 μm mean diameter), water-soluble copolymer of iso-butylene and maleic anhydride as dispersant and gelling agent, cationic surfactant cetyl trimethyl ammonium bromide and the anionic surfactant sodium N-lauroyl sarcosinate as the surface modifiers of the silica powders and the foaming agents.

The fabrication process starts with dispersing fused silica powders into DI water together with iso-butylene, silicon nitride powders and maleic anhydride (1 wt% based on the total weight of the powders) by ball milling at 300 rpm for 3 h in the milling pot (340 ml). The slurries prepared have specific volume of 65 ml. Then, the same amount of mixed surfactants solution was cast into the above slurries, followed by ball milling for 1 h to produce foam in the mix. The addition of the mixed surfactants was 0.3 wt% based on the total weight of the powders. The wet foams are then cast into plastic moulds and leave at ambient environment to dry for 48 h or more. This is followed by sintering at 1250 °C in air with heating rate 5 °C/min, dwell at peak temperature for 2 h (Du et al. 2020). Findings indicated that the solid content increase as the viscosity increases. Hence the volume expansion ratio decreases as the viscosity of the slurries increase due to difficulty of forming air-water interface. Figure 10 shows the SEM images of the silica foams synthesized by using slurries with different solid content. It can be seen from the figure that as the solid content decreases, bigger pores and more windows appear as in Fig. 10b-d. For lower solid content, the viscosity is lower hence weaker strength of the bubbles.
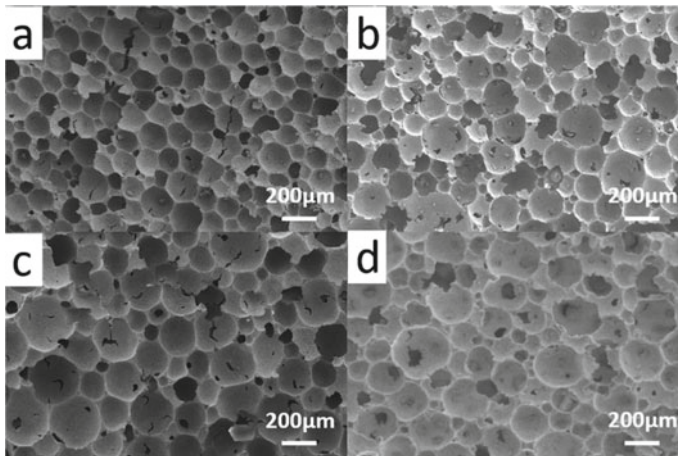
Fig. 10 SEM images of silica ceramic foams synthesized by using slurries with different solid content: **a** 33 vol%, **b** 31 vol%, **c** 29 vol%, **d** 27 vol%. Reprinted from Du et al. (2020), Copyright (2021), with permission from Elsevier

Therefore, the bubbles could easily coalesce and burst forming bigger pores and windows.

Another study by Stochero et al. (2020), fabricated open porous ceramic structure by producing ceramic shell foams through direct foaming and gel-casting of proteins with 35 vol.% solids. Ceramic shell powder (1.7 µm mean particle diameter) were mixed with DI water containing 1.5 vol.% (based on the ceramic powder content) of dispersant Dolapix® CE 64 by using the laboratory mixer for 20 min at 2000 rpm. After stirring for 10 min, the mix pH is adjusted with concentrated solutions (1 M) of sodium hydroxide, NaOH to values higher than 10 pH. This step is needed to control the stability, homogeneity of the mix and to eliminate sedimentation. 0.1 vol.% (based on the ceramic powder content) of nonionic surfactant Tergitol® TMN–10 (average molecular weight Mw = ~683 g/mol, HLB value ~14.1) were added to the suspensions with 35 vol.% of solids. Afterwards, the mix were aerated using a double shear mixer for 2 min at 500 rpm followed by addition of 5 wt.% (based on the ceramic powder content) of Ovalbumin (average molecular weight Mw = ~45,000 g/mol (62–88% of purity). This is the gelling agent to consolidate the foam and then, the mix were again stirred at 500 rpm for 3 min to achieve foaming.

The mixture were then poured into aluminium moulds (Ø ~ 60 mm, containing base and lid) and subjected to minimal vibration (manually), to eliminate defects. The foams were then heated to 80 °C (2 h 30 min) in an electric oven and dried for 24 h in atmospheric air. Sintering were conducted in two steps: first, the samples were pre-calcined at 650 °C (2 h, 1 °C/min heating rate), to remove the organic phase. Secondly, the samples were heated to 1550 °C (2 h, 2 °C/min heating rate) for complete consolidation of the structure. The produced sample contains interconnected pores as can be seen in Fig. 11. Using microtomography scanner, the data obtained were; total porosity 82.27 ± 2.75%, average pore diameter 956.26 ± 29,142 µm and average connection diameter of 240.38 ± 24.10 µm.
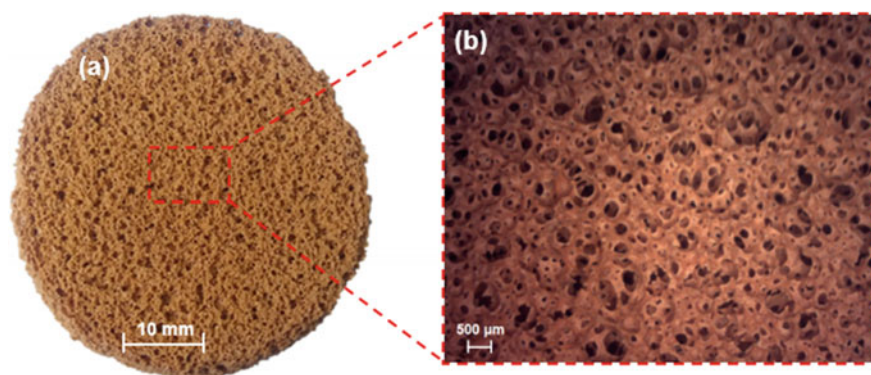
Fig. 11 **a** Photography and **b** Optical microscopy, of the pores microstructure of the fired ceramic shell foams. Reprinted from Stochero et al. (2020), Copyright (2021), with permission from Elsevier

3.5   Advantages and Limitations of Partial Sintering, Replica Template, Sacrificial Template and Direct Foaming

Looking at the available conventional process of synthesizing macro porous ceramic structure, each process have its own advantages and limitations. Table 1 show some of the common issues and advantages as mentioned from current literature.

4   Future Trends in Producing Porous Ceramics Components

Other than using the existing four synthesizing processes mentioned above on its own, some research also looked into combining the synthesizing process to tailor made pores. The reason behind this is to increase the percentage of porosity formed in the components and to increase the stability of the synthesizing process. The end in mind is for sustainability and repeatability of the produced porous ceramic components. Other than that, there is also special conditions in some of the processes where new terms emerge. This topic discussed the future trends emerging in the synthesizing methods of producing porous ceramic components.

As a start, biomorphic mineralization is a field of study where new materials were obtained using natural templates combined with synthetic compounds. The product, biomorphic combines natural geometry with synthetic material chemistry. The natural templates like biomolecules, plants, animal origin materials, or microorganisms can be ranging from nano- to micro- to mega-scale dimensions. There are two types of biomorphic mineralization processes; one that produces biomorphic material as a result of mineralization of precursor deposited on the template, or the template itself is the reagent and contributes to the final product (Sedmale et al. 2020). Depending on how the template is applied, it can be categorized into replica template or sacrificial template. Sedmale et al. (2020) prepared 40–45% water clay nanoparticles slurry from illite clay. The lichen as templates were washed in water and dried. Cylindrical and rectangular raw samples were formed by infiltration of slurry into templates during 24 h treatment followed by drying. Mineralization were done by sintering the samples at 800, 900 or 1000 °C in air and nitrogen environment for comparison. The highest porosity formed at 900 °C mineralization temperature with value of 65–70% porosity and pore size ranging from 1–2 nm up to 10 μm with visually visible ≥ 2 mm cells-voids.

In another study by Shavandi et al. (2016), waste kina shells were converted into hydroxyapatite with preserved porosity and interconnected porosity structure without addition of any other matrix. The process started with boiling and cleaning the kina shells from soft tissue and spine fragments. After drying overnight in the oven at 50°C, to obtain $CaCO_3$ and to remove the organic matter, the kina shells were divided into 30–30 g pieces and heated in the crucibles at 640 °C for 2 h. It was then left to cool down to room temperature inside the oven. Next is the conversion of the

Table 1 Advantages and limitations of partial sintering, replica template, sacrificial template and direct foaming

Synthesizing method	Advantage	Limitation	References
Partial sintering	Available equipment, facile and cost effective. Dry forming method (binder amount is low) means low possibility for drying shrinkage	Low porosity, limited sinterability for coarse powders, difficult to control the pores morphology and low mechanical properties	Chen et al. (2021), Hedayat et al. (2017) and Otitoju et al. (2020)
Replica template	Possible to copy exact features of the initial polymeric template; pore size and porosity. Hence enable to control pore distribution and pore morphology by simply changing the template foam used. Easy to produced high porosity open-cell units through this method	Shrinkage depends on the template used, e.g. marine sponge shrinkage around 50% shrinkage after sintering. High shrinkage percentage can be translated into higher chances for defects and cracking during sintering. During pyrolysis process of the template foam, the decomposition process produces gas that will flow out. Accumulated gas in the struts may burst out and induce cracking. Man-made template is preferred compared to naturally available foams due to natural template disadvantages such as low porosity, low mechanical strength, requires multiple steps of processing and production scale up issue. Issue with sustainable templates. More research is needed on naturally available foams like wood, marine sponge, etc. to see its effect on the produced porous ceramic structure. Impregnating foams with excessively narrow pores is difficult. Hence the minimum pore size is around 200 μm. Replica method results in high porosity amount with tailored pore size in the range of 200 μm–3 mm depending on the foam template. Porous ceramic can contain defects such as; (i) on the solid parts of the foam struts due to shrinkage of the slip during drying, (ii) internal defect due to pyrolysis of the polymer foam from the centre of struts. The defects will reduce the mechanical strength of the structure	Chen et al. (2021), Hedayat et al. (2017); Bowenn and Thomas (2015), Otitoju et al. (2020)

Table 1 (continued)

Synthesizing method	Advantage	Limitation	References
Sacrificial template	Well defined pore structure can be obtained by uniformly distributing the pore former and by controlling the ratio of the pore former used. The pores will take on the shape, size and amount of the pore former after burning process. When solid pore former were used, drying shrinkage is reduced compared to wet forming processes (ceramic in slurry form) Environment friendly templates available such as agrowaste, water and other organic materials. Capable to generate pores smaller than 10 μm	Quality of the porous ceramic produced depends highly on the pore former used Distribution process of the pore formed during mixing is important in producing homogeneous distribution of pores. Irregular pore distribution is an issue Mismatch in thermal expansion coefficient between the different materials can induce cracks formation during sintering process Impurities could easily generate in the ceramic structures after pyrolysis of the pore former	Chen et al. (2021), Hedayat et al. (2017), Otitoju et al. (2020), Deville (2008), Du et al. (2020)
Direct foaming	Simple, low-cost and fast process. Possible for mass production No additional template needed. No fugitive pore formers to be burned out	Stabilization of air bubbles in the suspension is an issue related to wet foam collapse or burst. One way to obtain ultra-stable wet foams is by modifying the mix with short chain or long chain surfactants and biomacromolecules. Narrow range of pore characteristics. Wet foam stabilized by surface modified particles has decreased the minimum pore size achievable through direct foaming to 10 μm. Direct foaming generates a high level of porosity with pore sizes ranging between 10 μm and 1.2 mm It is a costly and intricate process	Chen et al. (2021), Hedayat et al. (2017), Otitoju et al. (2020)

($CaCO_3$/CaO) into Hydroxyapatite using low-pressure and temperature method. 1 M solution of diammonium hydrogen phosphate $(NH_4)_2\ HPO_4$ ($\geq$ 98.0% purity, Sigma) was prepared and the pH was adjusted to 10 pH by adjusting the mix with ammonia hydroxide. The solution and the sample, at a size of 2 cm, were placed into a glass vessel equipped with a glass propeller. The vessel then goes through hydrothermal reaction using a silicon oil bath at 100 °C with continuous mechanical stirring. The pH maintained at 10 using a peristaltic pump supplying ammonia hydroxide solution throughout this stage of the process. The treatment was carried out for 8 h/day, up to 4 days. After exposure to heat each day for 8 h, the remaining hours, the samples were left to cool in the solution before it heats up again for the next day. Few samples were removed at days 1, 2 and 4 of treatment and rinsed with water to remove the residual phosphate until the rinse water tested neutral. This is followed by drying at 50 °C for 12 h. Figure 12 show the image of porous hydroxyapatite with the pore size distribution graph (Shavandi et al. 2016).

On another subject, for ceramic matrix composite, one of the methods used to improve its property is by formation of micro porosity, followed by liquid infiltration of another phase into the porosity to improve the composite property. In one example, a study by Flauder et al. (2021), the authors prepared C/C-SiC composite using three step process. Step one is carbon fiber-reinforced polymer (CFRP) with
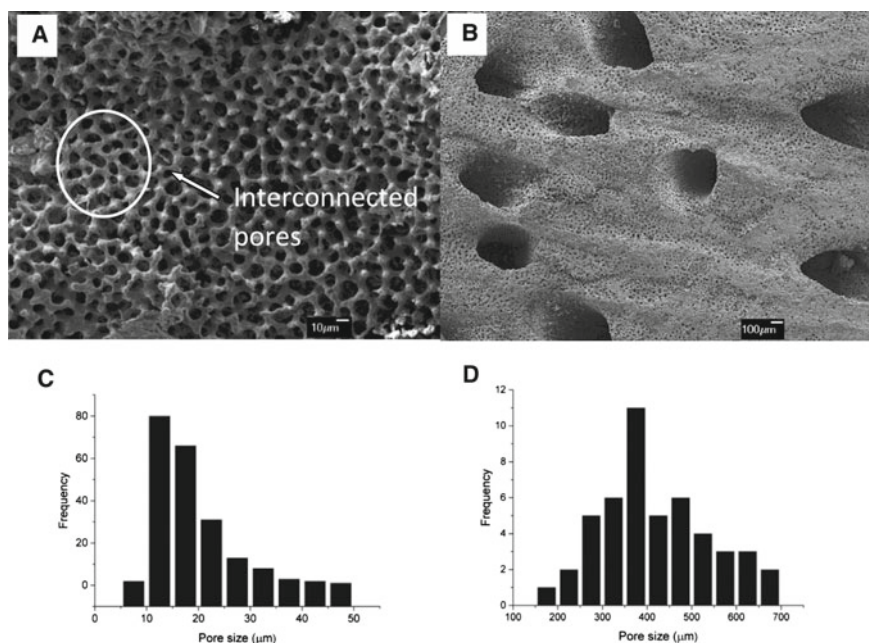
Fig. 12 SEM Micrographs (A, B) and histogram of pore size distribution (C, D) of small and large pores of kina shell derived hydroxyapatite after conversion process. Reprinted from Shavandi et al. (2016), Copyright (2021), with permission from Elsevier
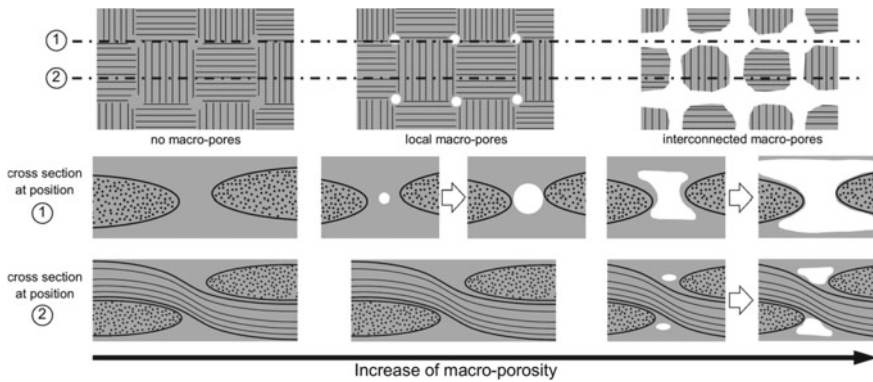
Fig. 13 Simplified conception for the shape and size development of macro-pores within a layer of a plain weave fabric. The macro-pores (white) appear in the fibre bundle gussets as local spherical pores and expand with an increased adjusted level of macro porosity. Reprinted from Flauder et al. (2021), Copyright (2021), with permission from Elsevier

thermoplastic polymer (matrix) of high carbon yield were fabricated and it goes through pyrolysis. Hence the CFRP convert into porous carbon reinforced carbon with pyrolysis temperature above 1000 °C, in this study, liquid pyrolysis initiated at 370 °C, holding time 30 min with load applied 0, 1, 2, 4, 8, 10 and 15 kPa perpendicular to the fibre axis orientation. After that, the porous C–C were infiltrated with molten silicon and produce C–C–SiC composite. It was mentioned that if the matrix used is thermoplastic, during pyrolysis, the term can be used is re-melting and liquid-phase pyrolysis, while if the matrix is thermoset, the matrix goes through solid phase pyrolysis. Pressure applied during the pyrolysis process also does influence the formation of the porosity. Figure 13 shows the schematic formation of the macro porosity.

The porosity started to form at the bulk of the matrix and eventually, it grows with time of liquid pyrolysis and pressure. Once interconnected porosity formed, liquid infiltration of Si were carried out and Si react with C forming SiC and filled in the pores (Flauder et al. 2021). The formation of SiC is to help increase the strength of the weakened structure due to the porosity formation. However, the SiC does not fill in all the porosity structures hence, there are certain percentages of porosity remained in the composite.

Another emerging process is additive manufacturing (AM) that has demonstrated great control and precision in its processes. It has also been explored in making tailored made porous ceramics components (Chen et al. 2021). However, most of the research using AM for porous ceramic are related to biomedical application due to the high precision needed in the component. AM is a manufacturing technology that allows synthesis of precise tailored porous ceramic structures with complex shapes using layer-by-layer process method based on a file of computer aided design (CAD), without using any other specific tooling (Galante et al. 2019; Lakhdar et al.

2021). This technology presents certain advantages over conventional manufacturing methods such as (Galante et al. 2019):

i.   Enable fabrication of customized near-net-shape pieces with intricate details and shape.
ii. Remove possibility for human error in the steps.
iii. Higher manufacturing sustainability since it reduces material waste and energy consumption.

Ceramic AM processes can be categorized into "single-step" or "multi-step" processes. For multi-step AM processes, the making of green body need subsequent drying and sintering thermal treatments to obtain final ceramic part. Most of the AM technologies and methods belong to this category (Lakhdar et al. 2021).

As an alternatively, another ceramic additive manufacturing route exists and is referred to as negative ceramic AM. In this method, AM is used just to shape the sacrificial polymer moulds which after that, will be impregnated with ceramic slurry by investment casting or gel-casting. The polymer after that will be removed by dissolution or thermal burn out. Since the method used AM just to shape the polymers moulds, it is both easier and cheaper to additively manufacture compared to directly AM the ceramics. Most polymer AM technologies can be used for this step. The indirect AM approach is readily scalable for high volume production and it enables relatively complex geometries, including functional grading and keeping the ability to customize each part independently. However, it has certain disadvantages such as no spatial control over material composition such as material grading and multi-material fabrication. The complexity of design is also reduced, especially when complex internal geometries are required. Finally, the negative AM method also requires multiple manufacturing steps that will increase lead times (Lakhdar et al. 2021; Baux et al. 2021).

Hence, the technology for ceramic additive manufacturing still requires much research and optimization due to the extremely high melting point of ceramics, low ductility, poor thermal shock resistance, high hardness, brittleness, scarce starting material, high cost, formation of cracks and defects during sintering and others (Lakhdar et al. 2021; Lee et al. 2017; Chang et al. 2020). Hence for application that does not require much precision, the conventional method of producing porous ceramic component is still the best option.

5   Conclusion

To conclude, each of the synthesizing processes have its own range of porosity and cell structure that can be produced. In order to synthesize the macro porous ceramic, any of the methods above can be applied. However, some method is more suitable to produce a certain structure, for example, if the structure is open-celled with high percentage of porosity for filters, replica template and sacrificial template would be more suitable to produce connected pores at high percentage. For closed-cell porous

structure, partial sintering, sacrificial template and direct foaming would be more suitable as the synthesizing method. Each of the processes also has its own advantage and limitations. Other than the individual process, combination of processes is also available to increase the efficiency of the synthesizing method. Modification to these techniques and exploration of other methods opens up future trends and possibilities in synthesizing porous ceramic components. Biomorphic mineralization, formation of other compounds to strengthen the porous ceramic structure and additive manufacturing are some of the future trends in this field. This opens up more research opportunities in optimizing the processes to suit the needs of each porous ceramic component produced in the quest towards sustainability.

References

Barg, S., Soltmann, C., Andrade, M., Koch, D., Grathwohl, G.: Cellular ceramics by direct foaming of emulsified ceramic powder suspensions. J. Am. Ceram. Soc. **91**(9), 2823–2829 (2008)

Baux, A., Jacques, S., Allemand, A., Vignoles, G.L., David, P., Piquero, T., Stempin, M.-P., Chollon, G.: Complex geometry macroporous SiC ceramics obtained by 3D-printing, polymer impregnation and pyrolysis (PIP) and chemical vapor deposition (CVD). J. Eur. Ceram. Soc. **41**(6), 3274–3284 (2021)

Bhaskar, S., Cho, G.H., Park, J.G., Kim, S.W., Kim, H.T., Kim, I.J.: Micro porous SiO_2–SiC ceramics from particle stabilized foams by direct foaming. J. Ceram. Soc. Jpn. **123**(5), 378–382 (2015)

Bowenn, C.R., Thomas, T.: Macro-porous Ti_2AlC MAX-phase ceramics by the foam replication method. Ceram. Int. **41**, 12178–12185 (2015)

Chang, H.-K., Chen, P.-Y.: Synthesis of silica-based scaffolds with high porosity and controllable microstructure by a sintering-free solegel/freeze-casting hybrid method under mild conditions. J. Market. Res. **9**(6), 16167–16178 (2020)

Chen, Y., Wang, N., Ola, O., Xia, Y., Zhu, Y.: Porous ceramics: light in weight but heavy in energy and environment technologies. Mater. Sci. Eng. R **143**, 1–65 (2021)

Dele-Afolabi, T.T., Azmah Hanim, M.A., Norkhairunnisa, M., Sobri, S., Calin, R.: Research trend in the development of macroporous ceramic components by pore forming additives from natural organic matters: a short review. Ceram. Int. **43**(2), 1633–1649 (2017)

Deville, S.: Freeze-casting of porous ceramics: a review of current achievements and issues. Adv. Eng. Mater. **10**(3), 155–169 (2008)

Di, F., Wang, N., Li, L., Geng, X., Yang, H., Zhou, W., Sun, C., An, B.: Coral-like porous composite material of silicon and carbon synthesized by using diatomite as self-template and precursor with a good performance as anode of lithium-ions battery. J. Alloy. Compd. **2021**(854), 157253 (2021). https://doi.org/10.1016/j.jallcom.2020.157253

Du, Y., Hedayat, N., Panthi, D., Ilkhani, H., Emley, B.J., Woodson, T.: Freeze-casting for the fabrication of solid oxide fuel cells: a review. Materialia **1**, 198–210 (2018)

Du, Z., Yao, D., Xia, Y., Zuo, K., Yin, J., Liang, H., Zeng, Y.-P.: Highly porous silica foams prepared via direct foaming with mixed surfactants and their sound absorption characteristics. Ceram. Int. **46**, 12942–12947 (2020)

Ferraro, C., Garcia-Tunon, E., Barg, S., Miranda, M., Bell, N.N.R., Saiz, E.: SiC porous structures obtained with innovative shaping technologies. J. Eur. Ceram. Soc. **38**(3), 823–835 (2018)

Flauder, S., Langhof, N., Krenkel, W.: Tailored macro-pores during the formation of C/C-SiC via liquid phase pyrolysis. J. Eur. Ceram. Soc. **41**(5), 2995–3001 (2021)

Galante, R., Figueiredo-Pina, C.G., Serro, A.P.: Additive manufacturing of ceramics for dental applications: a review. Dental Mater. **35**(6), 825–846 (2019)

Guo, R.-F., Mao, H.-R., Zhao, Z.-T., Shen, P.: Ultrafast high-temperature sintering of bulk oxides. Scripta Mater. **193**, 103–107 (2021)

Hammel, E.C., Ighodaro, O.R., Okoli, O.I.: Processing and properties of advanced porous ceramics: an application based review. Ceram. Int. **40**(10), 15351–15370 (2014)

Hedayat, N., Du, Y., Ilkhani, H.: Review on fabrication techniques for porous electrodes of solid oxide fuel cells by sacrificial template methods. Renew. Sustain. Energy Rev. **77**, 1221–1239 (2017)

Himoto, I., Yamashita, S., Kita, H.: Heat press molding of open-celled porous Si-SiC ceramics consisting of skeletal strut via gelcasting with flexible and thermosetting polyurethane resin. Adv. Powder Technol. **27**(3), 948–958 (2016)

Honda, S., Hashimoto, S., Iwata, S., Iwamoto, Y.: Anisotropic properties of highly textured porous alumina formed from platelets. Ceram. Int. **42**(1), 1453–1458 (2016)

Huh, T.-H., Kwark, Y.-J.: Fabrication of hierarchically micro/meso/macroporous silicon carbonitride T ceramic using freeze casting method with a silsesquiazane precursor. Ceram. Int. **46**, 11218–11224 (2020)

Jean, G., Sciamanna, V., Demuynck, M., Cambier, F., Gonon, M.: Macroporous ceramics: novel route using partial sintering of alumina-powder agglomerates obtained by spray-drying. Ceram. Int. **40**, 10197–10203 (2014)

Karageorgiou, V., Kaplan, D.: Porosity of 3D biomaterial scaffolds and osteogenesis. Biomaterials **26**(27), 5474–5491 (2005)

Lakhdar, Y., Tuck, C., Binner, J., Terry, A., Goodridge, R.: Additive manufacturing of advanced ceramic materials. Prog. Mater Sci. **116**, 100736 (2021). https://doi.org/10.1016/j.pmatsci.2020.100736

Lao, X., Xu, X., Jiang, W., Liang, J., Miao, L., Leng, G.: Effects of various sintering additives on the properties of β-SiAlON–SiC ceramics obtained by liquid phase sintering. Ceram. Int. **47**(9), 13078–13092 (2021)

Lee, J.-Y., An, J., Kai Chua, C.: Fundamentals and applications of 3D printing for novel materials. Appl. Mater. Today **7**, 120–133 (2017)

Liang, X., Li, Y., Liu, J., Sang, S., Chen, Y., Li, B., Aneziris, C.G.: Fabrication of SiC reticulated porous ceramics with multi-layered struts for porous media combustion. Ceram. Int. **42**(11), 13091–13097 (2016)

Marsh, A.C., Mellott, N.P., Crimp, M., Wren, A., Hammer, N., Chatzistavrou, X.: Ag-doped Bioactive Glass-Ceramic 3D Scaffolds: Microstructural, Antibacterial, and Biological Properties. J. Eur. Ceram. Soc. (2021). https://doi.org/10.1016/j.jeurceramsoc.2021.01.011

Mouiya, M., Bouazizi, A., Abourriche, A., El Khessaimi, Y., Benhammou, A., El hafiane, Y., Taha, Y., Oumam, M., Abouliatim, Y., Smith, A., Hannache, H.: Effect of sintering temperature on the microstructure and mechanical behavior of porous ceramics made from clay and banana peel powder. Results Mater. **4**, 100028 (2019). https://doi.org/10.1016/j.rinma.2019.100028

Naglieri, V., Bale, H.A., Gludovatz, B., Tomsia, A.P., Ritchie, R.O.: On the development of ice-templated silicon carbide scaffolds for nature-inspired structural materials. Acta Mater. **61**(18), 6948–6957 (2013)

Natividad Gómez-Cerezo, M., Peña, J., Ivanovski, S., Arcos, D., Vallet-Regí, M., Vaquette, C.: Multiscale porosity in mesoporous bioglass 3D-printed scaffolds for bone regeneration. Mater. Sci. Eng. C **120**, 111706 (2021). https://doi.org/10.1016/j.msec.2020.111706

Otitoju, T.A., Ugochukwu Okoye, P., Chen, G., Li, Y., Onyeka Okoye, M., Li, S.: Advanced ceramic components: materials, fabrication, and applications. J. Indus. Eng. Chem. **85**, 34–65 (2020)

Salleh, S.Z., Kechik, A.A., Yusoff, A.H., Ali Azhar Taib, M., Mohamad Nor, M., Mohamad, M., Guan Tan, T., Ali, A., Najmi Masri, M., Juliewatty Mohamed, J., Koriah Zakaria, S., Geng Boon, J., Budiman, F., Ter Teo, P.: Recycling food, agricultural, and industrial wastes as pore-forming agents for sustainable porous ceramic production: a review. J. Clean Prod **306**, 127264 (2021). https://doi.org/10.1016/j.jclepro.2021.127264

Santhosh, B., Ionescu, E., Andreolli, F., Biesuz, M., Reitz, A., Albert, B., Domenico Sorarù, G.: Effect of pyrolysis temperature on the microstructure and thermal conductivity of polymer-derived monolithic and porous SiC ceramics. J. Eur. Ceramic Soc. **41**, 1151–1162 (2021)

Scotti, K.L., Dunand, D.C.: Freeze casting—a review of processing, microstructure and properties via the open data repository. FreezeCasting.net. Progr. Mater. Sci. **94**, 243–305 (2018)

Sedmale, G., Rundans, M., Randers, M., Grase, L., Krumina, A.: Porous biomorphic ceramics for catalytic decomposition of phenol. Open Ceramics. **4**, 100024 (2020). https://doi.org/10.1016/j.oceram.2020.100024

Shavandi, A., Wilton, V., Bekhit, A.E.-D.A.: Synthesis of macro and micro porous hydroxyapatite (HA) structure from waste kina (Evechinus chloroticus) shells. J. Taiwan Inst. Chem. Eng. **65**, 437–443 (2016)

Sing, K.S.W.: Reporting physisorption data for gas/solid systems with special reference to the determination of surface area and porosity (Recommendations 1984). Pure Appl. Chem. **57**, 603–619 (1985)

Stochero, N.P., de Moraes, E.G., Moreira, A.C., Fernandes, C.P., Innocentini, M.D.M., Novaes de Oliveira, A.P.: Ceramic shell foams produced by direct foaming and gelcasting of proteins: Permeability and microstructural characterization by X-ray microtomography. J. Eur. Ceram. Soc. **40**, 4224–4231 (2020)

Studart, A.R., Gonzenbach, U.T., Tervoort, E., Gauckler, L.J.: Processing routes to macroporous ceramics: a review. J. Am. Ceram. Soc. **89**(6), 1771–1789 (2006)

Vakifahmetoglu, C., Zeydanli, D., Colombo, P.: Porous polymer derived ceramics. Mater. Sci. Eng. R **106**, 1–30 (2016)

Wang, K., Qiu, M., Jiao, C., Gu, J., Deqiao, X., Wang, C., Tang, X., Wei, Z., Shen, L.: Study on defect-free debinding green body of ceramic formed by DLP technology. Ceram. Int. **46**, 2438–2446 (2020)

Xu, G., Olorunyolemi, T., Carmel, Y., Lloyd, I.K., Wilson, O.C.: Design and construction of insulation configuration for ultra-high-temperature microwave processing of ceramics. J. Am. Ceram. Soc. **86**(12), 2082–2086 (2003)

Yang, L.-K., Jin, Q., Guo, R.-F., Shen, P.: Exploiting bio-inspired high energy-absorbent metal/ceramic composites through emulsion-ice-templating and melt infiltration. Materialia **14**, 100884 (2020). https://doi.org/10.1016/j.mtla.2020.100884

Emulsion Templated Hierarchical Macroporous Polymers

Hatice Hande Mert and Emine Hilal Mert

Abstract Emulsion templating is a versatile approach used for the preparation of hierarchical macroporous polymers with well-defined porosity. The basis of the approach is constituted on using concentrated emulsions as template for the creation of porous structures. With this approach, hierarchical polymer foams are usually produced by using high internal phase emulsions (HIPEs) as precursor templates. HIPEs, is defined as the emulsions having internal phase volume fraction (Ø) greater than 0.74. When a HIPE is prepared to contain monomer(s), polymerization of the monomer containing phase result in polymers known as polyHIPEs. PolyHIPEs are macroporous polymers exhibiting low density. The pore structure of polyHIPEs can be easily altered by variating the precursor HIPE templates. Thereby, polyHIPEs are good candidates to be used in the applications such as adsorption, chromatography, catalysis, tissue engineering, and storage of gases, liquids, and energy, where high permeability and shape stabilization is required. In this respect, numerous polyHIPEs exhibiting different chemistries and properties developed by scientists are in serve of the above-mentioned fields. To expand the use of polyHIPEs in industrial applications, it is necessary to adopt the emulsification process and properties of HIPEs, polymerization strategies and properties of polyHIPEs, and approaches and methods for their development. Regarding this, a retrospective analysis of HIPEs and polyHIPEs can be the key to developing novel materials for future applications.

H. H. Mert
Faculty of Engineering, Chemical Engineering Department, Yalova University, 77200 Yalova, Turkey

E. H. Mert (✉)
Faculty of Engineering, Department of Polymer Materials Engineering, Yalova University, 77200 Yalova, Turkey
e-mail: hmert@yalova.edu.tr

1   Introduction

Emulsions are dispersed systems which consist of two immiscible liquid phases. Emulsions are formed by dispersing the droplets of the first phase (known as disperse phase or droplet phase) in the second liquid phase (known as continuous phase). Therefore, emulsions are usually classified according to the state of the phases: if an aqueous phase is dispersed in an oil phase the formed emulsion is water-in-oil (w/o) type emulsion, and if an oil phase is dispersed in a continuous phase then it is an oil-in-water (o/w) type emulsion. They can also be classified based on their type (simple or multiple emulsions) and droplet size (macro-, micro-, and nanoemulsions). Macroemulsions and nanoemulsions are kinetically stable systems. Macroemulsions are known as opaque or milky emulsions due to the size of droplets. The average droplet size in macroemulsions usually changes in the range of 0.1–5 μm, while it is usually between 1–2 μm. As the average droplet size in nanoemulsions is ranging between 20 and 100 nm, they can be transparent, translucent, or opaque. Microemulsions, on the other hand, are often described as micellar systems. Because they are thermodynamically stable systems composed of droplets having average size changing between 5 and 50 nm (Tadros 2016).

Emulsions have been widely using in various industries; the most used fields include paint, cosmetics, food, and pharmaceuticals. On the other hand, high concentrated emulsions, which are known to be gel emulsions or foams, are also serving as templates for the preparation of macroporous polymer monoliths.

High concentrated emulsions or high internal phase emulsions (HIPEs) are characterized by their ratio of internal (or droplet) phases. In a HIPE the volume fraction (Ø) of the internal phase is greater than 0.74 and can be increased up to 0.99. According to Ostwald (1910) this figure is denoting the internal phase volume fraction at which mono-dispersed non-deformable rigid spheres are in the closest packing state. If a concentrated emulsion constitutes a continuous phase based on monomer(s), polymerization of this phase leads to the formation of hierarchical open-porous polymers. Hence, the polymers obtained from HIPEs are named poly(high internal phase emulsion)s or polyHIPEs (Barby and Haq 1985). The internal phase ratio, droplet size, and distribution of HIPEs can be altered by varying the emulsion compositions and emulsification conditions. This can be easily used as a tool for tuning the properties of polyHIPEs (Mert et al. 2019; Mert and Mert 2021).

In this chapter, HIPEs will be discussed first. It will be followed by the polymerization strategies of HIPEs and polyHIPE properties. Finally, polyHIPE applications will be discussed.

2 HIPE Formation and Structure of HIPEs

Emulsions can be classified under three groups by considering the internal phase volume ratios: emulsions having internal phase volume greater than 74.05% are defined as high internal phase emulsions (HIPEs), those having internal phase volume ratio between 74 and 20% are medium internal phase emulsions (MIPEs), and the ones having internal phases lower than 20% are low internal phase emulsions (LIPEs) (Lissant 1966). According to this classification, HIPEs are essentially emulsions that are rich in terms of one of the immiscible liquid phases. Since emulsions are usually prepared by using water and oil phases, in most cases, HIPEs are prepared by dispersing water-in-oil (w/o) or oil-in-water (o/w). The internal phase volume of a HIPE can be increased as high as 99%. The figure which describes the limiting volume fraction for the formation of HIPEs is not random. It is based on Ostwald's definition of critical volume fraction, which says that the volume fraction of mono-dispersed non-deformable spheres is 0.74 in the closest packing state (Ostwald 1910). So, this figure is representing the maximum volume at which deformable monodisperse rigid spheres are packed in an efficient manner. Over this volume fraction, emulsion droplets are no longer spherical. They are distorted with neighboring droplets and take the geometry of polyhedra. According to (Lissant 1966), HIPEs follow a rhomboidal dodecahedron (R.D.H.) packing from 74 vol% to approximately 94 vol% of the internal phase. Once the volume fraction of the internal phase exceeded 94% the tetrakaidecahedron (T.K.D.H.) packing is preferred. On the other hand, since theoretical calculations showed that the geometrical factor at any given percent internal phase is greater for polydispersed tessellations than it is for either R.D.H. or T.K.D.H., HIPEs are assumed as mono-dispersed systems. In this packing geometry, emulsion droplets are separated from each other with a thin layer of the continuous phase (Lissant 1966). The final structure is similar to ordinary foams (Pal 1999). Of course, as a result of the packing geometry of the emulsion droplets, HIPEs are highly viscous emulsions like creams. Hence, HIPEs are also known as cream emulsions, gel emulsions, or hydrocarbon gels.

The rheological properties of HIPEs are engaged with their three-dimensional (3D) interconnected network structure composed of thin liquid films of continuous phase. They show thixotropy or pseudoplasticity. According to (Lissant 1966) they show relaxation phenomena. Their rheological properties such as yield value and apparent viscosity gradually decrease as the emulsion ages as compared to the corresponding values in fresh emulsions (Lissant 1966). However, a more recent study showed that some of the rheological properties (i.e., steady shear, oscillatory shear, creep) exhibit negligible aging effects over a storage period of about 24 days (Pal 1999).

HIPEs are versatile emulsions and they have significant importance in many industrial fields such as cosmetics, pharmaceuticals, and food. In the last three decades, they also become very important in the preparation of low density polymer foams or monoliths (Cameron and Sherrington 1996).

HIPEs are usually prepared by dispersing high volume fraction of aqueous phase in the continuous oil phase, under constant stirring. However, vice versa is also used for some applications (Cameron and Sherrington 1996; Silverstein and Cameron 2010). However, due to the nature of emulsions and stability requirements, it is more common to use a highly hydrophobic oil phase as the continuous phase. Because emulsions are kinetically unstable systems a third component—an emulsifying agent (emulsifier or surfactant)—should be used to provide stability. However, emulsifier selection should be made carefully, because it has to have film-forming property and it should be effective against coalesce (Lissant 1966; Williams 1991). Related to emulsifier selection the two important properties that should be considered are the hydrophile-lipophile property of the emulsifier that is described by hydrophile-lipophile-balance (HLB) number, and the phase inversion temperature (PIT).

2.1 Stabilization of HIPEs

To provide and maintain the stability of HIPEs is crucial for the synthesis of poly-HIPEs. The stabilization of emulsions is mostly dependent on miscibility potential of organic and water phases in addition to surface tensions of droplets. Although stabilization of HIPEs usually achieved by using a surfactant, particle stabilization strategy which is based on using nano- or micro- sized amphiphilic particles can also be used for stabilization. Many parameters such as structure and composition of the surfactant, mass balance of the organic and water phases, presence of stabilizing agents (eg. addition of salts) in the water phase, and operation temperature extensively affect the stability of HIPEs. Due to the stabilization strategy HIPEs can be examined in two main groups: (1) surfactant-stabilized HIPEs and (2) particle-stabilized HIPEs (or Pickering-HIPEs).

2.1.1 Surfactant Stabilization (Surfactant-Stabilized HIPEs)

Surfactants are substances that reduce surface tension when dissolved in water or an aqueous solution. Surfactants are characterized by a molecule consisting of two groups; the hydrophilic part as a head group and the hydrophobic part as a tail group. The hydrophobic part tends to the oil phase while the hydrophilic part tends to the water phase. In this way, adsorption of surfactant molecules at the oil-water interface takes place and structures called micelles are formed (Fig. 1). Surfactants are classified according to the chemical structure of the hydrophilic head groups. Surfactants with a positively charged head group are called cationic surfactants (e.g., cetyl trimethyl ammonium bromide, octadecyltrimethyl ammonium bromide, trimethyl dodecyl ammonium chloride, etc.), while surfactants containing negatively charged head groups are called anionic surfactants (e.g., sodium dodecyl sulphate, sodium stearate, ammonium lauryl sulphate, etc.). Surfactants that have an uncharged head group are called nonionic surfactants (e.g., poly(alkylene-oxide) block copolymers,
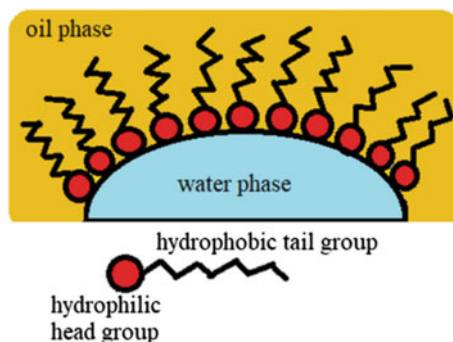
oligomeric alkyl-ethylene oxide, alkyl-phenol poly(ethylene oxide), sorbitan esters, etc.).

The surfactant concentration used in most of the surfactant-stabilized HIPEs usually varies between 5–30%. In some cases, this value can be up to 50%. However, remaining surfactant should be removed after obtaining polyHIPE due to its possible influence on the polyHIPE properties. In addition to relatively high cost of surfactants, removal processing costs required for the removal of the residual surfactant following the synthesis process limits the polyHIPE applications in large scale, due to not economically feasible (Silverstein 2014a; Zhang et al. 2019b). Moreover, conventional polyHIPEs prepared from surfactant-stabilized w/o HIPEs have poor mechanical properties and low permeability, due to the presence of cavities and interconnected pores.

There are many surfactant systems used to stabilize HIPEs. According to Bancroft rule, the medium in which the surfactant can mainly dissolve creates the continuous phase of the emulsion (Silverstein 2014b). Nonionic surfactants are frequently used in the organic phase for stabilization of w/o HIPEs, while HLB number is an important criterion during surfactant selection. This number is an indicator for surfactant molecules that reflects the ratio of hydrophilic/lipophilic groups. The HLB number of non-ionic surfactants, which are ideal for forming stable w/o HIPE is in the range of 3–6. For example; Span 80, which has an HLB number of 4.3, is frequently used for preparation of w/o HIPEs. Furthermore, presence of co-surfactants in HIPE formulations can also be influenced HIPE stabilization (Cameron and Sherrington 1996; Silverstein 2010). Based on the researches (Williams 1991), existence of a co-surfactant in addition to a non-ionic surfactant can cause reduced stability and lead to coalescence.

On the other hand, HLB number only considers the surfactant molecule itself at 25 °C, but not the overall interactions between the oil and water phases. However, molecular interactions between the components in the oil and water phases become more significant when the external emulsion phase consists of monomers with different polarities. For instance, while Span 80 (HLB 4.3) is very effective to prepare a stable w/o type HIPE of a hydrophobic monomer mixture, using a surfactant with

a lower HLB such as Pluronic® L121 (HLB 1.0) is more convenient to prepare more hydrophilic HIPEs.

2.1.2   Particle Stabilization (Particle-Stabilized Pickering-HIPEs)

Particle-stabilized emulsions have a considerable interest in recent years (Teixeira and Bon 2010; Esser-Kahn et al, 2011; Shen and Ye 2011; Chevalier and Bolzinger 2013). The adhesion of solid particles to the liquid-liquid interface of an emulsion droplet was first reported by Ramsden and Pickering in the 1900s (Ramsden 1903; Pickering 1907). The reason of settlement of solid particles in the liquid-liquid interface is partial wetting of them by two immiscible liquid phases. These types of emulsions which are stabilized by solid particles irreversibly adhered to the droplet interface is called "Pickering emulsions". Pickering emulsions are surfactant-free emulsions in which solid amphiphilic particles are used to ensure stabilization and the droplets are prevented from coalescence by positioning them at the oil-water interface (Ikem et al. 2008; Song 2009). Although the amount of solid particles used varies according to the monomer content, it is generally between 1–5% of the external emulsion phase.

Particle stabilization is also used to prepare stable HIPE templates. Pickering-HIPEs have many advantages in comparison with surfactant-stabilized HIPEs. In Pickering-HIPEs, liquid droplets existing in the dispersed phase can be stabilized by lower amount of solid particles instead of large amount of surfactant. Moreover, solid particles not only provide stabilization but also, can act as functional centers and participate in the formation of crosslinks between the polymer chains or can include new properties to polyHIPEs with thanks to functional groups they have (Zheng et al. 2013; Silverstein 2014b). For example, based on the type and functionality of solid particle, mechanical, thermal, or electrical properties of polyHIPEs can be improved (Silverstein 2014b). In addition, Pickering-HIPEs are more advantageous as solid particles are less toxic than surfactants and it is usually enough to use low amount of particles to stabilize emulsions.

Pickering emulsions can be replaced with conventional emulsions in many emulsion applications, owing to have the basic properties of surfactant-stabilized emulsions. Solid particles used as stabilizers in Pickering emulsions are smaller than emulsion droplets. Nano-sized solid particles (approximately 100 nm) allow stabilization of both droplets of a few micrometers and larger ones. On the other hand, micron-sized particles can stabilize droplets larger than a few millimeters in diameter.

Since Pickering emulsions are extremely stable due to the irreversible adhesion of solid particles at the liquid-liquid interface, small amounts of solid particles are sufficient for the stabilization of emulsions. Pickering emulsions can be prepared as o/w or o/w systems depending on the surface tension of solid particles. On the other hand, the adsorption mechanism of solid particles on the surface of emulsion droplets is different from the adsorption mechanism in the surfactant-stabilized emulsion droplets. The strong attachment of solid particles at the oil-water interface depends on the partial wetting of the surface of the solid particles with the

water and organic phases. The contact angle (α_w) of solid particles with water determines the stable position of the particle at the oil-water interface (Cauvin et al. 2005; Kralchevsky et al. 2005; Menner et al. 2007a, b). Thus, hydrophilic particles ($\alpha_w < 90º$) form o/w Pickering emulsions while hydrophobic particles ($\alpha_w > 90º$) create w/o Pickering emulsions (Fig. 2). Highly hydrophilic particles which can be able to stabilize o/w emulsions have a smaller contact angle with the water phase, whereas highly hydrophobic particles with higher contact angles are required to stabilize w/o emulsions. Considering the partial wetting with water and oil required for adsorption at the oil-water interface is essential for selection of appropriate solid particles. Where necessary, it is possible to alter the surface of the hydrophilic solid particles with a suitable modifying agent to impart hydrophobic properties and thus provide the partial wetting required by water and oil. In other words, surface modifying of the solid particle according to the desired type of emulsion allows the wetting properties to be controlled as desired. Thus, stabilization can be achieved by changing the surface chemistry of the solid particles. Many organic or inorganic particles, which provided the requirement of partial wetting can be used as stabilizer in the preparation of Pickering-HIPEs. For example; nanoclays (laponite, montmorillonite, halloysite) (Mert and Şen 2016; Mert et al. 2018), magnetic particles (Fe_3O_4) (Vílchez et al. 2014; Kovačič et al. 2014; Azhar et al. 2019), carbon nanotubes (CNT) (Menner et al. 2007a, b), silica (Ikem et al. 2008; Woodward et al. 2016), titania (Menner et al. 2007a, b; Yüce et al. 2017, graphene oxide (Yi et al. 2016b), etc.

PolyHIPEs prepared from particle-stabilized Pickering-HIPEs generally tend to form closed-cell structures depending upon the used solid particle. However, this is not preferable in some applications where permeability is important. But it is possible to prepare polyHIPEs with an open cellular structure with the use of a small amount of surfactant in addition to solid particles. The addition of surfactant leads to decrease in the interfacial tension, decreases the droplet size, and increases the number of droplets. Accordingly, wall thickness decreases and allows the formation of interconnected pores (pore throats) during polymerization. In particle and surfactant-stabilized HIPEs, variation of the morphology from closed to open cellular structure is a result of the presence or non-presence of interconnected pores between the cavities. Accordingly, permeability of the polyHIPE foam can also change. In
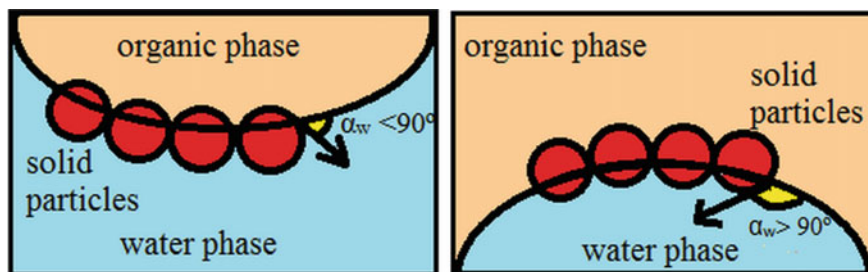
Fig. 2 The schematic representation of solid particles at oil-water interface

such a case, the addition of small amount of surfactant during the preparation of Pickering-HIPEs allows the formation of a more open structure with interconnected pores with larger dimensions. According to the desired morphology depending on the application area, particle-stabilized Pickering-HIPEs containing surfactant can be preferred.

3 Polymerization Strategies for HIPEs

An attractive application of HIPEs is the preparation of macroporous polymers by using them as precursor templates for the creation of porosity. While this approach is known as emulsion templating, resulting polymers are named as polyHIPEs (Barby and Haq 1985). PolyHIPEs are unique polymer foams exhibiting hierarchical pore structure which consists macropores interconnected by small pore throats. PolyHIPEs can be prepared by using either w/o or o/w type HIPEs (Cameron 2005). In the first case, due to the chemical structure of the used monomers, resulting polymers are highly hydrophobic, while the other one leads hydrophilic polymers. On the other hand, polyHIPEs from CO_2 HIPEs and non-aqueous HIPEs are also reported in the literature (Butler et al. 2003; Ma et al. 2020).

An important advantage of emulsion templating is the possibility of preparing polyHIPEs in the shape of beads, rods (Gokmen et al. 2009) and films (Pulko and Krajnc 2008) in addition to monoliths. It is also possible to obtain polyHIPEs from the polymerization of the HIPEs prepared by an extrusion process (Zhou et al. 2019), and with 3D printing (Yang et al. 2017; Hu et al. 2019). Thanks to their highly permeable structure polyHIPEs are attracting interest in the fields of adsorption, separation and chromatography, storage of gases, liquids and energy, catalysis, photocatalysis, tissue engineering, and, etc. (Silverstein 2014b). Moreover, polyHIPEs can serve as precursors of porous carbide derived carbons (CDCs) (Oschatz et al. 2012) and ceramics (Koler and Krajnc 2019).

In the literature, researchers reported many kinds of polyHIPEs by applying different polymerization and material preparation methodologies. The most used approaches among them are changing the chemical structure and material properties by varying the monomer type and composition, assembling polymer networks with nanoparticles, preparing interpenetrating or semi-interpenetrating polymer networks. In addition, preparation of functional polyHIPEs via post-functionalization or in-situ functionalization approaches was also extensively studied. In this case, it is required to use polar functional monomers during HIPE preparation (Silverstein 2014a).

PolyHIPEs were first prepared by the Unilever researchers Barby and Haq and patented in 1985 (Barby and Haq 1985). These polyHIPEs were obtained by free radical copolymerization of highly hydrophobic w/o HIPEs which contains styrene (S) and divinylbenzene (DVB) in continuous phase. As well as S and DVB based ones are the most studied and investigated polyHIPEs (Mert et al. 2019), strategies on polyHIPE synthesis have been extended by using various monomers. In this respect, scientists achieved polyHIPEs from chain-growth and step-growth polymerizations

of w/o, o/w, and even non-aqueous HIPEs containing monomers such as 4-vinyl benzyl chloride (VBC) (Krajnc et al. 2002; Jeřábek et al. 2008; Kovačič and Krajnc 2009; Koler and Krajnc 2021), glycidyl methacrylate (GMA) (Barbetta et al. 2009; Majer and Krajnc 2010; Mert et al. 2012; Jerenec et al. 2014; Pahovnik et al. 2016; Yang et al. 2018; Krajnc et al. 2015a), methyl methacrylate (MMA) (Mao et al. 2013; Huš and Krajnc 2014), 2-ethyl hexyl acrylate (EHA) (Cameron and Sherrington 1997; Jerenec et al. 2014; Moghbeli et al. 2017), glycerol 1,3-diglycerolate diacrylate (Parın and Mert 2020) ethylene glycol dimethacrylate (EGDMA) (Krajnc et al. 2005a; Livshina and Silverstein 2008; Rao et al. 2011), unsaturated polyester resin (Mert et al. 2012; Misra et al. 2016), acryl amide (AM) (Rao et al. 2011), acrylic acid (AAC) (Krajnc et al. 2005b; Kovačič et al. 2011), ε-caprolactone (CPL) (Busby et al. 2001; Pérez-García et al. 2016; Yadav et al. 2020), dicyclopentadiene (DCPD) (Kovačič et al. 2010, 2012; Mert et al. 2015; Kovačič and Slugovc 2020), trimethylolpropane tris(3-mercaptopropionate) (TMPTMP) (Chen et al. 2017; Lee et al. 2017), trimethylolpropane diallyl ether (TMPDAE) (Chen et al. 2017), pentaerythritol allyl ether (PEAE) (Chen et al. 2017), 1,7-octadiyne (ODY) (Chen et al. 2017), and β-myrcene (Mert and Kekevi 2020; Kekevi and Mert 2021) in the external phase were prepared and polymerized to obtain polyHIPEs through different polymerization mechanisms. In this respect, several polymerization mechanisms including chain-growth, step-growth, and ring opening homopolymerization and copolymerization have been successfully implemented in polyHIPE synthesis. General principles of polyHIPE synthesis via different polymerizations approaches are extensively explained below.

3.1 Chain-Growth Polymerization

Chain-growth polymerization is based on growth of polymer chains through an active center. Reactive centers are produced by a catalyst or initiator and due to the nature of the active center of growing chains; chain-growth polymerization has two types: free radical polymerization and ionic polymerization (IP) (Hamielec and Tobita 2012). Since most of the commercial monomers with C=C double bonds can easily undergo free radical polymerization, it is a convenient route to synthesize polyHIPEs by the polymerization of the external HIPE phases.

Purification and drying procedures following polymerization step are important in terms of the final pore morphology. However, additional stress on the polymer network arises during drying may cause collapse of the pore structure (Kovalenko et al. 2016). For this respect, crosslinking is used to obtain a solid material and to prevent the collapse of pore structures. The additional benefit of this approach is to obtain shape-stabilized polyHIPE materials exhibiting sufficient chemical and thermal stability for various applications.

Free radical copolymerization of mono- and difunctional vinyl monomers can be used to achieve crosslinking of the external HIPE phase. For this purpose, S and DVB are the most extensively used monomer and comonomer, as being the subject of

original polyHIPE patent (Barby and Haq 1985; Mert et al. 2019). These polyHIPEs are extensively studied and synthesized with different nominal porosities. Synthesis of poly(S-co-DVB) polyHIPEs from w/o HIPEs is quite simple. In this procedure, S, DVB, a non-ionic emulsifier (usually Span 80 is used; HLB: 4.3), and an oil-soluble initiator (such as 2,2'-asobisisobutyronitrile—AIBN or benzoyl peroxide—BPO) are mixed in a reaction vessel. Afterward internal phase (deionized water) is added dropwise under continuous constant stirring. Once the addition of the internal phase is completed stirring is continued for a specified time to obtain homogeneous dispersion of emulsion droplets. The resulting HIPE is moved to a sealed container and polymerization is proceeded under convenient conditions. Polymerization temperature is determined depending on the decomposition rate constant and 10 h half-life time ($t_{1/2}$) of the polymerization initiator. After polymerization, resulting solid poly-HIPE foam is purified via Soxhlet extraction and dried under vacuum until constant weighing is available. In this procedure, the amount of emulsifier used has a critical importance for the creation of open-porous structure. It is known from the previous studies that open-porous polyHIPEs are formed when the amount of emulsifier is varied between 4 and 50 vol %, while closed-cell polyHIPEs are formed when the ratio of the emulsifier is exceeded 80 vol % of the continuous phase. However, in most cases using emulsifiers with a ratio changing between 20 and 50 vol % is enough to obtain open porosity. On the other hand, HLB number of the emulsifier has also important to maintain stability until the completion of polymerization. As mentioned above, Span 80 is the most preferred surfactant used to stabilize w/o type HIPEs, however, this type of HIPEs can be stabilized with the emulsifiers usually having HLB value changing from 2 to 6. The amount of the initiator is usually equal to the 1 mol % regarding total mole number of the monomer(s). Apart from the oil-soluble initiator's water-soluble initiators such as potassium persulfate (KPS) are also used to initiate polymerization of the continuous phase of a HIPE.

In free radical polymerization, high molecular weight polymers are formed at the very beginning of the polymerization. As a result, the reaction medium becomes highly viscous with increasing polymer chain lengths at high monomer conversions. Viscosity affects mixing process and as well as heat and mass transfer in the reaction medium. Polymerization rates such as bimolecular termination reactions of living polymer chain radicals can also be affected in some cases. In addition to this, high viscosity also decreases the initiator efficiency by inhibiting their diffusion from the cage in which they are surrounded by the other molecules in the reaction medium. On the other hand, heterogeneous free radical polymerization processes such as emulsion and suspension polymerization already have more complex structures than homogeneous processes. From this point of view, free radical polymerization or copolymerization of the external phase of HIPEs dependent on several parameters. The most important parameter is maintaining the emulsion stability during polymerization or completion of the polymerization before destabilization processes occurred. Therefore, HIPEs are polymerized immediately after completion of the emulsification. In this respect, the activity of the polymerization initiator has importance.

A free radical initiator can be initiated by thermal energy, redox reactions, irradiation with ultraviolet (UV) and UV-visible (UV-vis) light, and radiation. It is

known that the decomposition rates of azo-based and peroxy-based initiators can be increased by UV and UV-vis light irradiation. A photo-initiated polymerization can be proceeded at lower temperatures (i.e., at room temperature) because the activation energy of photo chemical initiation is approximate zero. This is very advantageous in terms of preventing coalescence or Ostwald ripening during polymerization. On the other hand, using redox initiation systems is another advantageous choice for lowering the activation energy and to achieve polymerization at lower temperature conditions. Such that redox initiations can be used in a temperature range changing between 0 and 50 °C. Radiation initiation, which is used as a versatile for post-modifications, is also an alternative by its zero-activation energy for the formation of primary radicals. Radiation initiation can be used at low or high temperatures. Radiation induced polymerization of GMA-based HIPEs at room temperature is a preferable approach because of inhibiting hydrolysis of the epoxy groups (Yang et al. 2018).

Apart from the activation energies, initiator selection is also important in terms of locus of initiation. The locus of initiation is important for the polymer microstructure, final polyHIPE morphology, and other physical properties that are dependent on the microstructure. Depending on the locus of initiation open or closed-cell polyHIPEs can be formed. When polymerization initiated in the bulk phase resulting polyHIPEs generally exhibit an open-porous structure consisting of spherical pores (Fig. 3), whereas if it is initiated at the oil/water interface resulting polyHIPE might exhibit a closed-cell structure (Fig. 4). In the polymerization of w/o HIPEs, when the initiator radicals are generated in the oil phase, polymer is continuously formed in the external emulsion phase. In this case, primer monomer radicals are responsible for the initiation of the polymerization. During polymerization, external phase is
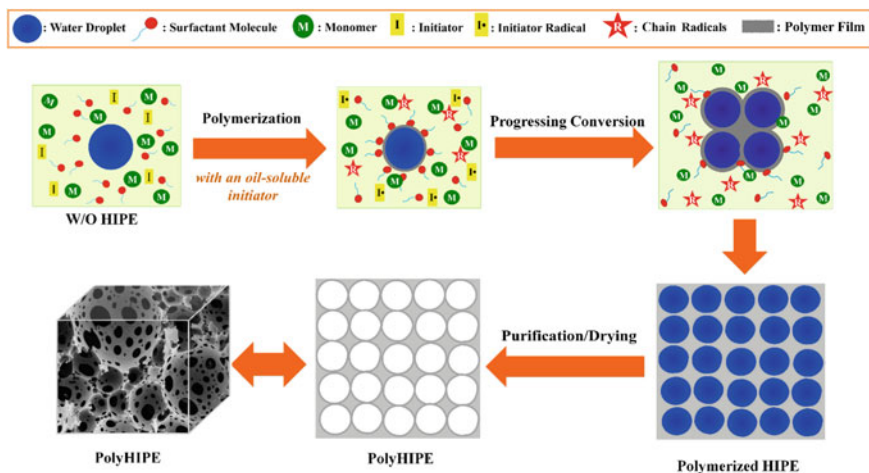
Fig. 3 Locus of initiation and progressing conversion in the polymerization of w/o HIPEs when an oil-soluble initiator is used. The possible morphology of the resulting polyHIPE
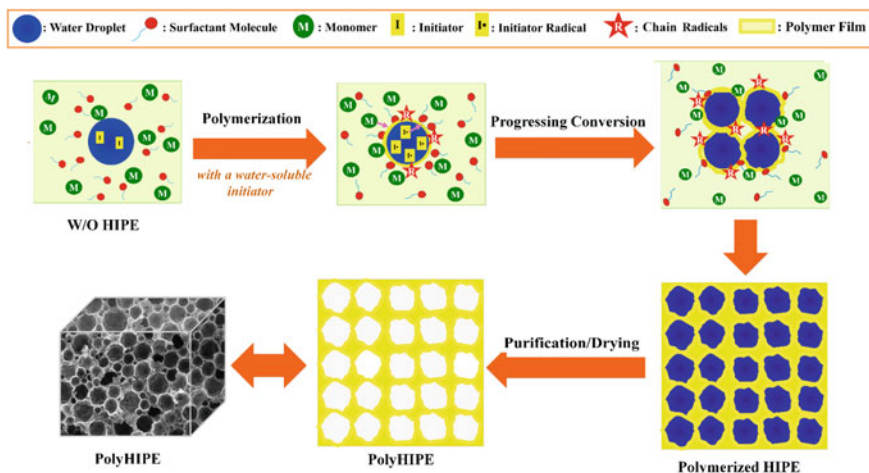
Fig. 4 Locus of initiation and progressing conversion in the polymerization of w/o HIPEs when a water-soluble initiator is used. The possible morphology of the resulting polyHIPE

the monomer reservoir. Monomer units are continually added to the active growing polymer chains and lead formation of a polymer film. Accordingly, internal phase droplets are surrounded by a continuous polymer film. This type of polymerization proceeds in a random manner (Fig. 3). If the initiator dissolved in the internal aqueous phase, initiator radicals are formed there and diffused to the water/oil interface. Monomers diffuse from the external oil phase to the interface and primary monomer radicals are also produced here. During the polymerization, external phase is the monomer reservoir and monomer units are continually diffuse from this phase to the interface and added to the active growing polymer chains (Fig. 4). At these conditions resulting polymers are rich in monomer(s) present in excess at the interface. Accordingly, it is adequate to say that monomer polarity and its ability of diffusing to the interface is determinative on the polymer microstructure.

O/W type HIPEs are also prepared by using highly hydrophilic water-soluble monomers such as acryl amide (AAm) (Livshina and Silverstein 2008), acrylic acid (AAC) (Krajnc et al. 2005b; Kovačič et al. 2011), N-isopropyl acrylamide (NiPAM) (Kovačič et al. 2011), and 2-hydroxyl ethyl methacrylate (HEMA) (Mezhouda et al. 2018). Because the external phase is composed of aqueous monomer solution and water-soluble initiator also dissolves in this phase free radical polymerization or copolymerization of an o/w HIPE is initiated and progressed in the external phase.

Thiol-ene reactions, which involve addition of a thiol to an ene bond, are also used as an efficient route to synthesize polyHIPEs. A reaction between a thiol and an ene can proceed via a radical chain or an anionic chain. While the first one is known as thiol-ene reactions the later one, which involves thiol-Michael addition, is known as thiol click reactions in the literature (Lowe 2010). Thiol-ene reactions are focused on the synthesis of polymer networks for various applications are mostly conducted through radical centers and proceeds via initiation, propagation, and termination

steps as in a chain-growth polymerization process. In many cases, photo-induced thiol-ene polymerization is preferred within the presence of a photoinitiator. An advantage of using this type of polymerization for the synthesis of crosslinked polymers is the ideal microstructure of resulting polymer networks and low shrinkage stress during polymerization (Lowe 2010; Hoyle and Bowman 2010). In general, a wide variety of highly functional thiols can be employed in thiol-ene based polymerizations. However, the reactivity of thiol species is varied due to the strength of S–H bond and monomer structure (i.e., substitution pattern of the C=C bond and monomer polarity). Another major advantage of thiol-ene based polymerizations is the extremely rapid reactions even at ambient conditions (Lowe 2010; Hoyle and Bowman 2010). On the other hand, due to the concerns related to emulsion stability, modest reaction conditions and fast reactions are usually preferred for HIPE polymerizations. Considering the tremendous advantages mentioned above, thiol-ene based crosslinking of HIPEs is also being studied by scientists (Sergent et al. 2012; Caldwell et al. 2012; Kirche et al. 2013; Lafleur et al. 2015). Thiol-ene reactions are also applied as a post-functionalization step to the polyHIPE monoliths or as an approach to improve specific surface area by hypercrosslinking via radical-mediated thiol-ene/yne addition (Mezhouda et al. 2018). In addition, thiol-yne polymerizations are also successfully implemented in polyHIPE synthesis due to their opportunity of expanding thiol-ene chemistry and ability in synthesizing polyHIPEs with novel properties (Lovelady et al. 2011; Chen et al. 2017).

Controlled radical polymerization techniques have been also used for the preparation of polyHIPEs with well-defined microstructure and specific functionality because of their advantages of providing simple and robust synthetic routes. Since controlled radical polymerization provides significant opportunity in material design, it is used as a versatile tool to prepare bioconjugates, organic/inorganic composites, and surface-tethered copolymers (Matyjaszewski and Spanswick 2005; Benaddi et al. 2021).

As distinct from the free radical polymerization, the control of the mechanism in controlled radical polymerization is based on the regulation of the chain propagation step by the activation/deactivation of the radical species during polymerization. There are several types of controlled radical polymerization including reversible addition-fragmentation chain transfer (RAFT) polymerization, atom transfer radical polymerization (ATRP), and nitroxide-mediated radical polymerization. Among them, RAFT has similarities to free radical polymerization in terms of initiation and termination mechanisms of polymerization, since reactions are initiated by the commonly used free radical initiators, and control of the mechanism depends on the RAFT agents responsible for chain transfer reactions (Perrier 2017; Benaddi et al. 2021). However, in ATRP equilibrium between propagating radicals and dormant polymer chains is generated by a redox reaction between a solubilized transition metal and alkyl halide, and it is controlled by the forward and back reaction rates. On the other hand, while the reaction follows first-order kinetics, low instantaneous radical concentration is responsible for the elimination of termination step (Matyjaszewski and Xia 2001; Ayres 2011; Matyjaszewski 2012). An important disadvantage of ATRP, easy oxidation of transition metal complexes to higher oxidation states, can

be overcome by using an electron transfer rather than organic radicals. This procedure, which is known as activator generated by electron transfer for ATRP (AGET-ATRP), has additional benefit of providing enhanced catalyst stability (Jakubowski and Matyjaszewski 2005). Since synthesis of polyHIPEs is achieved in complex HIPE mediums composed of aqueous and oil phases AGET-ATRP was applied by Gurevitch and Silverstein as a suitable approach to synthesize 2-EHA and DVB based polyHIPEs from HIPEs and Pickering-HIPEs. They revealed that the properties of resulting polyHIPEs including macromolecular structure, wall structure, and pore morphology are strongly related to the locus of initiation (Gurevitch and Silverstein 2011, 2012). Improving mechanical properties of polyHIPEs due to the creation of a uniform network is the most significant contribution of controlled radical polymerization to polyHIPE development. In this respect, Luo and co-workers demonstrated that RAFT of HIPE templates resulted in polyHIPEs exhibiting three-fold higher Young's modulus and crush strength in comparison with the polyHIPE produced by free radical polymerization (Luo et al. 2012). In another study, AGET-ATRP was implemented to synthesize fully biodegradable polyHIPEs with stiffer structure and higher Young's modulus from the copolymerization of 2-ethylhexyl methacrylate (EHMA) and bis(2-methacryloyloxyethyl) disulfide (DSDMA) (Lamson et al. 2013). Benaddi et al. showed that the void sizes, gap connectivity, and mechanical behavior of polyHIPEs were strongly influenced by the polymerization mechanism, initiator solubility, molar ratio of RAFT agent to initiator, and the amount of crosslinking comonomer (DVB) in RAFT applied polyHIPE synthesis (Benaddi et al. 2021).

3.2   Step-Growth Polymerization

In step-growth polymerizations, usually, one type of reaction is responsible for the formation of high polymers. Here, polymer chain length increases slowly, and high molecular weight polymers are not formed until the end of the polymerization and nearly complete conversion of monomer has occurred. During polymerization, the rate constants for the various steps are approximately equal (Flory 1946; Hamielec and Tobita 2012). Polyesters, polyamide, and polyurethanes are the important polymer classes produced by step-growth polymerization reactions.

   To obtain high molecular weight polymers by using step-growth polymerizations at least two bifunctional monomers with an almost exact equivalence in the number of functional groups is necessary. Moreover, reactants should be very pure, side reactions should be avoided, and low molecular mass condensation by-product, which is formed during polymerization, should be removed from the polymerization medium (Flory 1946; Hamielec and Tobita 2012). The main advantages of the step-growth polymerization are the possibility of constructing high polymers of accurately known structure, easy mixing, and thermal control due to low viscosity of the reaction medium, while removal of the by-product is the main difficulty. In addition, molecular weight distribution can be easily derived with the unity of the stoichiometric ratio of the monomers. While using bifunctional monomers resulted in linear

polymers, non-linear polymer networks with an infinite molecular weight are formed with the use of monomers with more than two functional groups per molecule (Flory 1946).

Preparation of network polymers by step-growth polymerization for various purposes can be achieved via several polymerization processes including bulk polymerization, solution polymerization, and emulsion polymerization. On the other hand, hierarchical macroporous polyesters, polyamides, and polyurethanes obtained from HIPE templating have also been reported by scientists in the literature. In this frame, polyurethane (David and Silverstein 2009; Barbara et al. 2017; Weinstock et al. 2019), urea-formaldehyde (Pan et al. 2016), melamine-formaldehyde (Yin et al. 2018), resorcinol-formaldehyde (Elmes et al. 1994), and polysiloxane type polyHIPEs (Grosse et al. 2008), and polyHIPEs from the polycondensation between 2-nitroresorcinol and cyanuric chloride (Audouin et al. 2008), mannitol, and poly(hexamethylene diisocyanate) (Zhang et al. 2019a) have been reported by researchers. However, using step-growth polymerization for synthesizing polyHIPEs is not as common as using free radical polymerization or copolymerization due to the limitation of polycondensation reactions (i.e., condensation by-product can inhibit the reaction or can promote alternative reactions, and polycondensations can be achieved usually above 100 °C) and disadvantageous such as relatively high densities and less open pore architecture of the obtained materials (Silverstein and Cameron 2010).

3.3 Ring Opening Polymerization (ROP)

Ring opening polymerization (ROP) is one of the most important synthetic routes used for the preparation of polymers exhibiting controllable specific properties. It is a versatile polymerization technique for preparing bio-derived and biodegradable polymeric materials for various applications (Nuyken and Pask 2013). Ring opening polymerization is classified into cationic, anionic, radical, metathesis, and coordination polymerizations according to the propagating species (Sanda and Endo 2001). Because the driving force for the ROP is the ring strain, the mechanism of ROP is different from step-growth polymerization or polycondensation. Moreover, polymerization mechanism is associated steric considerations and ring chain equilibrium. Accordingly, microstructure of the final polymer product is strongly dependent on the temperature (Nuyken and Pask 2013).

An important advantage of ROP is the opportunity of introducing a functional group to the polymer chains (ester, ether, amide, carbonate, etc.). On the other, due to the compact structures of the cyclic monomers, twice less volume shrinkage is occurred during polymerization, as compared to vinyl monomers (Sanda and Endo 2001). When compared with polycondensation, the milder reaction conditions and stoichiometry, absence of by-product formation, and possibility of controlling polymer microstructure (opportunity of synthesizing block copolymers and stereoregular polymers, possibility of controlling polymer molecular weight and

polydispersity) are the main advantageous (Sanda and Endo 2001). The above-mentioned features of ROP have been successfully utilized in HIPE templating to prepare biodegradable and biocompatible polyHIPEs, mostly for tissue engineering applications. In this respect poly(caprolactone) (PCL) (Utroša et al. 2019; Yadav et al. 2019; Agrawal et al. 2020; Yang et al. 2020), poly(L-lactide) (PLLA), poly(L-lactide)/poly(ε-caprolactone) PLLA/PCL (Pérez-García et al. 2016; García-Landeros et al. 2019) based polyHIPEs were reported by the researchers. Moreover, ROP of N-carboxyanhydrides (NCAs) was also used for the preparation of polypeptide based polyHIPEs (Onder et al. 2020).

Because of the very high catalytic activities of the catalysts provides short curing times as compared to free radical polymerizations, ring opening metathesis polymerization (ROMP) by using ruthenium-based metathesis catalyst was also extensively used for the synthesis of polyHIPEs (Benmachou et al. 2003). DCPD is a cheap monomer which is also very reactive. Since polyDCPD has excellent impact strength and is also being used as thermoset foam in the automative sector, polyDCPD type polyHIPEs have been also extensively studied in the literature (Benmachou et al. 2003; Kovačič et al. 2010, 2012, 2020; Mert et al. 2015). In addition to the advantage of short curing periods of the DCPD-based HIPE templates, polyDCPD type polyHIPEs also provide the advantage of unsaturated double bonds on the polymer main chains for post-functionalization (Kovačič et al. 2010; Kovačič and Slugovc 2020).

In the frame of polymerization methodologies utilized for polyHIPE synthesis, monomer, comonomer, and surfactant systems frequently used in polyHIPE preparation are tabulated in Table 1.

4 PolyHIPE Properties

PolyHIPEs are noted for their unique pore morphologies due to the need for open cellular structure in many applications (Silverstein 2014b). Although polyHIPEs are known by their hierarchical open-porous structure composed of large voids that are connected by small holes (Fig. 5a), formation of closed-cell morphology (Fig. 5b) is also possible depending on the synthetic conditions (Cameron et al. 2011; Zhang et al. 2019b; Mert et al. 2019). The main difference of polyHIPEs exhibiting closed-cell morphology from those with open pores is the absence of interconnected pores (pore throats) in the material morphology (Fig. 5). Since polyHIPEs are synthesized by using HIPEs as a template for the creation of porosity it would not be wrong to express that the resulting pore structure in polyHIPEs is the reflection of precursor HIPEs (Cameron et al. 2011; Mert et al. 2019). In this respect, cavities of a polyHIPE correspond to the droplets of HIPEs. Because a HIPE is usually composed of droplets with diameters changing in the range between 5 to 100 μm, cavities of polyHIPEs are also changing in the same size range (Cameron et al. 2011). Due to the highly porous structure polyHIPEs usually exhibit densities around 0.1 g/cm^3. However, it

Table 1 Frequently used monomer, comonomer, and surfactant systems in polyHIPE synthesis

Monomer	Monomer structure	Crosslinker comonomer	Emulsion type (o/w or w/o)	Surfactant	References
S		DVB	w/o	Span 80	Williams and Wrobleski (1988), Williams et al. (1990), Cameron et al. (1996), Li et al. (2008), Mert et al. (2018), Mert et al. (2019), Mert and Mert (2021)
HEMA		MBA or EGDMA	o/w or w/o	Pluronic F68 or Pluronic L121	Kovačič et al. (2007)
		MBA	o/w	Pluronic F68	Majer et al. (2016)
		MBA or EGDMA	o/w	Triton X-405	Kulygin and Silverstein (2007)
EHMA		S, DVB	w/o	Span 80	Cameron and Sherrington (1997)
MMA		EGDMA	w/o	Synperonic PEL121	Huš and Krajnc (2014)
		EGDMA	w/o	Pluronic L121	Althubeiti and Horozov (2019)
		DVB	w/o	Span 80	Li et al. (2016)

(continued)

Table 1 (continued)

Monomer	Monomer structure	Crosslinker comonomer	Emulsion type (o/w or w/o)	Surfactant	References
GMA		EGDMA	w/o	Symperonic PEL 121	Krajnc et al. (2005a)
		2-EHA, isobornyl acrylate (IBOA), TMPTA	w/o	Hypermer B246	Kimmins et al. (2012)
		EGDMA	w/o	Pluronic F127, Brij35, Span80, PVP, SDS	Yao et al. (2009)
		EHA and EGDMA	w/o	Symperonic PEL 121	Pulko et al. (2011)
		DVB	w/o	Span 80 or polyglycerol of a fatty acid (PGE 080/D)	Barbetta et al. (2009)
		DVB	w/o	Tripolyglycerol monostearate (TGPS)	Yang et al. (2014)
Butyl Methacrylate (BMA)		DVB	w/o	Span 80	Ma et al. (2014)

(continued)

Table 1 (continued)

Monomer	Monomer structure	Crosslinker comonomer	Emulsion type (o/w or w/o)	Surfactant	References
AN		DVB	w/o	Polyglycerol polyricinoleate (PGPR, Palsgaard 4125)	Cohen and Silverstein (2011)
AAC		MBA	o/w	Triton X-405	Krajnc et al. (2005b)
AAM		MBA	o/w	Span80	Nikjoo and Akhtar 2017
β-myrcene		EGDMA	w/o	Pluronic L121	Mert and Kekevi (2020), Kekevi and Mert (2021)
Polylactide (PLA)		S or MMA	w/o	Span 80, Span 85, and Tween 80	Busby et al. (2002)

(continued)

Table 1 (continued)

Monomer	Monomer structure	Crosslinker comonomer	Emulsion type (o/w or w/o)	Surfactant	References
DCPD			w/o	Pluronic L121, Brij 52, Span 80	Kovačič (2013)
			w/o	Pluronic L121	Trupej et al. (2017)
			w/o	Synperionic PEL121	Kovačič et al. (2012)
		–	w/o	Pluronic L121	Yüce et al. (2019)
		–	w/o	Span 80	Kovačič et al (2015)
Cyclooctene (COE)		–	w/o	Span 80	Benicewicz et al. (1998)
VBC		S and DVB	w/o	Span 80	Benicewicz et al. (1998)
		DVB	w/o	Span 80	Alexandratos et al. (1998)
TMPTA		–	w/o	Pluronic L121, Span 65	Sušec et al. (2013)
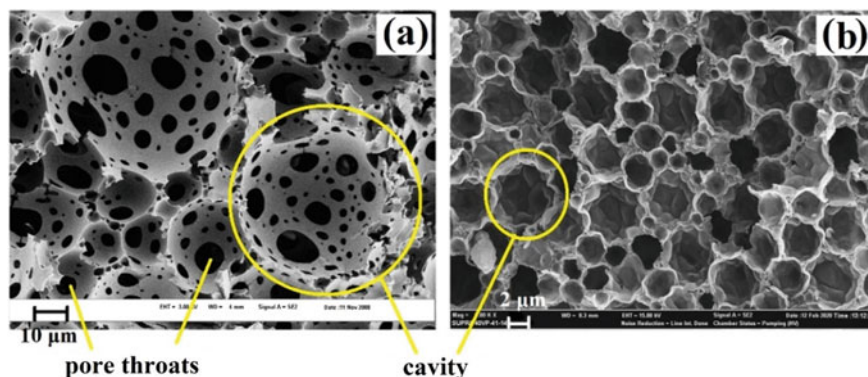
Fig. 5 SEM image of **a** an open-cell polyHIPE, and **b** a closed-cell polyHIPE

is also possible to prepare polyHIPEs with lower densities by changing the synthetic conditions (Silverstein and Cameron 2010).

The features that make the emulsion templating approach outstanding compared to other methods used for the synthesis of porous polymers is the controllability of the pore structure and the ability to prepare well-defined porous polymers (Silverstein 2014a; Mert et al. 2019). The key to controlling the pore structure is mainly dependent on the combination of several factors including HIPE formation and maintaining the emulsion stability until reaching the gel point during polymerization step (Mert et al. 2019; Rohm et al. 2019; Mert et al. 2021). Since the main issue is emulsion formation and stability, surfactants have great importance. To prepare a polyHIPE with a well-defined pore structure, the first step is to select suitable surfactant(s) by considering the external phase composition as described previously above, while the second step is to use the correct amount of surfactant(s) (Pulko and Krajnc 2012; Rohm et al. 2019). According to the literature, to obtain highly open cellular polyHIPE the surfactant content should be greater than the 7% of the external phase (Williams and Wrobleski 1988). On the other hand, HIPEs consisting surfactants below 5% of the external phase usually resulted in closed-cell morphology (Williams and Wrobleski 1988). As reported by Williams and Wrobleski, pores begin to develop at surfactant concentrations as low as 7–10% and are interrupted when the amount of surfactant is above 80% of the external phase (1988). On the other hand, surfactant concentrations changing between 20 and 50% of the external phase resulted in open-porous polyHIPE materials for all internal phase volumes (Cameron et al. 1996). Since the cavities reflect the emulsion droplet size, the decrease in the droplet size leads smaller cavities (Williams et al. 1990). According to Williams et al. (1990) small emulsion droplets that satisfy the radius constraints is made to the extent that the monomer/surfactant can surround them, and the remaining water is walled off. The cavity size distribution of polyHIPEs can be a clue for emulsion stability even at low surfactant concentrations. As the stability of the emulsion increases, cavity size distribution of the resulting polyHIPEs becomes more uniform (Williams

et al. 1990). The increase in the diameter of the emulsion droplets indicates that the destabilization processes are effective. Droplet coalescence and Ostwald ripening are the two main processes that cause emulsion destabilization and may increase the average droplet size in time (Kabalnov and Shchukin 1992; Taylor 1995). Eventually, they lead a polydispersed droplet size distribution, which reflects as a broader cavity size distribution in polyHIPEs. The driving force behind these two mechanisms is different from each other. While Ostwald ripening is occurred due to the differences between the chemical potential of emulsion droplets that have different in size (Taylor 1995), coalescence is eventuated as a result of the thinning and rupture of the thin interfacial films between the droplets (Freire et al. 2005; Carnachan et al. 2006). Therefore, the surfactant system itself and it is amount in the external emulsion phase are the important factors for maintaining the stability of precursor HIPEs and controlling the morphology of the obtained polyHIPEs.

Internal phase ratio is also of great importance in the formation of open cellular structures. The nominal porosity of the final polyHIPEs is related to the total internal phase volume, as cavities are formed upon removal of the internal phase droplets entrapped in the resulting continuous polymer film. However, earlier findings suggest that the surfactant concentration has more influence on the cellular pore structure as compared to internal phase volume (Cameron et al. 1996). According to Cameron et al. with the increase of surfactant concentration the film between the adjacent internal phase droplets become thinner and ruptured from the closest and thinnest points to form holes (pore throats) in the final polyHIPE morphology (Cameron et al. 1996). The importance of maintaining the emulsion stability until the gel point during the polymerization is based on this theory. It was suggested that the volume contraction during the conversion of vinylic monomer units to polymer chains also plays an important role in hole formation. It was predicted that there should be a correlation between the areas of the holes formed in the walls of the cavities and the ratio of certain volumes of the monomer/surfactant mixture and crosslinked polymer phase (Cameron et al. 1996). During the polymerization of HIPEs, holes can still form, although there is no significant shrinkage in volume. This has been attributed to the shrinkage of the polymer films during the drying process of the obtained polyHIPEs (Hainey et al. 1991; Cameron et al. 1996; Cameron 2005).

Menner and Bismarck suggested that the formation of holes in the cavity walls is a mechanical process and related to the purification and drying processes, and they were pointed to the importance of surfactant concentration one more time with their hypothesis (Menner and Bismarck 2006). Purification of a polyHIPE is usually performed by Soxhlet extraction by using low alcohol, and it is followed by drying of the material until constant weighing is available. According to Menner and Bismarck (Menner and Bismarck 2006), polymerizing HIPE cannot shrink externally due to the presence of incompressible droplet phase. In addition, holes are formed because the internal phase droplets rupture the polymer film that they are surrounded by. The perfect spherical geometry of the formed holes can be attributed to the change of the solubility of the surfactant in the emulsion phases during polymerization, and phase separation occurred during polymerization of the oil phase. At higher conversions, two different phases such as a surfactant-rich and a polymer-rich phase were formed.

Meanwhile, surfactant molecules were driven to diffuse oil/water interface between the neighboring droplets and created a weak point that could be ruptured easily during purification or following drying process under vacuum (Menner and Bismarck 2006). On the other side, a more recent study that focused on the statistical evaluation of the relationship between the experimental parameters used for HIPE preparation and polyHIPE properties suggested new findings (Mert et al. 2019). According to Mert et al. (2019) derived mathematical equations showed that while the internal phase ratio is the most effective factor on the variation of average cavity size, surfactant concentration is the second one, and crosslinker concentration also have an important influence. Moreover, internal phase ratio was also found to be the most effective parameter in the determination of interconnected pore size. Model equations showed that the diameters of the interconnected pores were increased with the increase of the internal phase volume. The crosslinker concentration, surfactant concentration, and mixing rate were also found to have significant importance (Mert et al. 2019).

Furthermore, the structure of the macropore walls and openness of the final structure is also associated with the locus of initiation. Based on the monomer type and polymerization mechanism it is possible to use different types of initiator systems that could lead to external phase initiation, interfacial initiation, and nanoparticle-based initiation. According to (Robinson et al. 2014), the influence of the locus of initiation in HIPE systems arises with the formation of open or closed-cell foams. It has been suggested that when polymerization begins at the interface, the resulting polyHIPE will exhibit a closed-cell structure where the pores are deformed polyhedra (Fig. 4), and if polymerization starts in the bulk phase, the resulting polyHIPEs will exhibit an open morphology consisting of spherical pores (Fig. 3). The change in pore morphology has been attributed to "the force of densification upon conversion of macromonomer to polymer". According to Robinson et al. (2014), the thin film between two adjacent droplets is stabilized by interfacial initiation and eventually interconnecting pores are formed. In other respects, Quell et al. (2016) proposed that closed-cell foams with a uniform pore wall thickness can be formed by interface initiation and explained their suggestion based on the osmatic pressure gradient. According to Quell and co-workers, osmotic pressure gradient could redistribute fluid from emulsion nodes to the contact points between the drops just before the template solidifies. However, when polymerization is initiated in the bulk phase, there is not an osmotic pressure gradient, and as the polymerization progresses, the spherical shaped emulsion droplets freeze without deforming. Thereby, spherical cavities are formed. In this phenomenon, the formation of interconnected pores is explained based on the shrinkage of the continuous phase by polymerization Quell et al. (2016).

Generally, polyHIPEs exhibit modest surface area due to the lack of meso- and micropores in their structure. Since macropores are dominated the morphology, surface area of polyHIPEs are usually varied between 5 and 20 m^2/g (Cameron et al. 2011). However, it is possible to improve the surface area by using experimental approaches such as adding a porogen in the precursor HIPE formulation, post-polymerization crosslinking, or hypercrosslinking (Koler et al. 2020). The basic principle of increasing the surface area by adding a porogen to the continuous

phase is based on promoting mesoporosity through early or late phase separation that occurs during polymerization (Sherrington and Hodge 1988). In this respect, Barbetta and Cameron were achieved obtaining polyDVB-based polyHIPEs with a surface area as high as 703 m^2/g by using a porogen (Barbetta and Cameron 2004). Post-polymerization crosslinking is a method based on the creation of meso- and micro-sized pores by crosslinking polymer chains (Davankov and Tsyurupa 1990; Tsyurupa and Davankov 2002). In post-polymerization crosslinking, polymer chains are distributed in a solvent and new bridges are formed between the chains. Since polymer chains are strongly solvated throughout the hypercrosslinking, phase separation cannot be occurred (Koler et al. 2020).

An efficient route for post-polymerization hypercrosslinking is creating new bridges between the chloromethyl groups of chloromethylated polystyrene by Friedel–Crafts alkylation. Hypercrosslinking of linear polystyrene (PS) or P(S-*co*-DVB) leads a polymer network consisting rigid connections. This is achieved by Friedel–Crafts alkylation in the presence of external crosslinker and Lewis acid catalyst (Davankov and Tsyurupa 1990). Another practical approach for synthesizing hypercrosslinked polymer networks is conducting Friedel–Crafts alkylation of vinylbenzyl chloride moieties in poly(vinylbenzyl chloride) (polyVBC) or poly(vinylbenzyl chloride-*co*-divinylbenzene) (poly(VBC-*co*-DVB)) chains. In the above-mentioned approaches, external crosslinker has a significant influence on the rigidity and morphology of the final hypercrosslinked polymer product. While the most used catalyst is FeCl$_3$, dichloroethane (DCE) is the most preferred solvent (Koler et al. 2020).

By conducting post-polymerization hypercrosslinking surface area of polymers can be remarkably increased due to the microporosity created by the formation of additional crosslinks. If the precursor polymer already exhibits microporosity, the resulting hypercrosslinked polymer also exhibits microporosity and unimodal pore size distribution. Whereas, hypercrosslinking of a precursor polyHIPE by Friedel–Crafts alkylation results in bimodal pore size distribution due to the incorporation of micro and mesopores into the macroporous structure. In addition, the morphology of the polyHIPEs is remaining unchanged after hypercrosslinking. In the literature ultra-high surface area, polyHIPEs obtained by hypercrosslinking are reported by several groups including (Pulko et al. 2010) (1100 m^2/g) and (Schwab et al. 2009) (1200 m^2/g).

Generally, polyHIPEs exhibit low mechanical properties as a result of highly porous polymer matrix (Menner et al. 2006; Yüce et al. 2019). Improving the mechanical properties of polyHIPEs without compromising the highly porous and interconnected structure is a major challenge, as opposed to easy control of pore morphology or improvement of surface area by relatively easy-to-apply methods. Poly(S-*co*-DVB)-based network is being the most studied polymer matrix, because it is economically feasible, and S and DVB can be easily copolymerized within a HIPE template. However, polyHIPEs based on poly(S-*co*-DVB) are chalky and fragile (Menner et al. 2006). This is a major drawback in terms of real industrial applicability.

Several approaches can be used to improve the mechanical property of a poly-HIPE. In this respect, increasing the density by increasing the volume fraction of

monomer (or decreasing the volume fraction of internal phase) is usually yields polyHIPEs with improved modulus values. However, high surfactant concentrations cause the polymer to plasticize and decrease mechanical strength (Williams et al. 1990). The ratio of crosslinking and copolymerization with monomers that add flexibility to the final polymer network also has a significant effect on mechanical properties (Mert et al. 2019). For example, increasing the ratio of crosslinking can increase the modulus of the polymer matrix while reducing toughness (Silverstein and Cameron 2010). Copolymerization of rigid monomer units with monomers consisting of flexible groups increases the toughness while decreasing the modulus. In addition, copolymerizing with monomers that possess low glass transition temperature (Tg) both reduces brittleness and modulus (Sergienko et al. 2002). Another way of improving the polyHIPE mechanical properties is using a cyclic monomer such as DCPD which provides excellent modulus values and reduces brittleness to the polymer network (Kovačič and Krajnc 2009; Barbetta et al. 2009; Majer and Krajnc 2010; Koler and Krajnc 2021). On the other hand, while polyDCPD-based polyHIPEs synthesized via ROMP of DCPD monomer in the external phase of a HIPE offers tremendous compression modulus as high as 278 MPa, susceptibility of the polyDCPD chain to oxidation leads significant decrement of the modulus in time (Yüce et al. 2019). However, this decrement caused by oxidation can be inhibited to a level by using antioxidants during polyHIPE synthesis (Yüce et al. 2019). In addition, supporting the polyHIPE matrix with fillers or nanoparticles can be also used as a tool for improving mechanical properties (Yüce et al. 2018; Mert and Mert 2021).

5 PolyHIPE Applications

PolyHIPEs find many application areas in the field of materials science. These polymeric materials can be used in many engineering applications such as separation and filtration processes, adsorption process, tissue engineering, catalysis, enzyme immobilization, energy storage, etc., due to their low density, open cellular structure, and high absorbance capacity. Among all, the main area of interest is separation applications, but tissue engineering also has an important place. In the last decade, energy storage has also become an important application for polyHIPEs due to the increasing interest in new energy sources. Therefore, some important applications of polyHIPEs is presented in this section.

5.1 *Adsorption/Separation/Filtration Processes*

PolyHIPEs provide desired properties for adsorption with their modest surface area and macropores and play a major role in increasing the adsorption capacity. However, high adsorption efficiency requires interactions between the polyHIPE and

the adsorbed species. In this respect, Van der Waals forces, hydrogen bonding, and π–π interactions play an important role (Luo et al. 2021). Based on the target, functional groups with high affinity for the substance can be incorporated into the polyHIPE skeleton to obtain highly selective functional materials with adsorbent properties. Thereby, cost-effective and highly efficient materials can be easily prepared by altering the experimental conditions.

PolyHIPEs are useful for adsorption of oil-based substances since most of the polyHIPES have a hydrophobic structure. Due to hydrophobicity, when they are placed in a mixture containing oil and water, they can be used as sorbents in removing undesired impurities from water by adsorbing only the oily phase. Until today, polyHIPEs were used for separation of metal ions, removal of aquatic pollutants, and adsorption of dyes from aqueous solutions. In this respect, magnetic polyHIPEs exhibiting highly macroporous structure was synthesized in the presence of humic acid modified Fe_3O_4 nanoparticles for separation of heavy metal ions from water, and adsorption of Hg(II) ions at pH 4, 7, and 10 were investigated (Mert et al. 2013). Hg(II) sorption capacities of magnetic polyHIPE monoliths with 30% by weight of modified Fe_3O_4 were found as 20.44 mmol/g at pH $= 4$, 7.44 mmol/g at pH $= 10$, and 3.45 mmol/g at pH $= 7$ (Fig. 6). In another study conducted by Barlık et al. (2015), styrene and divinyl based polyHIPE discs, which were modified by chloromethylation and amination for usage as anion exchange monoliths, were designed for Cr(VI) ion removal from aqueous solution. After anionic functionality was achieved, the obtained light-yellow polymer discs were used for Cr (VI) ion removal from aqueous solution in an adsorption test apparatus, and the maximum Cr (VI) adsorption of the designed adsorbent were found to be 126.58 mg Cr (VI)/g. In the follow up study, anionic polyHIPE monoliths were also evaluated in terms of removal of nitrate ions from aqueous solution (Barlık et al. 2016). According to the test results of experiments performed in the same test apparatus, it was concluded that polyHIPE monolith behaves as an anion exchanger resin and it was effective for anion removal.
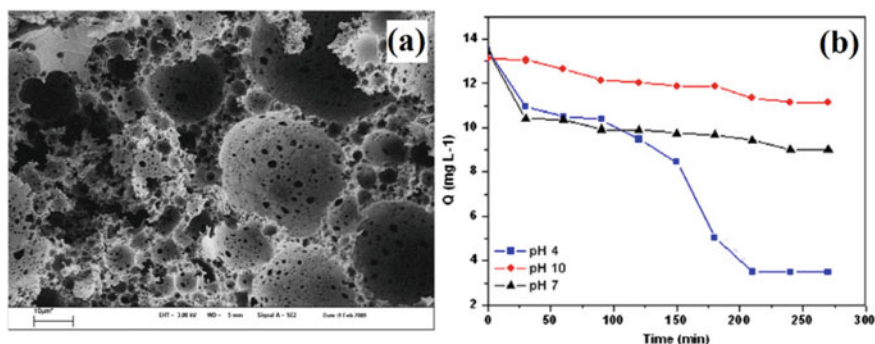
Fig. 6 a SEM image of the magnetic polyHIPE. **b** Hg(II) adsorption capacity of the magnetic polyHIPE monolith at different pH values. Reproduced from Mert et al. (2013), copyright 2013, with permission from Elsevier

More recently, a biosorbent material was also used for the development of poly-HIPE adsorbents by Mert et al. (2018). In this respect, a series of polyHIPE nanocomposites included Spirulina (Sp) immobilized nanoclay were used for cationic dye adsorption. Immobilization of Sp biosorbent onto montmorillonite (MMT) clay was achieved by two types of methods; conventional physical adsorption in solution (SOL) and cryoscopic expansion (C-XP). The higher adsorption capacity was found for the composite material which has modified clay with C-XP assisted (SpXPM clay). In addition, found that the polyHIPE composite prepared by using only 2% surfactant, 0.5% SpXPM clay loaded exhibited 578% higher Nile Blue adsorption capacity in comparison with the neat polyHIPE.

Macroporous foams prepared from Pickering-HIPEs which were stabilized with lignin particles were also used for the adsorption of Cu(II) ions from aqueous solution of $CuSO_4$ (Yang et al. 2013). It was observed that the adsorption capacity for Cu^{+2} increased regularly with the increasing pH. It was determined that the polyHIPE foams with an open-cell structure displayed higher adsorption capacity than those with a closed-cell structure, and the foam with the largest surface area demonstrated the highest adsorption capacity (73.2 mg/g). Moreover, researchers observed that the polyHIPE foam with higher permeability reached the adsorption equilibrium faster (72 min). The potential adsorbent was also proposed for removal of metal ions such as Cd^{+2}.

In another study, functionalized polyHIPE supports carrying piperazine parts were used for separating atrazine from aqueous solutions. It was observed that the polyHIPE support demonstrated better performance in comparison with chemically identical polymer beads thanks to their higher porosity (Pulko et al. 2007).

PolyHIPEs allow reactants and solvents to pass through their pores at very low pressures thanks to their structure composed of large cavities and interconnected pores. Accordingly, their usage is increasing gradually in separation media such as membrane systems. In this context, polyHIPEs also applied in chromatographic separation processes. For instance, methacrylate based polyHIPE monoliths were used for separation of standard protein mixtures as chromatographic support after modification of epoxy groups. By this study, researchers reported that polyHIPE monoliths have a developable potential as a support material for separation media (Krajnc et al. 2005a). In another work, researchers synthesized graphene oxide nanoparticle-modified (GONP-modified) polyHIPE stationary phases and used for reversed phase liquid chromatographic separation of alkylbenzenes (Choudhury et al. 2017). It was observed that, although a decrement in surface area was observed after addition of nanoparticles, GOBNP- modified column exhibited effective separation in comparison with existing GONP/silica stationary phases. Another chromatographic application of polyHIPEs as stationary phase of thin-layer chromatography (TLC) was reported by Yin et al. (2017). Yin and co-workers synthesized polyHIPE plates from HIPEs consisting of S, DVB and butyl acrylate (BuAc). The researchers used both herb extracts and herbs for the evaluation of the performance of TLC analysis and demonstrated the performance and reusability of polyHIPE plates in TLC.

Poly(butyl acrylate) based polyHIPE monoliths as microfiltration membranes composed of hydrophobic body with hydrophilic surface were designed and used

for separation of microalgae by Malakian et al. (2019). For this purpose, HIPEs consisted of BuAc in the continuous phase and sodium acrylate in the aqueous phase were used to obtain polyHIPEs with increased permeability. According to the permeation test, it was reported that the synthesized membranes have higher permeability and displayed better performance than available microfiltration membranes used for separating microalgae.

5.2   Tissue Engineering

Tissue engineering is an important field that requires multidisciplinary work in order to make a progress. Scientists have been doing research on new materials and material preparation techniques to prevent tissue loss and organ failure for many years. While the major aim is to produce scaffolds that are biocompatible, biodegradable, and enables production of healthy tissues, open cellular polymer scaffolds are of great interest (Akay et al. 2004). Porosity is an important feature in tissue engineering because matrixes have to allow nutrients to reach developing tissue and facilitate removal of waste products (Busby et al. 2001, 2002; O'Brien 2011). In the last two decades, polyHIPEs have shown increasing potential as tissue scaffolds due to their pore morphology allowing cell anchorage and growth.

In this respect, Busby et al. (2001) described preparation of highly permeable and partially biodegradable PCL based polyHIPEs by free radical copolymerization of a PCL macromonomer in the external phase of a HIPE. The resulting polyHIPEs were shown to be biocompatible to support cell function and growth of human fibroblasts over a period of 2.5 days. In the follow up study, Busby et al. (2002) reported synthesis of polyHIPE foams containing PLA. The biological efficiency of the obtained poly-HIPE foams was investigated with chicken embryo explants, rat skin explants, and individual human fibroblasts. It was demonstrated that polyHIPE foams had good biocompatibility to support adhesion, spread, and proliferation of cells.

Akay et al. (2004) reported that the hydroxyapatite (HA) modified poly(S-*co*-DVB) based polyHIPE supports osteoblast differentiation and bone growth in vitro, due to the increased penetration and migration of cells. However, polystyrene-based polyHIPEs are not biodegradable. But they are promising as routine 3D cell cultures which are cost-effective, non-degradable, and inert. In this respect Alvetex® is a novel industrial polystyrene-polyHIPE that was developed as a routine 3D cell culture for incorporation into existing cell culture products, such as multi-welled plates or well inserts (Knight et al. 2011).

Biodegradable polyHIPE scaffolds were also reported by several groups. In this respect, Christenson et al. (2007) described fully biodegradable fumarate-based polyHIPEs as potential bone graft materials. More recently, Naranda et al. (2016) reported biodegradable polyester-type polyHIPE with an open-porous architecture that promotes human derived chondrocyte proliferation and cartilage growth with all the other requirements of an ideal scaffold including biodegradability, biocompatibility, and mechanical strength (Fig. 7) (Naranda et al. 2016).
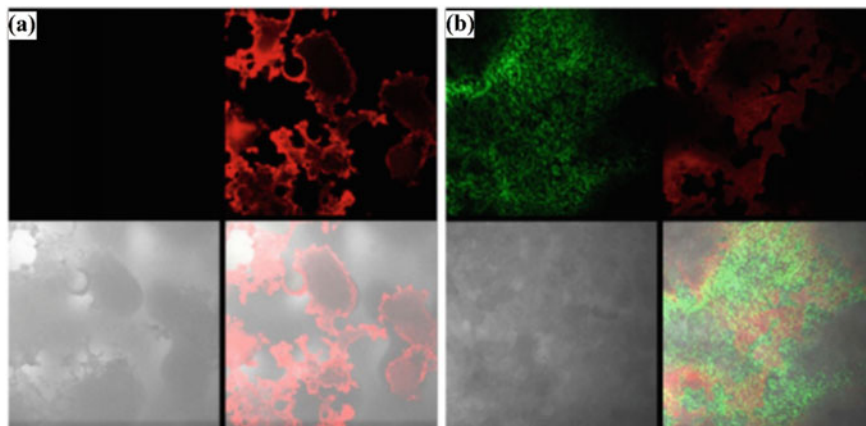
Fig. 7 Confocal microscopy of polyHIPE sample and polyHIPE-chondrocyte constructs. Confocal microscope images **a** polyHIPE sample (without cells) after live/dead staining, **b** polyHIPE-chondrocyte constructs after cell seeding (7 days) and live/dead staining. Reprinted from Naranda et al. (2016)

A combination of HIPE templating and microstereolithography was used by Owen et al. to fabricate polyHIPE scaffolds (Fig. 8) (Owen et al. 2016). In this respect, EHA and IBOA based polyHIPEs with varying nominal porosities and mechanical properties were described. Moreover, proliferation and penetration of human embryonic
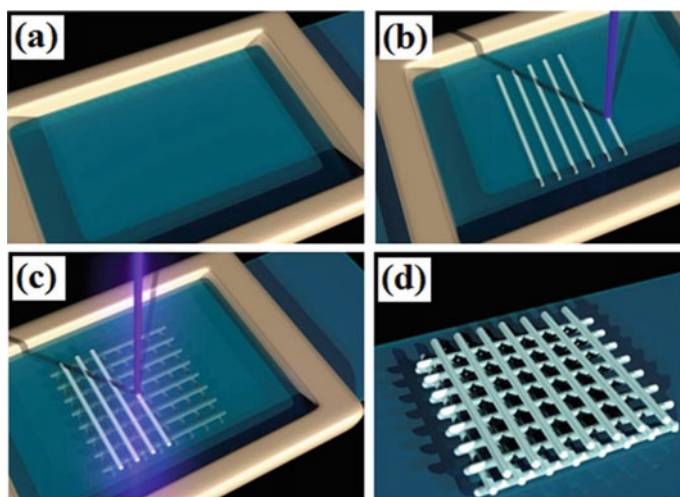
Fig. 8 Steps of production of a polyHIPE scaffold by microstereolithography: **a** Pipetting HIPE onto a functionalized coverslip, **b** Laser beaming of the coverslip-HIPE interface and writing the bottom layers, **c** Additional HIPE addition on the first layer of fibers, and laser beaming and writing of the second layer, **d** Resulting polyHIPE scaffold. Reprinted from Owen et al. (2016)

stem-cell derived mesenchymal progenitor cells into the micro and macroporous architecture was confirmed. Direct-write UV-stereolithography technique was also used to prepare HA incorporated polyHIPE scaffolds exhibiting multi-scale porosity and proposed as ideal scaffolds for tissue engineering vascularized bone (Wang et al. 2016).

5.3 Organic Reactions and Catalysis

Catalysis has great importance in chemical processes. Increasing the surface area to increase catalytic activity or supporting the catalyst is an important approach to facilitate rapid migration of reagents to active sites or migration of products from active sites. Therefore, supporting materials exhibiting micro-/mesoporosity are in the service of catalytic processes. PolyHIPEs also provide great advantages with their highly permeable pore structures as support materials for catalytic processes.

There are several important studies suggesting new application fields to poly-HIPEs in the catalysis of chemical reactions. So far, Pd-containing polyHIPEs were utilized as catalysts for the hydrogenation of allyl alcohol (Desforges et al. 2005a), Suzuki–Miyaura reaction (Desforges et al. 2005b), Heck coupling reaction (Ungureanu et al. 2008) and catalytic hydrogenation of phenylacetylene (PhAc) (Mrówka et al. 2020).

More recently, the efficiency of polyDCPD-based nanocomposite polyHIPE catalyst in advanced oxidation processes (AOP) was reported by Yeşil and Çetinkaya (2020). For this purpose, polyDCPD-based polyHIPEs were synthesized with various amounts of trimanganese tetraoxide (Mn_3O_4), and then the nanocomposite polyHIPE with 5 wt% of Mn_3O_4 was used as a model catalyst in heterogeneous oxidation of phenol. According to their results, while the highest kinetic constant achieved was $0.0611\ min^{-1}$, no significant activity loss was determined after four cycles.

PolyDCPD-based polyHIPE composites were also developed by Yüce et al. (2017) for the heterogeneous photocatalytic degradation of 4-nitrophenol (NP). For this purpose, surface modified TiO_2 was used to prepare Pickering-HIPEs, and to obtain polyHIPE/TiO_2 composites. It was shown that by using a Pickering-polyHIPE photocatalyst, photodegradation ratio of 4-nitrophenol irradiated 540 min can be reached up to 53%.

Recently, the preparation of polyHIPE by photo-initiated polymerization of HIPEs has also received increasing interest. In this respect, Wang et al. (2014) demonstrated the preparation of a π-conjugated polyHIPE showing high efficiency as a heterogeneous photosensitizer for singlet oxygen generation under visible light. Moreover, they tested the efficiency of the prepared polyHIPE initiator in the photopolymerization of MMA and reported the minimized odor, toxicity, and migration problems with the use of the novel polyHIPE photoinitiator. Yuan et al. (2018) prepared functional highly porous polyHIPE monolith which included immobilized gold nanoparticles on

its surface and investigated its catalytic performance for the catalytic reduction of 4-nitrophenol. The macroporous polyHIPE demonstrated reusability after a minimum 10 cycles without any observation of decline of activity.

5.4 Energy Storage

In recent works, polyHIPEs has been employed as support material for energy storage applications such as hydrogen storage, shape stabilization of phase change materials, etc. Macroporous polyHIPEs also have the potential of usage as support materials for hydrogen storage thanks to their unique structure composed of cavities with interconnected pores in addition to low density (Su et al. 2008). In this respect, carbon based polyHIPE foams (carboHIPEs) were also designed as electrocatalysts support for the applications in direct methanol fuel cell Yi et al. (2016a). The acrylonitrile/divinyl benzene-based template was used as support for PtRu alloy nanoparticles after hypercrosslinking and electrocatalytic performance of obtained materials was tested. According to the obtained results, PtRu/carboHIPE was displayed excellent performance in comparison with available commercial catalysts included approximately same Pt content.

Controllable porous structure and increasable surface area, improvable mechanical properties, facility of synthesis from chemicals coherent with energy storage materials have been also made emulsion templated polymers (polyHIPEs) an attractive matrix for preparation of shape-stabilized composite phase change materials (PCMs). PCMs are functional materials based on the latent heat storage approach which are preferred as thermal energy storage materials for sustainability of thermal comfort in many applications and thermal management of systems. These latent heat storage materials may cause serious damage in application areas such as electronic devices or energy systems because of leakage problems. Providing shape stabilization of these materials via limiting them in a proper supporting matrix has increasing interest due to disadvantage of direct usage of them.

Polystyrene-based polyHIPE foams were used for achieving microencapsulation of erythritol and xylitol as PCMs (Puupponen et al. 2016). For this purpose, polyol-polystyrene composites were prepared by dissolving polyols in the aqueous phase of emulsion system after optimizing the foam structure by controlling the experimental parameters. It was found that incorporation fractions of erythritol and xylitol into the foam was found to be 62 and 67 wt% in addition that obtained composite PCMs displayed more controlled and rapid heat release manners as compared to bulk PCMs. In another work, biobased PCMs were prepared via encapsulation of butyl stearate onto pullulan foam by emulsion templating approach (Balderrama et al. 2018). In this respect, while pullulan was used as the matrix, butyl stearate which was acting as PCM was used as the dispersed phase of emulsion. The optimum concentration of pullulan and butyl stearate in emulsion system besides drying methods for removing water was investigated. The latent heat of melting was found to be 33 J/g for synthesized pullulan poly(low internal phase emulsion) (polyLIPE) encapsulating butyl

stearate and phase change temperatures did not observe significant change. Based on their findings, emulsion templating strategy is reported as an applicable method for encapsulation of PCMs, by the researchers.

Shape stabilization of energy storage materials by employing polyHIPEs can be also achieved via incorporation PCM into porous polyHIPE support matrix by one step impregnation method after obtained polyHIPE monolith with well-designed porosity. In this context, Mert (2020) prepared polyHIPE composites containing surface modified montmorilonite clay for shape stabilization of n-hexadecane as PCM (Fig. 9). The polyHIPE composite, which possesses desirable morphology and highest compression modulus, was selected as framework for producing form-stable PCM by one step impregnation method. It was reported that the obtained form-stable PCM demonstrated high latent heat storage capacity (143.41 J/g), thermal stability, leakproof property, and has remarkable potential for thermal management of systems in building applications.

Closed-cell, flexible, PCM encapsulated-polyHIPE monoliths were synthesized via interfacial thiol-Michael addition by Zhang and co-workers using n-octadecane as PCM (Zhang et al. 2020). It was reported that the obtained flexible monoliths not only showed high heat storage capacity (up to 213 J/g) but also displayed reusability
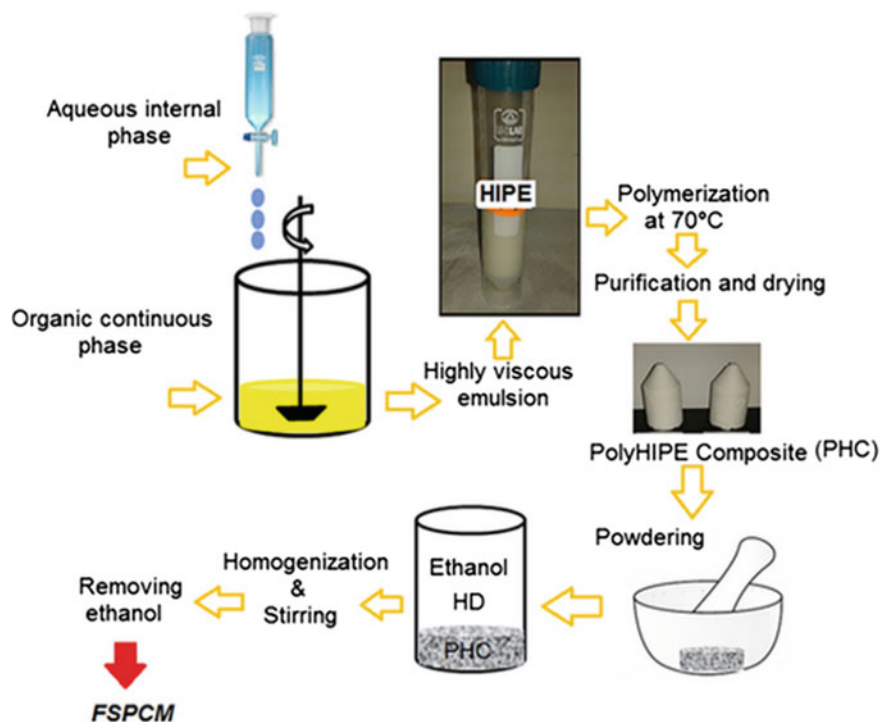
Fig. 9 Preparation route of shape-stabilized PCM via employing polyHIPE material. Reprinted from Mert (2020), copyright 2020, with permission from John Wiley & Sons, Inc

and chemical stability properties by maintaining heat capacity after heating–cooling for 100 cycles.

6 Conclusion

Emulsion templating provides the advantages of creating porous polymer foams, membranes, beads, or rods with a diverse morphology. Preparation of polymers exhibiting well-defined porosity and chemical functionality can be easily utilized by using HIPEs as templates. Since polyHIPEs are reflecting the precursor HIPE templates, by altering the droplet size and the chemical structure of the emulsion phases materials with notable properties can be obtained. Moreover, post-polymerization approaches can be also easily adapted to improve the surface area or include additional chemical functionality. In-situ or one-pot approaches can be also carried out easily to achieve functionalization of polyHIPEs. PolyHIPEs are being used in a wide range of areas including thermal and electrochemical energy storage applications, tissue engineering, 3D cell cultures, chromatography, and catalysis.

References

Agrawal, M., Yadav, A., Nandan, B., Srivastava, R.K.: Facile synthesis of templated macrocellular nanocomposite scaffold via emulsifier-free HIPE-ROP. Chem. Commun. **56**, 12604–12607 (2020). https://doi.org/10.1039/d0cc05331g

Akay, G., Birch, M.A., Bokhari, M.A.: Microcellular polyHIPE polymer supports osteoblast growth and bone formation in vitro. Biomaterials **25**, 3991–4000 (2004). https://doi.org/10.1016/j.biomaterials.2003.10.086

Alexandratos, S.D., Beauvais, R., Duke, J.R., Jorgensen, B.S.: Functionalized polymer foams as metal ion chelating agents with rapid complexation kinetics. J. Appl. Polym. Sci. **68**, 1911–1916 (1998). https://doi.org/10.1002/(SICI)1097-4628(19980620)68:12%3c1911::AID-APP3%3e3.0.CO;2-O

Althubeiti, K.M., Horozov, T.S.: Efficient preparation of macroporous poly(methyl methacrylate) materials from high internal phase emulsion templates. Reacti. Func. Polym. **142**, 207–212 (2019). https://doi.org/10.1016/j.reactfunctpolym.2019.06.015

Audouin, F., Birot, M., Pasquinet, É., Deleuze, H., Besnard, O., Poullain, D.: Synthesis of porous materials by 2-nitroresorcinol/cyanuric chloride thermal polycondensation in emulsions. J. Appl. Polym. Sci. **108**, 2808–2813 (2008)

Ayres, N.: Atom transfer radical polymerization: a robust and versatile route for polymer synthesis. Polym. Rev. **51**, 138–162 (2011). https://doi.org/10.1080/15583724.2011.566402

Azhar, U., Huyan, C., Wan, X., Zong, C., Xu, A., Liu, J., Ma, J., Zhang, S., Geng, B.: Porous multifunctional fluoropolymer composite foams prepared via humic acid modified Fe_3O_4 nanoparticles stabilized Pickering high internal phase emulsion using cationic fluorosurfactant as co-stabilizer. Arabian J. Chem. **12**, 559–572 (2019). https://doi.org/10.1016/j.arabjc.2018.04.003

Balderrama, J.A.M., Dourges, M.A., Magueresse, A., Maheo, L., Deleuze, H., Glouannec, P.: Emulsion-templated pullulan monoliths as phase change materials encapsulating matrices. Mater. Today Commun. **17**, 466–473 (2018). https://doi.org/10.1016/j.mtcomm.2018.10.012

Barbara, I., Dourges, M.A., Deleuze, H.: Preparation of porous polyurethanes by emulsion-templated step growth polymerization. Polymer **132**, 243–251 (2017). https://doi.org/10.1016/j.polymer.2017.11.018

Barbetta, A., Cameron, N.R.: Morphology and surface area of emulsion-derived (polyHIPE) solid foams prepared with oil-phase soluble porogenic solvents: three-component surfactant system. Macromolecules **37**, 3202–3213 (2004). https://doi.org/10.1021/ma035944y

Barbetta, A., Dentini, M., Leandri, L., Ferraris, G., Coletta, A., Bernabei, M.: Synthesis and characterization of porous glycidylmethacrylate–divinylbenzene monoliths using the high internal phase emulsion approach. React. Func. Polym. **69**, 724–736 (2009). https://doi.org/10.1016/j.reactfunctpolym.2009.05.007

Barby, D., Haq, Z.: US Patent 4522953 (1985)

Barlık, N., Keskinler, B., Kocakerim, M.M., Akay, G.: Surface modification of monolithic PolyHIPE polymers for anionic functionality and their ion exchange behavior. J. Appl. Polym. Sci. **132**, 42286 (2015). https://doi.org/10.1002/app.42286

Barlık, N., Keskinler, B., Kocakerim, M.M., Akay, G.: Functionalized PolyHIPE polymer monoliths as an anion-exchange media for removal of nitrate ions from aqueous solutions. Desalin. Water Treat. **57**, 26440–26447 (2016). https://doi.org/10.1080/19443994.2016.1164083

Benaddi, A.O., Cohen, O., Matyjaszewski, K., Silverstein, M.S.: RAFT polymerization within high internal phase emulsions: Porous structures, mechanical behaviors, and uptakes. Polymer **213**,(2021). https://doi.org/10.1016/j.polymer.2020.123327

Benmachou, K., Deleuze, H., Herogueza, V.: Ring opening polymerisation of highly concentrated inverse emulsions to obtain microcellular foams. React. Funct. Polym. **55**, 211–217 (2003). https://doi.org/10.1016/S1381-5148(02)00248-1

Benicewicz, B.C., Jarvinen, G.D., Kathios, D.J., Jorgensen, B.S.: Open-celled polymeric foam monoliths for heavy metal separations study. J. Radioanal. Nucl. Chem. **235**, 31–35 (1998). https://doi.org/10.1007/BF02385933

Busby, W., Cameron, N.R., Jahoda, C.A.B.: Emulsion-derived foams (polyHIPEs) containing poly(ε-caprolactone) as matrixes for tissue engineering. Biomacromol **2**, 154–164 (2001). https://doi.org/10.1021/bm0000889

Busby, W., Cameron, N.R., Jahoda, C.A.B.: Tissue engineering matrixes by emulsion templating. Polym. Int. **51**, 871–881 (2002). https://doi.org/10.1002/pi.934

Butler, R., Hopkinson, I., Cooper, A.I.: Synthesis of porous emulsion-templated polymers using high internal phase CO_2-in-water emulsions. J. Am. Chem. Soc. **125**, 14473–14481 (2003). https://doi.org/10.1021/ja037570u

Caldwell, S., Johnson, D.W., Didsbury, M.P., Murray, B.A., Wu, J.J., Przyborskibd, Stefan A., Cameron, N.R.: Degradable emulsion-templated scaffolds for tissue engineering from thiol–ene photopolymerisation. Soft. Matter **8**, 10344–10351 (2012). https://doi.org/10.1039/C2SM26250A

Cameron, N.R.: High internal phase emulsion templating as a route to well-defined porous polymers. Polymer **46**, 1439–1449 (2005). https://doi.org/10.1016/j.polymer.2004.11.097

Cameron, N.R., Sherrington, D.C.: High internal phase emulsions (HIPEs)—structure, properties and use in polymer preparation. In: Biopolymers Liquid Crystalline Polymers Phase, Emulsion. Advances in Polymer Science, vol. 126. Springer, Berlin (1996). https://doi.org/10.1007/3-540-60484-7_4

Cameron, N.R., Sherrington, D.C.: Preparation and glass transition temperatures of elastomeric PolyHIPE materials. J. Mater. Chem. **7**, 2209–2212 (1997). https://doi.org/10.1039/A702030I

Cameron, N.R., Sherrington, D.C., Albiston, L., Gregory, D.P.: Study of the formation of the open-cellular morphology of poly(styrene/divinylbenzene) polyHIPE materials by cryo-SEM. Colloid Polym. Sci. **274** (1996). https://doi.org/10.1007/BF00655236

Cameron, N.R., Krajnc, P., Silverstein, M.S.: Colloidal templating. In: Silverstein, M.S., Cameron, N.R., Marc, A. (eds.) Porous Polymers, pp. 119–172. Hillmyer. Wiley, Hoboken (2011)

Carnachan, R.J., Bokhari, M., Przyborskibc, S.A., Cameron, N.R.: Tailoring the morphology of emulsion-templated porous polymers. Soft Matter **2**, 608–616 (2006). https://doi.org/10.1039/B603211G

Cauvin, S., Colver, P.J., Bon, S.A.F.: Pickering stabilized miniemulsion polymerization: preparation of clay armored latexes. Macromolecules **38**, 7887–7889 (2005). https://doi.org/10.1021/ma051070z

Chen, C., Eissa, A.M., Schiller, T.L., Cameron, N.R.: Emulsion-templated porous polymers prepared by thiol-ene and thiol-yne photopolymerisation using multifunctional acrylate and non-acrylate monomers. Polymer **126**, 395–401 (2017). https://doi.org/10.1016/j.polymer.2017.04.021

Chevalier, Y., Bolzinger, M.A.: Emulsions stabilized with solid nanoparticles: pickering emulsions. Colloid Surf. A Physicochem. Eng. Asp. **439**, 23–34 (2013). https://doi.org/10.1016/j.colsurfa.2013.02.054

Christenson, E.M., Soofi, W., Holm, J.L., Cameron, N.R., Mikos, A.G.: Biodegradable fumarate-based polyHIPEs as tissue engineering scaffolds. Biomacromol **8**, 3806–3814 (2007). https://doi.org/10.1021/bm7007235

Cohen, N., Silverstein, M.S.: Synthesis of emulsion-templated porous polyacrylonitrile and its pyrolysis to porous carbon monoliths. Polymer **52**, 282–287 (2011). https://doi.org/10.1016/j.polymer.2010.11.026

Choudhury, S., Duffy, E., Connolly, D., Paull, B., White, B.: Graphene oxide nanoparticles and their influence on chromatographic separation using polymeric high internal phase emulsions. Separations **4**, 5 (2017). https://doi.org/10.3390/separations4010005

Davankov, V.A., Tsyurupa, M.P.: Structure and properties of hypercrosslinked polystyrene—the first representative of a new class of polymer networks. React. Polym. **13**, 27–42 (1990). https://doi.org/10.1016/0923-1137(90)90038-6

David, D., Silverstein, M.S.: Porous polyurethanes synthesized within high internal phase emulsions. J. Polym. Sci., Part a: Polym. Chem. **47**, 5806–5814 (2009). https://doi.org/10.1002/pola

Desforges, A., Deleuze, H., Mondain-Monval, O., Backov, R.: Palladium nanoparticle generation within microcellular polymeric foam and size dependence under synthetic conditions. Ind. Eng. Chem. Res. **44**, 8521–8529 (2005). https://doi.org/10.1021/ie040239e

Desforges, A., Backov, R., Deleuze, H., Mondain-Monval, O.: Generation of palladium nanoparticles within macrocellular polymeric supports: application to the heterogeneous catalysis of the Suzuki-Miyaura coupling reaction. Adv. Funct. Mater. **15**, 1689–1695 (2005). https://doi.org/10.1002/adfm.200500146

Elmes, A.R., Hammond, K., Sherrington, D.C.: EP 289238 (1994)

Esser-Kahn, A.P., Odom, S.A., Sottos, N.R., White, S.R., Moore, J.S.: Triggered release from polymer capsules. Macromolecules **44**, 5539–5553 (2011). https://doi.org/10.1021/ma201014n

Flory, P.J.: Fundamental principles of condensation polymerization. Chem. Rev. **39**(1), 137–197 (1946). https://doi.org/10.1021/cr60122a003

Freire, M.G., Dias, A.M.A., Coelho, M.A.Z., Coutinho, J.A.P., Marrucho, I.M.: Aging mechanisms of perfluorocarbon emulsions using image analysis. J. Colloid Interface Sci. **286**, 224–232 (2005). https://doi.org/10.1016/j.jcis.2004.12.036

García-Landeros, S.A., Cervantes-Díaz, J.M., Gutiérrez-Becerra, A., Pelayo-Vázquez, J.B., Landazuri-Gomez, G., Herrera-Ordonez, J., Soltero-Martínez, J.F.A., Mota-Morales, J.D., Pérez-García, M.G.: Oil-in-eutectic mixture HIPEs co-stabilized with surfactant and nanohydroxyapatite: ring-opening polymerization for nanocomposite scaffold synthesis. Chem. Commun. **55**, 12292–12295 (2019). https://doi.org/10.1039/C9CC06292K

Gokmen, M.T., Camp, W.V., Colver, P.J., Bon, S.A.F., Du Prez, F.E.: Fabrication of porous "clickable" polymer beads and rods through generation of high internal phase emulsion (HIPE) droplets in a simple microfluidic device. Macromolecules **42**, 9289–9294 (2009). https://doi.org/10.1021/ma9018679

Grosse, M.T., Lamotte, M., Birot, M., Deleuz, H.: Preparation of microcellular polysiloxane monoliths. J. Polym. Sci. Part A: Polym. Chem. **46**, 21–32 (2008). https://doi.org/10.1002/pola.22351

Gurevitch, I., Silverstein, M.S.: Nanoparticle-based and organic-phase-based AGET ATRP Poly-HIPE synthesis within Pickering HIPEs and surfactant-stabilized HIPEs. Macromolecules **44**, 3398–3409 (2011). https://doi.org/10.1021/ma200362u

Gurevitch, I., Silverstein, M.S.: One-pot synthesis of elastomeric monoliths filled with individually encapsulated liquid droplets. Macromolecules **45**, 6450–6456 (2012). https://doi.org/10.1021/ma301007s

Hainey, P., Huxham, I.M., Rowatt, B., Sherrington, D.C., Tetley, L.: Synthesis and ultrastructural studies of styrene-divinylbenzene polyHIPE polymers. Macromolecules **24**, 117–121 (1991). https://doi.org/10.1021/ma00001a019

Hamielec, A.E., Tobita, H.: Polymerization processes, 1. Fundamentals. In: Ullmann's encyclopedia of industrial chemistry, Wiley-VCH Verlag GmbH & Co. KGaA, Weinheim (2012). https://doi.org/10.1002/14356007.a21_305.pub2

Hoyle, C.E., Bowman, C.N.: Thiol–ene click chemistry. Angew. Chem. Int. Ed. **49**, 1540–1573 (2010). https://doi.org/10.1002/anie.200903924

Hu, Y., Wang, J., Li, X., Hu, X., Zhou, W., Dong, X., Wang, C., Yang, Z., Binks, B.P.: Facile preparation of bioactive nanoparticle/poly(ε-caprolactone) hierarchical porous scaffolds via 3D printing of high internal phase Pickering emulsions. J. Colloid. Interface Sci. **545**, 104–115 (2019). https://doi.org/10.1016/j.jcis.2019.03.024

Huš, S., Krajnc, P.: PolyHIPEs from methyl methacrylate: Hierarchically structured microcellular polymers with exceptional mechanical properties. Polymer **55**, 4420–4424 (2014). https://doi.org/10.1016/j.polymer.2014.07.007

Ikem, V.O., Menner, A., Bismarck, A.: High internal phase emulsions stabilized solely by functionalized silica particles. Angew. Chem. Int. Ed. **47**, 8277–8279 (2008). https://doi.org/10.1002/anie.200802244

Jakubowski, W., Matyjaszewski, K.: Activator generated by electron transfer for atom transfer radical polymerization. Macromolecules **38**, 4139–4146 (2005). https://doi.org/10.1021/ma0473891

Jeřábek, K., Pulko, I., Soukupova, K., Štefanec, D., Krajnc, P.: Porogenic solvents influence on morphology of 4-vinylbenzyl chloride based polyHIPEs. Macromolecules **41**, 3543–3546 (2008). https://doi.org/10.1021/ma8002104

Jerenec, S., Šimić, M., Savnik, A., Podgornik, A., Kolar, M., Turnšek, M., Krajnc, P.: Glycidyl methacrylate and ethylhexyl acrylate based polyHIPE monoliths: morphological, mechanical and chromatographic properties. React. Func. Polym. **78**, 32–37 (2014). https://doi.org/10.1016/j.reactfunctpolym.2014.02.011

Kabalnov, A.S., Shchukin, E.D.: Ostwald ripening theory: applications to fluorocarbon emulsion stability. Adv. Colloid Interface Sci. **38**, 69–97 (1992). https://doi.org/10.1016/0001-8686(92)80043-W

Kekevi, B., Mert, E.H.: Synthesis of β-myrcene-based macroporous nanocomposite foams: altering the morphological and mechanical properties by using organo-modified nanoclay. J. Appl. Polym. Sci. **138**, 50074 (2021). https://doi.org/10.1002/app.50074

Kimmins, S.D., Wyman, P., Cameron, N.R.: Photopolymerised methacrylate-based emulsion-templated porous polymers. React. Funct. Polym **72**, 947–954 (2012). https://doi.org/10.1016/j.reactfunctpolym.2012.06.015

Kirche, L., Theato, P., Cameron, N.R.: Reactive thiol-ene emulsion-templated porous polymers incorporating pentafluorophenyl acrylate. Polymer **54**, 1755–1761 (2013). https://doi.org/10.1016/j.polymer.2013.01.024

Knight, E., Murray, B., Carnachan, R., Przyborski, S.: Alvetex®: polystyrene scaffold technology for routine three dimensional cell culture. Methods Mol. Biol. **695**, 323–340 (2011). https://doi.org/10.1007/978-1-60761-984-0_20

Koler, A., Krajnc, P.: Macroporous titania monoliths from emulsion templated composites. Colloid Polym. Sci. **297**, 799–807 (2019). https://doi.org/10.1007/s00396-019-04504-7

Koler, A., Krajnc, P.: Surface modification of hypercrosslinked vinylbenzyl chloride polyHIPEs by grafting via raft. Macromol. Chem. Phys. **222**, 2000381 (2021). https://doi.org/10.1002/macp.202000381

Koler, A., Pulko, I., Krajnc, P.: Post polymerisation hypercrosslinking with emulsion templating for hierarchical and multi-level porous polymers. Acta Chim. Slov. **67**, 349–360 (2020). https://doi.org/10.17344/acsi.2020.5901

Kovačič, S.: Ring opening metathesis polymerisation (ROMP) as a tool for PolyHIPEs with extraordinary mechanical properties. Acta Chim. Slov. **60**, 448–454 (2013)

Kovačič, S., Krajnc, P.: Macroporous monolithic poly(4-vinylbenzyl chloride) columns for organic synthesis facilitation by in situ polymerization of high internal phase emulsions. J. Polym Sci. Part A Polym. Chem. **47**, 6726–6734 (2009). https://doi.org/10.1002/pola.23732

Kovačič, S., Slugovc, C.: Ring-opening metathesis polymerisation derived poly(dicyclopentadiene) based materials. Mater. Chem. Front. **4**, 2235–2255 (2020). https://doi.org/10.1039/D0QM00296H

Kovačič, S., Štefanec, D., Krajnc, P.: Highly porous open-cellular monoliths from 2-hydroxyethyl methacrylate based high internal phase emulsions (HIPEs): preparation and void size tuning. Macromolecules **40**, 8056–8060 (2007). https://doi.org/10.1021/ma071380c

Kovačič, S., Krajnc, P., Slugovc, C.: Inherently reactive polyHIPE material from dicyclopentadiene. Chem. Commun. **46**, 7504–7506 (2010). https://doi.org/10.1039/C0CC02610G

Kovačič, S., Jeřabek, K., Krajnc, P.: Responsive poly(acrylic acid) and poly(n-isopropylacrylamide) monoliths by high internal phase emulsion (HIPE) templating. Macromol. Chem. Phys. **212**, 2151–2158 (2011). https://doi.org/10.1002/macp.201100229

Kovačič, S., Jeřábek, K., Krajnc, P., Slugovc, C.: Ring opening metathesis polymerisation of emulsion templated dicyclopentadiene giving open porous materials with excellent mechanical properties. Polym. Chem. **3**, 325–328 (2012). https://doi.org/10.1039/C2PY00518B

Kovačič, S., Matsko, N.B., Ferk, G., Slugovc, C.: Nanocomposite foams from iron oxide stabilized dicyclopentadiene high internal phase emulsions: preparation and bromination. Acta Chim. Slov. **61**, 208–214 (2014)

Kovačič, S., Preishuber-Pflügl, F., Pahovnik, D., Žagar, E., Slugovc, C.: Covalent incorporation of the surfactant into high internal phase emulsion templated polymeric foams. Chem. Commun **51**, 7725–7728 (2015). https://doi.org/10.1039/C4CC09199J

Kovalenko, A., Zimny, K., Mascaro, B., Brunet, T., Mondain-Monval, O.: Tailoring of the porous structure of soft emulsion-templated polymer materials. Soft Matter **12**, 5154–5163 (2016). https://doi.org/10.1039/C6SM00461J

Krajnc, P., Brown, J.F., Cameron, N.R.: Monolithic scavenger resins by amine functionalizations of poly(4-vinylbenzyl chloride-co-divinylbenzene) polyHIPE materials. Org. Lett. **4**(15), 2497–2500 (2002). https://doi.org/10.1021/ol026115k

Krajnc, P., Leber, N., Štefanec, D., Kontrec, S., Podgornik, A.: Preparation and characterisation of poly(high internal phase emulsion) methacrylate monoliths and their application as separation media. J. Chrom. A **1065**, 69–73 (2005). https://doi.org/10.1016/j.chroma.2004.10.051

Krajnc, P., Štefanec, D., Pulko, I.: Acrylic acid "reversed" polyHIPEs. Macromol. Rapid Commun. **26**, 1289–1293 (2005). https://doi.org/10.1002/marc.200500353

Kralchevsky, P.A., Ivanov, I.B., Ananthapadmanabhan, K.P., Lips, A.: On the thermodynamics of particle-stabilized emulsions: curvature effects and catastrophic phase inversion. Langmuir **21**, 50–63 (2005). https://doi.org/10.1021/la047793d

Kulygin, O., Silverstein, M.S.: Porous poly (2-hydroxyethyl methacrylate) hydrogels synthesized within high internal phase emulsions. Soft Matter **3**, 1525–1529 (2007). https://doi.org/10.1039/b711610a

Lafleur, J.P., Senkbeil, S., Novotny, J., Nys, G., Bøgelund, N., Rand, K.D., Foret, F., Kutter, J.P.: Rapid and simple preparation of thiol–ene emulsion-templated monoliths and their application

as enzymatic microreactors. Lab Chip **15**, 2162–2172 (2015). https://doi.org/10.1039/C5LC00224A

Lamson, M., Epshtein-Assor, Y., Silverstein, M.S., Matyjaszewski, K.: Synthesis of degradable polyHIPEs by AGET ATRP. Polymer **54**, 4480–4485 (2013). https://doi.org/10.1016/j.polymer.2013.06.048

Lee, A., Langford, C.R., Rodriguez-Lorenzo, L.M., Thissen, H., Cameron, N.R.: Bioceramic nanocomposite thiol-acrylate polyHIPE scaffolds for enhanced osteoblastic cell culture in 3D. Biomater. Sci. **5**, 2035–2047 (2017). https://doi.org/10.1039/C7BM00292K

Li, Z., Liu, H., Zeng, L., Liu, H., Wang. Y.: The facile synthesis of PMMA polyHIPEs with highly interconnected porous microstructures. J. Mater. Sci. **51**, 9005–9018 (2016). https://doi.org/10.1007/s10853-016-0154-7

Li, X., Zhang, C., Du, Z., Li, H.: Preparation of hydrophilic/hydrophobic porous materials. J. Colloid Interface Sci. **323**, 120–125 (2008). https://doi.org/10.1016/j.jcis.2008.03.028

Lissant, K.J.: The geometry of high-internal-phase-ratio emulsions. J. Colloid Interface Sci. **22**, 462–468 (1966). https://doi.org/10.1016/0021-9797(66)90091-9

Livshina, S., Silverstein, M.S.: Cross-linker flexibility in porous crystalline polymers synthesized from long side-chain monomers through emulsion templating. Soft Matter **4**, 1630–1638 (2008). https://doi.org/10.1039/B802173B

Lovelady, E., Kimmins, S.D., Wu, J., Cameron, N.R.: Preparation of emulsion-templated porous polymers using thiol–ene and thiol–yne chemistry. Polym. Chem. **2**, 559–562 (2011). https://doi.org/10.1039/C0PY00374C

Lowe, A.B.: Thiol-ene '"click"' reactions and recent applications in polymer and materials synthesis. Polym. Chem. **1**, 17–36 (2010). https://doi.org/10.1039/B9PY00216B

Luo, J., Huang, Z., Liu, L., Wang, H., Ruan, G., Zhao, C., Du, F.: Recent advances in separation applications of polymerized high internal phase emulsions. J. Sep. Sci. **44**, 169–187 (2021). https://doi.org/10.1002/jssc.202000612

Luo, Y., Wang, A.N., Gao, X.: Pushing the mechanical strength of polyHIPEs up to the theoretical limit through living radical polymerization. Soft Matter **8**, 1824–1830 (2012). https://doi.org/10.1039/C1SM06756G

Ma, L., Luo, X., Cai, N., Xue, Y., Zhu, S., Fu, Z., Yu, F.: Facile fabrication of hierarchical porous resins via high internal phase emulsion and polymeric porogen. Appl. Surf. Sci. **305**, 186–193 (2014). https://doi.org/10.1016/j.apsusc.2014.03.036

Ma, C., Wang, J., Cho, L.: Preparation of macroporous hybrid monoliths via iron-based MOFs-stabilized CO_2-in-water HIPEs and use for β-amylase immobilization. Polym. Adv. Technol. **31**, 2967–2979 (2020). https://doi.org/10.1002/pat.5019

Majer, J., Krajnc, P.: Amine functionalisations of glycidyl methacrylate based polyHIPE monoliths. Macromol. Symp. **296**, 5–10 (2010). https://doi.org/10.1002/masy.201051002

Majer, J., Paljevac, M., Žagar, E., Kovačič, S., Krajnc, P.: Functionalization of 2-hydroxyethyl methacrylate-based polyHIPEs: effect of the leaving group. React. Funct. Polym. **109**, 99–103 (2016). https://doi.org/10.1016/j.reactfunctpolym.2016.10.008

Malakian, A., Zhou, M., Zowada, R.T., Foudazi, R.: Synthesis and insitu functionalization of micro-filtration membranes via high internal phase emulsion templating. Polym. Int. **68**, 1378–1386 (2019). https://doi.org/10.1002/pi.5828

Mao, D., Li, T., Liu, H., Li, Z., Shao, H., Li, M.: Preparation of macroporous polyHIPE foams via radiation-induced polymerization at room temperature. Colloid Polym. Sci. **291**, 1649–1656 (2013). https://doi.org/10.1007/s00396-013-2899-8

Matyjaszewski, K.: Atom transfer radical polymerization (ATRP): current status and future perspectives. Macromolecules **45**, 4015–4039 (2012). https://doi.org/10.1021/ma3001719

Matyjaszewski, K., Spanswick, J.: Controlled/living radical polymerization. Materialstoday **8**, 26–33 (2005). https://doi.org/10.1016/S1369-7021(05)00745-5

Matyjaszewski, K., Xia, J.: Atom transfer radical polymerization. Chem. Rev. **101**, 2921–2990 (2001). https://doi.org/10.1021/cr940534g

Menner, A., Bismarck, A.: New evidence for the mechanism of the pore formation in polymerising high internal phase emulsions or why polyHIPEs have an interconnected pore network structure. Macromol. Symp. **242**, 19–24 (2006). https://doi.org/10.1002/masy.200651004

Menner, A., Haibach, K., Powell, R., Bismarck, A.: Tough reinforced open porous polymer foams via concentrated emulsion templating. Polymer **47**, 7628–7635 (2006). https://doi.org/10.1016/j.polymer.2006.09.022

Menner, A., Ikem, V., Salgueiro, M., Shaffer, M.S.P., Bismarck, A.: High internal phase emulsion templates solely stabilised by functionalised titania nanoparticles. Chem. Commun. **41**, 4274–4276 (2007a). https://doi.org/10.1039/B708935J

Menner, A., Verdejo, R., Shaffer, M., Bismarck, A.: Particle-stabilized surfactant-free medium internal phase emulsions as templates for porous nanocomposite materials: poly-pickering-foams. Langmuir **23**, 2398–2403 (2007b). https://doi.org/10.1021/la062712u

Mert, E.H., Kaya, M.A., Yıldırım, H.: Preparation and characterization of polyester–glycidyl methacrylate polyHIPE monoliths to use in heavy metal removal. Des. Monomer. Polym. **15**, 113–126 (2012). https://doi.org/10.1163/156855511X615001

Mert, H.H.: PolyHIPE composite based-form stable phase change material for thermal energy storage. Int. J. Energy Res. **44**, 6583–6594 (2020). https://doi.org/10.1002/er.5390

Mert, E.H., Kekevi, B.: Synthesis of polyHIPEs through high internal phase emulsions of β-myrcene. Coloid. Polym. Sci. **298**, 1423–1432 (2020). https://doi.org/10.1007/s00396-020-04730-4

Mert, E.H., Mert, H.H.: Preparation of polyHIPE nanocomposites: Revealing the influence of experimental parameters with the help of experimental design approach. Polym. Compos. **42**, 724–738 (2021). https://doi.org/10.1002/pc.25861

Mert, H.H., Şen, S.: Synthesis and characterization of polyHIPE composites containing halloysite nanotubes. e-Polymers **16**, 419–428 (2016). https://doi.org/10.1515/epoly-2016-0175

Mert, E.H., Yıldırım, H., Üzümcü, A.T., Kavas, H.: Synthesis and characterization of magnetic polyHIPEs with humic acid surface modified magnetic iron oxide nanoparticles. React. Funct. Polym. **73**, 175–181 (2013). https://doi.org/10.1016/j.reactfunctpolym.2012.09.005

Mert, E.H., Slugovc, C., Krajnc, P.: Tailoring the mechanical and thermal properties of dicyclopentadiene polyHIPEs with the use of a comonomer. eXPRESS Polym. Lett. **9**, 344–353 (2015). https://doi.org/10.3144/expresspolymlett.2015.32

Mert, H.H., Tekay, E., Nugay, N., Nugay, T., Şen, S.: Adsorptive polyHIPE composites based on biosorbent immobilized nanoclay: effects of immobilization techniques. Polym. Eng. Sci. **58**, 1229–1240 (2018). https://doi.org/10.1002/pen.24684

Mert, H.H., Mert, M.S., Mert, E.H.: A statistical approach for tailoring the morphological and mechanical properties of polystyrene PolyHIPEs: looking through experimental design. Mater. Res. Express **6** (2019). https://doi.org/10.1088/2053-1591/ab437f

Mezhouda, S., Paljevac, M., Koler, A., Droumaguet, B.L., Grande, D., Krajnc, P.: Novel hypercrosslinking approach toward high surface area functional 2-hydroxyethyl methacrylate-based polyHIPEs. React. Func. Polym. **132**, 51–59 (2018). https://doi.org/10.1016/j.reactfunctpolym.2018.09.009

Misra, P., Chitanda, J.M., Dalai, A.K., Adjaye, J.: Selective removal of nitrogen compounds from gas oil using functionalized polymeric adsorbents: efficient approach towards improving denitrogenation of petroleum feedstock. Chem. Eng. J. **295**, 109–118 (2016). https://doi.org/10.1016/j.cej.2016.03.024

Moghbeli, M.R., Khajeh, A., Alikhani, M.: Nanosilica reinforced ion-exchange polyHIPE type membrane for removal of nickel ions: preparation, characterization and adsorption studies. Chem. Eng. J. **309**, 552–562 (2017). https://doi.org/10.1016/j.cej.2016.10.048

Mrówka, J., Gackowski, M., Lityńska-Dobrzyńska, L., Bernasik, A., Kosydar, R., Drelinkiewicz, A., Hasik, M.: Poly(methylvinylsiloxane)-based high internal phase emulsion-templated materials (polyHIPEs)—preparation, incorporation of palladium, and catalytic properties. Ind. Eng. Chem. Res. **59**, 19485–19499 (2020). https://doi.org/10.1021/acs.iecr.0c03429

Naranda, J., Sušec, M., Maver, U., Gradišnik, L., Gorenjak, M., Vukasović, A., Ivković, A., Rupnik, M.S., Vogrin, M., Krajnc, P.: Polyester type polyHIPE scaffolds with an interconnected porous structure for cartilage regeneration. Sci. Rep. **6**, 28695 (2016). https://doi.org/10.1038/srep28695

Nikjoo, D., Akhtar, F.: Structured emulsion-templated porous copolymer based on photopolymerization for carbon capture. J. CO2 Util. **21**, 473–479 (2017). https://doi.org/10.1016/j.jcou.2017.08.007

Nuyken, O., Pask, S.D.: Ring-opening polymerization—an introductory review. Polymers **5**, 361–403 (2013). https://doi.org/10.3390/polym5020361

O'Brien, F.J.: Biomaterials & scaffolds for tissue engineering. Mater. Today **14**, 88–95 (2011). https://doi.org/10.1016/S1369-7021(11)70058-X

Onder, O.C., Utroša, P., Caserman, S., Podobnik, M., Žnidarič, M.T., Grdadolnik, J., Kovačič, S., Žagar, E., Pahovnik, D.: Emulsion-templated synthetic polypeptide scaffolds prepared by ring-opening polymerization of N-carboxyanhydrides. Polym. Chem. **11**, 4260–4270 (2020). https://doi.org/10.1039/d0py00387e

Oschatz, M., Borchardt, L., Thommes, M., Cychosz, K.A., Senkovska, I., Klein, N., Frind, R., Leistner, M., Presser, V., Gogotsi, Y., Kaskel, S.: Carbide-derived carbon monoliths with hierarchical pore architectures. Angew. Chem. Int. Ed. **51**, 7577–7580 (2012). https://doi.org/10.1002/anie.201200024

Ostwald, W.: Beiträge zur kenntnis der emulsionen. Colloid Polym. Sci. **6**, 103–109 (1910). https://doi.org/10.1007/BF01465754

Owen, R., Sherborne, C., Paterson, T., Green, N.H., Reilly, G.C., Claeyssens, F.: Emulsion templated scaffolds with tunable mechanical properties for bone tissue engineering. J. Mech. Behav. Biomed. Mater. **54**, 159–172 (2016). https://doi.org/10.1016/j.jmbbm.2015.09.019

Pahovnik, D., Majer, J., Žagar, E., Kovačič, S.: Synthesis of hydrogel polyHIPEs from functionalized glycidyl methacrylate. Polym. Chem. **7**, 5132–5138 (2016). https://doi.org/10.1039/C6PY01122E

Pal, R.: Yield stress and viscoelastic properties of high internal phase ratio emulsions. Colloid Polym. Sci. **277**, 583–588 (1999). https://doi.org/10.1007/s003960050429

Pan, J., Luo, J., Cao, J., Liu, J., Huang, W., Zhang, W., Yang, L.: Competitive adsorption of three phenolic compounds to hydrophilic urea-formaldehyde macroporous foams derived from lignin-based Pickering HIPEs template. RSC Adv. **6**, 93894–93904 (2016). https://doi.org/10.1039/C6RA20919J

Parın, F.N., Mert, E.H.: Hydrophilic closed-cell macroporous foam preparation by emulsion templating. Mater. Lett. **277**,(2020). https://doi.org/10.1016/j.matlet.2020.128287

Pérez-García, M.G., Gutierrez, M.C., Mota-Morales, J.D., Luna-Barcenas, G., del Monte, F.: Synthesis of biodegradable macroporous poly(L-lactide)/ poly(ε-caprolactone) blend using oil-in-eutectic-mixture high internal phase emulsions as template. ACS Appl. Mater. Interfaces **8**, 16939–16949 (2016). https://doi.org/10.1021/acsami.6b04830

Perrier, S.: 50th anniversary perspective: RAFT polymerization—a user guide. Macromolecules **50**(19), 7433–7447 (2017). https://doi.org/10.1021/acs.macromol.7b00767

Pickering, S.U.: CXCVI.—Emulsions. J. Chem. Soc. Trans. **91**, 2001−2021 (1907). https://doi.org/10.1039/CT9079102001

Pulko, I., Kolar, M., Krajnc, P.: Atrazine removal by covalent bonding to piperazine functionalized polyHIPES. Sci. Total Environ. **386**, 114–123 (2007). https://doi.org/10.1016/j.scitotenv.2007.06.032

Pulko, I., Krajnc, P.: Open cellular reactive porous membranes from high internal phase emulsions. Chem. Commun. 4481–4483 (2008). https://doi.org/10.1039/B807095D

Pulko, I., Krajnc, P.: High internal phase emulsion templating—a path to hierarchically porous functional polymers. Macromol. Rapid Commun. **33**, 1731–1746 (2012). https://doi.org/10.1002/marc.201200393

Pulko, I., Wall, J., Krajnc, P., Cameron, N.R.: Ultra-high surface area functional porous polymers by emulsion templating and hypercrosslinking: efficient nucleophilic catalyst supports. Chem. Eur. J. **16**, 2350–2354 (2010). https://doi.org/10.1002/chem.200903043

Pulko, I., Smrekar, V., Podgornik, A., Krajnc, P.: Emulsion templated open porous membranes for protein purification. J. Chrom. a. **1218**, 2396–2401 (2011). https://doi.org/10.1016/j.chroma.2010.11.069

Puupponen, S., Mikkola, V., Ala-Nissila, T., Seppälä, A.: Novel microstructured polyol–polystyrene composites for seasonal heat storage. Appl. Energy **172**, 96–106 (2016). https://doi.org/10.1016/j.apenergy.2016.03.023

Quell, A., Bergolis, B., Drenckhan, W., Stubenrauch, C.: How the locus of initiation influences the morphology and the pore connectivity of a monodisperse polymer foam. Macromolecules **49**, 5059–5067 (2016). https://doi.org/10.1021/acs.macromol.6b00494

Ramsden, W.: Separation of solids in the surface-layers of solutions and suspensions (observations on surface-membranes, bubbles, emulsions and mechanical coagulation)-preliminary account. Proc. r. Soc. Lond. **72**, 156–164 (1903). https://doi.org/10.1098/rspl.1903.0034

Rao, K.M., Anbananthana, N., Rajulu, A.V.: Bicontinuous highly cross-linked poly(acrylamide-co-ethyleneglycol dimethacrylate) porous materials synthesized within high internal phase emulsions. Soft Matter **7**, 10780–10786 (2011). https://doi.org/10.1039/C1SM06084H

Robinson, J.L., Moglia, R.S., Stuebben, M.C., McEnery, M.A.P., Cosgriff-Hernandez, E.: Achieving interconnected pore architecture in injectable polyHIPEs for bone tissue engineering. Tissue Eng Part A **20**, 1103–11012 (2014). https://doi.org/10.1089/ten.tea.2013.0319

Rohm, K., Manas-Zloczower, I., Feke, D.: Poly(HIPE) morphology, crosslink density, and mechanical properties influenced by surfactant concentration and composition. Colloid Surf. A Physicochem. Eng. Asp. **583**,(2019). https://doi.org/10.1016/j.colsurfa.2019.123913

Sanda, F., Endo, T.: Radical ring-opening polymerization. J. Polym. Sci. Part A: Polym. Chem. **39**, 265–276 (2001). https://doi.org/10.1002/1099-0518(20010115)39:2<265::AID-POLA20>3.0.CO;2-D

Schwab, M.G., Senkovska, I., Rose, M., Klein, N., Koch, M., Pahnke, J., Jonschker, G., Schmitz, B., Hirscher, M., Kaskel, S.: High surface area polyHIPEs with hierarchical pore system. Soft Matter **5**, 1055–1059 (2009). https://doi.org/10.1039/B815143A

Sergent, B., Birot, M., Deleuze, H.: Preparation of thiol–ene porous polymers by emulsion templating. React. Func. Polym. **72**, 962–966 (2012). https://doi.org/10.1016/j.reactfunctpolym.2012.02.011

Sergienko, A.Y., Tai, H., Narkis, M., Silverstein, M.S.: Polymerized high internal-phase emulsions: properties and interaction with water. J. Appl. Polym. Sci. **84**, 2018–2027 (2002). https://doi.org/10.1002/app.10555

Shen, X., Ye, L.: Interfacial molecular imprinting in nanoparticle-stabilized emulsions. Macromolecules **44**, 5631–5637 (2011). https://doi.org/10.1021/ma200837n

Sherrington, D.C., Hodge, P.: Synthesis separations using functional polymers. Wiley-VCH Verlag GmbH&Co, KGaA (1988)

Silverstein, S.: Emulsion-templated porous polymers: a retrospective perspective. Polymer **55**, 304–320 (2014)

Silverstein, M.S.: PolyHIPEs: recent advances in emulsion-templated porous polymers. Prog. Polym. Sci. **39**, 199–234 (2014). https://doi.org/10.1016/j.progpolymsci.2013.07.003

Silverstein, M.S., Cameron, N.R.: PolyHIPEs—porous polymers from high internal phase emulsions. In: Encyclopedia of Polymer Science and Technology. Wiley, Hoboken (2010). https://doi.org/10.1002/0471440264.pst571

Song, X., Zhao, Y., Wang, H., Du, Q.: Fabrication of polymer microspheres using titania as a photocatalyst and Pickering stabilizer. Langmuir **25**, 4443–4449 (2009). https://doi.org/10.1021/la8039237

Su, F., Bray, C.L., Tan, B., Cooper, A.I.: Rapid and reversible hydrogen storage in clathrate hydrates using emulsion-templated polymers. Adv. Mater. **20**, 2663–2666 (2008). https://doi.org/10.1002/adma.200800550

Sušec, M., Ligon, S.C., Stampfl, J., Liska, R., Krajnc, P.: Hierarchically porous materials from layer-by-layer photopolymerization of high internal phase emulsions. Macromol. Rapid. Commun. **34**, 938–943 (2013). https://doi.org/10.1002/marc.201300016

Tadros, T.F.: Emulsions formation, stability, industrial applications, De Gruyter Textbook, De Gruyter (2016). ISBN: 9783110452242

Taylor, P.: Ostwald ripening in emulsions. Colloids Surf. A Physicochem. Eng. Asp. **99**, 175–185 (1995). https://doi.org/10.1016/0927-7757(95)03161-6

Teixeira, R.F.A., Bon, S.A.F.: Physical methods for the preparation of hybrid nanocomposite polymer latex particles. Adv. Polym. Sci. **233**, 19–52 (2010). https://doi.org/10.1007/12_2010_65

Trupej, N., Novak, Z., Knez, Ž., Slugovc, C., Kovačič, S.: Supercritical CO_2 mediated functionalization of highly porous emulsion-derived foams: $ScCO_2$ absorption and epoxidation. J. CO_2 Util. **21**, 336–341 (2017). https://doi.org/10.1016/j.jcou.2017.07.024

Tsyurupa, M.P., Davankov, V.A.: Hypercrosslinked polymers: basic principle of preparing the new class of polymeric materials. React. Funct. Polym. **53**, 193–203 (2002). https://doi.org/10.1016/S1381-5148(02)00173-6

Ungureanu, S., Deleuze, H., Sanchez, C., Popa, M.I., Backov, R.: First Pd@Organo-Si(HIPE) open-cell hybrid monoliths generation offering cycling heck catalysis reactions. Chem. Mater. **20**, 6494−6500 (2008). https://doi.org/10.1021/cm801525c

Utroša, P., Onder, O.C., Žagar, E., Kovacič, S., Pahovnik, D.: Shape memory behavior of emulsion-templated poly(εcaprolactone) synthesized by organocatalyzed ring-opening polymerization. Macromolecules **52**, 9291–9298 (2019). https://doi.org/10.1021/acs.macromol.9b01780

Vílchez, A., Rodríguez-Abreu, C., Menner, A., Bismarck, A., Esquena, J.: Antagonistic effects between magnetite nanoparticles and a hydrophobic surfactant in highly concentrated pickering emulsions. Langmuir **30**, 5064–5074 (2014). https://doi.org/10.1021/la4034518

Wang, Z.J., Landfester, K., Zhang, K.A.I.: Hierarchically porous p-conjugated polyHIPE as a heterogeneous photoinitiator for free radical polymerization under visible light. Polym. Chem. **5**, 3559–3562 (2014). https://doi.org/10.1039/c4py00323c

Wang, A., Paterson, T., Owen, R., Sherborne, C., Dugan, J., Li, J., Claeyssens, F.: Photocurable high internal phase emulsions (HIPEs) containing hydroxyapatite for additive manufacture of tissue engineering scaffolds with multi-scale porosity. Mater. Sci. Eng. C **67**, 51–58 (2016). https://doi.org/10.1016/j.msec.2016.04.087

Weinstock, L., Sanguramath, R., Silverstein, M.S.: Encapsulating an organic phase change material within emulsion-templated poly(urethane urea)s. Polym. Chem. **10**, 1498–1507 (2019). https://doi.org/10.1039/C8PY01733F

Williams, J.M.: High internal phase water-in-oil emulsions: influence of surfactants and cosurfactants on emulsion stability and foam quality. Langmuir **7**, 1370–1377 (1991). https://doi.org/10.1021/la00055a014

Williams, J.M., Gray, A.J., Wilkerson, M.H.: Emulsion stability and rigid foams from styrene or divinylbenzene water-in-oil emulsions. Langmuir **6**, 437–444 (1990). https://doi.org/10.1021/la00092a026

Williams, J.M., Wrobleski, D.A.: Spatial distribution of the phases in water-in-oil emulsions. Open and closed microcellular foams from cross-linked polystyrene. Langmuir **4**, 656–662 (1988). https://doi.org/10.1021/la00081a027

Woodward, R.T., Fam, D.W.H., Anthony, D.B., Hong, J., McDonald, T.O., Petit, C., Shaffer, M.S.P., Bismarck, A.: Hierarchically porous carbon foams from pickering high internal phase emulsions. Carbon **101**, 253–260 (2016). https://doi.org/10.1016/j.carbon.2016.02.002

Yadav, A., Pal, J., Nandan, B., Srivastava, R.K.: Macroporous scaffolds of cross-linked Poly(ε-caprolactone) via high internal phase emulsion templating. Polymer **176**, 66–73 (2019). https://doi.org/10.1016/j.polymer.2019.05.034

Yadav, A., Erdal, N.B., Hakkarainen, M., Nandan, B., Srivastava, R.K.: Cellulose-derived nanographene oxide reinforced macroporous scaffolds of high internal phase emulsion-templated cross-linked poly(ε-caprolactone). Biomacromol **21**, 589–596 (2020). https://doi.org/10.1021/acs.biomac.9b01330

Yang, T., Hu, Y., Wang, C., Binks, B.P.: Fabrication of hierarchical macroporous biocompatible scaffolds by combining Pickering high internal phase emulsion templates with three-dimensional

printing. ACS Appl. Mater. Interfaces **9**, 22950–22958 (2017). https://doi.org/10.1021/acsami. 7b05012

Yang, S., Wang, Y., Jia, Y., Sun, X., Sun, P., Qin, Y., Li, R., Liu, H., Nie, C.: Tailoring the morphology and epoxy group content of glycidyl methacrylate-based polyHIPE monoliths via radiation-induced polymerization at room temperature. Colloid Polym. Sci. **296**, 1005–1016 (2018). https://doi.org/10.1007/s00396-018-4307-x

Yang, Y., Wei, Z., Wang, C., Tong, Z.: Lignin-based Pickering HIPEs for macroporous foams and their enhanced adsorption of copper (II) ions. Chem. Commun. **49**, 7144–7146 (2013). https://doi.org/10.1039/C3CC42270D

Yang, X., Yin, Z., Zhang, X., Zhu, Y., Zhang, S.: Fabrication of emulsion-templated macroporous poly(ε-caprolactone) towards highly effective and sustainable oil/water separation. Polymer **204** (2020). https://doi.org/10.1016/j.polymer.2020.122852

Yang, S., Zeng, L., Li, Z.C., Zhang, X., Liu, H., Nie, C., Liu, H.: Tailoring the morphology of emulsion-based (glycidyl methacrylate-divinylbenzene) monoliths. Eur. Polym. J. **57**, 127–136 (2014). https://doi.org/10.1016/j.eurpolymj.2014.05.014

Yao, C.H., Qi, L., Jia, H.Y., Xin, P.Y., Yang, G.L., Chen, Y.: A novel glycidyl methacrylate-based monolith with sub-micron skeletons and well-defined macropores. J. Mater. Chem. **19**, 767–772 (2009). https://doi.org/10.1039/B816712E

Yeşil, R., Çetinkaya, S.: Mn_3O_4/p(DCPD)HIPE nanocomposites as an efficient catalyst for oxidative degradation of phenol. J. Nanopart. Res. **22**, 198 (2020). https://doi.org/10.1007/s11051-020-04931-6

Yi, F., Gao, Y., Li, H., Yi, L., Chen, D., Lu, S.: Nitrogen- and oxygen-codoped porous carbonaceous foam templated from high internal emulsion as PtRu catalyst support for direct methanol fuel cell. Electrochim. Acta **211**, 768–776 (2016a). https://doi.org/10.1016/j.electacta.2016.06.092

Yi, W., Wu, H., Wang, H., Du, Q.: Interconnectivity of macroporous hydrogels prepared via graphene oxide-stabilized pickering high internal phase emulsions. Langmuir **32**(4), 982–990 (2016b). https://doi.org/10.1021/acs.langmuir.5b04477

Yin, D., Guan, Y., Gu, H., Jia, Y., Zhang, Q.: Polymerized high internal phase emulsion monolithic material: a novel stationary phase of thin layer chromatography. RSC Adv. **7**, 7303–7309 (2017). https://doi.org/10.1039/C6RA27609A

Yin, J., Zhang, T., Schulman, E., Liu, D., Meng, J.: Hierarchical porous metallized poly-melamineformaldehyde (pmf) as low-cost and high-efficiency catalyst for cyclic carbonate synthesis from CO_2 and epoxides. J. Mater. Chem. A **6**, 8441–8448 (2018). https://doi.org/10.1039/C8TA00625C

Yuan, W., Chen, X., Xu, Y., Yan, C., Liu, Y., Lian, W., Zhou, Y., Li, Z.: Preparation and recyclable catalysis performance of functional macroporous polyHIPE immobilized with gold nanoparticles on its surface. RSC Adv. **8**, 5912–5919 (2018). https://doi.org/10.1039/C8RA00089A

Yüce, E., Krajnc, P., Mert, H.H., Mert, E.H.: Influence of nanoparticles and antioxidants on mechanical properties of titania/polydicyclopentadiene polyHIPEs: A statistical approach. J. Appl. Polym. Sci. **136**, 46913 (2019). https://doi.org/10.1002/app.46913

Yüce, E., Mert, E.H., Krajnc, P., Parın, F.N., San, N., Kaya, D., Yıldırım, H.: Photocatalytic activity of titania/polydicyclopentadiene polyHIPE composites. Macromol. Mater. Eng. **302**, 1700091 (2017). https://doi.org/10.1002/mame.201700091

Yüce, E., Parın, F.N., Krajnc, P., Mert, H.H., Mert, E.H.: Influence of titania on the morphological and mechanical properties of 1,3-butanediol dimethacrylate based polyHIPE composites. React. Funct. Polym. **130**, 8–15 (2018). https://doi.org/10.1016/j.reactfunctpolym.2018.05.009

Zhang, T., Gui, H., Xu, Z., Zhao, Y.: Hydrophobic polyurethane polyHIPEs templated from mannitol within nonaqueous high internal phase emulsions for oil spill recovery. J. Polym. Sci., Part a: Polym. Chem. **57**, 1315–1321 (2019a). https://doi.org/10.1002/pola.29392

Zhang, T., Sanguramath, R.A., Israel, S., Silverstein, M.S.: Emulsion templating: porous polymers and beyond. Macromolecules **52**, 5445–5479 (2019b). https://doi.org/10.1021/acs.macromol.8b02576

Zhang, T., Xu, Z., Li, X., Gao, G., Zhao, Y.: Closed-cell, phase change material-encapsulated, emulsion-templated monoliths for latent heat storage: flexibility and rapid preparation. Appl. Mater. Today **21** (2020). https://doi.org/10.1016/j.apmt.2020.100831

Zheng, Z., Zheng, X., Wang, H., Du, Q.: Macroporous graphene oxide−polymer composite prepared through Pickering high internal phase emulsions. Appl. Mater. Interfaces **5**, 7974–7982 (2013). https://doi.org/10.1021/am4020549

Zhou, C., Qiao, M., Zhang, X., Zhu, Y., Zhang, S., Chen, J.: Production of high internal phase emulsion with a miniature twin screw extruder. ACS Omega **4**, 9957–9963 (2019). https://doi.org/10.1021/acsomega.9b01156

Characterization of Macroporous Materials

Thabang R. Somo, Mpitloane J. Hato, and Kwena D. Modibane

Abstract Macroporous materials (with pore sizes of > 50 nm) have received little attention in the literature mainly due to their complexity but their pore diameters comparable to optical wavelengths are predicted to have unique and highly useful optical properties such as photonic bandgaps and optical stop-bands. Herein, the current state of characterization of these materials using a set of three-dimensional imaging techniques: computerized X-ray tomography, 3D electron tomography, dual-beam electron microscopy and magnetic resonance imaging is discussed. Each technique could be characterized by ambiguities resulting from various parameters. Nevertheless, employing the above-mentioned techniques in parallel or even coupling them can improve their precision and eliminate ambiguities when characterizing macroporous materials.

Keywords 3D imaging · Computerized X-ray tomography · 3D electron tomography · Dual-beam electron microscopy and magnetic resonance imaging

1 Introduction

Porous materials can simply be explained as any solid containing pores and are classified into three families (microporous, mesoporous and macroporous) according to their pore sizes (Tang et al. 2004). According to International Union of Pure and Applied Chemistry (IUPAC) classification, microporous materials (e.g. zeolites, graphene and nanotubes) are constituted of pores that are smaller than 2 nm in diameter. Mesoporous materials (e.g. clathrates and carbon molecular sieves) have pores ranging between 2 and 50 nm while any porous material with pores sizes over this range is referred to as macroporous material (polymers, foams, glasses, hydrogel scaffolds, TiO_2 and silica) (Rouquerol et al. 2012a). These materials, both well-ordered and low-ordered structures, have excelled in a wide range of applications in recent years. Examples of such applications include gas ad/absorption (Lyu and

T. R. Somo (✉) · M. J. Hato · K. D. Modibane
Nanotechnology Research Lab, Department of Chemistry, School of Physical and Mineral Sciences, University of Limpopo (Turfloop), Sovenga 0727, Polokwane, South Africa
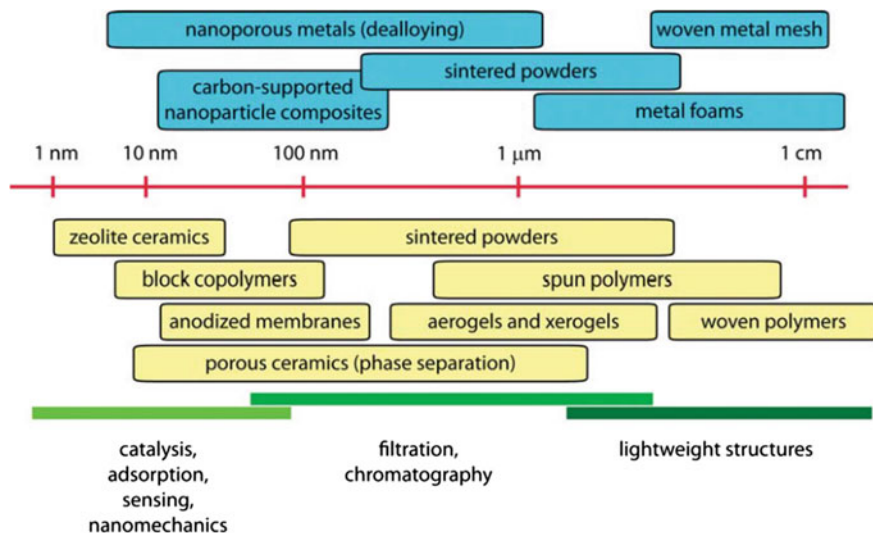
Fig. 1 A pecking order of macroporous materials, with average pore diameter. Conductive materials in blue while yellow ones are non-conductors. Their applications are presented in green. Reproduced with permission from Erlebacher and Seshadri (2009). Copyright 2009 Springer

Kudiiarov 2020; Somo et al. 2021a, b), cell immobilization (Bonin et al. 2017), water treatment (Jain and Kandasubramanian 2020), energy conversion (Somo et al. 2021a, b), electrical insulators (Shun et al. 2012), catalysis (Jeon et al. 2011), etc. Average pore size, average particle diameter, morphology, specific surface area and particle shape are some of the most relevant and significant parameters that are taken into consideration when porous materials are considered in the above-mentioned applications (Wang et al. 2017).

Of the three families, macroporous materials (Fig. 1, from 50 nm) have received little attention in the literature mainly due to their complexity but their pore diameters comparable to optical wavelengths are predicted to have unique and highly useful optical properties such as photonic bandgaps and optical stop-bands (Melicchio et al. 2016; Studart et al. 2006). Hydrogel scaffolds, which are frequently used in tissue engineering, have caught attention as macroporous materials that have thrived in most applications (Chen et al. 2011). Their macroporosity is thought to help facilitate cell migration, proliferation and signalling (Hoo et al. 2013). Freeze-drying, gasfoaming, stereolithography and porogen leaching are some of synthetic routes used to prepare macroporous hydrogel scaffolds (Al-Abboodi et al. 2013; Chen et al. 2011). Once prepared, it is of paramount importance to quantify the macroporosity through characterization techniques. The well-known traditional techniques for pore analysis are mercury intrusion porosimetry (MIP), scanning electron microscope (SEM), Brunauer–Emmett–Teller (BET), solute exclusion and small-angle X-ray scattering (Friedrich et al. 2007). Mercury intrusion porosimetry, which is functions on the basis of mercury infusion within material under increasing pressure to approximate

pore size, presents several concerns such as toxicity of mercury, as well as difficulty to analyze pressure sensitive materials (Rouquerol et al. 2012b). Moreover, the need for vacuum environment is not ideal as such an environment would boil away most of the water and thus drastically alter the structure of water-swollen hydrogels in case of hydrogel scaffolds (Hoo et al. 2013). Furthermore, the rapid expansion and collapse events that occur during syntheses of most macroporous materials such as foams make it difficult to precisely characterize these materials using the afore-mentioned techniques (Spowage et al. 2006). Additionally, foams and silica commonly consist of primary cells ranging from approximately 30–200 nm in diameter, a size range that is challenging to study fully using the traditional techniques (Yuan et al. 2009). On the other hand, the use of bulk techniques such as BET is not ideal as direct information on the actual location and distribution of the active particles within a bulk material is limited (Alvarez et al. 2019). SEM provides 2-dimensional (2D) static imaging and thus deepness of structures cannot be obtained and localized with 2D imaging (Manickam and McCutcheon 2012). As a result, new techniques which provide true structural properties and synthetic/crystallization mechanisms should be introduced. Consequently, the last few decades saw emergence of more accurate pore characterization methods better known as three-dimensional (3D) imagining techniques. These include computerized X-ray tomography, 3D electron tomography (3DET), dual-beam electron microscopy and magnetic resonance imaging (Zhao et al. 2020). Their outstanding advantages for characterization of macroporous materials are outlined in Fig. 2.

These imaging techniques are appropriate for analyses of porosity and morphologies on a variety of macroporous materials with varying length scales. For example, electron tomography is able to reach spatial resolutions down to $(1 \text{ nm})^3$ of volumes up to $(3 \text{ } \mu\text{m})^3$, while the resolution of computerized X-ray tomography can reach $(50 \text{ nm})^3$ with sample sizes of up to $(64 \text{ } \mu\text{m})^3$ (Apeleo Zubiri et al. 2019). So, each technique has its benefits and there is always a balance between spatial resolution and sample size. Imaging methods have greatly improved our ability to characterize the highly complex internal structures of macroporous materials. X-ray tomography and magnetic resonance imaging provide maps of the spatial distribution of local average accessible porosity for macroporous materials over macroscopic length scales (> 10 mm) (Karatas and Toy 2019). The next sections of this chapter elaborate and discuss in depth the application of these techniques for characterization of different macroporous materials.

2 Computerized X-Ray Tomography

Computerized X-ray tomography (CXT) employs a rotating chamber to view material from different angles. Subsequently, 3D images are reconstructed by recording the intensity of the X-ray beam (Rigby et al. 2020). The beam can only detect macropores of at least 100 nm if a synchrotron source is used and 1 µm if a desktop apparatus is used. Pore sizes of < 100 nm can be detected through the improvement of contrast
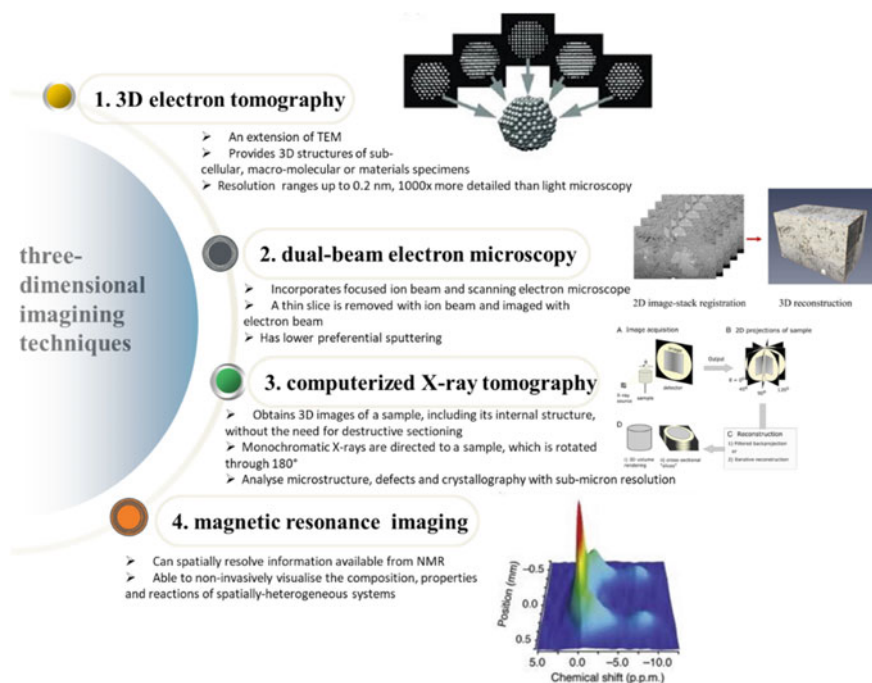
Fig. 2 Three-dimensional imaging techniques and their advantages for analyses of porous materials

by filling the pores with mercury (Rouquerol et al. 2012b). For example, LiFePO$_4$ nanoplates with 10 nm resolution enabled by soft X-ray and of catalysts with 23 nm space resolution, using synchrotron source have been recently reported (Alvarez et al. 2019). Such analyses require coupling of mercury porosimetry and MFX imaging techniques (Rigby et al. 2011). Another porous materials that are commonly difficult to characterize using XCT are polymers consisting of only light elements such as carbon, hydrogen, oxygen and nitrogen (Nishikawa et al. 2013). These materials possess relatively low X-ray absorptions as compared to the metal-containing materials and thus they are expected to be almost transparent under XCT. Thus, contrast enhancement can certainly permit the application of XCT to polymers. The X-ray absorption is directly proportional to density, energy of photons and atomic number. For polymers, changing the elements and density is challenging, making it impossible to make use of low energy X-rays as a traditional route to enhance contrast (Salomons et al. 2000). A recent study has shown that a suitable high contrast to characterize polymers is achievable by using a Coolidge-type X-ray tube and rather thin (125 mm) CsI scintillator for the detector (Nishikawa et al. 2013). The capability of the designed XCT apparatus with the above-mentioned specifications was validated by using typical polymers, polystyrene, poly (methymethacrylate) and their blends. The measured contrasts were in the same agreement with the predicted data on the basis of the energy dependencies of X-ray absorption coefficients.

CXT method is non-destructive and performs different in-situ time resolved experiments, while imaging. It has been employed to image macroporous alumina templated with expandable microspheres (Andersson et al. 2010), macroporous ceramic scaffolds (Jerban and Elkoun 2016) and macroporous zeolite (Apeleo Zubiri et al. 2019). Information that can be extracted from X-ray images includes pore and throat size distributions and the interconnected porosity. Microfocus X-ray tomography is able to map the density and porosity distributions for chemically and mechanically homogeneous materials (Zhao et al. 2017). The porosity distribution obtained in Zhao et al. (2017) consisted of entirely enclosed porosity and porosity accessible from the surface.

It has been reported that the binarisation of the original grey-scale XCT information using the "converging active contours" segmentation technique allows the capture of porous and solid phases (Andersson et al. 2010). Furthermore, CXT can also map the spatial location of entrapped mercury left behind after a mercury porosimetry intrusion and retraction cycle (Rigby et al. 2002). An example of such study was conducted by Rigby et al. (2011) and a macroporous α-alumina pellet was used to interpret ambiguous mercury porosimetry data. As shown in Fig. 3, the spatial distribution of entrapped mercury and pores accessible by necks of sizes above 6.96 mm is not homogeneous. To acquire Fig. 3 3D analysis in CT analyzer was achieved by choosing individual annular volumes of the pellets tested. Most importantly, quantitative analysis including the separation of individual pores as shown in Fig. 4 is possible with computerized X-ray tomography. The separation is based on interconnectivity points. Thus porosity (%) for different pore types (macropores, mesopores and micropores) can be determined and distinguished (Zhou et al. 2018a, b).

In the field of medicinal chemistry, CXT is mostly preferred over its competitors (SEM and MIP) for architectural features such as pore and interconnection sizes. MIP is limited by its insensitivity to macropores while the 2D images obtained by
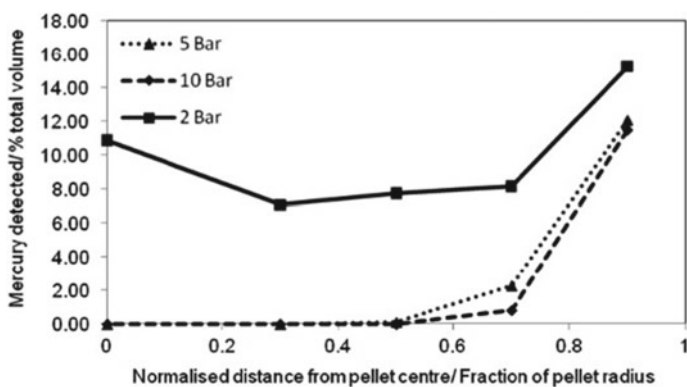
Fig. 3 Variation of apparent mercury entrapment in α-alumina pellets plotted against a normalized distance from the pellet centre. Reproduced with permission from Rigby et al. (2011)
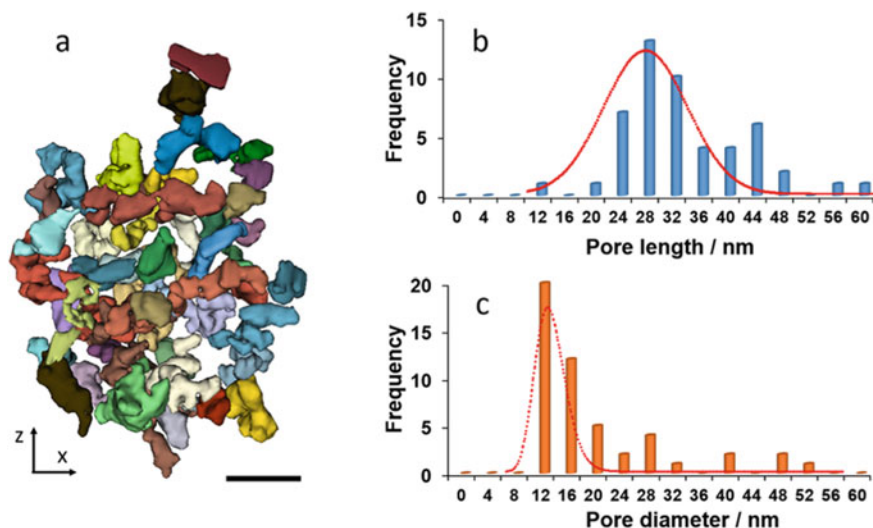
Fig. 4 **a** Individual pores selected from a highly porous region, pore length distribution (**b**) and pore diameter distribution (**c**) for Mo_3Si. Reproduced with permission from Zhou et al. (2018a, b). Copyright 2018 Nature Research

SEM provide insufficient information. Thus CXT has been used to visualize bone substitution by macroporous, interconnected and osteoconductive materials such as β-tricalcium phosphate (Jerban and Elkoun 2016). CXT is able to perform different in-situ time resolved experiments, while imaging (Villevieille 2015). This unique feature was explored by Ebner et al. (2013) when visualizing and quantifying the occurrence and evolution of electrochemical and mechanical degradation when a battery is operating. The investigation was performed on a tin oxide electrode to understand the influence of high-volume changes in cubic particles (Fig. 5c). X-ray attenuation coefficient histograms (Fig. 5a, b) were used to study phase evolution as they confirm conversion of SnO phase into Li_2O + Sn phase. Attenuation coefficient (Fig. 5d), which is closely related to the structure and density of the electrode, was able to reveal the following two major trends occurring during cycling process. First one is the conversion reaction that results in the formation of Li_2O and the second one is the formation of $Li_{3.5}Sn$ alloy (Fig. 5e). It was further reported that the sample developed cracks as a result of severe high-volume change undergone during lithiation. This information has acquired all thanks to CXT characterization (Table 1).
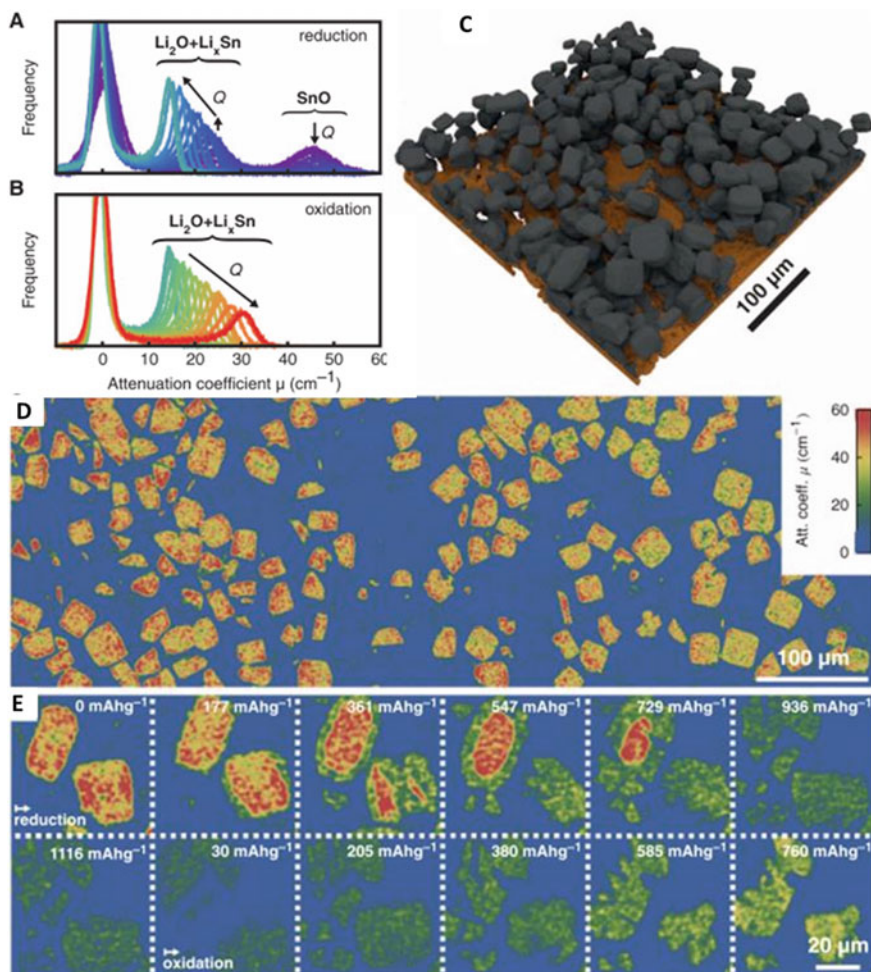
Fig. 5 X-ray attenuation coefficient histograms during electro-chemical **a** reduction and **b** oxidation. **c** 3D imaging assembled during battery operation. **d** Cross-section displaying SnO particles in the electrode. **e** A series of cross sections through two particles demonstrating a core-shell process, volume expansion and particle fracture. Reproduced with permission from Villevieille (2015)

3 Magnetic Resonance Imaging

Magnetic resonance imaging (MRI) has been given considerable attention in medicine since it provides high information content while not destructing the sample of interest (Hertel et al. 2013); but its applicability within materials science scope is still developing due to a number of technical challenges (Wang et al. 2012). Nonetheless, the last decade has seen emergence of numerous studies involving materials science MRI applications of composite and porous materials (Morozov et al. 2019).

Table 1 Macroporous materials characterized by CXT and parameters of the data acquisition processes for 3D visualization

Material	Current (μA)	Spatial resolution (μm)	Volume dimensions (μm)	Beam voltage (kv)	rotation angle (°)	Connected porosity (%)	Total porosity (%)	Pore size (μm)	References
Ni-based porogen	1×10^7	0.67	400 × 400 × 400	40	–	–	60.5	7.5–142	Ebner et al. (2013)
Intact loess	–	10	–	–	–	–	11.50	62.6–100	Li and Shao (2020)
Titanium powders	64	3	–	135	–	–	0.424	4.5–33.2	Heim et al. (2016)
Berea sandstone	20	0.35	–	100	–	85	19.4	0.25–25	Peng et al. (2012)
Macroporous alumina	100	3	1160 × 1160 × 580	80	360	16	75.5	60	Andersson et al. (2010)
Sandstone	130	2.9	500 × 500 × 1000	80	0–180	–	11.45	2.9–85.2	Fernandes et al. (2007)
Cement	10–2000	–	–	30–320	130	–	29.01	0.081	Cho et al. (2020)
Polymeric nonwovens	–	1–3	800 × 800 × 800	–	180	–	56.34	63	Manickam and McCutcheon (2012)
Leached cement paste	150	3	–	60	180	92	58	3.62	Bossa et al. (2015)
Carbon fibre-polymers	160	2.7–20	–	60	–	–	10.42	–	Kastner et al. (2010)
Boom clay	200	2.5	500 × 500 × 1000	55	–	87	12.95	–	Hemes et al. (2015)
Silica sludge	125	13–20	–	80	360	65.66	58.6	250–500	Korat et al. (2013)

Table 1 (continued)

Material	Current (μA)	Spatial resolution (μm)	Volume dimensions (μm)	Beam voltage (kv)	rotation angle (°)	Connected porosity (%)	Total porosity (%)	Pore size (μm)	References
Porous layer for PEFCs	30	0.05	–	40	–	99.9	54.2	0.54	Wargo et al. (2013)

Distinctive MRI analyses of macroporous materials involve ^{1}H NMR of suitably wetting probe fluids, such as water or hydrocarbons. This technique functions by attaining a resonance signal from the hydrogen nucleus (Karatas and Toy 2019). The positional data is programmed into the NMR signal by means of field gradients since the Larmor precession frequency is a function of field strength. Due to the nature of NMR relaxation processes, conventional ^{1}H MRI spin-lattice relaxation time contrast methods to quantitatively characterize pore structure (porosity and pore size) are more possible on relatively ordered porous materials, such as pure silica or alumina catalyst precursors (Cho et al. 2012). For macroporous materials with pore sizes from approximately 10 μm, direct characterization of void space is possible using MRI; but macroporous materials with pore sizes ranging between 50 nm and < 10 μm, as well as mesoporous and microporous materials, require additional contrast techniques; such as relaxation time or pulsed-field gradient methods (Stannarius 2017). These methods are coupled with elementary imaging experiments to provide spatially resolved maps of the local average porosity, pore size and network tortuosity for pore sizes down to the micropore range. The lower detection limit is determined by the very short relaxation time of the smallest pores. The resolution limit for coupled techniques generally relies on the root mean square speed of the probe fluid, as this hypothetically blurs the image (Gladden and Mitchell 2011). Pore size mapping, using relaxation time contrast techniques, are only really appropriate for use with chemically homogeneous materials, such as relatively pure silica and alumina catalyst supports and would generally be unsuitable materials with substantial concentrations of paramagnetic species, or for partially coked heterogeneous catalysts. This is because NMR relaxation of pore fluids would be affected by heterogeneous distributions of paramagnetic and pore size variation (Rouquerol et al. 2012a).

Due to its non-invasive and non-destructive nature, MRI is reliable in providing spatial information that is sufficient for a serial study of blockage and altered flow patterns with time in the same reactor. For example, Nott et al. (2001) visualized polyurethane foam after challenging with copper in citrate buffer supplemented with glycerol 2-phosphate. The MR images show that polyurethane foam is distinguishable from the neighbouring liquid. MRI technique can also be used to study adsorption, diffusion and flow propagator properties of macroporous materials. For flow propagator measurements of ^{1}H nuclei, the maximum observation time (Δ_{max}) is the spin-lattice (T_1) relaxation time multiplied by four. For bulk fluids, T_1 times of ^{1}H nuclei range from 1.5 to 3 s, making Δ_{max} to be about 6–12 s (Radakovi et al. 2015). In porous materials, T_1 times are much smaller, reducing Δ_{max} even more (Gladden and Mitchell 2011). To overcome such drawbacks, ^{13}C flow propagators, which possess considerably longer T_1 times and Δ_{max} of up to 40 s, can be measured instead. Nevertheless, ^{13}C is limited by its low natural abundance, reduced Larmor frequency and poor MR sensitivity (5870 times less than for ^{1}H) (Lucas-Oliveira et al. 2018). For quite a number of applications, it is not practical, physically or economically, to use ^{13}C isotopically enriched samples. In this regard, distortionless enhancement by polarization transfer (DEPT) is used to enhance the signal of [13]C.
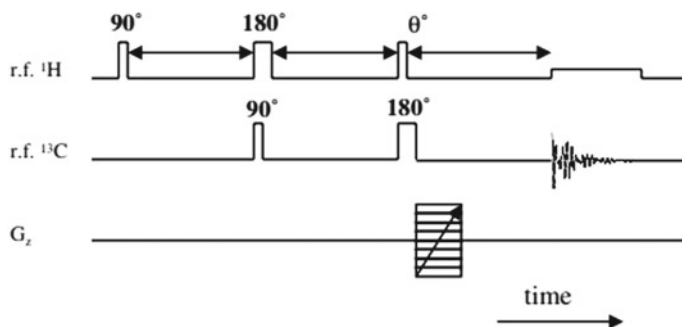
Fig. 6 ^{13}C DEPT MRI pulse sequence. The signal is acquired under conditions of ^{1}H decoupling. Reproduced with permission from Switendick (1979). Copyright 2005 Springer

DEPT is coupled with flow propagator measurement to assist in detecting ^{13}C signal (Gladden and Mitchell 2011).

^{13}C DEPT MRI has thus been used to map isomerization and conversion reactions such as those including hydrocarbons as this technique possess huge chemical shift range, simplifying identification of reactants; intermediates and products. For instance, Akpa et al. (2005) studied a competing etherification and hydration reaction of 2-methyl-2-butene. Another study by Sederman et al. (2005) involved conversion of 1-octene during hydrogenation over a macroporous Pd/Al$_2$O$_3$ material. The authors employed a proton-decoupled ^{13}C DEPT spectroscopy pulse sequence combined with an imaging sequence to map the reaction as depicted in Fig. 6.

Recently, Morozov et al. (2019) reported that the use of MRI to study H$_2$O absorption by macroporous ceramics is more precise compared to weight measurement techniques such as FTIR and ultraviolet-visible spectroscopy. This is because MRI is able to provide full information on the spatial distribution of H$_2$O inside the materials as well as its migration paths while the other techniques provide information on the amount and state of H$_2$O regardless of its local distribution. The authors utilized MRI to evaluate water absorption by a series of TZMK-25 specimens made in the form of a 10 × 10 × 20 mm parallelepiped and VTI-17 specimens treated with PPU-90 perfluorinated powder accelerators in sc-CO$_2$. Interpretation of MR images (Fig. 7) revealed that such macroporous materials contain a hygroscopic memory, existing in the adsorption of H$_2$O in some areas inside the material, repeating during consequent wettings with H$_2$O. The occupation of specimen volume takes place without impregnation front or moisture content gradient is formed. Heat treatment, which is used to control sorption mechanisms involving macroporous samples, could eliminate the possibility of impregnation front. Moisture formation can be avoided by impregnation of fluoroparaffin to oxide fibres as a way of making the material water-repellent (Proietti et al. 2006).

A similar study was conducted by Xue et al. (2018) when using MRI to evaluate pore size distribution of fractured coal by T$_2$ spectrum and to map water accumulation within the fractures of this material. T$_2$ spectrum distribution (Fig. 8a) revealed
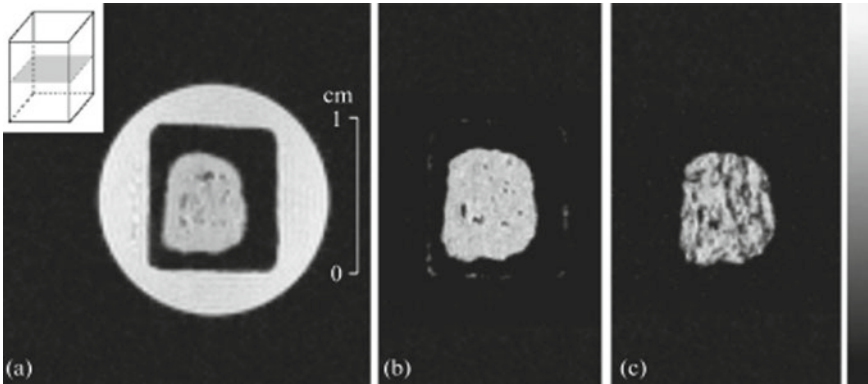
Fig. 7 MR images of the specimen **a** upon exposure to H$_2$O for 120 min, **b** immediately upon removal from H$_2$O and **c** upon overnight exposure to air. Reproduced with permission from Morozov et al. (2019). Copyright 2019 Springer

that fractured coal consists of three types of porosity, namely: adsorption, peculation and migration pores. Adsorption pores are micropores with high pressure flooding; peculation pores are mesopores with fluid accumulation pathways; while migration pores are macropores with fluid pools. Figure 8b–d display the MRI images of the spatial distribution of H$_2$O content in fractured coal. Water content is directly proportional to the relaxation time and signal. In Fig. 8b, red signifies higher water content and blue signifies lower content. The MRI results depict that the water content in coal is low, with nonhomogeneous water distribution.

In addition to the above-mentioned applications in different areas of material science, MRI can improve functionality of other techniques including mercury porosimetry (Rigby et al. 2002). Mercury porosimetry relies on the intrusion of mercury, which is difficult to penetrate and access all pores in the presence of macropores as such pores are usually shielded/concealed by surrounding smaller pores. Subsequently, the shape of a mercury intrusion curve is sensitive to the form of the pore size probability density function, the connectivity and spatial arrangement of the individual pores within the void space. Thus sensitivity to all these three aspects makes the evaluation of a mercury intrusion curve integrally ambiguous (Jerban and Elkoun 2016). To overcome this challenge, mercury porosimetry can be coupled with both MRI and BET. These distinct techniques can provide descriptors of particular structural properties of macroporous materials unconventionally without involving mercury porosimetry. This would therefore resolve ambiguities in the evaluation of mercury porosimetry. MRI can be used to provide maps of the macroscopic distribution of local average porosity and pore size (Cho et al. 2012). Although MRI is able to quantify the internal space of the measured substance, its applicability is limited by two aspects. First, the resolution of MRI imaging cannot achieve the standard that can be effectively utilized by image analysis software at this stage (Zhao et al. 2020). But for imaging of foam structure, 3D image processing algorithm and an image processing software package called FoamView were developed specifically
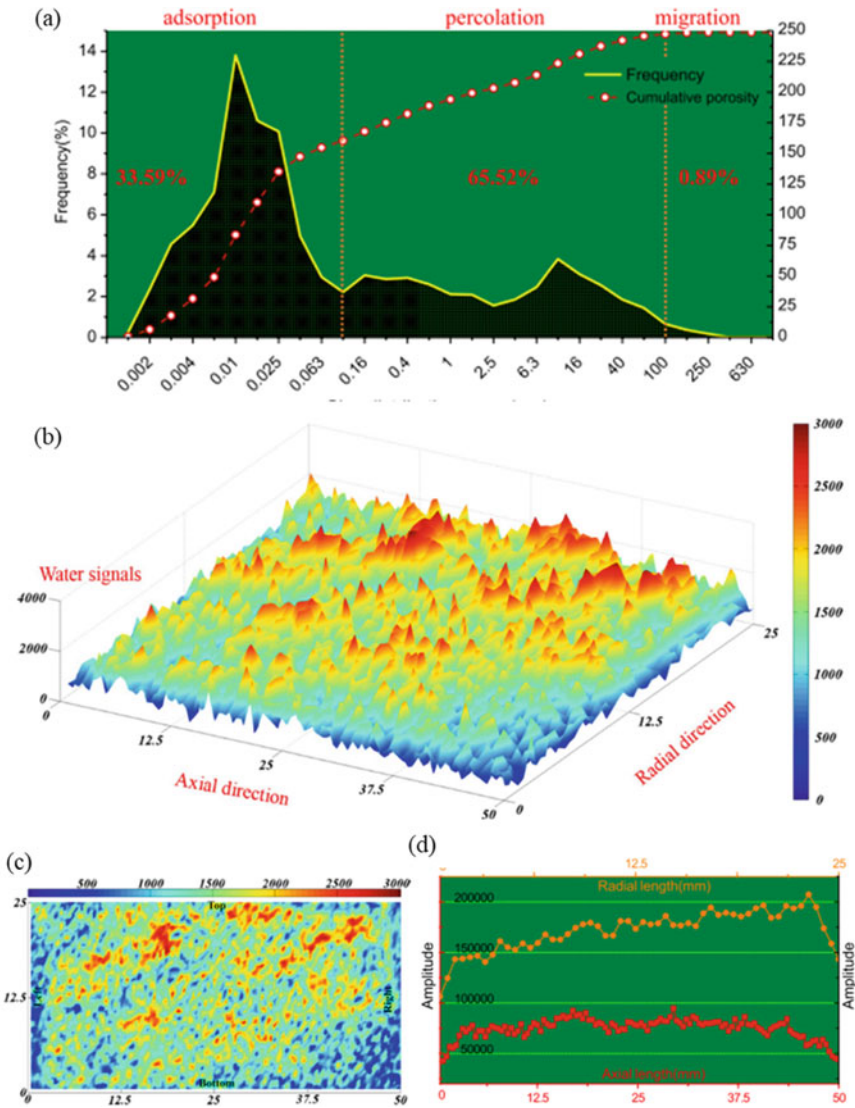
Fig. 8 **a** Pore size distribution and porosity evolution of fractured coal. **b** 3D-, **c** 2D- and **d** 1D-distribution of water content spatial distribution of fractured coal. Reproduced with permission from Xue et al. (2018). Copyright 2018 Springer

to extract structural information from 3D foam images (Hertel et al. 2013). Second, the water content of the substance to be tested has certain requirements and there are limitations in dynamically monitoring the change of material moisture (Zhao et al. 2020). These drawbacks limit the application of this technique in the characterization of porous materials.

4   Electron Microscopy

4.1   3D Electron Tomography (3DET) Technique

Transmission electron microscopy (TEM) is known to be a prevailing technique as it reveals structural properties in submicron detail. However, the resulting images are in first approximation a 2D projection of a 3D structure (Rohrer 2014). This means that in case of complex 3D materials, such as silica composites, the direct 3D location and distribution of the structure can never be evaluated from 2D TEM imaging. Electron tomography, which combines a series of tilted TEM images from different directions, provides 3D imaging (Chang et al. 2015; Kruk et al. 2018); making it easier to analyze structures to the depth. Theoretically, all probable angles and orientations could be imaged (on the order of 1°); however practically, the geometry of the crucible containing the material and the microscope customarily restrict the range of rotation (Zhou et al. 2018a, b). Although this may seem ambiguous and could result in some artefacts, it does not prevent application of the method. Upon completion of imaging, 3D volume as depicted in Fig. 9 is reassembled and imaged using computer algorithms.

3DET has similar working principle as computerized X-ray tomography, but the filtrating radiation is a beam of electrons, instead of X-rays. Its resolution, which depends on material size (example, for 500 nm, resolution is approximately 1 nm) and the angle through which the sample stage may be turned, is of the order of a few nanometres (Wang et al. 2016). Application of 3DET is more common in both biological and material sciences (Wang et al. 2006). In relation to material sciences, this technique was initially applied to heterogeneous catalysts with more emphasis on the qualitative analyses of nanoscale structures (Apeleo Zubiri et al. 2019). Recent studies have involved a posteriori image segmentation to quantitatively examine properties, including porosity, localization of the active phase and loading of active components (Friedrich et al. 2007). However, it should be noted that electron
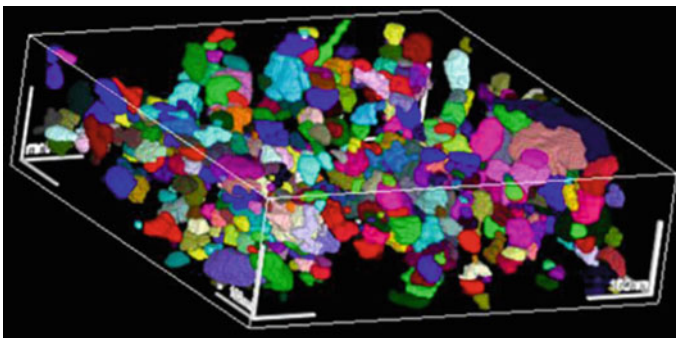
Fig. 9 Volume rendered view of the reconstructed mass density distribution of silica inclusions in a rubber matrix. Reproduced with permission from Rohrer (2014). Copyright 2014 Elsevier Ltd.
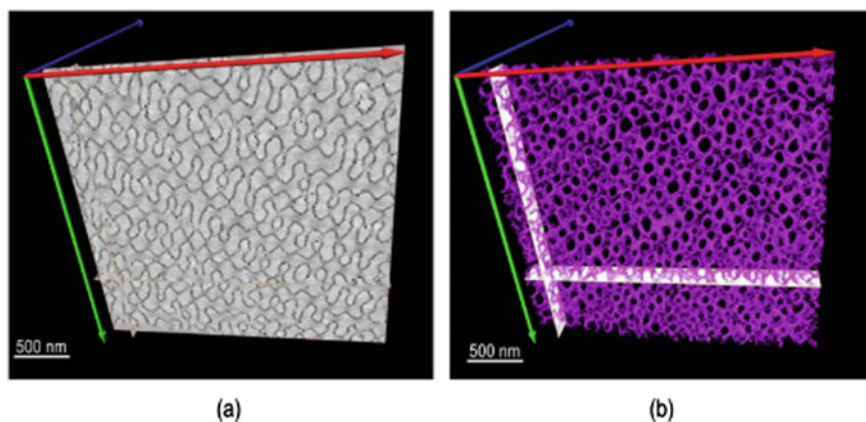
Fig. 10 TEM image **a**, **b** 3DET reconstruction of a 100 nm slice of PS-*b*-PAA porous particles. Reproduced with permission from Alvarez et al. (2019). Copyright 2019 Nature Research

tomography relies on representative images for the bulk material; and thus, bulk characterization is still relevant.

Recently it has been reported that a tilt series generated from TEM gives important information on the shape of the macropores on a macroscopic scale (50–1000 nm) (Sok et al. 2010). Alvarez et al. (2019) compared TEM and 3DET images of macroporous polystyrene-b-poly (acrylic acid) (PS-b-PAA) copolymer as shown in Fig. 10. TEM image just shows a simple periodic structure while 3DET image reveals the regular pore morphology, providing a clear illustration of the pore size and distribution at high magnification, highlighting the centre of the particles.

3DET can be used to locate small particles inside the macropores by imaging these materials in three dimensions. For example, Janssen and co-workers (Janssen et al. 2003) localized small gold (Au) particles inside the pores of SBA-15 using 3DET reconstruction. On the other hand, Yuan et al. (2009) used this particular technique to study the packing structures of macroporous ordered siliceous foams (MOSFs). Information for MOSFs with single-layered, double-layered and multi-layered structures was obtained. More importantly, the authors illustrate that these organic/inorganic composite foams follow the packing model of bubble-like soft materials, which sheds light on the formation principle of the surface area-minimization rule in nanoscience. 3DET can function with the aid of bright-field, dark-field or high-angle annular dark-field imaging as contrast mechanisms. However, the latter, which is sensitive to variations in the atomic number, is more popular since it creates clear phase contrast while the bright-field and dark-field imaging mechanisms can interfere with 3D reconstruction (Saheb et al. 2013). Apart from revealing porosity and structural properties of macroporous materials, 3DET can be coupled with electron energy loss or energy-dispersive spectroscopy to evaluate dislocation dynamics and magnetic domain structure (Rohrer 2014). The resolution of this technique is on the order of 1 nm.
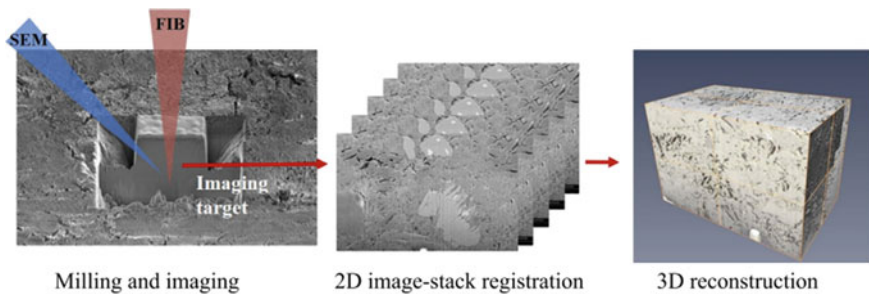
Fig. 11 Reconstruction of 3D volume using dual-beam electron microscopy. Reproduced with permission from Lim et al. (2018). Copyright 2018 Elsevier Ltd.

4.2 *Dual-Beam Electron Microscope*

Dual-beam electron microscope, popularly known as FIB/SEM, is a microstructural characterization technique that combines the merits of Focused Ion Beam (FIB) and SEM (Merchán-Pérez et al. 2014). This technique is well-known to produce high quality three-dimensional images of porous materials through serial milling using FIB and imaging by SEM (Fig. 11), providing characterization of nanopores ranging from 10 nm in diameter. Dual-beam SEM is able to obtain serial images with small and reproducible spacing between the single imaging planes (Lim et al. 2018). Unlike 3DET, which involves a serial tilting of 2D images to reconstruct the 3D volume, FIB/SEM tomography uses computer software for experimental raw data stack processing and graphics packages for 3D (Liu et al. 2019). It is possible to study features at spatial resolutions at the level of tens of nanometers and volumes up to tens of cube microns (Kruk et al. 2018).

Before the discovery of dual-beam electron microscopy, TEM was the only technique that could be used for analyses of structural properties of multi-layered materials. However, due to its in-situ cross-sectional investigation, the dual-beam instrument has become a strong competitor for characterizing multi-layer heterostructures (Alam et al. 2011). Dual-beam instruments can also be used for site-specific sample preparation for TEM (Zhou et al. 2018a, b). Porosity measurement using imaging microscopy is significantly dependent on the quality of material preparation. For example, a cross-section of an inappropriately prepared material could show several cracks, which are known to damage the original microstructure. A sawn-surface preparation leads to substantial damage, leaving a rough surface and residual particulate matter (Lin et al. 2018). FIB is able to provide a high quality surface for SEM imaging by milling the surface with nanometer accuracy. Figure 12 shows porosity evaluation of silica fume modified cement paste using dual-beam microscopy. 3D image in Fig. 12a was reconstructed by aligning and loading 1000 2D images into a 3D bounding container. Total porosity and pore size of the paste can be determined using Fig. 12b, c. Dual-beam electron microscopy addresses a technological void with regard to limited resolution that other 3D imaging techniques, including 3DET
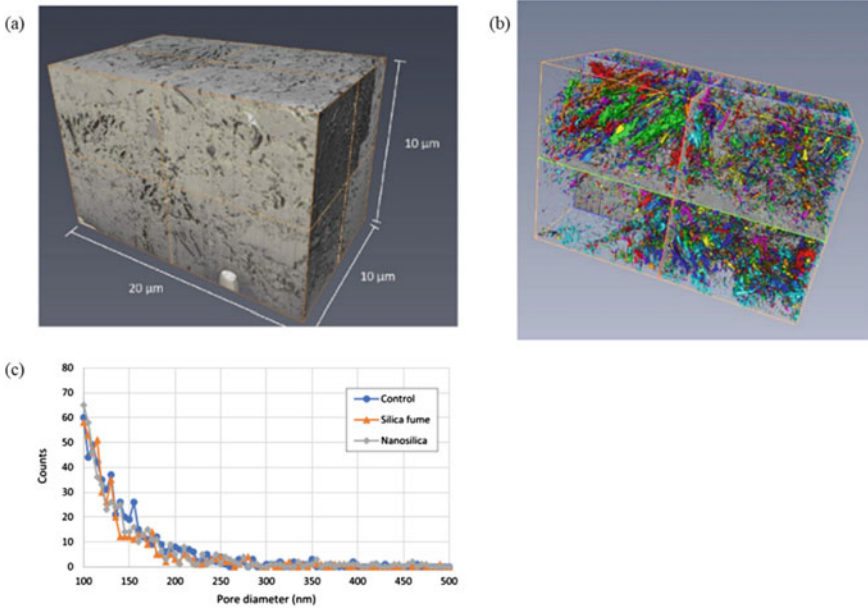
Fig. 12 3D model for the paste sample **a** 1000 slices of 2D SEM images were aligned and stacked, **b** segmentation of pore spaces and **c** pore size distribution measured by dual-beam microscope. Reproduced with permission from Lim et al. (2018). Copyright 2018 Elsevier Ltd.

and MRI, possess. Voxel dimension in the range of 10 nm enables detection of gel pores in cement-based materials (Lim et al. 2018).

Dual-beam tomography is able to demonstrate spatial 3D distribution of particles, an organic binder and pores within a macroporous material as shown in Fig. 13. Al_2O_3 brown body ceramic material was used for imaging analyses and the following information can be extracted from FIB/SEM characterization. The ceramic material consists of a wide range of pores ranging from micropores to macropores. Macroporosity formed due to development of multiple cavities and combined in the material during the removal of the organic binder. The pore shape and position within the structure are used to deduce two mechanisms of their origin development of dry areas (due to lack of binder or being too little) and air entrapment as a result of low homogenization of the ceramic material. However, the sintered material contains smaller pores.

Dual-beam microscopy is popularly applied to microporous materials, such as metal organic frameworks and zeolites. The application to polymers containing macropores can be very challenging and has not been explored much. This is because polymers are very sensitive to ion beam and the optimization of milling conditions have to be more precise (Gaboreau et al. 2016). The potential for this characterization is high and the application to polymers is now expanding. Examples are the 3D imaging of porous membranes and hierarchical systems and chiral gyroid block
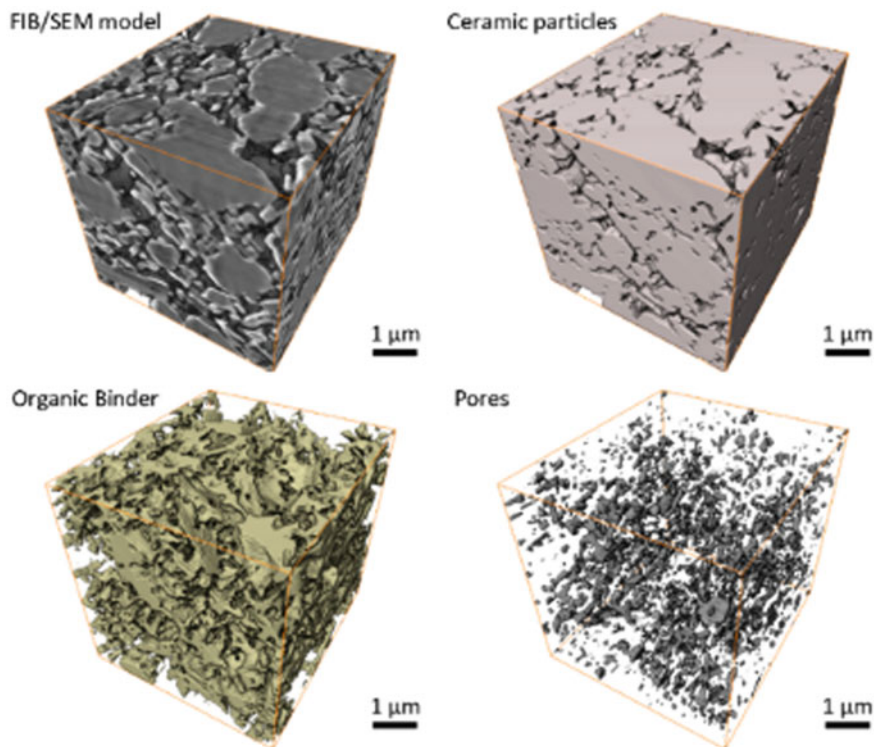
Fig. 13 FIB/SEM-based 3D images of Al_2O_3 ceramic sample. Reproduced with permission from Chugunov et al. (2020). Copyright 2020 Multidisciplinary Digital Publishing Institute

copolymers and molecular imprinted polymers (Alvarez et al. 2019). Another challenge associated with polymers is the difficulties in cross-sectioning the particle. This is usually observed from SEM images when a typical crystal structure is not perfectly clear (for instance, obscured cube in the case of hard materials). To overcome this, the current of the beam and the time of exposure could both be increased since this will increase the charging effects over the sample. Alvarez et al. (2019) successfully employed dual-beam microscopy to reconstruct 3D visualization of polystyrene-b-poly (acrylic acid) (PS-*b*-PAA) copolymer with complex ordered morphology and noted that the polymetric material consists of pores ranging from 32 to 54 nm and sampling volume of $(20 \, \mu m)^3$. Table 2 contains some macroporous materials with pore sizes ranging from 54 nm to 300 μm as well as macroporosity in the range of 3.2–86.7%. These porosity properties were acquired using dual-beam electron microscopy. The accuracy of this technique is affected by few parameters as a number of images acquired to reconstruct a 3D volume, volume dimensions and beam voltage. Gallium ion beam, which has a melting point of 30 °C and lowers vapour pressure compared to mercury, is preferred.

Table 2 Macroporous materials characterized by dual-beam electron microscope and parameters of the data acquisition processes for 3D visualization

Material	Synthetic route	No. of Images acquired	Volume dimensions (μm)	Beam voltage (kV)	Surface area (m²/g)	Connected porosity (%)	Total macroporosity (%)	Pore size (μm)	References
Cement paste	Astm c305	1000	10 × 10 × 20	30	–	14.5	11.55	0.1–0.28	Lim et al. (2018)
Carbonates	–	–	–	–	–	–	11	0.03–0.06	Sok et al. (2010)
Compacted clay	Hydraulic compaction	–	–	1.7	–	71	39	0.1–0.11	Gaboreau et al. (2016)
Al₂o₃ ceramics	Sintering	200	10 × 10 × 10	–	–	11.7	37.3	32	Chugunov et al. (2020)
Ps-*b*-paa	–	–	–	3	112	–	–	0.03–0.05	Alvarez et al. (2019)
Hydroxyapatite	Ultramicrotomy/fib milling	–	–	30	–	–	8.5	1–10	Porter et al. (2006)
Calcite	In-vitro mineralization	200	–	30	–	–	3.2		Chang et al. (2015)
Hydrogel scaffolds	Carbodiimide/active ester-mediated reaction	137	84 × 70 × 17	10	–	–	72	21	Al-Abboodi et al. (2013)
Coal	–	–	–	5	19.58	65.66	5.26	0.02–0.08	Zhou et al. (2018a, b)
Methacrylate scaffold	Azeotropic distillation	–	–	30		~90	86.7	30–300	Hoo et al. (2013)

5 Conclusions

Macroporous materials are characterized by pore sizes of 50 nm or greater. Examples of such materials are polymers, metal foams, sintered materials, glasses, hydrogel scaffolds, woven metal mesh and silica. There has been a sudden growing interest in macroporous materials since the discovery of their applications in drug delivery systems, diagnostics, optics, cosmetics, catalysis, coatings, bio-separation, gas-separation and nanotechnology. However, it is challenging to characterize macroporous materials using bulk techniques due to the nature and complexity of their structures. On the other hand, the use of mercury intrusion porosimetry is limited by several concerns such as toxicity of mercury, as well as difficulty to analyze pressure sensitive materials. Three-dimensional imaging techniques are promising alternative methods. 3D sample imaging is very significant instrument because it gives researchers a clear structural visualization for various materials, including porous materials. The current chapter reviewed a set of three-dimensional imaging techniques: computerized X-ray tomography, 3D electron tomography, dual-beam electron microscopy and magnetic resonance imaging used to image the morphological properties and porosity of macroporous materials. The main objectives herein were to summarize the current state of these techniques and to evaluate their applicability to characterization of macroporous materials. Three-dimensional imaging techniques discussed here can provide a very important information on several structural parameters as such pore size distribution and porosity. Moreover, it is possible to quantify the application of macroporous materials using these techniques. Such applications include water absorption and drainage and percolation of nitrogen—water flooding by macroporous materials. Nonetheless, each technique has drawbacks that may hinder their full potential use. For instance, CXT beam can only detect macropores of at least 100 nm if a synchrotron source is used and 1 μm if a desktop apparatus is used. With regard to MRI, the water content of the substance to be tested has certain requirements and there are limitations in dynamically monitoring the change of material moisture. The precision and validation of these techniques can be enhanced by employing them in parallel or coupling them with other techniques. For example, 3DET can be coupled with posterior image segmentation because this combination can retrieve 3D nearest neighbour distances and a loading model in the case of composite materials.

Progression in the design of macromaterials gradually depends on understanding the reliance of the performance of material on 3D analysis of its microstructure. 3D imaging methods grant the immediate characterization of microstructural properties that fundamentally impact functionality and durability, surface area, cyclability and triple phase boundary length. Moreover, advanced portrayals of imaged microstructures offer practical aspects for modelling.

If applied in concert, the 3D imaging techniques discussed in this chapter can offer a comprehensive, multi-scale understanding of how microstructural properties influence macroporous materials for different applications. Moreover, structural properties that are difficult to observe using bulk or 2D techniques are becoming more

accessible due to increasingly refined three-dimensional techniques. These properties involve, for instance, interface and boundary characteristics, contiguity and tortuosity. The emerging science of macroporous materials may potentially result in advancement of reliable cell immobilization and electrical insulating devices among other many applications of these materials. The three-dimensional imaging techniques reviewed in this article are well suited to aid in establishing the fundamental knowledge necessary for the design of materials for high performing, durable and economical energy technologies.

References

Akpa, B.S., Mantle, M.D., Sederman, A.J., Gladden, L.F.: In situ 13C DEPT-MRI as a tool to spatially resolve chemical conversion and selectivity of a heterogeneous catalytic reaction occurring in a fixed-bed reactor. Chem. Commun. **21**, 2741–2743 (2005). https://doi.org/10.1039/B501698C

Al-Abboodi, A., Fu, J., Doran, P.M., Chan, P.P.Y.: Three-dimensional nanocharacterization of porous hydrogel with ion and electron beams. Biotechnol. Bioeng. **110**(1), 318–326 (2013). https://doi.org/10.1002/bit.24612

Alam, M.Z., Saha, S., Sarma, B., Das, D.K.: Formation of WSi2 coating on tungsten and its short-term cyclic oxidation performance in air. Int. J. Refract Metal Hard Mater. **29**, 54–63 (2011)

Alvarez, J., Saudino, G., Musteata, V., Madhavan, P., Genovese, A., Behzad, A.R., Sougrat, R., Boi, C., Peinemann, K.V., Nunes, S.P.: 3D analysis of ordered porous polymeric particles using complementary electron microscopy methods. Sci. Rep. **9**(1), 1–10 (2019). https://doi.org/10.1038/s41598-019-50338-2

Andersson, L., Jones, A.C., Knackstedt, M.A., Bergström, L.: Three-dimensional structure analysis by X-ray micro-computed tomography of macroporous alumina templated with expandable microspheres. J. Eur. Ceram. Soc. **30**(12), 2547–2554 (2010). https://doi.org/10.1016/j.jeurceramsoc.2010.05.003

Apeleo Zubiri, B., Weissenberger, T., Przybilla, T., Wirth, J., Englisch, S., Drobek, D., Schwieger, W., Spiecker, E.: Scale-bridging 3D analysis of micro-/macroporous zeolite particles using X-ray nano-tomography and electron tomography. Microsc. Microanal. **25**(S2), 396–397 (2019). https://doi.org/10.1017/s143192761900271x

Bonin, J., Maurin, A., Robert, M.: Molecular catalysis of the electrochemical and photochemical reduction of CO$_2$ with Fe and Co metal based complexes. Recent Adv. Coord. Chem. Rev. **334**, 184–198 (2017). https://doi.org/10.1016/j.ccr.2016.09.005

Bossa, N., Chaurand, P., Vicente, J., Borschneck, D., Levard, C., Aguerre-Chariol, O., Rose, J.: Micro- and nano-X-ray computed-tomography: a step forward in the characterization of the pore network of a leached cement paste. Cem. Concr. Res. **67**, 138–147 (2015). https://doi.org/10.1016/j.cemconres.2014.08.007

Chang, E.P., Williamson, G., Evans, J.S.: Focused ion beam tomography reveals the presence of micro-, meso-, and macroporous intracrystalline regions introduced into calcite crystals by the gastropod nacre protein AP7. Cryst. Growth Des. **15**(4), 1577–1582 (2015). https://doi.org/10.1021/acs.cgd.5b00225

Chen, C., Betz, M.W., Ph, D., Fisher, J.P., Ph, D., Paek, A., Chen, Y., Ph, D.: Macroporous hydrogel scaffolds and their characterization by optical coherence tomography. Tissue Eng. Part C Methods **17**(1), 101–112 (2011). https://doi.org/10.1089/ten.tec.2010.0072

Cho, H.J., Sigmund, E.E., Song, Y.: Magnetic resonance characterization of porous media using diffusion through internal magnetic fields. Materials **5**(12), 590–616 (2012). https://doi.org/10.3390/ma5040590

Cho, W.J., Kim, M.J., Kim, J.S.: Study on the pore structure characteristics of ferronickel-slag-mixed ternary-blended cement. Materials **13**, 4863 (2020)

Chugunov, S., Adams, N.A., Akhatov, I.: Evolution of SLA-based Al_2O_3 microstructure during additive manufacturing process. Materials **13**, 3928 (2020)

Ebner, M., Stampanoni, M., Wood, V.: Visualization and quantification of electrochemical and mechanical degradation in Li Ion batteries visualization and quantification of electrochemical and mechanical degradation in Li Ion batteries. Science **342**, 716 (2013). https://doi.org/10.1126/science.1241882

Erlebacher, J., Seshadri, R.: Hard materials with tunable porosity. MRS Bull. **34**(8), 561–568 (2009). https://doi.org/10.1557/mrs2009.155

Fernandes, J.S., Appoloni, C.R., Moreira, A.C., Fernandes, C.P.: Porosity and pore size distribution determination of tumblagooda formation sandstone by x-ray microtomography. October, 1–7 (2007)

Friedrich, H., Sietsma, J.R.A., De Jongh, P.E., Verkleij, A.J., De Jong, K.P.: Measuring location, size, distribution, and loading of NiO crystallites in individual SBA-15 pores by electron tomography. J. Am. Chem. Soc. **129**(33), 10249–10254 (2007). https://doi.org/10.1021/ja0728876

Gaboreau, S., Robinet, J., Pr, D.: Optimization of pore-network characterization of a compacted clay material by TEM and FIB/SEM imaging. Microporous Mesoporous Mater. **224**, 116–128 (2016). https://doi.org/10.1016/j.micromeso.2015.11.035

Gladden, L.F., Mitchell, J.: Measuring adsorption, diffusion and flow in chemical engineering: applications of magnetic resonance to porous media. New J. Phys. **13**, 035001 (2011). https://doi.org/10.1088/1367-2630/13/3/035001

Heim, K., Bernier, F., Pelletier, R., Lefebvre, L.P.: High resolution pore size analysis in metallic powders by X-ray tomography. Case Stud. Nondestruct. Test. Evaluat. **6**, 45–52 (2016). https://doi.org/10.1016/j.csndt.2016.09.002

Hemes, S., Desbois, G., Urai, J.L., Schr, B.: Multi-scale characterization of porosity in Boom Clay (HADES-level, Mol, Belgium) using a combination of X-ray m-CT, 2D BIB-SEM and FIB-SEM tomography. Microporous Mesoporous Mater. **208**, 1–20 (2015). https://doi.org/10.1016/j.micromeso.2015.01.022

Hertel, S., Hunter, M., Galvosas, P.: Magnetic resonance pore imaging, a tool for porous media research. Phys. Rev. E Stat. Nonlinear Soft Matter Phys. **87**(3), 2–5 (2013). https://doi.org/10.1103/PhysRevE.87.030802

Hoo, S., Loh, Q., Yue, Z., Fu, J., Tan, T.: Preparation of a soft and interconnected macroporous hydroxypropyl cellulose methacrylate scaffold for adipose tissue engineering. J. Mater. Chem. B **1**(24), 3107–3117 (2013)

Jain, V., Kandasubramanian, B.: Functionalized graphene materials for hydrogen storage. J. Mater. Sci. **55**, 1865–1903 (2020). https://doi.org/10.1007/s10853-019-04150-y

Janssen, A.H., Yang, C.M., Wang, Y., Schüth, F., Koster, A.J., De Jong, K.P.: Localization of small metal (oxide) particles in SBA-15 using bright-field electron tomography. J. Phys. Chem. B **107**(38), 10552–10556 (2003). https://doi.org/10.1021/jp034750h

Jeon, K., Moon, H.R., Ruminski, A.M., Jiang, B., Kisielowski, C., Bardhan, R., Urban, J.J.: Air-stable magnesium nanocomposites provide rapid and high-capacity hydrogen storage without using heavy-metal catalysts. Nat. Mater. **10**(4), 1–5 (2011). https://doi.org/10.1038/nmat2978

Jerban, S., Elkoun, S.: Individual pore and interconnection size analysis of macroporous ceramic scaffolds using high-resolution X-ray tomography. Mater. Charact. **118**, 454–467 (2016). https://doi.org/10.1016/j.matchar.2016.06.030

Karatas, O.H., Toy, E.: Three-dimensional imaging techniques: a literature review. Eur. J. Dent. **8**(1), 132–140 (2019). https://doi.org/10.4103/1305-7456.126269

Kastner, J., Plank, B., Salaberger, D., Sekelja, J.: Defect and porosity determination of fibre reinforced polymers by X-ray computed tomography. NDT in Aerospace 2010 - We.1.A.2, 1–12 (2010)

Korat, L., Ducman, V., Legat, A., Mirtic, B.: Characterisation of the pore-forming process in lightweight aggregate based on silica sludge by means of X-ray micro-tomography (micro-CT) and mercury intrusion porosimetry (MIP). Ceram. Int. **39**, 6997–7005 (2013). https://doi.org/10.1016/j.ceramint.2013.02.037

Kruk, A., Cempura, G., Lech, S.: Application of analytical electron microscopy and tomographic techniques for metrology and 3D imaging of microstructural elements in Allvac® 718 Plus™. In: *Proceedings of the 9th International Symposium on Superalloy 718 & Derivatives: Energy, Aerospace, and Industrial Applications*, pp. 1035–1050 (2018). https://doi.org/10.1007/978-3-319-89480-5

Li, P., Shao, S.: Can X-ray computed tomography (CT) be used to determine the pore—size distribution of intact loess? Environ. Earth Sci. **79**(1), 1–12 (2020). https://doi.org/10.1007/s12665-019-8777-z

Lim, S., Lee, H.S., Kawashima, S.: Pore structure refinement of cement paste incorporating nanosilica: study with dual beam scanning electron microscopy/focused ion beam (SEM/FIB). Mater. Charact. **145**(April), 323–328 (2018). https://doi.org/10.1016/j.matchar.2018.08.045

Lin, G., Xi, S., Pan, C., Lin, W., Xie, K.: Growth of 2 cm metallic porous TiN single crystal. Mater. Horiz. **5**, 953–960 (2018). https://doi.org/10.1039/C8MH00494C

Liu, Y., Elam, F.M., Zoethout, E., Starostin, S.A., Van De Sanden, M.C.M., De Vries, H.W.: Atmospheric-pressure silica-like thin film deposition using 200 kHz/13.56 MHz dual frequency excitation. J. Phys. D: Appl. Phys. **52**(35) (2019). https://doi.org/10.1088/1361-6463/ab269b

Lucas-Oliveira, E., Araujo-Ferreira, A.G., Trevizan, W.A., Fortulan, C.A., Bonagamba, T.J.: Computational approach to integrate 3D X-ray microtomography and NMR data. J. Magn. Reson. **292**, 16–24 (2018). https://doi.org/10.1016/j.jmr.2018.05.001

Lyu, J., Kudiiarov, V.: An overview of the recent progress in modifications of carbon nanotubes for hydrogen adsorption. Nanomaterials **10**, 255 (2020)

Manickam, S., McCutcheon, J.R.: Characterization of polymeric nonwovens using porosimetry, porometry and X-ray computed tomography. J. Membr. Sci. **407–408**, 108–115 (2012). https://doi.org/10.1016/j.memsci.2012.03.022

Melicchio, A., Liguori, P.F., Russo, B., Golemme, G.: Strategy for the enhancement of H_2 uptake in porous materials containing TiO_2. Int. J. Hydrogen Energy **41**, 5733–5740 (2016). https://doi.org/10.1016/j.ijhydene.2016.02.050

Merchán-Pérez, A., Rodríguez, J.R., González, S., Robles, V., Defelipe, J., Larrañaga, P., Bielza, C.: Three-dimensional spatial distribution of synapses in the neocortex: a dual-beam electron microscopy study. Cereb. Cortex **24**(6), 1579–1588 (2014). https://doi.org/10.1093/cercor/bht018

Morozov, E.V., Buznik, V.M., Bespalov, A.S., Grashchenkov, D.V.: Magnetic resonance imaging of water absorption by highly porous ceramic materials. Dokl. Chem. **484**(2), 44–47 (2019). https://doi.org/10.1134/S0012500819020058

Nishikawa, Y., Baba, S., Takahashi, M.: Optimization of X-ray computerized tomography for polymer materials optimization of X-ray computerized tomography for polymer materials. Int. J. Polym. Mater. Polym. Biomater. **62**, 295–300 (2013). https://doi.org/10.1080/00914037.2012.664215

Nott, K.P., Paterson-Beedle, M., Macaskie, L.E., Hall, L.D.: Visualisation of metal deposition in biofilm reactors by three-dimensional magnetic resonance imaging (MRI). Biotech. Lett. **23**(21), 1749–1757 (2001). https://doi.org/10.1023/A:1012492216390

Peng, S., Hu, Q., Dultz, S., Zhang, M.: Using X-ray computed tomography in pore structure characterization for a Berea sandstone: Resolution effect. J. Hydrol. **472–473**, 254–261 (2012). https://doi.org/10.1016/j.jhydrol.2012.09.034

Porter, A.E., Buckland, T., Hing, K., Best, S. M., Bonfield, W., Al, P.E.T.: The structure of the bond between bone and porous silicon-substituted hydroxyapatite bioceramic implants. J. Biomed. Mater. Res. Part 1, **78**(1), 25–33 (2006). https://doi.org/10.1002/jbm.a

Proietti, N., Capitani, D., Cozzolino, S., Valentini, M., Pedemonte, E., Princi, E., Vicini, S., Segre, A.L.: In situ and frontal polymerization for the consolidation of porous stones: a unilateral NMR and magnetic resonance imaging study. J. Phys. Chem. B **110**(47), 23719–23728 (2006). https://doi.org/10.1021/jp063219u

Radakovi, J., Iordoc, M., Mirkovi, M., Batalovi, K.: ScienceDirect influence of Ta and Nb on the hydrogen absorption kinetics in Zr-based alloys. 4–9 (2015). https://doi.org/10.1016/j.ijhydene.2015.02.083

Rigby, S.P., Fletcher, R.S., Raistrick, J.H., Riley, S.N.: Characterisation of porous solids using a synergistic combination of nitrogen sorption, mercury porosimetry, electron microscopy and micro-focus X-ray imaging techniques. Phys. Chem. Chem. Phys. **4**(14), 3467–3481 (2002). https://doi.org/10.1039/b110781j

Rigby, S.P., Chigada, P.I., Wang, J., Wilkinson, S.K., Bateman, H., Al-Duri, B., Wood, J., Bakalis, S., Miri, T.: Improving the interpretation of mercury porosimetry data using computerised X-ray tomography and mean-field DFT. Chem. Eng. Sci. **66**(11), 2328–2339 (2011). https://doi.org/10.1016/j.ces.2011.02.031

Rigby, S.P., Stevens, L., Meersmann, T., Pavlovskaya, G.E., Rees, G.J., Henderson, J., Bryant, J., Edler, K.J., Fletcher, R.S.: Structural and chemical heterogeneity in ancient glass probed using gas. Mater. Charact. **167**, 110467 (2020). https://doi.org/10.1016/j.matchar.2020.110467

Rohrer, G.S.: Microstructural characterization of hard ceramics. In: Comprehensive Hard Materials, vol. 2, pp. 265–284. Elsevier Ltd. (2014) https://doi.org/10.1016/B978-0-08-096527-7.00027-1

Rouquerol, J., Baron, G., Denoyel, R., Giesche, H., Groen, J., Klobes, P., Levitz, P., Neimark, A.V., Rigby, S., Skudas, R., Sing, K., Thommes, M., Unger, K.: Liquid intrusion and alternative methods for the characterization of macroporous materials (IUPAC technical report). Pure Appl. Chem. **84**(1), 107–136 (2012b). https://doi.org/10.1351/PAC-REP-10-11-19

Rouquerol, J., Baron, G.V., Denoyel, R., Giesche, H., Groen, J., Klobes, P., Levitz, P., Neimark, A.V., Rigby, S., Skudas, R., Sing, K., Thommes, M., Unger, K.: The characterization of macroporous solids: an overview of the methodology. Microporous Mesoporous Mater. **154**, 2–6 (2012). https://doi.org/10.1016/j.micromeso.2011.09.031

Saheb, N., Iqbal, Z., Khalil, A., Hakeem, A.S., Aqeeli, N.Al., Laoui, T., Al-qutub, A.: Spark Plasma Sintering of Metals and Metal Matrix Nanocomposites: A Review (2013). https://doi.org/10.1155/2012/983470

Salomons, G.J., Park, Y.S., Kim, B.: Polymer gel dosimetry using x-ray computed tomography: a feasibility study. Phys. Med. Biol. **45**, 2559 (2000)

Sederman, A.J., Mantle, M.D., Dunckley, C.P., Huang, Z., Gladden, L.F.: In Situ MRI Study of 1-octene Isomerisation and Hydrogenation within a Trickle-bed Reactor. Catal. Lett. **103**(1–2), 1–8 (2005). https://doi.org/10.1007/s10562-005-7522-2

Shun, T.T., Chang, L.Y., Shiu, M.H.: Microstructure and mechanical properties of multiprincipal component CoCrFeNiMox alloys. Mater. Charact. **70**, 63–67 (2012)

Sok, R., Varslot, T.K., Knackstedt, M.: Pore scale characterization of carbonates at multiple scales: integration of micro-CT, BSEM and FIBSEM. J. Form. Evoluat. Reservoir **51**(06), 1–12 (2010)

Somo, T.R., Mabokela, T.E., Teffu, D.M., Sekgobela, T.K., Hato, M.J., Modibane, K.D.: Review on the effect of metal oxides as surface coatings on hydrogen storage properties of porous and non-porous materials. Chem. Pap. **10**, 1 (2021a). https://doi.org/10.1007/s11696-020-01466-x

Somo, T.R., Davids, M.W., Lototskyy, M.V., Hato, M.J., Modibane, K.D.: Improved hydrogenation kinetics of TiMn1.52 alloy coated with palladium through electroless deposition. Materials **14**, 1833 (2021b)

Spowage, A.C., Shacklock, A.P., Malcolm, A.A., May, S.L., Tong, L., Kennedy, A.R.: Development of characterisation methodologies for macroporous materials. J. Porous Mater. **13**(3), 431–438 (2006). https://doi.org/10.1007/s10934-006-8042-1

Stannarius, R.: Magnetic resonance imaging of granular materials. Rev. Sci. Instrum. **88**(5), 051806 (2017). https://doi.org/10.1063/1.4983135

Studart, R., Gonzenbach, U.T., Tervoort, E., Gauckler, L.J.: Processing routes to macroporous ceramics: a review. J. Am. Ceram. Soc. **89**(6), 1771–1789 (2006). https://doi.org/10.1111/j.1551-2916.2006.01044.x

Switendick, A.C.: Band structure calculations for metal hydrogen system. J. Phys. Chem. **117**, 89–112 (1979)

Tang, F., Fudouzi, H., Uchikoshi, T., Sakka, Y.: Preparation of porous materials with controlled pore size and porosity. J. Eur. Ceram. Soc. **24**(2), 341–344 (2004). https://doi.org/10.1016/S0955-2219(03)00223-1

Villevieille, C.: Electrochemical characterization of rechargeable lithium batteries. In Rechargeable Lithium Batteries: From Fundamentals to Applications. Elsevier Ltd. (2015). https://doi.org/10.1016/B978-1-78242-090-3.00007-9

Wang, H., Zhou, X., Yu, M., Wang, Y., Han, L., Zhang, J., Yuan, P., Auchterlonie, G., Zou, J., Yu, C.: Supra-assembly of siliceous vesicles. J. Am. Chem. Soc. **128**(50), 15992–15993 (2006). https://doi.org/10.1021/ja066707o

Wang, H., Liu, Y., Song, Y., Zhao, Y., Zhao, J., Wang, D.: Fractal analysis and its impact factors on pore structure of artificial cores based on the images obtained using magnetic resonance imaging. J. Appl. Geophys. **86**, 70–81 (2012). https://doi.org/10.1016/j.jappgeo.2012.07.015

Wang, D., He, H., Han, L., Lin, R., Wang, J., Wu, Z., Liu, H., Xin, H.L.: Three-dimensional hollow-structured binary oxide particles as an advanced anode material for high-rate and long cycle life lithium-ion batteries. Nano Energy **20**, 212–220 (2016). https://doi.org/10.1016/j.nanoen.2015.12.019

Wang, B., Prinsen, P., Wang, H., Bai, Z., Wang, H., Luque, R., Xuan, J.: Macroporous materials: microfluidic fabrication, functionalization and applications. Chem. Soc. Rev. **46**(3), 855–914 (2017). https://doi.org/10.1039/c5cs00065c

Wargo, E.A., Kotaka, T., Tabuchi, Y., Kumbur, E.C.: Comparison of focused ion beam versus nano-scale X-ray computed tomography for resolving 3-D microstructures of porous fuel cell materials. J. Power Sources **241**, 608–618 (2013). https://doi.org/10.1016/j.jpowsour.2013.04.153

Xue, D.J., Liu, H.W.Z.Y.T., Zhang, L.S.D.L.: Study of drainage and percolation of nitrogen—water flooding in tight coal by NMR imaging. Rock Mech. Rock Eng. **51**(11), 3421–3437 (2018). https://doi.org/10.1007/s00603-018-1473-6

Yuan, P., Zhou, X., Wang, H., Liu, N., Yifan, H., Auchterlonie, G.J., Drennan, J., Yao, X., Lu, G.Q., Zou, J., Chengzhong, Y.: Electron-tomography determination of the packing structure of mecroporous ordered siliceous foams assembled from vesicles. Small **5**(3), 377–382 (2009). https://doi.org/10.1002/smll.200801020

Zhao, Y., Zhu, G., Dong, Y., Noraei, N., Chen, Z.: Comparison of low-field NMR and microfocus X-ray computed tomography in fractal characterization of pores in artificial cores. Fuel **210**, 217–226 (2017). https://doi.org/10.1016/j.fuel.2017.08.068

Zhou, J., Taylor, M., Melinte, G.A., Shahani, A.J., Dharmawardhana, C.C., Heinz, H., Voorhees, P.W., Perepezko, J.H., Bustillo, K., Ercius, P., Miao, J.: Quantitative characterization of high temperature oxidation using electron tomography and energy-dispersive X-ray spectroscopy. Sci. Rep. **8**(1), 1–8 (2018). https://doi.org/10.1038/s41598-018-28348-3

Zhou, S., Liu, D., Cai, Y., Karpyn, Z., Yao, Y.: Comparative analysis of nanopore structure and its effect on methane adsorption capacity of Southern Junggar coal field coals by gas adsorption and FIB-SEM tomography. Microporous Mesoporous Mater. **272**, 117–128 (2018). https://doi.org/10.1016/j.micromeso.2018.06.027

Zhao, Z., Zhang, M., Liu, W., Li, Q.: Measurement of pore sized microporous-mesoporous materials by time-domain nuclear magnetic resonance. BioResourses **15**(1), 1407–1418 (2020)

Synthesis of Mesoporous Materials

Antony Rajendran, Hong-Xia Fan, and Wen-Ying Li

Abstract Mesoporous materials have become indispensable in every aspect of materials science due to their applications in various fields such as catalysis, adsorption, sensing, pharmaceutics and electrochemistry. The higher selectivity in performance highlights the ordered mesoporous materials (OMMs) as the most intriguing and continuously flourishing materials. The versatility in tuning the key properties of OMMs including pore size, pore volume, pore symmetry, surface area and stability by suitable synthetic strategies and conditions underlines the significance of synthetic methods. Since 1990s, the synthesis of OMMs has been a hot topic in materials science, and so far, the different methods have been attempted for preparing various OMMs. This chapter aims to cover all the possible synthetic methods and their key parameters for preparing various OMMs. The properties of mesoporous materials are discussed at the outset.

Keywords Ordered mesoporous materials · Surfactant · Micelle · Hard template · Metal-organic framework

Abbreviations

AMS	Anionic Surfactant Templated Mesoporous Silica
BET	Brunauer-Emmett-Teller
BJH	Barrett-Joyner-Halenda
CASH	Combined Assembly by Soft and Hard Chemistries
CMC	Critical Micelle Concentration
CMK	Carbon Material Korea
CMT	Critical Micelle Temperature
COF	Covalent Organic Framework
COK	Centre for Research Chemistry and Catalysis

A. Rajendran (✉) · H.-X. Fan · W.-Y. Li (✉)
State Key Laboratory of Clean and Efficient Coal Utilization, Taiyuan University of Technology, Taiyuan 030024, China
e-mail: ying@tyut.edu.cn

CP	Cloud Point
CTAB	Cetyltrimethylammonium Bromide
CTEAB	Cetyltriethylammonium Bromide
EIAA	Evaporation-Induced Aggregating Assembly
EIMCA	Evaporation-induced multicomponent co-assembly
EISA	Evaporation-Induced Self-Assembly
EO	Ethylene oxide
FDU	Fudan University Material
FSM	Folding Sheet Material
HMS	Hexagonal Mesoporous Silica
HMTA	Hexamethylenetetramine
IUPAC	International Union for Pure and Applied Chemistry
KIT	Korea Advanced Institute of Science and Technology
MCM	Mobil Catalytic Material
MOF	Metal Organic Framework
MSU	Michigan State University
NMR	Nuclear Magnetic Resonance
OMC	Ordered Mesoporous Carbon
OMCOF	Ordered Mesoporous Covalent Organic Framework
OMM	Ordered Mesoporous Material
OMMO	Ordered Mesoporous Metal Oxide
OMMOF	Ordered Mesoporous Metal Organic Framework
OMS	Ordered Mesoporous Silica
OMZ	Ordered Mesoporous Zeolite
TMAOH	Tetramethylammonium Hydroxide
TEAOH	Tetraethylammonium Hydroxide
PCH	Layered Silicate
PEO	Polyethylene Oxide
PMMA	Polymethyl Methacrylate
PMO	Periodic Mesoporous Organosilica
PO	Propylene oxide
PPO	Polypropylene oxide
PS	Polystyrene
SBA	Santa Barbara Amorphous
SDA	Surface Directing Agent
TEOS	Tetraethyl Orthosilicate
THF	Tetrahydrofuran
TMS	Titanium Metal Oxide Molecular Sieve
TPU	Tianjin Polytechnic University
XRD	X-Ray Diffraction

1 Introduction

Porous materials are of great importance as they provide highly accessible surface area in comparison with their non-porous counterparts (Wagner et al. 2013; Zhu and Yuan 2015; Wu and Zhao 2011). Regardless of composition and particle size, the International Union for Pure and Applied Chemistry (IUPAC) classifies the porous materials into three common types such as microporous (<2 nm), mesoporous (2–50 nm) and macroporous (<50 nm) materials on the basis of pore diameter (Sing 1982; Thommes et al. 2015). IUPAC adopted the Greek prefix "*meso*", which has the meaning of "in between", to define the mesoporous materials having the pore diameter between macropore and micropore (Pal and Bhaumik 2013). The mesoporous materials have received much attention than the other two because of their pore size and pore volume which are very much suitable for finding applications in almost all the areas including adsorption (Wu and Zhao 2011), catalysis (Tüysüz and Schüth 2012), sensors (Wagner et al. 2013), electrochemistry (Walcarius 2013; Du et al. 2019) and pharmaceutics (Vallet-Regí 2006; Zhou and Hartmann 2013). The mesoporous materials are either ordered or disordered, which is basically determined by pore size distribution. Ordered mesoporous materials (OMMs) possess the pores of uniform size (narrow pore size distribution) with long-range order (e.g. SBA-15, SBA: Santa Barbara Amorphous) whereas the disordered mesoporous materials do not exhibit such properties (e.g. clays) (McCusker et al. 2001). Therefore, OMMs are highly selective in performance and strongly recommended for the practical applications and provide the beneficial mass transfer of reactants and products (Wu and Zhao 2011; Taguch and Schüth 2005; Garcia-Bennett 2011). While the research interest on OMMs has been swiftly and continuously thriven to the next stage due to their extensive applications, the new research on disordered mesoporous materials is relatively slow. Thus, this chapter primarily focuses on the synthetic methods and key synthetic parameters regarding the preparation of OMMs reported so far.

OMMs constitute the materials of various kinds including silica (Florek et al. 2014), metal oxides (Ren et al. 2012), carbon (Ryoo et al. 2001), metal–organic frameworks (MOFs) (Song et al. 2012), zeolites (Chen et al. 2011) and covalent-organic frameworks (COFs) (Díaz an Corma 2016), while the templates are essential for the preparation of ordered mesoporous silicas (OMSs), ordered mesoporous metal oxides (OMMOs), ordered mesoporous carbons (OMCs), ordered mesoporous zeolites (OMZs), the preparation of ordered mesoporous MOFs (OMMOFs) and ordered mesoporous COFs (OMCOFs) usually do not require the templates. Before the in-depth discussion on the synthesis of diverse OMMs, giving a brief introduction about the first-ever reports of above-listed OMMs along with their synthetic details seems important. The timeline displaying the discovery of different OMMs is illustrated in Fig. 1. The invention of first OMS (MCM-41, MCM: Mobil Catalytic Material) in 1991 by Mobil is regarded as a milestone in materials science (Kresge et al. 1992c). Before this landmark achievement, Kuroda and his co-workers had already observed the generation of a complex containing cationic surfactants and
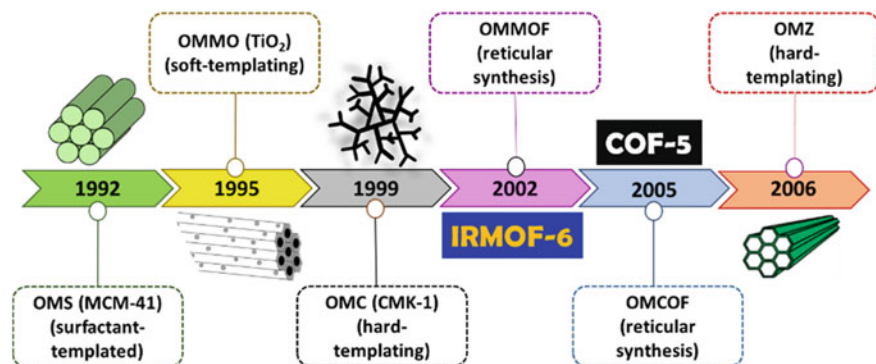
Fig. 1 Timeline showing the discovery of different OMMs. The structure of OMZ is adapted from (Fang and Hu 2006) with permission from American Chemical Society. For the structure of IRMOF-6 (Eddaoudi et al. 2002) and COF-5 (Côté et al. 2005), the corresponding articles may be referred

clays at basic conditions while pillaring the clay (Kanemite) using alkyltrimethyl-lammonium cations. However, they had prepared only a mixed phase of surfactant and silicate, i.e. the surfactant removal was not performed, and had not provided the enough characterization details and formation mechanism for the further proceedings (Yanagisawa et al. 1990). Few years later (1996), the observed complex material was regarded as a new OMS, i.e. FSM-16 (FSM: Folding Sheet Material) (Inagaki et al. 1996a, b). Coming to the first preparation of OMS (MCM-41), the Mobil researchers had initially applied a pillaring strategy of clays to zeolites for producing the zeolites with a large pore size. This is because the zeolites usually demonstrate a better thermal stability and catalytic activity in most of the petrochemical processes. The zeolite materials were obtained from the interrupted synthesis, i.e. the incomplete crystallization of zeolites, in order to facilitate the delamination of zeolite layers. To the interrupted zeolite precursor, a long-chain alkyltrimethylammonium salt and tetramethylammonium silicate were added as intercalator and potential pillaring agent, respectively. The obtained synthetic mixture was subjected to hydrothermal treatment that yielded the product with some very unusual properties. After repeating the same experiment for multiple times at different venues, the formation of same product was invariably confirmed. This same product was also obtained while adding the hexadecyltrimethylammonium hydroxide directly as a surface directing agent (SDA) in zeolite-like hydrothermal synthesis. Eventually, the Mobil researchers had established the formation of a very first OMM, i.e. MCM-41, an OMS. They had also proved that the different OMSs can be prepared simply by varying the concentration or the alkyl chain length of surfactant by keeping all the other reaction conditions same (Kresge et Kresge et al. 1992a, b, c; Beck et al. 1992). To know more details about the discovery of MCM-41, the highlight reported by Kresge and Roth would be useful (Kresge and Roth 2013). The generalized synthetic mechanism established by the researchers of Mobil company (Fig. 2) has paved the way for the discovery of different OMMs, which is still very much useful.
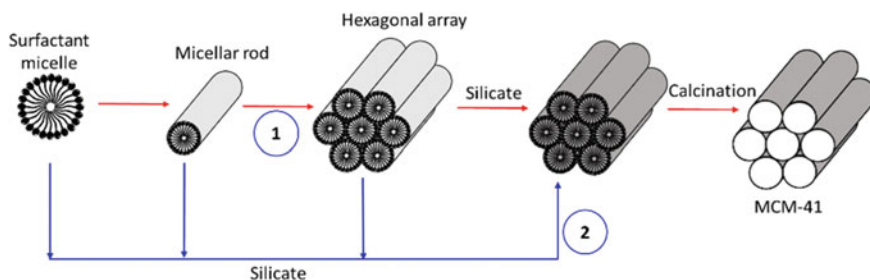
Fig. 2 Initially proposed liquid crystalline template mechanism of formation pathways. (1): liquid crystal initiated and (2) silicate-initiated pathway operating in almost all situations. Adapted from Beck et al. (1992) with permission from American Chemical Society

Following the strategy used in the formation of MCM-41, Antonelli and Ying had prepared the very first OMMO (titania) in 1995 using tetradecylphosphate as a soft template which involved a strong interaction with the titania framework via phosphorus (Antonelli and Ying 1995). Note that the OMS framework is stable and can be easily assembled from tetrahedral building blocks whereas the corresponding synthesis of OMMOs is challenging due to the vulnerability of metal oxide frameworks to hydrolysis, redox reactions and/or phase transitions and the collapse of porous structure during thermal treatment. As a result, the soft template-assisted synthesis of OMMOs still requires the major efforts to avoid the above-listed problems (Gu and Schüth 2014; Szczęśniak et al. 2020). Subsequently, the first OMC (CMK-1, CMK: Carbon Material Korea) with ordered uniform pores of 3 nm diameter was prepared in 1999 by Ryoo et al. While the preparation of first-ever OMS and OMMO was accomplished using the soft template, CMK-1 was first prepared using a hard template (MCM-48). CMK-1 was prepared in three sequential key steps: (i) impregnation of pores of MCM-48 with carbon precursor, (ii) carbonization of carbon precursor and (iii) silica etching (Ryoo et al. 1999). As this method requires the preparation of hard template (an another OMM, i.e. OMS) and hazardous treatment (NaOH or HF) for the template removal, few years later, the soft templates had been attempted for preparing OMCs (Liang and Dai 2006; Meng et al. 2006; Ma et al. 2013).

Next to OMC, OMMOF was joined the group of OMMs when the first mesoporous MOFs (Zn-containing MOFs with octahedral Zn–O–C clusters) with the pore diameter up to 2.9 nm was prepared in 2002 by Yaghi's research group using the large organic linkers like *p*-terphenyldicarboxylate (Eddaoudi et al. 2002). Few years later (2005), the same group had prepared the first OMCOF with a pore diameter of 2.7 nm and surface area of 1590 cm^2 g^{-1} by condensing 1,4-benzenediboronic acid and 2,3,6,7,10,11-hexahydroxytriphenylene that generated the boronate ester linkages (the backbone of formed OMCOF) (Côté et al. 2005). Unlike the preparation of OMSs, OMMOs and OMCs, the preparation of OMMOFs and OMCOFs commonly does not require any template but their structural network is basically built upon the chemical reactions occurring between chosen starting materials. Such chemical

reactions occur between the metal and ligands during the preparation of OMMOFs, but during the preparation of OMCOFs, those chemical reactions befall between two different organic molecules carrying unique reactive functional groups.

Despite the microporosity of zeolites is well-known for many decades, the first OMZ was prepared only in 2006. Fang and Hu had utilized CMK-5 as a hard template and prepared the first OMZ via three key sequential steps: (i) impregnation of Al-SBA-15/OMC composite with tetrapropylammonium hydroxide, (ii) recrystallization of amorphous silica SBA-15 walls at 175 °C for 48 h in an autoclave and (iii) removal of CMK-5 and organic templates at 550 °C for 5 h in air. In this preparation, besides being a hard template, CMK-5 kinetically controlled the crystallization process to form the large zeolite crystals (Fang and Hu 2006).

In the literature, OMSs, OMMOs, OMCs and OMZs have been often prepared using the templates (soft or hard templates). It is noticed in the literature that the nature of templates, preparation conditions, precursors and the methods of template removal could remarkably influence the properties of resultant OMMs. Regarding the preparation of OMMOFs and OMCOFs, the precursors and the synthetic conditions play a major role in deciding the properties of end products. This chapter discusses the different methods of preparing the OMMs with a special emphasis on soft-templating and hard-templating methods. We believe that the strong understanding on the different preparation methods of various OMMs can be attained through this chapter.

2 Properties of Mesoporous Materials

The important properties of mesoporous materials are listed here.

- Crystallinity
- Pore size and its distribution
- Surface area
- Pore shape
- Pore volume
- Pore symmetry
- Pore connectivity
- Stability
- Constituent elements (composition) and functional groups

The crystallinity of mesoporous materials is basically studied using powder X-ray diffraction (XRD) analysis. Thus, while defining the crystallinity of mesoporous materials, the crystallinity at atomic scale (arrangement of atoms) as well as the crystallinity at mesoscale (pore size distribution) need to be concerned. OMMs (e.g. SBA-15 and MCM-41) have the pores of uniform size with long-range order, and hence, exhibit powder XRD peaks at d-values reflecting the pore-to-pore distance (McCusker et al. 2001). Mesoporous materials with disordered pore structure (e.g. clay and phosphate materials), i.e. with wide pore size distribution (short-range

order), do not display this behaviour in powder XRD analysis. Even though the mesopores are ordered (uniform in size), the periodic arrangement of linked atoms in OMMs can be either ordered (crystalline OMMs) or disordered (amorphous OMMs). In crystalline OMMs, the atoms are periodically arranged with a long-range order, i.e. with minimum 10 replications in all directions, that results in the appearance of sharp maxima in powder XRD analysis. Contrary to this, the linked atoms are periodically arranged with a short-range order in amorphous OMMs, only displaying the sharp peaks corresponding to pore ordering. For example, MCM-41, being an amorphous OMM, shows the low angle powder XRD peaks corresponding to hexagonal pores study and does not reveal any significant peak in wide angle powder XRD analysis (Fig. 3a, b). OMZs are the unique examples to be called crystalline both at mesoscale and at atomic scale which can be evidenced by powder XRD and HR-TEM analyses (Fig. 3c, d).

The pore size, surface area, pore volume and pore shape are the properties of mesoporous materials usually derived by gas porosimetry using a very common Brunauer–Emmett–Teller method (BET, a multilayer extension of Langmuir monolayer adsorption theory). This experiment is mostly performed at 77 K using adsorbates like N_2. The pore size (pore diameter) is a very basic structural property of mesoporous materials. In structural perspective, the pores are actually the voids created by periodic arrangement of linked atoms forming the chemical structure of materials. The mesoporous materials, as mentioned earlier, display the pore diameter in 2–50 nm range.
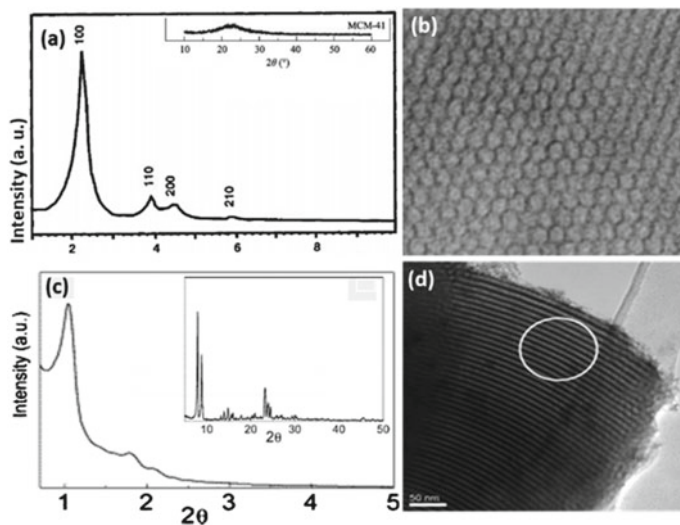
Fig. 3 **a** Small angle powder XRD pattern of MCM-41 (inset: wide angle powder XRD pattern of MCM-41, Adapted from Su et al. (2020) with permission from Elsevier) and **b** HR-TEM image of MCM-41. Adapted from Kresge et al. (1992c) with permission from Springer Nature; **c** powder XRD pattern of OMZ-1 (inset: wide angle powder XRD pattern of OMZ-1) and **d** HR-TEM image of OMZ-1. Adapted from Fang and Hu (2006) with permission from American Chemical Society

Applying Barrett–Joyner–Halenda (BJH) method on N_2 adsorption–desorption data is a typical method to calculate the pore size distribution of mesoporous materials, which is a very important property to distinguish OMMs from disordered mesoporous materials. Surface area of mesoporous materials is commonly quite high; however, it mainly depends upon the synthetic conditions. According to IUPAC definition, all the mesoporous materials either display Type IV (strong adsorbent–adsorbate interaction) or Type V (weak adsorbent–adsorbate interaction) sorption isotherms with hysteresis loops during BET adsorption–desorption studies. The hysteresis loops are observed due to the distinctive capillary condensation of gas adsorbates inside the mesopores. The characteristics of pore shape can be identified from the hysteresis loops as shown in Fig. 4. The mesoporous materials usually contain mesopores in any one of the four shapes listed here: open-ended cylindrical pores (H1 hysteresis), interconnected pores of progressive sizes and shapes (H2 hysteresis), slit-shaped pores (H3 hysteresis) and narrow slit-shaped pores (H4 hysteresis) (Broekhoff 1979; Horikawa et al. 2011; Rouquerol et al. 1999).

Though mesoporous materials are broadly characterized by their porosity and pore size, such characterization might be incomplete without pore symmetry that defines mesostructure and pore connectivity. This is because the pore symmetry of two mesoporous materials can be entirely different despite those materials display identical porosity and pore diameter. Pore symmetry indicates the arrangement explaining how the pore throats connect the neighbouring pores to each other (Sen and Barisik 2019). The diverse mesophase structures have been recognized (Gao 2009; Wan and
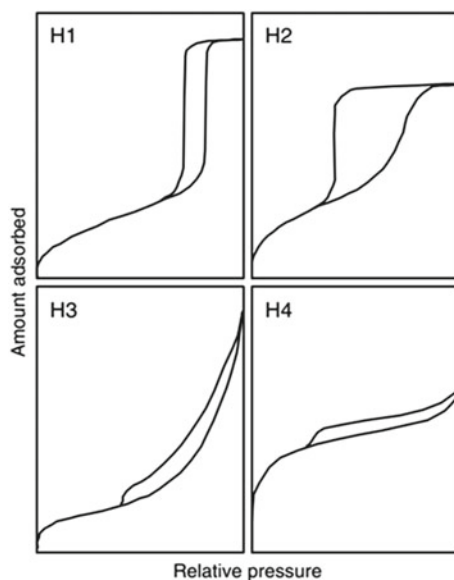
Fig. 4 IUPAC classification of hysteresis loop. Reprinted from Horikawa et al. (2011) with permission from Elsevier

Zhao 2007), which are listed as follows, (i) lamellar (*L*); (ii) hexagonal (*p6mm*); (iii) bicontinuous cubic (*Ia$\bar{3}$d*, *Pn$\bar{3}$m*, *Im$\bar{3}$m*); (iv) cage-type cubic (*Pm$\bar{3}$n*, *Fm$\bar{3}$m*, *Im$\bar{3}$m*, *Fd$\bar{3}$m*, etc.); (v) cage-type hexagonal (*P6$_3$/mmc*); and (vi) other mesophase structure (*P4$_2$/mnm*, *P4/mmm*, *c2mm*, etc.).

The mesophase structure of OMMs is usually exemplified using OMSs due to the wide range of pore symmetry in OMSs. The very common mesophase structures of OMSs are depicted in Fig. 5. While forming OMSs, two-dimensional (2D) hexagonal mesophase with *P6mm* symmetry (e.g. SBA-15 and MCM-41) is frequently reported than other mesophase structures. Next to this, amidst OMSs, cubic mesophase structures including face-centred cubic (*Fm$\bar{3}$m*, close packing of spherical mesopores with each connected to 12 nearest neighbouring mesopores), body-centred cubic (*Im$\bar{3}$m*, every mesopore is connected to 8 neighbouring mesopores) and bicontinuous cubic gyroid (*Ia$\bar{3}$d*, three-dimensional (3D) interconnected pores) are familiar. Among the OMSs having cubic mesostructure, the diffusion through 3D pore structure (*Ia$\bar{3}$d*) is better and attractive than that through 2D hexagonal pore structure (Fm$\bar{3}$m and Im$\bar{3}$m). The mesoporous structure with lamellar symmetry is made up of silica layers (Chew et al. 2010). The pore symmetry details of different mesoporous silicas are provided in Table 1.

The stability such as thermal stability, hydrothermal stability and mechanical stability is considered depending upon the nature of mesoporous materials. The thermal stability of mesoporous silica and aluminosilicates is quite higher than the
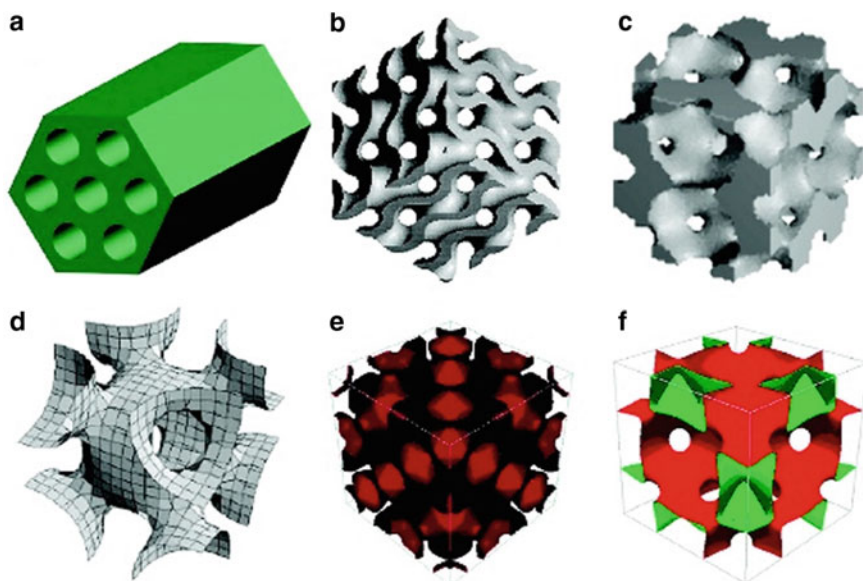
Fig. 5 Pore models of mesostructure with symmetries of **a** *p6mm*, **b** *Ia$\bar{3}$d*, **c** *Pm$\bar{3}$n*, **d** *Im$\bar{3}$m*, **e** *Fd$\bar{3}$m* and **f** *Fm$\bar{3}$m*. Reprinted from (Wan and Zhao 2007) with permission from American Chemical Society

Table 1 Pore symmetry details of OMSs (Chew et al. 2010)

Family	Mesophase symmetry				
	Hexagonal	Tetragonal	Cubic	Lamellar	Rectangular
M41S	MCM-41 ($P6mm$)	–	MCM-48 ($Ia\bar{3}d$)	MCM-50	–
SBA-n	SBA-2 ($P6_3/mmc$) SBA-3 ($P6mm$) SBA-12 ($P6_3/mmc$) SBA-15 ($P6mm$)	–	SBA-1 ($Pm\bar{3}n$) SBA-6 ($Pm\bar{3}m$) SBA-11 ($Pm\bar{3}m$) SBA-14 SBA-16 ($Im\bar{3}\,m$)	–	SBA-8 (cmm)
FSM	FSM-16 ($P6mm$)	–	–	–	–
AMS	AMS-1 ($P6_3/mmc$) AMS-3 ($P6mm$)	$P4_2/mmm$	AMS-2 ($Pm\bar{3}n$) AMS-4 ($Im\bar{3}m$) AMS-6 ($Ia\bar{3}d$) AMS-8 ($Fd\bar{3}m$) AMS-8 ($Fd\bar{3}m$)	AMS-5 ($p2$)	–
FDU	–	–	FDU-1 ($Im\bar{3}m$) FDU-5 ($Ia\bar{3}d$) FDU-12 (Fm$\bar{3}$m)	–	–
KIT	–	–	KIT-5 ($Fm\bar{3}m$) KIT-6 ($Ia\bar{3}d$)	–	–

AMS—anionic-surfactant-templated mesoporous silica; *FDU*—Fudan university material; *KIT*—Korea advanced institute of science and technology

mesoporous metal oxides. The thermal stability of mesoporous silicas is basically related to the thickness of their pore wall. Mesoporous silicas with thick pore walls generally exhibit a higher thermal stability (Zhao et al. 2013a). This is supported by the experimental results of Cassiers et al. who established the thermal stability order of different mesoporous silicas (KIT-1 > SBA-15 > FSM-16 = PCH > MCM-41 = MCM-48 = HMS) (Cassiers et al. 2002). To improve the thermal stability, the pore wall thickness of mesoporous silicas and aluminosilicates can be increased to a certain level by controlling the synthetic parameters; however, it is very difficult to reach the pore wall thickness of microporous zeolites. Compared to mesoporous zeolites, mesoporous silica displays a less thermal stability for the reason that the pore wall thickness of mesoporous silicas is relatively low due to the abundance of silanol groups in the pore walls and lack of crystallinity (Liang et al. 2017). Glass transition temperature (T_g) and crystallization temperature (T_x) are the two key factors deciding the thermal stability of mesoporous materials. A general consensus is that the increase of temperature in mesoporous materials facilitates the movement of atoms on the microscopic scale which is further accelerated at very high temperature. For the materials like mesoporous silicas, T_g seems very significant because the separated melts generated with the increase of temperature would combine together and grow in size to decrease the surface energy by which the mesostructure of mesoporous silicas is collapsed. The thermal stability of mesoporous metal oxides is defined according to their crystallization temperature. Mesoporous metal oxides initially begin to crystallize with the rise of temperature and the size of resultant crystalline particles would

simultaneously grow. At a particular point, the size of crystalline particle becomes larger than the pore wall thickness (~5 nm), and for mesoporous metal oxide, it is disabled to retain the mesostructure (Zhao et al. 2013a). The thermal stability of mesoporous metal oxides can be enhanced by decreasing the crystallization degree or size of crystalline particles by using the crystallization inhibitor (Grosso et al. 2003; Li et al. 2004a). Mesoporous carbons could preserve their mesostructure even at 1900 °C as they have no obvious glass transition and require minimum 2000 °C for the crystallization. Similarly, the non-oxide mesoporous materials like carbides and nitrides also demonstrate the high thermal stability (~1500 °C) because they also have no obvious glass transition and require the devitrification temperature around 1500 °C (Meng et al. 2005, 2006).

Rather than by treating with boiling water, the true hydrothermal stability of mesoporous materials is determined by treating the mesoporous materials with 100% steam at 600–800 °C as it is a common industrial process for the activating catalysts. The mesoporous materials with thick pore walls and condensation degree could exhibit a higher hydrothermal stability. Therefore, the hydrothermal stability of MCM-41 is typically lower than that of SBA-15. The incorporation of Al into the framework of mesoporous silicas can enhance the hydrothermal stability (Wang et al. 2006; Han et al. 2003). Compared to mesoporous silicas, the mesoporous zeolites show the higher hydrothermal stability due to their framework Al species which enable them to find the applications in petroleum refineries and chemical industries. Therefore, it is understood that the framework tetrahedral Al species and Si–O–Al bonds in the mesoporous materials are vital to attain a better hydrothermal stability (Han et al. 2003; Liu et al. 2001; Wang and Pinnavaia 2006; Liu et al. 2000). Besides through the addition of Al, the hydrothermal stability of mesoporous materials can be enhanced by other methods such as the addition of appropriate salt with a suitable molar ratio during the crystallization process (Yu et al. 2001; Ryoo and Jun 1997), post-thermal treatment (Zhang et al. 2005b; Jun et al. 2000) and hydrophobic treatment (Pham et al. 2012; Smeulders et al. 2012; Park et al. 2001).

The mechanical stability of mesoporous materials is mainly related to mesoporous silicas and aluminosilicates, which could withstand the pressure up to 600 MPa. However, due to the large number of pores and amorphous pore walls, the mechanical stability of mesoporous silicas is lesser than that of microporous zeolites (Zhao et al. 2013a). The mechanical stability is defined based on the ratio of pore wall thickness to lattice parameter. Therefore, MCM-41 is mechanically stable than SBA-15. The mesoporous silicas with 3D cubic mesostructure (e.g. MCM-48 and SBA-1) could display the higher mechanical stability than MCM-41 and SBA-15 (Vinu et al. 2003; Hartmann and Vinu 2002; Hartmann and Bischof 1999).

Thermal and hydrothermal stability of mesoporous MOFs and mesoporous COFs mainly depends on the nature of the bonds by which the framework structure is constructed. In addition to these backbone bonds, the other interactions like hydrogen bonding can remarkably increase the thermal stability of mesoporous MOFs and mesoporous COFs. However, the porosity collapse in MOFs and COFs is very familiar upon their activation. Due to the extraordinary porosity, the mechanical

stability of mesoporous MOFs and mesoporous COFs cannot be higher than that of zeolites (Evans et al. 2021; Howarth et al. 2016; Hisaki et al. 2019; Peng et al. 2019).

The composition of constituent elements and functionalization reactions can significantly tune the properties of mesoporous materials, especially the chemical properties. Mesoporous silicas are commonly built up of repeated SiO_4 tetrahedral networks, i.e. mesoporous silicas have Si and O as their constituent elements. The surface silanol (–OH) groups increase the hydrophilicity of mesoporous silicas but the surface of mesoporous silicas can be made hydrophobic by functionalizing the surface Si–OH groups using alkoxy/aryloxy silanes (Vivian et al. 2021; Jambhrunkar et al. 2014). Similarly, using different silanes, various types of functional groups can be introduced on mesoporous silicas through the condensation reactions, which yield the rich chemical properties to mesoporous silicas (Musso et al. 2015; Verma et al. 2020; Hartono et al. 2010). Considering the mesoporous carbons, they are basically hydrophobic in nature and can be made hydrophilic by being functionalized with different functional groups (Bazuła et al. 2008; Zhang et al. 2017; Qian et al. 2018; Song et al. 2016). Mesoporous zeolites are very famous for their intriguing acid properties that generated by the composition of constituent elements such as Si and Al. It is known that a higher Si/Al ratio reduces the number of acid sites (Brønsted acidity) but increases the acid strength and vice-versa (Serrano et al. 2011; Verma et al. 2011). The foreign element can be doped (doped mesoporous metal oxides) or the foreign material can be mixed (composite mesoporous metal oxides) to influence the properties of parent mesoporous metal oxide (Silva et al. 2013; Charan and Rao 2015; Yang et al. 2012; Sun et al. 2015). Regarding the mesoporous MOFs and mesoporous COFs, they can be made rich in constituents and functional groups due to their reactive chemical groups (Sun et al. 2015; Huang et al. 2016).

3 Preparation Methods of Mesoporous Materials

The principal methods for preparing the mesoporous materials are pictorially categorized in Fig. 6 and are broadly classified into two types such as template-assisted and template-free syntheses. Among these two broad types, the template-assisted methods, especially the soft-templating and hard-templating protocols, are very famous as they could routinely yield the highly desirable OMMs. The vivid growth of materials science has exposed the insights about the key factors (e.g. template and its concentration, precursors, template removal methods, etc.) involved in the synthesis of OMMs by soft-templating and hard-templating methods. Regarding the soft-templating method, it is intriguing to mention that the utilization of same procedure by different research groups to prepare a certain OMM has often led to the significant variations in properties. This indicates the opportunities for creating the different porous textures including novel mesoporous family members through the complicated combination of simple synthetic factors of the soft-templating method (Zhao et al. 2013a). Due to the familiarity, diverse opportunities and rich chemistry, the soft-templating method is comprehensively discussed in the following section
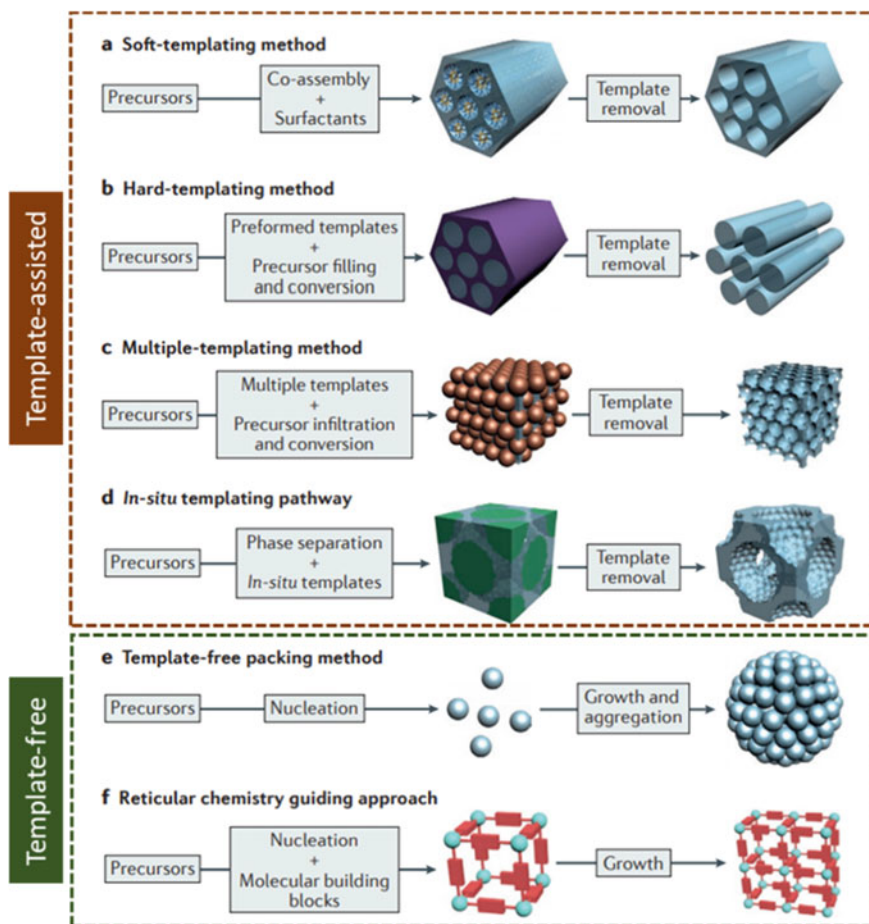
Fig. 6 Principal methods for synthesizing mesoporous materials. Adapted from (Li et al. 2016) with permission from Springer Nature

along with the details of precursors, surfactants and template removal methods. After this, the hard-templating method is adequately discussed. A brief discussion is also made on the template-free synthesis of mesoporous materials including OMMOF and OMCOF, and at the end, the merits and demerits of all the synthetic methods are compared.

4 Template-Assisted Synthesis of OMMs

This method essentially requires the templates to direct the generation of mesoporous structure. Briefly, the precursors of a particular OMM and the required template

cooperate with each other in a certain way to develop an ordered composite structure at a mesoscopic scale. Through specific chemical routes, the target components in composite structure are converted to three-dimensionally interconnected porous network. The subsequent removal of template by a suitable method yields the corresponding OMM (Cui et al. 2019). Two types of templates are used for creating the mesopores such as supramolecular aggregates (e.g. surfactant micelle arrays) and preformed rigid mesoporous solids (e.g. OMS). Accordingly, the template-assisted synthesis of OMMs is broadly classified into soft-templating and hard-templating methods (Li et al. 2013).

4.1 Preparation of OMMs by Soft-Templating Method

In the soft-templating approach, the organic template molecules like amphiphilic surfactants are used whose structure is critical for the formation of mesostructure. For this reason, the template molecules are regarded as the SDAs. Soft templates are constructed by the assembly of surfactant molecules under the preparative conditions. The inorganic precursors are arranged around the self-assembly of surfactant molecules to generate the inorganic–organic composite solid in liquid medium, i.e. the self-assembly of surfactant molecules is present within the assembly of inorganic precursors. Therefore, the soft-templating method is also known as endo-templating method. The choice of a suitable surfactant and its concentration play a very crucial part in determining the characteristics of OMMs. More details about the surfactants required for the generation of soft templates to prepare the OMMs can be seen in Sect. 4.1.2.

Two synthetic mechanisms are mainly considered for the synthesis of OMMs using soft-templating method. The initial liquid–crystal template mechanism proposed by the researchers of Mobil company is always considered true as it fundamentally embraces all the possibilities. The other popular mechanism is based on the cooperative self-assembly of surfactant molecules and the precursors of OMMs (Fig. 7) (Wan and Zhao 2007; Ying et al. 1999; Corma 1997; Schüth 2003; Pal and Bhaumik 2013). The driving force for the cooperative assembly of surfactant molecules and precursors is the spontaneous trend of reduction in interface energy (Hyde and Schröder 2003). During the cooperative assembly, a strong interaction between the surfactant and the precursors of OMM is desirable to overcome the macroscale phase separation (Zhao et al. 2013a).

Three basic steps are usually involved in the preparation of OMMs using soft-templating method as listed below, which can be easily understood from the mechanisms depicted in Fig. 7.

(i)   the self-assembly of surfactant molecules
(ii)   generation of a stable inorganic–organic hybrid via the arrangement of inorganic precursors around the preformed self-assembly of surfactant
(iii) removal of organic template (e.g. micelle rod array) by a suitable method
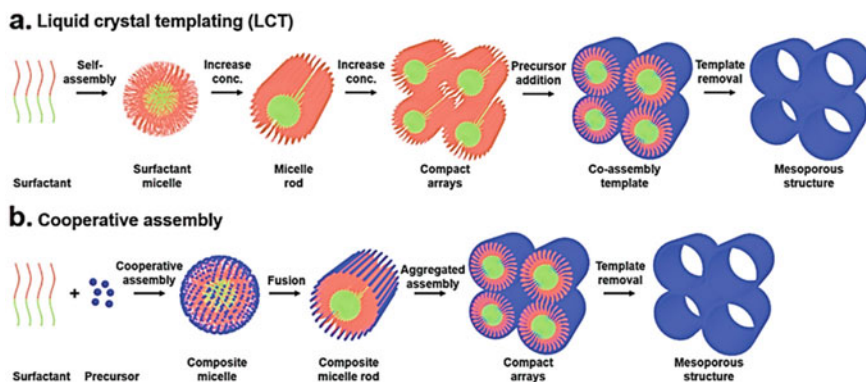
Fig. 7 Formation of mesoporous structures: **a** via true liquid–crystal templating process and **b** via cooperative self-assembly. Reprinted from Qiu et al. (2021) with permission from Wiley

During the synthesis of a certain OMM by soft-templating method, the nature of surfactant and its concentration, nature of the precursor of OMM, synthesis conditions and template removal method need to be very carefully chosen and maintained. Otherwise, the synthesis of OMMs may result in the formation of OMMs with unexpected properties or may get even failed.

Hydrothermal treatment is a significant step in the preparation of OMMs by soft-templating method. Though the mesostructure is usually generated prior to the hydrothermal treatment, the regularity of mesostructure is improved via the reorganization, growth and recrystallization process by the hydrothermal treatment. The hydrothermal treatment is commonly carried out at the moderate temperature (80–150 °C). The prolonged hydrothermal treatment (several days to weeks) is beneficial to attain the highly ordered mesoporous structure. Considering the procedure, the mother liquor is first safely transferred to the hydrothermal autoclave and heated at a static temperature for a prolonged time. Subsequent to this, the obtained solid is filtered and subjected to template removal to obtain the OMM (Zhao et al. 2013a).

Note that the soft-templating preparation of OMMs is usually performed in the aqueous media. Recently, the special soft-templating approach called evaporation-induced self-assembly (EISA) method has become very familiar which can be accomplished in the non-aqueous media.

Soft-templating has been so far successfully applied for the synthesis of various OMMs such as OMSs (Wan and Zhao 2007), OMMOs (Ren et al. 2012), OMCs (Ma et al. 2013) and OMZs (Chen et al. 2020).

OMSs are the exemplary mesoporous materials which are extensively prepared by soft-templating methods for various benefits such as a great variety of possible structures provided by flexible tetra-coordinated silicon atom, a precise control of the hydrolysis-condensation reactions, a better thermal stability of final amorphous networks, and the feasibility of adapting different organic functionalities into its main structural network, outer surface and pore walls (Pal and Bhaumik 2013; Verma et al. 2020; Rosenholm and Lindén 2007). Furthermore, for the preparation of OMSs

by soft-templating method, the availability of silica sources (precursors) is plenty, however tetraethyl orthosilicate (TEOS) is mostly used as silica source in laboratories (Verma et al. 2020; Zhao et al. 1998a, b, 2013a; Shukrun Farrell et al. 2020). Therefore, a special emphasis is given in this chapter for the synthesis of OMSs by the soft-templating method.

The precursors like TEOS are initially hydrolysed either under basic or acidic conditions and subsequently condensed together to form the oligomeric sol as shown in Scheme 1. The oligomeric sol is simultaneously arranged around the surfactant micelles via cooperative assembly that yields the inorganic–organic hybrid in the form of a gel. This gel is subsequently treated under the hydrothermal conditions to generate an ordered arrangement through further condensation, solidification and reorganization. The obtained product is cooled to room temperature, filtered, washed and dried. The resultant solid is subjected to template removal using a method like calcination to obtain the target OMS (Zhao et al. 2013a; Pal and Bhaumik 2013; Wan and Zhao 2007; Berggren et al. 2005).

The synthesis medium is crucial to obtain the desirable OMSs by soft-templating method. Concerning pH of the synthesis solution, it can be basic or acidic. The first-ever reported OMS, i.e. MCM-41, was prepared under basic conditions. In the synthesis of OMSs under basic conditions (pH range = 9.5–12.5), the silicate precursors remain present as anions during the hydrolysis. In this pH range, the cross-linking and polymerization of silicate precursors are reversible, which provides the opportunity to have a great variety of silicate precursors such as silica gels, colloidal sols, water glass (sodium silicates), silica aerogels and TEOS. The higher polymerization degrees of silicate precursors are generally observed while using the silicate precursors except TEOS. This is because all the condensed species are more likely to be ionized at pH > 7 and become mutually repulsive. Consequently, the polymerization proceeds mainly by the addition of monomers to more highly condensed particles rather than by particle aggregation (Zhao et al. 2013a; Brinker and Scherer 1990). To attain the desirable basic conditions during the synthesis of OMSs, different bases are used, for example, sodium hydroxide, potassium hydroxide, aqueous ammonia ($NH_3 \cdot H_2O$), tetramethylammonium hydroxide (TMAOH) and tetraethylammonium
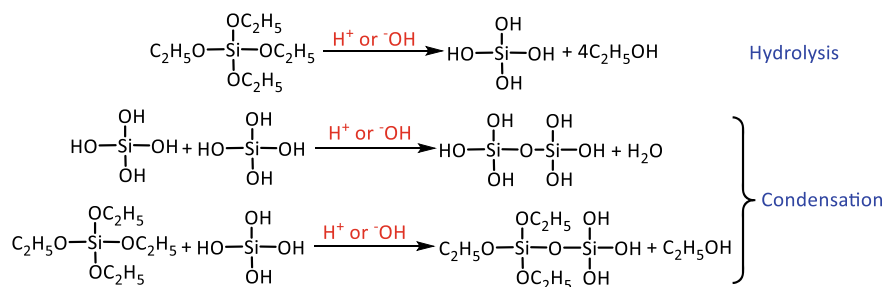
Scheme 1 Hydrolysis and condensation of silicate precursors exemplified using TEOS

hydroxide (TEAOH). Among these different bases, TMAOH and TEAOH are expensive and mostly used for the preparation of H-type aluminosilicates. Due to the weak alkalinity of $NH_3 \cdot H_2O$, the formation of disordered mesoporous silicas may occur sometimes (Zhao et al. 2013a). In the earlier days, hexagonal MCM-41 was easily prepared as compared to the synthesis of cubic MCM-48 under basic conditions. In the progress, the utility of surfactant with a large hydrophilic-head volume has erased down the difficulties that earlier observed in the synthesis of cubic MCM-48 under basic conditions (Kresge et al. 1992c; Zhao et al. 2013a). The increase in pH generally increases the charge density of silica. This promotes the electronic interactions between surfactants and silica, which is advantageous while using cationic surfactants (Berggren et al. 2005). Therefore, for the synthesis of OMSs via soft-templating method under basic conditions, the cationic surfactants like CTAB are generally used in the literature.

The acidic conditions were used for the first time by Huo et al. in 1994 to prepare SBA-3 using cetyltriethylammonium bromide (CTEAB) as a template (Huo et al. 1994b). Few years later, the acidic conditions were efficiently utilized by Stucky's research group for the preparation of a list of OMSs (SBA-11, SBA-12, SBA-13, SBA-15, SBA-16, etc.) using non-ionic surfactants (Zhao et al. 1998a; b). During the synthesis of OMSs under the acidic conditions, the strong acidity, i.e. the higher concentration of H^+ ions, is not recommendable because it might lead to the uncontrolled precipitation of silicate precursors, resulting in the low-quality products. This occurs due to the increase in the hydrophilicity of block copolymer, i.e. the ready protonation of polyethylene oxide moieties, with the increase of H^+ ions (Zhao et al. 2013a). Contrary to this, the low acidic concentration and addition of *n*-butanol slow down the precipitation of silicate precursors (the condensation of silicate oligomers). Moreover, the addition of *n*-butanol offers the extended domain for preparing SBA-16 (Kleitz et al. 2006) and MCM-48 (Kim et al. 2005).

It is commonly believed that the neutral solution is not appropriate for the formation of ordered mesostructure due to the rapid polymerization and cross-linking of silicates at pH of 6–8.5. However, Kim et al. have prepared the ordered MSU-H (MSU: Michigan State University) silica at pH = 6.5 using Pluronic P123 and sodium silicate at 60 °C. In this preparation, acetic acid was added to the hydroxide content of silicate for reaching the pH of 6.5 (Kim et al. 2001). In the other report, Wang et al. have prepared the new OMSs at a pH of 6.15 (quasi-neutral pH) using sodium silicate with the addition of phosphate (Na_2HPO_4). In the synthesis, HCl was added in excess for the neutralization of hydroxide content of sodium silicate and to control the required pH value. By keeping the same amount of phosphate and varying the amount of HCl in synthesis solution, the phosphate buffer with different compositions was generated. Consequently, five different pH conditions were attained that led to the formation of OMSs called TPU materials (TPU: Tianjin Polytechnic University) having similar pore diameter (8.6–8.9 nm) and different mesoporous volume and surface area (Wang et al. 2015). COK-12 was also prepared at the quasi-neutral pH range (5–6) using the citric acid/citrate buffer which limited the shifting of pH upon the addition of silica precursor (strongly basic sodium silicate, pH = 12) to the surfactant solution containing the buffer (Jammaer et al. 2009).

The status of silicate precursors after the hydrolysis at different pH conditions and their condensation is shown in Scheme 2. The comparison between the synthesis of OMSs under acidic and basic conditions (Zhao et al. 2013a; Pal and Bhaumik 2013) is made in Table 2.

While choosing the synthesis temperature for the preparation of OMSs, it is very essential to concern two factors such as Krafft temperature [or critical micelle temperature (CMT)] and cloud point (CP). CMT is the minimum temperature required for the surfactants to generate micelles. Below this CMT, the critical micelle concentration (CMC) cannot be attained, i.e. micelles cannot be generated. CP of surfactant is related to the temperature above which the surfactants become insoluble that leads to the phase separation and the precipitation of surfactant. CMT is usually considered for all the types of surfactants (ionic and non-ionic surfactants) but CP is commonly observed in the case of non-ionic surfactant. For the better understanding of CMT, the
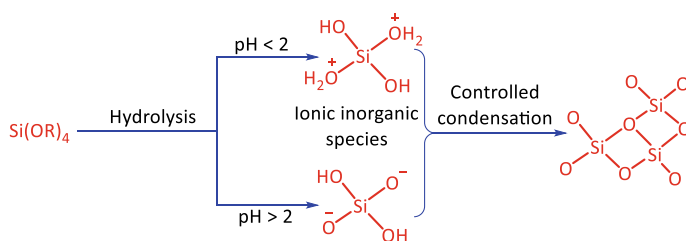
Scheme 2 Silica precursor at various pH conditions

Table 2 Comparison between the synthesis of OMSs under basic and acidic conditions

Basic conditions	Acidic conditions
Difficult to control morphology due to the fast polymerization and condensation of silicates. Spherical particles are very common	Suitable for the synthesis of OMSs in various morphologies (e.g. single crystals, thin films, fibres, spheres, etc.)
Reversible nature of silicate polymerization affirms the success of synthesis	Irreversible polymerization of silicates may sometimes lead to the failure of synthesis after the gel formation
Wide range of silica sources can be used as precursors due to the reversible nature of silicate polymerization	Siliceous oligomers and monomers are the suitable precursors
Mesophase transformation by varying the synthetic conditions is relatively common	Only a very few examples are noticed for such mesophase transformation
Synthesis of MCM-41 is most familiar	Synthesis of SBA-15 is most familiar
NaOH, KOH and $NH_3.H_2O$ are the commonly used inexpensive bases	Strong acids like HCl, HNO_3 and H_2SO_4 and weak acids like H_3PO_4 and CH_3COOH can be used
Synthesis of metal-doped OMSs with a higher metal loading is easy	Synthesis of metal-doped OMSs with high metal loading is not easy

schematic phase diagram of surfactant is illustrated in Fig. 8. The synthesis temperature for preparing OMSs should be above CMT and below CP because the formation of micelles will occur only under these conditions. The CMT value for the cationic surfactants is quite low and thus, they are generally prepared at room temperature. For instance, the CMT of the well-known cationic surfactant (CTAB) is in the range of 20–25 °C (Goyal and Aswal 2001; Grosse and Estel 2000). On the other hand, while using the non-ionic surfactants such as block copolymers, the synthesis temperature is quite high due to the higher CMT of block copolymer surfactants. This higher synthesis temperature should not be higher than the CP of non-ionic surfactants. The common consensus is that the decrease in synthesis temperature is desirable as it directs to the formation of OMSs with an improved crystalline regularity. Therefore, there are few attempts made to prepare the OMSs using the non-ionic surfactants under room temperature or reduced temperature. For instance, J. Jammaer et al. have prepared a new type of OMS (COK-12) under room temperature using Pluronic P123 and sodium silicate at quasi-neutral pH (5–6) (Jammaer et al. 2009).

The attempts are being continuously made to bring the innovation in the fundamental template-assisted synthesis of OMSs. It is known that, for the hydrolysis of TEOS, an acid or a base is required as a catalyst. Feng et al. have accomplished the synthesis of SBA-15 without the requirement of an acid and have called that method as a green synthesis. They have employed the ultraviolet (UV) radiation to generate the ·OH radicals in the synthetic mixture consisting of P123, TEOS and H_2O. These radicals facilitate the hydrolysis of TEOS and exhibit a higher catalytic activity than H^+ ions in the hydrolysis of TEOS (Feng et al. 2018). In the other method, Farrell et al. have effectively combined the basic soft-templating preparation of OMSs with the 3D printing technology (digital light processing), i.e.
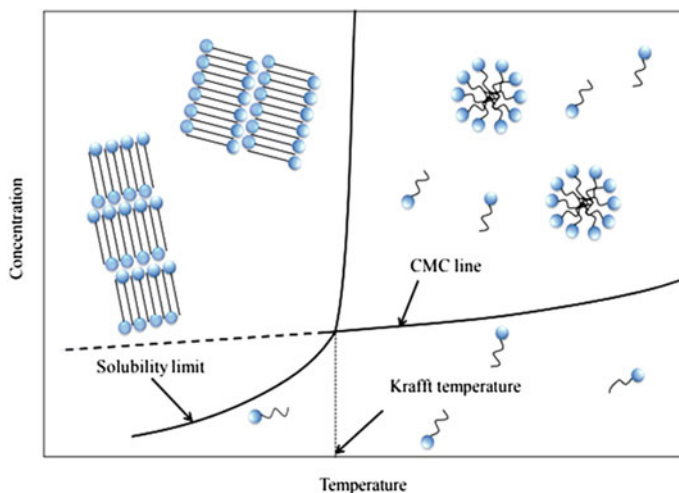
Fig. 8 Schematic phase diagram of surfactant. Usual surfactant solutions are above the CMC line and above CMT (Krafft temperature). Reprinted from Iwata (2017) with permission from Elsevier
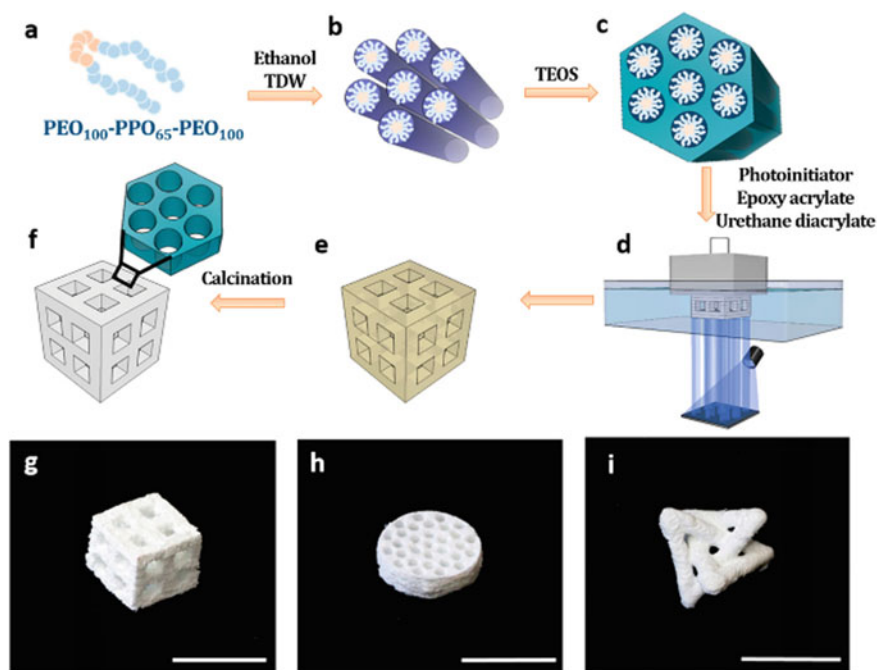
Fig. 9 Fabrication process of OMS monoliths. Schematic presentation of **a** the templating agent molecule, Pluronic F-127, **b** hexagonal liquid crystalline arrangement of the rod micelles, **c** hydrolysis and condensation of the TEOS precursor around the templating agent, resulting in the silica skeleton, **d** printing of the ink in a DLP printer, **e** printed hybrid object and **f** mesostructure of the calcined monoliths. Resulting objects: **g–i** printed OMS monoliths with high geometrical complexity (scale bars, 1 cm). Reprinted from Shukrun Farrell et al. (2020) with permission from American Chemical Society

stereolithography, to prepare OMS monoliths (Fig. 9). In this approach, a patterned UV light is applied to cure sequential 2D layers of UV-polymerizable ink to create 3D OMS objects (Shukrun Farrell et al. 2020). It is known that the water insoluble block copolymers having a long and rigid hydrophobic chain are generally used for the preparation of OMSs in the non-aqueous conditions (EISA). However, Wei et al. have adopted a new soft-templating strategy called solvent evaporation-induced aggregating assembly (EIAA) to prepare the OMSs with a pore tunability up to 37 nm by using home-made water insoluble block copolymer PEO-b-PMMA as a template, TEOS as a precursor and HCl as a catalyst in aqueous medium (THF/H_2O mixture, THF: tetrahydrofuran). After the slow evaporation of THF at room temperature, the obtained PEO-b-PMMA/silica composite is subjected to hydrothermal treatment and calcination, yielding the OMSs with a large pore diameter. EIAA process is water tolerant and the self-assembly occurs at the liquid–liquid interface, whereas in EISA, only a limited amount of water is used in the initial solution and ordered mesostructure is formed at the solid (substrate)–liquid (solution) interface (Wei et al. 2011).

It should be mentioned that the EISA has been found very useful in preparing the OMS thin films via dip-coating or spin-coating or casting method (Liu et al. 2003; Zhang et al. 2007; Glazneva et al. 2007; Chen et al. 2008; Horiuchi and Yamashita 2011; Jung and Park 2006). The more details about the EISA process can be known from the following paragraph dealing with the synthesis of OMMOs.

As mentioned in the introduction of this chapter, unlike the silicas that constructed from flexible tetrahedral building blocks, the metal oxides are mostly vulnerable to phase transitions, hydrolysis and/or redox reactions. Furthermore, the synthesis of OMMOs is challenging owing to the uncontrolled hydrolysis and condensation of metal precursors. Also, it is quite difficult to preserve the mesoporous structure of metal oxides due to the collapse of porous framework during the thermal treatment aiming to achieve the crystallinity (Szczęśniak et al. 2021; Gu and Schüth 2014; Huo et al. 1994a). The oxide/phosphate mesophase was firstly reported by Stucky's group (1994) but the OMMO was not obtained due to the collapse of mesophase structure while removing the surfactant by thermal treatment (Huo et al. 1994a). In the same period, Antonelli and Ying also made the attempts to prepare the mesoporous metal oxides via soft-templating method. The hydrolysis of titanium isopropoxide in the presence of alkyl(trimethyl)ammonium bromide surfactants at pH 8–10 resulted in the formation of anatase TiO_2. Also, the hydrolysis of titanium isopropoxide at a lower pH with alkyl(trimethyl)ammonium bromide surfactants, or with anionic sulphate, carboxylate and phosphate surfactants yielded either anatase or amorphous TiO_2 after the calcination. This was happened due to the rapid precipitation of oxide–alkoxide aggregates that disfavoured the gel formation. Subsequent to these attempts, Antonelli and Ying successfully synthesized the first-ever OMMO (hexagonally packed TiO_2) in 1995 by using titanium acetylacetonate tris-isopropoxide as a precursor which enabled the gel formation with tetradecyl phosphate surfactants at pH 3–6. After the calcination at 350 °C, the first-ever OMMO, i.e. Ti-TMS1 (TMS: titanium metal oxide molecular sieve), was obtained with 196 m^2g^{-1} surface area and 3.2 nm pore size (Antonelli and Ying 1995). In the late 1990s, this solution synthesis method was repeatedly applied for the preparation of various OMMOs such as Nb_2O_5 (Antonelli et al. 1996), VO_x (Liu et al. 1997) and ZrO_2 (Antonelli 1999; Wong et al. 1997). The early reports by Ying's research group and other subsequent reports on the preparation of OMMOs employing the soft templates typically follow the mechanism depicted in Fig. 7, i.e. cooperative assembly of metal oxide precursors and surfactant molecules.

For preparing OMMOs with controlled hydrolysis and condensation of metal oxide precursors, EISA has been recognized as the best strategy. EISA is very useful in the synthesis of ordered mesoporous Al_2O_3 (Xu et al. 2020; Wei et al. 2017a) and other transition metal oxides (Szczęśniak et al. 2021; Zhang et al. 2019a). EISA method deals with the cooperative self-assembly of surfactants (ionic or non-ionic) and suitable precursors of OMMs and generates the pore walls during the course of solvent evaporation (Fig. 10) (Deng et al. 2013; Wei et al. 2017b; Liu et al. 2018b). In the earlier days, the cationic surfactants like CTAB were used in the EISA protocol, which only yielded the OMMs of smaller pore size (Ogawa 1994; Lu et al. 1997). Therefore, to prepare the OMMOs displaying a larger pore size, the utilization of
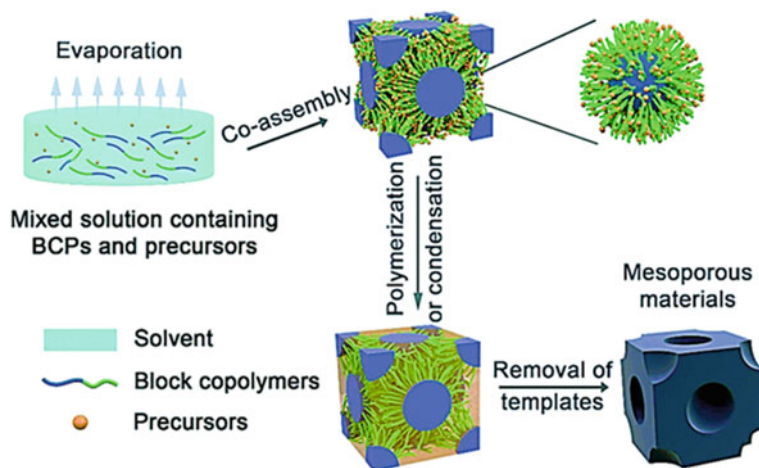
Fig. 10 Scheme illustration of a typical EISA process for the synthesis of mesoporous materials using block copolymers as the soft template. Reprinted from (Li et al. 2020a) with permission from Royal Society of Chemistry

high-molecular weight block copolymers has become familiar (Ma et al. 2018; Liu et al. 2015; Stefik et al. 2012; Weller et al. 2018; Zhu et al. 2017). In solution phase, the block copolymers interact with the soluble precursors via intermolecular interactions (e.g. hydrogen bonding and electrostatic interactions). As the solvent gets evaporated, the cooperative self-assembly is achieved between metal precursors (mostly metal alkoxides) and block copolymers, resulting in the microphase separation. Subsequently, a continuous network is constructed via the condensation or cross-linking of the precursors which may occur simultaneously or after the self-assembly process. Upon the successful removal of block copolymer template by calcination or solvent extraction, the mesoporous architecture is developed (Li et al. 2020a).

During EISA or other methods, the preparation of OMMOs with high crystallinity is a challenging task and thus, the special synthetic strategies are required to attain the crystalline OMMOs. This is mainly due to the decomposition of templates before the crystallization temperature of metal oxide, and thus, further increase of temperature to attain the crystallinity would damage the mesostructure. To avoid this, the combined assembly by soft and hard chemistries (CASH) has been employed for the first time by Weisner's group, which deals with the protection of mesostructure of metal oxide by carbon coating (Lee et al. 2008). Following this strategy, Feng et al. have employed a ligand-assisted EISA strategy using a home-made diblock copolymer (PEO_{125}-b-PS_{120}) to accomplish the ordered mesoporous TiO_2 thin films via a stepwise pyrolysis. The ligand (acetylacetonate) reduces the hydrolysis and polymerization of titanium precursor, and the polystyrene(PS) segment of copolymer template generates the carbon residues as a protection layer to support TiO_2 during the first pyrolysis in N_2. Therefore, the ordered mesostructure during the crystallization is saved. Upon the
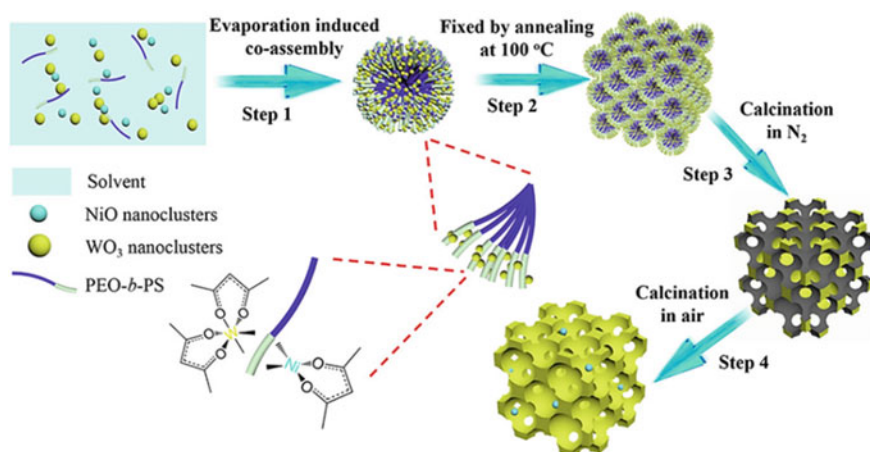
Fig. 11 Illustration of the synthesis of ordered mesoporous crystalline WO₃/NiO composites via solvent evaporation-induced multicomponent co-assembly (EIMCA) in combination with the combined assembly by CASH strategy. Reprinted from (Xiao et al. 2019) with permission from American Chemical Society

removal of carbon through calcination in air, the ordered mesoporous TiO_2 thin film is obtained (Feng et al. 2013). Similarly, the ordered mesoporous WO_3/NiO composite material (Xiao et al. 2019) (Fig. 11) and several other OMMOs have been prepared (Xiao et al. 2018; Zou et al. 2019). Figure 11 pictorially demonstrates the various steps of CASH process. CASH method can also be carried out to stabilize the mesostructure of TiO_2 during the crystallization at a higher temperature via the carbonization of polymer template using H_2SO_4 (Zhang et al. 2010). For the preparation of disordered mesoporous TiO_2, the titanium precursor having the ability to form the carbon residue coating can be utilized without a soft template (Marszewski et al. 2016).

Utilizing the crystalline nanoparticles of metal oxide as precursor and block copolymers as surfactants in non-aqueous media can also yield the crystalline OMMOs (Ba et al. 2005; Deshpande et al. 2005). For instance, Ba et al. have utilized nanosized crystalline SnO_2 as a precursor which is transformed into a stable sol in THF. The obtained sol serves as the building blocks in copolymer-assisted synthesis to yield the crystalline ordered mesoporous SnO_2 after the template removal (Ba et al. 2005). The crystallinity and the ordered mesostructure of prepared SnO_2 are evidenced by XRD and TEM analyses (Fig. 12). Similarly, boehmite gets fragmented into small nanoclusters and self-assembled with copolymer, and thus improves the crystallinity of the resultant mesoporous Al_2O_3 and related materials (Gonçalves et al. 2018; Fulvio et al. 2010).

During the formation of OMMOs, the water content should be neither too high nor too low. With excess water (H > 1, H denotes the number of water molecules per metal atom), the coordination bond between water and the metal is occurred. This weakens the interaction between surfactant and metal and hinders the hydrolysis and
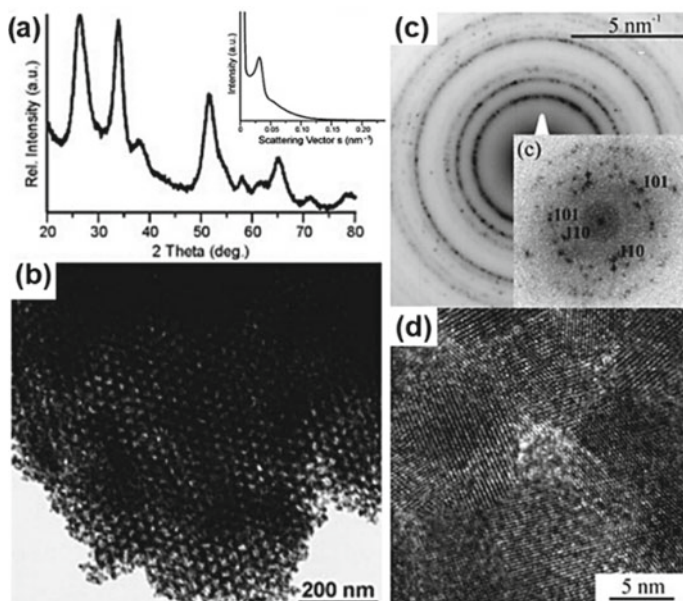
Fig. 12 **a** Powder XRD pattern (inset: small angle X-ray scattering pattern), **b** TEM image, **c** SAED pattern (insert: corresponding power spectrum) and **d** HRTEM image of ordered mesoporous SnO_2 prepared using crystalline SnO_2 nanoparticles as the precursor. Adapted from Ba et al. (2005) with permission from Wiley

condensation of inorganic sols, leading to phase separation and formation of non-porous metal oxides. On the other hand, while the very less water ($H \ll 1$) induces the strong interaction between the surfactant and metal precursors, it suppresses the surfactant–surfactant interactions. Consequently, the mesoporous materials without a regular mesostructure are obtained. As most of the syntheses are open to air, it becomes quite difficult to control the water content without the use of a humidity chamber (Grosso et al. 2004b). Surprisingly, Poyraz et al. have come up with a generic method (inverse sol–gel method) for the synthesis of diverse OMMOs (oxides of transition metals, early transition metals and lanthanides) in which the water content is not a concern. Figure 13 displays this inverse sol–gel method and roles of different components utilized for the preparation of OMMOs (Poyraz et al. 2013). This method has been efficiently utilized for the preparation of various OMMOs (Poyraz et al. 2013; Song et al. 2014; Poyraz et al. 2014).

The OMMOs can be converted to ordered mesoporous metal nitrides by nitriding at a higher temperature using NH_3 as a nitrogen source (Robbins et al. 2016; Beaucage et al. 2017; Kim et al. 2017).

It should be noted that, like the preparation of OMSs, the preparation of OMMOs with the desirable characteristics can be influenced by the various factors such as precursor, synthesis medium, pH of the solution and nature of surfactant.
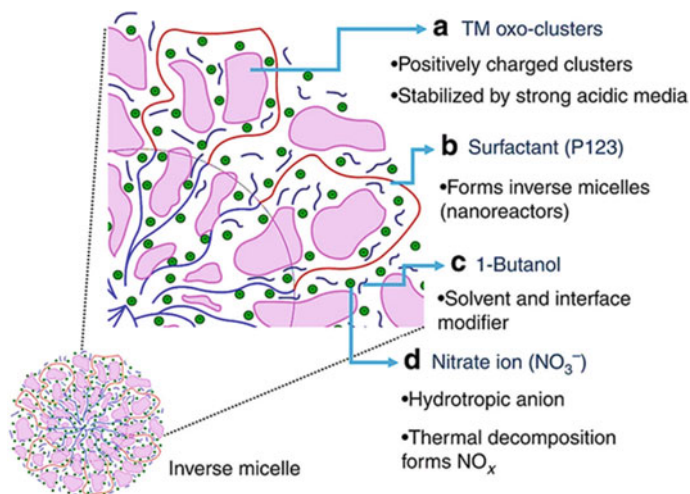
Fig. 13 **a** Transition metal (TM) oxo-clusters: positively charged oxo-clusters interact with surfactant via hydrogen bonding and the charge is balanced by negatively charged nitrate ions (NO^{3-}), **b** surfactant (P123): inverse micelles are formed by P123 (EO_{20}–PPO_{70}–PEO_{20}) surfactant. Later, the inverse micelles are packed to form the material, **c** 1-Butanol: solubilizes the surfactant (solvent) and stabilizes inverse micelles (modifier), **d** nitrate ion (NO^{3-}): hydrotropic nitrate anion penetrates into the core of inverse micelles to hydrate it and pulls positively charged oxo-clusters into the micelles. Thermal decomposition of nitrate ions forms nitric oxides (NO_x) to control the sol–gel chemistry. Formed NO_x is adsorbed on oxo-clusters to hinder uncontrolled condensation. Reprinted from (Poyraz et al. 2013) with permission from Springer Nature

Very recently, mechanochemistry has received attention for the synthesis of mesoporous metal oxides which shortens the preparation time and circumvents the requirement of solvent (Szczęśniak et al. 2021; Nie et al. 2020). The interaction and diffusion between the metal oxide precursors and surfactants are basically driven by the kinetic energy and frictional heating released during ball milling. This method seems very much suitable to prepare the high-entropy mesoporous metal oxides because ball milling generates the short-range heating which is sufficient for the synthesis of high-entropy mesoporous materials without the porosity deterioration (Szczęśniak et al. 2021; Zhang et al. 2019b). Very recently, Xiong et al. have accomplished the preparation of various crystalline mesoporous metal oxides such as ZrO_2, Nb_2O_5, HfO_2, Al_2O_3, TiO_2, Ta_2O_5 and TiO_2–Nb_2O_5 composite using the simple mechanochemical synthesis in which the metal alkoxide/polyethylenimine composite mesophase is obtained just by grinding physically for five minutes at room temperature (Xiong et al. 2020). Though the mechanochemical approach offers several benefits, it is thus far very difficult to achieve high crystallinity and ordered mesoporosity (Szczęśniak et al. 2021).

Regarding the synthesis of OMCs by soft-templating method, the two mechanistic pathways depicted in Fig. 7 are applicable. As a common fact, the interaction between the surfactant and the precursor of target OMM is crucial to construct

the mesophase structure via the cooperative self-assembly. In this view, Moriguchi et al. have utilized the electrostatic interaction between phenolic resin (phenol–formaldehyde) and cationic surfactant to generate the lamellar and disordered polymer mesophases (Moriguchi et al. 1999). However, the disordered mesostructure is destructed while removing the cationic surfactant. Similarly, the different precursors such as the oxidized polycondensed aromatic hydrocarbons containing oxygen-functional groups (e.g. carboxyl, ether, phenol or carbonyl) and resorcinol–formaldehyde aerogels have been utilized for the preparation of disordered mesoporous carbons. These precursors electrostatically interact with the cationic surfactants via their negatively charged groups under basic conditions (Li et al. 2004b; Nishiyama et al. 2005; Lee and Oh 2002). The major disadvantage of using the ionic surfactants for the preparation of mesoporous carbons is the formation of disordered mesostructure. The uncontrolled polymerization of organic precursors also befalls due to the very weak interaction of organic polymer frameworks with amphiphilic cationic surfactants. Furthermore, the insufficient charge density of ionic surfactants reduces the miscibility between the organic frameworks and surfactants after the polymerization, leading to the macroscopic phase separation (Zhao et al. 2013b).

Due to these abovementioned disadvantages of ionic surfactants, the non-ionic block copolymers have become attractive as they could accomplish the synthesis of OMCs. The key to the preparation of OMCs using the block copolymers is the choice of carbon precursors. The chosen precursors should be able to generate the 3D thermoset network and maintain the ordered mesostructure by strongly interacting with block copolymers. Phenolic resin is an attractive precursor due to its thermosetting, high carbon yield and miscibility with a variety of polar polymers. The resol-type phenolic resin is the widely used precursor which is generated under basic conditions (pH = 9). On the other hand, another phenolic resin (novolac, a linear long-chain polymer), which is generated under acidic conditions, is not very familiar due to its thermoplastic properties and melting at high temperature that disrupts the mesostructure during the pyrolysis and carbonization processes. This demerit of novolac can be solved by using the curing agent method which promotes the cross-linking between the linear novolac to yield the phenolic resin with the desired thermosetting properties. HMTA is utilized as a familiar curing agent for novolac (Jiao et al. 2013; Huang et al. 2009). This curing agent method for the preparation of OMC using a block copolymer as surfactant and novolac as precursor is schematically shown in Fig. 14. Hydrogen bonding interaction between the block copolymers and the phenolic resin plays a vital role because it drives the formation of ordered mesostructure of the phenolic resin/block copolymer composite. Those interactions can be understood from Fig. 15, which considers novolac, resol and phloroglucinol as the various carbon precursors, and the pyridine-containing and PEO-containing block copolymers as the non-ionic surfactants.

In common, the preparation of OMCs using the block copolymers typically involves few significant steps (i) the preparation of phenolic resin such as resol or novolac, (ii) the generation of hydrogen bonding between phenolic resin and block copolymer, (iii) the solidification of ordered mesophases through the polymerization of phenolic resin around the templates, (iv) the removal of templates to form ordered
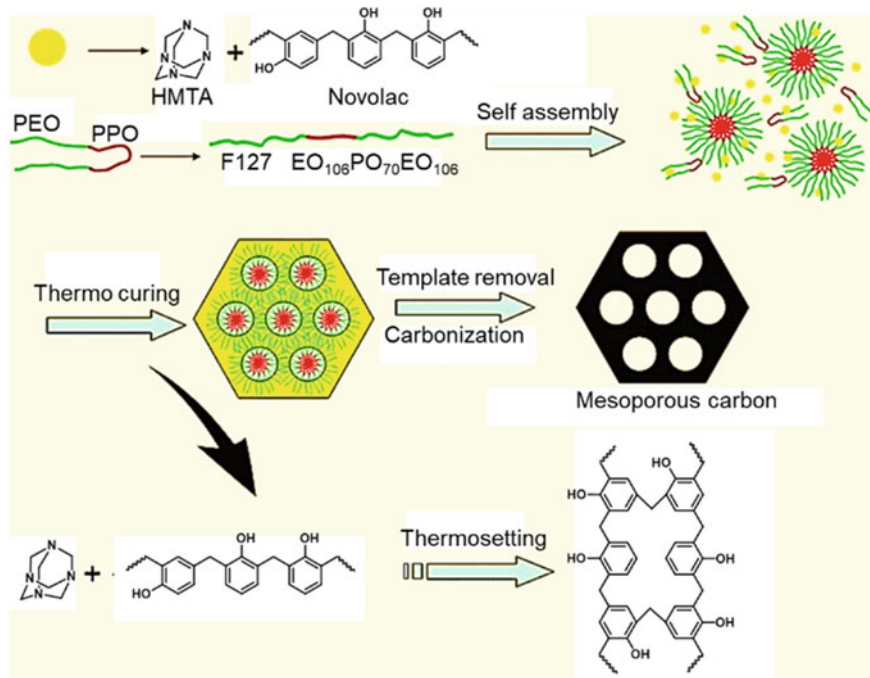
Fig. 14 Schematic showing the synthesis of OMCs with F127 as template, novolac cured with hexamethylenetetramine (HMTA) as carbon precursor by EISA. Adapted from Jiao et al. (2013) with permission from Springer Nature

mesoporous polymer and (v) the carbonization of polymer frameworks to the homologous OMCs (Libbrecht et al. 2017; Zhao et al. 2013b). Following these sequential steps, the preparation of OMCs can be achieved by one of the four methods such as hydrothermal autoclaving route, hydrothermal diluted route, EISA and phase separation (Libbrecht et al. 2017). The hydrothermal autoclaving route is performed under basic conditions using phenol as a precursor and P123 or F127 as a surfactant (García et al. 2013; Huang et al. 2008; Li and Xue 2014). The deprotonated phenol yields the phenoxide ion which is then subjected to formaldehyde substitution. Base (NaOH) promotes the formation of resols with the excessive addition of formaldehyde to phenol. The autogenous pressure generated inside the autoclave drives the formation of periodic assembly between precursor and template molecules (Libbrecht et al. 2017; Muylaert et al. 2012). In the hydrothermal diluted route, no autoclave is used, i.e. no autogenous pressure is generated. In this case, the hydrogen bonding between resol and surfactant drives the construction of desired periodic assembly that generates the mesophase in diluted media. Therefore, in this method, the precise control of pH is important to maintain the hydrogen bonding during the periodic assembly process (Enterría and Figueiredo 2016; Zhang et al. 2005a; Zhang et al. 2006). While a higher pH disrupts the hydrogen bonds, the neutral or weak acidic conditions slow
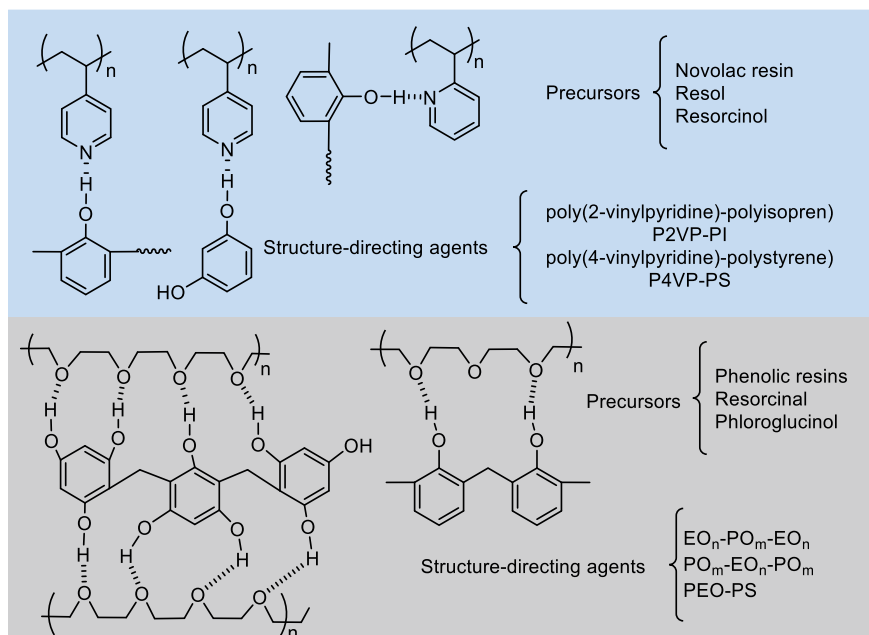
Fig. 15 Hydrogen bonding interaction of **a** pyridine-group-containing and **b** PEO-containing block copolymers with the hydroxyl-group-containing organic precursors. Adapted from (Wan et al. 2008) with permission from American Chemical Society

down the process. Therefore, a very narrow pH range should be maintained which is a limitation of this method (Libbrecht et al. 2017; Zhang et al. 2005a). During the macroscopic phase separation method, an acid is used as the catalyst to promote the reaction between the excess resorcinol or phloroglucinol with formaldehyde to generate novolac. The insolubility of novolac in water or ethanol allows the phase separation to occur. As phenol has very less activity under the acidic conditions, the reactive resorcinol and phloroglucinol have been mostly used as the precursors in this method (Libbrecht et al. 2017; Wang et al. 2008; Gao et al. 2008; Liu et al. 2010). Note that, like resols, novolacs also behave similarly during the curing process to yield the 3D interconnected polymer network (Wang et al. 2008).

The fourth method used for the preparation of OMCs is EISA process. The general description about the EISA protocol is already discussed above. EISA has been widely utilized for the preparation of OMCs due to the following benefits, (i) the applicability of different reaction conditions (e.g. pH range and various surfactants), (ii) choice with a variety of solvents like THF, methanol, etc. and (iii) enrichment of polymer concentration by the solvent evaporation that promotes the organic–organic self-assembly between the block copolymer and the resol (Libbrecht et al. 2017). The advantageous organic–organic self-assembly was reported by Zhao's research group using the low-molecular weight phenolic resol and a block copolymer in a solvent like ethanol. Initially, phenolic resol and block copolymer are mixed

in the solvent whose evaporation results in the self-assembly of block copolymer and resol. The hydrogen bonding drives the construction of phenolic resol/block copolymer composite showing the ordered mesostructure. The resol is cured at 100 °C to solidify the polymeric framework. Applying the difference in the chemical and thermal stability between resin and block copolymer, the template is removed either by calcination at 350–450 °C or by extraction with 48 wt% H_2SO_4. The obtained bakelite framework with ordered aligned voids is converted to the homologous OMC by heating above 600 °C (Meng et al. 2005; Huang et al. 2007; Deng et al. 2007; Zhao et al. 2013b). The whole process is pictorially illustrated in Fig. 16 by which the essential five steps required for the preparation of OMCs can be understood (Meng et al. 2006). It should be mentioned that the removal of template without the carbonization will result in the generation of ordered mesoporous polymers, i.e. the process should be ended at the step 4 according to Fig. 16.

Synthesis of OMZs basically means the introduction of additional mesoporosity in the zeolitic framework structure which contains the characteristic micropores of zeolites. Due to this bimodal porosity, the OMZs are termed as the hierarchical zeolites. To install this bimodal porosity, in general, two types of SDA are required (the common SDA for introducing micropores and the other SDA for introducing mesopores). During the preparation, the zeolite precursor slurry is initially
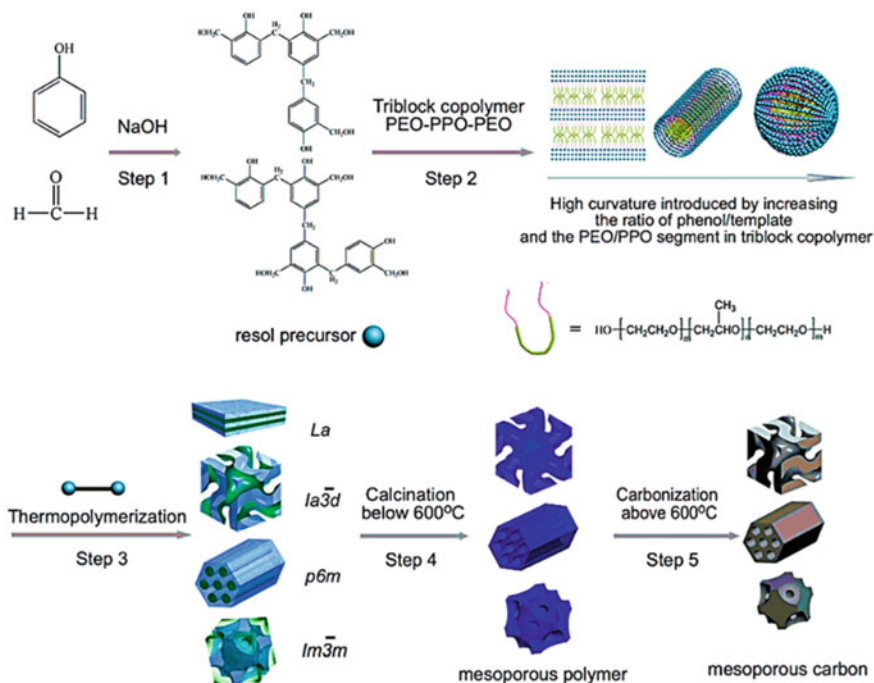
Fig. 16 Scheme for the preparations of the ordered mesoporous polymer resins and carbon frameworks. Reprinted from (Meng et al. 2006) with permission from American Chemical Society

arranged around the mesopore templates which are subsequently removed to generate the hierarchical mesoporous zeolites. Synthesis of hierarchical zeolites with meso-porosity can be performed by two different routes, (i) primary soft-templating and (ii) secondary soft-templating. In primary soft-templating method, all the components including the surfactant are added in the beginning to generate the synthesis mixture (Chen et al. 2020). Under the hydrothermal conditions, while the hydrophilic part of the surfactant induces the zeolite formation around it, the hydrophobic domain of the surfactant controls the growth of zeolite crystal to form the lamellar arrange-ment, leading to the zeolite crystallization in the form of thin sheets. The primary-templating method often uses the specially designed surfactant having the capacity to assemble the primary building units in zeolite crystallization that enables the generation of intra- or intercrystalline mesopores along with the typical micropores (Hartmann et al. 2021). The hierarchical zeolites with a layer-like morphology are frequently obtained by the primary soft-templating protocol (Choi et al. 2009a, b). However, the hierarchical zeolites with a sponge-like morphology can also be prepared but by increasing the concentration of surfactant which stimulates the phase separation (Choi et al. 2006). The primary-templating method seems very general but it is limited to very few topologies such as FAU (Faujasite), MFI (ZSM-5 (Five)), BEA (Beta), MEL (ZSM-11 (Eleven)) and MWW (MCM-22 (Twenty two)) (Hartmann et al. 2021).

The secondary soft-templating approach involves two sequential steps such as the preparation of zeolite nanocrystals (seeds) and the addition of surfactant to induce the self-assembly that generates the desired mesopores during the hydrothermal treat-ment. The commercially available surfactants (e.g. CTAB) and a classical SDA for micropores (e.g. tetrapropylammonium ion (TPA)) are used in secondary-templating process. The addition of surfactant in the second step, i.e. after the formation of zeolites seeds, prohibits the phase separation of mesoporous amorphous silica (Hartmann et al. 2021; Zhu et al. 2011).

As an intriguing phenomenon in the synthesis of hierarchical zeolites, Che's research group has utilized the π-π stacking for the hierarchical growth of zeolites containing the ordered mesostructure. This has been accomplished by using the amphiphilic surfactant possessing the aromatic groups which are engaged in the π-π stacking (Fig. 17). However, this strategy is thus far restricted only to MFI zeolites due to the geometric matching between the self-assembled aromatic tails and the MFI framework (Zhang and Che 2020; Xu et al. 2014).

The advantage of preparing the hierarchical zeolites in the soft-templating method is that both the surfactant (for additional mesopores) and the SDA (for typical micropores) can be optimized which provides the opportunity to design a great variety of hierarchical zeolites (Hartmann et al. 2021). For the preparation of hierarchical zeolites with mesoporosity by soft-templating method, the soft templates should possess the following characteristics, (i) stability under alkaline conditions even at 140–180 °C (the general reaction conditions for the preparation of zeolites), (ii) posi-tively charged to interact strongly with negative silica species, (iii) suitable mesoscale sizes in aqueous solution and (iv) low cost (Chen et al. 2020). For the extensive reading on the hierarchical mesoporous zeolites and their preparation, the recently
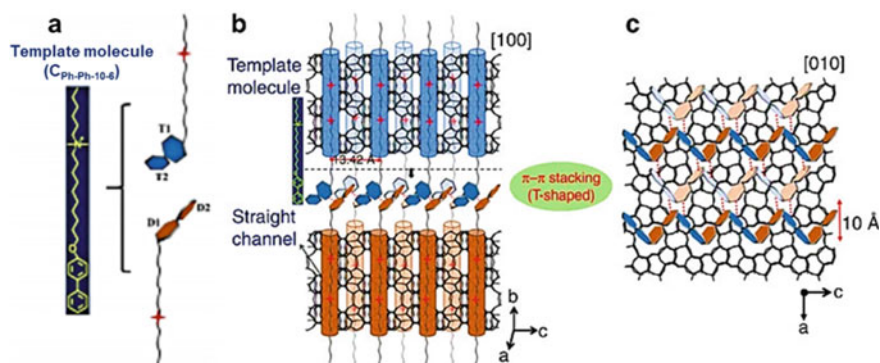
Fig. 17 **a** Single-head quaternary ammonium-type template with aromatic groups, **b** single quaternary ammoniums in the template molecules are located in the straight channel and serve as a template to direct the formation of hierarchical MFI zeolite and **c** the arrangement of biphenyl groups from adjacent MFI layers along the a–c plane orientation matching the MFI frameworks. Adapted from Xu et al. (2014) with permission from Springer Nature

published review articles may be referred (Chen et al. 2020; Hartmann et al. 2021; Feliczak-Guzik 2018; Schwieger et al. 2016; Wei et al. 2015).

Despite the OMMOFs are mostly prepared by the template-free synthesis (reticular synthesis), it is also possible to prepare the OMMOFs by soft-templating method using a suitable surfactant (Ma et al. 2012; Guan et al. 2018).

4.1.1 Precursors

For the preparation of OMSs by soft-templating method, the silicon atoms in chosen precursors are either attached to no silicon atom (0) or different number of silicon atoms (1–4) via siloxane (–Si–O–Si–) bonds. TEOS and other simple alkoxides are the precursors for OMSs, which do not have any siloxane bond. On the other hand, the other precursor, colloidal silica, is rich in the silicon atoms which have four neighbours linked by siloxane bonds. In the periphery, silicon atoms have three siloxane bonds and one silanol group. On the basis of the signals obtained in the ^{29}Si NMR spectral analysis, the suitability of silica sources for being the precursors of OMSs can be scrutinized. $Si(Q^n)$ is used as the nomenclature to indicate the ^{29}Si NMR signals of the silicon atoms (n denotes number of siloxane bonds that surround the silicon atom). For instance, water glass (sodium silicate) can display all the five possible ^{29}Si NMR signals ($Si(Q^0)$, $Si(Q^1)$, $Si(Q^2)$, $Si(Q^3)$ and $Si(Q^4)$) (Berggren et al. 2005; Setoguchi et al. 1997), with signals from higher coordination increasing with increasing SiO_2-to-Na_2O ratio. Note that $Si(Q^4)$ rules out the presence of silanol group whereas $Si(Q^0)$, $Si(Q^1)$, $Si(Q^2)$ and $Si(Q^3)$ could have four, three, two and one silanol group(s), respectively, under the hydrolysis conditions. The precursors with more $Si(Q^4)$ signals are not suitable for the preparation of OMSs. Therefore, the

water glass needs to be treated with NaOH to bring down the SiO_2-to-Na_2O ratio as two. TEOS shows only the $Si(Q^0)$ signal and is routinely used in the synthesis of OMSs. The synthesis solution predominantly contains $Si(Q^1)$ in the earlier stage and displays ordered mesophase, which becomes disordered with the increase of $Si(Q^3)$ species. This reveals the significance of low-condensed $Si(Q^{n<3})$ species in the initial stage to prepare OMSs (Berggren et al. 2005; Klotz et al. 2000). So far, TEOS has been known as the best precursor for preparing the OMSs despite its expensive nature than the water glass.

Other intriguing precursors (bis-silylated organosilanes, $(R'O)_3Si$-R-$Si(OR')_3$) are also available, which could yield the OMSs with the different properties. Utilizing TEOS and the monosilylated organosilanes results in the silicas with a hydrophobic coating (Macquarrie 1996) but using the bis-silylated organosilanes accomplishes the new type of OMSs, i.e. periodic mesoporous organosilicas (PMOs) (Fig. 18) (Guan et al. 2000; Melde et al. 1999; Asefa et al. 1999; Inagaki et al. 1999). The synthesis procedure of PMOs is similar to the synthesis of common OMSs but with a variation in the template removal. The template removal during the preparation of PMOs is performed by the solvent extraction due to the thermal instability of organic groups within the framework. The PMOs were reported for the first time by Inagaki et al. using 1,2-bis(trimethoxysilyl)ethane as precursor and octadecyltrimethylammonium chloride or hexadecyltrimethylammonium chloride as surfactant under basic conditions (Inagaki et al. 1999). As common in the other cases, the interaction between surfactant and hydrolysed organosilane precursor is crucial for preparing PMOs. It is not easy to prepare the PMOs possessing the bulky organic groups by using 100% bridged organosilane precursors that display the poor interaction capacity with surfactant. This can be rectified by enriching the silyl groups in the precursors; however, the preparation of such precursors is inherently difficult. On the other hand, this problem can be solved by the co-condensation with TEOS or bridged organosilanes having small organic groups (e.g. 1,2-bis(triethoxysilyl)ethane) (Goto et al. 2019). The organosilanes with the functional groups such as $-NH_2$, $-Cl$ and $-SH$ $((R'O)_3$-$(CH_2)_3$-FG, FG: functional group) can also be used as one of the silica precursors to yield the OMSs with rich reaction chemistry (Rajendran et al. 2020).

For the preparation of OMMOs, a wide variety of hydrolysable metal precursors is available such as alkoxides, acetylacetonates, nitrates and chlorides (Wei et al.
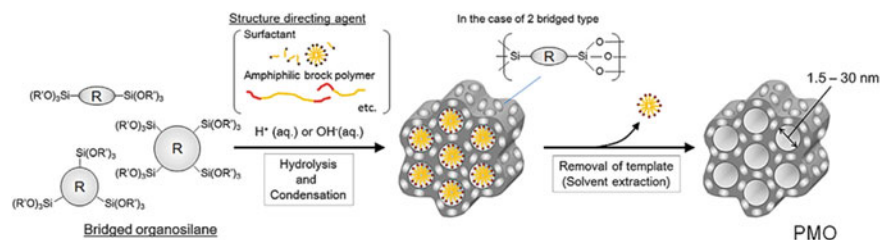
Fig. 18 Synthesis of a periodic mesoporous organosilica (PMO) from organic-bridged alkoxysilane precursors. Adapted from (Goto et al. 2019) with permission from Elsevier

2017a; Ge et al. 2019; Grosso et al. 2004a). OMCs are frequently prepared from the phenolic resin monomers which are mainly based on phenol or resorcinol or phloroglucinol. Though phenol was used in the earlier days, the noticed macroscopic phase separation has allowed the researchers to look for the other phenols and thus became resorcinol very attractive. Considering the reactivity of phenolic compounds, it is increased based on the number of hydroxyl groups, i.e. phenol < resorcinol < phloroglucinol. The polymerization time for phenol, resorcinol and phloroglucinol is about two to three weeks, about one week, and 40 min, respectively, at room temperature (Libbrecht et al. 2017; Ma et al. 2013; Liang and Dai 2006). The plant extracts containing phenolic-type compounds are also used as the precursors but the accomplishment of ordered mesoporous structure is not assured (Liu et al. 2013; Nelson et al. 2016; Schlienger et al. 2012).

The synthesis of OMZs (hierarchical zeolites) is commonly performed by using $NaAlO_2$ and TEOS as the precursors of Si and Al, respectively, in different ratios depending upon the nature of target zeolite materials.

4.1.2 Surfactants

Surfactant is a key component in the preparation of OMMs by soft-templating method. Surfactants are generally the amphiphiles, i.e. they have hydrophobic and hydrophilic parts. The hydrophobic part stabilizes the organic species and the hydrophilic part interacts with the inorganic precursors. Surfactants can be stabilized in water by two different ways, (i) the arrangement of surfactants in the surface by having the hydrophilic part interacting with water and the hydrophobic part expelling out from water to the air (occurs at lower surfactant concentration) that lowers the surface tension and (ii) the formation of aggregates with the orientation of hydrophobic parts inside the cluster and the exposure of hydrophilic parts to the water (higher concentration) (Alexandridis et al. 1998). The surface gets saturated at a particular concentration above which the formation of micelles is started. That particular concentration is defined as CMC above which the self-assembly of micelles occur, resulting in the construction of 3D spherical or 2D rod like array, i.e. a basic step for the pore generation.

Based on the dissociation in water, the surfactants are classified into three major types such as cationic, anionic and non-ionic (Pal and Bhaumik 2013; Zhao et al. 2013a).

Upon dissociation in water, the cationic surfactants produce an amphiphilic cation and an anion. Among the cationic surfactants, quaternary cationic surfactants are very familiar (e.g. CTAB). The other cationic surfactants such as the gemini surfactants, bolaform surfactants, multihead group surfactants and cationic fluorinated surfactants have also been used for the preparation of different mesostructures. The characteristics of cationic surfactants are the higher solubility, high CMT and applicability in both acidic and basic media. The size of the surfactants is important to tune the pore diameter of OMSs. As CTAB is a small surfactant, it only accomplishes the OMSs possessing the pore diameter less than 5 nm. Therefore, to prepare the

OMSs with large pore diameter (highly accessible pores), the surfactants having the long hydrophobic chains are needed which could enable the generation of a larger hydrophobic volume.

The dissociation in water breaks the anionic surfactants to yield the amphiphilic anion and a cation. Many anionic surfactants have been used such as carboxylates, sulphates, sulfonates and phosphates. Compared to the cationic and non-ionic surfactants, the utility of anionic surfactants is less reported for the preparation of OMMs.

Non-ionic surfactants have the widespread applications in the preparation of OMMs than the surfactants of any other type and have rich phase behaviours with low CMT values. Due to their non-ionic nature (no charge), these surfactants are not dissociated in water. For instance, in the famous PEO-PO block copolymer, the hydrophilicity arises from the polyethylene glycol chain obtained by the condensation of ethylene oxide. The polyether chain behaves as a lipophilic group, i.e. non-polar group.

Besides these surfactants, another type of surfactants called amphoteric surfactant also occasionally finds applications in the preparation of OMMs. These surfactants could display both anionic as well as the cationic dissociations (Pal and Bhaumik 2013; Zhao et al. 2013a). In Fig. 19, the structures of various surfactant types are illustrated.

The size of surfactant is important to control the pore size of OMMs. The big size surfactants (high-molecular-weight surfactants, generally, block copolymers) are found useful in expanding the pore width of OMMs. Besides tuning the size of surfactants, the pore width of OMMs can be expanded with the use of swelling agents such as hexane, polypropylene glycol, trimethylbenzene and *m*-xylene (Colmenares et al. 2018; Trivedi et al. 2019; Ma et al. 2017; Bolivar et al. 2017). These swelling agents typically enhance the volume of micelles by being inserted into the hydrophobic core of the micelle.

For the formation of ordered mesostructure, the interaction between surfactant and the precursor of OMM is very fundamental. The interactions between surfactants and the inorganic species during the preparation of OMMs include S^+I^-, $S^+X^-I^+$, S^-I^+, $S^-X^+I^-$, $S^0X^+I^-$, S^0I^0, $(S^0H^+)X^-I^+$, etc. (S: surfactant, I: inorganic species like silica, and X: inorganic salt) (Wan and Zhao 2007; Soler-Illia et al. 2002). As mentioned in the previous section, for example, silica species get protonated under acidic conditions (I^+) and deprotonated under basic conditions (I^-). The abovementioned interactions are illustrated in Fig. 20. Following the interactions of type S^+I^-, $S^+X^-I^+$, $S^0X^+I^-$, S^0I^0 and $(S^0H^+)X^-I^+$, various ordered mesostructures have been prepared using the cationic and non-ionic surfactants. On the other hand, S^-I^+ and $S^-X^+I^-$ interactions observed with anionic surfactants often result in the disordered mesoporous structures. This might be due to the protonation of anionic surfactants under acidic conditions and weakening of the interaction of counter-cations with surfactant and silicate ions under basic conditions (Gao 2009; Pal and Bhaumik 2013).

Fig. 19 List of common cationic, anionic and non-ionic surfactants and their structures

4.1.3 Template Removal

In common, the template removal is the last step in the preparation of OMMs. The template removal needs to be carried out without disturbing the ordered mesoporous structure. There are many methods available for the removal of templates such as calcination, solvent extraction, supercritical fluid extraction, microwave irradiation, ultraviolet radiation, microwave digestion and oxidation of ammonium perchlorate (Zhao et al. 2013a).

Amidst these methods, the calcination method is very much applicable to yield the OMSs, OMMOs, OMZs and OMCs due to its simplicity and less time consumption. While preparing the crystalline OMMs, the higher calcination temperature is required so that in such cases, the template removal occurs before the crystallization temperature. Despite the crystallinity is accomplished, the ordered mesostructure may be collapsed due to the premature removal of template before the crystallization
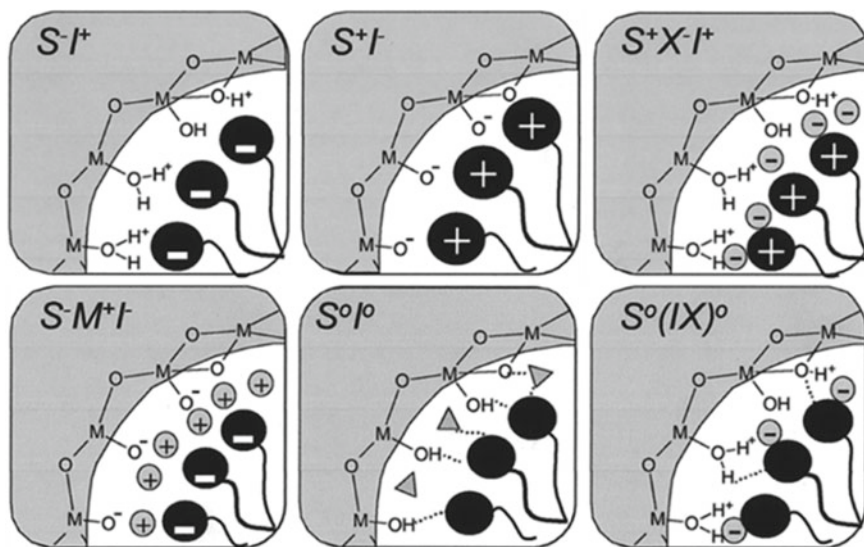
Fig. 20 Schematic representation of the different types of silica–surfactant interfaces. S represents the surfactant molecule and I, the inorganic framework. M^+ and X^- represent the corresponding counterions. Solvent molecules are not shown, except for the S^0I^0 case (triangles); dashed lines correspond to H-bonding interactions. Adapted from Soler-Illia et al. (2002) with permission from American Chemical Society

temperature. This concept is discussed above with the possible ways to prepare the crystalline OMMOs (Sect. 4.1). Unfortunately, the surfactants cannot be recovered during the calcination process and the surface hydroxyl groups may be also lost.

The calcination cannot be employed while the OMMs carry the important organic moieties in the framework structure (e.g. PMOs) or in the surface. Therefore, for the removal of templates during the preparation of PMOs, the solvent extraction is employed in order to preserve the organic groups affixed in the framework. Though the solvent extraction looks simple requiring no harsh condition and maintains the ordered mesoporous structure, it cannot assure the 100% removal of template (Pal and Bhaumik 2013; Zhao et al. 2013a). Therefore, it is not frequently utilized like calcination.

Supercritical fluid extraction mostly uses the supercritical CO_2 which could remove and recover the surfactant with more than 90% efficiency. The collapse of ordered mesostructure would be very rare, and hence, this method can be an ideal choice to prepare the OMMs possessing multiple components and various morphologies (Zhao et al. 2013a; van Grieken et al. 2003; Kawi and Lai 2002).

For the materials sensitive to microwave irradiation, the templates removal can be carried out using the microwave irradiation. By the heat produced from the microwave treatment of materials like Co_2O_3, NiO and activated carbon, the templates are removed (Gallis and Landry 2001). Despite being achieved within a short time

(10–30 min), the very high power involved in this method damages the ordered mesostructure and also results in the carbon deposition (Zhao et al. 2013a).

In the presence of ultraviolet radiation, the C–C bonds in the templates are initially broken which are subsequently removed by the oxidation using the strong oxidants like ozone and nascent oxygen (Hozumi et al. 2000a, b). Ultraviolet radiation process requires a very long time which makes it unsuitable for the industrial applications (Zhao et al. 2013a).

Microwave digestion is associated with the oxidation process in the presence of HNO_3 and H_2O_2 at an instantaneous high temperature (~200 °C) and pressure (1.3 MPa). The templates can be removed within a very short time (3–10 min) without the collapse of ordered mesostructure, and the reduction in surface area and pore volume (Tian et al. 2002). This method is facile and promising except for the materials like organic frameworks and titania which are sensitive to the acids (Zhao et al. 2013a).

In the ammonium perchlorate oxidation method, the templates are removed through the oxidizing ability of NH_4ClO_4 under the acidic conditions at temperature above 100 °C. This method can be even applied for the selective removal of block copolymers during the preparation of PMOs under the controlled reaction conditions (Cai and Zhao 2009). On the other hand, this selective removal is not known for the case of cationic surfactants like CTAB. Also, for the mesoporous polymers containing more oxygen-based groups, this method is not suitable (Zhao et al. 2013a).

4.2   Preparation of OMMs by Hard-Templating Method

Hard-templating method follows the procedure of traditional process called casting. As the porosity with nanoscale is the main focus in the hard-templating process, it is also known as the nanocasting method. This method is very simple as compared to the soft-templating method due to the absence of complicated sol–gel chemistry. As the structures of hard templates are fixed, the process is comparatively easy to control. On the other hand, the structures of soft templates are flexible and depend on the various factors such as temperature, solvent and ionic strength. Therefore, it is difficult to expect the structure showing the negative replica of the soft template (Lu and Schüth 2006). The hard templates like OMSs are very stable, and hence, the highly crystalline OMMs can be easily synthesized by the nanocasting method. The pore structure of target OMMs mainly depends on the characteristics (e.g. shape, size, pore structure, etc.) of the hard template. Contrary to soft-templating method (endo-templating), hard-templating method is defined as the exo-templating method in which the precursors of the target OMM are filled inside the pores of the template (Schüth 2003).

Figure 21 illustrates the traditional casting process of a key and replication of an ordered mesoporous replica. During the nanocasting protocol for preparing OMMs, the template with ordered mesostructure (mold) is first infiltrated with precursors of a
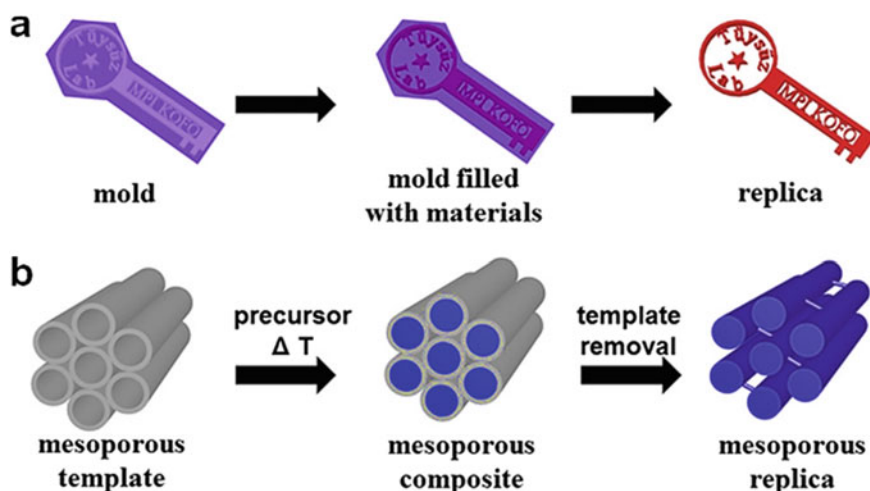
Fig. 21 Schematic illustration for **a** the casting process of a key with a mold and **b** nanocasting using OMMs as the hard template. Adapted from Deng et al. (2017) with permission from American Chemical Society

desired OMM. After removing the solvents by evaporation, the pores of template are partially or fully filled with the precursor which is subsequently converted to solid mostly by the thermal treatment. Eventually, the template is removed by a certain method (e.g. silica template by HF etching and carbon template by calcination) depending upon the nature of hard template, yielding the OMM. Thus, it is understood that the nanocasting process basically contains three major steps: (i) formation of the hard template, (ii) the casting step with target precursors including solidification of precursors and (iii) removal of the template (Deng et al. 2017; Lu and Schüth 2006). Note that the pore structure of templates is converted to the solid structure of the target OMMs and the pore walls of templates become the pore structure of target OMMs (replica) (Lu and Schüth 2006). Compared to the traditional casting process, the nanocasting method is mainly driven through the capillary condensation by which the fluids are transported into the ordered mesopores of the template. This indicates the importance of surface modification and wettability during the nanocasting. Moreover, unlike the traditional casting, the nanocasting is not merely a physical solidification because the chemical conversion is required for the conversion of precursors to yield the target OMMs (e.g. sucrose to carbon) inside the confined nanochannels (Lu et al. 2009). In the nanocasting method, the templates are usually removed by the chemical treatment instead of using the mechanical treatment. For instance, being the hard template, OMSs are removed by the etching process using aqueous HF or NaOH solution which erodes the silica template into movable gaseous or dissolvable products.

So far, the hard-template method has been very familiar and repeatedly used for the preparation of OMCs and OMMOs. For the preparation of an OMM, the nanocasting

method was firstly employed by Ryoo et al. who prepared the OMC (CMK-1) which is an ordered mesoporous replica of MCM-48. Sucrose, the carbon precursor, was impregnated inside the pores of MCM-48 and subsequently carbonized at 800 °C in the presence of H_2SO_4. After removing the silica template using NaOH in ethanol, CMK-1 was obtained (Ryoo et al. 1999). The interesting phenomenon with the hard-templated synthesis of OMCs is the enhanced crystallization degree (graphitization) which is usually quite difficult to accomplish by the soft-templated synthesis (Kim et al. 2003). For the soft-templated synthesis of OMCs, the choice of carbon sources is restricted to the phenolic resins which have the ability to interact with surfactants via hydrogen bonding and to undergo condensation. Alternatively, the hard-templating protocol provides the opportunity to look for a variety of precursors like sucrose (Yuan et al. 2018), tannin (Sanchez-Sanchez et al. 2017), palm oil (Sobrinho et al. 2019), pyrrole (Wan et al. 2015), o-phenylenediamine (Liu et al. 2018a), melamine (Liu et al. 2018a), etc. Note that it is beneficial to choose the precursors having the capacity to give a high carbon yield without being simply decomposed during the carbonization. This is because the well filling of the pores with carbon sources can ensure that the obtained OMC is the perfect replica of silica template (Lu and Schüth 2006). Contrary to this, by partially (coating) filling the pores of SBA-15 with furfuryl alcohol (carbon source), Joo et al. have prepared an OMC (CMK-5) with a different morphology (nanotubes) than the expected nanorod morphology (Joo et al. 2001). The utilization of nitrogen-containing carbon sources such as pyrrole (Wan et al. 2015), o-phenylenediamine (Liu et al. 2018a), melamine (Liu et al. 2018a) and phthalocyanine (Li et al. 2020b) does not yield the pure OMCs but results in the formation of nitrogen-doped OMCs. For instance, Li et al. have utilized the metal phthalocyanines as the carbon sources and silica spheres as the hard template which yield the metal and nitrogen-doped graphitic OMCs (Li et al. 2020b). Chao et al. have studied that the pore structure and surface chemistry characteristics of OMCs can be varied with the use of different precursors (Chao et al. 2017). In the other work, it is found that the OMC prepared from sucrose is more hydrophobic than the OMC prepared from anthracene using the same hard template (Li et al. 2018).

OMCs with dual porosity (micropores and mesopores) are very much intrigued for the supercapacitance applications due to the fact that the energy storage predominately occurs in the micropores and the mass-transport of electrolytes back and forth the micropores is facilitated by mesopores (Bhat et al. 2020; Zhai et al. 2011). The common template removal methods such as etching silica, chemical activation or metal extraction from mesoporous carbides do not always assure the mesopores with narrow size distribution. On the other hand, with these methods, it is also very difficult to tune the size and volume of micropores. To solve this issue, Yan et al. have adapted a hard-salt template strategy (multiple-templating strategy), i.e. mixture of a hard template (SBA-15) and a salt template ($ZnCl_2$), which leads to the formation of OMC with the micropores of narrow size distribution. Besides, the positively charged Zn^{2+} ions interact with the pore walls of the negatively charged electron lone pair rich SBA-15 during the impregnation. Hence, the salt template is distributed partly along the mesopore channel and partly inside the carbon precursor residing in the meso-pore channels of SBA-15. This enlarges the mesopore size in the ordered mesoporous

cylindrical carbon rods that obtained after the template removal. The mesopore size of OMC can be further enhanced with the increase of salt template but it may end up in the mesopores of broad size distribution (Yan et al. 2018).

The ordered micro-mesoporous carbon can also be obtained by utilizing the composite template (dual hard template, also an example of multiple-templating method) that is made up of an ordered mesoporous template (SBA-15) and an ordered microporous template (HZSM-5). The composite template is removed by stirring the sample with NaOH in ethanol–water mixture at 80 °C for 4 h (Sobrinho et al. 2019). Sun et al. have employed the dual-hard-templating protocol for synthesizing the 3D OMC with macropores. The dual hard template is prepared by the immersion of opal (macroporous silica template) in the precursor solution of OMS followed by the calcination. This dual hard template is impregnated into the precursor solution containing sucrose, urea and phytic acid. After drying, the obtained solid is pyrolysed under argon atmosphere, yielding the nitrogen and phosphorous-doped carbon containing 3D-ordered mesopores and macropores. The 3D-ordered macroporous-mesoporous carbon has also been prepared in this method (Sun et al. 2018).

The solvents for the preparation of OMCs should have the lower boiling point and the capacity to solve the carbon sources to ensure the efficient infiltration inside the mesopore channels of hard templates. The common solvents are water and ethanol (Lu et al. 2009) but in these solvents, the solubility of C_{60} is poor which inhibits the cross-linking of C_{60} and also results in the insufficient pore filling. Therefore, the generation of ordered mesoporous C_{60} was only a dream until Benzigar et al. have utilized 1-chloronapthalene as a solvent in which C_{60} has the higher solubility. After following the routine procedure using SBA-15 as a hard template, the ordered mesoporous C_{60} is successfully obtained. Furthermore, the cross-linking reactions between C_{60} clusters enable the polymerization and promote the generation of crystalline pore walls (ordered mesoporous C_{60} with a higher crystallinity) during the carbonization (Benzigar et al. 2018b). This similar strategy has also been applied for the preparation of another fullerene type material, i.e. ordered mesoporous C_{70} (Benzigar et al. 2018a).

For the preparation of OMCs by hard-templating methods, the OMSs of different types such as MCM, SBA, FDU, MSU-H, KIT and HMS have been routinely utilized as hard templates. According to the pore structures of OMS templates, the pore structures of OMCs are derived (Lu et al. 2009). Colloidal silica nanoparticles can also find applications as hard template for preparing OMCs (Chai et al. 2004). Iron oxide is an interesting hard template as it promotes the graphitization of OMC at the lower temperatures (Kim et al. 2004). Though OMSs, due to the excellent ordered mesostructure, are widespread as the hard templates for OMCs, the strong acid or base treatment required for the removal of OMSs is a key disadvantage. MgO, owing to the capacity to be removed under mild acid treatment, can be used but the regularity of mesopores in the resultant carbon materials is not up to the mark as that obtained by using OMSs (He et al. 2012; Morishita et al. 2010; Eftekhari and Fan 2017).

The procedure to prepare the OMMOs using the hard-template method is almost the same like the preparation of OMCs. The difference is that the metal precursors are converted to metal oxide by the calcination in air during the preparation of OMMOs

whereas the carbon precursors are converted to solid carbon by the carbonization or pyrolysis procedure at vacuum or inert atmosphere. Mostly, the common metal salts (e.g. metal nitrates) are used as the precursors for the preparation of OMMOs but it depends on the type of metals. Though the OMSs are the familiar hard templates for the preparation of OMMOs, the OMCs can be also used. Unlike the OMS templates, the strong acid or base treatment is not required for the removal of OMCs which can be easily burnt off. But the problem is that, during the removal of OMCs, a small content of metal oxide may be lost or the metal carbide may be formed (Szczęśniak et al. 2021). Note that the OMSs cannot be the promising templates for preparing the OMMOs of all kinds of metals because, depending on the metal type, a part of the metal oxides can be leached away by reacting with HF or NaOH during removal of OMS template (Lu and Schüth 2006). The major advantage in preparing OMMOs by hard-templating method is the accomplishment of ordered mesostructure together with the excellent crystallinity in a simple way, which usually requires the special strategy in soft-templating method. Despite the pore structure is controlled by the nature of hard template, the crystalline phase of a particular OMMO can be rationally designed. For instance, ordered mesoporous β-MnO_2, Mn_2O_3 and Mn_3O_4 can be prepared by varying the calcination temperatures or with the assistance of H_2 using the same hard template (KIT-6). Note that all these materials have the similar frameworks (Zhang et al. 2019a; Jiao and Bruce 2007; Jiao et al. 2007).

The challenging aspect in the synthesis of OMMOs is to accomplish the higher surface area. This is because of the structural shrinkage and sintering of the primary particles during the thermal treatment. Also, the complete pore system of the template is filled, and hence the surface area of the cast oxide corresponds to the previously exposed surface of the template, the achievable surface area is limited. To overcome this, the surface templating (surface casting) instead of pore filling templating has been proposed by Gu et al. For this, a special template, i.e. SBA-15 with abundant silanol groups, is initially prepared by using the oxidative removal of soft template instead of using the calcination method. These reactive silanol groups interact with the zirconia precursor which is consequently coated on the surface of pore walls in SBA-15. After removing the template by NaOH, the ordered mesoporous zirconia with high surface area is obtained. (Gu et al. 2017).

OMZs have also been prepared by the hard-templating method, which is usually carried out in two different ways. In the first method, the hard template is mixed with the synthetic precursor gel of the zeolite, i.e. the in situ crystallization occurs inside the pore channels of hard templates. The other method deals with the addition of preformed zeolite crystals into the hard templates. As indicated above, the hard-templating approach provides the improved crystallinity, which is a more desirable property for the zeolite materials. While OMCs are used as the templates, the phase separation of carbon is noticed because hydrophobic carbon and the hydrophilic zeolite precursors repel each other. To avoid this, the carbon templates are usually treated with HNO_3 (Chen et al. 2020; Hartmann et al. 2021).

For achieving the efficient nanocasting method to prepare the OMMs, the following requirements are crucial.

(i)   The first requisite is the interaction between template and precursors of target OMM, which promotes the efficient pore filling and ensures the regularity of mesostructure. For instance, OMSs having silanol groups can interact with the inorganic precursors.

(ii)   The template removal should be performed without disturbing the cast and the ordered mesostructure.

(iii)   Aggregation and migration of metal ions are important to accomplish the flawless replica of the chosen hard template during the preparation of OMMOs. This is because the volume contraction rate (~10%) is low for the metal oxides (Lu et al. 2009).

(iv)   The stability of hard template needs to be very high so that the OMMs with the higher crystallinity can be prepared.

(v)   The adequate knowledge about the pore structure of hard template is essential before performing the synthesis process.

(vi)   The solvents should have the capacity to be easily removed. Ethanol, water and THF are frequently used. Ethanol is relatively a better solvent than water for the inorganic precursors because water exposes a strong hydrating effect which may suppress the migration and aggregation of precursors on the silica surface. THF is a suitable solvent when the organic polymers are used as the precursors (Lu et al. 2009).

(vii)   The target OMM should be able to develop the interconnected framework to sustain the chemical treatment during and after the template removal. Or else, the discrete nanoparticles or nanowires would be obtained and the accomplishment of structurally stable replica would become a failure (Lu et al. 2009).

The templates, as shown in Fig. 6d, can be in situ generated by phase separation using various chemical species (e.g. salts, ions, molecules or sometimes the solvent), i.e. it is not always required for the hard templates to be formed before the preparation of mesoporous materials (Li et al. 2016).

5 Template-Free Synthesis of OMMs

MOFs and COFs are the exemplary porous materials prepared by the template-free synthesis. Similar to zeolites, metal–organic frameworks (MOFs) are the crystalline inorganic–organic hybrid materials having the atomic periodicity extending to the pores and channels (Guan et al. 2018). MOFs are a kind of porous materials constructed by the assembly of inorganic metal nodes or polynuclear secondary building units (SBUs) and organic linkers. Typically, like zeolites, the MOFs are microporous; however, the OMMOFs can be prepared by using the lengthy organic linkers.

Similarly, the covalent-organic frameworks (COFs) are a kind of porous materials in which the organic moieties (linkers) are assembled together through covalent

bonding which builds the periodic porous network. The OMCOFs can be prepared by utilizing the lengthy organic linkers. Topological design is an important factor to accomplish the mesoporosity in COFs (Abuzeid et al. 2021; Huang et al. 2016).

Unlike the other OMMs, the mesoporous MOFs and COFs are yet to be largely utilized in the various applications. For more details about the preparation of mesoporous MOFs (Xuan et al. 2012; Guan et al. 2018) and COFs (Huang et al. 2016; Abuzeid et al. 2021), it is recommended to read the already published review articles.

The mesoporosity in zeolites can be introduced without using any template via the post-modification method such as desilication and dealumination but the obtained mesostructure would be irregular. Note that, in this method, no template is used for introducing the mesoporosity but the typical template (tertiarypropylammonium) for preparing the microporous zeolites is required.

As shown in Fig. 6e, the mesoporous materials can be also prepared from the aggregation of nanoscale building blocks. However, in such materials, the pore architectures could be determined only for the materials with closed-packing structure (Li et al. 2016). It is very hard to construct the ordered mesostructure by this method.

6 Doping in OMMs

To facilitate the applications of OMMs in diverse fields like catalysis, the chemical species such as alkali metals, transition metal ions and nitrogen are doped in the OMMs. Especially, for the materials like OMCs and OMSs, the doping is very crucial due to their inert properties. Doping of different chemical elements in the OMMs can be done in one-pot, i.e. during the preparation of OMMs, or two-pot, i.e. after the synthesis of OMMs (Fig. 22). In the one-pot method, the precursors of OMMs and dopant are taken together and subjected to the chosen synthetic procedure (Yang et al. 2017; Wang et al. 2018; Li et al. 2017a). The nitrogen-doped OMCs are generally prepared from the carbon precursors containing nitrogen functional groups, i.e. no additional precursor is required for providing the nitrogen atoms (Wan et al. 2015; Liu et al. 2018a). Note that the dopants may sometimes influence the regularity of mesoporous structure in the resulting OMMs. More than one dopant can be incorporated in the chosen OMMs by the one-pot method (Liu et al. 2018a). In the two-pot method of doping, the OMM is initially prepared, and to this preformed OMM, the precursor of dopant is added (Budi et al. 2019; Cho et al. 2018; Kayal et al. 2019).

Similar to the dopant, the composite OMM materials can also be prepared. For preparing the composite OMM, instead of adding just the elements or ionic species in the OMM, another material of different type is mixed to the OMM. The composite OMM can be also prepared by either one-pot (Benzigar et al. 2019; Li et al. 2017b) or two-pot method (Glotov et al. 2019). In the composite OMM, either both the materials have the ordered mesostructure or one of the materials displays the ordered mesostructure.
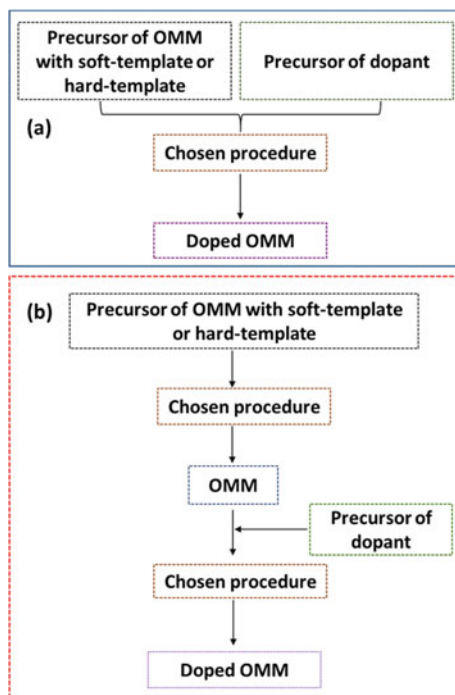
Fig. 22 Preparation of doped OMMs by **a** one-pot and **b** two-pot methods

Note that, depending upon the compatibility, the amount of dopant or a foreign material can be increased in the target doped OMM or composite OMM, respectively.

7 Advantages and Limitations of Different Preparation Methods

Considering the different methods for the preparation of mesoporous materials, every method has its own advantages and disadvantages. Despite the soft-templating and the hard-templating methods are very familiar as they often promise the ordered mesostructure, it seems significant to compare the advantages and disadvantages of each and every method. Such comparison is made in Table 3.

Table 3 A comparison of synthetic methods of mesoporous materials. Adapted from Li et al. (2016) with permission from Springer Nature

Methods	Advantages	Disadvantages
Soft-templating method	Controllable mesostructures and pore sizes Tuneable morphologies and easily processable High-quality product Large-scale production	Uses surfactants Mesostructure formation is highly sensitive to the reaction conditions Relatively low crystallinity
Hard-templating method	Low sensitivity to the reaction conditions High-quality product Highly crystalline product Ordered nanoarrays structure	Uses preformed hard templates High cost Time consuming
Multiple-templating method	Hierarchically porous structure	Requires multiple templates High cost Time consuming
In situ templating pathway	Simple method No preformed templates or surfactants required Low cost	Low quality Hard to obtain ordered structures
Template-free packing method	Simple method Easily processable No templates required Highly crystalline product	Hard to obtain ordered structures
Reticular chemistry guiding approach	Controllable mesostructures and pore volume No templates Highly crystalline product	Low stability Mesostructure formation is highly sensitive to the reaction conditions Not easily processable

8 Conclusion and Future Trends

OMMs have become very attractive than the disordered mesoporous materials as they provide excellent mass transfer and higher selectivity in applications. Relatively, the preparation of OMMs requires a very special and controlled procedure than that of disordered mesoporous materials. Among the so far reported methods, the soft-templating method, which mostly utilizes the surfactants as templates, is frequently reported and effective than the other synthetic routes of OMMs. However, soft-templating route is tedious as it involves the complicated sol–gel chemistry, and also, the synthetic conditions should be strictly maintained. Contrary to this, the other familiar method, i.e. the hard-templating method, is straightforward because it is similar to the traditional nanocasting method. EISA is found to be the efficient method for the preparation of different OMMOs; however, it can be also applied for the preparation of OMSs and OMCs. For the preparation of highly crystalline OMMOs using the soft-templating route, the CASH method is beneficial. Differently,

the hard-templating method can produce easily the high crystalline OMMOs due to the better thermal stability of hard templates such as OMSs and OMCs. The template-free method is so far successful in the preparation of OMMOFs and OMCOFs. The template-free synthesis basically depends on the strong chemical reactions whereas the template-assisted synthesis is generally built upon the electrostatic interactions (e.g. ionic and hydrogen bonding).

Considering the future trends, the innovations are highly possible in the synthesis of OMMs. This is because the tuning of simple synthetic parameter could lead to the excellent results in the preparation of OMMs. For example, just by changing the solvent, the synthesis of ordered mesoporous C_{60} and C_{70} has been made possible. Moreover, the template-assisted route has been successfully introduced for the synthesis of OMMOFs. Unfortunately, the biggest concern regarding the synthesis methods of OMMs is their industrialization. Despite the accomplishment of innovation, the high cost associated with the synthesis of OMMs hampers the industrial applications of OMMs. Furthermore, except the traditional OMMs (e.g. MCM-41 and SBA-15), the synthesis of other known OMMs is yet to be performed in the bulk scale. Therefore, the future trends on the synthesis of OMMs would be equally focused on two main concepts: (i) innovation in the synthesis of OMMs and (ii) industrialization of OMMs by reducing the total cost of preparation method. Furthermore, the regularity of mesoporosity in OMMs is generally vulnerable at the higher temperature conditions. Therefore, it seems very important to enhance the thermal stability of ordered mesoporous structure in OMMs for the repeated utilities in a specific industrial application.

References

Abuzeid, H.R., El-Mahdy, A.F.M., Kuo, S.-W.: Covalent organic frameworks: design principles, synthetic strategies, and diverse applications. Giant **6**, 100054 (2021). https://doi.org/10.1016/j.giant.2021.100054

Alexandridis, P., Olsson, U., Lindman, B.: A record nine different phases (four cubic, two hexagonal, and one lamellar lyotropic liquid crystalline and two micellar solutions) in a ternary isothermal system of an amphiphilic block copolymer and selective solvents (water and oil). Langmuir **14**(10), 2627–2638 (1998). https://doi.org/10.1021/la971117c

Antonelli, D.M.: Synthesis and mechanistic studies of sulfated meso- and microporous zirconias with chelating carboxylate surfactants. Adv. Mater. **11**(6), 487–492 (1999). https://doi.org/10.1002/(SICI)1521-4095(199904)11:6%3c487::AID-ADMA487%3e3.0.CO;2-2

Antonelli, D.M., Nakahira, A., Ying, J.Y.: Ligand-Assisted Liquid Crystal Templating in Mesoporous Niobium Oxide Molecular Sieves. Inorg. Chem. **35**(11), 3126–3136 (1996). https://doi.org/10.1021/ic951533p

Antonelli, D.M., Ying, J.Y.: Synthesis of hexagonally packed mesoporous TiO$_2$ by a modified sol-gel method. Angew. Chem. Int. Ed. Engl. **34**(18), 2014–2017 (1995). https://doi.org/10.1002/anie.199520141

Asefa, T., MacLachlan, M.J., Coombs, N., Ozin, G.A.: Periodic mesoporous organosilicas with organic groups inside the channel walls. Nature **402**(6764), 867–871 (1999). https://doi.org/10.1038/47229

Ba, J., Polleux, J., Antonietti, M., Niederberger, M.: Non-aqueous synthesis of Tin Oxide nanocrystals and their assembly into ordered porous mesostructures. Adv. Mater. **17**(20), 2509–2512 (2005). https://doi.org/10.1002/adma.200501018

Bazuła, P.A., Lu, A.-H., Nitz, J.-J., Schüth, F.: Surface and pore structure modification of ordered mesoporous carbons via a chemical oxidation approach. Microporous Mesoporous Mater. **108**(1), 266–275 (2008). https://doi.org/10.1016/j.micromeso.2007.04.008

Beaucage, P.A., Susca, E.M., Gruner, S.M., Wiesner, U.B.: Discovering synthesis routes to hexagonally ordered mesoporous niobium nitrides using poloxamer/pluronics block copolymers. Chem. Mater. **29**(21), 8973–8977 (2017). https://doi.org/10.1021/acs.chemmater.7b03834

Beck, J.S., Vartuli, J.C., Roth, W.J., Leonowicz, M.E., Kresge, C.T., Schmitt, K.D., Chu, C.T.W., Olson, D.H., Sheppard, E.W., McCullen, S.B., Higgins, J.B., Schlenker, J.L.: A new family of mesoporous molecular sieves prepared with liquid crystal templates. J. Am. Chem. Soc. **114**(27), 10834–10843 (1992). https://doi.org/10.1021/ja00053a020

Benzigar, M.R., Joseph, S., Baskar, A.V., Park, D.-H., Chandra, G., Umapathy, S., Talapaneni, S.N., Vinu, A.: Ordered mesoporous C70 with highly crystalline pore walls for energy applications. Adv. Funct. Mater. **28**(35), 1803701 (2018). https://doi.org/10.1002/adfm.201803701

Benzigar, M.R., Joseph, S., Ilbeygi, H., Park, D.-H., Sarkar, S., Chandra, G., Umapathy, S., Srinivasan, S., Talapaneni, S.N., Vinu, A.: Highly crystalline mesoporous C60 with ordered pores: a class of nanomaterials for energy applications. Angew. Chem. Int. Ed. **57**(2), 569–573 (2018). https://doi.org/10.1002/anie.201710888

Benzigar, M.R., Joseph, S., Saianand, G., Gopalan, A.-I., Sarkar, S., Srinivasan, S., Park, D.-H., Kim, S., Talapaneni, S.N., Ramadass, K., Vinu, A.: Highly ordered iron oxide-mesoporous fullerene nanocomposites for oxygen reduction reaction and supercapacitor applications. Microporous Mesoporous Mater. **285**, 21–31 (2019). https://doi.org/10.1016/j.micromeso.2019.04.071

Berggren, A., Palmqvist, A.E.C., Holmberg, K.: Surfactant-templated mesostructured materials from inorganic silica. Soft Matter **1**(3), 219–226 (2005). https://doi.org/10.1039/B507551N

Bhat, V., Supria, S., Jayeoye, T.J., Rujiralai, T., Sirimahachai, U., Chong, K.F., Hegde, G.: Influence of surface properties on electro-chemical supercapacitors utilizing Callerya atropurpurea pod derived porous nanocarbons: structure property relationship between porous structures to energy storage devices. Nano Select **1**(2), 226–243 (2020). https://doi.org/10.1002/nano.202000013

Bolivar, J.M., Gascon, V., Marquez-Alvarez, C., Blanco, R.M., Nidetzky, B.: Oriented coimmobilization of oxidase and catalase on tailor-made ordered mesoporous silica. Langmuir **33**(20), 5065–5076 (2017). https://doi.org/10.1021/acs.langmuir.7b00441

Brinker, C.J., Scherer, G.W.: Hydrolysis and condensation II: silicates (Chap. 3). In: Brinker, C.J., Scherer, G.W. (eds.) Sol-gel science, pp. 96–233. Academic Press, San Diego (1990)

Broekhoff, J.C.P.: Mesopore determination from nitrogen sorption isotherms: fundamentals, scope, limitations. In: Delmon, B., Grange, P., Jacobs, P., Poncelet, G. (eds.) Studies in Surface Science and Catalysis, vol. 3. pp. 663–684. Elsevier (1979)

Budi, C.S., Saikia, D., Chen, C.-S., Kao, H.-M.: Catalytic evaluation of tunable Ni nanoparticles embedded in organic functionalized 2D and 3D ordered mesoporous silicas from the hydrogenation of nitroarenes. J. Catal. **370**, 274–288 (2019). https://doi.org/10.1016/j.jcat.2018.12.025

Cai, H., Zhao, D.: A mild method to remove organic templates in periodic mesoporous organosilicas by the oxidation of perchlorates. Microporous Mesoporous Mater. **118**(1), 513–517 (2009). https://doi.org/10.1016/j.micromeso.2008.08.049

Cassiers, K., Linssen, T., Mathieu, M., Benjelloun, M., Schrijnemakers, K., Van Der Voort, P., Cool, P., Vansant, E.F.: A detailed study of thermal, hydrothermal, and mechanical stabilities of a

wide range of surfactant assembled mesoporous silicas. Chem. Mater. **14**(5), 2317–2324 (2002). https://doi.org/10.1021/cm0112892

Chai, G.S., Yoon, S.B., Yu, J.-S., Choi, J.-H., Sung, Y.-E.: Ordered porous carbons with tunable pore sizes as catalyst supports in direct methanol fuel cell. J. Phys. Chem. B **108**(22), 7074–7079 (2004). https://doi.org/10.1021/jp0370472

Chao, B., Konggidinata, M.I., Lin, L., Zappi, M., Gang, D.D.: Effect of carbon precursors and pore expanding reagent on ordered mesoporous carbon for resorcinol removal. J. Water Process Eng. **17**, 256–263 (2017). https://doi.org/10.1016/j.jwpe.2017.05.002

Charan, P.H.K., Rao, G.R.: Textural and morphological studies of transition metal doped SBA-15 by co-condensation method. J. Chem. Sci. **127**(5), 909–919 (2015). https://doi.org/10.1007/s12039-015-0847-5

Chen, A., Komura, M., Kamata, K., Iyoda, T.: Highly ordered arrays of mesoporous silica nanorods with tunable aspect ratios from block copolymer thin films. Adv. Mater. **20**(4), 763–767 (2008). https://doi.org/10.1002/adma.200702010

Chen, H., Wydra, J., Zhang, X., Lee, P.-S., Wang, Z., Fan, W., Tsapatsis, M.: Hydrothermal synthesis of zeolites with three-dimensionally ordered mesoporous-imprinted structure. J. Am. Chem. Soc. **133**(32), 12390–12393 (2011). https://doi.org/10.1021/ja2046815

Chen, L.-H., Sun, M.-H., Wang, Z., Yang, W., Xie, Z., Su, B.-L.: Hierarchically structured zeolites: from design to application. Chem. Rev. **120**(20), 11194–11294 (2020). https://doi.org/10.1021/acs.chemrev.0c00016

Chew, T.-L., Ahmad, A.L., Bhatia, S.: Ordered mesoporous silica (OMS) as an adsorbent and membrane for separation of carbon dioxide (CO_2). Adv. Coll. Interface. Sci. **153**(1), 43–57 (2010). https://doi.org/10.1016/j.cis.2009.12.001

Cho, J.M., Han, G.Y., Jeong, H.-K., Roh, H.-S., Bae, J.W.: Effects of ordered mesoporous bimodal structures of Fe/KIT-6 for CO hydrogenation activity to hydrocarbons. Chem. Eng. J. **354**, 197–207 (2018). https://doi.org/10.1016/j.cej.2018.07.205

Choi, M., Cho, H.S., Srivastava, R., Venkatesan, C., Choi, D.-H., Ryoo, R.: Amphiphilic organosilane-directed synthesis of crystalline zeolite with tunable mesoporosity. Nat. Mater. **5**(9), 718–723 (2006). https://doi.org/10.1038/nmat1705

Choi, M., Na, K., Kim, J., Sakamoto, Y., Terasaki, O., Ryoo, R.: Stable single-unit-cell nanosheets of zeolite MFI as active and long-lived catalysts. Nature **461**(7261), 246–249 (2009). https://doi.org/10.1038/nature08288

Choi, M., Na, K., Ryoo, R.: The synthesis of a hierarchically porous BEA zeolitevia pseudomorphic crystallization. Chem. Commun. **20**, 2845–2847 (2009b). https://doi.org/10.1039/B905087F

Colmenares, M.G., Simon, U., Schmidt, F., Dey, S., Schmidt, J., Thomas, A., Gurlo, A.: Tailoring of ordered mesoporous silica COK-12: Room temperature synthesis of mesocellular foam and multilamellar vesicles. Microporous Mesoporous Mater. **267**, 142–149 (2018). https://doi.org/10.1016/j.micromeso.2018.03.015

Corma, A.: From microporous to mesoporous molecular sieve materials and their use in catalysis. Chem. Rev. **97**(6), 2373–2420 (1997). https://doi.org/10.1021/cr960406n

Côté, A.P., Benin, A.I., Ockwig, N.W., Keeffe, M., Matzger, A.J., Yaghi, O.M.: Porous, crystalline, covalent organic frameworks. Science **310**(5751), 1166 (2005). https://doi.org/10.1126/science.1120411

Cui, Y., Lian, X., Xu, L., Chen, M., Yang, B., Wu, C.-E., Li, W., Huang, B., Hu, X.: Designing and fabricating ordered mesoporous metal oxides for CO_2 catalytic conversion: a review and prospect. Materials (basel) **12**(2), 276 (2019). https://doi.org/10.3390/ma12020276

Deng, X., Chen, K., Tüysüz, H.: Protocol for the nanocasting method: preparation of ordered mesoporous metal oxides. Chem. Mater. **29**(1), 40–52 (2017). https://doi.org/10.1021/acs.chemmater.6b02645

Deng, Y., Wei, J., Sun, Z., Zhao, D.: Large-pore ordered mesoporous materials templated from non-Pluronic amphiphilic block copolymers. Chem. Soc. Rev. **42**(9), 4054–4070 (2013). https://doi.org/10.1039/C2CS35426H

Deng, Y., Yu, T., Wan, Y., Shi, Y., Meng, Y., Gu, D., Zhang, L., Huang, Y., Liu, C., Wu, X., Zhao, D.: Ordered mesoporous silicas and carbons with large accessible pores templated from amphiphilic diblock copolymer poly(ethylene oxide)-b-polystyrene. J. Am. Chem. Soc. **129**(6), 1690–1697 (2007). https://doi.org/10.1021/ja067379v

Deshpande, A.S., Pinna, N., Smarsly, B., Antonietti, M., Niederberger, M.: Controlled assembly of preformed ceria nanocrystals into highly ordered 3D nanostructures. Small **1**(3), 313–316 (2005). https://doi.org/10.1002/smll.200400060

Díaz, U., Corma, A.: Ordered covalent organic frameworks, COFs and PAFs. From preparation to application. Coord. Chem. Rev. **311**, 85–124 (2016). https://doi.org/10.1016/j.ccr.2015.12.010

Du, G., Xu, Y., Zheng, S., Xue, H., Pang, H.: The state of research regarding ordered mesoporous materials in batteries. Small **15**(11), 1804600 (2019). https://doi.org/10.1002/smll.201804600

Eddaoudi, M., Kim, J., Rosi, N., Vodak, D., Wachter, J., Keeffe, M., Yaghi, O.M.: Systematic design of pore size and functionality in isoreticular MOFs and their application in methane storage. Science **295**(5554), 469 (2002). https://doi.org/10.1126/science.1067208

Eftekhari, A., Fan, Z.: Ordered mesoporous carbon and its applications for electrochemical energy storage and conversion. Mater. Chem. Front. **1**(6), 1001–1027 (2017). https://doi.org/10.1039/C6QM00298F

Enterría, M., Figueiredo, J.L.: Nanostructured mesoporous carbons: tuning texture and surface chemistry. Carbon **108**, 79–102 (2016). https://doi.org/10.1016/j.carbon.2016.06.108

Evans, A.M., Ryder, M.R., Ji, W., Strauss, M.J., Corcos, A.R., Vitaku, E., Flanders, N.C., Bisbey, R.P., Dichtel, W.R.: Trends in the thermal stability of two-dimensional covalent organic frameworks. Faraday Discuss. **225**(0), 226–240 (2021). https://doi.org/10.1039/D0FD00054J

Fang, Y., Hu, H.: An Ordered mesoporous aluminosilicate with completely crystalline zeolite wall structure. J. Am. Chem. Soc. **128**(33), 10636–10637 (2006). https://doi.org/10.1021/ja061182l

Feliczak-Guzik, A.: Hierarchical zeolites: synthesis and catalytic properties. Microporous Mesoporous Mater. **259**, 33–45 (2018). https://doi.org/10.1016/j.micromeso.2017.09.030

Feng, D., Luo, W., Zhang, J., Xu, M., Zhang, R., Wu, H., Lv, Y., Asiri, A.M., Khan, S.B., Rahman, M.M., Zheng, G., Zhao, D.: Multi-layered mesoporous TiO_2 thin films with large pores and highly crystalline frameworks for efficient photoelectrochemical conversion. J. Mater. Chem. A **1**(5), 1591–1599 (2013). https://doi.org/10.1039/C2TA00588C

Feng, G., Wang, J., Boronat, M., Li, Y., Su, J.-H., Huang, J., Ma, Y., Yu, J.: Radical-facilitated green synthesis of highly ordered mesoporous silica materials. J. Am. Chem. Soc. **140**(14), 4770–4773 (2018). https://doi.org/10.1021/jacs.8b00093

Florek, J., Guillet-Nicolas, R., Kleitz, F.: Ordered mesoporous silica: synthesis and applications (Chap. 4). In: Mario, L., Robert, G. (eds.) Functional Materials, pp. 61–100. De Gruyter, Berlin (2014)

Fulvio, P.F., Brosey, R.I., Jaroniec, M.: Synthesis of mesoporous alumina from boehmite in the presence of triblock copolymer. ACS Appl. Mater. Interfaces. **2**(2), 588–593 (2010). https://doi.org/10.1021/am9009023

Gallis, K.W., Landry, C.C.: Rapid calcination of nanostructured silicate composites by microwave irradiation. Adv. Mater. **13**(1), 23–26 (2001). https://doi.org/10.1002/1521-4095(200101)13:1%3c23::AID-ADMA23%3e3.0.CO;2-9

Gao, C.: Formation Mechanism of Anionic-Surfactant-Templated Mesoporous Silica (AMS). Department of Physical, Inorganic and Structural Chemistry, Stockholm University (2009)

Gao, P., Wang, A., Wang, X., Zhang, T.: Synthesis of highly ordered Ir-containing mesoporous carbon materials by organic-organic self-assembly. Chem. Mater. **20**(5), 1881–1888 (2008). https://doi.org/10.1021/cm702815e

Garcia-Bennett, A.E.: Synthesis, toxicology and potential of ordered mesoporous materials in nanomedicine. Nanomedicine **6**(5), 867–877 (2011). https://doi.org/10.2217/nnm.11.82

García, A., Nieto, A., Vila, M., Vallet-Regí, M.: Easy synthesis of ordered mesoporous carbon containing nickel nanoparticles by a low temperature hydrothermal method. Carbon **51**, 410–418 (2013). https://doi.org/10.1016/j.carbon.2012.08.074

Ge, J., Yang, X., Luo, J., Ma, J., Zou, Y., Li, J., Luo, W., Cheng, X., Deng, Y.: Ordered mesoporous CoO/CeO2 heterostructures with highly crystallized walls and enhanced peroxidase-like bioactivity. Appl. Mater. Today **15**, 482–493 (2019). https://doi.org/10.1016/j.apmt.2019.03.009

Glazneva, T.S., Rebrov, E.V., Schouten, J.C., Paukshtis, E.A., Ismagilov, Z.R.: Synthesis and characterization of mesoporous silica thin films as a catalyst support on a titanium substrate. Thin Solid Films **515**(16), 6391–6394 (2007). https://doi.org/10.1016/j.tsf.2006.11.058

Glotov, A., Levshakov, N., Stavitskaya, A., Artemova, M., Gushchin, P., Ivanov, E., Vinokurov, V., Lvov, Y.: Templated self-assembly of ordered mesoporous silica on clay nanotubes. Chem. Commun. **55**(38), 5507–5510 (2019). https://doi.org/10.1039/C9CC01935A

Gonçalves, A.A.S., Costa, M.J.F., Zhang, L., Ciesielczyk, F., Jaroniec, M.: One-pot synthesis of MeAl2O4 (Me = Ni Co, or Cu) supported on γ-Al$_2$O$_3$ with ultralarge mesopores: enhancing interfacial defects in γ-Al$_2$O$_3$ to facilitate the formation of spinel structures at lower temperatures. Chem. Mater. **30**(2), 436–446 (2018). https://doi.org/10.1021/acs.chemmater.7b04353

Goto, Y., Mizoshita, N., Waki, M., Ikai, M., Maegawa, Y., Inagaki, S.: Synthesis and applications of periodic mesoporous organosilicas. In: Douhal, A., Anpo, M. (eds.) Chemistry of Silica and Zeolite-Based Materials, vol. 2. pp. 1–25. Elsevier (2019)

Goyal, P.S., Aswal, V.K.: Micellar structure and inter-micelle interactions in micellar solutions: results of small angle neutron scattering studies. Curr. Sci. **80**(8), 972–979 (2001)

Grosse, I., Estel, K.: Thin surfactant layers at the solid interface. Colloid Polym. Sci. **278**(10), 1000–1006 (2000). https://doi.org/10.1007/s003960000364

Grosso, D., Boissière, C., Smarsly, B., Brezesinski, T., Pinna, N., Albouy, P.A., Amenitsch, H., Antonietti, M., Sanchez, C.: Periodically ordered nanoscale islands and mesoporous films composed of nanocrystalline multimetallic oxides. Nat. Mater. **3**(11), 787–792 (2004). https://doi.org/10.1038/nmat1206

Grosso, D., Cagnol, F., Soler-Illia, G.J.d.A.A., Crepaldi, E.L., Amenitsch, H., Brunet-Bruneau, A., Bourgeois, A., Sanchez, C.: Fundamentals of mesostructuring through evaporation-induced self-assembly. Adv. Funct. Mater. **14**(4), 309–322 (2004b). https://doi.org/10.1002/adfm.200305036

Grosso, D., Soler-Illia, G.J.d.A.A., Crepaldi, E.L., Charleux, B., Sanchez, C.: Nanocrystalline transition-metal oxide spheres with controlled multi-scale porosity. Adv. Funct. Mater. **13**(1), 37–42 (2003). https://doi.org/10.1002/adfm.200390002

Gu, D., Schmidt, W., Pichler, C.M., Bongard, H.-J., Spliethoff, B., Asahina, S., Cao, Z., Terasaki, O., Schüth, F.: Surface-casting synthesis of mesoporous zirconia with a CMK-5-like structure and high surface area. Angew. Chem. Int. Ed. **56**(37), 11222–11225 (2017). https://doi.org/10.1002/anie.201705042

Gu, D., Schüth, F.: Synthesis of non-siliceous mesoporous oxides. Chem. Soc. Rev. **43**(1), 313–344 (2014). https://doi.org/10.1039/C3CS60155B

Guan, H.-Y., LeBlanc, R.J., Xie, S.-Y., Yue, Y.: Recent progress in the syntheses of mesoporous metal–organic framework materials. Coord. Chem. Rev. **369**, 76–90 (2018). https://doi.org/10.1016/j.ccr.2018.05.001

Guan, S., Inagaki, S., Ohsuna, T., Terasaki, O.: Cubic hybrid organic−inorganic mesoporous crystal with a decaoctahedral shape. J. Am. Chem. Soc. **122**(23), 5660–5661 (2000). https://doi.org/10.1021/ja000839e

Han, Y., Li, N., Zhao, L., Li, D., Xu, X., Wu, S., Di, Y., Li, C., Zou, Y., Yu, Y., Xiao, F.-S.: Understanding of the high hydrothermal stability of the mesoporous materials prepared by the assembly of triblock copolymer with preformed zeolite precursors in acidic media. J. Phys. Chem. B **107**(31), 7551–7556 (2003). https://doi.org/10.1021/jp026899j

Hartmann, M., Bischof, C.: Mechanical stability of mesoporous molecular sieve MCM-48 studied by adsorption of benzene, n-heptane, and cyclohexane. J. Phys. Chem. B **103**(30), 6230–6235 (1999). https://doi.org/10.1021/jp991103a

Hartmann, M., Thommes, M., Schwieger, W.: Hierarchically-ordered zeolites: a critical assessment. Adv. Mater. Interfaces **8**(4), 2001841 (2021). https://doi.org/10.1002/admi.202001841

Hartmann, M., Vinu, A.: Mechanical stability and porosity analysis of large-pore SBA-15 mesoporous molecular sieves by mercury porosimetry and organics adsorption. Langmuir **18**(21), 8010–8016 (2002). https://doi.org/10.1021/la025782j

Hartono, S.B., Qiao, S.Z., Liu, J., Jack, K., Ladewig, B.P., Hao, Z., Lu, G.Q.M.: Functionalized mesoporous silica with very large pores for cellulase immobilization. J. Phys. Chem. C **114**(18), 8353–8362 (2010). https://doi.org/10.1021/jp102368s

He, X., Li, R., Qiu, J., Xie, K., Ling, P., Yu, M., Zhang, X., Zheng, M.: Synthesis of mesoporous carbons for supercapacitors from coal tar pitch by coupling microwave-assisted KOH activation with a MgO template. Carbon **50**(13), 4911–4921 (2012). https://doi.org/10.1016/j.carbon.2012.06.020

Hisaki, I., Xin, C., Takahashi, K., Nakamura, T.: Designing hydrogen-bonded organic frameworks (HOFs) with permanent porosity. Angew. Chem. Int. Ed. **58**(33), 11160–11170 (2019). https://doi.org/10.1002/anie.201902147

Horikawa, T., Do, D.D., Nicholson, D.: Capillary condensation of adsorbates in porous materials. Adv. Coll. Interface. Sci. **169**(1), 40–58 (2011). https://doi.org/10.1016/j.cis.2011.08.003

Horiuchi, Y., Yamashita, H.: Design of mesoporous silica thin films containing single-site photocatalysts and their applications to superhydrophilic materials. Appl. Catal. A **400**(1), 1–8 (2011). https://doi.org/10.1016/j.apcata.2011.04.027

Howarth, A.J., Liu, Y., Li, P., Li, Z., Wang, T.C., Hupp, J.T., Farha, O.K.: Chemical, thermal and mechanical stabilities of metal–organic frameworks. Nat. Rev. Mater. **1**(3), 15018 (2016). https://doi.org/10.1038/natrevmats.2015.18

Hozumi, A., Sugimura, H., Hiraku, K., Kameyama, T., Takai, O.: Low-temperature elimination of organic components from mesostructured organic−inorganic composite films using vacuum ultraviolet light. Chem. Mater. **12**(12), 3842–3847 (2000). https://doi.org/10.1021/cm000546k

Hozumi, A., Yokogawa, Y., Kameyama, T., Hiraku, K., Sugimura, H., Takai, O., Okido, M.: Photocalcination of mesoporous silica films using vacuum ultraviolet light. Adv. Mater. **12**(13), 985–987 (2000). https://doi.org/10.1002/1521-4095(200006)12:13<985::AID-ADMA985>3.0.CO;2-#

Huang, N., Wang, P., Jiang, D.: Covalent organic frameworks: a materials platform for structural and functional designs. Nat. Rev. Mater. **1**(10), 16068 (2016). https://doi.org/10.1038/natrevmats.2016.68

Huang, Y., Cai, H., Feng, D., Gu, D., Deng, Y., Tu, B., Wang, H., Webley, P.A., Zhao, D.: One-step hydrothermal synthesis of ordered mesostructured carbonaceous monoliths with hierarchical porosities. Chem. Commun. **23**, 2641–2643 (2008). https://doi.org/10.1039/B804716B

Huang, Y., Cai, H., Yu, T., Zhang, F., Zhang, F., Meng, Y., Gu, D., Wan, Y., Sun, X., Tu, B., Zhao, D.: Formation of mesoporous carbon with a face-centered-cubic Fd3m structure and bimodal architectural pores from the reverse amphiphilic triblock copolymer PPO-PEO-PPO. Angew. Chem. Int. Ed. **46**(7), 1089–1093 (2007). https://doi.org/10.1002/anie.200603665

Huang, Y., Yang, J., Cai, H., Zhai, Y., Feng, D., Deng, Y., Tu, B., Zhao, D.: A curing agent method to synthesize ordered mesoporous carbons from linear novolac phenolic resin polymers. J. Mater. Chem. **19**(36), 6536–6541 (2009). https://doi.org/10.1039/B908183F

Huo, Q., Margolese, D.I., Ciesla, U., Demuth, D.G., Feng, P., Gier, T.E., Sieger, P., Firouzi, A., Chmelka, B.F.: Organization of organic molecules with inorganic molecular species into nanocomposite biphase arrays. Chem. Mater. **6**(8), 1176–1191 (1994). https://doi.org/10.1021/cm00044a016

Huo, Q., Margolese, D.I., Ciesla, U., Feng, P., Gier, T.E., Sieger, P., Leon, R., Petroff, P.M., Schüth, F., Stucky, G.D.: Generalized synthesis of periodic surfactant/inorganic composite materials. Nature **368**(6469), 317–321 (1994). https://doi.org/10.1038/368317a0

Hyde, S.T., Schröder, G.E.: Novel surfactant mesostructural topologies: between lamellae and columnar (hexagonal) forms. Curr. Opin. Colloid Interface Sci. **8**(1), 5–14 (2003). https://doi.org/10.1016/S1359-0294(03)00014-1

Inagaki, S., Guan, S., Fukushima, Y., Ohsuna, T., Terasaki, O.: Novel mesoporous materials with a uniform distribution of organic groups and inorganic oxide in their frameworks. J. Am. Chem. Soc. **121**(41), 9611–9614 (1999). https://doi.org/10.1021/ja9916658

Inagaki, S., Koiwai, A., Suzuki, N., Fukushima, Y., Kuroda, K.: Syntheses of highly ordered mesoporous materials, FSM-16, derived from Kanemite. Bull. Chem. Soc. Jpn. **69**(5), 1449–1457 (1996). https://doi.org/10.1246/bcsj.69.1449

Inagaki, S., Sakamoto, Y., Fukushima, Y., Terasaki, O.: Pore wall of a mesoporous molecular sieve derived from Kanemite. Chem. Mater. **8**(8), 2089–2095 (1996). https://doi.org/10.1021/cm960115v

Iwata, T.: Lamellar gel network (Chap. 25). In: Sakamoto, K., Lochhead, R.Y., Maibach, H.I., Yamashita, Y. (eds.) Cosmetic Science and Technology, pp. 415-447. Elsevier, Amsterdam (2017)

Jambhrunkar, S., Qu, Z., Popat, A., Karmakar, S., Xu, C., Yu, C.: Modulating in vitro release and solubility of griseofulvin using functionalized mesoporous silica nanoparticles. J. Colloid Interface Sci. **434**, 218–225 (2014). https://doi.org/10.1016/j.jcis.2014.08.019

Jammaer, J., Aerts, A., D'Haen, J., Seo, J.W., Martens, J.A.: Convenient synthesis of ordered mesoporous silica at room temperature and quasi-neutral pH. J. Mater. Chem. **19**(44), 8290–8293 (2009). https://doi.org/10.1039/B915273C

Jiao, F., Bruce, P.G.: Mesoporous crystalline β-MnO$_2$—a reversible positive electrode for rechargeable lithium batteries. Adv. Mater. **19**(5), 657–660 (2007). https://doi.org/10.1002/adma.200602499

Jiao, F., Harrison, A., Hill, A.H., Bruce, P.G.: Mesoporous Mn$_2$O$_3$ and Mn$_3$O$_4$ with crystalline walls. Adv. Mater. **19**(22), 4063–4066 (2007). https://doi.org/10.1002/adma.200700336

Jiao, J., Cai, Y., Liu, P., Liu, P.: Influence of template on the structure of mesoporous carbon prepared with novalac resin as carbon precursor. J. Porous Mater. **20**(5), 1247–1255 (2013). https://doi.org/10.1007/s10934-013-9709-z

Joo, S.H., Choi, S.J., Oh, I., Kwak, J., Liu, Z., Terasaki, O., Ryoo, R.: Ordered nanoporous arrays of carbon supporting high dispersions of platinum nanoparticles. Nature **412**(6843), 169–172 (2001). https://doi.org/10.1038/35084046

Jun, S., Kim, J.M., Ryoo, R., Ahn, Y.-S., Han, M.-H.: Hydrothermal stability of MCM-48 improved by post-synthesis restructuring in salt solution. Microporous Mesoporous Mater. **41**(1), 119–127 (2000). https://doi.org/10.1016/S1387-1811(00)00279-1

Jung, S.-B., Park, H.-H.: Concentration-dependent mesostructure of surfactant-templated mesoporous silica thin film. Thin Solid Films **494**(1), 320–324 (2006). https://doi.org/10.1016/j.tsf.2005.08.160

Kawi, S., Lai, M.W.: Supercritical fluid extraction of surfactant from Si-MCM-41. AIChE J. **48**(7), 1572–1580 (2002). https://doi.org/10.1002/aic.690480719

Kayal, U., Mohanty, B., Bhanja, P., Chatterjee, S., Chandra, D., Hara, M., Kumar Jena, B., Bhaumik, A.: Ag nanoparticle-decorated, ordered mesoporous silica as an efficient electrocatalyst for alkaline water oxidation reaction. Dalton Trans. **48**(6), 2220–2227 (2019). https://doi.org/10.1039/C8DT04159H

Kim, B.G., Jo, C., Shin, J., Mun, Y., Lee, J., Choi, J.W.: Ordered mesoporous titanium nitride as a promising carbon-free cathode for aprotic lithium-oxygen batteries. ACS Nano **11**(2), 1736–1746 (2017). https://doi.org/10.1021/acsnano.6b07635

Kim, C.H., Lee, D.-K., Pinnavaia, T.J.: Graphitic mesostructured carbon prepared from aromatic precursors. Langmuir **20**(13), 5157–5159 (2004). https://doi.org/10.1021/la049602c

Kim, S.S., Karkamkar, A., Pinnavaia, T.J., Kruk, M., Jaroniec, M.: Synthesis and characterization of ordered, very large pore MSU-H silicas assembled from water-soluble silicates. J. Phys. Chem. B **105**(32), 7663–7670 (2001). https://doi.org/10.1021/jp010773p

Kim, T.-W., Kleitz, F., Paul, B., Ryoo, R.: MCM-48-like large mesoporous silicas with tailored pore structure: facile synthesis domain in a ternary triblock copolymer−butanol−water system. J. Am. Chem. Soc. **127**(20), 7601–7610 (2005). https://doi.org/10.1021/ja042601m

Kim, T.-W., Park, I.-S., Ryoo, R.: A synthetic route to ordered mesoporous carbon materials with graphitic pore walls. Angew. Chem. Int. Ed. **42**(36), 4375–4379 (2003). https://doi.org/10.1002/anie.200352224

Kleitz, F., Kim, T.-W., Ryoo, R.: Phase domain of the cubic Im$\bar{3}$m mesoporous silica in the EO106PO70EO106−butanol−H$_2$O system. Langmuir **22**(1), 440–445 (2006). https://doi.org/10.1021/la052047+

Klotz, M., Ayral, A., Guizard, C., Cot, L.: Synthesis conditions for hexagonal mesoporous silica layers. J. Mater. Chem. **10**(3), 663–669 (2000). https://doi.org/10.1039/A906181I

Kresge, C.T., Leonowicz, M.E., Roth, W.J., Vartuli, J.C.: Composition of Synthetic Porous Crystalline Material, Its Synthesis. United States of America Patent (1992a)

Kresge, C.T., Leonowicz, M.E., Roth, W.J., Vartuli, J.C.: Synthetic Mesoporous Crystaline Material. United States of America Patent (1992b)

Kresge, C.T., Leonowicz, M.E., Roth, W.J., Vartuli, J.C., Beck, J.S.: Ordered mesoporous molecular sieves synthesized by a liquid-crystal template mechanism. Nature **359**(6397), 710–712 (1992). https://doi.org/10.1038/359710a0

Kresge, C.T., Roth, W.J.: The discovery of mesoporous molecular sieves from the twenty year perspective. Chem. Soc. Rev. **42**(9), 3663–3670 (2013). https://doi.org/10.1039/C3CS60016E

Lee, J., Christopher Orilall, M., Warren, S.C., Kamperman, M., DiSalvo, F.J., Wiesner, U.: Direct access to thermally stable and highly crystalline mesoporous transition-metal oxides with uniform pores. Nat. Mater. **7**(3), 222–228 (2008). https://doi.org/10.1038/nmat2111

Lee, K.T., Oh, S.M.: Novel synthesis of porous carbons with tunable pore size by surfactant-templated sol–gel process and carbonisation. Chem. Commun. **22**, 2722–2723 (2002). https://doi.org/10.1039/B208052D

Li, B., Luo, X., Huang, J., Wang, X., Liang, Z.: One-pot synthesis of ordered mesoporous Cu-KIT-6 and its improved catalytic behavior for the epoxidation of styrene: effects of the pH value of the initial gel. Chin. J. Catal. **38**(3), 518–528 (2017). https://doi.org/10.1016/S1872-2067(17)62767-0

Li, C., Li, Q., Kaneti, Y.V., Hou, D., Yamauchi, Y., Mai, Y.: Self-assembly of block copolymers towards mesoporous materials for energy storage and conversion systems. Chem. Soc. Rev. **49**(14), 4681–4736 (2020). https://doi.org/10.1039/D0CS00021C

Li, D., Zhou, H., Honma, I.: Design and synthesis of self-ordered mesoporous nanocomposite through controlled in-situ crystallization. Nat. Mater. **3**(1), 65–72 (2004). https://doi.org/10.1038/nmat1043

Li, H., Liu, D., Zhu, X., Qu, D., Xie, Z., Li, J., Tang, H., Zheng, D., Qu, D.: Integrated 3D electrodes based on metal-nitrogen-doped graphitic ordered mesoporous carbon and carbon paper for high-loading lithium-sulfur batteries. Nano Energy **73**, 104763 (2020b). https://doi.org/10.1016/j.nanoen.2020.104763

Li, M., Ma, C., Zhu, Q.-C., Xu, S.-M., Wei, X., Wu, Y.-M., Tang, W.-P., Wang, K.-X., Chen, J.-S.: Well-ordered mesoporous Fe$_2$O$_3$/C composites as high performance anode materials for sodium-ion batteries. Dalton Trans. **46**(15), 5025–5032 (2017). https://doi.org/10.1039/C7DT00540G

Li, M., Xue, J.: Integrated synthesis of nitrogen-doped mesoporous carbon from melamine resins with superior performance in supercapacitors. J. Phys. Chem. C **118**(5), 2507–2517 (2014). https://doi.org/10.1021/jp410198r

Li, W., Liu, J., Zhao, D.: Mesoporous materials for energy conversion and storage devices. Nat. Rev. Mater. **1**(6), 16023 (2016). https://doi.org/10.1038/natrevmats.2016.23

Li, W., Yue, Q., Deng, Y., Zhao, D.: Ordered mesoporous materials based on interfacial assembly and engineering. Adv. Mater. **25**(37), 5129–5152 (2013). https://doi.org/10.1002/adma.201302184

Li, X., Forouzandeh, F., Fürstenhaupt, T., Banham, D., Feng, F., Ye, S., Kwok, D.Y., Birss, V.: New insights into the surface properties of hard-templated ordered mesoporous carbons. Carbon **127**, 707–717 (2018). https://doi.org/10.1016/j.carbon.2017.11.049

Li, Z., Yan, W., Dai, S.: A novel vesicular carbon synthesized using amphiphilic carbonaceous material and micelle templating approach. Carbon **42**(4), 767–770 (2004). https://doi.org/10.1016/j.carbon.2004.01.044

Liang, C., Dai, S.: Synthesis of mesoporous carbon materials via enhanced hydrogen-bonding interaction. J. Am. Chem. Soc. **128**(16), 5316–5317 (2006). https://doi.org/10.1021/ja060242k

Liang, J., Liang, Z., Zou, R., Zhao, Y.: Heterogeneous catalysis in zeolites, mesoporous silica, and metal-organic frameworks. Adv. Mater. **29**(30), 1701139 (2017). https://doi.org/10.1002/adma.201701139

Libbrecht, W., Verberckmoes, A., Thybaut, J.W., Van Der Voort, P., De Clercq, J.: Soft templated mesoporous carbons: Tuning the porosity for the adsorption of large organic pollutants. Carbon **116**, 528–546 (2017). https://doi.org/10.1016/j.carbon.2017.02.016

Liu, L., Wang, F.-Y., Shao, G.-S., Ma, T.-Y., Yuan, Z.-Y.: Synthesis of ultra-large mesoporous carbons from triblock copolymers and phloroglucinol/formaldehyde polymer. Carbon **48**(9), 2660–2664 (2010). https://doi.org/10.1016/j.carbon.2010.03.035

Liu, N., Assink, R.A., Smarsly, B., Brinker, C.J.: Synthesis and characterization of highly ordered functional mesoporous silica thin films with positively chargeable-NH2 groups. Chem. Commun. **10**, 1146–1147 (2003). https://doi.org/10.1039/B301910A

Liu, P., Moudrakovski, I.L., Liu, J., Sayari, A.: Mesostructured vanadium oxide containing dodecylamine. Chem. Mater. **9**(11), 2513–2520 (1997). https://doi.org/10.1021/cm970067u

Liu, S., Huang, Z., Wang, R.: A carbon foam with a bimodal micro–mesoporous structure prepared from larch sawdust for the gas-phase toluene adsorption. Mater. Res. Bull. **48**(7), 2437–2441 (2013). https://doi.org/10.1016/j.materresbull.2013.02.069

Liu, X., Li, W., Zou, S.: Cobalt and nitrogen-codoped ordered mesoporous carbon as highly efficient bifunctional catalysts for oxygen reduction and hydrogen evolution reactions. J. Mater. Chem. A **6**(35), 17067–17074 (2018). https://doi.org/10.1039/C8TA06864J

Liu, Y., Che, R., Chen, G., Fan, J., Sun, Z., Wu, Z., Wang, M., Li, B., Wei, J., Wei, Y., Wang, G., Guan, G., Elzatahry, A.A., Bagabas, A.A., Al-Enizi, A.M., Deng, Y., Peng, H., Zhao, D.: Radially oriented mesoporous TiO$_2$ microspheres with single-crystal–like anatase walls for high-efficiency optoelectronic devices. Sci. Adv. **1**(4), e1500166 (2015). https://doi.org/10.1126/sciadv.1500166

Liu, Y., Wang, Z., Teng, W., Zhu, H., Wang, J., Elzatahry, A.A., Al-Dahyan, D., Li, W., Deng, Y., Zhao, D.: A template-catalyzed in situ polymerization and co-assembly strategy for rich nitrogen-doped mesoporous carbon. J. Mater. Chem. A **6**(7), 3162–3170 (2018). https://doi.org/10.1039/C7TA10106F

Liu, Y., Zhang, W., Pinnavaia, T.J.: Steam-stable aluminosilicate mesostructures assembled from zeolite type Y seeds. J. Am. Chem. Soc. **122**(36), 8791–8792 (2000). https://doi.org/10.1021/ja001615z

Liu, Y., Zhang, W., Pinnavaia, T.J.: Steam-stable MSU-S Aluminosilicate mesostructures assembled from zeolite ZSM-5 and zeolite beta seeds. Angew. Chem. Int. Ed. **40**(7), 1255–1258 (2001). https://doi.org/10.1002/1521-3773(20010401)40:7%3c1255::AID-ANIE1255%3e3.0.CO;2-U

Lu, A.-H., Zhao, D., Wan, Y.: Principles of Nanocasting. In: Lu, A.-H., Zhao, D. (eds.) Nanocasting: A Versatile Strategy for Creating Nanostructured Porous Materials, pp. 1–44. The Royal Society of Chemistry, London (2009)

Lu, A.H., Schüth, F.: Nanocasting: a versatile strategy for creating nanostructured porous materials. Adv. Mater. **18**(14), 1793–1805 (2006). https://doi.org/10.1002/adma.200600148

Lu, Y., Ganguli, R., Drewien, C.A., Anderson, M.T., Brinker, C.J., Gong, W., Guo, Y., Soyez, H., Dunn, B., Huang, M.H., Zink, J.I.: Continuous formation of supported cubic and hexagonal mesoporous films by sol–gel dip-coating. Nature **389**(6649), 364–368 (1997). https://doi.org/10.1038/38699

Ma, J., Ren, Y., Zhou, X., Liu, L., Zhu, Y., Cheng, X., Xu, P., Li, X., Deng, Y., Zhao, D.: Pt Nanoparticles sensitized ordered mesoporous wo3 semiconductor: gas sensing performance and mechanism study. Adv. Func. Mater. **28**(6), 1705268 (2018). https://doi.org/10.1002/adfm.201705268

Ma, N., Zhang, Y., Yang, J., Huang, Y.: Facile preparation of hollow-structured mesoporous silica spheres with large and ordered mesochannels. Int. J. Appl. Ceram. Technol. **14**(5), 915–920 (2017). https://doi.org/10.1111/ijac.12728

Ma, T.-Y., Li, H., Deng, Q.-F., Liu, L., Ren, T.-Z., Yuan, Z.-Y.: Ordered mesoporous metal-organic frameworks consisting of metal disulfonates. Chem. Mater. **24**(12), 2253–2255 (2012). https://doi.org/10.1021/cm301256r

Ma, T.-Y., Liu, L., Yuan, Z.-Y.: Direct synthesis of ordered mesoporous carbons. Chem. Soc. Rev. **42**(9), 3977–4003 (2013). https://doi.org/10.1039/C2CS35301F

Macquarrie, D.J.: Direct preparation of organically modified MCM-type materials. Preparation and characterisation of aminopropyl–MCM and 2-cyanoethyl–MCM. Chem. Commun. **16**, 1961–1962 (1996). https://doi.org/10.1039/CC9960001961

Marszewski, M., Marszewska, J., Pylypenko, S., Jaroniec, M.: Synthesis of porous crystalline doped titania photocatalysts using modified precursor strategy. Chem. Mater. **28**(21), 7878–7888 (2016). https://doi.org/10.1021/acs.chemmater.6b03429

McCusker, L.B., Liebau, F., Engelhardt, G.: Nomenclature of structural and compositional characteristics of ordered microporous and mesoporous materials with inorganic hosts (IUPAC Recommendations 2001). Pure Appl. Chem. **73**(2), 381–394 (2001). https://doi.org/10.1351/pac200173020381

Melde, B.J., Holland, B.T., Blanford, C.F., Stein, A.: Mesoporous sieves with unified hybrid inorganic/organic frameworks. Chem. Mater. **11**(11), 3302–3308 (1999). https://doi.org/10.1021/cm9903935

Meng, Y., Gu, D., Zhang, F., Shi, Y., Cheng, L., Feng, D., Wu, Z., Chen, Z., Wan, Y., Stein, A., Zhao, D.: A family of highly ordered mesoporous polymer resin and carbon structures from organic−organic self-assembly. Chem. Mater. **18**(18), 4447–4464 (2006). https://doi.org/10.1021/cm060921u

Meng, Y., Gu, D., Zhang, F., Shi, Y., Yang, H., Li, Z., Yu, C., Tu, B., Zhao, D.: Ordered mesoporous polymers and homologous carbon frameworks: amphiphilic surfactant templating and direct transformation. Angew. Chem. Int. Ed. **44**(43), 7053–7059 (2005). https://doi.org/10.1002/anie.200501561

Moriguchi, I., Ozono, A., Mikuriya, K., Teraoka, Y., Kagawa, S., Kodama, M.: Micelle-templated mesophases of phenol-formaldehyde polymer. Chem. Lett. **28**(11), 1171–1172 (1999). https://doi.org/10.1246/cl.1999.1171

Morishita, T., Tsumura, T., Toyoda, M., Przepiórski, J., Morawski, A.W., Konno, H., Inagaki, M.: A review of the control of pore structure in MgO-templated nanoporous carbons. Carbon **48**(10), 2690–2707 (2010). https://doi.org/10.1016/j.carbon.2010.03.064

Musso, G.E., Bottinelli, E., Celi, L., Magnacca, G., Berlier, G.: Influence of surface functionalization on the hydrophilic character of mesoporous silica nanoparticles. Phys. Chem. Chem. Phys. **17**(21), 13882–13894 (2015). https://doi.org/10.1039/C5CP00552C

Muylaert, I., Verberckmoes, A., De Decker, J., Van Der Voort, P.: Ordered mesoporous phenolic resins: Highly versatile and ultra stable support materials. Adv. Coll. Interface. Sci. **175**, 39–51 (2012). https://doi.org/10.1016/j.cis.2012.03.007

Nelson, K.M., Mahurin, S.M., Mayes, R.T., Williamson, B., Teague, C.M., Binder, A.J., Baggetto, L., Veith, G.M., Dai, S.: Preparation and CO_2 adsorption properties of soft-templated mesoporous carbons derived from chestnut tannin precursors. Microporous Mesoporous Mater. **222**, 94–103 (2016). https://doi.org/10.1016/j.micromeso.2015.09.050

Nie, S., Yang, S., Zhang, P.: Solvent-free synthesis of mesoporous platinum-aluminum oxide via mechanochemistry: toward selective hydrogenation of nitrobenzene to aniline. Chem. Eng. Sci. **220**, 115619 (2020). https://doi.org/10.1016/j.ces.2020.115619

Nishiyama, N., Zheng, T., Yamane, Y., Egashira, Y., Ueyama, K.: Microporous carbons prepared from cationic surfactant–resorcinol/formaldehyde composites. Carbon **43**(2), 269–274 (2005). https://doi.org/10.1016/j.carbon.2004.09.009

Ogawa, M.: Formation of novel oriented transparent films of layered silica-surfactant nanocomposites. J. Am. Chem. Soc. **116**(17), 7941–7942 (1994). https://doi.org/10.1021/ja00096a079

Pal, N., Bhaumik, A.: Soft templating strategies for the synthesis of mesoporous materials: Inorganic, organic–inorganic hybrid and purely organic solids. Adv. Coll. Interface. Sci. **189–190**, 21–41 (2013). https://doi.org/10.1016/j.cis.2012.12.002

Park, D.-H., Nishiyama, N., Egashira, Y., Ueyama, K.: Enhancement of hydrothermal stability and hydrophobicity of a silica MCM-48 membrane by silylation. Ind. Eng. Chem. Res. **40**(26), 6105–6110 (2001). https://doi.org/10.1021/ie0103761

Peng, L., Yang, S., Jawahery, S., Moosavi, S.M., Huckaba, A.J., Asgari, M., Oveisi, E., Nazeeruddin, M.K., Smit, B., Queen, W.L.: Preserving porosity of mesoporous metal-organic frameworks through the introduction of polymer guests. J. Am. Chem. Soc. **141**(31), 12397–12405 (2019). https://doi.org/10.1021/jacs.9b05967

Pham, H.N., Anderson, A.E., Johnson, R.L., Schmidt-Rohr, K., Datye, A.K.: Improved hydrothermal stability of mesoporous oxides for reactions in the aqueous phase. Angew. Chem. Int. Ed. **51**(52), 13163–13167 (2012). https://doi.org/10.1002/anie.201206675

Poyraz, A.S., Kuo, C.-H., Biswas, S., King'ondu, C.K., Suib, S.L.: A general approach to crystalline and monomodal pore size mesoporous materials. Nat. Commun. **4**(1), 2952 (2013). https://doi.org/10.1038/ncomms3952

Poyraz, A.S., Kuo, C.-H., Kim, E., Meng, Y., Seraji, M.S., Suib, S.L.: Tungsten-promoted mesoporous group 4 (Ti, Zr, and Hf) transition-metal oxides for room-temperature solvent-free acetalization and ketalization reactions. Chem. Mater. **26**(9), 2803–2813 (2014). https://doi.org/10.1021/cm501216c

Qian, X., Ren, M., Fang, M., Kan, M., Yue, D., Bian, Z., Li, H., Jia, J., Zhao, Y.: Hydrophilic mesoporous carbon as iron(III)/(II) electron shuttle for visible light enhanced Fenton-like degradation of organic pollutants. Appl. Catal. B **231**, 108–114 (2018). https://doi.org/10.1016/j.apcatb.2018.03.016

Qiu, P., Zhao, T., Fang, Y., Zhu, G., Zhu, X., Yang, J., Li, X., Jiang, W., Wang, L., Luo, W.: Pushing the limit of ordered mesoporous materials via 2D self-assembly for energy conversion and storage. Adv. Func. Mater. **31**(7), 2007496 (2021). https://doi.org/10.1002/adfm.202007496

Rajendran, A., Rajendiran, M., Yang, Z.-F., Fan, H.-X., Cui, T.-Y., Zhang, Y.-G., Li, W.-Y.: Functionalized silicas for metal-free and metal-based catalytic applications: a review in perspective of green chemistry. Chem. Rec. **20**(6), 513–540 (2020). https://doi.org/10.1002/tcr.201900056

Ren, Y., Ma, Z., Bruce, P.G.: Ordered mesoporous metal oxides: synthesis and applications. Chem. Soc. Rev. **41**(14), 4909–4927 (2012). https://doi.org/10.1039/C2CS35086F

Robbins, S.W., Beaucage, P.A., Sai, H., Tan, K.W., Werner, J.G., Sethna, J.P., DiSalvo, F.J., Gruner, S.M., Van Dover, R.B., Wiesner, U.: Block copolymer self-assembly–directed synthesis of mesoporous gyroidal superconductors. Sci. Adv. **2**(1), e1501119 (2016). https://doi.org/10.1126/sciadv.1501119

Rosenholm, J.M., Lindén, M.: Wet-chemical analysis of surface concentration of accessible groups on different amino-functionalized mesoporous SBA-15 silicas. Chem. Mater. **19**(20), 5023–5034 (2007). https://doi.org/10.1021/cm071289n

Rouquerol, F., Rouquerol, J., Sing, K.: Assessment of mesoporosity (Chap. 7). In: Rouquerol, F., Rouquerol, J., Sing, K. (eds.) Adsorption by powders and porous solids, pp. 191–217. Academic Press, London (1999)

Ryoo, R., Joo, S.H., Jun, S.: Synthesis of highly ordered carbon molecular sieves via template-mediated structural transformation. J. Phys. Chem. B **103**(37), 7743–7746 (1999). https://doi.org/10.1021/jp991673a

Ryoo, R., Joo, S.H., Kruk, M., Jaroniec, M.: Ordered mesoporous carbons. Adv. Mater. **13**(9), 677–681 (2001). https://doi.org/10.1002/1521-4095(200105)13:9%3c677::AID-ADMA677%3e3.0.CO;2-C

Ryoo, R., Jun, S.: Improvement of hydrothermal stability of MCM-41 using salt effects during the crystallization process. J. Phys. Chem. B **101**(3), 317–320 (1997). https://doi.org/10.1021/jp962500d

Sanchez-Sanchez, A., Izquierdo, M.T., Ghanbaja, J., Medjahdi, G., Mathieu, S., Celzard, A., Fierro, V.: Excellent electrochemical performances of nanocast ordered mesoporous carbons based on tannin-related polyphenols as supercapacitor electrodes. J. Power Sources **344**, 15–24 (2017). https://doi.org/10.1016/j.jpowsour.2017.01.099

Schlienger, S., Graff, A.-L., Celzard, A., Parmentier, J.: Direct synthesis of ordered mesoporous polymer and carbon materials by a biosourced precursor. Green Chem. **14**(2), 313–316 (2012). https://doi.org/10.1039/C2GC16160E

Schüth, F.: Endo- and exotemplating to create high-surface-area inorganic materials. Angew. Chem. Int. Ed. **42**(31), 3604–3622 (2003). https://doi.org/10.1002/anie.200300593

Schwieger, W., Machoke, A.G., Weissenberger, T., Inayat, A., Selvam, T., Klumpp, M., Inayat, A.: Hierarchy concepts: classification and preparation strategies for zeolite containing materials with hierarchical porosity. Chem. Soc. Rev. **45**(12), 3353–3376 (2016). https://doi.org/10.1039/C5CS00599J

Sen, T., Barisik, M.: Pore connectivity effects on the internal surface electric charge of mesoporous silica. Colloid Polym. Sci. **297**(10), 1365–1373 (2019). https://doi.org/10.1007/s00396-019-04555-w

Serrano, D.P., García, R.A., Vicente, G., Linares, M., Procházková, D., Čejka, J.: Acidic and catalytic properties of hierarchical zeolites and hybrid ordered mesoporous materials assembled from MFI protozeolitic units. J. Catal. **279**(2), 366–380 (2011). https://doi.org/10.1016/j.jcat.2011.02.007

Setoguchi, Y.M., Teraoka, Y., Moriguchi, I., Kagawa, S., Tomonaga, N., Yasutake, A., Izumi, J.: Rapid room temperature synthesis of hexagonal mesoporous silica using inorganic silicate sources and cationic surfactants under highly acidic conditions. J. Porous Mater. **4**(2), 129–134 (1997). https://doi.org/10.1023/A:1009684801918

Shukrun Farrell, E., Schilt, Y., Moshkovitz, M.Y., Levi-Kalisman, Y., Raviv, U., Magdassi, S.: 3D printing of ordered mesoporous silica complex structures. Nano Lett. **20**(9), 6598–6605 (2020). https://doi.org/10.1021/acs.nanolett.0c02364

Silva, R., Voiry, D., Chhowalla, M., Asefa, T.: Efficient metal-free electrocatalysts for oxygen reduction: polyaniline-derived n- and o-doped mesoporous carbons. J. Am. Chem. Soc. **135**(21), 7823–7826 (2013). https://doi.org/10.1021/ja402450a

Sing, K.S.W.: Reporting physisorption data for gas/solid systems with special reference to the determination of surface area and porosity (Provisional). Pure Appl. Chem. **54**(11), 2201–2218 (1982). https://doi.org/10.1351/pac198254112201

Smeulders, G., Meynen, V., Silvestre-Albero, A., Houthoofd, K., Mertens, M., Silvestre-Albero, J., Martens, J.A., Cool, P.: The impact of framework organic functional groups on the hydrophobicity and overall stability of mesoporous silica materials. Mater. Chem. Phys. **132**(2), 1077–1088 (2012). https://doi.org/10.1016/j.matchemphys.2011.12.072

Sobrinho, R.A.L., Andrade, G.R.S., Costa, L.P., de Souza, M.J.B., de Souza, A.M.G.P., Gimenez, I.F.: Ordered micro-mesoporous carbon from palm oil cooking waste via nanocasting in HZSM-5/SBA-15 composite: preparation and adsorption studies. J. Hazard. Mater. **362**, 53–61 (2019). https://doi.org/10.1016/j.jhazmat.2018.08.097

Soler-Illia, G.J.d.A.A., Sanchez, C., Lebeau, B., Patarin, J.: Chemical strategies to design textured materials: from microporous and mesoporous oxides to nanonetworks and hierarchical structures. Chem. Rev. **102**(11), 4093–4138 (2002). https://doi.org/10.1021/cr0200062

Song, L., Zhang, J., Sun, L., Xu, F., Li, F., Zhang, H., Si, X., Jiao, C., Li, Z., Liu, S., Liu, Y., Zhou, H., Sun, D., Du, Y., Cao, Z., Gabelica, Z.: Mesoporous metal–organic frameworks: design and applications. Energy Environ. Sci. **5**(6), 7508–7520 (2012). https://doi.org/10.1039/C2EE03517K

Song, W., Poyraz, A.S., Meng, Y., Ren, Z., Chen, S.-Y., Suib, S.L.: Mesoporous Co_3O_4 with controlled porosity: inverse micelle synthesis and high-performance catalytic CO oxidation at − 60 °C. Chem. Mater. **26**(15), 4629–4639 (2014). https://doi.org/10.1021/cm502106v

Song, Y., Ye, G., Wu, F., Wang, Z., Liu, S., Kopeć, M., Wang, Z., Chen, J., Wang, J., Matyjaszewski, K.: Bioinspired polydopamine (PDA) chemistry meets ordered mesoporous carbons (OMCs): a benign surface modification strategy for versatile functionalization. Chem. Mater. **28**(14), 5013–5021 (2016). https://doi.org/10.1021/acs.chemmater.6b01729

Stefik, M., Wang, S., Hovden, R., Sai, H., Tate, M.W., Muller, D.A., Steiner, U., Gruner, S.M., Wiesner, U.: Networked and chiral nanocomposites from ABC triblock terpolymer coassembly

with transition metal oxide nanoparticles. J. Mater. Chem. **22**(3), 1078–1087 (2012). https://doi.org/10.1039/C1JM14113A

Su, M., Li, W., Ma, Q., Zhu, B.: Production of jet fuel intermediates from biomass platform compounds via aldol condensation reaction over iron-modified MCM-41 lewis acid zeolite. J. Bioresour. Bioprod. **5**(4), 256–265 (2020). https://doi.org/10.1016/j.jobab.2020.10.004

Sun, T., Shan, N., Xu, L., Wang, J., Chen, J., Zakhidov, A.A., Baughman, R.H.: General synthesis of 3D ordered macro-/mesoporous materials by templating mesoporous silica confined in Opals. Chem. Mater. **30**(5), 1617–1624 (2018). https://doi.org/10.1021/acs.chemmater.7b04829

Sun, X., Hu, X., Wang, Y., Xiong, R., Li, X., Liu, J., Ji, H., Li, X., Cai, S., Zheng, C.: enhanced gas-sensing performance of fe-doped ordered mesoporous nio with long-range periodicity. J. Phys. Chem. C **119**(6), 3228–3237 (2015). https://doi.org/10.1021/jp5124585

Szczęśniak, B., Choma, J., Jaroniec, M.: Major advances in the development of ordered mesoporous materials. Chem. Commun. **56**(57), 7836–7848 (2020). https://doi.org/10.1039/D0CC02840A

Szczęśniak, B., Choma, J., Jaroniec, M.: Recent advances in mechanochemical synthesis of mesoporous metal oxides. Mater. Adv. **2**(8), 2510–2523 (2021). https://doi.org/10.1039/D1MA00073J

Taguchi, A., Schüth, F.: Ordered mesoporous materials in catalysis. Microporous Mesoporous Mater. **77**(1), 1–45 (2005). https://doi.org/10.1016/j.micromeso.2004.06.030

Thommes, M., Kaneko, K., Neimark, A.V., Olivier, J.P., Rodriguez-Reinoso, F., Rouquerol, J., Sing, K.S.W.: Physisorption of gases, with special reference to the evaluation of surface area and pore size distribution (IUPAC Technical Report). Pure Appl. Chem. **87**(9–10), 1051–1069 (2015). https://doi.org/10.1515/pac-2014-1117

Tian, B., Liu, X., Yu, C., Gao, F., Luo, Q., Xie, S., Tu, B., Zhao, D.: Microwave assisted template removal of siliceous porous materials. Chem. Commun. **11**, 1186–1187 (2002). https://doi.org/10.1039/B202180C

Trivedi, M., Peng, F., Xia, X., Sepulveda-Medina, P.I., Vogt, B.D.: Control of Pore Size in Ordered Mesoporous Carbon-Silica by Hansen Solubility Parameters of Swelling Agent. Langmuir **35**(43), 14049–14059 (2019). https://doi.org/10.1021/acs.langmuir.9b02568

Tüysüz, H., Schüth, F.: Ordered mesoporous materials as catalysts (Chap. 2). In: Gates, B.C., Jentoft, F.C. (eds.) Advances in Catalysis, vol. 55. pp. 127–239. Academic Press, Amsterdam (2012)

Vallet-Regí, M.: Ordered mesoporous materials in the context of drug delivery systems and bone tissue engineering. Chem. Eur. J. **12**(23), 5934–5943 (2006). https://doi.org/10.1002/chem.200600226

van Grieken, R., Calleja, G., Stucky, G.D., Melero, J.A., García, R.A., Iglesias, J.: Supercritical fluid extraction of a nonionic surfactant template from SBA-15 materials and consequences on the porous structure. Langmuir **19**(9), 3966–3973 (2003). https://doi.org/10.1021/la026970c

Verma, D., Kumar, R., Rana, B.S., Sinha, A.K.: Aviation fuel production from lipids by a single-step route using hierarchical mesoporous zeolites. Energy Environ. Sci. **4**(5), 1667–1671 (2011). https://doi.org/10.1039/C0EE00744G

Verma, P., Kuwahara, Y., Mori, K., Raja, R., Yamashita, H.: Functionalized mesoporous SBA-15 silica: recent trends and catalytic applications. Nanoscale **12**(21), 11333–11363 (2020). https://doi.org/10.1039/D0NR00732C

Vinu, A., Murugesan, V., Hartmann, M.: Pore size engineering and mechanical stability of the cubic mesoporous molecular sieve SBA-1. Chem. Mater. **15**(6), 1385–1393 (2003). https://doi.org/10.1021/cm0213523

Vivian, A., Soumoy, L., Fusaro, L., Fiorilli, S., Debecker, D.P., Aprile, C.: Surface-functionalized mesoporous gallosilicate catalysts for the efficient and sustainable upgrading of glycerol to solketal. Green Chem. **23**(1), 354–366 (2021). https://doi.org/10.1039/D0GC02562C

Wagner, T., Haffer, S., Weinberger, C., Klaus, D., Tiemann, M.: Mesoporous materials as gas sensors. Chem. Soc. Rev. **42**(9), 4036–4053 (2013). https://doi.org/10.1039/C2CS35379B

Walcarius, A.: Mesoporous materials and electrochemistry. Chem. Soc. Rev. **42**(9), 4098–4140 (2013). https://doi.org/10.1039/C2CS35322A

Wan, K., Long, G.-F., Liu, M.-Y., Du, L., Liang, Z.-X., Tsiakaras, P.: Nitrogen-doped ordered mesoporous carbon: synthesis and active sites for electrocatalysis of oxygen reduction reaction. Appl. Catal. B **165**, 566–571 (2015). https://doi.org/10.1016/j.apcatb.2014.10.054

Wan, Y., Shi, Y., Zhao, D.: Supramolecular aggregates as templates: ordered mesoporous polymers and carbons. Chem. Mater. **20**(3), 932–945 (2008). https://doi.org/10.1021/cm7024125

Wan, Y., Zhao: On the controllable soft-templating approach to mesoporous silicates. Chem. Rev. **107**(7), 2821–2860 (2007). https://doi.org/10.1021/cr068020s

Wang, H., Pinnavaia, T.J.: MFI zeolite with small and uniform intracrystal mesopores. Angew. Chem. Int. Ed. **45**(45), 7603–7606 (2006). https://doi.org/10.1002/anie.200602595

Wang, J.-G., Liu, H., Sun, H., Hua, W., Wang, H., Liu, X., Wei, B.: One-pot synthesis of nitrogen-doped ordered mesoporous carbon spheres for high-rate and long-cycle life supercapacitors. Carbon **127**, 85–92 (2018). https://doi.org/10.1016/j.carbon.2017.10.084

Wang, K., Lin, Y., Morris, M.A., Holmes, J.D.: Preparation of MCM-48 materials with enhanced hydrothermal stability. J. Mater. Chem. **16**(41), 4051–4057 (2006). https://doi.org/10.1039/B607599A

Wang, X., Liang, C., Dai, S.: Facile synthesis of ordered mesoporous carbons with high thermal stability by self-assembly of resorcinol−formaldehyde and block copolymers under highly acidic conditions. Langmuir **24**(14), 7500–7505 (2008). https://doi.org/10.1021/la800529v

Wang, Y.-Q., Zheng, C.-M., Liu, Z.-J., Guo, M.-L.: Fabrication of highly ordered mesoporous silica with the assistance of phosphate. New J. Chem. **39**(10), 7763–7767 (2015). https://doi.org/10.1039/C5NJ01632K

Wei, J., Ren, Y., Luo, W., Sun, Z., Cheng, X., Li, Y., Deng, Y., Elzatahry, A.A., Al-Dahyan, D., Zhao, D.: Ordered mesoporous alumina with ultra-large pores as an efficient absorbent for selective bioenrichment. Chem. Mater. **29**(5), 2211–2217 (2017). https://doi.org/10.1021/acs.chemmater.6b05032

Wei, J., Sun, Z., Luo, W., Li, Y., Elzatahry, A.A., Al-Enizi, A.M., Deng, Y., Zhao, D.: New Insight into the synthesis of large-pore ordered mesoporous materials. J. Am. Chem. Soc. **139**(5), 1706–1713 (2017). https://doi.org/10.1021/jacs.6b11411

Wei, J., Wang, H., Deng, Y., Sun, Z., Shi, L., Tu, B., Luqman, M., Zhao, D.: Solvent Evaporation induced aggregating assembly approach to three-dimensional ordered mesoporous silica with ultralarge accessible mesopores. J. Am. Chem. Soc. **133**(50), 20369–20377 (2011). https://doi.org/10.1021/ja207525e

Wei, Y., Parmentier, T.E., de Jong, K.P., Zečević, J.: Tailoring and visualizing the pore architecture of hierarchical zeolites. Chem. Soc. Rev. **44**(20), 7234–7261 (2015). https://doi.org/10.1039/C5CS00155B

Weller, T., Deilmann, L., Timm, J., Dörr, T.S., Beaucage, P.A., Cherevan, A.S., Wiesner, U.B., Eder, D., Marschall, R.: A crystalline and 3D periodically ordered mesoporous quaternary semiconductor for photocatalytic hydrogen generation. Nanoscale **10**(7), 3225–3234 (2018). https://doi.org/10.1039/C7NR09251B

Wong, M.S., Antonelli, D.M., Ying, J.Y.: Synthesis and characterization of phosphated mesoporous zirconium oxide. Nanostruct. Mater. **9**(1), 165–168 (1997). https://doi.org/10.1016/S0965-9773(97)00044-5

Wu, Z., Zhao, D.: Ordered mesoporous materials as adsorbents. Chem. Commun. **47**(12), 3332–3338 (2011). https://doi.org/10.1039/C0CC04909C

Xiao, X., Liu, L., Ma, J., Ren, Y., Cheng, X., Zhu, Y., Zhao, D., Elzatahry, A.A., Alghamdi, A., Deng, Y.: Ordered mesoporous tin oxide semiconductors with large pores and crystallized walls for high-performance gas sensing. ACS Appl. Mater. Interfaces. **10**(2), 1871–1880 (2018). https://doi.org/10.1021/acsami.7b18830

Xiao, X., Zhou, X., Ma, J., Zhu, Y., Cheng, X., Luo, W., Deng, Y.: Rational synthesis and gas sensing performance of ordered mesoporous semiconducting WO_3/NiO composites. ACS Appl. Mater. Interfaces. **11**(29), 26268–26276 (2019). https://doi.org/10.1021/acsami.9b08128

Xiong, H., Zhou, H., Sun, G., Liu, Z., Zhang, L., Zhang, L., Du, F., Qiao, Z.-A., Dai, S.: Solvent-free self-assembly for scalable preparation of highly crystalline mesoporous metal oxides. Angew. Chem. Int. Ed. **59**(27), 11053–11060 (2020). https://doi.org/10.1002/anie.202002051

Xu, D., Ma, Y., Jing, Z., Han, L., Singh, B., Feng, J., Shen, X., Cao, F., Oleynikov, P., Sun, H., Terasaki, O., Che, S.: π–π interaction of aromatic groups in amphiphilic molecules directing for single-crystalline mesostructured zeolite nanosheets. Nat. Commun. **5**(1), 4262 (2014). https://doi.org/10.1038/ncomms5262

Xu, X., Megarajan, S.K., Zhang, Y., Jiang, H.: Ordered mesoporous alumina and their composites based on evaporation induced self-assembly for adsorption and catalysis. Chem. Mater. **32**(1), 3–26 (2020). https://doi.org/10.1021/acs.chemmater.9b03873

Xuan, W., Zhu, C., Liu, Y., Cui, Y.: Mesoporous metal–organic framework materials. Chem. Soc. Rev. **41**(5), 1677–1695 (2012). https://doi.org/10.1039/C1CS15196G

Yan, R., Heil, T., Presser, V., Walczak, R., Antonietti, M., Oschatz, M.: Ordered mesoporous carbons with high micropore content and tunable structure prepared by combined hard and salt templating as electrode materials in electric double-layer capacitors. Adv. Sustain. Syst. **2**(2), 1700128 (2018). https://doi.org/10.1002/adsu.201700128

Yanagisawa, T., Shimizu, T., Kuroda, K., Kato, C.: The preparation of alkyltriinethylaininonium-kaneinite complexes and their conversion to microporous materials. Bull. Chem. Soc. Jpn. **63**(4), 988–992 (1990). https://doi.org/10.1246/bcsj.63.988

Yang, D.-S., Bhattacharjya, D., Inamdar, S., Park, J., Yu, J.-S.: Phosphorus-doped ordered mesoporous carbons with different lengths as efficient metal-free electrocatalysts for oxygen reduction reaction in alkaline media. J. Am. Chem. Soc. **134**(39), 16127–16130 (2012). https://doi.org/10.1021/ja306376s

Yang, Q., Wang, Y., Liu, J., Liu, J., Gao, Y., Sun, P., Zheng, J., Zhang, T., Wang, Y., Lu, G.: Enhanced sensing response towards NO2 based on ordered mesoporous Zr-doped In_2O_3 with low operating temperature. Sens. Actuators, B Chem. **241**, 806–813 (2017). https://doi.org/10.1016/j.snb.2016.09.145

Ying, J.Y., Mehnert, C.P., Wong, M.S.: Synthesis and applications of supramolecular-templated mesoporous materials. Angew. Chem. Int. Ed. **38**(1–2), 56–77 (1999). https://doi.org/10.1002/(SICI)1521-3773(19990115)38:1/2%3c56::AID-ANIE56%3e3.0.CO;2-E

Yu, J., Shi, J.-L., Chen, H.-R., Yan, J.-N., Yan, D.-S.: Effect of inorganic salt addition during synthesis on pore structure and hydrothermal stability of mesoporous silica. Microporous Mesoporous Mater. **46**(2), 153–162 (2001). https://doi.org/10.1016/S1387-1811(01)00269-4

Yuan, S., Bo, X., Guo, L.: In-situ growth of iron-based metal-organic framework crystal on ordered mesoporous carbon for efficient electrocatalysis of p-nitrotoluene and hydrazine. Anal. Chim. Acta **1024**, 73–83 (2018). https://doi.org/10.1016/j.aca.2018.03.064

Zhai, Y., Dou, Y., Zhao, D., Fulvio, P.F., Mayes, R.T., Dai, S.: Carbon materials for chemical capacitive energy storage. Adv. Mater. **23**(42), 4828–4850 (2011). https://doi.org/10.1002/adma.201100984

Zhang, F., Meng, Y., Gu, D., Yan, Chen, Z., Tu, B., Zhao, D.: An aqueous cooperative assembly route to synthesize ordered mesoporous carbons with controlled structures and morphology. Chem. Mater. **18**(22), 5279–5288 (2006). https://doi.org/10.1021/cm061400+

Zhang, F., Meng, Y., Gu, D., Yan, Yu, C., Tu, B., Zhao, D.: A facile aqueous route to synthesize highly ordered mesoporous polymers and carbon frameworks with Ia3̄d bicontinuous cubic structure. J. Am. Chem. Soc. **127**(39), 13508–13509 (2005a). https://doi.org/10.1021/ja0545721

Zhang, F., Yan, Y., Yang, H., Meng, Y., Yu, C., Tu, B., Zhao, D.: Understanding effect of wall structure on the hydrothermal stability of mesostructured silica SBA-15. J. Phys. Chem. B **109**(18), 8723–8732 (2005). https://doi.org/10.1021/jp044632+

Zhang, J., Yi, X.-B., Ju, W., Fan, H.-L., Wang, Q.-C., Liu, B.-X., Liu, S.: Hydrophilic modification of ordered mesoporous carbons for supercapacitor via electrochemically induced surface-initiated atom-transfer radical polymerization. Electrochem. Commun. **74**, 19–23 (2017). https://doi.org/10.1016/j.elecom.2016.09.011

Zhang, L., Jin, L., Liu, B., He, J.: Templated growth of crystalline mesoporous materials: from soft/hard templates to colloidal templates. Front. Chem. **7**, 22 (2019)

Zhang, R., Tu, B., Zhao, D.: Synthesis of highly stable and crystalline mesoporous anatase by using a simple surfactant sulfuric acid carbonization method. Chem. Eur. J. **16**(33), 9977–9981 (2010). https://doi.org/10.1002/chem.201001241

Zhang, X., Wu, W., Wang, J., Liu, C.: Effects of sol aging on mesoporous silica thin films organization. Thin Solid Films **515**(23), 8376–8380 (2007). https://doi.org/10.1016/j.tsf.2007.04.041

Zhang, Y., Che, S.: π–π interactions between aromatic groups in amphiphilic molecules: directing hierarchical growth of porous zeolites. Angew. Chem. Int. Ed. **59**(1), 50–60 (2020). https://doi.org/10.1002/anie.201903364

Zhang, Z., Yang, S., Hu, X., Xu, H., Peng, H., Liu, M., Thapaliya, B.P., Jie, K., Zhao, J., Liu, J., Chen, H., Leng, Y., Lu, X., Fu, J., Zhang, P., Dai, S.: Mechanochemical nonhydrolytic sol–gel-strategy for the production of mesoporous multimetallic oxides. Chem. Mater. **31**(15), 5529–5536 (2019). https://doi.org/10.1021/acs.chemmater.9b01244

Zhao, D., Feng, J., Huo, Q., Melosh, N., Fredrickson, G.H., Chmelka, B.F., Stucky, G.D.: Triblock copolymer syntheses of mesoporous silica with periodic 50 to 300 Angstrom pores. Science **279**(5350), 548 (1998). https://doi.org/10.1126/science.279.5350.548

Zhao, D., Huo, Q., Feng, J., Chmelka, B.F., Stucky, G.D.: Nonionic triblock and star diblock copolymer and oligomeric surfactant syntheses of highly ordered, hydrothermally stable, mesoporous silica structures. J. Am. Chem. Soc. **120**(24), 6024–6036 (1998). https://doi.org/10.1021/ja974025i

Zhao, D., Wan, Y., Wuzong, Z.: Synthesis approach of mesoporous molecular sieves. ordered mesoporous materials. Wiley-VCH Verlag & Co., Weinheim (2013a)

Zhao, D., Wan, Y., Zhou, W.: Mesoporous nonsilica materials. In: Zhao, D., Wan, Y., Zhou, W. (eds.) Ordered Mesoporous Materials. Wiley Online Books, pp. 293–428. Wiley, Weinheim (2013b)

Zhou, Z., Hartmann, M.: Progress in enzyme immobilization in ordered mesoporous materials and related applications. Chem. Soc. Rev. **42**(9), 3894–3912 (2013). https://doi.org/10.1039/C3CS60059A

Zhu, Y., Hua, Z., Zhou, J., Wang, L., Zhao, J., Gong, Y., Wu, W., Ruan, M., Shi, J.: Hierarchical mesoporous zeolites: direct self-assembly synthesis in a conventional surfactant solution by kinetic control over the zeolite seed formation. Chem. Eur. J. **17**(51), 14618–14627 (2011). https://doi.org/10.1002/chem.201101401

Zhu, Y., Zhao, Y., Ma, J., Cheng, X., Xie, J., Xu, P., Liu, H., Liu, H., Zhang, H., Wu, M., Elzatahry, A.A., Alghamdi, A., Deng, Y., Zhao, D.: Mesoporous tungsten oxides with crystalline framework for highly sensitive and selective detection of foodborne pathogens. J. Am. Chem. Soc. **139**(30), 10365–10373 (2017). https://doi.org/10.1021/jacs.7b04221

Zhu, Y.P., Yuan, Z.Y.: Introduction. In: Zhu, Y.P., Yuan, Z.Y. (eds.) Mesoporous Organic-Inorganic Non-Siliceous Hybrid Materials, pp. 1–6. Springer, Berlin (2015)

Zou, Y., Zhou, X., Zhu, Y., Cheng, X., Zhao, D., Deng, Y.: sp2-hybridized carbon-containing block copolymer templated synthesis of mesoporous semiconducting metal oxides with excellent gas sensing property. Acc. Chem. Res. **52**(3), 714–725 (2019). https://doi.org/10.1021/acs.accounts.8b00598

Characterization of Mesoporous Materials

Sarita Kumar, Aarti Sharma, Drashya Gautam, and Sunita Hooda

Abstract Nanotechnology has emerged as an important and rapidly growing field in the area of instrumentation techniques for investigating and characterizing mesoporous materials in recent years. This chapter discusses the various instrumentation techniques that are used to investigate and characterize mesoporous materials in order to determine particle size, pore morphology, structure and surface information. The key biophysical techniques used to classify the most mesoporous materials are powder X-ray diffraction (XRD), transmission electron microscopy (TEM), scanning electron microscopy (SEM), energy dispersive X-ray (EDX), Fourier transform infrared spectroscopy (FTIR), nitrogen adsorption-desorption and solid-state nuclear magnetic resonance (NMR), thermal gravimetric analysis (TGA) and differential scanning calorimetry (DSC). Direct approaches to obtain data from electron micrographs of mesoporous materials include microscopy-based techniques such as SEM and TEM. The diffraction technique and TEM can reveal structural order in mesoporous materials, while SEM can reveal particle size and morphology. The porosity and surface area of the formulated materials are determined by N_2 adsorption analysis, while the porous structure is determined by DSC. The NMR measurements provide information about material surfaces, while EDX provides qualitative and quantitative information about elemental-chemical composition. A brief description of the principle and graphical analysis for each technique has been discussed in detail.

Keywords Characterization · Crystal structure mesoporous · Morphology · Pore size · Stability · Surface area

S. Kumar (✉) · A. Sharma · D. Gautam · S. Hooda
Acharya Narendra Dev College, University of Delhi, Kalkaji, New Delhi 110019, India
e-mail: saritakumar@andc.du.ac.in

S. Hooda
e-mail: sunitahooda@andc.du.ac.in

1 Introduction

Mesoporous materials are porous materials with pore diameter typically ranging between 2 and 50 nm (Rameli et al. 2018), whereas those with <2 nm pores are considered microporous and those with pore size of >50 nm are macroporous materials (Fig. 1). Mesoporous materials possess large accessible surface areas and tunable pore sizes, which are of particular advantage for mass transport and dispersion of electrons/reactants. Thus, mesoporous materials display inordinate potential in electrocatalysis, photocatalysis and, energy storage and conversion (Zhang et al. 2019).

The examples of typical mesoporous materials include some kinds of alumina, silica and various oxides of cerium, niobium, tantalum, tin, titanium and zirconium with mesopores (Fig. 2). However, the lead in the mesoporous materials is taken by mesoporous carbon that exhibits the direct applications in energy storage devices (Eftekhari and Zhaoyang 2017). Mesoporous carbon exhibits porosity within the range of mesopore materials, and this significantly raises the specific surface area. Activated carbon is another very common mesoporous material that is typically composed of a carbon framework with both microporosity and mesoporosity depending upon the conditions under which it was synthesized. According to International Union of Pure and Applied Chemistry (IUPAC), a mesoporous material can be
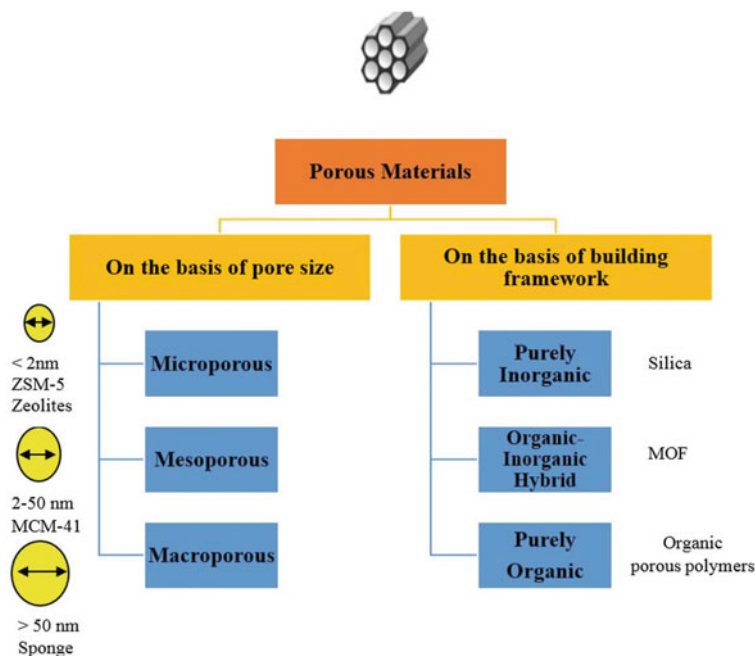
Fig. 1 IUPAC classification of porous materials depending on pore size

(a) Controllable Pore Size (2-50 nm)

(b) Tunable framework compositions
(C, SiO₂, metals, metal oxides etc.)

Nanofiber   Nanosheet   Nanosphere

(c) Morphology (1D, 2D and 3D)

(d) Nanoconfinement effect

(e) Enough space for accommodating volume change

(f) Transport pathway
(Efficient mass transport)
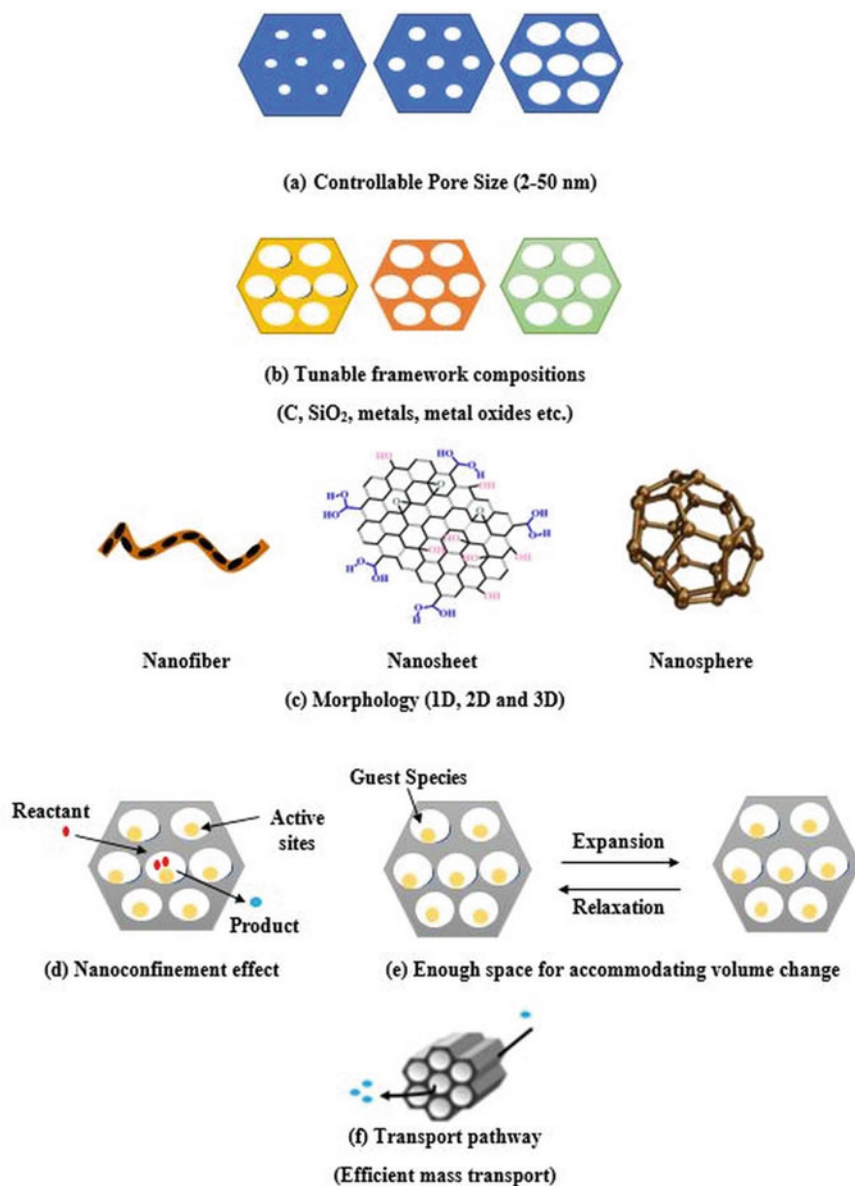
Fig. 2 Structural features and related properties of mesoporous materials with the features of **a** controllable pore sizes, **b** tunable framework compositions, and **c** diverse morphologies. Mesoporous materials with the mesostructured features can **d** work as nanoreactor with nanoconfinement effect for catalysis, and **e** provide enough space for accommodating volume change of an anode in the battery and **f** facilitate efficient mass transport

ordered or disordered in a mesostructure. In case of crystalline inorganic materials, the structure of mesoporous material markedly limits the number of lattice units, and this significantly changes the solid-state chemistry. For example, the battery performance of mesoporous electroactive materials is significantly different from that of their bulk structure (Eftekhari 2017).

With the progress of nanomaterials, substantial deliberation has been carried out regarding the application of mesoporous materials because of their exclusive advantages, such as even mesoporosity, 10–1000 nm particle size, flexible morphology, large surface area, large pore volume, facile surface functionalization, excellent biocompatibility and biodegradation. These excellent structural characteristics could possibly make them appropriate for a widespread array of biomedical applications, such as in drug delivery, sensors, photonics and various nano-devices (Ke et al. 2020).

In the 1970s, the zeolites industry signified the origin of mesoporous materials. The Mobil Corporation established a synthetic method in 1972 to convert methanol into gasoline in the presence of a catalyst, the Zeolite ZSM-5 (Zeolite Socony Mobil). The purpose of this research was to achieve cheaper gasoline from acid–base reactions taking place in the small voids of those zeolites. The failure of zeolite-based method motivated the researchers to synthesize and design materials with larger pores. The porous solids industry made efforts to discover the materials with pores larger than of zeolites, leading to production of the first silica-based mesoporous material almost simultaneously in the early 1990s by Mobil Corporation at the USA (Kresge et al. 1992) and Kuroda research team at Japan (Yanagisawa et al. 1990). Kuroda and team members formulated mesoporous silica by using the intercalated complex of a layered polysilicate kanemite with alkyltrimethylammonium cationic surfactant (Cn-TMA) whose mesoporous structure was established by N_2 adsorption. After two years, researchers at Mobil Research and Development Corporation stated preparation of mesoporous silica using alkyltrimethylammonium bromide (Cn-TAB) or chloride (Cn-TAC) as removable templates and sodium silicate as silica source under alkaline conditions. The materials were named M41S family comprising Mobil Composition of Matter (MCM) kind of materials, with a 2D hexagonal (MCM-41), bi-continuous cubic (MCM-48) or lamellar (MCM-50) mesostructures. The MCM-41 family of mesoporous sieves showed hexagonal array of uniform mesopores ranging from 15 Å to >100 Å in diameter, exhibiting surface area of >700 m^2/g and absorption capacities of 0.7 cm^3/g or greater. Alongside, another Mobil-independent researchers group from Japan established another technique to synthesize mesoporous material and termed them as FSM-16 (Folded Sheet Materials). These remarkable observations started copious exploration on mesoporous materials (Ariga et al. 2012). Gradually, several kinds of mesoporous materials were formulated using different compounds, such as FDU (Fudan University), KIT (Korean Advanced Institute of Science and Technology), MSU (Michigan State University) and SBA (Santa Barbara Amorphous).

Well-organized mesoporous materials can be classified as per their structural dimensions and pore geometry, e.g., either cage-type structures (3D) or cylindrical (2D/3D). Cage-type meso-caged solids such as FDU1 (*Imm*), SBA1 (*Pmn*) and AMS8 (*Fdm*) are made up of spherical or ellipsoidal cages that are interconnected

three dimensionally by smaller cage connecting windows, which could be used to manipulate the mass transfer of active agents. In contrast, cylindrical structures such as MCM48, AMS6 (*Iad*), MCM41, SBA15 and NFM1 (*p6mm*) possess uniform pore diameter and demonstrate potential toward applications in catalysis, adsorption and as drug delivery vehicles (Merck 2021).

2 Characterization of Mesoporous Materials

Characterization of the synthesized mesoporous material is an extremely important step in order to determine their particle size, pore morphology, structure and details study of surface. The major biophysical techniques used to characterize the most mesoporous materials are powder X-ray diffraction (XRD), transmission electron microscopy (TEM), scanning electron microscopy (SEM), energy dispersive X-ray (EDX), Fourier transform infrared spectroscopy (FTIR), nitrogen adsorption-desorption and solid-state nuclear magnetic resonance (NMR), thermal gravimetric analysis (TGA) and differential scanning calorimetry (DSC). Diffraction technique and TEM provide insights about structural order of mesoporous materials, while SEM gives information regarding particle size and morphology. Nitrogen adsorption analysis gives evidence about the porosity and surface area of the formulated materials and solid-state NMR measurements provide facts concerning the surfaces of materials. Various characterization techniques have been listed in Table 1 with their characteristic parametric measurements.

2.1 X-ray Diffraction (XRD)

X-ray diffraction is a rapid analytical technique typically used to determine the crystalline structure of mesoporous material and which can provide information on dimensions of a unit cell. The XRD technique works in accordance with the Bragg's law based on the wide-angle elastic scattering of X-rays and measuring the diffraction intensities in the range of 8–80° 2h angles. The average bulk composition of the material is analyzed after its fine grinding and homogenization. The technique helps to qualitatively recognize various compounds present in the material, and the diffraction principle quantitatively resolves the particle size and chemical species. The reflection of the X-ray on the crystalline structure of the material results in the development of different diffraction patterns indicating the physicochemical properties of the crystal structure.

The major advantage of XRD is its rapidity as it requires less than 20 min for identification of any unknown material. Additionally, requisite of minimal sample preparation and relatively straight forward data interpretation makes it beneficial. On the other hand, the technique has a few limitations, such as necessity of standard

Table 1 Characterization techniques and their corresponding parameters for analysis of mesoporous material

S. No.	Technique	Entity characterized
1	X-ray diffraction (XRD)	Crystal structure
2	Nitrogen adsorption-desorption	• Porosity • Surface area
3	Transmission electron microscopy (TEM)	• Size (structural properties) • Shape • Crystal structure • Single particle properties • Agglomeration state • Dispersion of particles in matrices/supports • Detection of particles
4	Fourier transform infrared spectroscopy (FTIR)	Ligand: • Binding • Composition • Density • Arrangement • Mass • Surface composition
5	Thermal gravimetric analysis (TGA)	Ligand: • Binding • Composition • Density • Arrangement • Mass • Surface composition
6	Energy dispersive X-ray (EDX)	Elemental-chemical composition
7	Differential scanning calorimetry (DSC)	Porous structure
8	Nuclear magnetic resonance (NMR)	• Size (structural properties) • Elemental-chemical composition • Ligand density and arrangement electronic core structure • Atomic composition • Ligand binding/composition/density/arrangement/mass, surface composition

reference file and probable occurrence of overlaying peaks in case of high-angle reflections (MacDonald 2004).

Awoke et al. (2020) characterized the two-ordered mesoporous materials, Santa Barbara Amorphous (SBA-15) material and periodic mesoporous organosilica (PMO), *via* low angle powder X-ray diffraction in order to obtain the information on pore arrangement. They observed a typical XRD pattern in the materials which comprised an ordered 2D hexagonal network arrangement of mesopores belonging
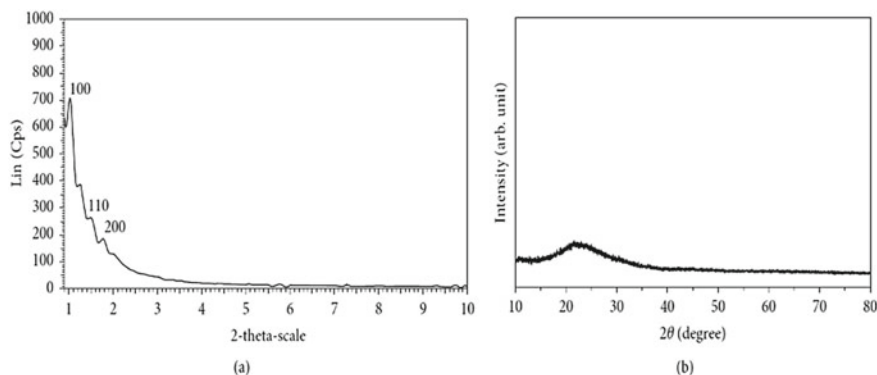
Fig. 3 XRD pattern of Santa Barbara Amorphous (SBA-15) mesoporous material. **a** small angle XRD (SAXRD) pattern and **b** high-angle XRD (HAXRD) pattern. Reproduced from: Nguyen et al. (2020) under the license (CC-BY 4.0)

to the *p6mm* space group. Nguyen et al. (2020) also characterized mesoporous Silica SBA-15 using X-ray diffraction. They recorded the diffraction patterns by the Bruker D8 advance using Cu Kα radiations ($\lambda = 1.54$ °A) with 2θ of 0.1°–10° (Fig. 3a) and by D2 phaser system using radiations at same wavelength but with 2θ of 10°–80° (Fig. 3b). The small-angle XRD pattern of SBA-15 exhibited three characteristic peaks, *viz.* (100), (110) and (200) planes at 2θ of 0.96°, 1.45° and 1.7° (Fig. 3a). These peaks were similar to those obtained in the XRD pattern of materials using tetraethyl orthosilicate (TEOS) as the silica source and denoted the 2D hexagonal structure of SBA-15, whereas the high-angle XRD pattern of SBA-15 presented in Fig. 3b showed the absence of SiO_2 crystal phase in SBA-15, confirming the SiO_2 amorphous porous structure of SBA-15.

The small-angle XRD (SAXRD) pattern of MCM-41 with characteristic intense peak (100) at $2\theta \approx 2.69$ and two obvious reflections [(110) and (200)] at $2\theta \approx 4.5$ and 5.4, respectively, is presented in Fig. 4a. The presence of strong peak (100) directly interprets the MCM-41 structure and the two weak peaks (110) and (200) can be indexed to the $P6mm$ space group, representing a hexagonal mesostructure material with a high degree of long-range order, whereas SAXRD pattern of SBA-3 displayed three peaks at slightly different $2\theta \approx 2.5$, 4.69 and 5.30, corresponding to typical (100), (110) and (200) reflections of one-dimensional hexagonal ($P6m$) mesostructure.

Instead, SAXRD pattern of SBA-15 demonstrated three well-resolved peaks at $2\theta \approx 1.01$, 1.77 and 2.01, characteristic of the planes (100), (110) and (200). Comparatively much lower 2θ values of the peaks indicate a significant degree of long-range ordering in the structure and a well-formed two-dimensional hexagonal lattice (Morsi and Mohamed 2018). On the other hand, the wide-angle X-ray powder diffraction (WAXRD) pattern of the synthesized silica material (MCM-41, SBA-3, SBA-15, SN and SM) showed a broad diffused or an amorphous peak centered at $2\theta = 23°$
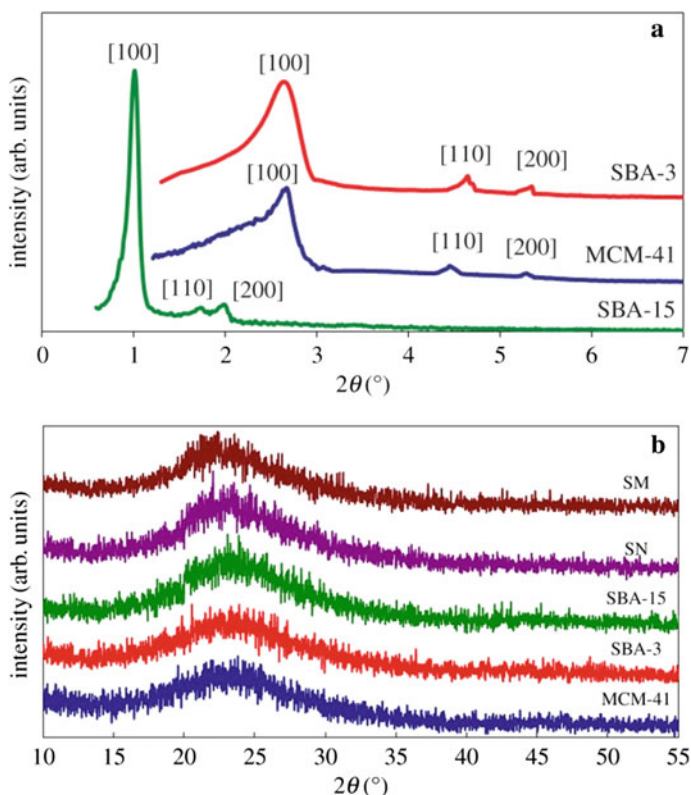
Fig. 4 XRD pattern of mesoporous silica material, **a** SAXRD patterns of ordered mesoporous silica samples: MCM-41; SBA-3 and SBA-15, **b** WAXRD patterns of the prepared silica samples: MCM-41; SBA-3; SBA-15; SN and SM. Reproduced from: Morsi and Mohamed (2018) under the license (CC-BY 4.0)

(equivalent Bragg angle) proposing the amorphous silica phase as the main substance of these materials (Fig. 4b).

Determination of pore-to-pore distance and pore diameter of SBA-15 mesoporous silica and MCM-41 mesoporous silica, using SAXRD technique, also suggested quasi two-dimensional hexagonal (*p6mm*) pore structure (Ishii et al. 2013). The small-angle XRD patterns of chemically modified ordered mesoporous carbon materials (FC-*x* samples) displayed three distinct Bragg diffraction peaks at (100), (110) and (200), which specified the formation of highly ordered 2D hexagonal mesostructure. It was also observed that the intensity of the diffraction peaks decreased with longer oxidation time (Li et al. 2006), whereas the XRD patterns of the mesoporous phenolic resin (MPR) and the mesoporous carbon (MC) showed a low angle (100) peak with *d*-spacing of 11.6 nm and 10.3 nm, respectively (Otero et al. 2014).

2.2 Nitrogen Adsorption-Desorption

The adsorption of gases onto porous solids is a popular way to describe the surface of ceramic materials. Analysis of the surface parameters may be used to infer or quantify the most significant parameter of these materials. The analysis is based on the relationship between the volume and the relative pressure of a physically adsorbing gas. The Brunauer–Emmett–Teller (BET) theory proposed by Stephen Brunauer, Paul Emmett and Edward Teller in 1938 is used to measure specific surface area in multilayer adsorption systems (Sing 1987). The theory, named after the first letter of each publisher's surname, typically uses probing gases (adsorbent) that do not chemically react with material surfaces as an adsorbate (the material on which the gas binds). However, the "monolayer principle" was pioneered by Langmuir which put all evidences together in support of the unifying concept of an ideal localized monomolecular layer. The Langmuir theory was then developed by Irving Langmuir in 1916, and the BET theory was an extension of it. The BET theory was the first to provide a theoretical foundation for understanding the stage of monolayer completion and the start of multilayer growth (Hwang and Barron 2011).

The most widely used gaseous adsorbate for surface probing by BET methods is nitrogen and thus, standard BET analysis is frequently performed at N_2 boiling temperature (77 K). Further probing adsorbates such as argon, carbon dioxide and water are often used, although at a lower frequency, to enable surface area measurements at various temperatures and scales. Since specific surface area is a scale-dependent property with no single true value, quantities of specific surface area calculated using BET theory vary depending on the adsorbate molecule and its adsorption cross-section (Equations numbers 1 and 2). The data collected is represented by a BET isotherm, which plots the amount of gas adsorbed as a function of relative pressure.

$$S_t = \frac{\upsilon_m N s}{V} \tag{1}$$

$$S_{\text{BET}} = \frac{S_t}{a} \tag{2}$$

where S_t, υ_m, N, s, V, a and S_{BET} are total surface area of material, monolayer absorbed gas volume, Avogadro's number (6.02×10^{23} molecules/mol), cross-sectional area of adsorbed gas molecule, molar volume of adsorbed gas, mass of material and specific surface area.

Adsorption-based methods, especially the BET method, are used to calculate porosity and surface area (Širc et al. 2012), because of their ability to measure porosity with a magnitude of 0.4–50 nm, ease of measurement and low cost. In fact, the sort, scale and shape of pores in the material may also be deduced from the type of isotherm. According to Fig. 5a, in the low-pressure field, the phosphorus-modified boehmite (BP) nitrogen isothermal IV type adsorption–desorption curve was biased toward the *y*-axis, suggesting a strong interaction between the sample and nitrogen.

Fig. 5 a N$_2$ adsorption–desorption isotherms and pore size distribution of phosphorus-modified boehmite (BP), **b** N$_2$ adsorption–desorption isotherms of corresponding alumina (AP) and resultant carbon materials (CCAP), **c** pore size distribution of AP and CCAP. Reproduced with permission from: Wang et al. (2021) under license number 5067591511405
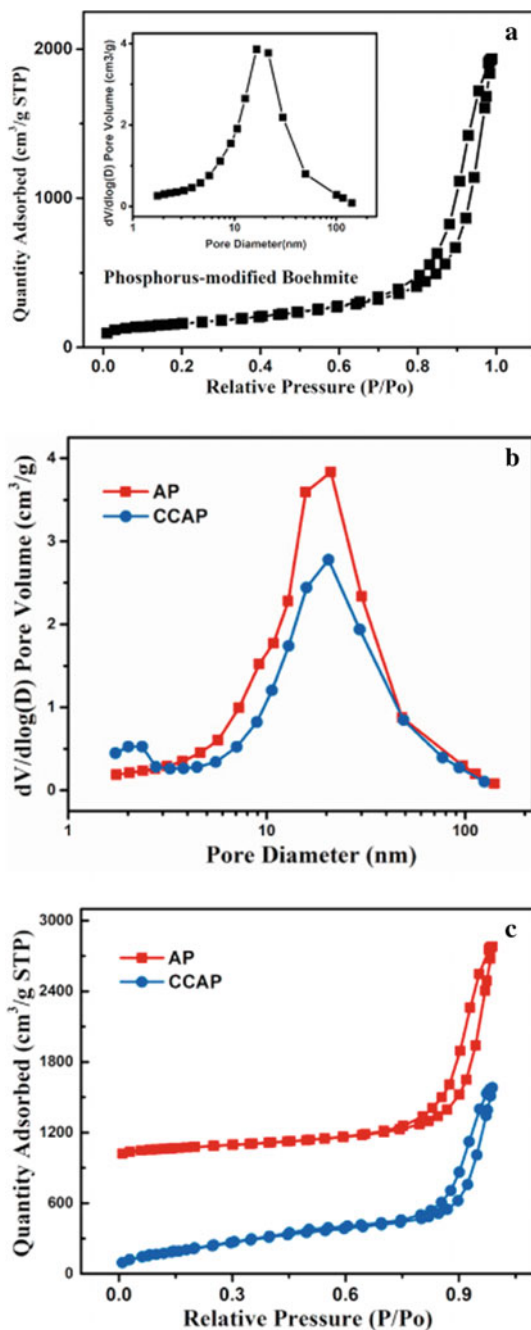
At high pressure, the sample had a capillary condensation effect, and the hysteresis loop was of the H3 kind, suggesting that the materials should be stacked on top of each other to create a slit hole.

Corresponding alumina (AP) and resultant carbon materials (CCAP) had isotherms with visible hysteresis loops, suggesting that the synthesized mesoporous carbon materials were normal mesoporous carbon materials, as shown in Fig. 5b. Using a pore size distribution curve, the BET surface area, pore volume, pore diameter and pore ratio (over 2 nm) of phosphorous-modified boehmite nanosheets (BP), the corresponding alumina (AP) and the resultant carbon materials (CCAP) were measured (Fig. 5c) (Wang et al. 2021).

Likewise, Qiu et al. (2021) investigated the precise controllability and flexibility, enabling the formation of mesoporous TiO_2 nanosheets with adjustable thickness and mesopore size by varying the precursor concentration or ethanol/glycerol ratio, as well as the addition of various amounts of swelling agents (e.g., trimethyl benzene—TMB).

The BET method tests the amount of surface that does not actually move through any of the gases if the sample contains large cavity values. As a result, this technique has a high measurement error. Furthermore, this process is time-consuming, insufficient for measuring low-level surfaces and is incompatible to powder samples with micrometric particle sizes.

2.3 Transmission Electron Microscope (TEM)

Comprehensive analysis of symmetry and pore order at the mesoscale can be carried out by employing high-resolution transmission electron microscopy (HRTEM) a technique vital for obtaining detailed information at these length scales. The samples of TEM can be in various forms, accordingly their preparation and the scope of application may vary. The TEM analysis of mesoporous materials can be done by dispersing a little amount of sample in water or ultrasonically dispersal of the powdered mesoporous particles in ethanol for 5 min. A drop of suspension is then deposited on the holey carbon-coated copper grids for analysis. In comparison with scanning electron microscopy (SEM) technique, TEM holds two advantages by offering better analytical measurement capability and enhanced spatial resolution (Williams and Carter 2009). These advantages make TEM characterization crucial for the systematic study of mesoporous materials.

Gunathilake et al. (2019) synthesized the Titania-incorporated mesoporous organosilica materials (Ti-MO) through a co-condensation process in the presence of the triblock copolymer. They used tris[3-(trimethoxysilyl) propyl] isocyanurate (ICS) and tetraethyl orthosilicate (TEOS) as silica precursors, while titanium isopropoxide (TiPO) was used as the titanium precursor. The TEM characterization of different titania-silica composites (Ti-I10-TS50) showed aggregation of small particles (Fig. 6a, b). It was predicted that branching of such mesostructures may be advantageous for catalytic applications in comparison with ordered structures as it
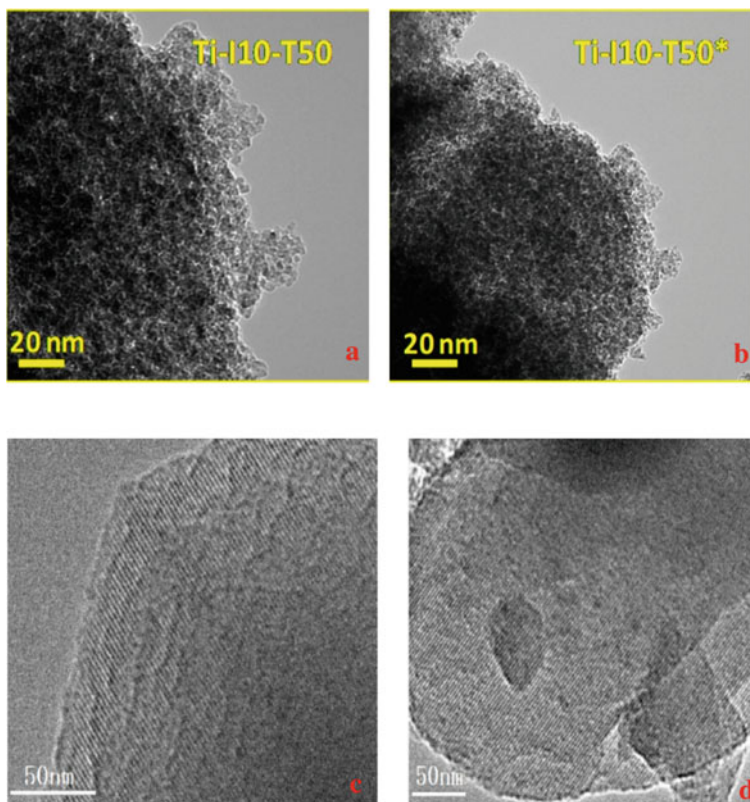
Fig. 6 HRTEM images, **a** Ti-I10-TS50 and **b** Ti-I10-TS50*. Reproduced from: Gunathilake et al. (2019) under the license (CC-BY 4.0), **c** Cry-Ni and **d** Cry-Co. Reproduced from: Qin et al. (2017) under the license (CC-BY 4.0)

gradually augments the capability of molecules to approach toward the active sites (Alba et al. 1996; Morey et al. 2000).

Qin et al. (2017) synthesized the crystalline heteroatom mesoporous MCM-41 (Cry-Ni and Cry-Co) using an ionic complex as template formed by interaction between cetyltrimethylammonium ions and metal complex ion $[M(EDTA)]^{2-}$ (M = Co or Ni)]. The pore morphology was scrutinized by high-resolution transmission electron microscopy (HRTEM) on a JEM-2100 microscope with an accelerating voltage of 200 kV. They observed that the synthesized mesoporous materials exhibited a uniform pore size with a highly ordered pore structure and the characteristic long-range ordered symmetry of a mesophase. The ordered mesopores of the crystals are shown in HRTEM images (Fig. 6c, d). Huang et al. (2014) TEM-characterized hexagon-symmetrical silica mesoporous particles (HMSNPs) synthesized by using cetyl trimethylammonium bromide and tetraethyl orthosilicate. They found consistent pore diameter of 2.07 ± 0.28 nm. The profiling of individual pore suggested

the permeation of HMSNPs by ordered arrays of channels of consistent diameter (Fig. 7).
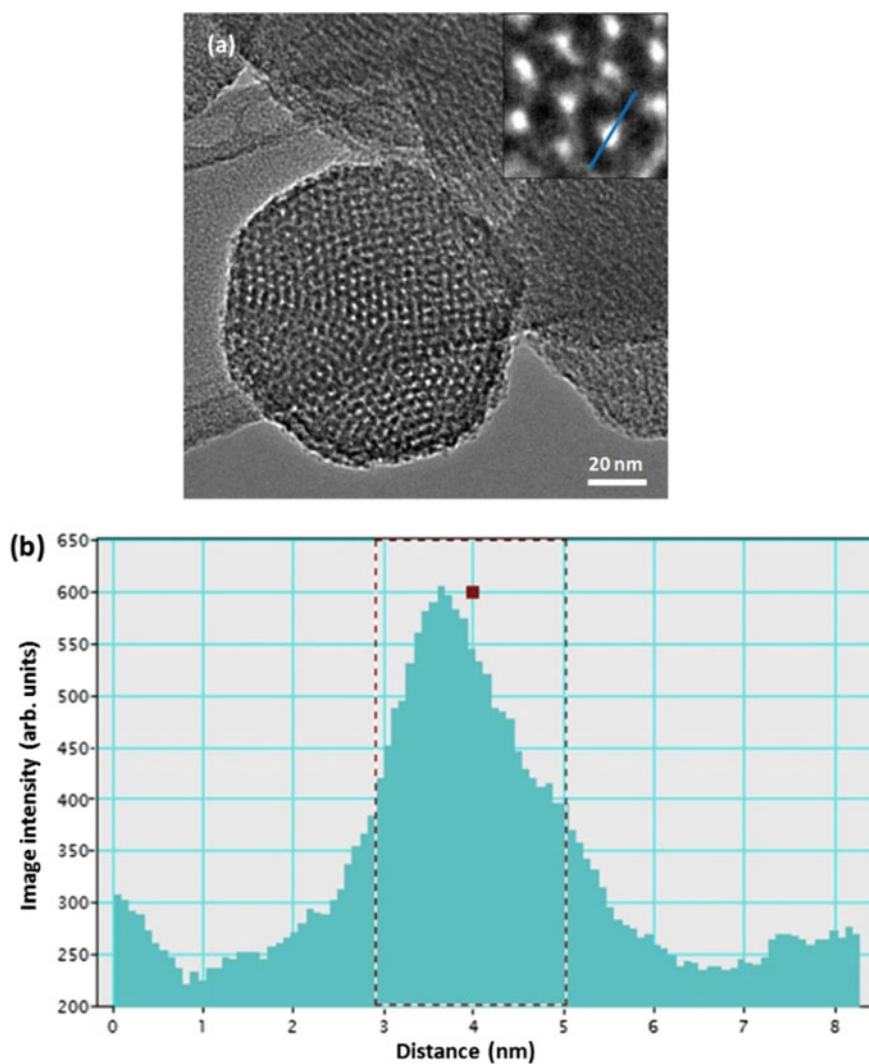
Fig. 7 HRTEM images **a** the pore structure, inset of figure shows the individual pores that are line profiled using the DigitalMicrograph software, **b** shows the resulting line profile, where the full width at half-maximum is extracted from the image intensity. Reproduced from: Huang et al. (2014) under the license (CC-BY 3.0)

2.4   Fourier Transform Infrared (FTIR) Spectroscopy

Among the non-destructive characterization methods, the Fourier transform infrared spectroscopy is highly beneficial tool for surface characterization of materials' surfaces. This technique provides a molecular fingerprint of materials depending on the vibration of their molecules. It determines the chemical composition of the nanoparticles' surface as well as recognizes the surface reactive sites responsible for the surface reactivity and chemical bonding (Baraton and Merhari 2007).

FTIR spectroscopy technique is based on the measurement of the infrared spectra of the substances by computing interferogram and performing Fourier transform of the interferogram, mostly composed of optical detecting part and computer part. Nowadays, a large number of IR spectral data of various substances have been summarized systematically. Different characteristics of the spectrum assist in the determination of unknown functional group, elucidation of the chemical structure, detection of the chemical reaction process, differentiation of the isomers and the purity assessment of the analyte, etc. Thus, FTIR spectroscopy has become a routine analytical method for qualitative and structural analysis.

Unlike, techniques explained earlier, FTIR is a time-efficient technique because of simple sample preparation requirement, brief time required for spectral analysis and enabling the analysis of samples in different states (liquid or solids). Additionally, it requires only small quantity of the sample; in μg (solids) or μL (liquid). FTIR is also a cost-effective technique and has three noteworthy advantages of providing; higher signal-to-noise ratio, high-energy throughput and, high accuracy and stability. However, surrounding environmental conditions of heterogeneous samples necessitate various background scans and sample scans to evade artifacts and discrepancies in the spectra. Pre-treatment of the samples may be critical to purify the sample and to prevent overlapping of the peaks in the spectra. This can be done by preparing a solid sample which is oven-dried at 80 °C for 6 h before being compacted into transparent disks (Faghihzadeh et al. 2016).

FTIR characterization of synthesized mesoporous silica nanoparticles (MSN) has revealed existence of a silanol (Si–OH) peak at 956 cm^{-1} indicative of physiosorbed water molecule for un-calcined MSN (MSN-T) (Rameli et al. 2018) (Fig. 8; Table 2). Similar observation was documented by Handke and Hwasny (2014), who advocated that Si–OH group peak was noticeable only in the spectrum of silica, as a result of the preparation method and hygroscopic properties. However, calcined MSN (MSN-C) demonstrated a noticeable increase in the Si–OH peaks. Further, peaks in all the MSN samples were characteristic of SiO_2 only, concluding that calcination removed the volatile component from MSN entirely (Chen et al. 2013). Successful formation of MSN can be recognized by the increase in intensity of the absorption peak of SiO_2 (Hu et al. 2011) (Fig. 8). Mesoporous silica nanoparticles (MSNp) MCM-41 have also been synthesized from natural waste rice husk (Purnawira et al. 2019). FTIR characterization of these particles recognized the existence of functional group of Si–O, Si–O–H, Si–O–Si, –OH, Si–H and Si–OH bonds at respective wavenumber of 3388.31, 1636.71, 1070.46, 956.95, 795.09 and 456.15 cm^{-1} of various compositions
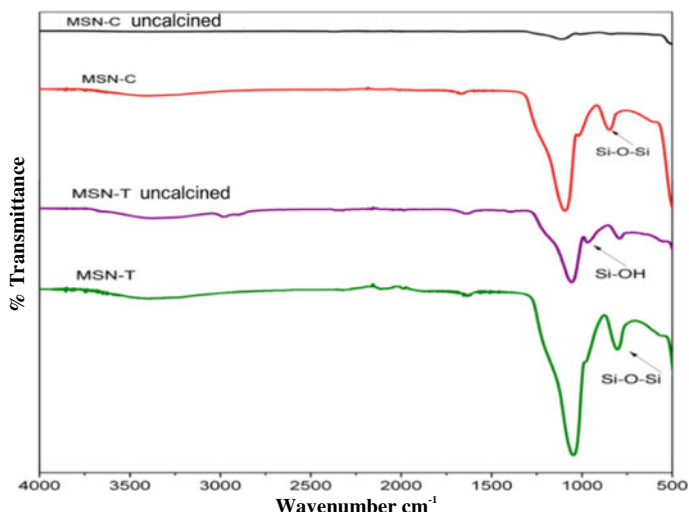
Fig. 8 FTIR spectra of MSN (mesoporous silica nanoparticles) of uncalcined and calcined MSN-C and MSN-T. Reproduced from: Rameli et al. (2018) under the license (CC-BY 3.0)

of Cetyl Trimethyl Ammonium Bromide (CTAB)-templated silica at 1, 1.25 and 1.5% (Fig. 9; Table 2).

2.5 Thermogravimetric Analysis (TGA)

Thermal gravimetric analysis (TGA), also known as thermogravimetric analysis, is the thermal analysis of the material based on the principle of measuring mass of a sample with the change in temperature over time. The analysis reveals not only physical phenomena such as phase transitions, absorption, adsorption and desorption, but also chemical phenomena such as chemisorption, thermal decomposition and solid–gas reactions (Saadatkhah et al. 2020). The material is characterized through analysis of characteristic decomposition patterns. It is especially useful for the study of polymeric materials, including thermoplastics, thermosets, elastomers, composites, plastic films, fibers, coatings, paints and fuels.

TGA measures and records the mass, time and temperature of the sample. Heating, cooling, isothermal stays or a combination of these can be used in the temperature program. Initially, the analyzer made up of a precise micro-balance is attached to a computer. The micro-balance also termed as thermo-balance is a sample pan inside a furnace with a temperature programmer and controller, used for weighing the sample in the closed furnace. The temperature range for commercial TGAs is typically ambient to 1000 °C or even more, a sufficient upper limit required for polymer applications. A purge gas flowing through the balance creates an atmosphere; the

Table 2 FTIR functional groups present in the mesoporous materials

S. No.	Mesoporous material	Functional groups	Peak-wave numbers (cm^{-1})	References
1	Mesoporous silica nanoparticles (MSN)	Silanol (Si–OH)	956	Rameli et al. (2018)
2	Mesoporous silica nanoparticles (MSNp) MCM-41	Si–O	3388.31	Purnawira et al. (2019)
		Si–O–H	1636.71	
		Si–O–Si	1070.46	
		– OH	956.95	
		Si–H	795.09	
		Si–OH	456.15	
3	Mesoporous silica synthesized using tetraethoxysilane (TEOS) SBA-16	Si–OH	960	Andrade et al. (2012)
4	Mercaptopropyltriethoxysilane (M-PTES)	– OH	1630–1650, 3200–3550	
5	Triethoxyphenylsilane (T-PTES)	– CH$_3$	2854	
		– CH	2970 and 2926	
		Si–O–Si	800, 1000–1100	
6	Santa Barbara Amorphous-15 (SBA-15)	C–H bonds	2900–3000	Liu et al. (2005)
7	Carbon/silica hybrid (S15N)	Si–O–Si	1090 and 800	
8	Carbon/silica hybrid (S15A)	Si–OH	810	
9	Modified mesoporous carbon (CMK-3)	O–H	3450	Li et al. (2006)
		– COOH	1643–1750	
		C–O	1100	

gas can be inert, such as nitrogen, argon or helium; oxidizing, such as air or oxygen; or reducing, such as forming gas (8–10 % hydrogen in nitrogen) (Fig. 10). With polymers, however, a reducing atmosphere is rarely needed. The moisture content of the purge gas can vary from dry to saturate (Prime et al. 2009).

The mass change of the sample as a function of temperature or time is graphically represented as TGA thermal curve, also known as a thermogram. Thermal stability, oxidative stability, multicomponent composition, product lifespan, decomposition kinetics, moisture, and volatile content are all communicated through thermograms, which are unique to each compound. Thermograms with several parts are known as generic thermograms. Some of the factors which can affect TGA results include thermal expansion, atmospheric turbulence, condensation, electrostatic and magnetic forces, electronic drift, heating rate, thermal conductivity, enthalpy of the processes and sample furnace sensor arrangement.
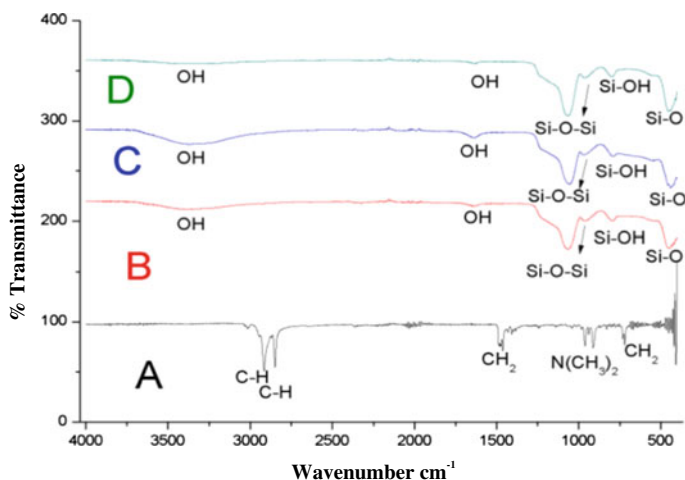
Fig. 9 FTIR spectra of mesoporous silica nanoparticles (MSNp) MCM-41 synthesized from natural waste rice husk with, **a** pure CTAB silica, **b** silica reflux at 1% CTAB, **c** silica reflux at 1.25% CTAB, **d** silica reflux at 1.5% CTAB. Reproduced from: Purnawira et al. (2019) under the license (CC-BY 3.0)
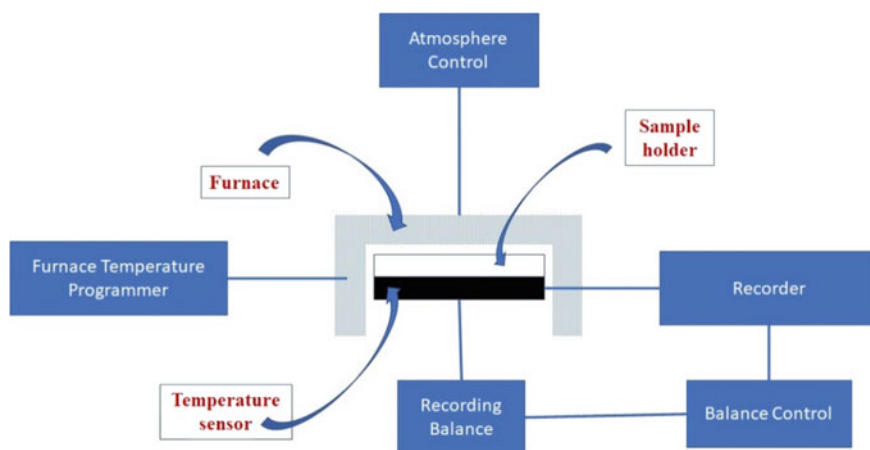
Fig. 10 Working diagram of TGA

TGA is an advantageous technique as it needs limited sample preparation (at least 0.1 mg) of powders, pellets and flakes. Also, with TGA, the furnace can be kept at 1000 °C without any balance drift, which is not possible with other thermo-balances. Since the cooling period is so low, a thermogram can be recorded. However, the TGA has limitation that only solid sample can be used in quantitative and qualitative analysis. Non-homogeneous material cannot be tested. The technique is sensitive to

heating rate and sample mass that results in shift in temperature. Thus, it is limited to sample which undergoes weight change, melting, crystal phase change, etc.

Costa et al. (2021) assessed the mesoporous matrix's thermal stability as well as inferred the percentage of changing groups within the system based on the mass variation of the matrix as a function of temperature. Figure 11a, b shows that TGA of the filtered mesoporous adsorbent confirmed the maximum amount of adsorbed amino acid, with a weight loss of 28.4 wt.% for cNGM-1(D-valine) and 20.3 wt% for cNFM 1 (L-valine) (Huang and Garcia-Bennett 2021).

Heba et al. (2021) investigated the thermostability of mesocellular foam MCFs, calcination of organic fragments presents in Benzyl groups with MCF (Bu-fMCF) and bonding of Ru-complex with MCF (Fig. 12a, b). The TGA curve for the non-covalently immobilized complex, Ru-complex with Bn-MCF (Ru(3)-ncBn-fMCF),
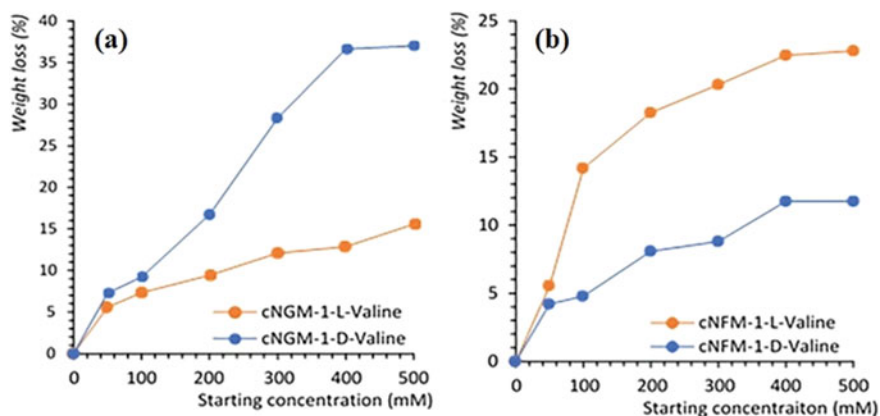
Fig. 11 Adsorbent % weight loss after filtration as measured by thermogravimetric analysis for **a** cNGM-1-L-Valine and **b** cNFM-1-L-Valine. Reproduced from: Huang and Garcia-Bennett (2021) under the license (CC-BY 4.0)
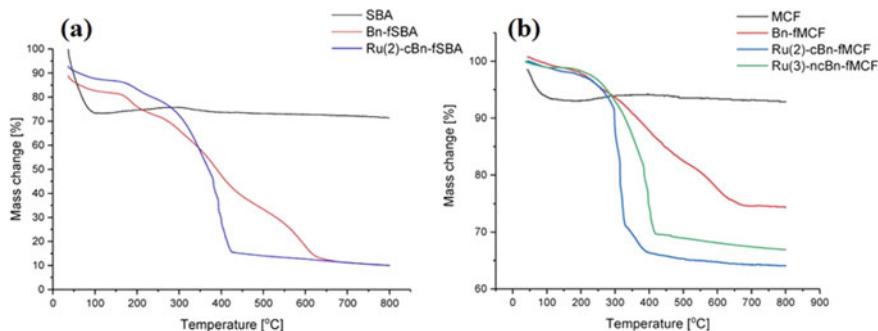
Fig. 12 a Thermogravimetry analysis (TGA) analysis of SBA compounds. **b** TGA of MCF compounds. Reproduced from: Heba et al. (2021) under the license (CC-BY 4.0)

was found to be similar to the Ru-complex with benzyl group Santa Barbara Amorphous (Ru(2)-cBn-fSBA) curve. It was proposed that SBA-15's narrower pores promoted phenyl group stacking interaction. It may also be blamed for the higher content of organic compounds in functionalized SBA, which obstructed substrate access to active sites, lowering catalytic activity.

2.6 Energy Dispersive X-ray (EDX)

The energy dispersive X-ray (EDX) microanalysis is a non-destructive analytical technique that is used to identify and characterize the elemental composition of sample. The sample of interest can be examined in situ through EDX technique with little or no sample preparation. Qualitative analysis of elements in samples and quantitative analysis of their mass concentration can be carried out rapidly.

This technique is linked to electron microscopy based on the generation of representative X-rays that expose the existence of elements in the sample material. EDX systems are basically attachments to the electron microscopy (EM) instruments [scanning electron microscopy (SEM) or transmission electron microscopy (TEM)] where the imaging capability of the microscope identifies the specimen. In a typical EDX spectrum: the y-axis defines the number of X-rays and the x-axis shows the energy of X-rays. The data generated by EDX analysis contains the spectra corresponding to the peaks of all the different elements in the sample. The position of the peak detects the elements, and the peak height quantifies the concentration of each element.

Figure 13a depicts an EDX spectrum that describes the elemental dispersion throughout the silica framework and affirms the incorporation of titanium species into the silica matrix (Gunathilake et al. 2019). The EDX characterization of mesoporous silica SBA-15 revealed weight composition of SBA-3 as Si = 44.81% and oxygen = 55.19%, while in SBA-5, weight composition of Si observed was 41.06% and the composition of oxygen was 58.94% (Thahir et al. 2019). The percentage of silica observed through EDX evidenced that the synthesis of silica material was successful with uniform composition (Fig. 13b).

2.7 Differential Scanning Calorimetry (DSC)

Differential scanning calorimetry (DSC) determines the amount of energy required to achieve a near-zero temperature difference between a sample and an inert reference material, subjected to similar conditions. The device, which measures energy directly and allows precise measurement of heat power, is known as a DSC. In order to preserve a zero-temperature difference, the energy consumed by the sample, is offset by an increased energy input into the sample during an endothermic transition (Pierella et al. 2005). Since this balancing energy has the exact same magnitude as the energy consumed in the transition, direct calorimetric measurement of the transition
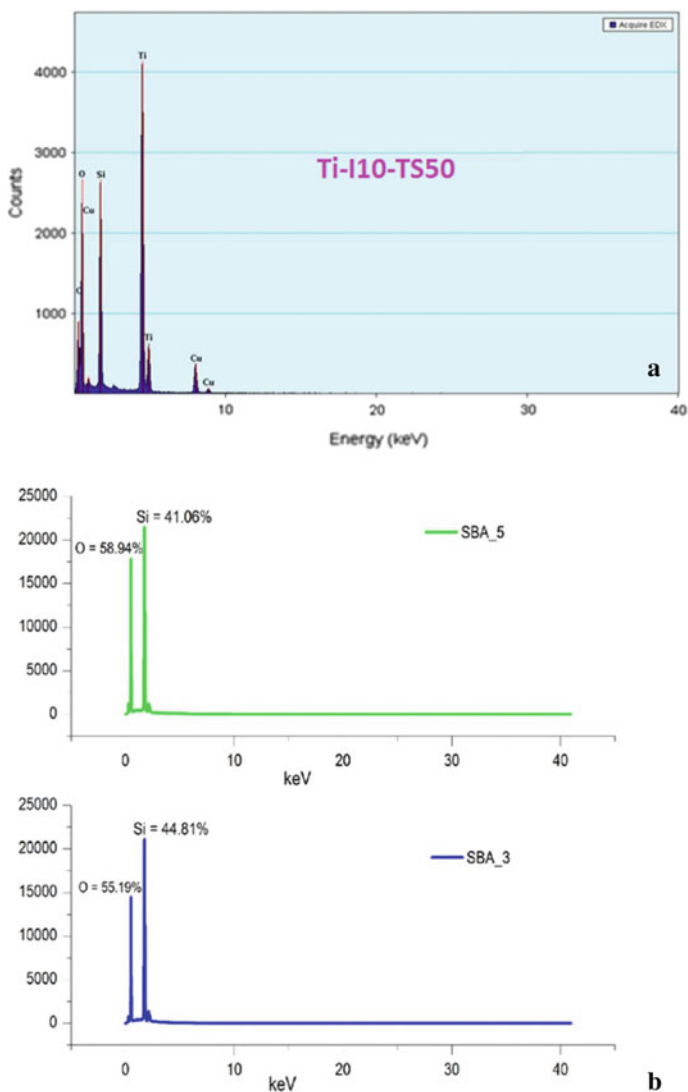
Fig. 13 EDX spectrum of **a** Ti-I10-TS50 sample [Ti-I10-TS50 indicates 10% (10% with regard to total titanium moles (0.011) = 0.0011 mol) of Tris [3-(trimethoxysilyl)propyl]isocyanurate (ICS) and 50% (50% with regard to total titanium moles (0.011) = 0.0055 mol) of tetraethylorthosilicate (TEOS).]. Reproduced from: Gunathilake et al. (2019) under the license (CC-BY 4.0) **b** Santa Barbara Amorphous-15 (SBA-15) sample. Reproduced from: Thahir et al. (2019) under the license (CC-BY 4.0)

is possible. The abscissa indicates the transition temperature on the DSC table, while the peak indicates total energy transfer to or from the sample. It measures accurate temperature as well as the amount of energy consumed or emitted by a sample while it is heated, cooled or kept at a constant temperature.

A heat flux versus temperature or time curve is obtained after a DSC experiment (Zhang et al. 2020). Exothermic reactions in the sample are represented by a positive or negative peak, depending on the type of technology employed in the experiment. The enthalpies of transformations can be calculated using this curve by incorporating the peak associated with a specific transformation. Equation (3) is used to express the enthalpy of transformation:

$$\Delta H = KA \tag{3}$$

where ΔH is the enthalpy of transition, K is the calorimetric constant and A is the region under the curve.

The calorimetric constant (K) varies with the instrument, but it can be obtained by analyzing a well-characterized sample with known transition enthalpies. Two types of DSC techniques are available; (a) heat flux DSC: used to measure the difference between the sample and the reference; (b) Power differential DSC: used to measure difference in power supplied to the sample and a reference. Several parameters; such as gas flow, purging of gas (N_2 or O_2), particle size, volume of sample, heating temperature, vessel used, and sample pre-treatment; all affect the thermal analysis performance. These elements can be divided into two main groups: (a) instrumental factors, which include furnace heat rate and furnace atmosphere and (b) sample characteristics, which include weight of sample and particle size. DSC is commonly used to evaluate the thermal transitions of polymeric materials. The glass transition temperature (T_g), crystallization temperature (T_c) and melting temperature are all important thermal transitions (T_m). Liquid crystals and oxidation stability of the sample is often characterized using DSC.

DSC characterization carries benefit in that it can be used at very high temperature, is highly sensitive, is flexible for sample volume, and provides high-resolution curves. However, the use of DSC is limited for thermal screening of isolated intermediates and products due to difficulties in test cell preparation in avoiding evaporation of volatile solvents.

Iza et al. (2000) used DSC to examine the solidification thermogram of a poly(N-(2-hydroxypropyl) methacrylamide (PHPMA) hydrogel saturated with water (Fig. 14). It was found that the temperature peak was caused solely by water crystallization within the silica mesopores. The form of water used in this study had showed two peaks; the temperature peak for fusion of "bulk" water was around 48 °C, while the temperature peak for fusion of water within mesopores was 218 °C. The literature has revealed that the poor thermal effect at 306–500 °C is followed by an apparent exothermic peak at around 470 °C which is shown in Fig. 15, indicating that the amorphous phase has crystallized into anatase (Janitabar-Darzi et al. 2009).
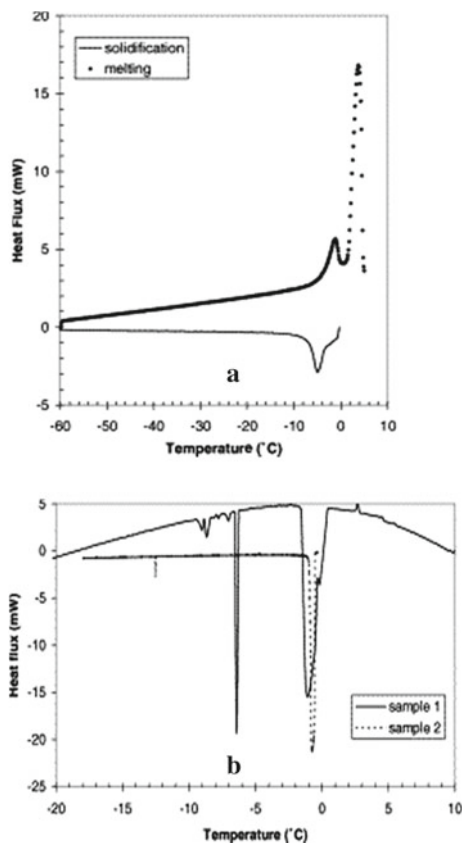
Fig. 14 Melting and solidification thermograms of **a** mesoporous silica and **b** sample 1. Reproduced from: Iza et al. (2000) with permission under the license number: 5067610763375

2.8 Nuclear Magnetic Resonance (NMR)

NMR spectroscopy is one of the most popular techniques for obtaining physical, chemical, electronic and structural knowledge about molecules because of the chemical change in the resonance frequencies of the nuclear spins in the sample.

The principle of NMR can be divided into three steps (Kirkpatrick 2018): (a) The magnetic nuclear spins is aligned (polarized) in an applied, constant magnetic field B_0. (b) A weak oscillating magnetic field, commonly referred to as a radio-frequency (R_F) pulse, disrupts the nuclear spin alignment. The frequency of oscillation required for significant perturbation is determined by the static magnetic field (B_0) and the nuclei under observation. (c) The NMR signal is detected during or after the R_F pulse as a result of the voltage caused in a detection coil by the nuclear spins precession around B_0. Precession normally occurs with the intrinsic Larmor frequency (When a nucleus is put in a magnetic field, it has a natural tendency to interact with field.
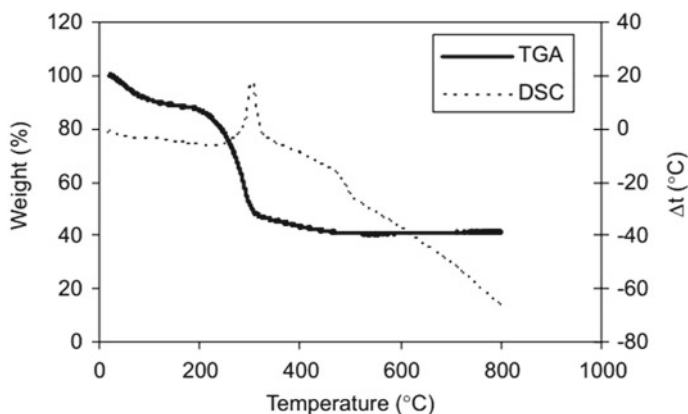
Fig. 15 TiO$_2$ TG–DSC curves prior to calcinations. Reproduced from: Janitabar-Darzi et al. (2009) with permission under the license number: 5067611246211

Larmor frequency is the propensity of a nucleus to align itself in a magnetic field in which it is put) of the nuclei after R_F pulse and does not require transitions between spin states or energy levels.

The functional groups, topology, dynamics, pore size distribution and three-dimensional structure of organic molecules in solution and solid state can all be studied using NMR spectroscopy (Reif et al. 2021). Peak integrals may be used to calculate composition quantitatively since the region under NMR peak is usually proportional to the number of spins involved. For several years, NMR has been a common method for determining the structure of organic molecules in solution. Only with the development of high-field superconducting magnets, magic-angle spinning (MAS) and the ability to study nuclides with a microscope progressed the field of nuclide research. It is now possible to deal with a wide variety of inorganic solids using the quadrupole moment.

NMR is a non-destructive technique. It is used to study a wide range of systems, from membrane proteins and amyloid fibrils in biochemistry to polymers, battery materials, photovoltaic perovskites and cements in chemistry and materials science. It provides high-resolution conformational structure of various organic compounds, cannot be applied to larger proteins (>800KD) and is very expensive tool for structure determination.

Trzeciak et al. (2021) conducted a high-resolution NMR assay to detect a multi-modal distribution of embedded GM (guest molecule in mesoporous material) spectral signals. NMR relaxometry and cryoporometry have been utilized to monitor the curing process and pore structures of metakaolin-based geopolymers with a narrow water-to-solid (w/s) ratio of 0.59–0.66 (Li et al. 2021). They used solid-state NMR spectroscopy and investigated the interaction and nature of surface sites for water and methanol sorption on MFI-type zeolites and mesoporous SBA-15. The material was characterized due to the larger mesopores of SBA-15 leading to the presence of

significantly higher total amounts of water and methanol in the pores in the adsorption equilibrium at room temperature in comparison with Silicalite-1 (Fig. 16).

Chen et al. (2021) studied the pore structure of potato starch (PS) using low-field NMR cryoporometry (LF-NMRC). As shown in Fig. 17, the NMR signal increased slowly as the temperature rose from $(-)30$ to $(-)5$ °C, but increased dramatically once the temperature surpassed $(-)5$ °C, suggesting a physical theory different from the current LT-NA. The melting point of small water domains trapped within different-sized pores determined the pore size distribution in LF-NMRC; the melting point of ice decreased as the pore size decreased. The comparison of LF-NMRC method to the conventional LT-NA method assessed the potential of using LF-NMRC to determine the pore size distribution of potato starch granules (Chen et al. 2021).
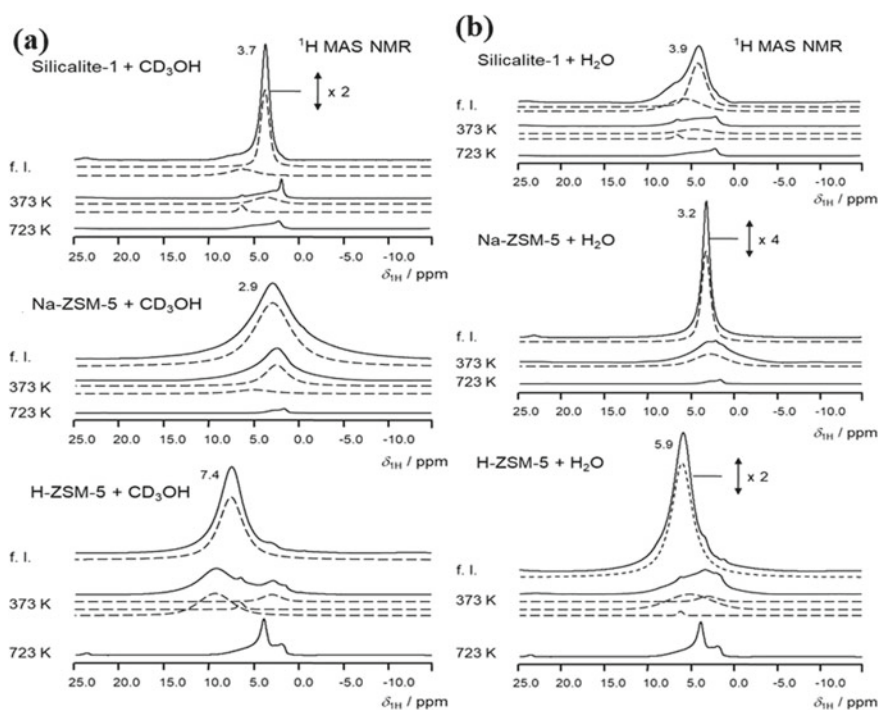
Fig. 16 a ^{1}H MAS NMR spectra of Silicalite-1, Na-ZSM-5 and H-ZSM-5 **a** recorded in the fully loaded state (f.l., top) and after desorption of water at 373 K (middle) and 723 K (bottom). The dashed curves indicate the shapes of the water signals used for simulating the experimental spectra, **b** ^{1}H MAS NMR spectra of Silicalite-1, Na-ZSM-5 and H-ZSM-5 recorded in the fully loaded state (f.l., top) and after desorption of methanol at 373 K (middle) and 723 K (bottom). The dashed curves indicate the shapes of methanol OH signals used for simulating the experimental spectra. Reproduced from: Li et al. (2021) under the license (CC-BY 4.0)
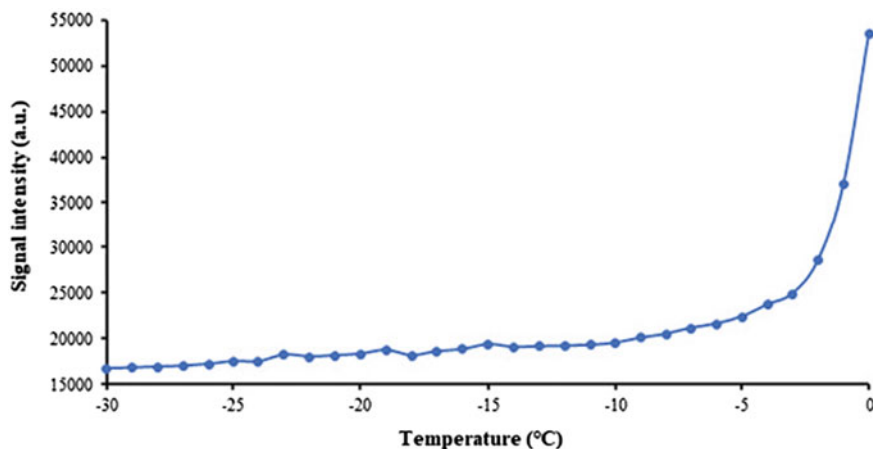
Fig. 17 LF-NMRC experiment melting curve. Chen et al. (2021) with permission under the license number: 5067760128798

3 Limitations of Techniques

S. No.	Name of the technique	Limitations
1	XRD	• The optimum material for identifying an unknown is homogeneous and single-phase material • It must have access to an inorganic compound standard reference file (d-spacings, hkls) • Tenths of a gram of material must be processed into a powder for analysis • The detection limit for mixed compounds is 2% of the sample • Pattern indexing for non-isometric crystal systems is difficult for unit cell determinations • Peak overlay is possible, and it gets worse for high-angle "reflections"
2	BET	• As the SSA value varies depending on the sorbent material, BET does not provide an absolute measurement (e.g., N_2) • The most significant disadvantage of this measuring method is that it can only be utilized with dried materials
3	FTIR	• IR spectroscopy is not a very sensitive technique • The absorption bands usually overlap in the IR spectrum of the complex mixtures • Complex mixtures are generally impossible to analyze without reference IR spectra of pure materials • Several materials completely absorb IR, and thus, it is impossible to obtain reliable results

(continued)

(continued)

S. No.	Name of the technique	Limitations
4	TEM	• It can only investigate a tiny portion of a material at any given time • The higher is the resolution, the lower are the sampling capabilities • TEM lets us see 2D images of 3D specimens
5	EDX	• Analysis is dependent on the concentration of an element in the sample. X-rays will give insufficient amount of energy after hitting the sample containing low concentrations of elements to adequately measure its proportion • EDX generally does not work for elements with a low atomic number • Sample thickness can bring energy levels closer together, thus making electrons easier to move to outer energy levels, which can in turn cause deviation in the results • X-rays are not particularly effective at penetrating beyond several nanometers in samples, so the only surface layers can be efficiently measured
6	TGA	• The higher reactivity of amorphous forms is not taken into account • As only volatile degradation can be identified, degradation start temperatures can lead to the incorrect conclusion that a material is thermally stable within a given temperature range while non-volatile degradation is actually occurring • The unequal mass loss of volatiles and the creation of degradants, severely limits their capacity to offer constant universal indicators of actual degradation extent • It supplies useful information only when there is a change in mass • Although some liquids may be measured, this is usually a tough task
7	DSC	• This technique requires excellent thermal contact with the bottom of the sample crucible • It is extremely sensitive to the heating rate
8	NMR	• This is beneficial for more precise structure determination, but not for the availability of greater molecular masses • As the information obtained from the same materials is substantially more complex, NMR has a lower resolving power than other types of investigations • Many times, one can predict two or more potential conformations from a given data collection • With increasing intensity and complexity of the determination, the expense of the experimental implementation rises

4 Conclusion

Given the growing variety of porous materials, it is easy to believe that a generic approach to characterization is becoming obsolete. In reality, there is still a high demand for current knowledge on both the old and new approaches, as well as advice on how to interpret experimental results. Characterization techniques have made a significant contribution to the processing of mesoporous materials in the desired form and operation. Some characterization techniques can track the synthesis and creation of nano-sized particles under controlled conditions at a very early stage of synthesis, making the process fast and simple. On the other hand, some characterization techniques offer knowledge and confirmation about the topography, 3D structure, chemical structure, elemental composition and metallic nanoparticle molecular fingerprinting. It is an odd scenario that some of the good user-friendly software presently accessible may be too easy to use, making it feasible to create a false impression of a complex pore structure without expert direction. As a countermeasure, and for other reasons, every effort should be made to sustain the existing tradition of worldwide pore structure characterization during symposia and workshops, and it is hoped that these events will continue to give opportunities for vigorous discussion. The importance of derived values of surface area, pore size, porosity, three-dimension and other parameters need to be evaluated more critically in the future. The creation of a variety of new reference materials with uniform pore structures is another challenge for the future.

References

Alba, M.D., Luan, Z.H., Klinowski, J.: Titanosilicate mesoporous molecular sieve MCM-41: synthesis and characterization. J. Phys. Chem. **100**, 2178–2182 (1996)

Andrade, G.F., Soares, D.C.F., Almeida, R.K.D.S., Sousa, E.M.B.: Mesoporous silica SBA-16 functionalized with alkoxysilane groups: preparation, characterization, and release profile study. J. Nanomater. **816496**, 1–10 (2012). https://doi.org/10.1155/2012/816496

Ariga, K., Vinu, A., Yamauchi, Y., Ji, Q., Hill, J.P.: Nanoarchitectonics for mesoporous materials. Bull. Chem. Soc. Japan **85**(1), 1–32 (2012)

Awoke, Y., Chebude, Y., Díaz, I.: Controlling particle morphology and pore size in the synthesis of ordered mesoporous materials. Molecules **25**(21), 4909 (2020)

Baraton, M.I., Merhari, L.: Dual contribution of FTIR spectroscopy to nanoparticles characterization: surface chemistry and electrical properties. In: Nanomaterials synthesis, interfacing, and integrating in devices, circuits, and systems II, vol 6768, p. 676806. International Society for Optics and Photonics (2007)

Chen, B., Quan, G., Wang, Z., Chen, J., Wu, L., Xu, Y., Li, G., Wu, C.: Hollow mesoporous silicas as a drug solution delivery system for insoluble drugs. Powder Tech. **240**, 48–53 (2013)

Chen, L., McClements, D.J., Ma, Y., Yang, T., Ren, F., Tian, Y., Jin, Z.: Analysis of porous structure of potato starch granules by low-field NMR cryoporometry and AFM. Int. J. Biol. Macromol. **173**, 307–314 (2021)

Costa, J.A.S., de Jesus, R.A., Santos, D.O., Neris, J.B., Figueiredo, R.T., Paranhos, C.M.: Synthesis, functionalization, and environmental application of silica-based mesoporous materials of the M41S and SBA-n families: a review. J. Environ. Chem. Eng. 105259 (2021)

Eftekhari, A.: Ordered mesoporous materials for lithium-ion batteries. Micropor. Mesopor. Mater. **243**:355–369 (2017). https://doi.org/10.1016/j.micromeso.2017.02.055

Eftekhari, A., Zhaoyang, F.: Ordered mesoporous carbon and its applications for electrochemical energy storage and conversion. Mater. Chem. Front. **1**(6), 1001–1027 (2017). https://doi.org/10.1039/C6QM00298F

Faghihzadeh, F., Anaya, N.M., Schifman, L.A., Oyanedel-Craver, V.: Fourier transform infrared spectroscopy to assess molecular-level changes in microorganisms exposed to nanoparticles. Nanotechnol. Environ. Eng. **1**(1), 1 (2016)

Gunathilake, C., Kalpage, C., Kadanapitiye, M., Dassanayake, R.S., Manchanda, A.S., Gangoda, M.: Facile synthesis and surface characterization of titania-incorporated mesoporous organosilica materials. J. Compos. Sci. **3**, 77 (2019)

Handke, M., Kwaśny, M.: Infrared spectroscopic study of octahydridooctasilsesquioxane hydrolytic polycondensation. Vib. Spectrosc. **74**, 127–131 (2014)

Heba, M., Stradomska, D., Szymańska, K., Jarzębski, A., Ambroziak, K., Masternak, M., Kolanowska, A., Pudło, W., Kuźnik, N.: Engineering and performance of ruthenium complexes immobilized on mesoporous siliceous materials as racemization catalysts. Catalysts **11**(3), 316 (2021)

Hu, Y., Wang, J., Zhi, Z., Jiang, T., Wang, S.: Facile synthesis of 3D cubic mesoporous silica microspheres with a controllable pore size and their application for improved delivery of a water-insoluble drug. J. Colloid Interf. Sci. **363**, 410–417 (2011)

Huang, X., Young, N.P., Townley, H.E.: Characterization and comparison of mesoporous silica particles for optimized drug delivery. Nanomater. Nanotechnol. **4**, 1–15 (2014)

Huang, Y., Garcia-Bennett, A.E.: Equilibrium and kinetic study of l- and d-valine adsorption in supramolecular-templated chiral mesoporous materials. Molecules **26**(2), 338 (2021)

Hwang, N., Barron, A.R.: BET surface area analysis of nanoparticles. Open Stax-CNX Module **m38278**, 1–11 (2011)

Ishii, Y., Nishiwaki, Y., Al-zubaidi, A., Kawasaki, S.: Pore size determination in ordered mesoporous materials using powder x-ray diffraction. J. Phys. Chem. C **117**(35), 18120–18130 (2013)

Iza, M., Woerly, S., Danumah, C., Kaliaguine, S., Bousmina, M.: Determination of pore size distribution for mesoporous materials and polymeric gels by means of DSC measurements: thermoporometry. Polymer **41**(15), 5885–5893 (2000)

Janitabar-Darzi, S., Mahjoub, A.R., Nilchi, A.: Investigation of structural, optical and photocatalytic properties of mesoporous TiO_2 thin film synthesized by sol–gel templating technique. Physica e: Low-Dimens. Syst. Nanostruct. **42**(2), 176–181 (2009)

Ke, J., Wang, Y., Wang, L., Yang, B., Gou, K., Qin, Y., Li. S., Li, H.: Synthesis and characterization of core-shell mesoporous silica nanoparticles with various shell thickness as indomethacin carriers: In vitro and in vivo evaluation. Micropor. Mesopor. Mater. **297**, 110043 (2020)

Kirkpatrick, R.J.: MAS NMR spectroscopy of minerals and glasses (Chap. 9). In: Berlin FC (ed) Spectroscopic Methods in Mineralogy and Geology. De Gruyter, Boston, pp. 341–404 (2018)

Kresge, C.T., Leonowicz, M.E., Roth, W.J., Vartuli, J.C., Beck, J.S.: Ordered mesoporous molecular sieves synthesized by a liquid-crystal template mechanism. Nature **359**(6397), 710–712 (1992)

Li, H., Zhu, S., Wen, Z., Wang, R.: Preparation, structural characterization, and electrochemical properties of chemically modified mesoporous carbon. Micropor. Mesopor. Mater. **96**(1–3), 357–362 (2006)

Li, Z., Rieg, C., Beurer, A.K., Benz, M., Bender, J., Schneck, C., Traa, Y., Dyballa, M., Hunger, M.: Effect of aluminum and sodium on the sorption of water and methanol in microporous MFI-type zeolites and mesoporous SBA-15 materials. Adsorption **27**(1), 49–68 (2021)

Liu, X., Chang, F., Xu, L., Yang, Y., Tian, P., Qu, L., Liu, Z.: Preparation of ordered carbon/silica hybrid mesoporous materials with specific pore size expansion. Micropor. Mesopor. Mater. **79**(1–3), 269–273 (2005)

Macdonald, H.: Geologic puzzles: Morrison formation. Retrieved on 14 May 2021 from http://serc.carleton.edu/introgeo/interactive/examples/morrisonpuzzle.html (2004)

Merck: Properties and applications of mesoporous materials. AZoM. Retrieved on 14 May 2021 from https://www.azom.com/article.aspx?ArticleID=19977 (2021)

Morey, M.S., O'Brien, S., Schwarz, S., Stucky, G.D.: Hydrothermal and post synthesis surface modification of cubic, MCM-48, and ultra large pore SBA-15 mesoporous silica with titanium. Chem. Mater. **12**, 898–911 (2000)

Morsi, R.E., Mohamed, R. S.: Nanostructured mesoporous silica: influence of the preparation conditions on the physical-surface properties for efficient organic dye uptake. R. Soc. Open Sci. **5**(3), 172021 (2018)

Nguyen, Q., Yen, N.T., Hau, N. D., Tran, H. L.: Synthesis and characterization of mesoporous silica SBA-15 and ZnO/SBA-15 photocatalytic materials from the ash of brickyards. J. Chem. **2020**, 1–8 (2020)

Otero, R., Esquivel, D., Ulibarri, M.A., Romero-Salguero, F.J., Van Der Voort, P., Fernández, J.M.: Mesoporous phenolic resin and mesoporous carbon for the removal of S-Metolachlor and Bentazon herbicides. Chem. Eng. J. **251**, 92–101 (2014)

Pierella, L.B., Renzini, S., Anunziata, O.A.: Catalytic degradation of high density polyethylene over microporous and mesoporous materials. Micropor. Mesopor. Mater. **81**(1–3), 155–159 (2005)

Prime, R.B., Bair, H.E., Vyazovkin, S., Gallagher, P.K., Riga, A.: Thermogravimetric analysis (TGA). In: Menczel, J.D., Prime, R.D. (ed.) Thermal Analysis of Polymers: Fundamentals and Applications. Wiley, USA, pp. 241–317 (2009)

Purnawira, B., Purwaningsih, H., Ervianto, Y., Pratiwi, V. M., Susanti, D., Rochiem, R., Purniawan, A.: Synthesis and characterization of mesoporous silica nanoparticles (MSNp) MCM 41 from natural waste rice husk. In: IOP Conference Series: Mater. Sci. Eng. **541** (1), 012018 (2019)

Qin, J., Li, B., Yan, D.: Synthesis, characterization and catalytic performance of well-ordered crystalline heteroatom mesoporous MCM-41. Curr. Comput.-Aided Drug Des. **7**(4), 89 (2017)

Qiu, P., Zhao, T., Fang, Y., Zhu, G., Zhu, X., Yang, J., Li, X., Jiang, W., Wang, L., Luo, W.: Pushing the limit of ordered mesoporous materials *via* 2D self-assembly for energy conversion and storage. Adv. Funct. Mater. **31**(7), 2007496 (2021)

Rameli, N., Jumbri, K., Wahab, R. A., Ramli, A., Huyop, F.: Synthesis and characterization of mesoporous silica nanoparticles using ionic liquids as a template. J. Phys. Conference Series, IOP Publishing, **1123**(1), 012068 (2018)

Reif, B., Ashbrook, S.E., Emsley, L., Hong, M.: Solid-state NMR spectroscopy. Nat. Rev. Methods Primers **1**(1), 1–23 (2021)

Saadatkhah, N., Carillo Garcia, A., Ackermann, S., Leclerc, P., Latifi, M., Samih, S., Patience, G.S., Chaouki, J.: Experimental methods in chemical engineering: thermogravimetric analysis—TGA. Can. J. Chem. Eng. **98**(1), 34–43 (2020)

Sing, K.S.: Obituary: Stephen Brunauer (1903–1986). Langmuir **3**(1), 2–3 (1987)

Širc, J., Hobzova, R., Kostina, N., Munzarová, M., Juklíčková, M., Lhotka, M., Kubinová, Š., Zajícová, A., Michálek, J.: Morphological characterization of nanofibers: methods and application in practice. J. Nanomater. **2012**, 327369 (2012)

Thahir, R., Wahab, A.W., La Nafie, N., Raya, I.: Synthesis of high surface area mesoporous silica SBA-15 by adjusting hydrothermal treatment time and the amount of polyvinyl alcohol. Open Chem. **17**(1), 963–971 (2019)

Trzeciak, K., Kaźmierski, S., Drużbicki, K., Potrzebowski, M.J.: Mapping of guest localization in mesoporous silica particles by solid-state NMR and *Ab Initio* modeling: new insights into benzoic acid and p-fluorobenzoic acid embedded in MCM-41 via ball milling. J. Phys. Chem. C **125**, 18, 10096–10109 (2021)

Wang, X., Chen, S., Sun, J., Zhang, D., Yan, Z., Xu, X., Song, J.: Synthesis of large pore sized mesoporous carbon using alumina-templated strategy for high-performance RhB removal. Micropor. Mesopor. Mater. **318**, 110993 (2021)

Williams, D.B., Carter, C.B.: The transmission electron microscope. In: Transmission Electron Microscopy. Springer, Boston, pp. 3–32 (2009)

Yanagisawa, T., Shimizu, T., Kuroda, K., Kato, C.: The preparation of alkyltriinethylaininonium–kaneinite complexes and their conversion to microporous materials. Bull. Chem. Soc. Japan **63**(4), 988–992 (1990)

Zhang, L., Jin, L., Liu, B., He, J.: Templated growth of crystalline mesoporous materials: from soft/hard templates to colloidal templates. Frontiers Chem. **7**, 22 (2019)

Zhang, T., He, W., Zhang, W., Wang, T., Li, P., Sun, Z., Yu, X.: Designing composite solid-state electrolytes for high performance lithium ion or lithium metal batteries. Chem. Sci. **11**(33), 8686–8707 (2020)

Role of Mesoporous Silica Nanoparticles as Drug Carriers: Evaluation of Diverse Mesoporous Material Nanoparticles as Potential Host for Various Applications

Sadhana Rajput, Nasir Vadia, and Mohit Mahajan

Abstract Effective treatment of patients suffering from fatal diseases such as cancer, AIDS, tuberculosis, etc., has always been a challenge, and new approaches are continuously explored so as to prevent or reduce the toxic side effects of such drugs. The exploration of silica-based mesoporous nanoparticles as a host for better therapeutic action of drugs has provided some very positive and encouraging outcomes. The characteristics of these mesoporous materials needed for maximum loading of the drug and then the subsequent release of drug from the host can give the idea about the suitability of these materials as drug carriers. The manuscript describes various morphological properties of mesoporous materials which can favour the maximum drug loading in the mesopores. The subsequent release of the drug trapped from the mesopores can be tailored to a specific site release (targeted drug delivery), release at a slow rate (sustained drug delivery) or fast or immediate release so that it can show maximum biological activity. Most of the studies have shown great potential of these mesoporous materials as a carrier to carry sufficient amount of the drug and release it in a desired manner. The review presents the current status of the applications of mesoporous materials as host for drug molecules.

Keywords Mesoporous nanoparticles · Drug trapping · Drug release

1 Introduction

Since the first nanoparticle was used as drug delivery carrier in the 1960s, immense research has been undertaken to explore new avenues for the development and use of nanoparticles as drug carriers. The great advantage of nanomaterial includes the possibilities of material engineering for the enhanced dissolution, targeted delivery and controlled release of different therapeutically active agents. The major concern of the modern drug delivery system is to minimize side effects, dose and dosage

S. Rajput (✉) · M. Mahajan
Pharmacy Department, The M. S. University of Baroda, Vadodara, Gujarat, India

N. Vadia
Department of Pharmaceutical Sciences, Saurashtra University, Rajkot, Gujarat, India

frequency. Generally, the material between 1 and 100 nm is classified as a nanomaterial. Owing to their size, they can transport active agents freely in systemic circulation as compared to conventional dosage forms. In the initial phase of nanoparticles-based drug delivery development, lipid-based nanoparticles were explored, and at the current time, FDA has approved liposomes and micelles form of lipid-based nanoparticles-based drug delivery systems (Shi et al. 2008). Various nanotechnology-based drug delivery systems (Suri et al. 2007) have been explored like polymeric nanoparticles, metallic nanoparticles, dendrimers, polymeric nanoparticles, magnetic nanoparticles, inorganic nanoparticles, organic nanocrystals, liposomes, biological nanocarrier, carbon nanotubes, quantum dots, etc., and have been reported in the literature as a drug delivery system not only for the treatment, but also for the prevention and diagnosis of different diseases and physiological conditions (Patra et al. 2018). The use of mesoporous material is a newly explored approach to the nanotechnology-based drug delivery system. The porous characteristic structure of silica (SiO_2) along with porous hollow structure, tunable size, high pore volume, high surface area, uniform pore size and biocompatibility make mesoporous material a potential drug carrier (Narayan et al. 2018; Vadia and Rajput 2019). In general, porous structured materials can be classified as macroporous, mesoporous and microporous (Pattnaik and Swain 2018). Their structures and pore size are presented in Fig. 1.

The primitive mesoporous structure and surface-functionalized mesoporous structure provide better opportunities as a drug carrier through the attachment of the functional groups of drug substance to the mesoporous material. The presence of numerous silanol groups on mesoporous material provides a free, active site to modify or change the properties of these materials according to the desirable release or delivery pattern of the pharmacologically active substance. For an instance, mesoporous material satisfies the polypharmaceutics approach where many molecules including drugs, genes, enzymes, proteins, etc., can be accommodated and extract their desired properties as a drug delivery system (Fig. 2).

2   Chemistry and Synthesis of Mesoporous Material

Porous solids with ordered structures have been created using a variety of materials, the most common of which is silica. According to IUPAC, microporous structures have pore diameters of less than 2 nm, whereas mesoporous materials have pore diameters ranging from 2 to 50 nm. The first-time innovative process as proposed by Kresge et al. presented aluminosilicates-mesoporous materials and this being synthesized with the use of a surfactant as a structure-directing agent and resulted in the creation of porous materials with uniform pore diameters in the range of 2–50 nm (Kresge et al. 1992). This discovery transformed the field of mesoporous materials. Mesoporous silica is appealing because of its consistent pore diameter, huge surface area, great chemical and thermal stability, and ability to be functionalized. Mesoporous materials are useful for a variety of applications, including catalysis (Taguchi et al. 2005), chemical separations (Kim et al. 2015) and biomedical applications
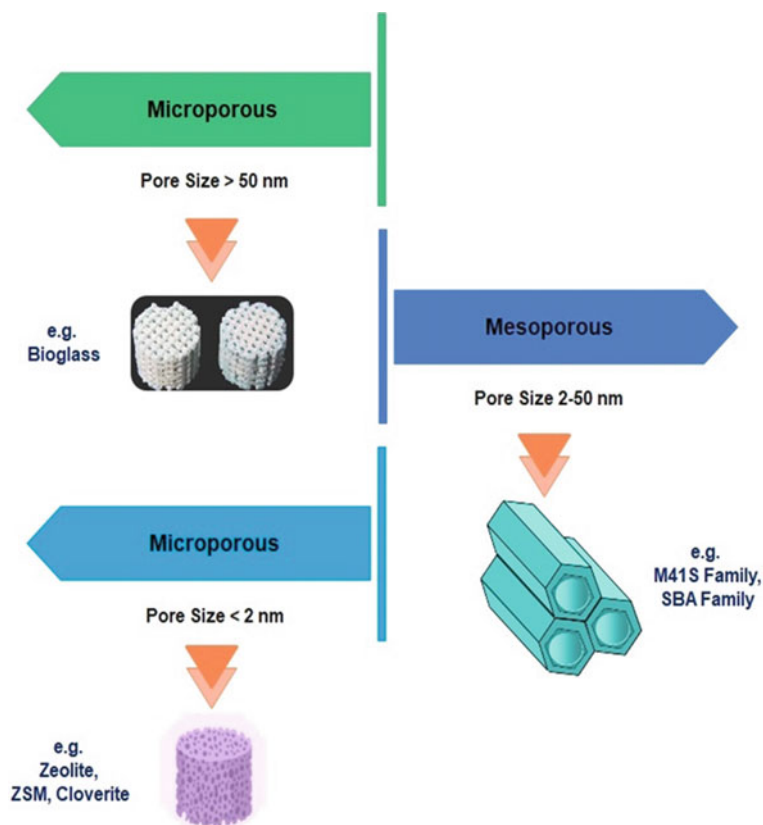
Fig. 1 Classification of porous material

such as bone tissue engineering implants and drug delivery (Li et al. 2012). Mesoporous materials grafted in a variety of morphologies, including thin films (Regev et al. 1999), powders (Vadia and Rajput 2019), and micro- and nanoparticles of various shapes (Vadia and Rajput 2019). Mesoporous material can be disordered or ordered in a mesostructure, according to IUPAC. In crystalline inorganic materials, the mesoporous structure significantly reduces the number of lattice units, altering the solid-state chemistry. Several patents have been filed in the late nineties (Chiola et al. 1971; Page et al.; Hanns et al. 1970); majority of them have used the concept of the Stöber process (Stöber et al. 1968) for synthesis. Afterwards, researchers in Japan independently synthesized mesoporous silica nanoparticles (MSNs) in 1990. Mobil Crystalline Materials, or MCM-41, were later developed at Mobil Corporation laboratories. The initial synthetic methods did not allow for control over the quality of the generated secondary level of porosity. Only by using quaternary ammonium, cations and silanization agents during the synthesis were the materials able to exhibit true hierarchical porosity and improved textural properties. The majority of ordered mesoporous materials have a two-dimensionally ordered array of cylindrical pores
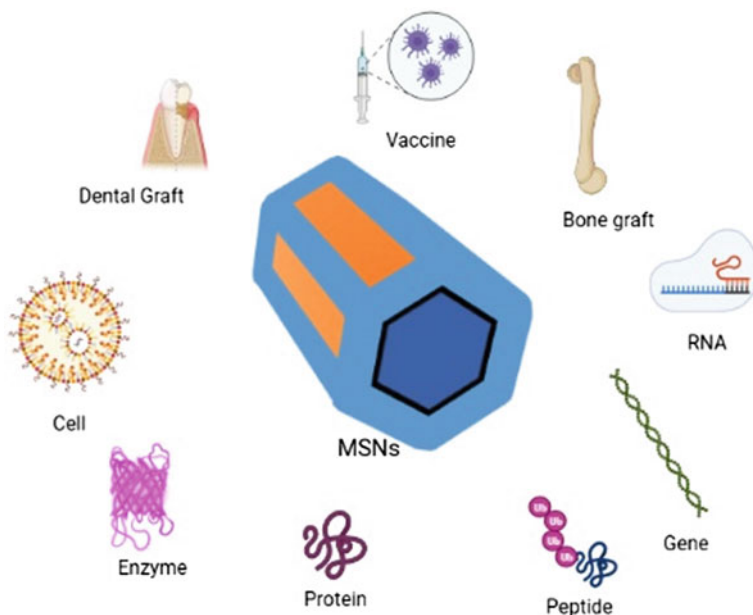
Fig. 2 Polypharmaceutics approach of mesoporous material

of uniform size disposed of parallel to each other and separated by thin walls (Vadia and Rajput 2019). Series of inorganic mesostructure, like MSU, MCM-41, MCM-48, TUD, HMS, SBA, etc., have been synthesized with different templating schemes. Among different such materials, some are listed in Table 1 with their structural characteristics.

Table 1 Structural characteristics different mesoporous material

Mesoporous material	Structural property
MCM-41	Hexagonal 1D
MCM-48	Bicontinuous 3D
MCM-50	Lamellar
SBA-11	Cubic-3D
SBA-12	Hexagonal 3D
SBA-15	Hexagonal 1D
SBA-16	Cage like arrangement
MSU	Hexagonal 2D
HMS	Hexagonal
FDU	Large pore 3D
KIT-6	Cubic-3D
COK	Hexagonal

Numerous reports are available in the literature suggesting various synthesis methods and mechanisms. Broadly porous materials can be categorized based on pore geometry and their frame structure. In general, mesoporous materials are synthesized through inorganic, organic, or a mixture of organic and inorganic elements or compounds. MCM-41, MCM-48, MCM-50, SBA-15, HMS, OMS, MCF, FSM, KIT, AMS, MSU and TUD are some of the most explored and used mesoporous materials (Vadia and Rajput 2011). Surfactant-guided self-assembly fabrication is the most common method for producing mesoporous materials with a particular chemical composition, structure and function. The formation of mesostructure is influenced by a variety of forces, including non-covalent and weak interactions such as hydrogen bonding, Van der Waals forces and electrostatic interactions between surfactant molecules. The design of the synthesis conditions used for different mesoporous materials determines the fundamental difference between them. These synthesis conditions produce mesoporous materials with a variety of physicochemical properties, including the form of a mesostructured system, surface area, wall thickness, pore characteristics, pore distribution, pore diameter and pore volume (Vadia and Rajput 2019, 2011). Mesoporous silica nanoparticles can be made by using a surfactant in an aqueous solution that can be charged or neutral in the environment. The formation of mesostructure occurs when an ester of ortho silicic acid, i.e. silicates is polymerized by a surfactant. The controlling parameters determining the pore size, surface area and overall morphology of the developed material are variables such as interaction rate, hydrolysis rate, polymerization rate and condensation of silica source. New strategies and modification techniques are constantly being investigated for the development of mesoporous materials with varying properties. Liquid crystal templating mechanism, charge density matching mechanism, folded sheet mechanism, silica tropic liquid crystal mechanism (Vadia and Rajput 2019) and other commonly used conventional methods are listed below. Different mechanisms produce materials with varying morphologies, some of which are listed in Table 2.

For the synthesis of mesoporous materials, a specific surfactant is used as a structure guiding agent, followed by polycondensation with various silica sources. The nature of the synthesis conditions used for distinct mesoporous materials determines the basic difference between them. These synthesis conditions produce mesoporous materials with various physiochemical properties, such as the type of mesostructure framework, surface area, wall thickness and pore characteristics, such as pore distribution, pore diameter and pore volume (Zainal et al. 2013). The composition and chemical nature of the surfactant, as well as many parameters such as surfactant concentration, pH, temperature, the presence of additives, etc., influence the mesoporosity produced by the liquid crystal mechanism. The surfactant is removed by heat degradation or solvent extraction once the silica source has condensed around the micelles in the synthetic process. The elimination of surfactants leads to the formation of a mesostructure framework. The developed materials generally have a surface area of more than 700 m^2/g and absorption capabilities of 0.7 cm^3/g and higher (Xia et al. 2010; Othaman et al. 2012). According to the structural requirements of the material, several inorganic mesostructures have been produced using various surfactants and experimental settings (Tanev et al. 1995; Bagshaw et al. 1995). These materials are

Table 2 Common synthesis mechanism/approach of mesoporous material

Synthesis mechanism	Driving force	Characteristic of material
Liquid crystal	Hydrocarbon chain length of the surfactant	Hexagonal, cubic and lamellar structures
Charge density matching	Electrostatic interaction between the anionic silicates and the cationic surfactant	Hexagonal mesostructure
Folded sheet mechanism	Interaction between the cationic surfactant and intercalated silicate phases at higher pH	A highly porous hexagonal structure
Silica tropic liquid crystals	Organization of inorganic and organic molecular species into a 3D structure	3D porous structure
Soft template (Endo template)	Use of organic molecule	Mesoporous material with good shape, size and characteristic
Hard template (Exo template)	Use of inorganic molecule	Mesoporous material with irregular and non-uniform morphology
Quenching approach	The reaction was quenched at neutral pH	Mesoporous material with a larger size
Evaporation-induced self-assembly	All the reactants undergo concentration changes during evaporation	Functionalized mesoporous material with high loading capacity

named after the firm or research organization or group that first introduced them or after the material's structural features (Fig. 3).

For the development of materials with various mesoporous properties, a variety of ionic and non-ionic surfactants have been utilized. Alkyl ammonium surfactants
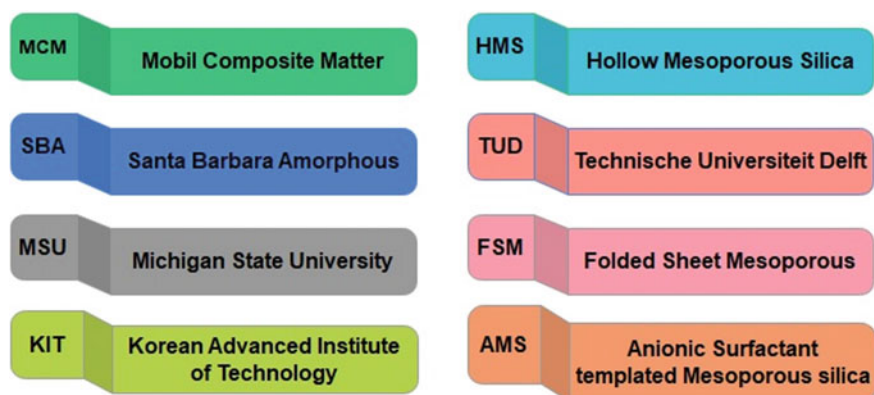
Fig. 3 Different mesoporous materials with their full name

and tetraethyl orthosilicate were used to create mesoporous materials having hexagonal, cubic and lamellar mesostructure and various morphologies, such as MCM-41, MCM-48 and MCM-50 (Kresge et al. 1992). The first SBA type material (Zhao et al. 1998) with different mesostructure and identical porosity properties to the MCM-type materials was made using cationic surfactants in an acidic solution. Non-ionic surfactants like polypropylene oxide and polyethylene oxide are used to manufacture Santa Barbara University type mesoporous materials like SBA-15 and SBA-16 with bigger pore sizes and thicker walls in acidic media. Other mesoporous materials known as MSU-X (Prouzet et al. 2002) were synthesized with neutral pH and non-ionic surfactants; the resulting mesostructure is more unstructured, with pore diameters and wall thicknesses of 2–8 nm and 1.5–4 nm, respectively. TUD-1 (Jansen et al. 2001), a member of the porous silica group, the main distinction between TUD-1 and the other porous silicas is that the TUD-1 silica production technique is completely surfactant-free. Pore formation is triggered by collections of smaller molecules rather than micelles or big chemical compounds. As a result, the procedure is cost-effective. Cu, Zn, Al, B, Ga, Fe, Cr, Ti, V Sn and other heteroatoms have been incorporated into mesoporous frame structures for various applications (Shylesh et al. 2008). The template synthesis method for preparing mesoporous silica has been extended to the creation of various mesoporous metal oxides.

3 Functionalization of Mesoporous Material

The wide range of possibilities for structural modification and/or chemical functionalization of the silanol groups, which are present on the internal or external surface of the material by various organic groups, is a cornerstone in the development of mesoporous silica as drug delivery systems (Vadia and Rajput 2011; Vallet-Regi et al. 2006, 2007). Because of the possibility of functionalization, mesoporous material has become a globally accepted material for a wide range of applications, including drug delivery systems. In general, the three most widely accepted and used methods for functionalization are co-condensation (one-pot synthesis) (Abboud et al. 2018; Yokoi et al. 2004; Burkett et al. 1996), grafting (post-synthesis modification) (Abboud et al. 2018; Yokoi et al. 2004; Burkett et al. 1996; Nhavene et al. 2018) and imprint coating (Moorthy et al. 2013; Dai et al. 1999).

The direct synthesis method is another name for the co-condensation method. Mesostructured silica material can be created using this method by co-condensing tetra alkoxy silanes with terminal tri-alkoxy organosilanes in the presence of structure-directing agents, most commonly a surfactant. Organically modified silica can be prepared by selecting structure-directing agents from the synthesis of pure mesoporous silica phases in such a way that the organic functionalities project into the pores. The surfactant is then removed using a suitable technique, such as solvent extraction or calcination. When compared to the grafting process, the organic units in direct synthesis are more uniformly distributed. However, the co-condensation method has some drawbacks, such as the fact that the degree of mesoporosity

decreases as the concentration of organosilanes in the reaction mixture increases, which can result in a completely disordered material. Furthermore, a greater extent of incorporated organic groups can result in a decrease in the pore diameter, pore volume and specific surface areas of the newly formed material. The process of functionalizing various groups or atoms within the interior pore of mesoporous materials is represented by grafting. These mesoporous materials are typically created through the post-synthesis grafting method. After the surfactant is removed, the mesopore wall surface of the prefabricated inorganic mesoporous materials is modified with organosilane compounds in this method. Because mesoporous materials contain silanol (Si–OH) groups, they facilitate the attachment of various organic functional groups to the mesoporous material's surface. The most common surface modification reactions are silylation and esterification. Silylation occurs on all silica surface groups, including free and/or geminal silanols. However, it was revealed that silanol groups attached via hydrogen bonds are less accessible for surface modification, which could be due to the formation of hydrophilic networks. To avoid self-condensation of the precursors in the presence of water molecules, the host materials should be completely dried before adding the modification precursor in the post-synthesis grafting method. Polymerization of metal alkoxides is carried out in the presence of a structure-directing agent in the imprint coating method, resulting in the formation of mesoporous materials with relatively large surface areas and uniform mesostructure. These materials with a large surface area are widely used in catalysis and the preparation of chromatographic resins. Selecting a target molecule as a template, incorporating the template into rigid solid networks through in situ copolymerizations and removing the template to leave cavities with a predetermined number and arrangement of ligands that selectively rebind to the target molecule at a later stage are all steps in the imprinting process. This imprinted mesoporous material is especially useful for separating racemic mixes and metal cation mixes. This technique has some limitations when compared to other known methods due to the unfavourable kinetics of the sorption/desorption process. Furthermore, because of the non homogeneous cavity formation, this process is being explored further in un disordered polymer matrices, which limits the selectivity of the final imprinted materials. Surface imprinting has been developed to address such molecular imprinting concerns. Imprint coating is used to introduce the functional group of interest onto the mesopore surface of a mesoporous material in this method. The covering of the mesopore surface with ligand complexes is a key characteristic of this approach. Metal ions, rather than free ligands, are the objective of this approach (Dai et al. 1999).

The addition of amino groups to mesoporous silica allows it to be used as an adsorbent, drug delivery system and solid base catalyst. Carbon dioxide, heavy metals and oxoanions adsorption, heterogeneous catalysis of epoxidation reactions, the creation of carbon–carbon bonds and the administration of salicylic acid are few examples. Mercurium and thiol groups (SH) have a strong bond (II). Some silicas that have been functionalized with thiol, thiourea or thioether have a high Hg^{2+} adsorption capability and good selectivity. Pollutant removal is another major application for functionalized materials; heavy metal ions and metalloids, inorganic anions, phenolic

chemicals, polyaromatic hydrocarbons, insecticides and dyes are the most targeted pollutants. Inorganic groups including metal oxides, complexes and nanoparticles, as well as more complex systems like clusters, polymers and enzymes, can be added to mesoporous silica. Functionalization can alter the host's physicochemical properties, such as hydrophobicity and, hence, have a significant impact on the guest molecule's adsorption capabilities. The organic modification should be chosen based on the medication or biomolecule to be adsorbed, as well as the guest molecule's functional groups. Different strategies can be used to control medication release from the mesopores. For medication delivery applications, functionalization is extremely beneficial. The drug diffusion kinetics can be improved controlled by modifying the carrier chemically with groups that interact with biologically active compounds (Wang et al. 2009). Furthermore, multifunctional mesoporous silica composites with magnetic or luminous qualities can be used to direct the medicine to the target place. The preferred strategy is to enhance drug surface contact, which can be accomplished via surface functionalization with chemical groups capable of forming ionic or ester interactions with drug molecules (Bharti et al. 2015). The functionalization of surface silanol groups by some hydrophobic species is another commonly utilized method to produce controlled-release medication formulations. This mechanism hampered drug release by preventing drug molecules from contacting the aqueous media. As a result, aqueous phase penetration is avoided, resulting in poor wettability, which hinders diffusion from the carrier. Functionalization provides a fantastic platform for targeted delivery systems nowadays; interactions with biomolecules, cells, and tissues allow for controlled drug release and modify the drug molecules' safety profile. Internalization routes may be influenced by surface functionalization, particle type and size, which may have an impact on cytotoxicity. Furthermore, biological interactions, bioavailability difficulties, cellular migration and auto-immune surveillance are all influenced by surface-functionalized mesoporous material (Vadia and Rajput 2019). Taking all the factors into account, personalized pharmacokinetic release profiles, improved solubility and bioavailability, target delivery and, hence, improved therapeutic efficacy with the fewest possible side effects will be conceivable. The overall strategy to develop a formulation with mesoporous nanoparticles is presented in Fig. 4.

4   Methods of Drug Loading and Release of Drugs from MSNs

The significant loading capacity of MSNs due to the large pore volume and surface engineering qualities both on the external and internal surface for improved drug targeting makes it a typically used carrier for drug delivery. The pore size of a mesoporous material is an important tool because it plays a role in drug entrapment and can be employed as a drug delivery system. The drug is frequently entrapped within the pores by soaking/impregnating the mesoporous material in a highly concentrated
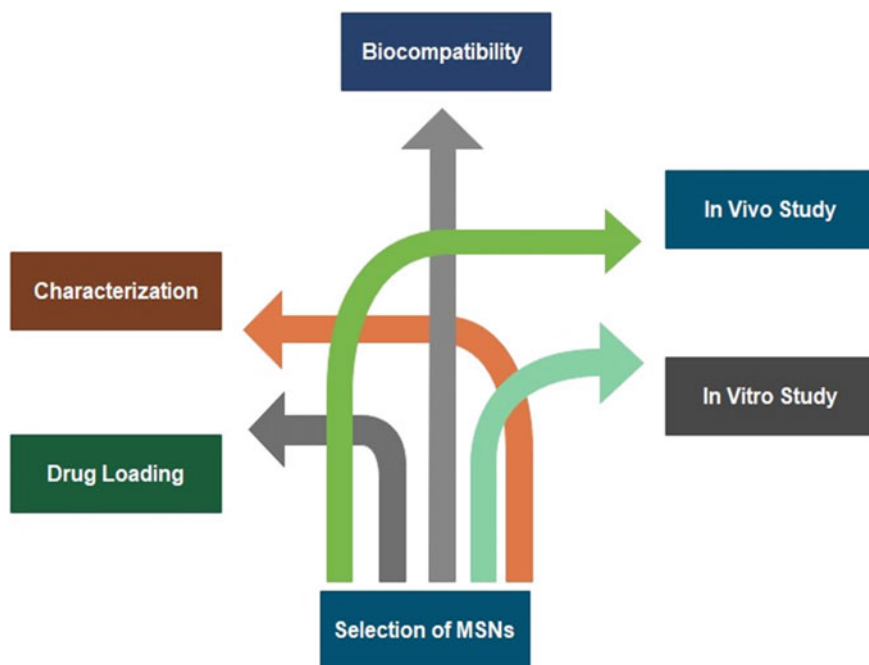
Fig. 4 Strategy for formulation development with mesoporous nanoparticles

drug solution (nearly saturated solution). The different factors governing the loading process are presented in Fig. 5.

The size of the molecule to be housed is determined by the diameter of the mesopore, and therefore, the size of the molecule to be selected for confinement must also be considered for suitable material selection. The drug would be trapped in the inner half of the mesopores if the molecule were smaller than the pore cavity. When the drug molecule is larger than the diameter of the mesopores, however, adsorption occurs solely on the exterior surface. The behaviour of drug molecules confined in pores differs from that of drug molecules in bulk. Their dynamical and thermodynamic properties will be altered once they are entrapped within the pores. Mesoporous materials with slightly larger mesopore sizes than drug molecule sizes should be explored for successful drug loading. For facile passage of drug molecules to mesopores, a pore-to-drug-molecule size ratio greater than one is ideal. Changing and manipulating different synthesis circumstances, such as the right selection of structure-directing agent, the addition of some auxiliary chemicals, and, most crucially, the chain length of the surfactant, may easily customize pore size from a single nanometre to several tens of nanometres (Kresge et al. 1992; Fan et al. 2003). The mesoporous material contains numerous silanol groups that will react with the drug's functional groups, and the strength of the interaction will have a big impact on the drug's release pattern (Fig. 7). The adsorptive characteristics of mesoporous material influence the drug
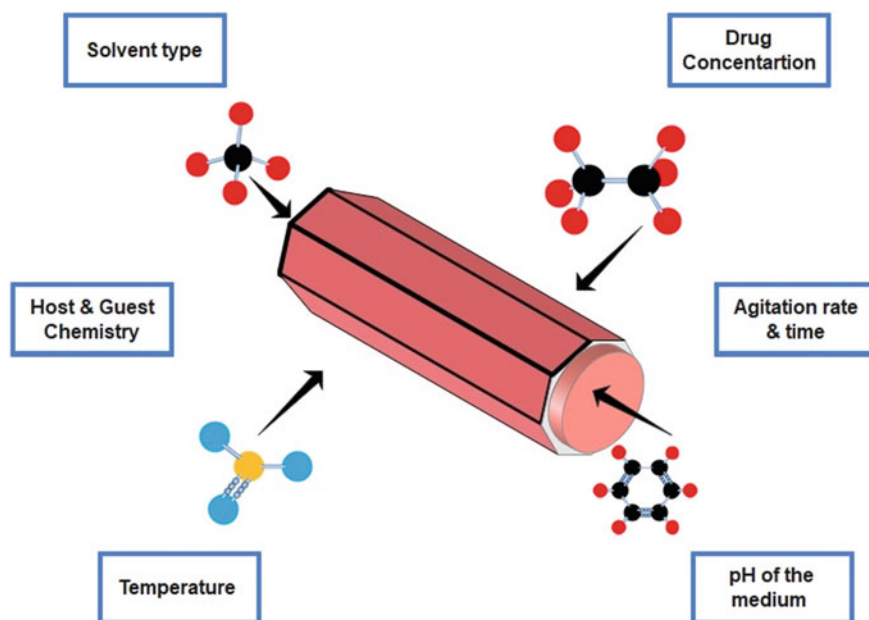
Fig. 5 Factors affecting drug loading process

loading process in the mesoporous system. As a result, the surface property of meso-
porous material is a critical parameter for drug adsorption and loading. The greater
surface area will facilitate the interaction time between the host and guest molecules.

Size, morphology, texture and porosity of mesoporous material all affect an overall
surface area. Emmett and Edward Teller devised a formula for calculating surface
area. Brunauer–Emmett–Teller (BET) is a calculation that measures the surface area
by measuring the adsorption of non-polar gases like nitrogen or argon (Brunauer et al.
1938). Mesoporous materials have an advantage over conventional drug carriers in
that drug molecules are not only entrapped in mesopores, but also adsorbed onto the
silica surface due to their high surface area. A large surface area allows for greater
drug adsorption potential. As previously stated, mesoporous materials have a high
number of silanol groups in their structure (both within mesopores and on the surface)
and are sensitive to chemical modification with a wide range of organic groups via the
functionalization process. This functionalization provides for better drug loading and
release control, and it can be used for either immediate or regulated active molecule
release. The functional groups of the molecules or substance of therapeutic interest
to be adsorbed would determine the pore and surface silanol group modification. By
increasing/reducing the surface area or altering the surface–drug affinity, it is feasible
to increase the payload and modify/control the drug's release pattern (Zhanga et al.
2020). The amount of drug entrapped in mesopores can be calculated by the following
equation.

% Entrapment efficiency $=$ Amount of drug entrapped/Total amount of drug added
$$* \ 100 \tag{1}$$

Encapsulation of pharmaceuticals with a high payload is possible owing to the massive surface area and high pore capacity. For high-volume compounds like proteins, antibiotics, amino acids and biomolecules, pore volume is critical. To evaluate pore size distribution, the Barrett–Joyner–Halenda (BJH) method is often used (Barrett et al. 1951). The BJH method of adsorption/desorption implies a theory comparable to the BET of the adsorption/desorption process. When saturation is reached and the adsorptive gas has filled all mesopores, the BJH is determined. Continuous, repeated and consecutive impregnations that result in total pore volume filling can achieve a high payload of drug molecules. The repeated impregnations enhanced the amount of drug loaded by promoting intermolecular drug-drug interactions.

Through the attractive interaction with the inside mesopore walls, the molecules are trapped inside the pores. It is reasonable to assume that the opposite process, namely the release of the adsorbed medication, will similarly be affected by the material surface area. Indeed, various tests have shown that when the surface area of MSNs is remarkably high, there is high molecule retention and, as a result, a slower drug release when compared to materials with smaller surface areas. The increased interactions of the drug molecules with a larger surface area accessible cause a delay in the drug's release kinetics. For large molecules, pore volume is a critical factor (Vallet-Regi et al. 2006). The available area to load therapeutic molecules is determined by the pore volume. The higher the pore volume, the larger the load, which has an impact on drug release. In the case of a small number of pores, the matrix's channel may become obstructed with drug molecules. The drug retention and release phenomenon are highly influenced by the presence of electrostatic interactions between the drug and the mesoporous host. Another important parameter is the hydrophobicity and lipophilicity of the guest–host system. The mesoporous silica matrix is hydrophilic in concept and does not dissolve in water, but this can change if the material is altered after it has been functionalized (Vallet-Regi et al. 2006, 2007). This characteristic affects the drug's adsorption as well as its release property. The other common factors affecting the release process are presented in Fig. 6.

5   Mesoporous Material as a Potential Drug Carrier

The encapsulation of drugs and pharmaceuticals with a high payload is made possible by the variable pore size, large surface area and high pore volume. Within the pores, the mesoporous channels maintain pharmaceuticals in an amorphous or noncrystalline state, allowing for drug breakdown. Furthermore, the high chemical stability and inert characteristics enable better drug loading and release management (Fig. 7). The important applications area is presented in Fig. 8. The function is
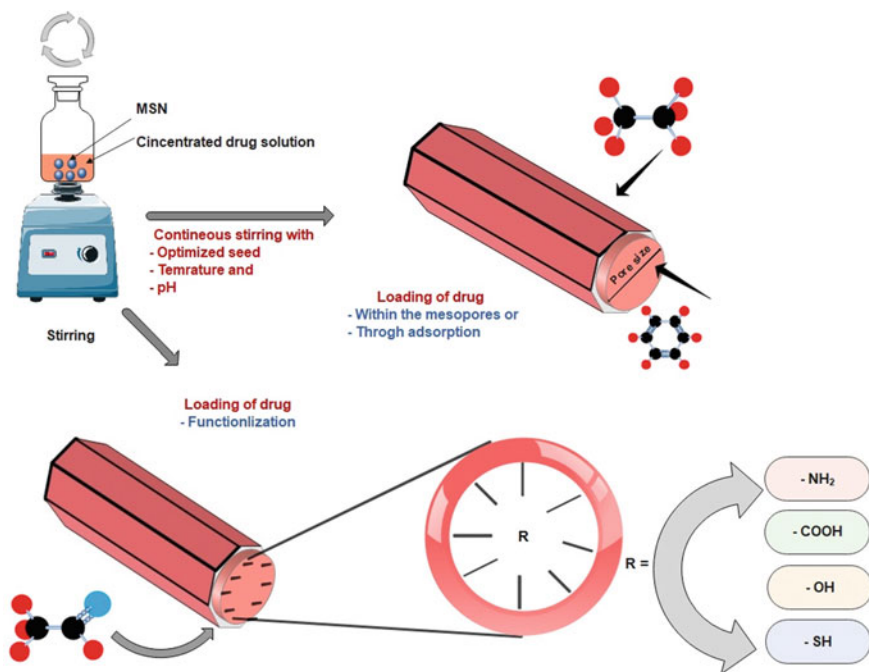
Fig. 6 Drug loading process
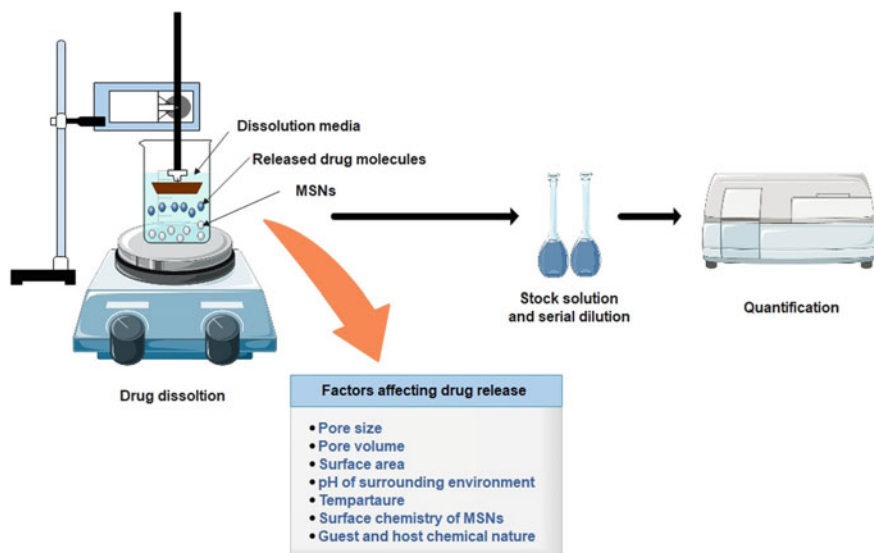
Fig. 7 Drug release process
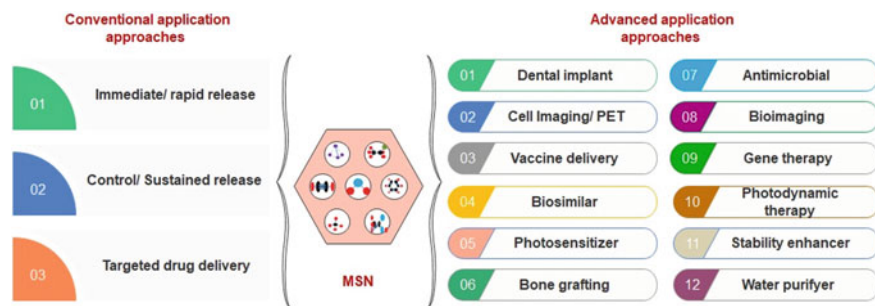
Fig. 8 Application approaches of MSNs

based on two factors: raising the active surface area of the medicinal ingredient and lowering its crystallinity. When molecules are confined in mesopores, their kinetic behaviour differs dramatically from that of molecules in a crystal lattice (Vadia and Rajput 2019).

Mesoporous silica has several important properties that make it useful in drug delivery applications. The small size of the pores confines the space of a drug and engages the effects of surface interactions of the drug molecules and the pore wall. The surface chemistry of the pore walls and the size of the pores can be easily changed and controlled. Increased or sustained release of the loaded drug can be obtained depending on the size and surface chemistry of the pores. Because purely siliceous mesoporous materials are biocompatible and even bioactive in some cases. Numerous studies have shown that mesoporous materials can be used as pharmaceutical carrier systems for both immediate and controlled drug release. Because of their larger pores and well-defined structure, mesoporous materials can be used as medical devices. Depending on the synthesis conditions, they have high surface areas and ordered mesopores. Higher surface area and pore size will favour drug loading. Grafting/functionalization of mesoporous silica alters pore size and the interaction between drug and substrate, resulting in lower drug loading and a slower release rate (Vadia and Rajput 2011; Vallet-Regi et al. 2006; Bharti et al. 2015).

Significant advances in the pharmaceutical industry and medicinal chemistry in recent decades have resulted in a comprehensive understanding of the physico-chemical properties of medical substances and the possibility of identifying cellular absorption techniques for effective therapies. Initially, treatments in some conditions, such as chemotherapy for cancer, relied on the use of toxic medications with unwanted side effects and limited beneficial results. Mesoporous silica materials are appealing because of their resistance to heat, pH and mechanical stress, and very small pore sizes and have more potential than other nanocarriers in terms of greater accuracy in the selective loading of various drug molecules and large pore volumes available for drug loading. MSNs are used for the delivery of bioactive compounds, and they may protect against degradation while permitting regulated release, longer blood circulation, enhanced disease targeting and fewer adverse effects (Vadia and Rajput 2019; Bharti et al. 2015; Singh et al. 2018). The applicability of MSNs in
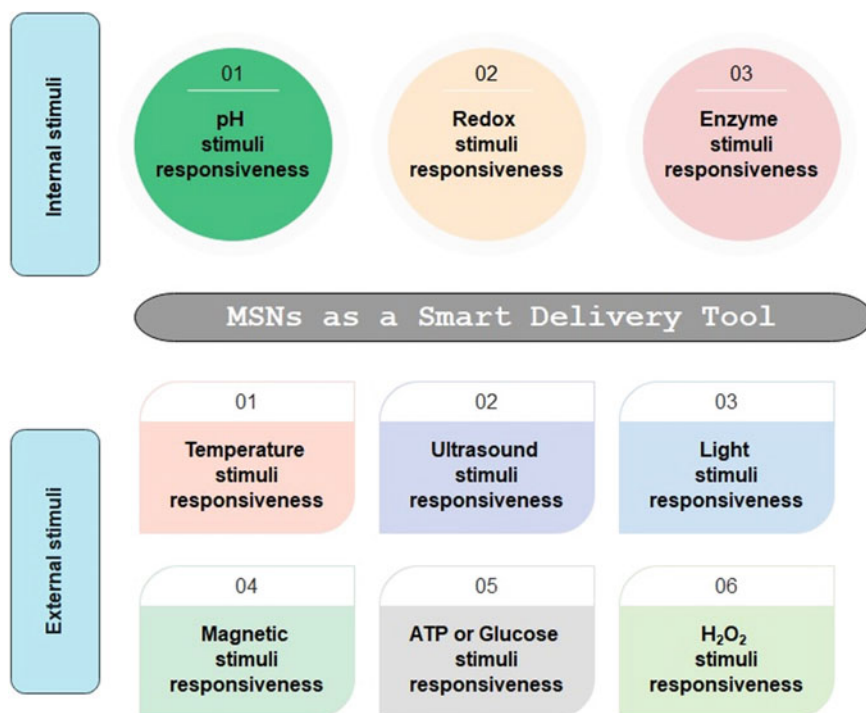
Fig. 9 Application of MSNs as smart drug delivery

the current time for the treatment of cancer and other such diseased conditions is presented in Fig. 9.

Vallet-Regi and colleagues were among the first to investigate the drug release properties of these materials, attempting to extend the release of ibuprofen using MCM-41 as a carrier (Vallet-Regi et al. 2001, 2007). Charnay demonstrated rapid and pH-dependent ibuprofen release from MCM-41 with a pore size of 3.5 nm 142. Later studies demonstrated the high mobility of ibuprofen within the pore system of MCM-41 at room temperature, as well as a weak interaction of ibuprofen with the silica matrix (Charnay et al. 2004). Aiello et al. investigated the use of mesoporous silicate as drug delivery devices. Four anti-inflammatory agents were used: diflunisal, naproxen, ibuprofen and sodium salt. Drug release studies were also carried out at pH levels of 1.1 and 6.8 to simulate gastrointestinal fluids. According to the release data, the matrix impregnated with diflunisal has a high potential as a system for modified drug release (Aiello et al. 2002). Zhu and colleagues have investigated the mesoporous MCM-41 system with water-soluble drug captopril (Zhu et al. 2006). Trewyn et al. presented research on the use of room-temperature ionic liquid to prepare mesoporous silica nanoparticle (MSN) materials with various particle morphologies such as spheres, ellipsoids, rods and tubes (RTIL). The pore morphology was tuned from

MCM-41 hexagonal mesopores to helical channels and wormhole-like porous structures by changing the RTIL template. These materials were then used as controlled-release delivery nanodevices to deliver antibacterial ionic liquids against E. coli K12. The antibacterial activity was proportional to the rate of diffusional release of the pore encapsulated RTIL, which was governed by mesoporous morphology (Trewyn et al. 2007). Jie et al. created biocompatible mesoporous silica nanoparticles containing the fluorescent dye fluorescein isothiocyanate, which offer a potential approach for paclitaxel delivery to cancer cells. They discovered that fluorescent mesoporous nanoparticles (FMSN) are readily absorbed by human cancer cells in this investigation. They also demonstrated that paclitaxel, a hydrophobic anticancer medication, may be stored in FMSN and delivered to human cancer cells, inhibiting their proliferation. These findings allude to FMSN's potential as an anticancer medication delivery mechanism (Jie et al. 2007). Another important application of mesoporous nanoparticles, as represented by Jie et al., is as a dissolution enhancer for the poorly soluble anticancer drug camptothecin, which was successfully entrapped into the pores of FMSN and delivered CPT into a variety of human cancer cells to induce cell death, demonstrating that mesoporous silica nanoparticles (Jie et al. 2007). Sun et al., reported similar findings when preparing MSN for lung cancer therapy, revealing the three-dimensional distribution of the MSN inside the cell (Sun et al. 2008). Shenmin Zhu et al. investigated the utilization of polymer containing mesoporous silica with large pore seize for drug release. They used hydrophobic polyisoprene (PI) in the pores network for free-radical polymerization, and the resultant materials (MCFPI) were examined as drug storage matrices. As model medicines, ibuprofen and vancomycin were loaded onto unmodified MCF and modified MCF. Because of the trap effects caused by polyisoprene chains inside the pores, the adsorption capabilities of these model medicines on MCFPI were found to be higher than those on pure MCF (Shenmin et al. 2009). Kamalakannan et al. reported on the pseudomorphic fabrication of MCM-41 silica spheres. Following surface modification of the mesoporous silica spheres, two silylating agents, noctadecyltrihydridosilane and noctadecyltrimethoxysilane produced varied surface morphology and prepared MCM-41 spheres are well ordered and have almost homogenous mesopores. Some research papers have reported on the post-synthesis treatment, which offers essential information about the surface geometry and morphology of mesopores (Kamalakannan et al. 2008).

6 Applicability of Mesoporous Material for Fast or Immediate Drug Delivery Systems

The mesoporous channels preserve pharmaceuticals in the pores in an amorphous or non-crystalline state, allowing for drug dissolution. Furthermore, the high chemical stability and inert nature enable better drug loading and release management. The function is based on two factors: enhancing the active surface area of the medicinal

ingredient and decreasing its crystallinity (Zhuravlev et al. 2000). When molecules are confined in mesopores, their kinetic behaviour varies considerably from that of molecules in a crystal lattice. The decrease in crystallinity frequently causes problems with stability since the non-crystalline disordered form has a high chemical potential and tends to transition to a crystalline form of a lower energy state. As a result, the contact between the drug molecules and the carrier must be sufficiently stable such that the molecules are neither chemically nor physically changed (Brás et al. 2011). By physically shielding the amorphous drug, the porous carrier inhibits these changes. Furthermore, drug molecule loading into porous particles has been shown to improve permeability. Small pore size has been reported to be a key component in the stabilization of disordered drugs (Horcajada et al. 2004). Because the pores are usually tiny enough to preclude the formation of an ordered crystal structure within them, the loaded substance is forced to remain amorphous, and phase transitions during storage are prohibited. By causing a steric barrier, the carrier structure may help shield the loaded molecule from external assault. This type of protection is especially important for peptides that are susceptible to enzymatic breakdown in the body. Although the mesopores are typically tiny enough to provide adequate protection for the loaded medication, acceptable mass transfer rates can be attained, which is critical in both dissolution and drug loading. Because the diameter of the mesopores is several orders of magnitude larger than the size of the drug molecule, crystallization inside the pores is not completely impossible. Although the medication is usually amorphous, it can also appear as microscopic, nano-sized crystals. The solubility of nanocrystals is significantly greater than that of the bulk substance. As a result, this form is also advantageous in terms of drug absorption, and the product's stability is superior to that of amorphous drugs. To produce drug loading in nanocrystal form, the loading process must be meticulously optimized and controlled (Joshi et al. 2019; Xu et al. 2018a, 2018b; Vadia and Rajput 2012).

7 Applicability of Mesoporous Material for Sustained or Controlled Drug Delivery Systems

Any pharmaceutical dosage form that provides sustained release will have a considerable advantage due to the ability to maintain constant blood concentration for an extended period. Two alternative strategies can be used to create a sustained drug delivery system utilizing mesoporous materials. Sustained drug release can be achieved with unmodified silica by managing the pore size, pore diameter and particle structure of the targeted substance. Modified silica materials, on the other hand, are conjugated to various chemical functional groups, such as organosilanes (Fengyu et al. 2006). Sustained drug release would be feasible for the requisite amount of time due to the interaction between the drug molecules and the functional groups of modified silica materials. Traditional mesoporous materials have been successfully used as long-term drug delivery systems by changing and/or manipulating their

physical-textural properties. The primary characteristics of mesoporous material as a regulated drug delivery system are unconnected pore volume, relatively small pore size, pore channel length and material form. Polarity, in addition to pore architecture, influences the loading and release of drug molecules from mesopores. Furthermore, the amount of medication entrapped within the pores determines the pace of release. It was discovered that the drug release rate reduced as the drug content increased. This is because the solvent molecules are poor at penetrating the pore channels, preventing drug release. MSNs offer careful regulation of the delivered medicinal drug pharmacokinetic profile. That is crucial since the concentration of this drug in the serum would be as high as possible when the drug is given independently if delivered orally or intravenously. This concentration would then be lowered until the next drug use, which would cause a concentration peak again. This approach would result in an erratic pattern of the concentration, and sometimes, the maximum might be higher than the levels of toxicity and the minimum may be lower. The use of MSNs as controlled drug delivery systems may maintain optimum drug concentration over long periods, improve therapy efficiency and reduce potential toxicity and consequent side effects. Therapeutic compounds are also protected during their passage throughout the body by MSNs employed for medication delivery. A possible cargo degradation, which is of particular concern when soft therapeutic molecules like genes, enzymes or proteins are delivered, would be prevented. The MSN's high loading capacity enables two or more medications to be carried in the same nanoparticles which enable combination therapy for tumour control. Furthermore, this capability enables the inclusion of specific contrast agents for biomedical imaging, which might be incredibly useful for tracking the progression of treatment in real-time. The possibility of reactive compliance is another benefit of using MSNs as drug delivery systems. This allows for exact checks on the release of cargo using a stimulus, whether internal and pathological characteristics are addressed or whether the physician is external. The regulation provided by the MSNs-responsive mechanism prevents the early release of the therapeutic substance, which could be important in preventing systemic toxicity (Cauda et al. 2020; Zhou et al. 2018; Vallet-Regí et al. 2018). By modifying the physicochemical parameters of the chosen mesoporous materials, the nature of the drug's interactions can be altered. As a result, changing the drug release pattern enables the development of improved drug formulations. Functionalization of mesoporous with appropriate functional groups will retard the diffusion of liquid resulting in a decrease in drug release. The amount of drug released is determined by the electrostatic force that exists between the host and guest molecules. In general, because the functionalization is specially designed to interact with the chemical groups of the drug, this effect is observed in all instances, resulting in drug retention within mesopores. As a result, it is critical to select a suitable functionalization group based on the chemical nature of the drug or biologically active ingredient to be entrapped in mesopores.

Among the other types, materials from M41S family are explored more for various applications including drug delivery system. The important materials from M41S

family are MCM-41, MCM-48 and SBA-15 (Fig. 10). For the synthesis of these materials, choice of surfactant plays a vital role in the overall development of mesostructured. In 1992, a research team from Mobil Oil presented a paper titled "A new family of mesoporous molecular sieves prepared with liquid crystal models" that was the first report on the synthesis of a new family of materials. This newly formed materials family is known as the M41S family (Kresge et al. 1992). The mesoporous materials from this family have ordered and uniform mesopores with a homogeneous size range of 2–10 nm. MCM-41 with hexagonal series, MCM-48 with cubic and MCM-50 with lamellar arranged structured. SBA-15 is a mesoporous silica sieve with uniform hexagonal pores, a narrow pore-size distribution and a pore diameter that can be adjusted between 5 and 15 nm. These materials are presented with mesostructured geometry that is uniform and regularly organized, and their dimensions can be greatly altered by using different surfactants, using organic and inorganic additives, and regulating various synthesis conditions. Their utility as a drug delivery mechanism has been scientifically investigated and documented. Fundamentally, MSNs are acting as a potential drug carrier.

The principle of host–guest chemistry can be used to describe how the loading of the molecule of interest inside the mesopores can be efficiently altered, regulated and updated according to the intended application. Material engineering's feasibility makes it a good choice for acting as a gatekeeper for a variety of drug molecules. Nowadays, these materials are gaining a lot of attention as drug carriers because of their ability to handle a large variety of molecules of varying sizes, because their pore sizes are close to most drug molecules, and if not, they can be effectively adapted to them (Mehmood et al. 2017). Mobil Composition of Matter No. 41, commonly named MCM-41, has a hexagonal array of one-dimensional mesopores with a narrow pore-size distribution that can be tailored with the proper selection of surfactants and other synthesis conditions such as the source of silica, the ratio of silica and surfactant, time, temperature, pH, etc., from 1.5 to 10 nm in diameter (Taguchi et al. 2005). The cubic phase of MCM-48 is formed by a three-dimensional pore system with a bicontinuous structure based on the gyroid minimal surface, which divides the accessible pore space into two nonintersecting subvolumes. MCM-48 is formed as a
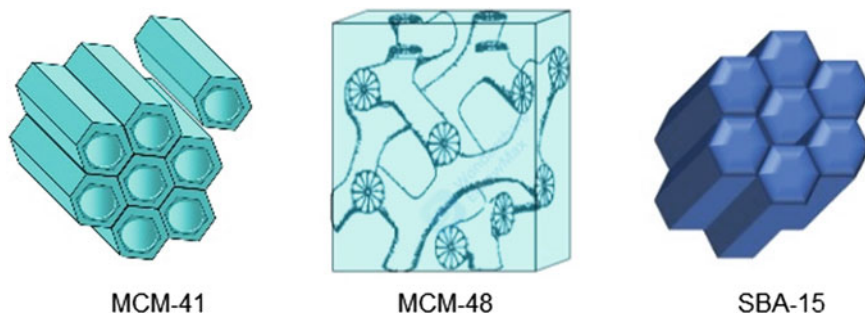
Fig. 10 Different types of mesoporous materials of M41S family

result of mesophase transformations, which are initially non-cubic and are influenced by pH, surfactant content and silica source (Schumacher et al. 2000). Santa Barbara Amorphous (SBA), another widely studied highly ordered mesoporous family, was first introduced and replicated in 1998 by Zhao et al. This material's pore size ranges from 2 to 30 nm, and it is made with an acidic environment and a non-ionic surfactant as a directing agent. The non-ionic triblock copolymer Pluronic P123 is used as a surfactant in the SBA-15, which is one of the most important materials in the SBA group (Zhao et al. 1998). When compared to the MCM-41 mesostructured, SBA-15 has a hexagonal structure, but the mesoporous silica SBA-15 has thicker silica walls (3.1–6.4 nm) and larger pores (4.6–30 nm), with greater hydrothermal stability. SBA-15 has a hexagonal structure and has a mixture of micro and mesopores, and these micropores were found to occupy up to 30% of the total pore volume.

8 Mesoporous Nanotechnology Approaches for Infectious Diseases

Infectious diseases are becoming a major cause of morbidity and mortality around the world since some diseases are caused by multi-resistant microorganisms to existing drugs (Ogunsona et al. 2020; Zaidi et al. 2017). When microorganisms such as bacteria, fungi, viruses and parasites are exposed to antimicrobial medications, they develop antimicrobial resistance to common drugs used as antibiotics, antifungals, antivirals, antimalarials and anthelmintics. This leads to ineffective medicines and to persistent infections within the body, increasing the risk of spread to others. Numerous reports are available in literature that revealed the use of mesoporous material as a host to deliver different therapeutic agents as expressed in Fig. 11. Medical procedures such as organ transplantation, cancer chemotherapy, diabetes management and major surgery become extremely risky in the absence of effective antimicrobials for infection prevention and treatment. Furthermore, as stated by the World Health Organization, antimicrobial resistance raises the cost of health care by requiring longer hospital stays and more intensive care.

The rapid emergence of drug resistance has put new antibiotics in place in the treatment of infectious diseases at the forefront. Conventional therapy is currently restricted to problems of drugs, such as low accumulation of intracellular drugs, efflux of drugs by efflux pumps and/or enzyme decay.

Currently, global burden of disease is dominated by infections. Lower respiratory infections, diarrhoea, tuberculosis (TB), human immunodeficiency virus (HIV) malaria and highly contagious coronavirus are associated with high mortality rates. In developing countries where resources such as vaccines and anti-infective substances can be limited, mortality rates are highest. Highly contagious coronavirus, which has, in 210 countries already affected more than 2 million individuals, caused a huge economic crisis because of actions taken by different Governments to restrict transmission. Many people worldwide infected have, thus, been put at great risk for their
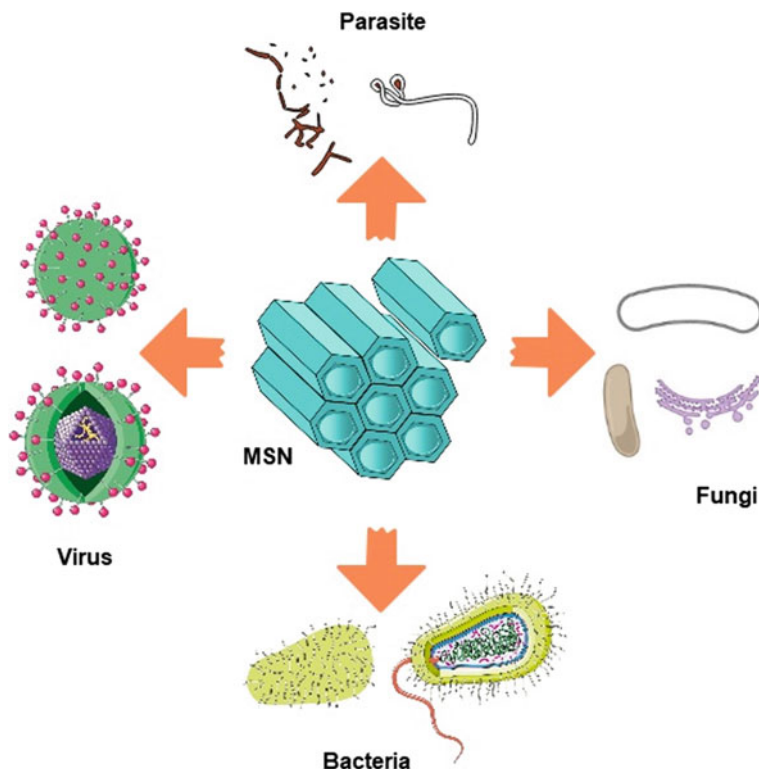
Fig. 11 Application of MSNs against various infectious microorganism

lives. No established or validated COVID-19 treatments that are approved worldwide are currently available. Unfortunately, these infectious diseases have not been clinically proven in comparison with other commonly found disease like cardiovascular and metabolic disorder, and therefore, practical and impactful strategies for better treatment of infectious diseases are urgently required. Pathogens, such as bacteria, fungi, viruses and parasites, are causes of infectious diseases, which invade the host cells for reproduction and damage disease causing tissues. These diseases are transmitted person by person (National Institutes of Health 2007; WHO 2020) directly or indirectly.

To improve access, the quantum leap in the intracellular transport and retention of drugs could be achieved using specialized nanocarriers. Mesoporous silica nanoparticles have the key advantages, such as large surfaces, easy functioning and biocompatibility. The MSNs provide additional benefits, like the accessible size and volume for a drug, which leads to the high loading capacity of drugs and can act as a powerful tool for the targeted supply of antimicrobials in the context of different infections to potentially reduce the impact of the high dosage of drugs and their secondary effects. The main merit of mesoporous silica-based nanoparticles over other particle types

comprises the firmness of the silica frame, which allows harsh reaction conditions and excellent textural characteristics for their modifications. The US Food and Drug Administration (FDA) consider silica to be "safe", and it is frequently used as an excipient in drug formulations and as a dietary supplement. Furthermore, the US FDA approved silica nanoparticles, i.e. c-dots of 7 nm for imaging purposes after a human clinical trial showed that they were well tolerated by patients and accumulated in the tumour location (Sahoo et al. 2003). As a result, silica-based nanoparticles are a powerful and promising tool that could be quickly translated into better medicines.

Bacterial Infections

The major challenge in the treatment of bacterial infections includes antibiotic resistance development in several the ineffectual treatment of bacteria species. One way to overcome this disadvantage involves using nanoparticles which can effectively interact to disrupt the bacterial surface the cell wall causing death in the cell. Multifunctional mesoporous nanoparticles (MSNs) can interact with bacteria's cellular organelles and biomolecules, making resistance development more difficult. The usage of MSNs containing antibacterial peptides has been reported, with the goal of preventing their enzymatic breakdown, which would potentiate their antimicrobial effect (Thomas et al. 2019). It can also ensure that antibacterial proteins are loaded in the same way (Xu et al. 2018a, 2018b). In other experiments, hydrophobic antimicrobial drugs-loaded MSNs were used to increase their action in biological mediums (Deaconu et al. 2019; Yang et al. 2018; Chen et al. 2018). MSNs, on the other hand, can enable regulated drug release in hydrophilic antimicrobial medicines that are particularly soluble in aqueous/biological environments. The combination of multifunctional MSNs and antimicrobial medicines allows for efficient uptake in the bacterial environment in addition to controlled drug release (Martínez-Carmona et al. 2019). Drug-loaded mesoporous silica carriers have been reported to access bone infections due to limited fluid circulation in this area, which reduces drug bioavailability when administered conventionally.

Traditional bacterial treatment is difficult, owing to weak antibiotic agent permeation into affected cells. Researchers (Zainal et al. 2013; Xu et al. 2018a, b) have prepared the rifampicin loaded MSNs of different sizes and proved that drug-loaded MSNs provide better intracellular bacterial infection treatment. Researchers (Martínez-Carmona et al. 2019; Vallet-Regí et al. 2019) created a smart nanocarrier based on antibiotic levofloxacin loaded MSNs decorated with the lectin concanavalin A, which was utilized to aggregate specificity to the nanosystem, promoting greater absorption into biofilm and then antimicrobial action. In another study, researchers have created norfloxacin loaded modified and unmodified MCM-type MSNs to test their antibacterial activity against *Escherichia coli* (Deaconu et al. 2019). The researchers concluded that norfloxacin loaded MCM-based nanocarriers had comparable antibacterial efficacy to free norfloxacin. These MSN-based nanosystems could be used to avoid using high concentrations of free norfloxacin while yet increasing antibacterial activity in any biological medium. Antibiotics that have been used in the past have shown to be ineffective against *Staphylococcus aureus* strain of bacteria. This bacterium can infiltrate and employ them as a reservoir for osteoblasts and

macrophages; hence, antibiotic activity is reduced, resulting in infection recurrence. In another finding, gentamicin-loaded MSNs were developed with a lipid bilayer, and its surface was modified with shell and ubiquicidin, a bacterial-targeting peptide onto a bilayer of lipids lead to provide promising results against *Staphylococcus aureus* (Yang et al. 2018). Similar findings are reported in literature for different antibacterial agents like vancomycin, ciprofloxacin, doxycycline, clofazimine, levofloxacin, etc.

Parasitic Infections

MSNs have been given due attention to the production of vaccines. The surface functionalization of MSNs with several molecules improves cell targeting and uptake while also favouring drug transport and release from the mesopores, resulting in interesting immune and cellular responses, making MSNs appealing as potential nanoplatforms for the fabrication of vaccines against any infectious diseases. Oliveira and colleague developed a vaccine for the protection against Schistosoma mansoni. Authors have reported the use as the new strategy for the treatment of *Schistosomiasis mansoni* infection with antigeic preparation of soluble worm loaded MSNs (Oliveira et al. 2016). Multifunctional MSNs based on MCM-41 functionalized with (3-glycidoxypropy) trimethoxysilane (GPTMS) and chitosan succinate (CS) containing benznidazole (BZ) was developed onto modified MSNs surface, with the goal of evaluating their action against the parasite Trypanosoma cruzi, which causes Chagas disease (Nhavene et al. 2018). In another study, praziquantel (PZQ)-loaded MSNs were developed to test their therapeutic efficacy against murine *Schistosomiasis mansoni* (Tawfeek et al. 2019). Whisker-formed SBA-15 nanoparticles were synthesized as a pH-sensitive metronidazole loaded nanocarrier. These findings point to this multifunctional nanoplatform as a promising and efficient metronidazole delivery system for the treatment of parasitic diseases (Yunessnia et al. 2019).

Fungal Infections

Multiple resistance mechanisms developed by biofilm formation make this pathogen (fungal) resistant to drugs such as fluconazole and amphotericin B, making it difficult to effectively treat these infections and contributing to high morbidity and mortality rates in immunocompromised patients. Researchers described a MSNs-based nanosystem with Rose Bengal as an antibacterial alternative to treat *Candida albicans* using photodynamic therapy (Paramanantham et al. 2018). Due to its low water solubility, econazole, an antifungal commonly used to treat cutaneous infections, has limited bioavailability (Firooz et al. 2015). Econazole-loaded MSNs modified with aminopropyl groups to circumvent econazole solubility issues (Montazeri et al. 2020). In another study, the authors created a pH-responsive gated MSNs-based nanosystem with the goal of treating fungal infections like vaginal candidiasis (Mas et al. 2014). In another study, silver nanoparticles were loaded into MSNs and tested for antifungal activity against *Candida albicans* 077 strains using green synthesis and Azadirachta indica leaf extract as a reducing agent (Eduardo et al. 2015).

Viral Infections

Only by interacting with host cells can viruses establish infections and spreadability. Understanding and elucidating the interaction between virus and host cells at the molecular level is critical to developing viral infection treatments. Furthermore, viruses can evolve through genetic mutation and become drug resistant, necessitating the development of new drugs. In today's medical scenario, the lack of antiviral broad-spectrum drugs, the rapid and widespread spreadability, and the lengthy time required to elucidate virus mechanism action in order to design safe and effective vaccines or treatments make viral infections like SARS-CoV-2 a major threat to human global health. Viruses are a dangerous infection for humans, responsible for millions of deaths each year. Despite the availability of some medicines, such as highly active antiretroviral therapy, to treat the human immunodeficiency virus, new medicines and vaccines are required to combat emerging infections.

Venezuelan equine encephalitis virus (VEEV) is a major public health concern; due to its potential use as a bioterrorism agent and the severe health consequences, it can cause in humans. In preclinical testing, the usefulness of a chemical VEEV inhibitor known as ML336 in preventing VEEV infection was validated. The main limitation for ML336 clinical translation is its low solubility and stability in biological media. Considering this, researchers created lipid-coated MSNs (LC-MSNs) as smart nanocarriers for ML336 delivery (LaBauve et al. 2018). The herpes simplex virus (HSV) causes a variety of infectious disorders, including orolabial and genital herpes, which are currently treated with guanine analogues like acyclovir, valaciclovir and others, which stop viral DNA replication. However, these compounds exhibit antiviral drug resistance, particularly in immunocompromised persons, as well as low absorption, prompting the administration of several and high doses. Glycosaminoglycan mimetic-functionalized MSNs were developed to cure HSV-1 and HSV-2 infections. Authors also tested glycosaminoglycan mimetic-functionalized MSNs as smart nanocarriers for acyclovir delivery, with the goal of inhibiting viral penetration and DNA replication at the same time (Lee et al. 2016, 2018). A customized MSNs were developed to test their biocompatibility and ability to block virus transduction of target cells in order to better understand the mechanism of antiviral MSNs action (Silva et al. 2016).

In the case of COVID-19, most early stage vaccines target the so-called spike protein. This protein is found on the surface of the virus and allows it to attach to the ACE2 receptor on the cell surface, causing the virus to fuse with and be taken up by the cell, triggering the cascade of events that leads to virus replication. Antigens derived from weakened or destroyed forms of the microbe/virus, its toxins, or one of its surface proteins are commonly used in vaccines. The antigen activates the immune system, causing it to recognize the agent as a threat and eliminate the virus linked with it. The antigen protein (s) can be given alone or in combination with an adjuvant to boost the immune response. The antigen in the instance of COVID-19 is the spike protein or epitopes, which include the receptor binding domain. Rather than administering the protein antigen, other approaches for administering the DNA or RNA that encodes the antigenic protein have been developed. A DNA/RNA vaccine

transfers DNA/RNA into the cell to generate the spike protein, which is subsequently processed internally by the cell and exposed to immune cells on the cell surface.

This presents the virus or its antigen in a similar fashion to when infected with the wildtype virus, eliciting a more natural immune response. To combat the virus, the immune system should activate both killer T cells and neutralizing antibodies. The most difficult aspect of DNA/RNA vaccine development is ensuring that the inserted genetic material is accepted by the host cell. The DNA/RNA is introduced into the host immune cells in one of two ways: via viral vectors or via a delivery system that carries the DNA/RNA across the cell membrane and promotes spike protein synthesis. Nuvec®, a new silica nanoparticle, has the potential to be useful in both ways. N4 Pharma is working on a new silica nanoparticle delivery system for vaccines and pharmaceuticals, with a special focus on cancer therapies and viral vaccines based on mRNA and pDNA. The original technology was created as a nanosilica system for the delivery of a hepatitis B vaccination that would reduce the number of doses per day from three to one. It was licenced from researchers at the University of Queensland (UQ) in Australia. Based on their previous experience, the founders of N4 Pharma licenced the UQ technology and collaborated to produce a unique silica nanoparticle particularly intended for nucleic acid delivery with an uneven (spiky) surface structure, which was functionalized by coupling with polyethyleneimine (PEI). This surface captures and shields nucleic acids (such as mRNA/pDNA) from nuclease enzymes as they go to the cells in a simple and effective manner. Once within the cell, the DNA/RNA is released, causing the foreign/target protein to be synthesised, activating the immune system and triggering both a cellular and humoral immune response.

The COVID-19 pandemic's worldwide urgency has brought more than 25 years of research into nucleic acid-based vaccines and medicines to the fore. The pharmaceutical sector, government institutions and the World Health Organization are all striving to develop a COVID-19 vaccine. Safe and effective alternatives to known technologies, including nanosilica-based developing technologies like Nuvec®, can be examined as researchers hunt for their perfect delivery platforms (Nigel 2020).

9   Conclusion

The common disadvantage of a number of medications is their insolubility that makes it necessary to give a higher dose of the drug for necessary therapeutic action which may lead to greater toxicity/side effects. The application of silica-based mesoporous materials as drug delivery systems has sparked the interest of researchers in drug delivery and applied sciences. A wide range of compounds can be efficiently contained and released through the mesopores. These particles, which have a diverse nature and are even tiny than eukaryotic cells in size, can cross the cell. Mesoporous silica nanoparticles with large surface area, tunable pore-size property and high pore volume make them ideal potential carriers to increase the solubility and bioavailability of low water-soluble medicines. These diverse MSNs are being explored as

a drug carrier and considerable dissolution and bioavailability enhancement have been observed for the selected drugs. Many cell-line studies using Caco-2 cells have shown good biocompatibility of MSNs. Furthermore, because there is no premature release, it is an ideal alternative to conventional techniques for oral delivery. Long-term therapy can manage the kinetic release of drugs more efficiently by modifying environmental stimuli. MSNs promise to carry toxic as well as a potent therapeutic agent such as anticancer drugs with site-specific features for only targeting the tumour cells. The efficient control of drug release is possible with specifically designed MSNs. Above all, with the internal and exterior stimulus concept, attractive tailored drug delivery application is also achievable. The diverse nature of MSNs is excellent in applications such as drug/biomolecules/gene delivery, targeted cancer medicines as diagnostic and imaging, biosensors, cell tracing and many more applications. Finding new nanomedicines for tailored therapy and diagnostics of a large variety of diseases is also the great adaptability of such clever nanosystems.

References

Abboud, M., Tahar, B.H., Fakhri, N., Sayari, A.: Synthesis of ferrocenylazobenzene-functionalized MCM-41 via direct co-condensation method. Microp. Mesop. Mater. **265**, 179–184 (2018)

Aiello, R., Cavallaro, G., Giammona, G., Pasqua, L., Pierro, P., Testa, F.: Nanostructured materials to porosity 'controlled applications for innovative technology.' Surf. Sci. Cat. **142**, 1165–1172 (2002)

Bagshaw, S.A., Prouzet, E., Pinnavaia, T.J.: Templating of mesoporous molecular sieves by nonionic polyethylene oxide surfactants. Science 1242–1244 (1995)

Brás, A.R., Merino, E.G., Neves, P.D., Fonseca, I.M., Dionísio, M., Schönhals, A., Correia, N.T.: Amorphous ibuprofen confined in nanostructured silica materials: a dynamical approach. J. Phys. Chem. C 4616–4623 (2011)

Barrett, E.P., Halenda, P.P.: The determination of pore volume and area distributions in porous substances. I. Computations from nitrogen isotherms. J. Am. Chem. Soc. 373–380 (1951)

Bharti, C., Nagaich, U., Pal, A.K., Gulati, N.: Mesoporous silica nanoparticles in target drug delivery system: a review. Int. J. Pharm. Investig. **5**(3), 124–133 (2015)

Brunauer, S., Emmet, p., Teller, E.: Adsorption of gases in multimolecular layers. J. Am. Chem. Soc. **60**(2), 309–319 (1938)

Burkett, S.L., Sims, S.D., Mann, S.: Synthesis of hybrid inorganic–organic mesoporous silica by co-condensation of siloxane and organosiloxane precursors. Chem. Commun. 1367–1368 (1996)

Cauda, V., Canavese, G.: Mesoporous materials for drug delivery and theranostics. Pharmaceutics **12**(11), 1108 (2020)

Charnay, C., Bégu, S., Péteilh, P.C., Nicole, D.A., Lerner, L., Devoisselle, J.M.: Inclusion of ibuprofen in mesoporous templated silica: drug loading and release property. Eur. J. Pharm. Biopharm. **57**, 533–540 (2004)

Chen, W., Cheng, C.A., Lee, B.Y., Clemens, D.L., Huang, W.Y., Horwitz, M.A.: Facile strategy enabling both high loading and high release amounts of the water-insoluble drug clofazimine using mesoporous silica nanoparticles. ACS Appl. Mater. Interfaces **10**(38), 31870–31881 (2018)

Chiola, V., Ritsko, J.E., Vanderpool, C.D.: Process for producing low-bulk density silica. US Patent 3556725D, 19 Jan 1971

Dai, S., Burleigh, M.C., Shin, Y., Morrow, C.C., Barnes, C.E., Xue, Z.: Imprint coating: a novel synthesis of selective functionalized ordered mesoporous sorbents. Angew. Chem. Int. Ed. **38**, 1235–1239 (1999)

Deaconu, M., Pintilie, L., Vasile, E., Mitran, R.A., Pircalabioru, G., Matei, C.: Norfloxacin delivery systems based on MCM-type silica carriers designed for the treatment of severe infections. Mater. Chem. Phys. **238**, 121886 (2019)

Eduardo, J.M., Francisco, A.C., Bruno, C., Auberson, M.M., Everardo, A.M., Pierre, B.A.F.: Antifungal activity of silver nanoparticles obtained by green synthesis. Rev. Inst. Med. Trop Sao Paulo **57**(2), 165–167 (2015)

Fan, J., Gao, F., Lei, J., Tian, B., Wang, L., Luo, Q., Tu, B., Zhou, W., Zhao, D.: Cubic mesoporous silica with large controllable entrance sizes and advanced adsorption properties. Angew. Chem. Int. Ed. 3254–3258 (2003)

Fengyu, Q.U., Huiming, L.I.N., Weiwei, Z., Jinyu, S.: A controlled release of ibuprofen by systematically tailoring the morphology of mesoporous silica materials. J. Solid State Chem. 2027–2035 (2006)

Firooz, A., Nafisi, S., Maibach, H.I.: Novel drug delivery strategies for improving econazole antifungal action. Int. J. Pharm. **495**(1), 599–607 (2015)

Hanns, B., Gotterred, K.: Application No. US 342525; Publication No. US 3383172

Horcajada, P., Pariente, P.J., Vallet-Regi, M.: Influence of pore size of MCM-41 matrices on drug delivery rate. Micropor. Mesopor. Mater. 105–109 (2004)

Jansen, J.C., Marchese, L., Zhou, W., Puil V.D., Maschmeyer, T.: A new templating method for three-dimensional mesopore networks. Chem. Commun. 713–714 (2001)

JieL, L., Monty, L., Sean, S., Tian, X., Michael, K., Andre, N., Jeffrey, Z.: Mesoporous silica nanoparticles for cancer therapy: energy-dependent cellular uptake and delivery of paclitaxel to cancer cells. NanoBiotechnology **3**, 89–95 (2007)

Joshi, K., Chandra, A., Jain, K., Talegaonkar, S.: Nanocrystalization: an emerging technology to enhance the bioavailability of poorly soluble drugs. Pharm. Nanotechnol. **7**(4), 259–278 (2019)

Kamalakannan, K., Klaus, M.: Physicochemical characterization of MCM-41 silica sphere made by the psudomorphic route and grafted with octadecyl chain. J. Chromatogr. Sci. **1191**, 125–135 (2008)

Kim, H.J., Yang, H.C., Chung, D.Y., Yang, I.H., Choi, Y.J., Moon, J.K.: Functionalized mesoporous silica membranes for CO_2 separation applications. J. Chem. **1**, 1–9 (2015)

Kresge, C.T., Roth, W.J., Vartuli, J.C., Beck, J.S.: Ordered mesoporous molecular sieves synthesized by a liquid-crystal template mechanism. Nature 710–712 (1992)

LaBauve, A.E., Rinker, T.E., Noureddine, A., Serda, R.E., Howe, J.Y., Sherman, M.B.: Lipid-coated mesoporous silica nanoparticles for the delivery of the ML336 antiviral to inhibit encephalitic alphavirus infection. Sci. Rep. **8**(1), 13990 (2018)

Lee, E.C., Davis-Poynter, N., Nguyen, C.T.H., Peters, A.A., Monteith, G.R., Strounina, E.: GAG mimetic functionalised solid and mesoporous silica nanoparticles as viral entry inhibitors of herpes simplex type 1 and type 2 viruses. Nanoscale **8**(36), 16192–16196 (2016)

Lee, E.C., Nguyen, C.T.H., Strounina, E., Davis-Poynter, N., Ross, B.P.: Structure–activity relationships of GAG mimetic-functionalized mesoporous silica nanoparticles and evaluation of acyclovirloaded antiviral nanoparticles with dual mechanisms of action. ACS Omega **3**(2), 1689–1699 (2018)

Li, Z., Barnes, J.C., Bosoy, A., Stoddart, J.F., Zink, J.I.: Mesoporous silica nanoparticles in biomedical applications. Chem. Soc. Rev. **41**(7), 2590–2605 (2012)

Martínez-Carmona, M., Izquierdo-Barba, I., Colilla, M., Vallet-Regí, M.: Concanavalin a-targeted mesoporous silica nanoparticles for infection treatment. Acta Biomater. **96**, 547–556 (2019)

Mas, N., Galiana, I., Hurtado, S., Mondragón, L., Bernardos, A., Sancenón, F.: Enhanced antifungal efficacy of tebuconazole using gated pH-driven mesoporous nanoparticles. Int. J. Nanomed. **9**(1), 2597–2606 (2014)

Montazeri, M., Razzaghi-Abyaneh, M., Nasrollahi, S.A., Maibach, H., Nafisi, S.: Enhanced topical econazole antifungal efficacy by amine-functionalized silica nanoparticles. Bull. Mater. Sci. **43**(1), 13 (2020)

Moorthy, M.S., Tapaswi, P.K., Park, S.S., Mathew, A., Cho, H.J., Ha, C.S.: Ion-imprinted meso-porous silica hybrids for selective recognition of target metal ions. Microp. Mesop. Mater. **180**, 162–171 (2013)

Narayan, R., Nayak, U.Y., Raichur, A.M., Garg, S.: Mesoporous silica nanoparticles: a comprehen-sive review on synthesis and recent advances. Pharmaceutics **10**, 118 (2018)

National Institutes of Health: Understanding emerging and reemerging infectious diseases. Biol. Sci. Curric study NIH Curric Suppl. Ser. Natl. Institutes Heal Bethesda, MD (2007)

Nhavene, E.P.F., Silva, W.M., Trivelato, R.R., Gastelois, P.L., Venâncio, T., Nascimento, R., Batista, R.J.C., Machado, C.R., Almeida, W.A., Sousa, E.M.B.: Chitosan grafted into mesoporous silica nanoparticles as benznidazol carrier for Chagas diseases treatment. Microp. Mesop. Mater. **272**, 265–275 (2018)

Nigel, T.: Emerging vaccine delivery systems for COVID-19. Drug Discov. Today. **25**(9), 1556–1558 (2020)

Ogunsona, E.O., Muthuraj, R., Ojogbo, E., Valerio, O., Mekonnen, T.H.: Engineered nanomaterials for antimicrobial applications: a review. Appl. Mater. Today. **18**, 100473 (2020)

Oliveira, D.C., Barros, A.L.B., Belardi, R.M., Goes, A.M., Oliveira, B.K., Soares, D.C.F.: Meso-porous silica nanoparticles as a potential vaccine adjuvant against schistosoma mansoni. J. Drug Deliv. Sci. Technol. **35**, 234–240 (2016)

Othman, A.L.: A review: fundamental aspects of silicate mesoporous materials. Materials (basel) **5**(12), 2874–2902 (2012)

Page, M.L., Beau, R., Duchene, J.: Application No. US 3493341D; Publication No. US 3493341 (1967)

Paramanantham, P., Antony, A.P., Sruthil, S.B., Sharan, A., Syed, A., Ahmed, M.: Antimicrobial photodynamic inactivation of fungal biofilm using amino functionalized mesoporus silica-rose Bengal nanoconjugate against Candida albicans. Sci. African. **1**, e00007 (2018)

Patra, J., Das, G., Fernandes, L., Vangelie, R.C.E., Pilar, R.T.M., Acosta, T.L., Diaz, L.T., Grillo, R., Swamy, M.K., Sharma, S., Habtemariam, S., Shin, H.: Nano based drug delivery systems: recent developments and future prospects. J. Nanobiotech. **16**, 71 (2018)

Pattnaik, S., Swain, K.: Mesoporous nanomaterials as carriers in drug delivery. In: Applications of Nanocomposite Materials in Drug Delivery, pp. 589–604. Woodhead Publishing, Cambridge, UK (2018)

Prouzet, E., Boissiere, C., Kooyman, P.J., Larbot, A.: Nanometric hollow spheres made of MSU-X-type mesoporous silica. J. Mater. Chem. 1553–1556 (2002)

Regev, S.P., Rozen, R.Y.: Thin films of mesoporous silica: preparation and characterization. Curr. Opin. Colloid Interface Sci. **4**(6), 420–427 (1999)

Sahoo, S.K., Labhasetwar, V.: Nanotech approaches to drug delivery and imaging. Drug Discov. Today. **8**(24), 1112–1120 (2003)

Schumacher, K., Ravikovitch, P.I., Chesne, A.D., Neimark, A.V., Unger, K.K.: Characterization of MCM-48 materials. Langmuir **16**, 4648–4654 (2000)

Shenmin, Z., Di, Z., Yang, N.: Hydrophobic polymers modification of mesoporous silica with large pore size for drug release. J. Nano. Res. **11**, 561–568 (2009)

Shi, X., Sun, K., Baker, Jr.: Spontaneous formation of functionalized dendrimer-stabilized gold nanoparticles. J. Phys. Chem. C. **112**, 8251–8258 (2008)

Silva, J.M., Hanchuk, T.D.M., Santos, M.I., Kobarg, J., Bajgelman, M.C., Cardoso, M.B.: Viral inhi-bition mechanism mediated by surface-modified silica nanoparticles. ACS Appl. Mater. Interfaces **8**(26), 16564–16572 (2016)

Singh, K., Bhori, M., Kasu, Y.A., Bhat, G., Marara, T.: Antioxidants as precision weapons in war against cancer chemotherapy induced toxicity–exploring the armoury of obscurity. Saudi Pharm. J. **26**(2), 177–190 (2018)

Shylesh, S., Samuel, P.P., Sisodiya, S., Singh, A.P.: Periodic mesoporous silicas and organosilicas: an overview towards catalysis. Catal. Surv. Asia **12**, 266 (2008)

Stöber, W., Fink, A., Bohn, E.: Controlled growth of monodisperse silica spheres in the micron size range. J. Coll. Interf. Sci. **26**(1), 62–69 (1968)

Suri, S., Fenniri, H., Singh, B.: Nanotechnology-based drug delivery systems. J. Occup. Med. Toxicol. **2**, 16 (2007)

Sun, W., Fang, N., Trewyn, B.G., Tsunoda, M.: Endocytosis of a single mesoporous silica nanoparticle into a human lung cancer cell observed by differential interference contrast microscopy. Anal. Bioanal. Chem. **391**, 2119–2125 (2008)

Taguchi, A., Schüth, F.: Ordered mesoporous materials in catalysis. Micropor. Mesopor. Mater. **77**(1), 1–45 (2005)

Tanev, P.T., Pinnavaia, T.J.: A neutral templating route to mesoporous molecular sieves. Science 865–867 (1995)

Tawfeek, G.M., Baki, M.H.A., Ibrahim, A.N., Mostafa, M.A.H., Fathy, M.M., Diab, M.S.E.D.M.: Enhancement of the therapeutic efficacy of praziquantel in murine *Schistosomiasis mansoni* using silica nanocarrier. Parasitol. Res. **118**(12), 3519–3533 (2019)

Thomas, S., Jambhrunkar, G., Prestidge, K.: Rifampicin-loaded mesoporous silica nanoparticles for the treatment of intracellular infections. Antibiotics **8**(2), 39 (2019)

Trewyn, B.G., Jennifer, A.N., Zhao, Y., Victor, S., Lin, Y.: Biocompatible mesoporous silica nanoparticles with different morphologies for animal cell membrane penetration. J. Chem. Eng. **137**, 23–29 (2007)

Vadia, N., Rajput, S.: Applications of mesoporous material for drug delivery. In: Importance and Applications of Nanotechnology, pp. 1–14. MedDocs Publishers LLC, USA (2019)

Vadia, N., Rajput, S.: Mesoporous material, MCM-41: a new drug carrier. Asian. J. Pharm Clin Res. **4**(2), 44–53 (2011)

Vadia, N., Rajput, S.: Study on formulation variables of methotrexate loaded mesoporous MCM-41 nanoparticles for dissolution enhancement. Eur. J. Pharma. Sci. **45**, 8–18 (2012)

Vallet-Regi, M., Ramila, A., Del, R.P., Perez, P.J.: A new property of MCM-41: drug delivery system. Chem. Mater. **13**, 308–311, (2001)

Vallet-Regi, M.: Revisiting ceramics for medical applications. Dalton Trans. 5211–5220 (2006)

Vallet-Regi, M., Daniel, A., Mesoporous materials for drug delivery. Angew. Chem. Int. Ed. 7548–7558 (2007)

Vallet-Regí, M., Colilla, M., Barba, I.I., Manzano, M.: Mesoporous silica nanoparticles for drug delivery: current insights. Molecules **23**(47), 1–19 (2018)

Vallet-Regí, M., González, B., Izquierdo-Barba, I.: Nanomaterials as promising alternative in the infection treatment. Int. J. Mol. Sci. **20**(15), 3806 (2019)

Wang, G., Otuonye, A.N., Blair, E.A., Denton, K., Tao, Z., Asefa, T.: Functionalized mesoporous materials for adsorption and release of different drug molecules: a comparative study. J. Solid State Chem. **182**(7), 1649–1660 (2009)

WHO | Infectious diseases; 2020 May 22. Available from: https://www.who.int/topics/infectious_diseases/en/

Xia, H.S., Zhou, C.H., Tong, D.S., Lin, C.X.: Synthesis chemistry and application development of periodic mesoporous organosilicas. J. Porous Mater. **17**, 225–252 (2010)

Xu, B., Su, Y., Chen, L., Cai, J., Huang, B.: Preparation of mesoporous silica nanoparticles with controlled pore size, particle diameter, morphology, and structure by two-step process of chlorosilane residue. Ceram. Int. **44**, 22241–22248 (2018)

Xu, C., He, Y., Li, Z., Ahmad, Y., Ye, Q.: Nanoengineered hollow mesoporous silica nanoparticles for the delivery of antimicrobial proteins into biofilms. J. Mater. Chem. B **6**(13), 1899–1902 (2018)

Yang, S., Han, X., Yang, Y., Qiao, H., Yu, Z., Liu, Y.: Bacteria targeting nanoparticles with microenvironment-responsive antibiotic release to eliminate intracellular *Staphylococcus aureus* and associated infection. ACS Appl. Mater. Interfaces **10**(17), 14299–14311 (2018)

Yokoi, T., Yoshitake, H., Tatsumi, T.: Synthesis of amino-functionalized MCM-41 via direct co-condensation and post-synthesis grafting methods using mono, di- and tri-amino-organoalkoxysilanes. J. Mater. Chem. **14**, 951–957 (2004)

Yunessnia, A., Shagholani, H., Nikpay, A., Ghorbani, M., Soleimani, L.M., Soltani, M.: Synthesis and modification of crystalline SBA-15 nanowhiskers as a pH-sensitive metronidazole nanocarrier system. Int. J. Pharm. **555**, 28–35 (2019)

Zaidi, S., Misba, L., Khan, A.U.: Nano-therapeutics: a revolution in infection control in post antibiotic era. Nanomed. Nanotechnol. Biol. Med. **13**(7), 2281–2301 (2017)

Zainal, N.A., Rizal, S., Shukor, A., Azwana, H., Wab, A., Razak, K.A.: Study on the effect of synthesis parameters of silica nanoparticles entrapped with rifampicin. Chem. Eng Trans. **32**, 2245–2250 (2013)

Zhanga, J., Rosenholmb, J.M.: Molecular and nanoscale engineering of porous silica particles for drug delivery. In: Nanoengineered Biomaterials for Advanced Drug Delivery, pp. 395–419. Woodhead Publishing Series in Biomaterials, Elsevier, Netherlands (2020)

Zhao, D., Huo, Q., Fena, J., Chemelka, B.F., Stucky, G.D.: Nonionic triblock and star diblock copolymer and oligomeric surfactant syntheses of highly ordered, hydrothermally stable, mesoporous silica structures. J. Amer. Chem Soc. **120**, 6024–6036 (1998)

Zhou, Y., Quan, G., Wu, Q., Zhang, X., Niu, B., Wu, B., Huang, Y., Pan, X., Wu, C.: Mesoporous silica nanoparticles for drug and gene delivery. Acta. Pharm. Sin. B **8**(2), 165–177 (2018)

Zhu, Q.F., Shougui, S.H.L., Qiu: Effective controlled release of captopril by silylation of mesoporous MCM-41. Chem. Phys. Chem. 400–406 (2006)

Zhuravlev, L.: The surface chemistry of amorphous silica. Zhuravlev model. Colloids Surf. A Physicochem. Eng. Asp. 1–38 (2000)

Applications and Future Trends in Mesoporous Materials

Jella Gangadhar, Barath Tirumuruhan, and Ravindran Sujith

Abstract Mesoporous materials have attracted a wide interest in the scientific community due to its exceptional physical and chemical properties. Typically these materials have large specific surface area with pore size ranging between 2 and 50 nm. The interconnected and ordered pores present in these materials provide an excellent access and diffusion pathways for various atomic species. Further, by functionalization it is possible to tune the surface chemistry of these materials. All these unique properties makes them exceptional materials for various frontier applications. In this chapter some of the major applications of these mesoporous materials such as in energy conversion and storage, filtration, catalysis, carbon capture, optics and drug delivery are discussed. Finally, future trends in the development of these materials towards various applications are summarized.

Keywords Energy storage · Catalysis · Fuel cells · Batteries · Carbon capture · Adsorbents · Drug carrier · Filtration · Optics

1 Introduction

Materials with porous features are extensively used in applications ranging from structural to energy technologies. On the basis of pore size IUPAC have classified these porous materials into micro, meso and macroporous materials. Microporous materials have a pore size of less than 2 nm and are useful for applications involving very large specific surface area. Zeolites are an excellent example for such microporous materials. However, synthesizing these materials are often challenging and in certain cases extremely small pore sizes may prove to be diadvantageous. For instance, Metal Organic Frameworks (MOF) with micropores are extensively studied for hydrogen storage, but its volumetric capacity is rather limited due to its low densities (Zhang et al. 2020). In case of macroporous materials the pore sizes are larger than 50 nm and hence are inefficient for those applications that requires high specific

J. Gangadhar · B. Tirumuruhan · R. Sujith (✉)
Mechanical Engineering Department, Birla Institute of Technology and Science,
Pilani-Hyderabad Campus, Telangana 500078, India
e-mail: sujith@hyderabad.bits-pilani.ac.in

surface area. Hence, mesoporous materials can be the considered as a suitable material for such applications because they have an intermediate pore size and thereby combine the advantages of both micro and macroporous materials.

In 1992, Kato and his colleagues from Mobil Research and Development Corporation were the first to propose a successful strategy for the synthesis of mesoporous materials. They have synthesized mesoporous silica from the calcination of aluminosilicate gels (Kresge et al. 1992). The pore channels of these mesoporous silica were regular and the pore size ranged between 1.5 and 2 nm. Because of its incredibly large surface areas they were considered as molecular sieves and Mobil composition of matter (MCM-41) is one such material which has gained a wide popularity (Zhao et al. 1996). Another significant development happened in 1998 which involved in the development of SBA-15 (Santa Barbara Amorphous) by a group of scientists from Santa Barbara (Zhao et al. 1998). Because of its interconnected pore structure and thicker mesopore walls they were found to be more stable than the MCM-41. The synthesis of these materials simulated further research into this area resulting in the development of materials which are highly stable and suitable for various applications. New types of mesoporous materials based on transition metal oxides, silica and organic frameworks were synthesized. Moreover, recent advances in manufacturing such as soft lithography have made possible the fabrication of these mesoporous materials with pore morphologies of various shapes and order. For example, soft lithography (micromolding, micromolding in capillaries and microtransfer molding) was combined with acidic sol–gel block copolymer templating chemistry to form mesostructured silica waveguides (Yang et al. 2000).

Currently the mesoporous materials have been envisaged for a variety of applications such as in energy conversion and storage, filtration, catalysis, optics, drug delivery and so on. The potential applications of these materials are many and is mainly because of the recent progress that has occurred in this area of research. Now it is possible to synthesize mesoporous materials that are highly stable having controlled pore morphology and tuned surface properties. This chapter focusses on the recent developments that has occurred in the applications of these mesoporous materials. Further the advantages of choosing these material over its dense counterpart is highlighted in the respective sections. Finally the existing challenges in realizing the commercial viability of these materials for the various applications are also discussed.

2 Energy Conversion and Storage

The growth of the global population has led to the heavy dependency on fossil fuels such as coal, petrol and natural gas, and the emissions released from these systems are harmful to the environment. To address this energy crisis and to preserve the environment, considerable research effort has been devoted globally to the development of new and renewable energy sources. Mesoporous materials owing to its interesting characteristics can provide a sustainable solution to this energy crisis.

Moreover, recent developments in energy storage systems and electric vehicles can be augmented by the usage of these mesoporous materials. One of the main reasons for the choice of these materials is its incredibly high SSA. Such large surface area provides a large number of active sites which could be beneficial for applications involving energy conversion and storage. Recent studies have shown that these pores could result in nanoconfinement effects which in turn enhances the suitability of these materials for various energy storage applications (Li et al. 2016). In this section we highlight the application of these materials toward batteries, super capacitors, fuel cells and solar cells.

2.1 Rechargeable Batteries

Recent research trends suggest that Li-ion batteries provide the best solution towards portable electronics as well as towards the electrification of the automotive industry. The widespread implementation of these rechargeable batteries arises from their high energy densities and long-term stability, but the power density is low at high charge and discharge cycles due to its high polarization effect (Vekariya et al. 2018). Among the different parts of a battery, the electrode, electrolyte, separator, and cell design are considered to be important. Further, the research on electrode materials has been extensively taken up to develop newer materials that are mesoporous, due to the fact that electrochemical performance greatly depends upon the presence of active sites in these electrodes (Ye et al. 2013). In the bulk form these materials suffer at higher power densities due to less surface to volume ratio and longer diffusion length for lithium ions and electrons (Eftekhari 2017). Hence, one of the most widely investigated approaches is to use mesoporous materials with controlled porosity or in some cases ordered/hierarchical porosity. Listed below are some of the major advantages of using such a mesoporous material for batteries.

- High surface area for electrochemical reactions in Li-ion batteries.
- Interconnected meso channels and nanosized mesopore walls that facilitate electrolyte and ionic transport.
- Shorter solid state diffusion path for the Li-ions in batteries, which is beneficial for a high charging and discharging rates.
- Large pore volumes that can accommodate the strain relaxation during the charging and discharging processes.

In conventional Li-ion batteries the material of choice for the anode is graphite. However, the theoretical specific capacity of graphite is 372 mAh/g and it is not high enough for heavy-duty commercial applications. So, the efforts were to develop an alternative material having high specific capacities. Silicon because of its high theoretical specific capacity ($\sim$4200 mAh/g) and low discharge potential (<0.5 V versus Li/Li$^+$) with an alloying/dealloying mechanism while lithiation and de-lithiation is an obvious material of choice (Salah et al. 2019). However, usage of Si in commercial applications is limited because it has a tendency to pulverize upon repeated cycling

leading to short circuiting issues and in some cases even explosion of batteries. This is because of the large volumetric expansion (~400%) that is being observed during the lithiation cycle. Though there are several solutions being proposed (Fig. 1), one of the most promising techniques is to use a mesoporous silicon. The strategy is that the porosity present in these Si particles could act as a buffer against the volumetric strains. Further, it was also observed that addition of graphene like particles into the silicon-based systems will be beneficial in improving the overall performance of these batteries (Cheng et al. 2021). In the present scenario the mesoporous silicon-based carbon composites are in the process of commercialization by various battery manufacturers such as Tesla, Nexon and Sila Nanotechnologies. Table 1 summarizes the electrochemical performances of the various mesoporous Si-based Li-ion batteries.

Flammable organic electrolytes are another major concern which limits the application of Li-ion batteries. Hence, an alternative solution that is being proposed is to use solid state electrolytes in place of liquid electrolytes. Commercially two types of solid-state electrolytes are available, namely: inorganic ceramic electrolytes
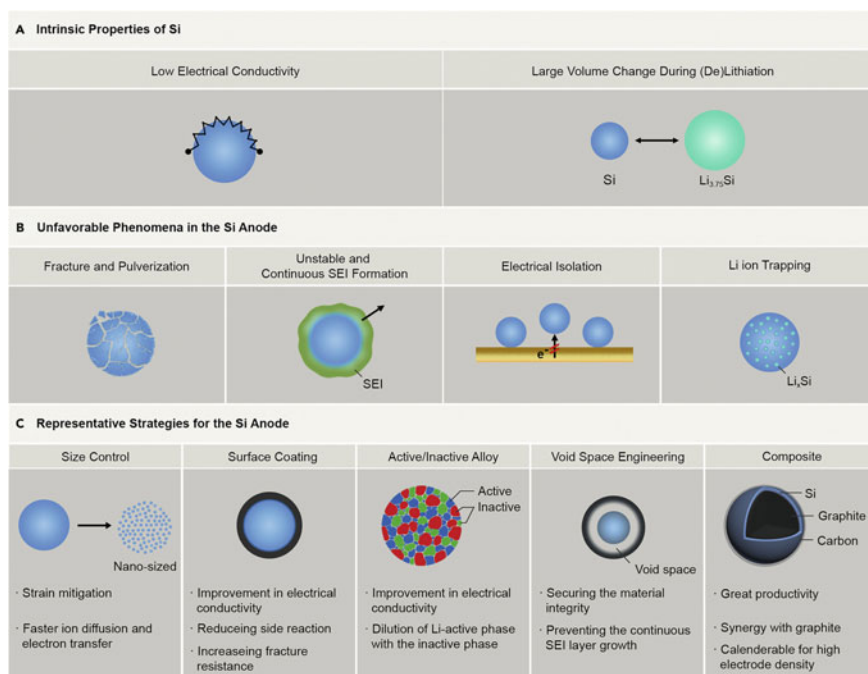
Fig. 1 Overview of the challenges and representative strategies associated with Si anode. **a** Intrinsic properties of Si is disadvantageous to charge transfer kinetics and stable cycling behavior. **b** Unfavorable phenomena in the Si anode causing the active material loss and consumption of lithium ion in the cell. **c** Various representative strategies for addressing the unfavorable phenomena such as size control, surface coating, active/inactive alloy, void space engineering, and composite is provided. Reprinted from ref. (Chae et al. 2017), Copyright (2021), with permission from Elsevier

Table 1 Summarizes the various types of mesoporous silicon used as anode materials along with its surface characteristics and electrochemical performances

S. No.	Sample	Specific surface area (m²/g)	Pore diameter (nm)	Pore volume (cm³/g)	Initial charge capacity (mAh/g)	Initial discharge capacity (mAh/g)	Stable capacity/ cycles/ C rate	Initial coulombic efficiency (%)	Ref.
1	Polysiloxane derived mesoporous Si	51	35.9	0.46	3572	3349	1564 mAh/g 100 cycles 0.1 C rate	96	(Lee et al. 2020)
2	Mesoporous silicon nanorod	254.6	12	0.636	3285	1586	1038 mAh/g 170 cycles at 0.2 A/g	48.2	(Zhou et al. 2014a)
3	Mg reduced silicon nano particle	128	20–40	0.66	3487	2452	910 mAh/g 50 cycles 1.2 A/g	73	(Wang et al. 2016)
4	Solution synthesis mesoporous silicon	190	3.8	–	3000	2200	847 mAh/g 320 cycles 2 A/g	73.3	Sun et al. 2017
5	Mesoporous Si@SiO	239	4	–	2789	1782	873 mAh/g 1.8 A/g 1400 cycles	64.1	Liang et al. 2016
6	Mesoporous silicon hollow nanocubes derived from MOF template	–	27.5	–	2160	1728	850 mAh/g 1 C rate 80 cycles	80	Yoon et al. 2017

(continued)

Table 1 (continued)

S. No.	Sample	Specific surface area (m²/g)	Pore diameter (nm)	Pore volume (cm³/g)	Initial charge capacity (mAh/g)	Initial discharge capacity (mAh/g)	Stable capacity/ cycles/ C rate	Initial coulombic efficiency (%)	Ref.
7	Zeolite-templated mesoporous silicon	90.7	19–31	0.4–0.5	1399	1031	1000 mAh/g 1.1 A/g	73.6	Kim et al. 2018
8	Silicon from Mg reduction	162	40	–	4819	2918	1004 mAh/g 50 cycles		Chen et al. 2011
9	3D-mesoporous silicon	74.2	28.5	0.559	2642	1945	1500 mAh/g 100 cycles 1 C rate	73.6	Jia et al. 2011
10	Mesoporous metallurgical silicon	219.4	17.9	0.97	3992	2111	2111 mAh/g 50 cycles 0.2 C rate	52.8	Li et al. 2015
11	Mesoporous silicon sponge	494	17	1.71	–	–	750 mAh/g	56	Li et al. 2014

and organic polymeric electrolytes. Ionic conductivity in these materials plays a crucial role in the selection of these materials as solid-state electrolytes. Typical ionic conductivities in these materials lie between 10^{-4} and 10^{-2} S/cm. These ionic conductivities can be further enhanced by the incorporation of mesoporous materials. Though there have been several breakthrough studies in this area, challenges like large interfacial resistance between the solid electrolyte and the electrode material, depletion of Li at the interface, dendritic growth, high cost of production of solid-state electrolytes etc., still exists (Lewis et al. 2019; Maekawa et al. 2008; Zheng et al. 2018). Recently, MXene based mesoporous silica nanosheets were developed as ion conducting agents to be embedded in poly propylene oxide (PPO) giving an ionic conductivity of 4.6×10^{-4} S/cm. The mesopores served as sites for dispersing active functional groups of MXene-Ti_3C_2, that form Lewis acid–base interactions with $TFSI^-$ to form Li^+ transport channels (Shi et al. 2020). An alternative study approached the problem by using MOP fillers in PEO-LiTFSI electrolyte membranes. These MOP fillers acted as scavengers for trace solvent impurities and decomposition products and hence increased the Li^+ conductivity upto 4.4×10^{-4} S/cm. Also, the enhancement of the mechanical strength by the fillers resisted Li dendrite growth and thus improved the long term stability of a full cell with 144 mAh/g after 300 cycles (Liu et al. 2018a). Further in-depth study is required to understand the structure and surface properties of these materials so as to ensure its commercial viability.

2.2 Supercapacitors

Compared to batteries supercapacitors have higher power densities and excellent cycle life (Li et al. 2016). There are two types of supercapacitors in usage: (i) electrochemical double layer capacitor (EDLC) and (ii) pseudo capacitors (Fig. 2). In EDLC energy is stored in the form of charged species in the surface of electrodes, whereas in pseudo capacitors energy is stored in the form of a series of Faradaic reactions. Since high surface area and pore channels are significant for energy storage in these devices, mesoporous materials play an important role in these applications. In EDLC's the usage of mesoporous carbon in the form of graphene has demonstrated a capacity of 166 Fg^{-1} in presence of an organic electrolyte (Zhu et al. 2011). Though ultra-high surface area is quite beneficial for achieving high storage capacities it has been observed that pore sizes and its distribution have a similar or a more significant effect in realizing high storage capacities. However, in case of pseudo capacitors, the major constraint is with respect to its low electrical conductivity, and hence the usage of mesoporous carbon materials as host materials is a viable option since it provides the required electrical pathway along with its stability. But this could lead to lower gravimetric capacities since carbon in this case acts like an inactive material. So, the solution could be to choose an active mesoporous material and studies have shown that mesoporous metal oxide thin films based on TiO_2, Nb_2O_5 and MoO_3 could exhibit much higher pseudo capacitive energy storage capacity in comparison to its non-mesoporous counterparts (Augustyn et al. 2013; Brezesinski et al.
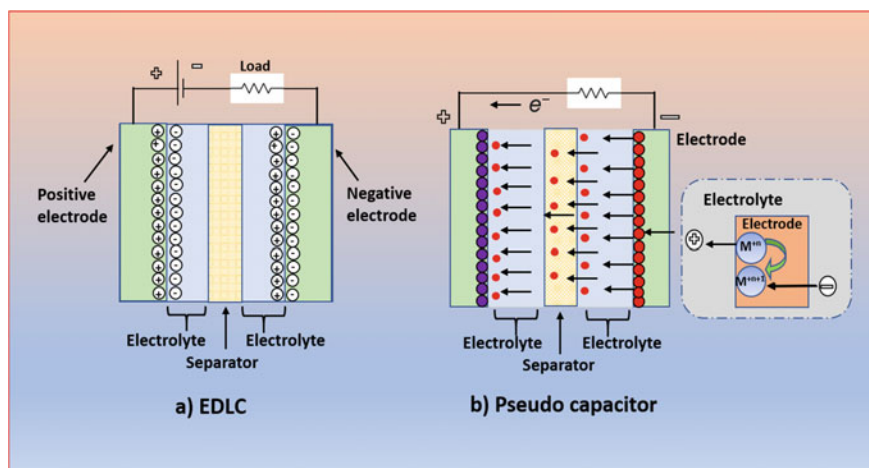
Fig. 2 Schematic representation of **a** electrochemical double layer capacitor (EDLC) and **b** pseudo-capacitor. Idea of schematic taken from (Vangari et al. 2013)

2010, 2009). The high surface area and the interconnected porous structure present in these materials could provide shorter diffusion paths for the mass transport of ions to the active sites. Another solution which is being offered in the literature is doping with heteroatoms like nitrogen to mesoporous carbon (Zhao et al. 2015). This could enhance the wettability and surface reactions leading towards higher capacitance. In general, it can be considered that further research towards optimizing the pore structures and modelling their properties are required to ensure the commercial viability of the usage of these supercapacitors.

2.3 Fuel Cells

In this section, the focus is on the usage of mesoporous materials for polymer electrolyte membrane fuel cells (PEMFC) wherein hydrogen is used as the fuel. It should be noted that other fuels such as menthol can be also used in PEMFC, but in this section the discussion is limited to hydrogen-based systems. The vision of realizing a hydrogen economy wherein hydrogen is used in all the stages of the energy life cycle is one of the forefront areas of research in recent years. Though there is considerable progress toward realization of this goal the usage of hydrogen as fuel is still in the nascent stages of development owing mainly to the difficulty in achieving high energy storage densities. The storage of hydrogen is often measured in terms of either gravimetric density or volumetric density (g/L). Today, the commonly adopted technology for storing hydrogen in on-board applications is by pressurizing hydrogen at 700 bar and storing in high pressure cylinders (Hirscher et al. 2020). This could result

in high storage densities of 40 g/L, but storing hydrogen at these extreme high pressures is enormously risky and costly. The cost is high because it requires specialized carbon fiber cylinders for enabling high pressure storage conditions. Hence, it was thought that materials with high levels of porosity could act as suitable adsorbents for hydrogen thereby enabling storing of hydrogen at relatively low pressures. In order to promote research in this area, the US Department of Energy (DoE) has come up with target values of hydrogen storage suitable for on-board applications. Several micro and mesoporous materials based on zeolites, carbonaceous materials, metal organic frameworks (MOF) and silicates (Sujith et al. 2018) have been developed and in many cases these materials were able to meet the target put forward by US-DoE. Among these materials MOFs have shown impressive performance mainly because of their large SSA and open porous structure enabling very fast adsorption and desorption kinetics (Panella et al. 2006). This is impressive but its application is practically limited because of the requirement of cryogenic conditions that enable the adsorption of hydrogen to these materials. Hence, the challenge is towards development of suitable adsorbents that are capable of achieving ambient temperature adsorption conditions. One of the basic requirements for achieving this is that the material should have a binding enthalpy in the range from -15 to -25 kJ/mol. In a recent study on vanadium-based MOFs it was reported that binding energies of -21 kJ/mol can be achieved and thereby realizing it's potential for ambient hydrogen storage (Jaramillo et al. 2021) (Fig. 3). It has been also observed that the pore sizes and SSA play an important role in achieving high storage densities. Hence efforts have been put forward to optimize the pore structures for maximizing the hydrogen uptake and recently various machine learning algorithms have been employed for this purpose. In one such study nearly half a million metal organic networks were screened and it was observed that capacity can be maximized by increasing the surface area and porosity (Ahmed et al. 2019). They were also able to predict a theoretical volumetric capacity limit of 40 g/L in these material systems.


Fig. 3 The low-pressure hydrogen adsorption isotherms for $V_2Cl_{2.8}$ (btdd) is shown. This material has shown significant adsorption under ambient conditions and exhibited an isosteric heat of adsorption of -21 kJ/mol. Reprinted with permission from (Jaramillo et al. 2021)
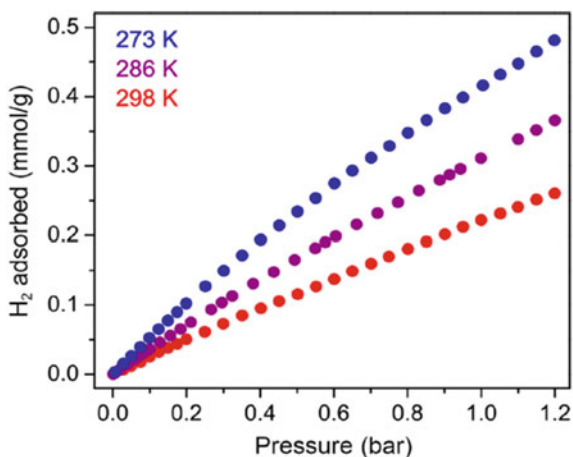
Another significant application of mesoporous materials in the PEMFC based technology is the adaptation of these materials to electrodes and electrolytes. In PEMFC the reaction kinetics is extremely sluggish in the cathode and hence it necessitates the usage of a catalyst. Pt is the most commonly used catalyst, but it is expensive and prone to issues like "poisoning" effects. Recently, ordered mesoporous Pt@graphitic carbon composites have been developed and the presence of these graphitic particles was observed to provide a shielding effect thereby enhancing the overall stability of the system, even in presence of fuels like methanol (Wu et al. 2012). Another strategy that is considered for reducing the usage of precious metals as catalysts is to develop non-metallic catalysts having mesoporous structure. For example, Si colloids (SBA-15) have been doped with Co and N and its considerably high surface area with its suitable composition was observed to exhibit an activity comparable to that of Pt-based catalysts (Liang et al. 2013). Another major challenge is in the development of a suitable electrolyte membrane. Nafion is the most commonly used membrane, but it has constraints like high cost, low permeability of fuels like methanol and operation difficulties at high temperature. Hence, there have been efforts to improve the existing system and it was reported that usage of mesoporous materials such as phosphotungstic acid functionalized mesoporous silica can be tried out because of its high stability at temperature above 100 °C and its high proton conductivity (Zhou et al. 2014b).

2.4 Solar Cells

Recent studies have shown that solar cells based on mesoporous materials offer an alternative solution to the conventional solid-state photovoltaics. Dye sensitized solar cells (DSSC) fabricated out of mesoporous TiO_2 electrodes is one such approach wherein high power conversion efficiency (PCE) can be expected. Recently, studies have shown that TiO_2 microspheres when used along with a commercial dye N719, a power conversion efficiency of 12% can be attained (Liu et al. 2015). These 3D mesoporous TiO_2 microspheres were synthesized via evaporation driven oriented assembly method (Fig. 4). However, challenges still exist in DSSC such as reducing the charge recombination at the electrode–electrolyte interface, improving light harvesting, dye regeneration reaction and so on. An alternative to DSSC is the perovskite based solar cells wherein organic halide perovskites are used as solid-state light absorbing and hole transporting materials. Here also, mesoporous TiO_2 scaffolds were found to be highly effective in suppressing the charge recombinations and achieving a PCE of 18% under 100 mW m^{-2} AM1.5G illumination (Liu et al. 2015). It was also observed that by depositing $FAPbI_3$ on a mesoporous TiO_2 electrode, PCE can be enhanced to 20% (Jeon et al. 2015). However, it should be noted that in these systems where high PCE is reported long term stability of perovskite is affected due to the hysteresis that is observed in the photocurrent–voltage curve. By enhancing the charge mobility the hysteresis can be inhibited and to achieve this strategies such as usage of TiO_2 nanowires and doping the TiO_2 with Li were
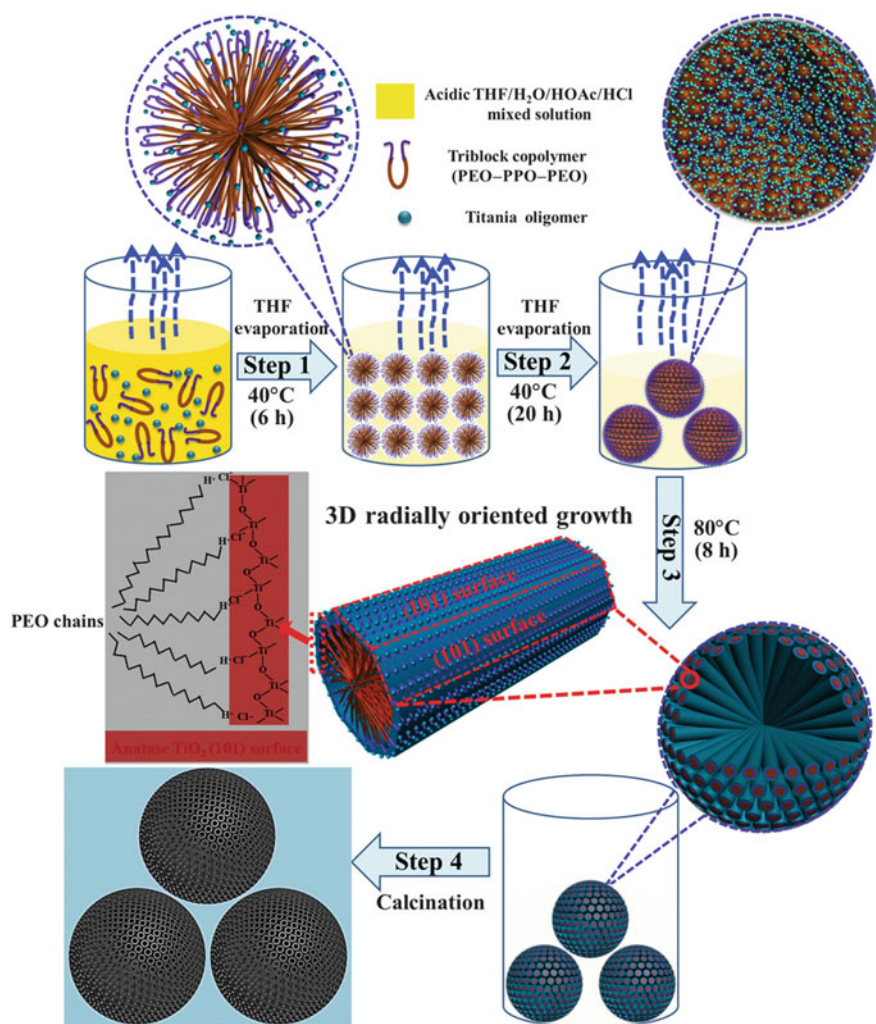
Fig. 4 Schematic representation of the formation process through evaporation-driven oriented assembly. Reprinted with permission from (Liu et al. 2015)

proposed (Yu et al. 2015). It has been also observed that long term exposure of these mesoporous TiO_2 based perovskite solar cells to UV radiation could lead to significant loss in efficiency (Li et al. 2016). Significant research has been carried out to develop coating materials that can block the exposure of UV radiation. One such strategy is to coat TiO_2 with Al_2O_3 scaffold (Leijtens et al. 2013).

In addition to its usage as solar cells, these materials can be also envisaged for solar fuel production purposes. For example, mesoporous Si due to its high surface area is observed to exhibit high photocatalytic activity in comparison to silicon nanopowder (Dai et al. 2014). However, it should be noted that an increased surface area could

lead to more charge recombination rates. Hence, producing mesoporous Si with fewer grain boundaries could be a solution leading to better performances. It has been reported that mesoporous TiO_2 because of its high activity towards hydrogen can be effectively used for hydrogen generation. Further, studies on mesoporous CoO have shown that its mesoporous structure can be effectively used for water splitting purposes by tuning its band edge positions in these semiconductors (Liao et al. 2014). From all these studies it can be summarized that the solutions these mesostructured materials offer towards energy storage and conversion is immense.

3 Carbon Capture

Carbon dioxide emissions have been the largest inducer of climate change and it seems the current level of CO_2 is at the highest point in the last 800,000 years (Lüthi et al. 2008). Carbon being released into the atmosphere is too much for natural sequestration by plants and we are also witnessing a constant increase in the annual emission rate. Hence, it is critical to develop technologies wherein we can capture CO_2 and store it in some safe places. The sequestration process is of three types- direct air capture, pre-combustion capture and post-combustion capture. Processes such as chemisorption, physisorption and membrane separation enable long-term and high volume storage of CO_2. Mesoporous materials due to its large SSA are excellent solid adsorbent materials. Several solid adsorbents ranging from porous carbon, metal oxides, MOF, porous polymers and covalent organic frameworks have been developed. Hierarchical and combinations of different pore types such as micro-mesoporous and macro-mesoporous have also been utilized to improve the adsorption potential (Fig. 5) (Dabbawala et al. 2020; Song et al. 2019). The sequestration for the post-combustion processes also requires specificity towards CO_2 over N_2 and other flue gases. This specificity is achieved by functionalization and doping. For example, it was shown that by doping N on ordered mesoporous carbon higher specificity towards CO_2 over N_2 can be attained (Chen et al. 2018b). The efficiency of CO_2 adsorption has also been significantly improved by the immobilization of amines on the surface. These supported amine sorbents (SAS) offer better adsorption rates and higher capacity (Licciulli et al. 2017). SAS either have amines impregnated or grafted on them. Among these two methods, the former suffers from thermal stability during regeneration while the latter is limited by surface functionalities available for grafting. Recently, amine ionic liquids supported on mesoporous alumina have been reported to circumvent the problems with SAS (Balsamo et al. 2018). Reactive porous oxide materials such as MgO and CaO as alternatives for SAS and MOFs are being developed for CO_2 capture (Harada and Hatton 2015; Park et al. 2020).
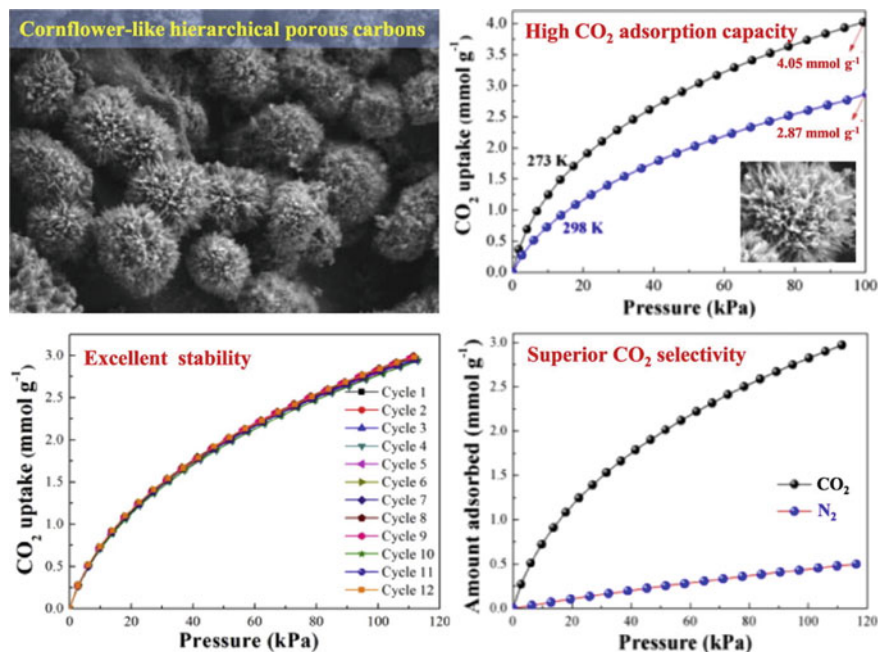
Fig. 5 Performance of hierarchical cornflower like porous carbon (FC4) adsorbent for CO_2 capture. **a** SEM image of FC4. The CO_2 adsorption isotherms display its, **b** high adsorption capacity of 4.05 and 2.87 m mol g^{-1} at 273 and 298 K, and, **c** excellent recyclability after 12 cycles. **d** The adsorption isotherms for CO_2 and N_2 reveal the trapping selectivity of FC4 for CO_2 from their initial and final CO_2/N_2 adsorption ratios of 24 and 6.4. Reprinted with permission from ref. (Chen et al. 2018a)

4 Filtration

Filtration is a physical separation process where we selectively isolate a particular substance from a mixture of substances. Our interest in filtration is parochial in using mesoporous membrane separation materials for liquid and gas phase separation. Filtration is crucial for the growing pollution across the world affecting air and water quality, especially in the urban regions. Air quality index is measured in terms of the concentration of particulate matter of diameter in the micro and nano scales in air. The particles of a size of less than 300 nm are the most dangerous for humans. Existing macroporous filters are not capable of handling these particles. Hence, mesoporous materials with lesser pore size have been developed. Likewise, water pollution is caused by large-scale contamination of water sources with a multitude of organic and inorganic contaminants. Mesoporous membranes serve as a cost-effective and efficient alternative to other filtration methods such as chemical precipitation, electrophoresis, electrodialysis, and magnetic separation. The large SSA and the specific pore size of mesoporous materials cater to this application too. Mesoporous silica was among the first explored for filtration and its properties such

as chemical inertness, thermal stability and tunability of the pore surface with functional groups for selective adsorption of particulate matter was hugely beneficial. One recurring problem with porous materials is the broad distribution of the pore size. In filtration the fraction of pores of a specific kind type (macro, meso and micro) and in certain cases uniformity in pore size is essential. For instance, it has been reported that mesopores contribute strongly to the capture of airborne nanoparticles while working with aerogels (Fig. 6) (Kim et al. 2016; Zhai and Jana 2017). In other work, selective separation of gold nanoparticles required tunable uniform pore sizes in the range from 2.8 to 11 nm (Liu et al. 2017). As mentioned earlier, functionalization of the mesoporous materials with groups like amines, thiol, dopamine and phosphates have resulted in high selectivity, high efficiency and faster adsorption (Bagheri et al. 2019; Enache et al. 2018; Giannakoudakis et al. 2021).

Selective removal of specific organic and inorganic pollutants such as pesticides, azo dyes, lead, phosphates, arsenic etc. using mesoporous adsorbents have been widely researched upon (Diagboya and Dikio 2018; Huang et al. 2017; Liu et al. 2018b). Nevertheless, most of those developments were laboratory studies and require extrapolation to large scale applications. An interesting modification is the magnetization of these adsorbents by designing magnetic core–shell systems such as Fe_3O_4@SBA-15 which could be easily removed from the solution after adsorption using an external magnetic force (Wang et al. 2015). Oil/water emulsion separation is essential for treating industrial wastewater and oil spills. It is an important future direction of exploration for mesoporous material application with the evolving global environmental policies. The small pore size of mesoporous materials enable speed and efficient separation of a range of oil/water emulsions compared to other
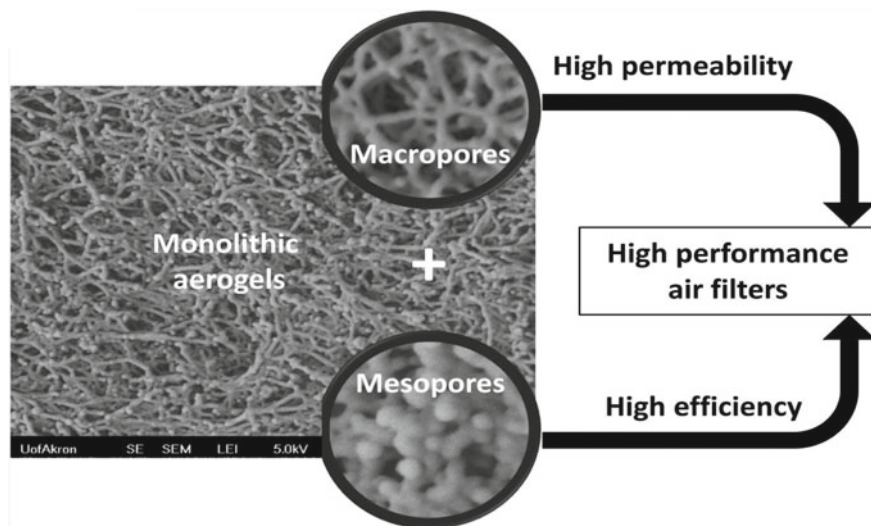
Fig. 6 The contribution of macro and mesopores in aerogel monoliths. Reprinted with permission from ref. (Kim et al. 2016)

traditional methods. But, the flow of heavy oil particles through small pores induce challenges such as lower influx and high infiltration pressure requirement (Gupta et al. 2017). Recently, mesoporous hafnium oxide was demonstrated as an excellent crude oil separation material (Hussain et al. 2020).

5 Catalysis

Catalysts are prevalent across various industries and processes such as energy processing, chemical synthesis (bulk and fine), environmental protection, pharmaceuticals and food processing. The catalytic reactions can be classified as acid-catalyzed, base-catalyzed, oxidation and hydrogenation reactions. Heterogeneous catalysis, i.e. the reaction where the catalyst and the mixture of reactants and products are of different phases, with nanoparticles has caveats due to sintering. Sintering is the degradation of the catalyst due to agglomeration or growth of the particle in the reaction environment (Hansen et al. 2013). The advent of MCM-14 led to new approaches in catalyst development. For example, mesoporous SBA-15 silica was loaded with nanostructured PdO/CeO_2 for a low-temperature methane oxidation reaction (Dai et al. 2018). Similar experiments were performed using other mesoporous support materials to negate the effects of sintering. The use of tubular halloysite lumens as support for palladium nanoparticles for 4-Nitrophenol reduction had been demonstrated earlier (Dedzo et al. 2016). Metal oxides like Cr_2O_3 and Co_3O_4 have also been used as mesoporous support materials and these were prepared by nanocasting method (Fig. 7). Recently, MIL-101(Cr) MOF was pre-impregnated with Pt NP and then calcined to get $Pt@Cr_2O_3$ catalyst for studying the toluene combustion reaction (Chen et al. 2018c). Apart from being protective shells, mesoporous materials benefit the catalysis via their large surface area enabling high nanoparticle loading and large pore size allowing diffusion pathways. Further, the pores of the support materials are tuned to improve the selectivity of the catalyst. Recent studies have shown that superior electrocatalytic activity can be achieved by tuning the pores and SSA for oxygen reduction reaction and ethanol oxidation (Li et al. 2019; Shah et al. 2017). For certain applications, the surface of mesoporous materials is functionalized with amines, cytosine, phenylamine, sulfonic acid, and so on to directly use them as catalysts (Doustkhah et al. 2019; Lakhi et al. 2017).

Two important industrial reactions involving mesoporous catalysts are fluid catalytic cracking (FCC) and Friedel crafts acylation. FCC is the process of converting heavy hydrocarbons in petroleum refineries to more usable low-molecular-weight products such as gasoline, diesel, and other lighter alkenes. Zeolite Y was a breakthrough in the petroleum industry. Currently, the directions of research in FCC is along creating highly mesoporous structures, introduction of different elements into the support and development of zeolite substitutes like ordered mesoporous silica. Friedel crafts acylation reaction enables attachment of different functional groups to the benzene ring and is one of the important reactions in chemical
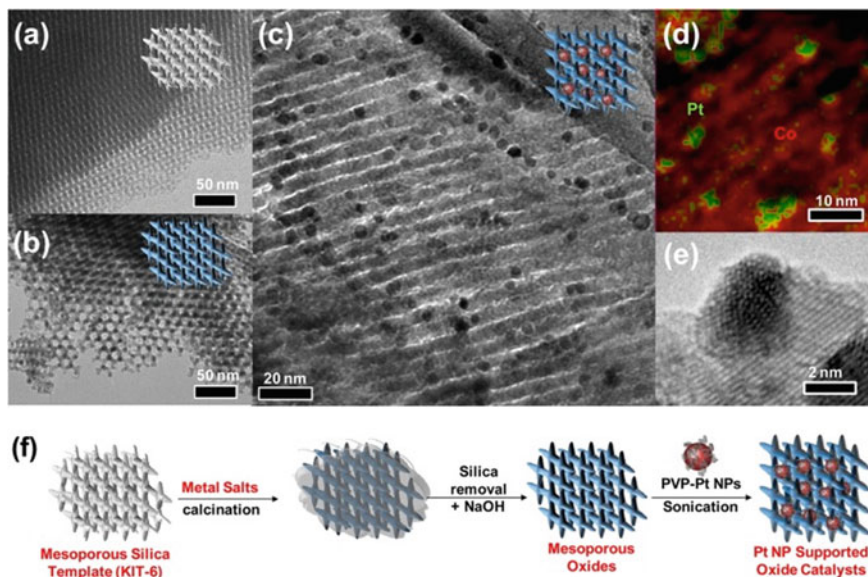
Fig. 7 TEM images of **a** the mesoporous silica template and, **b** the resulting Co_3O_4 replica. **c** TEM image of Pt/Co_3O_4 catalysts and, **d** their corresponding energy-dispersive spectroscopy (EDS) phase mapping, showing the merged image of the Co K (red) and Pt L (green) lines. **e** High-resolution TEM image of Pt/Co_3O_4 catalysts. **f** Illustration of the hard templating (nanocasting) approach for the preparation of mesoporous-oxide-supported Pt nanoparticle catalysts. Reprinted with permission from ref. (An et al. 2013)

manufacturing. The catalysis requires Lewis acidic centres. Many mesoporous silica-supported with Lewis acidic metallic centres and zeolites catalysts are used (Liang et al. 2017). Novel catalysts like mesoporous carbon nitride have also been proposed in literature (Yang et al. 2015). These studies show that catalysis is a major beneficiary of development in mesoporous materials.

6 Optics

Generally, the materials used for optical applications are synthesized by processes such as the sol–gel process, co-assembly of inorganic components, block copolymer templating and surfactants. It was observed that by introducing mesostructures into these materials its optical properties can be improved. Size confined structures. These mesostructures can act as active sites for doping and can produce size confined structures such as quantum dots (Scott et al. 2001). Surface functionalization/immobilization of mesostructured materials with photoactive species such as dyes impart optical properties in them. The main advantages of these mesoporous materials over the traditionally used materials for optical applications are

its (i) capability of achieving better dispersion of optically active components at higher concentrations of dyes without interactions. (ii) Possibility of rapid diffusion due to the availability of the open structures and uniform pores. (iii) Protective packaging of the optical species within the uniform three-dimensional arrays of the mesostructures. Some of the optical applications of these materials include optical sensing (molecules/ions), pH sensing, light-harvesting, laser applications, photochromic applications, and photoluminescence.

Recently, a fluorescent chemosensing material (2-MPT-SBA-15) was developed by the functionalization of SBA-15 along with a fluorescent chromophore 5-methoxy-2-thiazoles (2-MPT) for the multi-analyte sensing in water. This material exhibited both (1) pH-sensitive fluorescent behavior in the range of 1–1.57, and (2) a very fast and reproducible selective optical sensing ability towards Cu^{2+} ions in water (Li et al. 2007). In chemical sensing, the requirements such as negligible leaching and fast response are fulfilled by covalently attaching/anchoring the dye in the large pores during synthesis and removing the structure directing the block copolymer at a lower temperature (Wirnsberger et al. 2001). Photochromic materials are those which can change their color upon illumination. It is desirable to have a fast reaction and rapid switching between high/low transmission wavelength ranges for these materials. To attain this functionality, mesoporous structures with inorganic and organic components act as excellent hosts for photochromic dyes. Spiropyrane and spirooxazine derivatives are used for the color change phenomenon since these molecules undergo ring-opening upon light irradiation (Fig. 8). Mesoporous thin films prepared using dip coating of dye doped with precursor solution are colorless and exhibited complete transmission in the visible spectrum. When illuminated with 355 nm light, these films exhibited blue color immediately and became colorless with the removal of the UV lamp (Scott et al. 2001). Futher, it is possible to develop new optoelectronic devices with unique functionalities by extending the research towards other transition metal oxide systems.

Fig. 8 Photochromic mesostructured thin films doped with a spirooxazine. Transmission of the thin films during several on/off cycles. Reprinted with permission from ref. (Scott et al. 2001)
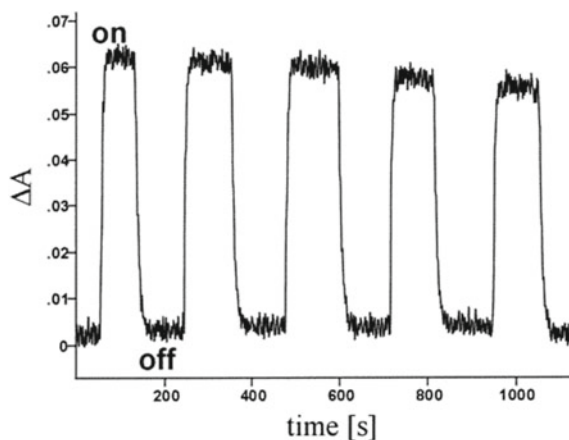
7 Drug Delivery

For the treatment of diseases like cancer, conventional treatment requires the usage of toxic chemicals leading to adverse side effects. The usage of such chemicals could lead to the damage of healthy cells as well. Hence, it is quintessential to develop a target specific drug delivery system that will attack only the malign cancerous cells. Some of the requirements for achieving this targeted drug delivery is to have a material which is biocompatible and at the same time have high drug loading capacity (Wen et al. 2017). Further, it should have zero premature release and respond precisely to the various endogenous and exogenous stimuli. Since 1992 after the discovery of MCM-41 material by the researchers at Mobil, different nanostructured materials such as gold nanoparticles, silicon nanoparticles and quantum dots have been developed for targeted delivery to treat the tumour growth. Mesoporous Silicon Nanoparticles (Fig. 9), commonly known as MSNs have gained immense popularity in this aspect. They have certain attractive properties like very large specific surface area (700 m^2/g), tunable pore sizes (2–50 nm), surface functionalization capability and good biocompatibility (Zhou et al. 2018). The flexibility in achieving different pore sizes make it suitable for incorporation of various guest agents. Furthermore, its porous structure can be enriched with functional groups such as silanol enabling interaction with other functional groups. These functional groups play an important role in determining controlled drug delivery under the influence of various stimuli. Recently, smart MSNs were developed and they are equipped as "controlled gate keepers" ensuring controlled drug release and preventing premature release (Wen et al. 2017). These studies show that by proper functionalization and nano-structuring of these MSNs it is possible to overcome many of the barriers associated with cancer treatment.

Fig. 9 Transmission electron images of mesoporous silicon nanoparticles. Reprinted with permission from (Zhou et al. 2018)
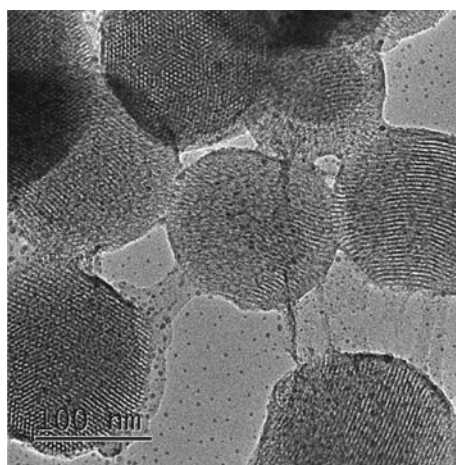
8 Conclusion and Future Scope

This chapter provides an overview of the various applications of mesoporous materials. In recent years significant progress has been made in the development of various mesoporous materials, however, challenges still remain. For example, the production of mesoporous materials in bulk and in a cost-effective manner is still a big challenge. Moreover, to realize its full potential, these materials should exhibit properties significantly better than the existing materials and/or at a cheaper cost. One of the main advantages of these mesoporous materials is the enormous flexibility it offers towards attaining different pore structures, surface functionalization and so on. However, methods to precisely control the pore morphologies at a bulk level to obtain the desired functionalities is still a big challenge. Off late there is an increasing demand for large quantities of such mesoporous materials. Hence, there is a need to develop novel synthesis routes that are capable of producing mesoporous materials in bulk quantities. Further, development in the characterization techniques to establish the properties of these materials in-situ also plays a key role in enhancing its commercial viability.

The difficulty in controlling unwanted side-reactions is another significant challenge in these mesoporous materials. High surface area and pore volumes provides enormous opportunities for various applications, but this could also act as sites for unwanted side reactions. These problems are prevalent in applications such as in batteries, fuel cells, solar cells and even in drug delivery. Several strategies have been proposed such as reducing the grain boundary area, surface functionalization and so on, to overcome these limitations. Recent developments like the usage of various artificial intelligence techniques to predict and optimize the desired pore structure requirements were found to be highly beneficial in developing new systems that could meet the requirements of specific applications. Moreover, significant developments in processing technology such as 3D printing, lithography and so on have made possible the fabrication of these materials with very high precision. Hence, with greater understanding coupled with the development in manufacturing and technology the future of these mesoporous materials looks promising.

References

Ahmed, A., Seth, S., Purewal, J., Wong-Foy, A.G., Veenstra, M., Matzger, A.J., Siegel, D.J.: Exceptional hydrogen storage achieved by screening nearly half a million metal-organic frameworks. Nat. Commun. **10**, 1568 (2019). https://doi.org/10.1038/s41467-019-09365-w

An, K., Alayoglu, S., Musselwhite, N., Plamthottam, S., Melaet, G., Lindeman, A.E., Somorjai, G.A.: Enhanced CO oxidation rates at the interface of mesoporous oxides and Pt nanoparticles. J. Am. Chem. Soc. **135**, 16689–16696 (2013). https://doi.org/10.1021/ja4088743

Augustyn, V., Come, J., Lowe, M.A., Kim, J.W., Taberna, P.-L., Tolbert, S.H., Abruña, H.D., Simon, P., Dunn, B.: High-rate electrochemical energy storage through Li$^+$ intercalation pseudocapacitance. Nat. Mater. **12**, 518–522 (2013). https://doi.org/10.1038/nmat3601

Bagheri, S., Amini, M.M., Behbahani, M., Rabiee, G.: Low cost thiol-functionalized mesoporous silica, KIT-6-SH, as a useful adsorbent for cadmium ions removal: a study on the adsorption isotherms and kinetics of KIT-6-SH. Microchem. J. **145**, 460–469 (2019). https://doi.org/10.1016/j.microc.2018.11.006

Balsamo, M., Erto, A., Lancia, A., Totarella, G., Montagnaro, F., Turco, R.: Post-combustion CO_2 capture: on the potentiality of amino acid ionic liquid as modifying agent of mesoporous solids. Fuel **218**, 155–161 (2018). https://doi.org/10.1016/j.fuel.2018.01.038

Brezesinski, T., Wang, J., Polleux, J., Dunn, B., Tolbert, S.H.: Templated nanocrystal-based porous TiO_2 films for next-generation electrochemical capacitors. J. Am. Chem. Soc. **131**, 1802–1809 (2009). https://doi.org/10.1021/ja8057309

Brezesinski, T., Wang, J., Tolbert, S.H., Dunn, B.: Ordered mesoporous α -MoO 3 with iso-oriented nanocrystalline walls for thin-film pseudocapacitors. Nat. Mater. **9**, 146–151 (2010). https://doi.org/10.1038/nmat2612

Chae, S., Ko, M., Kim, K., Ahn, K., Cho, J.: Confronting issues of the practical implementation of Si anode in high-energy lithium-ion batteries. Joule **1**, 47–60 (2017). https://doi.org/10.1016/j.joule.2017.07.006

Chen, W., Fan, Z., Dhanabalan, A., Chen, C., Wang, C.: Mesoporous silicon anodes prepared by magnesiothermic reduction for lithium ion batteries. J. Electrochem. Soc. **158**, A1055 (2011). https://doi.org/10.1149/1.3611433

Chen, C., Huang, H., Yu, Y., Shi, J., He, C., Albilali, R., Pan, H.: Template-free synthesis of hierarchical porous carbon with controlled morphology for CO_2 efficient capture. Chem. Eng. J. **353**, 584–594 (2018a). https://doi.org/10.1016/j.cej.2018.07.161

Chen, C., Yu, Y., He, C., Wang, L., Huang, H., Albilali, R., Cheng, J., Hao, Z.: Efficient capture of CO_2 over ordered micro-mesoporous hybrid carbon nanosphere. Appl. Surf. Sci. **439**, 113–121 (2018b). https://doi.org/10.1016/j.apsusc.2017.12.217

Chen, X., Chen, X., Cai, S., Chen, J., Xu, W., Jia, H., Chen, J.: Catalytic combustion of toluene over mesoporous Cr_2O_3-supported platinum catalysts prepared by in situ pyrolysis of MOFs. Chem. Eng. J. **334**, 768–779 (2018c). https://doi.org/10.1016/j.cej.2017.10.091

Cheng, H., Shapter, J.G., Li, Y., Gao, G.: Recent progress of advanced anode materials of lithium-ion batteries. J. Energy Chem. **57**, 451–468 (2021). https://doi.org/10.1016/j.jechem.2020.08.056

Dabbawala, A.A., Ismail, I., Vaithilingam, B.V., Polychronopoulou, K., Singaravel, G., Morin, S., Berthod, M., Al Wahedi, Y.: Synthesis of hierarchical porous Zeolite-Y for enhanced CO_2 capture. Microporous Mesoporous Mater. **303**, 110261 (2020). https://doi.org/10.1016/j.micromeso.2020.110261

Dai, F., Zai, J., Yi, R., Gordin, M.L., Sohn, H., Chen, S., Wang, D.: Bottom-up synthesis of high surface area mesoporous crystalline silicon and evaluation of its hydrogen evolution performance. Nat. Commun. **5**, 3605 (2014). https://doi.org/10.1038/ncomms4605

Dai, Y., Pavan Kumar, V., Zhu, C., MacLachlan, M.J., Smith, K.J., Wolf, M.O.: Mesoporous silica-supported nanostructured PdO/CeO$_2$ catalysts for low-temperature methane oxidation. ACS Appl. Mater. Interfaces **10**, 477–487 (2018). https://doi.org/10.1021/acsami.7b13408

Dedzo, G.K., Ngnie, G., Detellier, C.: PdNP decoration of halloysite lumen via selective grafting of ionic liquid onto the aluminol surfaces and catalytic application. ACS Appl. Mater. Interfaces **8**, 4862–4869 (2016). https://doi.org/10.1021/acsami.5b10407

Diagboya, P.N.E., Dikio, E.D.: Silica-based mesoporous materials; emerging designer adsorbents for aqueous pollutants removal and water treatment. Microporous Mesoporous Mater. **266**, 252–267 (2018). https://doi.org/10.1016/j.micromeso.2018.03.008

Doustkhah, E., Lin, J., Rostamnia, S., Len, C., Luque, R., Luo, X., Bando, Y., Wu, K.C.-W., Kim, J., Yamauchi, Y., Ide, Y.: Development of sulfonic-acid-functionalized mesoporous materials: synthesis and catalytic applications. Chem. Eur. J. **25**, 1614–1635 (2019). https://doi.org/10.1002/chem.201802183

Eftekhari, A.: Ordered mesoporous materials for lithium-ion batteries. Microporous Mesoporous Mater. **243**, 355–369 (2017). https://doi.org/10.1016/j.micromeso.2017.02.055

Enache, D.F., Vasile, E., Simonescu, C.M., Culita, D., Vasile, E., Oprea, O., Pandele, A.M., Razvan, A., Dumitru, F., Nechifor, G.: Schiff base-functionalized mesoporous silicas (MCM-41, HMS) as Pb(II) adsorbents. RSC Adv. **8**, 176–189 (2018). https://doi.org/10.1039/C7RA12310H

Giannakoudakis, D.A., Anastopoulos, I., Barczak, M., Antoniou, E., Terpiłowski, K., Mohammadi, E., Shams, M., Coy, E., Bakandritsos, A., Katsoyiannis, I.A., Colmenares, J.C., Pashalidis, I.: Enhanced uranium removal from acidic wastewater by phosphonate-functionalized ordered mesoporous silica: surface chemistry matters the most. J. Hazard. Mater. **413**, 125279 (2021). https://doi.org/10.1016/j.jhazmat.2021.125279

Gupta, R.K., Dunderdale, G.J., England, M.W., Hozumi, A.: Oil/water separation techniques: a review of recent progresses and future directions. J. Mater. Chem. A **5**, 16025–16058 (2017). https://doi.org/10.1039/C7TA02070H

Hansen, T.W., DeLaRiva, A.T., Challa, S.R., Datye, A.K.: Sintering of catalytic nanoparticles: particle migration or ostwald Ripening? Acc. Chem. Res. **46**, 1720–1730 (2013). https://doi.org/10.1021/ar3002427

Harada, T., Hatton, T.A.: Colloidal nanoclusters of mgo coated with alkali metal nitrates/nitrites for rapid, high capacity CO_2 capture at moderate temperature. Chem. Mater. **27**, 8153–8161 (2015). https://doi.org/10.1021/acs.chemmater.5b03904

Hirscher, M., Yartys, V.A., Baricco, M., Colbe, J.B., Blanchard, D., Bowman, R.C., Broom, D.P., Buckley, C.E., Chang, F., Chen, P., Cho, Y.W., Crivello, J.-C., Cuevas, F., David, W.I.F., de Jongh, P.E., Denys, R.V., Dornheim, M., Felderhoff, M., Filinchuk, Y., Froudakis, G.E., Grant, D.M., Gray, E.MacA., Hauback, B.C., He, T., Humphries, T.D., Jensen, T.R., Kim, S., Kojima, Y., Latroche, M., Li, H.-W., Lototskyy, M.V., Makepeace, J.W., Møller, K.T., Naheed, L., Ngene, P., Noréus, D., Nygård, M.M., Orimo, S., Paskevicius, M., Pasquini, L., Ravnsbæk, D.B., Veronica Sofianos, M., Udovic, T.J., Vegge, T., Walker, G.S., Webb, C.J., Weidenthaler, C., Zlotea, C.: Materials for hydrogen-based energy storage—past, recent progress and future outlook. J. Alloys Compd. **827**, 153548 (2020). https://doi.org/10.1016/j.jallcom.2019.153548

Huang, W., Zhang, Y., Li, D.: Adsorptive removal of phosphate from water using mesoporous materials: a review. J. Environ. Manage. **193**, 470–482 (2017). https://doi.org/10.1016/j.jenvman.2017.02.030

Hussain, F.A., Zamora, J., Ferrer, I.M., Kinyua, M., Velázquez, J.M.: Adsorption of crude oil from crude oil–water emulsion by mesoporous hafnium oxide ceramics. Environ. Sci.: Water Res. Technol. **6**, 2035–2042 (2020). https://doi.org/10.1039/D0EW00451K

Jaramillo, D.E., Jiang, H.Z.H., Evans, H.A., Chakraborty, R., Furukawa, H., Brown, C.M., Head-Gordon, M., Long, J.R.: Ambient-temperature hydrogen storage via vanadium(II)-dihydrogen complexation in a metal-organic framework. J. Am. Chem. Soc. **143**, 6248–6256 (2021). https://doi.org/10.1021/jacs.1c01883

Jeon, N.J., Noh, J.H., Yang, W.S., Kim, Y.C., Ryu, S., Seo, J., Seok, S.I.: Compositional engineering of perovskite materials for high-performance solar cells. Nature **517**, 476–480 (2015). https://doi.org/10.1038/nature14133

Jia, H., Gao, P., Yang, J., Wang, J., Nuli, Y., Yang, Z.: Novel three-dimensional mesoporous silicon for high power lithium-ion battery anode material. Adv. Energy Mater. **1**, 1036–1039 (2011). https://doi.org/10.1002/aenm.201100485

Kim, S.J., Chase, G., Jana, S.C.: The role of mesopores in achieving high efficiency airborne nanoparticle filtration using aerogel monoliths. Sep. Purif. Technol. **166**, 48–54 (2016). https://doi.org/10.1016/j.seppur.2016.04.017

Kim, N., Park, H., Yoon, N., Lee, J.K.: Zeolite-templated mesoporous silicon particles for advanced lithium-ion battery anodes. ACS Nano **12**, 3853–3864 (2018). https://doi.org/10.1021/acsnano.8b01129

Kresge, C.T., Leonowicz, M.E., Roth, W.J., Vartuli, J.C., Beck, J.S.: Ordered mesoporous molecular sieves synthesized by a liquid-crystal template mechanism. Nature **359**, 710–712 (1992). https://doi.org/10.1038/359710a0

Lakhi, K.S., Park, D.-H., Al-Bahily, K., Cha, W., Viswanathan, B., Choy, J.-H., Vinu, A.: Mesoporous carbon nitrides: synthesis, functionalization, and applications. Chem. Soc. Rev. **46**, 72–101 (2017). https://doi.org/10.1039/C6CS00532B

Lee, J.H., Choi, W.S., Woo, H.-Y., Nersisyan, H.H., Jin, E.M., Jeong, S.M.: Polysiloxane-derived silicon nanoparticles for Li-ion battery. J. Energy Storage **27**, 101141 (2020). https://doi.org/10.1016/j.est.2019.101141

Leijtens, T., Eperon, G.E., Pathak, S., Abate, A., Lee, M.M., Snaith, H.J.: Overcoming ultraviolet light instability of sensitized TiO_2 with meso-superstructured organometal tri-halide perovskite solar cells. Nat. Commun. **4**, 2885 (2013). https://doi.org/10.1038/ncomms3885

Lewis, J.A., Tippens, J., Cortes, F.J.Q., McDowell, M.T.: Chemo-mechanical challenges in solid-state batteries. Trends Chem. **1**, 845–857 (2019). https://doi.org/10.1016/j.trechm.2019.06.013

Li, L.-L., Sun, H., Fang, C.-J., Xu, J., Jin, J.-Y., Yan, C.-H.: Optical sensors based on functionalized mesoporous silica SBA-15 for the detection of multianalytes (H+ and Cu2+) in water. J. Mater. Chem. **17**, 4492–4498 (2007). https://doi.org/10.1039/B708857D

Li, X., Gu, M., Hu, S., Kennard, R., Yan, P., Chen, X., Wang, C., Sailor, M.J., Zhang, J.-G., Liu, J.: Mesoporous silicon sponge as an anti-pulverization structure for high-performance lithium-ion battery anodes. Nat. Commun. **5**, 4105 (2014). https://doi.org/10.1038/ncomms5105

Li, X., Yan, C., Wang, J., Graff, A., Schweizer, S.L., Sprafke, A., Schmidt, O.G., Wehrspohn, R.B.: Stable silicon anodes for lithium-ion batteries using mesoporous metallurgical silicon. Adv. Energy Mater. **5**, 1401556 (2015). https://doi.org/10.1002/aenm.201401556

Li, C., Iqbal, M., Jiang, B., Wang, Z., Kim, J., Nanjundan, A.K., Whitten, A.E., Wood, K., Yamauchi, Y.: Pore-tuning to boost the electrocatalytic activity of polymeric micelle-templated mesoporous Pd nanoparticles. Chem. Sci. **10**, 4054–4061 (2019). https://doi.org/10.1039/C8SC03911A

Liang, H.-W., Wei, W., Wu, Z.-S., Feng, X., Müllen, K.: Mesoporous metal-nitrogen-doped carbon electrocatalysts for highly efficient oxygen reduction reaction. J. Am. Chem. Soc. **135**, 16002–16005 (2013). https://doi.org/10.1021/ja407552k

Liang, J., Li, X., Hou, Z., Zhang, W., Zhu, Y., Qian, Y.: A deep reduction and partial oxidation strategy for fabrication of mesoporous Si anode for lithium ion batteries. ACS Nano **10**, 2295–2304 (2016). https://doi.org/10.1021/acsnano.5b06995

Liang, J., Liang, Z., Zou, R., Zhao, Y.: Heterogeneous catalysis in zeolites, mesoporous silica, and metal-organic frameworks. Adv. Mater. **29**, 1701139 (2017). https://doi.org/10.1002/adma.201701139

Liao, L., Zhang, Q., Su, Z., Zhao, Z., Wang, Y., Li, Y., Lu, X., Wei, D., Feng, G., Yu, Q., Cai, X., Zhao, J., Ren, Z., Fang, H., Robles-Hernandez, F., Baldelli, S., Bao, J.: Efficient solar water-splitting using a nanocrystalline CoO photocatalyst. Nat. Nanotechnol. **9**, 69–73 (2014). https://doi.org/10.1038/nnano.2013.272

Licciulli, A., Notaro, M., De Santis, S., Terreni, C., Kunjalukkal Padmanabhan, S.: CO_2 capture on amine impregnated mesoporous alumina-silica mixed oxide spheres. Fuel Process. Technol. **166**, 202–208 (2017). https://doi.org/10.1016/j.fuproc.2017.06.009

Liu, Y., Che, R., Chen, G., Fan, J., Sun, Z., Wu, Z., Wang, M., Li, B., Wei, J., Wei, Y., Wang, G., Guan, G., Elzatahry, A.A., Bagabas, A.A., Al-Enizi, A.M., Deng, Y., Peng, H., Zhao, D.: Radially oriented mesoporous TiO_2 microspheres with single-crystal-like anatase walls for high-efficiency optoelectronic devices. Sci. Adv. **1**, e1500166 (2015). https://doi.org/10.1126/sciadv.1500166

Liu, Y., Shen, D., Chen, G., Elzatahry, A.A., Pal, M., Zhu, H., Wu, L., Lin, J., Al-Dahyan, D., Li, W., Zhao, D.: Mesoporous silica thin membranes with large vertical mesochannels for nanosize-based separation. Adv. Mater. **29**, 1702274 (2017). https://doi.org/10.1002/adma.201702274

Liu, R., He, P., Wu, Z., Guo, F., Huang, B., Wang, Q., Huang, Z., Wang, C., Li, Y.: PEO/hollow mesoporous polymer spheres composites as electrolyte for all solid state lithium ion battery. J. Electroanal. Chem. **822**, 105–111 (2018a). https://doi.org/10.1016/j.jelechem.2018.05.021

Liu, Z., Chen, J., Wu, Y., Li, Y., Zhao, J., Na, P.: Synthesis of magnetic orderly mesoporous α-Fe_2O_3 nanocluster derived from MIL-100(Fe) for rapid and efficient arsenic(III,V) removal. J. Hazard. Mater. **343**, 304–314 (2018b). https://doi.org/10.1016/j.jhazmat.2017.09.047

Lüthi, D., Le Floch, M., Bereiter, B., Blunier, T., Barnola, J.-M., Siegenthaler, U., Raynaud, D., Jouzel, J., Fischer, H., Kawamura, K., Stocker, T.F.: High-resolution carbon dioxide concentration record 650,000–800,000 years before present. Nature **453**, 379–382 (2008). https://doi.org/10.1038/nature06949

Maekawa, H., Iwatani, T., Shen, H., Yamamura, T., Kawamura, J.: Enhanced lithium ion conduction and the size effect on interfacial phase in Li_2ZnI_4–mesoporous alumina composite electrolyte. Solid State Ionics **178**, 1637–1641 (2008). https://doi.org/10.1016/j.ssi.2007.10.018

Panella, B., Hirscher, M., Pütter, H., Müller, U.: Hydrogen adsorption in metal–organic frameworks: Cu-MOFs and Zn-MOFs compared. Adv. Funct. Mater. **16**, 520–524 (2006). https://doi.org/10.1002/adfm.200500561

Park, S.J., Kim, Y., Jones, C.W.: $NaNO_3$-promoted mesoporous MgO for high-capacity CO_2 capture from simulated flue gas with isothermal regeneration. Chemsuschem **13**, 2988–2995 (2020). https://doi.org/10.1002/cssc.202000259

Salah, M., Murphy, P., Hall, C., Francis, C., Kerr, R., Fabretto, M.: Pure silicon thin-film anodes for lithium-ion batteries: a review. J. Power Sources **414**, 48–67 (2019). https://doi.org/10.1016/j.jpowsour.2018.12.068

Scott, B.J., Wirnsberger, G., Stucky, G.D.: Mesoporous and mesostructured materials for optical applications. Chem. Mater. **13**, 3140–3150 (2001). https://doi.org/10.1021/cm0110730

Shah, S.S.A., Peng, L., Najam, T., Cheng, C., Wu, G., Nie, Y., Ding, W., Qi, X., Chen, S., Wei, Z.: Monodispersed Co in mesoporous polyhedrons: fine-tuning of ZIF-8 structure with enhanced oxygen reduction activity. Electrochim. Acta **251**, 498–504 (2017). https://doi.org/10.1016/j.electacta.2017.08.091

Shi, Y., Li, B., Zhu, Q., Shen, K., Tang, W., Xiang, Q., Chen, W., Liu, C., Luo, J., Yang, S.: MXene-based mesoporous nanosheets toward superior lithium ion conductors. Adv. Energy Mater. **10**, 1903534 (2020). https://doi.org/10.1002/aenm.201903534

Song, T., Zhao, H., Hu, Y., Sun, N., Zhang, H.: Facile assembly of mesoporous silica nanoparticles with hierarchical pore structure for CO_2 capture. Chin. Chem. Lett. **30**, 2347–2350 (2019). https://doi.org/10.1016/j.cclet.2019.07.024

Sujith, R., Chauhan, P.K., Gangadhar, J., Maheshwari, A.: Graphene nanoplatelets as nanofillers in mesoporous silicon oxycarbide polymer derived ceramics. Sci. Rep. **8**, 17633 (2018). https://doi.org/10.1038/s41598-018-36080-1

Sun, L., Wang, F., Su, T., Du, H.: Room-temperature solution synthesis of mesoporous silicon for lithium ion battery anodes. ACS Appl. Mater. Interfaces **9**, 40386–40393 (2017). https://doi.org/10.1021/acsami.7b14312

Vangari, M., Pryor, T., Jiang, L.: Supercapacitors: review of materials and fabrication methods. J. Energy Eng. **139**, 72–79 (2013). https://doi.org/10.1061/(ASCE)EY.1943-7897.0000102

Vekariya, R.L., Dhar, A., Paul, P.K., Roy, S.: An overview of engineered porous material for energy applications: a mini-review. Ionics **24**, 1–17 (2018). https://doi.org/10.1007/s11581-017-2338-9

Wang, C., Ren, J., Chen, H., Zhang, Y., Ostrikov, K. (Ken), Zhang, W., Li, Y.: Synthesis of high-quality mesoporous silicon particles for enhanced lithium storage performance. Mater. Chem. Phys. **173**, 89–94 (2016). https://doi.org/10.1016/j.matchemphys.2016.01.043

Wang, S., Wang, K., Dai, C., Shi, H., Li, J.: Adsorption of Pb2+ on amino-functionalized core–shell magnetic mesoporous SBA-15 silica composite. Chem. Eng. J. **262**, 897–903 (2015). https://doi.org/10.1016/j.cej.2014.10.035

Wen, J., Yang, K., Liu, F., Li, H., Xu, Y., Sun, S.: Diverse gatekeepers for mesoporous silica nanoparticle based drug delivery systems. Chem. Soc. Rev. **46**, 6024–6045 (2017). https://doi.org/10.1039/C7CS00219J

Wirnsberger, G., Yang, P., Scott, B.J., Chmelka, B.F., Stucky, G.D.: Mesostructured materials for optical applications: from low-k dielectrics to sensors and lasers. Spectrochim. Acta Part A Mol. Biomol. Spectrosc. **57**, 2049–2060 (2001). https://doi.org/10.1016/S1386-1425(01)00503-0

Wu, Z., Lv, Y., Xia, Y., Webley, P.A., Zhao, D.: Ordered mesoporous platinum@graphitic carbon embedded nanophase as a highly active, stable, and methanol-tolerant oxygen reduction electrocatalyst. J. Am. Chem. Soc. **134**, 2236–2245 (2012). https://doi.org/10.1021/ja209753w

Yang, P., Wirnsberger, G., Huang, H.C., Cordero, S.R., McGehee, M.D., Scott, B., Deng, T., Whitesides, G.M., Chmelka, B.F., Buratto, S.K., Stucky, G.D.: Mirrorless lasing from mesostructured waveguides patterned by soft lithography. Science **287**, 465–467 (2000). https://doi.org/10.1126/science.287.5452.465

Yang, Q., Wang, W., Zhao, Y., Zhu, J., Zhu, Y., Wang, L.: Metal-free mesoporous carbon nitride catalyze the friedel-crafts reaction by activation of benzene. RSC Adv. **5**, 54978–54984 (2015). https://doi.org/10.1039/C5RA08871B

Ye, Y., Jo, C., Jeong, I., Lee, J.: Functional mesoporous materials for energy applications: solar cells, fuel cells, and batteries. Nanoscale **5**, 4584 (2013). https://doi.org/10.1039/c3nr00176h

Yoon, T., Bok, T., Kim, C., Na, Y., Park, S., Kim, K.S.: Mesoporous silicon hollow nanocubes derived from metal-organic framework template for advanced lithium-ion battery anode. ACS Nano **11**, 4808–4815 (2017). https://doi.org/10.1021/acsnano.7b01185

Yu, Y., Li, J., Geng, D., Wang, J., Zhang, L., Andrew, T.L., Arnold, M.S., Wang, X.: Development of lead iodide perovskite solar cells using three-dimensional titanium dioxide nanowire architectures. ACS Nano **9**, 564–572 (2015). https://doi.org/10.1021/nn5058672

Zhai, C., Jana, S.C.: Tuning porous networks in polyimide aerogels for airborne nanoparticle filtration. ACS Appl. Mater. Interfaces. **9**, 30074–30082 (2017). https://doi.org/10.1021/acsami.7b09345

Zhang, X., Lin, R.-B., Wang, J., Wang, B., Liang, B., Yildirim, T., Zhang, J., Zhou, W., Chen, B.: Optimization of the pore structures of MOFs for record high hydrogen volumetric working capacity. Adv. Mater. **32**, 1907995 (2020). https://doi.org/10.1002/adma.201907995

Zhao, D., Feng, J., Huo, Q., Melosh, N., Fredrickson, G.H., Chmelka, B.F., Stucky, G.D.: Triblock copolymer syntheses of mesoporous silica with periodic 50–300 angstrom pores. Science **279**, 548–552 (1998). https://doi.org/10.1126/science.279.5350.548

Zhao, J., Lai, H., Lyu, Z., Jiang, Y., Xie, K., Wang, X., Wu, Q., Yang, L., Jin, Z., Ma, Y., Liu, J., Hu, Z.: Hydrophilic hierarchical nitrogen-doped carbon nanocages for ultrahigh supercapacitive performance. Adv Mater. **27**, 3541–3545 (2015). https://doi.org/10.1002/adma.201500945

Zhao, X.S., Lu, G.Q. (Max), Millar, G.J.: Advances in mesoporous molecular sieve MCM-41. Ind. Eng. Chem. Res. **35**, 2075–2090 (1996). https://doi.org/10.1021/ie950702a

Zheng, F., Kotobuki, M., Song, S., Lai, M.O., Lu, L.: Review on solid electrolytes for all-solid-state lithium-ion batteries. J. Power Sources **389**, 198–213 (2018). https://doi.org/10.1016/j.jpowsour.2018.04.022

Zhou, Y., Jiang, X., Chen, L., Yue, J., Xu, H., Yang, J., Qian, Y.: Novel mesoporous silicon nanorod as an anode material for lithium ion batteries. Electrochim. Acta **127**, 252–258 (2014a). https://doi.org/10.1016/j.electacta.2014.01.158

Zhou, Y., Yang, J., Su, H., Zeng, J., Jiang, S.P., Goddard, W.A.: Insight into proton transfer in phosphotungstic acid functionalized mesoporous silica-based proton exchange membrane fuel cells. J. Am. Chem. Soc. **136**, 4954–4964 (2014b). https://doi.org/10.1021/ja411268q

Zhou, Y., Quan, G., Wu, Q., Zhang, X., Niu, B., Wu, B., Huang, Y., Pan, X., Wu, C.: Mesoporous silica nanoparticles for drug and gene delivery. Acta Pharm. Sin. B **8**, 165–177 (2018). https://doi.org/10.1016/j.apsb.2018.01.007

Zhu, Y., Murali, S., Stoller, M.D., Ganesh, K.J., Cai, W., Ferreira, P.J., Pirkle, A., Wallace, R.M., Cychosz, K.A., Thommes, M., Su, D., Stach, E.A., Ruoff, R.S.: Carbon-based supercapacitors produced by activation of graphene. Science **332**, 1537–1541 (2011). https://doi.org/10.1126/science.1200770

Advanced Ordered Nanoporous Materials

G. T. M. Kadja, N. Nurdini, Y. K. Krisnandi, I. R. Saragi, Y. Yasmine, A. T. N. Fajar, L. Larasati, W. W. Lestari, A. Pangestu, and O. A. Saputra

Abstract Ordered nanoporous materials have attracted much attention due to their unique pore architecture, tunable physicochemical properties, which find applications in a broad spectrum of catalysis, separation, adsorption, drug delivery, energy storage, and sensing. In the past decades, the amount of research on ordered nanoporous materials has grown incrementally, resulting in diverse types of these materials with unprecedented structures. Herein, this chapter presents the recent advances of ordered nanoporous materials, including zeolites, ordered mesoporous materials (OMMs), metal–organic frameworks (MOFs), and covalent organic frameworks (COFs). Several vital aspects, i.e., structural and physicochemical properties,

G. T. M. Kadja (✉) · N. Nurdini
Division of Inorganic and Physical Chemistry, Institut Teknologi Bandung, Jl. Ganesha No. 10, Bandung 40132, Indonesia
e-mail: kadja@chem.itb.ac.id

G. T. M. Kadja
Research Center for Nanosciences and Nanotechnology, Institut Teknologi Bandung, Jl. Ganesha No. 10, Bandung 40132, Indonesia

Center for Catalysis and Reaction Engineering, Institut Teknologi Bandung, Jl. Ganesha No. 10, Bandung 40132, Indonesia

Y. K. Krisnandi · I. R. Saragi · Y. Yasmine
Solid Inorganic Framework Laboratory, Department of Chemistry, Faculty of Mathematics and Natural Science, Universitas Indonesia, Depok 16424, Indonesia

Y. K. Krisnandi
Inorganic Chemistry Division, Department of Chemistry, Faculty of Mathematics and Natural Science, Universitas Indonesia, Depok 16424, Indonesia

I. R. Saragi
Department of Chemistry, Faculty of Mathematics and Natural Science, Universitas Sumatera Utara, Medan 20155, Indonesia

A. T. N. Fajar
Department of Applied Chemistry, Graduate School of Engineering, Kyushu University, 744 Motooka, Fukuoka 819-0395, Japan

L. Larasati · W. W. Lestari · A. Pangestu · O. A. Saputra
Division of Inorganic Chemistry, Universitas Sebelas Maret, Jl. Ir. Sutami No 36A, Kentingan, Jebres, Surakarta 57216, Indonesia

synthesis, and applications, are comprehensively discussed. Finally, challenges and prospects for future improvement are also elaborated.

Keywords Nanopores · Zeolite · MOF · COF · Mesoporous materials

1 Introduction

Nanoporous materials are either inorganic, organic, or inorganic–organic hybrid materials, which possess pores within the nanoscale (<100 nm). International Union of Pure and Applied Chemistry (IUPAC) classifies nanoporous materials into three types based on the pore size, i.e., microporous (pore size less than 2 nm), meso-porous (pore size from 2 to 50 nm), and macroporous (pore size more than 50 nm) (Thommes et al. 2015). Highly open structure and large surface area have enabled their applications in established fields such as catalysis, separation, and adsorption, while rendering them up-and-coming in cutting-edge applications, e.g., sensor, drug delivery, and energy storage. Thus, tremendous efforts have been devoted to fabri-cating many novel nanoporous materials with desired structure and physicochemical properties.

It should be noted that the nanopores could be ordered and disordered based on their regularity. Nonetheless, this chapter will focus solely on the ordered nanoporous materials, which include zeolite (inorganic, microporous), ordered mesoporous mate-rials (inorganic, mesoporous), metal–organic frameworks (inorganic–organic hybrid, microporous), and covalent organic frameworks (organic, microporous). The hierar-chically porous materials comprising more than one porosity are also included in this chapter. Herein, we comprehensively discuss each ordered nanoporous material with the corresponding structure and physicochemical properties, synthetic techniques, and applications. This chapter is concluded with a summary and the prospects for future development.

2 Zeolites

2.1 Structure and Physicochemical Properties

Zeolites, in general, are crystalline inorganic materials composed of corner-sharing SiO_4 and AlO_4 tetrahedra linked through oxygen atoms creating a three-dimensional, highly regular microporous structure (<2 nm). The structures have cavities or cages connected by ring or pore openings with defined size and shape. The name zeolite ((from the Greek, zeo = to boil and lithos = stone; stone that boil) was given by Swedish mineralogist A.F. Cronstedt, who discovered these minerals in 1756 since when they were heated rapidly, they released water and seemed to boil. This silicate material belongs to the tectosilicate family that in nature can be found as minerals

in volcanic areas, alkaline desert lake sediments, soils, or marine sediments. Until today, there are about 67 natural zeolites that have been indexed by International Zeolite Association (IZA) that come with various shapes, pore and cavity sizes, and availability. The substitution of SiO_4 with AlO_4 introduces a negative charge to the counterbalanced structure by exchangeable cations (Na^+, K^+, Mg^{2+}, and Ca^{2+}) in the vicinity.

Zeolites have been utilized in various applications, ranging from daily activities in the household and agriculture to industrial processes due to some unique properties in one structure, such as reversible water molecule adsorption–desorption, cation exchangeability, large surface area, and regular pore shapes and sizes. More on structure, properties, and application will be discussed later in this section.

Although many natural zeolites are abundantly available, their limited structures and compositions, together with the presence of impurities, reduce their commercial application mainly to simple technologies such as building materials, water purification, agriculture, and animal care. On the other hand, for more sophisticated and high-end industrial applications such as adsorption, ion exchange, catalysis, membrane, synthetic zeolites, having well-defined structure and pore system, composition, tailored functional and active surface are employed. According to the Structure Commission of the International Zeolite Association (IZA-SC), at present, there are 254 structures officially registered in its database (consists of 232 framework types and 22 families of disordered frameworks, i.e., intergrowths of two or more different but structurally related frameworks) (Baerlocher and McCusker 2017). In the last three years, the database has been updated with 17 new approved frameworks. Later, it will be shown how computation and machine learning get involved in synthesizing new zeolite materials.

In 1997, a subcommittee of the Commission on New Minerals and Mineral Names of the International Mineralogical Association defined a zeolite mineral as:

> … a crystalline substance with a structure characterized by a framework of linked tetrahedra, each consisting of four O atoms surrounding a cation. This framework contains open cavities in the form of channels and cages. These are usually occupied by H_2O molecules and extra-framework cations that are commonly exchangeable. The channels are large enough to allow the passage of guest species. In the hydrated phases, dehydration occurs at temperature mostly below about 400°C and is largely reversible. The framework may be interrupted by (OH, F) groups; these occupy a tetrahedron apex that is not shared with adjacent tetrahedral. (Coombs et al. 1997)

This definition applies not only to natural aluminosilicate minerals but also to synthetic zeolites. Zeolite's framework structure determines its function and application.

It is mentioned earlier that the zeolite framework is built up from corner-sharing TO_4 tetrahedra that are called primary building units (PBU). Then, researchers developed a framework with one single secondary building unit (SBU). The database of zeolite structures contains 23 different SBUs, which can be found via framework-type pages. However, it is unlikely to create a single type of SBU; therefore, SBUs are no longer generated for the newer frameworks in IZA Database. Instead, the structures are described using composite building units (CBUs). CBUs represent

standard structural features, including cages, channels, chains, and layers, present in more than one zeolite. For example, the SOD framework type can be built up using six rings only (its SBU), as can 50 other frameworks, but its formation is better described by the sodalite cage (its CBU). This cage is present in 11 different zeolite frameworks (most notably FAU and LTA). The sodalite cage is not an SBU because it cannot build up the SOD framework exclusively; T-atoms in the sodalite cages overlap in the SOD framework. The examples of how zeolite frameworks are built from PBU and CBU are depicted in Fig. 1a (Smeets and Zou 2017).
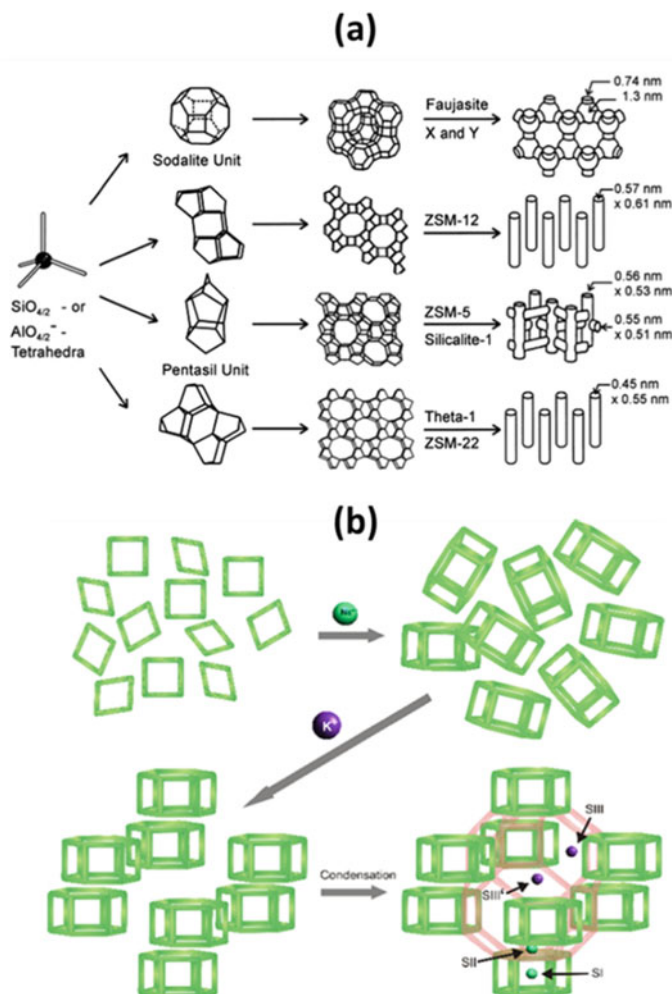
Fig. 1 Schematic illustrations of **a** four selected zeolite frameworks and their micropore systems (Smeets and Zou 2017) and the synergistic role of Na^+ and K^+ in directing the formation of CHA frameworks (Kadja et al. 2020a)

Due to the existence of such unique and comprehensive features in their structure, zeolites have some physicochemical properties as follows:

1. Crystal morphology: Zeolites with homogeneous and intracrystalline porosity have developed a microporous structure that causes very high surface areas and pore volumes, which confer these materials a high adsorption capacity that leads to the application as molecular sieves for gas separation and adsorbents (Wang and Peng 2010; Flanigen 2001; Wenten et al. 2020; Kurniawati et al. 2021). Recently, many have reported work on controllable and tunable morphology such as hierarchical porous structures, zeolite membranes, hollow zeolite spheres, core@shell structured zeolites (Li et al. 2019), 2D-zeolites, and nanosheets (Schulman et al. 2020).

2. Pore topology: Channels and/or cages of molecular dimensions in zeolites will allow discrimination among molecules of different sizes and shapes. The intracrystalline porosity also plays an essential role in catalytic application since it creates shape selectivity for reactant, transition state, and products (Martinez and Corma 2013).

3. Chemical composition: Classic zeolites are aluminosilicate frameworks having a composition of

$$\left(M^+\right)_a \left(M^{2+}\right)_b \left[Al^{(a+2b)}Si^{n-(a+2b)}O_{2n}\right].mH_2O$$
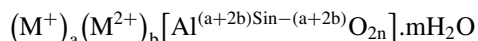
Typical tectosilicate family, zeolite has an atomic ratio $O/(Si + Al) = 2$, while according to Lowenstein's rule, the Si/Al ratio is always > 1 (Millini and Bellussi 2017).

In nature, some silicates (SiO_4) undergo isomorphous substitution with AlO_4, resulting in a negative charge in the framework that is compensated by exchangeable cations. This leads to applications based on cation exchange such as detergent, water softening, and heavy metal removal. Furthermore, in modern zeolites, Al and/or Si can be replaced (at least partially) by other elements, as in the case of replacing some Si with Ge in Thomsonite (Millini and Bellussi 2017) and exchanging Si and/or Al in crystalline microporous aluminophosphates and its derivatives (AlPO, SAPO, MeAPO, and MeAPSOs) (Hartmann and Kevan 2002).

2.2 Zeolite Synthesis

Many syntheses of commercial zeolites are carried out using silica, alumina, inorganic cation, hydroxide, water, and optionally OSDA reagents ingredients, through hydrothermal synthesis procedure at certain crystallization time and temperature, following the sequence of steps: (1) mixing of all of the ingredients to form a homogenous gel; (2) heating of the gel at a certain temperature (70 °C to 200 °C), in a Teflon-lined stainless steel autoclave; (3) evolution of the reaction mixture to form the

designated framework; and (4) recovery of the zeolite crystals by filtration or centrifugation, washing, and drying. The role of each compound to make the gel composition, crystallization time, and the temperature has been widely reviewed (Hartmann et al. 2016; Martinez and Corma 2013; Kadja et al. 2015, 2017; Mukaromah et al. 2016). The role of OSDA is mainly explained in this chapter since it could be reworded as the decisive factor in synthesizing most zeolites.

Organic structure-directing agents (OSDAs) are the ultimate strategy for synthesizing new zeolitic frameworks, especially those with a high Si/Al ratio (Hartmann et al. 2016). Suitable OSDAs are any species of organic or organometallic molecules that have a cationic charge and are stable in the synthesis mixture under crystallization conditions (Christensen et al. 2007). Tetraalkylammonium cations are the most widely used OSDAs, while the use of tetraphosphonium, phosphazenes, cationic metallocenes, neutral alcohols, amines, and cyclic ethers are also reported (Serrano et al. 2013). The main characteristics of an OSDA which will determine its suitability for the synthesis of a certain zeolite structure are its polarity (hydrophobic/hydrophilic character), its size, charge, shape, and rigidity (Jia et al. 2019).

OSDAs can have several roles in zeolite synthesis as follows:

1. To induce the formation of zeolite framework
2. To act as gel modifier resulting in different precursors of framework materials
3. To act as a template where silica and alumina species arrange themselves and condense to form a zeolite framework with cage and channel according to the size of the OSDA
4. To fill up the space (a space-filling) of internal cavities during the crystallization process.

In the latter role, the OSDA is much less specific such that a given zeolite could be formed from a vast number of OSDAs that can fill its pores. For instance, 22 possible molecules can be used to synthesize ZSM-5. Furthermore, OSDAs are sometimes added not to form a specific zeolite but to increase the Si/Al ratio of the product that can otherwise be prepared at lower Si/Al ratios without OSDAs (Martínez and Corma 2013).

However, OSDA has disadvantages because they are usually expensive compounds, and the most common way to remove the OSDA is through combustion. Some works reported that minimizing the amount of OSDAs used in the synthesis (Ferdov 2017; Kadja et al. 2017, 2020a, 2021a, 2021b; Rilyanti et al. 2016) will less damage the zeolite structure during the removal of the OSDAs. Furthermore, OSDAs are also utilized intensively to synthesize hierarchical and layered or two-dimensional (2D) zeolites.

The presence of OSDA can be excluded entirely using the addition of seed and/or the directing role of inorganic cations. Kadja and his coworkers (Kadja et al. 2020a) revisited the seed synthesis of CHA zeolites without the OSDA. They reported that the course of crystallization depends on seeds that provide sufficient active surface for direct crystal growth and the synergistic role of inorganic cations (Na^+ and K^+) for assisting the formation of CHA frameworks. Na^+ directs the formation of double-six

ring (d6r) from the four-membered ring (4-MR), while K$^+$ organizes the d6rs into CHA frameworks (Fig. 1b).

2.2.1 Hierarchical Zeolites

The slow diffusion of fitting molecules within the zeolite micropores, known as "configuration diffusion", frequently limits the catalytic application of zeolites. Molecular diffusivity rapidly drops to lower levels than in Knudsen diffusion and molecular diffusion, which are the dominant diffusion mechanism in mesopores and macropores, respectively. The low diffusivities in micropores decrease the transport of various compounds to and from the active sites. In applying zeolite as the catalyst, the delayed transport of reagents accelerates the formation of unwanted by-products and coke that can poison or deactivate the catalyst and shorten the catalyst lifetime (Hartmann et al. 2016; Kadja et al. 2020b; Maghfirah et al. 2020). The internal micropores of zeolites then become inactive since only the external surface of zeolites takes part in the catalytic reaction. Therefore, the synthesis of hierarchical zeolites with two different porous systems, mainly microporous and the additional mesopores (pore size according to IUPAC from 2 to 50 nm), is introduced. Such a solution aims to facilitate access of larger reagent molecules to active centers of the material while simultaneously maintaining acidity and crystallinity of zeolites (Hartmann et al. 2016; Wardani et al. 2019; Kadja et al. 2021b). So far, the methods of synthesis of hierarchical zeolites, consisting of microporous and mesoporous structures, are being developed. The biggest challenge in this work is that the materials must retain the essential properties of the microstructure while introducing the secondary porosity. Some general advantages associated with hierarchical zeolites are listed below:

1. The diffusion limitation can be significantly decreased, as the secondary porosity significantly shortens the length of the diffusional pathway (Christensen et al. 2007)
2. Less steric hindrance due to the introduction of mesopores and/or macropores because the active sites may exist in secondary porosity networks: (i) the external surface will have almost no steric hindrance; (ii) the entrance of the microporous network will potentially have a few steric limitations and affect the accessibility of bulky molecules (Serrano et al. 2013).
3. The hierarchical structure can be either beneficial or detrimental to the product selectivity of the reaction. Generally, it depends on the location of the active site in the structure. For example, p-xylene selectivity has decreased over hierarchical zeolites compared to conventional microporous ones (Musilová et al. 2010). However, the use of hierarchical zeolites increased the selectivity toward branched hydrocarbons during hydrocracking, probably due to the shortened reaction time and fast molecules diffusion inside zeolite microporous channels (Kim et al. 2017a; b; Firmansyah et al. 2016)
4. Decreased coke formation inside the micropores (Musilová et al. 2006; Kim et al. 2010)

5. The external acid sites in hierarchical zeolites may be weaker than the conventional zeolites but more robust than those in mesoporous silica such as MCM-41 (Jia et al. 2019).

2.2.2 Two-Dimensional Zeolites

The need for increasing the accessibility to the microporous structure, especially for catalytic applications, has directed research not only to the reduction of crystallite size (Jeong et al. 2017) and introduction of mesoporosity (Jia et al. 2019) but also to the separation of zeolite layers leading to the synthesis of 2D zeolites (Martínez and Corma 2013). As mentioned earlier, a zeolite is a covalently bonded continuous microporous aluminosilicate framework extended in three dimensions. A two-dimensional zeolite also has a covalently bonded framework, but it is propagated in only two directions.

Zeolite topologies in 2D structures are considered primary structures, while the various layered forms can be denoted as secondary structures (Roth et al. 2014a), with layers of one-unit cell or smaller thickness structures. The first synthesis of MFI zeolite nanosheets was approached using quaternary ammonium surfactant, $C_{22}H_{45}–N^+(CH_3)_2–C_6H_{12}–N^+(CH_3)_2–C_6H_{13}$ (C_{22-6-6}) as a structure-directing agent (SDA), which can be used to control microporous structures and nanolayer features (Dugkhuntod and Wattanakit 2020). More details in the synthesis of 2D zeolites are explained later. The extensive synthesis of zeolite nanosheets or nanolayers such as SAPO-34 (Chen et al. 2019), ZSM-5 (Tian et al. 2018), MFI (Choi et al. 2009), FAU (Inayat et al. 2012), FER (Wuamprakhon et al. 2016), MTW (Dugkhuntod et al. 2019), and many have increased over the years, owing to its remarkable advantages compared to 3D zeolites (Dugkhuntod et al. 2019). Roth et al. reported that from 16 commercially/industrially used zeolites, 13 are layered or 2D form zeolites (Roth et al. 2015, Schulman et al. 2020).

Zeolite nanosheets are suitable for catalytic application due to the abundance of acid sites on their external surface and high thermal and hydrothermal stability (Choi et al. 2009). Owing to their layered structure, the 2D zeolites have increased the advantages in catalytic activity due to superior accessibility and diffusion of bulky such as aromatics and long-chain hydrocarbons into its active site due to its hierarchical zeolite nanosheet structure (Park et al. 2011). Its usage as catalysis can also reduce coke deposition and have a long lifetime as catalysts in converting gasoline (MTG) from methanol (Choi et al. 2009).

Traditionally, zeolites grow into tridimensional crystals in sizes and shapes that can significantly differ, depending not only on the structure but also on the composition and/or synthesis conditions. Like the hierarchical zeolites, the methods of 2D zeolite synthesis can be divided into two categories: bottom-up and top-down methods. The bottom-up method usually requires direct synthesis of layered zeolite using hydrothermal methods. In contrast, the top-down approach requires post-synthesis disassembly of the 3D parent zeolites into layered zeolite precursors.

The first 2D zeolite nanosheets were MCM-22 with MWW topology synthesized by Mobil Company (Eliášová and Cejka 2017), where the MWW can be formed by direct synthesis and by the formation of a layered zeolitic precursor (LZP) called MCM-22P. The precursor has a structure of one-unit-cell thick layers separated by organic molecules used as a structure-directing agent. Moreover, various practices usually applied on clays (swelling and pillaring) can be applied on MCM-22 to produce another type of layered zeolites (Roth et al. 2015). The properties of 2D zeolites also can be improved after synthesis that includes the modification of inter-layer space (swelling, pillaring, and delamination). Other examples of bottom-up methods are reported by Ferdov et al. (2017) and Liu et al. (2019). Preparation of FAU zeolite nanosheets reported by Ferdov et al. (Ferdov 2017) was achieved only by kinetic control. The zeolite had a ball-like shape with a diameter of 2 μm. On the particle surface, the nanolayer patterns grew and branched with thickness between 20 to 60 nm and length between 50 nm to 2 μm. The evidence showed that the branching came from the recrystallization of zeolite nanoparticles followed by submicron faceted crystals.

Liu and coworkers prepared MFI-type zeolites with nanosheet assembly morphology by a seed-assisted hydrothermal approach using bola form surfactant as a structure-directing agent (Liu et al. 2019). The morphology of the zeolites varied depending on Si/Al ratio. By changing the ratio from 60 to 10, the morphology changed from MFI nanosheets with a randomly organized structure to nanosheet stacks to house-of-cards-like structures and nanosponges.

In 2011, Roth et al. (2011) successfully prepared a layered zeolite using the top-down method. They used zeolite UTL as a parent zeolite and transformed 3D zeolite into layered zeolite (IPC-IP) by hydrolysis treatment. The treatment resulted in the degradation of the UTL structure and the transformation into a 2D structure.

2.2.3 Prediction of New Structure of Zeolite Through Data Mining and Machine Learning

Traditional laboratory synthesis of zeolites is often a tedious process, where each synthesis parameter has to be modified one at a time without any guarantee of reaching the desired zeolite phases. The use of machine learning (ML) can be used to analyze the relation of synthetic conditions to the tendency to form certain zeolite phases, in which, initially, chemical compositions are used by ML to predict synthetic results (Jensen et al. 2019). Synthesis parameters, but not limited to temperature heating time, chemical composition, aging conditions, and sources of reactants, are usually used as synthesis descriptors for the construction of ML models. From datasets of synthesis, machine learning can also pinpoint the preference of framework formation concerning chemical composition. For example, an ML application has been able to determine the preference of FAU, LTA, and SOD formation in mixtures with higher Na/(Si + Al). Contrarily, the formation of MFI, MOR, and LTL is preferred in mixtures with lower Na/(Si + Al) (Schwalbe-Koda and Gómez-Bombarelli 2020).

In the past decade, various methods have been used to calculate the binding energies, where using high-throughput (HT) virtual screening has yielded meaningful binding affinity calculations of certain molecules to a zeolite framework using density functional theory (DFT) and force fields in the calculation of binding affinities with zeolites, such as certain organic structure-directing agents (OSDAs) interactions with zeolites (Schwalbe-Koda and Gómez-Bombarelli 2020). The employment of HT characterization and data mining techniques on designing experiments has also allowed the discovery of new zeolites, such as the ITQ-21, ITQ-30, and ITQ-24 in the employment of combinatorial synthesis (Martínez and Corma 2013).

Another extensive use of ML (Fig. 2) and data mining is in determining the relation of zeolite phases and the use of organic structure-directing agents (OSDAs). Generally, machine learning (ML) and data mining have been used without considering OSDA structure or analyzing OSDA–zeolite interactions within limited chemical space, OSDA-free zeolite systems, and inter-zeolite transformations (Corma et al. 2006). Certain OSDA can crystallize many different zeolite phases, which helps with charge balancing and space-filling in a templating manner. Using data mining, the size, flexibility, hydrophilicity, and charge of the OSDA can be analyzed. OSDA size correlates directly with zeolite pore size, while OSDA rigidity increases specificity or the formation of fewer zeolite phases (Jensen et al. 2021). Nonetheless, the dependence on heuristics limits the researchers from comparing vast amounts of databases.

Using high-throughput (HT) screening, silico data mining can identify materials from computationally generated databases or existing ones in vast amounts. The first HT approach was first performed in 1998, which involves evaluating the ternary phase system Na_2O–Al_2O_3–SiO_2-H_2O and identifying zeolite phases in it by varying its hydrothermal synthesis conditions via automated combinatorial methods in a multi-autoclave system, allowing 1000 combinations per experiment (Akporiaye et al. 1998).
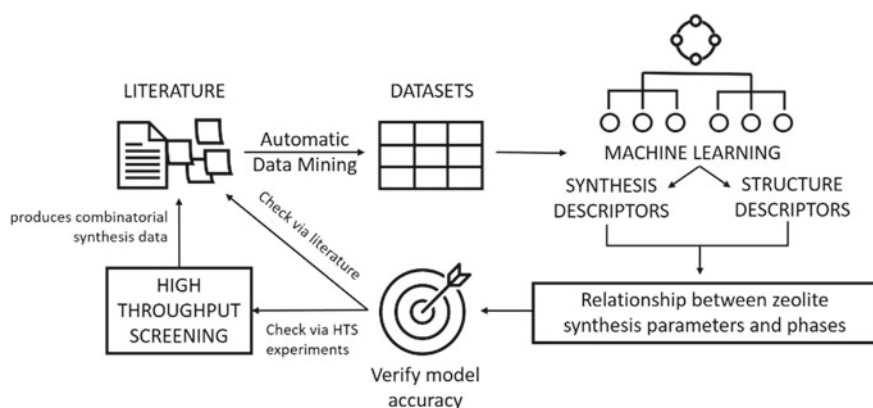
Fig. 2 Schematic diagram on utilization of machine learning and data mining in prediction of new zeolite structures

With the recent development of technology, using data mining with generative neural networks, impressive feats of processing vast amounts of datasets can be seen in a work of exploring 5663 synthesis routes obtained in 1996–2020 to model the interaction of OSDA with zeolites, which enabled the discovery of alternatives for the industrial OSDA trimethyladamantammonium (TMAda+) in the production of CHA zeolites (Jensen et al. 2021). Different methods, which do not utilize comparison of known molecules, could employ molecular mechanics to help generate meaningful physical predictions, such as calculating the energy binding calculations of generated molecules with SFW, which has shown good agreement with the binding energies of existing literature of OSDAs for SFW (Schwalbe-Koda and Gómez-Bombarelli 2020).

2.3 Applications of Zeolites

Because of their unique channel structure, good thermal stability, and high acidity and selectivity properties, natural and synthetic zeolites with conventional structures have been widely used both in the laboratory and industrial scales, as molecular sieves, adsorbent, cation exchanger, and heterogeneous catalyst (Jeong et al. 2017; Yulizar et al. 2016; Makertihartha et al. 2020; Kadja and Ilmi 2019; Puspitasari et al. 2019). Several examples of zeolite applications as molecular sieves are as follows. Membrane: hierarchical Linde Type-T (h-LTT) zeolite for the fabrication of hybrid membrane in CO_2/CH_4 separation (Hassan et al. 2021; Lestari et al. 2020, 2021a; b), adsorbent: Hierarchical HMOR and HZSM-5 zeolites as adsorbents for mesosulfuron-methyl removal in the aqueous phase (Rasamimanana et al. 2016), cation exchanger: the hierarchical X zeolite adsorbent and its Ca^{2+} ion-exchanged to enhance nitrogen adsorption capacity (Mousavi et al. 2021) and catalyst: zeolite type NaY has been tested for the catalytic activity and selectivity of n-Hexadecane Cracking products (Krisnandi et al. 2019a). However, due to its disadvantages from microporous characters, as mentioned above, many applications of zeolites depends on the advanced structure of the zeolite, such as hierarchical and 2D nanosheet structure.

Hierarchical zeolites have become an essential commercial heterogeneous catalyst due to Lewis and Brønsted's acidic properties. The amount and acid strength of the zeolite depend on the SiO_2/Al_2O_3 ratio of the zeolite framework for uniform pore size for the level of the primary pore. The introduction of secondary pores to its structure has dramatically enhanced the research in zeolite catalysts because of mass transfer for faster molecular diffusion. For example, various approaches have been utilized to modify ZSM-5 to enhance its efficiency for the catalytic pyrolysis of biomass (Che et al., 2019). Hierarchical Mn_3O_4/ZSM-5 has been reported as heterogeneous catalysts in biomass utilization, such as the conversion of cellulose from rice husks to levulinic acid (Krisnandi et al. 2019b) also HMF, formic acid, and levulinic acid (Pratama et al. 2020). Co_3O_4/ZSM-5 with hierarchical pores are reported to be used in catalytic partial oxidation conversion of methane to methanol with high (Beznis

et al. 2011; Krisnandi et al. 2015) and catalytic cracking to increase the octane number of gasoline and alkylated gasoline products (Klerk 2018).

Progress in the application of 2D zeolites is also related to heterogeneous catalysis, where zeolite can have several roles, such as acid, acid–base, solid acid catalyst, oxidative catalyst, and porous material for catalyst support. There are several advantages to using 2D zeolites, such as hierarchical characteristics, large external surface areas, and stable and abundant accessible base sites (Pang et al. 2020a; b). It is reported that an application [S4] of the prepared 2D Na/zeolites, especially the Na/ITQ-2 type, shows remarkably enhanced activity in the transesterification reactions to produce fatty acid methyl ester (FAME) as biodiesel (Pang et al. 2020a; b). In addition, the 2D materials as separation membranes provide exemplary performance in energy field applications, for example, 2D sheets zeolites for membrane separation process for H2 and biofuel purification (Dai et al. 2021), with beneficial properties including high chemical and mechanical stability, large modifiable functional group, and low mass transport resistance.

3 Ordered Mesoporous Materials

To expand applications of porous materials into various fields, an enlargement of pore opening of microporous materials was highly pursued in the late 1980s. Among various studies, ordered mesoporous materials (OMMs) have then emerged as a breakthrough to the limitation of micropores. Mesopores are, according to IUPAC, defined as pores with a diameter of between 2 and 50 nm (Sing 1985). Since then, OMMs has been immensely developed in structure design, preparation procedures, and applications. The unique features of OMMs, i.e., high specific surface area (up to $1000 \text{ m}^2 \text{ g}^{-1}$) and well-defined pore size, enable them to be used in many areas such as adsorption, separation, sensing, catalysis, and some bio-related fields. This section would elaborate on the developments and recent studies of the most common OMMs, e.g., mesoporous silica, mesoporous alumina, mesoporous metal/metal oxide, and mesoporous carbon.

3.1 Mesoporous Silica

Silica-based OMMs are the pioneer of mesoporous material with a well-ordered structure. Separately in the early 1990s, Japanese scientists (Yanagisawa et al. 1990) and a research team from Mobil Company (Kresge et al. 1992) first reported the preparation of mesoporous silica in the presence of organic molecules. Kresge et al. from Mobil used cetyltrimethylammonium bromide (CTAB) to prepare M41S mesoporous silicate molecular sieves (later known as MCM family) hydrothermal synthesis. The concept of "template" was introduced and considered a significant factor in synthesizing mesoporous silica. Later on, a detailed investigation of the crystallization
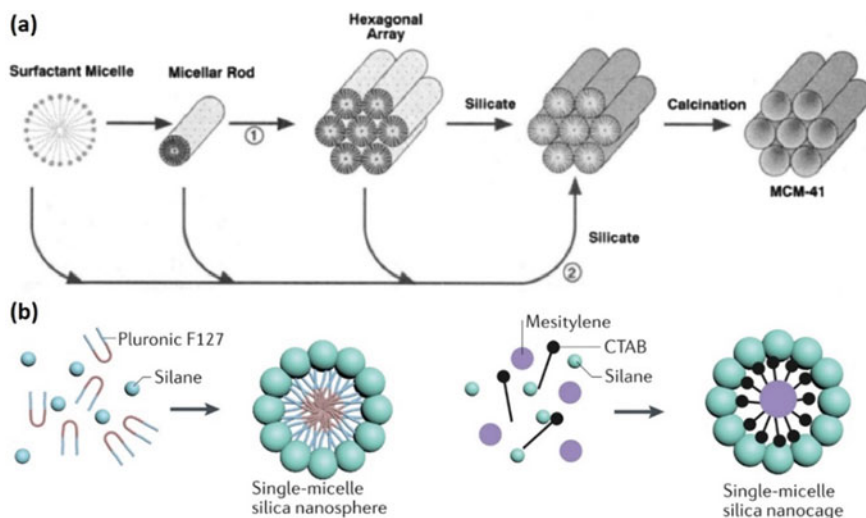
Fig. 3 a Schematic representation of MCM-41 formation mechanism initially proposed by Beck et al. Reproduced from Beck et al. (1992). Copyright 1992 American Chemical Society. **b** Formation of hollow silica out of single micelle mechanism using Pluronic F127 (left) and CTAB (right) as the surfactants. Reproduced from Wu and Lin (2013). Copyright 2019 Springer Nature

and pore formation mechanism was reported by the same group from Mobil. They proposed that surfactant micelles were assembled and formed liquid crystal array during sol to gel transformation of the initial precursors. Figure 3a shows a schematic illustration of the mechanistic pathway of the formation of M41S originally proposed by Becket al. (1992).

Various silica-based OMMs have been developed, including MCM family (e.g., MCM-41, MCM-48; MCM stands for Mobil Composition of Matter), SBA family (e.g., SBA-15, SBA-16; SBA stands for Santa Barbara Amorphous), FSM-16, KIT-6, etcetera. Likewise, methods for synthesizing mesoporous silica also have undergone much progress. The synthesis methods generally could be divided into two classes, i.e., hard-templating and soft-templating methods (Zhao et al. 2019). Hard-templating methods rely on pre-synthesized colloidal crystals or mesoporous solid, which then act as mesopores' mold. Complex templates are commonly relatively stable physically and chemically; thus, they facilitate the formation of mesopores with a wide range of compositions and features. However, this method is considered somewhat costly since the hard-template materials must be prepared in advance and sacrificed at the end of synthesis.

Moreover, since the templates are rigid, the mesopore formation is less tunable. On the other hand, soft-templating methods rely on micelles formation, which then dictates the construction of mesopores. The micelles are built up from amphiphilic surfactants or block copolymer and thus easily adjusted to create specific features. However, since the templates are organic molecules which generally removed through calculations, loosely implementing this method on a large scale may

contribute to increasing carbon emission. Therefore, some progress of synthesis methods commonly concerns the environmental impacts (Gérardin et al. 2013).

Synthesis of MCM family—the most commonly used silica-based OMMs— is frequently performed by mixing a silica precursor such as tetraethylorthosilicate (TEOS) and a template at essential condition (pH of 11) then treated under hydrothermal process at 30–60 °C (Martínez-Edo et al. 2018). When the silica precursor is dissolved under primary conditions, the alkoxide groups are hydrolyzed, and the resulting silanol groups polymerize to form macrostructures using Si–O–Si bonds. During aging, the negative charge of silica species is attracted to the positive part of the surfactants. Since the surfactants form a micelle structure, the silica species are directed to form a tubular structure around the micelles (see Fig. 3a). Subsequently, the particles would slowly grow until the electrostatic force reaches saturation, which the process determines the shape and size of the particles, including the crystal shape (hexagonal and cubic for MCM-41 and MCM-48, respectively). Recently, it was unraveled using cryo-electron microscopy that if the polymerization of silica species could be prevented, single micelles would form and lead to the formation of hollow silica particles, as illustrated in Fig. 3b (Wu and Lin 2013).

In contrast with the MCM family, the SBA family is prepared in acidic conditions. Typically, a silica precursor such as tetraethoxysilane (TEOS), tetramethoxysilane (TMOS), or tetrapropoxysiliane (TPOS) and a template are mixed into 2 M HCl aqueous solution (Kruk et al. 2000; Zhao et al. 1998). The mixture is then aged at 80 °C overnight. The template for SBA-15 synthesis is generally a non-ionic, triblock copolymer such as poly(ethylene oxide)-poly(propylene oxide)-poly(ethylene oxide) (PEO-PPO-PEO) or Pluronic 128. Depending on the length of the repeating unit of the polymer chain, the crystal shape of the SBA could be varied as cubic, hexagonal, lamellar, or other phases.

In recent years, the functionalization of silica-based OMMs was widely studied in order to employ materials in a wide variety of fields. In the field of catalysis, Méndez et al. reported Ti-modified MCM-41 as support for CoMoS and NiMoS hydrogenation catalysts (Méndez et al. 2021). Ti was incorporated into the MCM-41 structure by directly mixing the precursor into micellar solution. The catalysts demonstrated a remarkable improvement in terms of reaction rate as well as selectivity of products. Appaturi et al. reported a bifunctional MCM-41-alanine catalyst for selective synthesis of dioxolane biofuel (Appaturi et al. 2021). The MCM-41 was first grafted with 3-chloropropyl triethoxysilane (CPTES), which then managed [S1] to covalently bond to the alanine. The catalyst could carry out glycerol acetylation with the conversion of 90% and selectivity of 78% owing to the abundance of acid and base active sites. The catalyst also showed excellent stability as it had no significant depletion after six operations. MCM-41 also showed promising results as an absorbent. Madri et al. developed a composite of MCM-41 with 3-(2-aminoethylamino) propyl trimethoxysilane coordinated with Fe(III) as an effective adsorbent for Cr(IV) removal from aqueous solution (Madri et al. 2021). The composite could absorb Cr(IV) spontaneously using the chemisorption mechanism. In the bio-related fields, the possibilities of using MCM-41 as a drug delivery system

are intensely studied. Shariatinia et al. recently reported the use of tert-butylamine-functionalized MCM-41 as a carrier of cyclophosphamide anticancer drug (Shariatinia et al. 2021). The drug was loaded inside the mesopores as well as on the surface of the particles.

Interestingly, the kinetics of drug release could be controlled by varying the pH of the environments. Fuentes et al. demonstrated that a bare MCM-41 particle exhibited mild cytotoxicity toward HepG2 cells (Fuentes et al. 2021), showing the feasibility of being used in medical fields. They also showed that the cytotoxicity of the MCM-41 composite would be affected by the functional groups; thus, it could be easily tuned.

Silica-based OMMs also showed promising results as a sensing material. Gong et al. developed SBA-15 assembled with silicon nanoparticles for effective oxygen sensing (Gong et al. 2020). They found out that the oxygen-sensing performance would relate to the shape of SBA-15 particles. The SBA-15 with a prism-like shape showed the fastest sensing ability attributed to the large surface area. Fahmi et al. studied the fluorescence properties of SBA-15 grafted with 5-nitroisatin Schiff base as a chemosensory for Fe(III) ions (Gong et al. 2020). The Schiff base, which functions as the active sensing site, was easily anchored onto the surface of SBA-15 using APTES as the bridge. Han et al. recently investigated a new photocatalyst, i.e., SBA-15 impregnated with BiOBr (Han et al. 2020a; b). The photocatalytic (oxidation of rhodamine B) activity of BiOBr impregnated onto SBA surface was significantly higher than that of pure BiOBr, which demonstrated the vital role of SBA-15 support in photocatalysis applications. In a different photocatalytic reaction, Vibulyaseak et al. used a well-defined anatase phase of SBA-15 impregnated with TiO_2 to decompose acetic acid (Vibulyaseak et al. 2020). It was found that the photocatalytic activity of the SBA-15 composite was better than the commercial titania.

3.2 Mesoporous Alumina

After discovering mesoporous silica, the advancements in OMMs were extended to other oxide materials, including ordered mesoporous alumina (OMA), Al_2O_3. This development was mainly undertaken between 1992 and 1995 (Bagshaw et al. 1995). Like silica-based OMMs, OMA provides a large surface area and narrow pore distribution suitable for many applications. Furthermore, OMA shows exceptional thermal stability (González-Peña et al. 2001; Sun et al. 2011), thanks to the nature of alumina crystals. This particular feature enables OMA suitable to function as catalysts or catalyst supports for high-temperature reactors. The acid–base properties of OMA are also easily tuned using metal doping as well as surface functionalization.

Synthesis of OMA could be carried out using a complex template such as SBA-15 (Baca et al. 2008). However, the complex template techniques are less favorable since the templates themselves are not easy to prepare. Sol–gel processes in the presence of soft template have been widely employed (Cabrera et al. 1999; Valange et al. 2000; Niesz et al. 2005), such as the evaporation-induced self-assembly (EISA) method.

EISA is a sol–gel process in the company of a template using a non-aqueous solvent, typically ethanol, which is followed by a thermal treatment. Figure 4a [S1] shows the schematic illustration of the preparation of OMA using the EISA method (Xu et al. 2020). The process is begun [S2] by dissolving the template—typically a non-ionic surfactant or block copolymer such as F127—into the non-aqueous solvent
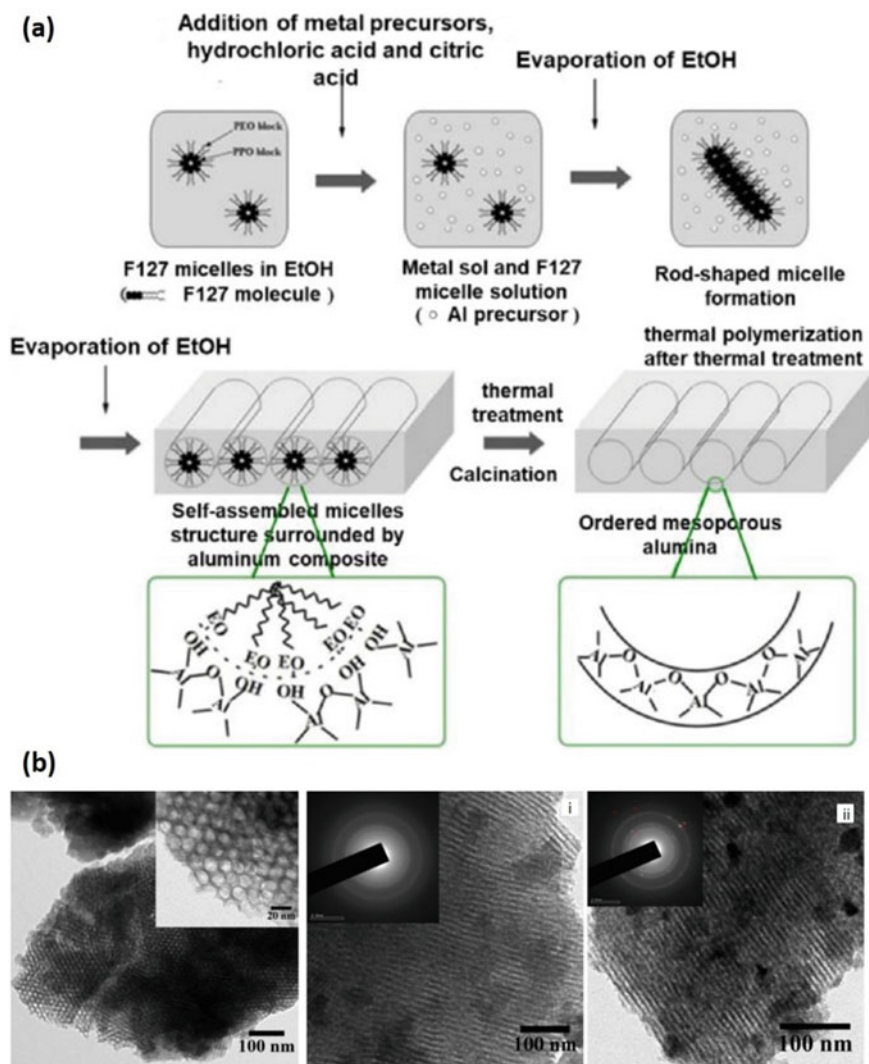
Fig. 4 a Schematic representation of the formation of OMAs prepared by the EISA method. Reproduced from Xu et al. (2020). Copy right 2019 American Chemical Society. **b** TEM images of OMA particles prepared using the EISA method. Reproduced from Yenumala et al. (2020). Copyright 2020 Elsevier

(ethanol). Subsequently, an alumina precursor and an acid are added to the mixture. Under the acidic condition, the alumina precursor undergoes hydrolysis and condensation to form a metal sol phase. The mixture is then preconcentrated by evaporating the solvent, which induces self-assembly of the micelles surrounded by the alumina species, comprising tubular shapes. Finally, thermal treatment at high temperatures is performed to remove the organic surfactant, which leads to the formation of mesopores.

The mesopores' structure and the alumina crystal phase of OMA prepared by the EISA method are highly dependent on some factors, as recently reviewed by Xu et al. (2020). The form of alumina precursors is an essential factor. Different anions in the precursors provide different sizes, charge, and affinity toward Al and thus affect the rate of reaction and assembly processes. The interaction of anions and Al is also affected by acids, which can act as a competitor. It was found that, in general, increasing the acid concentration would increase the pore width of the OMA. Templates—the non-ionic surfactants or block copolymers—indeed govern the mesopores' structure. The type of micelles determines the surface area and size of the pores. For instance, to increase the size of mesopores, a block copolymer with higher molecular weight could be employed. The other dominant factor is the temperature of the calcination process. This determines the crystal structure and thermal stability of the alumina.

In contrast with the EISA method, which typically uses non-ionic surfactants, hydrothermal synthesis of OMA could employ both ionic and non-ionic surfactants (Zhang et al. 2004; González-Peña et al. 2005). CTAB has commonly used the template in the hydrothermal method. Hydrothermal methods also allow various Al precursors due to their excellent solubility in water solvent (Fulvio et al. 2010; Liu et al. 2008). Therefore, despite the remark that the EISA method is superior, conventional hydrothermal methods are still popular for preparing OMA with desired properties.

As catalysts, commonly, OMA is prepared as a composite with transition metals such as nickel. Aljishi et al. prepared ordered nickel–alumina catalyst using the EISA method and investigated the catalytic activities toward CO_2 methanation (Aljishi et al. 2018). Different synthesis parameters—acid types, Ni loading, and calcination temperatures—lead to different porosity of the catalysts. It was found that the best performance of CO_2 conversion to CH_4 could be observed in a catalyst calcined at 700 °C. Using similar catalysts (mesoporous nickel–alumina composite), Yenumala et al. carried out hydrodeoxygenation (HDO) of Karanja oil (Yenumala et al. 2020). The results showed that the catalytic performance of catalysts prepared using the EISA method was much better than that of those designed using wet impregnation. This might be attributed to the interaction of Ni-complexes with alumina as well as the species distribution. Figure 4b shows TEM images of the OMA particles prepared using the EISA method. The optimum catalyst converted almost 100% of the oil to linear paraffin with about 70% selectivity to C17 alkane. Gholizadeh et al. developed cubic ordered mesoporous alumina (COMA)-supported nickel catalysts for dry reforming of methane (Gholizadeh et al. 2021). In the 15% loading of Ni, the catalyst could convert more than 90% of CH_4 and CO_2 with excellent stability.

After 210 h of operation, only a tiny amount of cokes (5 wt%) was found deposited on the catalyst.

Surprisingly, OMA also showed promising performance in bio-related applications. Wei et al. reported the development using ligand-assisted solvent evaporation-induced co-assembly as an absorbent of phospho-peptides (Wei et al. 2017). An ultra-large pore size (16.0–18.9 nm) could be constructed using a block copolymer—poly(ethylene oxide)-b-polystyrene (PEO-b-PS)—with high molecular weight as the template. The OMA demonstrated excellent performance as a bio-absorbent even in a shallow concentration or complicated samples such as human serum. Another potential application of mesoporous alumina is membranes. A comprehensive review on the mesoporous structures confined in anodic alumina membranes had been provided by Bein and coworkers elsewhere (Platschek et al. 2011).

3.3 Mesoporous Metal/Metal Oxide

After discovering silica-based OMMs in the early 1990s and OMA in the mid-1990s, the study of OMMs was further broadened to non-silica and non-alumina-based, including transition metals and their oxides (Ren et al. 2012). In this sub-section, ordered mesoporous metals and metal oxides would be referred to as metal-based OMM for the sake of simplicity and are elaborated alternately. Compared to silica or alumina, OMMs based on transition metals or metal oxides can provide d-shell electrons on the walls and redox-active surface. These particular features of metal-based OMMs offer excellent and unique performances in catalysis and electronic devices. However, the synthesis of metal-based OMMs is somewhat challenging compared to silica or alumina since the hydrolysis and condensation of the metal precursors are not easy to control (Schüth 2001). Thus, various efforts have been carried out in recent years. Synthesis of metal-based OMMs generally is classified into two routes, i.e., hard-templating methods and soft-templating methods, similar to the other types of OMMs.

In the hard-templating method, the mold to prepare metal-based OMMs can be provided by mesoporous silica, mesoporous alumina, or mesoporous carbon. The hard-templating method comprises several steps, i.e., (i) preparation of the template, (ii) deposition of the metal precursor into the template, and (iii) template removal. Typically, the structure of the products prepared using this method would limitedly follow the inverted shape of the original construction of the templates. The first successful preparation of ordered mesoporous transition metal oxide was reported in 2003 by Zhu et al. (2003). Crystalline Cr_2O_3 was prepared using APTS/SBA-15 as the template and $H_2Cr_2O_7$ as the precursor.

The soft-templating method to prepare metal-based OMMs includes the following strategies: (i) lyotropic liquid crystals (LLCs), (ii) LLCs through solvent evaporation, and (iii) micelle assembly. A comprehensive review of these strategies has been provided by Yamauchi and coworkers (Malgras et al. 2016). LLCs are an assembly of micelles in surfactant solution with high concentration ($\geq$30 wt%). The formed

LLCs would act as the structure-directing agent for mesoporous metal precursors. The first study on the successful preparation of mesoporous Pt was reported in 1997 by Attard et al. (1997).

Nonetheless, the application of LLCs is limited since it requires a high concentration of surfactants. As an alternative strategy to provide a soft template, the formation of LLCs could be manipulated by solvent evaporation, which essentially controls the concentration. Figure 5a illustrates the process of synthesizing mesoporous Pt using
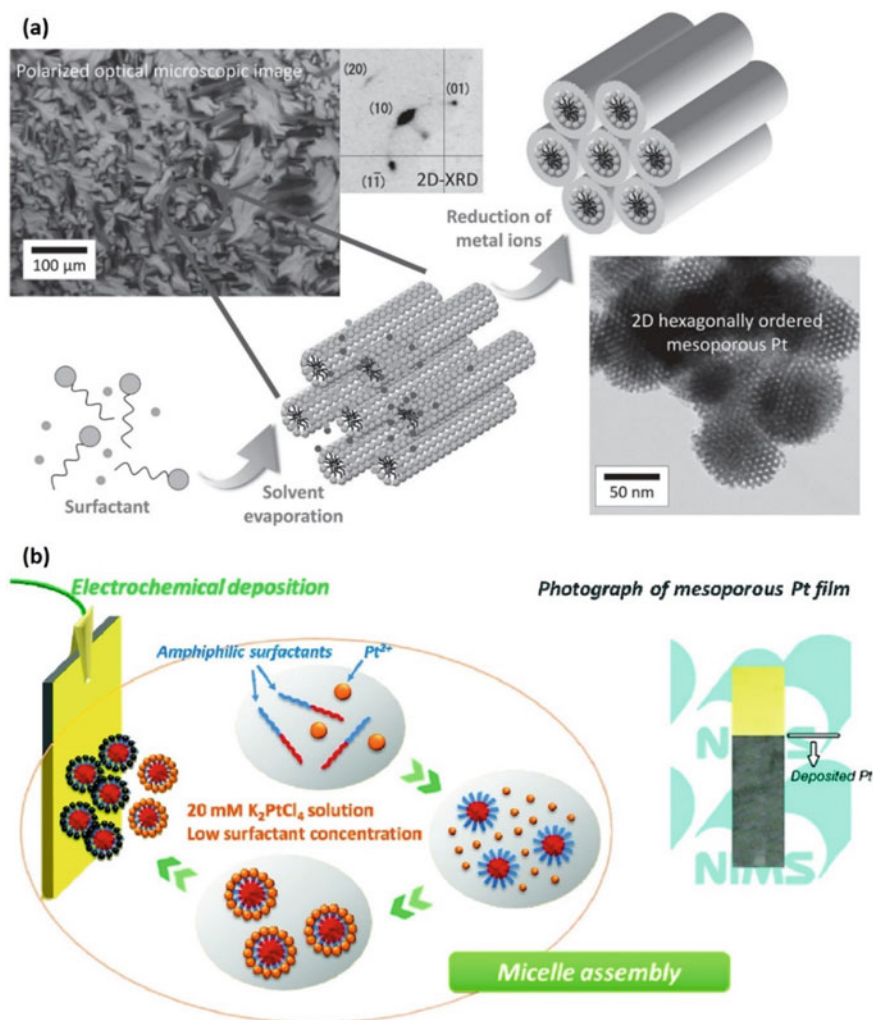
Fig. 5 a Schematic illustration of synthesizing mesoporous Pt using LLCs as the template through solvent evaporation strategy. Reproduced from Malgras et al. (2016). Copyright 2016 Wiley. **b** Schematic illustration of the synthesis of mesoporous Pt using micelles assembly strategy. Reproduced from Wang et al. (2012). Copyright 2012 American Chemical Society

LLCs as the template through solvent evaporation strategy. In this strategy, volatile solvents such as THF or ethanol should be employed.

In contrast to the LLC strategies, which require a high surfactant concentration, Yamauchi's group proposed an alternative approach, namely micelles assembly (Wang et al. 2012). The micelles assembly strategy integrates two additional mechanisms: coordination of the metal precursors and the surfactants via hydrogen bond and electrodeposition process. Figure 5b shows the schematic illustration of the synthesis of mesoporous Pt using a micelles assembly strategy.

Mesoporous metals or metal oxides, especially those of transition metals, are undoubtedly suitable for catalyst applications owing to their acid–base characteristics as well as having d orbital. Li et al. studied an ethanolysis of xilinguole lignite over a series of mesoporous metals catalyst MMgAlOx, where M was Cu, Zn, Co, or Ni (Li et al. 2021a; b, c). Using a simple co-precipitation technique, catalysts with mesoporous structure and tunable acidity could be prepared. The catalysts showed remarkable performance, except for Ni, in converting the lignite into arenes, phenols, alcohols, and esters with more than 97% yields. Halawy et al. investigated the effect of F-ions and K_2O addition onto mesoporous NiO catalyst to carry out the production of methyl ethyl ketone (MEK) (Halawy et al. 2021). The mesoporous NiO catalyst showed a conversion of 77%, while the mesoporous NiO catalysts modified with F-ions and K_2O showed conversions of 99 and 95%, respectively. CO_2-TPD analyses revealed that F-ions or K_2O provided primary sites at various strengths on the catalysts. Gai et al. developed a mesoporous TiO_2 catalyst dopped with a Ru cluster for the catalytic wet air oxidation of low-concentration ammonia (Gai et al. 2021). The Ru@TiO_2 catalyst showed excellent performance with a 95.5% conversion of NH_3 to N_2 without alkali. The catalyst also showed good durability in a 4-cycle of reusability test. Li et al. employed precious metals—Rh and Ru—to prepare mesoporous catalysts for hydrogen evolution reaction (HER) (Li et al. 2021a; b, c). Using hexadecylpyridinium chloride monohydrate (HDPC) as the structure-directing agent, high porosity RhRu catalyst could be prepared by a simple wet chemistry method. The catalyst demonstrated excellent performance with an overpotential of 25 mV at $10\,\text{mA cm}^{-2}$ and a Tafel slope of $47.5\,\text{mV dec}^{-1}$ in 1.0 M KOH, which is significantly higher than the commercial Pt/C catalyst. DFT calculations suggested that the d-band center was promoted toward the Fermi level owing to the charge redistribution on the RhRu alloy, which enabled bond cleavage and improved the adsorption/desorption processes.

3.4 Mesoporous Carbon

The discovery of novel mesoporous materials witnessed tremendous growth till the early 2000s. In 1999, Ryoo's group first reported the synthesis of ordered mesoporous carbon (OMC), namely CMK-1 (Ryoo et al. 1999). The synthesis of CMK-1 was carried out using sucrose as a carbon precursor and MCM-48 as the complex template. The mesopores of the MCM-48 were filled with the sucrose solution and sulfuric acid

as a catalyst. The mixture was then heated at 800–1000 °C under an inert atmosphere. The process would convert the sucrose into a carbon material, following the inverted shape of MCM-48. The silica of MCM-48 was removed by dissolution using NaOH and ethanol, resulting in a mesoporous carbon framework. Schematic representation of CMK-1 synthesis described by Ryoo et al. is depicted in Fig. 6a.

Later on, carbon scientists developed an alternative method to prepare OMCs using soft-templating methods since hard-templating methods are not practical. In 2004, Liang et al. first reported block copolymer as a soft template to prepare
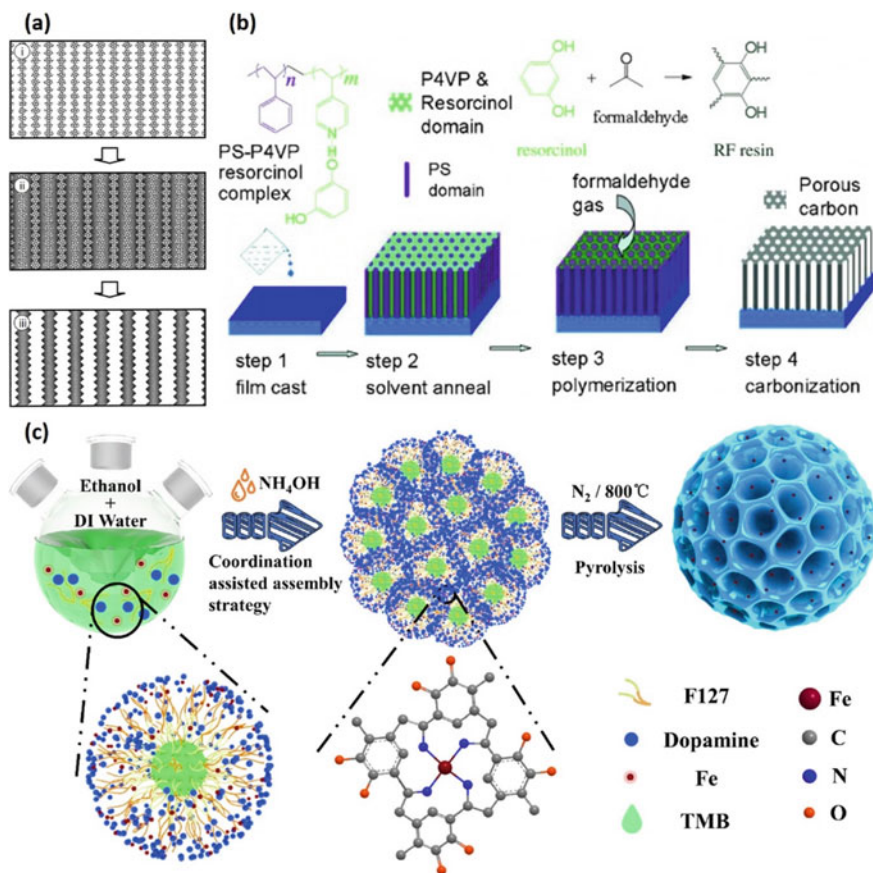
Fig. 6 a Schematic representation of the synthesis of CMK-1, the first reported OMC, initially described by Ryoo et al. Reproduced from Ryoo et al. (1999). Copyright 1999 American Chemical Society. **b** Schematic representation of the first OMC film synthesis using the soft-templating method. Reproduced from Liang et al. (2004). Copyright 2004 Wiley. **c** Schematic illustration of the preparation of atomic Fe dispersed hierarchical mesoporous Fe–N–C catalyst via coordination-assisted assembly technique. Reproduced from Zhou et al. (2021). Copyright 2021 American Chemical Society

OMC (Liang et al. 2004). Briefly, the polystyrene-block-poly(4-vinylpyridine) (PS-b-P4VP) block copolymer was dissolved in THF, heated at 100 °C to initiate self-assembly via a hydrogen bond, and then spin-coated onto a silica plate. After aging for several hours, the nascent film was carbonized by heating at 800 °C under an inert atmosphere. Figure 6b shows a schematic representation of the OMC film synthesis using the soft-templating method. Afterward, Tanaka et al. reported the preparation of mesoporous carbon COU-1 via direct carbonization of an organic–organic nanocomposite (Tanaka et al. 2005). The strategy was to employ an organic–organic interaction between a decomposable surfactant at high temperatures and a thermosetting polymer to form an ordered array. The polymer would be carbonized at high temperatures under an inert atmosphere to create a carbonaceous wall. This technique significantly reduces the steps in the preparation of OMCs.

The techniques for synthesizing OMCs are continuously developed in the early 2000s. A comprehensive review from Dai's group had highlighted this development (Liang et al. 2008). In recent years, scientists are focusing on preparing functionalized OMCs to match the demands of various fields. Mesoporous carbon nitrides (MCNs) and mesoporous heteroatom-doped carbon (MHC) are lately gaining much attention, as recently described by Dai and coworkers (Zhang et al. 2017). In MCNs, some carbon atoms are substituted by nitrogen atoms, which leads to the opening of an additional bandgap in the material. Thus, MCNs are widely studied for photocatalysis applications. In MHCs, heteroatoms such as B, P, S, and N are doped onto the surface or the backbone of carbon. The presence of heteroatom could manipulate the acidity or basicity of the material as desired in many applications.

Like the other type of OMMs, one of the significant applications of OMCs lands upon the field of catalysis. Han et al. recently reported the development of hierarchically ordered porous N-doped carbon with single-atomic Co sites embedded on the walls (ISA-Co/HOPNC) for oxygen reduction reaction (ORR) (Han et al. 2021a; b). The catalyst was prepared to utilize a single template pyrolysis strategy. Owing to the abundance of exposed co-active sites, the catalyst showed remarkable performance as well as stability. Similarly, Xu et al. also developed highly dispersed Co-Nx sites on mesoporous carbon for catalytic transfer hydrogenation (Xu et al. 2021). The catalyst demonstrated excellent performance as it could convert up to 100% 5-hydroxymethylfurfural with an 86% yield of 2,5-furandimethanol. Another ORR catalyst based on single-atomic sites of metal embedded on porous carbon was introduced by Zhou et al. (2021). An atomic Fe dispersed hierarchical mesoporous Fe–N–C catalyst was prepared via a coordination-assisted polymerization assembly strategy, as illustrated in Fig. 6c. The catalyst demonstrated outstanding performance and stability in carrying out the ORR reaction, which outperformed the conventional Pt/C electrocatalyst system. Similar catalysts with S moiety—atomically dispersed Fe-Nx and C–S–C ordered mesoporous carbons (Fe/S–N/C)—were studied by Han et al. (2021a, 2021b). The catalyst demonstrated an excellent oxygen reduction reaction in a microbial fuel cell, which was 20% better than the commercial Pt/C catalyst.

4 Metal–Organic Frameworks (MOFs)

4.1 Structure and Physicochemical Properties

Metal–organic frameworks (MOFs) are hybrid ordered porous materials constructed by metal ions or metal oxide clusters as the nodes interconnected by organic ligands as the linkers to form infinite three-dimensional frameworks. MOFs are well-known for their high tunability, where different structures could be obtained by easily customizing the building blocks. Different shapes and symmetry of the inorganic clusters commonly referred to as secondary building units (SBUs), and the chelating organic ligands lead to significant development of novel MOFs structures. Various common SBUs based on carboxylate moieties either from inorganic or organic units in MOFs are shown in Fig. 7. The diversity of MOFs is also a result of the reticular
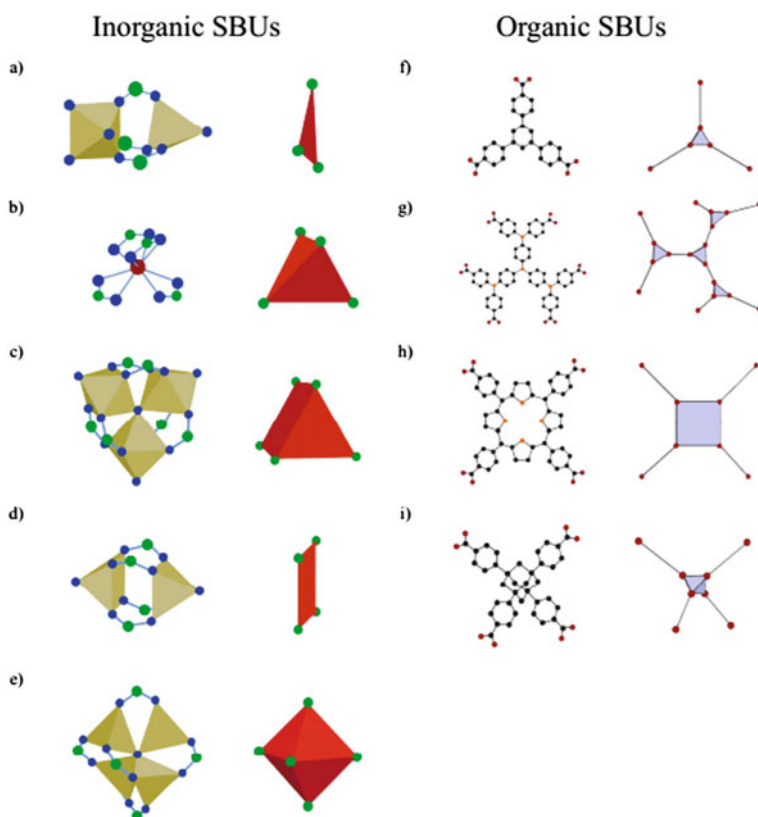
Fig. 7 Typical inorganic and organic SBUs based on carboxylate moieties in MOFs: **a** triangle, **b** tetrahedron, **c** trigonal prism, **d** square paddle wheel, **e** octahedral nodes and **f** tritopic, **g** multitopic and **h**, **i** tetratopic ligands

chemistry that enables the design of various frameworks from single inorganic SBU and organic ligands with similar symmetry but different in length, size, and attached functional groups (Yaghi et al. 2019). An early report on reticular synthesis of MOFs was reported by Eddaoudi et al. in which IRMOF series based on MOF-5 was obtained with different functionalities ($-Br$, $-NH_2$, $-OC_3H_7$, $-OC_5H_{11}$, $-C_2H_4$, and $-C_4H_4$) and long organic bridges (biphenyl, tetrahydropyrene, pyrene, and terphenyl) without changing the original topology (Eddaoudi et al. 2002). The formation of MOF structure from the SBU unit and the linkers is depicted in Fig. 8. More than 90,000 different structures of MOFs have been reported, and 500,000 were predicted since the discovery of the first MOF (Moosavi et al. 2020).

The invention of this material was started in 1989 when Robson et al. reported the preparation of three-dimensional coordination polymer from transition metal cations and linear ditopic organic ligands, and the term MOF was introduced in 1995 by Yaghi et al. (Hoskins and Robson 1989; Yaghi and Li 1995). Some of the well-known early reported MOFs are HKUST = Hong Kong University of Science and Technology (HKUST-1) that consist of paddle wheel $Cu_2(CO_2)_4$ metal clusters and tritopic H_3BTC ligand (H_3BTC = 1,3,5-benzenetricarboxylic acid) and
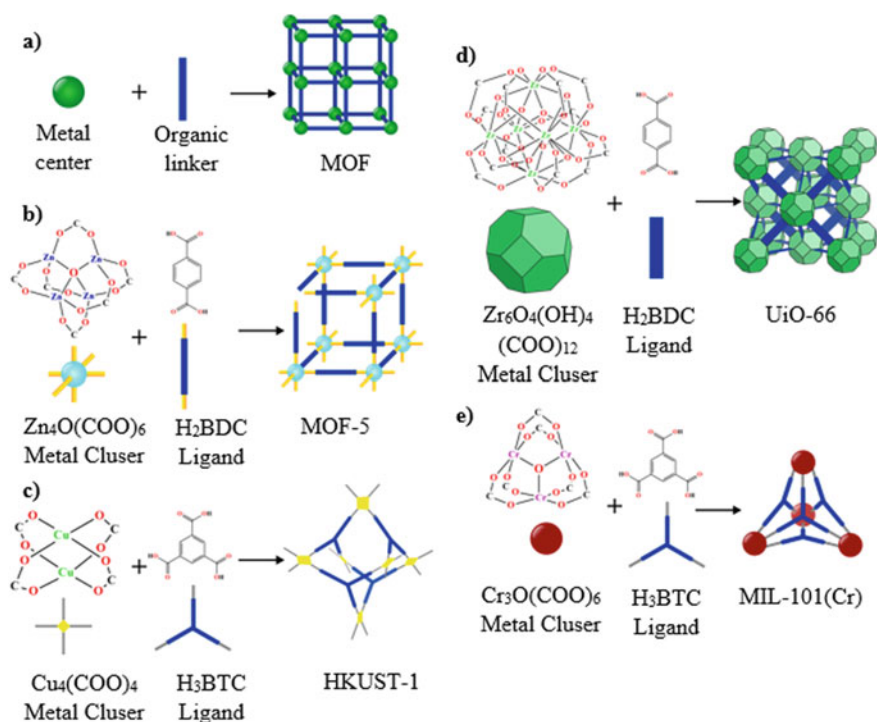
Fig. 8 Formation of MOFs in: **a** general, **b** MOF-5, **c** HKUST-1, **d** UiO-66, and **e** MIL-100(Cr) with linear ditopic linker and tritopic linker. It is clearly illustrated that difference in the inorganic SBU and organic ligand shape and symmetry would lead to different framework topology

MOF-5 (IRMOF-1) (IRMOF = Isoreticular MOF) that is composed of octahedra $Zn_4O(COO)_6$ and ditopic H_2BDC linkers (H_2BDC = 1,4-benzenedicarboxylic acid) (Chui et al. 1999; Li et al. 1999). The MIL-100 (MIL = Matériaux de l'Institut Lavoisier) and UiO-66 (UiO = University of Oslo) are also among the most widely developed MOFs. The MIL-100(Cr) is the first reported MIL family that is built from $Cr_3O(COO)_6$ nodes and H_3BTC ligand, while UiO-66 is Zr-based MOF comprised of $Zr_6O_4(OH)_4(COO)_{12}$ clusters and H2BDC linkers (Cavka et al. 2008; Férey et al. 2004). These MOFs are depicted in Fig. 8. This material class started gaining attention and growing progressively due to its unique features compared to other porous materials.

Ultrahigh porosity and surface area are some of the extraordinary features possessed by MOFs. For years, the record of highest porosity was held NU-110 (NU = Northwestern University) with BET surface area up to 7140 $m^2\ g^{-1}$ and total pore volume up to 4.4 $cm^3\ g^{-1}$, but in 2018, Kaskel and coworkers broke the record with the discovery of DUT-60 (DUT = Dresden University of Technology), whose specific area and total pore volume are 7839 $m^2\ g^{-1}$ and 5.02 $cm^3\ g^{-1}$. The novel MOF consists of $Zn_4O(CO_2)_6$ clusters that are linked by ditopic H_2bcpbd and tritopic H_3bbc organic ligands (H_2bcpbd = 1,4-bis-p-carboxyphenylbuta-1,3-diene; H_3bbc = 1,3,5-Tris(4′-carboxy[1,1′-biphenyl]-4-yl)benzene). A computational simulation study using less bulky organic linkers reveals an even more outstanding theoretical limit of MOFs surface area, up to 14,600 $m^2\ g^{-1}$ (Farha et al. 2012). This finding is surprising and indicates excellent development since the first reported MOF-5's surface area was only 2320 $m^2\ g^{-1}$, and another conventional porous material such as zeolite, silica, and carbon has a limited surface area below 2000 $m^2\ g^{-1}$. The adjustable pore size of MOFs also plays a significant role in MOFs as host molecules in drug delivery and gas separation since these fields of application commonly rely on size selectivity. Controlling the pore size of MOFs for specific functionalization could be done by organic ligand selection with a certain length or interpenetration of different frameworks via catenation, as described in the next part (Furukawa et al. 2013).

In the early years of exploration, the stability of MOFs is a challenging drawback because the frameworks are formed with vulnerable and labile coordination bonds. However, recent studies have reported the development regarding this issue. The chemical stability, for example, could be improved by the employment of high-valence metal nodes, insertion of stabilizing pillars, and interpenetration of frameworks in de novo synthesis and post-synthesis modifications. The high-valence metals such as Al^{3+}, Fe^{3+}, Ti^{4+}, and Zr^{4+} showed promising results in building water-stable MOFs. Zr-based MOFs also remain intact even in acidic aqueous conditions (Bosch et al. 2014; Ding et al. 2019a, b; Wang and Serre 2019). Thermal stability is also a critical point in the design of MOFs, as a broad range of applications of this material relies on thermal behavior. The well-known Zr-based MOF UiO-66 has a decomposition temperature ranging from 300 to 500 °C, while the highest thermally stable MOFs belong to the Li-based UL-MOFs (UL-MOF = Ultra-light MOF) that undergo degradation in the region of 600 °C. The thermal decomposition process of MOFs could be categorized into two types, ligand-centered and node-centered

mechanisms. As observed in several carboxylate MOFs, the first type involves the fragmentation of M–O, O–C and C–C bonds and results in the solid residue of metal oxides as well as gaseous CO_2 and volatile organic matter. Meanwhile, the latter involves the desolation of the metal nodes, leading to the fragmentation of the building blocks (Healy et al. 2020).

With the "empty spaces" inside the material, MOFs are considered vulnerable to mechanical stresses since the pressure could destroy the frameworks. Various synthetic efforts to gain higher stability are progressing, such as tuning the organic ligand flexibility, changing the solvent polarity, and inserting a "bending" bridge inside the cavity (Redfern and Farha 2019). Yaghi and coworker installed 4,4′-biphenyldicarboxylate (BPDC) into MOF-520 and found that the mechanical stability of the material is improved, in which the modified MOF maintained the crystallinity up to 5.5 GPa, while the pristine MOF started to form amorphous solid at 2.8 GPa (Kapustin et al. 2017).

4.2 Synthesis Techniques

As a rapidly growing porous material, scientists had put much effort into exploring various routes of preparing MOFs to meet scalable synthesis. Conventional heating is one of the most used methods in the early years, but while it provides highly crystalline materials, the long reaction time, high temperature, and severe environmental problems from excess solvents are some of the main obstacles faced in this strategy. A brief description of several methods to synthesize MOFs, including solvothermal or hydrothermal, microwave-assisted, electrochemical, sonochemical, and mechanochemical synthesis, will be discussed in this section.

4.2.1   Conventional Solvothermal and Hydrothermal Synthesis

Solvothermal is a synthesis procedure in a small sealed vial involving the use of solvent and heating of the ligand and metal salt precursors above the boiling point of the solvent, in which the driving force of the reaction comes from the high temperature. Organic solvents such as dimethyl formamide (DMF), diethyl formamide (DEF), ethanol, and methanol are usually used in solvothermal, and when the solvent is water, the process is termed as hydrothermal reaction (Sun and Zhou 2015). One of the early reported MOFs, HKUST-1 ([$Cu_3(BTC)_2(H_2O)_3$]n where BTC is 1,3,5-benzenetricarboxylic acid or trimesic acid), was synthesized using this method. The mixture of cupric nitrate trihydrate and trimesic acid in ethanol/water (50:50) solvent was placed in a Teflon-lined vessel and heated up to 180 °C for 12 h. Relying upon the entropic reasons, high temperature in the solvothermal method was expected to promote the formation of high-dimensionality of polymer frameworks. The obtained material displayed permanent porosity, in which the frameworks were maintained after the guest molecules removal (Chui et al. 1999).

Despite the wide use of the method in discovering novel MOFs structure because of the ability to generate high-quality crystals, it is not easy to use it in the scaling up for further commercialization. The reaction usually takes time up to 12–48 h, and a previous study on the scale-up procedure of MOF-5 reported that it needs almost 6 L of DEF to prepare a 50 g scale of the material (Meek et al. 2011). It also faces environmental issues from the excessive use of solvents, both in the reaction and the washing process. Various techniques were applied to assist solvothermal synthesis during the development, such as modulations and microwave assistance. In the first technique, modulation by changing typical parameters such as solvents, pH, and modulator acids like acetic or formic acid is used to control the crystallinity or other properties of the MOFs. Altering the metal source's initial oxidation state is also a rising strategy; as reported by Bosch and coworkers, the synthesis of Mn cluster and TCPS ligand-based MOFs (TCPS = tetrakis(4-carboxyphenyl)silane) using different metal sources under nearly identical conditions leads to different structure and properties of MOFs, named PCN-47, PCN-48, and PCN-49, respectively, for Mn12(Acetate), $Mn(CH_3COO)_2 \cdot 4H_2O$ and $KMnO_4$ as the metal sources (Bosch et al. 2016; Han et al. 2020a, b).

4.2.2   Microwave-Assisted Synthesis

The development of conventional heating into microwave-assisted technique was because of the ability of the electromagnetic wave to interact with polar molecules/ions and finally increase the kinetic energy as well as the temperature of the system, more rapidly compared to those in conventional solvothermal technique. In addition to the fast reaction, time also generates microcrystalline material with high phase selectivity, uniform size particle, and facile morphology control (Lee et al. 2013). Microwave-assisted synthesis offers a low-energy input method, but it involves strong interaction between the starting and microwave radiation. Therefore, appropriate selection of solvent and energy input is mandatory (Stock and Biswas 2012). A study reported the fast and effective route preparation of Hf- and Zr-UiO-66 using microwave-assisted synthesis, in which uniformly nano-sized particles (less than 50 nm) with high yields (up to 90% and 88% for Hf-UiO-66 and Zr-UiO-66, respectively) are obtained. The synthesis itself is conducted by placing the mixture of the precursors in a microwave tube followed by heating under microwave radiation at 100 °C, 90 W for three minutes in atmospheric conditions (Dang et al. 2020).

4.2.3   Electrochemical Synthesis

Electrochemical synthesis of MOFs uses metal plates as metal sources instead of metal salts or oxides. In this way, the release of undesired anions such as chloride or nitrate commonly included in metal salts could be eliminated. The metal ions produced through the anodic dissolution of the metal plate electrodes react with the ligands dissolved in the solvent and electrolyte solution.

The first preparation of MOFs using the electrochemical method was reported in 2005 by BASF researchers. Cu-BTC MOF was synthesized in an electrochemical cell using 5 mm thick copper plates as electrodes and 1,3,5-benzenetricarboxylic acid dissolved in methanol solvent at a voltage of 12–19 V for 120 min. The obtained Cu-BTC MOF develop a great Cu-environment and surface area of 1820 m^2 g^{-1}, better than the solvothermal-synthesized Cu-BTC MOF that having disturbed Cu environment and lower surface area of 917 m^2 g^{-1}, presumably from the occupation of nitrate moieties from the metal salts (Mueller et al. 2006).

4.2.4 Sonochemical Synthesis

Sonochemical synthesis involves the employment of ultrasound, acoustic energy with a frequency above ~20 kHz. Ultrasound irradiation of the starting material solution allows the cavitation process in which bubbles are formed, grown, and finally collapsed, and generates local high temperature and pressure up to ~5000 K and ~1000 bar, respectively. This process's heating and cooling rates are also high-speed (1010 K s^{-1}) (Lee et al. 2013). In this manner, the utilization of high-energy ultrasound in the synthesis of MOFs is a low-energy and environmental-friendly strategy to obtain large-scale fine crystalline materials within a short period. Lestari and coworkers (Lestari et al. 2018) reported the comparative study in the synthesis of [Zn$_3$(BTC)$_2$] MOFs (BTC = 1,3,5-benzenetricarboxylic acid) using facile and green electrochemical and sonochemical strategy. Both are using ethanol/water (1:1) solvent at ambient temperature and pressure, electrochemical synthesis is performed at a voltage of 15 V for 2 h, while the sonochemical synthesis is conducted at a frequency of 40 kHz for a variation of time of 30, 60, and 90 min. The result showed that the materials prepared by the electrochemical method develop larger average size particles (ca. 18.43 $\pm$ 8.10 μm) than that of the sonochemically synthesized materials (ca. 87.63 $\pm$ 22.86 nm for 30 min reaction (Lestari et al. 2018).

4.2.5 Mechanochemical Synthesis

Mechanochemical synthesis of MOFs relies on the cleavage of molecular bonds by mechanical forces, followed by chemical transformation of the starting materials. The synthesis is commonly conducted in a stainless steel ball mill grinder with rotation at a certain rate. This strategy is advantageous in environmental terms as it could be carried out solvent-free under atmospheric conditions. In addition, metal oxides could sometimes be more preferred than metal salts, resulting only in water as the by-products.

The early synthesis by ball milling the reactants alone without solvent is denoted as neat grinding (NG). During the development, this has been improved into liquid-assisted grinding (LAG) with liquids or ions. A small number of liquid solvents such as ethanol and water could enhance the molecules' mobility and increase the reactant activity, thus promoting a faster reaction. A study also reported that water crystals as

an auxiliary solvent in mechanochemical synthesis could improve crystallinity (Tao and Wang 2021).

Prochowicz et al. reported the first successful attempt of MOF-5 synthesis via the LAG mechanochemical route. Using DEF (DEF = N, N´-dietylformamide) as the liquid, the oxo-zinc benzoate and H_2BDC ligand were ground, and PXRD revealed that increasing the amount of DEF in the mixture showed improved crystallinity of the obtained MOF-5. As a comparison, the NG of the reactants showed only H2BDC ligand peaks in PXRD with no trace of MOF-5 (Prochowicz et al. 2015). A series of MOF-74 families have been successfully synthesized via mechanochemical method using Hünig's base (N, N´-diisopropylethylamine) as both the liquid for LAG and the base required to facilitate MOFs formation, resulting in a high-quality MOF-74 in a scalable and sustainable manner (Wang et al. 2020a; b).

4.2.6 Purification and Activation of MOFs

Before use, MOFs need to be purified and activated. Purification refers to the removal of unreacted precursors or other chemicals such as solvents and modulators. At the same time, activation is related to eliminating any pore-blocking impurities to expose the large surface area and the active sites both in the metal centers and organic struts. Purification and activation are the final steps in MOFs production, and while these processes are challenging since, during the removal of the solvents, the frameworks can collapse and result in significantly decreased porosity, some significant progress has been made. Farha et al. reported the purification of the mixtures of MOFs phases, MOFs containing single and multiple ligands, and catenated and non-catenated phases (Farha and Hupp 2010).

The most conventional technique used in the activation of MOFs is calcination, in which the materials were heated both in the presence and absence of vacuum. However, despite the simplicity, this technique could only be applied to the MOFs with high thermal stability, such as UiO-66 (activated at 300 °C) (Cavka et al. 2008). In many cases, loss of crystallinity and lack of porosity are also observed. Solvent exchange is an effective alternative strategy, where the solvent used in the synthesis, usually a high-boiling point solvent, is exchanged with solvent of lower boiling point, and the process is continued with mild heating under vacuum. Solvents with lower boiling points have weaker intermolecular and lower surface tension and capillary forces to avoid structural collapse. Other alternatives are the employment of supercritical CO_2 (SCD), in which the solvent was exchanged with ethanol and then liquid CO_2, followed by heating over the critical point of CO_2 and then vented. Freeze drying that involves the use of benzene and the repeated process of freezing and warming to room temperature to allow the natural solid-to-gas phase transition of the benzene is also an alternative strategy, but due to the toxic nature of benzene, it could be substituted by other solvents such as cyclohexane (Mondloch et al. 2013).

Very recently, Woodliffe et al. summarized updated techniques in purification and activation to meet sustainable and scalable MOFs production in terms of technical and circular economy perspectives. Besides the mentioned techniques before, microwave

heating, UV–Vis irradiation, and ultrasound treatment are explored for their low energy sources and environmental-friendly natures (Woodliffe et al. 2021). One of the successful activations of MOFs using microwave-assisted process is the complete removal of solvents (methanol or ethanol, acetonitrile, or DMF in 4, 8, and 35 min, respectively, at 600 W) in HKUST-1. In addition to the effective performance, it needs lower energy than that of thermal activation, i.e., 51 and 5400 W h, respectively, for microwave and thermal activation of methanol solvent (Lee et al. 2019).

4.3   Applications

Given such unique features of surface area, porosity, and tunability, MOFs are investigated as tremendous potential in a broad spectrum of applications, including but not limited to catalysis, drug delivery, gas storage, and separation and sensing. The following are brief descriptions of the recent progress of MOFs application in several fields (Fig. 7).

4.3.1   Catalysis

Metal–organic frameworks have many properties that give good points in the catalysis application. Generally, a heterogeneous catalyst needs to exhibit a large surface area for higher contact possibility of the substrate molecules. It also requires a high density of active catalytic sites for high reaction kinetic rates per unit volume. These features could be found in MOFs, which makes them a potential candidate for catalyst materials. MOFs are well-known for their ultrahigh surface area and high density of active sites that come from both the inorganic and organic building blocks and the incorporated complementary catalytic groups within the frameworks. In addition, the tailored pore sizes and structures of MOFs allow shape and size selectivity, thereby enabling reactants diffusion and stable encapsulation of the guest species (Yang and Gates 2019).

The role of MOFs in catalysis involves three essential parts: the metal centers, organic linkers, and the pores. Catalysis in the inorganic center of MOFs comes from the coordinatively unsaturated metal sites formed upon the removal of coordinated labile ligands, commonly solvent molecules. The open metal sites will then provide a free coordination position for the substrates. To serve ascatalytic sites, the organic component of MOFs should contain reactive functional groups, other than the coordinative functional groups that coordinate to the metal centers to maintain the frameworks. One of the simplest organic ligands with such functional groups is 2-aminoterephtalate, which bears two terminal carboxylic groups as coordinative functional groups and one amino ($-NH_2$) group as a reactive functional group. It is widely explored to prepare the various MOFs such as UiO-66-NH_2 and MIL-101-NH_2 series. Further functionalization of this group could also give derivatives with certain catalytic activity and selectivity (Xamena et al. 2013).

Besides serving as Lewis acid by forming vacant orbitals in the metal centers, MOFs could also act as Brønsted acid by the encapsulation of Brønsted acid molecules within the pores and covalently bound Brønsted acid groups in the organic linkers. Both Lewis and Brønsted acid sites could be found in superacid MOFs. One of the MOFs with great acidity is sulfated Zr-based MOF, MOF-808-2.5SO$_4$ that was reported as the first evidence of superacid in MOFs with Hammett acidity function H0 $\leq$ −14.5. The nonstructural formate in the structure was replaced with sulfate by soaking the material in aqueous sulfuric acid (Jiang and Yaghi 2015; Jiang et al. 2014). In 2017, a similar method was applied to obtain Hafnium-based MOF VNU-11-SO$_4$ (VNU = Vietnam National University), which was reported as a new superacid with precisely the same Hammett indicator MOF-808-2.5SO$_4$. The catalyst showed high activity in the solvent-free synthesis of benzoxazoles, with reaction yield up to 95% (Nguyen et al. 2017). Recently, Peng et al. developed ionic liquids grafted UiO-66 superacid by quaternization of UiO-66 1,3-propane sultone, ion-exchanging with H$_2$SO$_4$ or HSO$_3$CF$_3$, and employed the material as a catalyst in biodiesel production via transesterification. The catalyst was slightly less acidic than MOF-808-2.5SO$_4$ or VNU-11-SO$_4$ (H0 $\leq$ −12.5) but was more muscular than 100% H$_2$SO$_4$ (Peng et al. 2020). In addition to the size and shape selectivity obtained by tailoring the porosity, enantioselectivity in MOFs as catalysts could also be obtained by functionalizing MOFs using certain modalities. Having these features, MOFs in catalysis has received significant interest.

The diversity of the building blocks and design allows for many MOFs applications as heterogeneous catalysts in various reactions such as the Friedel–Crafts reaction, Knoevenagel condensation, Aldol condensation, oxidation coupling reaction, cyanosilylation, and CO$_2$ fixation (Remya and Kurian 2019). In a recent report, Chen et al. demonstrated the employment of chiral MOFs (CMOFs) catalyst with tunable catalytic selectivity in the asymmetric transfer hydrogenation reaction. In a combination strategy of both metal and ligand design using Ca-, Sr-, and Zn-metals and enantiopure phospono-carboxylate ligands of 1,1′-bisphenol with functionalization, high enantioselectivity of catalysis in the asymmetric transfer hydrogenation of heteroaromatic imines was afforded, up to 97% for Ca-based MOFs with 2,4,6-trimethyl groups functionalization (Chen et al. 2021).

4.3.2 Drug Delivery

In biomedical applications such as drug carrier, MOFs should satisfy several requirements such as biocompatibility and stability. Biocompatibility could be achieved by using non-toxic metal centers such as calcium (Ca), copper (Cu), manganese (Mn), magnesium (Mg), zinc (Zn), iron (Fe), titanium (Ti), or zirconium (Zr) instead of the toxic chromium (Cr), cadmium (Cd), nickel (Ni), or cobalt (Co), also by employing exogenous linkers that are synthesized from natural compounds or endogenous spacers that also exist in the body composition (Sun et al. 2013; Wang and Serre 2019). Biodegradability and stability of MOFs are also key point that it is expected to be able to degrade in situ, and the products could be excreted with the body

metabolism to avoid dangerous endogenous accumulation. A recent review suggested that several MOFs could undergo biodegradation and elimination in urine and feces and also showed low acute toxicity as the particles were sequestered rapidly by liver and spleen (Sun et al. 2020).

The ultrahigh porosity is the main advantageous feature of MOFs application in drug delivery, as it indicates high loading capacity of a drug carrier. In addition to the exceptional porosity, tunability in the building blocks of MOFs allows the design of material with high biocompatibility and desired bioactivity. The first investigation of MOFs as a potential drug delivery system was pioneered by Ferey and coworkers using MIL family, MIL-101, and MIL-100. Ibuprofen was loaded into the MOFs, and the storage and release profile were observed. The ibuprofen loading in the MIL-101 (1.376 g ibuprofen/g MOF) is higher than that of MIL-100 (0.347 g ibuprofen/g MOF), attributed to the larger pore sizes of the former (12,700 and 20,600 Å) compared to the latter (8200 and 12,700 Å). The release study of the cargo was studied in simulated body fluid (SBF) at 37 °C, in which complete slow release of ibuprofen was achieved after three days and six days for MIL-100 and MIL-101, respectively. While the frameworks contained the toxic chromium metal centers, the alternative non-toxic homologue MIL-101(Fe) was developed in the following years (Horcajada et al. 2006).

Apart from the direct encapsulation of the drug within the MOFs porosity, drug delivery in MOFs could also be carried out via direct assembly and post-synthesis strategy. In direct assembly strategy, the drug molecules are directly employed as the ligand in the framework formation, while in the post-synthesis strategy, the drugs are introduced into MOFs via coordination bond with the metal nodes or covalent bond with the active sites in the organic linkers (Wang et al. 2018). A study reported the incorporation of anticancer agent cisplatin into MOFs via two different strategies, namely encapsulation and conjugation. Using UiO-66 and UiO-66-NH$_2$ as the drug vehicle, cisplatin was directly incorporated into the both MOFs, and cisplatin-derived Pt(IV) prodrug was conjugated via EDC/NHS coupling reaction with the –NH$_2$ groups in UiO-66-NH$_2$. Platinum loading test showed that the higher content was observed in conjugation strategy (30.7 wt%) than in the encapsulation strategy (4.9 wt%), and this translates into greater toxicity in the in vitro cell viability test (Mocniak et al. 2015).

4.3.3 Gas Storage and Separation

The utilization of porous material in gas storage emerges from the disadvantageous traditional storage systems that are commonly energy-expensive. In the hydrogen storage techniques, for example, cryogenic storage requires extremely low temperature, pressured tank needs high pressure, and metal hydrides formation requires high temperature to release the gas. The porous material, in the opposites, offers safer and cheaper alternative to store gas by adsorption. A gas storage porous material is expected to adsorb a reasonably high uptake of gas at room temperature and relatively low pressure (Durbin and Malardier-Jugroot 2013). Owing to an extraordinary

porosity and surface area with tunable pore size and functionalities, MOFs are highly potential gas storage materials.

Hydrogen storage in MOFs was first reported in the early years of exploration, in which MOF-5 could adsorb hydrogen up to 4.5 wt% at 78 K and 1.0 wt% at room temperature and pressure of 20 bar (Rosi et al. 2003). In a very recent report, a study computationally screened nearly 500,000 of real and hypothetical data of MOFs structure and assessed experimentally the hydrogen uptake of the most promising compounds, SNU-70 (SNU = Seoul National University), UMCM-9 (UMCM = University of Michigan Crystalline Material), and PCN-610/NU-100 (PCN = Porous Coordination Network). The assessment leads to the result that these three MOFs, especially PCN-610/NU-100 as the most superior, surpassed the hydrogen storage capacity of two benchmark MOFs, MOF-5 and IRMOF-20, the record-holder for highest performance with gravimetric capacity of 10.1 wt%, 4.5 wt%, and 5.7 wt%, respectively, for PCN-610/NU-100, MOF-5, and IRMOF-20 (Ahmed et al. 2019).

With the same manner as gas storage, gas separation materials should possess high selectivity toward different types of gas as the additional requirement. High shape selectivity could be achieved by tuning the pore size with isoreticular principle, framework interpenetration, or pore space partition. The pore will act as molecular sieves that allow gas with small and proper shape and size to diffuse, while excluding other gases. The specific and selective separation in MOFs could be increased by using and modifying linker functional sites and open metal sites. One of the most widely investigated applications is the CO_2 capture and separation (Lin et al. 2020).

The CO_2 capture by MOFs could be performed in four types, namely post-combustion, pre-combustion, oxy-fuel combustion, and direct capture from air. The Mg-MOF-74 is one of MOFs with notable CO_2 uptake at low pressure (5.28 mmol g^{-1} at 40 °C and 0.15 bar). The MOF is composed by 1D hexagonal channels with open metal sites (OMs) at the SBUs. The high adsorption of CO_2 mostly involves the strong interaction of CO_2 molecules with the OMs (Li et al. 2017). In addition, introduction of Lewis base sites (LBs) into MOFs could also enhance the CO_2 binding affinities. The employment of 2-aminoterephtalatic acid in the preparation of IRMOF-3 (a MOF isoreticular to MOF-5) resulted in greater CO_2 uptake capacity (up to 14.7 mmol g^{-1}) than MOF-5 (up to 14.0 mmol g^{-1}) at 298 K and a wide range of pressure (0–12.3 bar). Incorporation of alkylamine also showed improved CO_2 uptake via chemisorption manner (Ding et al. 2019a; b).

4.3.4 Sensing

As highly porous material with high tunability, MOFs could be designed as chemical sensors, such as anions, metal cations, organic compounds, and gases. There are several types of MOFs sensing, including luminescence sensing that involves spontaneous emission of light during the molecule detection, electrochemical sensing that works based on redox reaction with the analyte in electrochemical system, colometric sensing from the chromogenic reaction of colored compounds, magnetic sensing that

relies on the change of spin states, and chemiresistive sensing that works based on the change in the electronic properties or resistance (Koo et al. 2019; Li et al. 2020).

Among those types, the work on luminescence sensing is the most widely reported. Luminescent MOFs (LMOFs) with tunable photoluminescence properties could be obtained by utilizing relevant fluorescent structures. Photo-induced electron transfer (PET), ligand-centered emission, ligand-to-metal charge transfer (LMCT), metal-to-ligand charge transfer (MLCT), and guest-induced luminescence are some of typical processes involved in luminescence sensing in MOFs (Kanan and Malkawi 2021).

The LMOF-263 is one of which possessing strong luminescence and high water-stability, making it a great candidate as chemical sensor in aqueous conditions. High sensitivity of the MOF is observed in the detection of heavy metals at trace level, up to 3.3 ppb and 19.7 ppb for Hg^{2+} and Pb^{2+} metal ions, respectively, with impressive selectivity toward Hg^{2+} over other metal ions (Rudd et al. 2016). Very recently, Garcia-Valvidia et al. developed three isostructural MOFs based on 2-aminoisonicotinate, $\{[M(\mu-2ain)_2]\cdot DMF\}$ (2ain = 2-aminoisonicotinate), that combine both photoluminescence and magnetic sensing. The study revealed that these MOFs modulate their properties according to solvent exchange and/or capture of metal ions in liquid media (García-valdivia et al. 2020).

5 Covalent Organic Frameworks

Covalent organic frameworks (COFs) are, firstly introduced by Côté and coworkers in 2005 (Côté et al. 2005), constructed with covalently bonded organic building units demonstrating a new family of porous organic materials (Ding and Wang 2013). The elegant assemble of the organic units creates a well-defined porous and crystalline structure of COFs with tailored functional groups offering superior properties for a wide range of applications, such as adsorption, catalysis, gas storage, energy, drug delivery, optoelectronics, and so forth (Wu and Yang 2017). Herewith, we demonstrated the sophisticated architecture and properties of several groups of COFs with their recent and advanced synthesis strategy for various purposes of application.

5.1 Structure and Physicochemical Properties

The COFs serve as a promising platform for vital application owing to their structure design, topology, and functional group diversity, as well as the most important is porosity. The structure of COFs, two- or three-dimensional, symmetric or asymmetric topology, even their architectures, is highly influenced by building block units of the monomers which creating a diversity of COFs structure and properties. Therefore, design synthesis of COFs concerning the monomer symmetry having specific geometry is recommended following basic topology design diagram as shown in Fig. 9. (Geng et al. 2020). Each rigid backbone of the monomer has reactive sites
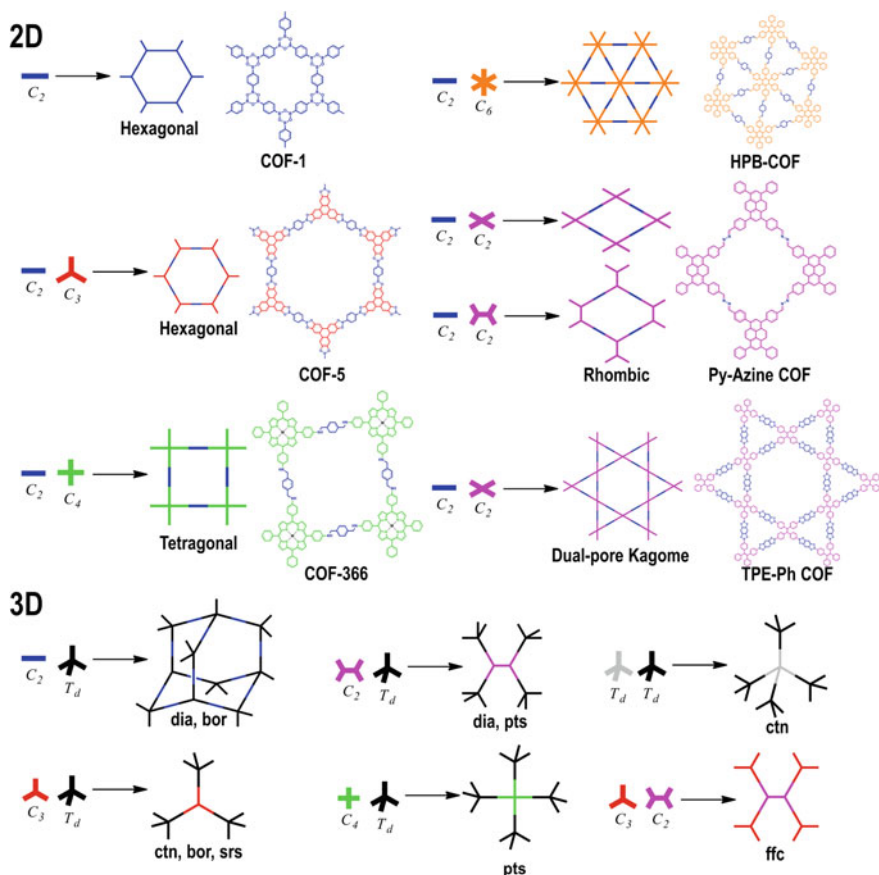
Fig. 9 Two- and three-dimensional basic topology of COFs structure. Some examples of COFs represent the two-dimensional COFs lattice, a combination of various monomer symmetries

distributed in a different geometry that can be covalently bonded to form two- or three-dimensional polymer backbone growth in a specific direction. This ordered assemble creates various crystalline porous structures with different textural properties. Figure 9 indicates that a combination of planar monomers controls the growth of COFs in a two-dimensional pathway generating a two-dimensional atomic layer with specific topologies. For example, both combinations of $C_3 + C_2$ and $C_2 + C_2$ indeed formed hexagonal 2D COFs, but they fashioned different lattice and topology which generating diversity in pore size and π-ordering (Côté et al. 2007; Wan et al. 2008; Xie et al. 2015).

The structure and physicochemical properties of COFs depend on the precursors and the organic linker that was employed during assembling their structure connected through a strong and dynamic covalent bond. To date, at least four common linkages are widely reported and investigated by the researcher in preparing the diversity
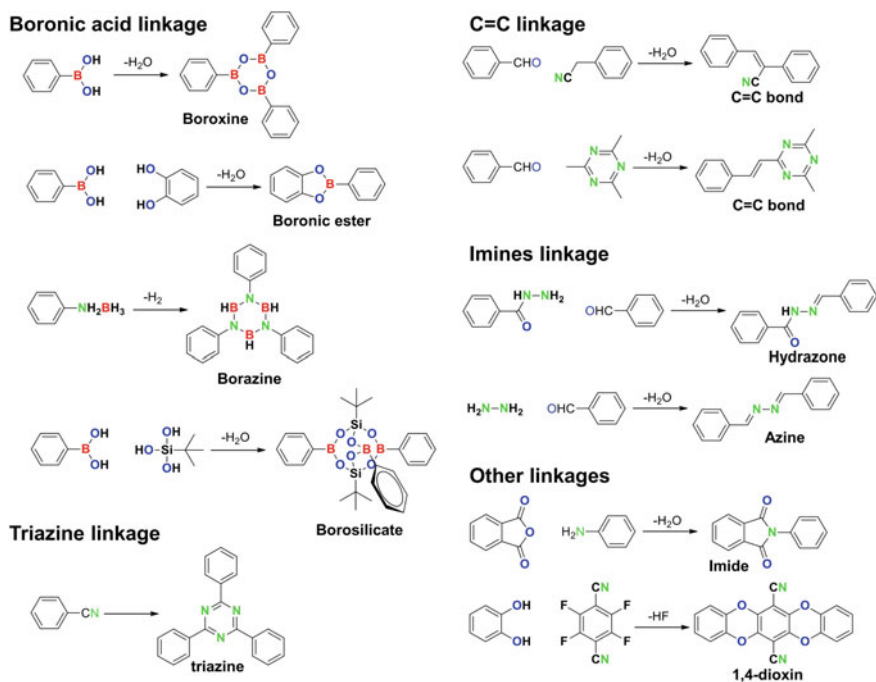
Fig. 10 Some examples of linkages employed to synthesize COFs

of COFs, such as boronic acid (including boronic ester, borazine, and borosilicate bonds), triazines, C=C bond, and imines linkages. The common examples of linkages are summarized in Fig. 10.

5.1.1 Boronic Acid Linkage

Boronic acid linkage pioneered the creation of COFs by assembling the B_3O_3 ring to give the first COFs, namely COF-1 and COF-5 (Côté et al. 2005). These materials are topologically designed and successfully prepared by researchers, Côté and his co-worker from Arizona State University, via condensation reaction of phenyl diboronic acid (DBBA) to yield crystalline material $(C_3H_2BO)_6 \cdot (C_9H_{12})_1$ or known as COF-1, or reacting DBBA with hexahydroxytriphenylene (HHTP) producing a highly crystalline product $C_9H_4BO_2$ (COF-5). The self-condensation of DBBA through "one-pot" protocol under the mild condition could be highly efficient to produce COF-1. This process was followed by dehydration reaction of boronic acid molecules unite to create a planar six-membered B_3O_3 ring by eliminating water molecules. A typical molecule of cyclotrimerized boronic acid is seized in planar confirmation via $C-H_{(o-ph)} \cdots O_{(BO)}$ with 2.975(2) Å of hydrogen bonds. This fundamental concept was adopted to extend a reaction of DBBA which expectedly forming a layered

hexagonal framework. As for COF-5, similar reaction analogs were applied upon condensation reaction of DBBA with a trigonal building block of HHTP to form a five-membered ring BO_2C_2. A study of X-ray diffraction revealed the crystal structure of extended staggered-graphitic layer P6$_3$/*mmc* COF-1 and eclipsed-graphitic layer P6/*mmm* COF-5, with a hexagonal pore size of 15 Å and 27 Å, respectively. The N_2 adsorption–desorption experiment was performed to confirm the architecture and porosity of both COF-1 and COF-5, revealing a typically type-IV isotherm characteristic with high BET surface area of 711 m^2 g^{-1} and 1590 m^2 g^{-1}, respectively, which surpass other layered porous materials, like graphite, clay, and pillared-clay. This finding inspired researchers to develop high-quality COFs architectures following the fundamental concept of B–O linkage analogs. For examples, boronic ester linkage with different combination of backbone units, such as benzene, biphenyl, biphenyl acetate, porphyrin, thiophene, triphenylene, and triphenylbenzene, leads to generating different crystal system and porosity of COFs, including COF-6, COF-8, COF-10, COF-66, COF-366, H$_2$P-COF, ZnP-COF, CuP-COF, T-COF 1-4, TT-COF, TP-COF, and many more (Côté et al. 2007; Wan et al. 2008, 2011; Xie et al. 2015; Bertrand et al. 2013; Dogru et al. 2013a, b; Zhao et al. 2019). Not only having a two-dimensional structure, but a reticular synthesis of COFs using boronic acid-based linkage also generates a three-dimensional network by extending the chemical reaction of molecules connected by borosilicate linkage. Yaghi and *co*-worker successfully prepared COF-202 through a condensation reaction of *tert*-butylsilanetriol and tetra(4-hydroxyboryl-phenyl)methane, in which the boron atoms of the borosilicate cage form a triangle (Hunt et al. 2008). This material was chemically and physically stable proven by its capability to maintain its structure up to 450 °C or immersing in common organic solvents (alkenes, THF, DMF, acetone, and alcohols). Additionally, a low-pressure argon adsorption–desorption study shows a type I isotherm indicating a microporous structure of COF 202 with a BET surface area of 2690 m^2 g^{-1}.

5.1.2   Imines Linkage

In addition to the boric acid-based linkages, the construction of COFs can also involve the imines bond. The crystallinity of COFs constructed via imine linkages, unfortunately, is much lower than the boric acid linkage, but their chemical stability against water, acids, and alcohol is greatly improved (Huang et al. 2016). Chemically, the imine linkage can be normally formed by reacting amines and aldehydes. Similar to the B–O linkage, the structural diversity and properties of COFs-based imines linkage are also determined by the monomer. For example, TPB-DMTP-COF, developed by chemically combining symmetrical group C$_3$ triphenylbenzene (TPB) and electron-donating C$_2$ dimethoxy terephthaldehyde (DMTP), possessed a hexagonal pore shape with BET surface area of 2105 m^2 g^{-1} and provided high chemical stability in the water, acid and base (Xu et al. 2015). Jiang's group developed four series of imine-linked pyrene COFs, namely Py-DHPh COF, Py-2,3-DHPh COF, Py-2,2'-BPyPh COF, and Py-3,3'-BPyPh COF, having ordered docking sites featured on their channel wall for providing non-covalent interaction, which may open a new

insight for the novel synthesis of COF-based material (Xiong et al. 2014). Since the presence of open docking sites channeled through one-dimensional walls of 2D COFs, those Py-DHPh COF, Py-2,3-DHPh COF, Py-2,2'-BPyPh COF, and Py-3,3'-BPyPh COF are expected to have high BET surface area which measured using N_2 adsorption–desorption, found SBET = 1895, 1932, 2349 and 2200 $m^2 g^{-1}$, respectively. Besides, those COFs also have high thermal stability (stable up to 400 °C) and crystallinity which make them a versatile platform in desired applications. A unique flexible structure (having AA eclipsed- and AB staggered-stacking architecture system) of imine-based COF was recently prepared by irradiating 2,4,6-tris(4-formylphenoxy)-1,3,5-triazine and 2,4,6-tris(4-formylphenoxy)-1,3,5-triazine using 100 kGy of electron beam for 160 s, which later denoted as EB-COF 1 (Zhang et al. 2020). This material possesses type I reversible isotherm which is determined by the N_2 adsorption–desorption method and also has 738 $m^2 g^{-1}$ of BET surface area.

5.1.3 Triazine Linkage

As revealed in Fig. 10, a simple COF can be prepared from cyanides benzene to afford a triazine-linked COF. One example reporting a COF construction through triazine linkage is research performed by Khun et al. (Kuhn et al. 2008). The porous and crystalline polytriazine framework was obtained via ionothermal employing molten $ZnCl_2$ as a structure-directing agent. The reaction of 1,4-dicyanobenzene under high temperature gave CTF-1 as a product with hexagonal pore system and BET surface area of 791 $m^2 g^{-1}$ and total pore volume of 0.40 $cm^3 g^{-1}$. Bhanja et al. reported a new triazine-linked COF, denoted as TDFP-1 integrated from 1,3,5-tris-(4-aminophenyl)triazine (TAPT) and 2,6-diformyl-4-methylphenol (DFP) (Bhanja et al. 2017). The combination of C3 TAPT and C2 DFP produced a two-dimensional COF structure with a hexagonal pore shape. This layered graphitic-like structure has a BET surface area of 651 $m^2 g^{-1}$.

5.1.4 Other Linkages

Besides the common linkages described previously, the alternative linkages, for example, dioxane and C=C bond, are also widely used in the synthesis of functional COFs. The dioxin-linked COFs also offer unique structure and properties compliment with cyanides as side functional groups for further post-modification. The hexagonal pore shape of COF-316 and COF-318 was successfully synthesized by Zhang et al. (2018a; b). The reaction of C_3 knot 2,3,6,7,10,11-hexahydroxytriphenylene (HHTP) and C_2 linker tetrafluoro-phthalonitrile (TFPN) or 2,3,5,6-tetrafluoro-4-pyridinecarbonitrile (TFPC) gave a yellow microcrystalline powder of 2D COF-316 and COF-318, respectively, which are chemically stable against acetone, alcohols, DCM, THF, and DMF. Besides, the textural evaluation revealed a relatively high S_{BET} of 557 $m^2 g^{-1}$ for COF-316 and 579 $m^2 g^{-1}$ for COF-318. A reversible

C=C to C–C linked COF, called CCOF-17 and CCOF-18, was successfully integrated via Knoevenagel polycondensation of dibinaphthyl-22-crown-6 with 2,2′-(1,4-phenylene)diacetonitrile or 2,2′-(biphenyl-4,4′-diyl) diacetonitrile (Yuan et al. 2021). The unique two-dimensional tetragonal structure of CCOF-17 was easily transformed into CCOF-17 R by the addition of NaBH$_4$ as a reducing agent. This feature also applies to CCOF-18. The change of their structure and framework leads to elevate the chemical stability of both CCOF-17 and CCOF-18 over various inorganic solvents. Almost no weight loss was found after soaking CCOF-17 R and CCOF-18 R, but little loss (less than 10%) in a strong acid solvent.

5.2 Synthesis Techniques

Over the past decades, the chemistry of COFs has received incredible attention as a high class of organic-based porous materials. Although a novel synthesis strategy of COFs has been rapidly and massively reported, efficient, green chemistry, reproducible, sustainable, and environmental-friendly protocols are still progressively developed and as a key point in achieving recommended and high-quality COFs to serve the various promising applications. The high-quality COFs depend on several factors, namely energy sources (thermal, mechanics, microwave radiation, high electron beam, ultrasound, and so forth), catalyst (basically acid homogenous catalyst), solvents (organic or green solvents), monomer (combination of various knots and linker), or crystallization activation. This section discussed and highlighted a progress synthesis procedure of COFs, from conventional solvothermal and ionothermal methods to green and advanced methods, including mechanochemistry, microwave-assisted synthesis, and photo-induced techniques (Li et al. 2020).

5.2.1 Solvothermal

Most COFs are prepared by the solvothermal synthesis method (Côté et al. 2005; Wan et al. 2011; Bertrand et al. 2013; Dogru et al. 2013a, b; Feng et al. 2012; Hunt et al. 2008; Xu et al. 2015; Xiong et al. 2014). This method is still popular among researchers since the first COFs (COF-1 and COF-5) were established in the recent study synthesizing TpPa-COF, TbPa-COF, and TpBD-COF nanosheets (Shi et al. 2020). The solvothermal method involves several variables that directly or indirectly determine the quality of COFs, such as temperature, pressure, solvents volume ratio, and reaction time. To obtain high yield, purity, and quality of COFs, many efforts have been conducted in terms of optimization. The advantages of this method are capable to produce high crystallinity with relatively good yield. Unfortunately, this method generally requires a high synthesis temperature (up to 120 °C) and long reaction time (up to 15 days), which becomes the major issue for preparing COFs. Additionally, the solvothermal method employs harmful solvents, usually a combination of mesitylene

or o-dichlorobenzene (*o*-DCB) with common organic solvents, such as dioxane, acetone, alcohols, and toluene, which basically increase its hazardous parameters.

5.2.2 Ionothermal

A similar strategy that eliminates at least the use of harmful solvents is developed, called ionothermal. This method used inorganic salt (ionic liquid), such as $ZnCl_2$, either as the solvent at high temperature or as a structure-directing agent (Kuhn et al. 2008; Maschita et al. 2020). Mostly, the synthesis of COFs through this pathway involves a solid-state reaction, in which the molten-inorganic salt catalyzing the formation of two-dimensional COFs architecture. Khun et al. prepared CTF-1, a triazine-based COF, through ionothermal strategy catalyzed with molten $ZnCl_2$ under high temperature up to 400 °C for 40 h (Kuhn et al. 2008). The COF synthesis by this method not only preserved the chemical, physical and crystalline stability, but also produced a high quantity of product due to the reactivity and chemical selectivity of molten $ZnCl_2$ salt toward trimerization reaction. This leads to a high yield of TAPB-PTCDA COF, synthesized using ionothermal by reacting trigonal 2,4,6-tris(4-aminophenyl)-benzene (TAPB) and perylene-3,4,9,10-tetracarboxylic dianhydride (PTCDA) under vacuum condition and catalyzed with anhydrous $ZnCl_2$ at 300 °C, acquired up to 88% (Kuhn et al. 2008). Nevertheless, applying high temperature and long reaction time becomes an issue both environmentally and economically. An advanced and innovative ionothermal strategy was developed by Fang's group which only needs 3 min to obtain three-dimensional ionic liquid COF (3D-IL-COF 1 and 3D-IL-COF 2) (Guan et al. 2018).

5.2.3 Mechanochemistry

Mechanochemistry is one of a technique to afford high-quality of COFs, which required mild reaction condition, short reaction time, high energy saving, eco-friendly, economically benefit and simple protocol. The COF prepared by this method (Schiff base mechanochemistry) was firstly reported in 2013 by Biswal et al., synthesizing TpPa-1 through grinding 1,3,5-triformylphloroglucinol and *p*-phenylenediamine in a mortar at room temperature (Biswal et al. 2013). The progress formation of TpPa-1 (~90% of yield) was indicated from the vicissitudes of the product's color over time which completely formed at 45 min of reaction monitored by PXRD, FTIR, and ^{13}C CP-MAS solid-state NMR. However, moderate crystallinity and low BET surface areas (61 m^2 g^{-1}) were the drawbacks of this method. A moderate crystallinity of hydrazine-linked COF (TpTh) was also reported by the same research group, even though they had applied the liquid-assisted grinding (LAG) method as an innovation of the mechanochemical technique (Das et al. 2014). Nevertheless, this new insight pioneered and encouraged the researcher to develop a high-quality COF prepared through mechanochemistry. The combination of mechanochemistry and thermal crystallization method on the synthesis of TpPa-1

gave a better result both crystallinity and BET surface area compared to simple mechanochemistry or solvothermal method (Karak et al. 2017). In their report, a Brønsted acid (*p*-toluenesulfonic acid) and *p*-phenylenediamine were ground in mortar for 5 min, followed by the addition of 1,3,5-triformyl phloroglucinol, and continuous ground for 10 min. In the final step, water was added, and the mixture was transferred into a vessel for thermal crystallization at 170 °C for around 60 s. The TpPa-1 obtained via this method has a high BET surface area of 1432 m^2 g^{-1}.

5.2.4 Microwave-Assisted Method

Another fast-synthesis route is a microwave-assisted synthesis that was first introduced in 2009 toward the synthesis of COF-5 (Campbell et al. 2009). A rapid formation of the gray purple powder of boronate ester-linked COF-5, reacting BDBA and HTTP with a molar ratio of 3:2 in a mixture of 1:1 mesitylene:1,4-dioxane under microwave irradiation of 200 W, only takes 20 min which is 200 times faster than the conventional solvothermal method (Côté et al. 2005). In addition, the product yielded 68% of pure material and showed a higher BET surface area of 2019 m^2 g^{-1} than COF-5 previously prepared by the solvothermal method (S$_{BET}$ = 1590 m^2 g^{-1}). Another boronate ester-linked COF, BTD-COF, was also successfully achieved through the microwave-assisted method (Dogru et al. 2013a, b). The transesterification reaction of 4,7-bis[4-(4,4,5,5)-tetramethyl-[1,3,2]dioxaborolan-2-yl)-phenyl]-56 benzo[1,2,5]-thiadiazole and HTTP irradiated with 200 W of microwave radiation for 40 min produced the green BTD-COF powder with 75% of yield. Ji et al. also reported a high yield TH-COF synthesized from the nucleophilic substitution of 2,3,5,6-tetrafluoro-4-pyridinecarbonitrile with HHTP in a mixture solvent of 1:1 mesitylene/dioxin catalyzed by trimethylamine under 100 W microwave irradiation for 30 min (Ji et al. 2020). Not only that, the product also has high crystallinity and BET surface area of 1254 m^2 g^{-1} which greatly improved compared to a similar COF structure (COF-318) prepared through the solvothermal method, having a BET surface area of 576 m^2 g^{-1} (Zhang et al. 2018a; b).

5.2.5 Photo-Induced Method

The photo-induced method also known as the photochemistry approach has been firstly introduced in the synthesis of COF in 2017 by Choi's and Lim's groups (Kim et al. 2017a, b). They demonstrated a rapid photochemical synthesis of "sea urchin-shaped" UV-COF-5. The growth rate of UV-COF-5 synthesized under UV light exposure was 48-fold faster than the conventional solvothermal method. Additionally, the reaction of BDBA and HTTP exposed by UV light for 1 h yielded 75% of COF-5. The ultimate yield of COF-5 was obtained after exposure for 72 h (yield = 90%). The BET surface area of UV-COF-5 exposed by Hg lamp (λ = 325–580 nm), denoted as Hg-UV-COF-5, was found to be 2026.9 m^2 g^{-1}, much higher than th-COF-5 (solvothermal, BET = 1608.1 m^2 g^{-1}). In recent years, Kim and Choi reported a

synthesis of highly conjugated crystalline pyrazine-fused COF (hcc-COF) promoted by light energy (Kim and Choi 2019). A reaction of 1,2,4,5-benzenetetramine tetrahydrochloride and hexaketocyclohexane octahydrate was conducted in a vial containing mesitylene, chloroform, and acetic acid and further exposed using simulator sunlight (λ = 200–2500 nm).

5.2.6 Sonochemistry

Synthesis of COFs through sonochemistry approach provides a low-cost, low-energy consumption, and short synthesis route to achieve highly efficient and affordable protocols. This method can accelerate the crystallization rate through cavitation in the solution, thereby generating extremely high local temperature and pressure which featuring fast heating and cooling rates (Hangxun et al. 2013). Yang et al. employed this method to prepare COF-1 and CPF-5 (Yang et al. 2012), published in 2012, and limited research involving this method afterward. In a typical reaction, a self-condensation of BDBA was irradiated by 100% power of ultrasound wave for 1 h produced a relatively high surface area of COF-1 by 732 m^2 g^{-1} with a pore volume of 0.55 cm^3 g^{-1}. They also generated COF-5 with a BET surface area of 2122 m^2 g^{-1} which was higher than COF-5 prepared with the solvothermal method. This method also allowed a huge-scale synthesis of COF-5 with a relatively faster and high yield compared to the solvothermal method.

5.2.7 Post-synthesis Strategy

Owing to their functional group availability, such as –OH, –CN, –COOH, saturated C–C bonds, etc., the post-synthesis strategy of COFs becomes an interesting subject to study. This strategy engineers the functionality of COFs allowing them to have superior properties compared to their origins. The post-synthesis approach could be followed simple chemical reactions, for example, esterification, imid-amide transformation, and addition, or by other advanced chemical reactions, such as click chemistry, tautomerization, protonated–deprotonated reaction, and so on (Liu et al. 2021). The following post-reaction of CuP-DMNDA-COF with iron(III) in acetone media to form Fe-coordinated CuP-DMNDA-COF (denoted as CuP-DMNDA-COF/Fe) revealed a high adsorption capacity toward rhodamine B (up to ~100%) compared to the CuP-DMNDA-COF which could not exceed 20% (Hou et al. 2017). A similar result was also reported by Yue and coworkers that embedded nickel and calcium ions on the carboxylic group of COF-COOH to form COF-COONi and COF-COOCa. The presence of those ions could significantly improve the adsorption capacity of COFs toward Congo red dyes (Yue et al. 2019). The key point of this approach is that the COFs should have a specific functional group acted as a molecular anchor point for further modifications.

5.3 Applications

Since their luxurious features, such as high surface area, ordered structure and porosity, high physical and chemical stability, high crystallinity, and providing active functional groups, COFs are widely employed in various applications, including energy storage, contamination treatments, catalysis, and drug delivery. Herewith, some examples of the recent and most outstanding results of COFs are reported by researchers.

5.3.1 Optoelectronic

Assemble of aromatic-based ligands to construct two-dimensional graphitic-like COFs delivers the advantage of framework diversity, molecular flexibility, structure tunability, physicochemical stability, π-π interaction behavior, and so forth, given an exhilarating prospect for optoelectronic application (Yang et al. 2018). Furthermore, the conductivity and optical properties (either in visible or NIR region) of several COFs allow them to serve various optoelectronic applications, such as sensors, photocatalysts, supercapacitors, and solar harvesting devices (Keller and Bein 2021). According to the COFs structural aspects, the electronic behavior is strongly affected by linker geometry, lattice symmetry, linkage motif, π-stacking, and self-assembled eclipsed alignment (H-aggregate) or shifted alignment (J-aggregate). Linker geometry and lattice symmetry control the COFs pore structure and size, respectively. Variety of geometry and lattice symmetry of linker molecules forms various pore shapes of two-dimensional COFs, such as hexagonal, tetragonal, rhombic, triangular, kagome as revealed in Fig. 9, resulting in different pore size and π-density.

In 2019, Thomas et al. investigated for the first time a relationship between chemical structure and lattice symmetry (trigonal and tetragonal nodes), related to the electronic properties by applying the DFT approach (Thomas et al. 2019a). The C_3 symmetry axes of a 2D benzene–ethylene COF gave an inherent property of kagome lattice which generally leads to an almost flat band around the Fermi level featuring the very high charge-carrier effective masses. This could be tracked from the characteristic of cycloproprenyl moieties representing triangular structure in kagome lattice. The four-arm core is more interesting to have large bandwidths. In this regard, zinc porphyrin and pyrene cores connected via diacetylene bridges represent high band dispersion at the Fermi level. In the same year, this group extends their study to specifically investigate the electronic structure of four-arm cores (pyrene, porphyrin, and Zn-porphyrin) connected with diacetylene linker generating Pyr-COF, Por-COF, and ZnPor-COF (Thomas et al. 2019b). The Pyr-COF, owing to their distorted square structure, has high band dispersion compared to other COFs which produces light hole and electron with stronger anisotropic characteristic.

5.3.2 Energy Storage

Nowadays, the utilization of porous materials for energy storage applications is massively reported. The COFs, as the chemically stable complemented by excellent textural properties, become a potential candidate to be applied in the energy storage field. A two-dimensional NT-COF reveals its capability to directly convert and store solar to electrochemical energy (Lv et al. 2018). This material used as cathode in solar Li-ion battery could reduce the charge voltage and increased discharge voltage, resulting in an extra 38.7% of battery efficiency. The high performance of converting and storing solar to electrochemical energy is due to a combination of naphthalene diimide (NDI) and triphenylamine (TPA) units enabling an ultrahigh efficient charge transfer and inducing a reversible electrochemical reaction. Another feature that makes COF a potential material for energy storage application is due to its graphitic-like structure promoting π-conjugation. It is showed through a study conducted by Bhaumik's group (Bhanja et al. 2017). The π-conjugation of graphitic-like triazine-linked COF (TDFP-1) presented an excellent energy storage ability proven by the high specific capacitance of 354 Fg^{-1} at a scan rate of 2 mV s^{-1} and good cycles stability (relatively constant about 95% of retention even after 1000 cycles at 10 A g^{-1}).

5.3.3 Environmental Protection

Owing to their porous structure and functional group diversity, the COFs have been utilized in environmental applications, such as a sensor for detecting contaminant or adsorbent for removing hazardous species. Bisphenol A (BPA) and bisphenol S (BPS) are known as toxic compounds that are widely used in the manufacturing industry. Detection of BPA and BPS in the water sample is highly recommended to avoid serious diseases to humans. Therefore, Pang's group developed CTpPa-2 COF-modified glassy carbon electrode to sensitively detect those molecules, having a low limit of detection (LoD) ranging from 0.02 to 0.09 μM and high recovery (87.0–92.2%) (Pang et al. 2020a, b). The use of EB-COF:Br on the adsorption of phosphorus (V) and arsenic (V) hazardous compounds in water samples was reported, having high adsorption capacity up to 35.3 mg g^{-1} and 53.1 mg g^{-1}, respectively (Yang et al. 2020a). Yang et al. also employed EB-COF:Br on the adsorption of the excess phosphorous acid at extremely acid conditions (pH = 0.86–0.65) with high maximum adsorption capacity ranging from 6520 to 6980 mg g^{-1} at 25–45 °C (Yang et al. 2020b). The sulfonated COF ($SO_3H@COF$) also showed satisfactory results toward adsorption of Cd^{2+}, Co^{2+}, and Cr^{3+} heavy metal ions, revealing high maximum adsorption capacity at 298 K of 81.97, 77.52, and 105.26 mg g^{-1}, respectively (Wang et al. 2020a, b).

5.3.4 Biomedicine

The high surface area, the presence of tailored-porous structure, chemically stable, and enriched-functional groups, as well as biocompatibility feature, increase the applicability of COFs in biomedical application, for example, drug delivery system (Scicluna and Vella-Zarb 2020). High pore volume and low density of COFs serve more room for storing a high dosage of drug molecules. Moreover, the tenability of their pore structure engineered either via pre or post-modification resulting in the customized COFs improves the efficiency of drug administration to the targeted cells (Machado et al. 2021). Those features also allow COFs to control the rate of diffusion and release of drugs which makes them a potential candidate as a drug carrier. Zhang et al. developed a smart and water-dispersible drug carrier-based PEG-curcumin/amine-modified COF-1 (PEG-CCM/APTES-COF-1) for targeted delivery of a highly toxic cancer chemo agent, doxorubicin (DOX) (Zhang et al. 2018a; b). The DOX-loaded PEG-CCM/APTES-COF-1 significantly reduced the tumor weight indicating apoptosis of cancer cells. A porphyrin-based nano-COF, COF-366 prepared via ultrasound method, also showed significant results on the in vivo study of photodynamic (PDT) and photo-thermal (PTT) cancer treatments (Wang et al. 2019). The study revealed unique properties of COF-366 which not only response to PDT but also PTT induced by a single wavelength (635 nm laser with a power of 200 mW cm^{-2}). Due to its conjugation system, the COF-366 is effectively capable to adsorb NIR and increase its performance to reduce the volume of tumor cells even with one-time injection.

6 Summary and Prospects

It has been demonstrated that ordered nanoporous materials possess unique structures and properties desired in diverse applications. Progress in zeolite science and technology is strongly dependent on developing the materials' structure, morphology, and properties. Since it was found in nature back in 1756 until the present time, the work in zeolites has greatly expanded, not only directly utilize the natural zeolites but also synthesize new zeolite structure to enhance its inherent properties such as porous, intracrystalline, thermal stability, acidity, and ion exchange capacity. Structure modifications are sometimes required, such as hierarchical and 2D layered structures, to improve their performances in various applications. This leads to the synthesis of zeolitic or zeotype materials. Zeolite has proven to be one of the frontiers in porous material synthesis and inspires the development of new materials such as mesoporous silica, mesoporous carbon, MOFs, and COFs. With recent advancements in computing such as data mining, machine learning, and increased usage in high-throughput screening, we are getting closer to understanding the complex relationship between zeolite synthesis, its outcome, and its energy landscape. In approaching rational synthesis, we should anticipate novel uses and modifications of zeolites and discover new branches of zeolites.

In preparing ordered mesoporous materials (silica, alumina, metal, and carbon), soft and hard templating are the most commonly utilized techniques. A more rational synthetic strategy should be pursued to realize desired ordered mesoporous materials with high accuracy and precision for their future development. An extensive collection of publications on ordered mesoporous materials should be revisited to draw a clear line of significant factors determining the formation of particular structures. Similar to zeolites, advanced computing methods could be applied to understand the complicated mechanism better and assist the discovery of many novel structures.

Metal–organic frameworks (MOFs) are of interest to researchers due to their exceptional chemical and physical properties, including highly tunable ultra-porosity and surface area and thermal, chemical, and mechanical stability. Being flexibly prepared via various synthesis methods, MOFs have received significant attention for their application in a wide range of fields such as catalysis, drug delivery, gas storage, and sensors. While facing several aspects such as environmental issues, the materials are developing progressively, and in the future, it is expected that a more advanced strategy will lead to the large-scale green fabrication of MOFs.

Design synthesis of high-quality COFs becomes a challenge among researchers. A combination of various monomers and linkers produced a variety of COFs structures with dynamic properties. To date, the common linkages that still play an essential role in the design and development of COFs are boric acid, imines-, azides- and C=C based linkages that resulted in a diversity of COFs summarized in Table 3. Additionally, the sound properties, high crystallinity, and yield of MOFs are also strongly affected by synthesis methods, including energy sources, catalysts, solvents, and crystallization activation. Although the solvothermal method shows advantages in producing high yield and crystalline COFs, this method lacks an environmental-friendly aspect. Therefore, sustainable chemistry on the synthesis of green COF is still developed. The high-quality COFs remarkably have high BET surface area, tailored-porous structure, and unique structure and functionalities, making them versatile porous material for various purposes, from energy to biomedical application.

References

Ahmed, A., Matzger, A.J., Seth, S., Purewal, J., Wong-foy, A.G., Veenstra, M., Siegel, D.J.: Exceptional hydrogen storage achieved by screening nearly half a million metal-organic frameworks. Nat. Commun. **10**(1568), 1–9 (2019)

Akporiaye, D.E., Dahl, I.M., Karlsson, A., Wendelbo, R.: Combinatorial approach to the hydrothermal synthesis of zeolites. Angew. Chem. Int. Ed. **37**(5), 609–611 (1998). https://doi.org/10.1002/(SICI)1521-3773(19980316)37:5%3c609::AID-ANIE609%3e3.0.CO;2-X

Aljishi, A., Veilleux, G., Lalinde, J.A.H., Kopyscinski, J.: The effect of synthesis parameters on ordered mesoporous nickel alumina catalyst for CO_2 methanation. Appl. Catal. A Gen. **549**, 263–272 (2018). https://doi.org/10.1016/j.apcata.2017.10.012

Appaturi, J.N., Ramalingam, R.J., Al-Lohedan, H.A., Khoerunnisa, F., Ling, T.C., Ng, E.P.: Selective synthesis of dioxolane biofuel additive via acetalization of glycerol and furfural enhanced by MCM-41-alanine bifunctional catalyst. Fuel **288**, 119573 (2021). https://doi.org/10.1016/j.fuel.2020.119573

Attard, G.S., Corker, J.M., Göltner, C.G., Henke, S., Templer, R.H.: Liquid-crystal templates for nanostructured metals. Angew. Chem. Int. Ed. English **36**, 1315–1317 (1997). https://doi.org/10.1002/anie.199713151

Baca, M., de la Rochefoucauld, E., Ambroise, E., Krafft, J.M., Hajjar, R., Man, P.P., Carrier, X., Blanchard, J.: Characterization of mesoporous alumina prepared by surface alumination of SBA-15. Microporous Mesoporous Mater. **110**, 232–241 (2008). https://doi.org/10.1016/j.micromeso.2007.06.010

Baerlocher, C., McCusker, L.: Database of zeolite structures. http://www.iza-structure.org/databases/ (2017). Accessed 22 Apr 2021

Bagshaw, S.A., Prouzet, E., Pinnavaia, T.J.: Templating of mesoporous molecular sieves by nonionic polyethylene oxide surfactants. Science **269**, 1242–1244 (1995). https://doi.org/10.1126/science.269.5228.1242

Beck, J.S., Vartuli, J.C., Roth, W.J., Leonowicz, M.E., Kresge, C.T., Schmitt, K.D., Chu, C.T.W., Olson, D.H., Sheppard, E.W., McCullen, S.B., Higgins, J.B., Schlenker, J.L.: A new family of mesoporous molecular sieves prepared with liquid crystal templates. J. Am. Chem. Soc. **114**, 10834–10843 (1992). https://doi.org/10.1021/ja00053a020

Bertrand, G.H.V., Michaelis, V.K., Ong, T.C., Griffin, R.G., Dincâ, M.: Thiophene-based covalent organic frameworks. Proc. Natl. Acad. Sci. USA **110**, 4923–4928 (2013). https://doi.org/10.1073/pnas.1221824110

Beznis, N.V., Van Laak, A.N.C., Weckhuysen, B.M., Bitter, J.H.: Oxidation of methane to methanol and formaldehyde over Co-ZSM-5 molecular sieves: tuning the reactivity and selectivity by alkaline and acid treatments of the zeolite ZSM-5 agglomerates. Microporous Mesoporous Mater. **138**(1–3), 176–183 (2011). https://doi.org/10.1016/j.micromeso.2010.09.009

Bhanja, P., Bhunia, K., Das, S.K., Pradhan, D., Kimura, R., Hijikata, Y., Irle, S., Bhaumik, A.: A new triazine-based covalent organic framework for high-performance capacitive energy storage. Chemsuschem **10**, 921–929 (2017). https://doi.org/10.1002/cssc.201601571

Biswal, B.P., Biswal, B.P., Chandra, S., Chandra, S., Kandambeth, S., Kandambeth, S., Lukose, B., Lukose, B., Heine, T., Heine, T., Banerjee, R., Banerjee, R.: Mechanochemical synthesis of chemically stable isoreticular covalent organic frameworks. J. Am. Chem. Soc. **135**, 5328–5331 (2013). http://pubs.acs.org/doi/abs/10.1021/ja4017842%5Cn

Bosch, M., Zhang, M., Zhou, H.C.: Increasing the stabiilty of metal-organic frameworks. Adv. Chem. Ser. **2014**, 182327 (2014)

Bosch, M., Sun, X., Yuan, S., Chen, Y.P., Wang, Q., Wang, X., Zhou, H.C.: Modulated synthesis of metal-organic frameworks through tuning of the initial oxidation state of the metal. Eur. J. Inorg. Chem. **27**, 4368–4372 (2016)

Cabrera, S., El Haskouri, J., Alamo, J., Beltrán, A., Beltrán, D., Mendioroz, S., Marcos, M.D., Amorós, P.: Surfactant-assisted synthesis of mesoporous alumina showing continuously adjustable pore sizes. Adv. Mater. **11**, 379–381 (1999). https://doi.org/10.1002/(SICI)1521-4095(199903)11:5%3c379::AID-ADMA379%3e3.0.CO;2-6

Campbell, N.L., Clowes, R., Ritchie, L.K., Cooper, A.I.: Rapid microwave synthesis and purification of porous covalent organic frameworks. Chem. Mater. **21**, 204–206 (2009). https://doi.org/10.1021/cm802981m

Cavka, J.H., Jakobsen, S., Olsbye, U., Guillou, N., Lamberti, C., Bordiga, S., Lillerud, K.P.: A new zirconium inorganic building brick forming metal organic frameworks with exceptional stability. J. Am. Chem. Soc. **130**(42), 13850–13851 (2008)

Che, Q., Yang, M., Wang, X., Yang, Q., Chen, Y., Chen, X., Xhen, W., Hu, J., Zeng, K., Yang, H., Chen, H.: Preparation of mesoporous ZSM-5 catalysts using green templates and their performance in biomass catalytic pyrolysis. Bioresour. Technol. **289**, 121729 (2019). https://doi.org/10.1016/j.biortech.2019.121729

Chen, H., Wang, M., Yang, M., Shang, W., Yang, C., Liu, B., Hao, Q., Zhang, J., Ma, X.: Organosilane surfactant-directed synthesis of nanosheet-assembled SAPO-34 zeolites with improved MTO catalytic performance. J. Mater. Sci. **54**(11), 8202–8215 (2019). https://doi.org/10.1007/s10853-019-03485-w

Chen, X., Qiao, Z., Hou, B., Jiang, H., Gong, W., Dong, J., Li, H.Y., Cui, Y.: Chiral metal-organic frameworks with tunable catalytic selectivity in asymmetric transfer hydrogenation reactions. Nano Res. **14**, 466–472 (2021)

Choi, M., Na, K., Kim, J., Sakamoto, Y., Terasaki, O., Ryoo, R.: Erratum: stable single-unit-cell nanosheets of zeolite MFI as active and long-lived catalysts. Nature **461**(7265), 828–828 (2009). https://doi.org/10.1038/nature08493

Christensen, C.H., Johannsen, K., Törnqvist, E., Schmidt, I., Topsøe, H., Christensen, C.H.: Mesoporous zeolite single crystal catalysts: diffusion and catalysis in hierarchical zeolites. Catal. Today **128**(3–4), 117–122 (2007). https://doi.org/10.1016/j.cattod.2007.06.082

Chui, S.S.Y., Lo, S.M.F., Charmant, J.P.H., Orpen, A.G., Williams, I.D.: A chemically functionalizable nanoporous material [Cu$_3$(TMA)$_2$(H$_2$O)$_3$]N. Science **283**, 1148–1150 (1999)

Coombs, D.S., Alberti, A., Armbruster, T., Artioli, G., Colella, C., Galli, E., Grice, J.D., Liebau, F., Mandarino, J.A., Minato, H., Nickel, E.H., Passaglia, E., Peacor, D.R., Quartieri, S., Rinaldi, R., Ross, M., Sheppard, R.A., Tillmanns, E., Vezzalini, G.: Recommended nomenclature for zeolite minerals: report of the subcommittee on zeolites of the International Mineralogical Association, Commission on new Minerals and Mineral names. Canad. Mineral. **35**(6), 1571–1606 (1997)

Corma, A., Moliner, M., Serra, J.M., Serna, P., Díaz-Cabañas, M.J., Baumes, L.A.: A new mapping/exploration approach for HT synthesis of zeolites. Chem. Mater. **18**(14), 3287–3296 (2006). https://doi.org/10.1021/cm060620k

Côté, A.P., Benin, A.I., Ockwig, N.W., O'Keeffe, M., Matzger, A.J., Yaghi, O.M.: Porous, crystalline, covalent organic frameworks. Science (80-.) **310**, 1166–1171 (2005)

Côté, A.P., El-Kaderi, H.M., Furukawa, H., Hunt, J.R., Yaghi, O.M.: Reticular synthesis of microporous and mesoporous 2D covalent organic frameworks. J. Am. Chem. Soc. **129**, 12914–12915 (2007). https://doi.org/10.1021/ja0751781

Dai, L., Huang, K., Xia, Y., Xu, Z.: Two-dimensional material separation membranes for renewable energy purification, storage, and conversion. Green Energy Environ. (2021). https://doi.org/10.1016/j.gee.2020.09.015

Dang, Y.T., Hoang, H.T., Dong, H.C., Bui, K.B.T., Nguyen, L.H.T., Phan, T.B., Kawazoe, Y., Doan, T.L.H.: Microwave-assisted synthesis of nano Hf- and Zr-based metal-organic frameworks for enhancement of curcumin adsorption. Microporous Mesoporous Mater. **298**, 110064 (2020)

Das, G., Balaji Shinde, D., Kandambeth, S., Biswal, B.P., Banerjee, R.: Mechanosynthesis of imine, β-ketoenamine, and hydrogen-bonded imine-linked covalent organic frameworks using liquid-assisted grinding. Chem. Commun. **50**, 12615–12618 (2014). https://doi.org/10.1039/c4cc03389b

Ding, S.Y., Wang, W.: Covalent organic frameworks (COFs): from design to applications. Chem. Soc. Rev. **42**, 548–568 (2013). https://doi.org/10.1039/c2cs35072f

Ding, M., Cai, X., Jiang, H.L.: Improving MOF stability: approaches and applications. Chem. Sci. **10**, 10209–10230 (2019a)

Ding, M., Flaig, R.W., Jiang, H.L., Yaghi, O.M.: Carbon capture and conversion using metal-organic frameworks and MOF-based materials. Chem. Soc. Rev. **48**(10), 2783–2828 (2019b)

Dogru, M., Handloser, M., Auras, F., Kunz, T., Medina, D., Hartschuh, A., Knochel, P., Bein, T.: A photoconductive thienothiophene-based covalent organic framework showing charge transfer towards included fullerene. Angew. Chem. **125**, 2992–2996 (2013a). https://doi.org/10.1002/ange.201208514

Dogru, M., Sonnauer, A., Zimdars, S., Doblinger, M., Knichel, P., Bein, T.: Facile synthesis of a mesoporous benzothiadiazole-COF based on a transesterification process. Cryst. Eng. Commun. **15**, 1500–1502 (2013b). https://doi.org/10.1039/b000000x

Dugkhuntod, P., Wattanakit, C.: A comprehensive review of the applications of hierarchical zeolite nanosheets and nanoparticle assemblies in light olefin production. Catalysts **10**(2), 245 (2020). https://doi.org/10.3390/catal10020245

Dugkhuntod, P., Imyen, T., Wannapakdee, W., Yutthalekha, T., Salakhum, S., Wattanakit, C.: Synthesis of hierarchical ZSM-12 nanolayers for levulinic acid esterification with ethanol to ethyl levulinate. RSC Adv. **9**(32), 8087–18097 (2019). https://doi.org/10.1039/c9ra03213d

Durbin, D.J., Malardier-Jugroot, C.: Review of hydrogen storage techniques for on board vehicle applications. Int. J. Hydrog. Energy **38**(34), 14595–14617 (2013)

Eddaoudi, M., Kim, J., Rosi, N., Vodak, D., Wachter, J., O'Keeffe, M., Yaghi, O.M.: Systematic design of pore size and functionality in isoreticular MOFs and their application in methane storage. Science **295**, 469–472 (2002)

Eliášová, P., Cejka, J.: Two-dimensional Zeolites. In: Čejka, J., Morris, R.E., Nachtigall, P. (eds.) Zeolites in catalysis: properties and applications, pp. 146–193. Royal Society of Chemistry, Cambridge (2017)

Farha, O.K., Hupp, J.T.: Activation of metal-organic framework materials. Cryst. Eng. Commun. **15**, 9258–9264 (2010). https://doi.org/10.1039/C3CE41232F

Farha, O.K., Eryazici, I., Jeong, N.C., Hauser, B.G., Wilmer, C.E., Sarjeant, A.A., Snurr, R.Q., Nguyen, S.T., Yazaydin, A.O., Hupp, J.T.: Metal-organic frameworks materials with ultrahigh surface areas: is the sky the limit? J. Am. Chem. Soc. **134**(36), 15016–15021 (2012)

Feng, X., Liu, L., Honsho, Y., Saeki, A., Seki, S., Irle, S., Dong, Y., Nagai, A., Jiang, D.: High-rate charge-carrier transport in porphyrin covalent organic frameworks: switching from hole to electron to ambipolar conduction. Angew. Chem. **124**, 2672–2676 (2012). https://doi.org/10.1002/ange.201106203

Ferdov, S.: FAU-type zeolite nanosheets from additives-free system. Microporous Mesoporous Mater. **242**, 59–62 (2017). https://doi.org/10.1016/j.micromeso.2017.01.018

Férey, G., Serre, C., Mellot-Draznieks, C., Millange, F., Surble, S., Dutour, J., Margiolaki, I.: A hybrid solid with giant pores prepared by a combination of targeted chemistry, simulation, and powder diffraction. Angew. Chem. Int. Ed. **43**(46), 6296–6301 (2004)

Firmansyah, M.L., Jalil, A.A., Triwahyono, S., Hamdan, H., Salleh, M.M., Ahmad, W.F.W., Kadja, G.T.M.: Synthesis and characterization of fibrous silica ZSM-5 for cumene hydrocracking. Catal. Sci. Technol. **6**(13), 5178–5182 (2016). https://doi.org/10.1039/c6cy00106h

Flanigen, E.M.: Zeolites and molecular sieves: an historical perspective. Stud. Surf. Sci. Catal. **137**, 11–35 (2001). https://doi.org/10.1016/s0167-2991(01)80243-3

Fuentes, C., Ruiz-Rico, M., Fuentes, A., Barat, J.M., Ruiz, M.J.: Comparative cytotoxic study of silica materials functionalised with essential oil components in HepG2 cells. Food Chem. Toxicol. **147**, 111858 (2021). https://doi.org/10.1016/j.fct.2020.111858

Fulvio, P.F., Brosey, R.I., Jaroniec, M.: Synthesis of mesoporous alumina from boehmite in the presence of triblock copolymer. ACS Appl. Mater. Interfaces **2**, 588–593 (2010). https://doi.org/10.1021/am9009023

Furukawa, H., Cordova, K.E., O'Keeffe, M., Yaghi, O.M.: The chemistry and applications of metal-organic frameworks. Science **341**, 974–986 (2013)

Gai, H., Liu, X., Feng, B., Gai, C., Huang, T., Xiao, M., Song, H.: An alternative scheme of biological removal of ammonia nitrogen from wastewater–highly dispersed Ru cluster @mesoporous TiO_2 for the catalytic wet air oxidation of low-concentration ammonia. Chem. Eng. J. **407**, 127082 (2021). https://doi.org/10.1016/j.cej.2020.127082

García-valdivia, A.A., Pérez-yáñez, S., García, J.A., Fernández, B., Cepeda, J., Rodríguez-diéguez, A.: Magnetic and photoluminescent sensors based on metal-organic frameworks built up from 2-Aminoisonicotinate. Sci. Rep. **10**, 8843 (2020)

Geng, K., He, T., Liu, R., Dalapati, S., Tan, K.T., Li, Z., Tao, S., Gong, Y., Jiang, Q., Jiang, D.: Covalent organic frameworks: design, synthesis, and functions. Chem. Rev. **120**, 8814–8933 (2020). https://doi.org/10.1021/acs.chemrev.9b00550

Gérardin, C., Reboul, J., Bonne, M., Lebeau, B.: Ecodesign of ordered mesoporous silica materials. Chem. Soc. Rev. **42**, 4217–4255 (2013). https://doi.org/10.1039/c3cs35451b

Gholizadeh, F., Izadbakhsh, A., Huang, J., Zi-Feng, Y.: Catalytic performance of cubic ordered mesoporous alumina supported nickel catalysts in dry reforming of methane. Microporous Mesoporous Mater. **310**, 110616 (2021). https://doi.org/10.1016/j.micromeso.2020.110616

Gong, T., Li, Y., Zhang, H., Zhou, J., Xie, G., Lei, B., Zhuang, J., Liu, Y., Zhang, H.: Synthesis of SBA-15 assembled with silicon nanoparticles with different morphologies for oxygen sensing. Microporous Mesoporous Mater. **296**, 110001 (2020). https://doi.org/10.1016/j.micromeso.2020.110001

González-Peña, V., Díaz, I., Márquez-Alvarez, C., Sastre, E., Pérez-Pariente, J.: Thermally stable mesoporous alumina synthesized with non-ionic surfactants in the presence of amines. Microporous Mesoporous Mater. **44–45**, 203–210 (2001). https://doi.org/10.1016/S1387-1811(01)00185-8

González-Peña, V., Márquez-Alvarez, C., Díaz, I., Grande, M., Blasco, T., Pérez-Pariente, J.: Sol–gel synthesis of mesostructured aluminas from chemically modified aluminum sec-butoxide using non-ionic surfactant templating. Microporous Mesoporous Mater. **80**, 173–182 (2005). https://doi.org/10.1016/j.micromeso.2004.12.011

Guan, X., Ma, Y., Li, H., Yusran, Y., Xue, M., Fang, Q., Yan, Y., Valtchev, V., Qiu, S.: Fast, ambient temperature and pressure ionothermal synthesis of three-dimensional covalent organic frameworks. J. Am. Chem. Soc. **140**, 4494–4498 (2018). https://doi.org/10.1021/jacs.8b01320

Halawy, S.A., Osman, A.I., Abdelkader, A., Yang, H.: Boosting NiO catalytic activity by x wt% F-ions and K2O for the production of methyl ethyl ketone (MEK) via catalytic dehydrogenation of 2-butanol. Chem. Cat. Chem. **13**, 1–15 (2021). https://doi.org/10.1002/cctc.202001954

Han, Y., Yang, H., Guo, X.: Synthesis methods and crystallization of MOFs. In: Marzouki, R. (ed.) Synthesis Methods and Crystallization. IntechOpen, London (2020)

Han, Y.J., Wang, S., Liu, H., Shi, L., Song, J.Y., Huang, Y.H., Ji, Z.X., Lu, X.L., Shen, S.B., Zhang, Z.W., Song, A.J.: BiOBr@SBA-15 system as a novel photocatalyst with high photocatalytic performance. Mater. Lett. **278**, 128462 (2020b). https://doi.org/10.1016/j.matlet.2020.128462

Han, H., Wang, X., Zhang, X.: A hierarchically ordered porous nitrogen-doped carbon catalyst with densely accessible Co-Nx active sites for efficient oxygen reduction reaction. Microporous Mesoporous Mater. **317**, 111002 (2021a). https://doi.org/10.1016/j.micromeso.2021.111002

Han, W., Li, C., Jiang, Y., Ma, Z., Zhang, Y., Yan, X., Zheng, X.: Atomically-dispersed Fe-Nx and C-S-C ordered mesoporous carbons as efficient catalysts for the oxygen reduction reaction in a microbial fuel cell. J. Alloys Compd. **852**, 156994 (2021b). https://doi.org/10.1016/j.jallcom.2020.156994

Hangxun, X., Zeiger, B.W., Suslick, K.S.: Sonochemical synthesis of nanomaterials. Chem. Soc. Rev. **42**, 2555–2567 (2013). https://doi.org/10.1039/c2cs35282f

Hartmann, M., Kevan, L.: Substitution of transition metal ions into aluminophosphates and silicoaluminophosphates: Characterization and relation to catalysis. Res. Chem. Intermed. **28**(7–9), 625–695 (2002). https://doi.org/10.1163/15685670260469357

Hartmann, M., Machoke, A.G., Schwieger, W.: Catalytic test reactions for the evaluation of hierarchical zeolites. Chem. Soc. Rev. **45**(12), 3313–3330 (2016). https://doi.org/10.1039/c5cs00935a

Hassan, T.N.A.T., Jusoh, N., Yeong, Y.F.: Synthesis and characterization of PEBAX 1657 and hierarchical Linde Type-T (h-LTT) zeolite for the fabrication of hybrid membranes. Mater. Today Proc. (2021). https://doi.org/10.1016/j.matpr.2021.02.792

Healy, C., Patil, K.M., Wilson, B.H., Hermanspahn, L., Harvey-reid, N.C., Howard, B.I., Kleinjan, C., Kolien, J., Payet, F., Telfer, S.G., Kruger, P.E., Bennett, T.D.: The thermal stability of metal-organic frameworks. Coord. Chem. Rev. **419**, 213388 (2020)

Horcajada, P., Serre, C., Vallet-Regí, M., Sebban, M., Taulelle, F., Férey, G.: Metal-organic frameworks as efficient materials for drug delivery. Angew. Chem. Int. Ed. **45**(36), 5974–5978 (2006)

Hoskins, B.F., Robson, R.: Infinite polymeric frameworks consisting of three dimensionally linked rod-like segments. J. Am. Chem. Soc. **111**, 5962–5964 (1989)

Hou, Y., Zhang, X., Wang, C., Qi, D., Gu, Y., Wang, Z., Jiang, J.: Novel imine-linked porphyrin covalent organic frameworks with good adsorption removing properties of RhB. New J. Chem. **41**, 6145–6151 (2017). https://doi.org/10.1039/c7nj00424a

Huang, N., Wang, P., Jiang, D.: Covalent organic frameworks: a materials platform for structural and functional designs. Nat. Rev. Mater. **1**, 1–19 (2016). https://doi.org/10.1038/natrevmats.2016.68

Hunt, J.R., Doonan, C.J., LeVangie, J.D., Côté, A.P., Yaghi, O.M.: Reticular synthesis of covalent organic borosilicate frameworks. J. Am. Chem. Soc. **130**, 11872–11873 (2008). https://doi.org/10.1021/ja805064f

Inayat, A., Knoke, I., Spiecker, E., Schwieger, W.: Assemblies of mesoporous FAU-type zeolite nanosheets. Angew. Chem. Int. Ed. **51**(8), 1962–1965 (2012). https://doi.org/10.1002/anie.201105738

Jensen, Z., Kim, E., Kwon, S., Gani, T.Z.H., Román-Leshkov, Y., Moliner, M., Corma Am Olivetti, E.: A machine learning approach to zeolite synthesis enabled by automatic literature data extraction. ACS Cent. Sci. **5**(5), 892–899 (2019). https://doi.org/10.1021/acscentsci.9b00193

Jensen, Z., Kwon, S., Schwalbe-Koda, D., Paris, C., Gómez-Bombarelli, R., Román-Leshkov, Y., Corma, A., Moliner, M., Olivetti, E.A.: Discovering relationships between OSDAs and zeolites through data mining and generative neural networks. ACS Cent. Sci. (2021). https://doi.org/10.1021/acscentsci.1c00024

Jeong, S., Yang, S., Kim, D.H.: Depolymerization of protobind lignin to produce monoaromatic compounds over Cu/ZSM-5 catalyst in supercritical ethanol. Mol. Catal. **442**, 140–146 (2017). https://doi.org/10.1016/j.mcat.2017.09.010

Ji, W., Guo, Y.S., Xie, H.M., Wang, X., Jiang, X., Guo, D.S.: Rapid microwave synthesis of dioxin-linked covalent organic framework for efficient micro-extraction of perfluorinated alkyl substances from water. J. Hazard Mater. **397**, 122793 (2020). https://doi.org/10.1016/j.jhazmat.2020.122793

Jia, X., Khan, W., Wu, Z., Choi, J., Yip, A.C.K.: Modern synthesis strategies for hierarchical zeolites: bottom-up versus top-down strategies. Adv. Powder Technol. **30**(3), 467–484 (2019). https://doi.org/10.1016/j.apt.2018.12.014

Jiang, J., Yaghi, O.M.: Brønsted acidity in metal-organic frameworks. Chem. Rev. **115**(14), 6966–6997 (2015)

Jiang, J., Gándara, F., Zhang, Y.B., Na, K., Yaghi, O.M., Klemperer, W.G.: Superacidity in sulfated metal–organic framework-808. J. Am. Chem. Soc. **136**(37), 12844–12847 (2014)

Kadja, G.T.M., Ilmi, M.M.: Indonesia natural mineral for heavy metal adsorption: a review. J. Environ. Sci. Sustain. Dev. **2**(2) (2019). https://doi.org/10.7454/jessd.v2i2.1033

Kadja, G.T.M., Mukti, R.R., Marsih, I.N., Ismunandar: A comparative study of the synthesis of MFI zeolite by using high- and low-temperature heating. Adv. Mater. Res. **1112**, 201–204 (2015). https://doi.org/10.4028/www.scientific.net/amr.1112.201

Kadja, G.T.M., Fabiani, V.A., Aziz, M.H., Fajar, A.T.N., Prasetyo, A., Suendo, V., Ng, E.P., Mukti, R.R.: The effect of structural properties of natural silica precursors in the mesoporogen-free synthesis of hierarchical ZSM-5 below 100 °C. Adv. Powder Technol. **28**(2), 443–452 (2017). https://doi.org/10.1016/j.apt.2016.10.017

Kadja, G.T.M., Kadir, I.R., Fajar, A.T.N., Suendo, V., Mukti, R.R.: Revisiting the seed-assisted synthesis of zeolites without organic structure-directing agents: Insights from the CHA case. RSC Adv. **10**(9), 5304–5315 (2020a). https://doi.org/10.1039/c9ra10825d

Kadja, G.T.M., Suprianti, T.R., Ilmi, M.M., Khalil, M., Mukti, R.R., Subagjo: Sequential mechanochemical and recrystallization methods for synthesizing hierarchically porous ZSM-5 zeolites. Microporous Mesoporous Mater. **308**(10), 110550 (2020). https://doi.org/10.1016/j.micromeso.2020.110550

Kadja, G.T.M., Azhari, N.J., Mukti, R.R., Khalil, M.: A mechanistic investigation of sustainable solvent-free, seed-directed synthesis of ZSM-5 zeolites in the absence of an organic structure-directing agent. ACS Omega **6**(1), 925–933 (2021a). https://doi.org/10.1021/acsomega.0c05070

Kadja, G.T.M., Rukmana, M.D., Mukti, R.R., Mahyuddin, M.H., Saputro, A.G., Wungu, T.D.K.: Solvent-free, small organic lactam-assisted synthesis of ZSM-5 zeolites. Mater. Lett. **290**, 129501 (2021b). https://doi.org/10.1016/j.matlet.2021.129501

Kanan, S.M., Malkawi, A.: Recent advances in nanocomposite luminescent metal-organic frameworks sensors for detecting metal ions. Comments Inorg. Chem. **41**(1), 1–66 (2021)

Kapustin, E.A., Lee, S., Alshamari, A.S., Yaghi, O.M.: Molecular retrofitting adapts a metal-organic framework to extreme pressure. ACS Cent. Sci. **3**(6), 662–667 (2017)

Karak, S., Kandambeth, S., Biswal, B.P., Sasmal, H.S., Kumar, S., Pachfule, P., Banerjee, R.: Constructing ultraporous covalent organic frameworks in seconds via an organic terracotta process. J. Am. Chem. Soc. **139**, 1856–1862 (2017). https://doi.org/10.1021/jacs.6b08815

Keller, N., Bein, T.: Optoelectronic processes in covalent organic frameworks. Chem. Soc. Rev. **50**, 1813–1845 (2021). https://doi.org/10.1039/d0cs00793e

Kim, S., Choi, H.C.: Light-promoted synthesis of highly-conjugated crystalline covalent organic framework. Commun. Chem. **2**, 1–8 (2019). https://doi.org/10.1038/s42004-019-0162-z

Kim, J., Choi, M., Ryoo, R.: Effect of mesoporosity against the deactivation of MFI zeolite catalyst during the methanol-to-hydrocarbon conversion process. J. Catal. **269**(1), 219–228 (2010). https://doi.org/10.1016/j.jcat.2009.11.009

Kim, M.Y., Kim, J.K., Lee, M.E., Lee, S., Choi, M.: Maximizing biojet fuel production from triglyceride: importance of the hydrocracking catalyst and separate deoxygenation/hydrocracking steps. ACS Catal. **7**(9), 6256–6267 (2017a). https://doi.org/10.1021/acscatal.7b01326

Kim, S., Park, C., Lee, M., Song, I., Kim, J., Lee, M., Jung, J., Kim, Y., Lim, H., Choi, H.C.: Rapid photochemical synthesis of sea-urchin-shaped hierarchical porous COF-5 and its lithography-free patterned growth. Adv. Funct. Mater. **27**, 1–8 (2017b). https://doi.org/10.1002/adfm.201700925

Klerk, A.: Zeolites as catalysts for fuels refining after indirect liquefaction processes. Molecules **23**(1), 115 (2018). https://doi.org/10.3390/molecules23010115

Koo, W.T., Jang, J.S., Kim, I.D.: Metal-organic frameworks for chemiresistive sensors. Chem **5**, 1938–1963 (2019)

Kresge, C.T., Leonowicz, M.E., Roth, W.J., Vartuli, J.C., Beck, J.S.: Ordered mesoporous molecular sieves synthesized by a liquid-crystal template mechanism. Nature **359**, 710–712 (1992). https://doi.org/10.1038/359710a0

Krisnandi, Y.K., Putra, B.A.P., Bahtiar, M., Zahara, A.I., Howe, R.F.: Partial oxidation of methane to methanol over heterogeneous catalyst Co/ZSM-5. Procedia Chem. **14**, 508–515 (2015). https://doi.org/10.1016/j.proche.2015.03.068

Krisnandi, Y.K., Saragi, I.R., Sihombing, R., Ekananda, R., Sari, I.P., Griffith, B.E., Hanna, J.V.: Synthesis and characterization of crystalline NaY-zeolite from Belitung kaolin as catalyst for n-hexadecane cracking. Curr. Comput.-Aided Drug Des. **9**(8), 404 (2019a). https://doi.org/10.3390/cryst9080404

Krisnandi, Y.K., Nurani, D.A., Agnes, A., Pertiwi, R., Antra, N.F., Anggraeni, A.R., Azaria, A.P., Howe, R.F.: Hierarchical MnOx/ZSM-5 as heterogeneous catalysts in conversion of delignified rice husk to levulinic acid. Indones. J. Chem. **19**(1), 115–123 (2019). https://doi.org/10.22146/ijc.28332

Kruk, M., Jaroniec, M., Ko, C.H., Ryoo, R.: Characterization of the porous structure of SBA-15. Chem. Mater. **12**, 1961–1968 (2000). https://doi.org/10.1021/cm000164e

Kuhn, P., Antonietti, M., Thomas, A.: Porous, covalent triazine-based frameworks prepared by ionothermal synthesis. Angew. Chem. Int. Ed. **47**, 3450–3453 (2008). https://doi.org/10.1002/anie.200705710

Kurniawati, M., Azhari, N.J., Kadja, G.T.M., Mukti, R.R., Notodarmojo, S.: Conversion of coal fly ash into advanced crystalline materials. IOP Conf. Ser.: Earth Environ. Sci. **623**(1), 012040 (2021). https://doi.org/10.1088/1755-1315/623/1/012040

Lee, Y.R., Kim, J., Ahn, W.S.: Synthesis of metal-organic frameworks: a mini review. Korean J. Chem. Eng. **30**(9), 1667–1680 (2013)

Lee, E.J., Bae, J.H., Choi, K.M., Jeong, N.C.: Exploiting microwave chemistry for activation of metal–organic frameworks. ACS Appl. Mater. Interfaces **11**, 35155–35161 (2019)

Lestari, W.W., Arvinawati, M., Martien, R., Kusumaningsih, T.: Green and facile synthesis of MOF and nano MOF containing zinc(II) and benzene-1,3,5-tricarboxylate and its study in ibuprofen slow-release. Mater. Chem. Phys. **204**, 141–146 (2018)

Lestari, W.W., TE Irwinsyah, S., Krisnandi, Y.K., Arrozi, U.S.F., Heraldy, E., Kadja, G.T.M.: Composite material consisting of HKUST-1 and Indonesian activated natural zeolite and its application in CO_2 capture. Open Chem. **17**(1), 1279–1287 (2020). https://doi.org/10.1515/chem-2019-0136

Lestari, W.W., Yunita, L., Saraswati, T.E., Heraldy, E., Khafidhin, M.A., Krisnandi, Y.K., Arrozi, U.S.F., Kadja, G.T.M.: Fabrication of composite materials MIL-100(Fe)/Indonesian activated natural zeolite as enhanced CO_2 capture material. Chem Pap 100 (2021). https://doi.org/10.1007/s11696-021-01558-2

Lestari, W.W., Khafidhin, M.A., Wijiyanti, R., Widiastuti, N., Handayani, D.S., Arrozi, U.S.F., Kadja, G.T.M.: Novel mixed matrix membranes based on polyethersulfone and MIL-96 (Al) for CO_2 gas separation. Chem. Pap. **96**(0123456789) (2021). https://doi.org/10.1007/s11696-021-01562-6

Li, H., Eddaoudi, M., O'Keeffe, M., Yaghi, O.M.: Design and synthesis of an exceptionally stable and highly porous metal-organic framework. Nature **402**, 276–279 (1999)

Li, H., Wang, K., Sun, Y., Lollar, C.T., Li, J., Zhou, H.C.: Recent advances in gas storage and separation using metal-organic frameworks. Mater. Today **21**(2), 108–121 (2017)

Li, S., Li, J., Dong, M., Fan, S., Zhao, T., Wang, J., Fan, W.: Strategies to control zeolite particle morphology. Chem. Soc. Rev. **48**(3), 885–907 (2019). https://doi.org/10.1039/c8cs00774h

Li, H.Y., Zhao, S.N., Zang, S.Q., Li, J.: Functional metal–organic frameworks as effective sensors of gases and volatile compounds. Chem. Soc. Rev. **49**, 6364–6401 (2020)

Li, Z.K., Wang, H.T., Yan, H.L., Yan, J.C., Lei, Z.P., Ren, S.B., Wang, Z.C., Kang, S.G., Shui, H.F.: Catalytic ethanolysis of Xilinguole lignite over layered and mesoporous metal oxide composites to platform chemicals. Fuel **287**, 119560 (2021a). https://doi.org/10.1016/j.fuel.2020.119560

Li, Y., Guo, Y., Yang, S., Li, Q., Chen, S., Lu, B., Zou, H., Liu, X., Tong, X., Yang, H.: mesoporous RhRu nanosponges with enhanced water dissociation toward efficient alkaline hydrogen evolution. ACS Appl. Mater. Interfaces **13**, 5052–5060 (2021b). https://doi.org/10.1021/acsami.0c19571

Li, Y., Chen, W., Xing, G., Jiang, D., Chen, L.: New synthetic strategies toward covalent organic frameworks. Chem. Soc. Rev. **49**, 2852–2868 (2021). https://doi.org/10.1039/d0cs00199f

Liang, C., Hong, K., Guiochon, G.A., Mays, J.W., Dai, S.: Synthesis of a large-scale highly ordered porous carbon film by self-assembly of block copolymers. Angew. Chem. Int. Ed. **43**, 5785–5789 (2004). https://doi.org/10.1002/anie.200461051

Liang, C., Li, Z., Dai, S.: Mesoporous carbon materials: synthesis and modification. Angew. Chem. Int. Ed. **47**, 3696–3717 (2008). https://doi.org/10.1002/anie.200702046

Lin, R.B., Shengchang, X., Wei, Z., Banglin, C.: Microporous metal-organic framework materials for gas separation. Chem **6**, 337–363 (2020)

Liu, Q., Wang, A., Wang, X., Gao, P., Wang, X., Zhang, T.: Synthesis, characterization and catalytic applications of mesoporous γ-alumina from boehmite sol. Microporous Mesoporous Mater. **111**, 323–333 (2008). https://doi.org/10.1016/j.micromeso.2007.08.007

Liu, B., Chen, Z., Huang, J., Chen, H., Fang, Y.: Direct synthesis of hierarchically structured MFI zeolite nanosheet assemblies with tailored activity in benzylation reaction. Microporous Mesoporous Mater. **273**, 235–242 (2019). https://doi.org/10.1016/j.micromeso.2018.07.019

Liu, X., Pang, H., Liu, X., Li, Q., Zhang, N., Mao, L., Qiu, M., Hu, B., Yang, H., Wang, X.: Orderly porous covalent organic frameworks-based materials: superior adsorbents for pollutants removal from aqueous solutions. The Innovation **2**, 100076 (2021). https://doi.org/10.1016/j.xinn.2021.100076

Lv, J., Tan, Y.X., Xie, J., Yang, R., Yu, M., Sun, S., De Li, M., Yuan, D., Wang, Y.: Direct solar-to-electrochemical energy storage in a functionalized covalent organic framework. Angew. Chem. Int. Ed. **57**, 12716–12720 (2018). https://doi.org/10.1002/anie.201806596

Machado, T.F., Serra, M.E.S., Murtinho, D., Valente, A.J.M., Naushad, M.: Covalent organic frameworks: synthesis, properties and applications—an overview. Polymers (basel) **13**(6), 970 (2021). https://doi.org/10.3390/polym13060970

Madri, R.K., Tiwari, D., Sinha, I.: Efficient removal of chromate ions from aqueous solution using a highly cost-effective ferric coordinated [3-(2-aminoethylamino)propyl]trimethoxysilane–MCM-41 adsorbent. RSC Adv. **11**, 11204–11214 (2021). https://doi.org/10.1039/d0ra07425j

Maghfirah, A., Ilmi, M.M., Fajar, A.T.N., Kadj, G.T.M.: A review on the green synthesis of hierarchically porous zeolite. Mater. Today Chem. **17** (2020). https://doi.org/10.1016/j.mtchem.2020.100348

Makertihartha, I.G.B.N., Kadja, G.T.M., Gunawan, M.L., Mukti, R.R., Subagjo: Exceptional aromatic distribution in the conversion of palm-oil to biohydrocarbon using zeolite-based catalyst. J. Eng. Technol. Sci. **52**(4), 584–597 (2020). https://doi.org/10.5614/j.eng.technol.sci.2020.52.4.9

Malgras, V., Ataee-Esfahani, H., Wang, H., Jiang, B., Li, C., Wu, K.C.W., Kim, J.H., Yamauchi, Y.: Nanoarchitectures for mesoporous metals. Adv. Mater. **28**, 993–1010 (2016). https://doi.org/10.1002/adma.201502593

Martínez, C., Corma, A.: Zeolites. In: Reedijk, J., Poeppelmeier, K. (eds.) Comprehensive Inorganic Chemistry II (Second Edition): From Elements to Applications. Elsevier, Amsterdam, pp 103–131 (2013). https://doi.org/10.1016/B978-0-08-097774-4.00506-4

Martínez-Edo, G., Balmori, A., Pontón, I., Del Rio, A.M., Sánchez-García, D.: Functionalized ordered mesoporous silicas (MCM-41): synthesis and applications in catalysis. Catalysts **8**(12), 617 (2018). https://doi.org/10.3390/catal8120617

Maschita, J., Banerjee, T., Savasci, G., Haase, F., Ochsenfeld, C., Lotsch, B.V.: Ionothermal synthesis of imide-linked covalent organic frameworks. Angew. Chem.-Int. Ed. **59**, 15750–15758 (2020). https://doi.org/10.1002/anie.202007372

Meek, B.S.T., Greathouse, J.A., Allendorf, M.D.: Metal-organic frameworks: a rapidly growing class of versatile nanoporous materials. Adv. Mater. **23**(2), 249–267 (2011)

Méndez, F.J., Vargas, R., Blanco, J., Rojas-Challa, Y., Bastardo-González, E., García-Macedo, J.A., Puello-Polo, E., Brito, J.L.: Titanium-modified MCM-41 molecular sieves as efficient supports to increase the hydrogenation abilities of NiMoS and CoMoS catalysts. J. Ind. Eng. Chem. **95**, 340–349 (2021). https://doi.org/10.1016/j.jiec.2021.01.003

Millini, R., Bellussi, G.: Zeolite Science and Perspectives (Chapter 1). In: Čejka, J., Morris, R.E., Nachtigall, P. (eds.) Zeolites in Catalysis: Properties and Applications, pp. 1–36. Royal Society of Chemistry, Cambridge (2017)

Mocniak, K.A., Kubajewska, I., Spillane, D.E.M., Williams, G.R., Morris, R.E.: Incorporation of cisplatin into the metal-organic frameworks UiO66-NH2 and UiO66-encapsulation vs. conjugation. RSC Adv. **5**(102), 83648–83656 (2015)

Mondloch, J.E., Karagiaridi, O., Farha, O.K., Hupp, J.T.: Activation of metal-organic framework materials. Cryst. Eng. Commun. **15**(45), 9258–9264 (2013)

Moosavi, S.M., Nandy, A., Jablonka, K.M., Ongari, D., Janet, J.P., Boyd, P.G., Lee, Y., Smit, B., Kulik, H.J.: Understanding the diversity of the metal-organic framework ecosystem. Nat. Commun. **11**, 4068–4078 (2020)

Mousavi, H., Darian, J.T., Mokhtarani, B.: Enhanced nitrogen adsorption capacity on Ca^{2+} ion-exchanged hierarchical X zeolite. Sep. Purif. Technol. **264**, 118442 (2021). https://doi.org/10.1016/j.seppur.2021.118442

Mueller, U., Schubert, M., Teich, F., Puetter, H., Schierle-Arndt, K., Pastre, J.: Metal-organic frameworks-prospective industrial applications. J. Mater. Chem. **16**(7), 626–636 (2006)

Mukaromah, A.H., Kadja, G.T.M., Mukti, R.R., Pratama, I.R., Zulfikar, M.A., Buchari: Surface-to-volume ratio of synthesis reactor vessel governing low temperature crystallization of ZSM-5. J. Math. Fundam. Sci. **48**(3), 241–251 (2016). https://doi.org/10.5614/j.math.fund.sci.2016.48.3.5

Musilová, R., Choi, M., Ryoo, R.: Mesoporous materials with zeolite framework: Remarkable effect of the hierarchical structure for retardation of catalyst deactivation. Chem. Commun. **43**, 4489–4491 (2006). https://doi.org/10.1039/b612116k

Musilová, Z., Žilková, N., Park, S.E., Čejka, J.: Aromatic transformations over mesoporous ZSM-5: advantages and disadvantages. Top. Catal. **53**(19–20), 1457–1469 (2010). https://doi.org/10.1007/s11244-010-9606-5

Nguyen, L.H.T., Nguyen, T.T., Nguyen, H.L., Doan, T.L.H., Tran, P.H.: A new superacid hafnium-based metal–organic framework as a highly active heterogeneous catalyst for the synthesis of benzoxazoles under solvent-free conditions. Catal. Sci. Technol. **7**, 4346 (2017)

Niesz, K., Yang, P., Somorjai, G.A.: Sol-gel synthesis of ordered mesoporous alumina. Chem. Commun. 1986–1987 (2005). https://doi.org/10.1039/B419249D

Pang, H., Yang, G., Li, L., Yu, J.: Efficient transesterification over two-dimensional zeolites for sustainable biodiesel production. Green Energy Environ. **5**(4), 405–413 (2020a). https://doi.org/10.1016/j.gee.2020.10.024

Pang, Y.H., Huang, Y.Y., Wang, L., Shen, X.F., Wang, Y.Y.: Determination of bisphenol A and bisphenol S by a covalent organic framework electrochemical sensor. Environ. Pollut. **263**, 114616 (2020b). https://doi.org/10.1016/j.envpol.2020.114616

Park, W., Yu, D., Na, K., Jelfs, K.E., Slater, B., Sakamoto, Y., Ryoo, R.: Hierarchically structure-directing effect of multi-ammonium surfactants for the generation of MFI zeolite nanosheets. Chem. Mater. **23**(23), 5131–5137 (2011). https://doi.org/10.1021/cm201709q

Peng, W., Mi, J., Liu, F., Xiao, Y., Chen, W., Liu, Z., Yi, X., Liu, W., Zheng, A.: Accelerating biodiesel catalytic production by confined activation of methanol over high-concentration ionic liquids grafted UiO-66 solid superacids. ACS Catal. 11848–11856 (2020)

Platschek, B., Keilbach, A., Bein, T.: Mesoporous structures confined in anodic alumina membranes. Adv. Mater. **23**, 2395–2412 (2011). https://doi.org/10.1002/adma.201002828

Pratama, A.P., Rahayu, D.U.C., Krisnandi, Y.K.: Levulinic acid production from delignified rice husk waste over manganese catalysts: heterogeneous versus homogeneous. Catalysts **10**(3), 327 (2020). https://doi.org/10.3390/catal10030327

Prochowicz, D., Sokotowski, K., Justyniak, I., Kornowicz, A., Fairen-Jimenez, D., Friscic, T., Lewinski, J.: A mechanochemical strategy for IRMOF assembly based on pre-designed oxo-zinc precursors. Chem. Commun. **51**, 4032–4035 (2015)

Puspitasari, T., Ilmi, M.M., Nurdini, N., Mukti, R.R., Radiman, C.L., Darwis, D., Kadja, G.T.M.: The physicochemical characteristics of natural zeolites governing the adsorption of Pb^{2+} from aqueous environment. Key Eng. Mater. **811**, 92–98 (2019). 10.4028/www.scientific.net/KEM.811.92

Rasamimanana, S., Mignard, S., Batonneau-Gener, I.: Hierarchical zeolites as adsorbents for mesosulfuron-methyl removal in aqueous phase. Microporous Mesoporous Mater. **226**, 153–161 (2016). https://doi.org/10.1016/j.micromeso.2015.12.014

Redfern, L.R., Farha, O.K.: Mechanical properties of metal-organic frameworks. Chem. Sci. **10**, 10666–10679 (2019)

Remya, V.R., Kurian, M.: Synthesis and catalytic applications of metal-organic frameworks: a review on recent literature. Int. Nano Lett. **9**, 17–29 (2019)

Ren, Y., Ma, Z., Bruce, P.G.: Ordered mesoporous metal oxides: synthesis and applications. Chem. Soc. Rev. **41**, 4909–4927 (2012). https://doi.org/10.1039/c2cs35086f

Rilyanti, M., Mukti, R.R., Kadja, G.T.M., Ogura, M., Nur, H., Ng, E.P., Ismunandar: On the drastic reduction of organic structure directing agent in the steam-assisted crystallization of zeolite with hierarchical porosity. Microporous Mesoporous Mater. **230**, 30–38 (2016). https://doi.org/10.1016/j.micromeso.2016.04.038

Rosi, N.L., Eckert, J., Eddaoudi, M., Vodak, D.T., Kim, J., O'Keeffe, M., Yaghi, O.M.: Hydrogen atorage in microporous metal-organic frameworks. Science **300**(5622), 1127–1129 (2003)

Roth, W.J., Shvets, O.V., Shamzhy, M., Chlubná, P., Kubů, M., Nachtigall, P., Čejka, J.: Postsynthesis transformation of three-dimensional framework into a lamellar zeolite with modifiable architecture. J. Am. Chem. Soc. **133**(16), 6130–6133 (2011). https://doi.org/10.1021/ja200741r

Roth, W.J., Gil, B., Marszalek, B.: Comprehensive system integrating 3D and 2D zeolite structures with recent new types of layered geometries. Catal. Today **227**, 9–14 (2014a). https://doi.org/10.1016/j.cattod.2013.09.032

Roth, W.J., Nachtigall, P., Morris, R.E., Čejka, J.: Two-dimensional zeolites: current status and perspectives. Chem. Rev. **114**, 4807–4837 (2014b). https://doi.org/10.1021/cr400600f

Roth, W.J., Čejka, J., Millini, R., Montanari, E., Gil, B., Kubu, M.: Swelling and interlayer chemistry of layered MWW zeolites MCM-22 and MCM-56 with high Al content. Chem. Mater. **27**(13), 4620–4629 (2015). https://doi.org/10.1021/acs.chemmater.5b01030

Rudd, N.D., Wang, H., Fuentes-Fernandez, E.M., Teat, S.J., Chen, F., Hall, G., Chabal, Y.J., Li, J.: Highly efficient luminescent metal-organic frameworks for the simultaneous detection and removal of heavy metals from water. ACS Appl. Mater. Interfaces **8**, 30294–30303 (2016)

Ryoo, R., Joo, S.H., Jun, S.: Synthesis of highly ordered carbon molecular sieves via template-mediated structural transformation. J. Phys. Chem. B **103**, 7743–7746 (1999). https://doi.org/10.1021/jp991673a

Schulman, E., Wu, W., Liu, D.: Two-dimensional zeolite materials: structural and acidity properties. Materials **13**(8) (2020). https://doi.org/10.3390/MA13081822

Schüth, F.: Non-siliceous mesostructured and mesoporous materials. Chem. Mater. **13**, 3184–3195 (2001). https://doi.org/10.1021/cm011030j

Schwalbe-Koda, D., Gómez-Bombarelli, R.: Accuracy and reproducibility of host-guest interactions in zeolites. ChemRxiv (2020). https://doi.org/10.26434/chemrxiv.13270184.v1

Scicluna, M.C., Vella-Zarb, L.: Evolution of nanocarrier drug-delivery systems and recent advancements in covalent organic framework-drug systems. ACS Appl. Nano Mater. **3**(4), 3097–3115 (2020). https://doi.org/10.1021/acsanm.9b02603

Serrano, D.P., Escola, J.M., Pizarro, P.: Synthesis strategies in the search for hierarchical zeolites. Chem. Soc. Rev. **42**(9), 4004–4035 (2013). https://doi.org/10.1039/c2cs35330j

Shariatinia, Z., Pourzadi, N., Darvishi, S.M.R.: tert-Butylamine functionalized MCM-41 mesoporous nanoparticles as drug carriers for the controlled release of cyclophosphamide anticancer drug. Surf. Interfaces **22**, 100842 (2021). https://doi.org/10.1016/j.surfin.2020.100842

Shi, X., Ma, D., Xu, F., Zhang, Z., Wang, Y.: Table-salt enabled interface-confined synthesis of covalent organic framework (COF) nanosheets. Chem. Sci. **11**, 989–996 (2020). https://doi.org/10.1039/c9sc05082e

Sing, K.S.W.: Reporting physisorption data for gas/solid systems with special reference to the determination of surface area and porosity (Recommendations 1984). Pure Appl. Chem. **57**, 603–619 (1985). https://doi.org/10.1351/pac198557040603

Smeets, S., Zou, X.: Zeolite structures. In: Čejka, J., Morris, R.E., Nachtigall, P. (eds.) Zeolites in Catalysis: Properties and Applications, pp. 37–72. Royal Society of Chemistry, Cambridge (2017)

Stock, N., Biswas, S.: Synthesis of metal-organic frameworks (MOFs): routes to various MOF topologies, morphologies, and composites. Chem. Rev. **112**(2), 933–969 (2012)

Sun, Y., Zhou, H.C.: Recent progress in the synthesis of metal-organic frameworks. Sci. Technol. Adv. Mater. **16**, 054202 (2015)

Sun, Q., Zheng, Y., Zheng, Y., Xiao, Y., Cai, G., Wei, K.: Synthesis of highly thermally stable lanthanum-doped ordered mesoporous alumina. Scr. Mater. **65**, 1026–1029 (2011). https://doi.org/10.1016/j.scriptamat.2011.09.013

Sun, C.Y., Qin, C., Wang, X.L., Su, Z.M.: Metal-organic frameworks as potential drug delivery systems. Expert Opin. Drug Deliv. **10**(1), 89–101 (2013)

Sun, Y., Zheng, L., Yang, Y., Qian, X., Fu, T., Li, X., Yang, Z., Yan, H., Cui, C., Tan, W.: Metal–organic framework nanocarriers for drug delivery in biomedical applications. Nano-Micro Lett. **12**, 103 (2020)

Tanaka, S., Nishiyama, N., Egashira, Y., Ueyama, K.: Synthesis of ordered mesoporous carbons with channel structure from an organic–organic nanocomposite. Chem. Commun. **2005**, 2125–2127 (2005). https://doi.org/10.1039/B501259G

Tao, C.A., Wang, J.F.: Synthesis of metal organic frameworks by ball-milling. Crystal **11**(15), 1–20 (2021)

Thomas, S., Li, H., Zhong, C., Matsumoto, M., Dichtel, W.R., Bredas, J.L.: Electronic structure of two-dimensional π-conjugated covalent organic frameworks. Chem. Mater. **31**, 3051–3065 (2019a). https://doi.org/10.1021/acs.chemmater.8b04986

Thomas, S., Li, H., Dasari, R.R., Evans, A.M., Castano, I., Allen, T.G., Reid, O.G., Rumbles, G., Dichtel, W.R., Gianneschi, N.C., Marder, S.R., Coropceanu, V., Brédas, J.L.: Design and synthesis of two-dimensional covalent organic frameworks with four-arm cores: prediction of remarkable ambipolar charge-transport properties. Mater. Horizons **6**, 1868–1876 (2019b). https://doi.org/10.1039/c9mh00035f

Thommes, M., Kaneko, K., Neimark, A.V., Olivier, J.P., Rodriguez-Reinoso, F., Rouquerol, S.K.S.W.: Physisorption of gases, with special reference to the evaluation of surface area and pore size distribution (IUPAC Technical Report). Pure Appl. Chem. **87**(9–10), 1051–1069 (2015). https://doi.org/10.1515/pac-2014-1117

Tian, Y., Liu, H., Wang, L., Zhang, X., Liu, G.: Controllable fabrication and catalytic performance of nanosheet HZSM-5 films by vertical secondary growth. AIChE J. **64**(6), 1923–1927 (2018). https://doi.org/10.1002/aic.16158

Valange, S., Guth, J.L., Kolenda, F., Lacombe, S., Gabelica, Z.: Synthesis strategies leading to surfactant-assisted aluminas with controlled mesoporosity in aqueous media. Microporous Mesoporous Mater. **35–36**, 597–607 (2000). https://doi.org/10.1016/S1387-1811(99)00253-X

Vibulyaseak K (Guy), Ohtani B, Ogawa M (2020) Crystallization of well-defined anatase nanoparticles in SBA-15 for the photocatalytic decomposition of acetic acid. RSC Adv. **10**, 32350–32356. https://doi.org/10.1039/d0ra04528d

Wan, S., Guo, J., Kim, J., Ihee, H., Jiang, D.: A belt-shaped, blue luminescent, and semiconducting covalent organic framework. Angew. Chem.-Int. Ed. **47**, 8826–8830 (2008). https://doi.org/10.1002/anie.200803826

Wan, S., Gándara, F., Asano, A., Furukawa, H., Saeki, A., Dey, S.K., Liao, L., Ambrogio, M.W., Botros, Y.Y., Duan, X., Seki, S., Stoddart, J.F., Yaghi, O.M.: Covalent organic frameworks with high charge carrier mobility. Chem. Mater. **23**, 4094–4097 (2011). https://doi.org/10.1021/cm201140r

Wang, S., Peng, Y.: Natural zeolites as effective adsorbents in water and wastewater treatment. Chem. Eng. J. **156**(1), 11–24 (2010). https://doi.org/10.1016/j.cej.2009.10.029

Wang, S., Serre, C.: Toward green production of water-stable metal-organic frameworks based on high-valence metals with low toxicities. ACS Sustain. Chem. Eng. **7**, 11911–11927 (2019)

Wang, H., Wang, L., Sato, T., Sakamoto, Y., Tominaka, S., Miyasaka, K., Miyamoto, N., Nemoto, Y., Terasaki, O., Yamauchi, Y.: Synthesis of mesoporous Pt films with tunable pore sizes from aqueous surfactant solutions. Chem. Mater. **24**, 1591–1598 (2012). https://doi.org/10.1021/cm300054b

Wang, L., Zheng, M., Xie, Z.: Nanoscale metal-organic frameworks for drug delivery: a conventional platform with new promise. J. Mater. Chem. B **6**(5), 707–717 (2018)

Wang, D., Zhang, Z., Lin, L., Liu, F., Wang, Y., Guo, Z., Li, Y., Tian, H., Chen, X.: Porphyrin-based covalent organic framework nanoparticles for photoacoustic imaging-guided photodynamic and photothermal combination cancer therapy. Biomaterials **223**, 119459 (2019). https://doi.org/10.1016/j.biomaterials.2019.119459

Wang, H., Wang, T., Ma, R., Wu, K., Li, H., Feng, B., Li, C., Shen, Y.: Facile synthesis of sulfonated covalent organic framework for the adsorption of heavy metal ions. J. Taiwan Inst. Chem. Eng. **112**, 122–129 (2020a). https://doi.org/10.1016/j.jtice.2020.07.005

Wang, Z., Li, Z., Ng, M., Milner, P.J.: Rapid mechanochemical synthesis of metal-organic frameworks using exogenous organic base. Dalton Trans. **49**(45), 16238–16244 (2020b)

Wardani, M.K., Kadja, G.T.M., Fajar, A.T.N., Subagjo, M.I.G.B.N., Gunawan, M.L., Suendo, V., Mukti, R.R.: Highly crystalline mesoporous SSZ-13 zeolite obtained via controlled post-synthetic treatment. RSC Adv. **9**(1), 77–86 (2019). https://doi.org/10.1039/C8RA08979E

Wei, J., Ren, Y., Luo, W., Sun, Z., Cheng, X., Li, Y., Deng, Y., Elzatahry, A.A., Al-Dahyan, D., Zhao, D.: Ordered mesoporous alumina with ultra-large pores as an efficient absorbent for selective bioenrichment. Chem. Mater. **29**, 2211–2217 (2017). https://doi.org/10.1021/acs.chemmater.6b05032

Wenten, I.G., Khoiruddin, K., Kadja, G.T.M., Mukti, R.R., Sutrisna, P.D.: Modified zeolite-based polymer nanocomposite membranes for pervaporation. In: Thomas, S., George, S.C., Jose, T. (eds.) Polymer Nanocomposite Membranes for Pervaporation. Elsevier, Amsterdam (2020). https://doi.org/10.1016/b978-0-12-816785-4.00011-2

Woodliffe, J.L., Ferrari, R.S., Ahmed, I., Laybourn, A.: Evaluating the purification and activation of metal-organic frameworks from a technical and circular economy perspective. Coord. Chem. Rev. **428**, 213578 (2021)

Wu, S.H., Lin, H.P.: Synthesis of mesoporous silica nanoparticles. Chem. Soc. Rev. **42**, 3862–3875 (2013). https://doi.org/10.1039/c3cs35405a

Wu, M.X., Yang, Y.W.: Applications of covalent organic frameworks (COFs): from gas storage and separation to drug delivery. Chin. Chem. Lett. **28**, 1135–1143 (2017). https://doi.org/10.1016/j.cclet.2017.03.026

Wuamprakhon, P., Wattanakit, C., Warakulwit, C., Yutthalekha, T., Wannapakdee, W., Ittisanronnachai, S., Limtrakul, J.: Direct synthesis of hierarchical ferrierite nanosheet assemblies via an organosilane template approach and determination of their catalytic activity. Microporous Mesoporous Mater. **219**, 1–9 (2016). https://doi.org/10.1016/j.micromeso.2015.07.022

Xamena, L.I., Francesc, X., Gascon, J.: Metal Organic Frameworks as Heterogeneous Catalysts. The Royal Society of Chemistry, Cambridge (2013)

Xie, Y.F., Ding, S.Y., Liu, J.M., Wang, W., Zheng, Q.Y.: Triazatruxene based covalent organic framework and its quick-response fluorescence-on nature towards electron rich arenes. J. Mater. Chem. C **3**, 10066–10069 (2015). https://doi.org/10.1039/c5tc02256h

Xiong, C., Ning, H., Jia, G., Hong, X., Fei, X., Donglin, J.: Towards covalent organic frameworks with predesignable and aligned open docking sites. Chem. Commun. **50**, 6161–6163 (2014). https://doi.org/10.1039/c4cc01825g

Xu, H., Gao, J., Jiang, D.: Stable, crystalline, porous, covalent organic frameworks as a platform for chiral organocatalysts. Nat. Chem. **7**, 905–912 (2015). https://doi.org/10.1038/nchem.2352

Xu, X., Megarajan, S.K., Zhang, Y., Jiang, H.: Ordered mesoporous alumina and their composites based on evaporation induced self-assembly for adsorption and catalysis. Chem. Mater. **32**, 3–26 (2020). https://doi.org/10.1021/acs.chemmater.9b03873

Xu, L., Nie, R., Chen, X., Li, Y., Jiang, Y., Lu, X.: Formic acid enabled selectivity boosting in transfer hydrogenation of 5-hydroxymethylfurfural to 2,5-furandimethanol on highly dispersed Co–Nx sites. Catal. Sci. Technol. **11**, 1451–1457 (2021). https://doi.org/10.1039/D0CY01969K

Yaghi, O.M., Li, H.: Hydrothermal asnthesis of a metal-organic framework containing large rectangular channels. J. Am. Chem. Soc. **117**, 10401–10402 (1995)

Yaghi, O.M., Kalmutzi, M.J., Diercks, C.S.: Introduction to Reticular Chemistry. Wiley-VCH Verlag GmbH & Co., Weinheim (2019)

Yanagisawa, T., Shimizu, T., Kuroda, K., Kato, C.: The preparation of alkyltrimethylammonium-kanemite complexes and their conversion to microporous materials. Bull. Chem. Soc. Jpn. **63**, 988–992 (1990). https://doi.org/10.1246/bcsj.63.988

Yang, D., Gates, B.C.: Catalysis by metal organic frameworks: perspective and suggestions for future research. ACS Catal. **9**, 1779–1798 (2019)

Yang, S.T., Kim, J., Cho, H.Y., Kim, S., Ahn, W.S.: Facile synthesis of covalent organic frameworks COF-1 and COF-5 by sonochemical method. RSC Adv. **2**, 10179–10181 (2012). https://doi.org/10.1039/c2ra21531d

Yang, F., Cheng, S., Zhang, X., Ren, X., Li, R., Dong, H., Hu, W.: 2D organic materials for optoelectronic applications. Adv. Mater. **30**, 1–27 (2018). https://doi.org/10.1002/adma.201702415

Yang, C.H., Cheng, C.C., Lee, D.J.: Excess adsorption of phosphoric acid from extremely acidic solutions by covalent organic framework EB-COF:Br. Chemosphere **257**, 127244 (2020a). https://doi.org/10.1016/j.chemosphere.2020.127244

Yang, C.H., Chang, J.S., Lee, D.J.: Covalent organic framework EB-COF: Br as adsorbent for phosphorus (V) or arsenic (V) removal from nearly neutral waters. Chemosphere **253**, 126736 (2020b). https://doi.org/10.1016/j.chemosphere.2020.126736

Yenumala, S.R., Kumar, P., Maity, S.K., Shee, D.: Hydrodeoxygenation of karanja oil using ordered mesoporous nickel-alumina composite catalysts. Catal. Today **348**, 45–54 (2020). https://doi.org/10.1016/j.cattod.2019.08.040

Yuan, C., Fu, S., Yang, K., Hou, B., Liu, Y., Jiang, J., Cui, Y.: Crystalline C - C and C=C bond-linked chiral covalent organic frameworks. J. Am. Chem. Soc. **143**, 369–381 (2021). https://doi.org/10.1021/jacs.0c11050

Yue, J.Y., Wang, L., Ma, Y., Yang, P., Zhang, Y.Q., Jiang, Y., Tang, B.: Metal ion-assisted carboxyl-containing covalent organic frameworks for the efficient removal of Congo red. Dalt. Trans. **48**, 17763–17769 (2019). https://doi.org/10.1039/c9dt04175c

Yulizar, Y., Kadja, G.T.M., Safaat, M.: Well-exposed gold nanoclusters on Indonesia natural zeolite: a highly active and reusable catalyst for the reduction of p-nitrophenol. React. Kinet. Mech. **117**(1), 353–363 (2016). https://doi.org/10.1007/s11144-015-0916-2

Zhang, X., Zhang, F., Chan, K.Y.: The synthesis of large mesopores alumina by microemulsion templating, their characterization and properties as catalyst support. Mater. Let. **58**, 2872–2877 (2004). https://doi.org/10.1016/j.matlet.2004.05.008

Zhang, P., Zhang, J., Dai, S.: Mesoporous carbon materials with functional compositions. Chem.-A Eur. J. **23**, 1986–1998 (2017). https://doi.org/10.1002/chem.201602199

Zhang, B., Wei, M., Mao, H., Pei, X., Alshmimri, S.A., Reimer, J.A., Yaghi, O.M.: Crystalline dioxin-linked covalent organic frameworks from irreversible reactions. J. Am. Chem. Soc. **140**, 12715–12719 (2018a). https://doi.org/10.1021/jacs.8b08374

Zhang, G., Li, X., Liao, Q., Liu, Y., Xi, K., Huang, W., Jia, X.: Water-dispersible PEG-curcumin/amine-functionalized covalent organic framework nanocomposites as smart carriers for in vivo drug delivery. Nat. Commun. **9**, 1–11 (2018b). https://doi.org/10.1038/s41467-018-04910-5

Zhang, M., Zhang, M., Zhang, M., Chen, J., Zhang, S., Zhou, X., He, L., Sheridan, M.V., Yuan, M., Zhang, M., Chen, L., Dai, X., Ma, F., Wang, J., Hu, J., Wu, G., Kong, X., Zhou, R., Albrecht-Schmitt, T.E., Chai, Z., Wang, S.: Electron beam irradiation as a general approach for the rapid synthesis of covalent organic frameworks under ambient conditions. J. Am. Chem. Soc. **142**, 9169–9174 (2020). https://doi.org/10.1021/jacs.0c03941

Zhao, D., Huo, Q., Feng, J., Chmelka, B.F., Stucky, G.D.: Nonionic triblock and star diblock copolymer and oligomeric sufactant syntheses of highly ordered, hydrothermally stable, mesoporous silica structures. J. Am. Chem. Soc. **120**, 6024–6036 (1998). https://doi.org/10.1021/ja974025i

Zhao, T., Elzatahry, A., Li, X., Zhao, D.: Single-micelle-directed synthesis of mesoporous materials. Nat. Rev. Mater. **4**, 775–791 (2019). https://doi.org/10.1038/s41578-019-0144-x

Zhou, Y., Yu, Y., Ma, D., Foucher, A.C., Xiong, L., Zhang, J., Stach, E.A., Yue, Q., Kang, Y.: Atomic Fe dispersed hierarchical mesoporous Fe–N–C nanostructures for an efficient oxygen reduction reaction. ACS Catal. **11**, 74–81 (2021). https://doi.org/10.1021/acscatal.0c03496

Zhu, K., Yue, B., Zhou, W., He, H.: Preparation of three-dimensional chromium oxide porous single crystals templated by SBA-15. Chem. Commun. 98–99 (2003). https://doi.org/10.1039/b210065g

Characterization of Nanoporous Materials

Leila Keshavarz, Mohammad Reza Ghaani, Omid Saremi, and Niall J. English

Abstract Nanoporous materials have aroused huge attention in research and development due to their capability in numerous areas such as gas storage, separation, and catalysis processes, membranes, microdevices, etc. The properties of nanoporous materials are controlled by the arrangement of atoms in the crystal as well as the specific surface area and porosity. Detailed information about textural properties, such as pore size, shape, surface morphology, and connectivity, and composition of nanoporous materials has a significant effect on their efficiency and performance, and therefore, it is necessary to determine their properties. The development of nanoporous materials featuring uniform, tailor-made pore structures, and offers the tremendous capability for these applications. In this respect, this chapter emphasizes and explains both existing and novel methods for the synthesis and characterization of nanoporous materials, which is essential to galvanize yet more progress in these materials' further development.

Keywords Nanoporous · Characterization · Crystalline structure · Oxidation state & coordination · Chemical composition · Pore analysis

1 Introduction

There is a wide variety of solid nanoporous materials, including nanoporous carbons, zeolites, nanoporous inorganic oxides, together with nanoporous polymers. With advances in fabricating nanoporous materials with tailor-made pore structures and with changing synthesis conditions, it is possible to control the size of these channels and their surface properties; excitingly, this offers huge potential for different applications. There is a great, renewed interest in the characterization of novel

L. Keshavarz (✉) · M. R. Ghaani · O. Saremi · N. J. English (✉)
School of Chemical and Bioprocess Engineering, University College Dublin,
Belfield, Dublin 4, Ireland
e-mail: leila.keshavarz@ucd.ie

N. J. English
e-mail: niall.english@ucd.ie

nanoporous materials, owing to impressive recent achievements in modern characterization methods. To produce a repeatable synthesis of nanomaterials, their characterization is rightly considered to be pivotal. Also, consideration of a detailed textual analysis of nanoporous materials is vital to acquiring precise information on, *inter alia*, the pore size, surface area, and network connectivity. Incorporation of this data with studies on process performance helps to coordinate the structural properties of materials with their performance for gas storage, separation, and catalytic processes. A variety of techniques with different degrees of uncertainty are available for the textual and structural characterization of nanoporous materials, such as gas adsorption, electron microscopy, nuclear magnetic resonance methods, X-ray analysis, and various spectroscopic methods (Senthil Kumar et al. 2019). Every technique has some advantages as well as limitations in application range. This chapter contains a brief description of different characterization methods and demonstrates their application to characterize the surface and structural properties of nanoporous material, while also summarizing recent progress in the field of nanoporous materials characterization; to do so, we adopt a nanoporous materials-characterization "categorization scheme" as depicted in Fig. 1.
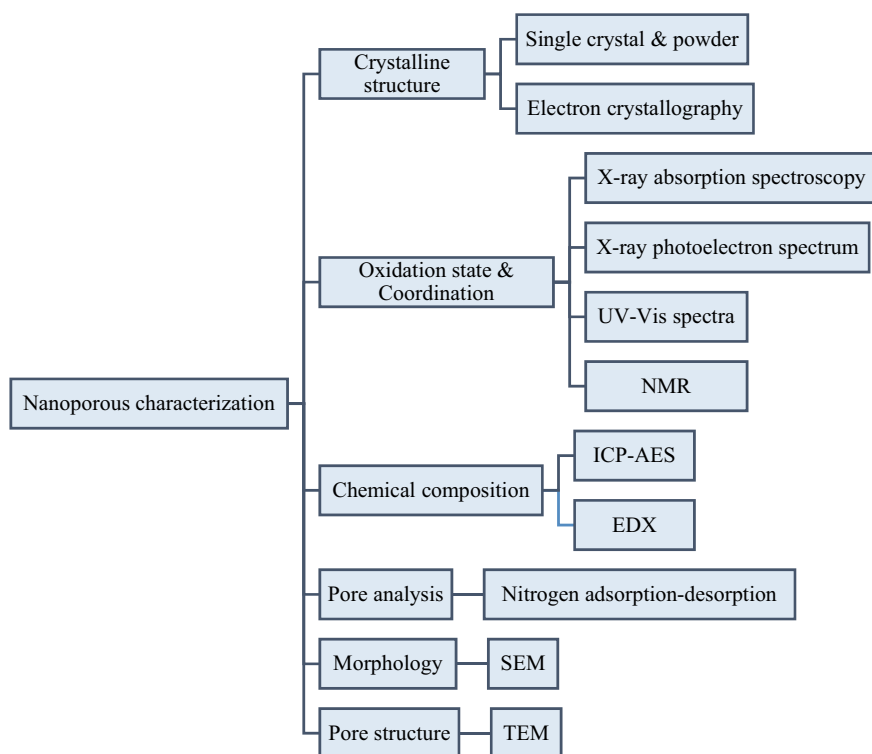

Fig. 1 Classification of characterization methods for nanoporous materials

2 Crystalline Structure

Usually, the structural resolution of porous materials is challenging as most porous materials are polycrystalline with complex featuring large unit cells, and the materials are indeed sometimes disordered. Moreover, the group of species included in the pores of the crystal cause more difficulty for the structure determination of nanoporous materials. Common solid nanoporous materials can be classified as polymeric, metals, carbon, aluminosilicate, and oxides (Fayed et al. 2016). Nanoporous materials have increased the domain of zeolites, and new nanoporous materials developed such as new porous metal-organic frameworks (MOFs) and coordination polymers (PCPs), porous metalophosphates, and hybrid materials. Consequently, new challenges are facing for the structural characterization of these nanoporous crystals. To determine the structure of nanoporous materials, it is of paramount importance to determine the periodic arrangement of the material within the bulk of the crystal and averaged structures and then probe the structural deflection from perfect infinite crystal, such as surface- and defect-based fine structures, as well as incommensurate structures. As reported by the International Union of Pure and Applied Chemistry (IUPAC), there are three categories of nanoporous materials: micropores (pore sizes < 2 nm), mesoporous (2–50 nm), and macrospores (>50 nm). A comparison of these different pore systems of mesoporous is shown in Fig. 2 (Fayed et al. 2016).

For example, MOF structures (Helliwell et al. 2008) have pores of uniform size up to 3 nm containing metal salts as the inorganic source, together with organic molecules featuring O or N donor atoms. For finding the framework structure of this nanoporous material, the challenge lays first in detecting the non-framework groups, including template molecules. The next step that is more challenging is finding the location of the site(s) of the replaced metal atoms and the acidic sites. However, during the production of these materials formed by heating the "as-synthesized" materials, it is necessary to consider changes that occurred especially the oxidation state changes of the incorporated metal atoms.
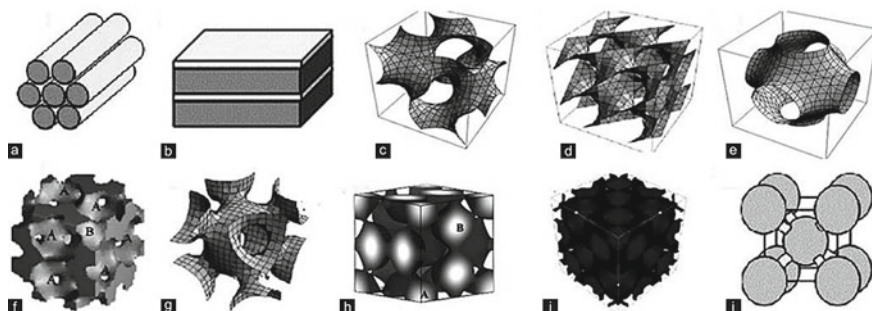
Fig. 2 Various structures of mesoporous silicates, **a** 2D-hexagonal, **b** lamellar, **c** Ia-3d, **d** Pn-3 m, **e** Im-3, **f** Pm-3n, **g** Fm-3 m, **h** Im-3 m, **i** Fd-3 m and **j** body-centered cubic structures (reproduced, with permission, from Fayed et al. 2016)

Among the existing structure determination tools, single-crystal and powder X-ray diffraction and electron crystallography are the most common characterization methods for the crystalline structure of nanoporous materials (Liu et al. 2013). Distance ordered-arrangement of pores could be measured by electron crystallography (EC). Single-crystal XRD (SXRD) is a non-destructive analytical technique and enables detailed information about the crystal, such as cell dimension, bond length, bond angle, etc. Powder X-ray diffraction (PXRD) is another technique applied to determine the crystallographic analysis of a powder sample.

2.1 Single Crystal and Powder XRD

X-ray diffraction (XRD) technique is among the common techniques for characterization of the long-range order in materials including nanoporous materials. XRD is a quick, non-destructive analysis of multicomponent mixtures that provides information regarding the microstructure of 3D crystalline structure (including grain size, lattice constant, and strains, nature of the phase), without the need for extensive sample preparation. The diffraction pattern achieved from the XRD analysis provides a sharp and considerable peak for the crystalline compound.

W. L. Bragg proposed that when X-ray incident onto a crystal surface, the interaction of X-rays defined based on the reflection from crystal planes, which is called Bragg's Law (Bragg and Bragg 1913):

$$n\lambda = 2d \sin\theta \tag{1}$$

Here θ is the angle of the incident X-ray beam, d is the spacing of the crystal layers (path difference), λ is the wavelength of the incident beam, and n is a constant.

In the constant wavelength, Bragg's law expresses that the angles of X-rays reflect by a set of lattice planes only depending on the d-spacing. In Fig. 3, two sets of reflections from the A and B planes which reflect at the same angle are different in

Fig. 3 Reflection of X-rays beam from two lattice planes attributed to the family $H \equiv (h, k, l)$
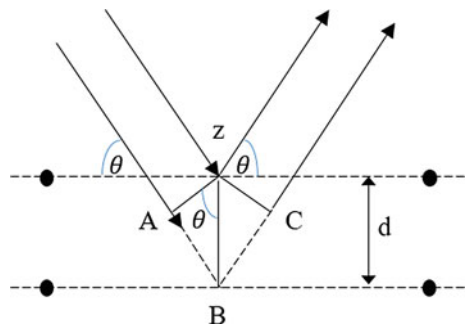
phase depending on d, λ, and they are different in amplitude if they are not from the same atoms (Martis 2011).

Single-Crystal X-Ray Diffraction

The most feasible and well-established technique for characterization of crystalline materials and understanding the atomic arrangement is single-crystal X-ray diffraction (SXRD). Generally, larger crystals of nanoporous material are suitable for characterization by SXRD. The angles and intensities of X-ray diffraction apply to generate a 3D image of the density of electrons, which reflects the average positions of atoms in the crystal. Three-dimensional XRD intensity data from a single crystal require approximately less than 10 h. This method has some limitations, in that when the crystals are too small. Therefore, the main difficulty of structure determination by SXRD lies in the crystal size itself, despite the brightest synchrotron light sources needing to be at least a few micrometers.

In the case of nanoporous materials, SXRD has been applied to determine the structure of various open-framework oxides and metal-organic frameworks, as it is relatively easy to form crystals large enough for SXRD of such materials (Kaskel 2017). Contrarily, this method is not very popular for zeolites, and only a limited number of zeolites have been solved by SXRD. High internal stress during solvent removal of nanoporous materials tends to induce cracking in single crystals. Therefore, crystal fragmentation and defect formation of nanoporous materials can be often caused by desolvation, none of which is favorable for SXRD studies. Another challenge explaining the paucity of such studies in the literature centers on the inherent difficulty in carrying out structure determination of disordered crystals. Moreover, some nanoporous materials are usually isolated as microcrystalline powders, and resultant structures are mainly determined from powder-XRD data.

Halder and Kerpet developed a novel in situ SXRD technique to ascertain, as a function of temperature and vapor pressure which enables continuous monitoring of the single-crystal structure during the desorption and adsorption of different guest species into a porous coordination framework (Halder and Kepert 2005). In this method, mechanisms of structural rearrangements of the framework, together with desirable adsorption sites for gases, can be determined at the same time. Structure modeling can also be performed by XRD diffraction patterns using various software (e.g., TOPAS, Materials Studio), in conjunction with the Scherrer-equation treatment of broadening of the most intense peak of XRD measurements for specific samples.

When nanoporous single-crystal growth is difficult, structure solution from powder-diffraction data itself can be achieved.

Powder X-Ray Diffraction

This technique can be applied to determine information for crystalline materials and periodically arranged clusters, such as, *inter alia*, phase identification, phase quantification, percent crystallinity, lattice-parameter refinement, Rietveld refinement, expansion tensors and bulk modulus, crystallite size, and strain. The 2D diffraction pattern illustrates concentric rings of scattering peaks refer to the different d spacings in the crystal lattice because the nanoscale powder is randomly oriented. PXRD data

collect data from millions of randomly oriented crystallite; therefore, it can provide strong and reliable diffraction intensities. The intensities and positions of the peaks are employed to identify the structure of the material. After the collection of the powder-diffraction pattern is performed, extraction of line intensities is performed by a variety of approaches methods; for instance, the Le Bail or Pawley approaches can be performed to search for structure models and sifted through to select plausible ones.

It must be remarked that the majority of nanoporous materials is synthesized in powder form, and thus, SXRD may not offer all kinetic information during the adsorption process, because the collection of a complete 3D data set from the single crystal is highly time-consuming compared to PXRD. Although PXRD provides accuracy in intensity measurements, it must be admitted that sometimes prediction structure with PXRD is challenging due to significant overlapping in the powder-diffraction patterns even for high-resolution data. In general, nanoporous materials possess relatively poor crystallinity, which renders the resolution of their structures barely possible from PXRD data. This problem is more significant in the case of nanocrystals featuring large unit-cell sizes and low symmetry. In such cases, a structureless pattern refinement of the experimental diffraction diagram gives the possibility to obtain the cell parameters as well as the space-group symmetry of these nanoporous materials.

As a representative example, Fig. 4 shows some examples of the structure of MCM-41, MCM-48, and MSM-50 by their PXRD.

Developing these ideas further, Fig. 5a shows the crystal structure of nanoporous Si-ZSM-5, as verified by XRD (Kokotailo et al. 1978).

Figure 5b illustrates the three-dimensional channels of the nanoporous ZSM-5 zeolite. The [−101], [011], and [101] reflections located at $2\theta = 7.92°$, $7.93°$, and $8.01°$, respectively, led to a total peak at ~8.0 (Hernández et al. 2018).

XRD also can be applied to specify the effect of modification on the structure of the nanoporous materials. For example, Fig. 6 illustrates the XRD result of a nanoporous LUS-1 silica samples before and after loading of TiO_2. The TiO_2-containing LUS-1 spectra show hexagonal symmetry with (100), (110), and (200) diffraction peaks
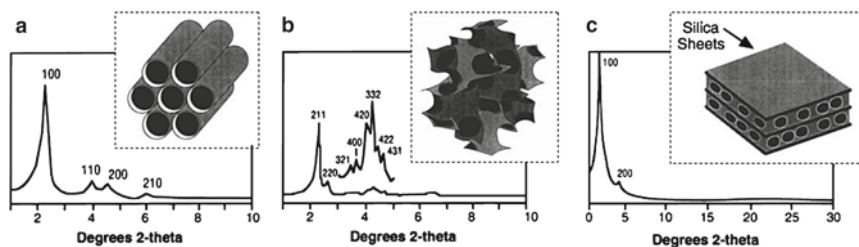
Fig. 4 XRD patterns and the assigned pore structures of **a** MCM-41 (hexagonal), **b** MCM-48 (cubic), and **c** MCM-50 (stabilized lamellar) (reproduced, with permission, from Barton et al. 1999)
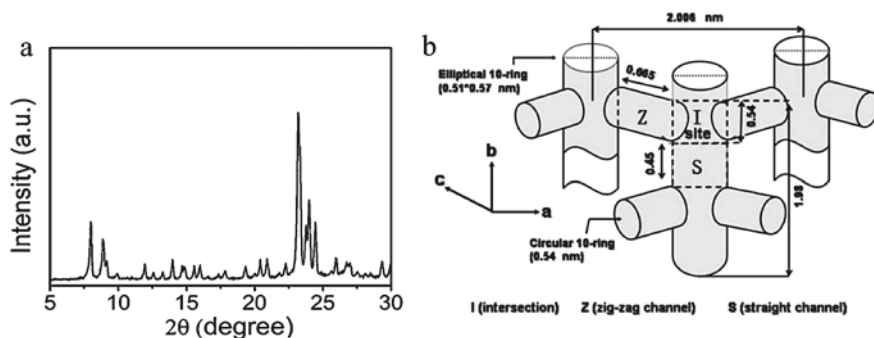
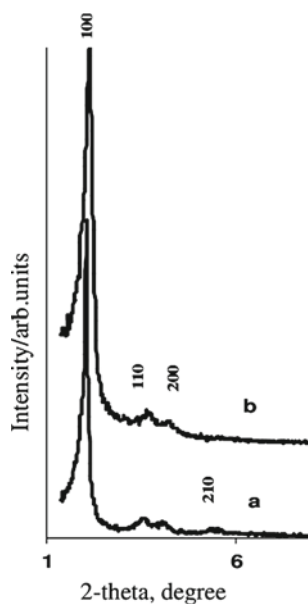**Fig. 5** Structure characterizations. **a** XRD pattern of nanoporous Si-ZSM-5, **b** A schematic illustration displaying the intrinsic microporous structure in a ZSM-5 crystal (reproduced, with permission, from Hernández et al. 2018)

Fig. 6 XRD pattern of **a** LUS-1 nanoporous silica, **b** Ti/LUS-1 nanoporous silica (Badiei et al. 2009)

that assignable to hexagonal P6mm symmetry. The (100) peak demonstrates a well-defined mesostructure with a pore diameter of 2–50 nm. It was found from the XRD patterns the loading of TiO_2 on LUS-1 in solution did not have any effect on the order of the mesostructure (Badiei et al. 2009).

Many nanoporous materials are known to be electrical insulators, and their electron-beam sensitivity depends on the binding nature of the material. To overcome this challenge, more research is needed. Despite this weakness, the high-resolving power of electrons renders them very powerful for the characterization of nanoporous materials (Liu et al. 2013).

Fig. 7 Structure envelope generation using selected reflection (reproduced, with permission, from Chen et al. 2015)
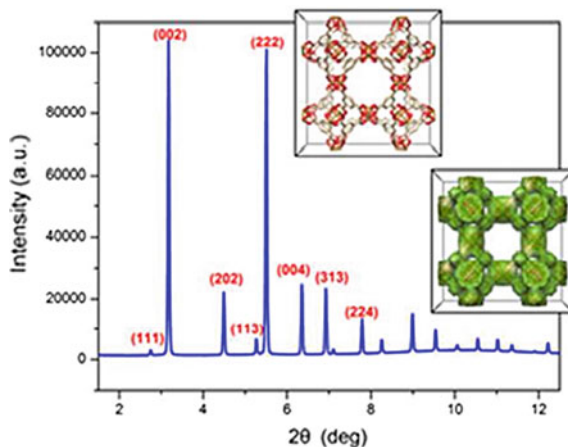
Yakovenko et al. developed a method to characterize the structure envelope (SE) of a nanoporous MOF from either single-crystal or PXRD patterns (Yakovenko et al. 2013). To envelop the structure, the intensities of reflection were employed in SUPERFLIP software, to solve the structure of MOF, as shown in Fig. 7 (Chen et al. 2015).

However, in many cases, regardless of using the highest-quality powder-diffraction data sets, XRD fails to predict a good structure model. It frequently happens for nanoporous solids that often feature a 2D periodicity but exhibit no long-range order in the third dimension. Moreover, low electronic contrast, pore fillers with no or different periodicity, lamellar compounds, etc., provide an extra challenge in this regard. In a conclusion, to characterize structural transformations in the flexible structure of MOFs, incorporation of the gas adsorption with X-ray powder diffraction enables to determine and obtaining information about the mechanism and kinetics of "gate opening," swelling, and breathing which is significantly important for innovative materials design for future applications (Krause et al. 2016).

2.2 Electron Crystallography

In cases that the crystals are too small for characterizing by SXRD or the structures too complex for determining by PXRD, electron crystallography (EC) offers the best alternative tool for the structural determination of materials (Liu et al. 2013). By utilizing the diffracted electron beams in an electron, EC entails solving the crystal structure of a very small single crystal. Moreover, this method can probe smaller length-scale electrons due to their intrinsically smaller wavelengths vis-à-vis X-ray crystallography. Due to the much stronger interaction of the electron with matter compared to the X-ray, this technique gives the ability to study nano-sized crystals. In another word, X-ray powder sample reacts like a single crystal under electron beams.

Moreover, electrons are negatively charged, and they can be focused by electromagnetic lenses to form images. Indeed, EC is becoming a more common technique for the determination of unknown zeolites structure (Terasaki et al. 2004). High-resolution transmission electron microscopy (HR-TEM) images as a powerful technique can offer comprehensive information about atomic arrangements in a crystal, and it gives direct information about possible disorders.

The three-dimensional electron tomography (3DTEM) technique has been used to monitor some materials that possess composition variations on a nanoscopic scale in a non-periodic manner. This method has been applied to study biological systems (Anderson et al. 2004), but the applications to materials science more broadly are just beginning to be realized, with a great deal of promise.

Sakamoto et al. created a method that uses EC to predict 3D structures of mesoporous materials with disordered structures by use of high-resolution electron microscopy (HREM) (Sakamoto et al. 2000). By applying this technique, the 3D structure can solve at the nanoscale level, including the sizes and shapes of the pores and cages, their arrangements as well as their connectivity, as well as the sizes of openings. Their technique was developed particularly for periodic structural arrangements with mesoscale ordering and showed a good capability for characterizing a variety of mesoporous silica SBA structures.

Later, in 2013, electron diffraction was applied for the determination of the structure of a protein in 3D using a method called MicroED (Shi et al. 2013). MicroED is a cryoelectron microscopy (cryoEM) method that establishes the atomic resolution of structures from very small three-dimensional crystals (Shi et al. 2013). As such, this is a highly applicable technique if crystals can only be synthesized on a scale that is too small for analysis via X-rays (i.e., typically less than 1 μm) (Anderson et al. 2004). This allows for ready determination of crystals with particularly short crystal morphology, such as needle crystals, and also nanocrystals that are deliberately grown at a very small scale. Some structure solutions are shown in Fig. 8.

3 Oxidation State and Coordination

Detailed information about the oxidation station, coordination number, and interactions of adjacent compounds is essential in a composite material, as this allowed for optimization of material characteristics, which can trigger improved device performance. These factors sometimes change depending on the reaction conditions.

In nanoporous metal oxide, controlling these metal oxides with stable and tunable oxidation states, and coordination geometries are crucial for tailoring their catalytic, electronic, and optical properties. Local arrangements of atoms (coordination environment) are achieved by applying methods like X-ray absorption spectra (XAS)—Solid-state NMR—IR & Raman. For the oxidation state of nanoporous techniques included—X-ray photoelectron spectra (XPS), XAS—UV-Vis spectra are used.
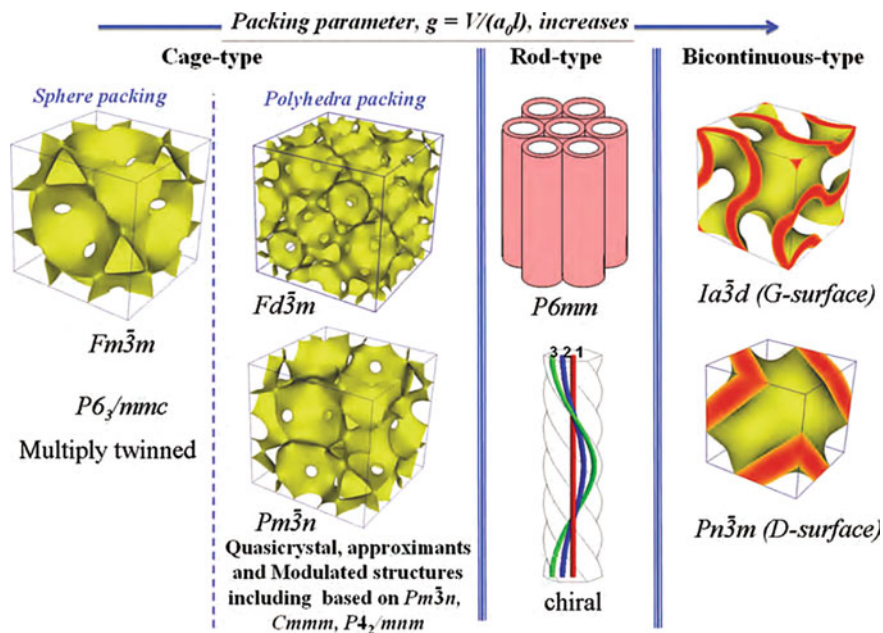
Fig. 8 Representative solved structure types of nanoporous materials via electron crystallography (reproduced, with permission, from Liu et al. 2013)

3.1 X-Ray Absorption Spectrum

X-ray absorption spectroscopy (XAS) is an enormously capable tool that provides information about the local structure around specific elements at the atomistic and molecular level (Koningsberger et al. 2000; Van Bekkum et al. 2001). X-ray absorption spectroscopy refers to experiments that the X-ray absorption coefficient $\mu(E)$ of the sample measures as a function of incoming energy (E) of the incident X-ray beam, in the vicinity of an absorption edge (at energy E_0) for one of the elements of the sample, denoted as the absorber.

Basic Principles of XAS

Passing a monochromatic beam of X-rays through a sample resulting partly scattered (diffracted) and partly absorbed (cf. Fig. 9a). Part of the incoming absorbed photons by atoms of the material causes a reduction in the intensity of the transmitted X-ray beam. Accordingly, the incident intensity I_0 will decrease depending on the absorption characteristics of the material. The Beer-Lambert Law (Eq. 2) is an empirical relationship between the absorption of X-rays to the properties of a matter that X-rays are passing through (Koningsberger et al. 2000).

$$I_t = I_0 e^{-\mu(E)t} \tag{2}$$
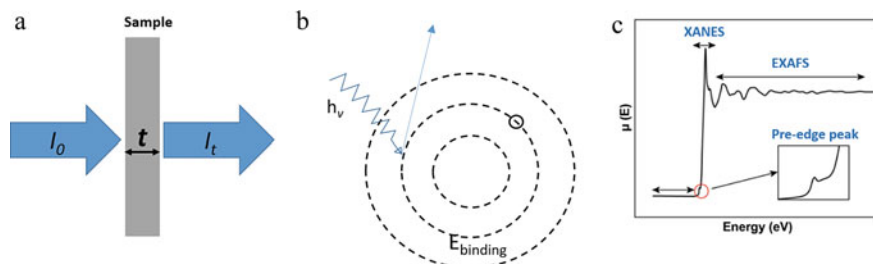
Fig. 9 **a** Schematic of the incident and transmitted X-ray beam, **b** Schematic of the photoelectric effect in terms of excitation of the different orbital, **c** Schematic of XAS including the pre-edge, XANES, and EXAFS regions

where $\mu(E)$ indicates the linear absorption coefficient, I_0 shows the incident X-ray intensity, I_t indicates the transmitted X-ray intensities, and t shows the thickness of the sample (Wang et al. 2019). When the binding energy of the core level is less than the energy of the incident X-ray, the electronic core level absorbs the X-ray (Van Oversteeg et al. 2017).

The flat area observed in Fig. 9c is for the situation that the incident X-ray energy is not sufficiently strong to excite the electrons to the highest unoccupied state or the vacuum and less than the binding energy of the electron in the element's orbital. Although, sometimes there are some unfavored transitions, including $1s$ to $3d$ in transition metals, which are indicated as a pre-edge peak (Fig. 9c). X-ray absorption near-edge structure (XANES) is called when the X-ray energy is strong enough to excite core electrons to the unoccupied state (the threshold energy or absorption edge), then X-ray is highly absorbed and leads to a sharp rise in the spectrum (Fig. 9c) (Martis 2011).

The XANES region is between 50 eV below the absorption edge toward 100 eV beyond the edge. As the spectrum is depending on the chemistry of the absorbing atom, thus, it is capable of extracting information for determining the oxidation state as well as the geometry of the element of interest. With further increase in X-ray energies, the area of the absorption spectra follows by the extended X-ray absorption fine structure (EXAFS), where expands into the range of thousands of eV beyond the absorption edge energy. The EXAFS function provides information on the next neighbor coordination shell of atoms; thus, information about the structure as well as the short-range environment of the X-ray absorbing atom can be achieved. The EXAFS function $\chi(E)$ is calculated from the:

$$\chi(E) = (\mu(E) - \mu_0(E))/\Delta\mu_0 \tag{3}$$

Here $\chi(E)$ represents the removal of X-ray absorption coefficient ($\mu(E)$) from background $\mu_0(E)$ and division by $\Delta\mu_o$ represents the normalization of the function.

To calculate $\chi(k)$ from the μ_{total} (experimentally acquired), a few steps are required to follow as shown in Fig. 10. The EXAFS function can be obtained from the absorption coefficients of the absorbing atom and the condensed phase:
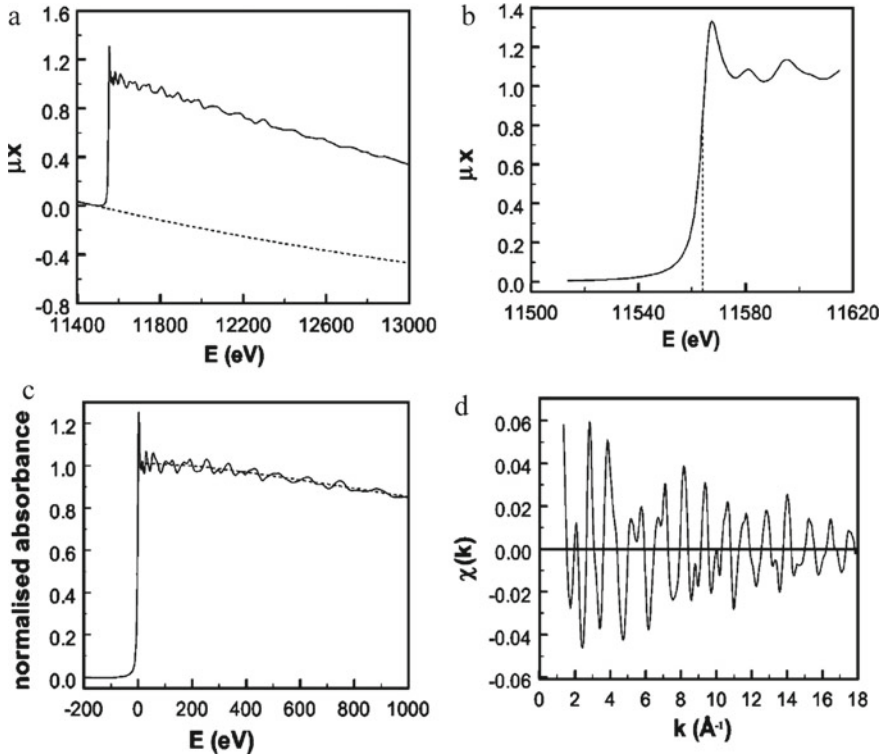
Fig. 10 Steps of extraction of the oscillatory part of an X-ray absorption spectrum for platinum foil: **a** removing the pre-edge background (- - -); **b** detecting the location of edge; **c** removing the post-edge background (- - -) and normalization; **d** transforming of the EXAFS spectrum to k scale through Eq. (4) after normalization (not displayed) (reproduced, with permission, from Koningsberger and Ramaker 2006)

$$\chi(k) = \sum_j \frac{N_j}{k R_j^2} \sin(2k \cdot R_j + 2\delta + \varnothing_j) \cdot |f_j(k)|$$

$$\cdot \exp(-2\sigma_j^2 k^2) \cdot \exp\left(-\frac{2V_i R_j}{k}\right) \tag{4}$$

Here N_j is the average coordination number of the jth shell; R_j is the average interval between the absorbent atom and the jth shell; δ is the phase shift of emitting atom σ_j is the Debey-Waller factor, k is the photoelectron wave vector, $f_j(k)$ is the amplitude of the back-scattering factor of the jth neighboring atom, φ_j is the phase shift of back-scattering atom in jth shell, and V_i is the inelastic scattering of photoelectron wave. Information on the local molecular coordination environment can be achieved by analyzing the EXAFS data.

In the study done by *Sinfelt and Meitzner*, the X-ray absorption edge was employed to investigate the oxidation states of pre-cursors during different steps in the preparing
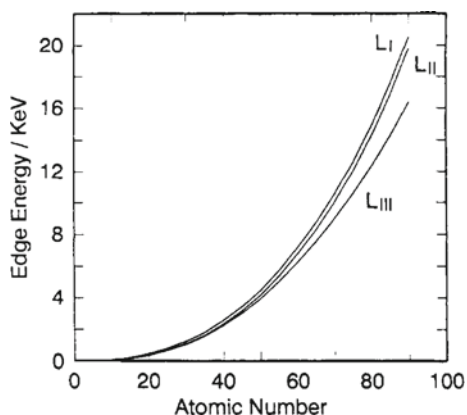
of a metal catalyst (Sinfelt and Meitzner 1993). Figure 11 indicates that in an absorption spectrum for each element, the absorption edges are observed at certain energies characteristic of the element. As shown in Fig. 11, the energies of the L_I edges (L_I edge is due to the excitation of electrons from 2s states) are more than L_{II} and L_{III} (L_{II} and L_{III} edges are due to the excitation of electrons from 2p states (Sinfelt and Meitzner 1993).

   As mentioned earlier, the absorption edge position reveals the information about the oxidation state, whereas a higher oxidation state is resulting in a shift of the absorption edge to larger energy. As shown in Fig. 12, there is a linear correlation between the Co K-edge position and the Co oxidation state (Timoshenko and Cuenya 2021). Therefore, for finding the oxidation state for the new materials, an established relationship between the edge location and oxidation state for known reference materials can be employed. In Fig. 12, E_s corresponding to 80% of the total area under the pre-edge and near-edge for Co_3O_4 and E_r shows 80% of the total area under
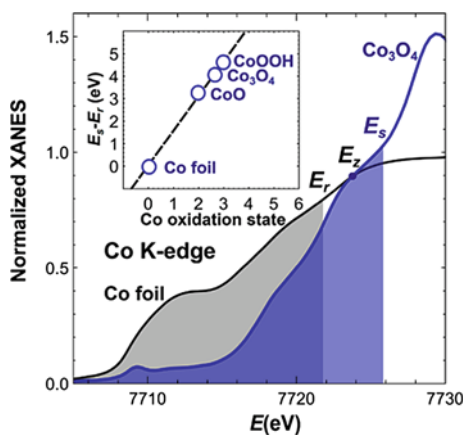
Fig. 13 Cu K-edge XANES spectra of Cu foil, CuO, and Cu_2O (Klaiphet et al. 2018)
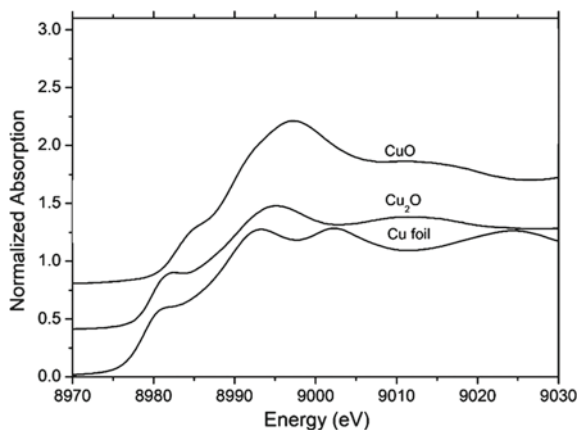
the pre-edge and near-edge for Co foil, whereas E_z is referring to the point that Co foil spectrum crosses the of Co_3O_4 spectrum. Figure 12 displays a nearly linear relationship between $E_s - E_r$ and the Co oxidation state.

Figure 13 shows an example of a comparison of obtained XAS spectra from Cu foil (0 oxidation state), CuO (+2 oxidation state), and $CuCl_2$ (+2 oxidation state) (Klaiphet et al. 2018). As shown in this figure, the $\mu(E)$ of both Cu_2O and CuO at pre-edge is shifted to higher energies compared to Cu foil, which is expected based on their higher oxidation states.

3.2 X-Ray Photoelectron Spectrum

X-ray photoelectron (XPS) is a technique for the determination of the energy of photoelectrons released from the sample impacted by irradiating with X-rays. The measured kinetic energy of core electrons allows calculation of the binding energy of the ejected electron in the material. While the binding energy of the core electrons is unique to each element, any slight change in the binding energy of elements is dependent on the environment and oxidation state of the atom. Therefore, XPS is one of the most established and non-destructive methods for the determination of oxidation states (Alov 2005).
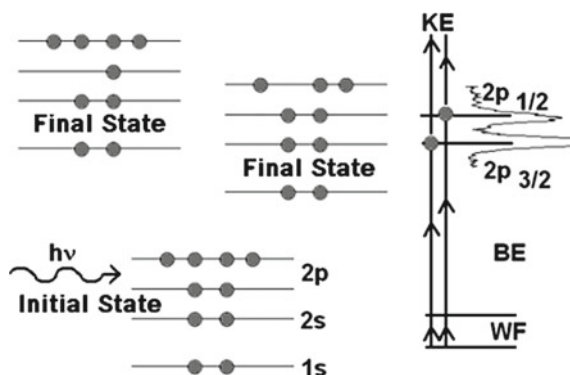
Principles of XPS
The relative positions of electronic energy levels and XPS Peaks are illustrated in Fig. 14. Generally, Mg Kα ($h\nu = 1253.6$ eV) or Al Kα ($h\nu = 1486.6$ eV) were applied as the X-ray light sources.

The kinetic energy (E_k) of the electron is express as:

$$E_k = h_\nu - BE - \phi \tag{5}$$

Fig. 14 Electronic energy levels and XPS peaks

where h is Planck's constant, ν is the frequency of the incident radiation, *BE* is the binding energy of the photoelectron, and ϕ is the work function (Son et al. 2020). When energy applies to the specimen, the electron excites and tends to depart from the nucleus and reaching the level that the binding energy of the nucleus is equal to the binding energy of the electron. The irradiated X-ray has high energy and is needed to emit the electrons of the *K* shell with considerable binding energy by the photoelectric effect (Fig. 14). As each element has its specified bonding energy, then analyzing the binding state of particular atomic orbitals of particular elements is feasible. Changing binding energy can be used to determine the oxidation state of the metal.

Lee et al. (2014) studied the porous properties of nanoporous manganese oxides. Among them, Mn_3O_4 and Mn_5O_8 exhibit similar textual properties including similar morphology, surface area, and crystal size of framework, but different oxidation states (Lee et al. 2014). Figure 15 shows the oxidation states of three nanoporous manganese samples (MnO, Mn_3O_4, and Mn_5O_8) determined by XPS. The Mn 3s XPS spectra revealed that the increase in the oxidation number of samples resulting in a gradual shift of the location of peak corresponded to the lower binding energy to the higher energy.

Along with subtracting background spectra, peaks from XPS are usually a combination of several smaller peaks, as shown in Fig. 15, so it is important to split the peaks (Raja and Barron 1934). This can be done with the software bundled with XPS equipment. Generally, the binding energy of each metal increases with a higher oxidation state.

Figure 16a shows a high-resolution Fe $2p_{3/2}$ XPS of a mixture of iron oxide powder with FeO (Fe^{2+}) and Fe_2O_3 (Fe^{3+}) (Wright and Barron 2017). The change in the oxidation state of the iron results in a shift in binding energy to higher levels. Another example is Cr_2O_3 $2p_{3/2}$, which appears as multiple peaks (Fig. 16b) (Wright and Barron 2017). Multiple peaks could also appear due to "charge-transfer satellites," from the sudden creation of a core-hole due to the XPS process.

Reference compounds of the metal with known oxidation states can be used to assist in the determination of oxidation states, from analysis of the peaks. For
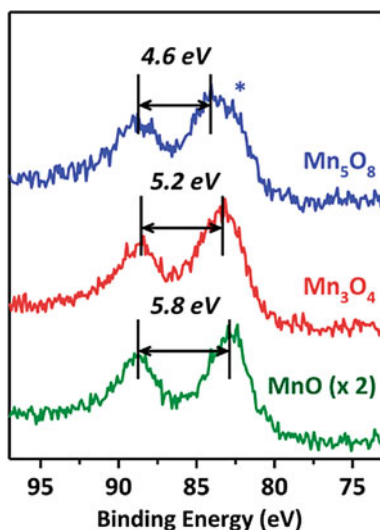
Fig. 15 Mn 3s XPS spectra of MnO, Mn_3O_4, and Mn_5O_8. The blue star shows the existence of low-valent (Mn^{2+}) manganese species in Mn_5O_8 (reproduced, with permission, from Lee et al. 2014)
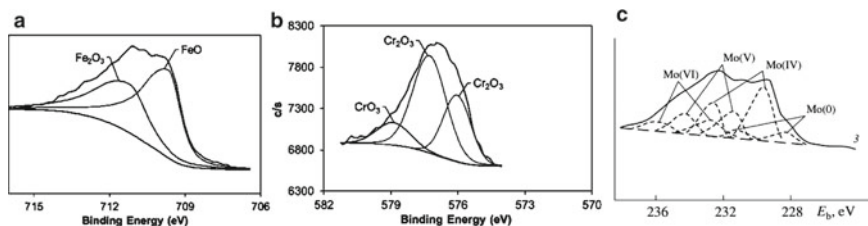
Fig. 16 a High-resolution Fe $2p_{3/2}$ XPS of mixed iron oxide powder, **b** High-resolution Cr $2p_{3/2}$ XPS peak for Cr_2O_3 showing an example of complex splitting, **c** Mo 3d XPS spectra of surface cleaned molybdenum crystals before (top solid line) and after (bottom dashed lines)

unknown vanadium oxide, for example, spectra of known vanadium oxides can be obtained and binding energies compare with the unknown. Moreover, the integration of the peaks can specify the relative amounts of each oxidation state.

The XPS database and binding energies of various metal complexes can be compared to those achieved in the *National Institute of Standards and Technology* (NIST).

However, there are some limitations in determining the oxidation state by XPS. The binding energy commonly increases with oxidation states, overlapping binding energy can happen for some compounds with the same metal but different oxidation states. For example, as illustrated in Table 1, $FeSO_4$ (Fe^{2+}) has a higher $2p_{3/2}$ binding energy than Fe_2O_3 (Fe^{3+}) *(*Raja and Barron 1934).

Table 1 Fe $2p_{3/2}$ XPS binding energy for various iron species

Species	Fe oxidation state	Fe $2p_{3/2}$ binding energy (eV)
Fe	0	706.3
FeO	2+	709.1
FeSO$_4$	2+	711.0
Fe$_2$O$_3$	3+	710.6

Even with limitations, XPS is a powerful technique that provides information on oxidation states materials including nanoporous materials.

3.3 UV–Vis Spectra

UV/Visible spectroscopy use to quantify the extinction (scatter + absorption) of light passing through a sample. This method is utilized to identify, characterize, and study nanomaterials, as these materials boast special properties which are sensitive to the size, shape, concentration, and refractive index near their surface. Because of its distinctive twin advantages, sporting inexpensive and facile analysis of substances, a UV-visible spectrometer is utilized in many disparate fields.

The UV radiation excites the electrons from the ground state to the state with a higher level of energy. The electromagnetic radiation between 190 and 800 nm and is divided into the range between the ultraviolet region (190–380 nm), and the visible region falls between 380 and 750 nm (Fig. 17).

To quantifying the sample's wavelength-dependent extinction spectrum, the intensity of UV/visible beam is quantified before and after passing through the sample and compared at each wavelength. By applying the Beer-Lambert Law, the absorption of spectra generated from these samples at given wavelengths can be related directly to the sample concentration. Indeed, the Beer-Lambert Law is based on the concept
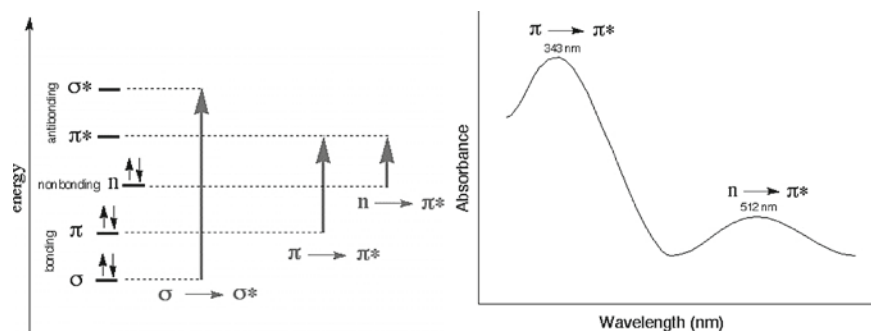
Fig. 17 *n* to π* and π to π* transitions occur in the UV-vis range, while σ to σ* transition needs absorption of a photon with a wavelength out of UV-vis region

Fig. 18 UV-visible absorption spectra of 1 (Co^{III}) and its reduced Co^{II} analog with $\lambda = 480$ nm and Co^{I} analog with $\lambda = 572$ nm and $\lambda = 685$ nm (reproduced, with permission, from Basu et al. (2016)
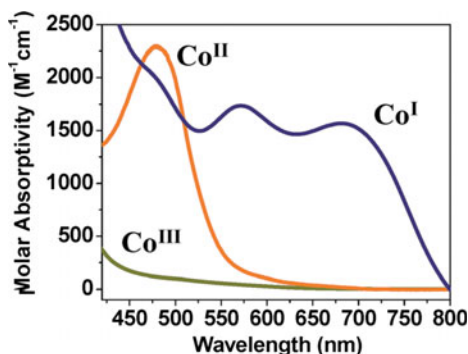
that the larger the number of molecules able to absorb light of a specific wavelength, the larger the extent of light absorption. Indeed, in such a way, it is possible to access molecular structure and oxidation state via UV-VIS spectroscopy.

To illustrate this important concept, the UV-Vis applied for different oxidation states of e 3+, 2+, and 1+ oxidation states of the metal (Co) is illustrated in Fig. 18 (Basu et al. 2016).

3.4 Nuclear Magnetic Resonance (NMR)

To characterize nanoporous materials, even with using very high-quality powder-diffraction data sets, a traditional strategy such as X-ray fails in finding a good structure model for many cases (Taulelle et al. 2013). This limitation is more significant in the case of nanoporous solids, due to some of their properties, for example, some nanoporous have a 2D periodicity without order in the third dimension, low electronic contrast, pore fillers without or with various periodicities. Among the substitute strategies, nuclear magnetic resonance (NMR) crystallography is an important analytical method that offers an efficient way to determine the structure of nanoscale materials.

The phenomenon of NMR relies on the nuclei of atoms featuring magnetic properties which can be used to provide chemical information. In the NMR technique, when the nuclei that have non-zero spin located in a strong magnetic field, it creates a small energy difference between the spin-up and spin-down states. Physiochemical characteristics, such as structure, purity, and functionality, can be analyzed by this method. Recently, pulsed field-gradient NMR has been applied for evaluation of the diffusivity of nanomaterials, resulting in determining the size and species interaction. However, there are several disadvantages to this technique such as time-consuming and low detection sensitivity. Over the last decades, NMR has been widely used as a

non-destructive technique to characterize nanoporous materials featuring pore sizes from 1 to 100 nm.

The Basic Principle of NMR

A general Hamiltonian, H, describing the interactions experienced by a nucleus of spin I may be expressed as:

$$H = H_Z + H_D + H_{CS} + H_{SC} + H_Q \tag{6}$$

where H_Z: Zeeman interaction, H_D: dipolar interaction, H_{CS}: chemical shift, H_{SR}: spin-rotation interaction; H_Q: nuclear spin and quadruple (Table 2).

Therefore, the precise energy-level splitting is sensitive to some nuclear spin interactions, which are assessed by the physical and chemical properties of the nuclear spin system.

Owing to the sensitivity of changes in the coordination environment, this technique is applied as an element-specific structure-analyzing technique. Each of the nuclei in a crystal has its characteristics, such as the spin number, which can be 1/2 or more. When the number of measurable nuclei is larger, the number of possible one-dimensional (1D) and two-dimensional (2D) NMR experiments which can be obtained is much larger.

Solis state NMR (SsNMR) has been demonstrated as a complementing technique to diffraction techniques for determining the structure of nanoporous materials.

The environments of framework atoms of porous materials can investigate by the NMR spectroscopy of ^{29}Si, ^{27}Al, ^{31}P, ^{69}Ga, or ^{71}Ga nuclei, or ^{1}H, ^{7}Li, ^{23}Na nuclei that are charge-compensating ions. These measurements can give information about the number of inequivalent atomic sites as well as the multiplicity of these sites. Some recent developments in NMR are the ability to probe inter-nuclear distances, increase the power of NMR (Taulelle et al. 2013).

Taulelle and coworkers studied the application of NMR crystallography for nanoporous materials (Taulelle et al. 2013). They (Taulelle et al. 2013) showed that the use of NMR data associated with diffraction methods and modeling can provide systematic ways to achieve the structure models. This is especially important for the structure determination of the complex nanoporous crystals.

1D collection of data can provide different structural information. From the isotropic chemical shifts, information such as the nature of the neighboring atom and the coordination number of the atom can be achieved. For instance, ^{7}Al in 4-, 5-

Table 2 Approximate range of different spin interaction (in Hz) (NMR Interactions 2020)

Zeeman	10^8
Dipolar	10^3
Chemical Shift	10^3
Scalar Coupling	10
Quadrupolar	10^6

Fig. 19 ^{27}Al chemical shift variation in most types of porous solid
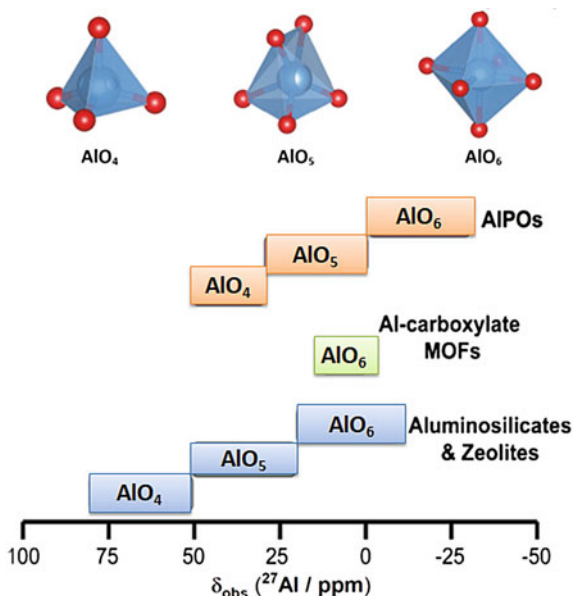
or 6-fold coordinated (Fig. 19), or ^{13}Cin 2-, 3- or 4-coordination state (hybridization sp, sp^2, sp^3), or the environment of SiO$_4$ in Q^4, Q^3, Q^2, Q^1, Q^0 environments (n of Qn refers to the number of bridged oxygen atoms in the first coordination sphere of the Si atom) can be determined as 1D ^{27}Al, ^{13}C and ^{29}Si MAS NMR spectra, respectively (Taulelle et al. 2013).

Wen et al. using NMR in both 1D and 2D to investigate the electrochemical redox activity between V^{5+} and V^{2+} oxidation states (Wen et al. 2019). Solid-state 2D ^{27}Al 3Q-MAS and 1D ^{27}Al single-pulse NMR spectrum obtained from precipitation of reaction between V$_2$O$_5$ and Al$_2$Cl$_7$ (cf. Fig. 20a, b, respectively). The ^{27}Al single-pulse NMR spectrum showed that the precipitate contains aluminum moieties for three different coordination environments: Al^{IV} (~85 ppm), Al^V (~34 ppm), and Al^{VI} (~4 ppm). The 2D ^{27}Al 3Q-MAS spectrum correlates the MAS dimension (horizontal) with an isotropic dimension (vertical). The 1D slices of the different Al coordination environments are shown in Fig. 20c.

Another example to emphasize the determination of oxidation state from NMR is shown in Fig. 21. ^{31}P MAS NMR spectrum was obtained to determine the oxidation state of phosphorus. Two peaks at −10 (A$_1$) and −6 (A$_2$) ppm indicated two non-equivalent positions of the phosphine present in the framework. Another peak was shown at 35 ppm is corresponding to oxidized phosphine (B). A phosphine fraction of 85% was observed for the peak area of combining A$_1$ and A$_2$ compared to the peak area of B (Morel et al. 2015).
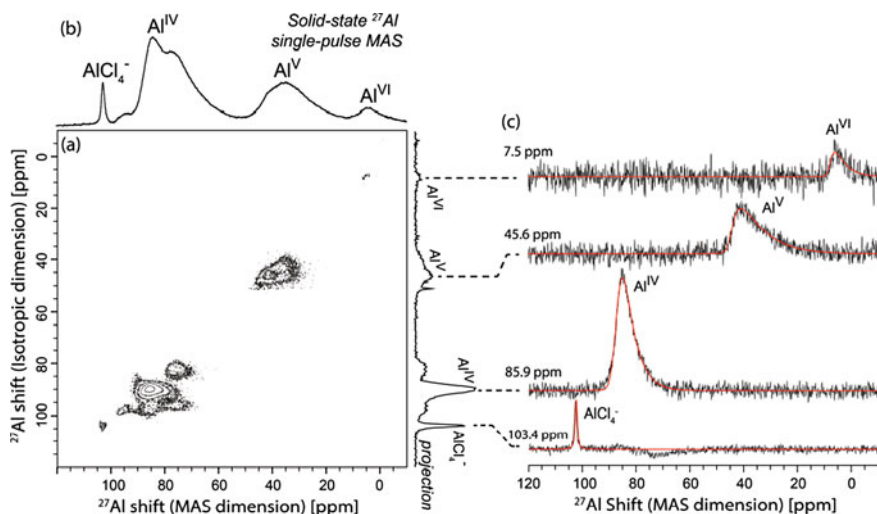
Fig. 20 **a** SsNMR of 2D ^{27}Al triple-quantum (3Q)-MAS NMR spectra. **b** A separately acquired quantitative 1D ^{27}Al single-pulse MAS spectrum is displayed, where ^{27}Al signals associated with 4-, 5-, and 6-coordinated Al moieties are labeled. **c** 1D slices of different Al coordination environments (reproduced, with permission, from Wen et al. 2019)

Fig. 21 ^{31}P MAS NMR spectra (right) of LSK-15. NMR signals are labeled according to phosphorus oxidation state (with permission from Morel et al. 2015)
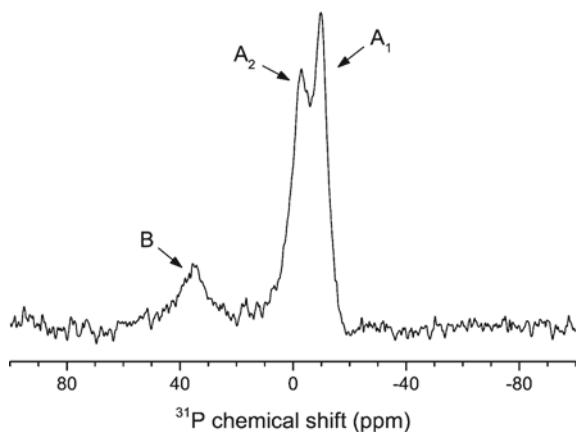
4 Chemical Composition

The chemical composition of nanoporous materials can be determined by elemental analysis techniques, including inductively coupled plasma-atomic emission spectroscopy ICP-AES and energy dispersive X-Ray spectroscopy (EDX).

ICP-AES is an emission-based spectrophotometric method to detect more than 70 elements with a concentration range of ppb to ppm. ICP-AES employs the fact that
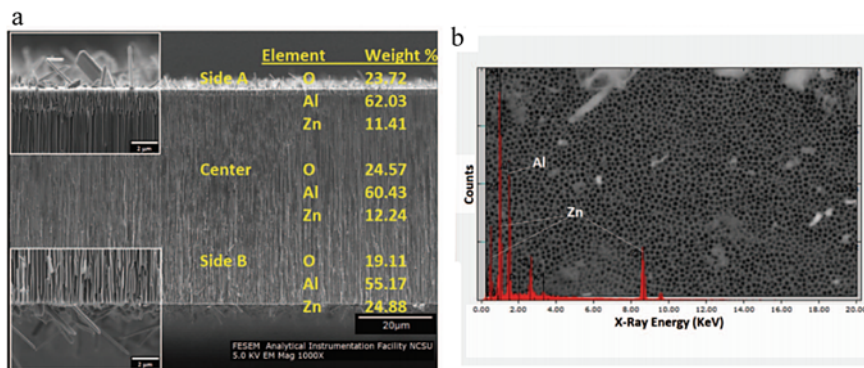
Fig. 22 **a** Cross-section view of a 20 nm nanoporous anodized aluminum oxide with an 8 nm ZnO coating membrane, showing the crystals present on the surface. **b** EDX spectrum obtained from the 200 nm circular pore side, showing Al and Zn peaks (reproduced, with permission, from Petrochenko et al. 2013)

when excited electrons return to the ground state, they emit energy at a given wavelength. Every element emits energy at unique wavelengths particular to its chemical character and ICP-AES select a single or a very few wavelengths for a given element (Ghodke 2015). By determining the emitted wavelengths and their intensities (with intensity proportional to concentration), this technique can determine the elemental composition of the sample. This technique can analyze all elements, except argon.

The elements present in the nanoporous materials can be identified by applying EDX analysis (Zhao et al. 2019). EDX technique incorporates with imaging tools such as scanning electron microscopy (SEM) and transmission electron microscopy (TEM) can detect the elemental composition of the imaged area. The data provided by EDX analysis contain spectra presenting peaks corresponding to making up the composition of the analyzed sample.

As an example, Fig. 22b shows an EDX spectrum of a nanoporous ZnO-coated anodized aluminum-oxide membrane (Petrochenko et al. 2013). Distinguished Zn and Al peaks were observed on spectra that were acquired from the membrane (Petrochenko et al. 2013).

A comparison between elemental analysis performed by CP-AES for Phosphotungstates (MPW) and EDX is presented in Table 3 (Ghodke 2015).

5 Pore Analysis

The gas-sorption analysis is among the most useful experimental techniques for structural characteristics of open porous solids such as specific and external surface area, total and micropore volume of nanoporous materials (Thommes and Schlumberger 2021). Generally, gas-sorption probes the interaction between gas and the sample,

Table 3 Elemental analysis by ICP-AES and EDX

Materials	% by ICP-AES analysis			% by EDX analysis (atomic %)			
	M (IV)	P	W	M (IV)	P	W	O
ZrPW	Zr = 26.88	4.96	25.37	Zr = 6.79	18.53	20.67	–
TiPW	Ti = 14.84	4.64	24.97	Ti = 46.61	37.99	15.40	–
SnPW	Sn = 36.82	4.67	29.41	Sn = 59.33	23.31	17.37	–
12-TPA/ZrO$_2$-20	Zr = 58.62	0.09	16.48	Zr = 28.75	0.11	3.44	67.70
12-TPA/TiO$_2$-20	Ti = 46.76	0.08	16.17	Ti = 28.63	0.15	0.88	70.34
12-TPA/SnO$_2$-20	Sn = 60.01	0.08	18.04	Sn = 18.40	0.12	2.57	78.92

From Ghodke 2015, with permission

this can happen in microporous or mesoporous adsorption, also in monolayer and multilayer adsorption (Keshavarz et al. 2021). Brunauer, Emmett, and Teller (BET) are the most popular method based on physical adsorption of a gas on the adsorbent surface for the determination of the specific surface area of porous materials. The BET isotherm is applicable for a sample covered by more than one layer of gas molecules:

$$\frac{P}{P_0} = \frac{1}{a_m C} + \frac{p_0(C-1)}{a_m C} \tag{7}$$

where P_0 is the tension of saturated vapor at a particular temperature, a_m is the specific monolayer capacity (mol/g), and the parameter C is a constant including adsorption and condensation heat (Širc et al. 2012).

The adsorption isotherm represents the dependency of the adsorbed gas on pressure at a constant temperature. The specific surface area can be measured according to

$$A_{sp}(\text{BET}) = N_A . a_m . \sigma \tag{8}$$

where A_{SP} (BET) is the BET specific surface area of adsorbent, N_A is the Avogadro constant, and σ is the area of the sample occupied by the adsorbate in the monolayer.

The original derivation of the BET relation is based on the assumption that a statistical multilayer coverage of a non-microporous surface (Reichenauer 2011). BET theory assumes the interactions between neighbor adsorbed molecules just happen in a vertical direction. Another assumption of this theory is that the adsorption energy is not dependent on the type of the adsorption sites (Sing et al. 1985; Lowell 2004).

The Barrett, Joyner, and Halenda (BJH) method which is based on the Kelvin equation (which relates the pressure to pore size) is the most widespread method to calculate the pore volume and pore size distribution in a mesoporous solid (Barrett and Halenda 1951). BJH theory assumes that the shape of the pore is cylindrical.

It was shown that the BJH method for narrow mesopores (pore diameter < 10 nm) underestimates pore size by approximately 20–30% (Thommes et al. 2015). This error can be minimized by applying methods based on molecular simulation or density-functional theory (DFT) software which is applicable for different types of pore geometries.

Advanced statistical thermodynamics models, including DFT, molecular dynamics (MD), and Monte Carlo (MC) simulations, yield a molecular-level acquaintance of adsorption in pores and apply to characterize nanoporous materials. A nonlocal density-functional rheory (NLDFT) approach is a precise method that is offered for the characterization of nanoporous materials. The NLDFT has been established to predict the adsorption/desorption isotherms in nanopores of various geometries with pore diameters about 0.3–100 nm (Reichenauer 2011). The results of pore-size distributions of mesoporous calculating from the NLDFT method are in good agreement with other techniques applied for characterization of pore structure (transmission electron microscopy and X-ray diffraction).

The International Union of Pure and Applied Chemistry (IUPAC) recommended the classification of isotherms regarding physical-adsorption characterization that is shown in Fig. 23. Based on their classifications: Pores are typically microporous which yield to Type I isotherms; nonporous or pores with diameters exceeding micropores adsorbents give Type II isotherm; Type III and V isotherms observed when there are small adsorbent-adsorbate interactions potential and are associated with a pore diameter in the range of 1.5–100 nm; Type IV isotherms represent mesoporous

Fig. 23 Classification of adsorption isotherms (reproduced, with permission, from Barton et al. 1999)
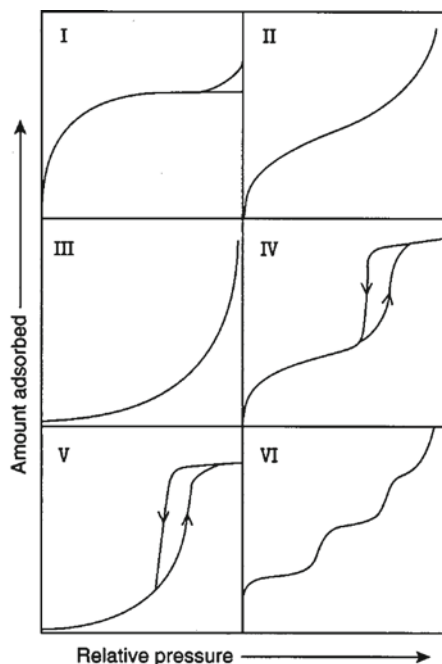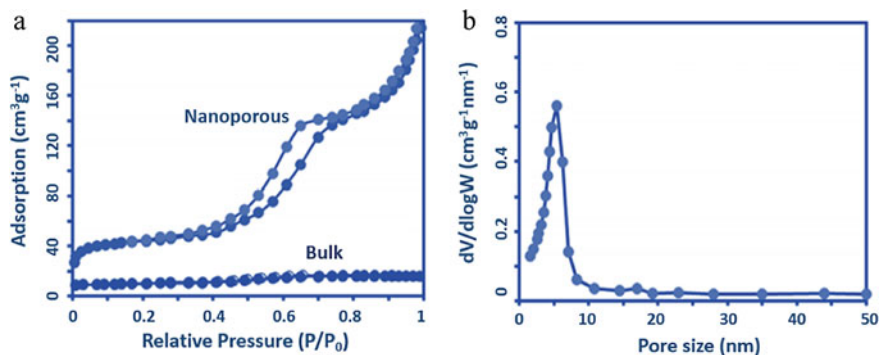
Fig. 24 **a** N_2 adsorption-desorption isotherms of the balk and nanoporous $NiMoO_4$ samples, **b** BJH pore-size distribution plot of the nanoporous $NiMoO_4$

materials; and Type VI isotherms indicate layer-by-layer adsorption on a nonporous surface. The suitable selection of the adsorption isotherm, along with the proper pore-size calculation such as molecular simulation or DFT, allows the possibility to evaluate precisely the pore-size distribution within the porous material.

As an example for this section, the N_2 adsorption-desorption isotherms, as well as the BJH pore-size distribution for nanoporous and bulk NiMoO4, are illustrated in Fig. 24 (Moosavifard et al. 2014). As shown in Fig. 24a, the nano-cast sample has a type IV isotherm that is characteristic of nanoporous or mesoporous materials, while the bulk sample has a type II isotherm representing nonporous or macroporous materials. Moreover, the pore-size distribution of nanoporous $NiMoO_4$ calculated by BJH (Fig. 24b) shows a uniform pore-size distribution. Then their sample showed a high-ordered nanoporous structure with narrow pore-size distribution and large surface area.

Determination of pore sizes and pore-size distributions from N_2 isotherms of some nanoporous materials like microporous polymers suffer from an absence of proper models. As shown in Fig. 25b, the acquired results from the same isotherm were compared by the NLDFT and Horvarth–Kawazoe (HK) analysis, which are two predominant methods. Although both models are based on the same assumption, significant differences between the models are evident.

Using nitrogen in gas-sorption experiments has a certain drawback in comparison to noble gases such as Argon: it experiences a stronger interaction with polar moieties of polymers because of its quadruple moment. Moreover, it is possible that some of the pores are not occupied by nitrogen due to the relatively large size of nitrogen. Despite these limitations, nitrogen sorption is the most used technique for the analysis of nanoporous materials mostly due to its accessibility in many laboratories. Recently, the use of carbon dioxide as an adsorbent to characterize ultra-micropores has become more common in the analysis of microporous materials. This method is well known for analyzing activated carbons.
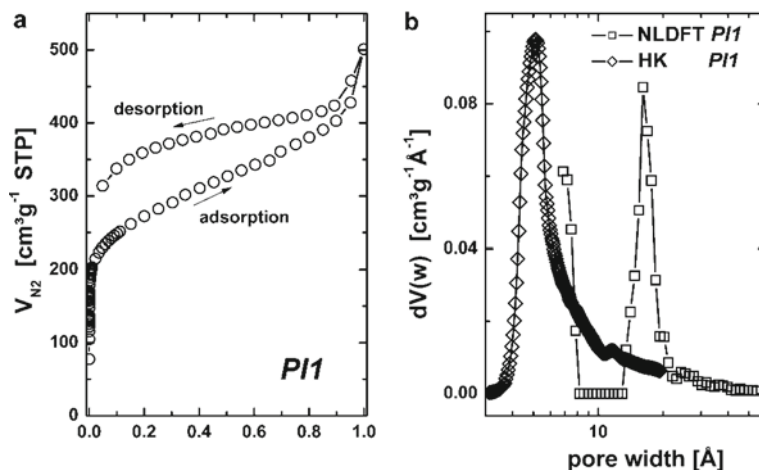
Fig. 25 a Nitrogen sorption isotherm of a spirobiuorene-based polyimide network. **b** Comparison of the micropore analysis data obtained from the HK and NLDFT model (Weber et al. 2008, with permission)

6 Morphology: SEM

Scanning electron microscope (SEM) is a very common technique for observing and quantifying the shape, surface texture, and particle distribution of materials and provides information about morphology, topography, composition, and crystallography of materials, including nanoporous materials. This imaging technique allows for direct visualization and investigation of nanoporous materials with advanced structures. Due to high resolution along with a deep depth of focus, SEM is considered a powerful visualization tool for nanostructures analysis, including nanoporous materials. Recent progress in the resolution of SEM and the large depth of field allows for the capture of the microstructures of the sample with three-dimensional information. Therefore, analysis of SEM images has highlighted attention in the nanostructured world, especially in nanoporous materials, as the complex networks between the pores and the walls appear vividly under an SEM. The structure of various places of the nanoporous sample can be visualized directly by SEM. Therefore, so-obtained images from SEM enable useful and important details to compare the local structures with the whole sample and are considered as an alternative to observing pores.

Applying a method developed by Zhou & Qiao through a large number of SEM images were used to provide detailed structural information such as 2D pore and wall size, fractal dimension, and porosity (Zhao and Qiao 2016). This method for SEM-image polishing (SIP), according to the quantitative SEM-image analysis (QSIA) technique for nanoporous materials, provides the possibility of fast and accurate data mining at the nanoscale in nanoporous materials. However, the lack of structural

information is one of the foundational difficulties in allowing for quantitative image analysis.

The Basic Principle of SEM

In an SEM, a high-energy beam is emitted from electrons that interact with atoms on the surface of the specimen or near it. The resolution attained by SEM is mainly dependent upon the operating parameters (around 1 nm). To prevent a repulsive reaction of an electron beam, the surface of a non-conductive sample is usually coated with a very thin layer of gold or platinum. However, the sputter coating can lead to removing the atomic number-contrast and elemental composition analysis.

The depth of field (Δf) defines as the distance within which the sample remains in acceptable focus which depends on two factors including magnification (M) and the beam convergence (α_0):

$$\Delta f \approx \frac{0.2\,\text{mm}}{M\alpha_0} \tag{9}$$

where the factor of 0.2 mm is regarding the resolution of the human eye over the SEM images.

Figures 26a–c illustrates that the three-dimensional pore structure of the nanoporous polyethylene was analyzed by SEM.

SEM images provide images of the sample with information about surface defects like cracks, etching residues, depressions, differential swelling, and perforations. However, there are some drawbacks of SEM, such as degradation of the sample, which alters or destroys details and consequently changes results and conclusions. Moreover, there is the possibility of damage to the sample by the SEM's electron beam. In addition, SEM is not able to image wet samples, due to possible damage
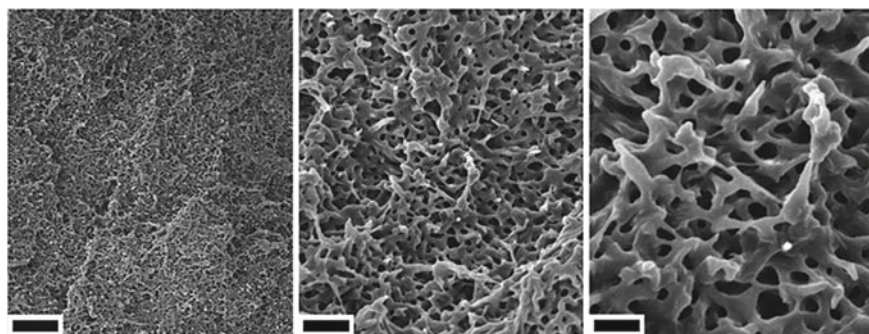
Fig. 26 Morphology of a bicontinuous microemulsion-derived, nanoporous polyethylene using SEM, two right images are a higher-magnification view of the central part of the area illustrated in the left image. The scale bars from left to right: 3 μm, 750 nm, and 300 nm, respectively (Jones and Lodge 2012, with permission)

during vacuum required during operation. Another limitation of SEM is when applied to capture measurement involving height or process color image.

7 Pore Structure: TEM

Transmission electron microscopy (TEM) is considered the most widely used technique in characterizing nanomaterials, due to its sub-nanometer resolution and the capability of directly observing very small pore structure. The image of nanomaterials provided by TEM at a resolution of atomic dimensions ranging from ~100 nm to single atom size. This method has the ability of imaging a variety of nanostructures such as nanoporous materials. The highly detailed images provide valuable insight into structural information including particle size and morphology and high-resolution images of the framework at an atomic level.

Similar to SEM, imaging the non-conductive samples is challenging for TEM; therefore, for some metal oxides before imaging, covering the sample with a thin layer of gold is recommended. One disadvantage of TEM is the difficulty in preparing the samples since the grids for the sample holder are very tiny, and the sample must be sufficiently small (100 nm thin) or a very fine powder. However, the methods of preparing the sample for TEM might change the underlying pore size and pore structure.

Recently, this technique has encountered very promising breakthrough progress in the aberration correction for atomic-level imaging, the cryogenic TEM for imaging biological specimens, and the new in situ instrumentation. Excitingly, in situ TEM started to be a prevailing technique to observe reactions at the nanoscale level. TEM boasts providing high temporal and spatial resolution, as well as direct visualization of any changes in structural, morphological, or elemental distribution at the nanoscale which considered as an advantage of this method compared with other in situ techniques such as scanning-tunneling microscopy (STM), atomic force microscopy (AFM), and various X-ray methods.

TEM images of nanoporous materials include micropores pore (size < 2 nm), mesoporous (2–50 nm), and macrospores (size > 50 nm) with examples are shown in Fig. 27 (Fayed et al. 2016, with permission).

TEM offers more advantages compared to SEM to provide spatial resolution in high-quality and analytical measurements. Moreover, by utilizing TEM, it is possible to visualize the internal connectivity. TEM images offering instant feedback and consequently allowing control during the nanopore drilling processes.

To glean a better comparison between two imaging technologies for nanoporous materials, Fig. 28 shows the SEM and TEM of nanoporous manganese oxides (Lee et al. 2014).
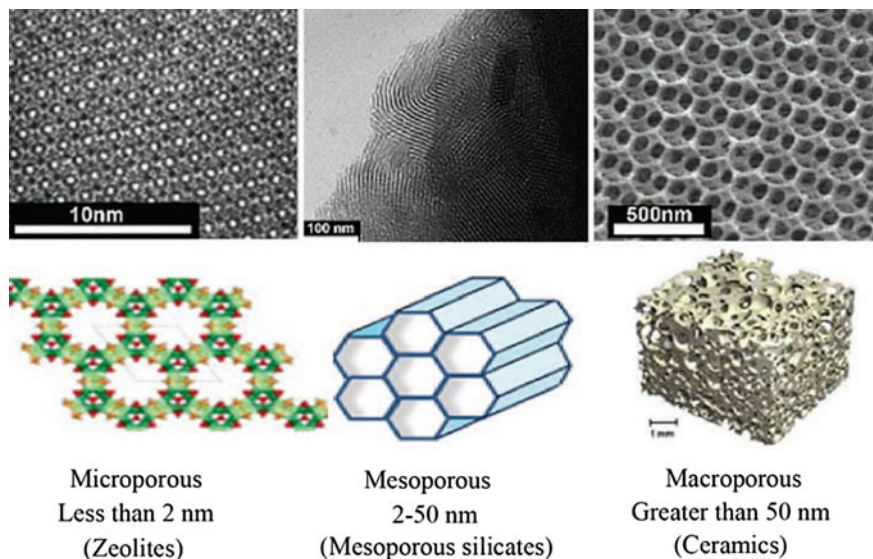
Fig. 27 Three categories of nanoporous materials and their TEM images (Fayed et al. 2016, with permission)
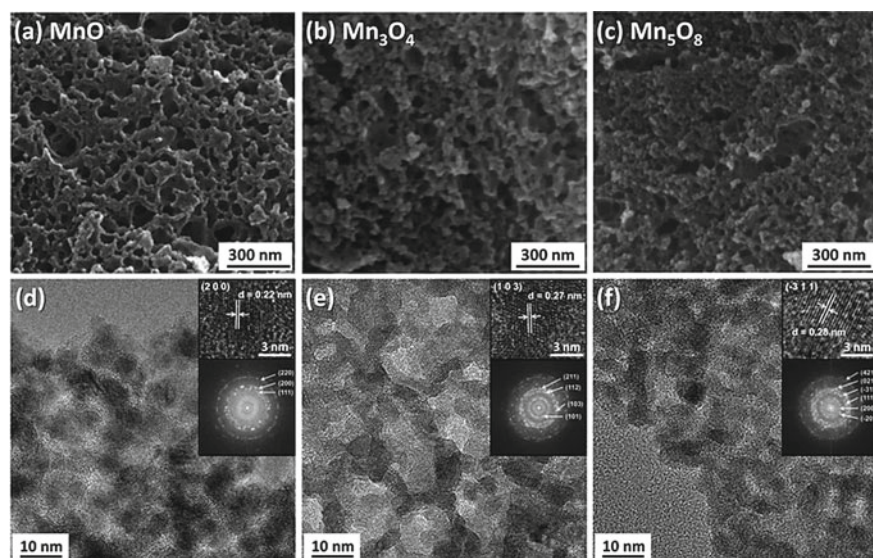
Fig. 28 Comparing the SEM images (**a–c**) and TEM images (**d–f**) of converted manganese oxides. (**d–f**, inserts) HR-TEM images of nanoporous MnO (**a, d**), Mn_3O_4 (**b, e**), and Mn_5O_8 (**c, f**) (Lee et al., 2014, with permission)

8 Conclusions

Comprehensive knowledge of the structural properties including pore size and connectivity can assist to improve the efficiency of nanoporous materials in a disparate different fields, such as, *inter alia*, gas storage, separation, and catalytic processes. From this perspective, huge advances have been done recently regarding the physisorption characterization of nanoporous materials. The IUPAC technical report in 2015 outlined their suggestions for the surface and pore-size analysis.

Structural and morphological characterization for nanoporous materials can obtain by various techniques including X-ray diffraction techniques, electron crystallography, small-angle X-ray, gas adsorption, and neutron scattering, together with mercury porosimetry, scanning electron microscopy, and transmission electron microscopy, as well as nuclear magnetic resonance (NMR) methods. The oxidation state and coordination properties can be analyzed adopting UV-Vis, X-ray absorption spectroscopy, NMR, etc. Inductively coupled plasma mass spectrometry (ICP-MS), energy dispersive analysis of X-rays (EDAX), and X-ray photoelectron spectroscopy (XPS) are generally using for elemental analysis of nanoporous materials. Evaluation of surface area and pore size is performed by N_2 adsorption-desorption isotherm. Each of these methods has advantages, disadvantages as well as a limited application range.

One important future direction in nano- and porous-materials analysis lies in the use of molecular simulation as an important method to accompany experimental materials characterization. Using both empirical-potential models and electronic-structure methods allows for the simulation of atomic- and nanoscale defects and surface/bulk features, and the extraction of spectroscopy results therefrom, which can then be compared with experimentally. However, excitingly, this approach can be used for predictive materials design as a prototyping tool in nanomaterials discovery. In such a way, we can determine desirable spectral features from molecular simulation and "tune" material properties, such as defects and nanoscale geometry features, to arrive at an optimal porous-materials design.

References

Alov, N.V.: Determination of the states of oxidation of metals in thin oxide films by X-ray photo-electron spectroscopy. J. Anal. Chem. **60**(5), 431–435 (2005). https://doi.org/10.1007/s10809-005-0114-x

Anderson, M.W., Ohsuna, T., Sakamoto, Y., Liu, Z., Carlsson, A., Terasaki, O.: Modern microscopy methods for the structural study of porous materials. Chem. Commun. **4**(8), 907–916 (2004). https://doi.org/10.1039/b313208k

Badiei, A., Gholami, J., Khaniani, Y.: Synthesis and characterization of titanium supported on high order nanoporous silica and application for direct oxidation of Benzene to Phenol. E-J. Chem. **6**(Suppl. 1), 324–329 (2009). https://doi.org/10.1155/2009/292483

Barrett, E.P., Joyner, L.G., Halenda, P.P.: The determination of pore volume and area distributions in porous substances. I. Computations from nitrogen isotherms. J. Am. Chem. Soc. **73**(1), 373–380

Barton, T.J., Bull, L.M., Klemperer, W.G., Loy, D.A., McEnaney, B., Misono, M., Monson, P.A., et al.: Tailored porous materials. Chem. Mater. **11**(10), 2633–2656 (1999). https://doi.org/10.1021/cm9805929

Basu, D., Mazumder, S., Niklas, J., Baydoun, H., Wanniarachchi, D., Shi, X., Staples, R.J., Oleg Poluektov, H., Schlegel, B., Verani, C.N.: Evaluation of the coordination preferences and catalytic pathways of heteroaxial cobalt oximes towards hydrogen generation. Chem. Sci. **7**(5), 3264–3278 (2016). https://doi.org/10.1039/c5sc04214c

Bragg, P.W.H., Bragg, W.L.: The reflexion of X-rays by crystals. Proc. r. Soc. Lond. a. **88**(605), 428–438 (1913)

Chen, Y.P., Liu, Y., Liu, D., Bosch, M., Zhou, H.C.: Direct measurement of adsorbed gas redistribution in metal-organic frameworks. J. Am. Chem. Soc. **137**(8), 2919–2930 (2015). https://doi.org/10.1021/ja5103579

Fayed, T.A., Shaaban, M.H., El-Nahass, M.N., Hassan, F.M.: Hybrid organic-inorganic mesoporous silicates as optical nanosensor for toxic metals detection. Int. J. Chem. Appl. Biol. Sci. **1**(2), 1–18 (2016)

Ghodke, U.C., Shrinivas: A comparative study on catalytic activity of solid acid catalysts towards microwave assisted synthesis of coumarin derivatives. Int. J. Sci. Res. (IJSR) **4**(1), 1933–1939 (2015). https://www.ijsr.net/archive/v4i1/SUB15710.pdf

Halder, G.J., Kepert, C.J.: In situ single-crystal X-ray diffraction studies of desorption and sorption in a flexible nanoporous molecular framework material. J. Am. Chem. Soc. **127**(21), 7891–7900 (2005). https://doi.org/10.1021/ja042420k

Helliwell, M., Helliwell, J.R., Logar, N.Z., Mali, G., Tušar, N.N., Kaučič, V.: Structure characterisation of nanoporous materials using state-of-the-art single-crystal X-ray and neutron diffraction techniques. Acta Chim. Slov. **55**(4), 709–718 (2008)

Hernández, M.A., Abbaspourrad, A., Petranovskii, V., Rojas, F., Portillo, R., Salgado, M.A., Hernández, G., de los Angeles Velazco, M., Ayala, E., Quiroz, K.F.: Estimation of nanoporosity of ZSM-5 zeolites as estimation of nanoporosity of ZSM-5 zeolites as hierarchical materials. In: Zeolites and Their Applications Size, pp. 73–90. https://doi.org/10.5772/intechopen.73624

Jones, B.H., Lodge, T.P.: Nanocasting nanoporous inorganic and organic materials from polymeric bicontinuous microemulsion templates. Polym. J. **44**(2), 131–146 (2012). https://doi.org/10.1038/pj.2011.136

Kaskel, S. (2017). The chemistry of metal-organic frameworks: synthesis, characterization, and applications. Johnson Matthey Technol. Rev. **61**. https://doi.org/10.1595/205651317X695091

Keshavarz, L., Ghaani, M.R., Don MacElroy, J.M., English, N.J.: A comprehensive review on the application of aerogels in CO_2-adsorption: materials and characterisation. Chem. Eng. J. **412**, 128604 (2021). https://doi.org/10.1016/j.cej.2021.128604

Klaiphet, K., Saisopa, T., Pokapanich, W., Tangsukworakhun, S., Songsiriritthigul, C., Saiyasombat, C., Céolin, D., Songsiriritthigul, P.: Structural study of Cu(II): glycine solution by X-ray absorption spectroscopy. J. Phys.: Conf. Ser. **1144**(1) (2018). https://doi.org/10.1088/1742-6596/1144/1/012063

Kokotailo, G.T., Lawton, S.L., Olson, D.H., Meier, W.M.: Structure of synthetic zeolite ZSM-5. Nature (1978). https://doi.org/10.1038/272437a0

Koningsberger, D.C., Ramaker, D.E.: Applications of X-ray absorption spectroscopy in heterogeneous catalysis: EXAFS, atomic XAFS and delta XANES. In: Chapter 3.1.3.2 Structure and Morphology, pp. 774–803 (2006)

Koningsberger, D.C., Mojet, B.L., Van Dorssen, G.E., Ramaker, D.E.: XAFS spectroscopy; fundamental principles and data analysis. Top. Catal. **10**(3–4), 143–155 (2000). https://doi.org/10.1023/a:1019105310221

Krause, S., Bon, V., Senkovska, I., Stoeck, U., Wallacher, D., Többens, D.M., Zander, S., et al.: A pressure-amplifying framework material with negative gas adsorption transitions. Nature **532**(7599), 348–352 (2016). https://doi.org/10.1038/nature17430

Lee, J.H., Sa, Y.J., Kim, T.K., Moon, H.R., Joo, S.H.: A transformative route to nanoporous manganese oxides of controlled oxidation states with identical textural properties. J. Mater. Chem. A **2**(27), 10435–10443 (2014). https://doi.org/10.1039/c4ta01272k

Liu, Z., Fujita, N., Miyasaka, K., Han, L., Stevens, S.M., Suga, M., Asahina, S., et al.: A review of fine structures of nanoporous materials as evidenced by microscopic methods. J. Electron Microscopy **62**(1), 109–146 (2013). https://doi.org/10.1093/jmicro/dfs098

Lowell, S.: Characterization of Porous Solids and Powders: Surface Area, Pore Size and Density. Edited by LLC SPRINGER SCIENCE+BUSINESS MEDIA. Kluwer Academic Publishers (2004)

Martis, M.: In Situ and Ex Situ Characterization Studies of Transition Metal Containing Nanoporous Catalysts, pp. 1–216 (2011). http://discovery.ucl.ac.uk/1334587/

Moosavifard, S.E., Shamsi, J., Fani, S., Kadkhodazade, S.: 3D Ordered Nanoporous NiMoO4 for high-performance supercapacitor electrode materials. RSC Adv. **4**(94), 52555–52561 (2014). https://doi.org/10.1039/c4ra09118c

Morel, F.L., Pin, S., Huthwelker, T., Ranocchiari, M., Van Bokhoven, J.A.: Phosphine and phosphine oxide groups in metal-organic frameworks detected by P K-Edge XAS. Phys. Chem. Chem. Phys. **17**(5), 3326–3331 (2015). https://doi.org/10.1039/c4cp05151c

NMR Interactions (2020, August 15). Retrieved September 10, 2021, from https://chem.libretexts.org/@go/page/1823

Petrochenko, P.E., Skoog, S.A., Zhang, Q., Comstock, D.J., Elam, J.W., Goering, P.L., Narayan, R.J.: Cytotoxicity of cultured macrophages exposed to antimicrobial zinc oxide (ZnO) coatings on nanoporous aluminum oxide membranes. Biomatter **3**(3) (2013). https://doi.org/10.4161/biom.25528

Raja, P.M.V., Barron, A.R.: Physical methods in chemistry. Nature **134**(3384), 366–367 (1934). https://doi.org/10.1002/jctb.5000533702

Reichenauer, G.: Structural characterization of aerogels. Aerogels Handbook (2011). https://doi.org/10.1007/978-1-4419-7589-8

Sakamoto, Y., Kaneda, M., Terasaki, O., Zhao, D.Y., Kim, J.M., Stucky, G., Shin, H.J., Ryoo, R.: Direct imaging of the pores and cages of three-dimensional mesoporous materials. Nature **408**(6811), 449–453 (2000). https://doi.org/10.1038/35044040

Senthil Kumar, P., Grace Pavithra, K., Naushad, M.: Characterization techniques for nanomaterials. In: Nanomaterials for Solar Cell Applications. Elsevier Inc. (2019). https://doi.org/10.1016/B978-0-12-813337-8.00004-7

Shi, D., Nannenga, B.L., Iadanza, M.G., Gonen, T.: Three-dimensional electron crystallography of protein microcrystals. Elife **2**, 1–17 (2013). https://doi.org/10.7554/elife.01345

Sinfelt, J.H., Meitzner, G.D.: X-ray absorption edge studies of the electronic structure of metal catalysts. Acc. Chem. Res. **26**(1), 1–6 (1993). https://doi.org/10.1021/ar00025a001

Sing, K.S.W., Everett, D.H., Haul, R.A.W., Moscou, L., Pierotti, R.A., Rouquérol, J., Siemieniewska, T.: Reporting physisorption data for gas/solid systems with special reference to the determination of surface area and porosity. Pure Appl. Chem. **57**(4), 603–619 (1985). https://doi.org/10.1515/iupac.57.0007

Širc, J., Hobzová, R., Kostina, N., Munzarová, M., Juklíčková, M., Lhotka, M., Kubinová, Š., Zajícová, A., Michálek, J.: Morphological characterization of nanofibers: methods and application in practice. J. Nanomater. 2012 (2012). https://doi.org/10.1155/2012/327369

Son, D., Sanghoscho@kist re kr Cho, Nam, J., Lee, H., Kim, M.: X-ray-based spectroscopic techniques for characterization of polymer nanocomposite materials at a molecular level. Polymers **12**(5) (2020). https://doi.org/10.3390/POLYM12051053

Taulelle, F., Bouchevreau, B., Martineau, C.: NMR crystallography driven structure determination: nanoporous materials. CrystEngComm **15**(43), 8613–8622 (2013). https://doi.org/10.1039/c3ce41178h

Terasaki, O., Ohsuna, T., Liu, Z., Sakamoto, Y., Garcia-Bennett, A.E.: Structural study of mesoporous materials by electron microscopy. Stud. Surf. Sci. Catal. **148**, 261–288 (2004). https://doi.org/10.1016/s0167-2991(04)80201-5

Thommes, M., Schlumberger, C.: Characterization of nanoporous materials. Annu. Rev. Chem. Biomol. Eng. **12**(5), 5.1–5.23 (2021). https://doi.org/10.1201/9781420082753-c6

Thommes, M., Kaneko, K., Neimark, A.V., Olivier, J.P., Rouquerol, F.-R., Sing, K.S.W.: Physisorption of gases, with special reference to the evaluation of surface area and pore size distribution. Pure Appl. Chem. **87**, 1051–1069 (2015). https://doi.org/10.1515/pac-2014-1117

Timoshenko, J., Cuenya, B.R.: In situ/operando electrocatalyst characterization by X-ray absorption spectroscopy. Chem. Rev. **121**(2), 882–961 (2021). https://doi.org/10.1021/acs.chemrev.0c00396

Van Bekkum, H., Flanigen, E.M., Jacobs, P.A., Jansen, J.C.: Introduction to Zeolite Science and Practice: Preface 1st Edition. Studies in Surface Science and Catalysis, vol. 137 (2001)

Van Oversteeg, C.H.M., Doan, H.Q., De Groot, F.M.F., Cuk, T.: In situ X-ray absorption spectroscopy of transition metal based water oxidation catalysts. Chem. Soc. Rev. **46**(1), 102–125 (2017). https://doi.org/10.1039/c6cs00230g

Wang, M., Árnadóttir, L., Xu, Z.J., Feng, Z.: In situ X-ray absorption spectroscopy studies of nanoscale electrocatalysts. Nano-Micro Lett. **11**(1), 1–18 (2019). https://doi.org/10.1007/s40820-019-0277-x

Weber, J., Antonietti, M., Thomas, A.: Microporous networks of high-performance polymers: elastic deformations and gas sorption properties. Macromolecules **41**(8), 2880–2885 (2008). https://doi.org/10.1021/ma702495r

Wen, X., Liu, Y., Jadhav, A., Zhang, J., Borchardt, D., Shi, J., Wong, B.M., Sanyal, B., Messinger, R.J., Guo, J.: Materials compatibility in rechargeable aluminum batteries: chemical and electrochemical properties between vanadium pentoxide and chloroaluminate ionic liquids. Chem. Mater. **31**(18), 7238–7247 (2019). https://doi.org/10.1021/acs.chemmater.9b01556

Wright, K., Barron, A.: Catalyst residue and oxygen species inhibition of the formation of hexahapto-metal complexes of group 6 metals on single-walled carbon nanotubes. J. Carbon Res. **3**(4), 17 (2017). https://doi.org/10.3390/c3020017

Yakovenko, A.A., Reibenspies, J.H., Bhuvanesh, N., Zhou, H.C.: Generation and applications of structure envelopes for porous metal-organic frameworks. J. Appl. Crystallogr. **46**(2), 346–353 (2013). https://doi.org/10.1107/S0021889812050935

Zhao, C., Qiao, Y.: Characterization of nanoporous structures: from three dimensions to two dimensions. Nanoscale **8**(40), 17658–17664. https://doi.org/10.1039/c6nr05862k

Zhao, C., Zhang, Y., Wang, C.C., Hou, M., Li, A.: Recent progress in instrumental techniques for architectural heritage materials. Heritage Sci. **7**(1), 1–50 (2019). https://doi.org/10.1186/s40494-019-0280-z

Emerging Biomedical and Industrial Applications of Nanoporous Materials

Neha Suvindran, Amir Servati, and Peyman Servati

Abstract Nanoporous materials is a fast-growing subset of nanomaterials with unique intrinsic properties. The advances in fabrication and characterization techniques have enabled scientists to tailor the properties and design a wide range of application specific nanoporous materials. This chapter highlights the key technological advancements that nanoporous materials have achieved in the frontiers of biomedical engineering across analyses, diagnostics and therapeutics. It draws attention to progressive studies like the membrane based organ-on-a-chip (OOC) models of the blood brain barrier and human alveolar that contributed to the advancements in the drug development studies of neurological diseases and COVID-19 to neurochemical biosensing and artificial portable kidneys (Fan et al., ACS Nano 13:8374–8381, 2019; Wang et al., Biotechnol. Bioeng. 114:184–194, 2017; Zhang et al., Adv. Sci. 8:1–14, 2021; Zhou et al., Anal. Chem. 91:3645–3651, 2019). A brief account of the versatile industrial applications of nanoporous materials in chromatography, nanoreactors, energy storage and cutting-edge concepts like nanosized photonic data storage is also illustrated with representative cases.

Keywords Nanoporous materials · Nanobiomedicine · Theranostics · Biosensors · Bioelectronics · Chromatography · Nanoreactors · Photonic data storage · Energy harvesting

N. Suvindran (✉)
School of Biomedical Engineering, University of British Columbia, Vancouver, BC V6T 1Z4, Canada
e-mail: nehas@ece.ubc.ca

A. Servati · P. Servati (✉)
Department of Electrical and Computer Engineering, University of British Columbia, Vancouver, BC V6T 1Z4, Canada
e-mail: peymans@ece.ubc.ca

A. Servati
e-mail: amir.servati@ubc.ca

A. Servati
Department of Materials Engineering, University of British Colombia, Vancouver, BC V6T 1Z4, Canada

1   Introduction

Today, nearly 70 years after Richard Feynman first introduced the term, 'nanotechnology' in his talk 'There's Plenty of Room at the Bottom', it has burgeoned into a conglomerate of subdisciplines, continually redefining the frontiers of science.

Nanoporous materials are one such subset of nanotechnology that has captured the attention of the scientific community and become the focal point of research for the past few decades. Biomimetic studies elucidated nature's repletion of biological nanoporous structures such as cell membranes, bone matrix, lipid-coated olfactory nanochannels of insects, that possess intricate pore morphologies and multifunctional capabilities far superior than their synthetic counterparts (Gaidash et al. 2011; Jakšić and Jakšić 2020; Yusko et al. 2011). The recent advances in micro- and nanomaterial fabrication has enabled researchers to emulate these characteristics producing intelligent nanoporous-based systems for a seemingly disparate number of fields like health care, agro-food industry, manufacturing, flexible electronics, renewable energy, separation technology and informatics as shown in Fig. 1.

Like all other nanomaterials, nanoporous materials possess a large and functionalizable-specific surface area, along with intrinsic mechanical, optical and electrical characteristics. However, they possess a unique set of properties that sets it apart from the other nanomaterials such as its tunable pore size, pore shape, pore density, pore distribution and selective permeability of the nanochannels (Fig. 1). A bare bone definition of nanoporous materials is 'organic, inorganic or hybrid porous structures that possess high aspect ratios along with a thickness below 100 nm'. Additionally, the term nanoporous membranes (NPMs) has also been extensively used across literature for structures with thicknesses in the micrometer scale but containing nanosized pores (Jakšić and Jakšić 2020). This is due to the fact that nanomaterials are defined as materials with at least 1 dimension within the range
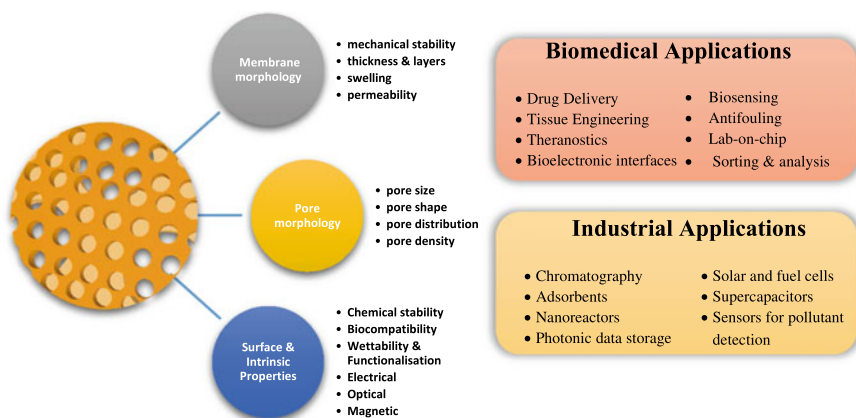
Fig. 1   Properties and potential applications of nanoporous materials

of 1–100 nm (Yin and Sheng 2018). Early on, the NPM technology was limited to practical applications like filtration and separation. The rapid advancements in fabrication techniques revolutionized the nanoporous membrane technology leading to the low-cost, large-scale production of various types of novel NPMs. Previously, NPMs used in filtration would be supported by a microporous substrate, however the advances in material science led to novel concepts such as self-healing, stimuli responsive, free-standing and biomimetic NPMs. This, along with the integration of micro-electro-mechanical-systems (MEMS) technology led to the development of smart applications across various disciplines. Being a nanomaterial, nanoporous materials possess a large surface area to volume ratio, as most of the atoms are present at the surface and there is an absence of bulk. This greatly increases the contact with the external environment with reduced spatial dimensions making it an attractive option for sensing applications. Furthermore, researchers exploited the intrinsic electrical, magnetic and optical properties of nanoporous materials to revolutionize the sensing technology by developing sensors with enhanced molecular level sensing capabilities.

NPMs are fabricated from a large array of materials which are broadly classified into (i) organics such as polymers, (ii) inorganics such as metals and semiconducting materials and (iii) composites which are hybrids containing ceramics mixed with metals, etc. Nanoporous metals are an interesting subclass due to their intrinsic optical and electrical characteristics (Fujita 2017). As an example, nanoporous gold is extensively being explored to design ultrafast and accurate optical sensors that outperform their conventional metallic bulk counterparts (Collinson 2013). In terms of pore morphology, nanoporous materials can be broadly classified based on the pore size, shape and order. Pore sizes are chosen based on the desired application and range from microporous (<2 nm), mesoporous (2–50 nm) and macroporous (50 nm) structures. Several novel and cutting-edge fabrication techniques like focused ion beam, lithography, electrospinning, self-assembly, layer by layer, dealloying, etc., have allowed researchers to precisely control the pore shape and assembly while fabricating the NPMs (Sun et al. 2021). Today, apart from cylindrical and conical pore shapes, there are several irregular shapes such as hexagonal, star, clover leaves, triangular and square, which can be arranged in a random or uniform order during fabrication (Sun et al. 2021). The ability to accurately tailor pore morphology enabled researchers to control and manipulate transport at the molecular level leading to several novel applications in therapeutics and energy systems.

2 Nanobiomedicine Applications

It is a well-known fact that cells are the fundamental building blocks of all living organisms. However, the lesser-known fact is that the cellular walls, which perform vital functions that sustain life, are in fact biological nanoporous membranes. These biological NPM structures perform a multitude of functions such as the definition of the cell boundaries and shape, protection of the interior cellular contents, selective

membrane transfer of ions, signal reception and so forth (Jakšić and Jakšić 2020). This finding pushed researchers to synthesize artificial nanoporous membranes that mimic the multifunctional capabilities of their biological counterparts.

Today, engineering innovation in synthetic nanoporous membrane (NPM) technology has significantly advanced the frontiers of nanobiomedicine. NPM technology has enabled researchers to effectively diagnose and develop treatments at the cellular level for medical conditions such as cancer, renal failure, tissue injury, diabetes and neurological disorders.

Several material properties of NPMs come into play while implementing them in biomedical applications. The pore size and morphology are critical in drug delivery, therapeutic and bioassay applications to control the transport and separation at the molecular level. For instance, the pore size of NPMs for protein separation and molecular analysis is around 100 nm (Garle et al. 2020; Sun et al. 2021). Another important characteristic is the mechanical durability and biocompatibility of the NPMs while being implemented in in vitro and in vivo applications. The materials used should not evoke a foreign body response which in turn will wall it off and reduce its functionality. Often, researchers perform surface modifications to enhance the biocompatibility of the surfaces. It is also critical that the materials remain stable in the host environment and resist biofouling. Several advanced fabrication techniques have allowed researchers to functionalize and activate the surfaces of the NPMs thereby tailoring them for specific biosensing and therapeutic applications.

Table 1 (Adiga et al. 2009; Sun et al. 2021) highlights a few of the NPM materials, their surface properties and respective biomedical applications that were discussed in previous reviews. The following section covers the emerging trends of NPMs in nanobiomedical areas like therapeutics, tissue engineering, diagnostics, artificial organs and smart biointerfaces.

2.1 Drug Delivery Systems (DDS) and Tissue Engineering

When it comes to designing effective medical interventions, scientists believe 'the smaller the better'. Initial pilot studies implemented nanoparticles as carriers in an effort to design targeted drug delivery systems (DDS) for cancer therapy. Several inorganic nanoparticles like iron oxide, gold, quantum dots, colloidal systems like HA-IONP (hyaluronic acid-iron oxide nanoparticle) and polymeric nanoparticles like star-shaped PLGA-TPGS(poly(d,l-lactide-co-glycolide)-d-α-tocopheryl polyethylene glycol 1000 succinate), dendrimers, etc. were functionalized to produce theranostic solutions combining molecular imaging with chemotherapy (Quigley and Dalhaimer 2018; Wang et al. 2018). However, this approach faced several drawbacks like poor targeting due to the uncontrolled circulation of the nanoparticles along with the untimely release of the drugs leading to tissue damage and severe side effects. Furthermore, issues related to nanotoxicity and ethical considerations cropped up resulting in very few nanoparticle-based DDS gaining FDA (Food and Drug Safety) approval and going mainstream.

Table 1 Material properties and biomedical applications of NPMs (Adiga et al. 2009; Sun et al. 2021)

Material type	Material	Pore size and morphology	Properties	Biomedical applications
Inorganic	Anodic aluminium oxide (AAO)	5 nm–10 µm Uniform pores High density	Chemical and thermal stability, biocompatible, tailored surface properties	Cell culture, biosensing; drug delivery, molecular sieving, nano-patterning, chromatography
	Si, SiO₂, other semiconductors	2 nm–3 µm Uniform pores High density	Good mechanical strength, chemically inert, biocompatible	Biosensing, cell culture, drug delivery, biomimicking, microfiltration, ultrafiltration Micropatterning
Organic (*pore morphology defined by fabrication process*)	Polydimethylsiloxane (PDMS)	800 nm–500 µm	Chemically inert, biocompatible, high permeability, transparent	Micropatterning, microfiltration, cell operation, organ-on-chip, bioassay
	Polycarbonate (PC)	1 nm–1 mm	Chemical and thermal stability, good mechanical strength, biocompatible	Bioassay, separation, filtration, drug delivery
	Polyethylene (PE)	>20 nm	Chemical stability and good mechanical strength	Organ-on-chip, microfiltration
	Polystyrene (PS)	0.7 nm–1 µm	Chemically stable and biocompatible	Ultrafiltration, nano-patterning, drug delivery
	Parylene	5 nm–1 mm	Chemically stable and biocompatible	Cell culture, drug delivery, microfiltration

Table 1 (continued)

Material type	Material	Pore size and morphology	Properties	Biomedical applications
	Polyethylene terephthalate (PET)	100 nm–8 μm	Good mechanical strength and transparency	Bioparticle operation, cell culture, organ chips
	Polymethyl methacrylate (PMMA)	0.7 nm–5 μm	Chemically inert, biocompatible and transparent	Water purification, drug delivery
	Polylactic acid (PLA)	300 nm–1 μm	Biocompatible, high adhesiveness, transparent	Wound dressing, bone regeneration, adhesive anchor
	Poly(3,4-ethylenedioxythiophene)polystyrene Sulfonate (PEDOT:PSS)	13–several hundred μm	Biocompatible, highly conductive, biodegradable, stretchability	Drug delivery, electrical stimulation, smart scaffolds, flexible bioelectronics devices
	Polyethylene glycol (PEG)	100 nm–several hundred μm	Biocompatible, hydrophilic, transparent, antifouling, functionalized biodegradability	Drug delivery, theranostic devices, wound dressing, tissue engineering, bioelectronics
Composite	Ceramics/polymer	nm pore size by pore-filling coating	Chemically stable, good mechanical strength, superior biocompatibility, multimodal functionality	Microfiltration, ultrafiltration
	Oxide + polymer			

However, the discovery that cell membranes were biological NPMs shed light on the pharmacokinetic behavior of drugs in relation to the NPMs. Targeted therapeutic treatments also involve subcellular mechanisms that use nanocarriers to target drugs onto cellular organelles present inside the cells. The nanocarriers interact with the biological NPMs which function as the cell wall that controls their passage into the cell (Jakšić and Jakšić 2020). Several of the aforementioned drawbacks were solved by using synthetic NPMs as carriers for targeted drug delivery systems. For instance, NPMs comprise of several organic and inorganic materials such as PDMS, PE, AAO and nanoporous gold, as shown in Table 1 that tend to be highly biocompatible and durable. The mechanical and chemical stability aids in securely storing the drugs within the NPMs and preventing the uncontrolled release. Furthermore, the pore size and morphology also play a very crucial role. The nanopores and nanochannels present in the membranes aid in precisely tuning the amount and discharge rate of the drugs. In addition, the ability to modify and functionalize the surface of NPMs makes it an attractive candidate capable of carrying multiple drugs and providing on-demand release for effective therapeutic treatments. In short, nanoporous materials with their large multifunctional surface areas and well-defined porosity are the perfect carriers for targeted and controlled DDS.

Targeted and controlled DDS are broadly classified into two types based on the desired pharmacokinetics. First is the continuous discharge of the drug throughout the whole treatment and the other is the pulsatile release of the drug based on demand (Fig. 2a). For the former application, nanoporous membranes with uniform pore sizes are employed. The reduction in size of pores of the NPMs restricts the drug flow rate and stabilizes it over time. This technique is popularly known as single file diffusion. Kim et al. (2015) illustrated the single file diffusion phenomena in 20 nm channels of SiO_2 NPMs. The latter application employs nanoporous membranes whose surfaces are functionalized to respond to stimuli thereby enabling pulsatile delivery of drugs (Jeon et al. 2012). The NPMs that are activated by stimuli can be active or passive in nature based on the clinical condition they aim to cure. Artificially controlled stimuli such as electrical, magnetic and optical triggers are used while designing the passive NPMs-based DDS while biological factors like pH, ions, proteins, enzymes, antibody agents, etc., are used to design active NPMs-based systems. Cai et al. (2009) successfully demonstrated a magnetically stimulated pulsatile DDS to deliver DNA and vitamin B12. A nanoporous PC membrane with 125 nm pores was embedded with Fe_3O_4 nanoparticles that controlled the release of the drugs stored in a PDLLA (poly(D,L-lactic acid)) reservoir. Some research groups used passive stimuli like specific proteins to trigger the DDS. The surface of the nanoporous membranes was functionalized with ionizable polymer brushes such as diethylamino or sulfonic acid to entangle aminoacylase protein molecules that stimulate the drug release from the nanochannels by widening the pores.

The aforementioned studies elucidate the extensive use of polymers in designing nanoporous membranes for DDS. In the last decade, a new class of polymers known as conductive polymers and their composites began gaining traction in designing controlled DDS. Aleman's group reviewed the work of Schmidt who incorporated
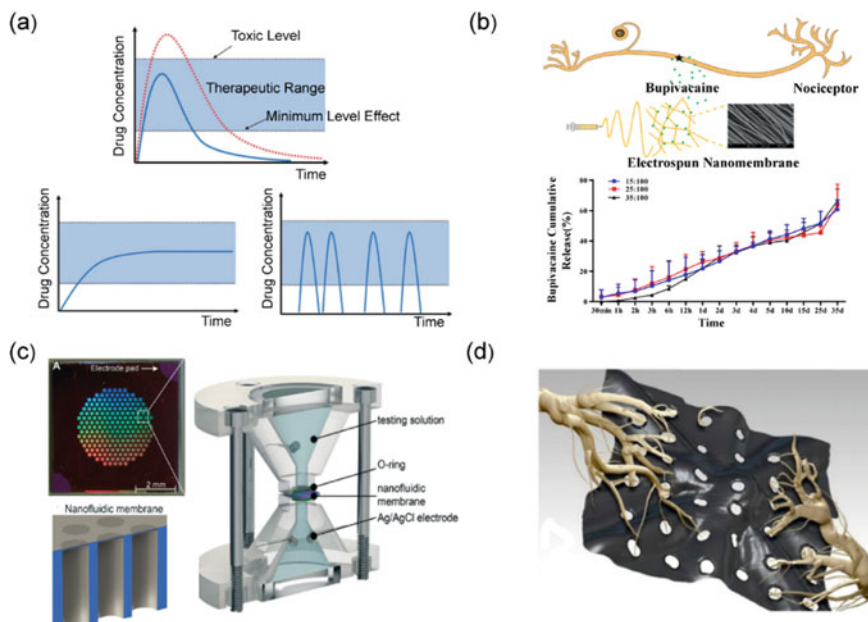
Fig. 2 Nanoporous membrane applications in DDS and tissue engineering: **a** the drug release profiles of oral medication, continuous DDS and pulsatile DDS. Republished with permission of Royal Society of Chemistry, from Jeon et al. (2012) permission conveyed through Copyright Clearance Center, Inc. **b** Electrospun PLGA nanomembrane as an analgesic carrier for postoperative pain treatment. Reproduced from He et al. (2020). **c** Next generation DDS using a electrostatically gated nanofluidic membrane for personalized medicine. Reproduced from Di Trani et al. (2020). **d** Illustration of a nanoporous membrane used for regeneration of damaged neural tissue. Reproduced from Jakšić and Jakšić (2020)

electroactive oligoaniline linked PEG as a DDS for anti-inflammatory drugs (Pérez-Madrigal et al. 2015), while Dubey et al. (2020) reviewed the use of nanoporous composites like PLGA/CS for cancer therapy. Recently, He et al. (2020) proposed a non-toxic and efficient nanomembrane DDS as an analgesic carrier for postoperative pain therapy. They fabricated an aligned PLGA nanomembrane via electrospinning and loaded with bupivacaine (Fig. 2b). The in vitro and in vivo studies presented a biocompatible and more efficient analgesic delivery system in comparison to the existing systems.

The objective of the next-generation drug delivery systems is to achieve patient centric, personalized and precise therapeutic management by replacing the existing stimuli responsive NPMs. Currently, researchers are integrating sensory and feedback control systems into the DDS architecture that enables higher precision in drug release with remote communication capabilities. In 2020, Grattoni's group presented a smart and high-density DDS system using a nanofluidic membrane controlled via electrostatic gating (Di Trani et al. 2020). They fabricated SiO$_2$ micro-nanochannels using semiconductor technology with each chip featuring 278,600 nanochannels

coated in SiC (Fig. 2c). The use of electrostatic particles enabled molecular level control in the nanochannels for drug administration. The in vitro experiments revealed that hormonal drug administration controlled by electrostatic gating was able to mimic the circadian hormone cycles. When coupled with a feedback system, their device sets the foundation for the next-generation drug delivery systems.

Nanoporous materials found one of its earliest biomedical applications in tissue engineering. Tissue engineering requires a supportive scaffolding to promote the regeneration, restoration and regrowth of cells and tissue in either in vitro or in vivo environments (Fig. 2d). The artificial scaffolds need to be biocompatible and biodegradable such that they do not trigger an inflammatory reaction and undergo a benign decomposition in the host once the regenerative process is complete. The swell index is also a crucial mechanical property for tissue engineering. The water retention capacity of the scaffold promotes transport and cellular regeneration. Additionally, the scaffolds need to be porous structures providing the embedded stimulants and cells passage to interact with the host for tissue regeneration. NPMs met all the afore-mentioned requirements and served as the perfect template for artificial scaffolds. Today, NPMs-based artificial scaffolds are used across a wide range of regenerative applications in bones, neural tissues, cardiovascular tissues, lungs, liver, kidney, brain damage, spinal cord injury and wound healing.

Typically, organic and ceramic-based nanoporous materials were used for designing the artificial scaffolds. Currently, polymer scaffolds have become extremely popular due to their high biocompatibility and swelling behaviour. Special types of polymer-based NPMs such as free-standing, conductive, composite-based smart designs have gained traction in tissue engineering applications (Dubey et al. 2020; Pérez-Madrigal et al. 2015). Early on, Zhang et al. (2007) illustrated the use of PPy (polypyrrole) NPM composites with butane sulphonic acid dopants that successfully promoted neuronal regrowth in nerve regeneration studies. Pérez-Madrigal et al. (2014) prepared a novel polymer NPM composite for cell regeneration. They spin coated a mixture of TPU and P3TMA in a 40:60 ratio to produce hydrophilic nanoporous membranes that revealed biodegradable and cell regeneration capabilities in their in vitro collagen study.

Advancements in the fabrication technologies have enabled researchers to develop novel multifunctional nanomembranes for tissue engineering. Kong et al. (2016) presented a novel free-standing 3D CHI/ALG (chitosan-alginate) nanomembrane for stem cell delivery in wound healing treatments. They used the layer-by-layer self-assembly technique with gelatin as the sacrificial substrate to create the free-standing NPM. A 15 multilayer CHI/ALG nanomembrane scaffold was developed and embedded with bone marrow stem cells and mesenchymal stem cells that aid in wound healing. The in vitro and in vivo studies successfully demonstrated a biocompatible NPM scaffold for skin tissue reconstruction. Deng et al. (2019) designed functionalized NPMs for tissue and organ repair with excellent antibio-fouling and antithrombosis properties. Hydrophilic NPM with porosity of 20–24 nm

was designed using PEG and programmable carboxyl-terminated SS-PLLA (Gn-$(COOH)_x$) (poly(L-lactic acid)) as the self-assembly block via an emulsification-induced self-assembly technique. Their study revealed that the length of the PEG chain directly affected the antifouling property making it a tunable property.

2.2 Bioseparation, Sorting and Analysis

Bioseparation is an important biomedical technology used by researchers for cell and biomolecule separation, culture purification and biomarker isolation prior to performing analytical studies. Bioseparation techniques are broadly classified into active or passive techniques based on the nature of the manipulating forces (Catarino et al. 2019). Active techniques involve the use of mobile components like MEMS actuators, optical tweezers or external forces, i.e. magnetophoresis, acoustophoresis and dielectrophoresis, while passive techniques lack mobile parts and perform bioseparation by manipulating the hydrodynamic flow, i.e. chromatography, channel morphology or incorporating filters. As early as the 1970s, membrane technology was used for molecular separation (Stroeve and Ileri 2011). It was an attractive option being a size selective, passive filter that enabled separation at room temperatures with low-cost maintenance in comparison to the other techniques. Microporous track etched membranes made of polycarbonate (PC) or polyethylene terephthalate (PET) were extensively used in the early days for molecular separation. However, major deficiencies such as non-uniform porosity and morphology, large pore sizes, poor mechanical strength and biocompatibility limited the large-scale applicability of these porous membranes.

The advances in nanofabrication techniques enabled researchers to precisely control parameters, like the pore size and shape, pore density, membrane thickness, and functionalize the surface of the NPM. This coupled with low-cost fabrication, mechanical and chemical durability in biological environments made NPMs the ideal interface for bioseparation. Today, NPM-based bioseparation has made tremendous strides in biomedical research and is used in cancer cell separation, blood fractioning, plasma enrichment, pathogen isolation, specific macromolecules like DNA, RNA and protein isolation. Parameters such as pore morphology and membrane thickness play a very important role in determining the efficiency of the NPM filter. Traditionally, NPMs possess cylindrical pores, however recent advances have enabled the fabrication of conical-, hexagonal-, pyramidal- and asymmetric-shaped pores that provide greater selectivity and precision in molecular level control of the separation process. Ileri et al. (2012) compared the performance of polycarbonate track etch (PCTE) and Si membranes containing the same pore size but varying membrane thickness. Laser interferometric lithography (LIL) was incorporated to fabricate Si and Si_3N_4 NPMs with cylindrical, pyramidal pores of 250 nm diameter and membrane thickness of 220 nm while PCTE membranes were 6 μm thick. The thinner Si NPM had a higher separation flux rate for pyridine solution in comparison with the thicker PCTE membranes. This is because thinner NPM possess shorter nanochannels leading

to faster diffusion of the mixture and bioseparation of the target molecules. The aforementioned experiment validated the theoretical notion that pore flux is directly proportional to the pore size and density and inversely proportional to the channel length.

Several inorganic and organic-based NPM separation filters exist pertaining to the target mixture. Early on, several groups used aluminium anodic oxide (AAO) nanoporous membranes for applications like bioseparation of DNA molecules (Stroeve and Ileri 2011). Anodic oxidation was used to produce the AAO NPM with hexagonal pores with the pore size varying between 10 and 200 nm depending on the target molecule. However, AAO NPM possess a thickness in the range of tens of micrometers which was a huge drawback since bioseparation required thin, flexible membranes. Several studies also examined the efficacy of organic polymer-based NPMs in bioseparation. PTCE membranes with pore size of 10 nm were fabricated with cylinder and conical pore shapes. Polydimethylsilane (PDMS)-based NPMs fabricated by soft lithographic techniques was also extensively explored for bioseparation application. However, such polymer compounds faced drawbacks due to absorption and swelling. Despite the high throughput and low-cost fabrication, both AAO and polymeric membranes possessed several limitations that were overcome with the implementation of semiconductor fabrication technology. Several groups investigated inorganic silicon-based NPMs for bioseparation. Advanced fabrication techniques like electron beam lithography (EBL) and focused ion beam (FIB) enabled the fabrication of silicon (Si) and silicon nitride (Si_3N_4)-based NPMs with precise pore morphology and distribution. Furthermore, bioseparation studies revealed that Si and Si_3N_4 filters possessed excellent mechanical and chemical stability along with being ultrathin. Shankles et al. (2015) used electron beam lithography (EBL) and photolithography to demonstrate a multiscale NPM device for bioseparation (Fig. 3b). The first NPM device had a pore size of 150 nm enabling bioseparation of lower molecular weight molecules from the mixture, while the second NPM had a pore size of 200 nm and served as medium between culture chamber and nutrient channels.

The current trend is the development of smart NPM for bioseparation based on surface functionalization and external stimuli. Metals such as gold, silver and copper are coated onto the NPMs to develop charge stimulated pores that enable the selective separation of ionic biomolecules. Similarly, pH was used as a stimulus for selective smart separation (Catarino et al. 2019). Sabirova et al. (2020) demonstrated a novel isoporous nanomembrane design for selective bioseparation. They employed photolithography and dry reactive etching (DRIE) to pattern Mylar and Kapton with isopores ranging from 787 nm to 50 μm with a tenfold higher porosity in comparison to commercial membranes. A stack of these isoporous membranes was successfully used for organelle fractionation, and they outperformed the existing commercial microporous membranes (Fig. 3a).

Cell sorting is a powerful diagnostic technique with high resolution that allows researchers to sort out cells into distinct groups based on their intra- and extracellular properties like surface protein, DNA and RNA expressions. Fluorescence-activated
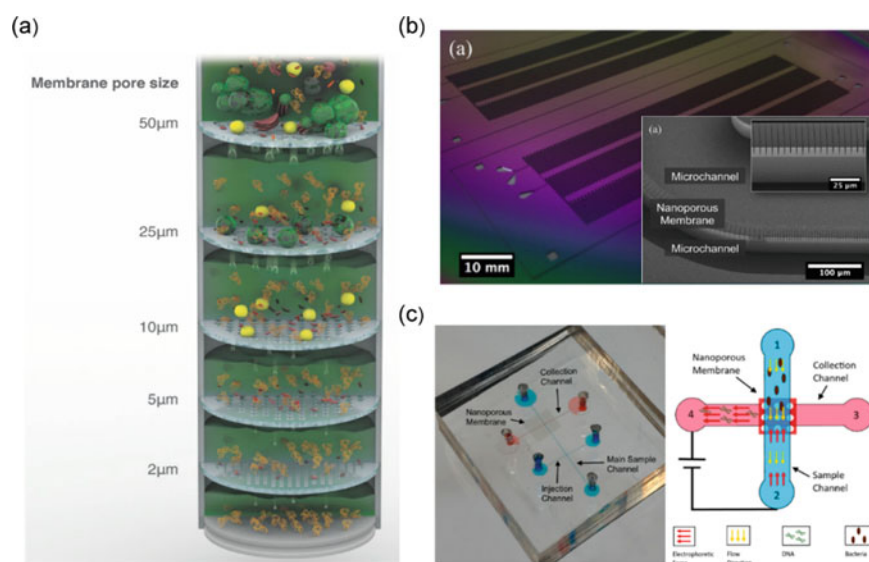
Fig. 3 NPM applications in separation and analysis: **a** illustration of layered cell sorting using different pore sized nanomembranes. Reproduced from Sabirova et al. (2020). **b** Multiscale fluidic device using nanoporous membranes for separation and culturing. Reprinted with permission from Shankles et al. (2015). Copyright 2015, American Vacuum Society. **c** Microfluidic device integrating nanoporous membrane for separation and subsequent lysis of bacteria. Reproduced from Islam et al. (2017)

cell sorting (FACS) and magnetic-activated cell sorting (MACS) are two of the traditionally used sorting techniques. The advances in nanofabrication and microfluidics led to the development of cost-effective, higher-resolution, benchtop cell sorting devices. Furthermore, the ability to functionalize the surface of NPM and precisely tailor its pore morphology made it a simple, cost-effective candidate for cell sorting applications. Several groups developed novel sorting chips using NPMs to achieve rapid separation and analysis (Wei 2013; Sajeesh and Sen 2014). Polymeric porous membranes like PDMS and PMMA are extensively used in cancer and white blood cell sorting studies. Wei et al. (2011) successfully presented a novel sorting chip that used a single membrane with customized pore sizes and distribution to achieve rapid and cost-effective sorting. Instead of stacking several NPMs of varying pore sizes in the sorting chip, their study fabricated multiple pore sizes on a single PDMS membrane using lithography. The size and arrangement of the pores can be tailored based on the application and user specifications. Their customized porous membrane device successfully achieved a 99% efficacy in sorting blood cells.

Apart from bioseparation and sorting, the integration of NPMs in these chips has led to rapid analysis and point of care diagnostic devices. Early on, NPMs

replaced polymeric micromembranes in single-molecule analysis applications. Polymeric NPMs also gained traction in 3D cell culture growth, tumour sorting and analysis. Multiple cell types were cultured on the PDMS NPM with a pore size of 810 nm and incorporated into microfluidic platforms to perform analytical studies.

A major advantage of using membrane technology apart from the aforementioned ones is the ability to easily integrate it with other technologies. In 2017, Selvaganapathy's group demonstrated a novel microfluidic device capable of cell separation, analysis and electrical lysis of bacteria using NPM technology (Islam et al. 2017). Commercially available polycarbonate (PC) NPM with pore size of 400 nm was coated with PVP and sandwiched between the microchannels (Fig. 3c). An electrical field was applied which created an electrophoretic force when the bacteria accumulate on the NPM and once the threshold is reached the potential is increased to 200–300 V to lysis the bacteria.

2.3 Antifouling and Antibacterial Coatings

Microbial contamination of diagnostic and therapeutic devices like surgical equipment, medical implants, DDS and biosensors continues to be the leading cause of infection and device failure. Biofouling is mediated by the adhesion of proteins on the surface (Damodaran and Murthy 2016). This creates a host environment for the proliferation of microorganisms and the subsequent formation of a biofilm that encapsulates the device thus impairing its functionality. Several strategies have been incorporated over the years to tackle this issue. Based on the mode of action, they are broadly classified as antifouling and antimicrobial coatings (Francolini et al. 2017). Antifouling coatings possess surface properties that repel the microorganisms and prevent the accumulation, while antimicrobial coatings contain compounds that interact with microorganisms to either inhibit their growth or cause microbial cell death.

Extensive research has been done to develop nanofilms from several 2D organic, inorganic and composite materials like PEG, PU, graphene, zwitterionic, nafion with antifouling and antimicrobial properties. However, with the discovery of the antifouling and antimicrobial characteristics of nanoporous cellular membranes, the research trend has shifted towards designing synthetic nanoporous membrane coatings that mimic the biological counterpart. Furthermore, the high mechanical strength, chemical stability and biocompatibility make NPMs an attractive candidate for antifouling and antimicrobial coatings.

The popularly used hydrophilic polymer coatings that possess excellent antifouling properties by forming a hydration layer to resist protein fouling. However, they often become susceptible to biofouling in blood-based environments due to the adhesion of non-specific proteins that contain hydrophilic patches which subsequently creates a platform for biofilm formations. Researchers explored several alternatives like nafion, bovine serum albumin (BSA), silica, fibronectin, base-hydrolyzed
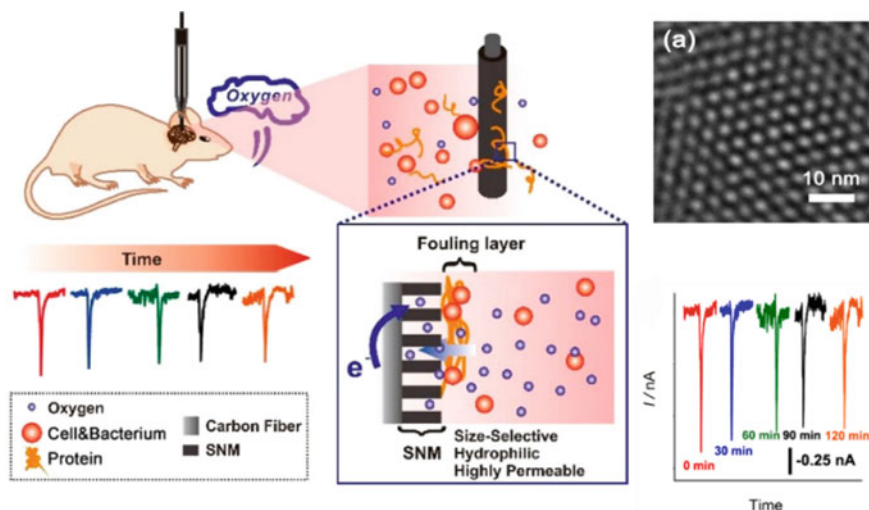
Fig. 4 Application of silica-nanoporous membrane used as an antifouling layer over carbon fibre electrodes for in vivo monitoring of O_2 in the rat brain. Reprinted with permission from Zhou et al. (2019). Copyright 2019, American Chemical Society

cellulose acetate (BSA) and so forth. Advances in the semiconductor fabrication techniques made NPM coatings based on inorganic materials like silica popular due to unique features like vertical orientation, high porosity, uniform distribution and selective permeability. Zhou et al. (2019) demonstrated a silica NPM as an antifouling coating for microelectrodes used in vivo oxygen monitoring. Electro-assisted self-assembly was used to grow 2 nm wide porous silica on the carbon fibre electrode (Fig. 4). The in vitro and in vivo characterization revealed excellent antifouling capabilities and selective permeability to oxygen. However, most of the carbon- and silica-based porous coatings required complex fabrication techniques making researchers explore other avenues for large-scale commercialization. In 2021, Li et al. (2021) developed a novel nanoporous composite coating on a biosensor showcasing excellent antifouling and selective detection of dopamine. They prepared a hydrophobic Nafion-coated porous boron-doped diamond (NAF/pBDD) electrode by thermally etching the BDD with nanopores to develop pBDD and covering the surface with a Nafion membrane. The ionic property of Nafion enables it to separate dopamine from the serum mixture, and the porosity of the pBDD surface greatly increased the biosensing sensitivity. Furthermore, their study validated that hydrophobic NPMs offered durable and efficient antifouling resistance in comparison to the traditionally used hydrophilic nanoporous polymers.

The advent of preventive medical interventions popularized antimicrobial coatings. Several groups began designing NPMs embedded with antibacterial agents. Polymerization of the agents was done to produce polymeric biocides such as vancomycin-PEG-methacrylate making them chemically stable and non-volatile in biological environments. Similarly, nanoporous metals such as gold (Au) gained a

lot of attention for its antimicrobial properties. Miyazawa et al. (2018) fabricated a nanoporous Au coating for antimicrobial activity. Nanoporous Au was synthesized by dealloying the sputtered gold surface. The simulation and in vitro culture characterizations revealed that NP Au achieved cell death by negatively hyperpolarizing the bacterial cells.

Recently, nanocomposites consisting of conductive polymers dopped with various metals gained traction to develop antimicrobial coatings capable of killing all types of microbes. Shaban et al. (2018) demonstrated a facile and large-scale technique to fabricate nanoporous Ag/PANI composite coatings for antimicrobial activity. Ag/PANI with a pore size of 20 nm was fabricated via oxidative polymerization. Their characterization studies revealed that the nanosized spherical shape Ag/PANI particles enabled them to easily penetrate microbial membranes depicting excellent antimicrobial capabilities against all bacterial strains.

2.4 Microfluidic Bioassays and Organ-on-Chip Devices

Bioassay is an important analytical technique that determines both the concentration and potency of a substance by monitoring the response against it in in vivo or in vitro environments. Apart from detection and monitoring of toxins, it is also extensively used to determine the dosage-toxicity profile in drugs for regulatory approval. The advances in nanofabrication and microfluidics led to the development of miniature devices capable of performing entire analytical assays (Dalili et al. 2019). Membrane-based bioassay chips have been extensively covered in literature due to its low-cost fabrication and multifunctional capabilities. Apart from being biocompatible, durable and aiding in molecular level transport, the nanoporous membranes replace the traditional complex parts on the chip and act as a platform that simultaneously promotes cell culture growth while also performing cell separation and sorting. Owing to their rapid analysis and ease of use, these nanoporous membrane-based bioassay chips are gradually replacing routine diagnostic tests at hospitals and providing point of care treatment in home settings. At present, several novel assay applications and organ-on-chip systems that precisely mimic our biological functions have been designed with the aid of organic and inorganic nanoporous membrane technology. In 2013, Glynn's group designed a nanoporous membraned-based chip for the bioassay of antitumour chemotic agent mitomycin C (MMC) on myeloid leukaemia cells (HL60) (Vereshchagina et al. 2013). Two PMMA microfluidic platforms were designed for flow through and diffusion-based control using PCTE nanoporous membranes with pore sizes between 15 and 400 nm (Fig. 5a). The PCTE membranes acted as a support for the cell culture while also selectively permitting the controlled exposure of the cells to the chemotoxic agent. They studied the rapid and long-term exposure of the chemotoxic agent and obtained results which were consistent with the traditional laboratory results. Nanoporous membranes have also been employed in co-culture assay systems. Traditionally, several micrometre thick porous membranes were used that hindered both, contact between the different cells and the subsequent imaging
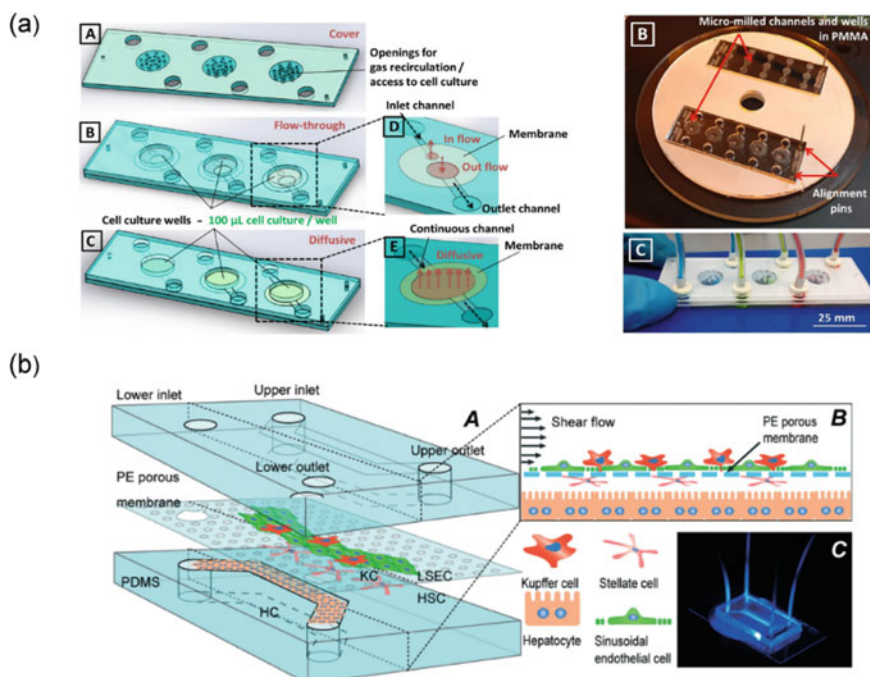
Fig. 5 NPM applications in bioassays and OOC: **a** microfluidic assay system for screening HL60 leukemia cells using a nanoporous PCTE membrane. Reprinted from Vereshchagina et al. (2013), with the permission of AIP Publishing. **b** In vitro liver chip mimicking the physiology of the liver using a nanoporous PE membrane. Republished with permission of Royal Society of Chemistry from Du et al. (2017); permission conveyed through Copyright Clearance Center, Inc.

for analysis. The incorporation of thin nanoporous membranes has helped design realistic co-culture models that accurately mimic biological processes and aid in drug development studies. Carter et al. (2017) demonstrated a transparent inorganic NPM for in vitro co-culture assays of endothelial and stem cells. Photolithography and etching were employed to design SiO_2 membranes with hexagonal pores of 300–500 nm diameter and membrane thickness of 300 nm. The nanoscale porosity enabled cell cultures of the endothelial and stem cells on either side, while the nanoscale thickness enabled communication between both cultures. Furthermore, the optical transparency of the SiO_2 membranes allowed the group to successfully use live fluorescence and phase imaging to visualize the cultures. Apart from polymeric and silica based nanoporous materials, researchers are also exploring several unconventional materials like the human nail and hen egg as perm-selective nanoporous materials. Park et al. (2021) demonstrated two novel nanofluidic devices using human nail and denatured hen egg as NPM suited for nanoelectrokinetic applications. Both the nanofluidic devices were made from PDMS with the membranes sandwiched in them. The nail membrane contains nanopores of 1.04 nm diameter with Pt electrodes while the albumen-based membrane contained nanopores of 60–90 nm diameter

with Ag electrodes. Their study revealed the perm-selectivity of the NPM caused by concentration polarization phenomenon (ICP) when a DC bias is applied to the devices.

The past few years have witnessed the emergence of the lab-on-chip technology. The miniature microfluidic device is capable of detection and performing several analytical functions. With the aid of functional nanoporous membranes, researchers have been able to incorporate several bioassay techniques onto chips. The surface enhanced Raman scattering (SERS) is a very important bioassay technique capable of providing molecular level information of the target toxins. Krafft et al. (2020) demonstrated a novel lab-on-chip SERS platform using electrical stimuli-responsive nanoporous PCTE membranes. Commercial PCTE membranes with pore size of 200 nm had one side coated with Ag and AgNP. The nanostructured AgNP coating performed SERS detection with a greater efficacy. The membrane also performed bioseparation by acting as a fluidic gate enabling electrokinetic transport when excited by a 10mW laser light. They successfully demonstrated the LOC capability by testing it to detect toxic melamine in milk.

The ability of synthetic nanoporous materials to precisely mimic the multifunctionality of the biological counter-parts coupled with advances in microfluidic fabrication and microelectronics has led to the evolution of organ-on-chip (OOC) systems. Today, OOC accurately epitomizes the complex biological structure and multiple functionalities of organs enabling researchers to study the pathophysiology, immune and drug responses in in vitro environments thereby replacing the need for animal models. A few popular OOC systems that incorporate porous membranes are the human intestine (Bein et al. 2018; Kim et al. 2012), kidney (Frohlich et al. 2013), pulmonary alveolus lung model (Zhang et al. 2020) and very recently a lung-SARS-COV-2 OOC to mimic the injury and immune responses of COVID-19 (Zhang et al. 2021). They were able to design this OOC using 5 μm porous PDMS membranes mimicking the lung tissue and to study the effect of the SAR-CoV-2 virus and remdesivir drug response to it thereby providing a rapid, miniature platform to assist in the drug development to fight the global pandemic. Most of the OOCs incorporate organic polymeric-based nanoporous membranes whose surfaces are functionalized to perform multiple functions. Similar to the aforementioned lab-on-chip technology, the membranes act as a support to promote co-cultures and control the molecular-level transport. Wang et al. (2017) used the organ-on-chip platform to develop a novel pumpless blood brain barrier (BBB) model for drug permeability studies across the BBB. Previous in vitro models found it hard to mimic the neurovasculature and were unable to perform controlled transport. They designed a three-layer microfluidic device using stereolithography. It consists of the chamber layer, a medium perfusion layer that contains the cell insert and a perfusion layer. The cell insert contains co-cultures grown on silicone sheets with a 400 nm pore size PC membrane sandwiched between them. The NPM membrane is used to separate the co-cultures of collagen IV on one side and primary rat astrocytes on the other side. The selective permeability of the NPM was tested using fluorescein isothiocyanate (FITC)-dextran and other drugs. The results obtained from the BBB closely resembled the in vivo values. Traditional in vitro systems also found it hard to mimic the human liver.

The liver sinusoid is a complex structure containing four types of cells, i.e. LSEC (liver sinusoidal endothelial cells), KC (Kupffer cells), HSC (hepatic stellate cells) and HC (hepatocytes). Furthermore, the liver performs several functions ranging from metabolism to immune response thereby making it difficult to emulate all of them onto a single 2D model. Du et al. (2017) successfully designed a liver-based OOC using a nanoporous membrane. They used templating to fabricate the PDMS chip with a 400 nm pore sized PE membrane covering the two channels. The four types of cells were seeded onto the PE membrane that acted as a co-culture support. Their characterization revealed that the 400 nm pore size was similar in size to the gaps present in the liver sinusoid. They were also successfully able to control the transport using the NPM and mimic liver functions similar to in vivo conditions (Fig. 5b).

2.5 Biosensors and Theranostic Devices

Biosensing is a bourgeoning analytical technique replacing existing diagnostic systems with rapid, low-cost, point-of-care counterparts. A biosensor typically consists of a physiochemical transducer that detects biomarkers like antibodies, enzymes, aptamers and so forth (Amouzadeh Tabrizi et al. 2020). Advances in nanotechnology and microfabrication enabled researchers to explore an array of nanomaterials for biosensing. Quintessential metallic surfaces were replaced by nanoparticles, nanoporous membranes and nanoporous metals to improve the biomolecule immobilization and subsequent sensor sensitivity and durability. However, poor biocompatibility and high costs limited the application of nanoparticles (Guo et al. 2017). Today, nanoporous materials like nanoporous gold and AAO membranes dominate the scene in designing rapid, ultrasensitive and highly selective biosensing platforms. Several intrinsic characteristics of nanoporous materials like the large specific surface area, mechanical durability, electrical and optical properties, biocompatibility, tunable pore morphology and surface functionality make them the ideal candidate for precise molecular level biosensing. The large functionizable surface area amplifies the contact with the specific biomolecules from the mixture thereby reducing noise and further enhancing the sensitivity. Furthermore, apart from the surface area, the pore morphology also plays a very crucial role in tuning the biosensors sensitivity (Basu and Roychaudhuri 2018; Zhang and Li 2012). The porosity enables successful immobilization of the biomolecules to the sensor surface unlike the conventional metal counterparts that face denaturing issues. Studies by several groups elucidated the direct impact of pore size and shape on the sensor performance wherein the best results were produced when the pore size was tuned to that of the specific biomolecule. Hence, tuning the pore size and shape of the large specific surface area to the desired biomolecule is crucial. Owing to their intrinsic electrical and optical properties, there are several types of nanoporous biosensors with functionalized selectivity present today such as electrochemical, optical and field

effect transistors (FET) biosensors (Nguyen et al. 2020). Electrochemical biosensors are the most commercially prevalent, used for applications such as glucose and cancer detection. Wang's group demonstrated a novel glucose biosensor based on free-standing hollow TiO_2 nanofibres (Guo et al. 2017). The hollow nanofiber film with 300–350 nm diameter fibres were fabricated using electrospinning and sol–gel techniques. The hollow fiber diameter was similar to the size of the glucose oxidase biomolecules. The similar porosity coupled with the intrinsic charge of the TiO_2 nanofibers helped immobilize the glucose oxidase with an excellent coverage of 99.2%. Their study also revealed the excellent stability of the biosensor wherein the response reduced by 2.5% in oxygen-free conditions. Mo et al. (2018) designed an electrochemical biosensor using a porous anodized aluminium (PAA) membrane coated with graphene oxide (GO) for aflatoxin B_1 (AFB_1) detection. In short, PAA with a 200 nm pore size and hexagonal shape was fabricated and modified with a GO coating and AFB_1 aptamer. The surface functionalization enabled selective detection of AFB_1. Recent advances in semiconductor technology enabled researchers to incorporate semiconducting porous materials and design FET-based biosensors. FET biosensors possess remarkable sensitivity along with real-time detection, i.e. SARS-CoV-2 biosensing platform (Seo et al. 2020). Several groups are exploring nanoporous graphene-based FET biosensors to achieve ultrasensitivity.

The intrinsic optical properties of nanoporous materials have also been extensively used by several studies to develop novel optical biosensors. The unique optical properties facilitate the development of ultrafast and ultrasensitive sensors that surpass the performance of existing electrical biosensors (Nguyen et al. 2020). One such optical nanoporous material that has drawn the attention of researchers is nanoporous anodic alumina (NAA). Apart from its electrical properties, NAA possesses unique optical properties such as reflectivity, transmittance, chemiluminescence and photoluminescence which have been exploited to develop highly efficient optical biosensors for pathogen, protein, small molecule detection and so forth (Rajeev et al. 2018a). Voelcker's group demonstrated a novel optical biosensor using functionalized NAA for tumour necrosis factor-alpha (TNF-α) biomarker detection in chronic wounds (Rajeev et al. 2018b). NAA is fabricated with nanopores ranging between 30 and 70 nm and functionalized with a thin platinum coating to improve the reflectivity. The functionalized NAA surface is used to execute the interferometric reflectance spectroscopy (IRS) method for the detection of TNF-α (Fig. 6a). Their study revealed that NAA was capable of providing accurate real-time detection using the IRS technique. Amouzadeh Tabrizi et al. (2020) also designed an IRS-based optical biosensor using NAA for trypsin detection. NAA membrane was fabricated with a pore size of 54 nm and functionalized by immobilizing urease and FLITC. The characterization of their IRS technique using NAA revealed a very high analytical performance of 86% for 2.0 µg mL^{-1} of trypsin in comparison with the existing quantum dot-based fluorescence biosensing. Recently, researchers have been exploring nanoporous metals such as gold for biosensing applications. In comparison with conventional metallic gold, nanoporous gold possesses unique plasmonic properties apart from typical nanoporous material characteristics making it a good candidate for electrochemical analysis (Collinson 2013). Scaglione et al. (2019) demonstrated a novel optical
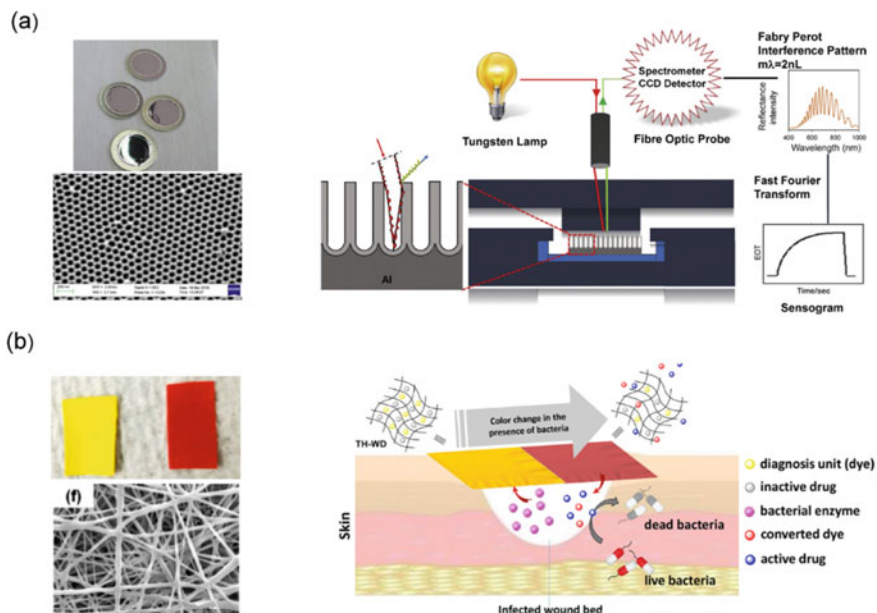
Fig. 6 NPM applications in biosensing and theranostics: **a** optical interferometric biosensing platform using NAA membranes to detect biomarkers in chronic wounds. Reprinted from Rajeev et al. (2018a). Copyright 2018, with permission from Elsevier. **b** Porous PU membrane as a theranostic wound dressing capable of detection and treatment. Reprinted with permission from Singh et al. (2019). Copyright 2019, American Chemical Society

biosensor performing SERS to detect human serum albumin (HSA) using functionalized nanoporous gold. In brief, nanoporous gold was synthesized by dealloying amorphous $Au_{20}Cu_{48}Ag_7Pd_5Si_{20}$ to create a free-standing membrane with a pore size of 40–200 nm. The surface was functionalized to enhance the SERS sensitivity enabling the optical biosensor to obtain a detection limit down to 10^{-14} M.

The current diagnostic and therapeutic platforms used by physicians are standalone devices leading to slow diagnosis. The advent of precision medicine and point-of-care services led to the emergence of a new discipline coined as 'theranostics' wherein intelligent platforms contain both diagnostics and therapeutic capabilities that can be tailored to be patient-specific. This technology is in its infancy stage and yet to go mainstream. However, a few groups have successfully demonstrated the potential of theranostic systems by exploiting the multifunctional capabilities of nanoporous materials such as nanoporous graphene for cancer research (Ghasemipour Afshar et al. 2020). In 2019, Liu's group demonstrated a facile theranostic wound dressing using a nanoporous substrate (Singh et al. 2019). The nanoporous PU membrane was fabricated using electrospinning with a diameter of 203 nm and functionalized with chromogenic (H-Cy) and ciprofloxacin prodrug (Pro-Cip). In short, Pro-Cip acts as the diagnostic probe for bacterial detection in the wound and H-Cy is the therapeutic drug released to inhibit the infection (Fig. 6b).

The porosity enabled controlled and timely release of the drug. The ex vivo characterization studies revealed that the H-Cy changed the dressing colour from yellow to red to indicate bacterial infection while the Pro-Clip membrane demonstrated a 95% success rate in incubating the bacterial pathogen upon detection.

2.6 Flexible Bioelectronics and Biointerfaces

The rise of flexible electronics has revolutionized the healthcare sector. Gradually, the existing rigid and bulky diagnostic systems are being replaced by miniature wearable counterparts that provide real-time monitoring in the home setting. This reduces hospital care costs and the need for patients to be confined to bed rest. Initially, the biggest challenge lay in designing a flexible substrate that was conformal, biocompatible and capable of multifunctional capabilities (Yin and Sheng 2018). Scientists explored an array of materials from silicon substrates to thin-film polymer sheets yet the mechanical mismatch and limited multifunctionality persisted. It was the ability to fabricate synthetic NPM to mimic its biological counterparts and the subsequent integration of microelectronics that brought about the revolutionary change. The material properties of NPMs enable it to be flexible yet possess mechanical strength to withstand buckling. Furthermore, it could be used as a substrate to print flexible electronics on it and functionalized for molecular-level detection and therapeutics. For instance, functionalized NPMs are used in artificial dialysis machines aiming to improve the quality of life for patients with renal and kidney diseases (Dang et al. 2020). Hill et al. (2020) used ultrathin nanoporous membranes to develop a wearable hemodialysis machine. The chips were designed using ultrathin silicon nitride membranes with a pore size tuned to filter out the specific toxins. The in vivo characterization revealed a 26% reduction in urea after 4 hours, demonstrating improved efficacy in contrast to the conventional thicker microporous membranes. Similarly, Fan et al. (2019) illustrated a wearable dialysis device capable of filtration and adsorption using nanoporous materials. In brief, their design consisted of two serpentine microfluidic channels separated by a porous polyamide membrane popularly used in dialysis. Sponge-inspired amphiphilic PAA-PSDVB (poly(acrylic acid)-poly(styrene divinylbenzene)) nanoporous particles were placed at the bottom channel for adsorption (Fig. 7a). The characterization studies revealed the influence of flow rate, pore size and pore density on the filtration and adsorption efficiency. Using a flow rate of 8 mL h^{-1}, the device achieved a 70% lysozyme cleaning efficiency. Nanoporous metals such as gold are also being extensively used to overcome the drawbacks of bulk metals in sensing and stimulation applications (Chapman et al. 2015; Shi et al. 2020). Bae et al. (2019) demonstrated a wearable sweat-based glucose sensor for continuous real-time monitoring based in nanoporous gold. Nanoporous gold was fabricated with a 30 nm pore size via dealloying and implemented as the working electrode. In brief, a microfluidic channel was designed to enable continuous supply of sweat and the entire set-up was placed on a flexible PDMS substrate (Fig. 7b). The sensor characterization against blood glucose and commercial kit measurements revealed that
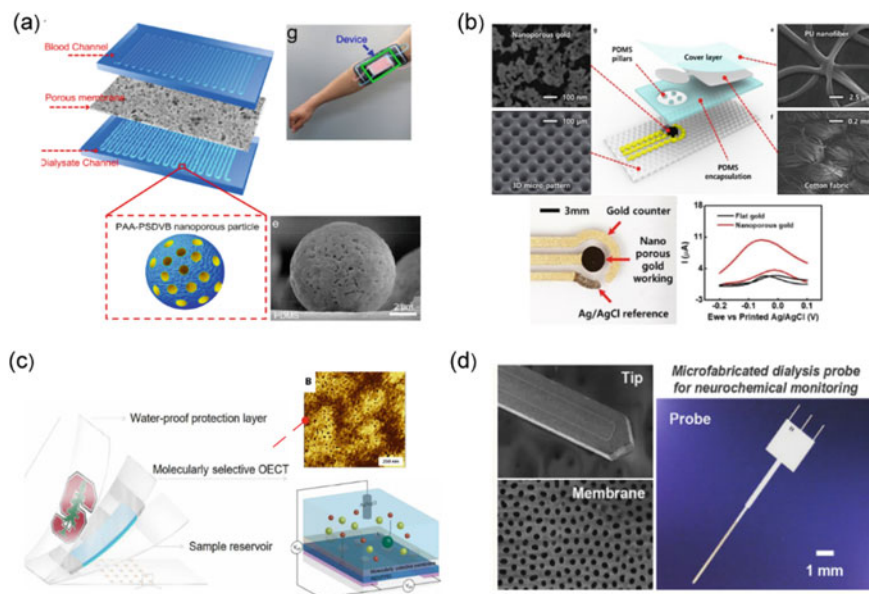
Fig. 7 Nanoporous materials in flexible electronics and biointerface applications: **a** wearable kidney-mimicking device using porous PAM membrane for filtration and nanoporous PAA-PSDBD particles for adsorption. Reprinted with permission from Fan et al. (2019). Copyright 2019, American Chemical Society. **b** Flexible glucose monitoring sensor using nanoporous gold for biosensing. Reprinted with permission from Bae et al. (2019). Copyright 2019, American Chemical Society. **c** Flexible OCET membrane-based wearable sensor for cortisol monitoring. Reproduced from Parlak et al. (2018). **d** Nanoporous AAO membrane probe for in vivo neurochemical monitoring. Reprinted with permission from Lee et al. (2016). Copyright 2016, American Chemical Society

the nanoporous gold possessed a very high glucose sensitivity of 253.4 μA cm^{-2} mM^{-1} coupled with biocompatibility. Sweat is an important biomarker that reveals a significant amount of information about a person and the ability to tune the pore morphology, surface selectivity and functionality of NPM has enabled researchers to use sweat to continuously monitor and detect various diseases, toxins and physiological conditions in a person. In 2018, Salleo's group demonstrated a novel wearable device for non-invasive cortisol sensing based on sweat (Parlak et al. 2018). In brief, they incorporated a nanoporous membrane to act as a molecularly selective membrane (MSM) sandwiched between the gate electrode of the organic electrochemical transistors (OECT) layer and channel reservoir layer (Fig. 7c). The MSM with a porosity of 10 nm diameter is highly selective and demonstrated a cortisol sensitivity of 2.68 μA dec^{-1}. Furthermore, their non-invasive sweat-based sensor produced cortisol measurements similar to in vivo enzyme-linked immunosorbent assay (ELISA) testing.

Nanoporous materials have also made tremendous strides in improving neural interfaces. The replacement of conventional silicon shanks with membrane-based designs has greatly minimized the foreign body attack and immune responses.

Furthermore, it has also enabled the development of multifunctional neural probes. Lee et al. (2016) demonstrated a novel probe for neurochemical monitoring using a nanoporous membrane as the interface. In short, they fabricated 8 mm long AAO membranes with 60–80 nm diameter pores which were used to etch polysilicon membranes. Due to the fragility of the polysilicon membranes, the AAO membranes act as a mechanical support while simultaneously enabling molecular-level transport. These membranes were placed over microchannels supported by a holder (Fig. 7d). Their in vitro and in vivo characterization revealed that the nanoporous membrane enabled detection of up to 14 neurochemicals with good signal-to-noise ratio (SNR).

2.7 Future Horizon and Challenges

Despite the rapid progress and illustration of novel NPM prototypes, they are yet to cover extensive grounds. The lack of a defined framework of protocols for nanosafety has dampened the testing and certification process. Moreover, some of the nanoporous-based devices face a few critical design challenges. For instance, the NPM used in blood cell separation, sorting and hemodynamic studies continues to face challenging issues such as clogging and rupture of the NPM due to the high pressure (Catarino et al. 2019). The polymeric membranes used with antifouling and antimicrobial properties raise elicit concerns about reduced efficacy due to the rise of drug-resistant microorganisms. The implementation of superhydrophobic and biocidal properties in the near future could tackle this challenge (Li et al. 2021). Also, the incorporation of commercial membranes in microfluidic chips faces a major sealing challenge. The fragility and antisticking properties of polymeric membranes lead to leakage if not sealed properly in the device (Vereshchagina et al. 2013).

Still, the future horizon for nanoporous materials is brimming with endless opportunities. Studies have predicted that the next-generation biomedical toolbox will contain NPMs made from metamaterials, shape memory materials that possess new functionalities like quantum effects and living plasmonics (Jakšić and Jakšić 2020). Pilot concepts like body-on-chips based on NPMs emulating the entire human body are being explored.

3 Industrial Applications

The incorporation of nanoporous materials has reinvented entire processes in several industrial sectors. The ability to tune the pore morphology and surface selectivity has led to faster and more efficient processes. Moreover, nanoporous material-based techniques are cost-effective due to their lower fabrication costs and energy saving compared to the traditional analytical techniques used by the industries (Al Mamun et al. 2020; Arabmofrad et al. 2020; Sun et al. 2021). In addition, the ability to manipulate the intrinsic magnetic, electrical and optical properties of nanoporous materials has directed several scientific breakthroughs for pharmaceutical and computing industries. The following section highlights only a few of the main applications

alongside pioneering innovations such as nanoreactors and incorporation of photonic nanoporous materials in informatics.

3.1 Chromatography and Filtration Applications

Chromatography is one of the oldest analytical techniques that has been in use since the nineteenth century. Today, it is the strongest purification method capable of providing qualitative and quantitative data and is routinely used by pharmaceutical and biotechnological industries. Conventional chromatography techniques like liquid- and gas-based chromatography have several drawbacks such as long separation time and cracking of the porous beds thereby making it expensive and time consuming for industrial applications (Kumeria and Santos 2015). The advances in nanotechnology popularized micro- and nanoporous membrane-based chromatography. The ability to precisely tune the pore morphology and surface selectivity makes membrane chromatography a cost-effective and high-performance technique. Polymer-based NPMs are a popular candidate for biomolecules due to their hydrophilicity. Furthermore, inorganic NPMs like AAO are also extensively used in the pharmaceutical industry to purify drugs due to their mechanical stability, biocompatibility and aligned porosity (Kumeria and Santos 2015). Several groups also explored nanocomposite-based membranes to improve the selectivity and multifunctionality. Asgari et al. (2014) demonstrated a nanoporous agar–nickel membrane for bioproduct adsorption using expanded bed chromatography. In brief, the nanocomposite surface with a tuned porosity of 38–130 nm was immobilized with Reactive Blue 4 (RB4) dye and the magnetic properties of Ni were used for adsorption bovine serum albumin (BSA) protein.

Filtration is another age-old technique that uses membrane technology. The properties of nanoporous materials such as the mechanical durability, shorter channels for faster diffusion along with tunable porosity and selectivity have significantly expanded the filtration applications. Early on, it was restricted to water purification applications, today due to the tuneable nanoscale porosity it is used in the food, pulp and paper, water treatment and biotechnological industries for filtering minute toxins, contaminants, biomolecules and viruses. It is an efficient, scalable option over expensive chromatography techniques. Russell's group demonstrated an asymmetric nanoporous membrane for filtration of viruses (Yang et al. 2006). They fabricated a PS-b-PMMA membrane with a 10–40 nm pore diameter, which was supported by a polysulfone (PSU) membrane layer. The NPM demonstrated excellent selectivity for HRV14 viruses. This was due to the similarity in size between the pores and molecules. Similarly, Schuster et al. (2018) demonstrated a novel polymer NPM for protein ultrafiltration. They fabricated 25 nm diameter poly(o-cresyl glycidyl ether)-co-formaldehyde with branched polyethyleneimine (PCGF/PEI) membranes. Chen et al. (2020) demonstrated the use of ceramic NPM for the precise filtration of extremely minute polysaccharides for the food industry.

They fabricated ZrO_2 membranes using the sol–gel technique with a tuned porosity of 5.9 nm that demonstrated a very high separation factor of 11.5.

3.2 Photocatalytic and Adsorption Applications

Photocatalysis is an innovative technique that uses light and semiconducting nanomaterial for oxidation and subsequent degradation of toxins (Rios et al. 2011). Membrane filtration coupled with photocatalytic capabilities is drawing a lot of attention for designing low-cost, efficient systems that simultaneously filter and purify industrial wastewater. Several nanoporous materials like TiO_2, ZnO and composites with ceramic, metallic and conducting polymers have been explored for their photocatalytic activity. To date, TiO_2-based NPMs are the most widely used for industrial water treatments due to its high performance using UV illumination (Riaz and Park 2020). The large specific surface area of porous materials enables greater catalytic activity while simultaneously performing filtration through the nanopores along with its intrinsic charge and long excitation state. Ma et al. (2009) demonstrated a novel silicon-doped TiO_2 photocatalytic membrane on an Al_2O_3 filtration membrane for wastewater treatment. The addition of SiO_2 improved the surface wettability while the combined operation had a 40% better efficiency than stand-alone filtration and purification processes. Athanasekou et al. (2015) studied the effect of porosity, surface area and charge for photocatalysis by comparing four types of composite TiO_2 NPMs. The organic shell layer modified membrane outperformed graphene oxide and activated TiO_2. Advances in fabrication has also led to the creation of hybrid photocatalytic membranes capable of treating low-concentration toxins which are extremely difficult to remove by conventional methods. Xu et al. (2020) demonstrated a novel platinum-implanted TiO_2 for UV and vacuum UV (VUV) excitation-based photocatalysis of ethenzamide. In brief, embedded platinum increases the number of active sites on the NPM and acts an electron capture centre. Their characterization study revealed 94.52% performance efficiency by 0.1Pt-embedded TiO_2 nanoporous membrane for removal of ethenzamide from 500 ppb using VUV illumination (Fig. 8a). Furthermore, they compared the efficacy of porous and non-porous membranes. Porosity and the amount of platinum embedded were crucial parameters defining the efficiency, the nanoporous membranes with 0.1 concentration of platinum outperforming the other 0.05 Pt, 0.25 Pt porous and non-porous membranes.

Adsorption is another popular technique employed by several industries to tackle global water shortages due the industrial consumption and subsequent generation of massive amounts of toxic wastewater. The large surface area, mechanical stability, tunable porosity and selectivity of nanoporous adsorbents have made it an efficient and cost-effective industrial application. Today, nanoporous adsorbents yield high-quality water by purifying, decolourizing, deodorizing and accumulating the contaminants (Arabmofrad et al. 2020). Several organic and inorganic nanoporous materials such as polymeric membranes, activated carbon (AC), zeolites, metal–organic frameworks (MOFs) and graphene have been widely explored for adsorption.
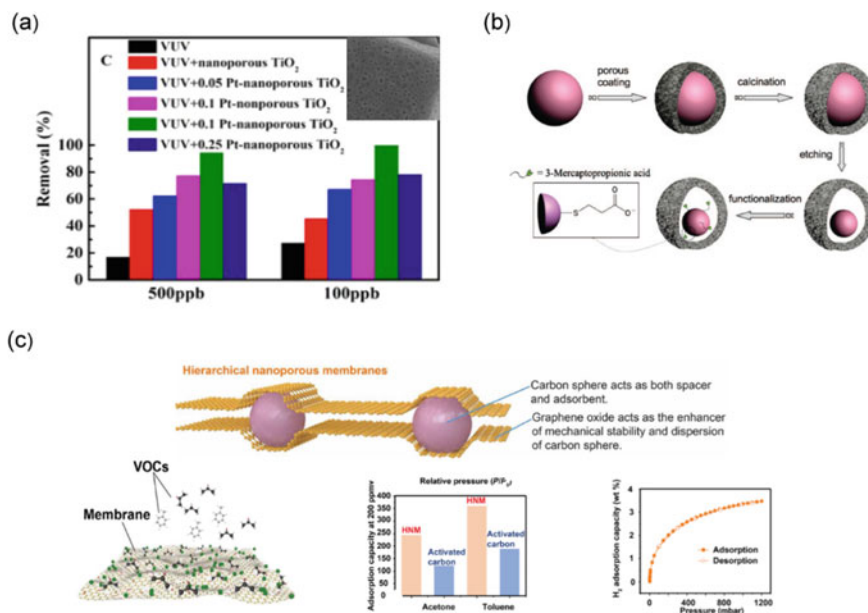
Fig. 8 Nanoporous material applications in photocatalysis, nanoreactors and adsorption: **a** Nanoporous TiO$_2$ with atomically dispersed Pt used for photocatalysis of pollutants. Reprinted from Xu et al. (2020). Copyright 2020, with permission from Elsevier. **b** Functionalized porous Au@SiO$_2$ nanoreactors. Reprinted with permission from Lee et al. (2008). Copyright 2008, American Chemical Society. **c** Hierarchical nanoporous GO and carbon sphere membrane for adsorption of VOC and H$_2$ storage. Reproduced from Mao et al. (2020)

To date, porous AC is the most extensively used due to its ability to effectively adsorb a variety of contaminants. Sava Gallis et al. (2017) explored the efficiency of various adsorbents in capturing radiological iodine gas, a highly toxic by-product of nuclear processes. Their study revealed that the large surface area and pore morphology were critical features that controlled the efficiency of adsorption and a mismatch in adsorbate molecule and adsorbent size would greatly impede the efficiency. The advances in material science have greatly improved the mechanical durability and multifunctionality of polymers. Furthermore, polymers cost less than their inorganic counterparts and have simpler fabrication procedures thereby encouraging scientists to explore polymer-based adsorption for applications like desalination and water filtering equipment at homes. Suzuki et al. (2020) demonstrated a novel self-standing polymer NPM using liquid crystal molecular assembly. The nanoporous membranes were functionalized with charge- and size-dependent properties which greatly improved the selective adsorption of ionic dyes from mixtures. With nanotechnological advances, scientists are designing multifunctional nanoporous membranes to selectively remove toxic gases and act as a storage carrier for useful gases like hydrogen and oxygen. Mao et al. (2020) demonstrated a novel multifunctional nanoporous membrane capable of adsorbing volatile organic compounds (VOCs)

and storage of H_2 gas. In brief, carbon spheres were fabricated from wood cellulose and sandwiched between graphene oxide sheets to create a hierarchical NPM with 0.7–2 nm diameter pores (Fig. 8c). Their characterization revealed a high adsorption rate of VOCs and H_2 with a 98.5% efficiency over five cycles.

3.3 Nanoreactors

Nanoreactors are a relatively new field, which consists of nanoscale vessels that isolate molecules from the outside and produce chemical reactions within them to alter the molecule's chemistry. They gained popularity in medical and environmental applications like diagnostics, therapeutics and pollutant decontamination due to their ability to be very precise and target the desired molecules. A crucial requirement for their functioning is the need for a large surface area to carry out the chemical reactions. The large surface area and tunable characteristics of nanoporous materials make it an ideal candidate to design nanoreactors. Various organic and inorganic nanoporous materials have been explored to design nanoreactors. Xu et al. (2018) demonstrated a novel graphene-based electrochemical enzyme nanoreactor to investigate steroid hormones. It was constructed using polydopamine-modified nanoporous graphene with the steroid enzyme CYP3A4 immobilized inside it. Similarly, Mikhraliieva et al. (2020) demonstrated a silica gel nanoreactor to synthesize fluorescent carbon dots from citric acid encapsulated within it. The pore size is a crucial feature that determines the efficiency, a 4–11 nm pore size was successful in synthesizing carbon dots. Song's group also illustrated the importance of tuning the pore size and selectivity for enhancing the performance of the nanoreactors (Lee et al. 2008). They designed a nanoporous Au@SiO_2 reactor (Fig. 8b). In order to enhance the catalytic efficiency, the porosity of SiO_2 was controlled using C_{18}TMS porogen and the Au was functionalized using 3-mercaptopropionic acid (3-MPA). Their characterization study revealed a 13-fold enhancement due to the controlled porosity and surface functionality.

3.4 Biosensing and Photonic Applications

There is a growing demand for a rapid and cost-effective detection of toxins in food and water sources. Conventional analytical techniques are bulky, expensive, time-consuming and require skilled labour thereby increasing the costs exponentially for industries. The advent of portable and miniature biosensors that provide rapid analysis without requiring skilled labour makes it an attractive option for these industries. Furthermore, the incorporation of nanoporous materials significantly enhances the biosensors performance to meet the industrial standards. This is due to their large surface area along with the ability functionalize the surface to detect specific molecules from the mixture. Ghosh and Roychaudhuri (2013) demonstrated

an immunosensor based on nanoporous silicon oxide for detection of aflatoxin B1 (AfB1), a carcinogenic toxin found in food and water. In brief, they used anodic etching to fabricate the NPM with 200–400 nm pore sizes. Their characterization studies revealed that the smaller pore sizes exhibited excellent impedance sensitivity to varying concentrations of the toxin. Similarly, Wujcik et al. (2016) demonstrated a colorimetric sensor based on nanoporous syndiotactic polypropylene (sPP) for the detection of trihalomethanes (THMs), a potent contaminant found in drinking water. They electrospun hydrophobic, nanoporous sPP membranes and coupled it with the colourimetric Fujiwara reaction to design their novel sensor. The characterization revealed that the selectivity of the sPP greatly enhanced the sensitivity and colour intensity of the colorimetric response. Several groups have also manipulated the unique optical properties of nanoporous materials for developing sensors for industrial applications. Knoll et al. (2020) reviewed the novel optical waveguide spectroscopy based on nanoporous materials for sensing and communication-based industrial applications. For instance, AAO-based NPM can be fabricated with aligned porosity creating uniform nanochannels that do not scatter or deflect light like the non-uniform random membranes. Furthermore, the large surface area also increases the sensitivity of the optical sensor.

Nanotechnological advances continue to miniaturize computing chips and data storage devices. One exciting domain is the ability to optically encode and store binary data in the spectral signature of nanoscale materials. The unique optical properties and tuneable selectivity of nanoporous materials make it the ideal candidate over their counterparts such as quantum dots and photonic crystals. Several inorganic nanoporous materials like AAO, silicon, gold possess unique optical properties can be manipulated for optical encoding of information. Santos et al. (2016) illustrated a novel method of storing 8-bit ASCII-based information in the spectral signature of AAO-based nanoporous crystals. In brief, they designed a novel anodization technique called multisinusoidal pulse anodization (MSPA) to create complex etching profiles containing encoded information. This was physically encoded onto the NAA photonic crystals. Their characterization studies revealed that the NAA crystals also exhibited unique interferometric colours characteristic of each binary data. This feature could be used to design nanosized photonic barcodes wherein the corresponding width of the photonic bars indicates the 0/1 state in the 8-bit code (Fig. 9a).

3.5 *Energy Harvesting and Storage Applications*

Nanoporous materials have facilitated the large-scale implementation of affordable and efficient renewable energy harvesting and storage systems. Today, nanoporous thin-film solar cells have replaced bulky photovoltaic cells. The tunable porosity helps trap the desired spectrum of light while the short nanochannels enable rapid transport. Hodes and Cahen (2012) proposed a new design for extremely thin absorber (ETA) solar cells. In order to improve the efficiency, they proposed reversing the
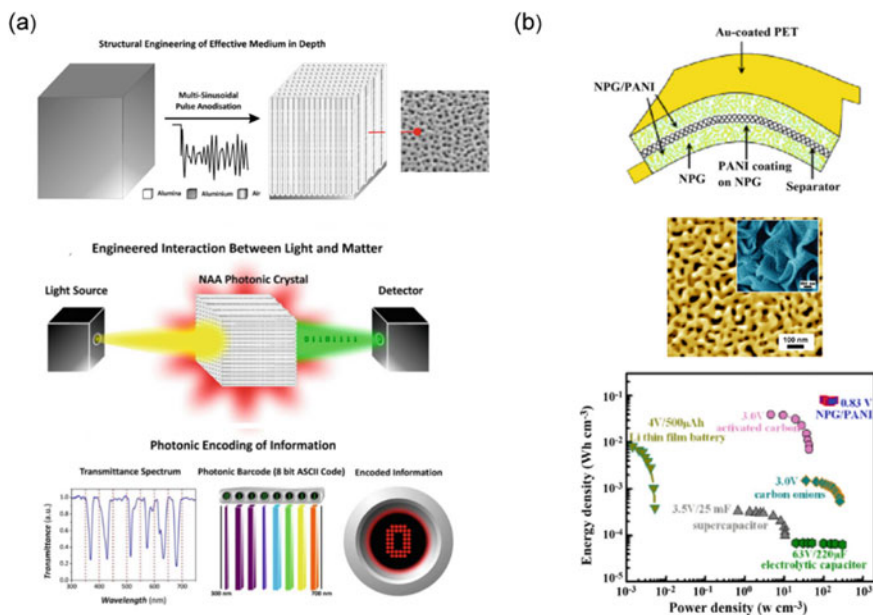
Fig. 9 NPM applications in photonics and energy storage: **a** NPM from photonic AA used as photonic barcodes by encoding data into the spectrum signature. Republished with permission of The Royal Society of Chemistry, from Santos et al. (2016); permission conveyed through Copyright Clearance Center, Inc. **b** Nanoporous Au/PANI thin films as supercapacitors. Reprinted from Lang et al. (2012). Copyright 2012, with permission from Elsevier

layers and depositing the porous hole conductor first. Inorganic nanoporous silicon is also extensively used in solar cell technology for different functionalities. Porous Si wafers possess direct and wide bandgaps that can be utilized by carefully tuning the pore morphology to absorb the desired spectrum range (Al Mamun et al. 2020). Another popular application is using it as antireflective coatings for solar cells. Miao et al. (2013) demonstrated a hybrid SiO_2-TiO_2 coating for solar cells. Porous SiO_2 films with 11 nm nanopore diameter behaves as the antireflective layer while the porous TiO_2 layer acts as a self-cleaning surface protecting the SiO_2 pores from clogging. The coating helped achieve a 3.4% transmittance gain over uncoated solar cells. Another novel solar harvesting technology is the dye sensitized solar cells (DSSC) which use nanoporous TiO_2 membranes functionalized with dye molecules to capture the solar energy (Rios et al. 2011).

Fuel cells, popularly used to power electric vehicles, have also greatly advanced due to the incorporation of NPMs. The membrane pore size, pore density and selectivity are the main controlling factors for scaling the efficiency. Traditional polymer electrolyte fuel cells (PEFC) used thick microscale Nafion membranes which when replaced with NPM-enabled faster proton transport (Jakšić and Jakšić 2020). Karan's group demonstrated a novel double-layer carbon scaffold for higher current density in PEFC (Islam et al. 2020). In short, their design used a double layer, nanoporous

carbon scaffold with 85 nm pore diameter neat the catalyst layer. One membrane is functionalized with hydrophilic wettability while the other possessed hydrophobic wettability. The hydrophilic layers attract water and allow O_2 transport while the hydrophobic layers keep the water trapped within the catalyst layer.

The rise in portable electronic devices and electronic vehicles demands for more efficient energy storage devices. Lithium-ion batteries are the gold standard in energy devices. A crucial component of any battery is the separator membrane whose porosity, surface wettability and thickness effect its storage and discharge efficiency (Rios et al. 2011). Several research groups studied the implementation of nanoporous materials as a separator membrane in order to increase the energy density while simultaneously minimizing the battery size. The NPM features such as large surface area to volume, shorter nanochannels, tuneable porosity and functionalization enable faster diffusion and greater storage capacity at reduced dimensions. Tour's group proposed a nanoporous Fe_2O_3/Fe_3C-graphene-based anode electrode to enhance the capacity and cyclability of lithium-ion batteries (Yang et al. 2014). The galvanostatic tests revealed that the thin membrane with a 40 nm pore size achieved a storage capacity of 346 $\mu A\ cm^{-2}\ \mu m^{-1}$. Several studies have also been conducted to develop flexible batteries that can be easily integrated into flexible electronic devices. Wan et al. (2019) demonstrated a solid-state electrolyte based on a polymer nanocomposite for ultrathin flexible lithium batteries. The conventional liquid electrolytes were replaced with nanoporous polyamide film (PI) filled with polyethylene oxide/lithium bis(trifluoromethanesulfony)imide (PEO/LiTFSI) to enhance the ionic conductivity. The 200 nm diameter porous membrane retained the flexibility of polymers while the shorter nanochannels and aligned porosity enhanced the performance of the solid-state electrolyte. Nanoporous metal-based electrodes have also attracted the attention of researchers as they outperform their bulk counterparts due to their intrinsic conductivity and large surface (Wu et al. 2020).

Supercapacitors are a new class of energy storage devices garnering a lot of attention due to their high energy density and ultrafast charge/discharge rates that outperform the conventional electrolytic capacitors. This is due to the implementation of various nanoporous materials to form the electrodes and separator creating a large surface area for storage and shorter channels for faster transport (Ding and Zhang 2016). Several groups explored metallic and conducting polymer-based NPM composites to achieve high capacitance rates. Lang et al. (2011) demonstrated a composite of NPG embedded with nanocrystalline MnO_2 to enhance the supercapacitance. Chen's group also developed a flexible solid-state supercapacitor composed of composite NPM films (Lang et al. 2012). The composite was prepared using nanoporous gold with polyaniline (NPG/PANI). In brief, NPG is prepared via dealloying $Ag_{65}Au_{35}$ and then embedded PANI in the nanopores (Fig. 9b). The characterization studies revealed an ultrahigh volumetric capacitance of 1500 F cm^{-3} outperforming the previous supercapacitors depicted in the Ragone plot.

3.6 Future Horizons and Challenges

The advancements bought about by nanoporous materials in the aforementioned industrial applications face a few critical issues. A major challenge is the cost of metallic nanoporous materials while implementing them at an industrial scale. This can be overcome by improving the durability and functional properties organic polymeric nanoporous materials. In filtration applications, clogging and sealing challenges continue to persist. This can be tackled by finding a scalable technique to functionalize the surface wettability. In addition, researchers are also exploring simple, eco-friendly, low-cost alternatives like nanocellulose-based energy storage devices, which will pave the way towards sustainable green energy.

A bright future can be envisioned for nanoporous materials in industrial applications. NPMs will be a key contributor towards a sustainable future through its energy and environmental applications. Furthermore, pilot concepts like optical encoding of data to design self-reporting smart membranes in DDS and other applications will lay the foundation for the next-generation technology.

4 Conclusion

This chapter covered numerous applications of nanoporous materials in an attempt to highlight its profound potential across various disciplines. In particular, nanoporous materials have made tremendous progress in the healthcare sector by paving the way towards personalized treatments via multimodal devices capable of therapeutics and diagnostics. Today, several nanotheranostic devices based on NPM technology have garnered a lot of attention due to its capability to efficiently detect, diagnose and treat at a molecular level. Apart from these commercial applications, the scientific community also relies greatly on synthetic nanoporous membranes to mimic the biological counterparts in their respective studies using microfluidic and lab-on-chip systems.

In the industrial realm, we briefly covered the advancements nanoporous materials have made in traditional applications like chromatography and adsorption. Today, the advances in nanoporous membrane technology have led to several cutting-edge inventions like NPM-based photonic data storage that are completely redefining the way we can store and manipulate binary data. It is certain that the perfection of synthetic nanoporous structures that can accurately mimic the complex multifunctionalities of their biological counterparts will spearhead many new possibilities that improves the quality of life and assist in realizing the zero emission revolution.

References

Adiga, P.S., Jin, C., Curtiss, A.L., Monteiro-Riviere, A.N., Narayan, J.R.: Nanoporous membranes for medical and biological applications. Wiley Interdiscip. Rev. Nanomed. Nanobiotechnol. **1**(5), 1–7 (2009). https://doi.org/10.1002/wnan.50

Al Mamun, M.A., Noor, M., Hasanuzzaman, M., Hashmi, M.S.J.: Nano-porous materials for use in solar cells and fuel cells. In: Encyclopedia of Renewable and Sustainable Materials. Elsevier Inc. (2020). https://doi.org/10.1016/B978-0-12-803581-8.11267-6

Amouzadeh Tabrizi, M., Ferré-Borrull, J., Marsal, L.F.: Remote biosensor for the determination of trypsin by using nanoporous anodic alumina as a three-dimensional nanostructured material. Sci. Rep. **10**(1), 1–10 (2020). https://doi.org/10.1038/s41598-020-59287-7

Arabmofrad, S., Bagheri, M., Rajabi, H., Jafari, S.M.: Nanoadsorbents and nanoporous materials for the food industry. In: Handbook of Food Nanotechnology. Elsevier Inc. (2020). https://doi.org/10.1016/b978-0-12-815866-1.00004-2

Asgari, S., Jahanshahi, M., Rahimpour, A.: Cost-effective nanoporous Agar-Agar polymer/Nickel powder composite particle for effective bio-products adsorption by expanded bed chromatography. J. Chromatogr. A **1361**, 191–202 (2014). https://doi.org/10.1016/j.chroma.2014.08.016

Athanasekou, C.P., Moustakas, N.G., Morales-Torres, S., Pastrana-Martínez, L.M., Figueiredo, J.L., Faria, J.L., Silva, A.M.T., Dona-Rodriguez, J.M., Romanos, G.E., Falaras, P.: Ceramic photocatalytic membranes for water filtration under UV and visible light. Appl. Catal. B Environ. **178**, 12–19 (2015). https://doi.org/10.1016/j.apcatb.2014.11.021

Bae, C.W., Toi, P.T., Kim, B.Y., Lee, W.I., Lee, H.B., Hanif, A., Lee, E.H., Lee, N.E.: Fully stretchable capillary microfluidics-integrated nanoporous gold electrochemical sensor for wearable continuous glucose monitoring. ACS Appl. Mater. Interfaces **11**(16), 14567–14575 (2019). https://doi.org/10.1021/acsami.9b00848

Basu, J., Roychaudhuri, C.: Graphene nanoporous FET biosensor: influence of pore dimension on sensing performance in complex analyte. IEEE Sens. J. **18**(14), 5627–5634 (2018). https://doi.org/10.1109/JSEN.2018.2841060

Bein, A., Shin, W., Jalili-Firoozinezhad, S., Park, M.H., Sontheimer-Phelps, A., Tovaglieri, A., Chalkiadaki, A., Kim, H.J., Ingber, D.E.: Microfluidic organ-on-a-chip models of human intestine. Cell. Mol. Gastroenterol. Hepatol. **5**(4), 659–668 (2018). https://doi.org/10.1016/j.jcmgh.2017.12.010

Cai, K., Luo, Z., Hu, Y., Chen, X., Liao, Y., Yang, L., Deng, L.: Magnetically triggered reversible controlled drug delivery from microfabricated polymeric multireservoir devices. Adv. Mater. **21**(40), 4045–4049 (2009). https://doi.org/10.1002/adma.200900593

Carter, R.N., Casillo, S.M., Mazzocchia, A.R., DesOrmeauxc, J.-P.S., Roussiec, J.A., Gaborski, T.R.: Ultrathin transparent membranes for cellular barrier and co-culture models. Biofabrication **9**(1), 015019 (2017). https://doi.org/10.1088/1758-5090/aa5ba7

Catarino, S.O., Rodrigues, R.O., Pinho, D., Miranda, J.M., Minas, G., Lima, R.: Blood cells separation and sorting techniques of passive microfluidic devices: from fabrication to applications. Micromachines **10**(9) (2019). https://doi.org/10.3390/mi10090593

Chapman, C.A.R., Chen, H., Stamou, M., Biener, J., Biener, M.M., Lein, P.J., Seker, E.: Nanoporous gold as a neural interface coating: effects of topography, surface chemistry, and feature size. ACS Appl. Mater. Interfaces **7**(13), 7093–7100 (2015). https://doi.org/10.1021/acsami.5b00410

Chen, X., Qi, T., Zhang, Y., Wang, T., Qiu, M., Cui, Z., Fan, Y.: Facile pore size tuning and characterization of nanoporous ceramic membranes for the purification of polysaccharide. J. Membr. Sci. **597**, 117631 (2020). https://doi.org/10.1016/j.memsci.2019.117631

Collinson, M.M.: Nanoporous gold electrodes and their applications in analytical chemistry. ISRN Anal. Chem. **2013**, 1–21 (2013). https://doi.org/10.1155/2013/692484

Dalili, A., Samiei, E., Hoorfar, M.: A review of sorting, separation and isolation of cells and microbeads for biomedical applications: microfluidic approaches. Analyst **144**(1), 87–113 (2019). https://doi.org/10.1039/c8an01061g

Damodaran, V.B., Murthy, S.N.: Bio-inspired strategies for designing antifouling biomaterials. Biomater. Res. **20**(1), 1–11 (2016). https://doi.org/10.1186/s40824-016-0064-4

Dang, B.V., Taylor, R.A., Charlton, A.J., Le-Clech, P., Barber, T.J.: Toward portable artificial kidneys: the role of advanced microfluidics and membrane technologies in implantable systems. IEEE Rev. Biomed. Eng. **13**, 261–279 (2020). https://doi.org/10.1109/RBME.2019.2933339

Deng, X., Zhang, M., Tan, L., Zeng, T., Lai, X., Geng, X., Huang, C., Li, A., Pan, Y., Hu, J.: Hydrophilic porous poly(l-lactic acid) nanomembranes: self-assembly, and anti-biofouling and anti-thrombosis effects. ChemPlusChem **84**(7), 989–998 (2019). https://doi.org/10.1002/cplu.201900256

Di Trani, N., Silvestri, A., Sizovs, A., Wang, Y., Erm, D.R., Demarchi, D., Liu, X., Grattoni, A.: Electrostatically gated nanofluidic membrane for ultra-low power controlled drug delivery. Lab Chip **20**(9), 1562–1576 (2020). https://doi.org/10.1039/d0lc00121j

Ding, Y., Zhang, Z.: Nanoporous metals for supercapacitor applications. In: Nanoporous Metals for Advanced Energy Technologies, pp. 1–223. Springer International Publishing (2016). https://doi.org/10.1007/978-3-319-29749-1_4

Du, Y., Li, N., Yang, H., Luo, C., Gong, Y., Tong, C., Gao, Y., Lü, S., Long, M.: Mimicking liver sinusoidal structures and functions using a 3D-configured microfluidic chip. Lab Chip **17**(5), 782–794 (2017). https://doi.org/10.1039/c6lc01374k

Dubey, N., Kushwaha, C.S., Shukla, S.K.: A review on electrically conducting polymer bionanocomposites for biomedical and other applications. Int. J. Polym. Mater. Polym. Biomater. **69**(11), 709–727 (2020). https://doi.org/10.1080/00914037.2019.1605513

Fan, J.B., Luo, J., Luo, Z., Song, Y., Wang, Z., Meng, J., Wang, B., Zhang, S., Zheng, Z., Chen, X., Wang, S.: Bioinspired microfluidic device by integrating a porous membrane and heterostructured nanoporous particles for biomolecule cleaning. ACS Nano **13**(7), 8374–8381 (2019). https://doi.org/10.1021/acsnano.9b03918

Francolini, I., Vuotto, C., Piozzi, A., Donelli, G.: Antifouling and antimicrobial biomaterials: an overview. APMIS **125**(4), 392–417 (2017). https://doi.org/10.1111/apm.12675

Frohlich, E.M., Luis Alonso, J., Borenstein, J.T., Zhang, X., Arnaout, M.A., Charest, J.L.: Topographically-patterned porous membranes in a microfluidic device as an in vitro model of renal reabsorptive barriers. Lab Chip **13**(12), 2311–2319 (2013). https://doi.org/10.1039/c3lc50199j

Fujita, T.: Hierarchical nanoporous metals as a path toward the ultimate three-dimensional functionality. Sci. Technol. Adv. Mater. **18**(1), 724–740 (2017). https://doi.org/10.1080/14686996.2017.1377047

Gaidash, A.A., Sinitsa, L.N., Babenko, O.A., Lugovskoy, A.A.: Nanoporous structure of bone matrix at osteoporosis from data of atomic force microscopy and IR spectroscopy. J. Osteoporos. **2011**, 1–7 (2011). https://doi.org/10.4061/2011/162041

Garle, A., Miller, A., Sarrafian, T., Tonne, J., Ikeda, Y., Grande, J., Wigle, D., Yaszemski, M., Kudva, Y.: Development of nanoporous polyurethane hydrogel membranes for cell encapsulation. Regen. Eng. Transl. Med. **6**(2), 217–227 (2020). https://doi.org/10.1007/s40883-019-00125-2

Ghasemipour Afshar, E., Zarrabi, A., Dehshahri, A., Ashrafizadeh, M., Dehghannoudeh, G., Behnam, B., Mandegary, A., Pardakhty, A., Mohammadinejad, R., Tavakol, S.: Graphene as a promising multifunctional nanoplatform for glioblastoma theranostic applications. FlatChem **22**, 2452–2627 (2020). https://doi.org/10.1016/j.flatc.2020.100173

Ghosh, H., Roychaudhuri, C.: Ultrasensitive food toxin biosensor using frequency based signals of silicon oxide nanoporous structure. Appl. Phys. Lett. **102**(24) (2013). https://doi.org/10.1063/1.4811409

Guo, Q., Liu, L., Zhang, M., Hou, H., Song, Y., Wang, H., Zhong, B., Wang, L.: Hierarchically mesostructured porous TiO_2 hollow nanofibers for high performance glucose biosensing. Biosens. Bioelectron. **92**, 654–660 (2017). https://doi.org/10.1016/j.bios.2016.10.036

He, Y., Qin, L., Fang, Y., Dan, Z., Shen, Y., Tan, G., Huang, Y., Ma, C.: Electrospun PLGA nanomembrane: a novel formulation of extended-release bupivacaine delivery reducing postoperative pain. Mater. Des. **193**, 108768 (2020). https://doi.org/10.1016/j.matdes.2020.108768

Hill, K., Walker, S.N., Salminen, A., Chung, H.L., Li, X., Ezzat, B., Miller, J.J., DesOrmeaux, J.P.S., Zhang, J., Hayden, A., Burgin, T., Piraino, L., May, M.N., Gaborski, T.R., Roussie, J.A., Taylor, J., DiVincenti, L., Shestopalov, A.A., McGrath, J.L., Johnson, D.G.: Second generation nanoporous silicon nitride membranes for high toxin clearance and small format hemodialysis. Adv. Healthcare Mater. **9**, 1900750 (2020). https://doi.org/10.1002/adhm.201900750

Hodes, G., Cahen, D.: All-solid-state, semiconductor-sensitized nanoporous solar cells. Acc. Chem. Res. **45**(5), 705–713 (2012). https://doi.org/10.1021/ar200219h

Ileri, N., Stroeve, P., Palazoglu, A., Faller, R., Zaidi, H.S., Nguyen, T.H., Britten, A.J., Létant, E.S., Tringe, W.J.: Fabrication of functional silicon-based nanoporous membranes. J. Micro/nanolithogr. MEMS MOEMS **11**(1), 013012 (2012). https://doi.org/10.1117/1.jmm.11.1.013012

Islam, M.S., Shahid, A., Kuryllo, K., Li, Y., Deen, M.J., Selvaganapathy, P.R.: Electrophoretic concentration and electrical lysis of bacteria in a microfluidic device using a nanoporous membrane. Micromachines **8**(2) (2017). https://doi.org/10.3390/mi8020045

Islam, M.N., Shrivastava, U., Atwa, M., Li, X., Birss, V., Karan, K.: Highly ordered nanoporous carbon scaffold with controllable wettability as the microporous layer for fuel cells. ACS Appl. Mater. Interfaces **12**(35), 39215–39226 (2020). https://doi.org/10.1021/acsami.0c10755

Jakšić, Z., Jakšić, O.: Biomimetic nanomembranes: an overview. Biomimetics **5**(2) (2020). https://doi.org/10.3390/biomimetics5020024

Jeon, G., Yang, S.Y., Kim, J.K.: Functional nanoporous membranes for drug delivery. J. Mater. Chem. **22**(30), 14814–14834 (2012). https://doi.org/10.1039/c2jm32430j

Kim, H.J., Huh, D., Hamilton, G., Ingber, D.E.: Human gut-on-a-chip inhabited by microbial flora that experiences intestinal peristalsis-like motions and flow. Lab Chip **12**(12), 2165–2174 (2012). https://doi.org/10.1039/c2lc40074j

Kim, S., Ozalp, E.I., Sundar, V., Zhu, J.G., Weldon, J.A.: Modeling of electrically controlled molecular diffusion in a nanofluidic channel. J. Appl. Phys. **118**(7), 074301 (2015). https://doi.org/10.1063/1.4928607

Knoll, W., Azzaroni, O., Duran, H., Kunze-Liebhäuser, J., Lau, K.H.A., Reimhult, E., Yameen, B.: Nanoporous thin films in optical waveguide spectroscopy for chemical analytics. Anal. Bioanal. Chem. **412**(14), 3299–3315 (2020). https://doi.org/10.1007/s00216-020-02452-8

Kong, Y., Xu, R., Darabi, M.A., Zhong, W., Luo, G., Xing, M.M.Q., Wu, J.: Fast and safe fabrication of a free-standing chitosan/alginate nanomembrane to promote stem cell delivery and wound healing. Int. J. Nanomed. **11**, 2543–2555 (2016). https://doi.org/10.2147/IJN.S102861

Krafft, B., Panneerselvam, R., Geissler, D., Belder, D.: A microfluidic device enabling surface-enhanced Raman spectroscopy at chip-integrated multifunctional nanoporous membranes. Anal. Bioanal. Chem. **412**(2), 267–277 (2020). https://doi.org/10.1007/s00216-019-02228-9

Kumeria, T., Santos, A.: Nanoporous alumina membranes for chromatography and molecular transporting. In: Springer Series in Materials Science, vol. 219. Springer International Publishing, pp. 293–318 (2015). https://doi.org/10.1007/978-3-319-20334-8_10

Lang, X., Hirata, A., Fujita, T., Chen, M.: Nanoporous metal/oxide hybrid electrodes for electrochemical supercapacitors. Nat. Nanotechnol. **6**(4), 232–236 (2011). https://doi.org/10.1038/nnano.2011.13

Lang, X., Zhang, L., Fujita, T., Ding, Y., Chen, M.: Three-dimensional bicontinuous nanoporous Au/polyaniline hybrid films for high-performance electrochemical supercapacitors. J. Power Sources **197**, 325–329 (2012). https://doi.org/10.1016/j.jpowsour.2011.09.006

Lee, J., Park, J.C., Bang, J.U., Song, H.: Precise tuning of porosity and surface functionality in Au@SiO$_2$ nanoreactors for high catalytic efficiency. Chem. Mater. **20**(18), 5839–5844 (2008). https://doi.org/10.1021/cm801149w

Lee, W.H., Ngernsutivorakul, T., Mabrouk, O.S., Wong, J.M.T., Dugan, C.E., Pappas, S.S., Yoon, H.J., Kennedy, R.T.: Microfabrication and in vivo performance of a microdialysis probe with embedded membrane. Anal. Chem. **88**(2), 1230–1237 (2016). https://doi.org/10.1021/acs.analchem.5b03541

Li, H., Cao, J., Wei, Q., Ma, L., Zhou, K., Yu, Z., Zeng, S., Zhu, R., Yang, W., Lin, C.T., Meng, L.: Antifouling nanoporous diamond membrane for enhanced detection of dopamine in human serum. J. Mater. Sci. **56**(1), 746–761 (2021). https://doi.org/10.1007/s10853-020-05344-5

Ma, N., Quan, X., Zhang, Y., Chen, S., Zhao, H.: Integration of separation and photocatalysis using an inorganic membrane modified with Si-doped TiO_2 for water purification. J. Membr. Sci. **335**(1–2), 58–67 (2009). https://doi.org/10.1016/j.memsci.2009.02.040

Mao, H., Tang, J., Chen, J., Wan, J., Hou, K., Peng, Y., Halat, D.M., Xiao, L., Zhang, R., Lv, X., Yang, A., Cui, Y., Reimer, J.A.: Designing hierarchical nanoporous membranes for highly efficient gas adsorption and storage. Sci. Adv. **6**(41), 1–10 (2020). https://doi.org/10.1126/sciadv.abb0694

Miao, L., Su, L.F., Tanemura, S., Fisher, C.A.J., Zhao, L.L., Liang, Q., Xu, G.: Cost-effective nanoporous SiO_2-TiO_2 coatings on glass substrates with antireflective and self-cleaning properties. Appl. Energy **112**, 1198–1205 (2013). https://doi.org/10.1016/j.apenergy.2013.03.043

Mikhraliieva, A., Zaitsev, V., Aucélio, R.Q., da Motta, H.B., Nazarkovsky, M.: Benefit of porous silica nanoreactor in preparation of fluorescence carbon dots from citric acid. Nano Express **1**(1), 010011 (2020). https://doi.org/10.1088/2632-959x/ab7e0d

Miyazawa, N., Hakamada, M., Mabuchi, M.: Antimicrobial mechanisms due to hyperpolarisation induced by nanoporous Au. Sci. Rep. **8**(1), 1–8 (2018). https://doi.org/10.1038/s41598-018-22261-5

Mo, R., He, L., Yan, X., Su, T., Zhou, C., Wang, Z., Hong, P., Sun, S., Li, C.: A novel aflatoxin B1 biosensor based on a porous anodized alumina membrane modified with graphene oxide and an aflatoxin B1 aptamer. Electrochem. Commun. **95**, 9–13 (2018). https://doi.org/10.1016/j.elecom.2018.08.012

Nguyen, E.P., De Carvalho Castro Silva, C., Merkoçi, A.: Recent advancement in biomedical applications on the surface of two-dimensional materials: from biosensing to tissue engineering. Nanoscale **12**(37), 19043–19067 (2020). https://doi.org/10.1039/d0nr05287f

Park, S., Hong, S., Kim, J., Son, S.Y., Lee, H., Kim, S.J.: Eco friendly nanofluidic platforms using biodegradable nanoporous materials. Sci. Rep. **11**(1), 1–11 (2021). https://doi.org/10.1038/s41598-021-83306-w

Parlak, O., Keene, S.T., Marais, A., Curto, V.F., Salleo, A.: Molecularly selective nanoporous membrane-based wearable organic electrochemical device for noninvasive cortisol sensing. Sci. Adv. **4**(7) (2018). https://doi.org/10.1126/sciadv.aar2904

Pérez-Madrigal, M.M., Giannotti, M.I., Del Valle, L.J., Franco, L., Armelin, E., Puiggalí, J., Sanz, F., Alemán, C.: Thermoplastic polyurethane:polythiophene nanomembranes for biomedical and biotechnological applications. ACS Appl. Mater. Interfaces **6**(12), 9719–9732 (2014). https://doi.org/10.1021/am502150q

Pérez-Madrigal, M.M., Armelin, E., Puiggalí, J., Alemán, C.: Insulating and semiconducting polymeric free-standing nanomembranes with biomedical applications. J. Mater. Chem. B **3**(29), 5904–5932 (2015). https://doi.org/10.1039/c5tb00624d

Quigley, K.J., Dalhaimer, P.: Nanobiomaterials for cancer therapy. In: Nanobiomaterials: Classification, Fabrication and Biomedical Applications, 1st edn, pp. 305–327. Wiley-VCH Verlag GmbH & Co. KGaA (2018). https://doi.org/10.1002/9783527698646.ch13

Rajeev, G., Prieto Simon, B., Marsal, L.F., Voelcker, N.H.: Advances in nanoporous anodic alumina-based biosensors to detect biomarkers of clinical significance: a review. Adv. Healthcare Mater. **7**(5), 1–18 (2018a). https://doi.org/10.1002/adhm.201700904

Rajeev, G., Xifre-Perez, E., Prieto Simon, B., Cowin, A.J., Marsal, L.F., Voelcker, N.H.: A label-free optical biosensor based on nanoporous anodic alumina for tumour necrosis factor-alpha detection in chronic wounds. Sens. Actuators B Chem. **257**, 116–123 (2018b). https://doi.org/10.1016/j.snb.2017.10.156

Riaz, S., Park, S.J.: An overview of TiO_2-based photocatalytic membrane reactors for water and wastewater treatments. J. Ind. Eng. Chem. **84**, 23–41 (2020). https://doi.org/10.1016/j.jiec.2019.12.021

Rios, G., Centi, G., Kanellopoulos, N.: Nanoporous Materials for Energy and the Environment, 1st edn. Pan Stanford Publishing (2011). https://doi.org/10.1201/b11168

Sabirova, A., Pisig, F., Rayapuram, N., Hirt, H., Nunes, S.P.: Nanofabrication of isoporous membranes for cell fractionation. Sci. Rep. **10**(1), 1–9 (2020). https://doi.org/10.1038/s41598-020-62937-5

Sajeesh, P., Sen, A.K.: Particle separation and sorting in microfluidic devices: a review. Microfluid. Nanofluid. **17**(1), 1–52 (2014). https://doi.org/10.1007/s10404-013-1291-9

Santos, A., Law, C.S., Pereira, T., Losic, D.: Nanoporous hard data: optical encoding of information within nanoporous anodic alumina photonic crystals. Nanoscale **8**(15), 8091–8100 (2016). https://doi.org/10.1039/c6nr01068g

Sava Gallis, D.F., Ermanoski, I., Greathouse, J.A., Chapman, K.W., Nenoff, T.M.: Iodine gas adsorption in nanoporous materials: a combined experiment-modeling study. Ind. Eng. Chem. Res. **56**(8), 2331–2338 (2017). https://doi.org/10.1021/acs.iecr.6b04189

Scaglione, F., Alladio, E., Damin, A., Turci, F., Baggiani, C., Giovannoli, C., Bordiga, S., Battezzati, L., Rizzi, P.: Functionalized nanoporous gold as a new biosensor platform for ultra-low quantitative detection of human serum albumin. Sens. Actuators B Chem. **288**, 460–468 (2019). https://doi.org/10.1016/j.snb.2019.03.005

Schuster, C., Rodler, A., Tscheliessnig, R., Jungbauer, A.: Freely suspended perforated polymer nanomembranes for protein separations. Sci. Rep. **8**(1), 1–11 (2018). https://doi.org/10.1038/s41598-018-22200-4

Seo, G., Lee, G., Kim, M.J., Baek, S.H., Choi, M., Ku, K.B., Lee, C.S., Jun, S., Park, D., Kim, H.G., Kim, S.J., Lee, J.O., Kim, B.T., Park, E.C., Kim, S.I.: Rapid detection of COVID-19 causative virus (SARS-CoV-2) in human nasopharyngeal swab specimens using field-effect transistor-based biosensor. ACS Nano **14**(4), 5135–5142 (2020). https://doi.org/10.1021/acsnano.0c02823

Shaban, M., Rabia, M., Fathallah, W., El-Mawgoud, N.A., Mahmoud, A., Hussien, H., Said, O.: Preparation and characterization of polyaniline and Ag/polyaniline composite nanoporous particles and their antimicrobial activities. J. Polym. Environ. **26**(2), 434–442 (2018). https://doi.org/10.1007/s10924-017-0937-1

Shankles, P.G., Timm, A.C., Doktycz, M.J., Retterer, S.T.: Fabrication of nanoporous membranes for tuning microbial interactions and biochemical reactions. J. Vac. Sci. Technol. B **33**(6), 06FM03 (2015). https://doi.org/10.1116/1.4932671

Shi, Y., Liu, R., He, L., Feng, H., Li, Y., Li, Z.: Recent development of implantable and flexible nerve electrodes. Smart Mater. Med. **1**, 131–147 (2020). https://doi.org/10.1016/j.smaim.2020.08.002

Singh, H., Li, W., Kazemian, M.R., Yang, R., Yang, C., Logsetty, S., Liu, S.: Lipase-responsive electrospun theranostic wound dressing for simultaneous recognition and treatment of wound infection. ACS Appl. Bio Mater. **2**(5), 2028–2036 (2019). https://doi.org/10.1021/acsabm.9b00076

Stroeve, P., Ileri, N.: Biotechnical and other applications of nanoporous membranes. Trends Biotechnol. **29**(6), 259–266 (2011). https://doi.org/10.1016/j.tibtech.2011.02.002

Sun, M., Han, K., Hu, R., Liu, D., Fu, W., Liu, W.: Advances in micro/nanoporous membranes for biomedical engineering. Adv. Healthcare Mater. **2001545**, 1–19 (2021). https://doi.org/10.1002/adhm.202001545

Suzuki, Y., Sakamoto, T., Yoshio, M., Kato, T.: Development of functional nanoporous membranes based on photocleavable columnar liquid crystals—selective adsorption of ionic dyes. Eur. Polym. J. **134**, 109859 (2020). https://doi.org/10.1016/j.eurpolymj.2020.109859

Vereshchagina, E., Mc Glade, D., Glynn, M., Ducrée, J.: A hybrid microfluidic platform for cell-based assays via diffusive and convective trans-membrane perfusion. Biomicrofluidics **7**(3) (2013). https://doi.org/10.1063/1.4804250

Wan, J., Xie, J., Kong, X., Liu, Z., Liu, K., Shi, F., Pei, A., Chen, H., Chen, W., Chen, J., Zhang, X., Zong, L., Wang, J., Chen, L.Q., Qin, J., Cui, Y.: Ultrathin, flexible, solid polymer composite electrolyte enabled with aligned nanoporous host for lithium batteries. Nat. Nanotechnol. **14**(7), 705–711 (2019). https://doi.org/10.1038/s41565-019-0465-3

Wang, Y.I., Abaci, H.E., Shuler, M.L.: Microfluidic blood–brain barrier model provides in vivo-like barrier properties for drug permeability screening. Biotechnol. Bioeng. **114**(1), 184–194 (2017). https://doi.org/10.1002/bit.26045

Wang, G., Gao, S., Tian, R., Miller-Kleinhenz, J., Qin, Z., Liu, T., Li, L., Zhang, F., Ma, Q., Zhu, L.: Theranostic hyaluronic acid-iron micellar nanoparticles for magnetic-field-enhanced in vivo cancer chemotherapy. ChemMedChem **13**(1), 78–86 (2018). https://doi.org/10.1002/cmdc.201700515

Wei, H.: Studying Cell Metabolism and Cell Interactions Using Microfluidic Devices Coupled with Mass Spectrometry, vol. 53, issue 9. Springer, Berlin Heidelberg (2013). https://doi.org/10.1007/978-3-642-32359-1

Wei, H., Chueh, B.H., Wu, H., Hall, E.W., Li, C.W., Schirhagl, R., Lin, J.M., Zare, R.N.: Particle sorting using a porous membrane in a microfluidic device. Lab Chip **11**(2), 238–245 (2011). https://doi.org/10.1039/c0lc00121j

Wu, X., He, G., Ding, Y.: Dealloyed nanoporous materials for rechargeable post-lithium batteries. ChemSusChem (2020). https://doi.org/10.1002/cssc.202001069

Wujcik, E.K., Duirk, S.E., Chase, G.G., Monty, C.N.: A visible colorimetric sensor based on nanoporous polypropylene fiber membranes for the determination of trihalomethanes in treated drinking water. Sens. Actuators B Chem. **223**, 1–8 (2016). https://doi.org/10.1016/j.snb.2015.09.004

Xu, X., Zheng, Q., Bai, G., Dai, Q., Cao, X., Yao, Y., Liu, S., Yao, C.: Polydopamine functionalized nanoporous graphene foam as nanoreactor for efficient electrode-driven metabolism of steroid hormones. Biosens. Bioelectron. **119**, 182–190 (2018). https://doi.org/10.1016/j.bios.2018.08.009

Xu, T., Zhao, H., Zheng, H., Zhang, P.: Atomically Pt implanted nanoporous TiO_2 film for photocatalytic degradation of trace organic pollutants in water. Chem. Eng. J. **385**, 123832 (2020). https://doi.org/10.1016/j.cej.2019.123832

Yang, S.Y., Ryu, I., Kim, H.Y., Kim, J.K., Jang, S.K., Russell, T.P.: Nanoporous membranes with ultrahigh selectivity and flux for the filtration of viruses. Adv. Mater. **18**(6), 709–712 (2006). https://doi.org/10.1002/adma.200501500

Yang, Y., Fan, X., Casillas, G., Peng, Z., Ruan, G., Wang, G.: Three-dimensional nanoporous Fe_2O_3/Fe_3C-graphene heterogeneous thin films for lithium-ion batteries. ACS Nano **8**(4), 3939–3946 (2014). https://doi.org/10.1021/nn500865d

Yin, L., Sheng, X.: Nonconventional biosensors based on nanomembrane materials. In: Nanobiomaterials: Classification, Fabrication and Biomedical Applications, 1st edn, pp. 241–257. Wiley-VCH Verlag GmbH & Co. KGaA (2018). https://doi.org/10.1002/9783527698646.ch10

Yusko, E.C., Johnson, J.M., Majd, S., Prangkio, P., Rollings, R.C., Li, J., Yang, J., Mayer, M.: Controlling protein translocation through nanopores with bio-inspired fluid walls. Nat. Nanotechnol. **6**(4), 253–260 (2011). https://doi.org/10.1038/nnano.2011.12

Zhang, J., Li, C.M.: Nanoporous metals: fabrication strategies and advanced electrochemical applications in catalysis, sensing and energy systems. Chem. Soc. Rev. **41**(21), 7016–7031 (2012). https://doi.org/10.1039/c2cs35210a

Zhang, Z., Rouabhia, M., Wang, Z., Roberge, C., Shi, G., Roche, P., Li, J., Dao, L.H.: Electrically conductive biodegradable polymer composite for nerve regeneration: electricity-stimulated neurite outgrowth and axon regeneration. Artif. Organs **31**(1), 13–22 (2007). https://doi.org/10.1111/j.1525-1594.2007.00335.x

Zhang, F., Liu, W., Zhou, S., Jiang, L., Wang, K., Wei, Y., Liu, A., Wei, W., Liu, S.: Investigation of environmental pollutant-induced lung inflammation and injury in a 3D coculture-based microfluidic pulmonary alveolus system. Anal. Chem. **92**(10), 7200–7208 (2020). https://doi.org/10.1021/acs.analchem.0c00759

Zhang, M., Wang, P., Luo, R., Wang, Y., Li, Z., Guo, Y., Yao, Y., Li, M., Tao, T., Chen, W., Han, J., Liu, H., Cui, K., Zhang, X., Zheng, Y., Qin, J.: Biomimetic human disease model of SARS-CoV-2-induced lung injury and immune responses on organ chip system. Adv. Sci. **8**(3), 1–14 (2021). https://doi.org/10.1002/advs.202002928

Zhou, L., Hou, H., Wei, H., Yao, L., Sun, L., Yu, P., Su, B., Mao, L.: In vivo monitoring of oxygen in rat brain by carbon fiber microelectrode modified with antifouling nanoporous membrane. Anal. Chem. **91**(5), 3645–3651 (2019). https://doi.org/10.1021/acs.analchem.8b05658

Fundamentals of Hierarchically Porous Materials and Its Catalytic Applications

Hiran Mayookh Lal, Arya Uthaman, and Sabu Thomas

Abstract The evolution of hierarchical porous materials has enhanced the productivity of the energy storage system owing to their higher surface area, space availability, low density, interconnected porosity at diverse scales, variable chemical composition, and excellent accommodation capability with thermal variation and space volume. The hierarchical porous structure benefits ion and electron transport, and diffusion, and mass transfer. With the varying pore structures, the electrochemical properties of hierarchical porous material vary. With the exact knowledge on the dependency of the pore dimensions and structures, the highly effective hierarchical porous structured materials could be fabricated with enriched catalytic performance. In this chapter, we have deliberated the characteristic properties of the hierarchically structured pores to summarize their recent development which mainly emphasized their catalytic applications. The first section of this chapter included brief discussions on the fundamentals, classification, and synthesis of the hierarchical porous materials. In the next section of this chapter, we mainly emphasized on application of hierarchical porous based on their catalytic activity. In the final section, the conclusion and the future aspects of hierarchical porous materials are included.

Keywords Hierarchical porous · Mesoporous · Nanoporous · Macroporous · Catalytic application

1 Introduction

The porous materials arranged in hierarchical structure according to the combination of entities, compositions, and geometric structures with various properties (e.g., viscosity and density) in a single system. In addition, hierarchical porous systems can be organized in a continuous/discontinuous, or homogeneous/heterogeneous manner, they are composed of components of different geometries and arranged into several

H. M. Lal (✉) · A. Uthaman (✉)
School of Civil Engineering, Harbin Institute of Technology, Harbin 150090, China

S. Thomas
School of Energy Materials, Mahatma Gandhi University, Kottayam, India

orders of magnitude (Fu et al. 2019). Therefore, in order to suit the name 'hierarchical', a material must require two basic criteria: first, its structural elements (compartments) should be defined by scales of more than one unit, and secondly, each structural elements must be having different structures but complementary function (Cao et al. 2018). By organizing the individual pore entities arranged in a hierarchy, the characteristic property of the resulting hierarchical material can far outweigh the materials with individual porous entities or porous structures.

According to researchers and chemical engineers, the main aim is always to design and develop the object with specific properties, which is the major aspect of their work pattern. Thus, from the point of view t of designing a material with such a property, the hierarchy can be divided in to three various forms:

(1) Structural hierarchy, which involves the steady construction with a deliberate repeating mixture of structural entities (e.g., ceramics, woods, bones, etc.)
(2) Transport hierarchy, which enables fast transport of distribution of a flow (e.g., river delta, lung, information system, etc.)
(3) Compositional hierarchy, which involves the assembling of the compartments of a material (e.g., atoms, molecules, larger entities, etc.) that permits the formation of a structure with systematically and locally changing composition by reorganization self-organization mechanisms that are induced by slight forces (e.g., ordered alloys, human body, and biomolecules) (Wu et al. 2020).

The structural hierarchical materials frequently exhibit very explicit organizing of their entities with functional subunits. The structural elements, which itself exhibits their discrete structure and they are ordered over a varying scale length composed of forming a macroscopic "super element", comparable to the cellular structure of bones. Hierarchical structures can show the enhanced properties associated to materials with an even bulk structure, such as features high compressive strength and other behavior associated to thermal expansion or oriented piezoelectricity. Moreover, the transport based hierarchical system exhibits a well-organized open path (transport), related to that in an interconnected pore system.

On discussing the organization of such hierarchical systems, Clauset et al. (2008) wrote: "Recent studies specified that networks often display hierarchical organization, in which the vertices are separated into groups, and it is again distributed into groups of groups so forth over various scales. In most circumstances, groups come to an agreement with well-known functional units such as environmental niches in food webs and modules in biochemical networks". Consequently, the levels of entities in hierarchical structure need to be a flat range or a branched arrangement. There are various examples that demonstrating the hierarchal pattern in nature, sometimes with a number of patterns but with very specific structures. Some typical examples for the natural hierarchically structures porous materials are represented in Fig. 1 that expressions the diversity of the formation of the hierarchical properties.

The highly developing economy of the world has caused an obvious growth in global energy necessity, resulting in the growing concerns of global warming and energy shortage problems. The development of clean, renewable and efficient energy sources such as solar, wind, and ocean energy has converted progressively critical
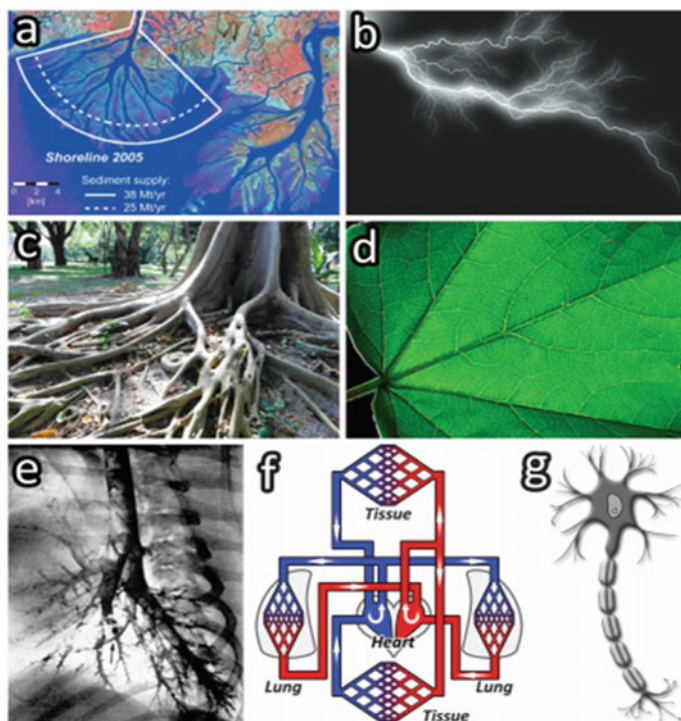
Fig. 1 Examples representing natural hierarchical systems. Reproduced from Schwieger et al. (2016) with permission of Royal Society of Chemistry

and vital. On the other hand, intermittence is one of the major disadvantages of the renewable energy basis. Implementing more investment in energy storage is one of the recovering solutions to challenge those renewable intermittence energy sources. Recently, many research has been focused on the various reversible and rechargeable energy storage devices such as Li-ion batteries, Li-sulphur batteries, sodium-ion batteries, and supercapacitors. Due to the, large available space, high interconnection among each porous space, various levels of porosity, high surface area, exceptional volume change accommodation, low density, and the orderliness of pores in each level, the hierarchical porous materials are largely useful for photo catalysis application, absorption, energy conversion and storage, separation, and functional materials in catalysis (Yang et al. 2017). The hierarchical porous material with interconnected and vascularized porosity can at various scale lengths decrease the ion transmission pathway to increase the gravity of electrochemical reaction that promotes the capacity of the electrode material and enhances the energy density. In addition, it can increase the structural constancy of the electrode material for enhancing the life of energy storage equipment.

2 Catalytic Applications of Hierarchical Porous Materials

2.1 Photocatalytic Materials

The magnitudes of macropores are similar to the wavelength of both UV light and visible light and can aid scattering of light within the porous structure. It reveals that the combination of these porous materials advances the photo catalytic effectiveness of the material owing to the potentially harvesting and increased light scattering, which includes the enhanced multiple internal reflections that may results in the cascade effect enhancing the illumination of active cites in pores and hence improves the photocatalytic efficiency.

Gas-phase process

The crystalline hierarchical organization of bismuth subcarbonate benefits in the enhanced diffusional properties and the improved photon harvesting, the surpassing particulate bismuth subcarbonate over the traditional C-doped titanium oxide is dynamic for the photocatalytic decomposition of NO in UV light (Dong et al. 2011). The hierarchically arranged porous structure of bismuth subcarbonate possesses an identical structure with a flower, in which an ordered packing of nanosheets around a central large cavity. The hierarchical porous structure ascends from the self-assembly mechanism with the larger mesopores/macropores (10–100 nm) situated in the space between the nanosheets and mesopores (3 nm) which are situated within the successive nanosheets. Zhu et al. (2010) detected the same morphology for the bismuth-oxychloride/oxyiodide and a composite of iodise-chloride that also exhibited the photocatalytic activity over C-doped TiO_2 (with iodine incorporated). The hierarchically porous structured catalyst reveals high stability, recyclability, which is adjusted by the temperature of the hydrothermal process. The improved photon absorption, through the multiple scattering processes, enhances the irradiation of the catalyst internal surfaces and thus acquires photocatalytic efficiency. The macroporous nature also enables more effective photo-degradation of the bulky dye molecules such as methyl orange.

Liquid-phase process

In the presence of soft templates, the mixed oxides of ceria and zinc can form the materials with hierarchically structures possessing flower like morphology. These materials are dynamic for the decomposition of rhodamine B under UV light and visible light. During the solvothermal treatment of the iron III oxide cores coated with tungsten VI oxide perpendicular needles formed tungsten oxide needles with mesoporous and macroporous region (3–20 nm), which endorses rhodamine B decomposition under visible light (Zhou et al. 2009). The incorporation of sacrificial poly styrene colloidal crystal template, the 3D well-ordered macroporous magnesium alumina double layer hydroxide was produced, which contains internal mesopores and macropores (650 nm), which is more functionalized using decatungstate anions (Géraud et al. 2008). The tungstated materials showed more active photocatalytic property.

The hexagonally close packed poly styrene crystals with P123, permit the development of a three dimensional ordered macroporous structured (170–200 nm) titania holding a secondary mesoporosity (3 nm) (Du et al. 2011). The organically functionalized metal phosphate porous material has been examined by Parlett et al. (2013). The hierarchically porous structured titania diphosphonate designed by self-assembly of nanorods in the occurrence of hydroxyethylidene with mesopores (2.2 nm) and macropores (90–400 nm). The subsequent hierarchically porous structured material have effective photocatalytic activity in decomposition of rhodamine B under UV irradiation.

2.2 Fuel Chemistry

Catalysts are widely applied for petrochemical industries in petroleum refining, with certain routes such as isomerization, cracking, and Fischer–Tropsch chemistry integral to production of petroleum fuels. The requirements on the improvement of the application of fossil based and petroleum resources, and the environmental requirements for the transportation of fuels, presents significant challenges to the design of heterogeneous catalysts (Parlett et al. 2013).

Catalytic cracking method

It is an important method for the large-scale manufacturing of commodity products. Zeolites, due to their microporous nature are generally used as catalysts. They can provide the lower mass transfer of bulky molecule; however, the common problem arises is the pore blockage and coking. Integration of a secondary mesoporous network is a solution for this problem. Recently, the incorporation of macropore is also used as a solution for the aforementioned problem, and the research work related to macropore incorporation is mainly highlighted in this chapter.

In the study conducted by Louis et al. (2010), crystals of ZSM-5 were grown on the 3D trimodal glass scaffold surface. The evaporation prompted self-assembly, with methyl cellulose and P123 as macropore and mesopore directing agents, allows the creation of ordered large macropores (300–500 µm), ordered mesopores (4–5 nm) with a P6 symmetry, and with disordered macropores (10–100 µm). The prepared hierarchically structured porous composites of ZSM-5/glass exhibited a greater n-hexane cracking activity. In another study by Yang et al. (2011), well-ordered micropores (0.5 nm), mesopores (7 nm), and macroporous (2–5 µm) solid was prepared using post synthesis recrystallization of macro/mesoporous alumina silicate. These hierarchical porous structures material permits the cracking at external and internal surfaces and thereby increased the active cites compared to the ordinary ZSM-5.

Fischer–Tropsch (FT) reaction

The conversion of CO and H_2 to hydrocarbons through FT preparation is a well-known route to develop liquid transportation fuels. This reaction generates a range

of products, with selectivity generally reported on the hydrocarbon chain length. In addition, the water gas shift reaction can affect in situ created water reacting through CO to yield H_2 and CO_2.

Martínez et al. (2009) reported that the nanofiber alumina doped with ruthenium and cobalt to prepare a Fischer–Tropsch catalyst which is more reactive than mesoporous alumina-based catalysts. The mesopores of 16 nm size and macropores sized 240 nm, were arranged randomly between the fibers packing. The enhanced catalytic activity is achieved from the bimodal pores in the fibrous support. Witoon et al. (2011) reported a green route to develop mesoporous-macroporous silica and has been validated, soft template as chitosan husk ash as silica source. The Fischer–Tropsch catalytic activity was achieved through the cobalt impregnation, with higher C5$^+$ selectivity over that obtained for a conventional mesoporous silica based catalyst.

Fuel cell applications

The durability and performance of support material applied in the fuel cell greatly depend on the design of proton exchange membrane used in it. According to Zhang et al. (2010) the incorporation of macropores into the carbon supports exhibited obvious advantages for their application in direct methanol fuel cells. Chai et al. (2004) the author deposited Pt–Ru alloys have been onto a high periodicity of about 300 nm sized pore diameter three dimensional ordered macroporous structure (3DOM), prepared from silica skeleton and having 10 nm sized regularly packed mesopores, and related with hollow core capsules consisting of mesoporous shells with 4 nm sized pores and macropores with 220 nm arranged in internal structures. Yan et al. (2010) synthesized active site proficient for alcohol electro-oxidation doping Pd nanoparticles. The developed hierarchical porous materials exhibited an enhanced performance due to superior Pd dispersion. The catalytic reforming of hydrogen from methanol, which is an efficient approach for the safe production of the H_2 for fuel cells. Holladay et al. (2004) reported a 3DOM zinc oxide copper oxide composites which were produced by using poly styrene as a hard template for preparation of 300 nm sized macropores and 6 and 3 nm sized disordered mesopores. The resultant framework is represented in Fig. 2, which exhibited low thermal activity at 230 °C, shows a conversion rate twice that of conversion of equivalent dense film composites.

2.3 Valorisation of Biomass

The biomass upgrading, for example, esterification of free fatty acids for biodiesel preparation, conversion of mono/di/polysaccharides into 5-hydroxy metylfurfural, a platform molecule that always consisting of bulky groups, has also aided from hierarchical macroporous structure catalysts.
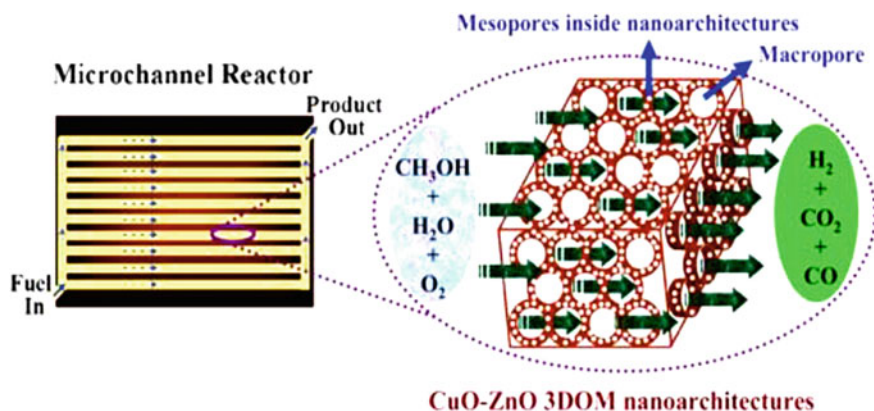
Fig. 2 Micro reactor for methanol reforming. Reproduced with permission from Lin et al. (2010) with permission of Royal Society of Chemistry

Dhainaut et al. (2010) prepared 3DOM silica with SBA-15 (ordered) walls using a polystyrene macropore template and P123 mesoporous structure. The functionalization of these affords with sulfonic acids active catalyst for the biodiesel production. Woodford et al. (2012) incorporated macropores to microporous magnesium aluminium hydrotalcite through a polystyrene hard template. The macroporous does not affect the interlayer micropores/Magnesium: Aluminium compositions of these solid bases, showed a significant rate enhancement in lower temperature transesterification of C18 triolein and C12 trilaurin in methanol.

Carbohydrate conversion process

The conversion of sugar from glucose and fructose to chemicals is an important overlook for sustainable chemical production. For such reactions and conversions, the porosity of the catalysts requires well designed structure to ensure the potential mass transport in liquid phase.

Kim et al. (2009) reported that the disordered porosity of both mesopores and macropores titanium phosphate were prepared through the evaporation-induced assembly with P123 as an agent direct for the generation of the mesopores. These catalysts were active for the conversion of the mono fructose, mannose, and glucose, di sucrose, and cellulose (polysaccharides) to 5-hydroxymethylfurfural.

Pyrolysis oil upgrading process

Fast pyrolysis is an efficient method to obtain bio-oils through rapid heating of biomass under anaerobic conditions, with higher liquid hydrocarbon yields. However, such bio-oils prepared have high moister content and oil content, polar mixtures of aldehydes, aromatics, alcohols, esters, sugars, and phenolic compounds that cause reduced stability and high viscosity. Czernik and Bridgwater (2004) reported that Bio-oils require pre-treatment before processing for fuel applications, in which catalytic hydrodeoxygenation is one of the most efficient methods for dropping their

oxygen content. The viscous nature of oil makes it favorable for the conversion by a hierarchically structured catalyst.

## 2.4 Selective Organic Transformation Process

The process of selective transformation of the organic molecules is necessary for the pharmaceutical and chemical industries. The implementation of hierarchically porous structured catalysts could potentially improve the active cite accessibility/dispersion and internal heat/mass transfer, mainly for low heat, liquid-phase interaction.

Epoxidation

The particles of copper oxide with well-ordered sea urchin morphology are active catalysts for epoxidation of alkenes. Xu et al. (2009) reported that the self-assembled structure obtained during the decomposition of copper nitrate hydroxide to form hierarchically structured copper oxide, with 11 nm sized mesopores and 100 nm size macropores are highly active compared to commercial copper oxides (Fig. 3). Kamegawa et al. (2011) reported hexagonally arranged 3DOM with spherical cavity 300 nm possessing mesopores, prepared by soft octadecyl trimethylammonium chloride templates and PMMA. This could be used to support tetrahedral Ti oxide moieties as epoxidation catalysts with tetrabutyl hydrogen peroxide. Chen et al. (2011) prepared meso-microporous silicate and found more effective for epoxidation of organic compounds with bulky groups, comparatively at a higher rate than conventional zeolitic titania silicate.

Selective oxidation

The hierarchically structured titanium silicate shows outstanding catalytic activity in oxidation of saturated hydrocarbons to ketones and alcohol (Poladi and Landry
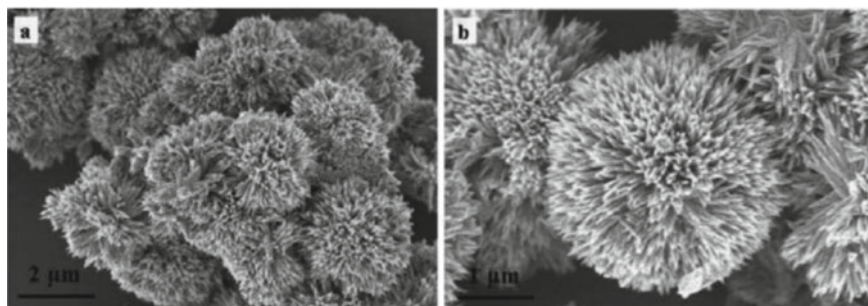
Fig. 3 CuO sea urchin morphology of alkene epoxidation catalyst. Reprinted from Xu et al. (2009) with permission of American Chemical Society

2002), with enhanced conversion rate than conventional mesoporous and microporous equivalents. Bronstein et al. (2004) found the occurrence of micropores in this trimodal organization could also reveal the shape and size dependent selectivity during the process. The incorporation of 1.6 nm Pt nanoparticles in the commercial hyper-cross-polystyrene that comprising disordered macro and mesopore, likewise exhibits the conversion rate-enhancements than the correspondent microporous polymer supports for the oxidation of L-sorbose to 2-keto-L-gulonic acid.

Isomerization

Valtchev et al. (2011) incorporated pore channels throughout the crystals of ZSM-5, through vacuum UV irradiation and HF treatment. The pore size of 50 nm improved the enactment in m-xylene while compared with traditional ZSM-5 isomerization. Wang et al. (2010) produced hierarchical porous structure with macropore size 450–900 nm through the hydrothermal conversion of betazeolites to a metaphorsis to acquire the macropore structure, which is dynamic to alpha-pinene isomerization. Further, the alkene treatment of ZSM-5 brought secondary meso-macro sized pores 0–100 nm. The incorporation of secondary pores improved the 1-hexane isomerization which is more dynamic than commercial ZSM-5.

Hydrogenation process

Florea et al. (2009) synthesized hierarchical porous structure catalyst which is used for hydrogenation of cinnamaldehyde. The Pd impregnation of commercial silicon carbide with 55 mm macropores and 15 nm mesopores has been used as the catalyst. Zhou et al. (2010) found that the hierarchical porous structures with meso-macropores alumina-based Pd are a potential catalyst for the selective hydrogenation of styrene and diolefin impurities. The acquired hierarchically porous structured catalysts were additionally active compared with the traditional mesoporous alumina support as represented in Fig. 4.

The hierarchically structured porous catalysts support that forms by a spontaneous self-assembly pathway hold a parallel 14 nm mesopores and 500 nm macropores combined within the framework.

2.5 Pollution Abatement

Harmful waste material treatment through the elimination of unwanted compounds and the emission of non-harmful chemical species, or the total chemical decomposition of harmful compounds present in the waste materials, are widely used commercial processes that are discussed as follows:

Catalytic combustion process

Kamperman et al. (2009) synthesized highly ordered, Pt doped SiC ceramic, comprising hierarchically porous structured with 300 nm and 2.5 μm macropores, and periodic 11 nm mesopores, through a one-pot method by means of PS spheres as
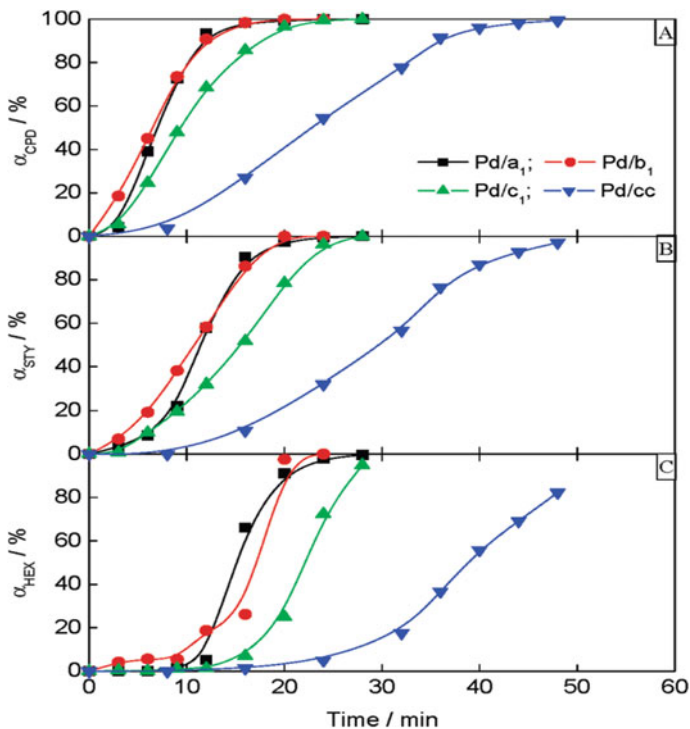
Fig. 4 a Conversion of cyclopentadiene, **b** conversion of styrene, and **c** conversion of 1-hexane, over hierarchical Pd/a, Pd/b, and Pd/c and commercial Pd/cc catalysts. Reprinted from Zhou et al. (2010) with permission of American Chemical Society

a co-polymer as the soft-mesoporous template and by using poly styrene sphere co-block polymer as hard-macroporous template as represented in Fig. 5. The designed structure is thermally stable structure and withstands up to 1000 °C under reducing conditions and up to 600 °C in an oxidizing environment. The hierarchical structure's porous material exhibited good activity towards methane combustion.

Jang et al. (2012) synthesized an irregular arrangement of macropores and mesopores in Ir/r-alumina, as represented in Fig. 6. The disintegration of hydrazine to H_2, NH_3 and N_2 for powering earth-orbiting satellites. The bimodal porous support (alumina), which consequences in a broad distribution of 3 nm sized mesoporous and 10–1000 μm sized macropores, has been tested in ethanol dehydration to diethyl ether realize the impact of hierarchically porous structured support to the acidity/basicity on product selectivity.

CO oxidation process

Yu et al. (2011) reported Cu doped porous (trimodal) ceria for the selective oxidation of CO in H_2. This catalyst consist of enhanced thermal stability that could operate at 80 °C with achieving full CO conversion, and high Cu dispersion. The enhanced
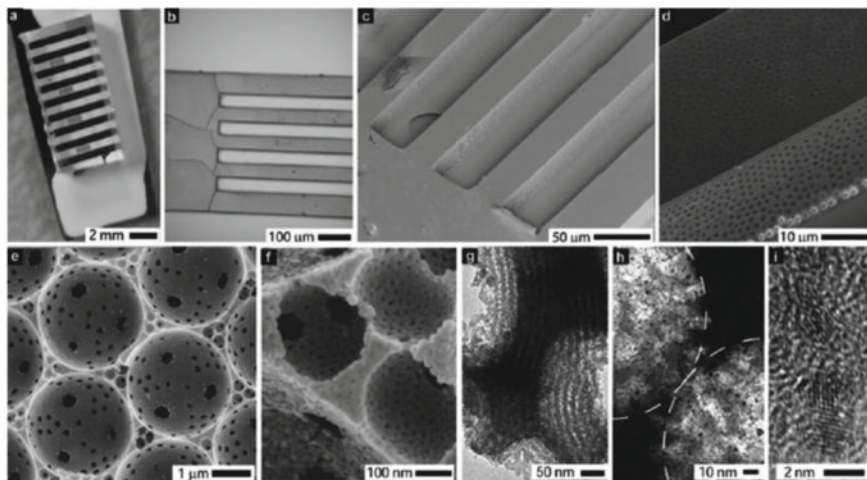
Fig. 5 **a** Photo; **b** micrograph; and **c** scanning electron microscopic image of SiC ceramic mold; **d** scanning electron microscopic of the molded ceramic; **e**, **f** Scanning electron microscopic highlighting macropores and ordered framework mesopores at higher resolution; **g**, **h** transmission electron microscopic of meso and macropores, and uniformly distributed 1–2 nm platinum nanoparticles; **i** high-resolution transmission electron microscopic revealing Pt lattice fringes. Reprinted from reference Kamperman et al. (2009), copyright from American Chemical Society

surface area of the porous ceria rises from a morphology that consists of flakes arranged into microspheres. The arrangement of P123 surfactant soft templating and poly styrene spheres hard template method has also been employed for the preparation of a 3DOM ϒ-alumina with ordered mesoporosity. The resultant hierarchically structured porous supports have been applied in Pt nanoparticle CO oxidation. Lu et al. (2010) synthesized hierarchically structure porous materials comprising mesoporous and macroporous ϒ-alumina shell and α-alumina core, while impregnated with Ni and Pt enhanced the catalytic capability of selective CO oxidation in H_2 stream. Ma et al. (2011) produced the successive impregnation of a macroporous silica skeleton by hydrothermal treatment to prepare a $CuO–Fe_2O_3$ mixed oxide that comprising of 14 nm mesopores. CO oxidation by the resultant support was exhibited at lower temperature than over conventional catalysts prepared from silica skeletons, and those hierarchically structures porous catalysts can also oxidize dichlorobenzene.

3 Recent Studies in Hierarchical Porous Materials

The enhanced performances that are relevant to the nanoparticle components have also been developed for the obtained nanoparticles/covalent organic framework (COF) which is a new class of porous materials (Shi et al. 2017). These composites are widely used in organic catalysis and hydrogen storage applications. This kind of
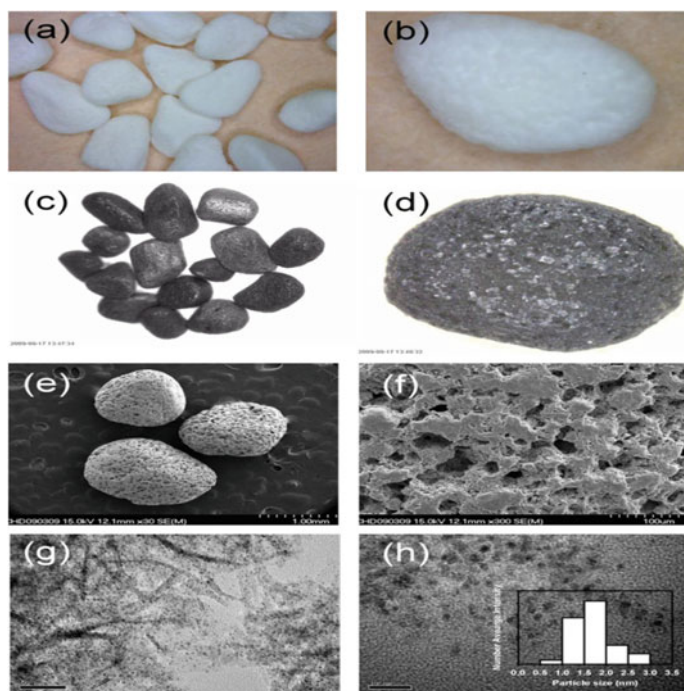
Fig. 6 Photographs (**a**, **b**); scanning electron microscopy (**c**, **d**); and transmission electron microscopy (**e**, **f**), of an Ir-impregnated alumina catalyst. Reprinted from Jang et al. (2012) with permission of Elsevier

composite could be prepared by encapsulating the pre-prepared nanoparticles during the COF synthesis. This method is attractive since, the sizes, shapes, and composition associated with the physical and chemical properties of nanoparticles and can be feasibly tuned by their strategic synthesis. COF materials can be hierarchically nucleated and could grow around the surfaces of some nanosized objects to give a core in shell structures. It is possible to tailor the encapsulated strategy, in principle, is capable of incorporating any type of nanoparticles owing to their desired mechanical and thermal properties. It is well-known that nanoparticles pose excellent mechanical and chemical properties (Uthaman et al. 2021b; Lal et al. 2021a). The modification of nano particles with surfactants enhances the stability of the nanoparticle (Uthaman et al. 2021a). Shi et al. (2017) reported the simple encapsulation method for incorporation of catalytically active PVP coated gold (Au) nanoparticles with various geometries in a two-dimensional (2D) COF synthesized by the condensing 1,3,5-tris(4-aminophenyl) benzene with 2,5-dimethoxyterephthaldehyde (DMTP). The encapsulation of nanoparticles does not vary the thermal stability, crystallinity, and pore structures of the COF matrices. Other than the catalytic applications these composites are commonly used in biomedical applications owing to the excellent antimicrobial activities of nanoparticles such as silver nanoparticles (Lal

et al. 2021b; Uthaman et al. 2021c). Mudassir et al. (2017) developed silver nanoparticle decorated hierarchically porous beads with excellent antibacterial properties for the water treatment. Recently the incorporation of hierarchical porous structure to polymer composites to improve the properties by improving the filler polymer interaction. The epoxy resins are major components that are commonly used as a resin matrix in fabricating composites for structural applications owing to their enhanced mechanical, thermal durability, and creep performance (Lal et al. 2020; Uthaman et al. 2020). Zaman et al. (2020) embedded lingocellulosic form with embedded Hierarchical porous structures to the surface of epoxy composite to enhance the property. The synthesized lignocellulosic form exhibited a hierarchical pores structure with diameter ranging between 10 and 0.001 µm. The interconnected 3D pore structure induced interlocking sites for the epoxy to impregnate and thus developed an interpenetrating polymerization network.

4 Conclusion and Future Aspects on Hierarchical Porous Materials

The success and improvement in the design, manufacturing, and development of hierarchical porous materials have contributed to the possibility to modify their chemical kinetics and diffusion properties. This may superiorities the manipulation of the various energy storage materials and potential catalytic application compared to the conventional single pore structured materials. The hierarchically porous structured materials exhibit outstanding structural advantages that also abbeys the laws of nature and showing an outperformed potential in their numerous application fields such as in catalytic applications. The future design and development of tailored hierarchically structured porous architectures, and control over the link between different pore sizes, necessitates continued researches for the evolution of new templates and motifs for self-assembly. The preparation of the new surfactants that shows expectable mesophases have a key role to play in emerging such innovations. On the other hand, their commercialization may unaffordable unless simple strategies of retrieval and re-use are also implemented. For the Large-scale production of hierarchically structured catalysts necessitates the use of low cost macroporous templates which could be sustainably sourced or could be recycled, and the use of bio-polymers is an attractive overlook. Although the substantial development in the improvement of hierarchically structured porous materials, some critical shortcomings still exist and hinder their commercial applications. Generally, hierarchically porous structures delivered the materials with high surface area and fast mass transport. This can intensify the probability of the occurrence of side reaction. The solutions to overcome these difficulties of the hierarchically structured porous materials may open new possibilities for discoveries and new thoughts, which enhances the stimulating opportunities for those entering different fields of application.

References

Bronstein, L.M., Goerigk, G., Kostylev, M., Pink, M., Khotina, I.A., Valetsky, P.M., Matveeva, V.G., Sulman, E.M., Sulman, M.G., Bykov, A.V., Lakina, N.V., Spontak, R.J.: Structure and catalytic properties of Pt-modified hyper-cross-linked polystyrene exhibiting hierarchical porosity. J. Phys. Chem. B **108**, 18234–18242 (2004). https://doi.org/10.1021/jp046459n

Cao, J., Zhu, C., Aoki, Y., Habazaki, H.: Starch-derived hierarchical porous carbon with controlled porosity for high performance supercapacitors. ACS Sustain. Chem. Eng. **6**, 7292–7303 (2018). https://doi.org/10.1021/acssuschemeng.7b04459

Chai, G.S., Shin, I.S., Yu, J.S.: Synthesis of ordered, uniform, macroporous carbons with meso-porous walls templated by aggregates of polystyrene spheres and silica particles for use as catalyst supports in direct methanol fuel cells. Adv. Mater. **16**, 2057–2061 (2004). https://doi.org/10.1002/adma.200400283

Chen, L.H., Li, X.Y., Tian, G., Li, Y., Rooke, J.C., Zhu, G.S., Qiu, S.L., Yang, X.Y., Su, B.L.: Highly stable and reusable multimodal zeolite TS-1 based catalysts with hierarchically interconnected three-level micro-meso-macroporous structure. Angew. Chem. Int. Ed. **50**, 11156–11161 (2011). https://doi.org/10.1002/anie.201105678

Clauset, A., Moore, C., Newman, M.E.J.: Hierarchical structure and the prediction of missing links in networks. Nature **453**, 98–101 (2008). https://doi.org/10.1038/nature06830

Czernik, S., Bridgwater, A.V.: Overview of applications of biomass fast pyrolysis oil. Energy Fuels **18**, 590–598 (2004). https://doi.org/10.1021/ef034067u

Dhainaut, J., Dacquin, J.P., Lee, A.F., Wilson, K.: Hierarchical macroporous–mesoporous SBA-15 sulfonic acid catalysts for biodiesel synthesis. Green Chem. **12**, 296–330 (2010). https://doi.org/10.1039/b919341c

Dong, F., Lee, S.C., Wu, Z., Huang, Y., Fu, M., Ho, W.K., Zou, S., Wang, B.: Rose-like monodisperse bismuth subcarbonate hierarchical hollow microspheres: one-pot template-free fabrication and excellent visible light photocatalytic activity and photochemical stability for NO removal in indoor air. J. Hazard. Mater. **195**, 346–354 (2011). https://doi.org/10.1016/j.jhazmat.2011.08.050

Du, J., Lai, X., Yang, N., Zhai, J., Kisailus, D., Su, F., Wang, D., Jiang, L.: Hierarchically ordered macro-mesoporous TiO_2-graphene composite films: improved mass transfer, reduced charge recombination, and their enhanced photocatalytic activities. ACS Nano **5**, 590–596 (2011). https://doi.org/10.1021/nn102767d

Florea, I., Houllé, M., Ersen, O., Roiban, L., Deneuve, A., Janowska, I., Nguyen, P., Pham, C., Pham-Huu, C.: Selective deposition of palladium nanoparticles inside the bimodal porosity of-SiC investigated by electron tomography. J. Phys. Chem. C **113**, 17711–17719 (2009). https://doi.org/10.1021/jp905968n

Fu, A., Wang, C., Pei, F., Cui, J., Fang, X., Zheng, N.: Recent advances in hollow porous carbon materials for lithium–sulfur batteries (2019)

Géraud, E., Rafqah, S., Sarakha, M., Forano, C., Prevot, V., Leroux, F.: Three dimensionally ordered macroporous layered double hydroxides: preparation by templated impregnation/coprecipitation and pattern stability upon calcination. Chem. Mater. **20**, 1116–1125 (2008). https://doi.org/10.1021/cm702755h

Holladay, J.D., Wang, Y., Jones, E.: Review of developments in portable hydrogen production using microreactor technology. Chem. Rev. **104**, 4767–4789 (2004). https://doi.org/10.1021/cr020721b

Jang, I.J., Shin, H.S., Shin, N.R., Kim, S.H., Kim, S.K., Yu, M.J., Cho, S.J.: Macroporous-mesoporous alumina supported iridium catalyst for hydrazine decomposition. Catal. Today **185**, 198–204 (2012)

Kamegawa, T., Suzuki, N., Che, M., Yamashita, H.: Synthesis and unique catalytic performance of single-site Ti-containing hierarchical macroporous silica with mesoporous frameworks. Langmuir **27**, 2873–2879 (2011). https://doi.org/10.1021/la1048634

Kamperman, M., Burns, A., Weissgraeber, R., Van Vegten, N., Warren, S.C., Gruner, S.M., Baiker, A., Wiesner, U.: Integrating structure control over multiple length scales in porous high temperature ceramics with functional platinum nanoparticles. Nano Lett. **9**, 2756–2762 (2009). https://doi.org/10.1021/nl901293p

Kim, Y.-S., Guo, X.-F., Kim, G.-J.: Asymmetric ring opening reaction of catalyst immobilized on silica monolith with bimodal meso/macroscopic pore structure. Top. Catal. (2009). https://doi.org/10.1007/s11244-008-9140-x

Lal, H.M., Xian, G., Thomas, S., Zhang, L., Zhang, Z., Wang, H.: Experimental study on the flexural creep behaviors of pultruded unidirectional carbon/glass fiber-reinforced hybrid bars. Materials **13**, 11–13 (2020). https://doi.org/10.3390/ma13040976

Lal, H.M., Thomas, S., Li, T., Maria, H.J.: Polymer Nanocomposites Based on Silver Nanoparticles. Springer International Publishing (2021a)

Lal, H.M., Uthaman, A., Thomas, S.: Silver Nanoparticle as an Effective Antiviral Agent. Springer Nature (2021b)

Lin, Y.G., Hsu, Y.K., Chen, S.Y., Chen, L.C., Chen, K.H.: O_2 plasma-activated CuO-ZnO inverse opals as high-performance methanol microreformer. J. Mater. Chem. **20**, 10611–10614 (2010). https://doi.org/10.1039/c0jm02605k

Louis, B., Ocampo, F., Yun, H.S., Tessonnier, J.P., Pereira, M.M.: Hierarchical pore ZSM-5 zeolite structures: from micro- to macro-engineering of structured catalysts. Chem. Eng. J. **161**, 397–402 (2010). https://doi.org/10.1016/j.cej.2009.09.041

Lu, S., Liu, Y., Wang, Y.: Meso-macro-porous monolithic Pt-Ni/Al_2O_3 catalysts used for miniaturizing preferential carbon monoxide oxidation reactor. Chem. Commun. **46**, 634–636 (2010). https://doi.org/10.1039/b912769k

Ma, X., Feng, X., He, X., Guo, H., Lü, L.: Preparation, characterization and catalytic behavior of hierachically porous CuO/α-Fe_2O_3/SiO_2 composite material for CO and o-DCB oxidation. J. Nat. Gas Chem. **20**, 618–622 (2011). https://doi.org/10.1016/S1003-9953(10)60253-8

Martínez, A., Prieto, G., Rollán, J.: Nanofibrous γ-Al_2O_3 as support for Co-based Fischer-Tropsch catalysts: pondering the relevance of diffusional and dispersion effects on catalytic performance. J. Catal. **263**, 292–305 (2009). https://doi.org/10.1016/j.jcat.2009.02.021

Mudassir, M.A., Hussain, S.Z., Rehman, A., Zaheer, W., Asma, S.T., Jilani, A., Aslam, M., Zhang, H., Ansari, T.M., Hussain, I.: Development of silver-nanoparticle-decorated emulsion-templated hierarchically porous poly(1-vinylimidazole) beads for water treatment. ACS Appl. Mater. Interfaces **9**, 24190–24197 (2017). https://doi.org/10.1021/acsami.7b05311

Parlett, C.M.A., Wilson, K., Lee, A.F.: Hierarchical porous materials: catalytic applications. Chem. Soc. Rev. **42**, 3876–3893 (2013). https://doi.org/10.1039/c2cs35378d

Poladi, R.H.P.R., Landry, C.C.: Oxidation of octane and cyclohexane using a new porous substrate, Ti-MMM-1. Microporous Mesoporous Mater. **52**, 11–18 (2002). https://doi.org/10.1016/S1387-1811(02)00272-X

Schwieger, W., Machoke, A.G., Weissenberger, T., Inayat, A., Selvam, T., Klumpp, M., Inayat, A.: Hierarchy concepts: classification and preparation strategies for zeolite containing materials with hierarchical porosity. Chem. Soc. Rev. **45**, 3353–3376 (2016). https://doi.org/10.1039/c5cs00599j

Shi, X., Yao, Y., Xu, Y., Liu, K., Zhu, G., Chi, L., Lu, G.: Imparting catalytic activity to a covalent organic framework material by nanoparticle encapsulation. ACS Appl. Mater. Interfaces **9**, 7481–7488 (2017). https://doi.org/10.1021/acsami.6b16267

Uthaman, A., Xian, G., Thomas, S., Wang, Y., Zheng, Q., Liu, X.: Durability of an epoxy resin and its carbon fiber-reinforced polymer composite upon immersion in water, acidic, and alkaline solutions. Polymers **12** (2020). https://doi.org/10.3390/polym12030614

Uthaman, A., Lal, H.M., Li, C., Xian, G., Thomas, S.: Mechanical and water uptake properties of epoxy nanocomposites with surfactant-modified functionalized multiwalled carbon nanotubes. Nanomaterials **11**, 1–16 (2021a). https://doi.org/10.3390/nano11051234

Uthaman, A., Lal, H.M., Thomas, S.: Fundamentals of Silver Nanoparticles and Their Toxicological Aspects. Springer Nature (2021b)

Uthaman, A., Lal, H.M., Thomas, S.: Silver Nanoparticle on Various Synthetic Polymer Matrices: Preparative Techniques, Characterizations, and Applications. Springer Nature (2021c)

Valtchev, V., Balanzat, E., Mavrodinova, V., Diaz, I., El Fallah, J., Goupil, J.M.: High energy ion irradiation-induced ordered macropores in zeolite crystals. J. Am. Chem. Soc. **133**, 18950–18956 (2011). https://doi.org/10.1021/ja208140f

Wang, D., Liu, Z., Wang, H., Xie, Z., Tang, Y.: Shape-controlled synthesis of monolithic ZSM-5 zeolite with hierarchical structure and mechanical stability. Microporous Mesoporous Mater. **132**, 428–434 (2010). https://doi.org/10.1016/j.micromeso.2010.03.023

Witoon, T., Chareonpanich, M., Limtrakul, J.: Effect of hierarchical meso-macroporous silica supports on Fischer-Tropsch synthesis using cobalt catalyst. Fuel Process. Technol. **92**, 1498–1505 (2011). https://doi.org/10.1016/j.fuproc.2011.03.011

Woodford, J.J., Dacquin, J.P., Wilson, K., Lee, A.F.: Better by design: nanoengineered macroporous hydrotalcites for enhanced catalytic biodiesel production. Energy Environ. Sci. **5**, 6145–6150 (2012). https://doi.org/10.1039/c2ee02837a

Wu, L., Li, Y., Fu, Z., Su, B.L.: Hierarchically structured porous materials: synthesis strategies and applications in energy storage. Natl. Sci. Rev. **7**, 1667–1701 (2020). https://doi.org/10.1093/nsr/nwaa183

Xu, L., Sithambaram, S., Zhang, Y., Chen, C.H., Jin, L., Joesten, R., Suib, S.L.: Novel urchin-like CuO synthesized by a facile reflux method with efficient olefin epoxidation catalytic performance. Chem. Mater. **21**, 1253–1259 (2009). https://doi.org/10.1021/cm802915m

Yan, Z., He, G., Zhang, G., Meng, H., Shen, P.K.: Pd nanoparticles supported on ultrahigh surface area honeycomb-like carbon for alcohol electrooxidation. Int. J. Hydrogen Energy **35**, 3263–3269 (2010). https://doi.org/10.1016/j.ijhydene.2010.01.031

Yang, X.Y., Tian, G., Chen, L.H., Li, Y., Rooke, J.C., Wei, Y.X., Liu, Z.M., Deng, Z., Van Tendeloo, G., Su, B.L.: Well-organized zeolite nanocrystal aggregates with interconnected hierarchically micro-meso-macropore systems showing enhanced catalytic performance. Chem. A Eur. J. **17**, 14987–14995 (2011). https://doi.org/10.1002/chem.201101594

Yang, X.Y., Chen, L.H., Li, Y., Rooke, J.C., Sanchez, C., Su, B.L.: Hierarchically porous materials: synthesis strategies and structure design (2017). www.rsc.org/chemsocrev

Yu, Y., Hou, S., Meng, M., Tao, X., Liu, W., Lai, Y., Zhang, B.: Converting inorganic-organic hybrid sulfides into oxides: a general strategy to hierarchical-porous-structured thermal-stable metal oxides with improved catalytic performance. J. Mater. Chem. **21**, 10525–10531 (2011). https://doi.org/10.1039/c1jm11057h

Zaman, A., Huang, F., Jiang, M., Wei, W., Kadhim, N., Zhou, Z.: Fabrication of enhanced epoxy composite by embedded hierarchical porous lignocellulosic foam. Renew. Energy **150**, 1066–1073 (2020). https://doi.org/10.1016/j.renene.2019.10.146

Zhang, W., Sherrell, P., Minett, A.I., Razal, J.M., Chen, J.: Carbon nanotube architectures as catalyst supports for proton exchange membrane fuel cells (2010). https://pubs.rsc.org/en/content/articlehtml/2010/ee/c0ee00139b

Zhou, L., Wang, W., Xu, H., Sun, S., Shang, M.: Bi_2O_3 hierarchical nanostructures: controllable synthesis, growth mechanism, and their application in photocatalysis. Chem. A Eur. J. **15**, 1776–1782 (2009). https://doi.org/10.1002/chem.200801234

Zhou, Z., Zeng, T., Cheng, Z., Yuan, W.: Preparation of a catalyst for selective hydrogenation of pyrolysis gasoline. Ind. Eng. Chem. Res. **49**, 11112–11118 (2010)

Zhu, L.P., Liao, G.H., Bing, N.C., Wang, L.L., Yang, Y., Xie, H.Y.: Self-assembled 3D BiOCl hierarchitectures: tunable synthesis and characterization. CrystEngComm **12**, 3791–3796 (2010). https://doi.org/10.1039/c0ce00038h

Characterization of Hierarchical Porous Materials

Mohd Asyadi Azam, Nur Ezyanie Safie, and Mohd Fareezuan Abdul Aziz

Abstract A pivotal function to verify the synthesis material is to comprehend the hierarchically porous material through the material characterization. This chapter discusses the vital characterization, especially for the as-prepared hierarchically porous materials, for further analyzing and understanding their behavior and properties. X-ray diffraction (XRD) is the most powerful technique in examining the crystallographic structure of a material. Chemical compounds can be identified using diffraction techniques based on their crystalline form. On the other hand, scanning electron microscope (SEM) analysis is essential for examining the hierarchically porous material's microstructure and surface morphology. Besides, the approach which indicates and discloses the porous structure of the materials is characterized by the transmission electron microscope (TEM). The measurement determining and resulting in particular surface area of the materials are often preferred using Brunauer–Emmett–Teller (BET) characterization.

Keywords Characterization · XRD · SEM · TEM · BET · Microstructure · Morphology

1 Introduction

Hierarchically porous materials, with remarkable structuring and role, mimicking the natural materials counterparts have been developed over the decades, which provide an opportunity for various applications, including photocatalysis (Zhang et al. 2018), adsorption (Luca et al. 2019), drug delivery (Zhao et al. 2018), photovoltaic solar cells (Abdelhamid et al. 2019), energy storage (Chang et al. 2018; Seman and Azam 2020; Azam et al. 2021), and chemical sensing (Wang et al. 2019). In general, hierarchically porous materials contain multimodal pores that are interconnected over different length scales and pore sizes. The pore sizes having over 50 nm are classified as macro-size (Xing et al. 2017), while pore size between 2 and 50 nm is considered

M. A. Azam (✉) · N. E. Safie · M. F. Abdul Aziz
Fakulti Kejuruteraan Pembuatan, Universiti Teknikal Malaysia Melaka, Hang Tuah Jaya, 76100 Durian Tunggal, Melaka, Malaysia
e-mail: asyadi@utem.edu.my

meso-size (Bera et al. 2017). However, materials with pore size lower than 2 nm are known as micro-size (Yang et al. 2020). With these various pore sizes, hierarchically porous materials are significant for the future material development, contributing to excellent properties including shape selectivity, high-contact surface areas, high-capacity volume storage, uniform and well-controlled porosity over variety length scales, as well as proficient mass transport.

Manufacturing hierarchically porous materials could be done by employing structure-directing agents. Often, the self-assembled molecular aggregates, or known as supramolecular assemblies, are used. Meanwhile, colloidal crystals, polymers, cellulose, emulsions, vesicles, inorganic salts, and even ice crystals are added to the synthesis to direct the formation of microporous structures. The hierarchical pore structure can also be created by carefully controlling the phase separation in the synthesis gel. In order to verify the as-prepared hierarchically porous materials, several material characterizations are essential to consider. This chapter introduces this book with contributions of the material characterization to the development of the hierarchically porous materials, which includes four types of characterizations which are in orders: 1. X-ray diffraction; 2. scanning electron microscope; 3. transmission electron microscopy; and 4. Brunauer–Emmett–Teller.

2 Characterization of Hierarchical Porous Materials by X-Ray Diffraction (XRD)

Since the discovery of X-ray diffraction (XRD) in 1912, it has been the most widely investigated and utilized method for material characterization. Generally, XRD techniques are usually categorized into two types which are known as spectroscopic and photographic. Among these two, the most frequently used diffraction method is spectroscopy, especially in modern laboratories compared to photographic techniques that are not widely utilized. Besides, X-ray powder diffractometry or X-ray diffractometry is the common name for the spectroscopy technique. In the X-ray diffraction pattern, we can obtain the synthesized materials' average crystallite particle sizes by using the Scherrer formula. The formula stated that the average crystalline particle size, d, is equal to the $K \cdot \lambda$ divided by $\beta \cdot \cos \theta$. The value of K is always close to unity which is ~ 0.9 (dimensionless shape factor). λ and β is the X-ray wavelength and full width at half maximum (FWHM), respectively. The value of theta, θ, is the Bragg angle of the crystal plane.

2.1 Oxide

In a novel ultra-porous hierarchical architecture of iridium-based nanocatalysts produced by spray drying, Faustini et al. (2019) observed extremely porous iridium-based materials ($Ir_{0.7}Ru_{0.3}O_2$) outperform industrial iridium oxide. These compounds are also a great way to test the oxygen species involved in the oxygen evolution process and the reactivity of the iridium. In situ X-ray diffraction (XRD) was utilized to study the material's dimension evolution when heated from ambient temperature to 800 °C. The rutile IrO_2 structure's X-ray diffractogram peak occurs around 450 °C and expands as the temperature rises. The volume of a unit cell declines with temperature, reaching a plateau around 800 °C (64.77 Å) above 650 °C. The decrease is primarily due to a reduction in the a-axis parameter from 4.56 to 4.53 Å, while the c-axis parameter remains nearly constant throughout the temperature range. Diffraction peaks narrow, indicating sintering effects as post-treatment temperature rises. The structure and size of porogen are retained when calcined to 600 °C, opening up various ways of preparing hollow, pore materials with tuned pores. Controlling the annealing conditions is essential for optimizing the crystallite size, surface area, and iridium surface oxidation state to obtain catalytic activity that is more remarkable than commercial iridium oxide.

Zhang et al. (2020) described a facile but effective polymer-templating route to manufacture porous ternary oxide zinc stannate (Zn_2SnO_4) nanospheres that interconnected and hierarchically ordered. This nanosphere, also known as zinc tin oxide (ZTO), is analyzed as an effective electron transport layer (ETL) to obtain high-performance organolead halide perovskite solar cells. Figure 1 shows the X-ray diffraction (XRD) of as-prepared p-ZTO, which confirmed its structure and phase composition. The sharp peaks were detected at similar exact diffraction locations for porous ZTO nanospheres (denoted as p-ZTO nanospheres) and ZTO nanoparticles in solid form (denoted as s-ZTO nanoparticles). The ZTO's crystalline structure and

Fig. 1 XRD pattern of p-ZTO nanospheres. The bottom panel is the peaks designated for cubic ZTO with JCPDS No. 21-1272 as reference. Reprinted with permission from Zhang et al. (2020)
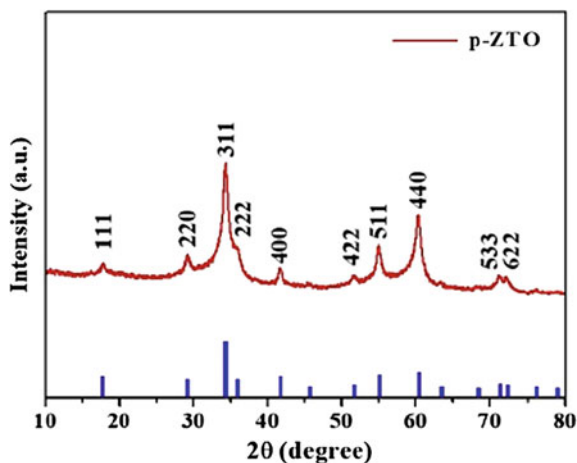
composition did not change during PS template removal and incorporation. Nevertheless, pyrolysis of the former resulted in better crystallization of p-ZTO than s-ZTO. From the entire width at half maximum of the (311) peak, the average diameters of the ZTO nanoparticles are observed to be around 4.3 and 6.7 nm, respectively. The resultant p-ZTO has a wide surface area with high porosity, which encourages perovskite material's penetration and growth, which is essential for efficiency enhancement. In addition, the polymer-templating technique dramatically facilitates access to a broad range of nanostructure material with semiconductor and related porous characteristics as stable charges transport materials for solar cell applications.

2.2 Carbon

Zhang et al. (2018) developed a general strategy for preparing an iron (Fe)-based catalyst on a hierarchically structured porous carbon (HPC) substrate with atomic Fe dispersion. This catalyst has demonstrated high oxygen reduction reaction (ORR) efficiency in both alkaline and acidic electrolytes, making it a viable replacement for Pt-based ORR catalysts in the application of fuel cells. X-ray diffraction (XRD) was used to examine the Fe and carbon crystalline structures. When compared to commercial graphitic carbon (26.48°), the single-atom (SA)-Fe-HPC and nanoparticle (NP)-Fe-HPC displayed peak matched to C (002), by a broad diffraction peak of approximately 23.18°, with just a low-angle change. There were no characteristic peaks for metallic iron, iron nitrate, or iron carbide crystals observed in the SA-Fe-HPC. On the other hand, the Fe–N–C revealed a succession of intense peaks indicating iron carbide at 37.78°, 43.78°, 44.98°, and 48.68°, respectively. Despite the microporous structure's ability to stabilize Fe atoms and limit the Fe aggregation, the NP-Fe-HPC sample also showed a couple of small but noticeable distinctive peaks at 43.78° and 44.98°.

On the other hand, MWCNT/ZIF-8 composite electrodes for supercapacitors were prepared by decorating zeolitic imidazolate frameworks (ZIF-8) onto the surface of multi-walled carbon nanotubes (MWCNTs), and MWCNT/NPCs were obtained by direct carbonization of MWCNT/ZIF-8 (Li et al. 2017). The crystal structure of the as-prepared hybrids was investigated using XRD. As seen in Fig. 2a, the diffraction peaks of the MWCNT/ZIF-8-L, which denotes a composite with large-sized ZIF-8 that is around 500 nm, matched well with the simulated ZIF-8 crystals. In addition, since the intensity is low, there is no peak for MWCNTs was seen in the figure. Furthermore, the XRD pattern of annealed products, which are denoted as MWCNT/NPC-L and NPC-L in this study, revealed carbon (002) diffractions characteristics that show as one prominent peak at around 26° (Fig. 2b). This peak indicates some graphitization and long-range two-dimensional ordering located in the material's carbon matrices. Markedly, no extra diffraction peaks is detected to represent the impurities, suggesting that the carbonaceous materials were fully converted during the annealing treatment.
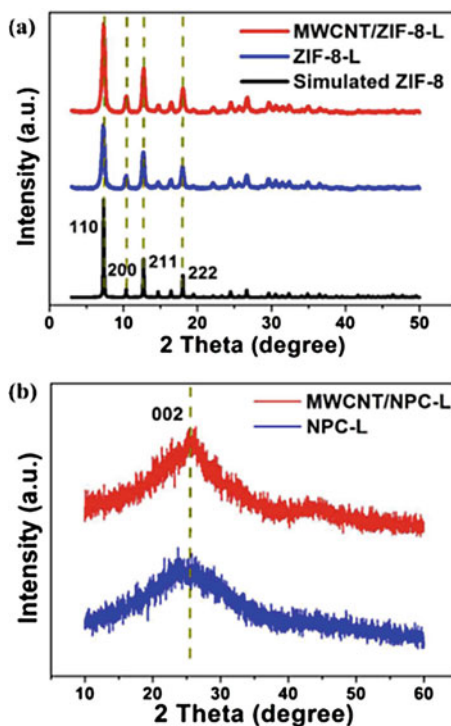
2.3 Metal

Zhou et al. (2017) investigated a new design of MOF template-directed technique by oxidizing, sulfurizing, carbonizing, and phosphorizing premade cobalt carbonate hydroxide@zeolitic imidazolate framework-67, denoted as CCH@ZIF-67, to create hierarchically ordered Co_3O_4@X composites, where X is Co_3O_4, CoS, C, and CoP. These composites are mainly applied for catalyst application. The film and powder forms of cobalt carbonate hydroxide (CCH) show a pattern of similar peaks at 2 of 28.65°, 30.47°, 33.71°, 35.11°, 39.46°, and 59.93°, which indicate good crystallization on the ground by the CCH corresponding to the (400), (101), (111), (220), (221), and (002) reflections, respectively. The CCH@ZIF-67 film displayed a superposed XRD pattern of CCH and ZIF-67 around the diffraction peaks of CCH (Fig. 5a, curve b) and ZIF-67 crystalline powder. Therefore, indicated that the high specific surface area and large exposed active sites by the unique hierarchical structure of these composites result in low overpotential and favorable reaction kinetics, enhancing oxygen evolution reaction (OER) performance.

Besides, Chen et al. (2017) studied in situ self-assembly of metal–organic framework (MOF) with mesoporous silica to create the HKUST-1@ Santa Barbara Amorphous-15 composites with hierarchical pore structure for the application of CO_2 adsorption. XRD was used to describe the pristine HKUST-1 (a blue cubic crystal
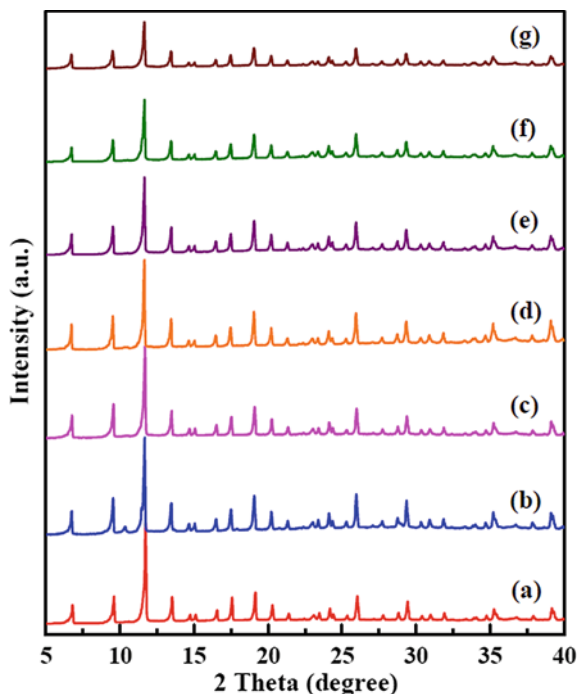
of copper-based ultramicroporous metal framework (MOF) or also known as MOF-
199) and composites containing varying amounts of Santa Barbara Amorphous-15
(SBA-15) as depicted in Fig. 3. The critical feature of exposed HKUST-1 peaks firmly
matched with those mentioned in the report. Peak intensities steadily declined as the
amount of SBA-15 added increased. However, it has discovered that no new peaks
have discovered due to the composites' high distribution and a comparatively small
amount of Santa Barbara Amorphous-15 material. The introduction of a high SBA-
15 content can cause a minor distortion of the structure and decrease crystallinity.
The Santa Barbara Amorphous-15 matrix worked as a forming factor while directing
the growth of HKUST-1 nanoparticles; however, it further gave the composite fixed
morphology and hierarchical arrangement. Therefore, the particle sizes of HKUST-1
and textural properties of composites are regulated by varying the amount of Santa
Barbara Amorphous-15 in materials.

3   Characterization of Hierarchical Porous Materials by Scanning Electron Microscope (SEM)

The most common kind of electron microscope is the scanning electron microscope
(SEM). A SEM image is created by a directed electron beam that scans over the

surface area of a specimen instead of a transmission electron microscope (TEM) image, which is created by instantaneous illumination of the entire region. Because of its vast depth of field, the three-dimensional appearance of an SEM's photographs is, perhaps, its most significant function. At $10^3\times$ magnification, for example, the depth of field will approach the order of tens of micrometers and the order of micrometers at $10^4\times$ magnification. Compared to a TEM, the SEM is comparatively simple to run and manage. This subtopic describes the characteristics of an SEM for examining the hierarchically porous material's microstructure and surface morphology.

3.1 Oxide

Previous research has shown that forming a new pore structure can affect the catalytic efficiency of porous catalysts in terms of action, selectivity, and stability. The epoxide-mediated sol–gel synthesis of mixed metal oxides, $NiAl_2O_4$ and $CoAl_2O_4$, with spinel phase structure and hierarchical pore structure was investigated by Herwig et al. (2018). The macropore size can be changed by varying the polymer and metal (Ni or Co) concentration. For instance, Fig. 4 shows that the presence of $Co_2 +$ influences the morphology of the macropore system: low Co contents (3Co-1, Fig. 4a) result in a well-defined interconnected structure with distinct struts. Higher Co contents (33Co-1 and 33Co-2) result in an entangled system with a more particle-like form (Fig. 4c, f). In addition to higher Co contents, raising the poly(ethylene oxide) (PEO) content to 3.5 106 mol percent resulted in a specific form of the macropore structure (Fig. 4d–f) due to an improved inclination for phase separation.
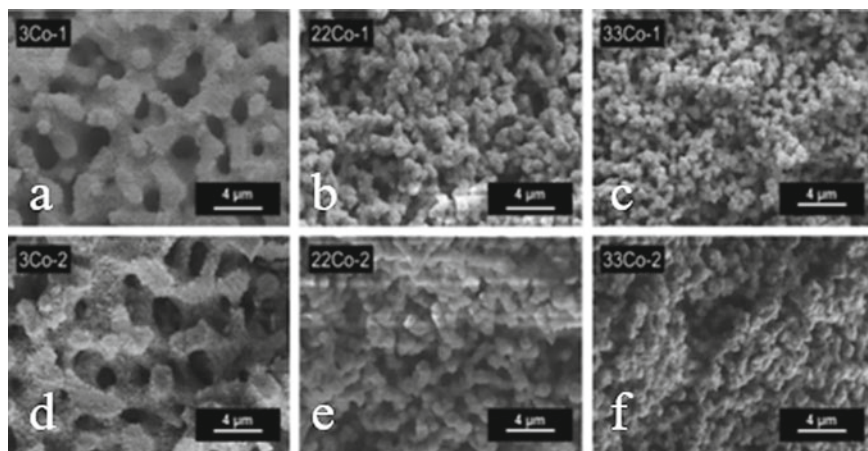
Fig. 4 SEM images for each sample studied which explain both conditions: (1) the increasing of Co content in the direction of **a–c**, and **d–f**; (2) the increasing of PEO content in the direction of top (**a–c**) to bottom (**d–f**). Reprinted with permission from Herwig et al. (2018)
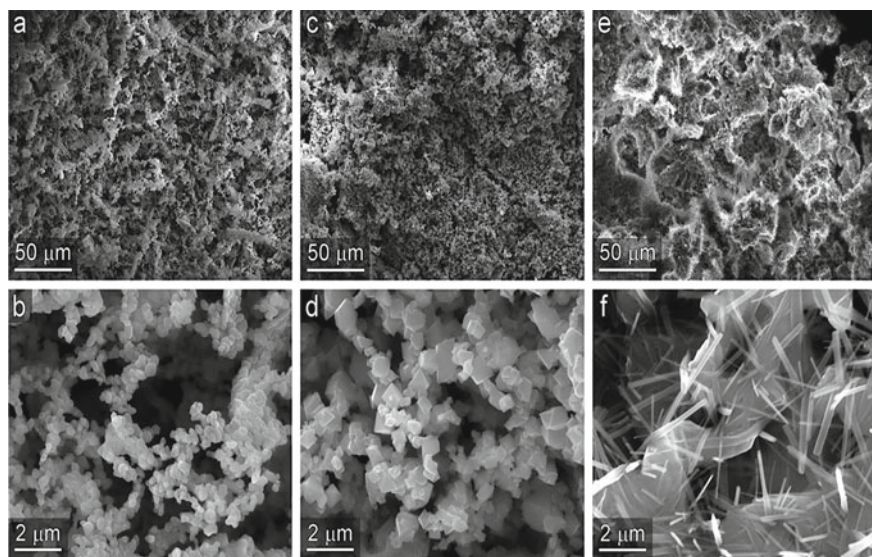
Fig. 5 SEM images for templated materials which are prepared form, **a**, **b** NiCl₂, **c**, **d** FeCl₂, and **e**, **f** MgCl₂. Reprinted with permission from Moyer et al. (2019)

Besides, Moyer et al. (2019) discovered a simple, low-cost, scalable synthesis method that allows for the templating of metal oxide structures using sustainable, bio-derived materials, resulting in tunable porosity and morphology. This study investigates the applicability of the nanocellulose (NC)-based templating approach to other oxide products while substituting some other metal chlorides, comprising $NiCl_2$, $FeCl_2$, and $MgCl_2$ for $CeCl_3$. Figure 5 shows SEM micrographs of the resulting products. Hierarchically ordered materials were observed in each event. The low magnification images in the top row (a, c, and e) of Fig. 5 display high-surface-area materials with macroporosity. Higher magnification images in the bottom panel of Fig. 5 indicate that the material's nanostructure is a three-dimensional integrated arrangement of micro- and nanostructures. Each material's nanoscale properties are noticeably different from one another and reflect the crystal structure created by the oxide produced during the high-temperature oxidation and template removal step. These findings show that NC can be used as an efficient templating agent by incorporating regulated porosity and morphology into catalyst particles to increase surface area and develop higher order architecture.

3.2 Polymer

The volume of integrated polyhedral oligomeric silsesquioxanes (POSS) has a substantially influences the composition of the composite film, capable of adjusting
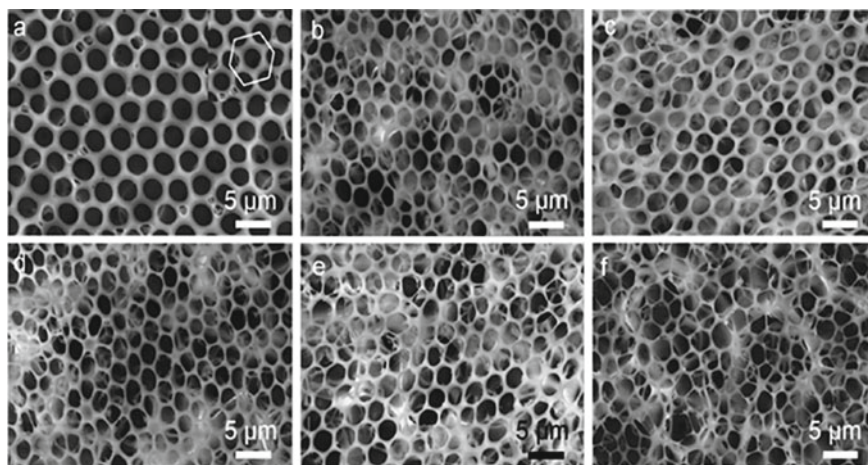
Fig. 6 **a** P-FPI. **b–f** P-polyhedral oligomeric silesquioxanes-PIs that contain varying amount of POSS, 10, 20, 30, 40, and 50%, respectively. Reprinted with permission from He et al. (2021)

the water resistance, tuning dielectric and mechanical characteristics as reported by He et al. (2021). The polyhedral oligomeric silsesquioxanes-contained hierarchical porous arrangement significantly decreased the water absorption and porosity of the polyimide (PI) film. As shown in Fig. 6, SEM was used to investigate the morphology of P-polyhedral oligomeric silsesquioxanes-PIs. When the POSS concentration fluctuated from 10 to 50%, honeycomb-patterned porous structures are created, but the regularity and pore size are varied. Furthermore, the increased amount of polyhedral oligomeric silsesquioxanes reduced the pore diameter and rim width substantially. According to the researchers, these discoveries provide a prominent approach for creating low-dielectric-constant materials with outstanding overall characteristics. As a result, the material may be a good candidate for dielectric materials utilized in microelectronics.

In developing functional devices composed of porous nanofibers, hierarchical control over structure is essential, like in the case of piezoelectric nanogenerators made of poly (vinylidene fluoride-trifluoroethylene) (P(VDF-TrFE)) nanofibers, for example, were built and thoroughly analyzed, giving information on the influence of various porous structures on outcomes. Abolhasani et al. (2020) proved that the high bulk porosity of the nanofibers might withstand significantly more significant volumetric stresses and offers much better power output while having a lower effective dielectric constant. On the other hand, porous nanofibers are not restricted to nanogenerators and may create polymer membranes applied for battery applications. SEM images of P(VDF-TrFE) nanofibers electrospun from tetrahydrofuran (THF) dopes that focus on surface and cross-sectional, as well as their diameter distribution, are shown in Fig. 7. The dopes contained 0 wt% water, 5.1 wt% water, 10.2 wt% water, and 12.7 wt% water (THF-1 to 4 dopes). Bulk porosity is driven by phase separation induced by the water intrusion and initial water content into the drying
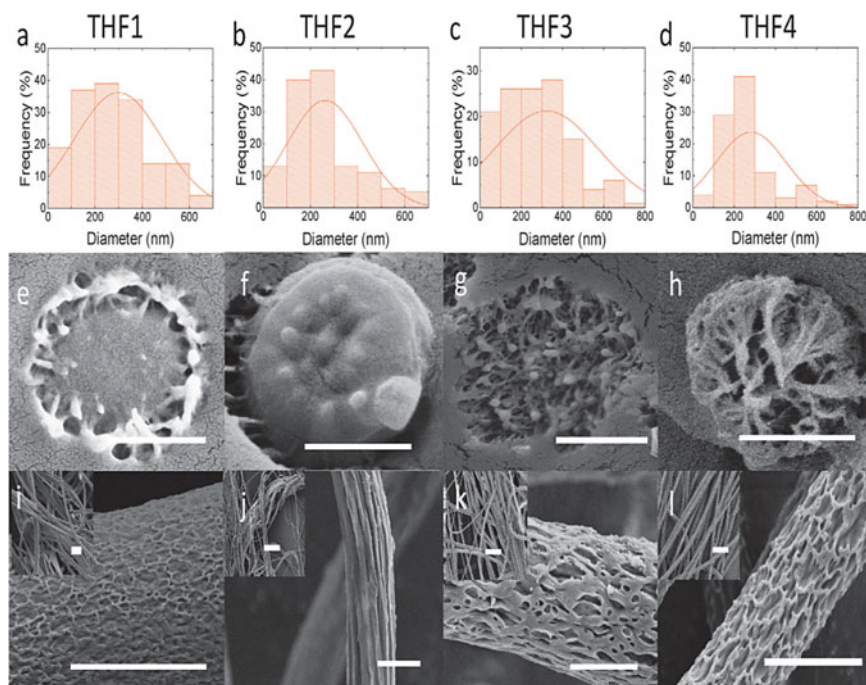
Fig. 7 a–d Histogram distribution of nanofiber diameter for all samples; SEM images of **e–h** the sample cross-sectional view and **i–l** their single fiber surface. The pictures in the insets are nanofibers with low magnification view. Reprinted with permission from Abolhasani et al. (2020)

fiber. For example, THF2 has a strong core despite 5.1 percent water at the beginning. Otherwise, phase separation of THF3 and THF4 L-L is resulting in a porous morphology. Surface porosity in THF-processed fibers, on the other hand, is most likely the result of the process of a "breath-figure"-type. The heat loss during fast evaporation leads to a sudden decrease in local temperature. Thus, water nanodroplets tend to condense and eventually will be precipitated onto the drying fiber. Thus, full knowledge of solvents, nonsolvents, and PVDF ternary phase diagram is essential for designing the procedure. Precise positioning of the pores occurs only on the surface and inside the bulk of the nanofibers. Careful selection of the solvent with the deliberate presence of water that acts as a non-solvent enabled the placement of the pores.

3.3 Metal

Hierarchically structured metal–organic frameworks (H-MOFs) where it comprise metal ions and organic ligands or cluster, because of their outstanding features of

adaptable pore structure flexibility at all hierarchical levels, have gained considerable attention. Duan et al. (2018) describe a simple, green-route, and flexible synthetic method to generate hierarchically ordered metal–organic frameworks (H-MOFs) with high space–time yields (STYs) where the hydroxy double salt (HDS) was employed as the template synergy. The SEM picture of C-HKUST-1 obtained not only reveals a typical single-crystal structure. The smooth and visible edges of the surfaces of the octahedral crystals are indicating a particle size of about 10 μm. The SEM image of H-HKUST-1 A shows that it successfully preserves the parent MOF's simple morphology. Nonetheless, there are noticeable variations in the particle sizes and crystal surfaces. For example, the crystal surface of the H-HKUST-1 A contains a consistent pattern of visible worm-like holes and structural defects. Furthermore, the H-HKUST-1 A's particle size measurement is lower than the particle size of C-HKUST-1, which is around 1 μm. This discovery might be attributed to the exchange rate of HDS's high anion, which causes the fast expansion of HKUST-1 and results in smaller nanocrystals.

4 Characterization of Hierarchical Porous Materials by Transmission Electron Microscope (TEM)

4.1 Oxide

Park et al. (2018) studied oxygen diffusion through the interface between two grains in the zirconium oxide (ZrO_2). The significant grain size of oxide produces a more critical oxidation-inhibiting impact due to fewer oxygen diffusion paths. In the study of oxide grain structure in exposed zirconium metal and the anodized zirconium metal (after oxidation process with the temperature of 1000 °C in normal air condition), TEM characterization has conducted. When zirconium metal was exposed and then oxidized, the small grains (10 nm) were formed successfully in the oxide (Fig. 8a). However, substantial ZrO_2 grains (micrometer) were grown vertically arranged under the nanoporous oxide layer when the anodized sample was oxidized. The TEM (dark-field) displayed and revealed the single-crystalline ZrO_2 in micrometer size of tetragonal phase grains with supported analysis by selected area electron diffraction pattern (SAED) (Fig. 8b). For the oxidation resistance process, the diffusion path length of oxygen is more significant for the latter than the former, resulting in columnar grains being the better choice than equiaxed grains. Therefore, large single-crystalline and columnar ZrO_2 grains are formed under the nanoporous oxide layer, and such oxide grains prevent further oxidation if the anodized zirconium metal is oxidized.

Using the TEM instrument, Saravanan et al. (2021) studied the physical properties of titanium dioxide and carbon core–shell nanowire used in optical engineering. The report revealed that titanium dioxide (TiO_2) and carbon shells nanowire are in rutile form where the nanowire has various thickness shell from ~ 1 to ~ 300 nm by testing with significant temperature. From Fig. 9, TEM results that the core diameter of TiO_2
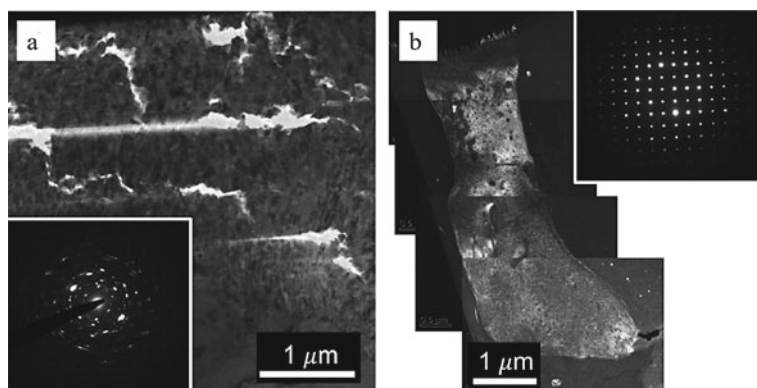
Fig. 8 **a** Oxide structure of exposed zirconium metal; **b** Oxide structure of zirconium metal with an anodic nanoporous oxide layer (dark field TEM) with SAED pattern of grain in the anodized sample identifying a single crystal grain. Both have gone through the oxidation process in normal air condition at the temperature of 1000 °C. Reprinted with permission from Park et al. (2018)

crystalline is unchanged for each various temperature (650, 750, 850, and 950 °C). However, the thickness of the carbon shell displays the increasing value for each temperature, which shows ~ 1, ~ 40, ~ 50, and ~ 300 nm. This report concludes that growing the titanium dioxide and carbon core–shell nanowire with the temperature at 850 °C has a high apparent quantum yield (AQY), which is the suitable thickness of carbon shell may assist in preventing the recombination, thus give importance to obtainability of electrons on the surface of the nanowires.

4.2 Carbon

Wu et al. (2021) proposed that the energy density of carbon-based supercapacitor can be improved by constructing the porous carbon with doping of heteroatoms (nitrogen and sulfur). In this work, it shows that the optimized samples which are nitrogen-sulfur dual-doped porous carbon (NSPC-700) has a large specific capacitance, C_{sp} of 360 F g^{-1} at 1.0 A g^{-1}. As referred to Fig. 10, the TEM images for these optimized samples have additionally highlighted massive micropores, mesopores and macropores in the surface of carbon structures. This shows that this sample has well-developed porosity behavior.

Some researchers work on porous carbon embedded with cerium oxide (CeO_2)/core–shell structure for performance lithium-sulfur batteries (Chen et al. 2021). In this work, the core–shell CeO_2/porous carbon (CS-CeO_2-PC) and S/CS-CeO_2/PC cathode materials have been prepared, and TEM characterization has been done. As referred to Fig. 11a, b, TEM images proved the existence of CeO_2 spherical shell structure. From Fig. 12, TEM images of S/CS-CeO_2/PC cathode material display that the S successfully occupies the inner area of cerium oxide
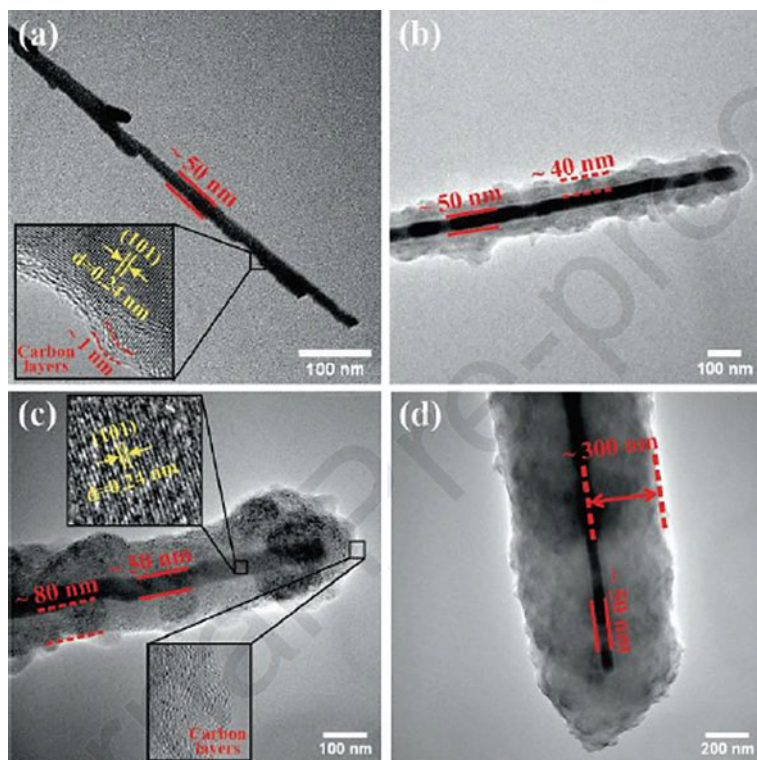
Fig. 9 TiO_2@carbon core–shell nanowires incorporated with variation temperature, T ($T = 650$, 750, 850, and 950 °C) in 100 nm scale. The inset shows the atomic-resolution TEM images for the crystalline TiO_2 cores and amorphous carbon shells. Reprinted with permission from Saravanan et al. (2021)
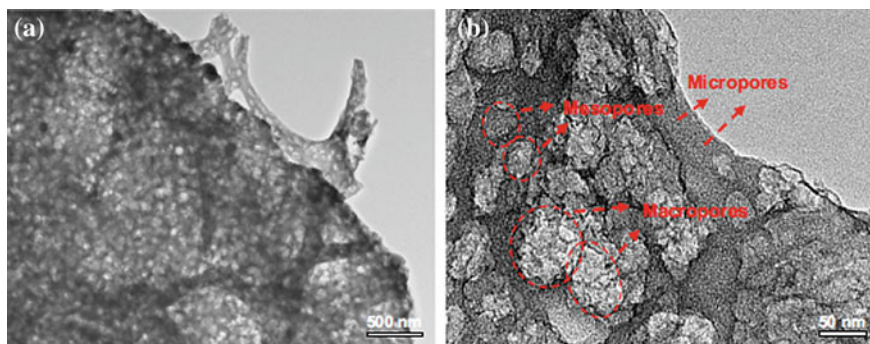
Fig. 10 **a**, **b** Nitrogen–sulfur dual-doped porous carbon (NSPC) in 500 µm and 50 nm scales. Reprinted with permission from Wu et al. (2021)
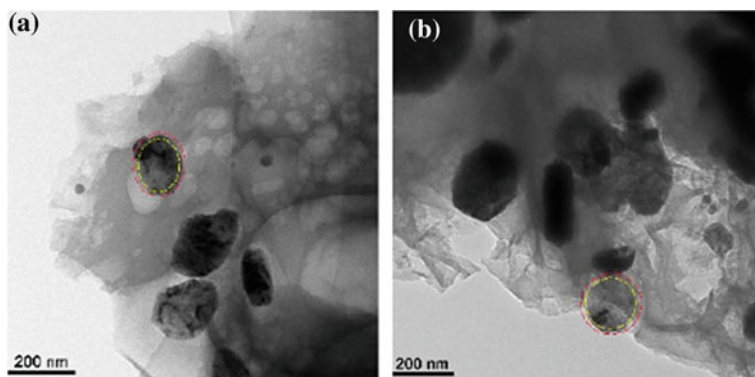
Fig. 11 a, **b** Core–shell cerium oxide/porous carbon in 200 nm scale. Reprinted with permission from Chen et al. (2021)
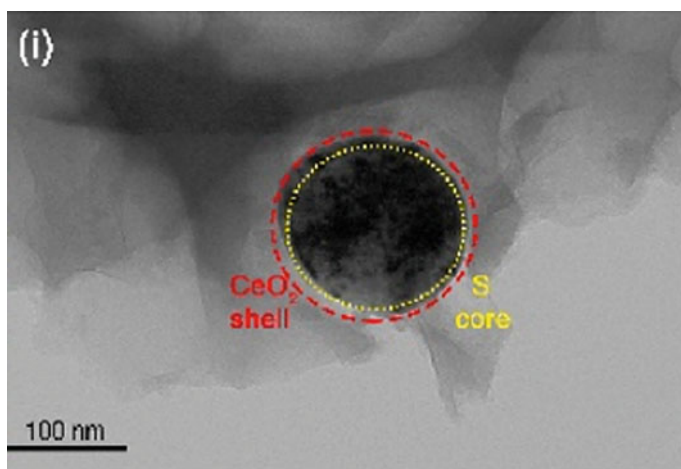
Fig. 12 S/CS-CeO$_2$/PC in 100 nm scale. Reprinted with permission from Chen et al. (2021)

(CeO$_2$), creating a core–shell material with CeO$_2$ as the shell and S as the core. It proves that this is S/CS-CeO$_2$/PC structure. In summary, the core–shell structure of cerium oxide (CeO$_2$) produces S reaction area and relieves its volume increase while together adsorbing more sulfides inhibits the shuttle effect. It will be resulting in high-performance lithium-sulfur batteries.

Xue et al. (2021) have investigated the hierarchical porous carbon derived from durian shell as the cathode precursor for Li–S batteries. Figure 13 shows the high-resolution TEM (HRTEM) images of durian porous carbon samples with two various areas and proves the porous identity of obtaining carbon after activation. Furthermore, by referring to these HRTEM images, it can be confirmed that not particularly pores with diameter, D, of approximately 1 nm (Fig. 13a) but pores with D of 2–4 nm
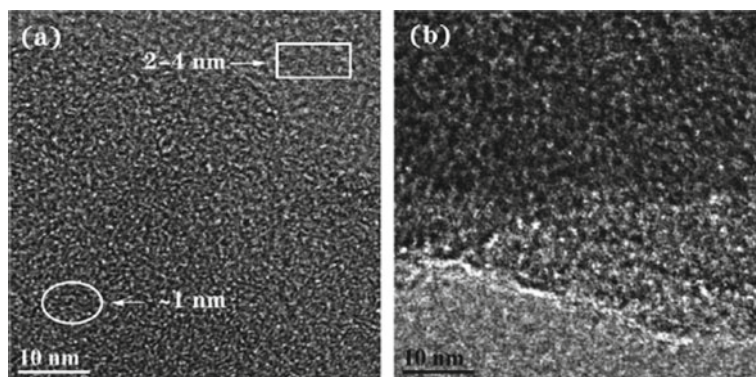
Fig. 13 Pore size **a** Small; **b** large. Reprinted with permission from Xue et al. (2021)

(Fig. 13a) and D around 4 nm (Fig. 13b) obeyed this, showing a hierarchical porous characteristic in the durian porous carbon.

4.3 Ceramic

Peng et al. (2010) researched on the morphology of silicon carbide formation in carbon fiber-reinforced carbon for the performance brake materials by using TEM analysis. For the TEM samples preparation, resin cross-section holders have been used for C/C-SiC stabilization. Then, ion beam thinning has been performed at an ion energy of 6×105 V with incident angle of $6°$. In results, the nano-SiC crystallites with average crystal size of 100–800 nm which indicates that neither the pyrocarbon matrix nor the carbon fibers are preferred reaction sites. Siliconization leads to a steady conversion of both fiber and matrix.

4.4 Polymer

Some porous polymers have investigated by using TEM characterization for the high-performance device. Won et al. (2021) explored the morphology of porous polymerized vinyl acetate (p-PVAc) thin films for lithium-sulfur batteries. The synthesis of p-PVAc/S/G has been done by distributed homogenously the S nanoparticles (S NP) which anchored on the graphene sheet. However, the S NPs has difficulty to cover within the polymer matrix. Figure 14a shows the TEM images of PVAc/S/G (before heat treatment), and S NPs located on graphene have selectively encapsulated by a densely packed PVAc layer. It is supposed that the S nanoparticles of PVAc/S/G have not revealed to the surface upon ion transfer. After the heat treatment process
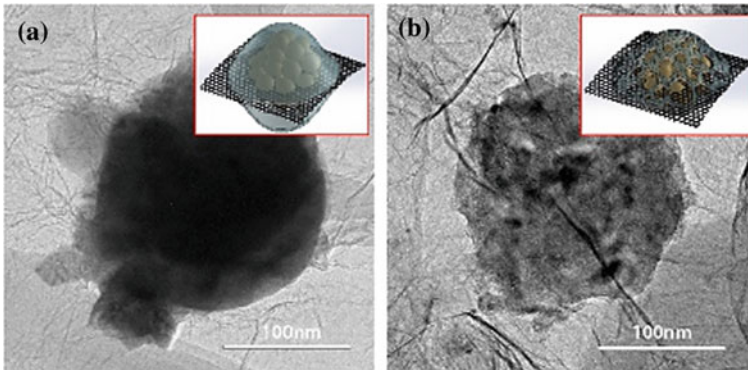
Fig. 14 **a** PVAc/S/G; **b** porous-PVAc/S/G. Reprinted with permission from Won et al. (2021)

(Fig. 14b), precise changes in the different values within the image confirm that the thin porous layer on the S NP has made upon by the PVAc molecules. This results that the heat treatment generates pores on the thin polymer layer by influencing the thermal decomposition of PVAc and enables the utilization of numerous ion channels.

Zang et al. (2020) have studied the porous organic polymers (POPs)-derived porous carbon (DPC) used for supercapacitor with high energy density and durability. As referred to Fig. 15a, b, TEM image is showing the POPs-DPC. POPs-derived porous carbon materials are block structures made of thin nanofilm by way of sequentially accumulated. TEM image is shown in Fig. 15c, d proves that large pores in DPC materials would produce a higher specific surface area.

Fig. 15 POPs-DPC materials. Reprinted with permission from Zang et al. (2020)
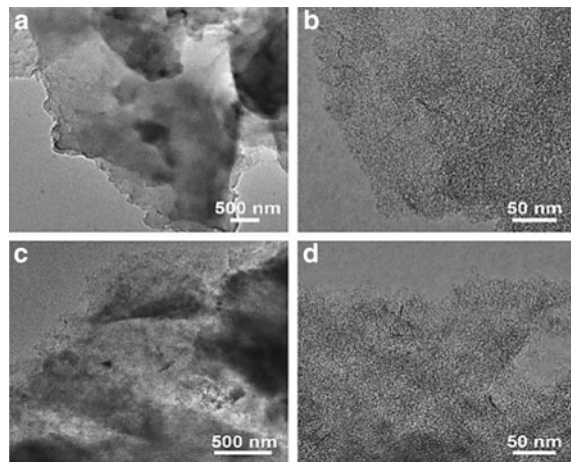
5 Characterization of Hierarchical Porous Materials by Brunauer–Emmett–Teller (BET)

5.1 Oxide

Othman et al. (2021) discovered that by using BET measurement, the surface area of activated carbon nanofibers (ACNFs) included with various types of metal oxide such as magnesium oxide (MgO), manganese dioxide (MnO_2), zinc oxide (ZnO) and calcium oxide (CaO) has been obtained. In this work, ACNFs incorporated with metal oxides that has high surface area indicate an improvement for adsorption of carbon dioxide (CO_2) saturating in the atmosphere area. The large BET surface area has been shown by the ACNFs incorporated with MgO which is the largest surface area compared to the others ACNFs + metals oxide (MnO_2, ZnO, and CaO). The identity of magnesium compounds as well as MgO is well-known as pore creating agents in carbon-based materials. The metallic Mg ions have high energy at high temperature and place porosity into carbon nanofibers. In other side, the suitable amount of metal oxide should be considered to prevent the pore blockage of nanofibers caused by inhomogeneous of polymer and metal oxides.

Li et al. (2020) investigated the surface area of the activated carbon fiber (ACF) with different metal oxides catalysts has affected the catalytic hydrolysis activity. The results show that nickel (Ni) metal oxides with ACF have large BET surface area compared to the other metal oxide (Fe, Cu, Zn, Co) used. On the other side, Fe and Zn metal oxides are expected to disperse in the micropores of ACF. Thus, this type of metal oxides is blocking the micropores and decreases the BET surface area. In the same work, the amount of Ni metal oxides also has been considered wisely. The amount of Ni metal oxides seems likely constant (not more than 5 wt.%) in the ACF. This is because if the amount of Ni metal oxides is more than 5 wt.%, the surface area is decreased where the active groups of these catalysts block the micropores of ACF.

In BET analysis, larger surface area of a nanoparticles size has high ability to remove the organic effluent from the water by employing in the detox process with multiple dyes. This has been revealed by Rabani et al. (2021) which demonstrates that the ZnO nanoparticles have the largest surface area compared to the other metal oxides such as cobalt hexahydrate (II) (Co_3O_4) and titanium dioxide (TiO_2). Larger surface area of ZnO nanoparticles promises that larger active surface sites are resulting higher performance of photocatalyst activity. Thus, author concludes that ZnO metal oxide particles were found to be an effective catalyst for photocatalytic application due to the high surface area compared to Co_3O_4 and TiO_2 metal oxide particles.

5.2 Carbon

Saka 2012 has revealed that the high BET surface area of the activated carbon is produced from an agricultural waste (acorn shell from Q petraea species of oak) by using zinc chloride ($ZnCl_2$) as chemical activation. The report results that the maximum BET surface area of activated carbons is 1289 $m^2 g^{-1}$ at constant activation temperature and time of 600 °C and 30 min, respectively. The author concludes that the prepared activated carbons from acorn shell is probably used for adsorption applications (depends on different activation conditions).

In porous carbon-based studies, Folaranmi et al. (2020) had compared the activated carbon (AC) electrode and AC/graphite oxide (GO) composite electrode. By using BET method, the surface area of activated carbon electrode is larger than surface area of activated carbon/graphene oxide composite electrode. This is because the existence of graphene oxide (GO) and incorporation of polyvinylidene fluoride (PVDF) has reduced the surface area of activated carbon. Even though the surface area of AC/GO is decreased, the specific capacitance (Csp) for AC/GO electrode which is obtained from cyclic voltammetry (CV) curves is high compared to other electrode prepared. In summary, author stated that the electrode prepared by combination of activated carbon and graphene oxide with suitable composition exhibits better electrochemical performance.

Some researchers work on the multi-wall carbon nanotube (MWCNT) as an improvement in the surface area of materials. Haque et al. (2021) show that the existence of MWCNT in the polymer has increased the BET surface area of polymer/MWCNT nanocomposites for proton exchange membrane fuel cells (PEMFCs) application. Polymer/multi-wall carbon nanotube-based electrocatalyst exhibited better electrochemical activity because the polymer binder has high abilities to assist electrochemical interaction using high surface areas of the catalyst supporting material. The author stated that the high surface area made by more exposure to the nanotube structure provides enough space to conduct the catalyst nanoparticles. In this research, the multi-wall carbon nanotube/Nafion has assigned to the highest surface area of 319 $m^2 g^{-1}$ compared to the other nanocomposites. The high surface area of catalyst-supporting materials has favorable for platinum (Pt) nanoparticles distributions. In addition, the polymer-coated MWCNT-based nanocomposites has high electrochemical activity demonstrated by cyclic voltammogram.

Liu et al. (2021) have examined the underlying mechanism for the difference between activated carbon (AC) and graphene nanoplate (GNP) electrodes using the BET analysis to determine specific surface area (SSA). The Brunauer–Emmett–Teller SSA obtained for the activated carbon electrode is ~ 1735.4 $m^2 g^{-1}$ and the graphene nanoplate electrode is 678.6 $m^2 g^{-1}$. From this researcher, although the BET SSA of the activated carbon electrode is higher than the graphene nanoplate electrode, the specific capacitance (C_{sp}) of the graphene nanoplate electrode is much higher than the activated carbon electrode. In electric double layer capacitor (EDLC) mechanism, electrical charges are stored through the reversible adsorption–desorption method. The mobility of ions through the porous electrode depends on the specific surface

area of materials, but suiting pore size in electrodes with ions mobility represents a vital purpose in the energy storage of EDLC.

5.3 Polymer

In porous polymer research, the microporous organic polymer (MOPs) is considered as one of the best candidates for trapping the carbon dioxides (CO_2) in the air. This research has been done by Krishnan and Suneesh (2021) which investigated the synthesis hyper-crosslinked polymer from tetraphenylcyclopentadienone (tetracyclone) and the modification of this type of polymer with amine group. In this research, the result from synthesis hyper-crosslinked polymer shows high surface area of 762 m^2g^{-1}, but it reduces to 490 $m^2 \, g^{-1}$ upon post-synthetic amine modification. This is because the surface area of post-synthetic amine modification hyper-crosslinked polymer expected has been blocked by the alkylamine groups grafted on the surface of smaller pores. However, the research concludes that the post-synthetic amine modification hyper-crosslinked polymer has high carbon dioxide capture capability.

Nickel–cobalt oxide—polyvinyl alcohol nanocomposite (NCO-PVA)—is one example of porous polymer type that has been studied by Siwatch et al. (2021). This experiment reveals that NCO-PVA nanocomposite has large surface area of 112.74 $m^2 \, g^{-1}$ which is calculated from BET equation. This can contribute large number of active sites for improvement of electrochemical performance. El-Shamy and Zayied (2020) have used polyvinyl alcohol (PVA) for PVA/carbon quantum dots (CQDs) nanocomposites film which is expected to be used in some application in anti-ultraviolet, catalytic water decomposition, and desalination. By using BET analysis, the surface area of PVA/CQDs nanocomposite ($82 \times 10^{-2} \, m^2 \, g^{-1}$) is larger than surface area of green PVA ($1.6 \times 10^{-3} \, m^2 \, g^{-1}$). This author also described that the high surface area is promising more active sites, producing an enhancement in the efficiency of adsorption capacity. By the results, the large surface area has high contribution number of active sites.

Zang et al. (2020) show that the porous organic polymers (POPs) derived with porous carbon exhibit a large SSA of 3270 m^2/g. Compared with conventional activated carbon, POPs-DPC show many advantages for energy storage, such as designable pore arrangement and morphology. Furthermore, profiting from the favorable formation and interface characteristics between polymer and DPC electrode, the electric double-layer capacitor (EDLC) displays outstanding electrochemical performance, which is the specific capacitance, C_{sp} is ~ 180 F/g at 0.5 A/g. Besides, the capacity retention shows ~ 70% at 10 A/g. Another example that deploys the porous organic polymers (POP) for supercapacitor has done by Mohamed et al. (2020). This researcher has successfully synthesized hyper-crosslinked porous organic polymers (CPOPs) with tetraphenylanthraquinone, showing Brunauer–Emmett–Teller surface area (approximately 1000 $m^2 \, g^{-1}$) high specific capacitance of 98.4 F/g at a current density of 0.5 A/g. The cycling stability shows 95.3% capacitance retention over 2000

cycles. This concludes that the CPOPs based on tetraphenylanthraquinone could be used as good materials for the supercapacitor.

6   Conclusion

In summary, understanding the hierarchically porous material through the material characterization plays an important role to verify the synthesis material. For discovering the crystal arrangement of materials, XRD analysis is the most powerful method. Chemical compounds can be identified using diffraction techniques based on their crystalline form rather than their chemical element composition. This implies that various compounds or phases of the same structure may be distinguished. On the other hand, SEM analysis is important for examining the hierarchically porous material's microstructure and surface morphology. It studies microscopic arrangement by examining the surface of materials in the same way as scanning confocal microscopes do but with much greater accuracy and intensity of the area. The outside surface morphology of the synthesized nanoparticles is shown by SEM photographs.

From the TEM characterization, this method indicates and reveals the porous structure of the materials. In porous metal oxide section, the large single-crystalline and columnar zirconium oxide grain's structure can be seen under nanoporous oxide has been confirmed. Another discussion titanium dioxide (TiO_2) and carbon shells nanowire are in rutile form has been revealed, and by TEM analysis, the core diameter of TiO_2 crystalline is clearly unchanged for different temperature. TEM for hierarchical porous carbon has been discussed. TEM images for nitrogen-sulfur dual-doped porous carbon have confirmed where bulky micropores (diameter smaller than 2 nm), mesopores (diameter between 2 and 50 nm), and macropores (diameter more than 50 nm) exist in the carbon structure's surface. This shows that the samples have well-developed porosity behavior. The formation of core–shell cerium oxide (CeO_2) and S as the core in the $S/CS-CeO_2/PC$ composition have confirmed by the TEM method. Other example of hierarchical porous carbon is durian porous carbon (DPC) sample. TEM characterization confirms the porous structure existence in DPC materials. Hierarchical porous ceramic has been characterized with TEM analysis. The result shows that the nano-SiC crystallites (average crystal size of 100–800 nm) indicate both pyrocarbon matrix and carbon fibers are not favorable for reaction sites. For hierarchically porous polymer TEM characterization, pores on the porous polymerized vinyl acetate (p-PVAc) have been confirmed. Other example, porous organic polymer (POPs)-derived porous carbon has been confirmed by TEM that the existence of abundant pores.

For BET characterization, the analysis is proving and resulting in the specific surface area (SSA) of the elements. The SSA ACNFs with metal oxide have been measured. ACNFs incorporated with metal oxides have large surface area which indicates an improvement for adsorption of carbon dioxide (CO_2) saturating in the atmosphere area. Surface area of activated carbon fiber (ACF) with different of metal oxides has been shown. Some types of metal oxides have blocked the micropores and

decrease the BET surface area. On the other hand, a large surface area for porous metal oxides has been confirmed and was an efficient catalyst for photocatalytic application. Hierarchically porous carbon shows that the large surface area provides excellent performance in electrochemical analysis. Large surface area has been chosen for the nanoparticles to be mobile and distribute in the materials. However, some cases show that the large surface area is not only role for ions mobility, but the matching of pore size in electrodes with ions size is another big reason for energy storage mechanisms. The hierarchically porous polymer shows that large surface area will result for good carbon dioxide (CO_2) capture, promising more active sites and suggesting as good materials for energy storage application.

References

Abdelhamid, H., El-Zohry, A., Cong, J., Thersleff, T., Karlsson, M., Kloo, L., Zou, X.: Towards implementing hierarchical porous zeolitic imidazolate frameworks in dye-sensitized solar cells. R. Soc. Open Sci. **6**(7), 5–12 (2019)

Abolhasani, M., Naebe, M., Hassanpour Amiri, M., Shirvanimoghaddam, K., Anwar, S., Michels, J., Asadi, K.: Hierarchically structured porous piezoelectric polymer nanofibers for energy harvesting. Adv. Sci. **7**(13), 1–9 (2020)

Azam, M.A., Ramli, N., Nor, N., Nawi, T.: Recent advances in biomass-derived carbon, mesoporous materials, and transition metal nitrides as new electrode materials for supercapacitor: a short review. Int. J. Energy Res. **45**, 8335–8346 (2021)

Bera, S., Pal, M., Sarkar, S., Jana, S.: Hierarchically structured macro with nested mesoporous zinc indium oxide conducting film. ACS Appl. Mater. Interfaces. **9**(5), 4420–4424 (2017)

Chang, Z., Ding, B., Dou, H., Wang, J., Xu, G., Zhang, X.: Hierarchically porous multilayered carbon barriers for high-performance Li-S batteries. Chem. - A Eur. J. **24**(15), 3768–3775 (2018)

Chen, C., Li, B., Zhou, L., Xia, Z., Feng, N., Ding, J., Wang, L., Wan, H., Guan, G.: Synthesis of hierarchically structured hybrid materials by controlled self-assembly of metal-organic framework with mesoporous silica for CO_2 adsorption. ACS Appl. Mater. Interfaces. **9**(27), 23060–23071 (2017)

Chen, X., Li, L., Shan, Y., Zhou, D., Cui, W., Zhao, Y.: Synergistic effect of cerium oxide with core-shell structure embedded in porous carbon for high-performance lithium-sulfur batteries. Mater. Today Commun. **27**, 102381 (2021)

Duan, C., Li, F., Li, L., Zhang, H., Wang, X., Xiao, J., Xi, H.: Hierarchically structured metal–organic frameworks assembled by hydroxy double salt–template synergy with high space–time yields. Cryst. Eng. Commun. **20**(8), 1057–1064 (2018)

El-Shamy, A., Zayied, H.: New polyvinyl alcohol/carbon quantum dots (PVA/CQDs) nanocomposite films: structural, optical and catalysis properties. Synth. Met. **259**, 116218 (2020)

Faustini, M., Giraud, M., Jones, D., Rozière, J., Dupont, M., Porter, T., Nowak, S., Bahri, M., Ersen, O., Sanchez, C., Boissière, C., Tard, C., Peron, J.: Porous electrocatalysts: hierarchically structured ultraporous iridium-based materials: a novel catalyst architecture for proton exchange membrane water electrolyzers. Adv. Energy Mater. **9**(4), 1–11 (2019)

Folaranmi, G., Bechelany, M., Sistat, P., Cretin, M., Zaviska, F.: Comparative investigation of activated carbon electrode and a novel activated carbon/graphene oxide composite electrode for an enhanced capacitive deionization. Materials (basel). **13**(22), 5185 (2020)

Haque, M., Sulong, A., Shyuan, L., Majlan, E., Husaini, T., Rosli, R.: Synthesis of polymer/MWCNT nanocomposite catalyst supporting materials for high-temperature PEM fuel cells. Int. J. Hydrogen Energy. **46**(5), 4339–4353 (2021)

He, Z., Xie, J., Liao, Z., Ma, Y., Zhang, M., Zhang, W., Yue, H., Gao, X.: Hierarchical porous structure contained composite polyimide film with enhanced dielectric and water resistance properties for dielectric material. Prog. Org. Coatings. **151**, 106030 (2021)

Herwig, J., Titus, J., Kullmann, J., Wilde, N., Hahn, T., Gläser, R., Enke, D.: Hierarchically structured porous spinels via an epoxide-mediated sol-gel process accompanied by polymerization-induced phase separation. ACS Omega **3**(1), 1201–1212 (2018)

Krishnan, S., Suneesh, C.: Post-synthetic modification of tetraphenylcyclopentadienone based hypercrosslinked microporous polymers for selective adsorption of CO_2. Mater. Today Commun. **27**, 102251 (2021)

Li, X., Hao, C., Tang, B., Wang, Y., Liu, M., Wang, Y., Zhu, Y., Lu, C., Tang, Z.: Supercapacitor electrode materials with hierarchically structured pores from carbonization of MWCNTs and ZIF-8 composites. Nanoscale **9**(6), 2178–2187 (2017)

Li, K., Wang, C., Ning, P., Li, K., Sun, X., Song, X., Mei, Y.: Surface characterization of metal oxides-supported activated carbon fiber catalysts for simultaneous catalytic hydrolysis of carbonyl sulfide and carbon disulfide. J. Environ. Sci. **96**, 44–54 (2020)

Liu, J., Khanam, Z., Ahmed, S., Wang, H., Wang, T., Song, S.: A study of low-temperature solid-state supercapacitors based on Al-ion conducting polymer electrolyte and graphene electrodes. J. Power Sources. **488**, 229461 (2021)

Luca, V., Sizgek, D., Sizgek, E., Arrachart, G., Rey, C., Scales, N., Aly, Z., Drisko, G.: Actinide and lanthanide adsorption onto hierarchically porous carbons beads: a high surface affinity for Pu. Nanomaterials **9**(10), 1464 (2019)

Mohamed, M.G., Zhang, X., Mansoure, T.H., EL-Mahdy, A.F.M., Huang, C.F., Danko, M., Xin, Z., Kuo, S.W.: Hypercrosslinked porous organic polymers based on tetraphenylanthraquinone for CO_2 uptake and high-performance supercapacitor. Polymer (Guildf). **205**, 122857 (2020)

Moyer, K., Conklin, D., Mukarakate, C., Vardon, D., Nimlos, M., Ciesielski, P.: Hierarchically structured CeO_2 catalyst particles from nanocellulose/alginate templates for upgrading of fast pyrolysis vapors. Front. Chem. **7**, 1–12 (2019)

Othman, F., Yusof, N., Samitsu, S., Abdullah, N., Hamid, M., Nagai, K., Abidin, M., Azali, M., Ismail, A., Jaafar, J., Aziz, F., Salleh, W.: Activated carbon nanofibers incorporated metal oxides for CO2 adsorption: Effects of different type of metal oxides. J. CO2 Util. **45**, 101434 (2021)

Park, Y., Kim, J., Ali, G., Cho, S.: Enhancement of oxidation resistance of zirconium alloy with anodic nanoporous oxide layer in high-temperature air/steam environments. Corros. Sci. **140**, 217–222 (2018)

Peng, X., Zhuan, L., Zi-bing, Z., Xiang, X.: The morphology and mechanism of formation of SiC in C/C-SiC composites fabricated by liquid silicon infiltration. J. Ceram. Process. Res. **11**, 335–340 (2010)

Rabani, I., Bathula, C., Zafar, R., Rabani, G., Hussain, S., Patil, S., Seo, Y.: Morphologically engineered metal oxides for the enhanced removal of multiple pollutants from water with degradation mechanism. J. Environ. Chem. Eng. **9**(1), 104852 (2021)

Saka, C.: BET, TG–DTG, FT-IR, SEM, iodine number analysis and preparation of activated carbon from acorn shell by chemical activation with $ZnCl_2$. J. Anal. Appl. Pyrolysis. **95**, 21–24 (2012)

Saravanan, L., Patil, R., Gultom, P., Kumar, B., Manikandan, A., Fu, Y., Chueh, Y., Cheng, C., Yeh, W., Ma, Y.: Rutile-phase TiO2@carbon core-shell nanowires and their photoactivation in visible light region. Carbon **181**, 280–289 (2021)

Seman, R., Azam, M.A.: Hybrid heterostructures of graphene and molybdenum disulfide: the structural characterization and its supercapacitive performance in 6M KOH electrolyte. J. Sci-Adv. Mater. Dev. **5**, 554–559 (2020)

Siwatch, P., Sharma, K., Manyani, N., Kang, J., Tripathi, S.: Characterization of nanostructured nickel cobalt oxide-polyvinyl alcohol composite films for supercapacitor application. J. Alloys Compd. **872**, 159409 (2021)

Wang, Z., Guan, X., Huang, H., Wang, H., Lin, W., Peng, Z.: Piezoresistive sensors: full 3D printing of stretchable piezoresistive sensor with hierarchical porosity and multimodulus architecture. Adv. Funct. Mater. **29**(11), 1–8 (2019)

Won, J., Kim, M., Jeong, H.: Porous polymer thin film encapsulated sulfur nanoparticles on graphene via partial evaporation for high-performance lithium–sulfur batteries. Appl. Surf. Sci. **547**, 149199 (2021)

Wu, X., Wang, Y., Zhong, R., Li, B.: Nitrogen and sulfur dual-doped hierarchical porous carbon derived from bacterial cellulose for high performance supercapacitor. Diam. Relat. Mater. **116**, 108447 (2021)

Xing, Y., Zhao, K., Shan, P., Zheng, F., Zhang, Y., Fu, H., Liu, Y., Tian, M., Xi, C., Liu, H., Feng, J., Lin, X., Ji, S., Chen, X., Xue, Q., Wang, J.: Ising superconductivity and quantum phase transition in macro-size monolayer NbSe2. Nano Lett. **17**, 6802–6807 (2017)

Xue, M., Xu, H., Tan, Y., Chen, C., Li, B., Zhang, C.: A novel hierarchical porous carbon derived from durian shell as enhanced sulfur carrier for high performance Li-S batteries. J. Electroanal. Chem. **893**, 115306 (2021)

Yang, Y., Zhu, H., Xiao, J., Geng, H., Zhang, Y., Zhao, J., Li, G., Wang, X., Li, C., Liu, Q.: Achieving ultrahigh-rate and high-safety Li+ storage based on interconnected tunnel structure in micro-size niobium tungsten oxides. Adv. Mater. **32**(12), 1905295 (2020)

Zhang, Y., Chen, J., Tang, H., Xiao, Y., Qiu, S., Li, S., Cao, S.: Hierarchically-structured SiO2-Ag@TiO2 hollow spheres with excellent photocatalytic activity and recyclability. J. Hazard. Mater. **354**, 17–26 (2018)

Zang, S., Jiang, J., An, Y., Li, Z., Guo, H., Sun, Y., Dou, H., Zhang, X.: A novel porous organic polymer-derived hierarchical carbon for supercapacitors with ultrahigh energy density and durability. J. Electroanal. Chem. **876**, 114723 (2020a)

Zhang, M., Cui, X., Wang, Y., Wang, B., Ye, M., Wang, W., Ma, C., Lin, Z.: Simple route to interconnected, hierarchically structured, porous Zn2SnO4 nanospheres as electron transport layer for efficient perovskite solar cells. Nano Energy. **71**, 104620 (2020b)

Zhou, J., Dou, Y., Zhou, A., Guo, R., Zhao, M., Li, J.: MOF template-directed fabrication of hierarchically structured electrocatalysts for efficient oxygen evolution reaction. Adv. Energy Mater. **7**(12), 1–10 (2017)

Zhao, X., Liu, Y., Yu, Y., Huang, Q., Ji, W., Li, J., Zhao, Y.: Hierarchically porous composite microparticles from microfluidics for controllable drug delivery. Nanoscale **10**(26), 12595–12604 (2018)

Hierarchical Porous Zeolitic Imidazolate Frameworks: Microporous to Macroporous Regime

Hani Nasser Abdelhamid

Abstract The creation of different pore size regimes into zeolitic imidazolate frameworks (ZIFs) to form hierarchical porous structures enhanced the material's performance for various applications. This book chapter focuses on the synthetic strategies for creating ZIFs with pore structures containing multiple pore regimes and provides readers with a broader scope of the strategies available for the fabrication of hierarchical porous ZIFs. Hierarchical porous ZIFs can be synthesized using in situ and ex situ synthesis procedures. Different synthesis procedures were reported, including template-based method, template-free procedure, and three-dimensional (3D) printing. The material's porosity can be characterized using nitrogen adsorption–desorption isotherms, mercury intrusion porosimetry, transmission electron microscopy, and scanning electron microscopy. Hierarchical porous ZIFs offered a complex porous structure. Thus, the combination of different techniques to characterize the material's porosity is highly required. Overall, this chapter offered a roadmap that may guide the scientists and researchers to design and develop hierarchical porous ZIFs materials with different pore size regimes and high molecular precision.

Keywords Metal–organic frameworks · Zeolitic imidazolate frameworks · Hierarchical porous · Porous materials

1   Introduction

Porous materials with a discrete form of pores play a crucial role in several applications (Singh et al. 2020; Szczęśniak et al. 2020). They can be classified as microporous (pore size < 2 nm), mesoporous (pore size of 2–50 nm), and macroporous (pore

H. N. Abdelhamid (✉)
Advanced Multifunctional Materials Laboratory, Department of Chemistry, Assiut University, Assiut 71516, Egypt
e-mail: hany.abdelhamid@aun.edu.eg

Proteomics Laboratory for Clinical Research and Materials Science, Department of Chemistry, Assiut University, Assiut 71516, Egypt

size > 50 nm). Large pore size is desirable for enabling faster molecular diffusion and mass transfer of large molecules. It also enables the diffusion of viscous solutions. Large pore size ensures high throughput diffusion with low-pressure gradients. Hierarchical pore materials refer to the integration of multi-domain or multi-level pore apportionments within the same porous system. Several types of porous materials were reported, including porous carbon, silica, zeolites, metal–organic frameworks (MOFs), covalent-organic frameworks (COFs), and intrinsic porous polymers (PIMs). They can be classified as inorganic (e.g., zeolite, silica, carbon), organic-based materials (e.g., COFs, PIMs), or hybrid materials (e.g., MOFs). These materials have been applied for a wide range of applications, including gas adsorption/storage, environmental-based applications, energy, and biomedical applications. They exhibit superior performance compared to non-porous materials.

Metal–**o**rganic **f**rameworks (MOFs) are porous materials assembled from inorganic nodes and organic linkers (Zhou et al. 2012a). They can also be denoted as **p**orous **c**oordination **p**olymers (PCPs) and **p**orous **c**oordination **n**etworks (PCNs). The combination of organic and inorganic moieties offered several advantages, including structural tunability that offers precise integration of functional groups inside the framework. There are more than 70,000 unique MOFs structures in Cambridge structure database (CSD) (Moghadam et al. 2017). However, very few examples of MOFs are common such as UiO-66 (**U**niversitetet **i O**slo), *HKUST-1* (**H**ong **K**ong **U**niversity of **S**cience and **T**echnology, copper-based MOFs), *MIL-53* (**M**aterials of **I**nstitute **L**avoisier, Al-based MOFs), and zeolitic imidazolate frameworks (e.g., ZIF-8 for Zn node and ZIF-67 for Co node). The material's porosity can be tailored through judicious choices of the material's building blocks or via other methods, including modulation, template-based method, or modern energy technologies such as microwave, ultrasonic, or plasma. MOFs offer fascinating properties such as high surface area, tunable pore size, high active metal sites, and their ability to encapsulate enzyme, protein, polysaccharides, and inorganic nanomaterials. They advanced both science and engineer fields. They have been tested for both fundamental aspects and practical applications, including adsorption (Canivet et al. 2014), photocatalysis (Alkhatib et al. 2020), fuel cells (Ramaswamy et al. 2014), environmental applications (Dhaka et al. 2019), and drug delivery (Abánades Lázaro and Forgan 2019).

Zeolitic imidazolate frameworks (ZIFs) are a subclass of MOFs that are topologically isomorphic with zeolites (Abdelhamid 2021a; Furukawa et al. 2013; Horcajada et al. 2012; Li et al. 2009; Murray et al. 2009; Park et al. 2006; Shekhah et al. 2011; Yang et al. 2016; Zhou et al. 2012b; Zhou and Kitagawa 2014). They are composed of tetrahedrally coordinated metal ions, e.g., Co, Cu, Zn, connected with an imidazolate-based linker. They exhibited a metal (M)–imidazole (Im)–metal (M) angle of 145° like Si–O–Si angle in zeolites. There are more than 105 ZIF topologies in the literature. They exhibit high thermal and chemical stability with high surface areas. Most of the reported ZIFs are micropore regimes (< 2 nm) (Abdel-Magied et al. 2019). The small pore of micropore ZIFs limits the diffusion rate of large molecules. Thus, several approaches, including template and template-free methods, were reported to create mesopore and macropore inside ZIF crystals, i.e., hierarchical porous structures (Abdelhamid 2020a; Abdelhamid et al. 2017; Zheng et al. 2016).

   This book chapter summarized the synthesis of hierarchical porous ZIFs. Synthesis procedures including template and template-free procedures, are included. The new porosity can be created inside the crystals via in situ and ex situ procedures. Hierarchical porous ZIFs can be achieved via other methods such as in situ growth of ZIFs material on a rigid template. Three-dimensional (3D) printing of ink-containing ZIFs materials can also be used to create hierarchical porous materials containing different pore regimes. The characterization techniques for the material's porosity are also summarized. This book chapter offered a guide for the scientists who work in ZIF's research area.

2   Structure of ZIFs

ZIFs materials are constructed from tetrahedral metal (M) centers such as Co and Zn, which coordinated via nitrogen atoms in imidazolate (1,3-diazolate, Im) ligand. The angle of M–Im–M in ZIFs is 145° and coincides with that of Si–O–Si in zeolites (Fig. 1, Table 1). Thus, the name of the materials was coined as **z**eolitic **i**midazolate **f**rameworks (ZIFs). ZIFs can be crystalline in several classes according to their topologies, such as Linde Type A (LTA), sodalite (SOD), zeolite rho (RHO), gmelinite (GME), gismondite (GIS), merlinoite (MER), and analcite (ANA).

   Zeolitic imidazolate frameworks (ZIFs) can be synthesized as hierarchical porous structures (Doan et al. 2019). The structure of ZIF depends on the type of imidazolate linker and the solvent used during the synthesis process. The variation in the functional linker groups or building blocks offered various ZIFs with different structures
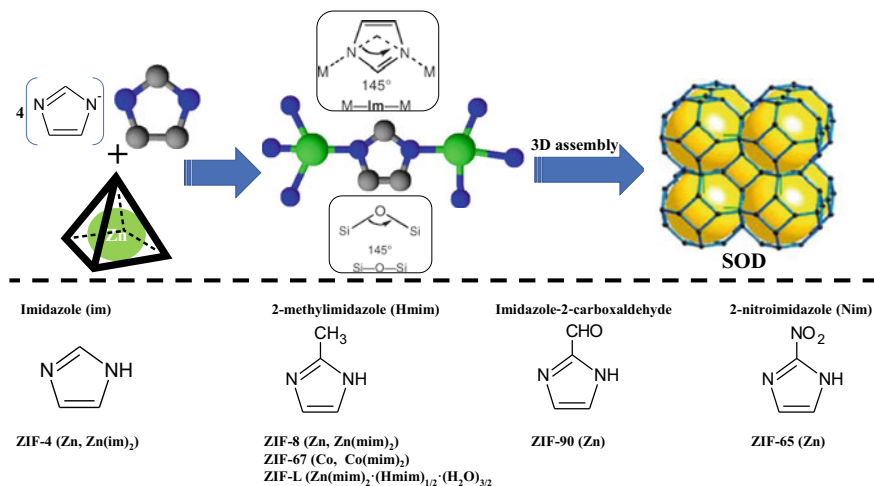
Fig. 1 Coordination of Zn and imidazole and some examples for imidazole linker and their corresponding ZIFs

**Table 1** Comparison between the zeolites and ZIFs

	Zeolites	ZIFs
Types	Inorganic	Hybrid (inorganic–organic)
History	Over 250 years (1765)	10 years (2010)
Composition	Si, Al, and O (dopant, e.g., Sn, Ti)	C, H, N, Co, Zn, Cu,
Secondary building units	$[SiO_4]$ and $[AlO_4]$	M(imidazole)$_2$, and M=Co, Zn, Cu
Existence	Natural and synthetic	Synthetic
Synthesis	High temperature, long reaction time (several days), and requires structure-directing agents (SDA)	Can be synthesized at room temperature, short reaction time (30 min), and no SDA
Structure	314	>400
Thermal Stability	High (up to 1000 °C)	High (thermal stability up to 500 °C)
Chemical stability	Depends on the Si/Al ratio, acid-sensitive, and exhibits high affinity to water	High chemical stability in basic condition, acid-sensitive, and low water affinity
Application prospects	Low cost and large scale for industry applications	Promising for industry applications

(Fig. 1). There are more than 400 ZIFs with unique structures in the literature. This makes it unique compared to zeolites that have only 314 different structures (Table 1). The same linkers and metal ions can offer different structures or morphology. For instance, 2-methylimidazole (Hmim) and zinc ions offer different structures such as ZIF-8, ZIF-L, and diaZIF. The same linker can coordinate with cobalt and offers ZIF-67 with the same structure and topology.

3   Synthesis of ZIFs

The synthesis of conventional porous ZIFs can be achieved using different methods, including hydrothermal, solvothermal, ionothermal, stirring at room temperature, microfluidic synthesis, dry-gel, electrospray, mechanochemical, sonochemical approach, microwave, steam-assisted, vapor-assisted, heating-assisted, and electrochemical synthesis (Fig. 2) (Jin and Shang 2021; Szczęśniak et al. 2020). These methods offer ZIFs materials with high crystallinity, high specific surface areas, and the ability to produce the materials in the forms of powder, thin film, and three-dimensional (3D) objects. The judicious choice of the synthesis method is the best option to obtain the target structure with the optimal properties.
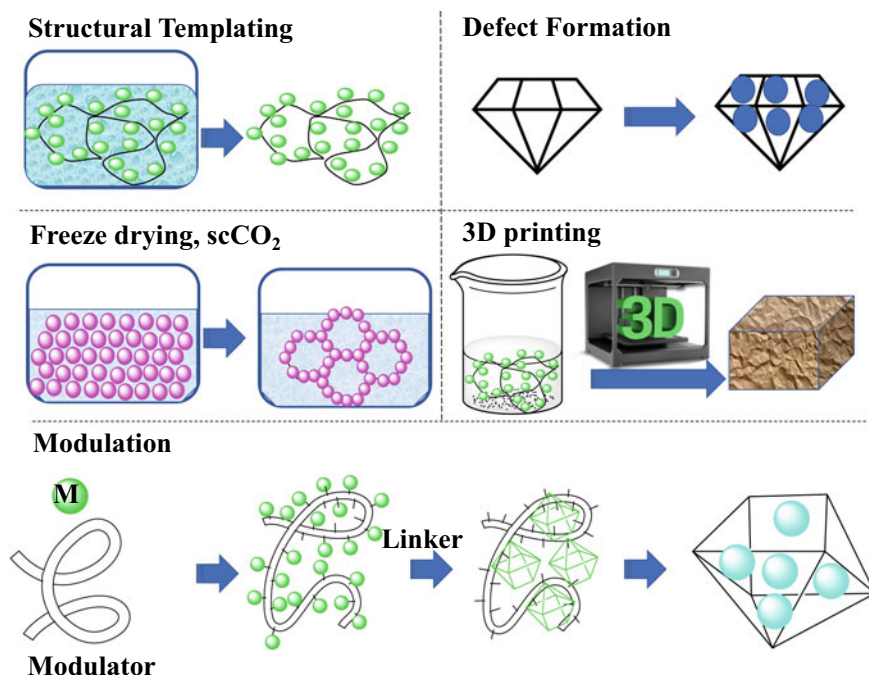
Several parameters affect the synthesis procedure of ZIFs. The synthesis of ZIFs can be achieved in different amide solvents such as N, N-dimethylformamide (DMF), N, N-diethyl formamide (DEF), and N-methyl pyrrolidine (NMP). These solvents
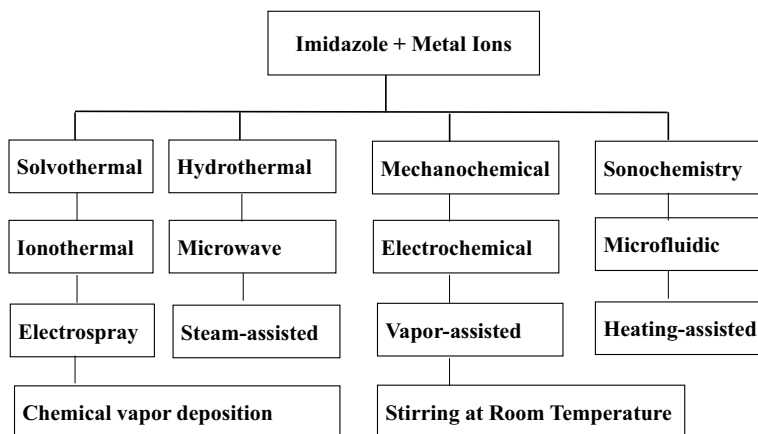
Fig. 2 Common procedures for the synthesis of ZIFs

required usually removing steps via different methods such as a solvent exchange. The synthesis can also be achieved in water and aqueous solution such as methanol and ethanol. The process of nucleation or crystal growth can be accelerated or modulated using reagents that control the crystal formation and control the size and shape of the synthesized ZIFs. Organic amines such as trimethylamine (TEA), pyridine (Py), and a base such as ammonium hydroxide (NH_4OH) or sodium hydroxide (NaOH) can be added to the reaction systems. These reagents play different roles, such as modulators, and can act as deprotonating agents of imidazole linkers. They facilitate the reaction between the metal cation and the imidazole-based linkers. Thus, they accelerate the synthesis of ZIFs and control the size of ZIFs crystals. A high concentration of imidazole linker can also be used to modulate and control the crystal's size. Auxiliary agents such as poly(diallyldimethylammonium chloride), N-heterocycle, carboxylate, alkylamine, or sodium formate can also be added as competitive ligands and bases during the nucleation and growth process of ZIFs.

The conventional synthesis procedure offered a facile method for the direct synthesis of hierarchical porous ZIFs. ZIFs materials such as ZIF-8 and ZIF-67 were synthesized using ammonium hydroxide and triblock copolymer (poly(ethylene oxide)–poly(propylene oxide)–poly(ethylene oxide), PEO–PPO–PEO) as a deprotonating agent and modulator, respectively (Yao et al. 2013). The synthesis procedure offered ZIFs materials with high purity and yield. The size of the ZIF-90 crystal can be decreased using alcohol and polyvinylpyrrolidone (PVP) (Shieh et al. 2013). The synthesis using water and PVP offered ZIF-90 with the size of microparticles. The size can be decreased to the nano-size range using water, alcohol, and PVP (Shieh et al. 2013). The synthesis can also be modulated using ionic liquids (ILs) that prevent competitive interactions between the solvent and the template framework (Parnham and Morris 2007). The use of ILs offered several advantages being environmentally friendly and cost-effective and can be recyclable.

Structural Templating

Defect Formation

Freeze drying, scCO$_2$

3D printing

Modulation

M

Linker

Modulator

Fig. 3 Schematic representation for the methods used to synthesis of hierarchical porous ZIFs

Hierarchical porous ZIF can be synthesized via pre-synthetic or post-synthetic (Fig. 3, Table 2). The new porosity can be created inside the crystal, i.e., intracrystal or between the crystal, i.e., intercrystals. The microporous ZIFs materials can contain mesopore via a modulator (Fig. 3, Table 2). Different modulators such as surfactants, polymers, and organic dyes were reported. The pre-synthetic procedure involved the use of template molecules to grow the ZIF-8 crystals. The template could be hard or soft structural template agents. The sacrificial template of the metal can be used for template-free procedures. The post-synthetic procedure involves defect formation and three-dimensional (3D) printing. A non-classical method such as the microwave-assisted method was used for the synthesis of hierarchical porous ZIF-65 (Butova et al. 2020). The following sections summarized some of these methods.

3.1   Modulation-based Method

Hierarchical porous ZIFs materials can be synthesized using a modulator (Fig. 4). The modulation can be achieved using a base such as triethylamine (TEA), sodium formate (HCOONa), surfactant, organic dyes (Abdelhamid 2020a), and inorganic salts (Abdelhamid 2020b).

Table 2 Synthesis methods for hierarchical porous ZIFs

Techniques	Procedures	Description	Advantages	Disadvantages
Modulation	In situ synthesis	Modulates the synthesis procedure	Simple and no template	Uncontrolled porosity
Hard structural templating	Direct synthesis	Uses a template to grow the crystal surround it	Offers tunable porosity The size of the template determines the material's porosity	Requires template and requires further steps to remove the template, and the final products sometimes contain a residual of the template materials
	Post-synthetic treatment			
Soft structural templating	Direct synthesis			
	Post-synthetic treatment			
Template-free procedure	In situ synthesis	Creates a sacrificial template inside the reaction's solution	No template, simple, and can be further modified with inexpensive reagents	Small mesopore size and no macroporosity
Defect formation	Post-synthetic treatment	Acid etching	Simple and no template	Uncontrolled porosity, requires high control condition to avoid framework dissolution, and only use for acid-sensitive materials
Supercritical CO_2 or freeze-drying	Post-synthetic treatment	$scCO_2$ drying and freeze-drying	Simple, offers large pore structure, tunable properties, and easy to proceed into commercial products such as foams or aerogels	Requires additives and expensive
	Direct synthesis	Expanded solvent		
3D printing	Post-synthetic incorporation	Processing a mixture containing ZIF materials and a binder into a 3D object	Easy for operation, offers tunable porosity, high-through procedures, and offers a product with the potential for commercialization	Requires experience and reagents such as binder for processing
	Direct synthesis	Produces an ink-containing ZIFs material before processing into a 3D object		
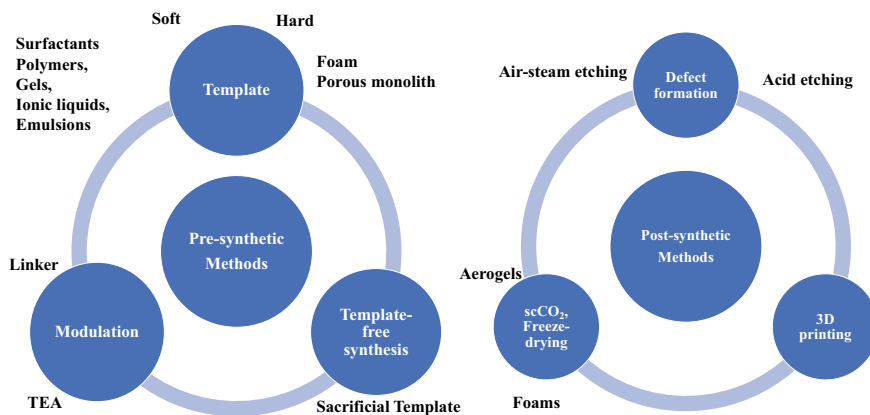
Fig. 4 Pre-synthetic and post-synthetic procedures for the synthesis of hierarchical porous ZIFs

The first synthesis of ZIFs involved solvothermal synthesis using organic solvent systems such as DMF, DEF, and NMP (Park et al. 2006). Organic modulators such as organic amines such as pyridine and TEA were added as the deprotonating agent that modulates the formation of the crystals. These modulators affect mainly the crystal's size. However, a recent study revealed that TEA could modulate the material's porosity (Abdelhamid et al. 2017). The procedure involved the synthesis of ZIF-8 and ZIF-67 at room temperature using water as a solvent. The synthesis mechanism showed the formation of zinc oxide nanocrystals that serve as a template. The material's porosity can be increased using an organic dye such as rhodamine B or methylene blue (Abdelhamid et al. 2017).

3.2 Template-based Method

The synthesis of hierarchical porous ZIFs can be synthesized using the template-based method. The template can be classified as; (1) hard template, e.g., a foam or porous monolith or (2) soft template, e.g., a gel or emulsion. The template can be retained or removed after the synthesis of ZIFs materials. The pore properties such as size, shape, and interconnectivity can be controlled through the judicious choice of the template types, size, and other properties.

Soft templates such as surfactants, polymers 31,32, gels, nucleotide 33, and emulsions can be used to synthesize hierarchical porous ZIFs. Polymers such as polyimide (PI) (Shahid et al. 2021) and polystyrene (PS) spheres (Shen et al. 2018) were reported as a template. Soft template such as cellulose acetate (CA) was used for the synthesis of ZIF-8/CA aerogel (Bo et al. 2018). The synthesis procedure involves the addition of zinc ions in a cellulose solution before the addition of 2-methylimidazole (Hmim) to form ZIFs. This method can be used for ZIFs materials such as ZIF-8 (Bo et al.

2018), ZIF-9, and ZIF-12 on CA (Ren et al. 2018). ZIF-8 can be synthesized into flexible cellulose aerogels via a sol–gel and freeze-drying process (Zhu et al. 2016). The synthesis of hierarchical porous using soft templates offers several advantages. The soft template can be removed via a simple post-synthetic procedure. For example, a polymer such as polystyrene (PS) spheres was used as a soft sacrificial template to form a single-crystal ordered macropore ZIF-8 (SOM-ZIF-8), a hierarchical porous structure (Shen et al. 2018). The synthesis procedure involves the impregnation of ZIF-8 precursors in a mixture of methanol/ammonia into PS polymer. A single crystal of ZIF-8 was uniformly grown surround the PS template. The PS template can be the removed via dissolving the PS template using tetrahydrofuran (THF) (Shen et al. 2018). This method offered macropores in the size of 80–470 nm via using different diameters of PS templates (Shen et al. 2018). PS can also be used for the synthesis of macro-microporous ZIF-67 (Zhao et al. 2021).

A surfactant-assisted dip-coating method was reported for the synthesis of a flexible 3D hierarchically porous ZIF-67 using melamine sponge (Andrew Lin and Chang 2015). The method involves dipping a melamine sponge into a solution of ZIF nanocrystals with stirring for three hours. The ZIF-67 crystals are self-assembled on the modified melamine sponge that occurs via non-covalent interactions such as electrostatic and π–π stacking interactions. The synthesis conditions can be tuned using different types of surfactants, including anionic sodium dodecylbenzene sulfonate (SDBS), cationic cetyltrimethylammonium bromide (CTAB), non-ionic hydrophobic sorbitan monooleate (SPAN-80), and non-ionic hydrophilic Triton X-100. The authors reported that the ZIF-67 loading could be increased by increasing the concentration of SPAN-80 and SDBS. On the other side, they did not observe this phenomenon for CTAB and Triton X-100. This effect could be due to the charge of the surfactant; ZIF-67 is positive surface charge particles, Triton X-100 is neutral, CTAB is positive surface charges, and SDBS and SPAN are negative surface charges surfactants. Surfactant with negative charge surface offered electrostatic interaction with melamine sponge (Andrew Lin and Chang 2015).

Hierarchical porous ZIFs can be synthesized using ZIFs as templates or seeds. For example, ZIF-67@ZIF-8 core–shell structures can be synthesized using ZIF-67 as seeds (Yang et al. 2015). Hierarchical yolk-shell nanoparticle@ZIF-8 was achieved via assembled ZIF-8 crystals on Cu_2O nanoparticles as a template (Kuo et al. 2012). ZIF-8 can be synthesized on the surface of mesoporous silica foam via the layer-by-layer method (Shekhah et al. 2012).

3.3 Template-free Synthesis

Hierarchical porous ZIFs can be synthesized via template-free procedure (Abdelhamid 2021b, 2017; Abdelhamid and Zou 2018). The procedure involves the in situ synthesis of the sacrificial template of the metal ions inside the reaction solution. An inorganic base such as NaOH can induce the formation of zinc hydroxy nitrate

that can serve as a sacrificial template for the synthesis of hierarchical porous ZIFs materials.

3.4 Defect Formation

Defect formation can be used for the synthesis of hierarchical porous ZIFs. The method depends on the disruption of the periodic crystalline structure of the ZIF crystal. It can be achieved via several methods, including (1) in situ method via incorporating a sizeable ligand or modulator during synthesis (linker modulation) or (2) via post-synthetic acid etching ZIF crystals. The in situ method depends on the encapsulation of molecules inside the crystal, which can be removed selectively to produce pores. This method is called linker modulation and linked labilization methods that produce mesoporous defects in a MOF containing microporous structure.

Defect formation can be achieved via air–steam etching, acid etching, and other methods. Air–steam etching of ZIF-8 offered hierarchical porous structure (Huang et al. 2021). This method offered a green and facile approach to construct hierarchical porous ZIF-8 without the need for templates or solvents. The degree of mesoporosity created inside ZIF-8 crystals can be controlled by regulating the etching temperature and time. The acid etching approach can be useful for the preparation of the hierarchical porous structure of ZIFs. This method is a comparatively facile procedure compared to templating methods. It can be carried out on larger samples of ZIFs. The method depends on the choice of etching agent and etching conditions to obtain controllable new porosity without the loss of material's crystallinity or cause complete dissolution of the crystals. The properties of the interactions within the frameworks must be well understood to optimize the optimal type of etching agent and their concentration.

The synthesis of hierarchical porous ZIFs materials using the defect formation method suffers from limitations. The creation of the new pore regime is usually uncontrolled and lacks homogenous distribution inside the crystal. Methods such as the acid etching method are unsuitable for water unstable ZIFs.

3.5 Freeze-drying and Supercritical Carbon Dioxide (CO_2)

Compressed or supercritical carbon dioxide (CO_2) was used for the activation of MOFs (Figs. 3 and 4). It was used to remove solvents and can be severed as a soft template. It can be further used to produce porous aerogel structures of ZIFs materials. Other methods such as freeze-drying can also be used to synthesis hierarchical porous materials containing ZIFs materials.

The hierarchical porous ZIF-L was reported using cellulose (Valencia and Abdelhamid 2019). Nanocellulose ZIF-L was fabricated as foams. The method involved

the in situ growth of ZIF-L inside nanocellulose material. It depends on the formation of zinc oxide nanocrystal inside cellulose using a base modulator, e.g., TEA. The crystal of ZIF-L was then formed after the addition of organic linker Hmim. The resultant materials were then fabricated as foam using a freeze-drying procedure. The formed foams are lightweight materials with good mechanical properties (Valencia et al. 2019).

3.6 3D Printing Method

3D printing technology is additive manufacture or robocasting technology. It can be used to fabricate monoliths with controlled 3D shapes. The method is relatively new for the processing of advanced materials such as MOFs and ZIFs.

ZIF-8 powder (up to 50 wt.%) was incorporated into either polylactic acid (PLA) or thermoplastic polyurethane to produce a filament feedstock for 3D printing (Evans et al. 2018). PLA and polyurethane are rigid and flexible polymer matrices, respectively. The rigidity of the PLA offered no re-organization around ZIF-8 crystals during extrusion. Thus, PLA provided various voids in different sizes in the range of micro-, meso-, and macroporous, offering a hierarchical porous monolith with preserved crystallinity. On the other side, the flexible polymer of polyurethane resulted in almost complete pore occlusion with a low specific surface area of the monolith (Evans et al. 2018).

A water-based in situ growth of ZIF-8 was reported for 3D printing (Sultan et al. 2018). The ink was prepared using anionic 2,2,6,6-tetramethylpiperidine-1-oxylradical-mediated oxidized cellulose nanofibers (TOCNFs), sodium alginate binder, and $CaCl_2$ as a crosslinker (Sultan et al. 2018). The ink preparation has been achieved via one pot at room temperature. It can be directly printed using a 3D printer as scaffolds with a large pore size (1 mm). The ink can be modified with drugs such as curcumin or dye such as methylene blue. The printed objects can be used for applications such as drug delivery (Sultan et al. 2018).

3D-printed technology can be used in both providing a monolith and adding hierarchical porosity into ZIF-based materials. However, 3D printing procedure using FDM (Fused Deposition Modeling) required high processing temperatures (> 230 °C) or ultraviolet curing, and thus they cannot be used for unstable MOF in the air because the process depends on a layer-by-layer printing process in air exposure for extended periods (15–120 h). It cannot also be used for thermal labile ZIFs.

4 Characterization of Porosity

The porosity of ZIF's materials can be characterized using several methods, including fluid penetration techniques, which involve the filling of pores with a liquid or a gas (Fig. 5). The information on the pore sizes and volumes can be obtained based on
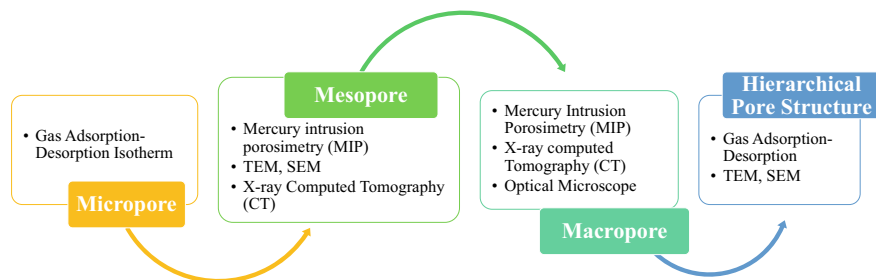
Fig. 5 Characterization techniques used for the determination of ZIF's porosity

the quantity of the adsorbed molecules. Fluid penetration techniques are helpful for the characterization of interconnected pores ("open" porosity) that are accessible to penetration by the fluid species. Other techniques such as imaging or diffraction can also help characterize the material's porosity (Fig. 5). Each method can be suitable for the characterization of a specific pore size range. The combination of more than one technique is highly preferable for accurate determination of the material's pore size and obtaining their pore size distribution. This option becomes obligatory in hierarchical porous materials that may contain multiple ranges of different pore size regimes.

Conventional microporous ZIFs materials are widely characterized using nitrogen (N_2) gas sorption (generally at temperature 77 K and pressure up to 1 bar). Nitrogen adsorption–desorption isotherms can be used to calculate the specific surface area, pore volume, and pore size distributions. Specific surface areas can be calculated using Brunauer–Emmett–Teller (BET, S_{BET}) method and the Langmuir model (S_{Lang}). The external surface area (S_{Ext}) can be calculated using the t-plot method. The pore size distribution can be estimated using different methods such as density functional theory (DFT), Horvath–Kawazoe (H–K) method, and Barrett–Joyner–Halenda (BJH). H–K method is used for the calculation of the pore size distribution in the micropore region. At the same time, the BJH method is used for mesopore distribution (Klobes et al. 2006). The total pore volume is usually calculated at high pressure of 0.98 bar. Nitrogen adsorption–desorption isotherm is very useful for the calculation of specific areas and pore size determination. However, the method cannot provide information on macropores larger than 100 nm (Klobes et al. 2006).

Hierarchical porous materials containing pores in the mesopore and macropore ranges (4 nm–60 μm) can be analyzed using an alternative method such as mercury intrusion porosimetry (MIP). MIP confirmed the presence of macropores in SOM-ZIF8 MOF with the size of 80–470 nm (Shen et al. 2018). MIP method uses non-wetting mercury to penetrate the pores under pressure. It consists of a pressurized chamber to force mercury to intrude into the pores or voids in the investigated materials. Mercury fills the larger pores first. At high pressure, mercury fills the smaller pore sizes. MIP characterizes both the interparticle pores and the intraparticle pores. However, this method uses a toxic compound for characterization and cannot be

used on soft or deformable structures. It is also a destructive method compared to gas adsorption.

Porosity can also be determined using scattering techniques. The scattering techniques involve bombarding the sample with X-rays, neutrons, or electrons. The scattered particles or radiation produces a pattern that can be used to calculate the pore size of the materials. These methods are non-destructive. Small-angle X-ray scattering (SAXS) can be used to probe the variations in scattering length density which occur over distances exceeding typical interatomic spacing to determine larger particle or pore sizes. Neutron and X-ray scattering can be used to provide information on the pore dimensions in a bulk sample. It is a beneficial method for the characterization of isolated or "closed" pores in the material. However, these techniques require appropriate scattering length contrast between the pores and the surrounding material. This requirement is difficult to achieve for ZIFs because the pores are often filled with air or solvent molecules.

Furthermore, the materials contain predominantly light organic moieties, giving low contrast. The contrast may be increased via filling the pores with a suitable contrast agent or using small-angle neutron scattering (SANS), which is independent of atomic number. Thus, SANS can distinguish between even light atoms such as hydrogen and carbon. Moreover, neutron source is a rarely used technique because of the high cost and the presence of these facilities in specific places.

Imaging using optical and electron microscopies such as transmission electron microscopy (TEM), high-resolution TEM, and scanning electron microscopy (SEM) can be helpful for the direct determination of the pore size. An optical microscope can be used for imaging larger macropores (microns to millimeters in size). These techniques offer a very straightforward method for evaluating pore size and their distribution inside the crystals. They can distinguish between interparticle and intraparticle porosity. They require a small amount of sample. The formation of the hierarchical pore can be characterized using liquid cell transmission electron microscopy (LCTEM). LCTEM offers information of the nucleation and growth at high magnification in real time allowing direct visualization of the hierarchical pore formation. However, they suffer from several limitations. These techniques are not bulk techniques. SEM images are restricted to the analysis of surface features. They can be used for the analysis of a small number of particles. Therefore, they may not be representative of the bulk porosity. They cannot be used to evaluate the connectivity or tortuosity of the interior pore network.

X-ray computed tomography (CT) can also be used to determine the pore size and their distribution. X-ray radiation penetrates light materials. CT can be used to obtain a series of two-dimensional (2D) X-ray images that can be computationally compiled and reassembled to obtain a 3D image. Thus, it is a valuable technique to characterize large pores in monolithic structures. However, the current technology using CT imaging is limited to a few tens of microns. Thus, it cannot be used to obtain the full range of pore sizes.

Based on the reviewing method for pore size determination, it is highly recommended to combine several techniques to describe the material's porosity fully.

This combination is essential for ZIFs materials with a complex pore size structure combining multiple pore size regimes.

5 Conclusion

Hierarchical porous ZIFs materials showed unique properties compared to ZIFs with a single pore size regime. Thus, they have been advanced several applications and hold a promising future for further investigation. The standard techniques for fabricating hierarchical porous ZIFs-based materials can be summarized into five general approaches: template-based method, template-free method, defect formation, freeze-drying/supercritical CO_2, and 3D printing. These methods offered the formation of hierarchically porous structures inside and between the crystals. They can be helpful for the commercialization of the materials into a custom form.

References

Abánades, I., Forgan, R.S.: Application of zirconium MOFs in drug delivery and biomedicine. Coord. Chem. Rev. **380**, 230–259 (2019). https://doi.org/10.1016/j.ccr.2018.09.009

Abdel-, A.F., Abdelhamid, H.N., Ashour, R.M., Zou, X., Forsberg, K.: Hierarchical porous zeolitic imidazolate frameworks nanoparticles for efficient adsorption of rare-earth elements. Microporous Mesoporous Mater. **278**, 175–184 (2019). https://doi.org/10.1016/j.micromeso.2018.11.022

Abdelhamid, H.N.: Lanthanide Metal-Organic Frameworks and Hierarchical Porous Zeolitic Imidazolate Frameworks: Synthesis, Properties, and Applications (2017). http://su.diva-portal.org/smash/record.jsf?aq2=%5B%5B%5D%5D&c=27&af=%5B%5D&searchType=LIST_COMING&query=&language=en&pid=diva2%3A1137293&aq=%5B%5B%5D%5D&sf=all&aqe=%5B%5D&sortOrder=author_sort_asc&onlyFullText=false&noOfRows=50&dswid=7329

Abdelhamid, H.N.: Dye encapsulated hierarchical porous zeolitic imidazolate frameworks for carbon dioxide adsorption. J. Environ. Chem. Eng. **8**, 104008 (2020a). https://doi.org/10.1016/j.jece.2020.104008

Abdelhamid, H.N.: Salts induced formation of hierarchical porous ZIF-8 and their applications for CO_2 sorption and hydrogen generation via $NaBH_4$ hydrolysis. Macromol. Chem. Phys. **221**, 2000031 (2020b). https://doi.org/10.1002/macp.202000031

Abdelhamid, H.N.: Biointerface between ZIF-8 and biomolecules and their applications. Biointerface Res. Appl. Chem. **11**, 8283–8297 (2021a). https://doi.org/10.33263/BRIAC111.82838297

Abdelhamid, H.N.: Dehydrogenation of sodium borohydride using cobalt embedded zeolitic imidazolate frameworks. J. Solid State Chem. **297**, 122034 (2021b). https://doi.org/10.1016/j.jssc.2021.122034

Abdelhamid, H.N., Huang, Z., El-, A.M., Zheng, H., Zou, X.: A fast and scalable approach for synthesis of hierarchical porous zeolitic imidazolate frameworks and one-pot encapsulation of

target molecules. Inorg. Chem. **56**, 9139–9146 (2017). https://doi.org/10.1021/acs.inorgchem.7b01191

Abdelhamid, H.N., Zou, X.: Template-free and room temperature synthesis of hierarchical porous zeolitic imidazolate framework nanoparticles and their dye and CO_2 sorption. Green Chem. **20**, 1074–1084 (2018). https://doi.org/10.1039/C7GC03805D

Alkhatib, I.I., Garlisi, C., Pagliaro, M., Al-Ali, K., Palmisano, G.: Metal-organic frameworks for photocatalytic CO_2 reduction under visible radiation: a review of strategies and applications (2020)

Andrew Lin, K.-Y., Chang, H.-A.: A zeolitic imidazole framework (ZIF)–sponge composite prepared via a surfactant-assisted dip-coating method. J. Mater. Chem. **3**, 20060–20064 (2015). https://doi.org/10.1039/C5TA04427H

Bo, S., Ren, W., Lei, C., Xie, Y., Cai, Y., Wang, S., Gao, J., Ni, Q., Yao, J.: Flexible and porous cellulose aerogels/zeolitic imidazolate framework (ZIF-8) hybrids for adsorption removal of Cr(IV) from water. J. Solid State Chem. **262**, 135–141 (2018). https://doi.org/10.1016/j.jssc.2018.02.022

Butova, V.V., Polyakov, V.A., Bulanova, E.A., Soldatov, M.A., Yahia, I.S., Zahran, H.Y., Abd, A.F., Algarni, H., Aboraia, A.M., Soldatov, A.V.: MW synthesis of ZIF-65 with a hierarchical porous structure. Microporous Mesoporous Mater. **293**, 109685 (2020). https://doi.org/10.1016/j.micromeso.2019.109685

Canivet, J., Fateeva, A., Guo, Y., Coasne, B., Farrusseng, D.: Water adsorption in MOFs: fundamentals and applications. Chem. Soc. Rev. **43**, 5594–5617 (2014). https://doi.org/10.1039/c4cs00078a

Dhaka, S., Kumar, R., Deep, A., Kurade, M.B., Ji, S.-W., Jeon, B.-H.: Metal–organic frameworks (MOFs) for the removal of emerging contaminants from aquatic environments. Coord. Chem. Rev. **380**, 330–352 (2019). https://doi.org/10.1016/j.ccr.2018.10.003

Doan, H.V., Amer, H., Karikkethu, P., Petrillo, C., Ting, V.P.: Hierarchical metal-organic frameworks with macroporosity: synthesis, achievements, and challenges. Nano-Micro Lett. **11**, 54 (2019). https://doi.org/10.1007/s40820-019-0286-9

Evans, K.A., Kennedy, Z.C., Arey, B.W., Christ, J.F., Schaef, H.T., Nune, S.K., Erikson, R.L.: Chemically active, porous 3D-printed thermoplastic composites. ACS Appl. Mater. Interfaces. acsami.7b17565 (2018). https://doi.org/10.1021/acsami.7b17565

Furukawa, H., Cordova, K.E., O'Keeffe, M., Yaghi, O.M.: The chemistry and applications of metal-organic frameworks. Science **341**(80), 1230444–1230444 (2013). https://doi.org/10.1126/science.1230444

Horcajada, P., Gref, R., Baati, T., Allan, P.K., Maurin, G., Couvreur, P., Férey, G., Morris, R.E., Serre, C.: Metal-organic frameworks in biomedicine. Chem. Rev. **112**, 1232–1268 (2012). https://doi.org/10.1021/cr200256v

Huang, H., Sun, Y., Jia, X., Xue, W., Geng, C., Zhao, X., Mei, D., Zhong, C.: Air-steam etched construction of hierarchically porous metal-organic frameworks. Chinese J. Chem. cjoc.202000718 (2021). https://doi.org/10.1002/cjoc.202000718

Jin, C.-X., Shang, H.-B.: Synthetic methods, properties and controlling roles of synthetic parameters of zeolite imidazole framework-8: a review. J. Solid State Chem. **297**, 122040 (2021). https://doi.org/10.1016/j.jssc.2021.122040

Klobes, P., Meyer, K., Munro, R.G.: Porosity and Specific Surface Area Measurements for Solid Materials (2006)

Kuo, C.-H., Tang, Y., Chou, L.-Y., Sneed, B.T., Brodsky, C.N., Zhao, Z., Tsung, C.-K.: Yolk-shell nanocrystal@ZIF-8 nanostructures for gas-phase heterogeneous catalysis with selectivity control. J. Am. Chem. Soc. **134**, 14345–14348 (2012). https://doi.org/10.1021/ja306869j

Li, J.-R., Kuppler, R.J., Zhou, H.-C.: Selective gas adsorption and separation in metal–organic frameworks. Chem. Soc. Rev. **38**, 1477 (2009). https://doi.org/10.1039/b802426j

Moghadam, P.Z., Li, A., Wiggin, S.B., Tao, A., Maloney, A.G.P., Wood, P.A., Ward, S.C., Fairen, D.: Development of a Cambridge structural database subset: a collection of metal-organic frameworks

for past, present, and future. Chem. Mater. **29**, 2618–2625 (2017). https://doi.org/10.1021/acs.chemmater.7b00441

Murray, L.J., Dincă, M., Long, J.R.: Hydrogen storage in metal–organic frameworks. Chem. Soc. Rev. **38**, 1294 (2009). https://doi.org/10.1039/b802256a

Park, K.S., Ni, Z., Cote, A.P., Choi, J.Y., Huang, R., Uribe-, F.J., Chae, H.K., O'Keeffe, M., Yaghi, O.M.: Exceptional chemical and thermal stability of zeolitic imidazolate frameworks. Proc. Natl. Acad. Sci. **103**, 10186–10191 (2006). https://doi.org/10.1073/pnas.0602439103

Parnham, E.R., Morris, R.E.: Ionothermal synthesis of zeolites, metal-organic frameworks, and inorganic-organic hybrids. Acc. Chem. Res. **40**, 1005–1013 (2007). https://doi.org/10.1021/ar700025k

Ramaswamy, P., Wong, N.E., Shimizu, G.K.H.: MOFs as proton conductors—challenges and opportunities. Chem. Soc. Rev. **43**, 5913–5932 (2014). https://doi.org/10.1039/c4cs00093e

Ren, W., Gao, J., Lei, C., Xie, Y., Cai, Y., Ni, Q., Yao, J.: Recyclable metal-organic framework/cellulose aerogels for activating peroxymonosulfate to degrade organic pollutants. Chem. Eng. J. **349**, 766–774 (2018). https://doi.org/10.1016/j.cej.2018.05.143

Shahid, S., Baron, G.V., Denayer, J.F.M., Martens, J.A., Wee, L.H., Vankelecom, I.F.J.: Hierarchical ZIF-8 composite membranes: enhancing gas separation performance by exploiting molecular dynamics in hierarchical hybrid materials. J. Memb. Sci. **620**, 118943 (2021). https://doi.org/10.1016/j.memsci.2020.118943

Shekhah, O., Fu, L., Sougrat, R., Belmabkhout, Y., Cairns, A.J., Giannelis, E.P., Eddaoudi, M.: Successful implementation of the stepwise layer-by-layer growth of MOF thin films on confined surfaces: mesoporous silica foam as a first case study. Chem. Commun. **48**, 11434 (2012). https://doi.org/10.1039/c2cc36233c

Shekhah, O., Liu, J., Fischer, R.A., Wöll, C.: MOF thin films: existing and future applications. Chem. Soc. Rev. **40**, 1081 (2011). https://doi.org/10.1039/c0cs00147c

Shen, K., Zhang, L., Chen, X., Liu, L., Zhang, D., Han, Y., Chen, J., Long, J., Luque, R., Li, Y., Chen, B.: Ordered macro-microporous metal-organic framework single crystals. Science **359**(80), 206–210 (2018). https://doi.org/10.1126/science.aao3403

Shieh, F.-K., Wang, S.-C., Leo, S.-Y., Wu, K.C.-W.: Water-based synthesis of zeolitic imidazolate framework-90 (ZIF-90) with a controllable particle size. Chem. A Eur. J. **19**, 11139–11142 (2013). https://doi.org/10.1002/chem.201301560

Singh, G., Lee, J., Karakoti, A., Bahadur, R., Yi, J., Zhao, D., AlBahily, K., Vinu, A.: Emerging trends in porous materials for CO_2 capture and conversion. Chem. Soc. Rev. **49**, 4360–4404 (2020). https://doi.org/10.1039/D0CS00075B

Sultan, S., Abdelhamid, H.N., Zou, X., Mathew, A.P.: CelloMOF: nanocellulose enabled 3D printing of metal-organic frameworks. Adv. Funct. Mater. 1805372 (2018). https://doi.org/10.1002/adfm.201805372

Szczęśniak, B., Borysiuk, S., Choma, J., Jaroniec, M.: Mechanochemical synthesis of highly porous materials. Mater. Horizons. **7**, 1457–1473 (2020). https://doi.org/10.1039/D0MH00081G

Valencia, L., Abdelhamid, H.N.: Nanocellulose leaf-like zeolitic imidazolate framework (ZIF-L) foams for selective capture of carbon dioxide. Carbohydr. Polym. **213**, 338–345 (2019). https://doi.org/10.1016/j.carbpol.2019.03.011

Valencia, L., Monti, S., Kumar, S., Zhu, C., Liu, P., Yu, S., Mathew, A.P.: Nanocellulose/graphene oxide layered membranes: elucidating their behaviour during filtration of water and metal ions in real time. Nanoscale **11**, 22413–22422 (2019). https://doi.org/10.1039/C9NR07116D

Yang, J., Zhang, F., Lu, H., Hong, X., Jiang, H., Wu, Y., Li, Y.: Hollow Zn/Co ZIF particles derived from core-shell ZIF-67@ZIF-8 as selective catalyst for the semi-hydrogenation of acetylene. Angew. Chemie. **127**, 11039–11043 (2015). https://doi.org/10.1002/ange.201504242

Yang, Y., Xie, X., Xu, X., Xia, X., Wang, H., Li, L., Dong, W., Ma, P., Yang, Y., Liu, Y., Mei, X.: Thermal and magnetic dual-responsive liposomes with a cell-penetrating peptide-siRNA conjugate for enhanced and targeted cancer therapy. Colloids Surf. B Biointerfaces. **146**, 607–615 (2016). https://doi.org/10.1016/j.colsurfb.2016.07.002

Yao, J., He, M., Wang, K., Chen, R., Zhong, Z., Wang, H.: High-yield synthesis of zeolitic imidazolate frameworks from stoichiometric metal and ligand precursor aqueous solutions at room temperature. CrystEngComm **15**, 3601 (2013). https://doi.org/10.1039/c3ce27093a

Zhao, Z., Duan, H., Pang, H., Zhu, R.: A hierarchically porous ZIF@LDH core-shell structure for high-performance supercapacitors. Chem. Asian J. **16**, 845–849 (2021). https://doi.org/10.1002/asia.202100087

Zheng, H., Zhang, Y., Liu, L., Wan, W., Guo, P., Nyström, A.M., Zou, X.: One-pot synthesis of metal-organic frameworks with encapsulated target molecules and their applications for controlled drug delivery. J. Am. Chem. Soc. **138**, 962–968 (2016). https://doi.org/10.1021/jacs.5b11720

Zhou, H.-C., Kitagawa, S.: Metal-organic frameworks (MOFs). Chem. Soc. Rev. **43**, 5415–5418 (2014). https://doi.org/10.1039/C4CS90059F

Zhou, H.-C., Long, J.R., Yaghi, O.M.: Introduction to metal–organic frameworks. Chem. Rev. **112**, 673–674 (2012a). https://doi.org/10.1021/cr300014x

Zhou, H.-C., Long, J.R., Yaghi, O.M.: Introduction to metal-organic frameworks. Chem. Rev. **112**, 673–4 (2012b). https://doi.org/10.1021/cr300014x

Zhu, H., Yang, X., Cranston, E.D., Zhu, S.: Flexible and porous nanocellulose aerogels with high loadings of metal-organic-framework particles for separations applications. Adv. Mater. **28**, 7652–7657 (2016). https://doi.org/10.1002/adma.201601351

Porous Metals

S. Vijayan, K. F. Anna Dilfi, and S. Venkatachalapathy

Abstract Porous or cellular metals are developed with advanced materials processing techniques to fulfil the emerging requirements of structural and functional applications. This chapter presents an overview of different methods of fabricating process involved in porous metal preparation and the important properties to analyse their characteristics. Finally, the structural and functional applications are presented.

Keywords Porous metals · Fabrication methods · Mechanical properties · Applications · Metal foam

1 Introduction

In nature, certain categories of materials have adequate strength at low weight like wood, sponge, bones and some stone materials such as limestone and pumice stone (Fig. 1). The excellent characteristics of these materials have led to the development of artificial porous materials like cement, ceramics, metal foams, etc. (Fig. 2). Porous materials find a wide variety of usages in various fields, viz. automobile, aerospace, processing industries, heat transfer, separation, filtration, environment protection, energy storage, etc. (Davies and Zhen 1983). Porous materials are usually prepared to meet the specific requirements for their either functional or structural desirable features. A different class of materials is used to make a variety of products, and generally, they may be brought under the classifications as metals and non-metals; further non-metal group may be divided into ceramics and polymers. The development of artificial porous materials was started a century ago, but in the last few decades, a quite number of commercial products have been developed using polymer and ceramic materials.

S. Vijayan · S. Venkatachalapathy
Department of Mechanical Engineering, National Institute of Technology, Tiruchirappalli, Tamil Nadu 620015, India

K. F. Anna Dilfi (✉)
School of Civil Engineering, Harbin Institute of Technology, Harbin 150090, China
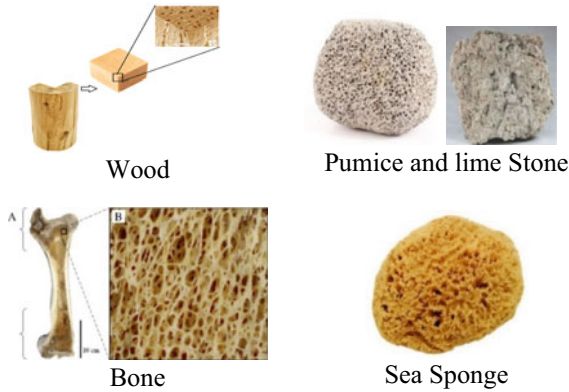
Fig. 1 Natural porous materials

Fig. 2 Artificial porous materials

The material which has distributed internal spaces throughout the volume and is filled with fluids (liquids or gases) is commonly known as porous media. If the solid part is made up of any metal, then it may be termed as porous metals. Usually, the internal spaces, i.e. porosity, should be at a considerable percentage (> 50%) to call porous metal. The free or internal spaces are denoted as cells, and the solid region is termed as parent metal (Goodall and Andreas 2014).

Cellular materials or porous materials are interchangeably used in many places. Usually, metallic foams are also called porous metals. In recent days, the usage of porous or cellular materials is plenty due to their exceptional behaviour and the advancements in the field of manufacturing have made it possible of achieving ultra-lightweight structures with tailor-made properties. Most of the porous metals or

cellular metals are produced through either the solid-state (powder or fibre metallurgy) or liquid-state methods. Apart from these methods, few novel methods like electrochemical deposition and metal vapour processing have also been proposed for laboratory-scale capacity (Atwater et al. 2018).

2 Types of Porous Metals

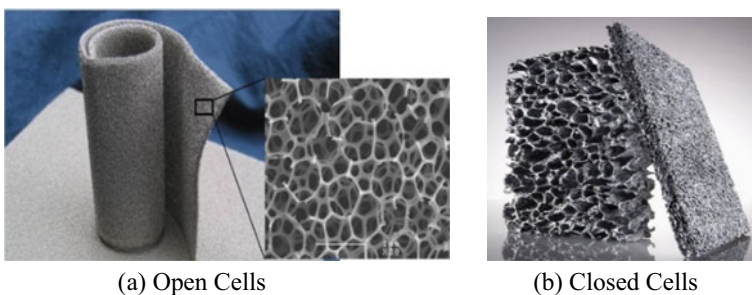Generally, porous metals are categorized based on their pore shape, size and distribution, etc. The pore connectivity is one of the significant parameters opted for the selection of the appropriate structure for the applications. Sometimes, the categorization is also made according to the cell structure and connectivity as open cells and closed cells. If the pores in the structure are interconnected with other pores, it can be called as open cells; otherwise, it is termed as closed cells as shown in Fig. 3. Closed-cell walls separate the pores or voids from others, but not in all cells, and few cells may be connected with each other due to missing cell walls (Kränzlin and Niederberger 2015).

Porous metals are mostly categorized based on the state at which the metal is processed, i.e. liquid-state processed or solid-state processed. The fabrication method influences the fundamental characteristics of the porous or cellular materials. The melting temperature of the metals also plays a significant role in selecting the method of fabrication of porous metals. For example, aluminium-based porous structure is usually obtained through liquid-state processing since the melting temperature is low. The cost of melting increases with an increase in the melting temperature of the solid metals. A few other methods also established to achieve specific properties of the porous materials with different porosities, macroscopic shapes, materials, pore sizes, etc. There are some other ways to classify the porous metals based on the pore arrangement as ordered or disordered, and oriented or non-oriented.

In certain places, the classification of porous metals is expressed based on their purpose as a structural material or functional material. The structural application materials should possess high strength-to-weight ratio, and the porous materials

(a) Open Cells   (b) Closed Cells

Fig. 3 Open and closed cells

<div align="center">Powder sintered   Fibre sintered   Wire mesh sintered</div>

Fig. 4 Sintered porous products

especially the closed cell-based structures readily exhibit adequate strength with low weight. On the other hand, the functional applications require some exclusive properties like high permeability, good sound absorption, well insulation ability, high thermal conductivity, etc. The partially open or complete open cells are well suitable for functional purposes. The major method involved in solid-state processing is powder metallurgy, where the porous metals are produced from the powders. During the last three decades, technological advancements have moved the methods of fabrication to a new horizon. Initially, porous metals are produced from powders and later from many fibres, wires, spheres, sheets, etc. Simple components produced through powder, fibre and wire mesh sintering are shown in Fig. 4.

3   Fabrication of Porous Metals

Fabrication of porous materials was demonstrated by Sosnik during 1948 using mercury (Sosnick 1948). Over the years, a variety of manufacturing methods has been reported for fabricating porous structures using different materials with different porosity levels. Among those, a very few methods have attained commercial status because of their desirable features like inexpensiveness, ease of processing, controlling parameters, etc. Nowadays, 98% porosity levels can be achieved.

Primarily introducing the voids or pores in material results in porous form, and the methods of introducing the pores should not have an adverse effect on the basic characteristics of the materials. Fabrication methods play a key role in determining the properties of the porous metals as well as achieving the desired macroscopic structure of the materials. Achieving the required structure along with the desired porosity levels as well as the properties is very important for a fabrication method. Therefore, the selection of appropriate route is the major attention of the researchers and commercial manufactures.

The usage of porous metals in a specific application is influenced by important parameters such as the composition, the macroscopic shape and the cell arrangement. The composition of the solid metal decides the basic properties such as density, strength, elasticity, thermal conductivity, corrosion resistance and oxidation stability.
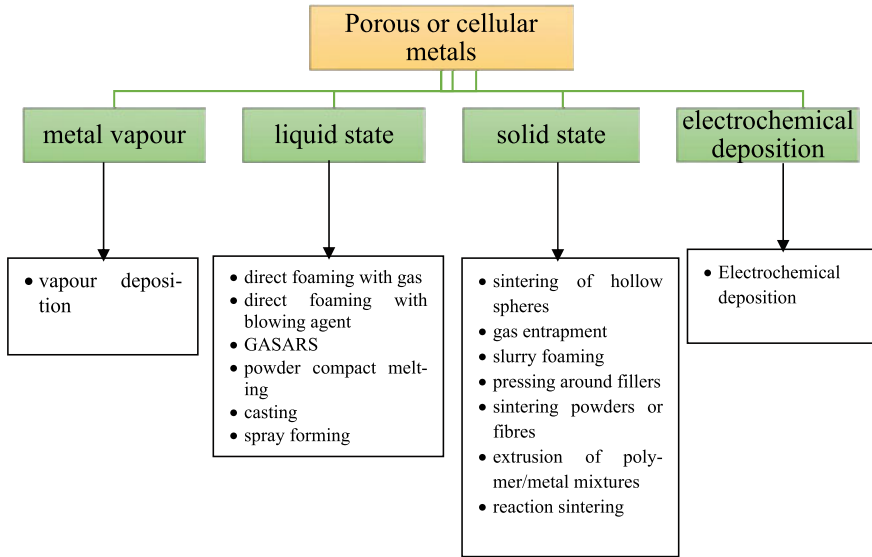
Fig. 5 Fabrication methods of cellular materials (Banhart 2001) (reproduced with permission from Elsevier)

The final shape of the cellular materials is crucial when it gets assembled with the other parts. Another important parameter is of pore or void structure as they primarily influence the relative density, surface area, porosity levels, gas permeability, cell connectivity, cell wall/edge stability, etc. (Kränzlin and Niederberger 2015).

There are numerous ways to fabricate porous metal structures. Initially, the technology development begun with the foaming of polymeric materials using gas blowing agents and later similar kind of process was adopted for metals also. Cellular or porous materials are commercially produced from either liquid- or solid-state processing routes (Banhart 2001) as indicated in Fig. 5. The methods are

(i)   liquid-state processing methods
(ii) solid-state processing methods
(iii) metal deposition from the metal vapour
(iv) electrochemical deposition.

3.1 Liquid-State Processing Routes

One of the most commonly used methods of producing porous metals or metal foams is liquid-state processing. The parent metal is processed after melting into liquid or semi-solid and the pore or void creation throughout the metal with the aid of the external gas source or dissolved gases. The methods may be categorized as direct or indirect foaming process. In the case of the direct foaming process, the pores

are created by introducing gases into the melt or employing the blowing agents which produce the gas after the chemical reaction. Indirect foaming process and the space holders are introduced into the melt for the creation of pores. The liquid-state processing routes can be further divided into three groups as shown in Fig. 6 (Srivastava and Sahoo 2007).

External Gas Source

Direct Foaming

The cellular materials can be directly obtained through the direct foaming process which means the voids or pores are created using the inert gas bubbles inside the melt. The gas bubbles are injected either directly or with the aid of gas releasing (blowing) agents. The viscosity of the molten metal is increased through the addition of ceramic powders to slow down the gas bubble movement since the density is much lower than the liquid-state metal, so quickly it will reach the surface (Banhart 2001). The way of introducing the gas bubbles into the melt is usually carried out by means of gas injection or by adding the blowing agents.

Gas Injection Method

The metals like aluminium, zinc, magnesium and their alloys can be foamed directly through the gas injection or air bubbling method, where any one of the gases like air, water, carbon dioxide, nitrogen, inert gases like argon, etc., is injected. Initially, the parent metal is melted to liquid state and the ceramic particles like aluminium oxide, silicon carbide or magnesium oxide are added into the melt to improve the melt viscosity. The next step is to inject the gas bubbles into the melt with the help of rotating or stirring paddle injector or nozzles. The gas bubble size and distribution are also controlled by means of the nozzle. A conveyor belt carries the foamed semi-solid metal and gets solidified. Schematic depiction of the experimental set-up is shown in Fig. 7. The foam is then cut into required length depending upon the application. Mostly, this method is for aluminium alloys since they do not get oxidized by atmospheric air and having a wide range of applications due to their favourable low density.
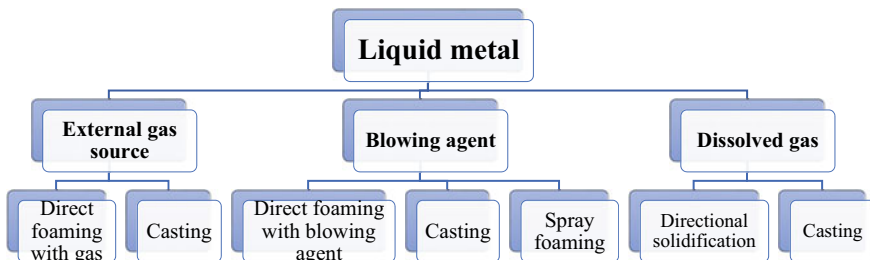
Fig. 6 Liquid-state processing routes
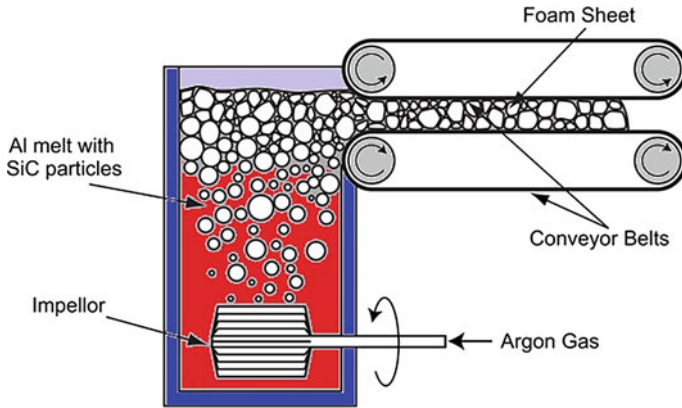
Fig. 7 Gas injection foaming process (Goodall and Andreas 2014) (reproduced with permission from Elsevier B.V.)

Katayose et al. (2016) demonstrated the fabrication of closed-cell foam using ultrasonic atomizer with a step horn, which produces the microbubble at the interface of melt and the gas supply horn. The fabrication set-up and the porous metal produced are shown in Fig. 8. The closed-cell metal foam with less than 100 μm porosity can be easily achieved through ultrasonic bubbling method, and the foam produced is highly suitable for energy and sound-absorbing applications.

Gas-Releasing Particle Decomposition

Other way of introducing the gas bubbles into the liquid metal is of adding blowing or gas releasing agents. The nature of these blowing agents is of undergoing decomposition and to release gas when they are heated up. Predominantly used agents for generating voids or pores in the melt are hydrides, carbonates or oxides (e.g. TiH_2, $CaCO_3$, $MgCO_3$ and ZrH_2) (Singh and Bhatnagar 2018). Usually, these blowing or gas releasing agents are added less than 1% and mixed well by means of any external
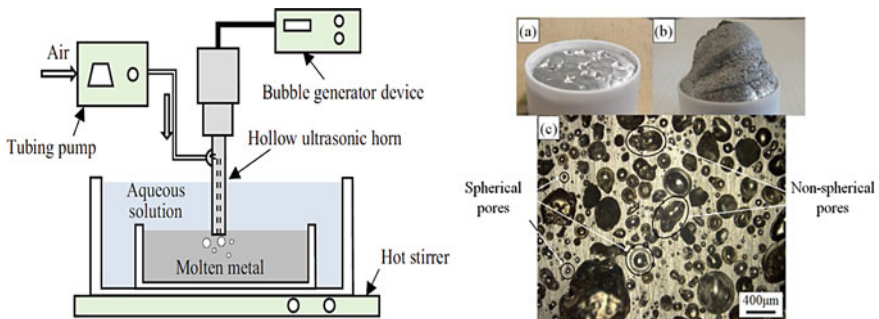
Fig. 8 Fabrication set-up of closed-cell ultrasonic atomizer and the prepared porous metal (Katayose et al. 2016) (reproduced with permission from Elsevier)

Fig. 9 Gas-releasing agent decomposition-based metal foaming process (Kränzlin and Niederberger 2015)
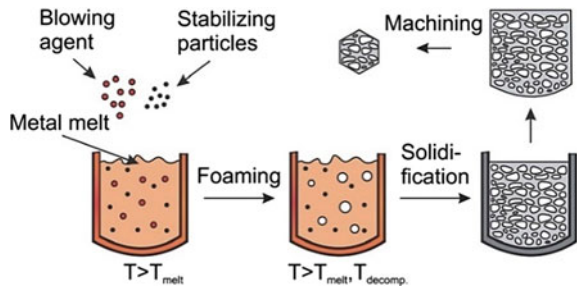
arrangements like stirrer during the process. The most commonly used blowing agent in the fabrication of aluminium foams is titanium hydrides (TiH_2) because it begins to decompose at 465 °C temperature which is lower than the melting temperature of aluminium (660 °C). Figure 9 shows the stages of direct foaming using the blowing agents. Aluminium melt is prepared by the application of heat, and the viscosity of the melt has been increased by adding 1–2% of calcium powders. Further, titanium hydride (TiH_2) powder is mixed into the thickened melt to produce gas bubbles inside the melt. Due to higher viscosity of the melt, gas bubble movement from the inside to surface is reduced and they get entrapped inside to form pores. A mechanical stirrer is used to produce homogeneous mixture of metal powder and foaming agents.

Spray Forming Process

Spray forming method is also used to produce foams of various metal alloys and composites with the desired porosity even lower than that of direct foaming methods. In this method, the metal melt is first atomized as small droplets by means of a continuous heating source and collected on cold substrate to form the desired shape of the foams based on die. Steps involved in the spray foaming process are indicated in Fig. 10. The metal composite foams can be produced by injecting oxide or carbide particles in the spray droplets (Banhart 2001; Srivastava and Sahoo 2007).

Dissolved Gas

Some technologies have been developed to produce directional porous metal through the advanced technologies. Solid–gas solidification is a special type of casting method
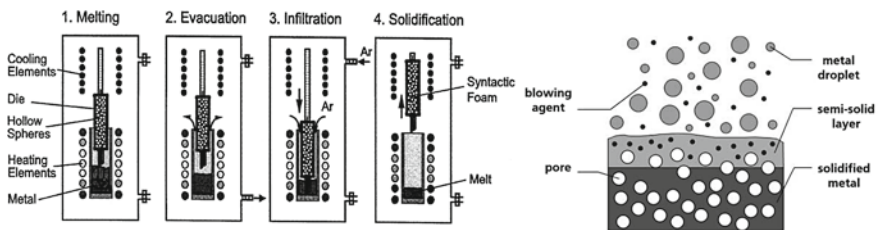
Fig. 10 Manufacture of metal foam by spray forming (reproduced with permission from Elsevier)

known as GASAR. In this process, metal–hydrogen eutectic reaction takes place. The liquid melt is prepared with hydrogen gas under high-pressure environment, which results in liquid metal with dissolved gas (heterogeneous mixture). During the solidification, the heterogeneous mixture solidifies at eutectic temperature (Liquid → Solid + Gas), where the hydrogen gas separated due to low solubility (Banhart 2001; Shapovalov 1994). The GASAR experimental set-up is shown in Fig. 11. This solid–gas eutectic transition continued in the direction of solidification, which induces the directional pores. The pore structure depends on the hydrogen pressure, solidification rate and the hydrogen content.

Investment Casting Method

In this process, the metal foam structure to be obtained is initially created using the polymer material called polymer foam template. This template is covered with the ceramic material and heated for two purposes: (i) to remove the polymer material and (ii) to bake the ceramic fillers. The removed polymer has created the cavity, and this can be filled with liquid metal for producing the metallic foams after solidification and removal of ceramic materials. The process steps are shown in Fig. 12.

Fig. 11 GASAR fabrication set-up (Goodall and Andreas 2014) (reproduced with permission from Elsevier B.V.)
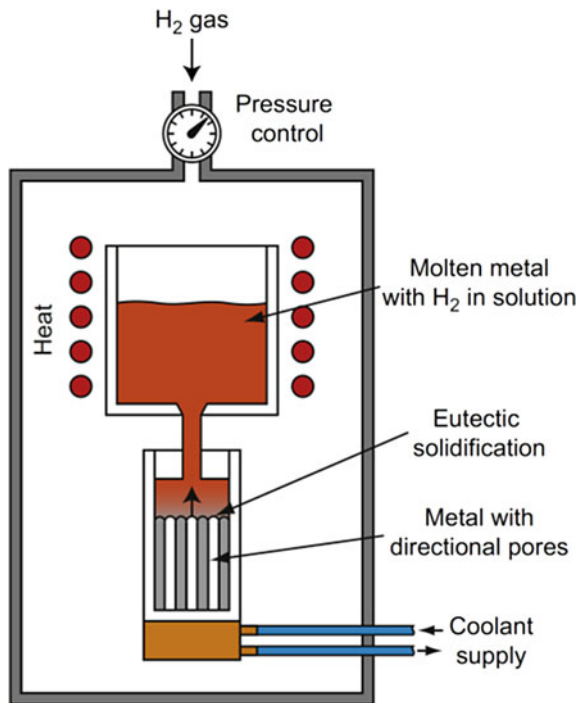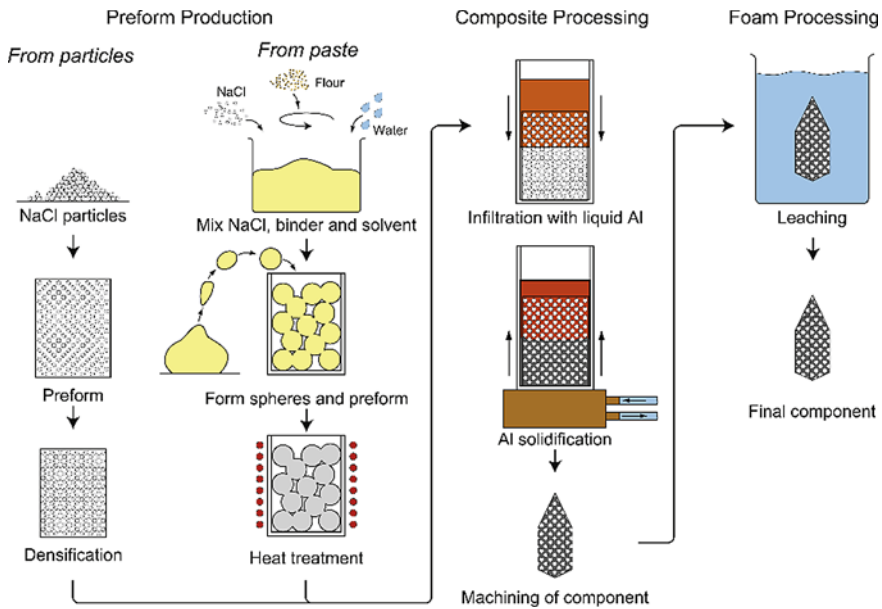
Fig. 12 Investment casting method stages (Goodall and Andreas 2014) (reproduced with permission from Elsevier B.V.)

3.2 Solid-State Processing Route

Porous metals or cellular materials can be produced through solid-state processing methods. Liquid-state processing route is energy-intensive process because of melting the metals. In most of the solid-state processing methods, metal powders are used to form porous structure and they remain in same solid state during the forming process. Powder metallurgy is comparatively simple and easy method to produce both open and closed cellular structures at low cost. In this process, the general steps involved are (i) mixing of metal powders with blowing agents, (ii) compaction or moulding and (iii) sintering with a heating source (Liu and Chen 2014).

Sintering of Metal Powders/Fibres

This method is the simplest technique to fabricate the porous metals through powder metallurgy. A wide variety of materials ranging from low to high melting point metals like aluminium, bronze, titanium, steel and alloys can be processed easily. Metal powders or fibres are poured into a container, and with or without the application of pressure, the desired shape is obtained. It is, then, heated to a temperature lower than the melting temperature to execute sintering; after cooling, it forms the porous structure. Loose packed or gravity sintered cellular materials have low compressive strength and are adopted mainly for bronze foams. Relative porosity obtained through

the process without pressure (compaction) is higher than with pressure, but they exhibit lower mechanical characteristics (Atwater et al. 2018). Compaction of the powders is carried out using either axial die, hydraulic press or rollers to enhance the strength and density (Banhart 2001).

Slurry Foaming Method

A slurry of metal powders, blowing agents and biding additives is prepared and poured into cavity for making metal foam. The slurry is heated to high temperature to induce the chemical reaction between the blowing agent and additives, which results in releasing of gases and expansion of the slurry (Fig. 13). The slurry is then stabilized in the expanded form to have adequate pores and sintered to enhance the strength.

Space Holder Method

The introduction of pores or voids inside the metal can be done by mixing the metal powder with the space holding materials (e.g. carbamide, dolomite, titanium hydride, etc.). Selecting the right space holder is important since they directly influence the pore characteristics (i.e. pore size, shape, porosity, etc.) of the resulted porous metal (Xie et al. 2017). Sometimes, binders are also used to enhance the bonding between the metal powder and space holders and moulded with or without pressure. The removal of space holder materials from the sintered metal can be carried out in two

Fig. 13 Solid-state processing steps (Kränzlin and Niederberger 2015)
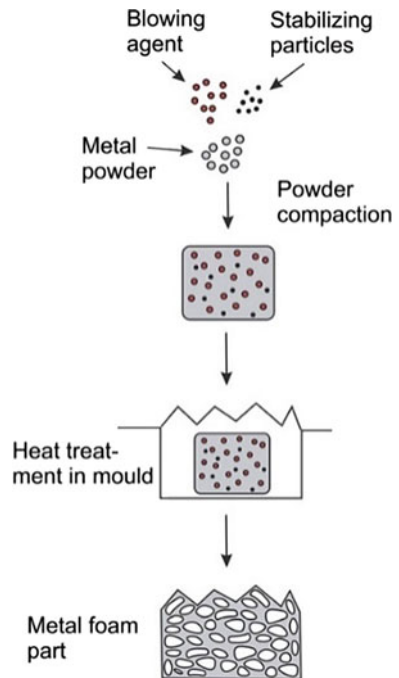
methods: (i) removal of the space holder materials through the application of heat (i.e. wax, PMMA, etc.) and (ii) dissolution method (dissolving in water or any other chemical solvents).

Stainless-steel, titanium and their alloy based porous metals can be fabricated successfully using powder space holder method. The porous structure such as cell type (open or closed), volume fraction etc can be controlled in a better manner through powder space holder method. Manonukul et al. (2010) demonstrated the fabrication of 316L porous metal with various volume fraction using spherical polymethyl methacrylate (PMMA) powders in powder space-holder method. Two different types of shrinkages were reported: (i) due to compaction of the powders and (ii) removal of space holders. Xie et al. (2017) fabricated titanium foam through the sintering and dissolution process using calcium chloride as space holder material. Titanium powder and anhydrous calcium chloride particles were mixed along with ethanol-based binder and compacted. Then, the binder was removed via oven drying method and sintered in two steps (800 °C for 2 h and 1200 °C for 3 h). The sintered specimen was kept in boiling water for 2 h and cleaned with ultrasonic cleaner to completely remove the space holder traces.

Additive Manufacturing Method

In addition to the above-mentioned methods, some advanced manufacturing techniques have also been introduced in fabrication of porous metals to achieve desired functional characteristics in micro- or nano-sizes. Earlier discussed methods mostly deal with the random structured porous metals. Additive manufacturing method is successfully employed to produce structured and controlled pore structured porous metals through layer-by-layer processing. Directional pore structured porous metals are exclusively preferred for significant and crucial applications like biomedical implants, aerospace and automotive parts (Yavari et al. 2013). Additive manufacturing method produces complex structures in a shorter duration through layer-by-layer processing of the materials with computer-aided design techniques. This method also uses powder processing method, initially the powder is placed as a thin layer on a platform, and according to the geometrical detail sintering of powder is done by means of a heating source (electron or laser beam). Then, next layer of powder is spread and sintered; likewise, the process is repeated till achieving the net shape. Biological implants are mostly fabricated using through additive manufacturing process. Most of the implants are produced using selective laser sintering or selective electron beam sintering processes, and the materials opted are titanium and zinc (Guddati and Kiran 2019).

3.3   Metal Deposition Methods

Porous metal structure can be obtained from the gaseous metal compounds or vapour from the metal ion. Metal deposition may take place in vacuum condition or ambient condition. The process involved the evaporation of metal using heating

sources (electron beam and electric arc) and depositing on a cold porous substrate (Liu and Chen 2014). There are many methods such as physical vapour deposition (PVD), chemical vapour deposition (CVD) and electron beam directed vapour deposition (EB-DVD). Among these, CVD is the wide preferred method for commercial production of nickel and copper foams for electrodes in batteries (Atwater et al. 2018). The desirable features of CVD are higher metal deposition rate, lower cost of the equipment and the ability to deposit both elemental metal and alloys. On the other hand, the polymer foam material should be able to withstand very high temperature, which makes the process costly. Queheillalt et al. (2001) demonstrated the electron beam directed vapour deposition (EB-DVD) method for the fabrication of nickel-based superalloy (Inconel 625) open-cell foam. The deposition of metal on polymer foam was done with the assistance of supersonic inert gas jet transport, and uniform deposition on the foam was achieved through the rotating and axial motion of polymer substrate. The high-speed gas jet transports the metal vapour around the substrate and gets deposited on the surface, which ensures the deposition on non-line of sight cells. The experimental set-up and the metal foam fabricated are shown in Figs. 14 and 15.

Fig. 14 EB-DVD process set-up (Queheillalt et al. 2001)
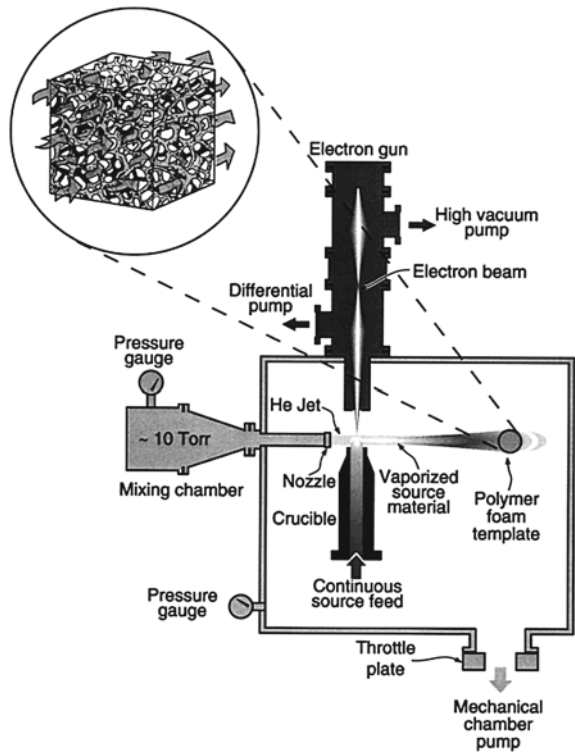
Fig. 15 Micrographs of **a** polymer foam and **b** Inconel foam (Queheillalt et al. 2001)
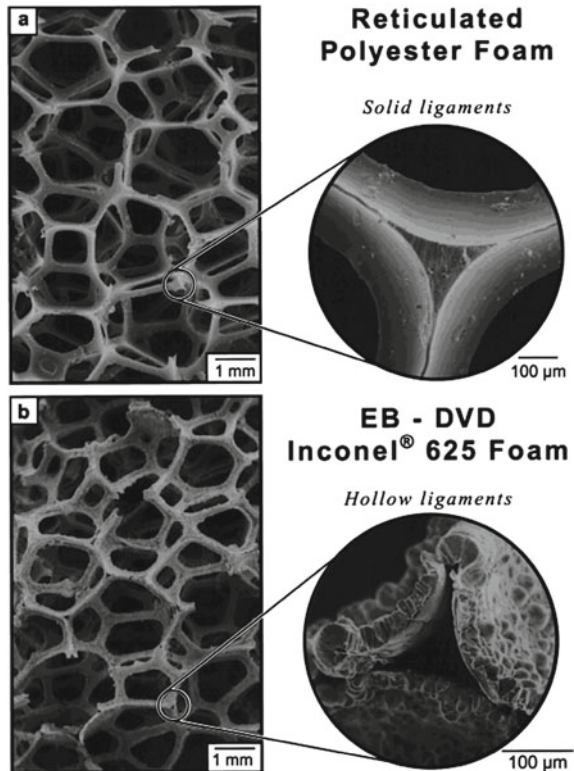
Electrochemical deposition method is another advanced technique to fabricate well-structured pore surface. The pore morphology can be produced through controlling of the process parameters. In this process, the metal ions from an electrolyte are produced and electro-deposition method is adopted to deposit on a polymer foam surface as like in investment casting method (Banhart 2001; Plowman et al. 2015). A polymer foam is formed for the required porosity and is coated with an electrically conducting materials to deposit the metal ions. This coating can be done either immersion or coating a layer through sputtering process.

4 Properties of Porous Metals

The properties of these special category materials are explored to ensure the applicability for the selected application. The excellent properties are catered to meet the requirements of the growing demands. Introduction of pores into the solid phase has adverse effect on their mechanical properties. For example, the strength of the

material has drastically affected while increasing the porosity. There are some properties of these materials that closely match with the properties of the parent (solid phase) material, for example, the properties like resistance to corrosion, elasticity, thermal conductivity, etc. Similarly, the porous metals exhibit surprising behaviour depending upon the nature of the material, type of fabrication, etc. In the following subsections, certain significant properties of the porous metals are discussed.

4.1 Microstructure of Porous Metals

The major significant parameter of the porous metals is pore characteristics such as pore size, distribution, type of pore (open or closed), morphology and surface area. The ratio between the densities of the porous metal to the parent metal density is called relative density. Closed cell-based porous metals have higher relative density than the open-cell type due to the absence of interconnection between the pores or voids. Closed-cell type of porous metals has adequate strength, and therefore, they are widely used for structural applications. On the other hand, the cells are interconnected with each other which enable them as a suitable candidate for the fluid flow systems for separation/filtration and thermal management applications. The microstructure of open-cell aluminium metal foam in different pore sizes (200–600 μm) fabricated using centrifugal casting method is shown in Fig. 16 (Wang et al. 2018).

Porous metals are also used as electrodes in fuel cells/batteries, and the desirable characteristics for that application are large cells for the movement of electrolytic
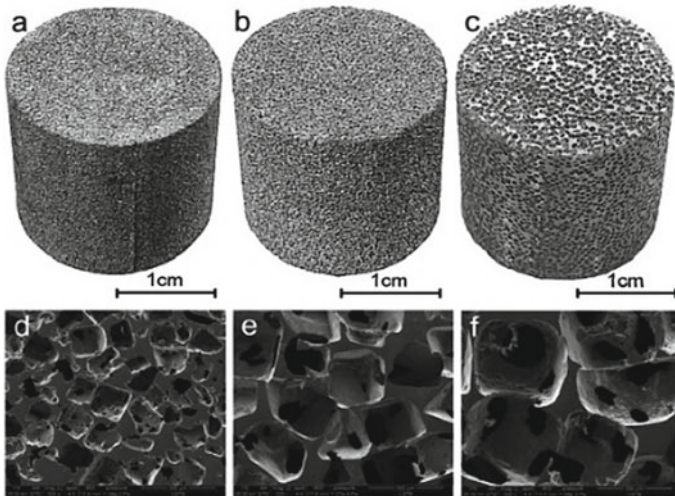
Fig. 16 Open-cell aluminium metal foam with a different porosity (Wang et al. 2018) (reproduced with permission from Royal Society of Chemistry)

solution and smaller cells to increase the surface area for enhancing the electrochemical reactions inside the electrodes (Wada et al. 2018). The dealloyed nanoporous metals satisfy the needs of the electrodes, catalysts, optical and sensing elements (Erlebacher et al. 2001). Hierarchical porous metals consist of both large and small pore structures, and the associated properties can be easily controlled independently.

## *4.2 Mechanical Properties*

The most significant properties for the structural applications are their mechanical properties, and they are highly influenced by the method of manufacturing and their resulting parameters such as pore size and porosity levels. The ratio between the densities of the porous metal to the parent metal is called relative density, which is a significant parameter to evaluate the mechanical properties. In porous metals, the stress concentration is higher in the cell edges/walls which lead to a reduction in mechanical properties like strength, plasticity, energy absorption, etc. The level of reduction is also affected by the manufacturing method; i.e. strength of fibre sintered metals is better than the powder sintered components. In the case of powder sintering, the processing parameters such as particle size, sintering temperature, duration and compaction pressure are also playing a significant role. Superior mechanical properties can be achieved by increasing the number of particles and area of contact (Liu 2006). Mechanical behaviour of cellular materials is majorly influenced by their internal structural arrangements of cells and edges. Understanding the relation between the structure and behaviour is an essential element in designing and controlling properties of cellular materials to meet the requirements. But establishing the relation is a difficult task due to complex 3D structure of the cells. Therefore, numerous researchers have proposed many numerical and analytical models to predict the properties in relation to their easy quantifiable parameters like cell size, porosity, density, arrangement, etc. (James Ren and Silberschmidt 2008). Michailidis et al. (2011) developed a finite simulation-based simulation methodology to model open-cell metal foams, where they have adopted two different methods such as X-ray tomography and a serial sectioning (Fig. 17). The mechanical behaviour under load (deformation) of nickel and aluminium foams was monitored using microscopic images (Fig. 18).

Porous metals usually exhibit better characteristics under compressive loads and are capable of absorbing a considerable amount of energy without much stress. Open-cell porous metals are superior to closed-cell materials for thermal management applications such as heat storage or dissipation purposes since they have good thermal conductivity and fluid permeability (Gibson 2000). Mechanical characteristics of metallic foams are tested under compressive load, and the stress–strain relationship is plotted to determine its ability. Figure 19 shows a typical stress–strain curve of an aluminium ($AlCu_4$) foam (83% porosity) compared with a polyethylene foam (87% porosity). Both exhibit a similar trend, but the magnitude of aluminium foam is almost 30 times larger than polyethylene (Yu and Banhart 2016).
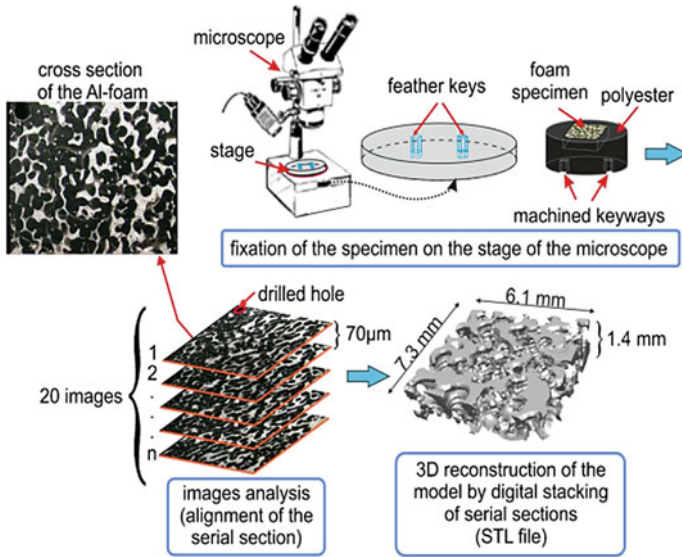
Fig. 17 Steps to obtain 3D model through image processing (Michailidis et al. 2011) (reproduced with permission from Elsevier B.V.)

Fig. 18 SEM image of failed foam and FEM simulation results (Michailidis et al. 2011) (reproduced with permission from Elsevier B.V.)
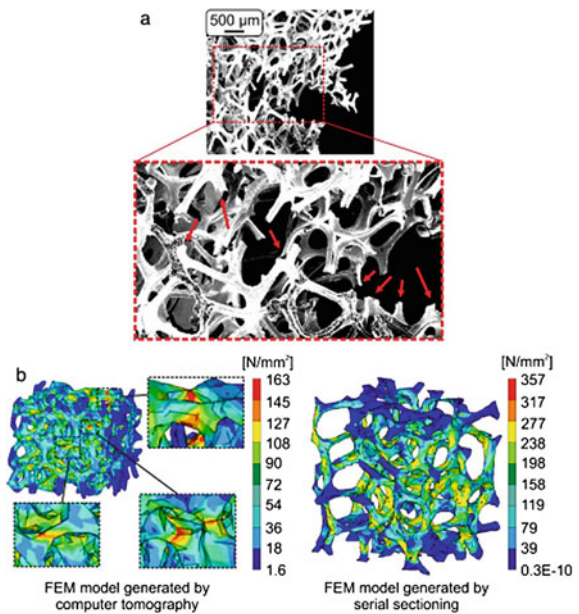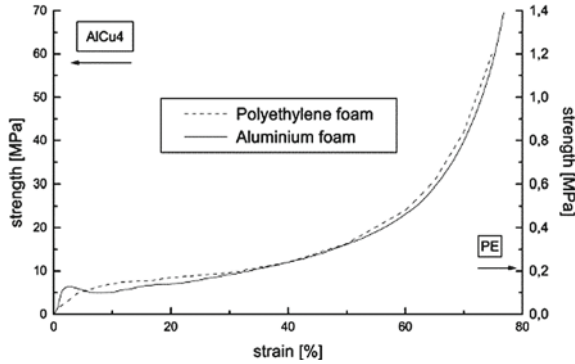
Fig. 19 Strength of aluminium foam versus polyethylene foam

Wang et al. (2018) reported the compressive strength of open-cell aluminium metal foam with different pore sizes (200–600 μm). The stress–strain curve is comprised of three regions: small linear elastic region, pore collapse region and densification region (Fig. 20).

Energy Absorption

Porous metals possess an excellent mechanical property of good energy absorption which enhances potential usage in structural applications. When these materials subject to a sudden impact load, they readily control the stress induced by absorbing the kinetic energy due to plateau region (Grilec et al. 2010). The compressive stress–strain curve has a plateau region, where the stress is almost flat (i.e. constant stress region). Aluminium foam exhibits a better energy absorption capability than the dense metal. Similarly, titanium metal foams are also exhibiting good energy absorption characteristics. Xie et al. (2017) have investigated the energy absorption behaviour of titanium foams at different porosity levels (71–88%), and
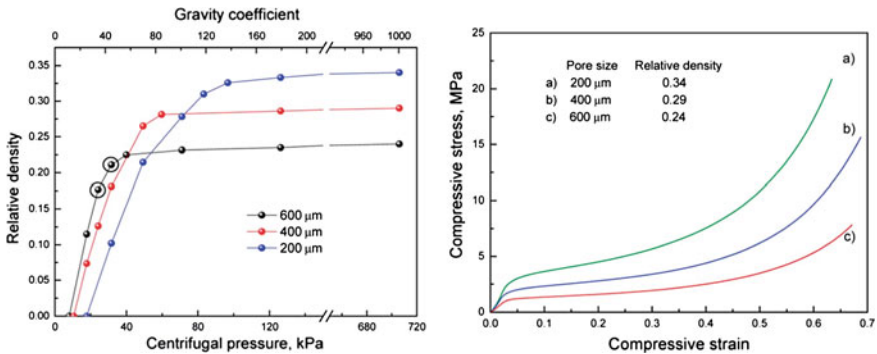
Fig. 20 Relative density and compressive strength of open-cell Al foam (Wang et al. 2018) (reproduced with permission from Royal Society of Chemistry)

they observed that the plateau stress was in the range of 18.1–150.6 MPa. Increase in relative density of the foam resulted in increase of plateau stress and energy absorption per unit volume.

4.3 Acoustic Properties

One of the important properties of porous metals is sound absorption, and they are used in a variety of sound-absorbing structures. Sound absorption is suppressing the effect of reflection of sound waves, which are highly essential in the places like theatres, auditorium, meeting halls, etc. Porous materials are majorly used to cover the side walls and ceilings to absorb the sounds. In most of the cases, these materials are made up of organic or inorganic fibre materials such as cotton, polyester, glass wool and rockwool. The major problem with these materials is of low load-bearing capability, thermal conductivity, energy absorption and stiffness. The materials which combine the advantages of metals and sound absorption are highly needed for construction; especially, in automotive vehicles releasing exhaust gas is creating a lot of noise pollution. The applications which utilize the pneumatic systems require powder sintered porous metals to absorb the sound energy along with vibrations and thermal transfer. The combined advantages of porous metals such as sound absorption with the structural and thermal energy absorption created the opportunity in a wide range of applications. Open-cell foams have better acoustic property than the closed-cell foams (Arjunan et al. 2019). Aluminium, copper and nickel Inconel superalloy are mostly preferred for sound absorption applications. Further, sound absorption characteristics of metallic foams can be enhanced through the introduction of air gap at the back side, multilayer compression and combination (Otaru 2019; Shen et al. 2020). Open-cell superalloy foam sound absorption takes place due to the combined actions of thermal loss, viscous loss and mechanical damping, while the sound wave passes through the pores. Zhai et al. (2018) investigated the sound absorption characteristics of IN625 foam with different porosity levels varying from 94 to 98% fabricated through template replication method. Different parameters related to the foams are indicated in Table 1. The response of IN625 samples for different sound frequencies is shown in Fig. 21, and it clearly indicates that the increase in porosity leads to better sound absorption.

Table 1 IN625 foam sample characteristics (Zhai et al. 2018)

Type	Porosity %	Relative density	Cell size (μm)
A25	98	2.0	686 and 876
B25	96.5	3.5	508 and 620
C25	94.2	5.8	368 and 470
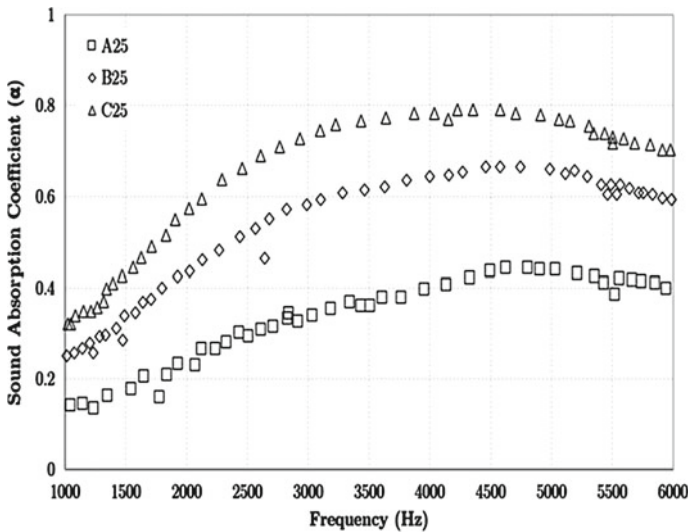
Fig. 21 Sound absorption coefficients of open-cell IN625 foam (25 mm thick) (Arjunan et al. 2019; Zhai et al. 2018) (reproduced with permission from Elsevier)

4.4 Thermal Properties

Porous metals are widely used in thermal devices for enhancing the thermal performance of the systems. The attractive features of porous metals have adequate thermal conductivity, which facilitates them to use it in the thermal applications like heat exchanger, heat sink, heat pipes, etc. Recent developments in the field of thermal energy storage have incorporated the metal foams and porous metals in the latent heat storage medium to enhance their heat transfer rate since the porous metals are having good thermal conductivity. Porous metals have complex structure with enhanced surface area per unit volume. This is an idealistic property essential for thermal management applications, as the permeability characteristics could improve the fluid flow as well as heat transfer enhancement (Tan et al. 2018).

5   Applications of Porous Metals

Porous metals are very attractive for their superior characteristics, and they are very useful in many applications. Based on the purpose for which the material is intended in an application, the materials may be categorized as structural or functional materials. The primary requirement of a material to use it for structural applications is possession of adequate strength to withstand the load, and the major advantageous feature of porous metals is exhibiting higher strength along with superior mechanical
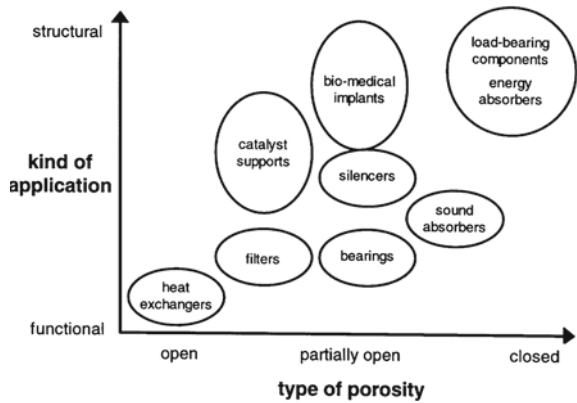
properties at lower density than the solid parts. In addition, with superior mechanical properties, possession of good thermal conductivity, sound absorption, electrical conductivity, large surface area, allowing the fluids to occupy, etc., can be utilized for functional applications. The suitability of the porous metals is opted based on certain parameters like type of porosity, size of pore, surface area, compatibility of the parent metal, cost, manufacturability, etc. Banhart (2001) summarized these factors into four as morphology (pore characteristics), metallurgy (material characteristics), processing method and economy.

Cellular materials are having comparatively superior characteristics like low density, high stiffness-to-mass ratio, better specific strength, high energy and sound absorption, excellent heat transfer and permeability, etc. These attractive properties make the porous metals as advantageous one for structural and functional or both applications. Some of the applications of porous metals based on the porosity levels are presented in Fig. 22.

5.1 Structural Applications

The primary requirement of any structural material is to exhibit excellent load-bearing ability with low or no deformation, and also, they are capable of absorbing sound, energy, thermal radiation, etc. These desirable properties of porous metals make them the best candidate for the structural applications in automotive, aerospace, marine applications, railway and building constructions. Nowadays, the demands of the automotive sectors are focusing on ensuring the safety as well as the fuel economy using low-cost materials. The porous materials offer low weight and considerably good stiffness-to-mass ratio than the bulk materials. Popularly used metal foams for structural applications are of aluminium foams since they are very easy to fabricate and they are widely accepted construction material.

Structural applications and sandwich panels (i.e. metal foam is covered with plain sheets) are preferred as they exhibit a better load carrying ability (i.e. high stiffness) than plain metal foam. However, the fabrication of sandwich panels is slightly expensive and perfect engineering is needed for designing the structure based on the application environment. There are some additional benefits that can be achieved through porous structures like suppression of vibration and noise, energy absorption, etc.

Biomedical Applications

High strength–weight ratio property of porous materials has attracted the biomedical applications to produce biological implants using the biocompatible materials like titanium, cobalt-chromium, etc. Day by day, the application of metallic foams in the biomedical field gets more attention due to their favourable properties and advancements in processing technologies (Patel et al. 2018; Singh and Bhatnagar 2018). Materials like 316L stainless steel, Co-29Cr-6Mo and Ti-6Al-4 V alloys are considered as biological compatible materials. Among these materials, titanium-based alloys are the most preferable porous implant due to their good corrosive resistance. Porous implants can be used in three ways: (i) partial or complete porous coated solid substrates, (ii) complete porous and (iii) porous segment connected to a solid part. Certain possible applications of porous implants are spinal fixation, fracture plates, artificial ligament attachments, etc. (Ryan et al. 2006; Wang et al. 2016). Titanium-based alloys are advantageous selection for implants subject to higher loads since they offer relatively high strength-to-weight ratio along with good corrosive resistance. Moreover, titanium alloys are well biocompatible materials. Porous metals for implant applications can be fabricated with desired pore characteristics through additive manufacturing process. Figure 23 shows few samples of titanium implant samples with different porosities fabricated using selective laser melting (SLM) process (Soro et al. 2019).

Fig. 23 Additive manufactured Ti–25Ta samples for implants (Soro et al. 2019) (reproduced with permission from Elsevier)
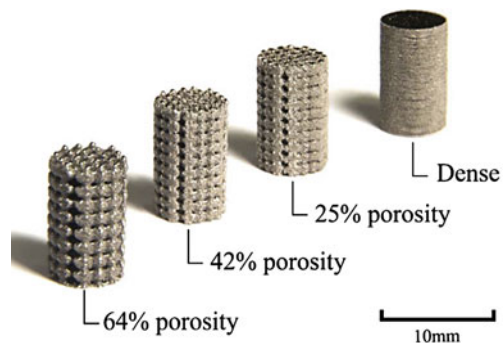
5.2 Functional Applications

Porous structure of the metals is quite useful in the applications where permeability, thermal and electrical conductivities, absorptivity, acoustic properties, etc., play a significant role in enhancing the process. The fundamental pore characteristics such as type (open or closed), size and shape are the key parameters in selecting the appropriate porous metal for an application. For example, the pore size of the metal is selected based on the size of the materials to be separated or filtered. Some of the functional applications of porous metals are as follows.

(a) **Filtration and Separation**

Permeability nature of the porous materials is utilized to filtering specific solid elements from a liquid or gas medium. Separation of specific element from gas–liquid and liquid–liquid is also possible by utilizing the wettability and molecular weight characteristics. For purifying hydraulic oil in gyroscopes and fuel lines, porous stainless steel filters are utilized in aerospace industries. Porous materials with higher thermal stability and corrosive resistance are also desirable for achieving longer life. Cellular materials made up of stainless steel and nickel are also employed to separate radiative pollutants from coolant in nuclear power plants (Liu and Chen 2014).

Porous metals are popularly used in the exhaust gas filters of gasoline direct injection (GDI) engines to prevent the escaping of particulate emission to the environment since the stringent emission norms are followed to reduce air pollution. Usage of ceramic foams is inefficient for GDI engines due to low filtering efficiency, and high back pressure has forced the engineers to introduce the metallic foams. There are different porous metallic filters employed such as (i) sintered metal powder, (ii) fibre or wire mesh and (iii) porous metal foam. Among these types, spherical powder sintered and metal wire sintered porous structures are recommended than metal foams due to relatively higher filtering efficiency and operational performance. Metallic fibre filters fabricated from long fibres with very high porosity are very much suitable for capturing micro-sized soot particles by interception, inertia and gravitational sedimentation principles (Liu and Chen 2014; Ou et al. 2017). Commonly selected porous materials for filter applications are of stainless steel, nickel and bronze.

(b) **Sound Absorption**

Sound absorption behaviour of materials including organic, inorganic and metals is desirable for the fabrication of damp proof and acoustic structures. Organic materials including cotton, fabric, wood, leather are the traditional material interest, but they lack much in fire and damp proofing and corrosion resistance. On the other hand, the inorganic materials cause different kinds of problems like material degradation and dust accumulation over the period of usage. In recent days, the utilization of porous metals in acoustic applications has acquired a good position. Open-cell metal foams and fibre sintered metal foams are possessing good acoustic properties (Wang et al. 2015).

(c)   **Heat Exchanger**

Porous metals are having higher surface area which sought an important behaviour for thermal management applications when it is used along with the fluid medium. The expanded surface area of porous metals drastically improves the heat transfer rate and results in better energy output. Metal foams like copper and aluminium materials are finding a good place in the design of thermal energy storage devices (Tan et al. 2018). The power density of the fuel cells can also be enhanced via metal foam electrodes. Nowadays, coated metal foams are used as electrodes to have a longer life by preventing the corrosion. Metal foams are widely used in heat exchangers, electronic cooling and heat sink applications (Han et al. 2012). Porous metals are getting popular in designing efficient heat exchangers with compact size and low weight systems for exchanging heat at higher rate in various applications like thermal energy storage, chemical reactor, radiators, etc. The desirable characteristics of higher heat transfer rate along with the other functional behaviours like structural stability, flow distribution, lower pressure loss, etc can be achieved by controlling the permeability and porosity of the porous metal via selecting the appropriate fabrication method (Tianjian 2002). Metallic foams are used for filtration and separation applications to remove/separate the solid particles from a fluid medium by allowing the media to flow through the porous structure.

Applications are not limited to the mentioned, and they have a wide range of applications in the fields like water purifications, electrodes of battery and fuel cells, heat exchangers, decoration structures, flame arrestors, fuel burners, etc. (Banhart 2001).

6   Conclusion

Porous or cellular materials have attained a greater position in a wide range of applications due to their attractive behaviour as well as the technological advancements in processing methods of different materials and their capability of controlling the parameters to produce the desired structure. Porous metals are produced in different scales varying from nano- to macro-sizes. One of the challenging aspects in manufacturing of cellular metals is of reducing the manufacturing cost. Technological advancements with interdisciplinary research can help to develop economically favourable porous metals with highly controllable characteristics to cater the exact needs of the emerging applications. Porous metal applications are going to reach a new horizon in mere future since the rapid addition of advanced manufacturing methods for a wide range of materials is progressing at a faster rate.

References

Arjunan, A., Baroutaji, A., Praveen, A.S., Olabi, A.G., Wang, C.J.: Acoustic performance of metallic foams. In: Reference Module in Materials Science and Materials Engineering, pp. 1–16. Elsevier (2019). https://doi.org/10.1016/b978-0-12-803581-8.11561-9

Atwater, M.A., Guevara, L.N., Darling, K.A., Tschopp, M.A.: Solid state porous metal production: a review of the capabilities. Charact. Challenges **1700766**, 1–33 (2018). https://doi.org/10.1002/adem.201700766

Banhart, J.: Manufacture, characterisation and application of cellular metals and metal foams. Prog. Mater. Sci. **46**, 559–632 (2001)

Davies, G.J., Zhen, S.: Metallic foams: their production, properties and applications. J. Mater. Sci. **18**, 1899–1911 (1983). https://doi.org/10.1007/BF00554981

Erlebacher, J., Aziz, M.J., Karma, A., Dimitrov, N., Sieradzki, K.: Evolution of nanoporosity in dealloying. Nature **410**, 450–453 (2001). https://doi.org/10.1038/35068529

Gibson, L.J.: Mechanical behavior of metallic foams. Annu. Rev. Mater. Sci. **30**, 191–227 (2000)

Goodall, R., Andreas, M.: Porous metals. In: Laughlin, D., Kazuhiro, H. (eds.) Physical Metallurgy, pp. 2399–2595. Elsevier B.V. (2014). https://doi.org/10.1016/B978-0-444-53770-6.00024-1

Grilec, K., Marić, G., Jakovljević, S.: A study on energy absorption of aluminium foam. BHM Berg-Huettenmaenn. Monatsh. **155**, 231–234 (2010). https://doi.org/10.1007/s00501-010-0567-6

Guddati, S., Kiran, A.S.K.: Recent advancements in additive manufacturing technologies for porous material applications **105**, 193–215 (2019)

Han, X.H., Wang, Q., Park, Y.G., T'Joen, C., Sommers, A., Jacobi, A.: A review of metal foam and metal matrix composites for heat exchangers and heat sinks. Heat Transf. Eng. **33**, 991–1009 (2012). https://doi.org/10.1080/01457632.2012.659613

James Ren, X., Silberschmidt, V.V.: Numerical modelling of low-density cellular materials. Comput. Mater. Sci. **43**, 65–74 (2008). https://doi.org/10.1016/j.commatsci.2007.07.038

Katayose, A., Yokose, R., Makuta, T.: Fabrication of closed-cell porous metals by using ultrasonically generated microbubbles. Mater. Lett. **185**, 211–213 (2016). https://doi.org/10.1016/j.matlet.2016.08.132

Kränzlin, N., Niederberger, M.: Controlled fabrication of porous metals from the nanometer to the macroscopic scale. Mater. Horizons **2**, 359–377 (2015). https://doi.org/10.1039/c4mh00244j

Liu, P.S.: Mechanical behaviors of porous metals under biaxial tensile loads. Mater. Sci. **422**, 176–183 (2006). https://doi.org/10.1016/j.msea.2006.01.083

Liu, P.S., Chen, G.F.: Chapter three—Application of porous metals. In: Liu, P.S., Chen, G.F.B.T.-P.M. (eds.) Porous Materials: Processing and Applications, pp. 113–188. Butterworth-Heinemann, Boston (2014a). https://doi.org/10.1016/B978-0-12-407788-1.00003-4

Liu, P., Chen, G.: Making porous metals. In: Porous Materials: Processing and Applications, pp. 21–112. Elsevier (2014b). https://doi.org/10.1016/B978-0-12-407788-1.00002-2

Manonukul, A., Muenya, N., Léaux, F., Amaranan, S.: Effects of replacing metal powder with powder space holder on metal foam produced by metal injection moulding. J. Mater. Process. Technol. **210**, 529–535 (2010). https://doi.org/10.1016/j.jmatprotec.2009.10.016

Michailidis, N., Stergioudi, F., Omar, H., Papadopoulos, D., Tsipas, D.N.: Colloids and surfaces A: physicochemical and engineering aspects experimental and FEM analysis of the material response of porous metals imposed to mechanical loading. Colloids Surf. A Physicochem. Eng. Asp. **382**, 124–131 (2011). https://doi.org/10.1016/j.colsurfa.2010.12.017

Otaru, A.J.: Enhancing the sound absorption performance of porous metals using tomography images. Appl. Acoust. **143**, 183–189 (2019). https://doi.org/10.1016/j.apacoust.2018.09.007

Ou, Q., Maricq, M.M., Pui, D.Y.H.: Evaluation of metallic filter media for sub-micrometer soot particle removal at elevated temperature. Aerosol. Sci. Technol. **51**, 1303–1312 (2017). https://doi.org/10.1080/02786826.2017.1349871

Patel, P., Bhingole, P.P., Makwana, D.: ScienceDirect manufacturing, characterization and applications of lightweight metallic foams for structural applications: review. Mater. Today Proc. **5**, 20391–20402 (2018). https://doi.org/10.1016/j.matpr.2018.06.414

Plowman, B.J., Jones, L.A., Bhargava, S.K.: Building with bubbles: the formation of high surface area honeycomb-like films via hydrogen bubble templated electrodeposition. Chem. Commun. **51**, 4331–4346 (2015). https://doi.org/10.1039/C4CC06638C

Queheillalt, D.T., Hass, D.D., Sypeck, D.J., Wadley, H.N.G.: Synthesis of open-cell metal foams by templated directed vapor deposition. J. Mater. Res. **16**, 1028–1036 (2001)

Ryan, G., Pandit, A., Apatsidis, D.P.: Fabrication methods of porous metals for use in orthopaedic applications. Biomaterials **27**, 2651–2670 (2006). https://doi.org/10.1016/j.biomaterials.2005.12.002

Shapovalov, V.: Porous metals. MRS Bull. **19**, 24–28 (1994)

Shen, X., Bai, P., Chen, L., To, S., Yang, F., Zhang, X., Yin, Q.: Development of thin sound absorber by parameter optimization of multilayer compressed porous metal with rear cavity. Appl. Acoust. **159**, 107071 (2020). https://doi.org/10.1016/j.apacoust.2019.107071

Singh, S., Bhatnagar, N.: A survey of fabrication and application of metallic foams (1925–2017). J. Porous Mater. **25**, 537–554 (2018). https://doi.org/10.1007/s10934-017-0467-1

Soro, N., Attar, H., Brodie, E., Veidt, M., Molotnikov, A., Dargusch, M.S.: Evaluation of the mechanical compatibility of additively manufactured porous Ti–25Ta alloy for load-bearing implant applications. J. Mech. Behav. Biomed. Mater. **97**, 149–158 (2019). https://doi.org/10.1016/j.jmbbm.2019.05.019

Sosnick, B.: Process for Making Foamlike Mass of Metal (1948)

Srivastava, V.C., Sahoo, K.L.: Processing, stabilization and applications of metallic foams. Art Sci. Mater. Sci. **25**, 733–752 (2007)

Tan, W.C., Saw, L.H., Thiam, H.S., Xuan, J., Cai, Z., Yew, M.C.: Overview of porous media/metal foam application in fuel cells and solar power systems. Renew. Sustain. Energy Rev. **96**, 181–197 (2018). https://doi.org/10.1016/j.rser.2018.07.032

Tianjian, L.: Ultralight porous metals: from fundamentals to applications. Acta Mech. Sin. **18**, 457–479 (2002)

Wada, T., Geslin, P., Kato, H.: Scripta Materialia preparation of hierarchical porous metals by two-step liquid metal dealloying. Scr. Mater. **142**, 101–105 (2018). https://doi.org/10.1016/j.scriptamat.2017.08.038

Wang, J.Z., Ao, Q.B., Tang, H.P., Bao, T.F.: Effect of characterization of porous metal fiber media on sound absorption coefficient **29**, 1–8 (2015). https://doi.org/10.1142/S0217979215400020

Wang, X., Xu, S., Zhou, S., Xu, W., Leary, M., Choong, P., Qian, M., Brandt, M., Min, Y.: Biomaterials topological design and additive manufacturing of porous metals for bone scaffolds and orthopaedic implants: a review. Biomaterials **83**, 127–141 (2016). https://doi.org/10.1016/j.biomaterials.2016.01.012

Wang, Z., Gao, J., Chang, K., Meng, L., Zhang, N., Guo, Z.: Manufacturing of open-cell aluminum foams via infiltration casting in super-gravity fields and mechanical properties. RSC Adv. **8**, 15933–15939 (2018). https://doi.org/10.1039/c7ra13689g

Xie, B., Fan, Y.Z., Mu, T.Z., Deng, B.: Fabrication and energy absorption properties of titanium foam with $CaCl_2$ as a space holder. Mater. Sci. Eng. A **708**, 419–423 (2017). https://doi.org/10.1016/j.msea.2017.09.123

Yavari, S.A., Wauthle, R., Stok, J., Van Der Riemslag, A.C., Janssen, M., Mulier, M., Kruth, J.P., Schrooten, J., Weinans, H., Zadpoor, A.A.: Fatigue behavior of porous biomaterials manufactured using selective laser melting. Mater. Sci. Eng. C **33**, 4849–4858 (2013). https://doi.org/10.1016/j.msec.2013.08.006

Yu, C.-J., Banhart, J.: Mechanical properties of metal foams. In: Proceedings of Fraunhofer USA Metal Foam Symposium, pp. 37–48 (2016)

Zhai, W., Yu, X., Song, X., Ang, L.Y.L., Cui, F., Lee, H.P., Li, T.: Microstructure-based experimental and numerical investigations on the sound absorption property of open-cell metallic foams manufactured by a template replication technique. Mater. Des. **137**, 108–116 (2018). https://doi.org/10.1016/j.matdes.2017.10.016

Porous Ceramic Properties and Its Different Fabrication Process

Arya Uthaman, Hiran Mayookh Lal, and Sabu Thomas

Abstract The unique compositions and outstanding properties of porous ceramic products make them useful in various application fields such as high-temperature thermal insulation, filtration, and catalytic reactions. This chapter aims to review the porous ceramics properties, classifications, and the different types of fabrication methods of porous ceramics. The readers can get a profound view of porous ceramic materials and their different fabrication methods such as particle stacking sintering, the addition of foaming, gel casting, sol–gel process, polymeric sponge, and freeze-drying method. The fabrication process of porous ceramics can influence the quality of the final products.

Keywords Porous ceramics · Ceramics · Fabrication process · Porous materials · Polymeric sponge method

1 Introduction

Recently, the utilization of porous ceramics has become great consideration due to its outstanding mechanical strength, chemical, abrasion resistance, etc. (Eom et al. 2013; Colombo 2008). Some benefits of porous ceramics are illustrated in Fig. 1. The broadly considering porous ceramics are silica, alumina, titania, magnesium oxide, zirconia, etc. (Colombo 2002). The pore structure, morphology, pore size, pore wall, porosity, the density of the pore strut, and interconnection of pores have a significant role in the properties of porous ceramics (Sakka 2005; Liu and Chen 2014). The particle size distribution of ceramic powders, the concentration of binder, types of binders, fabrication, etc., can influence the porosity and pore size (Ohji and Fukushima 2012). Typically, the particle size of raw ceramic powder is about two to five times greater than pores, for acquiring the needed pore size. And, the greatest service temperature of porous ceramics is around 1000–2000 °C. The pores are

A. Uthaman (✉) · H. M. Lal (✉)
School of Civil Engineering, Harbin Institute of Technology, Harbin 150090, China

S. Thomas
School of Energy Materials, Mahatma Gandhi University, Kerala, India

averted in ceramic materials due to intrinsically brittle behaviour than the polymeric or metallic products. The enhanced usage of porous ceramics in environments such as elevated temperatures, wear, and corrosive media (Studart et al. 2006; Guzman 2003; Gauckler et al. 2009). The applications of porous ceramics are mainly implemented in the field of environmental protection, energy and in chemical engineering as liquid gas filters, catalysis supports (Gao and Shi 1999; Scheffler and Colombo 2005). In addition, porous ceramics are widely considering in biological applications, due to their eminent melting point, resistance to surface damage, and electronic properties (Pokhrel et al. 2013). The porous ceramics can be used in water treatment by decorating the silver nano-particles (Uthaman et al. 2021b) on porous ceramic composites (Lv et al. 2009). The porous ceramics itself does not have the ability to prevent the growth of bacteria. The incorporation of metal nanoparticles such as silver nanoparticles that possess excellent antibacterial properties (Lal et al. 2021a, b; Uthaman et al. 2021c) by coating on the ceramic surface induce antibacterial properties. Furthermore, the porous ceramics can either have interrelated voids surrounded through ceramic or have a closed void within an uninterrupted ceramic matrix. Interrelated or reticulated porous ceramics are utilised in industrial filters, diesel engine exhaust filters, etc. (Al-Naib 2018).
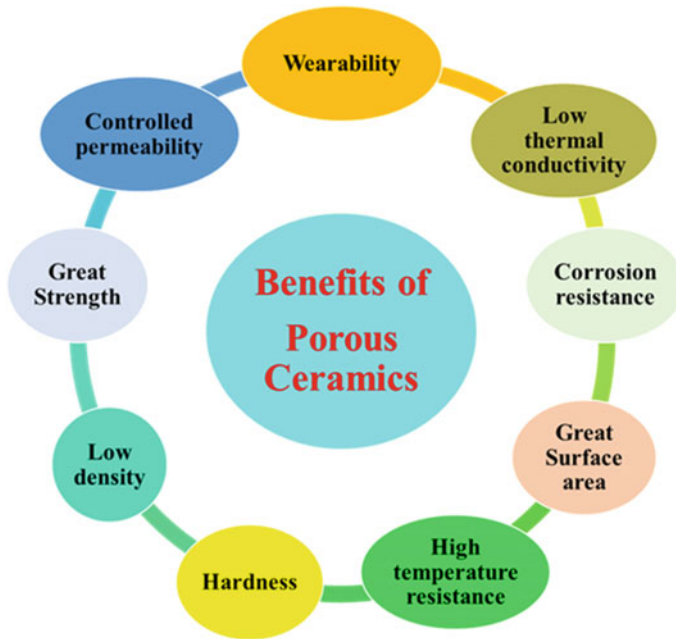
Fig. 1 Benefits or properties of porous ceramics

2 Classification of Porous Ceramics

In the case of porous ceramics, there is not a commonly admitted classification because these are mainly depending on the application purposes and principles. However, the fundamental characteristics of porous ceramics is depending on the classification of pores. The classification of porous ceramics (Al-Naib 2018) is shown in Fig. 2. These classifications aim to arrange the pores, based on structure, shape, etc. (Ohji and Fukushima 2012).

1. According to chemical components: The chemical components of the initial materials such as silicate, oxide, aluminosilicate, etc. (Guzman and Sysoev 1975).
2. According to inner structure: Fibrous, cellular, and granular.
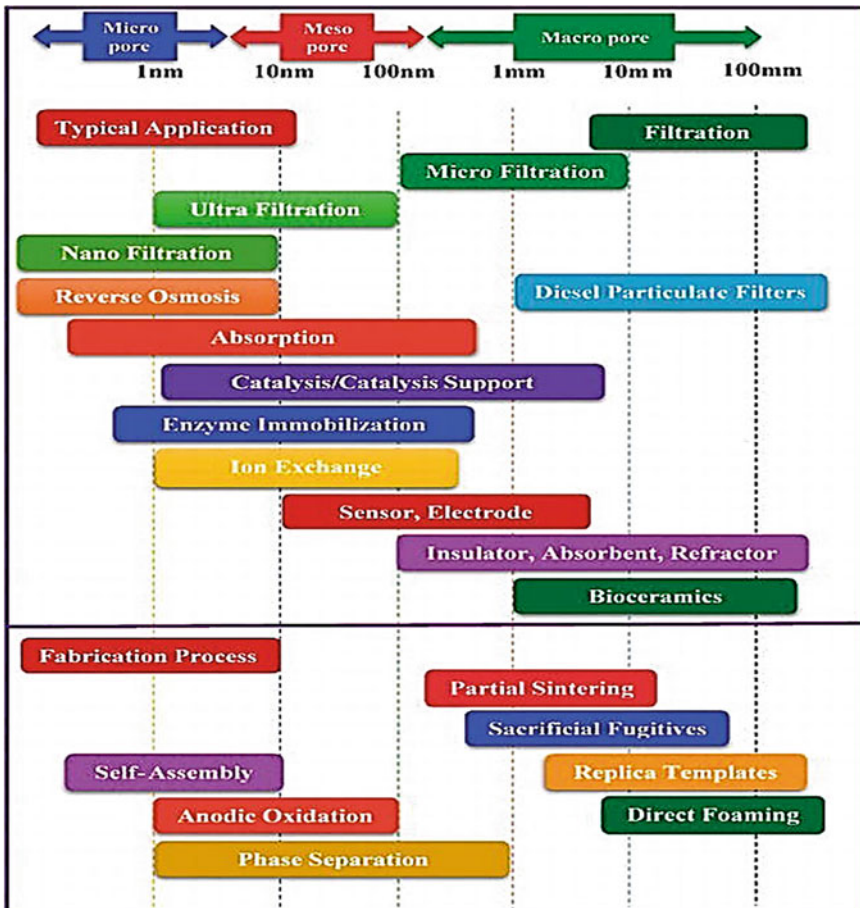
Fig. 2 Classification of porous ceramics: reproduced with permission from Al-Naib (2018)

3. According to porosity: Based on porosity, super-high, high, and moderate. Super-high is above 75%, high is in between 60 and 75%, and moderate is between 30 and 50% (Guzman and Sysoev 1975). These types contain two phases as solid ceramic and gas-filled porous phase (German 2013). The closed pores comprised of gases are independent of the environment (Misyura 2016). The porosity of ceramic body can be divided into two such as open and closed porosity. Open porosity means that can access from the outside and are of two types such as open dead-end pores and open pore channels. The addition of open and closed porosity is called total porosity. The open porosity enhances frictional porosity. The closed porosity can dominate if the materials have less frictional porosity.
4. According to nature of porosity, size and volume fraction of pores (Gaydardzhiev 2008), there are two kinds of nature of porosities are found; natural and synthetic ceramics. The porosity nature of natural ceramics depends on their genesis, while in the case of synthetic ceramics, it depends on their production, which could control.
5. According to pore size, there are three types, such as microporous (<2 nm), macroporous (>50 nm), and mesoporous (2–50 nm). The pore size is determined through mercury intrusion porosimetry technique.

2.1 Different Methods for Enhancing the Porosity of Porous Ceramic Materials

1. For the primary moulding mixture, the choosing of granular composition (Berkmam and Mel'nikova 1969).
2. Incorporating the synthesized or natural filler grains into the mixture (Kitaitsev 1970).
3. Incorporating additives in the primary mixture and then followed removal through the evaporation, sublimation, dissolution, etc.
4. By thermal treatment, swelling of the individual or total mixture.
5. Through mechanical treatment, the involvement of air into ceramics suspensions.
6. Polymer cellular matrix and ceramic suspension were impregnated and followed by squeezing, drying, and thermal treatments.
7. Addition of ceramic fibres in to a mixture and moulding with binder and thermal treatment of moulded materials (Kashcheev and Strelov 1992).
8. The formation of a honeycomb structure by extrusion moulding of plasticised ceramic mixture.

3 Fabrication of Porous Ceramics

3.1 Particle Stacking Sintering

In this process, the porous ceramics are made through the sintering of the aggregate particles. Similar particle sizes as the aggregate particles are incorporated for the interconnection. The additives containing thermal expansion coefficient (TEC) capable with aggregate particles, solid reactions with the aggregate particles, and wettable in the liquid phases at high temperatures (Zhang and Li 2003). The formation of porous ceramics can happen through the stacking of ceramic particle sintering because of the ceramic particles sinterability. Initially, tiny similar-type particles are imparted after that sintered, in order to connect high aggregate particles (Zhu and Su 2000). The aggregate particles are joined with others by a number of points to produce great number of three-dimensional interconnected networks. Generally, the higher aggregate particles can have higher average pore sizes, and besides, the lesser the aggregate particles can have greater pore distribution. Moreover, through calcination or low-density ceramic powders can produce solid-sintered pores (Sepulveda 1997). Usually, the sintering process is partially implemented and isothermal static pressing could be considered for ceramics having greater than 50 nm pore sizes (Nettleship 1996).

The porous ceramics having great strain bearing capability, low weight and young's modulus are commonly utilised in structural portions (Yang et al. 2001). The low porosity (<0.4) is produced through pressing ceramic powders to the needed size and density control via the amount of powders. In addition, the improvement in contact strength could protect the porous materials from mechanical collapsing. The schematic representation of the changes occurring with particles under sintering (Dorozhkin 2013) is shown in Fig. 3.
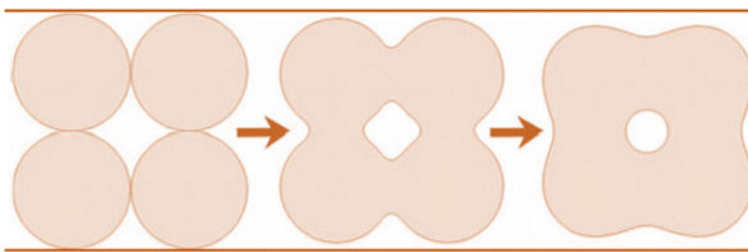
Fig. 3 Schematic representation of the changes occurring with particles under sintering: reproduced with permission from Dorozhkin (2013)

3.2 Addition of Pore-Forming Agent

3.2.1 Powders

There are several applications that are considered with the addition of a pore-forming agent to produce porous ceramics. In the case of ceramic powders, the volatile-type pore-forming agents are incorporated and the formation of pores, later the volatilisation at high temperatures, and subsequently, the products can be developed with complicated shapes and various pore structures (Zhu and Su 2000). This method is almost same as to the common ceramic preparation. To attain the porous ceramics, the ceramic powders were combined with carbon powders, fibres, wood scraps and organic powders such as flour, naphthalene and later pressed and sintered. The content of agent has a significant role in the pore size, volume and pore distribution. Furthermore, the open-cell porosity enhances with the content of the agents (Li and Wu 2000; Sepulveda 1997). The ceramic powders can combine not only with organic powders but also with inorganic salts. However, the inorganic salts are difficult to melt though dissolvable after sintering (Li and Wu 2000). Incrementing the sintering temperature and expanding, the time can decrease the porosity and improve the density, and thereby, the pore wall and porous ceramics strength can enhance (Zhang et al. 2002). The pore structures contain tiny and big pores and can prevent the content of the polymer powders to recognize the accurate control of the permeability of the final product. The schematic representation of the pore-forming agent method for porous ceramic production (Ribeiro et al. 2019) is shown in Fig. 4.

In the case of porous hydroxyapatite, the manufacturing process is occurred by the addition of pore-forming agents like olefin, naphthalene and PMMA. While heating, the TEC of the pore-forming agents may raise and can achieve 10 times than the hydroxyapatite at thermal decomposition temperature. Furthermore, the higher variation in TEC could results a great number of cracks and decrease in strength (Yao et al. 2000). However, the carbon powders TEC is around near to the hydroxyapatite and less cracks are formed and growth in mechanical strength can be found. The porous hydroxyapatite having improved sinterability and strength was developed via the incorporation of carbon powder agents and biological glass. The hydroxyapatite
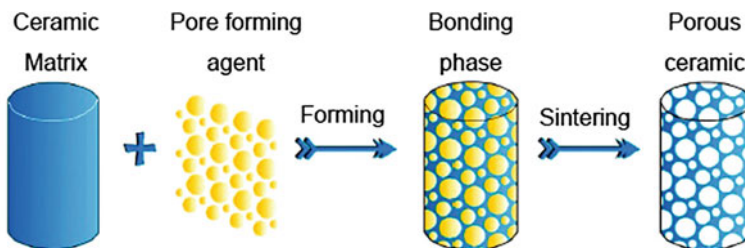
Fig. 4 Schematic representation of the pore-forming agent method for porous ceramic production. Reprinted from Ribeiro et al. (2019), with permission

is a type of biological active material. The development of green body can take place through the combining of binders, hydroxyapatite powders, biological glass, carbon powders and dispersants together and followed ball milling, drying, pressing and isostatic moulding. The commonly considering pore-forming agents, particle size is about 124–147 μm and around 30 volume % content. For the green product, the disperser is organic phosphate and about 1200 °C sintering temperature. Yao et al. reported that PMMA can use as pore-forming agent for producing porous hydroxyapatite ceramics (Yao et al. 2001). It was observed that porous structure was similar and pore size and porosity are <200 μm and <50% respectively (Yao et al. 2000).

3.2.2 Slurry

The carbon powders or organic volatile pore-forming agents are implemented into the ceramic slurry. While sintering, these agents may burn and remains several pores are formed as porous ceramic. Nowadays, the eco-friendly type of porous ceramics is developed by using starch as the pore-forming agent. The starch and the aqueous slurry of the ceramic powders are produced and subsequently added into the mould (infiltration is not required) and heated at a temperature of 50–70 °C (Bowden and Rippey 2002). Then, the starch powders interacted with water can extend the expansion of the powders and the absorption of water. And the liquid slurry can convert to a solid body as the shape of the mould. After demoulding, drying, and sintering, the final product can be achieved. The porosity and the pore size are depending on the starch powder content and size since, after sintering agents burned and remains pores. However, this method has several benefits such as easy to operate, less expensive, and porosity can be controlled. Instead of starch, the rice, potato powders, or the combination of this also can be considered as the binder and forming agent.

For the application purposes, some significant properties of starch powders are binding, gel, densification and generate membranes. Moreover, these are insoluble in water below 50 °C so the starch powders could be use and not influence on the structure. At the same time, above 55–80 °C can destroy the intermolecular bond and by absorbing the water, and the powders may expand. The thermal insulation components, infiltration components, gas combustors, and biological ceramics, etc., are produced by using this method and some products with different shapes.

3.3 Polymeric Sponge Impregnation Process

In 1963, the organic foam impregnation was patented (Schwartzwalder and Somers 1963). This is the most commonly considering method for producing the porous ceramics. These are most widely utilised to produce open-cell three-dimensional reticulated porous ceramic materials. Here, the organic foam is impregnated as preformed ceramic slurry and followed burning, for attaining porous ceramics. Rather

Fig. 5 Schematic representation of polymeric sponge impregnation method
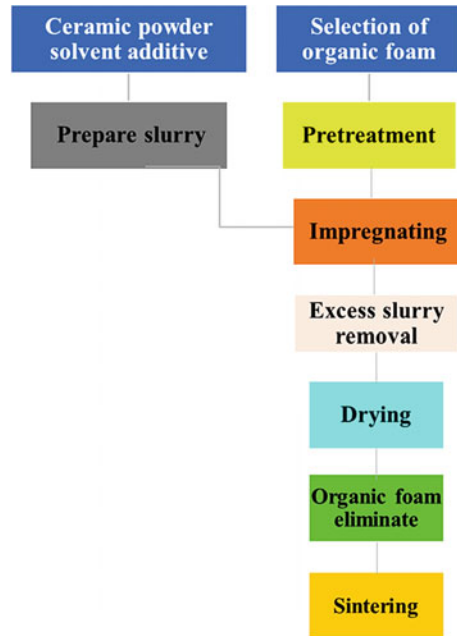
than ceramic slurry, the colloidal solution or sol–gel could be applied (Li and Wu 2000). The schematic representation of polymeric sponge impregnation method is shown in Fig. 5. Impregnating organic slurry process can attain great porosity of around 70–95% moreover and is simple and cheap fabricating method (Zhu and Jiang 2000). Compared with other process, the speciality of this method is that the products pore structure, i.e., open-cell three-dimensional reticulated, is about similar to that of organic foam precursors. The pores in the organic foam can influence the pore size and also the coated layer thickness, slurry drying and shrinkage while sintering.

3.3.1 Choosing Organic Foam and Pretreatment

While choosing an organic foam, the pore size must have an importance since; plastic foams pore sizes can decide the porous ceramic products pore size. So, the organic plastic foam should carefully determine according to the necessity of pore sizes and porosity of the products (Zhu and Jiang 2000; Wang 1997). Besides, the foam contains sufficient resilience and their vaporization temperature is less than the sintering temperature. Some fundamental factors for the organic foams are

- Enough rebound resilience to remove excess slurry.
- Open-cell reticulated structure to assure the impregnation of ceramic slurry and inter bonding.
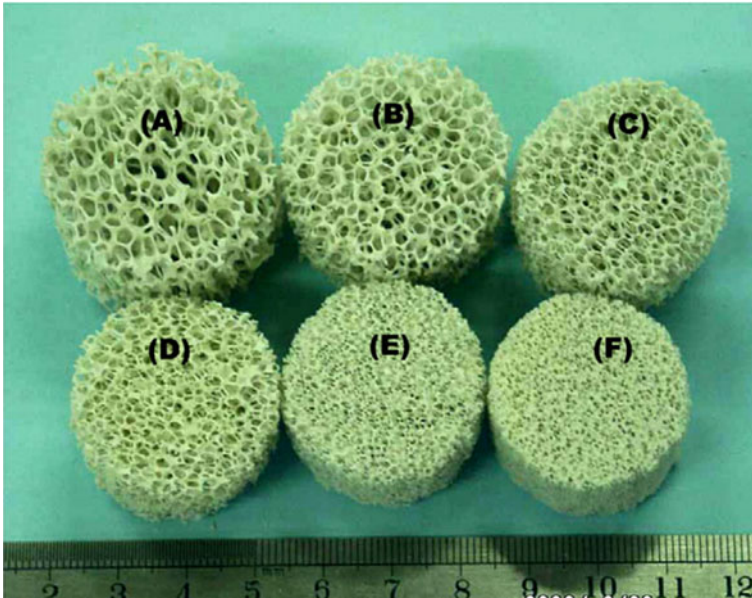
Fig. 6 Morphology of the porous silica ceramics with different pore sizes **a** 5.7 mm pore size and 78 vol.% porosity, **b** 5.3 mm pore size and 77.8 vol.% porosity, **c** 4.4 mm pore size and 77.3 vol.% porosity, **d** 3.2 mm pore size and 76.2 vol.% porosity, **e** 2.4 mm pore size and 74.9 vol.% porosity, **f** 2.2 mm pore size and 74.6 vol.% porosity. Reproduced from Wen et al. (2007) with permission of Elsevier

- Hydrophilicity to ingest the ceramic slurry.
- Volatilisation at lower sintering temperature.

The organic foams having these fundamental factors are polymerised sponges after exposed to some foaming methods. For example, polyurethane, cellulose, polyvinyl chloride, etc. (Zhu and Jiang 2000; Montanaro et al. 1998). The morphology of the porous silica ceramics with different pore sizes is shown in Fig. 6 (Wen et al. 2007). And also, these are open-cell reticulated structure, and the cells are linked by solid 3D skeletons forming connected open channels. The template of organic polymer sponge can influence the cell size of porous ceramics.

3.3.2 Preparation of Slurry and Impregnation

The proper selection of ceramic powders is a significant factor for the application purposes (Zhu and Jiang 2000). The slurry contains liquid solvents, ceramic powders and additives. Commonly, the liquid solvent is aqueous and also organic solvent, such as ethanol, is considered. The additives usually used are plasticizers, surfactants, binders, defoamers, and dispensers. The solid part of the slurry must be as much as possible higher, in order to control the shrinkage and cracking that can happen after

molding and drying and also for enhancing the coating content in the organic foam. The solid part is about 50–70%, and water is around 10–40% (Zhu and Jiang 2000).

The use of binders could increase the strength of a green body after drying and also protect breakage when removing the organics to assure the mechanical strength of the sintered product. Different types of binders are found such as organic and inorganic binders. Some examples of organic binders are poly vinyl alcohol, and inorganic binders are potassium/sodium silicate, phosphate, borate, etc. The type of binder can influence the properties of the final products.

Another important factor is the rheological properties of the slurry. The slurry should be flowable and is thixotropic. The flowability can assure the impregnation of the slurry into the organic foam and homogeneous coating on the pore wall. Thixotropy can decrease the viscosity and boost the moulding process. After moulding, the slurry viscosity can improve and the flowability reduces and adhesion of slurry on the pore wall solidifies.

The surfactant also has a significant role in the preparation of slurry. In the case of liquid slurry, if the organic foam has very less wettability, then the slurry will be thick in the area of cross section of the foam. This can induce cracking in sintering and decrease the strength of the porous ceramics. The usage of surfactant can increase the adhesion and properties of the materials (Uthaman et al. 2021a).

After preparation of the slurry, next section is the impregnation of slurry. The organic foam contains air that must be moved out through vacuum adsorption, hand rubbing, or any other methods before impregnation. After impregnation of the organic foam, the excessive slurry needs to removed (Wang 1997). In the organic foam impregnating method, the moulding of the slurry dipped organic foam have an important role.

3.3.3 Drying and Sintering of Green Bodies

After extrusion of the excess slurry, the porous green bodies ensure to be dried. The drying can be done in shade, oven drying, or any other way. For sintering, the green bodies are added to a kiln; during this, the content of water is less than 1% (Zhu and Jiang 2000). The sintering can be occurred in two phases such as high-temperature and low-temperature phase. In low temperature phase, the green bodies are slowly heated for completely removing the organic foam. And if fast heating, the decomposition of organic ejects higher amount of gas to break and pulverize the green bodies. The organic foam slurry impregnation method, the continuous impregnating, spraying, drying, and fibre reinforcement can be implemented to increase the structure and properties of the final products (Zhu and Jiang 2000). The presintering treatment needs to be considered for the green bodies to acquire the strength.

3.3.4 High Strength of the Ceramic Foam

The strength of the porous ceramics is an important factor. The strength of the ceramic foams could be improved through a higher content of coated slurry, modified sintering, and siliconizing (Zhai et al. 2008). Another method to enhance the properties of ceramic foams is by second coating, second phase toughening, siliconizing, and sintering modification (Zhai et al. 2008). The method of impregnation of slurry is illustrated in Fig. 7.

3.4 Foaming Process

In 1970s, this method was discovered for the production of porous ceramics with the foaming agents such as calcium hydroxide, aluminium sulphate, hydrogen peroxide, etc. (Wang 1997). The pre-processed raw materials are put into the mould and heated at around 900–1000 °C. Upon the pressure and in the oxidizing atmosphere, the powders were bonded and eject gas from the foaming agents to fill in the mold and after cooling the porous ceramics were incurred. There are different types of process; green body foaming, slurry foaming etc. The slurry foaming process is the cheap and much better way to produce high-strength porous ceramics (Sepulveda 1997). This method is impelled via the gaseous phases in the ceramic slurry, comprised of water, ceramic powders, polymer binders, gels, and surfactants. In addition, the anionic surfactants are more stable and have great foaming ability. The generation of foam can be prepared by mechanical foaming, exothermic reaction gas releasing, foaming agent, and evaporating low melting point solvent, etc.

The foaming method was discovered in 1974, for the manufacturing of polyurethane foam and ceramic foaming were conducted together to form a homogeneous distribution of ceramic powders in the organic foam (Wang 1997; Wood et al. 1974). The fabrication procedure of foam (Ishikawa 2010) is shown in Fig. 8.

The porous ceramics were produced at room temperature, and atmospheric pressure was invented in 1978. The materials used are acids and phosphates, alkali
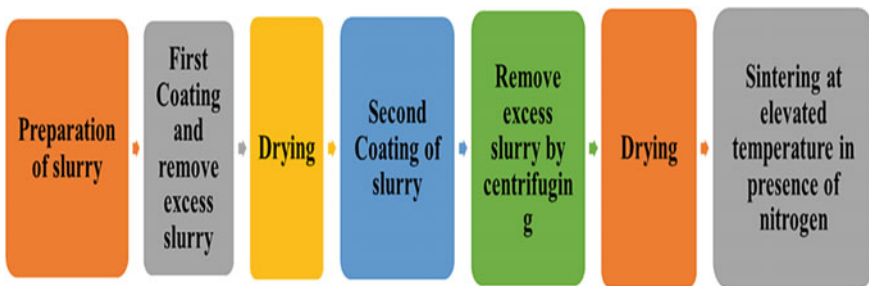
Fig. 7 Slurry impregnating method
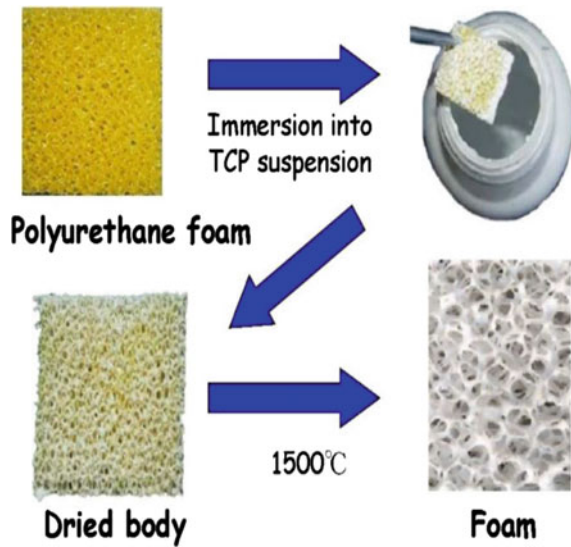
metal silicates, foam stabilizers, etc. (Wang 1997). The ceramic foams could produce
through foaming by blending aqueous solution of the metal carbonates having multi-
valences and metal phosphates (Hirschfeld et al. 1996; Yoshino and Iwami 1980).
The slurry formed by the ejection of carbonates as CO_2 and the oxides plays as a
curing agent. The viscosity can measure by the content of water; if the water content
is very less, the developed foaming structure is protected from shrinkage. Another
type is partly closed-cell porous ceramics, produced via blending surfactants, silica
gel, and methanol. Then the foaming agent of freon is imparted to the foam and
solidified followed by sintering (Fujiu et al. 1990). The increase in solid content can
enhance the mechanical properties of the product. However, the greater amount of
solid content can raise the slurry viscosity and pretends the formability and making
cracks in the materials. Some of the benefits of foaming gel method is that it is easy
to prevent the shape, density, and the compositions (Chen et al. 2009). Based on
(Xu et al. 2016) report, Fig. 9a–c represents the SEM images of the pore structure
of Al_2O_3 ceramics and magnified images of pore ridge, pore wall. And Fig. 9d, e
represents the good permeability of porous Al_2O_3 ceramics to water and ethanol.

Compared with the organic foam impregnation, the slurry foaming could be
considered for the preparation of open-cell and closed-cell foamed bodies. The
organic foam impregnation can be used for developing only open-cell materials.
The importance of surfactant usage is that, can keep the stability either in the liquid-
gas interface of the slurry or the solution in the slurry foaming method. And also,
the type of surfactant can affect the density and pore of the ceramic foams.
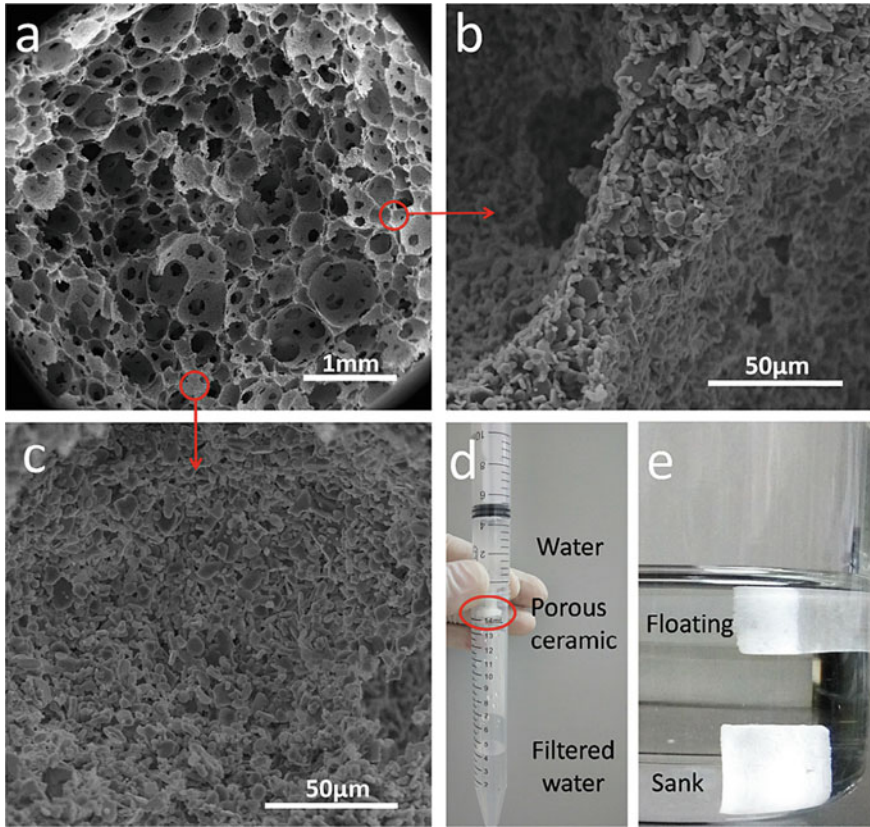
Fig. 9 a SEM images of pore structure of Al_2O_3 ceramics, and magnified images of pore ridge (**b**) and pore wall (**c**); **d** porous Al_2O_3 ceramics having good permeability to water; and **e** porous Al_2O_3 ceramics with (floating) and without (sank) a silicone layer outside the ceramic showing different floating status in ethanol. Reproduced from Xu et al. (2016) with permission of Elsevier

3.5 Sol–Gel Process

The microporous ceramic materials are commonly developed with the sol–gel process having nanometre range pore size (Zhang and Li 2003). Besides, these can consider for producing the porous materials contain high regularity (Zhu and Lu 2001). In this method, there are mainly three steps (Nettleship 1996) such as

- The metal oxide sol needs to be attained through the hydrolysis of the metal alkoxides dissolved in less alcohol mixed with water.
- The amorphous gel could be achieved via the polycondensation of the nanosized metal oxide particles through regulating the pH.
- The porous metal oxide ceramics can obtain through drying the gel and then organic material decomposing by heating.
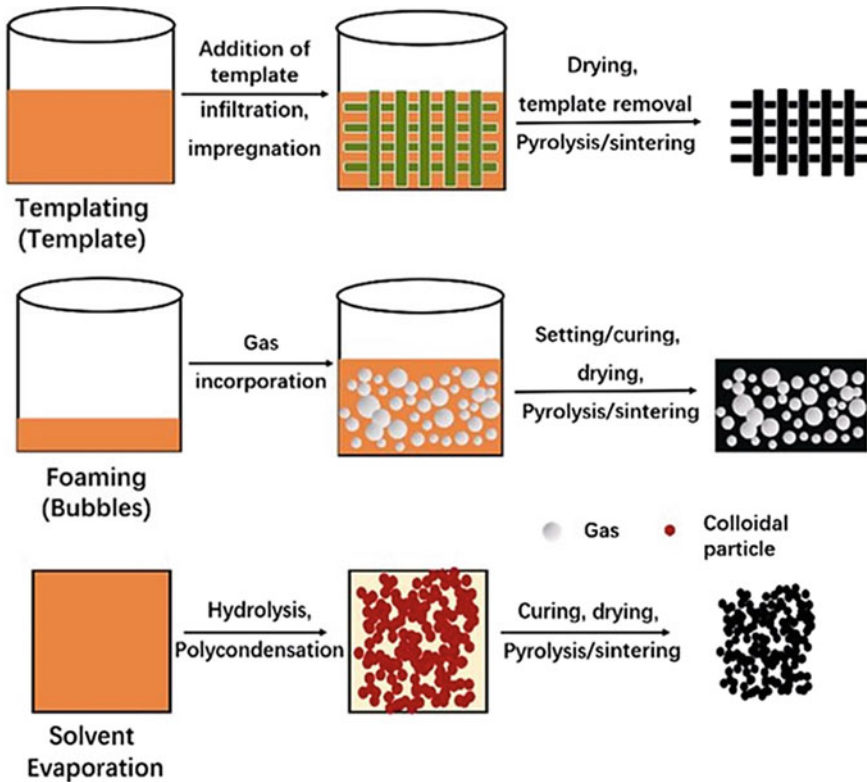
Fig. 10 Schematic representation of sol–gel process (Li et al. 2020)

The foam products could develop via the sol–gel process through stabilizing the bubbles since the viscosity gets incremented while the transformation of sol to gel (Sepulveda 1997). By foaming the SiO_2 gel system, many ceramic systems such as silica colloid, zirconia, and boehmite can be produced. In this method, the porous structures developed in the green body can be considered as the three categories such as templating, foaming, and solvent evaporation method (Li et al. 2020) as schematic represented in Fig. 10.

3.5.1 Templates

The templates play an important role in the case of sol–gel method. There are various types of templates found.

(a) Stacking with Uniform Particles Template

Recently, the products having same structure as to the natural opals are synthesized, and a process to produce this type of new material is by replicating the colloidal crystal

structure. These materials have a broad range of periodic structures produced with template as the aggregate of colloidal crystalline grains and subsequently transfer the sol into the interspaces and taking out the colloidal particles (Velev and Kaler 2000). To develop the template, the colloidal particles are filtered by a smooth filter membrane, and after accumulating, the particles are crystallized. Then, by using a cationic surfactant, the latex layer is washed. The zirconia, porous titania, silica, etc., were developed using sol–gel process having the template of the colloidal crystal through the agglomeration of latex particles.

(b) **Organic Foam Template**

The materials or products have around 97% porosities, <200 μm pore sizes can obtain from the sol–gel process or coating of a colloidal solution on organic foam (Brown et al. 1993; Hirschfeld et al. 1996). The range of pore size for organic foam is about 100–45 pores per inch and about 8–10 μm pore wall thickness. The organic foam is dipped in to the sol–gel solution, and to absorb the solution, the foam is enlarged. This enlarged foam is rolled in order to eliminate the excess solution. After that, it is dried at room temperature for two days and aged at temperatures around 40–60 °C for two days, then at 110 °C for 10 h, and lastly sintered at a temperature of 1200 °C for 24 h.

3.6 Other Processing Process of Porous Ceramics

3.6.1 Gel Casting

This method is applied for developing near reticulated ceramic materials (Kazumichi et al. 1997). In this method, by internal chemical interactions and in-situ solidification, a green body having uniform microstructure with great density can be produced (Jiao and Zhu 2007; Omatete and Janney 1991). The slurry could be foamed and solidified from the in-situ polymerization, and the reticulated green body has high strength. The premixing, casting, drying, and sintering are the main steps (Zhu and Lu 2001). Generally, this method was generated for the compact materials, and this was used to produce the porous ceramics to enhance the ceramic slurry foaming method. The monomer in the slurry could be in-situ polymerised to produce gel structures; can protect from collapsing of the foamed body. This foamed body attains high strength by the combination of gel and foaming (Sepulveda 1997). The schematic representation of gel-casting process (Hooshmand et al. 2019) is shown in Fig. 11.

The uniform slurry is produced with a solution of ceramic powder, dispersers, waters, and monomers. Then in the container, without the presence of oxygen, the surfactants are incorporated; can form the slurry. Also, the initiators and catalyst are imparted to boost the polymerisation. Following, the gel (rubber structure) is dried and burned to move out the polymer, and the dense ceramics are incurred. The ceramic powders like hydroxyapatite, alumina, zirconia, etc., could consider for this
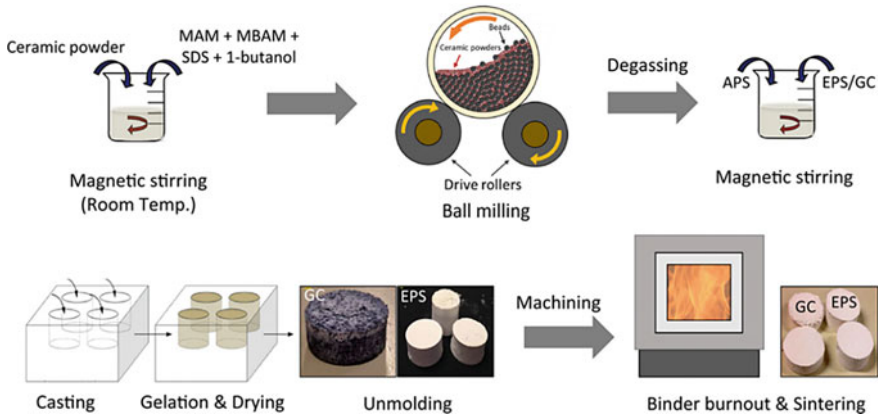
Fig. 11 Schematic representation of gel-casting process. Republished from Hooshmand et al. (2019)

method (Sepulveda 1997). This type of processing can be broadly considered in the automobile, electronics, and defence industries.

The addition of surfactants into the gas–liquid interface of bubbles in the slurry for stabilization. The surfactants contains hydrophilic and hydrophobic parts (Uthaman et al. 2021a). While sintering, the surfactants transmit to the gas–liquid interface and the hydrophobic component is tailored towards the gas surface in order to decrease the surface tension and also to stabilize the bubbles. Non-ionic surfactants are commonly considered for this method.

The gel casting method have many characteristic properties such as controllability in casting and solidifying steps, high amount of solid components having large particle powders, high strength and processability of green body, and low shrinkage while drying and sintering (Wang et al. 1995).

3.6.2 Wood Ceramics

When woods undergo physical and chemical treatments, for attaining a porous carbon material, porous oxide, and porous ceramic base composites and to the final products are generated by the process are known as wood ceramics (Qian et al. 2003). The materials such as wood, bamboo, waste paper, etc., are used. These are classified into two types such as carbon base and SiC base ceramics. The carbon base ceramics are the porous carbon materials achieved by carbonisation at elevated temperature of soaked wood or wood powders with thermosetting resin as phenolic resin followed by drying and solidifying (Zeng et al. 2007, 2008). The amorphous carbon is attained via the carbonisation of porous wood powders, and its high strength assures that the wood ceramics contain high mechanical properties. The SiC base ceramics are formed through the elevated temperature pyrolysis of natural wood in an inert atmosphere and then infiltration into liquid silicon at 1600 °C.
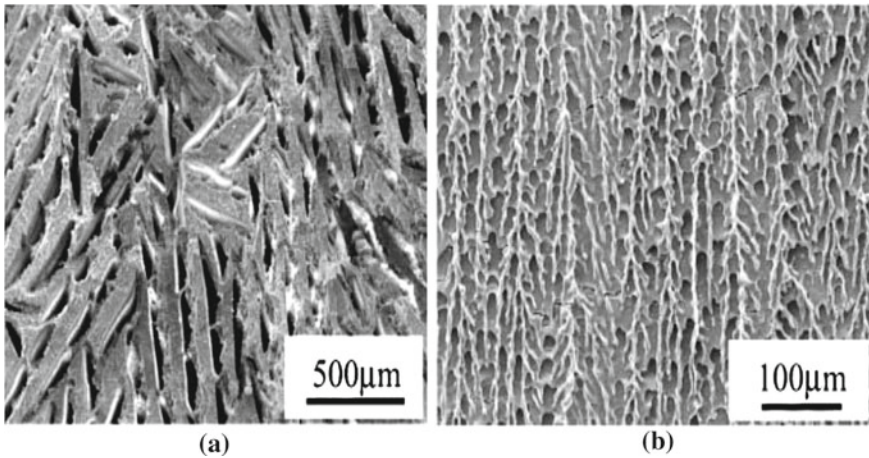
Fig. 12 Microstructures of porous ceramics fabricated by freeze-dry process **a** cross-sectional perpendicular to the macroscopic ice growth direction and **b** cross-sectional parallel to the macroscopic ice growth direction. Reproduced from Fukasawa et al. (2001) with permission of Springer Nature

For high-temperature applications, the materials need the properties such as high mechanical strength, thermal, and corrosion resistance (Lal et al. 2020; Uthaman et al. 2020). Porous SiC ceramics contains all these properties and are broadly applied as structural materials in high-temperature applications such as filters and carriers for catalyst (Liu and Chen 2014; Sieber et al. 2002). Nowadays, the production of porous SiC ceramics by transmitting of biological organic materials as wood is popular.

3.6.3 Freeze-Drying Process

The benefit of freeze-drying process is that the freezing effect of aqueous slurry, prevents the direction of ice formation and results the sublimation of ice by drying in low pressure, leading in a green body. And then, the porous ceramics having complex pore structure are formed after sintering. The sintering temperature and freezing temperatures can affect the pore size distribution and microstructure. Compared with freezing of chemical solutions, these have better *p*roperties like low shrinkage, high mechanical properties, wide range of porosity control, and eco-friendly (Fukasawa et al. 2001). The microstructure of porous ceramic fabricated by using freeze-drying method is shown in Fig. 12.

3.6.4 Hollow Sphere Sintering

This method is widely used for producing closed-cell ceramics and these are simple and easiest process for producing the porous ceramics (Green 1988; Hirschfeld et al.
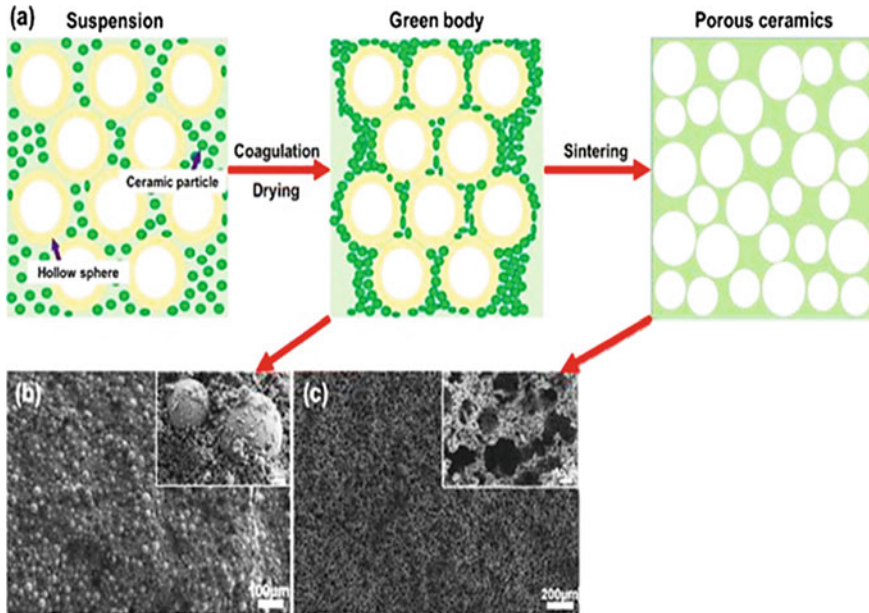
Fig. 13 Schematic representation of **a** fabrication of hollow sphere ceramic process, **b** SEM image of green body, and **c** SEM image of porous ceramics and pore size distribution. Reproduced from Zhang et al. (2019) with permission of Springer Nature

1996). The schematic representation of hollow sphere fabrication (Zhang et al. 2019) process is shown in Fig. 13. In this method, the hollow spheres were added in to the mould under pressure to accomplish a green body. Microwave heating is used for sintering the hollow spheres. The blending of glycerol and binders could increase the energy absorption, and then sintering can carried out in air. The SEM image of silica hollow spheres and fly ash hollow spheres (Zhang et al. 2019) are shown in Fig. 14.

4 Porous Ceramic Honeycombs

The honeycomb structure is created by using extrusion moulding technique; contains raw materials, extrusion, drying and burning (Chen et al. 2009). The materials such as binder, plasticiser, ceramics, and lubricants were added into the pug and mix homogenously in a stirrer. Then, the pug needs to under ageing in order to form uniformly distributed liquid phases. By extrusion using a reticulated mould, the ceramic honeycomb green body is produced. Followed by drying and sintering, the regular-shaped porous ceramic honeycomb can develop (Pu et al. 2004). The limitations of these ceramic honeycomb are poor strength, fast deformation, bubbles, cracks can happen.
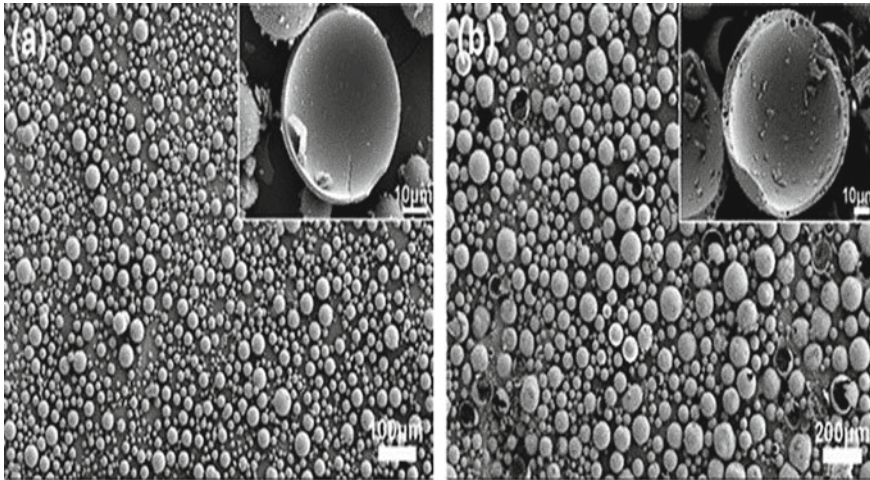
Fig. 14 SEM image of hollow spheres of **a** silica and **b** fly ash. Reproduced from Zhang et al. (2019) with permission of Springer Nature

The topologies of extruded and sintered ceramic honeycomb (Zhang et al. 2015) and FeCrAl honeycomb (Zhou et al. 2007) are shown in Fig. 15. Generally, the ceramic honeycombs have square, triangle, hexagonal parallel channels. The materials like aluminium titanate, cordierite, zeolite, etc., are used to produce the ceramic honeycombs. The honeycomb ceramics have high surface area, corrosion resistance and low thermal expansion. However, the metallic-type honeycombs are better than ceramic honeycomb since, they have high thermal conductivity, fracture toughness, etc. (Zhang et al. 2015).

5 Porous Ceramic Composites

Porous ceramic composites are divided into two kinds such as porous-reinforced ceramic composites and porous ceramic composite materials. Porous-reinforced ceramic composite is a composite generated from the infiltration of other materials in to the open-cell porous ceramics (Mclean 1997; Ning et al. 2001). Porous ceramic composites contain a base ceramics and other materials. Some examples of porous ceramic composites are Cu, α-SiC and graphite added to Si–O–C base ceramics for generating a conductive modified porous material (SiC and C are conductive materials, and conductivity is about 1×10^2–2.2×10^7 Ω^{-1} m^{-1}) (Liu 2010).
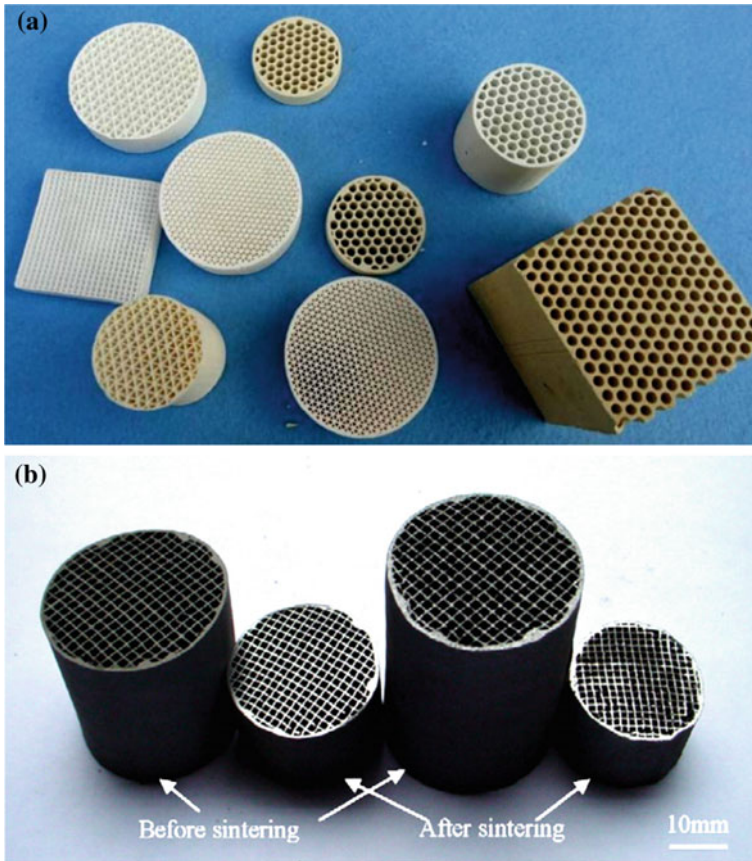
Fig. 15 Topologies of extruded and sintered **a** ceramic honeycombs and **b** FeCrAl honeycombs. Reproduced from Zhang et al. (2015) with permission of Elsevier

6 Conclusion

Porous ceramics are highly considering in many applications due to their attractive properties. The porosity of the material has a significant role in porous ceramics. The fabrication methods such as particle stacking sintering, the addition of pore foaming agents, polymeric sponge impregnation, sol–gel, foaming, gel casting, freeze-drying, etc., are profoundly emphasized in this chapter. Among these, the most commonly using fabrication technique is the polymeric sponge method. Each method possesses its advantages and disadvantages. The porous ceramics are widely considering in industrial application, due to the inherent properties such as cost effectiveness, mechanical strength, corrosion resistance, etc. Several problems are still required to be solved based on the preparative techniques of porous ceramic materials. In addition, the need for eco-friendly fabrication of porous ceramic materials is in

higher demand. The future works on the porous ceramic material need to solve all these related problems.

References

Al-Naib, U.M.B.: Introductory chapter: a brief introduction to porous ceramic. In: Recent Advances in Porous Ceramics. IntechOpen (2018)

Berkmam, A.S., Mel'nikova, I.G.: Porous Permeable Ceramics. Stroiizdat, Leningrad (1969)

Bowden, M.E., Rippey, M.S.: Porous ceramics formed using starch consolidation. Key Eng. Mater. **206**, 1957–1960 (2002)

Brown, J.J., Hirschfeld, D.A., Li, T.K.: Alkalai corrosion resistant coatings and ceramic foams having a superfine cell structure and method of processing (1993)

Chen, J.C., Ren, F.Z., Ma, Z.H., Li, F.J., Zhao, S.Y.: Preparation methods and application of foam ceramics. Chin. Ceram. **45**, 8–12 (2009)

Colombo, P.: Ceramic foams: fabrication, properties, and applications. Key Eng. Mater. **206**, 1913–1918 (2002)

Colombo, P.: In praise of pores. Science (80-) **32**, 381–383 (2008)

Dorozhkin, S.V.: Calcium orthophosphate-based bioceramics. Materials 3840–3942 (2013). https://doi.org/10.3390/ma6093840

Eom, J.-H., Kim, Y.-W., Raju, S.: Processing and properties of macroporous silicon carbide ceramics: a review. J. Asian Ceram. Soc. **1**, 220–242 (2013)

Fujiu, T., Messing, G., Huebner, W.: Processing and properties of cellular silica synthesized by foaming sol-gels. J. Am. Ceram. Soc. **73**, 85–90 (1990)

Fukasawa, T., Deng, Z.Y., Ando, M., Ohji, T., Goto, Y.: Pore structure of porous ceramics synthesized from water-based slurry by freeze-dry process. J. Mater. Sci. **36**, 2523–2527 (2001). https://doi.org/10.1023/A:1017946518955

Gao, Z.Y., Shi, X.L.: Preparation techniques of porous ceramics. Foshan Ceram. **4**, 19–20 (1999)

Gauckler, L.J., Studart, A., Tervoort, E., Gonzanbech, U.T., Akartuna, I.: Ultrastable particle stabilized foams and emulsions (2009)

Gaydardzhiev, S.: Gel-casted porous Al_2O_3 ceramics by use of natural fibers as pore developers. J. Porous Mater. **15**, 475–480 (2008)

German, R.M.: Liquid Phase Sintering. Springer Science & Business Media, New York (2013)

Green, D.J.: Fabrication and mechanical properties of lightweight ceramics produced by sintering of hollow spheres. J. Am. Ceram. Soc. **68**, 403–409 (1988)

Guzman, I.Y.: Certain principles of formation of porous ceramic structures. Properties and applications (a review). Glass Ceram. **60**, 280–283 (2003). https://doi.org/10.1023/B:GLAC.0000008227.85944.64

Guzman, I.Ya., Sysoev, E.P.: Technology of Porous Ceramics Materials and Articles (1975)

Hirschfeld, D.A., Li, T.K., Liu, D.M.: Processing of porous oxide ceramics. Key Eng. Mater. **115**, 65–80 (1996)

Hooshmand, S., Nordin, J., Akhtar, F.: Porous alumina ceramics by gel casting: effect of type of sacrificial template on the properties. Int. J. Ceram. Eng. Sci. **1**, 77–84 (2019). https://doi.org/10.1002/ces2.10013

Ishikawa, K.: Bone substitute fabrication based on dissolution-precipitation reactions. Materials (Basel) **3**, 1138–1155 (2010). https://doi.org/10.3390/ma3021138

Jiao, F.F., Zhu, G.Y.: Research progress of ceramic foams. Ceram **8**, 9–11 (2007)

Kashcheev, I.D., Strelov, K.K.: Fibrous Refractory Materials. Ekaterinburg (1992)

Kazumichi, Y., Koji, I., Nakamichi, Y.: Formation of anatase porous ceramics by hydrothermal hot-pressing of amorphous titania spheres. J. Am. Ceram. Soc. **80**, 1303–1306 (1997)

Kitaitsev, V.A.: Technology of Heat-Insulating Materials. Stroiizdat, Moscow (1970)

Lal, H.M., Xian, G., Thomas, S., Zhang, L., Zhang, Z., Wang, H.: Experimental study on the flexural creep behaviors of pultruded unidirectional carbon/glass fiber-reinforced hybrid bars. Materials **13**, 11–13 (2020). https://doi.org/10.3390/ma13040976

Lal, H.M., Thomas, S., Li, T., Maria, H.J.: Polymer Nanocomposites Based on Silver Nanoparticles: Synthesis, Characterization and Applications. Springer Nature Switzerland AG (2021a)

Lal, H.M., Uthaman, A., Thomas, S.: Silver Nanoparticle as an Effective Antiviral Agent, pp. 247–265 (2021b). https://doi.org/10.1007/978-3-030-44259-0_10

Li, Y.Q., Wu, J.Q.: Preparation, application, and development prospect of porous ceramics. Ceram. Eng. **12**, 44–47 (2000)

Li, F., Huang, X., Liu, J.X., Zhang, G.J.: Sol-gel derived porous ultra-high temperature ceramics (2020)

Liu, P.S.: Point defects in crystals (2010)

Liu, P.S., Chen, G.F.: Fabricating porous ceramics. In: Porous Mater, pp. 221–302 (2014). https://doi.org/10.1016/b978-0-12-407788-1.00005-8

Lv, Y., Liu, H., Wang, Z., Liu, S., Hao, L., Sang, Y., Liu, D., Wang, J., Boughton, R.I.: Silver nanoparticle-decorated porous ceramic composite for water treatment. J. Membr. Sci. **331**, 50–56 (2009). https://doi.org/10.1016/j.memsci.2009.01.007

Mclean, J.W.: The science and art of dental ceramics. Oper. Dent. **16**, 149–156 (1997)

Misyura, S.Y.: The influence of porosity and structural parameters on different kinds of gas hydrate dissociation. Sci. Rep. **6**, 30324 (2016)

Montanaro, L., Jorand, Y., Fantozzi, G., Negro, A.: Ceramic foams by powder processing. J. Eur. Ceram. Soc. **18**, 1339–1350 (1998)

Nettleship, I.: Application of porous ceramics. Key Eng. Mater. **122**, 305–324 (1996)

Ning, Q.J., Miao, H.Y., Wu, S.H.: Making composite porcelain crown material with Al_2O_3 and glass by melt infiltration. China Ceram. Ind. **8**, 18–21 (2001)

Ohji, T., Fukushima, M.: Macro-porous ceramics: processing and properties. Int. Mater. Rev. **57**, 115–131 (2012)

Omatete, O.O., Janney, M.A.: Gel casting—a new ceramic-forming process. Am. Ceram. Soc. Bull. **70**, 1641–1650 (1991)

Pokhrel, A., Seo, D.N., Lee, S.T., Kim, I.J.: Processing of porous ceramics by direct foaming: a review. J. Korean Ceram. Soc. **50**, 93–102 (2013)

Pu, X.P., Zheng, F.G., Liu, X.J., Huang, L.P.: Fabrication of porous ceramics. Ceram. Sci. Art **1**, 37–42 (2004)

Qian, J.M., Jin, Z.H., Qiao, G.J.: Recent progress in research on wood ceramics. J. Inorg. Mater. **18**, 716–724 (2003)

Ribeiro, G.C., Fortes, B.A., da Silva, L., Castro, J.A., Ribeiro, S.: Evaluation of mechanical properties of porous alumina ceramics obtained using rice husk as a porogenic agent. Cerâmica **65**, 70–74 (2019). https://doi.org/10.1590/0366-6913201965S12604

Sakka, Y.: Fabrication of porous ceramics with controlled pore size by colloidal processing. Sci. Technol. Adv. Mater. **6**, 915–920 (2005)

Scheffler, M., Colombo, P.: Cellular Ceramics: Structure, Manufacturing, Properties and Applications. Wiley-VCH, Weinheim (2005)

Schwartzwalder, K.H.S., Somers, A.V.: Method of making porous ceramic articles (1963)

Sepulveda, P.: Gelcasting foams for porous ceramics. Am. Ceram. Soc. Bull. **76**, 61–65 (1997)

Sieber, H., Vogli, E., Muller, F.P.G., Popovska, N., Gerhard, H.: CVI-R gas phase processing of porous, biomorphic SiC-ceramics. Key Eng. Mater. **206–213**, 2013–2016 (2002)

Studart, A.R., Gonzenbach, U.T., Tervoort, E., Gauckler, L.J.: Processing routes to macroporous ceramics—a review. J. Am. Ceram. Soc. **89**, 1771–1789 (2006)

Uthaman, A., Xian, G., Thomas, S., Wang, Y., Zheng, Q., Liu, X.: Durability of an epoxy resin and its carbon fiber-reinforced polymer composite upon immersion in water, acidic, and alkaline solutions. Polymers **12** (2020). https://doi.org/10.3390/polym12030614

Uthaman, A., Lal, H.M., Li, C., Xian, G.: Mechanical and water uptake properties of epoxy nanocomposites with surfactant-modified functionalized multiwalled carbon nanotubes. Nanomaterials **11**, 1–15 (2021a). https://doi.org/10.3390/nano11051234

Uthaman, A., Lal, H.M., Thomas, S.: Fundamentals of silver nanoparticles and their toxicological aspects. In: Lal, H.M., et al. (eds.) Polymer Nanocomposites Based on Silver Nanoparticles, pp. 1–24. Springer Nature Switzerland AG (2021b)

Uthaman, A., Lal, H.M., Thomas, S.: Silver nanoparticle on various synthetic polymer matrices: preparative techniques, characterizations, and applications (2021c)

Velev, O.D., Kaler, E.W.: Structured porous materials via colloidal crystal templating: from inorganic oxides to metals. Adv. Mater. **12**, 531–534 (2000)

Wang, L.X.: Development of porous ceramics. Refractories **31**, 55–58 (1997)

Wang, H.T., Liu, X.Q., Meng, G.Y.: Porous α-Al$_2$O$_3$ ceramics prepared by gel-casting. Mater. Res. Bull. **32**, 1705–1712 (1995)

Wen, Z., Han, Y., Liang, L., Li, J.: Preparation of porous ceramics with controllable pore sizes in an easy and low-cost way. Mater. Charact. **59**, 1335–1338 (2007). https://doi.org/10.1016/j.matchar.2007.11.010

Wood, L.L., Messina, P., Frisch, K.: Method of preparing porous ceramic structures by firing a polyurethane foam that is impregnated with organic material (1974)

Xu, C., Liu, H., Yang, H., Yang, L.: A green biocompatible fabrication of highly porous functional ceramics with high strength and controllable pore structures. J. Mater. Sci. Technol. **32**, 729–732 (2016). https://doi.org/10.1016/j.jmst.2016.07.002

Yang, J.F., Zhang, G.J., Ohji, T.: Porosity and microstructure control of porous ceramics by partial hot pressing. J. Mater. Res. **16**, 1908–1916 (2001)

Yao, X.M., Tan, H.T., Jiang, D.L.: Preparation of porous hydroxyapatite ceramics. J. Inorg. Mater. **15**, 467–472 (2000)

Yao, X.M., Tan, H.T., Jiang, D.L.: Preparation and processing of porous hydroxyapatite ceramics with controlled pore size. J. Funct. Mater. Dev. **7**, 152–156 (2001)

Yoshino, A., Iwami, I.: Inorganic foam and preparation thereof (1980)

Zeng, L.K., Hu, D.L., Shui, A.Z., Ren, X.T., Liu, P.A., Wang, H.: The novel techniques and development of preparation of porous ceramics (1). Chin. Ceram. **43**, 3–6 (2007)

Zeng, L.K., Hu, D.L., Shui, A.Z., Ren, X.T., Liu, P.A., Wang, H.: The novel techniques and development of preparation of porous ceramics (2). Chin. Ceram. **44**, 7–11 (2008)

Zhai, G.J., Ren, F.Z., Ma, Z.H., Li, F.J.: Techniques of preparing high-intensity foam ceramic. Chin. Ceram. **44**, 48–51 (2008)

Zhang, Z.H., Li, N.: Manufacturing process of porous ceramic materials. Mater. Rev. **17**, 30–31 (2003)

Zhang, Y.M., Liu, D.K., Han, J.C., Hao, X.D.: Progress in fabrication of porous ceramics. Ord. Mater. Sci. Eng. **25**, 62–67 (2002)

Zhang, Q., Yang, X., Li, P., Huang, G., Feng, S., Shen, C., Han, B., Zhang, X., Jin, F., Xu, F., Lu, T.J.: Bioinspired engineering of honeycomb structure—using nature to inspire human innovation. Prog. Mater. Sci. **74**, 332–400 (2015). https://doi.org/10.1016/j.pmatsci.2015.05.001

Zhang, X., Huo, W., Lu, Y., Gan, K., Yan, S., Liu, J., Yang, J.: Porous Si$_3$N$_4$-based ceramics with uniform pore structure originated from single-shell hollow microspheres. J. Mater. Sci. **54**, 4484–4494 (2019). https://doi.org/10.1007/s10853-018-3118-2

Zhou, Y., Zuo, X.Q., Sun, J.H., Mei, J., Sun, J.L.: Effects of sintering parameters on the structures of Fe-Cr-Al extruded honeycombs. Mater. Sci. Eng. A **457**, 329–333 (2007). https://doi.org/10.1016/j.msea.2006.12.117

Zhu, X.W., Jiang, D.L.: The polymeric sponge impregnation process—a type of economic and suitable process for preparing porous ceramics. Bull. Chin. Ceram. Soc. **3**, 45–51 (2000)

Zhu, C.X., Lu, Q.H.: Progress in the preparation of 3D-ordered porous material from the viewpoint of "science" and "nature" articles. New Chem. Mater. **29**, 22–25 (2001)

Zhu, X.L., Su, X.J.: Porous ceramics materials. Chin. Ceram. **36**, 36–39 (2000)

Application of Porous Ceramics

Omid Saremi, Mohammad Reza Ghaani, Leila Keshavarz, and Niall J. English

Abstract Ceramic materials are receiving more research attention due to their superior properties and characteristics. Porous ceramics, as a category of this kind of materials, provide a vast array of beneficial features of high pertinence to scientists and industries for application in disparate and varied applications. Chemical and thermal stability, high mechanical strength, abrasion resistance, high permeability, and desired selectivity are some of their interesting features. In this chapter, porous ceramic membranes and their applications regarding to the common physical, mechanical, chemical, and thermal properties of these kinds of materials are investigated, as well as new functional properties that could be achieved by altering and modifying their structures and formations. After introducing these membranes with an overall view about their synthesis methods and their properties, their applications are presented in six main categories including ion exchange, catalyst carriers, porous electrodes and membranes, filtration and separation, functional materials, and finally combustion and fire retardance. Although some of these applications have been utilized for a long time, recent studies are reviewed in particular in this chapter.

Keywords Ceramic membrane · Ion exchange · Catalysis carriers · Porous electrode · Battery · Solid electrolyte · Fuel cell · Filtration · Separation · Fire retardance

1 Introduction

During the last decade, porous ceramics have been employed in different industries and applications because of their superior properties such as chemical and thermal stability, besides high mechanical strength and significant resistance against abrasion

O. Saremi · M. R. Ghaani (✉) · L. Keshavarz · N. J. English (✉)
School of Chemical and Bioprocess Engineering, University College Dublin, Dublin, Ireland
e-mail: Mohammad.ghaani@ucd.ie

N. J. English
e-mail: Niall.english@ucd.ie

(Obada et al. 2017; Ohji and Fukushima 2012). On the other hand, high permeability and, in some cases, desired selectivity of porous ceramics highlight their use in filtration and separation technologies. The whole block of a porous ceramic can be described as a ceramic body with open porosity and media which fills the empty spaces and are accessible from the outside (German et al. 2009). However, in some cases during the formation of porous ceramics, closed porosity can be created which will result in the formation of some pores without any access to the surrounding media (Misyura 2016). The combination of open and closed porosity and the size and structure of the pores are key elements in developing the final application of the porous ceramic. As a result, to cautiously tailor the property of the porous ceramic without significant effect on the mechanical properties of the main ceramic body, four main fabrication techniques have been developed as follows:

1. Direct foaming: The gas will be added to a ceramic slurry. This gas can be provided either directly from a gas source or as a result of a chemical reaction.
2. Partial sintering: A modified heat treatment (lower sintering temperature or shorter sintering time) is applied to prepare the porous body.
3. Template-assisted techniques, such as replica and sacrificial templates: In these techniques, an existing porous structure immersed into the ceramic slurry (replica template) or a template acts as the pore-forming agent (sacrificial template). The remaining template will be removed later by the heat treatment process.
4. Additive manufacturing such as 3D printing is a new emerging technology that enables the creation of lighter, stronger parts with the desired pore structure.

Figure 1 summarizes the above-mentioned techniques, according to the range of achievable pore size and porosity level (He et al. 2012). Possible applications for each presented range are also presented in this figure for better understanding.
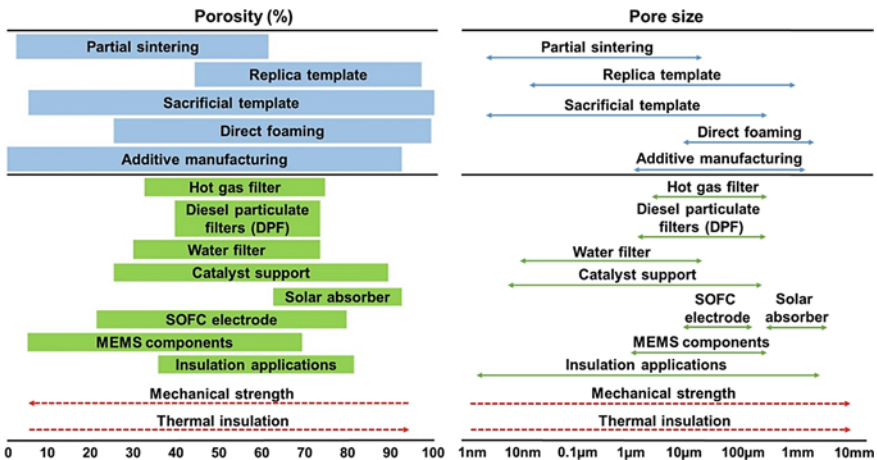

Fig. 1 Porosity and pore size distribution of porous ceramics for each selected fabrication techniques. Reprinted from Chen et al. (2021) with permission from Elsevier

This chapter covers a wide range of different applications of porous ceramics in industry. The first three sections are mainly focused on advanced applications in the chemical engineering field. Later, the role of ceramic membranes in filtration and separation techniques will be discussed. Next, the advanced application of porous ceramics in functional materials and materials for combustion and fire retardance systems will be reviewed.

2 Ion Exchange

With industrialization in high-speed growth, a lot of problems that endanger not only the environment but also the ecological systems, as well as human and livings health, have come to the fore. Nowadays, human and aquatic lives are in danger according to the ability of bioaccumulation and high toxicity of heavy metals that are among the most dangerous pollutants in the supply and treated water (Miretzky and Cirelli 2010; Sarin and Pant 2006). Longtime exposure, accumulation, and transportation of heavy metals like arsenic (As), lead (Pb), cadmium (Cd), mercury (Hg), and chromium (Cr) can comprise reverse effects on the mental and neurological system, gastrointestinal, and skin-associated illness leading to cancer (Dong et al. 2017; Gardea-Torresdey et al. 2000; Rehman et al. 2017; Vo et al. 2020). In this regard, heavy-component removal is a very important issue. One of the most recommended methods for heavy metal removal is ion exchange.

The first accurately formulated description of ion exchange processes dates back to 1850, where Way and Thompson explained the fundamental principles of ion exchange in four parts. They claimed that (i) the ion exchange is different from physical adsorption, (ii) the exchange happens in an equivalent amount, (iii) the process is reversible, and (iv) the exchange in some ions takes place more favorably (Thompson 1850; Way 1850). There were some obstacles in developing this technology including finding ion exchangers that are stable in a harsh chemical environment. Eighty-five years later, Adams and Holmes presented the first organic-based cation exchanger (Adams and Holmes 1935), and after that, the progress of ion exchange advances and applications grew faster.

An ion exchanger could be defined as a fixed co-ions framework that can be permeated and is neutralized electrically in an aqueous phase by mobile counterions. The framework in this definition is a continuous-phase skeleton, and fixed co-ions are electric surplus charges on the framework. Mobile counterions are movable solutes with charges opposite to fixed ions that can be replaced by other ions with the same sign and can permeate, while the complex is neutral electronically.

In an ion exchange complex, fixed co-ions, which are known as an ionogenic or functional groups, are attached to an insoluble phase covalently, and exchangeable counterions permeate through the insoluble phase where the complex is neutral for the presence of co- and counterions; the capacity of ion exchange complex is due to fixed co-ions' concentration. Figure 2 shows a cation exchanger schematic with a functional group of sulfonic acid and counterions of sodium (SenGupta 2017).
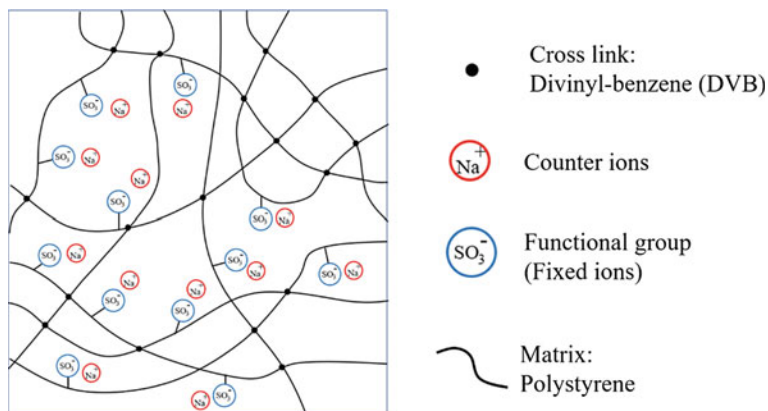
Fig. 2 Schematic of a cation exchange where fixed co-ions are shown by $-SO_3^-$ and counterions/exchanging ions by Na^+

In the following, some examples of porous ceramics usage with the aim of ion removal from aqueous solution are presented.

2.1 As, Zn, Cd, Cs

Arsenic is one of the most important compounds that threaten human health which is almost found in polluted waters (Pilicita et al. 2021). The highest contaminant level of arsenic, according to the United States Environmental Protection Agency (US EPA) and World Health Organization (WHO) in drinking water is 10 µg/L (USEPA 2001). Choi et al. used a flat ceramic membrane with commercial ion exchange fibers at room temperature to treat metal ions like arsenic and zinc as well as turbidity of wastewater (Choi et al. 2020). Chen et al. also adsorb heavy metal ions such as cadmium, cesium, and arsenic from water in ambient conditions by utilizing the Al–Fe type of PBA as a porous compound (Chen et al. 2019).

2.2 Li⁺

Collecting lithium as a very common material in different applications such as batteries has got huge attention in recent years (U.S. Geological Survey 2019). This increasing use of this nature of rare-find metal (Choubey et al. 2016) causes scientists to seek efficient ways for its extraction. In this regard, a lithium-ion conducting glass-ceramic membrane (LICGC) was utilized by Choubey et al. to increase the efficiency of lithium-ion selection. The experiments were performed at 25 ± 0.5 °C which resulted in a selectivity coefficient of 376 and 364 for Li^+/Na^+ and Li^+/K^+, respectively (Ounissi et al. 2020). Figure 3 shows Li-ion selectivity via LICGC in a membrane, while other ions like sodium are rejected.
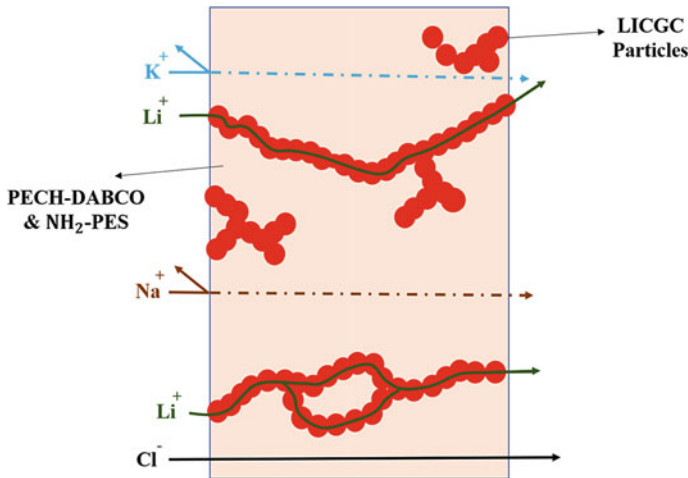
Fig. 3 Selectivity of lithium-ion via LICGC particles

2.3 Na⁺

One of the most important applications of ion exchange is removing ion material from ceramic foams in order to achieve better performance. Some alkali ions such as Na^+ and K^+ could possibly occupy the crystalline structure voids, which causes feldspathoid phase creation (Beall and Duke 1983). In this regard, Romero et al. remove Na^+ ions from green foams in the process of producing highly porous cordierite foams. They used a 0.1 M NH_4NO_3 solution in which the foam (consists of metakaolin, γ-Al_2O_3, and talc powder) was immersed for 24 h before drying and ceramization. The cordierite-based ceramic showed remarkable strength to density ratio (Romero et al. 2020).

2.4 NH₄⁺

The other critical water pollutant which not only affects Aquas livings, but also accelerates metal corrosion and lowers water disinfection efficiency, is ammonia (Atkins and Scherger 1975; Shi et al. 2011). Natural zeolite which is known as a low-cost ceramic membrane is a good choice for ammonia removal (Kouvelos et al. 2007). Hollow fiber natural zeolite ceramic membrane (HFCM), which was used as a ceramic compound, resulted in over 96% of ammonia adsorption in the presence of ion exchange fabric combining with polyethylene. In addition, the study revealed that by lowering the powder size of the zeolite, better rejection performance is expected (Adam et al. 2020).

2.5 O^{2-}

Oxygen purification is one of the growing demands in different areas, such as pharmaceuticals, medicine, and nanoelectronics (Kerry 2007). Ion exchange deployment could cause a reduction in the operating temperature in the process of oxygen permeation with the same value of transportation (Yaroslavtsev 2016). Solovieva et al. utilized a Co_2SiO_4 porous ceramic with a thin-film layer of dense composite based on Co_3O_4 and Bi_2O_3 at a temperature of 790 °C in order to separate oxygen from the air (Solovieva and Kulbakin 2018). In another study by this team, an oxygen selectivity over nitrogen of above 1000 was achieved by using a composite of NiO-30 wt% Ag-40 wt% Bi_2O_3 at a temperature of 725 °C (Kulbakin and Fedorov 2018). In a study conducted by Han et al., a ruddlesden-popper (RP) membrane of $La_2Ni_{1-x}Mo_xO_{4+\delta}$ at a temperature of 900 °C to improve oxygen permeation in a CO_2 atmosphere was adopted. The results illustrated a good efficiency of Mo-doped ceramics in improving oxygen permeability and also stability of (RP) membranes (Han et al. 2019).

3 Catalyst Carrier

Developing multifunctional materials is promising, while challenges in new pollutants and their complex interactions made scientists find new ways to detect, quantify, and control them. Developing ceramic supports, ceramic carriers, and other types of structures for their different properties attract much research. These properties vary from thermal characteristics to engender chemical stability and low-cost production, thus rendering them optimal choices for catalyst carriers in many applications (Bardhan 1997). Advances in synthesizing ceramics added the value of low greenhouse gas (GHG) emissions, due to low-energy inputs for their fabrication, to its property as safe material in the environment.

Although catalysts are the main part of a catalytic process, the role of their supports should not be neglected. Most catalytic processes in the environment utilize a carrier, which is a high-surface material to maximize catalytic activity by spreading catalysts on it, and support or substrate, which is defined as the final application structure of the catalyst, in their industrial applications. The complex microstructure of carriers provides a high-surface area and appropriate mass transfer rate for different applications such as gaseous reactants. Although the main aims of their usages are regarded to catalyst dispersing and stabilizing, their interactions with catalysts also affect the process (Labhsetwar et al. 2012). Figure 4 depicts a catalyst carrier in which catalytic sites dispersed on a monolith with a coating to increase the surface area.

Various structures of ceramic compositions like mullite, alumina, and cordierite are used as ceramic supports in both stationary and mobile catalytic applications (Cerri et al. 2000). Porous ceramics for their high-surface area are one of the best choices for catalyst supports and carriers.
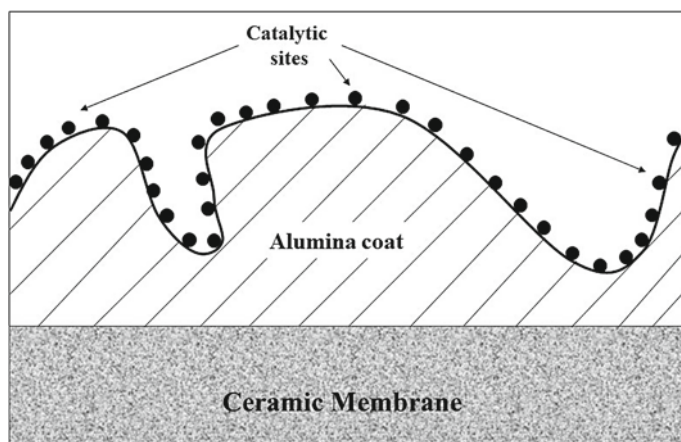
Fig. 4 Dispersed catalytic sites on a high-surface area carrier

In the following discussion, some applications of porous ceramics as catalyst carriers are presented. Styrene is a monomer, which has the most important role in producing polymers like foamed plastics, ABS, styrene-modified polyesters, and polystyrene is produced over 30 million tons per year. The best way of achieving styrene is the dehydrogenation of ethylbenzene over a catalyst. Fedotov et al. used a γ-Al_2O_3(K,Ce)/α-Al_2O_3 porous ceramic with Re–W (rhenium–tungsten) catalyst synthesized by the molecular layering of colloidal solution of precursors in order to dehydrogenate the ethylbenzene to styrene in the temperature of 200 °C (Fedotov et al. 2021). In another study, they used Re–W and Fe–Cr catalysts on a similar ceramic substrate at a temperature of 625 °C to dehydrogenation of cumene to α-methylstyrene (Fedotov et al. 2020).

Catalysis has been proven as an effective way to reduce and eliminate pollutants like organic, heavy metals, and other contaminants in water and wastewater treatment. The corrosion resistance, high-temperature stability, high permeability, low bulk density, and medium thermal conductivity render porous ceramics a good choice as supports for catalysts in both gas and liquid phases (Fraga et al. 2017a, b; Judkins et al. 1996; Ledoux et al. 1988; Taslicukur et al. 2007; Wei 1984). Li et al. deployed gold nanoparticles (Au NPs) as the catalyst on a bead of hydroxyapatite nanowire (HN)-sintered porous ceramic in ambient temperature for degrading nitrobenzene compounds to corresponding amino derivatives (Li et al. 2021a).

For the application of oil removal from wastewater, mullite-bonded SiC ceramics (MBSC), which was synthesized by facile solid-state reaction process with MoO_3 catalyst, were studied and showed good behavior for oil separation (Das et al. 2020). Dong et al. applied carbon nanotubes as a catalyst on a sepiolite porous ceramic in both high and low temperatures to separate oil from water (Dong et al. 2020). In another study, a Ni-ceramic membrane was used to treat oily sludge at 500 °C (Gao et al. 2020).

In other applications of wastewater treatment, a catalytic ceramic membrane of $CuMn_2O_4/g\text{-}C_3N_4$ was used to degrade benzophenone-4 (BP-4) and eliminate bromate (BrO_3^-) at ambient temperature (Liu et al. 2021). Figure 5 depicts the schematic of the catalytic ozonation process by using catalytic ceramic membrane for water treatment applications. Wu et al. and Scharnberg et al. provided TiO_2 as a catalyst in the presence of ceramic membrane in order to desulfurize and degrade Rhodamine B (RhB) in wastewater treatment, respectively (De Araujo Scharnberg et al. 2020; Wu et al. 2021). CuO catalyst was also studied in an investigation for peroxymonosulfate (PMS) activation in drinking water treatment over a ceramic hollow membrane (CIM) consisting of 96% of Al_2O_3 and 4% of TiO_2 (Wang et al. 2021). Figure 6 shows pollutants degradation processes by using CDF and CIM systems, and the status of their feed and permeation according to the study has been done by Wang et al.

One of the gaseous products that derived from human activities and has adverse effects on human health and the environment is volatile organic compounds (VOCs) (Bari and Kindzierski 2018; Gallon et al. 2020). Catalyst oxidation is known as one of the most efficient ways for ensuring VOCs' degradation (Zagoruiko et al. 2017). Toluene as a volatile organic compound could be degraded via Cu–Mn–Ce oxides on a bed of porous ceramic membrane that is shown schematically in Fig. 7 (Feng et al. 2021). In another study, Ni/P (nickel–phosphorous) catalyst used in the presence of 3D-printed biomimetic alumina ceramics in 800 °C for methane and tar reforming as well as VOC catalysis (Huo et al. 2021). Krivoshapkina et al. presented CuO–Co_3O_4–CeO_2 on kaolinite (with 40% porosity) and cordierite (with 25% porosity) for oxidation of carbon monoxide (Krivoshapkina et al. 2015).
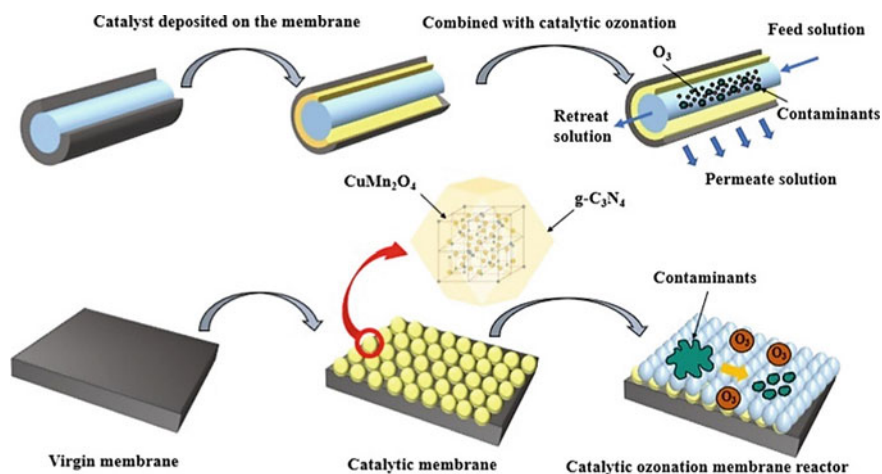
Fig. 5 Catalytic ozonation ceramic membrane for water purification. Reprinted from Liu et al. (2021) with permission from Elsevier
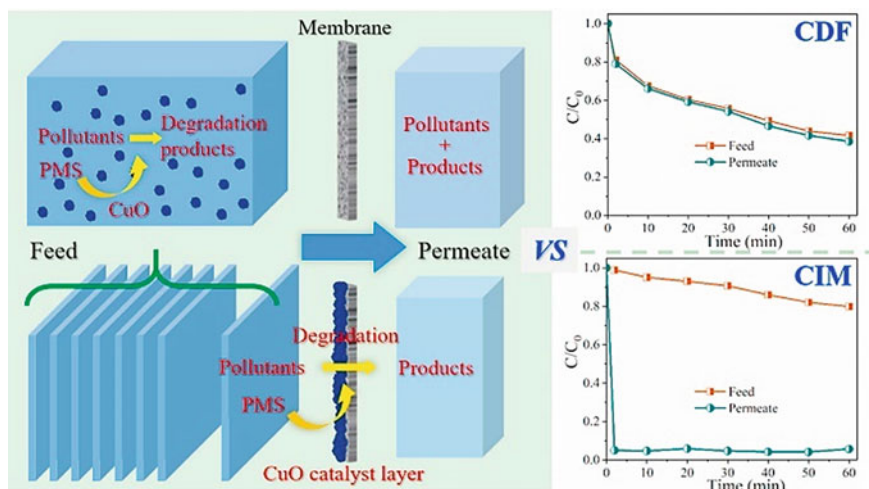
Fig. 6 Pollutants degradation in two processes of catalyst dispersed in the feed water (CDF) and catalyst immobilized on the ceramic hollow fiber membrane (CIM). Reprinted from Wang et al. (2021) with permission from Elsevier
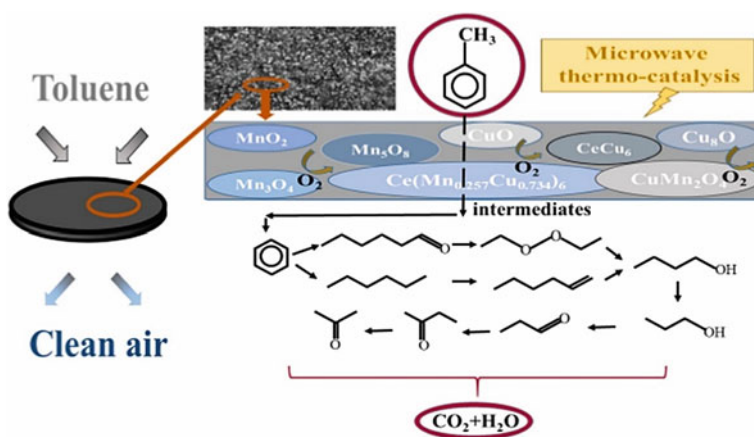
Fig. 7 Mechanism of toluene catalytic oxidation. Reprinted from Feng et al. (2021) with permission from Elsevier

4 Porous Electrodes and Membranes

Proton-conducting ceramics (PCCs) are a group which consists of materials that allow protonic or a mixture of protonic and one other charged carrier conduction in some high temperatures (400–700 °C). The latter could be mixed protonic–electronic conductors or triple-conducting oxides (TCO) that conduct three charge carriers of

protons, oxygen ions, and electron holes (or electrons) (Duan et al. 2015). Proton-conducting ceramics (PCC) have various applications like gas sensors (Iwahara 1996; Molenda et al. 2017), hydrogen separation membranes (Phair and Badwal 2006; Tao et al. 2015), fuel cells (Coors 2003; Duan et al. 2015; Iwahara 1996; Norby 1999), electrolyzers (Iwahara 1996; Sakai et al. 2009), and new interesting applications of electrochemical ammonia synthesis (Marnellos and Stoukides 1998), methane conversion to aromatics (Morejudo et al. 2016), and hydrogen thermos-electrochemical production from methane (Malerød-Fjeld et al. 2017). Hydrogen production according to hydrogen-fuelled vehicle applications is taking interests. Proton ceramic fuel cells (PCFCs) also introduce high efficiency and lower cost in comparison with solid oxide fuel cells (SOFCs) regarding their working temperature of (300–600 °C) and (800–1000 °C), respectively (Løken et al. 2018).

There are some issues, like boundary resistivity, electrolyte stability, and chemical resistivity of the electrode–electrolyte complex that is very crucial and has a key role in developing proton-conducting electrolyzers (Lei et al. 2019; Medvedev 2019), and PCFCs (Duan et al. 2020; Kim et al. 2019). So researchers are trying to overcome these issues in order to gain effective energy materials (Chiara et al. 2020).

4.1 Battery

Lithium-ion batteries (LIBs) are first appeared in 1991 and became the most used energy storage systems due to their capacity, high specific energy, and low cost (Ortiz-Vitoriano et al. 2017; Terada et al. 2001). Although this type of battery has many benefits, there are some difficulties toward their usage. The possibility of ignition of the flammable organic electrolyte due to internal short circuiting and overcharging that may cause overheating and explosion (Li et al. 1994) is some of these important issues and also inability as well as undesired happenings of using conventional carbonate-based electrolytes in the condition of exposure to more than 4.3 V when are coupled with high-voltage cathodes (Liu et al. 2014).

On the other hand, oxidative decomposition and a solid non-permeable interface formation on the cathode that lowers the battery life cycle and also the shortage of Li$^+$ in a liquid electrolyte made interests to use solid-state batteries (SSBs) instead. In SSBs, the solid electrolyte is the physical barrier between anode and cathode while permitting Li-ions to permeate, where its avoidance of dendrite growth makes it possible to use Li metal as the anode. The solid electrolyte has the ability to work in a wide temperature range that is an important advantage at high temperatures. Also good chemical and potential stability are essential to avoid electrode unwanted reactions and having good stability against cathodes with high voltages (Campanella et al. 2021).

Although polymer materials have many advantages, there are some major limitations with them. Ion conducting and electronic insulating are two important required properties of solid electrolytes while most of the polymer materials have little electronic conduction but usually show a low value of cationic transference. Moreover,

poor mechanical strength, rapid deterioration in the case of coupling with Li-metal anodes, and limited cationic transfer, which could lead to local inhomogeneities at the electrode interface that consequently could cause dendrites formation and conductivity loss in sequence (Brissot et al. 1999), are other limitations for using polymers as a solid electrolyte.

For improving mechanical properties of polymer electrolytes, some studies have been done. But the more mechanical properties improve, the more ionic conductivity decreases (Snyder et al. 2007). Inorganic solid electrolytes like oxides ($Li_7La_3Zr_2O_{12}$ (Murugan et al. 2007), $Li_{3x}La_{2/3-3x}TiO_3$ (Inaguma et al. 1993)) beside sulfides ($Li_{10}GeP_2S_{12}$ (Kamaya et al. 2011), $Li_7P_3S_{11}$ (Braga et al. 2016)) and phosphates ($Li_{1+x}Al_xGe_{2-x}(PO_4)_3$ (Fu 1997a), $Li_{1+x}Al_xTi_{2-x}(PO_4)_3$ (Fu 1997b)) are kinds of porous ceramic materials that have the property of Li-ion conduction while providing better mechanical strength (Campanella et al. 2021). The evolution of solid electrolyte in recent years is provided in Fig. 8.

Metal-air batteries are another type of battery in which a gas diffusion electrode (GDE) controls the oxygen transport process (Dhanushkodi et al. 2015). Most commercial GDEs consist of a bilayer structure one with macroporosity and another with microporosity with deposited electrocatalyst (Dhanushkodi et al. 2015; Jayakumar et al. 2017; Omrani and Shabani 2019; Ozden et al. 2018; Schweiss et al. 2016). Moni et al. utilized a silicon oxycarbide porous conductive ceramic instead of carbon nanotubes as an α-cathodic gas diffusion layer that increased oxygen diffusion rate and the battery's cycle life (Moni et al. 2020).
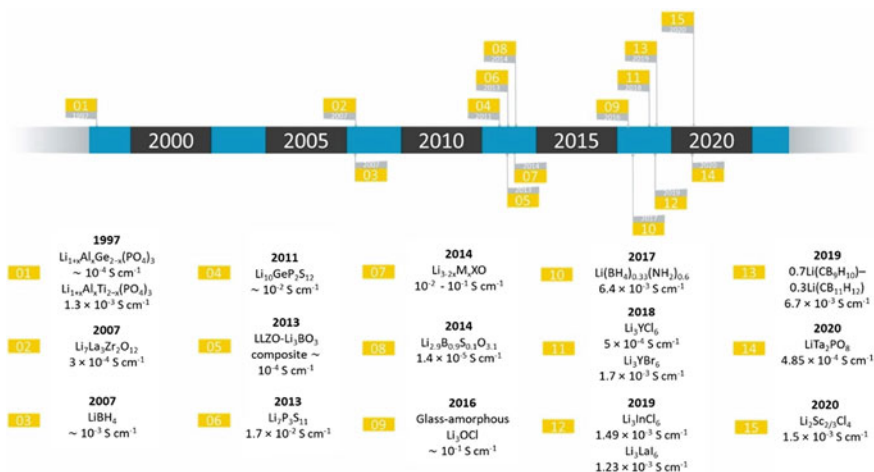
Fig. 8 Examples of solid electrolyte evolution in recent years. Reprinted from Campanella et al. (2021) with permission from Elsevier

4.2 Photo-Fenton

Micropollutants (MPs), which are increasingly found in wastewater streams, groundwater, surface water, and landfills, are creating concerns worldwide (Adamson et al. 2017; Karges et al. 2018; McElroy et al. 2019; Mohr et al. 2020; Sun et al. 2016; Tian et al. 2017). The recalcitrant nature of some micropollutants made scientists seek for advanced oxidation processes (AOPs) for degrading these pollutants according to the formation of non-selective and highly reactive radicals like $\cdot OH$, SO_4, and $\cdot Cl$ (Mao et al. 2018; Varanasi et al. 2018; Wei et al. 2019). Photo-Fenton is one of these advanced oxidation processes that Xue et al. studied. They deployed a porous ceramic membrane with a photocatalyst of goethite (α-FeOOH) coat to create a photo-Fenton reactive membrane. The mentioned membrane led to removing 1,4-dioxane up to 16% in combination with H_2O_2 and UV_{365} irradiation (Xue et al. 2021).

4.3 Fuel Cell

Fuel cells are attracting attention for use in different applications, ranging from stationary ones to transport and portable power. They have different types that operate in different temperatures and usually named according to the type of electrolyte material or fuels are used. High-energy density, high efficiency, low chemical emissions, high-quality power, and fuel flexibility are some of their advantages (Badwal et al. 2014). Porous ceramic membranes are ideal cases to use in such cells for their ability to conduct ions and also their physical properties like high-temperature stability.

4.3.1 Solid Oxide Fuel Cell

A solid oxide fuel cell (SOFC) is a kind of fuel cell that operates by using some gases like H_2 and CO as fuel. The operating temperature for this kind of fuel cell is between 700 and 1000 °C, in which an oxygen ion goes through the electrolyte toward the anode and reacts with H_2 and/or CO to produce water and CO_2 as shown in Fig. 9. In a research study, Dogdibegovic et al. used a more conductive and thinner, porous ceramic of 10Sc1CeSZ instead of conventional yttria-stabilized zirconia (YSZ) to improve the efficiency of metal-supported solid oxide fuel cell (MS-SOFC). The cathode catalyst was also replaced by Pr_6O_{11} with Ni content, which reached a peak of 1.56 W/cm^2 for exposure to air at 700 °C (Dogdibegovic et al. 2019).
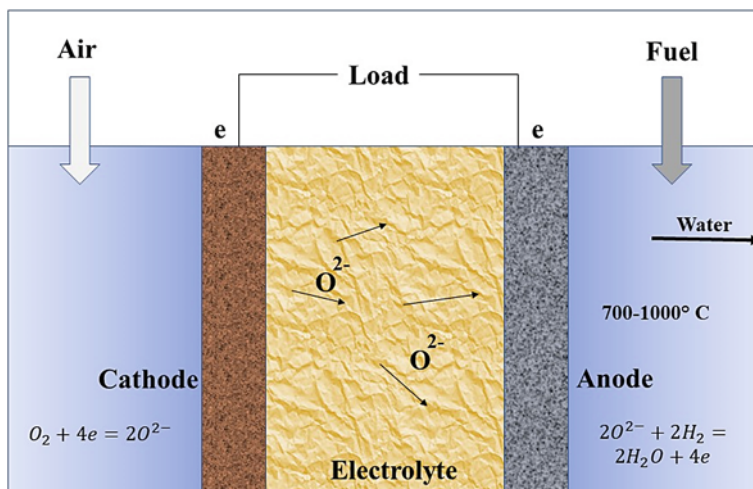
Fig. 9 Schematic of SOFC operation

4.3.2 Microbial Fuel Cell

According to the action of exo-electrogens, microbial fuel cells (MFCs) can produce electricity from the wastewater (Do et al. 2020). By means of these fuel cells, not only electricity could be produced but also wastewater would be treated. The biggest problem in using these kinds of fuel cells is their high production cost (Gajda et al. 2020). In this regard, Rodriguez et al. presented a cost-effective microbial fuel cell with a Pt-free catalyst cathode. They presented a tubular microbial fuel cell with slip-casted porous ceramic and CuO-based catalyst that reached 40% higher-power density than previous MFCs (Rodríguez et al. 2021).

5 Filtration and Separation

Generally, filtration and separation are two main applications of ceramics including porous and dense ones. These features for porous ceramics are regarding their pore sizes, thicknesses, and surface porosity where filtration and permeation mechanisms are totally different and complex. The porosity of the porous membrane defines the mechanism of permeation. According to International Union of Pure and Applied Chemistry (IUPAC), ceramic membranes are divided into four branches. In macroporous membranes with pore size more than 50 nm, sieving is the dominant permeation mechanism, while in mesoporous (2–50 nm pore size), microporous (less than 2 nm pore size) and dense ceramic membranes (without porosity), and permeation mechanisms are Knudsen diffusion, micropore diffusion, and diffusion, respectively (Koros et al. 1996).

Usually, ceramic membranes consist of a macro-porous layer as support, one or two layers of mesopore material as a bridge of porosity difference, and finally a layer of micropore or dense for separation purposes. These membranes can be only fabricated from one material or combinations of them. The most common materials for ceramic membranes are Al_2O_3, TiO_2, ZrO_2, SiO_2, etc. For having such multilayer membranes, a multistep process is required (Li 2007).

Ceramic membranes are fabricated in different shapes like plate, disk, tubular form, etc., according to their applications. One of the aims of having different shapes is increasing the surface area to volume ratio to achieve better efficiency in separation. Creating multichannel membranes is one of the methods to increase the surface area (Hsieh et al. 1988). Other actions to increase surface are making ceramic tubes, honeycomb channels, sandwiched sheets with spacers, and hollow fiber modules that create various spaces with different area to surface ratio for materials to be permeated through (Dyer et al. 2000).

5.1 Hot-Gas Filtration

The interest in removing particles from the hot gas is growing due to its advantages rather than cold filtration. The main benefits of this kind of filtration are (1) very high dew points, (2) the possibility of implementing energy conservation, (3) protecting the units of downstream heat recovery, and (4) being able to simplify the process (Li et al. 2021b). Also, there are other beneficial points, like lower-pressure drop during the filtration process as well as removing other pollutants and contaminants like SO_2 and HCl with dry reactions (Deng et al. 2019; Szul et al. 2020). It is also preferable to add some catalysts in order to functionalize the process to remove volatile organic compound (VOC) oxidation and NO_x.

According to high-temperature environment of hot gases that could possibly reach 1000 °C, some of the conventional methods like dedusting and filtering by cyclones, bag fabric filters, and electrostatic precipitators (ESP) cannot fully meet the required removal efficiency and energy recovery. According to the above points, seeking methods and materials to filter hot gases is important. One of the materials that have both properties of filtration and withstanding high-temperature is porous ceramics. The stability of this kind of materials in high temperature attracts many attentions to them. In this regard, Szul et al. presented membranes to simultaneously dedust and adsorb contaminants of syngas. The experiments were operated at the temperature of 350–500 °C, and the differential pressure of the filter was about 1–2 kPa. They evaluated the performance of the membranes including CaO, CaO–MgO, and AlO–SiO in high-molecular-weight tar, and Cl showed that these membranes can be used in the first sections of syngas purification (Szul et al. 2020).

In another study, Eterigho-Ikelegbe et al. studied the separation of a gas mixture. They used a nanocomposite of sodalite/α-Al_2O_3 tubular membrane produced by pore-plugging hydrothermal (PPH) synthesis in order to separate the H_2/CO_2 mixture. The experiments were done for single gas, and the mixture in different temperatures that

the results revealed that increasing the temperature highly affects H_2 permeation (Eterigho-Ikelegbe et al. 2020).

Another application of hot-gas filtration using porous ceramic membranes is related to the high demand for the oxygen purification industry. As described in ion exchange subpart of this chapter, the permeation of oxygen under different atmospheres, including air or CO_2, happens at high temperatures which are above 800 °C. The point is that by using porous ceramic membrane at that temperature, the high selectivity of oxygen, rather than other gases like N_2 or CO_2, is observed, and high purification of resulted oxygen could be expected.

5.2 Fluid Separation

Porous ceramic membranes, regarding their characteristics such as thermal and chemical stability, higher porosity, pore size, and mechanical strength are obtaining growing attention for separation and filtration processes (Dong et al. 2012; Hofs et al. 2011). Indeed, fluids separation is one of the main applications of porous ceramic membranes. One of the worrying issues in recent years is water pollution for oil spillage and also the production of oily wastewater regarding industrial development in areas like petrochemicals, transportation, and steel (Hubadillah et al. 2020; Statistics 2010). According to the limitations, some conventional separation methods are justifiably gleaning more attention, such as de-emulsification, air flotation, gravity separation, coagulation, and flocculation (Bensadok et al. 2007; Binner et al. 2013; Stack et al. 2005; Zhong et al. 2003) for their low efficiency, complex operations, and expenses, using porous membranes—especially ceramic ones (Koros and Mahajan 2000). In a research study on oily–wastewater separation, Hubadillah et al. used kaolin hollow fiber membrane (KHFM) at room temperature with a pressure of 2 bar to remove 99.99% of oil from water that the process and some experimental samples are shown in Fig. 10 (Hubadillah et al. 2020). In another study, Liu et al. utilized a dual-layer hollow fiber ceramic composite membrane with inner and outer α-Al_2O_3 powders doped in order to achieve 97.5% of oil rejection in oily–water separation (Liu et al. 2020). Hollow fiber ceramic membranes showed proper efficiency in oil–water separation. Raji et al. rejected 97% of oil by using a low-cost magnesium bentonite hollow fiber ceramic membrane. The process was done with a high flow rate of 544 l/m^{2}h and under a pressure of 3.5 bar (Raji et al. 2020). On the other hand, Kamarudin et al. presented a green ceramic hollow fiber membrane (h-MCa) by using metakaolin and corn cob ash that resulted in a higher flow flux of 1359.93 L/m^{2}h with an oil removal efficiency of 74.73% (Kamarudin et al. 2020).

In terms of industrialization and negative impacts of burning fossil fuels, seeking renewable and sustainable energy which decreases emission of pollution and heat trapped gases is essential (Shuit et al. 2012). Biodiesel, as a biodegradable fuel with no toxicity, has high similarity to petroleum-derived fuels, and its low cost and available sources made it a good choice for future energies (Atadashi et al. 2011; di Bitonto and Pastore 2019; Fonseca et al. 2019). In a research study on the purification
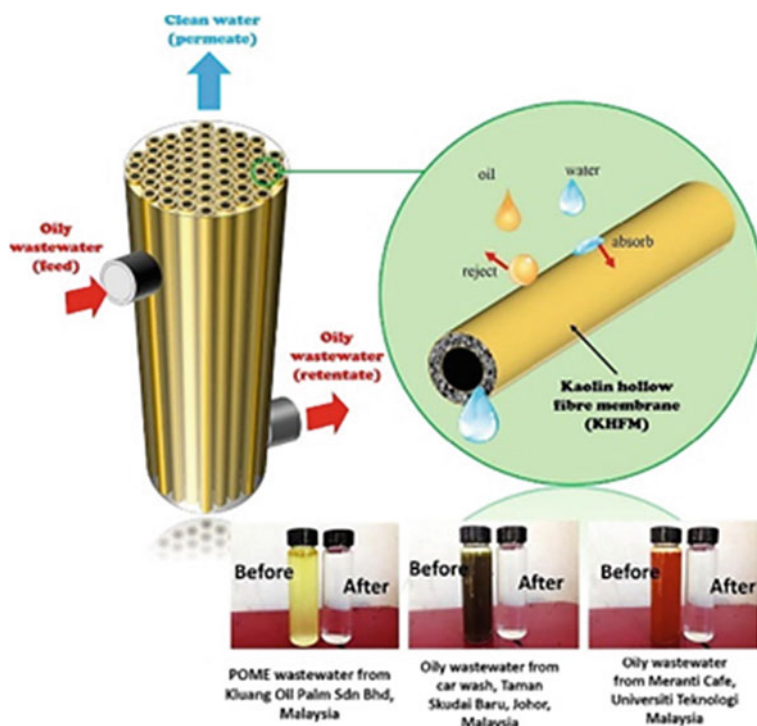
Fig. 10 Oil rejection by kaolin hollow fiber membranes (KHFM). Reprinted from Hubadillah et al. (2020) with permission from Elsevier

of biodiesel, Moreira et al. deployed α-Al_2O_3/TiO_2 porous ceramic membrane in the presence of acidified water to separate glycerol. The separation process, which was performed at 50 °C temperature and flow rate of 700 l/h, showed a high efficient separation and great reduction in water consumption for 1 g of biodiesel purification in comparison with conventional methods (Moreira et al. 2020).

In other applications of fluid separations by using porous ceramic membrane, Wang et al. used NaA zeolite membranes on the inner surface of four-channel ceramic hollow fibers in order for ethanol and water separation in 75 °C (Wang et al. 2018).

Water transfer through porous media imitates some systems that can be found in nature (Fisher et al. 2017; Hillel 2013); soils, crushed ores, and transpiration are some prominent examples of these systems. Membrane distillation (MD) is one of the systems that uses similar phenomena and is used for desalination of ocean water by using a porous hydrophobic membrane (Drioli et al. 2015; Khayet 2011; Souhaimi and Matsuura 2011; Wang and Chung 2015). If the process comprises a stream of hot salty water on one side and cold deionized water on the other, it is called direct-contact membrane distillation (DCMD) (Souhaimi and Matsuura 2011). In a recent research study, Subramanian et al. evaluated the potential of a superhydrophobic nano-porous ceramic for direct-contact membrane distillation. They used nano-porous anodized

aluminum oxide (AAO) ceramic membrane for desalination of seawater at 70 °C with the stream of 19 °C deionized water at the other side (Subramanian et al. 2019).

5.3 Filtration of Molten Metals

Non-metallic inclusions could affect the mechanical properties of metals like their strength, machinability, and toughness. In this regard, this inclusions' removal from molten metals is a great step to achieve high-quality products (Hoppach et al. 2020). The high-temperature atmosphere of the process environment restricts the usage of many filtering methods. Ceramic-foam filters due to their high thermal resistance and high mechanical properties such as high strength while having a complex network of cavities are good candidates for use as molten metal filters. In the following paragraphs, some of the aspects of different ceramic foam filters for molten metal filtration are presented.

5.3.1 Aluminum

In a research study, Demir fabricated a ceramic foam filter of Al_2O_3 with bentonite to filter molten aluminum and aluminum alloys. The reticulated ceramic membrane that was made by using replica technique and bentonite as a binding agent between the alumina particles showed a better performance of sponge-like ceramic filters in laminar flow and controlling the velocity of molten aluminum rather than honeycomb ceramic filters (Demir 2018). There are different ways to remove some impurities like adding some chemicals or by in-line spinning nozzle units, furnace fluxing, and so on. But some impurities that are referred to as non-reactive like Fe and Si are very hard to remove by ordinary fluxing processes (Damoah and Zhang 2011). Although there are some methods to remove impurities by reactions, the need to remove reaction impurities is another problem (Gorner et al. 2006). AlF_3 is a choice for alkali and alkaline earth metals removal from molten aluminum. Therefore, Damoah and Zhang deployed an Al_2O_3 ceramic filter with AlF_3 coating in order to remove impurities from molten aluminum. Their theoretical calculations revealed that the AlF_3-coated ceramic filter could achieve above 99% of Ca removal within 30 s of the residence time of molten aluminum featuring the filter (Damoah and Zhang 2011).

In a comparison between SiC and Al_2O_3 ceramic filters that were done by Bao et al., the wettability of the SiC filter was better than alumina filters, while the time-dependent filtration behavior of alumina membrane was better than the SiC filter. Although the Al_2O_3 filtration efficiency was increased during a one-hour test, while it decays faster for SiC filter, the SiC ceramic filter required less pressure drop in the filtration process that made it a clear choice for molten metal filtration (Bao et al. 2016).

5.3.2 Steel

Ceramic-foam filters made of zirconia and carbon-bonded alumina have been used in molten steel filtration for many years. But the disadvantage of creep exhibition in zirconia filters and shrinkage in carbon-bonded filters, which causes a decrease in molten steel flow rate made scientists seek a way for overcoming this problem (Aneziris et al. 2008; Emmel et al. 2014). The combination of Al_2O_3–C and MgO–C ceramic filter materials could lead to spinel forming that leads to expansion in the material and counteracts the filter shrinkage (Bavand-Vandchali et al. 2009; Mazzoni et al. 2003; Sainz et al. 2004; Tripathi and Ghosh 2010). In this regard, Emmel et al. presented an in-situ spinel-formation method for Al_2O_3–MgO–C ceramic foams to filter steel melt. The study revealed that the formation of spinel, which was increased by aumenting the heating temperature during the filtration process reduced the overall shrinkage of the filter, and avoided a permeation reduction. On the other hand, it caused a more stable flow rate in comparison to current filters and made it easier to create bigger filters for higher casting capacities due to its improved thermal-shock performance (Emmel et al. 2014).

As mentioned before, the Al_2O_3–C ceramic is one of the mainly used filters for molten steel filtration. Its high creep resistance, low weight, and thermal mass are beneficial in filtration applications (Aneziris et al. 2008). But the reaction between alumina-C filter with steel catalyzed by iron causes CO gas generation, the steel carbon take-up, and the creation of a new phase (Khanna et al. 2012). To overcome this problem, Gehre et al. presented two coatings for alumina-C ceramic foam filters. They compared use of porous alumina coated by slip spraying and dense alumina coated by flame spraying. The results demonstrated that slip-sprayed alumina coating showed some cracks and also some small plate-like crystals and vitreous alumina-bearing layer formation, while for flame-sprayed coating, these problems did not occur, and it also covered by alumina-graphite cracks too. Oxygen reduction was observed in the melt in both cases, and this drop was more for flame-sprayed coating. This suggested using alumina coating with the flame-spraying method for alumina-graphite ceramic foam filters to utilize in steel industries (Gehre et al. 2018).

5.4 Microfiltration

There are many organic and inorganic particles in water sources that could be potentially dangerous for human health. Indeed, the demand for high-quality water has made scientists seek ways of achieving the purpose. Centralized water treatment facilities, especially for drinking purposes, are challenging due to their expense, personnel demand, their way of operation, and maintenance (Mkandawire and Banda 2009). Porous ceramic filters (PCF) are one of the most efficient, low-cost, and facile-operation materials to use as microfilters (Abebe et al. 2016; Huang et al. 2018). Other advantages of porous ceramic membranes for use in filtration are their low-energy consumption, as they can even be used for water purification by using water

gravity, together with the availability of raw materials for ceramic membranes, such as clay and other natural substances (Farrow et al. 2018; Thi Thuy et al. 2013). Diana et al. utilized a porous ceramic membrane from mixed clay and fly ash material with different mixtures to create a filter to remove *Escherichia coli* (*E. coli*) bacteria in river water for drinking purposes. They sintered different mixtures at 700 °C and filtered the water at various operating pressures. The results showed that the mixture of 40% clay–60% fly ash can remove *E. coli* up to 99.048% under 0.25 bar operating pressure (Diana et al. 2019).

Although using porous ceramic membranes is very interesting, it has its own challenges too. Trapped micro-pollutants in the filter are one of the reasons that make it hard to use this kind of filters (Murphy et al. 2010). Unfortunately, this blockage of filters becomes worse with the progress of time, as it grows and reduces the performance and permeation of the filters drastically. In a research study by Liu et al., a high-permeability alumina ceramic membrane, which was synthesized by using UV curing-assisted drying method before sintering, was used to filter a slurry of TiO_2. The results revealed that, although good permeation and rejection performance were observed, the permeation flux was reduced during the time (Liu et al. 2018). Seeking a way to overcome this problem is essential.

In a study, Zhao et al. used a porous ceramic disk filter functionalized with Fe/TiO_2 nanocomposite to remove *E. coli* from drinking water (Zhao et al. 2020). TiO_2 nanoparticles are semiconductors with photocatalytic properties that have a bactericidal function (Pelaez et al. 2012). The Fe/TiO_2 composite was a product of $NaBH_4$ chemical reduction (Diao et al. 2017; Liu et al. 2012), which coated on the porous ceramic filter made of rice husk and clay. The experiments took place with and without VIS and UV light (300–800 nm) irradiation that showed using coated filters could enhance the performance of bacteria removal due to porous media and the Fe/TiO_2 behavior of bactericidal action. The removal mechanism is depicted in Fig. 11.

In another study, Saifuddin et al. worked on optimizing a porous membrane made of clay and modified by activated carbon and zeolite which is combusted at 800 °C to remove Fe, Mn, and *E. coli* bacteria from peat water. The mixed behavior of zeolite and activated carbon in enhancing the chemical and mechanical properties of the porous ceramic membrane caused to remove 100% of Fe^{2+} and to reach removal efficiency of 99.94 and 82.58% of Mn^{2+} and total dissolved solids (TDS). They also reported that the ceramic membrane is able to reduce turbidity up to 95.65% (Saifuddin et al. 2020). Due to the antimicrobial action of silver and controlled release of Ag nanoparticles, Peng et al. presented a porous ceramic membrane that semi-encapsulated Ag nanoparticles grafted on it by means of a loose polyimide (PI). They showed that Ag nanoparticles with the size of 50–80 nm were uniformly embedded on the surface of grafted PI-enhanced antibacterial activity as well as silver stability and anti-biofouling performance of the membrane in bovine serum albumin and *E. coli* filtration (Peng et al. 2020).

As a filter in the separation process, high permeability and selectivity are desirable. Obtaining high permeability is referred to the use of coarse grain size for making porous membrane (Awang Chee et al. 2020). But the coarse grain size of containing
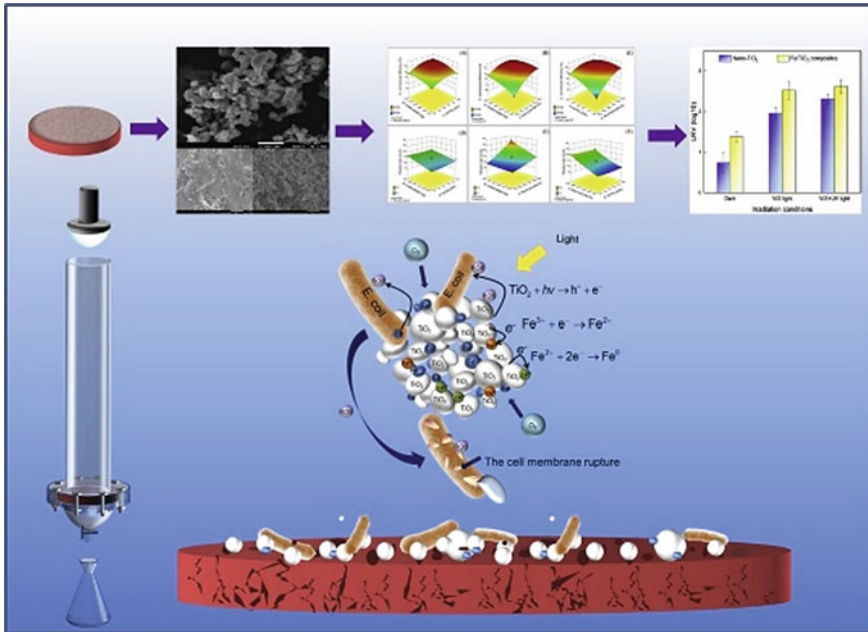
Fig. 11 *E. coli* removal mechanism of porous ceramic membrane functionalized with Fe/TiO$_2$. Reprinted from Zhao et al. (2020) with permission from Elsevier

materials in a porous media requires higher sintering temperature and also decreases the mechanical properties of the media too. In this regard, Awang Chee et al. worked on the influence of particle size of alumina hollow fiber for protein separation. They showed that a high amount of coarse particles produced more porous media, since finer sizes caused better mechanical properties. They achieved up to 66% of bovine serum albumin (BSA) rejection (Awang Chee et al. 2020). The mentioned process is depicted schematically in Fig. 12.

Gas–solid separations a one of the issues that has gained in importance due to the aggravation of air pollution. Fine particulate matter (PM$_{2.5}$) is a pollutant that can affect human health seriously (Shi et al. 2018). Indeed, the filtration of different dusty particles that are emitted from some industries like cement factories, metallurgical industries, and thermal power plants is essential in order to avoid the entrance of these fine particles into the air. Although some filters such as bag filters can reduce them, the high-temperature environment in some cases does not allow to use them (Saleem and Krammer 2007; Zhou et al. 2012). There are some other methods like electrostatic precipitators (Gallimberti 1998), and its expense makes it hard to use; however, its filtration efficiency is high. Using porous ceramic membrane is a highly efficient and low-cost solution for this problem. In this regard, Song et al. deployed a ceramic membrane by using short fibers in order to reject solids from gas with low filter resistance and high filtration efficiency. They compare two different ceramic membranes made of Al$_2$O$_3$ powders and CaO–MgO–SiO$_2$ ceramic fibers

Alumina Particle Size Distribution
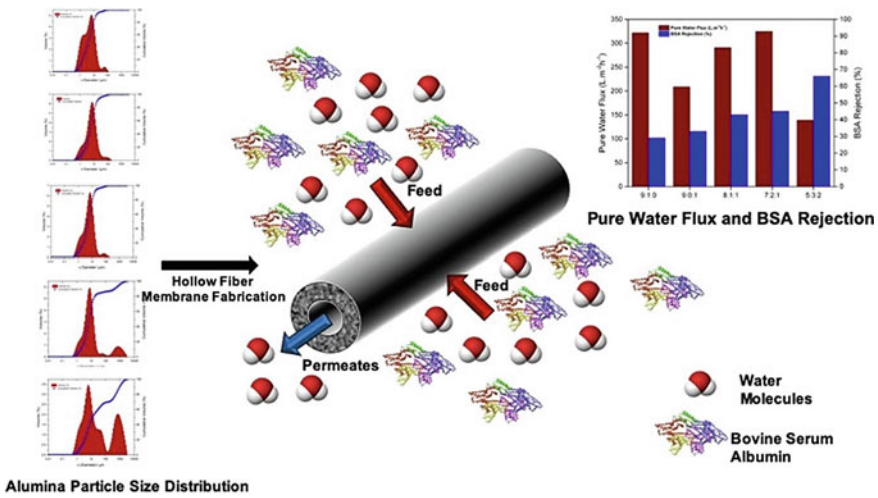
Fig. 12 Hollow aluminum fiber BSA protein filtration. Reprinted from Awang Chee et al. (2020) with permission from Elsevier

that are coated by carboxymethyl cellulose (CMC) for this purpose. These results have demonstrated that the membrane made of short ceramic fibers has an excellent filtration performance, while its regeneration performance was better than the membrane made of ceramic powders (Song et al. 2018).

6 Functional Materials

According to the broad variety of applications in which ceramics, and especially advanced ceramics, play a role, they can be divided into two main parts of structural and functional ceramics, in which functional ceramics assign a larger part to itself. Although ceramics are reasonably established, functional ceramics have a key role in modern technology development. Functional materials are used in different industries, according to their wide range of applications. It is worth noting that their production value is three times larger than structural ceramics, and it has reached 7 billion USD in 2009 (Yin et al. 2010). They are fabricated through various compounds such as zinc, silicon, titanium, lithium, manganese, gallium, indium, copper, aluminum, and boron and are utilized in different industries such as smart labels manufacturing, smart packaging, PCBs and electronic devices, computers, telecommunication, and space technology. The big part of growth in the market is due to the rapid progress of electric and electronic industries in developed regions.

On the other hand, reflecting on the increasing usage of porous ceramics in different applications from aviation and aerospace to chemical processes and filtration, the need to improve the properties of these membranes in order to achieve better

characteristics is essential. Although they presented some features, like a lightweight nature, high strength (Hwa et al. 2017; Zocca et al. 2015), and high-temperature resistance, their complex molding processes, as well as poor toughness, are some of their disadvantages (Ben et al. 2017; Eckel et al. 2016; Li et al. 2018b). 3D-printing methods facilitate the complex structure fabrication of porous ceramic membranes with high precision (An et al. 2017; Doreau et al. 2000; Mei et al. 2019; Ngo et al. 2018; Owen et al. 2018). Mei et al. studied the structure design and sintering temperature of a 3D-printed porous ceramic membrane of $Al_6Si_2O_{13}$ in order to optimize its compressive strength and fracture work and investigate 3D-printing influence on the final product. By increasing the sintering temperature, the compressive strength improved, but the fracture work was maximized at 1400 °C. They also showed that the compressive strength of structures with a coordination number of 6 was better than others and also a triangular hollow structure with 0° rotation angle exhibited the best bearing capacity among others (Mei et al. 2021). Figure 13 depicts 3D porous structures with different coordination numbers, while in Fig. 14, structures with different 3D-printed rotation angles are shown.

In order to improve the structure and properties of porous ceramic membranes, Yuan et al. presented a new pectin-based gel casting freeze-drying method to fabricate calcium hexaluminate (CA_6). They investigated the effect of solid contents on the properties of the final product and revealed that the membrane had a high degree of porosity, while introduced low thermal conductivity and good compressive strength (Yuan et al. 2021).

One of the areas that has been attracting growing interest is orthodontic appliances. Orthodontic materials, such as polycrystalline and monocrystalline alumina as ceramics and polycarbonate and polyurethane as polymers, are currently used to
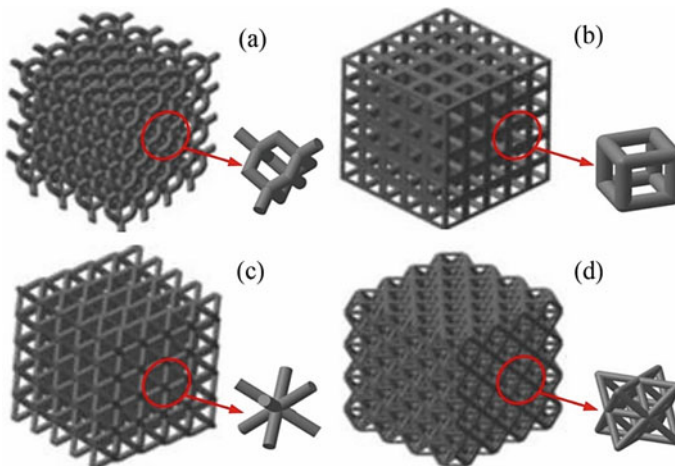
Fig. 13 Different 3D-printed structure with 4, 6, 8, and 12 coordination numbers. Reprinted from Mei et al. (2021) with permission from Elsevier
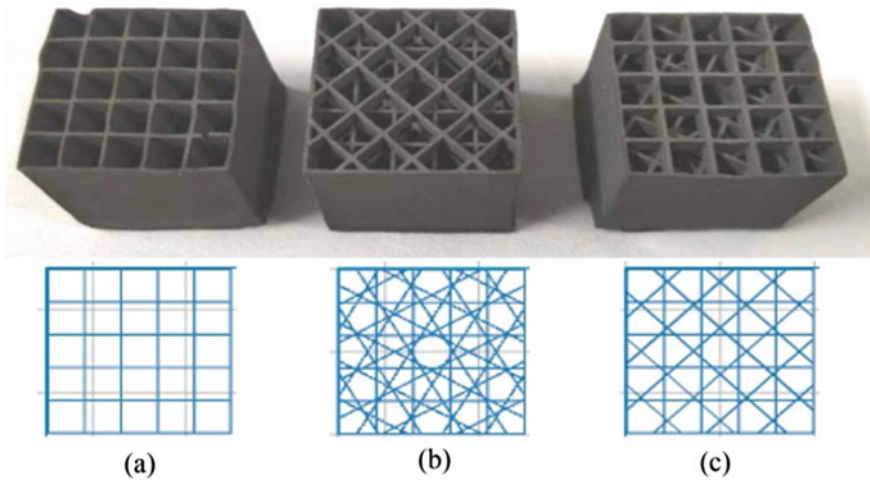
Fig. 14 3D-printed structures with **a** 0°, **b** 30°, and **c** 45° rotation angles. Reprinted from Mei et al. (2021) with permission from Elsevier

make fixed orthodontic brackets (Al-Jawoosh et al. 2020). According to the water absorption property of polymeric brackets that causes discoloration and also low wear resistance, as well as creep, their demand has decreased (Arici and Regan 1997; Faltermeier et al. 2007; Feldner et al. 1994; Göhring et al. 2005). On the other hand, good color stability and better wear resistance of ceramics (Eliades 2007; Karamouzos et al. 1997; Meguro et al. 2006), rather than polymers, could not conceal their adverse effects, such as excessive enamel wear due to high hardness, enamel surface fracture for their high compressive strength, and also their brittle nature (Arici and Regan 1997; Buzzitta et al. 1982; Douglass 1989; Jena et al. 2007). Therefore, Al-Jawoosh et al. worked on an alumina-polycarbonate (Al_2O_3-PC) composite material in order to achieve a combination of good strength and fracture toughness. The results revealed that the new composite could provide safe bonding and debonding, while it resists wear due to the rich ceramic surface. It has also eliminated creep that was seen in polymeric materials and led to a reduction in failures (Al-Jawoosh et al. 2020).

6.1 Flexible Porous Ceramics

As porous ceramics are rarely flexible, finding a way to functionalize ceramic membranes in order to provide flexibility as well as their common properties such as thermal stability, wear, creep, and corrosion resistance is promising. Silicon nitride (Si_3N_4) is one of the ceramic materials with balance features like toughness and mechanical properties (Qin et al. 2019; Yuan et al. 2019; Zeuner et al. 2011). It has also

the flexibility that due to the sintering in high pressure and high-temperature environment could be reduced and shows fragility (Li et al. 2018a; Zhang et al. 2017). Therefore, Yue et al. combined hard silicon nitride with soft MnO_2 nanowires to reach flexible ceramic membranes. Their flexible membrane, made with a facile vacuum filtration, anchored Si_3N_4 particles to porous flexible ultra-long MnO_2 nanowires. The membrane exhibited high porosity, superior flexibility, and high interface stability (Yue et al. 2020).

6.2 Dielectric, Ferroelectric, and Piezoelectric Effect

Some of the applications of porous ceramic membranes, including sensors, transducers, actuators, energy harvesters, and Wi-Fi communications, require some properties that are achieved via piezoelectricity, pyroelectricity, tunability, and electro-optic behavior of materials (Khachaturyan et al. 2016; Xu 2013). The porosity, as a defect in material structure, could play an important role in introducing some features, like acoustic-impedance reduction. This reduction is applicable in medical ultrasound, non-destructive testing, SONAR, and mechanical parts (Bosse et al. 2012; Challagulla and Venkatesh 2012). In high-strain actuators and ferroelectric memory, porosity has effects on fatigue behavior of the material in multiple polarization reversals (Jiang and Cross 1993). Curecheriu et al. investigated functional properties of porosity effects in lead-free piezoelectric $BaZr_{0.15}Ti_{0.85}O_3$ porous ceramics. The study, in which the porous material was prepared by using PMMA microspheres as a sacrificial template, revealed that by pore interconnectivity and anisotropy control, features of permittivity and tunability of the porous ceramic could be controlled (Curecheriu et al. 2020). Therefore, achieving different properties for the mentioned applications is reachable via porous ceramic materials.

7 Combustion and Fire Retardance

Regarding the thermo-mechanical behavior of ceramic materials, they can be used in different multifunctionality applications. The utilization of these materials includes structures which are lightweight (Evans et al. 1998) and are intended for energy-absorption systems (Ashby et al. 2000), absorption of sounds (Lu et al. 1999), heat exchangers (Lu et al. 1998), porous burners (Gauthier et al. 2008), combustion (Bubnovich et al. 2021), and fire retardant (Lu and Chen 1999). In this section, the last two applications will be explained in more detail.

7.1   Combustion

Efficient use of energy is a very important issue due to the shortage of sources and also environmental problems, which are multiplying around the world. One attractive area that has gained important traction in recent years is the technology of using porous media in combustion. This issue has its own difficulties such as material selection and the strategy of flame stabilization within porous media (Gao et al. 2014; Howell et al. 1996; Trimis 2000; Trimis and Durst 1996; Zheng et al. 2010). Although it may take a lot of effort to solve such problems, the beneficiary of this technology, as opposed to conventional free-flame combustion, is not negligible. Some of the important advantages of porous ceramic combustion, besides high radiation, hinge on combustion stability in a range of equivalence ratio, $0.4 < \varphi < 0.9$, very low dangerous gases emissions (CO and NO_x), energy concentration, high combustion efficiency, and a wide range of power modulation (Bubnovich et al. 2021).

The necessity of flame stabilization lies in a predefined and specific part of porous material and low dangerous gases (CO and NO_x) emissions, while having high process efficiency and are the two most important issues in the applications of such stationary-régime operating burners (Trimis and Durst 1996). Flame stabilization by two porous-media layers for the upper and lower parts which have a Péclet number lower and higher than 65, respectively, is that one of the methods is utilized for porous-media combustion (Babkin et al. 1991; Trimis and Durst 1996). Another method includes after-burning zone cooling at the outlet of the burner (Bouma and De Goey 1999; Brenner et al. 2000). The third method lies in implementing a periodic change between the input of reactants and the output of the products of combustion by a reciprocating flow reactor (Contarin et al. 2003; Hoffmann et al. 1997). The last method lies in making variations in a porous-media cross section of the burner (Bakry et al. 2011).

The most popular method for industrial applications is using two-layer porous-media burners. The design of these types of burners is divided into two parts, in line with the gas flow direction. The pore size of the first part is less than the critical size (~30 pores per centimeter, ppc), and the pore size of the second part is much bigger than the critical size (~4 ppc). The Péclet number also is defined as follows according to the pore size:

$$Pe = S \cdot d \cdot c_p \cdot \rho / \lambda$$

where S is free laminar flame speed, d is the equivalent pore diameter, c_p is the specific heat of gaseous mixture, ρ demonstrates the density of the mixture of gases, and λ is their mixture thermal conductivity. Due to the fact that flame development and extinguishment happen for Péclet numbers of more than 65 (Pe > 65) and less than 65 (Pe < 65), respectively, the stabilization of the flame could be in the interface of porous structures with different pore sizes (Bubnovich et al. 2021).

Volatile organic compounds (VOCs) are some kind of dangerous pollutants that are the result of production processes. One of the environmental issues is controlling

these compounds and their vapors and in avoiding their emission into the air. There are two ways to control these compounds: The first, which is more complex and expensive, entails their recovery from contaminated air, and the second (more inexpensive and more facile) way is to burn them. Bubnovich et al. presented a two-layer porous ceramic burner in order to overcome this problem. They examined different types of porous media with different shapes and materials to achieve better performance of the burner. Finally, they reached the minimum propane–air ratio of $\varphi = 0.5$ for flame stabilization. The process was without CO and NO_x emissions that showed an almost complete burn during combustion (Bubnovich et al. 2021). Hashemi et al. studied the effect of different porous walls on flame stability and its temperature distribution. They evaluated the relations of the inner diameter of porous wall, pore density, and porous wall length on flame stability and the flame's axial temperature (Hashemi et al. 2020).

7.2 Fire Retardance

The equivalent thermal conductivity of the foam is responsible for their fire-resisting property. Increasing reach time of the material to critical temperature is due to its low thermal conductivity, and it gives more time to the unexposed part of the material to reach high temperatures. For example, in the case of aluminum foams, when they are exposed to fire and high temperature, the oxide coatings that existed in the surfaces of the foam act as a barrier toward heat transfer and also avoid structural collapse even if the inner part of the structure exceeds the melting temperature for the solid phase of the material (Coquard et al. 2012).

As an example of porous ceramic application regarding its fire-resistant property is useful to consider here. Rashad, in an insightful overview, studied a lightweight expanded clay aggregate (LECA) as a porous ceramic for the application as a building material. LECA is a non-combustible ceramic foam, which can increase fire resistance for different applications, and is also a good choice for a thermal insulator, owing to its intrinsically low thermal conductivity. On the other hand, by combining LECA with other materials, the fire resistance of the resulting composite will be increased, as observed in some concrete containing LECA or some geopolymers (Rashad 2018). In another study, and according to the multifunctional performance of ceramic foams, Zhang et al. studied the effect of porous materials on gas explosion propagation. The results revealed that ceramic foams have a good capacity for fire resistance, according to a large number of conducted experiments, and featured good blast-wave attenuation that made them suitable for use in such applications (Zhang et al. 2013).

8 Conclusion and Future Trends

Ceramic materials have, justifiably, enjoyed increasing research focus in recent years, due to their judicious combination of various intrinsic desirable properties (e.g., inter alia, chemical/thermal stability, mechanical strength, abrasion resistance, good permeability, etc.) and great promise in a wide variety of industrial applications, are getting more attraction due to their superior properties and characteristics. In this chapter, we have discussed, in particular, porous ceramic membranes and their industrial applicability vis-à-vis physical, mechanical, chemical, and thermal characteristics of industrial applications, focusing, in part, on their underlying synthesis. In terms of applications per se, we have also reviewed ion exchange, filtration and separation, catalyst carriers, functional materials, porous electrodes and membranes, and, of course, combustion and fire resilience.

In terms of future prospects and challenges, we have identified herein, albeit in a preliminary manner, that a universal underpinning theme to porous ceramics design lies in both the control, manipulation and characterization of defect and pore size distributions. To achieve tangible future progress in this field, this is the great underlying challenge and prospect—in a very real sense, one and the same. In this respect, the establishment of "molecular-design rules" is of paramount importance to realize this goal.

Elaborating on this universal underlying challenge, another important future direction in and porous ceramics design, characterization, and analysis lies in the application of molecular simulation as an important and canny strategy in accompanying experimental materials development and characterization. Using both empirical potential models and electronic structure methods allows for the simulation of ceramic materials' atomic- and nanoscale defects and surface/bulk features; indeed, the extraction of *in-silico* spectroscopy results from these prototype systems is most instructive. Pragmatically, these simulation predictions can then be compared and validated with experiment in a process of "spectral matching," with iterative potential model refinement or *in-silico* "molecular redesign." Most excitingly, moreover, this approach can be applied to predictive materials design as a prototyping tool in porous ceramics discovery, akin to "materials genomics." In such a way, we may determine, a priori, molecular design rules and paradigms for desirable spectral features from molecular simulation and "tune" material properties, such a defects and nanoscale geometry features, to arrive at optimal porous ceramics "catalogs" equipped for the bespoke industrial application at hand.

References

Abebe, L.S., Chen, X., Sobsey, M.D.: Chitosan coagulation to improve microbial and turbidity removal by ceramic water filtration for household drinking water treatment. Int. J. Environ. Res. Public Health **13**, 269 (2016)

Adam, M.R., Othman, M.H.D., Kadir, S.H.S.A., Sokri, M.N.M., Tai, Z.S., Iwamoto, Y., Tanemura, M., Honda, S., Puteh, M.H., Rahman, M.A., Rahman, M.A., Jaafar, J.: Influence of the natural zeolite particle size toward the ammonia adsorption activity in ceramic hollow fiber membrane. Membranes (Basel) **10** (2020). https://doi.org/10.3390/membranes10040063

Adams, B.A., Holmes, E.L.: Adsorptive properties of synthetic resins. J. Soc. Chem. Ind. **54**, 1–6 (1935)

Adamson, D.T., Piña, E.A., Cartwright, A.E., Rauch, S.R., Anderson, R.H., Mohr, T., Connor, J.A.: 1, 4-dioxane drinking water occurrence data from the third unregulated contaminant monitoring rule. Sci. Total Environ. **596**, 236–245 (2017)

Al-Jawoosh, S., Ireland, A., Su, B.: Characterisation of mechanical and surface properties of novel biomimetic interpenetrating alumina-polycarbonate composite materials. Dent. Mater. **36**, 1595–1607 (2020). https://doi.org/10.1016/j.dental.2020.09.016

An, D., Li, H., Xie, Z., Zhu, T., Luo, X., Shen, Z., Ma, J.: Additive manufacturing and characterization of complex Al_2O_3 parts based on a novel stereolithography method. Int. J. Appl. Ceram. Technol. **14**, 836–844 (2017)

Aneziris, C.G., Ansorge, A., Jaunich, H.: New approaches of carbon bonded foam filters for filtration of large castings. In: Cfi-Ceramic Forum International, pp. E100–E103. Goller Verlag GMBH, Baden Baden (2008)

Arici, S., Regan, D.: Alternatives to ceramic brackets: the tensile bond strengths of two aesthetic brackets compared ex vivo with stainless steel foil-mesh bracket bases. Br. J. Orthod. **24**, 133–137 (1997)

Ashby, M., Evans, A., Fleck, N., Gibson, L., Hutchinson, J., Wadley, H., Delale, F.: Metal foams: a design guide (2000)

Atadashi, I.M., Aroua, M.K., Aziz, A.A.: Biodiesel separation and purification: a review. Renew. Energy **36**, 437–443 (2011)

Atkins, P.F., Scherger, D.A.: Review of Physical-Chemical Methods for Nitrogen Removal From Wastewaters. Elsevier Ltd (1975)

Awang Chee, D.N., Ismail, A.F., Aziz, F., Mohamed Amin, M.A., Abdullah, N.: The influence of alumina particle size on the properties and performance of alumina hollow fiber as support membrane for protein separation. Sep. Purif. Technol. **250** (2020). https://doi.org/10.1016/j.seppur.2020.117147

Babkin, V.S., Korzhavin, A.A., Bunev, V.A.: Propagation of premixed gaseous explosion flames in porous media. Combust. Flame **87**, 182–190 (1991)

Badwal, S.P.S., Giddey, S., Munnings, C., Kulkarni, A.: Review of progress in high temperature solid oxide fuel cells. J. Aust. Ceram. Soc. **50**, 23–37 (2014)

Bakry, A., Al-Salaymeh, A., Al-Muhtaseb, A.H., Abu-Jrai, A., Trimis, D.: Adiabatic premixed combustion in a gaseous fuel porous inert media under high pressure and temperature: novel flame stabilization technique. Fuel **90**, 647–658 (2011). https://doi.org/10.1016/j.fuel.2010.09.050

Bao, S., Syvertsen, M., Nordmark, A., Kvithyld, A., Engh, T., Tangstad, M.: Plant scale investigation of liquid aluminium filtration by Al_2O_3 and SiC ceramic foam filters (2016)

Bardhan, P.: Ceramic honeycomb filters and catalysts. Curr. Opin. Solid State Mater. Sci. **2**, 577–583 (1997). https://doi.org/10.1016/S1359-0286(97)80048-4

Bari, M.A., Kindzierski, W.B.: Ambient volatile organic compounds (VOCs) in Calgary, Alberta: sources and screening health risk assessment. Sci. Total Environ. **631**, 627–640 (2018)

Bavand-Vandchali, M., Sarpoolaky, H., Golestani-Fard, F., Rezaie, H.R.: Atmosphere and carbon effects on microstructure and phase analysis of in situ spinel formation in MgO–C refractories matrix. Ceram. Int. **35**, 861–868 (2009)

Beall, G.H., Duke, D.A.: Glass-ceramic technology. In: Glass: Science and Technology, p. 404 (1983)

Ben, Y., Zhang, L., Wei, S., Zhou, T., Li, Z., Yang, H., Wong, C., Chen, H.: Improved forming performance of β-TCP powders by doping silica for 3D ceramic printing. J. Mater. Sci. Mater. Electron. **28**, 5391–5397 (2017)

Bensadok, K., Belkacem, M., Nezzal, G.: Treatment of cutting oil/water emulsion by coupling coagulation and dissolved air flotation. Desalination **206**, 440–448 (2007)

Binner, E.R., Robinson, J.P., Kingman, S.W., Lester, E.H., Azzopardi, B.J., Dimitrakis, G., Briggs, J.: Separation of oil/water emulsions in continuous flow using microwave heating. Energy Fuels **27**, 3173–3178 (2013)

Bosse, P.W., Challagulla, K.S., Venkatesh, T.A.: Effects of foam shape and porosity aspect ratio on the electromechanical properties of 3–3 piezoelectric foams. Acta Mater. **60**, 6464–6475 (2012)

Bouma, P.H., De Goey, L.P.H.: Premixed combustion on ceramic foam burners. Combust. Flame **119**, 133–143 (1999). https://doi.org/10.1016/S0010-2180(99)00050-4

Braga, M.H., Murchison, A.J., Ferreira, J.A., Singh, P., Goodenough, J.B.: Glass-amorphous alkali-ion solid electrolytes and their performance in symmetrical cells. Energy Environ. Sci. **9**, 948–954 (2016). https://doi.org/10.1039/c5ee02924d

Brenner, G., Pickenäcker, K., Pickenäcker, O., Trimis, D., Wawrzinek, K., Weber, T.: Numerical and experimental investigation of matrix-stabilized methane/air combustion in porous inert media. Combust. Flame **123**, 201–213 (2000)

Brissot, C., Rosso, M., Chazalviel, J.-N., Lascaud, S.: Dendritic growth mechanisms in lithium/polymer cells. J. Power Sources **81–82**, 925–929 (1999). https://doi.org/10.1016/S0378-7753(98)00242-0

Bubnovich, V., Hernandez, H., Toledo, M., Flores, C.: Experimental investigation of flame stability in the premixed propane-air combustion in two-section porous media burner. Fuel. **291** (2021). https://doi.org/10.1016/j.fuel.2020.120117

Buzzitta, V.A.J., Hallgren, S.E., Powers, J.M.: Bond strength of orthodontic direct-bonding cement-bracket systems as studied in vitro. Am. J. Orthod. **81**, 87–92 (1982)

Campanella, D., Belanger, D., Paolella, A.: Beyond garnets, phosphates and phosphosulfides solid electrolytes: new ceramic perspectives for all solid lithium metal batteries. J. Power Sources **482**, 228949 (2021). https://doi.org/10.1016/j.jpowsour.2020.228949

Cerri, I., Saracco, G., Specchia, V.: Methane combustion over low-emission catalytic foam burners. Catal. Today **60**, 21–32 (2000). https://doi.org/10.1016/S0920-5861(00)00313-8

Challagulla, K.S., Venkatesh, T.A.: Electromechanical response of piezoelectric foams. Acta Mater. **60**, 2111–2127 (2012)

Chen, J.H., Liu, P.S., Cheng, W.: PBA-loaded albite-base ceramic foam in application to adsorb harmful ions of Cd, Cs and As(V) in water. Multidiscip. Model. Mater. Struct. **15**, 659–672 (2019). https://doi.org/10.1108/MMMS-07-2018-0140

Chen, Y., Wang, N., Ola, O., Xia, Y., Zhu, Y.: Porous ceramics: light in weight but heavy in energy and environment technologies. Mater. Sci. Eng. R Rep. **143**, 100589 (2021). https://doi.org/10.1016/j.mser.2020.100589

Chiara, A., Giannici, F., Pipitone, C., Longo, A., Aliotta, C., Gambino, M., Martorana, A.: Solid–solid interfaces in protonic ceramic devices: a critical review. ACS Appl. Mater. Interfaces (2020)

Choi, N.C., Cho, K.H., Kim, M.S., Park, S.J., Lee, C.G.: A hybrid ion-exchange fabric/ceramic membrane system to remove As(V), Zn(II), and turbidity from wastewater. Appl. Sci. **10** (2020). https://doi.org/10.3390/app10072414

Choubey, P.K., Kim, M.S., Srivastava, R.R., Lee, J.C., Lee, J.Y.: Advance review on the exploitation of the prominent energy-storage element: lithium. Part I: from mineral and brine resources. Miner. Eng. **89**, 119–137 (2016). https://doi.org/10.1016/j.mineng.2016.01.010

Contarin, F., Saveliev, A.V., Fridman, A.A., Kennedy, L.A.: A reciprocal flow filtration combustor with embedded heat exchangers: numerical study. Int. J. Heat Mass Transf. **46**, 949–961 (2003). https://doi.org/10.1016/S0017-9310(02)00371-X

Coors, W.G.: Protonic ceramic fuel cells for high-efficiency operation with methane. J. Power Sources **118**, 150–156 (2003)

Coquard, R., Rochais, D., Baillis, D.: Conductive and radiative heat transfer in ceramic and metal foams at fire temperatures. Fire Technol. **48**, 699–732 (2012). https://doi.org/10.1007/s10694-010-0167-8

Curecheriu, L., Lukacs, V.A., Padurariu, L., Stoian, G., Ciomaga, C.E.: Effect of porosity on functional properties of lead-free piezoelectric $BaZr_{0.15}Ti_{0.85}O_3$ porous ceramics. Materials (Basel) **13** (2020). https://doi.org/10.3390/ma13153324

Damoah, L.N.W., Zhang, L.: AlF_3 reactive Al_2O_3 foam filter for the removal of dissolved impurities from molten aluminum: preliminary results. Acta Mater. **59**, 896–913 (2011). https://doi.org/10.1016/j.actamat.2010.09.064

Das, D., Nijhuma, K., Gabriel, A.M., Daniel, G.P.F., Murilo, D.D.M.I.: Recycling of coal fly ash for fabrication of elongated mullite rod bonded porous SiC ceramic membrane and its application in filtration. J. Eur. Ceram. Soc. **40**, 2163–2172 (2020). https://doi.org/10.1016/j.jeurceramsoc.2020.01.034

De Araujo Scharnberg, A.R., Loreto, A.C.D., Wermuth, T.B., Alves, A.K., Arcaro, S., Santos, P.A.M.D., Rodriguez, A.D.A.L.: Porous ceramic supported TiO_2 nanoparticles: enhanced photocatalytic activity for Rhodamine B degradation. Bol. Soc. Esp. Ceram. Vidr. **59**, 230–238 (2020). https://doi.org/10.1016/j.bsecv.2019.12.001

Demir, A.: Fabrication of alumina ceramic filters and performance tests for aluminium castings. Acta Phys. Pol. A. **134**, 332–334 (2018). https://doi.org/10.12693/APhysPolA.134.332

Deng, Y., Ansart, R., Baeyens, J., Zhang, H.: Flue gas desulphurization in circulating fluidized beds (2019)

Dhanushkodi, S.R., Capitanio, F., Biggs, T., Merida, W.: Understanding flexural, mechanical and physico-chemical properties of gas diffusion layers for polymer membrane fuel cell and electrolyzer systems. Int. J. Hydrogen Energy **40**, 16846–16859 (2015)

di Bitonto, L., Pastore, C.: Metal hydrated-salts as efficient and reusable catalysts for pre-treating waste cooking oils and animal fats for an effective production of biodiesel. Renew. Energy **143**, 1193–1200 (2019)

Diana, S., Fauzan, R., Elfiana, E.: Removing *Escherichia coli* bacteria in river water using ceramic membrane from mixed clay and fly ash material (2019)

Diao, Z.-H., Xu, X.-R., Jiang, D., Liu, J.-J., Kong, L.-J., Li, G., Zuo, L.-Z., Wu, Q.-H.: Simultaneous photocatalytic Cr(VI) reduction and ciprofloxacin oxidation over TiO_2/Fe^0 composite under aerobic conditions: performance, durability, pathway and mechanism. Chem. Eng. J. **315**, 167–176 (2017)

Do, M.H., Ngo, H.H., Guo, W., Chang, S.W., Nguyen, D.D., Liu, Y., Varjani, S., Kumar, M.: Microbial fuel cell-based biosensor for online monitoring wastewater quality: a critical review. Sci. Total Environ. **712**, 135612 (2020)

Dogdibegovic, E., Wang, R., Lau, G.Y., Tucker, M.C.: High performance metal-supported solid oxide fuel cells with infiltrated electrodes. J. Power Sources **410–411**, 91–98 (2019). https://doi.org/10.1016/j.jpowsour.2018.11.004

Dong, H., Li, J., Li, Y., Hu, L., Luo, D.: Improvement of catalytic activity and stability of lipase by immobilization on organobentonite. Chem. Eng. J. **181**, 590–596 (2012)

Dong, H., Lin, Z., Wan, X., Feng, L.: Risk assessment for the mercury polluted site near a pesticide plant in Changsha, Hunan, China. Chemosphere **169**, 333–341 (2017). https://doi.org/10.1016/j.chemosphere.2016.11.084

Dong, L., Zhang, H., Zhang, J., Wu, W., Jia, Q.: Carbon nanotube modified sepiolite porous ceramics for high-efficient oil/water separation. Wuji Cailiao Xuebao/J. Inorg. Mater. **35**, 689–696 (2020). https://doi.org/10.15541/jim20190382

Doreau, F., Chaput, C., Chartier, T.: Stereolithography for ceramic part manufacturing. Ceram. Reliab. Tribol. Wear **12**, 69–74 (2000)

Douglass, J.B.: Enamel wear caused by ceramic brackets. Am. J. Orthod. Dentofac. Orthop. **95**, 96–98 (1989)

Drioli, E., Ali, A., Macedonio, F.: Membrane distillation: recent developments and perspectives. Desalination **356**, 56–84 (2015)

Duan, C., Tong, J., Shang, M., Nikodemski, S., Sanders, M., Ricote, S., Almansoori, A., O'Hayre, R.: Readily processed protonic ceramic fuel cells with high performance at low temperatures. Science (80-) **349**, 1321–1326 (2015)

Duan, C., Huang, J., Sullivan, N., O'Hayre, R.: Proton-conducting oxides for energy conversion and storage. Appl. Phys. Rev. **7**, 11314 (2020)

Dyer, P.N., Richards, R.E., Russek, S.L., Taylor, D.M.: Ion transport membrane technology for oxygen separation and syngas production. Solid State Ionics **134**, 21–33 (2000)

Eckel, Z.C., Zhou, C., Martin, J.H., Jacobsen, A.J., Carter, W.B., Schaedler, T.A.: Additive manufacturing of polymer-derived ceramics. Science (80-) **351**, 58–62 (2016)

Eliades, T.: Orthodontic materials research and applications: part 2. Current status and projected future developments in materials and biocompatibility. Am. J. Orthod. Dentofac. Orthop. **131**, 253–262 (2007)

Emmel, M., Aneziris, C.G., Sponza, F., Dudczig, S., Colombo, P.: In situ spinel formation in Al_2O_3-MgO-C filter materials for steel melt filtration. Ceram. Int. **40**, 13507–13513 (2014). https://doi.org/10.1016/j.ceramint.2014.05.033

Eterigho-Ikelegbe, O., Bada, S.O., Daramola, M.O.: Preparation and evaluation of nanocomposite sodalite/α-Al_2O_3 tubular membranes for H_2/CO_2 separation. Membranes (Basel) **10**, 1–18 (2020). https://doi.org/10.3390/membranes10110312

Evans, A.G., Hutchinson, J.W., Ashby, M.F.: Cellular metals. Curr. Opin. Solid State Mater. Sci. **3**, 288–303 (1998). https://doi.org/10.1016/S1359-0286(98)80105-8

Faltermeier, A., Behr, M., Müßig, D.: In vitro colour stability of aesthetic brackets. Eur. J. Orthod. **29**, 354–358 (2007)

Farrow, C., McBean, E., Huang, G., Yang, A., Wu, Y., Liu, Z., Dai, Z., Fu, H., Cawte, T., Li, Y.: Ceramic water filters: a point-of-use water treatment technology to remove bacteria from drinking water in Longhai City, Fujian Province, China. J. Environ. Inform. **32**, 63–68 (2018)

Fedotov, A.S., Uvarov, V.I., Tsodikov, M.V., Paul, S., Simon, P., Marinova, M., Dumeignil, F.: Dehydrogenation of cumene to α-methylstyrene on [Re, W]/γ-Al_2O_3(K, Ce)/α-Al_2O_3 and [Fe, Cr]/γ-Al_2O_3(K, Ce)/α-Al_2O_3 porous ceramic catalytic converters. Pet. Chem. **60**, 1268–1283 (2020). https://doi.org/10.1134/S0965544120110080

Fedotov, A.S., Uvarov, V.I., Tsodikov, M.V, Paul, S., Simon, P., Marinova, M., Dumeignil, F.: Production of styrene by dehydrogenation of ethylbenzene on a [Re, W]/γ-Al_2O_3 (K, Ce)/α-Al_2O_3 porous ceramic catalytic converter. Chem. Eng. Process. Process Intensif. **160** (2021). https://doi.org/10.1016/j.cep.2020.108265

Feldner, J.C., Sarkar, N.K., Sheridan, J.J., Lancaster, D.M.: In vitro torque-deformation characteristics of orthodontic polycarbonate brackets. Am. J. Orthod. Dentofac. Orthop. **106**, 265–272 (1994)

Feng, S., Liu, J., Gao, B., Bo, L., Cao, L.: The filtration and degradation mechanism of toluene via microwave thermo-catalysis ceramic membrane. J. Environ. Chem. Eng. **9** (2021). https://doi.org/10.1016/j.jece.2021.105105

Fisher, J.B., Melton, F., Middleton, E., Hain, C., Anderson, M., Allen, R., McCabe, M.F., Hook, S., Baldocchi, D., Townsend, P.A.: The future of evapotranspiration: global requirements for ecosystem functioning, carbon and climate feedbacks, agricultural management, and water resources. Water Resour. Res. **53**, 2618–2626 (2017)

Fonseca, J.M., Teleken, J.G., de Cinque Almeida, V., da Silva, C.: Biodiesel from waste frying oils: methods of production and purification. Energy Convers. Manag. **184**, 205–218 (2019)

Fraga, M.C., Sanches, S., Crespo, J.G., Pereira, V.J.: Assessment of a new silicon carbide tubular honeycomb membrane for treatment of olive mill wastewaters. Membranes (Basel) **7**, 12 (2017a)

Fraga, M.C., Sanches, S., Pereira, V.J., Crespo, J.G., Yuan, L., Marcher, J., de Yuso, M.M., Rodríguez-Castellón, E., Benavente, J.: Morphological, chemical surface and filtration characterization of a new silicon carbide membrane. J. Eur. Ceram. Soc. **37**, 899–905 (2017b)

Fu, J.: Fast Li^+ ion conducting glass-ceramics in the system Li_2O–Al_2O_3–GeO_2–P_2O_5. Solid State Ionics **104**, 191–194 (1997a). https://doi.org/10.1016/S0167-2738(97)00434-7

Fu, J.: Superionic conductivity of glass-ceramics in the system Li_2O–Al_2O_3–TiO_2–P_2O_5. Solid State Ionics **96**, 195–200 (1997b). https://doi.org/10.1016/S0167-2738(97)00018-0

Gajda, I., Obata, O., Salar-Garcia, M.J., Greenman, J., Ieropoulos, I.A.: Long-term bio-power of ceramic microbial fuel cells in individual and stacked configurations. Bioelectrochemistry **133**, 107459 (2020)

Gallimberti, I.: Recent advancements in the physical modelling of electrostatic precipitators. J. Electrostat. **43**, 219–247 (1998)

Gallon, V., Le Cann, P., Sanchez, M., Dematteo, C., Le Bot, B.: Emissions of VOCs, SVOCs, and mold during the construction process: contribution to indoor air quality and future occupants' exposure. Indoor Air **30**, 691–710 (2020)

Gao, H.B., Qu, Z.G., Feng, X.B., Tao, W.Q.: Methane/air premixed combustion in a two-layer porous burner with different foam materials. Fuel **115**, 154–161 (2014)

Gao, N., Li, J., Quan, C., Wang, X., Yang, Y.: Oily sludge catalytic pyrolysis combined with fine particle removal using a Ni-ceramic membrane. Fuel **277** (2020). https://doi.org/10.1016/j.fuel.2020.118134

Gardea-Torresdey, J.L., Tiemann, K.J., Armendariz, V., Bess-Oberto, L., Chianelli, R.R., Rios, J., Parsons, J.G., Gamez, G.: Characterization of Cr(VI) binding and reduction to Cr(III) by the agricultural byproducts of *Avena monida* (Oat) biomass. J. Hazard. Mater. **80**, 175–188 (2000). https://doi.org/10.1016/S0304-3894(00)00301-0

Gauthier, S., Nicolle, A., Baillis, D.: Investigation of the flame structure and nitrogen oxides formation in lean porous premixed combustion of natural gas/hydrogen blends. Int. J. Hydrogen Energy **33**, 4893–4905 (2008). https://doi.org/10.1016/j.ijhydene.2008.06.012

Gehre, P., Schmidt, A., Dudczig, S., Hubálková, J., Aneziris, C.G., Child, N., Delaney, I., Rancoule, G., DeBastiani, D.: Interaction of slip- and flame-spray coated carbon-bonded alumina filters with steel melts. J. Am. Ceram. Soc. **101**, 3222–3233 (2018). https://doi.org/10.1111/jace.15431

German, R.M., Suri, P., Park, S.J.: Review: liquid phase sintering. J. Mater. Sci. **44**, 1–39 (2009). https://doi.org/10.1007/s10853-008-3008-0

Göhring, T.N., Gallo, L., Lüthy, H.: Effect of water storage, thermocycling, the incorporation and site of placement of glass-fibers on the flexural strength of veneering composite. Dent. Mater. **21**, 761–772 (2005)

Gorner, H., Engh, T.A., Syvertsen, M.: Light Metals 2006, p. 756. Warrendale TMS (2006)

Han, N., Wei, Q., Zhang, S., Yang, N., Liu, S.: Rational design via tailoring Mo content in $La_2Ni_{1-x}Mo_xO_{4+\delta}$ to improve oxygen permeation properties in CO_2 atmosphere. J. Alloys Compd. **806**, 153–162 (2019). https://doi.org/10.1016/j.jallcom.2019.07.209

Hashemi, S.A., Alsulaiei, Z.M.A., Mollamahdi, M.: Experimental analysis of the effects of porous wall on flame stability and temperature distribution in a premixed natural gas/air combustion. Heat Transf. **49**, 2282–2296 (2020). https://doi.org/10.1002/htj.21720

He, X., Su, B., Tang, Z., Zhao, B., Wang, X., Yang, G., Qiu, H., Zhang, H., Yang, J.: The comparison of macroporous ceramics fabricated through the protein direct foaming and sponge replica methods. J. Porous Mater. **19**, 761–766 (2012). https://doi.org/10.1007/s10934-011-9528-z

Hillel, D.: Introduction to Soil Physics. Academic Press (2013)

Hoffmann, J.G., Echigo, R., Yoshida, H., Tada, S.: Experimental study on combustion in porous media with a reciprocating flow system. Combust. Flame **111**, 32–46 (1997). https://doi.org/10.1016/S0010-2180(97)00099-0

Hofs, B., Ogier, J., Vries, D., Beerendonk, E.F., Cornelissen, E.R.: Comparison of ceramic and polymeric membrane permeability and fouling using surface water. Sep. Purif. Technol. **79**, 365–374 (2011)

Hoppach, D., Werzner, E., Demuth, C., Löwer, E., Lehmann, H., Ditscherlein, L., Ditscherlein, R., Peuker, U.A., Ray, S.: Experimental investigations of the depth filtration inside open-cell foam filters supported by high-resolution computed tomography scanning and pore-scale numerical simulations. Adv. Eng. Mater. **22** (2020). https://doi.org/10.1002/adem.201900761

Howell, J.R., Hall, M.J., Ellzey, J.L.: Combustion of hydrocarbon fuels within porous inert media. Prog. Energy Combust. Sci. **22**, 121–145 (1996). https://doi.org/10.1016/0360-1285(96)00001-9

Hsieh, H.P., Bhave, R.R., Fleming, H.L.: Microporous alumina membranes. J. Memb. Sci. **39**, 221–241 (1988)

Huang, J., Huang, G., An, C., He, Y., Yao, Y., Zhang, P., Shen, J.: Performance of ceramic disk filter coated with nano ZnO for removing *Escherichia coli* from water in small rural and remote communities of developing regions. Environ. Pollut. **238**, 52–62 (2018)

Hubadillah, S.K., Othman, M.H.D., Rahman, M.A., Ismail, A.F., Jaafar, J.: Preparation and characterization of inexpensive kaolin hollow fibre membrane (KHFM) prepared using phase inversion/sintering technique for the efficient separation of real oily wastewater. Arab. J. Chem. **13**, 2349–2367 (2020). https://doi.org/10.1016/j.arabjc.2018.04.018

Huo, C., Tian, X., Chen, C., Zhang, J., Nan, Y., Zhong, Q., Huang, X., Hu, J., Li, D.: Hierarchically porous alumina catalyst carrier with biomimetic vein structure prepared by direct ink writing. J. Eur. Ceram. Soc. **41**, 4231–4241 (2021). https://doi.org/10.1016/j.jeurceramsoc.2021.02.016

Hwa, L.C., Rajoo, S., Noor, A.M., Ahmad, N., Uday, M.B.: Recent advances in 3D printing of porous ceramics: a review. Curr. Opin. Solid State Mater. Sci. **21**, 323–347 (2017)

Inaguma, Y., Liquan, C., Itoh, M., Nakamura, T., Uchida, T., Ikuta, H., Wakihara, M.: High ionic conductivity in lithium lanthanum titanate. Solid State Commun. **86**, 689–693 (1993). https://doi.org/10.1016/0038-1098(93)90841-A

Iwahara, H.: Proton conducting ceramics and their applications. Solid State Ionics **86**, 9–15 (1996)

Jayakumar, A., Singamneni, S., Ramos, M., Al-Jumaily, A.M., Pethaiah, S.S.: Manufacturing the gas diffusion layer for PEM fuel cell using a novel 3D printing technique and critical assessment of the challenges encountered. Materials (Basel) **10**, 796 (2017)

Jena, A.K., Duggal, R., Mehrotra, A.K.: Physical properties and clinical characteristics of ceramic brackets: a comprehensive review. Trends Biomater. Artif. Organs **20**, 101–115 (2007)

Jiang, Q.Y., Cross, L.E.: Effects of porosity on electric fatigue behaviour in PLZT and PZT ferroelectric ceramics. J. Mater. Sci. **28**, 4536–4543 (1993)

Judkins, R.R., Stinton, D.P., DeVan, J.H.: A review of the efficacy of silicon carbide hot-gas filters in coal gasification and pressurized fluidized bed combustion environments (1996)

Kamarudin, N.H., Harun, Z., Othman, M.H.D., Abdullahi, T., Syamsul Bahri, S., Kamarudin, N.H., Yunos, M.Z., Wan Salleh, W.N.: Waste environmental sources of metakaolin and corn cob ash for preparation and characterisation of green ceramic hollow fibre membrane (h-MCa) for oil-water separation. Ceram. Int. **46**, 1512–1525 (2020). https://doi.org/10.1016/j.ceramint.2019.09.118

Kamaya, N., Homma, K., Yamakawa, Y., Hirayama, M., Kanno, R., Yonemura, M., Kamiyama, T., Kato, Y., Hama, S., Kawamoto, K.: A lithium superionic conductor. Nat. Mater. **10**, 682–686 (2011)

Karamouzos, A., Athanasiou, A.E., Papadopoulos, M.A.: Clinical characteristics and properties of ceramic brackets: a comprehensive review. Am. J. Orthod. Dentofac. Orthop. **112**, 34–40 (1997)

Karges, U., Becker, J., Püttmann, W.: 1, 4-dioxane pollution at contaminated groundwater sites in western Germany and its distribution within a TCE plume. Sci. Total Environ. **619**, 712–720 (2018)

Kerry, F.G.: Industrial Gas Handbook: Gas Separation and Purification. CRC Press (2007)

Khachaturyan, R., Zhukov, S., Schultheiß, J., Galassi, C., Reimuth, C., Koruza, J., Von Seggern, H., Genenko, Y.A.: Polarization-switching dynamics in bulk ferroelectrics with isometric and oriented anisometric pores. J. Phys. D Appl. Phys. **50**, 45303 (2016)

Khanna, R., Kongkarat, S., Seetharaman, S., Sahajwalla, V.: Carbothermic reduction of alumina at 1823 K in the presence of molten steel: a sessile drop investigation. ISIJ Int. **52**, 992–999 (2012)

Khayet, M.: Membranes and theoretical modeling of membrane distillation: a review. Adv. Colloid Interface Sci. **164**, 56–88 (2011)

Kim, J., Sengodan, S., Kim, S., Kwon, O., Bu, Y., Kim, G.: Proton conducting oxides: a review of materials and applications for renewable energy conversion and storage. Renew. Sustain. Energy Rev. **109**, 606–618 (2019). https://doi.org/10.1016/j.rser.2019.04.042

Koros, W.J., Mahajan, R.: Pushing the limits on possibilities for large scale gas separation: which strategies? J. Memb. Sci. **175**, 181–196 (2000)

Koros, W.J., Ma, Y.H., Shimidzu, T.: Terminology for membranes and membrane processes (IUPAC Recommendations 1996). Pure Appl. Chem. **68**, 1479–1489 (1996). https://doi.org/10.1351/pac199668071479

Kouvelos, E., Kesore, K., Steriotis, T., Grigoropoulou, H., Bouloubasi, D., Theophilou, N., Tzintzos, S., Kanelopoulos, N.: High pressure N_2/CH_4 adsorption measurements in clinoptilolites. Microporous Mesoporous Mater. **99**, 106–111 (2007). https://doi.org/10.1016/j.micromeso.2006.07.036

Krivoshapkina, E.F., Vedyagin, A.A., Krivoshapkin, P.V., Desyatykh, I.V.: Carbon monoxide oxidation over microfiltration ceramic membranes. Pet. Chem. **55**, 901–908 (2015). https://doi.org/10.1134/S0965544115100096

Kulbakin, I.V., Fedorov, S.V.: Promising NiO–30 wt % Ag–40 wt % Bi_2O_3 membrane material for separation of oxygen from air. Inorg. Mater. Appl. Res. **9**, 868–872 (2018). https://doi.org/10.1134/S2075113318050180

Labhsetwar, N., Doggali, P., Rayalu, S., Yadav, R., Mistuhashi, T., Haneda, H.: Ceramics in environmental catalysis: applications and possibilities. Chin. J. Catal. **33**, 1611–1621 (2012). https://doi.org/10.1016/S1872-2067(11)60440-3

Ledoux, M.J., Hantzer, S., Huu, C.P., Guille, J., Desaneaux, M.-P.: New synthesis and uses of high-specific-surface SiC as a catalytic support that is chemically inert and has high thermal resistance. J. Catal. **114**, 176–185 (1988)

Lei, L., Zhang, J., Yuan, Z., Liu, J., Ni, M., Chen, F.: Progress report on proton conducting solid oxide electrolysis cells. Adv. Funct. Mater. **29**, 1903805 (2019)

Li, K.: Ceramic Membranes for Separation and Reaction. Wiley (2007)

Li, W., Dahn, J.R., Wainwright, D.S.: Rechargeable lithium batteries with aqueous electrolytes. Science (80-) **264** 1115–1118 (1994)

Li, B., Li, G., Chen, J., Chen, H., Xing, X., Hou, X., Li, Y.: Formation mechanism of elongated β–Si_3N_4 crystals in Fe–Si_3N_4 composite via flash combustion. Ceram. Int. **44**, 9395–9400 (2018a)

Li, S., Duan, W., Zhao, T., Han, W., Wang, L., Dou, R., Wang, G.: The fabrication of SiBCN ceramic components from preceramic polymers by digital light processing (DLP) 3D printing technology. J. Eur. Ceram. Soc. **38**, 4597–4603 (2018b)

Li, J., Wu, M., Du, H., Wang, B., Li, Y., Huan, W.: Highly effective catalytic reduction of nitrobenzene compounds with gold nanoparticle-immobilized hydroxyapatite nanowire-sintered porous ceramic beads. New J. Chem. **45**, 4601–4610 (2021a). https://doi.org/10.1039/d0nj06209j

Li, S., Baeyens, J., Dewil, R., Appels, L., Zhang, H., Deng, Y.: Advances in rigid porous high temperature filters. Renew. Sustain. Energy Rev. **139** (2021b). https://doi.org/10.1016/j.rser.2021.110713

Liu, L., Chen, F., Yang, F., Chen, Y., Crittenden, J.: Photocatalytic degradation of 2, 4-dichlorophenol using nanoscale Fe/TiO_2. Chem. Eng. J. **181**, 189–195 (2012)

Liu, D., Zhu, W., Trottier, J., Gagnon, C., Barray, F., Guerfi, A., Mauger, A., Groult, H., Julien, C.M., Goodenough, J.B.: Spinel materials for high-voltage cathodes in Li-ion batteries. RSC Adv. **4**, 154–167 (2014)

Liu, Y., Zhu, W., Guan, K., Peng, C., Wu, J.: Preparation of high permeable alumina ceramic membrane with good separation performance: via UV curing technique. RSC Adv. **8**, 13567–13577 (2018). https://doi.org/10.1039/c7ra13195j

Liu, J., Zhang, Y., Hong, Z., Liu, H., Wang, S., Gu, X.: Fabrication of dual-layer hollow fiber ceramic composite membranes by Co-extrusion. Wuji Cailiao Xuebao/J. Inorg. Mater. **35**, 1333–1339 (2020). https://doi.org/10.15541/jim20200182

Liu, Y., Song, Z., Wang, W., Wang, Z., Zhang, Y., Liu, C., Wang, Y., Li, A., Xu, B., Qi, F.: A $CuMn_2O_4/g$-C_3N_4 catalytic ozonation membrane reactor used for water purification: membrane fabrication and performance evaluation. Sep. Purif. Technol. **265** (2021). https://doi.org/10.1016/j.seppur.2020.118268

Løken, A., Ricote, S., Wachowski, S.: Thermal and chemical expansion in proton ceramic electrolytes and compatible electrodes. Crystals **8** (2018). https://doi.org/10.3390/cryst8090365

Lu, T.J., Chen, C.: Thermal transport and fire retardance properties of cellular aluminium alloys. Acta Mater. **47**, 1469–1485 (1999). https://doi.org/10.1016/S1359-6454(99)00037-3

Lu, T.J., Stone, H.A., Ashby, M.F.: Heat transfer in open-cell metal foams. Acta Mater. **46**, 3619–3635 (1998). https://doi.org/10.1016/S1359-6454(98)00031-7

Lu, T.J., Hess, A., Ashby, M.F.: Sound absorption in metallic foams. J. Appl. Phys. **85**, 7528–7539 (1999). https://doi.org/10.1063/1.370550

Malerød-Fjeld, H., Clark, D., Yuste-Tirados, I., Zanón, R., Catalán-Martinez, D., Beeaff, D., Morejudo, S.H., Vestre, P.K., Norby, T., Haugsrud, R.: Thermo-electrochemical production of compressed hydrogen from methane with near-zero energy loss. Nat. Energy **2**, 923–931 (2017)

Mao, J., Quan, X., Wang, J., Gao, C., Chen, S., Yu, H., Zhang, Y.: Enhanced heterogeneous Fenton-like activity by Cu-doped $BiFeO_3$ perovskite for degradation of organic pollutants. Front. Environ. Sci. Eng. **12**, 1–10 (2018)

Marnellos, G., Stoukides, M.: Ammonia synthesis at atmospheric pressure. Science (80-) **282**, 98–100 (1998)

Mazzoni, A.D., Sainz, M.A., Caballero, A., Aglietti, E.F.: Formation and sintering of spinels ($MgAl_2O_4$) in reducing atmospheres. Mater. Chem. Phys. **78**, 30–37 (2003)

McElroy, A.C., Hyman, M.R., Knappe, D.R.U.: 1, 4-Dioxane in drinking water: emerging for 40 years and still unregulated. Curr. Opin. Environ. Sci. Health **7**, 117–125 (2019)

Medvedev, D.: Trends in research and development of protonic ceramic electrolysis cells. Int. J. Hydrogen Energy **44**, 26711–26740 (2019)

Meguro, D., Hayakawa, T., Kawasaki, M., Kasai, K.: Shear bond strength of calcium phosphate ceramic brackets to human enamel. Angle Orthod. **76**, 301–305 (2006)

Mei, H., Huang, W., Zhao, Y., Cheng, L.: Strengthening three-dimensional printed ultra-light ceramic lattices. J. Am. Ceram. Soc. **102**, 5082–5089 (2019)

Mei, H., Tan, Y., Huang, W., Chang, P., Fan, Y., Cheng, L.: Structure design influencing the mechanical performance of 3D printing porous ceramics. Ceram. Int. **47**, 8389–8397 (2021). https://doi.org/10.1016/j.ceramint.2020.11.203

Miretzky, P., Cirelli, A.F.: Cr(VI) and Cr(III) removal from aqueous solution by raw and modified lignocellulosic materials: a review (2010)

Misyura, S.Y.: The influence of porosity and structural parameters on different kinds of gas hydrate dissociation. Sci. Rep. **6**, 30324 (2016). https://doi.org/10.1038/srep30324

Mkandawire, T., Banda, E.: Assessment of drinking water quality of Mtopwa village in Bangwe Township, Blantyre. Desalination **248**, 557–561 (2009)

Mohr, T.K.G., DiGuiseppi, W.H., Hatton, J.W., Anderson, J.K.: Environmental Investigation and Remediation: 1, 4-Dioxane and Other Solvent Stabilizers. CRC Press (2020)

Molenda, J., Kupecki, J., Baron, R., Blesznowski, M., Brus, G., Brylewski, T., Bucko, M., Chmielowiec, J., Cwieka, K., Gazda, M.: Status report on high temperature fuel cells in Poland—recent advances and achievements. Int. J. Hydrogen Energy **42**, 4366–4403 (2017)

Moni, P., Deschamps, A., Schumacher, D., Rezwan, K., Wilhelm, M.: A new silicon oxycarbide based gas diffusion layer for zinc-air batteries. J. Colloid Interface Sci. **577**, 494–502 (2020). https://doi.org/10.1016/j.jcis.2020.05.041

Moreira, W.M., da Igreja, G., Viotti, P. V, Baptista, C.M.S.G., Gimenes, M.L., Gomes, M.C.S., Pereira, N.C.: Soybean biodiesel purification through an acid-system membrane technology: effect of oil quality and separation process parameters. J. Chem. Technol. Biotechnol. **95**, 1962–1969 (2020). https://doi.org/10.1002/jctb.6395

Morejudo, S.H., Zanón, R., Escolástico, S., Yuste-Tirados, I., Malerød-Fjeld, H., Vestre, P.K., Coors, W.G., Martínez, A., Norby, T., Serra, J.M.: Direct conversion of methane to aromatics in a catalytic co-ionic membrane reactor. Science (80-) **353**, 563–566 (2016)

Murphy, H.M., McBean, E.A., Farahbakhsh, K.: A critical evaluation of two point-of-use water treatment technologies: can they provide water that meets WHO drinking water guidelines? J. Water Health **8**, 611–630 (2010)

Murugan, R., Thangadurai, V., Weppner, W.: Fast lithium ion conduction in garnet-type $Li_7La_3Zr_2O_{12}$. Angew. Chem. Int. Ed. **46**, 7778–7781 (2007). https://doi.org/10.1002/anie.200701144

Ngo, T.D., Kashani, A., Imbalzano, G., Nguyen, K.T.Q., Hui, D.: Additive manufacturing (3D printing): a review of materials, methods, applications and challenges. Compos. Part B Eng. **143**, 172–196 (2018)

Norby, T.: Solid-state protonic conductors: principles, properties, progress and prospects. Solid State Ionics **125**, 1–11 (1999)

Obada, D.O., Dodoo-Arhin, D., Dauda, M., Anafi, F.O., Ahmed, A.S., Ajayi, O.A.: Pressureless sintering and gas flux properties of porous ceramic membranes for gas applications. Results Phys. **7**, 3838–3846 (2017). https://doi.org/10.1016/j.rinp.2017.10.002

Ohji, T., Fukushima, M.: Macro-porous ceramics: processing and properties. Int. Mater. Rev. **57**, 115–131 (2012). https://doi.org/10.1179/1743280411Y.0000000006

Omrani, R., Shabani, B.: Gas diffusion layers in fuel cells and electrolysers: a novel semi-empirical model to predict electrical conductivity of sintered metal fibres. Energies **12**, 855 (2019)

Ortiz-Vitoriano, N., Drewett, N.E., Gonzalo, E., Rojo, T.: High performance manganese-based layered oxide cathodes: overcoming the challenges of sodium ion batteries. Energy Environ. Sci. **10**, 1051–1074 (2017)

Ounissi, T., Dammak, L., Larchet, C., Fauvarque, J.-F., Selmane Bel Hadj Hmida, E.: Novel lithium selective composite membranes: synthesis, characterization and validation tests in dialysis. J. Mater. Sci. **55**, 16111–16128 (2020). https://doi.org/10.1007/s10853-020-05147-8

Owen, D., Hickey, J., Cusson, A., Ayeni, O.I., Rhoades, J., Deng, Y., Zhang, Y., Wu, L., Park, H.-Y., Hawaldar, N.: 3D printing of ceramic components using a customized 3D ceramic printer. Prog. Addit. Manuf. **3**, 3–9 (2018)

Ozden, A., Alaefour, I.E., Shahgaldi, S., Li, X., Colpan, C.O., Hamdullahpur, F.: Gas Diffusion Layers for PEM Fuel Cells: Ex- and In-Situ Characterization. Elsevier (2018)

Pelaez, M., Nolan, N.T., Pillai, S.C., Seery, M.K., Falaras, P., Kontos, A.G., Dunlop, P.S.M., Hamilton, J.W.J., Byrne, J.A., O'Shea, K.: A review on the visible light active titanium dioxide photocatalysts for environmental applications. Appl. Catal. B Environ. **125**, 331–349 (2012)

Peng, S., Chen, Y., Jin, X., Lu, W., Gou, M., Wei, X., Xie, J.: Polyimide with half encapsulated silver nanoparticles grafted ceramic composite membrane: enhanced silver stability and lasting anti–biofouling performance. J. Memb. Sci. **611** (2020). https://doi.org/10.1016/j.memsci.2020.118340

Phair, J.W., Badwal, S.P.S.: Review of proton conductors for hydrogen separation. Ionics (Kiel) **12**, 103–115 (2006)

Pilicita, V., Páez Fajardo, G.J., Ormaza, R., Piper, L.F.J., Silva-Yumi, J.: Filter design for arsenic species in aqueous environments: An ab initio optimization of the absorbing capacity of magnetite-based arsenic filters. Mater. Lett. **295**, 129794 (2021). https://doi.org/10.1016/j.matlet.2021.129794

Qin, H., Li, Y., Nie, X., Yan, M., Jiang, P., Xue, W.: Combined effect of Fe-Si alloys and carbon on Si_3N_4 stability at elevated temperatures. Ceram. Int. **45**, 3290–3296 (2019)

Raji, Y.O., Othman, M.H.D., Nordin, N.A.H.S.M., ShengTai, Z., Usman, J., Mamah, S.C., Ismail, A.F., Rahman, M.A., Jaafar, J.: Fabrication of magnesium bentonite hollow fibre ceramic membrane for oil-water separation. Arab. J. Chem. **13**, 5996–6008 (2020). https://doi.org/10.1016/j.arabjc.2020.05.001

Rashad, A.M.: Lightweight expanded clay aggregate as a building material—an overview (2018)

Rehman, Z.U., Khan, S., Brusseau, M.L., Shah, M.T.: Lead and cadmium contamination and exposure risk assessment via consumption of vegetables grown in agricultural soils of five-selected regions of Pakistan. Chemosphere **168**, 1589–1596 (2017). https://doi.org/10.1016/j.chemosphere.2016.11.152

Rodríguez, J., Mais, L., Campana, R., Piroddi, L., Mascia, M., Gurauskis, J., Vacca, A., Palmas, S.: Comprehensive characterization of a cost-effective microbial fuel cell with Pt-free catalyst cathode and slip-casted ceramic membrane. Int. J. Hydrogen Energy (2021). https://doi.org/10.1016/j.ijhydene.2021.01.066

Romero, A.R., Elsayed, H., Bernardo, E.: Highly porous cordierite ceramics from engineered basic activation of metakaolin/talc aqueous suspensions. J. Eur. Ceram. Soc. **40**, 6254–6258 (2020). https://doi.org/10.1016/j.jeurceramsoc.2020.06.072

Saifuddin, S., Lisa, A., Amalia, Z., Faridah, F., Elfiana, E.: Applications of micro size anorganic membrane of clay, zeolite and active carbon as filters for peat water purification (2020)

Sainz, M.A., Mazzoni, A.D., Aglietti, E.F., Caballero, A.: Thermochemical stability of spinel (MgO·Al₂O₃) under strong reducing conditions. Mater. Chem. Phys. **86**, 399–408 (2004)

Sakai, T., Matsushita, S., Matsumoto, H., Okada, S., Hashimoto, S., Ishihara, T.: Intermediate temperature steam electrolysis using strontium zirconate-based protonic conductors. Int. J. Hydrogen Energy **34**, 56–63 (2009)

Saleem, M., Krammer, G.: Optical in-situ measurement of filter cake height during bag filter plant operation. Powder Technol. **173**, 93–106 (2007)

Sarin, V., Pant, K.K.: Removal of chromium from industrial waste by using eucalyptus bark. Bioresour. Technol. **97**, 15–20 (2006). https://doi.org/10.1016/j.biortech.2005.02.010

Schweiss, R., Meiser, C., Damjanovic, T., Galbiati, I., Haak, N.: SIGRACET gas diffusion layers for PEM fuel cells, electrolyzers and batteries. White Pap. SGL Gr. (2016)

SenGupta, A.K.: Ion Exchange in Environmental Processes: Fundamentals, Applications and Sustainable Technology. Wiley (2017)

Shi, P., Wang, Q., Xu, Y., Luo, W.: Corrosion behavior of bulk nanocrystalline copper in ammonia solution. Mater. Lett. **65**, 857–859 (2011). https://doi.org/10.1016/j.matlet.2010.12.014

Shi, Y., Matsunaga, T., Yamaguchi, Y., Li, Z., Gu, X., Chen, X.: Long-term trends and spatial patterns of satellite-retrieved PM2.5 concentrations in South and Southeast Asia from 1999 to 2014. Sci. Total Environ. **615**, 177–186 (2018)

Shuit, S.H., Ong, Y.T., Lee, K.T., Subhash, B., Tan, S.H.: Membrane technology as a promising alternative in biodiesel production: a review. Biotechnol. Adv. **30**, 1364–1380 (2012)

Snyder, J.F., Carter, R.H., Wetzel, E.D.: Electrochemical and mechanical behavior in mechanically robust solid polymer electrolytes for use in multifunctional structural batteries. Chem. Mater. **19**, 3793–3801 (2007)

Solovieva, A.A., Kulbakin, I.V.: The obtaining and properties of asymmetric ion transport membrane for separating of oxygen from air. IOP Conf. Ser. Mater. Sci. Eng. (2018)

Song, X., Jian, B., Jin, J.: Preparation of porous ceramic membrane for gas-solid separation. Ceram. Int. **44**, 20361–20366 (2018). https://doi.org/10.1016/j.ceramint.2018.08.026

Souhaimi, M.K., Matsuura, T.: Membrane Distillation: Principles and Applications (2011)

Stack, L.J., Carney, P.A., Malone, H.B., Wessels, T.K.: Factors influencing the ultrasonic separation of oil-in-water emulsions. Ultrason. Sonochem. **12**, 153–160 (2005)

Statistics, O.T.S.: The International Tanker Owners Pollution Federation (2010)

Subramanian, N., Qamar, A., Alsaadi, A., Gallo, A., Jr., Ridwan, M.G., Lee, J.-G., Pillai, S., Arunachalam, S., Anjum, D., Sharipov, F., Ghaffour, N., Mishra, H.: Evaluating the potential of superhydrophobic nanoporous alumina membranes for direct contact membrane distillation. J. Colloid Interface Sci. **533**, 723–732 (2019). https://doi.org/10.1016/j.jcis.2018.08.054

Sun, M., Lopez-Velandia, C., Knappe, D.R.U.: Determination of 1, 4-dioxane in the Cape Fear River watershed by heated purge-and-trap preconcentration and gas chromatography–mass spectrometry. Environ. Sci. Technol. **50**, 2246–2254 (2016)

Szul, M., Iluk, T., Sobolewski, A.: High-temperature, dry scrubbing of syngas with use of mineral sorbents and ceramic rigid filters (2020)

Tao, Z., Yan, L., Qiao, J., Wang, B., Zhang, L., Zhang, J.: A review of advanced proton-conducting materials for hydrogen separation. Prog. Mater. Sci. **74**, 1–50 (2015)

Taslicukur, Z., Balaban, C., Kuskonmaz, N.: Production of ceramic foam filters for molten metal filtration using expanded polystyrene. J. Eur. Ceram. Soc. **27**, 637–640 (2007)

Terada, N., Yanagi, T., Arai, S., Yoshikawa, M., Ohta, K., Nakajima, N., Yanai, A., Arai, N.: Development of lithium batteries for energy storage and EV applications. J. Power Sources **100**, 80–92 (2001)

Thi Thuy, P., Viet Anh, N., Van der Bruggen, B.: Low-cost technologies for safe drinking water in South-East Asia: overview and application to the north of Vietnam. Environ. Eng. Manag. J. **12** (2013)

Thompson, H.S.: On the absorbent power of soils. J. R. Agric. Soc. Engl. **11**, 68–74 (1850)

Tian, G.-P., Wu, Q.-Y., Li, A., Wang, W.-L., Hu, H.-Y.: Promoted ozonation for the decomposition of 1, 4-dioxane by activated carbon. Water Sci. Technol. Water Supply **17**, 613–620 (2017)

Trimis, D.: Stabilized combustion in porous media—applications of the porous burner technology in energy- and heat-engineering. In: Fluids 2000 Conference and Exhibit, p. 2298 (2000)

Trimis, D., Durst, F.: Combustion in a porous medium-advances and applications. Combust. Sci. Technol. **121**, 153–168 (1996)

Tripathi, H.S., Ghosh, A.: Spinelisation and properties of Al_2O_3–$MgAl_2O_4$–C refractory: effect of MgO and Al_2O_3 reactants. Ceram. Int. **36**, 1189–1192 (2010)

U.S. Geological Survey: Mineral Commodity Summaries 2019 (2019)

USEPA: Federal register. In: Federal Register, pp. 6976–7066 (2001)

Varanasi, L., Coscarelli, E., Khaksari, M., Mazzoleni, L.R., Minakata, D.: Transformations of dissolved organic matter induced by UV photolysis, hydroxyl radicals, chlorine radicals, and sulfate radicals in aqueous-phase UV-based advanced oxidation processes. Water Res. **135**, 22–30 (2018)

Vo, T.S., Hossain, M.M., Jeong, H.M., Kim, K.: Heavy metal removal applications using adsorptive membranes. Nano Converg. **7** (2020). https://doi.org/10.1186/s40580-020-00245-4

Wang, P., Chung, T.-S.: Recent advances in membrane distillation processes: membrane development, configuration design and application exploring. J. Memb. Sci. **474**, 39–56 (2015)

Wang, X.-L., Zhang, Y.-T., Gao, B., Zhang, C., Gu, X.-H.: Preparation and characterization of NaA zeolite membranes on inner-surface of four-channel ceramic hollow fibers. Wuji Cailiao Xuebao/J. Inorg. Mater. **33**, 339–344 (2018). https://doi.org/10.15541/jim20170174

Wang, S., Tian, J., Jia, L., Jia, J., Shan, S., Wang, Q., Cui, F.: Removal of aqueous organic contaminants using submerged ceramic hollow fiber membrane coupled with peroxymonosulfate oxidation: comparison of CuO catalyst dispersed in the feed water and immobilized on the membrane. J. Memb. Sci. **618** (2021). https://doi.org/10.1016/j.memsci.2020.118707

Way, J.T.: On the power of soils to absorb manure (1850)

Wei, G.C.: Method for forming fibrous silicon carbide insulating material (1984)

Wei, S., Zeng, C., Lu, Y., Liu, G., Luo, H., Zhang, R.: Degradation of antipyrine in the Fenton-like process with a La-doped heterogeneous catalyst. Front. Environ. Sci. Eng. **13**, 1–11 (2019)

Wu, Z., Hou, Y., Li, X., Li, Y., Cao, H.: Pilot study on catalyzed oxidation-ceramic membrane-high pressure reverse osmosis for desulfurization wastewater recovery (2021)

Xu, Y.: Ferroelectric Materials and Their Applications. Elsevier (2013)

Xue, S., Sun, S., Qing, W., Huang, T., Liu, W., Liu, C., Yao, H., Zhang, W.: Experimental and computational assessment of 1,4-dioxane degradation in a photo-Fenton reactive ceramic membrane filtration process. Front. Environ. Sci. Eng. **15** (2021). https://doi.org/10.1007/s11783-020-1341-y

Yaroslavtsev, A.B.: Solid electrolytes: main prospects of research and development. Russ. Chem. Rev. **85**, 1255 (2016)

Yin, Q., Zhu, B., Zeng, H.: Microstructure, Property and Processing of Functional Ceramics. Springer Science & Business Media (2010)

Yuan, Y., Li, Z., Cao, L., Tang, B., Zhang, S.: Modification of Si_3N_4 ceramic powders and fabrication of Si_3N_4/PTFE composite substrate with high thermal conductivity. Ceram. Int. **45**, 16569–16576 (2019)

Yuan, L., Jin, E., Li, C., Liu, Z., Tian, C., Ma, B., Yu, J.: Preparation of calcium hexaluminate porous ceramics by novel pectin based gelcasting freeze-drying method. Ceram. Int. **47**, 9017–9023 (2021). https://doi.org/10.1016/j.ceramint.2020.12.024

Yue, X., Zhang, T., Yang, D., Qiu, F.: Fabrication of flexible ceramic membranes derived from hard Si_3N_4 and soft MnO_2 nanowires. Ceram. Int. **46**, 8478–8482 (2020). https://doi.org/10.1016/j.ceramint.2019.11.226

Zagoruiko, A.N., Mokrinskii, V.V., Veniaminov, S.A., Noskov, A.S.: On the performance stability of the MnO_x/Al_2O_3 catalyst for VOC incineration under forced adsorption-catalytic cycling conditions. J. Environ. Chem. Eng. **5**, 5850–5856 (2017)

Zeuner, M., Pagano, S., Schnick, W.: Nitridosilicates and oxonitridosilicates: from ceramic materials to structural and functional diversity. Angew. Chem. Int. Ed. **50**, 7754–7775 (2011)

Zhang, J.-F., Zheng, Y.-M., Sun, Z.-Q., Hou, L.-M.: Study on effect disciplines of porous materials on gas explosion propagation. Dongbei Daxue Xuebao/J. Northeast. Univ. **34**, 290–293 (2013)

Zhang, T., Kong, L., Dai, Y., Yue, X., Rong, J., Qiu, F., Pan, J.: Enhanced oils and organic solvents absorption by polyurethane foams composites modified with MnO_2 nanowires. Chem. Eng. J. **309**, 7–14 (2017)

Zhao, Y., Huang, G., An, C., Huang, J., Xin, X., Chen, X., Hong, Y., Song, P.: Removal of *Escherichia coli* from water using functionalized porous ceramic disk filter coated with Fe/TiO_2 nano-composites. J. Water Process Eng. **33** (2020). https://doi.org/10.1016/j.jwpe.2019.101013

Zheng, C.-H., Cheng, L.-M., Li, T., Luo, Z.-Y., Cen, K.-F.: Filtration combustion characteristics of low calorific gas in SiC foams. Fuel **89**, 2331–2337 (2010)

Zhong, J., Sun, X., Wang, C.: Treatment of oily wastewater produced from refinery processes using flocculation and ceramic membrane filtration. Sep. Purif. Technol. **32**, 93–98 (2003)

Zhou, R., Shen, H., Zhao, M.: Simulation studies on protector of pulse-jet cleaning filter bag. Energy Procedia **16**, 426–431 (2012)

Zocca, A., Elsayed, H., Bernardo, E., Gomes, C.M., Lopez-Heredia, M.A., Knabe, C., Colombo, P., Günster, J.: 3D-printed silicate porous bioceramics using a non-sacrificial preceramic polymer binder. Biofabrication **7**, 25008 (2015)

Electrospun Porous Biobased Polymer Mats for Biomedical Applications

Fatma Nur Parin and Pınar Terzioğlu

Abstract The electrospinning method provides fabrication of nonwoven mats from nano to micrometers in size with controllable pores. Porous electrospun scaffolds have attracted increasing attention in biomedical applications especially due to their ability to mimic the extracellular matrix. This chapter presents a comprehensive overview of the advancements in the last five years through the design and preparation of porous biobased polymer mats using the electrospinning method for biomedical applications. Firstly, fundamentals of the electrospinning process are presented and followed by a discussion of the possible biomedical applications of micro- and nanostructured porous mats for drug delivery, wound dressing, tissue engineering, and other applications. Various crucial points for limitations and possible future trends are presented.

Keywords Biomimetic · Biomedical application · Electrospun mats · Drug delivery · Porous scaffold · Biobased polymer

1 Introduction

Along with developments in structural and functional materials over the last few decades, there has been a growth in the design and production of materials for use in biomedical technologies (Klee and Höcker 1999). The first synthetic biomaterials were successfully used and also save and extend human life more than 50 years ago (Ratner 1989). These materials include the first artificial heart valves, pacemakers, vascular grafts, and kidney dialysis. Afterward, orthopedic tools including knee and hip joint replacements and also intraocular lenses began to be used in the healing of cataract patients. Since there have been a lot of trial and error to select suitable materials for this concern (Ratner 1993; Klee and Höcker 1999).

Polymer-based materials are of high relevance for biomedical applications. Among the polymers, biobased ones are gaining more attention. Biobased polymers

F. N. Parin (✉) · P. Terzioğlu
Polymer Materials Engineering Department, Faculty of Engineering and Natural Sciences, Bursa Technical University, Bursa, Turkey
e-mail: nur.parin@btu.edu.tr

are classified into three types as (i) biopolymers, (ii) synthetic polymers, and (iii) bioengineering polymers (Nakajima et al. 2017; Bhatia 2012). "Biopolymers" are polymers that exist naturally in plants, animals, and microorganisms. This category includes both naturally occurring and chemically treated polymers such as alginate, chitosan, collagen, dextran, gelatin, and lignin (Reddy et al. 2021; Langer and Tirrell 2004). Biopolymers are known as natural polymers that are biodegradable and can be used directly from their sources. The main disadvantage of these polymers is that they have poor mechanical characteristics. It is reported that polycaprolactam (PCL), poly(lactic acid) (PLA), poly(butylenes succinate) (PBS), bio-polyolefins (bio-PP, bio-PE), and bio-poly(ethylene terephthalic acid) are in the category of biobased synthetic polymers (Place et al. 2009). To overcome the low tensile strength of natural polymers, they are blended with biobased synthetic polymers. Bioengineering polymers such as poly(hydroxy alkanoates) (PHAs), poly(glutamic acid) are bio-synthesized using microorganisms and plants (Nakajima et al. 2017).

As well as polymer type, the design parameters, method, and properties of the final material are the key parameters for the application of the material in a specific bio-related field. In particular, porous structure is one of the most critical factors considered during the design and fabrication of a material. The significance of the existence of the pores in polymers and the polymeric materials containing pores are regarded as excellent candidates for a wide variety of applications (Ahumada et al. 2018). Porous polymer-based materials are becoming increasingly popular in the biomedical field, especially in tissue engineering. Pores lead to enhancing the properties of biomaterials.

Nanofibers have a diameter of less than 1000 nm owing to lightweight, multiscaled porous structure, small diameter, and outstanding mechanical properties (Wang et al. 2016; Jeevanandam et al. 2018; Pathak et al. 2019).

Porous nanofibers can be fabricated by using various biobased polymers and hence have a wide range of physical properties as well as application possibilities. In medical applications, natural polymers are favored over synthetic polymers. Natural polymers are preferred in medical and life science fields for two major reasons: increased bioactivity and enhanced biocompatibility (Vasita and Katti 2006).

Many methodologies such as freeze drying (Jazaeri et al. 2011), self-assembly (Hong et al. 2003), phase separation (Ma and Zhang 1999), island-in-sea (Pike 1999), and electrospinning (Doshi and Reneker 1995; Xue et al. 2009) have been used to prepare nanofibers. Each of these methodologies, except electrospinning, has some limitations. Electrospinning is a versatile and effective technique for nanofiber production from polymer solutions (Parin et al. 2021). Over the years, significant advances in this process of nanofiber production from biobased polymers have been made.

This chapter describes concisely porous-structured biobased nanofibers and also summarizes the studies in the biomedical field including tissue engineering, drug, and therapeutic delivery, wound dressing, cosmeceutical, and also other applications. The significance of electrospun fibers with unique properties such as excellent piezo-electric properties, bioactivity, biodegradability, release behavior, good in vitro and in vivo biocompatibility, and so on is presented in detail. Lastly, future challenges and

many suggestions about electrospun fiber production as well as commercial usage of them have been discussed.

2 Electrospinning Process

Electrospinning is an electrohydrodynamic process that spins a polymer solution using a high potential electric field to produce nanofibers (Bhardwaj and Kundu 2010; He et al. 2017; Zahmatkeshan et al. 2018). Electrospinning is a low-cost, one-of-a-kind process for producing polymer fibers with diameters in the 100 nm range. The method has been extensively researched.

In electrospinning, an electrostatic force can be used to shape a fine fiber from polymer solution (Raval and Ramani 2019). The electrospun fibers are usually finer than melt-spun fibers owing to the evaporation of the solvent in the former case (Buschle-Diller et al. 2006).

According to the studies, the typical electrospinning device consisted of four major components: a syringe containing a polymer solution, a needle or nozzle, a power supply, and a conducting collector (with different configurations) (Kamble et al. 2017; Haider et al. 2018). Once an electric field is applied to a polymer solution, an electrostatic voltage builds up at the droplet's surface. It is known that the high voltage value (0–40 kV) changes from polymer to polymer. In immobilizing charges on the surface of a droplet, electrospinning produces a continuous jet. When the electric field is increased more, the spherical droplet deforms and brings on a conical structure that is known as the "Taylor cone" (Taylor 1964; Mirjalili and Zohoori 2016). After a fiber jet strains from the cone, it directly moves to the collector, and the solvent evaporates. Thus, solid thin fibers are deposited on the conductive collector.

Though electrospinning is regarded as an easy manufacturing process, several parameters can affect the morphology of the formed fibers (Erdal and Güngör 2020). Many factors affect electrospinning of fibers, making study and analysis in this area difficult (Fig. 1). Even evaporation patterns significantly affect the porosity of nanofibers. Moreover, the main argument about the electrospinning technique has been its relatively slow, and nanofiber fabrication on the industrial scale is a handicap.

2.1 Porous Nanofibers

Generally, electrospun nanofibers have a solid smooth structure. Nevertheless, nanofibers with different morphologies and structures may be electrospun, as well. A wide variety of different shaped nanofiber architectures, including thin smooth nanofibers, porous nanofibers, ribbon-like nanofibers, core–shell nanofibers, branched nanofibers, and nanofibers with fractal surface structures/configurations, spindle-type structures, or odd-shaped fibers could be fabricated by electrospinning.

Electrospinning

Nanofibers

Polymer properties	**Process Parameters**	**Ambient Conditions**
✓Molecular weight	✓Applied voltage	✓Temperature
✓Solvent	✓Nozzle – collector	✓Humidity
✓Chemical structure	distance	✓Air flow in the device
✓Viscosity	✓Polymer flow rate	
✓Polarity	✓Collector type	
✓Polymer concentration		
✓Additives		
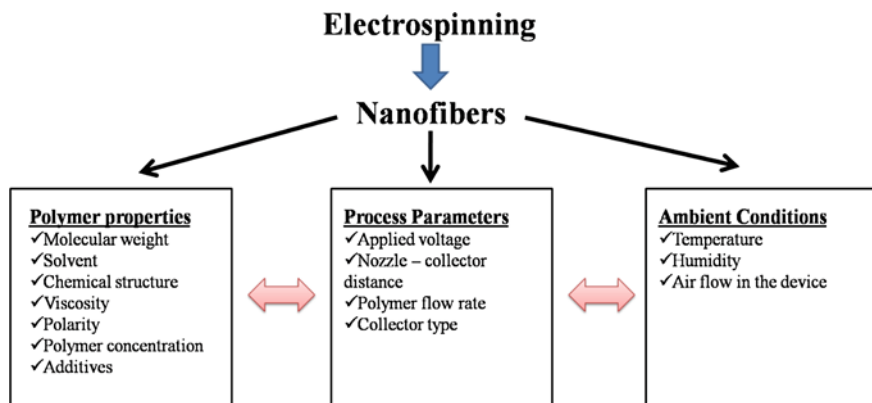
Fig. 1 Crucial parameters for electrospinning

Depending on the polymer used, various methods such as chemical and physical pre-treatment, solution mixture, humidity effect, and post-modification methods are carried out to achieve the desired porosity in nanofibers.

To increase the surface area much more, pores and dimples may be formed on the surface of the nanofibers. There are two ways to do this: adjusting the spinning atmosphere and solution interaction and using sacrificial matter. The morphology of nanofibers has been shown in both electrospun nanofibers and sintered inorganic nanofibers. Porous fibers have many ellipses and sphere-like cavities on their surface or within them, resulting in a wide surface area and lightweight. Therefore, it has the potential to be used in a variety of fields, including tissue engineering, sensing, filtration, separation, catalysis, superhydrophobic coatings, and encapsulating materials (Wei and Xia 2012). Especially, in tissue engineering and drug release applications, pores can serve as cell support. Pores can change the wetting properties of nanofibers and the drug release behaviors and affect the biodegradation kinetics of biodegradable fibers (Yousefzadeh and Ghasemkhah 2018). For example, carbon fibers have high porosity. This is making them ideal for use in enzyme immobilization and tissue engineering (Ji and Zhang 2009). Moreover, it has been reported that dimpled (porous) nanofibers have more surface area compared to smooth fibers. In a study, a larger surface area of nanofiber for protein adsorption was presented to obtain increased cell attachment and proliferation efficiency (Leong et al. 2009). In another study, it was found that nerve cells cultured on roughened nanofiber proliferated more than the cultured on smooth nanofiber (Zamani et al. 2013).

There have been several studies about nanoporous spheres being produced by the electrospinning method as a direct production of biological forms. The pores could serve as a favorable template for the surface of nanofibers with the formation of second-generation nanostructures. Eventually, the loading capacity of fibers can be increased (Yousefzadeh and Ghasemkhah 2018).

A range of techniques has been produced for the fabrication of porous nanofibers. There are primarily two approaches for obtaining porous structures (Megelski et al.

2002; Casper et al. 2004). During the electrospinning process, porous nanofibers production is possible via phase separation and breathing (BF) mechanisms (figures) (Wei and Xia 2012; Yousefzadeh and Ghasemkhah 2018).

Phase separation occurs by temperature, relative humidity, presence of insoluble matter, and relative volatility of solvent systems or some modifications of electrospinning devices. Due to a very humid environment, small water droplets precipitate on the polymer jet and form phase separation. If there is excess humidity in the system, phase separation forms as the hydrophobic-based polymer collapse in the solution. Then, polymer-rich and polymer-poor regions are formed. As a result, the highly volatile solvent evaporates quickly, and then, phase-separated geometry causes pores on the fiber surfaces (Yousefzadeh and Ghasemkhah 2018).

The suitable ratios of good and bad solvents play an essential role in the effective pore structure of nanofibers. Porous polycaprolactone (PCL) filament was developed for tissue engineering applications and analyzed the cell growth characteristics on these nonwoven fabrics (Khil et al. 2005; Lubasova and Martinova 2011).

Hussain and Yusoff (2012) prepared silver-loaded electrospun PVC nanofibers. In this study, tetrahydrofuran (THF) was used as a solvent, and dimpled structure on the fibers is caused by rapid evaporation of THF. The authors predicted the availability of the medical diagnostic of the resulting fibers around 1.5 µm fiber diameter and the dimple size ranging from 200 to 350 nm.

Studies on porosity have indicated that coaxial electrospun fibers have higher release behavior than non-porous ones (Nguyen et al. 2012). Ramos et al. (2020) suggested that antibacterial PCL fibers can be used as porous wound care products. Antibacterial agent chloramphenicol (CAM) was loaded into PCL solutions, and humidity conditions influence drug release behavior due to the changing of fiber topology. Although the same solvent system was used, porous structures were observed in higher humidity conditions. The largest pores were found on PCL fibers with the highest diameters obtained by electrospinning in a THF: dimethyl sulfoxide (DMSO) solvent solution with high humidity condition (RH, 65%). Nanofibers produced in lower humidity (around 19%) conditions have no pores on the fiber surface. Moreover, non-porous PCL nanofibers released more antibacterial drugs than porous PCL microfibers, with initial burst release values of $66.9 \pm 4.0\%$ and $53.5 \pm 7.0\%$, respectively.

As a result, nanofibers are unique materials with high porosity, and the porous structure depends on their morphology.

2.2 Polymer Used in Nanofiber Fabrication

Polymer-based nanofibers have attracted the interest of research and industry alike as a significant category of materials. Polymer nanofibers with submicrometer (<1 µm) diameters are produced both from natural and synthetic polymers (Bhattarai et al. 2018) The selection of polymer is crucial for the manufacture of nanofibers (Erdal and Güngör 2020). Natural and synthetic polymers are used to produce polymer

nanofibers. Thus far, it has been recorded that over 100 polymers have been used to obtain electrospun fibers with nanoscale (Zahmatkeshan et al. 2018). To eliminate each other's missing properties, especially natural and synthetic polymers are blended, and nanofiber fabrication is carried out. Polymers commonly used in the biomedical field are described as follows:

Polyvinyl alcohol (PVA) is a hydrophilic-based synthetic polymer that is nontoxic, biocompatible, biodegradable, and generally blend with other polymers (Erdal and Güngör 2020; Parın et al. 2021). Due to the good chemical and mechanical properties of PVA, it can be used in various medical applications in different forms including film, membrane, hydrogel, and fiber. During the electrospinning process, PVA interacts strongly with PVA or other polymers via hydrogen bonding that can provide strong spinnability. The adhesive nature of PVA enables elastic property, allowing it to be used as a regeneration scaffold and drug carrier in tissue engineering (Kumar 2017; Parın et al. 2021; Asiri et al. 2021).

Synthetic biobased polymers including polycaprolactone (PCL), polylactic acid (PLA), and poly lactic-co-glycolic acid (PLGA) have been used/applied to produce a fibrous matrix with nanoscale for biomedical applications. Polycaprolactone is one of the most researched hydrophobic polyesters due to its biocompatible, slow biodegradability, and non-immunogenic nature (Middleton and Tipton 2000; Wang et al. 2011; Manavitehrani et al. 2016; Espinoza et al. 2020). Despite its many advantages, the main drawback of polycaprolactone (PCL) is its hydrophobicity, which reduces cell attachment. This problem can be overcome by using pore-generating polymers such as polyethylene glycol (PEG), and gelatin as well as high vapor pressure solvents such as dichloromethane (DCM) are used. Kluge and Mauck (2011) reported that surface modification of PCL nanofibrous scaffolds using ethanol can result in a hydrophilic surface that allows for effective cell attachment. Moreover, incorporating hydrophilic drugs into the PCL matrix can be difficult for drug release applications requiring long times (Zupančič et al. 2018).

Chitosan is a hydrophilic biodegradable polysaccharide with β-(1 → 4)-D-glycosamine groups that are obtained by partially or completely deacetylation of chitin in alkaline media (Vega-Cázarez et al. 2018). It is often used in gel, microparticle, film, and particularly (nonwoven) nanofiber studies, due to its antimicrobial, biocompatible, and non-toxic properties. Many amino groups in chitosan increase hydrogen bonding between its chains that lead to a good swelling capacity (Rohindra et al. 2004; Ahmadi et al. 2015). Therefore, it is suitable for use in infected wound healing procedures. The polycationic character comes from the presence of several amino groups in its composition in acidic solutions. Since this polycationic character raises the surface tension of a chitosan solution, the electrospinnability of neat chitosan is limited. Chitosan-based nanofibers were utilized for wound dressing, bone scaffold, and ligands for epithelial cells. There are studies in the literature on chitosan-based nanofibers for wound dressing, bone scaffold, ligands for epithelial cells as a mixture of synthetic polymers such as polyethylene oxide (PEO), polyamide (PA6), PCL, and PVA (Alhosseini et al. 2012; Charernsriwilaiwat et al. 2014; Mendes et al. 2016; Kuntzler et al. 2018; Nokhasteh et al. 2019).

Gelatin (GE) is a water-soluble and biocompatible natural biopolymer extracted from partial hydrolysis of collagen derived from skin and bones that is a heterogeneous mixture of polypeptides containing 300–4000 amino acids (Heydarkhan-Hagvall et al. 2008; Gönen et al. 2015). GE has been widely utilized concerning various medical applications, such as burn dressing, drug carrier, surgical treatments, bone, skin, and nerve regeneration (Nguyen and Lee 2010; Aktürk and Keskin 2016; Erdal and Güngör 2020). It can enhance the hydrophilicity of some polymers like PCL and PLGA. Furthermore, it has been reported that three-dimensional (3D) porous structures can also be formed by the physical interaction or chemical reaction of gelatin with polycationic polymers such as PVA and chitosan (Nguyen and Lee 2010). On the other hand, porous GE fibrous structures have low mechanical properties and very brittle (Gönen et al. 2015; Mahnama et al. 2017). Thus, GE generally can be blended with other polymers.

Sodium alginate is a linear polysaccharide, consisting of (1,4)-b-D mannuronic acid and alpha L-glucuronic acid units, which has been broadly utilized in various biological fields, due to its relatively low cost, non-immunogenic character (Rafiq et al. 2018). While natural polymers are biocompatible and biodegradable, they have poor mechanical properties and some processing challenges as compared to synthetic polymers (Reddy et al. 2021). Therefore, the rigid and fragile nature of alginate can be improved by blended synthetic polymers (Arthanari et al. 2016).

Electrospun **collagen** mesh is the most plentiful protein in the human body that is derived from skin, tendon, bone, and cartilage. Collagen fibers resemble extracellular matrix (ECM) and mimic the architecture of natural human tissues due to cell adhesion and cell growth (Matthews et al. 2002; Parenteau-Bareil et al. 2010; Law et al. 2017). To develop their mechanical properties and prevent rapid degradation in aqueous media applications, collagen nanofibers are usually crosslinked with agents such as genipin, glutaraldehyde, and *N*-(3-dimethylaminopropyl)-*N*-ethylcarbodiimide hydrochloride (EDC) (Aktürk and Keskin 2016).

Silk is a long-chain protein with a β-nucleated layer structure that is made up of repeating glycine-sericin-glycine-alanine amino acid sequences (Kunz et al. 2016). Silk fibroin (SF) is also a natural polymer with outstanding properties including water and oxygen permeability, anti-inflammatory, and great blood compatibility. SF promotes collagen biosynthesis, re-epithelialization, and wound healing and assists in the treatment of atopic dermatitis and scarring. Unlike other natural polymers, silk fibroin has excellent mechanical properties (Bhardwaj and Kundu 2010; Wenk et al. 2011). Recently, a wide range of silk fibroin-based nanofibers have been focused on drug release, wound healing, and tissue regeneration (Pollini and Paladini 2020; Koh et al. 2015).

Polylactic acid (PLA) is a biodegradable polyester that can be produced by condensation polymerization and ring opening polymerization (ROP) methods (Kanmaz et al. 2018). Although PLA, alone or by combining with other biodegradable polymers, provides the environment for cell growth due to its excellent physical properties, its hydrophobic structure can limit cell affinity (Xu et al. 2017).

Polyurethane (PU) owns good blood compatibility and elastomeric properties as well as toughness, tear-resistant, and also wear resistance (Burke and Hasirci

2004). Therefore, polyurethane nanofibers may be preferred over other materials. Further, the very effective moisture-carrying properties of PU enhance wound fluid transfer from the contaminated layer (Akduman and Kumbasar 2017). Many studies reported on PU broadly used in medical fields as artificial heart, wound dressing, and pacemaker devices (Kim et al. 2014; Wróblewska-Krepsztul et al. 2019; Jatoi 2020).

3 Biomedical Applications of Porous Biobased Polymer Mats

As diameters of polymer-based fiber materials are reduced to low diameters (micrometers or nanometers), various properties occur, such as an improved surface area to volume ratio, versatility in surface functionalities, and superior mechanical strength compared with other forms of polymeric carriers.

The advantages of electrospun nanofibers, such as degradability and biocompatibility, as well as mechanical properties or porosity, allow for their use in a wide range of biomedical applications.

Consequently, porous fibers are ideal candidates for a variety of biomedical applications due to their excellent properties. Electrospun polymeric nanofibers have benefits over other drug delivery mechanisms, such as PVA, PEO, PCL, chitosan (CHS), poly(acrylic acid) (PAA), ethyl cellulose (EC), cellulose acetate (CA), hydroxypropylmethyl cellulose (HPMC), poly(L-lactic acid) (PLLA), PLGA, poly(acrylonitrile) (PAN), cellulose acetate phthalate (CAP), and poly(urethane) (PU) (Torres-Martínez et al. 2018).

In this chapter, electrospun porous fibers are used in biomedicine for four purposes: tissue engineering, drug delivery, wound dressing, and cosmeceutical applications.

3.1 Tissue Engineering Applications

As a multidisciplinary area, tissue engineering withstands the utilization of artificial porous scaffolds combined with cells or molecules to restore, maintain, or improve tissues (Das et al. 2020; Terzioglu et al. 2018). Electrospun porous structures are widely employed as scaffolds in tissue engineering applications for artificial vascular grafts (Awad et al. 2018), wound dressings, cartilage, and nerve regeneration.

The composition, specific functionalities, and structural requirements of scaffolds are key points that vary depending on the application. These factors are firstly very important from the cell adhesion, the biocompatibility, and optionally the biodegradability point of view (Das et al. 2020). Electrospun macro/nanofibrous scaffolds obtained from biobased polymers have attracted widespread interest due to

mimicking the microenvironment of extracellular matrix (ECM) (Awad et al. 2018; Lee et al. 2015; Hasan et al. 2014). Additionally, surface pores promote cell attachment, which is essential for the regeneration of damaged tissues. Moreover, the electrospinning process enables the engineering of a broad range of tunable mechanical and structural features as required for specific applications (Hasan et al. 2014).

3.1.1 Bone Tissue Engineering Scaffolds

Bone tissue engineering is a treatment option for damaged bones using bio-artificial bone scaffolds (Udomluck et al. 2020). It is expected from bio-artificial bone implants to mimic ECM and provide mechanical assistance for the growth of the new bone (Ranganathan et al. 2019). Structure of bone is composed of both organic and inorganic composite materials, including hydroxyapatite (up to 70%) and organic compounds (up to 35%) (Shitole et al. 2019). As bone is made up of osteoblasts, osteoclasts, osteocytes, and bone lining cells, the osteoconductive, osteoinductive, and osteogenic function scaffold (Fig. 2) are key factors for scaffold design (Ranganathan et al. 2019). It is known that interconnected pores, high porosity, and a high surface area are favorable properties to enhance bone regeneration (Udomluck et al. 2020). High surface area of the material may bring advantages by providing more sites for cells attachment and contact areas with surrounding tissues (Lu et al. 2020). Therefore, there is an increasing trend in the development of electrospun fibers as potential candidates for bone tissue engineering applications due to their highly porous structures (Lu et al. 2020).
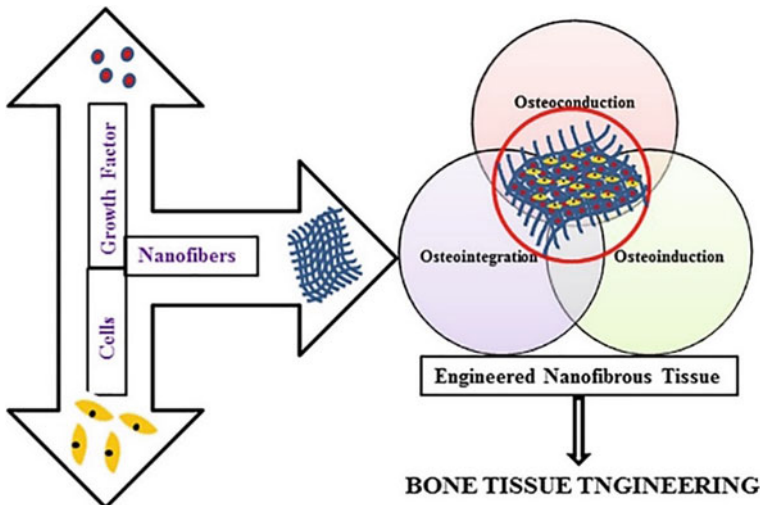
Fig. 2 Schematic diagram of a nanofiber-based engineered bone scaffold. Reprinted from Ranganathan et al. (2019), Copyright (2021), with permission from Elsevier

Porous and smooth PCL fibers were electrospun to be used in bone tissue engineering applications (Fig. 3). Cell material interaction, biomineralization, and the effect of the surface potential of fibers were investigated in detail. Higher mineralization and greater cell number were determined on the porous fibers as surface porosity and surface topography encourage the mineral nucleation and the initial cell adhesion, respectively. Higher surface potential improved collagen mineralization on the 7th day, while the negative zeta potential enhanced calcium mineralization. The results were presented that morphology and surface potential are important parameters in controlling cell function as well as behavior in physiological conditions. Therefore, these parameters should be taken into consideration in designing biomaterials for bone tissue engineering applications (Metwally et al. 2020).
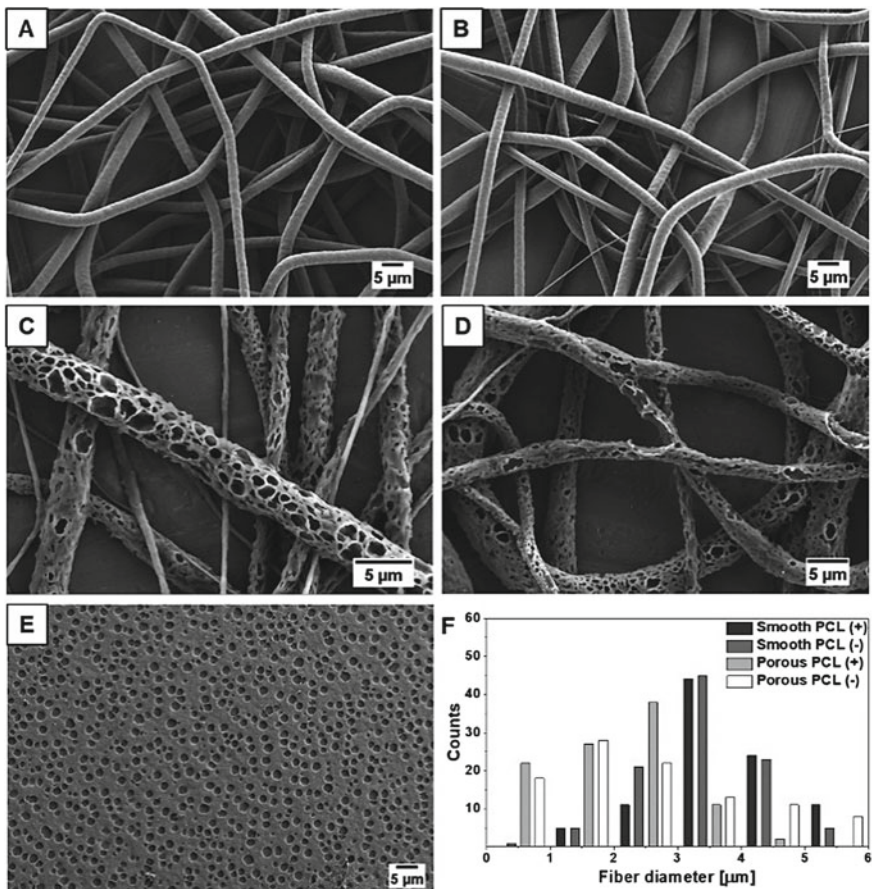
Fig. 3 SEM images of smooth (**a**, **b**), porous PCL (+) and PCL (−) (**c**, **d**) electrospun fibers PCL film (**e**), and histogram of fiber diameter distribution (**f**) (Metwally et al. 2020)

Incorporation of nanoparticles to electrospun porous fibers is also a widely investigated subject to design suitable materials with enhanced functional properties for bone regeneration. Silica is considered as one of the essential components of bone regeneration materials to obtain better bone cell attachment, mechanical properties, and biocompatibility (Karakuzu-Ikizler et al. 2020; Lu et al. 2020). From this point of view, Lu et al. (2020) developed highly porous membranes based on dopamine-modified porous PLLA fibers with silica nanoparticles coating to guide bone regeneration. As expected, the obtained membrane exhibited good biocompatibility, enhanced cell attachment, and proliferation.

Silver nanoparticles (AgNPs) are also interesting to study owing to their broad-spectrum antibacterial activity. AgNPs and hydroxyapatite nanoparticles incorporated PLA/CA or PCL nanofibrous scaffolds were fabricated to be applied as guided tissue regeneration and guided bone regeneration material for the repair of damaged periodontal tissues (Abdelaziz et al. 2021). In vitro tests demonstrated that the addition of hydroxyapatite nanoparticles to scaffolds improved the cell viability by approximately 50% and AgNPs notably improved the antibacterial activity. Despite in vitro tests provided enhanced in vivo bone formation predictions, in vivo studies are necessary to switch to clinical practice.

Jin et al. (2018) also demonstrated the antibacterial potential of silver by fabricating silver ion-loaded calcium phosphate/chitosan antibacterial electrospun fibrous scaffolds as potential guided bone regeneration membranes. Additionally, zinc oxide (ZnO) nanoparticles could be a good choice to obtain antibacterial electrospun biobased scaffolds for bone tissue regeneration to provide better cell adhesion and osteogenesis (Shitole et al. 2019; Felice et al. 2018; Harikrishnan and Sivasamy 2020; Rahmani et al. 2019). Moreover, calcium carbonate seems to be an attractive abundant, biocompatible, and low-cost filler to obtain hybrid electrospun fibers to be utilized in several applications such as dental fillers, bone grafting, and guided tissue regeneration which could be used instead of hydroxyapatite, with an additional advantage of biodegradability (Elsayed et al. 2019; Fujihara et al. 2005) and antibacterial effect (Terzioglu 2021).

Some of the recent approaches turned to combinations of cell-derived extracellular matrix (ECM) with biobased polymers to produce electrospun scaffolds that mimic the architecture, structure, and additionally composition of ECM (Fu et al. 2018; Carvalho et al. 2019; Junka and Yu 2020; Padalhin et al. 2021). This novel design strategy for engineering artificial bone implants resulted in an improvement in bone regeneration capacity (Junka and Yu 2020; Padalhin et al. 2021). This strategy also provides a better mimicry of the bone ECM composition and structure that may bring advantages in future bone tissue engineering designs to fabricate clinically relevant implants.

Besides cell-derived ECM and bone morphogenetic proteins (Aragón et al. 2018; Ye et al. 2019; Da Silva et al. 2019; Bhattarai et al. 2020; Toprak et al. 2021; Cheng et al. 2019; Huang et al. 2020) loaded porous biobased electrospun membranes, drug-loaded ones have also gained widespread interest to accelerate bone regeneration (Gong et al. 2018; Mathew et al. 2017; Balagangadharan et al. 2019; Zhu et al. 2019,

2020; He et al. 2018). These studies paved the road for designing and building more effective and suitable biomaterials to be applied in bone tissue engineering.

3D nanofibrous biomimetic bone tissue scaffolds have been another important development in the field (Miszuk et al. 2018; İşoğlu et al. 2019; Ye et al. 2019; Lin et al. 2020). The 3D electrospinning method maintains the possibility of preparation of nanofibrous bone regeneration scaffolds with larger pore size, greater porosity, and interconnected porous structure (Ye et al. 2019; Lin et al. 2020). Further studies are necessary to enhance the architecture and morphology of scaffolds with nano/macro channels (Qasim et al. 2019) and also to incorporate various active components to the scaffolds for better performance (Ye et al. 2019).

In sum, despite the progress through various strategies in the bone tissue repair and regeneration field, the design of electrospun nano/micro biobased polymer fibrous membranes and in vivo testing of the developed materials is still a challenge.

3.1.2 Artificial Vascular Grafts

The native blood vessels in the human body have complex three-dimensional structures with distinct properties (Hasan et al. 2014). Artificial vascular grafts are special biomaterials that are preferred in the treatment of cardiovascular diseases to replace or bypass an entire section of a damaged blood vessel (Gao et al. 2019; Park et al. 2019; Yalcin-Enis and Gok-Sadikoglu 2018). The primary requirements for vascular grafts are bioactivity, good biocompatibility, adequate elasticity, and implantability (Hasan et al. 2014; Zhao et al. 2021). The pore structure of graft in terms of pore type, size, and interconnectedness is considered as one of the most significant factors that can influence the mechanical properties as well as long-term patency and cell filtration (Rodriguez et al. 2020). The scaffolds should have sufficient strength to withstand endogenous biological forces, assist tissue regeneration, and enhance host tissue remodeling (Zhang et al. 2011; Gao et al. 2019). Large-diameter blood vessels have commercial availability (Zhu et al. 2021). Unfortunately, grafts that have a vessel diameter smaller than 6 mm are rejected by the body's immune system within a few months (Hasan et al. 2014). Therefore, polymer-based small-diameter vascular grafts are seldom commercialized, because of delayed re-endothelialization, thrombosis formation, and thrombotic occlusion (Park et al. 2019). The fabrication of sufficiently small-diameter blood vessels with strong physical structure and bioactivity is still a great challenge in the tissue engineering field.

Especially, PCL, PLA, polyglycolic acid (PGA), and polylactic-co-glycolic acid (PLGA) are commonly investigated biobased polymers to fabricate artificial vascular grafts due to maintaining sufficient mechanical strength and biocompatibility (Palumbo et al. 2014; Das et al. 2020; Gao et al. 2019). These polymers are approved by the U.S. Food and Drug Administration for clinical use (Radke et al. 2018).

PCL has poor hydrophilicity, hypersensitivity to plasma proteins, poor cellular activity, and slow biodegradation (Sun et al. 2006; Park et al. 2019). The long-term performance of a macroporous PCL electrospun vascular graft was explored by

suturing in the rat abdominal artery (Wu et al. 2018). The results provided important insight for the evaluation of PCL grafts in the shelf-ready vascular graft applications. The scaffolds exhibited good patency, mechanical strength, and fast endothelialization. However, the physiological function of the grafts was decreased because of the slow degradation behavior of the vascular wall. The degradation of grafts is important to leave adequate space for the ECM and cells to succeed in the native physiological structure and function. It is stated that additional investigations must be considered to obtain advanced PCL-based vascular grafts.

Best et al. (2019) engineered a poly-ε-caprolactone-co-L-lactic acid (PCLA) nonwoven scaffold for small-diameter vascular graft applications. The long-term performance of biomaterial conducted using in vivo and in silico assays. The sub-1 μm diameter polymeric fibers demonstrated a three-dimensional porosity, a lumen diameter of 526.4 ± 22.6 μm, and a wall thickness of 234.8 ± 20.3 μm (Fig. 4). Feret pore diameters of grafts were between 3.3 and 6.3 μm. It was reported that the porosity of the scaffold allowed cellular infiltration; however, overall cellularity was underwhelming. As a result of inadequate vascular neotissue formation, catastrophic graft failure was experienced at 14 weeks.
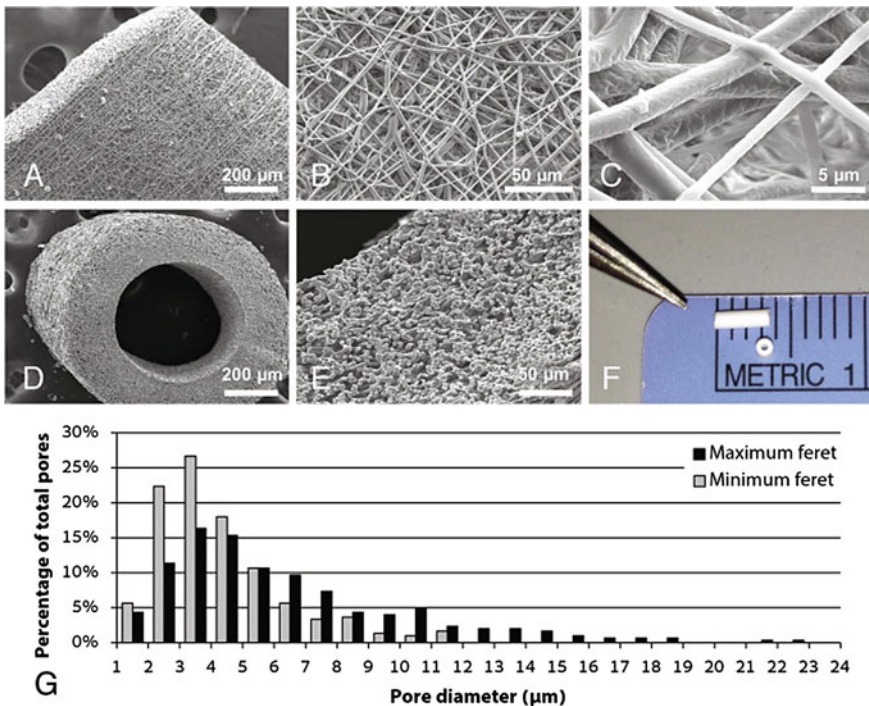
Fig. 4 SEM images of **a–c** the graft wall and **d–e** the scaffold in cross section **f** a gross image of the scaffold prior to implantation **g** pore size distribution of grafts. Reprinted from Best et al. (2019), Copyright (2021), with permission from Elsevier
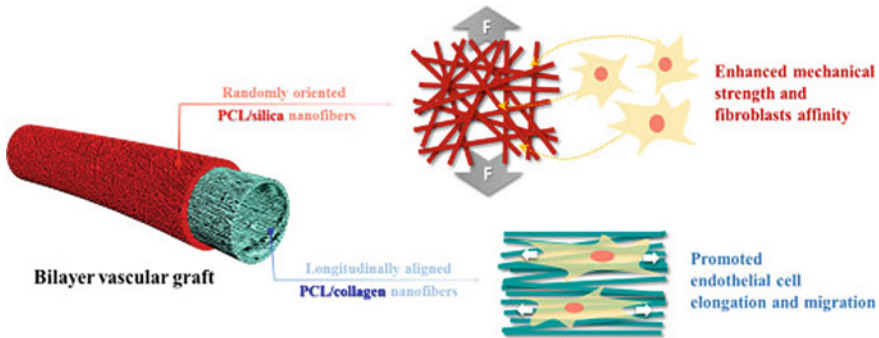
Fig. 5 Schematic illustration of the electrospun bilayer vascular graft. Reprinted from Park et al. (2019), Copyright (2021), with permission from Elsevier

Therefore, single polymer-based scaffolds should be insufficient in tissue-engineered vascular graft applications. This situation has directed researches toward the development of electrospun porous composite fibers. In recent years, Gao et al. (2019) combined the superior properties of PCL and PLGA as flexibility degradability, respectively, to obtain electrospun porous vascular grafts. The results demonstrated that the blended fibers with average diameters of ~700 nm had smooth surfaces. The tensile strength of the scaffolds fulfills the demands of artificial blood vessels. Another work (Park et al. 2019) contributed to the development of new combinations by exploring the PCL/collagen (inner layer) and PCL/silica (outer layer) nanofibers as small-diameter vascular graft with a bilayered tubular structure (Fig. 5). The natural polymer collagen incorporated inner layer enhanced the cellular affinity and enabled the rapid endothelialization of the luminal surface of the graft. It was stated that PCL-based bilayer vascular grafts could be a promising clinical potential for vascular tissue engineering applications.

PCL/fibrin-based porous nanofibers were also reported to be convenient small-diameter vascular scaffolds with cell compatibility, excellent mechanical properties, and degradation (Zhao et al. 2021; Yang et al. 2020). The electrospun PCL/fibrin tubular vascular scaffold had a length of 1 cm, an inner diameter of 3 mm, and a wall thickness of 0.2 mm (Fig. 6). The nanofibers had a porous structure that was advantageous for cell adhesion, migration, and proliferation. The in vivo experiments showed that the vascular function of the PCL/fibrin scaffolds was very similar to native arteries. Additionally, numerous functional microvessels are required in the design of artificial blood vessels. Besides, microvessel ingrowth is a significant phenomenon to remodel the degradable scaffolds. It was prognosticated that PCL/fibrin grafts could efficiently support the microvessels formation, which may be owing to the existence of fibrin with good biocompatibility. As also a solution for graft calcification, PCL/fibrin grafts (up to 9 months) demonstrated considerably fewer calcification areas compared with PCL grafts which may be related to the high pore structure of the composite graft (Zhao et al. 2021).
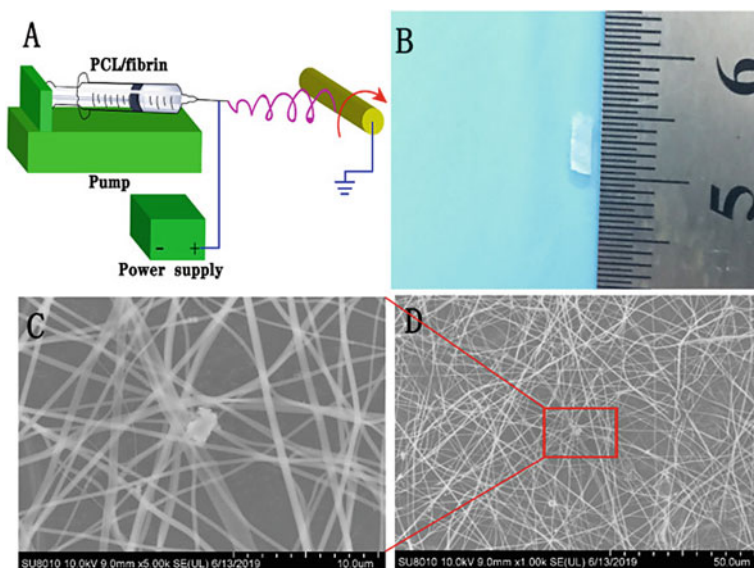
Fig. 6 **a** The schematic diagram **b** macroscopic appearances **c**, **d** SEM micrographs of electrospun PCL /fibrin vascular grafts. Reprinted from Zhao et al. (2021), Copyright (2021), with permission from Elsevier

Fiqrianti et al. (2018) reported the preparation of electrospun tubular PLLA/chitosan/collagen scaffolds for vascular graft applications. Results showed that the wall thickness and tube diameters within the heart coronary artery size range (~2.97–4.08 mm), while the pore sizes were suitable for human vascular prosthesis applications which should be optimally 20–30 μm.

To overcome the limitations of PCL, gelatin is another attractive natural polymer derived from native collagen that elicits differentiation signaling cues, granting improved cell adhesion and migration. Thus, many researchers have focused on the development of PCL/gelatin-based hybrid grafts (Shi et al. 2019; Jiang et al. 2017; Li et al. 2018; Joy et al. 2019; Suresh et al. 2018; Strobel et al. 2018). Shi et al. (2019) engineered heparin-loaded PCL/gelatin vascular grafts. The performances of heparin-loaded PCL/gelatin hybrid fibers were examined in vivo (Fig. 7). The vascular graft had an inner diameter of 2.0 mm and a wall thickness of about 500 μm. The incorporation of gelatin lowered the average fiber diameter of graft from 6.6 ± 0.7 to 3.7 ± 0.3 μm when compared with the pure PCL fibers. An effective approach was developed to handle each polymer's shortcoming as well heparin prevented the thrombosis. The electrospun grafts provided promotion of endothelialization and regulation of smooth muscle regeneration. It was stated that the combination of PCL and gelatin may provide a good opportunity for engineering small-diameter artificial blood vessels with enhanced performance.

Instead of blending the two polymers, Xing et al. (2021) coated the internal surface of electrospun PCL vascular grafts with gelatin. The porosity of the heparinized PCL
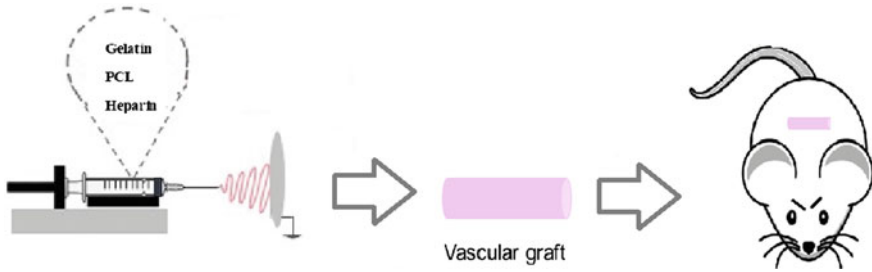
Fig. 7 Development of heparin-loaded PCL/gelatin hybrid vascular grafts for use in vivo

graft was found to be 85.2 ± 2.8%, and the gelatin coating lowered the porosity of the graft to 82.4 ± 1.5%. Coating the lumen side of PCL grafts with gelatin provided enhancement in smooth muscle cells and ECM regeneration. This can be applied as a simple and effective approach to promote the endothelialization of PCL vascular grafts.

Recently, a research group decided to verify the potential of electrospun recombinant spider silk protein/PCL/gelatin to be applied as small caliber vascular tissue engineering scaffolds through the in vitro and in vivo biocompatibility tests (Xiang et al. 2018). The tubular scaffolds were developed with a length, wall thickness, and an inner diameter of 2 cm, 0.3 mm, and 5 mm, respectively. The fibers exhibited interconnected pore structure and smooth surface. Silk protein/PCL/gelatin fiber had wider fiber diameter distribution, larger fiber diameters, and a faster degradation rate than silk protein/PCL and PCL ones. Silk protein/PCL/gelatin fiber simplified host cell ingrowth and showed excellent in vitro and in vivo blood and tissue biocompatibility which makes this scaffold a good candidate for vascular grafts.

Some efforts also realized on the combination of chitosan and PCL electrospun fibers for the preparation of tissue-engineered vascular grafts (Sultana et al. 2017; Rez et al. 2017). The blended PCL/chitosan tubular scaffolds showed promising features to be used as a replacement in blood vessel applications.

Chitosan/poly(L-lactide-co-epsilon-caprolactone) electrospun scaffolds were fabricated by Du et al. (2019), and then, dextran sulfate modification was applied to improve the properties of scaffolds. The mats showed a nanofibrous network with interconnected micropores, which could be similar to the native ECM structure. The modification provided to enhance the anticoagulation and hemocompatibility of the scaffolds. The modified scaffolds exhibited suitable degradation property which is important for the application of vascular grafts.

In conclusion, great efforts have been performed on artificial vascular grafts from biobased polymers which resulted in important progress in terms of accomplishing the tissue remodeling like the native blood vessels. However, further development needed for small-diameter blood vessels.

3.1.3 Cartilage Regeneration Scaffolds

Articular cartilage facilitates the resistance of complex loading patterns and articulation of joints. Because of several reasons (e.g., aging, traumatic injury, osteoarthritis, and other diseases), cartilage can be damaged (Patel et al. 2019). However, the damaged cartilage tissue has limited self-repair ability. Traditional surgical therapies are still lacking completely regenerating functional cartilage tissue and finding a solution for long-term outcomes (Li et al. 2019; Wang et al. 2016). Therefore, new strategies are developing in the tissue engineering field to replace the damaged cartilage. Adequate mechanical properties to preserve its shape, the capability to maintain the load-bearing function, biocompatibility, analog structure to ECM for cell adhesion, convenient porosity for cell ingrowth, and biodegradability are the expected features for an ideal tissue engineering cartilage regeneration scaffold (Li et al. 2019). Extensive research has been conducted on tissue-engineered electrospun cartilage regeneration scaffolds in the past few decades due to their outstanding properties such as high surface-to-volume ratio (Chen et al. 2021). Nevertheless, the existing electrospun scaffolds had insufficient biomechanical properties, limited thickness, and non-native articular cartilage structure (Wang et al. 2016; Chen et al. 2021). The recent researches focused on the development of cells and growth factors loaded electrospun scaffolds (Wang et al. 2016; Silva et al. 2017; Kadir et al. 2021), composite scaffolds (Chen et al. 2020; Jia et al. 2020; Sharifi et al. 2020), and 3D fibers instead of conventional two-dimensional (2D) ones (Chen et al. 2019, 2021).

Biochemical support to the surrounding cells may be maintained with the presence of significant bioactive components such as collagen, growth factors, glycosaminoglycan, and proteoglycan in the ECM matrix. Moreover, they are promoting cell growth and remodeling (Feng et al. 2020).

The coaxial electrospinning method had been applied to encapsulate glucosamine sulfate into the core of PCL nanofibers (Fig. 8) by Chen et al. (2020) for cartilage regeneration. The cell attachment and proliferation tests showed that composite nanofibrous scaffolds had an important impact on the proliferation and growth of rat articular chondrocytes. It was also reported that a suitable glucosamine sulfate amount in the fiber network was critical.

Another nanofibrous composite scaffold was fabricated by Jia et al. (2020) using fish collagen and PCL. Fish collagen was preferred as an alternative source to mammalian collagen for tissue engineering owing to its adequate biodegradability, good biocompatibility, inert immunogenicity, and low cost. The collagen/PCL scaffold was suggested as a promising biomaterial for cartilage regeneration due to showing good results in terms of in vitro supporting chondrocyte proliferation and cartilage formation.

Sharifi et al. (2020) reported the co-electrospinning of PCL with chondroitin sulfate and gelatin as a cartilage extracellular matrix component to develop composite nanofibrous scaffolds for chondrogenesis differentiation of human mesenchymal stem cells that exist in the bone marrow. It was shown that co-electrospun composite scaffold is suitable for successful cartilage tissue engineering application owing to providing mesenchymal stem cells without using any external differential agent.

Fig. 8 Schematic diagram of the glucosamine sulfate incorporation into PCL nanofibers via coaxial electrospinning. Reprinted from Chen et al. (2020), Copyright (2021), with permission from Elsevier
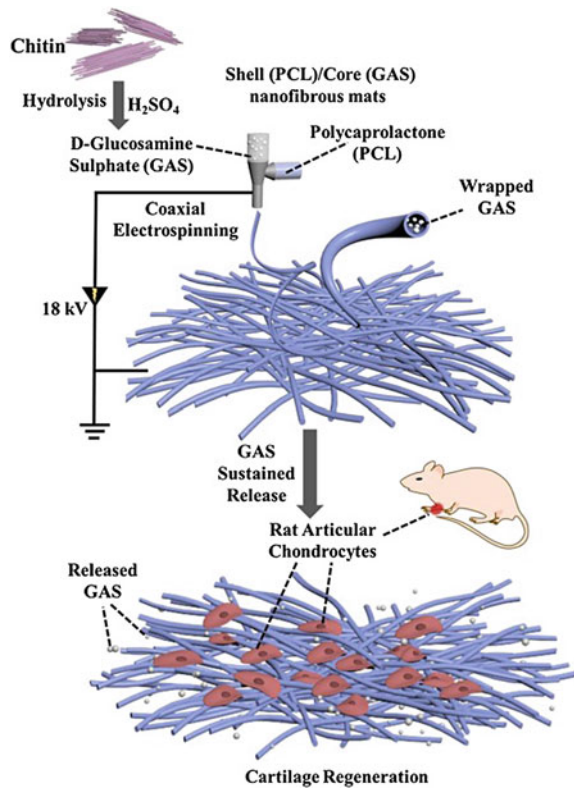
As the most prevailing recent trend, the 3D electrospun scaffolds with controllable shapes and large pores should bring the advantage of regulating cellular biological behaviors, intercellular interactions, and efficient biomimetic structure (Chen et al. 2019). The study of Li et al. (2019) reported that the preparation of porous 3D scaffolds composed of gelatin/PCL nanofibers and decellularized cartilage extracellular matrix. The biomimetic scaffolds served as a skeleton with good mechanical properties as well as good biocompatibility. Superior performance for cartilage defect repair was achieved with the developed composite scaffolds which demonstrated the potential for clinical applications.

3D porous electrospun PLA-gelatin-based scaffold functionalized by the crosslinking of chondroitin sulfate was performed by Chen et al. (2021). The scaffolds were formed of nanofibers with interconnected and cellular structure that mimicked the native ECM. Good results were obtained with the study that the composite scaffolds exhibited appropriate biocompatibility, reversible compressibility, and mechanical property. Superior anti-inflammation effects, as well as effectively promoted cartilage repair, were observed in the in vivo studies on rabbit cartilage defects.

As another critical challenge, Girão et al. (2020) focused on the fabrication of biomimetic arcade-like electrospun scaffolds. A hierarchical 3D bilayered biocompatible PCL-based scaffold with pore interconnectivity and mechanical features adequate for cell culture protocols was engineered which could be evaluated in the cartilage regeneration after detailed cell response and its modulation by mechanical stimuli investigations.

Continued efforts are needed to investigate in vivo biotoxicity, biodegradability, and mechanical performance to open the way for clinical applications (Zhou et al. 2019).

3.1.4 Nerve Tissue Engineering Scaffolds

Nerve tissue repair is a worthy treatment concept to restore nerve systems in human health care because of the incapability of self-regeneration (Ghasemi-Mobarakeh et al. 2008; Altun et al. 2019). Biobased electrospun artificial scaffolds have been a matter of great interest to be used in nerve tissue repair as in other biomedical applications. Currently, grand attention is drawn toward the design of highly effective scaffolds. The development of scaffolds with appropriate properties including chemical, physical, morphological, and electrical is crucial for nerve cell adhesion and proliferation (Zha et al. 2020). It has been reported that in clinical applications electrically conductive biomaterials play a key role in axonal growth and nerve regeneration by promoting the proliferation, adhesion, and migration of Schwann cells (Pan et al. 2018). Moreover, different recent approaches such as drug-loaded, 3D, and nanocomposite electrospun neural materials were summarized in the present part.

Gold nanoparticles (AuNPs) are metallic agents that have gained attention in neural tissue engineering treatments owing to providing enhanced cellular response and mechanical features of the scaffolds (Saderi et al. 2018; Afjeh-Dana et al. 2019; Jaswal et al. 2020). In addition, AuNPs stimulate axonal elongation and sprouting axons. Saderi et al. (2018) stated that nanofibrous scaffolds with electrical cues could be hopeful candidates in the nerve tissue engineering field. Gold nanoparticles are special components to provide improved electrical signal transfer between neural cells by increasing the conductivity of materials. Conductive nanofibrous electrospun scaffolds based on PCL/chitosan/AuNPs were developed that showing up to 15×10^{-3} S/cm electrical conductivity. It is known that in neural tissue engineering applications, the conductivity of the proper conductive material which could stimulate the migration and proliferation of Schwann cells should be higher than 1.0×10^{-3} S/cm, and thus the developed AuNPs doped PCL/chitosan nanofibrous scaffolds could be vastly applicable in the related field.

Polypyrrole is among the most significant intrinsically conductive polymers (Zarei et al. 2021). It was chosen due to being a very stable conductive organic polymer with no toxicity to cells and good biocompatibility features (Pan et al. 2018). Investigations have shown that polypyrrole-containing electrospun scaffolds have the potential of being used in nerve tissue engineering (Zarei et al. 2021; Pan

et al. 2018; Sadeghi et al. 2019). In a previous study, nerve guidance conduits with polypyrrole-coated polycaprolactone nano yarns as inner filler and PCL nanofibers as outer shells were prepared to have a unidirectional arrangement. The research opened a new way for peripheral nerve repair or regeneration with fabricated materials that have good mechanical properties (Pan et al. 2018). Further, Sadeghi et al. (2019) PCL/chitosan/polypyrrole nanofibrous scaffold is a promising graft for neural tissue engineering. The average fiber diameters were ranged between 36 and 181 nm. Chitosan provided enhanced cell adhesion and proliferation, while the availability of polypyrrole improved the growth of PC12 neural-like cells via rising the electro-activity of scaffolds.

Graphene and graphene oxide-enriched scaffolds have been highlighted as promising candidates for neural regeneration applications (Ginestra 2019; Heidari et al. 2019; Golafshan et al. 2018; Zhao et al. 2017; Aznar-Cervantes et al. 2017; Qi et al. 2019; Girão et al. 2020; Magaz et al. 2021). Graphene and graphene oxide are fascinating carbon-based materials that are preferred in the field of neuroscience applications due to their electrical conductivity and mechanical strength (Qi et al. 2019; Magaz et al. 2021). In the study of Ginestra (2019), functional electrospun porous scaffold production from PCL and graphene powders was achieved with the aim to embed neural cells in appropriate matrices that support cell adhesion and differentiation. The scaffolds were tested using mouse stem cells to determine cell growth behavior. The fibers were found to be highly compatible due to support stem cells adhesion, and proliferation. The differentiation of the stem cell into dopaminergic neurons was strongly promoted by the insertion of graphene. The research showed that the PCL-graphene scaffolds might be evaluated as a biomaterial in nerve endoprostheses and nerve injury treatments for clinical applications.

PCL can also be combined with gelatin to be used as nerve tissue repair material with the aim of highly enhanced mechanical, biological, and physical properties. Heidari et al. (2019) designed smooth and bead-free nanofibrous scaffolds composed of PCL/gelatin/graphene. Composite nanofibers showed improved biocompatibility as well as excellent antibacterial activity against *Staphylococcus aureus* and *Escherichia coli* bacteria. As it was mentioned in their article, PCL/gelatin/graphene-based electrospun fibers appeared to be a good candidate in tissue engineering and other biomedical field applications.

In another study, to determine the synergic effect of graphene and gold nanoparticles, a conducting hybrid fibrous material was developed by combining poly-3 hydroxybutyrate-co-12 mol.% hydroxyhexanoate and graphene-decorated gold nanoparticles. The scaffolds exhibited a permeable mat-shaped matrix assembly with a fibrous nature. Positive results were obtained in vitro biological studies for the proliferation and migration of Schwann cells (Liu et al. 2020).

Nanocomposite scaffolds are also important materials with unique properties providing new opportunities in nerve regeneration treatments. Fascinating research was executed by fabricating bacterial cellulose/PCL nanofibrous composite scaffolds as probable biomaterial candidates for neural renewal (Altun et al. 2019). The

morphological evaluation showed that composite scaffolds had well-defined inter-connected nanofiber (70–120 nm) networks with hollow micro/nanobeads (100 nm–1.6 µm). The structural properties of bacterial cellulose/PCL scaffolds mimicked neurological networks. In addition, these biocompatible scaffolds with promoted cell adhesion and enhanced neurite outgrowth feature were suggested as biomimetic materials in nerve tissue engineering applications.

Saravani et al. (2019) also fabricated an electrospun nanocomposite scaffold composed of polyglycerol sebacate/chitosan/gelatin. The diameters and porosities of fibers were determined approximately 80 nm and 63–83%, respectively. The scaf-fold containing more gelatin demonstrated the maximum proliferation of the PC12 cells after 3 days of cell culture. Furthermore, the nerve tissue layer was formed apparently. The authors suggested in vivo investigations for further research.

Lignin is considered a promising natural ingredient for tissue engineering composite scaffolds. Lignin nanoparticle-incorporated polycaprolactone nanocom-posite fibers were evaluated for potential peripheral nerve regeneration applications by Amini et al. (2020) toward in vitro and in vivo studies. The fibers promoted PC12 and human adipose-derived stem cells viabilities. The PCL fibers with 15% of lignin were found to be convenient to peripheral nerve regeneration. This fiber could promote axonal sprouting which is extremely accepted for nerve regeneration and reconstruction.

A cell-free and 3D artificial nerve implant design that mimics structural properties of ECM was developed by Kriebel et al. (2017) based on sub-micron fibers of PCL and collagen/PCL blends embedded in gelatin and then inserted in collagen tubes. The acellular scaffolds were tested through in vivo experiments by replacing 15 mm-long segments of rat sciatic nerves. All artificial implants provide the environment for Schwann cell migration and axonal regeneration. In addition, the artificial implant represents an important step for clinical applications of artificial nerve bridges due to the recovery of motor functions and physiological assessment of the regenerated nerves.

Silk fibroin is also a significant biobased polymer for biomedical applications that is preferred due to its highly biocompatible, permeable as well as exhibiting good mechanical properties, and controllable degradation rate (Türkkan et al. 2018; Oztoprak and Okay 2017; Lalegül-Ülker et al. 2019). Another in vivo study on dogs was conducted using silk fibroin-based conduit inserted with silk fibers to bridge a 30 mm-long sciatic nerve gap. The study demonstrated that the neural scaffold succeeded in satisfactory regenerative outcomes at 12 months after surgery presenting its potential for peripheral nerve injury treatment (Xue et al. 2018).

Drug-loaded electrospun neural conduits also hold great attention (Mahumane et al. 2020; Haidar et al. 2021; Farzamfar et al. 2018). In this concept, a gabapentin-loaded cellulose acetate/gelatin wet-electrospun scaffold was fabricated for neural tissue regeneration (Farzamfar et al. 2018). The scaffold that had approximately 70% porosity, 63.67° ± 3.21° wettability, and 2.80 ± 0.01 MPa tensile strength were chosen for in vivo tests. Then, the investigation toward in vivo tests in a sciatic nerve defect model in Wistar rats was carried out to determine neural regenera-tion efficacy of composite scaffold. Improved regeneration of the created injury was

achieved with the drug-loaded scaffold when compared with the gabapentin-free scaffold. *N*-acetylcysteine-incorporated PLGA biomimetic neuro-scaffold for traumatic brain injury was also found to be neurocompatible through ex vivo cytotoxicity assays that were realized on rat pheochromocytoma (PC12) and human glioblastoma multiform (A172) cell lines with a positive influence on cell proliferation (Mahumane et al. 2020). In another study, the combined multi-technologies were used to determine the neuroprotective effects of atorvastatin and alpha-lipoic acid as active pharmaceutical ingredients in a composite scaffold. The effective scaffolds were obtained by embedding atorvastatin-loaded chitosan nanoparticles into alpha-lipoic acid containing PLGA nanofibers to be evaluated in the peripheral nerve injury treatments for local delivery of neuroprotective drugs (Haidar et al. 2021).

In brief, composite functional scaffolds developed by the use of biobased polymers retain considerable potential in the field of implantable biomaterials for nerve tissue repair. PCL seems to be the most studied polymer in this field. Further efforts should be realized on in vivo stability and detailed toxicity tests of artificial implants for clinical applications.

3.2 Drug Delivery

Nanocarriers such as liposomes, sponges, foams, nanoparticles, hydrogels, and emulsions have been shown to enhance drug absorption, stability, penetration, half-life, bioavailability, as well (Agrahari et al. 2017; Singh et al. 2019). Among the other types of nanocarrier systems, nanofibers have conclusively demonstrated to be a robust carrier system for therapeutics due to their extraordinary properties such as high drug-loading ability, high encapsulation efficiency, target-specific, sustained drug delivery, and easy processing (Ramalingam and Ramakrishna 2017).

Drug release systems are mainly focused on minimizing drug degradation or loss, increasing the bioavailability of the drug, preventing side effects, and improving drug accumulation in the targeted area (Jain 2008). Furthermore, it is aimed to increase the effectiveness of the drug and treat the damaged area. These systems consisting of synthetic or natural polymers can consist of liposomes, micro/nanoparticle, dendrimer, micelle, hydrogel, or nanofiber forms (Jayaraman et al. 2015).

Thanks to its high drug-loading capacity, nanofiber mats increase the drug flow by increasing the drug concentration in the carrier system. Controlled drug release allows the release of active substances to the target area at a certain speed for a certain period. In addition, the fabrication methods of nanofibers are less costly compared to the other nanostructured drug carrier systems (Groeber et al. 2011; Kataria et al. 2014).

Polymeric nanofibers have been studied as drug delivery systems for ocular, nasal, mucosal, parenteral, dermal, and transdermal routes over the last few decades (Erdal and Güngör 2020; Jain 2020).

Modern drug delivery systems face problems such as poor solubility, bioavailability, and selective delivery of drugs with short half-lives (Abdelhady et al. 2015).

Several factors affect the drug-loading capacity and controlled release behavior of porous fibers. Among the most important factors influencing drug-loading efficiency and controlled release of nanofibers are polymer/drug ratio, polymer viscosity, variables in the electrospinning process, drug solubility in the chosen solvent system, and drug-loading technique (Cagil et al. 2019). Furthermore, using electrospun porous fibers will locally minimize the minimum necessary dose, resulting in fewer systemic ingestion and less unintended side effects (Zamani et al. 2013).

Drug release can be extended by using lipophilic polymers or crosslinking hydrophilic polymers. The use of these materials can bring many advantages including (i) achievement in prolongation of drug release (ii) prevention of sudden drug release (iii) increase of the stability of nanofibers in water or (iv) improvement of the mechanical, thermal, and chemical properties of nanofibers. Glutaraldehyde is the least cytotoxic among other crosslinking agents, and it is used to crosslink hydroxyl (–OH) containing polymers such as PVA, starch, and gelatin (Moreno-Cortez et al. 2015; Wang et al. 2016; Laha et al. 2016).

Due to their high surface-to-volume ratio and pore connectivity, electrospun nanofiber scaffolds have proven useful for drug delivery systems. Polymeric electrospun nanofibers can be used to advance drug delivery systems for a variety of water-soluble and insoluble drugs (Gupta et al. 2014).

In recent years, nanofibers have many advantages, which have become widely used in topical drug delivery fields. Nanofibers containing both hydrophilic and lipophilic drugs can be used for controlled release purposes, and the release rate of the drugs (active substances) can be changed by nanofiber morphology, porosity, and composition.

Nanofiber formulation is complicated and dependent on several variables, but the nature of the formulation provides many options for achieving the desired nanofiber drug release properties.

Ma et al. (2011) fabricated paclitaxel-loaded porous nanofibers to use for prostate cancer. In this study, chitosan-PEO nanofibers were obtained using PEO template, and the porous fibers were immersed in an ethanol solution of 0.1 wt% of PXT for almost 8 h to become adhesive to the fiber. Consequently, the resulting fibers showed almost 85% drug release from nanofibers in pH 7.4 for 48 h.

The drug's bioavailability should be close to the ideal dosage, which maximizes therapeutic effectiveness while minimizing possible side effects in the treatment (Nguyen et al. 2011). The formation of pores on the surfaces of individual nanofibers changed fiber surface morphology and allows for an increase in specific surface area. Therefore, both rate of the drug release from the nanofibers and the nanoporous morphology can affect the adhesion of the drug to the host cell. In this scope, porous core/sheath composite nanofibers were prepared with the use of salicylic acid (SA) and poly(ethylene glycol) (PEG) as core and PLA as the shell (Nguyen et al. 2011). SEM images of the composite fibers indicated that irregular pores have occurred in

the outer layers. According to in vitro study, it was found that the drug release from the porous structured fibers was higher than the non-porous counterpart.

In the last 10 years, many researchers have focused their efforts on drug-loaded nanofibers in local drug release to treat tumors and prevent tumor reformation. There are studies in the literature that have been performed by adding various anti-cancer drugs into the electrospun fibers, such as doxorubicin (DOX), paclitaxel, and dichloroacetate.

Wang et al. (2016) produced rapamycin-loaded PEO/PDLLA nanofibers at 0.5, 1, and 2% (w/w) using conventional electrospinning. In the study, encapsulation activity was 93.2, 96.1, and 86.4, respectively. A burst release was around 26% from the 0.5% rapamycin-loaded membrane in the first 24 h, while a slow release of 33.4% in the first 1-week period.

Salinomycin-loaded PLGA nanofibers were developed by a study group for use in the treatment of glioblastoma (Norouzi et al. 2018). It was found that 80% salino-mycin was released from the fibers through a diffusion mechanism in 4 days (Fig. 9). During the two-weeks when nanofiber started to degrade, the residual drug was sustain released.

Drugs that lose their activity in the digestive tract or have the first-pass effect in the liver when ingested orally are absorbed through the skin and added to the systemic circulation. The transdermal route is an alternative to the oral and intravenous routes for drug administration. However, changing the required amount and surface area of the drug utilized in these applications makes it difficult to release the drug in a repeatable dosage.

The drug storage device is mounted on the skin in transdermal therapy devices, and the drug transported by the system is liberated in a regulated fashion and enters

Fig. 9 Schematic illustration of drug release from fibers
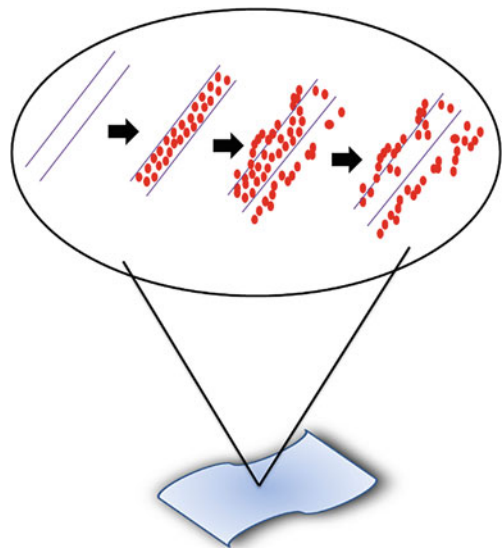
the systemic blood supply via the skin. In transdermal therapeutic systems, the drug stored system is placed on the skin, where it is carried by the system in a controlled manner until it enters the systemic bloodstream via the skin (Jain 2008; Alkilani et al. 2015).

At the same time, the drug dosage/formulation can be painlessly applied to the skin. The drug initially penetrates to the stratum corneum and then passes through the deeper epidermis and dermis without drug accumulation in the dermal layer. When the drug reaches the dermal layer, it becomes available for systemic absorption through dermal microcirculation. Thus, toxic side effects of drugs are minimized, and bioavailability increases, as well (Wen et al. 2015; Alkilani et al. 2015; Solomon 2015).

Hydrophilic drugs can show burst release behavior in the PBS buffer or in vivo conditions due to their high solubility. Heydari et al. (2018) prepared hydrophobic paracetyl-cyclodextrin (AcCDP) nanofibers containing riboflavin (vitamin B_2) and purposed to use them as tissue scaffold. As a result of release analysis, it was confirmed that the obtained materials have a two-phase release profile that involves burst and continuous release in both release media (pH 1.2 and pH 7.4). The presence of the burst release behavior can be related to the release of free vitamin molecules that interact with the nanofiber structure through non-cyclodextrin part interactions.

Li et al. (2016) found that crosslinking with glutaraldehyde increases vitamin A and E-loaded gelatin fibers. The FTIR spectra indicated characteristic peaks of vitamins in the gelatin fibers, and the peak intensities of vitamin-loaded fibers decreased to pristine gelatin fibers. Furthermore, the bioactive fibers prevented the *E. coli* versus *S. aureus* bacteria and increased fibroblast proliferation and collagen production. The literature studies on drug-loaded nanofibers used in wound care applications are given in Table 1.

Many attempts have been made to combine medicinal ingredients with nanofibers for use in transdermal applications.

DOX is a chemotherapy drug, which is used in many drug release forms. DOX-loaded PAN/PMMA fibrous materials developed by an unusual perspective (Dai et al. 2020). To obtain carbon nanofibers with porous structure, blend PAN/PMMA fibers were carbonized and then modified with acid treatment. This process increases the hydrophilicity of NF and therefore also increases the DOX release rate. Moreover, the new DOX-loaded PCNFs system exhibited a double-acting drug release behavior that accelerated DOX release in an acidic environment and by NIR irradiation.

Porous, eroded, wrinkled, and rough nanofiber topography has been observed in a study showing that the solvent system (single or binary solvent) and moisture can directly affect fiber morphology. Şimşek (2020) claimed that porous structured fibers are preferred in supporting cellular behavior in tissue engineering and drug release applications, due to their higher specific surface area. According to SEM micrographs, an acetone-DMSO binary solvent system (in 60% room humidity) may be favored in the fabrication of electrospun porous PCL fibers (Şimşek 2020).

Table 1 Drug-loaded nanofibers that have been performed in the last decade

Study group	Matrix	Active ingredient	Results
Abid et al. (2018)	PEO/Alginate	Acetaminophen	Fast release rate (~80% in 60 min)
Aminipour et al. (2018)	PVA	Theophylline	Uniform encapsulation
Tugcu-Demiröz et al. (2020)	PVP	Metronidazole (MET)	More than 80% of the MET in 15 min
Nguyen-Vu (2018)	PCL	Insulin and paclitaxel	Hydrophobic drug (PTX) and hydrophilic drug (insulin) miscibility with PCL
Parın and Yıldırım (2021)	PVA, gelatin and PVP	Folic acid	Fast release rate, more than 75% of FA in 20 min
Mendes et al. (2016)	Chitosan/fosfolipit	Curcumin, diclofenac, vitamin B$_{12}$	More than 75% of curcumin
Song et al. (2016)	PLGA	Daidzein-loaded nanocarriers	Approximately 70% of Daidzein in 60 min
Wang et al. (2015)	PVP	Curcumin	Dissolution rate above 90% within 15 min
Shen et al. (2014)	PVA	Prazosin hidrochloride (PRH)	PRH release rate around 25% in 24 h
Akduman et al. (2016)	PU	Naproxen	Burst release profile at 15–30 min
Opanasopit et al. (2013)	PVA/CA	Capsicum extract (CE)	More than 65% CE encapsulation efficiency
Rychter et al. (2018)	Poly(ε-Caprolactone)	Cilostazol (CIL)	Ritger-Peppas and Peppas-Sahlin models, >80% CIL release
Hamzah et al. (2021)	Polyvinylidene fluoride/Pectin	Benzalkonium chloride (BAC)	78.9 ± 1.7% Swelling capacity, Higuchi and Korsmeyer-Peppas kinetic models

3.3 Wound Dressings

Wound dressing materials are very substantial segments in the medical and pharmaceutical wound care marketing area (Boateng et al. 2008; Aavani et al 2019). Nanofibers have potential use as controlled drug release systems to human skin and covering material for the treatment of a wound and burn of the skin. It is associated with the fact that fibrous structure of nanofibers is similar to the skin structure. Due to their large surface area and nanoporous structure, nanofibers activate stimulating pathways at the wound site, and then, they attract fibroblasts to the dermis

layer (Rameshbabu et al. 2018). The wound healing process includes well-organized biological and molecular activities such as cell migration, cell proliferation, extracellular matrix deposition, angiogenesis, and remodeling (Schultz et al. 2011; Gonzalez et al. 2016). Extracellular matrix molecules provide tissue hydration, nutrition, cell proliferation, and differentiation (Yang et al. 2017; Giobbe et al. 2019). Biocompatible and biodegradable polymers can be used/accomplished to promote cell adhesion and proliferation as well as active drug substances. In conclusion, it helps heal wounds and regenerate tissue. The pore sizes of nanofibers used as wound dressings are between 500 nm and 1 μm (Gomes et al. 2015; Arthanari et al. 2016). The pore size allows cells in the wound region to exchange gas while serving as a barrier to infectious bacteria. A large surface area of about 5–100 m^2/g is very efficient for the absorption of fluids in the wound site (Heunis and Dicks 2010). It provides the wound discharge caused by the wound to be absorbed and oxygen and air transmission to the wound. Therefore, the flexible structure of nanofiber mats is very useful in wounds with a large surface (Kai et al. 2014).

Because of their high specific surface area, interconnectivity, and porous structure, electrospun nanofibers are an excellent wound dressing candidate (Fang et al. 2008; Lim 2017). Nanofibers are used both to remove extra body fluids from the wound site and for wound healing (Mohammadian and Eatemadi 2017).

Membrane mats (nonwoven) with pore sizes ranging from 1 to 500 nm are useful in preventing bacterial penetration. These membranes with large pore size and high surface area (5–150 m^2/g) proved effective for dermal drug release (Abdelhady et al. 2015).

Traditional wound care consisted mainly of ointments, local antimicrobial agents, and sterile bandages. There were a wide variety of wound dressings available in the early 1980s, and they mostly consisted of conventional dressings, paste bandages, and related preparations. Current wound care products first appeared in the mid-1980s, and hospitals all over the world continued to use them in a limited capacity (Dhivya et al. 2015). Recently, bioactive agents are released by using hydrocolloids, hydrogels, alginates, polyurethane films, and porous fibers (Ghomi et al. 2019).

Due to their porosity, high surface area to volume ratio, and biocompatibility, antibiotic-loaded nanofibers are useful as wound dressing materials. The composition of the nanofiber matrix is critical to drug release behavior. The rate of drug release decreases over time in a homogeneous nanofiber system. In homogenous fiber systems, it takes more time for the drug to go longer to spread around the porous fibers.

Depending on the chronic state, the average time for wound healing is 2–3 days (Abdelhady et al. 2015). As previously mentioned, wound dressing materials can be loaded with different drug and biologically active agents such as vitamins, growth factors, small molecules of nitric oxide, antibiotics, minerals, and oxygen or other molecules carriers (Aavani et al 2019).

To control infections without causing any side effects in acute trauma and wound healing, active ingredients are required to be quickly released. Therefore, PVA is usually used in a fast-dissolving release system due to its hydrophilic structure. PVA nanofibers containing ascorbic acid and caffeine were prepared and characterized

by Avizheh et al. (2019) to utilize in wound healing applications. It was observed that the ascorbic acid and caffeine were released from the hydrophilic fibers with 65% and 69% of release amount, respectively, in the first 6 h. PVA/caffeine samples released all caffeine in their structure after 90 min, while PVA/ascorbic acid samples released ascorbic acid in their structure after 150 min. According to FTIR results, active substances were well encapsulated in fibers during electrospinning, and it may be related to the formation of peak shifts in the spectrum. Besides, PVA/ascorbic acid/caffeine samples also showed antifungal effects; however, regeneration and wound closure rate found to be better in the PVA/ascorbic acid sample. This condition has been associated with ascorbic acid being a good antioxidant.

Barbak et al. (2020) developed PCL/PEO nanofiber structures loaded with silver sulfadiazine (SSD), and they investigated the utility of these structures as patches in local drug release. SEM analysis revealed that porous nanofibers with a smooth and regular morphology were seen by SEM analysis. The reason for this morphology was explained by the homogenous mixing of polymer matrix without phase separation, and the SSD-loaded blend nanofibers had a single-phase SSD release profile (SSD was released from the fibers at a rate of approximately 82% for 24 h). Physical interactions between drug-polymer matrix were proven by FTIR spectra, as well.

In another study, Galkina et al. (2015) investigated the availability of electrospun cellulose fibers containing three different drugs (diclofenac sodium, penicillamine-D, and fosfomycin) and nano TiO_2 in dermal applications. It has been proved that the physical interaction between nano TiO_2 and drug molecules influences the release rate and kinetic profile depending on the drug type.

There are many studies on the use of antibiotic-loaded nanofiber forms in skin treatment (Heunis and Dicks 2010; Soscia et al. 2010; Rasouli and Barhoum 2018; Khoshbakht et al. 2020; Homaeigohar and Boccaccini 2020). A study about the preparation of PVA, gum tragacanth, graphene oxide, and tetracycline hydrochloride nanofibers was conducted by Abdoli et al. (2020). It was determined that none of the nanofibers with less than 100 nm diameters showed any toxicity. Moreover, the addition of graphene oxide delayed the release of antibiotics and allowing the controlled release behavior. The electrostatic attraction between PVA and graphene oxide during the electrospinning process caused this controlled release behavior. The antibacterial activity of nanofibers containing graphene oxide was found to be higher than pure PVA counterparts.

In a similar study, the effect of graphene oxide on drug release profile was reported. The release of tetracycline from PCL/dextran/graphene oxide patches with less than 50 nm was more controlled with the addition of graphene oxide. Despite the same amount of tetracycline release, it increased the release time twice. These patches demonstrated antibacterial activity to *E. coli* and *S. aureus* bacteria. Consequently, it has been claimed that it can be utilized as a drug carrier system that releases drugs sustained and controlled for up to 3 days in chronic infections.

The literature studies on porous nanofiber patches used in wound care applications are given in Table 2.

Natural antibacterial components obtained from plants have been encapsulated in fiber forms. Chen et al. (2020) produced thymol-loaded porous CA nanofibers

Table 2 Studies on nanofibers used in wound care applications

Study group	Matrix	Active ingredient	Results
Tammaro et al. (2015)	PCL	Linezolid	Effective antibacterial activity (*Staphylococcus aureus*, zone area 8.9 cm^2)
Li et al. (2013)	PVA/SA	Ciprofloxacin	More than 240% swelling ratio, almost 60% release rate in 30 min
Rezai et al. (2019)	PEO/SA	Vitamin C	Effective to skin disorders
Sangnim et al. (2018)	PVA ve tamarind gum	Clindamycin	Efficient to *Staphylococcus aureus* growth
Zahid et al. (2019)	PCL/PLA	Vitamin E	Effectively promote angiogenesis
Garcia-Orue et al. (2019)	PLGA	Aleo vera	Maximum wound closure 95.53%
Ahlawat et al. (2019)	PVA/gelatin	Papaya	Strong antibacterial activity to *S. aureus* and *E. coli*
Poornima and Korrapati (2017)	Chitosan/PCL	Ferulic acid and resveratrol	Resveratrol and ferulic acid up to 48% and 55%, respectively, in 120 h, >85% wound closure
Dadras Chomachayi et al. (2018)	Gelatin/silk fibroin	Thyme essential oil and doxycycline	Extended release rate, effective to *Staphylococcus aureus* and *Klebsiella pneumoniae*
Shoba et al. (2017)	Gelatin/PVA/PCL	Bromelain (Br) and salvianolic acid (Sa)	Around 80% (Br) and 60% (Sa) release rate, total wound area closure in 15 days
Kiliç et al. (2018)	PU	Doxorubicin	Fast release behavior, more than 70% of DOX in the first 10 min
Razzaq et al. (2021)	Gelatin/Polyvinyl alcohol	Cephradine	>90% release rate in 24 h, effective to *S. aureus*

for the biomedical field. These nanofibers have 32–33 μm and 86% porosity. When skin regeneration and wound healing were studied, it was assigned that the pore size for the optimum cellular function was in the range of 20–120 m. Besides, porous patterned fibers have shown over 60% drug release for 48 h.

3.4 Cosmeceutical Applications

Electrospun nanofibers have a wide range of cosmetic uses, including the development of face masks, perfumes, deodorants, and antiperspirants (Kamble et al. 2017). Since electrospun fibers contain active ingredients, they are also ideal for cosmetic applications. In this regard, Manatuga et al. (2020) reported polyethylene oxide and gelatin (PEO-Gel) fibers with Au nanoparticles can be potential beauty masks. It demonstrated release only 30 min, and nanofibers containing orange peel-Au had a higher Au release than NFs containing green tea extract-Au NPs. It was assumed to be due to poor interaction between large particle-sized orange peel-Au NPs and polymer caused to prevent release.

The herbal extracts (*Centella asiatica*, *Portulaca oleracea*, and *Houttuynia cordata*) incorporated in PVA/chitosan nanofibers were aimed to be used as alternative acne therapy. PVA and chitosan were used as carrier matrix in this study due to their excellent hydrophilicity, biocompatibility, and biodegradability in a variety of wound dressing applications. Moreover, chitosan is an effective antimicrobial agent against dermal bacteria, and chitosan-based carrier systems have been shown to have synergistic effects in inhibiting *Propionibacterium acnes* and decreasing skin inflammation (Tang et al. 2021).

Solar ultraviolet radiation is the primary cause of skin damage due to the activation of reactive oxygen species (ROS), which leads to skin collagen imperfection, skin roughness, allergy even skin cancer, and ultimately, premature aging (Pillai et al. 2005). Topical formulations have recently attracted great concern as a tool for drug carriers to the human skin. The utilization of herbal phenolics and antioxidants to the skin is one method of reducing skin aging. Folic acid (FA) is an important member of antioxidant-rich B-complex vitamins, which help to facilitate the development of healthy skin cells (Gisondi et al. 2007). The use of folic acid has been evaluated as a beauty patch by spraying it onto nanofiber surfaces. However, hydrophilic-based polymers (PVA, alginate, and gelatin) limited the slow release of folic acid, and the release process was completed almost in 45 min. Furthermore, two different cytocompatibility tests, 3-(4,5-dimethylthiazol-2-yl)-2,5-diphenyltetrazolium bromide (MTT) assay and neutral red uptake (NRU) assay in L929 have revealed that FA has 120 and 109% cell growth (Parın et al. 2021).

In a similar strategy, Laosirisathian et al. (2021) developed Punica granatum peel extract-loaded PVA/PVP fibrous materials. The antioxidant activities of NFs were determined by 1,1-diphenyl-2-picrylhydrazyl (DPPH) and 2,2-azinobis (3-ethylbenzothiazoline-6-sulphonic acid) (ABTS) assay. The DPPH scavenging activity of NFs increased from 57% to 83.5 ± 6.7%, while the incorporation amount

of Punica granatum peel extract (PE) increased from 0.1 to 0.5 wt%. ABTS scavenging activity also showed that the NFs with the highest PE concentration have the highest antioxidant activities with 99.1 ± 3.4%. Besides, they were safe to be applied topical product due to no toxic effect on human dermal fibroblast (HDF) and human keratinocyte (HaCaT) cells.

Researchers suggested that 30 min is enough for the release of the active ingredients in commercial skin masks (Golubovic-Liakopoulos et al. 2011). Su and Hu (2020) produced PVA/gelatin/magnesium ascorbyl phosphate/tranexamic acid fibrous mats by the electrospinning method to be used as a skin mask. In vitro release study indicated that these mats had burst release magnesium ascorbyl phosphate and tranexamic acid within the first 10–15 min due to hydrophilic matrix. According to SEM micrographs, the resulting mats have a relatively lower diameter (600–800 nm) than commercial masks (15–30 μm).

Byeon et al. (2017) produced a cosmetic patch consisting of two different layers using electrospinning. Firstly, electrospun PCL was formed as the base layer, and then, the second layer consisting of PEO, alginate (Alg), and spirulina extract (0%, 1.41%, 2.35%, and 3.76% (w/v)) was electrospunned to the base layer. As spirulina (Spi) was incorporated into the nanofibers, the bead structure was formed, and the fiber morphology was disrupted. The hydrophilicity of the patches was improved with spirulina concentration, with the 3.76% (w/v) Spi/Alg-PCL patch being the most hydrophilic base. Moreover, 2.35% spirulina/alginate-PCL nanofibers have the best mechanical properties. The authors claimed that release results indicated that these spirulina patches NF cannot be used without crosslinked due to the sudden releases of spirulina from nanofiber forms. The findings of the cytotoxicity tests showed that spirulina extracts enhanced bioactive potency and adhesiveness to human skin.

In the previous section, it was mentioned that herbal extracts are added to nanofibers and used in drug release applications. A group of researchers investigated the release of e (E)-1-(3,4-dimethoxyphenyl) butadiene (DMPBD) from PLA nanofibers loaded with plai oil (Zingiber cassumunar Roxb.). Different concentrations of PLA (8, 10, and 12%) and different proportion of plai oil (15, 20 and 30%) significantly effected fiber morphology. According to optimum PLA (12%) concentration, all oil loaded-mats had similar amount of DMPBD release from the mats and were found that they are suitable to Higuchi kinetic model (Wongkanya et al. 2020).

Electrospun polymeric nanofibers have been identified for use as soft tissue prostheses, such as in vascular, blood vessel, or breast applications, among others (Abdelhady et al. 2015). Nanofibers can be designed on a tissue prosthesis device and as a coating material similar to thin films. The coated film is made up of fibrous and gradient structures, and it is lubricated between the tissues of the host and the prosthesis device, thereby minimizing stiffness.

3.5   Other Applications

Although nanofibers have less than 1000 nm, they have a remarkably high surface area to volume ratio, a variety of surface modifying sites, appropriate orientation or aggregation, and tunable surface topographic features.

Other medical applications using nanofibers and already on the literature include stent (Heo et al. 2011; Feng et al. 2017; Chu et al. 2020), implants (Eap et al. 2014; Rezk et al. 2019), hemostatic agents (Ranjbar et al. 2021; Udangawa et al. 2019; Hsu et al. 2015), prosthesis (Le et al. 2021; Liu et al. 2015), biosensors (Li et al. 2021; Supraja et al. 2020; Matlock-Colangelo and Baeumner 2012), and medical face mask (Xu et al. 2021; Kadam et al. 2021; Chowdhury et al. 2021).

4   Future Insights and Challenges

The global nanofiber market is projected to expand at a rapid growth over the forecast period, owing primarily to increased commercialization as a result of increasing end-user industrial applications. Nanofibers can change the properties of a variety of materials and also allow the development of completely new materials.

The biomedical industry is a significant contributor to the increasingly global market for nanofibers. Nanofibers are used in a variety of applications in the healthcare and pharmaceutical industries, including drug distribution, wound treatment, tissue engineering, and barrier textiles (Rezvani et al. 2019). Nanofiber membrane produced of biopolymers is commonly used as a bioactive substance or drug carrier in drug delivery applications (Buschle-Diller et al. 2006). Nanofiber layers made of biopolymers (chitosan, gelatin, collagen, polycaprolactone, etc., or blends of these materials) may also be used as wound care to substantially/seriously assist in wound healing. These materials can also be used as cell growth substrates. Furthermore, nanofibers serve as strong protection against microorganism penetration (viruses, bacteria, and molds).

In 2020, the healthcare and life sciences category had the highest demand. Biodegradable nanofiber materials are suitable for the medical and healthcare industries. Furthermore, the incorporation of additives enables these nanofibers to be multifunctional. They can be used in tissue engineering because their shape and size can be adjusted. Drug delivery, wound repair, tissue engineering, and barrier textiles are mostly a number of the main applications of nanofibers in the life sciences and pharmaceutical industries (Ramalingam and Ramakrishna 2017). The global nanofiber market is worth US $1263.6 million in 2017 and is estimated to expand by 25.0% to 2025, reaching US $7238.3 million. The nanofibers also for the medical and Cosmetics Market are expected to hit $4.2 billion by 2026, expanding by 15.7% between 2021 and 2026.

Nanofiber experiments and analyses are moving at a breakneck rate. New nanofiber synthesis techniques and applications are being published in the literature at a growing pace, with no signs of slowing down. But it is a fact that to go beyond the current state of nanofiber production and applications in commercial and industrial environments, various challenges must be faced and solved. Firstly, the scale-up problem in industrial applications is a disadvantage of using nanofibers (Lim 2017). Secondly, we should remember that the majority of the experimental trials were already carried out in vitro, and nanofiber technology has yet to make a significant impact in vivo application. Numerous in vitro assays and a limited number of in vivo trials, especially on animal models, have yielded encouraging results with varying categories and degrees of tissue injury.

Secondly, innovative modifications of traditional electrospinning, such as multi-needle and needleless electrospinning, can be further introduced to improve the performance of nanofiber synthesis.

5 Conclusion

Porous polymeric materials have been produced in various structures, such as gel, film, monolith, sponge, and fiber forms. In the last decade, nano-scaled porous fibers have become interesting especially for biomedical applications. The porous nanofibers to be used in biomedical applications are required to be biocompatible, biodegradable, and non-allergenic. Using the electrospinning technique, nanofibrous materials can be fabricated from biocompatible and biodegradable polymers. Electrospinning is increasing as an interdisciplinary field of study with considerable potential for advancement through the use of suitable biomaterials and the control of process parameters. Active agent-loaded electrospun nanofibers have high specific surface area, low density, and a high porosity that are utilized in medical fields such as artificial organ parts, tissue engineering, implant products, drug release, wound healing, and medical textile materials.

References

Aavani, F., Khorshidi, S., Karkhaneh, A.: A concise review on drug-loaded electrospun nanofibres as promising wound dressings. J. Med. Eng. Technol. **43**(1), 38–47 (2019)

Abdelaziz, D., Hefnawy, A., Al-Wakeel, E., El-Fallal, A., El-Sherbiny, I.M.: New biodegradable nanoparticles-in-nanofibers based membranes for guided periodontal tissue and bone regeneration with enhanced antibacterial activity. J. Adv. Res. **28**, 51–62 (2021)

Abdelhady, S., Honsy, K.M., Kurakula, M.: Electro spun-nanofibrous mats: a modern wound dressing matrix with a potential of drug delivery and therapeutics. J. Eng. Fibers Fabr. **10**(4), 155892501501000420 (2015)

Abdoli, M., Sadrjavadi, K., Arkan, E., Zangeneh, M.M., Moradi, S., Zangeneh, A., Khaledian, S.: Polyvinyl alcohol/Gum tragacanth/graphene oxide composite nanofiber for antibiotic delivery. J. Drug Deliv. Sci. Technol. **60**, 102044 (2020)

Abid, S., Hussain, T., Nazir, A., Zahir, A., Khenoussi, N.: Acetaminophen loaded nanofibers as a potential contact layer for pain management in Burn wounds. Mater. Res. Express **5**(8), 085017 (2018)

Afjeh-Dana, E., Naserzadeh, P., Nazari, H., Mottaghitalab, F., Shabani, R., Aminii, N., et al.: Gold nanorods reinforced silk fibroin nanocomposite for peripheral nerve tissue engineering applications. Int. J. Biol. Macromol. **129**, 1034–1039 (2019)

Agrahari, V., Agrahari, V., Mandal, A., Pal, D., Mitra, A.K.: How are we improving the delivery to back of the eye? Advances and challenges of novel therapeutic approaches. Expert Opin. Drug Deliv. **14**(10), 1145–1162 (2017)

Ahlawat, J., Kumar, V., Gopinath, P.: Carica papaya loaded poly (vinyl alcohol)-gelatin nanofibrous scaffold for potential application in wound dressing. Mater. Sci. Eng.: C **103**, 109834 (2019)

Ahmadi, F., Oveisi, Z., Samani, S.M., Amoozgar, Z.: Chitosan based hydrogels: characteristics and pharmaceutical applications. Res. Pharm. Sci. **10**(1), 1 (2015)

Ahumada, M., Jacques, E., Calderon, C., Martínez-Gómez, F.: Porosity in biomaterials: a key factor in the development of applied materials in biomedicine. In: Handbook of Ecomaterials, pp. 1–20. Springer International, Cham, Switzerland (2018)

Akduman, C., Kumbasar, E.P.A.: Electrospun polyurethane nanofibers. In: Aspects of Polyurethanes, vol. 17 (2017)

Akduman, C., Özgüney, I., Kumbasar, E.P.A.: Preparation and characterization of naproxen-loaded electrospun thermoplastic polyurethane nanofibers as a drug delivery system. Mater. Sci. Eng. C **64**, 383–390 (2016)

Aktürk, Ö., Keskin, D.: Collagen/PEO/gold nanofibrous matrices for skin tissue engineering. Turk. J. Biol. **40**(2), 380–398 (2016)

Aktürk, A., Cenik, B., Aydoğdu, Z., Taygun, M.E., Güler, F.K., Küçükbayrak, S.: Fabrication and characterization of polyvinyl alcohol/gelatin/silver nanoparticle nanocomposite materials. Eurasian J. Biol. Chem. Sci. **2**(1), 1–6

Alhosseini, S.N., Moztarzadeh, F., Mozafari, M., Asgari, S., Dodel, M., Samadikuchaksaraei, A., et al.: Synthesis and characterization of electrospun polyvinyl alcohol nanofibrous scaffolds modified by blending with chitosan for neural tissue engineering. Int. J. Nanomed. **7**, 25 (2012)

Alkilani, A.Z., McCrudden, M.T., Donnelly, R.F.: Transdermal drug delivery: innovative pharmaceutical developments based on disruption of the barrier properties of the stratum corneum. Pharmaceutics **7**(4), 438–470 (2015)

Altun, E., Aydogdu, M.O., Togay, S.O., Sengil, A.Z., Ekren, N., Haskoylu, M.E., et al.: Bioinspired scaffold induced regeneration of neural tissue. Eur. Polymer J. **114**, 98–108 (2019)

Alves da Silva, M., Martins, A., Costa-Pinto, A.R., Monteiro, N., Faria, S., Reis, R.L., Neves, N.M.: Electrospun nanofibrous meshes cultured with Wharton's jelly stem cell: an alternative for cartilage regeneration, without the need of growth factors. Biotechnol. J. **12**(12), 1700073 (2017)

Amini, S., Saudi, A., Amirpour, N., Jahromi, M., Najafabadi, S.S., Kazemi, M., et al.: Application of electrospun polycaprolactone fibers embedding lignin nanoparticle for peripheral nerve regeneration: in vitro and in vivo study. Int. J. Biol. Macromol. **159**, 154–173 (2020)

Aminipour, Z., Kolouei, Z., Tohidi, S., Bonakdar, S.: Encapsulation of Theophylline in Poly (vinyl alcohol) using electrospraying method. J. Tissues Mater. **1**(1), 32–39 (2018)

Aragón, J., Salerno, S., De Bartolo, L., Irusta, S., Mendoza, G.: Polymeric electrospun scaffolds for bone morphogenetic protein 2 delivery in bone tissue engineering. J. Colloid Interface Sci. **531**, 126–137 (2018)

Arthanari, S., Mani, G., Jang, J.H., Choi, J.O., Cho, Y.H., Lee, J.H., et al.: Preparation and characterization of gatifloxacin-loaded alginate/poly (vinyl alcohol) electrospun nanofibers. Artif. Cells Nanomed. Biotechnol. **44**(3), 847–852 (2016)

Asiri, A., Saidin, S., Sani, M.H., Al-Ashwal, R.H.: Epidermal and fibroblast growth factors incorporated polyvinyl alcohol electrospun nanofibers as biological dressing scaffold. Sci. Rep. **11**(1), 1–14 (2021)

Avizheh, L., Peirouvi, T., Diba, K., Fathi-Azarbayjani, A.: Electrospun wound dressing as a promising tool for the therapeutic delivery of ascorbic acid and caffeine. Ther. Deliv. **10**(12), 757–767 (2019)

Awad, N.K., Niu, H., Ali, U., Morsi, Y.S., Lin, T.: Electrospun fibrous scaffolds for small-diameter blood vessels: a review. Membranes **8**(1), 15 (2018)

Aznar-Cervantes, S., Pagán, A., Martínez, J.G., Bernabeu-Esclapez, A., Otero, T.F., Meseguer-Olmo, L., et al.: Electrospun silk fibroin scaffolds coated with reduced graphene promote neurite outgrowth of PC-12 cells under electrical stimulation. Mater. Sci. Eng., C **79**, 315–325 (2017)

Balagangadharan, K., Trivedi, R., Vairamani, M., Selvamurugan, N.: Sinapic acid-loaded chitosan nanoparticles in polycaprolactone electrospun fibers for bone regeneration in vitro and in vivo. Carbohyd. Polym. **216**, 1–16 (2019)

Barbak, Z., Karakas, H., Esenturk, I., Erdal, M.S., Sarac, A.S.: Silver sulfadiazine loaded poly (ε-caprolactone)/poly (ethylene oxide) composite nanofibers for topical drug delivery. NANO **15**(06), 2050073 (2020)

Best, C.A., Szafron, J.M., Rocco, K.A., Zbinden, J., Dean, E.W., Maxfield, M.W., et al.: Differential outcomes of venous and arterial tissue engineered vascular grafts highlight the importance of coupling long-term implantation studies with computational modeling. Acta Biomater. **94**, 183–194 (2019)

Bhardwaj, N., Kundu, S.C.: Electrospinning: a fascinating fiber fabrication technique. Biotechnol. Adv. **28**(3), 325–347 (2010)

Bhatia, S.K.: Bio-based materials step into the operating room. Chem. Eng. Prog. **108**(9), 49–53 (2012)

Bhattarai, D.P., Aguilar, L.E., Park, C.H., Kim, C.S.: A review on properties of natural and synthetic based electrospun fibrous materials for bone tissue engineering. Membranes **8**(3), 62 (2018)

Bhattarai, D.P., Kim, M.H., Park, H., Park, W.H., Kim, B.S., Kim, C.S.: Coaxially fabricated poly-lactic acid electrospun nanofibrous scaffold for sequential release of tauroursodeoxycholic acid and bone morphogenic protein2 to stimulate angiogenesis and bone regeneration. Chem. Eng. J. **389**, 123470 (2020)

Boateng, J.S., Matthews, K.H., Stevens, H.N., Eccleston, G.M.: Wound healing dressings and drug delivery systems: a review. J. Pharm. Sci. **97**(8), 2892–2923 (2008)

Burke, A., Hasirci, N.: Polyurethanes in biomedical applications. Biomaterials 83–101 (2004)

Buschle-Diller, G., Hawkins, A., Cooper, J.: Electrospun nanofibers from biopolymers and their biomedical applications. In: Modified Fibers with Medical and Specialty Applications, pp. 67–80. Springer, Dordrecht (2006)

Byeon, S.Y., Cho, M.K., Shim, K.H., Kim, H.J., Song, H.G., Shin, H.S.: Development of a spirulina extract/alginate-imbedded pcl nanofibrous cosmetic patch. J. Microbiol. Biotechnol. **27**(9), 1657–1663 (2017)

Cagil, E.M., Hameed, O., Ozcan, F.: Production of a new platform based calixarene nanofiber for controlled release of the drugs. Mater. Sci. Eng., C **100**, 466–474 (2019)

Carvalho, M.S., Silva, J.C., Udangawa, R.N., Cabral, J.M., Ferreira, F.C., da Silva, C.L., et al.: Co-culture cell-derived extracellular matrix loaded electrospun microfibrous scaffolds for bone tissue engineering. Mater. Sci. Eng., C **99**, 479–490 (2019)

Casper, C.L., Stephens, J.S., Tassi, N.G., Chase, D.B., Rabolt, J.F.: Controlling surface morphology of electrospun polystyrene fibers: effect of humidity and molecular weight in the electrospinning process. Macromolecules **37**(2), 573–578 (2004)

Charernsriwilaiwat, N., Rojanarata, T., Ngawhirunpat, T., Opanasopit, P.: Electrospun chitosan/polyvinyl alcohol nanofibre mats for wound healing. Int. Wound J. **11**(2), 215–222 (2014)

Chen, H., Cheng, R., Zhao, X., Zhang, Y., Tam, A., Yan, Y., ... Deng, L.: An injectable self-healing coordinative hydrogel with antibacterial and angiogenic properties for diabetic skin wound repair. NPG Asia Mater. **11**(1), 1–12 (2019)

Chen, H., Wang, X., Sutrisno, L., Zeng, T., Kawazoe, N., Yang, Y., & Chen, G.: Folic acid–functionalized composite scaffolds of gelatin and gold nanoparticles for photothermal ablation of breast cancer cells. Front. Bioeng. Biotechnol. **8**, 1214 (2020)

Chen, S., Chen, W., Chen, Y., Mo, X., Fan, C.: Chondroitin sulfate modified 3D porous electrospun nanofiber scaffolds promote cartilage regeneration. Mater. Sci. Eng.: C **118**, 111312 (2021)

Cheng, G., Yin, C., Tu, H., Jiang, S., Wang, Q., Zhou, X., et al.: Controlled co-delivery of growth factors through layer-by-layer assembly of core–shell nanofibers for improving bone regeneration. ACS Nano **13**(6), 6372–6382 (2019)

Chowdhury, M.A., Shuvho, M.B.A., Shahid, M.A., Haque, A.M., Kashem, M.A., Lam, S.S., et al.: Prospect of biobased antiviral face mask to limit the coronavirus outbreak. Environ. Res. **192**, 110294 (2021)

Chu, J., Chen, L., Mo, Z., Bowlin, G.L., Minden-Birkenmaier, B.A., Morsi, Y., et al.: An atorvastatin calcium and poly (L-lactide-co-caprolactone) core-shell nanofiber-covered stent to treat aneurysms and promote reendothelialization. Acta Biomater. **111**, 102–117 (2020)

da Silva, T.N., Gonçalves, R.P., Rocha, C.L., Archanjo, B.S., Barboza, C.A.G., Pierre, M.B.R., et al.: Controlling burst effect with PLA/PVA coaxial electrospun scaffolds loaded with BMP-2 for bone guided regeneration. Mater. Sci. Eng., C **97**, 602–612 (2019)

Dadras Chomachayi, M., Solouk, A., Akbari, S., Sadeghi, D., Mirahmadi, F., Mirzadeh, H.: Electrospun nanofibers comprising of silk fibroin/gelatin for drug delivery applications: thyme essential oil and doxycycline monohydrate release study. J. Biomed. Mater. Res., Part A **106**(4), 1092–1103 (2018)

Dai, J., Luo, Y., Nie, D., Jin, J., Yang, S., Li, G., et al.: pH/photothermal dual-responsive drug delivery and synergistic chemo-photothermal therapy by novel porous carbon nanofibers. Chem. Eng. J. **397**, 125402 (2020)

Das, P., Remigy, J.C., Lahitte, J.F., van der Meer, A.D., Garmy-Susini, B., Coetsier, C. et al.: Development of double porous poly (ε-caprolactone)/chitosan polymer as tissue engineering scaffold. Mater. Sci. Eng.: C **107**, 110257 (2020)

Dhivya, S., Padma, V.V., Santhini, E.: Wound dressings–a review. BioMedicine **5**(4) (2015)

Doshi J, Reneker DH.: Electrospinning process and applications of electrospun fibers. J. Electrostat. **35**, 151–160 (1995)

Du, H., Tao, L., Wang, W., Liu, D., Zhang, Q., Sun, P., et al.: Enhanced biocompatibility of poly (l-lactide-co-epsilon-caprolactone) electrospun vascular grafts via self-assembly modification. Mater. Sci. Eng., C **100**, 845–854 (2019)

Eap, S., Bécavin, T., Keller, L., Kökten, T., Fioretti, F., Weickert, J.L., et al.: Nanofibers implant functionalized by neural growth factor as a strategy to innervate a bioengineered tooth. Adv. Healthcare Mater. **3**(3), 386–391 (2014)

Elsayed, N.A., Zada, S., Allam, N.K.: Mineralization of electrospun gelatin/CaCO₃ composites: a new approach for dental applications. Mater. Sci. Eng., C **100**, 655–664 (2019)

Erdal, M.S., Güngör, S.: Electrospun nanofibers as carriers in dermal drug delivery. In: Nanopharmaceuticals: Principles and Applications, vol. 3, pp. 139–163. Springer, Cham (2020)

Espinoza, S.M., Patil, H.I., San Martin Martinez, E., Casañas Pimentel, R., Ige, P.P.: Poly-ε-caprolactone (PCL), a promising polymer for pharmaceutical and biomedical applications: focus on nanomedicine in cancer. Int. J. Polym. Mater. Polym. Biomater. **69**(2), 85–126 (2020)

Fang, J., Niu, H., Lin, T., Wang, X.: Applications of electrospun nanofibers. Chin. Sci. Bull. **53**(15), 2265–2286 (2008)

Farzamfar, S., Naseri-Nosar, M., Vaez, A., Esmaeilpour, F., Ehterami, A., Sahrapeyma, H., ... Salehi, M.: Neural tissue regeneration by a gabapentin-loaded cellulose acetate/gelatin wet-electrospun scaffold. Cellulose **25**(2), 1229–1238 (2018)

Felice, B., Sánchez, M.A., Socci, M.C., Sappia, L.D., Gómez, M.I., Cruz, M.K., et al.: Controlled degradability of PCL-ZnO nanofibrous scaffolds for bone tissue engineering and their antibacterial activity. Mater. Sci. Eng., C **93**, 724–738 (2018)

Feng, W., Liu, P., Yin, H., Gu, Z., Wu, Y., Zhu, W., et al.: Heparin and rosuvastatin calcium-loaded poly (l-lactide-co-caprolactone) nanofiber-covered stent-grafts for aneurysm treatment. New J. Chem. **41**(17), 9014–9023 (2017)

Feng, B., Ji, T., Wang, X., Fu, W., Ye, L., Zhang, H., Li, F.: Engineering cartilage tissue based on cartilage-derived extracellular matrix cECM/PCL hybrid nanofibrous scaffold. Mater. Des. **193**, 108773 (2020)

Fiqrianti, I.A., Widiyanti, P., Manaf, M.A., Savira, C.Y., Cahyani, N.R., Bella, F.R.: Poly-L-lactic acid (PLLA)-chitosan-collagen electrospun tube for vascular graft application. J. Funct. Biomater. **9**(2), 32 (2018)

Fu, Y., Liu, L., Cheng, R., Cui, W.: ECM decorated electrospun nanofiber for improving bone tissue regeneration. Polymers **10**(3), 272 (2018)

Fujihara, K., Kotaki, M., Ramakrishna, S.: Guided bone regeneration membrane made of polycaprolactone/calcium carbonate composite nano-fibers. Biomaterials **26**(19), 4139–4147 (2005)

Galkina, O.L., Ivanov, V.K., Agafonov, A.V., Seisenbaeva, G.A., Kessler, V.G.: Cellulose nanofiber–titania nanocomposites as potential drug delivery systems for dermal applications. J. Mater. Chem. B **3**(8), 1688–1698 (2015)

Gao, J., Chen, S., Tang, D., Jiang, L., Shi, J., Wang, S.: Mechanical properties and degradability of electrospun PCL/PLGA blended scaffolds as vascular grafts. Trans. Tianjin Univ. **25**(2), 152–160 (2019)

Garcia-Orue, I., Gainza, G., Garcia-Garcia, P., Gutierrez, F.B., Aguirre, J.J., Hernandez, R.M., Igartua, M.: Composite nanofibrous membranes of PLGA/Aloe vera containing lipid nanoparticles for wound dressing applications. Int. J. Pharm. **556**, 320–329 (2019)

Ghasemi-Mobarakeh, L., Prabhakaran, M.P., Morshed, M., Nasr-Esfahani, M.H., Ramakrishna, S.: Electrospun poly (ε-caprolactone)/gelatin nanofibrous scaffolds for nerve tissue engineering. Biomaterials **29**(34), 4532–4539 (2008)

Ginestra, P.: Manufacturing of polycaprolactone-graphene fibers for nerve tissue engineering. J. Mech. Behav. Biomed. Mater. **100**, 103387 (2019)

Giobbe, G.G., Crowley, C., Luni, C., Campinoti, S., Khedr, M., Kretzschmar, K., et al.: Extracellular matrix hydrogel derived from decellularized tissues enables endodermal organoid culture. Nat. Commun. **10**(1), 1–14 (2019)

Girao, A.F., Sousa, J., Dominguez-Bajo, A., Gonzalez-Mayorga, A., Bdikin, I., Pujades-Otero, E., et al.: 3D Reduced graphene oxide scaffolds with a combinatorial fibrous-porous architecture for neural tissue engineering. ACS Appl. Mater. Interfaces **12**(35), 38962–38975 (2020)

Gisondi, P., Fantuzzi, F., Malerba, M., Girolomoni, G.: Folic acid in general medicine and dermatology. J. Dermatol. Treat. **18**(3), 138–146 (2007)

Golafshan, N., Kharaziha, M., Fathi, M., Larson, B.L., Giatsidis, G., Masoumi, N.: Anisotropic architecture and electrical stimulation enhance neuron cell behaviour on a tough graphene embedded PVA: alginate fibrous scaffold. RSC Adv. **8**(12), 6381–6389 (2018)

Golubovic-Liakopoulos, N., Simon, S.R., Shah, B.: Nanotechnology use with cosmeceuticals. Semin. Cutan. Med. Surg. **30**(3), 176 (2011)

Gomes, S.R., Rodrigues, G., Martins, G.G., Roberto, M.A., Mafra, M., Henriques, C.M.R., Silva, J.C.: In vitro and in vivo evaluation of electrospun nanofibers of PCL, chitosan and gelatin: a comparative study. Mater. Sci. Eng., C **46**, 348–358 (2015)

Gong, M., Chi, C., Ye, J., Liao, M., Xie, W., Wu, C., et al.: Icariin-loaded electrospun PCL/gelatin nanofiber membrane as potential artificial periosteum. Colloids Surf., B **170**, 201–209 (2018)

Gönen, S.Ö., Taygun, M.E., Küçükbayrak, S.: Effects of electrospinning parameters on gelatin/poly (ε-caprolactone) nanofiber diameter. Chem. Eng. Technol. **38**(5), 844–850 (2015)

Gonzalez, A.C.D.O., Costa, T.F., Andrade, Z.D.A., Medrado, A.R.A.P.: Wound healing—a literature review. An. Bras. Dermatol. **91**(5), 614–620 (2016)

Groeber, F., Holeiter, M., Hampel, M., Hinderer, S., Schenke-Layland, K.: Skin tissue engineering—in vivo and in vitro applications. Adv. Drug Deliv. Rev. **63**(4–5), 352–366 (2011)

Gupta, K.C., Haider, A., Choi, Y.R., Kang, I.K.: Nanofibrous scaffolds in biomedical applications. Biomater. Res. **18**(1), 1–11 (2014)

Haidar, M.K., Timur, S.S., Demirbolat, G.M., Nemutlu, E., Gürsoy, R.N., Ulubayram, K., et al.: Electrospun nanofibers for dual and local delivery of neuroprotective drugs. Fibers Polym. **22**(2), 334–344 (2021)

Haider, A., Haider, S., Kang, I.K.: A comprehensive review summarizing the effect of electrospinning parameters and potential applications of nanofibers in biomedical and biotechnology. Arab. J. Chem. **11**(8), 1165–1188 (2018)

Hamzah, M.S.A., Ng, C., Sukor, J.A., Ali, K.S.M., Nayan, N.H.M.: Electrospinning, preparation and characterization of polyvinylidene fluoride/pectin electrospun loaded with benzalkonium chloride as a drug reservoirs. J. Mech. Eng. **18**(1), 39–51 (2021)

Harikrishnan, P., Sivasamy, A.: Preparation, characterization of electrospun polycaprolactone-nano zinc oxide composite scaffolds for osteogenic applications. Nano-Struct. Nano-Objects **23**, 100518 (2020)

Hasan, A., Memic, A., Annabi, N., Hossain, M., Paul, A., Dokmeci, M.R., et al.: Electrospun scaffolds for tissue engineering of vascular grafts. Acta Biomater. **10**(1), 11–25 (2014)

He, L., Zhao, Y., Tian, L., Ramakrishna, S.: Electrospraying and electrospinning for nanobiomaterial fabrication. In: Nanobiomaterials: Classification, Fabrication and Biomedical Applications (2017)

He, P., Zhong, Q., Ge, Y., Guo, Z., Tian, J., Zhou, Y., et al.: Dual drug loaded coaxial electrospun PLGA/PVP fiber for guided tissue regeneration under control of infection. Mater. Sci. Eng., C **90**, 549–556 (2018)

Heidari, M., Bahrami, S.H., Ranjbar-Mohammadi, M., Milan, P.B.: Smart electrospun nanofibers containing PCL/gelatin/graphene oxide for application in nerve tissue engineering. Mater. Sci. Eng. C **103**, 109768 (2019)

Heo, D.N., Lee, J.B., Bae, M.S., Hwang, Y.S., Kwon, K.H., Kwon, I.K.: Development of nanofiber coated indomethacin—eluting stent for tracheal regeneration. J. Nanosci. Nanotechnol. **11**(7), 5711–5716 (2011)

Heunis, T.D.J., Dicks, L.M.T.: Nanofibers offer alternative ways to the treatment of skin infections. J. Biomed. Biotechnol. **2010** (2010)

Heydari, A., Mehrabi, F., Shamspur, T., Sheibani, H., Mostafavi, A.: Encapsulation and controlled release of vitamin B2 using peracetyl-β-cyclodextrin polymer-based electrospun nanofiber scaffold (2018)

Heydarkhan-Hagvall, S., Schenke-Layland, K., Dhanasopon, A.P., Rofail, F., Smith, H., Wu, B.M., et al.: Three-dimensional electrospun ECM-based hybrid scaffolds for cardiovascular tissue engineering. Biomaterials **29**(19), 2907–2914 (2008)

Homaeigohar, S., Boccaccini, A.R.: Antibacterial biohybrid nanofibers for wound dressings. Acta Biomater. **107**, 25–49 (2020)

Hong, Y., Legge, R.L., Zhang, S., & Chen, P.: Effect of amino acid sequence and pH on nanofiber formation of self-assembling peptides EAK16-II and EAK16-IV. Biomacromolecules **4**(5), 1433–1442 (2003)

Hsu, B.B., Conway, W., Tschabrunn, C.M., Mehta, M., Perez-Cuevas, M.B., Zhang, S., Hammond, P.T.: Clotting mimicry from robust hemostatic bandages based on self-assembling peptides. ACS Nano **9**(9), 9394–9406 (2015)

Huang, C., Yang, G., Zhou, S., Luo, E., Pan, J., Bao, C., Liu, X.: Controlled delivery of growth factor by hierarchical nanostructured core-shell nanofibers for the efficient repair of critical-sized rat calvarial defect. ACS Biomater. Sci. Eng. **6**(10), 5758–5770 (2020)

Hussain, F.S.J., Yusoff, M.B.M.: Fabrication and characterization of electrospun silver nanofibers with unmatched porosity. In: 12th IEEE International Conference on Nanotechnology (IEEE-NANO), pp. 1–4. IEEE (2012)

İşoğlu, İA., Bölgen, N., Korkusuz, P., Vargel, İ, Çelik, H.H., Kılıç, E., et al.: Stem cells combined 3D electrospun nanofibrous and macrochannelled matrices: a preliminary approach in repair of rat cranial bones. Artif. Cells Nanomed. Biotechnol. **47**(1), 1094–1100 (2019)

Jain, K.K.: Drug delivery systems-an overview. In: Drug Delivery Systems, pp. 1–50 (2008)

Jain, K.K.: An overview of drug delivery systems. In: Drug Delivery Systems, pp. 1–54 (2020)

Jaswal, R., Shrestha, S., Shrestha, B.K., Kumar, D., Park, C.H., Kim, C.S.: Nanographene enfolded AuNPs sophisticatedly synchronized polycaprolactone based electrospun nanofibre scaffold for peripheral nerve regeneration. Mater. Sci. Eng.: C **116**, 111213 (2020)

Jatoi, A.W.: Polyurethane nanofibers incorporated with ZnAg composite nanoparticles for antibacterial wound dressing applications. Compos. Commun. **19**, 103–107 (2020)

Jayaraman, P., Gandhimathi, C., Venugopal, J.R., Becker, D.L., Ramakrishna, S., Srinivasan, D.K.: Controlled release of drugs in electrosprayed nanoparticles for bone tissue engineering. Adv. Drug Deliv. Rev. **94**, 77–95 (2015)

Jazaeri, E., Zhang, L., Wang, X., Tsuzuki, T.: Fabrication of carbon nanofiber by pyrolysis of freeze-dried cellulose nanofiber. Cellulose **18**(6), 1481–1485 (2011)

Jeevanandam, J., Barhoum, A., Chan, Y.S., Dufresne, A., Danquah, M.K.: Review on nanoparticles and nanostructured materials: history, sources, toxicity and regulations. Beilstein J. Nanotechnol. **9**(1), 1050–1074 (2018)

Ji, L., Zhang, X.: Fabrication of porous carbon nanofibers and their application as anode materials for rechargeable lithium-ion batteries. Nanotechnology **20**(15), 155705 (2009)

Jia, Z., Li, H., Cao, R., Xiao, K., Lu, J., Zhao, D., et al.: Electrospun nanofibrous membrane of fish collagen/polycaprolactone for cartilage regeneration. Am. J. Transl. Res. **12**(7), 3754 (2020)

Jiang, Y.C., Jiang, L., Huang, A., Wang, X.F., Li, Q., Turng, L.S.: Electrospun polycaprolactone/gelatin composites with enhanced cell–matrix interactions as blood vessel endothelial layer scaffolds. Mater. Sci. Eng., C **71**, 901–908 (2017)

Jin, S., Li, J., Wang, J., Jiang, J., Zuo, Y., Li, Y., Yang, F.: Electrospun silver ion-loaded calcium phosphate/chitosan antibacterial composite fibrous membranes for guided bone regeneration. Int. J. Nanomed. **13**, 4591 (2018)

Joy, J., Pereira, J., Aid-Launais, R., Pavon-Djavid, G., Ray, A.R., Letourneur, D., et al.: Electrospun microporous gelatin–polycaprolactone blend tubular scaffold as a potential vascular biomaterial. Polym. Int. **68**(7), 1367–1377 (2019)

Junka, R., Yu, X.: Polymeric nanofibrous scaffolds laden with cell-derived extracellular matrix for bone regeneration. Mater. Sci. Eng.: C **113**, 110981 (2020)

Kadam, V., Truong, Y.B., Schutz, J., Kyratzis, I.L., Padhye, R., Wang, L.: Gelatin/β–cyclodextrin bio–nanofibers as respiratory filter media for filtration of aerosols and volatile organic compounds at low air resistance. J. Hazard. Mater. **403**, 123841 (2021)

Kadir, N.D., Yang, Z., Hassan, A., Denslin, V., Lee, E.H.: Electrospun fibers enhanced the paracrine signaling of mesenchymal stem cells for cartilage regeneration. Stem Cell Res. Ther. **12**(1), 1–17 (2021)

Kai, D., Liow, S.S., Loh, X.J.: Biodegradable polymers for electrospinning: towards biomedical applications. Mater. Sci. Eng., C **45**, 659–670 (2014)

Kamble, P., Sadarani, B., Majumdar, A., Bhullar, S.: Nanofiber based drug delivery systems for skin: a promising therapeutic approach. J. Drug Deliv. Sci. Technol. **41**, 124–133 (2017)

Kanmaz, D., Toprakci, H.A.K., Olmez, H., Toprakci, O.: Electrospun polylactic acid based nanofibers for biomedical applications. Mater. Sci. Res. India **15**(3), 224–240 (2018)

Karakuzu-Ikizler, B., Terzioğlu, P., Basaran-Elalmis, Y., Tekerek, B.S., Yücel, S.: Role of magnesium and aluminum substitution on the structural properties and bioactivity of bioglasses synthesized from biogenic silica. Bioact. Mater. **5**(1), 66–73 (2020)

Kataria, K., Gupta, A., Rath, G., Mathur, R.B., Dhakate, S.R.: In vivo wound healing performance of drug loaded electrospun composite nanofibers transdermal patch. Int. J. Pharm. **469**(1), 102–110 (2014)

Khil, M.S., Bhattarai, S.R., Kim, H.Y., Kim, S.Z., Lee, K.H.: Novel fabricated matrix via electro-spinning for tissue engineering. J. Biomed. Mater. Res. Part B: Appl. Biomater. **72**(1), 117–124 (2005)

Khoshbakht, S., Asghari-Sana, F., Fathi-Azarbayjani, A., Sharifi, Y.: Fabrication and charac-terization of tretinoin-loaded nanofiber for topical skin delivery. Biomater. Res. **24**(1), 1–7 (2020)

Kiliç, E., Yakar, A., Bayramgil, N.P.: Preparation of electrospun polyurethane nanofiber mats for the release of doxorubicine. J. Mater. Sci.—Mater. Med. **29**(1), 8 (2018)

Kim, J.I., Pant, H.R., Sim, H.J., Lee, K.M., Kim, C.S.: Electrospun propolis/polyurethane composite nanofibers for biomedical applications. Mater. Sci. Eng., C **44**, 52–57 (2014)

Klee, D., Höcker, H.: Polymers for biomedical applications: improvement of the interface compatibility. In: Biomedical Applications Polymer Blends, pp. 1–57 (2000)

Kluge, J.A., Mauck, R.L.: Synthetic/biopolymer nanofibrous composites as dynamic tissue engineering scaffolds. In: Biomedical Applications of Polymeric Nanofibers, pp. 101–130 (2011)

Koh, L.D., Cheng, Y., Teng, C.P., Khin, Y.W., Loh, X.J., Tee, S.Y., Han, M.Y.: Structures, mechanical properties and applications of silk fibroin materials. Prog. Polym. Sci. **46**, 86–110 (2015)

Kriebel, A., Hodde, D., Kuenzel, T., Engels, J., Brook, G., Mey, J.: Cell-free artificial implants of electrospun fibres in a three-dimensional gelatin matrix support sciatic nerve regeneration in vivo. J. Tissue Eng. Regen. Med. **11**(12), 3289–3304 (2017)

Kumar, A., Han, S.S.: PVA-based hydrogels for tissue engineering: A review. Int. J. Polym. Mater. Polym. Biomater. **66**, 159–182 (2017). https://doi.org/10.1080/00914037.2016.1190930

Kuntzler, S.G., Costa, J.A.V., de Morais, M.G.: Development of electrospun nanofibers containing chitosan/PEO blend and phenolic compounds with antibacterial activity. Int. J. Biol. Macromol. **117**, 800–806 (2018)

Kunz, R.I., Brancalhão, R.M.C., Ribeiro, L.D.F.C., Natali, M.R.M.: Silkworm sericin: properties and biomedical applications. BioMed Res. Int. **2016** (2016)

Laha, A., Yadav, S., Majumdar, S., Sharma, C.S.: In-vitro release study of hydrophobic drug using electrospun cross-linked gelatin nanofibers. Biochem. Eng. J. **105**, 481–488 (2016)

Lalegül-Ülker, Ö., Vurat, M.T., Elçin, A.E., Elçin, Y.M.: Magnetic silk fibroin composite nanofibers for biomedical applications: fabrication and evaluation of the chemical, thermal, mechanical, and in vitro biological properties. J. Appl. Polym. Sci. **136**(41), 48040 (2019)

Langer, R., Tirrell, D.A.: Designing materials for biology and medicine. Nature **428**, 487–492 (2004)

Laosirisathian, N., Saenjum, C., Sirithunyalug, J., Eitssayeam, S., Chaiyana, W., Sirithunyalug, B.: PVA/PVP K90 nanofibers containing punica granatum peel extract for cosmeceutical purposes. Fibers Polym. **22**(1), 36–48 (2021)

Law, J.X., Liau, L.L., Saim, A., Yang, Y., Idrus, R.: Electrospun collagen nanofibers and their applications in skin tissue engineering. Tissue Eng. Regenerative Med. **14**(6), 699–718 (2017)

Le, A.N.M., Tran, N.M.P., Phan, T.B., Tran, P.A., Dai Tran, L., Nguyen, T.H.: Poloxamer addi-tive as luminal surface modification to modulate wettability and bioactivities of small-diameter polyurethane/polycaprolactone electrospun hollow tube for vascular prosthesis applications. Mater. Today Commun. **26**, 101771 (2021)

Lee, S.J., Heo, D.N., Park, J.S., Kwon, S.K., Lee, J.H., Lee, J.H., et al.: Characterization and prepara-tion of bio-tubular scaffolds for fabricating artificial vascular grafts by combining electrospinning and a 3D printing system. Phys. Chem. Chem. Phys. **17**(5), 2996–2999 (2015)

Leong, M.F., Chian, K.S., Mhaisalkar, P.S., Ong, W.F., Ratner, B.D.: Effect of electrospun poly (D, L-lactide) fibrous scaffold with nanoporous surface on attachment of porcine esophageal epithelial cells and protein adsorption. J. Biomed. Mater. Res. Part A **89**(4), 1040–1048 (2009)

Li, Z.Q., Li, Z., Zhao, H., Zheng, W., Li, L.: Preparation and characterization of sodium alginate-polyvinyl alcohol wound dressing system containing ciprofloxacin hydrochloride. In: Advanced Materials Research, vol. 749, pp. 388–393. Trans Tech Publications Ltd. (2013)

Li, H., Wang, M., Williams, G.R., Wu, J., Sun, X., Lv, Y., Zhu, L.M.: Electrospun gelatin nanofibers loaded with vitamins A and E as antibacterial wound dressing materials. RSC Adv. **6**(55), 50267–50277 (2016)

Li, Z., Zhou, P., Zhou, F., Zhao, Y., Ren, L., Yuan, X.: Antimicrobial eugenol-loaded electrospun membranes of poly (ε-caprolactone)/gelatin incorporated with REDV for vascular graft applications. Colloids Surf., B **162**, 335–344 (2018)

Li, Y., Liu, Y., Xun, X., Zhang, W., Xu, Y., Gu, D.: Three-dimensional porous scaffolds with biomimetic microarchitecture and bioactivity for cartilage tissue engineering. ACS Appl. Mater. Interfaces **11**(40), 36359–36370 (2019)

Li, T., Qu, M., Carlos, C., Gu, L., Jin, F., Yuan, T., et al.: High-performance poly (vinylidene difluoride)/dopamine core/shell piezoelectric nanofiber and its application for biomedical sensors. Adv. Mater. **33**(3), 2006093 (2021)

Lim, C.T.: Nanofiber technology: current status and emerging developments. Prog. Polym. Sci. **70**, 1–17 (2017)

Lin, Y., Umebayashi, M., Abdallah, M.-N., Dong, G., Roskies, M.G., Zhao, Y. F., Murshed, M., Zhang, Z., Tran, S.D.: Combination of polyetherketoneketone scaffoldand human mesenchymal stem cells from temporo-mandibular joint synovial fluid enhances bone regeneration. Sci. Rep. (2019)

Liu, K.S., Lee, C.H., Wang, Y.C., Liu, S.J.: Sustained release of vancomycin from novel biodegradable nanofiber-loaded vascular prosthetic grafts: in vitro and in vivo study. Int. J. Nanomed. **10**, 885 (2015)

Liu, Q., Liu, G., Liu, X., Yang, M., Xing, S., Du, Y., Xiong, X.: Synthesis of an electrospun PHA/RGO/Au scaffold for peripheral nerve regeneration: an in vitro study. Appl. Nanosci. **10**(3), 687–694 (2020)

Lu, Z., Wang, W., Zhang, J., Bártolo, P., Gong, H., Li, J.: Electrospun highly porous poly (L-lactic acid)-dopamine-SiO$_2$ fibrous membrane for bone regeneration. Mater. Sci. Eng.: C **117**, 111359 (2020)

Lubasova, D., Martinova, L.: Controlled morphology of porous polyvinyl butyral nanofibers. J. Nanomat. **2011** (2011)

Ma, G., Liu, Y., Peng, C., Fang, D., He, B., & Nie, J.: Paclitaxel loaded electrospun porous nanofibers as mat potential application for chemotherapy against prostate cancer. Carbohydr. Polym. **86**(2), 505–512 (2011)

Ma PX, Zhang RY.: J Biomed Mater Res **46**, 60 (1999)

Magaz, A., Li, X., Gough, J.E., Blaker, J.J.: Graphene oxide and electroactive reduced graphene oxide-based composite fibrous scaffolds for engineering excitable nerve tissue. Mater. Sci. Eng.: C **119**, 111632 (2021)

Mahnama, H., Dadbin, S., Frounchi, M., Rajabi, S.: Preparation of biodegradable gelatin/PVA porous scaffolds for skin regeneration. Artif. Cells Nanomed. Biotechnol. **45**(5), 928–935 (2017)

Mahumane, G.D., Kumar, P., Pillay, V., Choonara, Y.E.: Repositioning N-acetylcysteine (NAC): NAC-loaded electrospun drug delivery scaffolding for potential neural tissue engineering application. Pharmaceutics **12**(10), 934 (2020)

Manatunga, D.C., Godakanda, V.U., Herath, H.M.L.P.B., de Silva, R.M., Yeh, C.Y., Chen, J.Y., et al.: Nanofibrous cosmetic face mask for transdermal delivery of nano gold: synthesis, characterization, release and zebra fish employed toxicity studies. Roy. Soc. Open Sci. **7**(9), 201266 (2020)

Manavitehrani, I., Fathi, A., Badr, H., Daly, S., Negahi Shirazi, A., Dehghani, F.: Biomedical applications of biodegradable polyesters. Polymers**8**(1), 20 (2016)

Mathew, A., Vaquette, C., Hashimi, S., Rathnayake, I., Huygens, F., Hutmacher, D.W., Ivanovski, S.: Antimicrobial and immunomodulatory surface-functionalized electrospun membranes for bone regeneration. Adv. Healthcare Mater. **6**(10), 1601345 (2017)

Matlock-Colangelo, L., Baeumner, A.J.: Recent progress in the design of nanofiber-based biosensing devices. Lab Chip **12**(15), 2612–2620 (2012)

Matthews, J.A., Wnek, G.E., Simpson, D.G., Bowlin, G.L.: Electrospinning of collagen nanofibers. Biomacromol **3**(2), 232–238 (2002)

Megelski, S., Stephens, J.S., Chase, D.B., Rabolt, J.F.: Micro-and nanostructured surface morphology on electrospun polymer fibers. Macromolecules **35**(22), 8456–8466 (2002)

Mendes, A.C., Gorzelanny, C., Halter, N., Schneider, S.W., Chronakis, I.S.: Hybrid electrospun chitosan-phospholipids nanofibers for transdermal drug delivery. Int. J. Pharm. **510**(1), 48–56 (2016)

Metwally, S., Ferraris, S., Spriano, S., Krysiak, Z.J., Kaniuk, Ł., Marzec, M.M., et al.: Surface potential and roughness controlled cell adhesion and collagen formation in electrospun PCL fibers for bone regeneration. Mater. Des. **194**, 108915 (2020)

Middleton, J.C., Tipton, A.J.: Synthetic biodegradable polymers as orthopedic devices. Biomaterials **21**(23), 2335–2346 (2000)

Mirjalili, M., Zohoori, S.: Review for application of electrospinning and electrospun nanofibers technology in textile industry. J. Nanostruct. Chem. **6**(3), 207–213 (2016)

Miszuk, J.M., Xu, T., Yao, Q., Fang, F., Childs, J.D., Hong, Z., et al.: Functionalization of PCL-3D electrospun nanofibrous scaffolds for improved BMP2-induced bone formation. Appl. Mater. Today **10**, 194–202 (2018)

Mohammadian, F., Eatemadi, A.: Drug loading and delivery using nanofibers scaffolds. Artif. Cells Nanomed. Biotechnol. **45**(5), 881–888 (2017)

Moreno-Cortez, I.E., Romero-García, J., González-González, V., García-Gutierrez, D.I., Garza-Navarro, M.A., Cruz-Silva, R.: Encapsulation and immobilization of papain in electrospun nanofibrous membranes of PVA cross-linked with glutaraldehyde vapor. Mater. Sci. Eng., C **52**, 306–314 (2015)

Nakajima, H., Dijkstra, P., Loos, K.: The recent developments in biobased polymers toward general and engineering applications: polymers that are upgraded from biodegradable polymers, analogous to petroleum-derived polymers, and newly developed. Polymers **9**(10), 523 (2017)

Nguyen, T.H., Lee, B.T.: Fabrication and characterization of cross-linked gelatin electro-spun nanofibers. J. Biomed. Sci. Eng. **3**(12), 1117 (2010)

Nguyen, T.T.T., Chung, O.H., Park, J.S.: Coaxial electrospun poly (lactic acid)/chitosan (core/shell) composite nanofibers and their antibacterial activity. Carbohyd. Polym. **86**(4), 1799–1806 (2011)

Nguyen, T.T.T., Ghosh, C., Hwang, S.G., Chanunpanich, N., Park, J.S.: Porous core/sheath composite nanofibers fabricated by coaxial electrospinning as a potential mat for drug release system. Int. J. Pharm. **439**(1–2), 296–306 (2012)

Nguyen-Vu, V.L.: Fabrication drug loaded polycaprolactone microparticles by electrospraying method. In: International Conference on the Development of Biomedical Engineering in Vietnam, pp. 313–317. Springer, Singapore (June, 2018)

Nokhasteh, S., Molavi, A.M., Khorsand-Ghayeni, M., Sadeghi-Avalshahr, A.: Preparation of PVA/Chitosan samples by electrospinning and film casting methods and evaluating the effect of surface morphology on their antibacterial behavior. Mater. Res. Express **7**(1), 015401 (2019)

Norouzi, M., Abdali, Z., Liu, S., Miller, D.W.: Salinomycin-loaded nanofibers for glioblastoma therapy. Sci. Rep. **8**(1), 1–10 (2018)

Opanasopit, P., Sila-On, W., Rojanarata, T., Ngawhirunpat, T.: Fabrication and properties of capsicum extract-loaded PVA and CA nanofiber patches. Pharm. Dev. Technol. **18**(5), 1140–1147 (2013)

Oztoprak, Z., Okay, O.: Reversibility of strain stiffening in silk fibroin gels. Int. J. Biol. Macromol. **95**, 24–31 (2017)

Padalhin, A. R. (2021). Brief retrospect on the use of photobiomodulation (PBM) therapy for augmented bone regeneration (ABR). Med. Lasers Eng. Basic Res. Clin. Appl. **10**(1), 15–21

Palumbo, V.D., Bruno, A., Tomasello, G., Damiano, G., Lo Monte, A.I.: Bioengineered vascular scaffolds: the state of the art. Int. J. Artif. Organs **37**(7), 503–512 (2014)

Pan, X., Sun, B., Mo, X.: Electrospun polypyrrole-coated polycaprolactone nanoyarn nerve guidance conduits for nerve tissue engineering. Front. Mater. Sci. **12**(4), 438–446 (2018)

Parenteau-Bareil, R., Gauvin, R., Berthod, F.: Collagen-based biomaterials for tissue engineering applications. Materials **3**(3), 1863–1887 (2010)

Parın, F.N., Yıldırım, K.: Preparation and characterisation of vitamin-loaded electrospun nanofibres as promising transdermal patches. Fibres Text. Eastern Eur. (2021)

Parin, F.N., Terzioğlu, P., Sicak, Y., Yildirim, K., Öztürk, M.: Pine honey–loaded electrospun poly (vinyl alcohol)/gelatin nanofibers with antioxidant properties. J. Text. Inst. **112**(4), 628–635 (2021a). https://doi.org/10.1080/00405000.2020.1773199

Parın, F.N., Aydemir, Ç.İ., Taner, G., Yıldırım, K.: Co-electrospun-electrosprayed PVA/folic acid nanofibers for transdermal drug delivery: preparation, characterization, and in vitro cytocompatibility. J. Ind. Text. 1528083721997185 (2021b)

Park, S., Kim, J., Lee, M.K., Park, C., Jung, H.D., Kim, H.E., Jang, T.S.: Fabrication of strong, bioactive vascular grafts with PCL/collagen and PCL/silica bilayers for small-diameter vascular applications. Mater. Des. **181**, 108079 (2019)

Patel, J.M., Saleh, K.S., Burdick, J.A., Mauck, R.L.: Bioactive factors for cartilage repair and regeneration: improving delivery, retention, and activity. Acta Biomater. **93**, 222–238 (2019)

Pathak, C., Vaidya, F.U., Pandey, S.M.: Mechanism for development of nanobased drug delivery system. Appl. Target. Nano Drugs Deliv. Syst. 35–67 (2019)

Pike, R.D.: U.S. Patent No. 5,935,883. Washington, DC: U.S. Patent and Trademark Office (1999)

Pillai, S., Oresajo, C., Hayward, J.: Ultraviolet radiation and skin aging: roles of reactive oxygen species, inflammation and protease activation, and strategies for prevention of inflammation-induced matrix degradation–a review. Int. J. Cosmet. Sci. **27**(1), 17–34 (2005)

Place, E.S., George, J.H., Williams, C.K., Stevens, M.M.: Synthetic polymer scaffolds for tissue engineering. Chem. Soc. Rev. **38**, 1139 (2009)

Pollini, M., Paladini, F.: Bioinspired materials for wound healing application: the potential of silk fibroin. Materials **13**(15), 3361 (2020)

Poornima, B., Korrapati, P.S.: Fabrication of chitosan-polycaprolactone composite nanofibrous scaffold for simultaneous delivery of ferulic acid and resveratrol. Carbohyd. Polym. **157**, 1741–1749 (2017)

Qasim, M., Chae, D.S., Lee, N.Y.: Advancements and frontiers in nano-based 3D and 4D scaffolds for bone and cartilage tissue engineering. Int. J. Nanomed. **14**, 4333 (2019)

Qi, Z., Guo, W., Zheng, S., Fu, C., Ma, Y., Pan, S., et al.: Enhancement of neural stem cell survival, proliferation and differentiation by IGF-1 delivery in graphene oxide-incorporated PLGA electrospun nanofibrous mats. RSC Adv. **9**(15), 8315–8325 (2019)

Radke, D., Jia, W., Sharma, D., Fena, K., Wang, G., Goldman, J., Zhao, F.: Tissue engineering at the blood-contacting surface: a review of challenges and strategies in vascular graft development. Adv. Healthcare Mater. **7**(15), 1701461 (2018)

Rafiq, M., Hussain, T., Abid, S., Nazir, A., Masood, R.: Development of sodium alginate/PVA antibacterial nanofibers by the incorporation of essential oils. Mater. Res. Express **5**(3), 035007 (2018)

Rahmani, A., Hashemi-Najafabadi, S., Eslaminejad, M.B., Bagheri, F., Sayahpour, F.A.: The effect of modified electrospun PCL-nHA-nZnO scaffolds on osteogenesis and angiogenesis. J. Biomed. Mater. Res., Part A **107**(9), 2040–2052 (2019)

Ramalingam, M., Ramakrishna, S.: Introduction to nanofiber composites. In: Nanofiber Composites for Biomedical Applications, pp. 3–29. Woodhead Publishing (2017)

Rameshbabu, A.P., Datta, S., Bankoti, K., Subramani, E., Chaudhury, K., Lalzawmliana, V., et al.: Polycaprolactone nanofibers functionalized with placental derived extracellular matrix for stimulating wound healing activity. J. Mater. Chem. B **6**(42), 6767–6780 (2018)

Ramos, C., Lanno, G.M., Laidmäe, I., Meos, A., Härmas, R., Kogermann, K.: High humidity electrospinning of porous fibers for tuning the release of drug delivery systems. Int. J. Polym. Mater. Polym. Biomater. 1–13 (2020)

Ranganathan, S., Balagangadharan, K., & Selvamurugan, N.: Chitosan and gelatin-based electrospun fibers for bone tissue engineering. Int. J. Biol. Macromol. **133**, 354–364 (2019)

Ranjbar, J., Koosha, M., Chi, H., Ghasemi, A., Zare, F., Abdollahifar, M.A., et al.: Novel chitosan/gelatin/oxidized cellulose sponges as absorbable hemostatic agents. Cellulose **28**(6), 3663–3675 (2021)

Rasouli, R., Barhoum, A.: Advances in nanofibers for antimicrobial drug delivery. In: Handbook of Nanofibers, pp. 1–42 (2018)

Ratner, B.D.: Biomedical applications of synthetic polymers. In: The Synthesis Characterization Reaction and Application of Polymers, p 201. Pergamon Press (1989)

Ratner, B.D.: J Biomed Mat Res **27**, 837 (1993)

Raval, D., Ramani, V.: A review on electrospinning technique and its application in the field of nanoencapsulation of bioactive compounds. Int. J. Curr. Microbiol. App. Sci. **8**(7), 2724–2730 (2019)

Razzaq, A., Khan, Z.U., Saeed, A., Shah, K.A., Khan, N.U., Menaa, B., et al.: Development of cephradine-loaded gelatin/polyvinyl alcohol electrospun nanofibers for effective diabetic wound healing: in-vitro and in-vivo assessments. Pharmaceutics **2021**(13), 349 (2021)

Reddy, M., Ponnamma, D., Choudhary, R., Sadasivuni, K.K.: A comparative review of natural and synthetic biopolymer composite scaffolds. Polymers **13**(7), 1105 (2021)

Rezaei, S., Valipouri, A., Hosseini Ravandi, S.A., Kouhi, M., Ghasemi Mobarakeh, L.: Fabrication, characterization, and drug release study of vitamin C–loaded alginate/polyethylene oxide nanofibers for the treatment of a skin disorder. Polym. Adv. Technol. **30**(9), 2447–2457 (2019)

Rezk, A.I., Mousa, H.M., Lee, J., Park, C.H., Kim, C.S.: Composite PCL/HA/simvastatin electrospun nanofiber coating on biodegradable Mg alloy for orthopedic implant application. J. Coat. Technol. Res. **16**(2), 477–489 (2019)

Rezvani Ghomi, E., Khalili, S., Nouri Khorasani, S., Esmaeely Neisiany, R., Ramakrishna, S.: Wound dressings: current advances and future directions. J. Appl. Polym. Sci. **136**(27), 47738 (2019)

Rodriguez, M., Kluge, J.A., Smoot, D., Kluge, M.A., Schmidt, D.F., Paetsch, C.R., et al.: Fabricating mechanically improved silk-based vascular grafts by solution control of the gel-spinning process. Biomaterials **230**, 119567 (2020)

Rohindra, D.R., Nand, A.V., Khurma, J.R.: Swelling properties of chitosan hydrogels. South Pac. J. Nat. Appl. Sci. **22**(1), 32–35 (2004)

Rychter, M., Baranowska-Korczyc, A., Milanowski, B., Jarek, M., Maciejewska, B.M., Coy, E.L., Lulek, J.: Cilostazol-loaded poly (ε-Caprolactone) electrospun drug delivery system for cardiovascular applications. Pharm. Res. **35**(2), 1–20 (2018)

Sadeghi, A., Moztarzadeh, F., Mohandesi, J.A.: Investigating the effect of chitosan on hydrophilicity and bioactivity of conductive electrospun composite scaffold for neural tissue engineering. Int. J. Biol. Macromol. **121**, 625–632 (2019)

Saderi, N., Rajabi, M., Akbari, B., Firouzi, M., Hassannejad, Z.: Fabrication and characterization of gold nanoparticle-doped electrospun PCL/chitosan nanofibrous scaffolds for nerve tissue engineering. J. Mater. Sci.—Mater. Med. **29**(9), 1–10 (2018)

Sangnim, T., Limmatvapirat, S., Nunthanid, J., Sriamornsak, P., Sittikijyothin, W., Wannachaiyasit, S., Huanbutta, K.: Design and characterization of clindamycin-loaded nanofiber patches composed of polyvinyl alcohol and tamarind seed gum and fabricated by electrohydrodynamic atomization. Asian J. Pharm. Sci. **13**(5), 450–458 (2018)

Saravani, S., Ebrahimian-Hosseinabadi, M., Mohebbi-Kalhori, D.: Polyglycerol sebacate/chitosan/gelatin nano-composite scaffolds for engineering neural construct. Mater. Chem. Phys. **222**, 147–151 (2019)

Schultz, G.S., Chin, G.A., Moldawer, L., Diegelmann, R.F.: 23 Principles of wound healing. In: Mechanisms of Vascular Disease: A Reference Book for Vascular Specialists, p. 423 (2011)

Sharifi, F., Irani, S., Azadegan, G., Pezeshki-Modaress, M., Zandi, M., Saeed, M.: Co-electrospun gelatin-chondroitin sulfate/polycaprolactone nanofibrous scaffolds for cartilage tissue engineering. Bioact. Carbohydr. Dietary Fibre **22**, 100215 (2020)

Shen, X., Xu, Q., Xu, S., Li, J., Zhang, N., Zhang, L.: Preparation and transdermal diffusion evaluation of the prazosin hydrochloride-loaded electrospun poly (vinyl alcohol) fiber mats. J. Nanosci. Nanotechnol. **14**(7), 5258–5265 (2014)

Shi, J., Chen, S., Wang, L., Zhang, X., Gao, J., Jiang, L., et al.: Rapid endothelialization and controlled smooth muscle regeneration by electrospun heparin-loaded polycaprolactone/gelatin hybrid vascular grafts. J. Biomed. Mater. Res. B Appl. Biomater. **107**(6), 2040–2049 (2019)

Shitole, A.A., Raut, P.W., Sharma, N., Giram, P., Khandwekar, A.P., Garnaik, B.: Electrospun polycaprolactone/hydroxyapatite/ZnO nanofibers as potential biomaterials for bone tissue regeneration. J. Mater. Sci.—Mater. Med. **30**(5), 1–17 (2019)

Shoba, E., Lakra, R., Kiran, M.S., Korrapati, P.S.: Fabrication of core–shell nanofibers for controlled delivery of bromelain and salvianolic acid B for skin regeneration in wound therapeutics. Biomed. Mater. **12**(3), 035005 (2017)

Şimşek, M.: Tuning surface texture of electrospun polycaprolactone fibers: effects of solvent systems and relative humidity. J. Mater. Res. **35**(3), 332–342 (2020)

Singh, A.P., Biswas, A., Shukla, A., Maiti, P.: Targeted therapy in chronic diseases using nanomaterial-based drug delivery vehicles. Signal Transduct. Target. Ther. **4**(1), 1–21 (2019)

Solomon, A.O.: Making drugs safer: improving drug delivery and reducing side-effect of drugs on the human biochemical system. J. Pharm. Drug Deliv. Res. **4**(4) (2015)

Song, J., Fan, X., Shen, Q.: Daidzein-loaded nanostructured lipid carriers-PLGA nanofibers for transdermal delivery. Int. J. Pharm. **501**(1–2), 245–252 (2016)

Soscia, D.A., Raof, N.A., Xie, Y., Cady, N.C., Gadre, A.P.: Antibiotic-loaded PLGA nanofibers for wound healing applications. Adv. Eng. Mater. **12**(4), B83–B88 (2010)

Strobel, H.A., Calamari, E.L., Beliveau, A., Jain, A., Rolle, M.W.: Fabrication and characterization of electrospun polycaprolactone and gelatin composite cuffs for tissue engineered blood vessels. J. Biomed. Mater. Res. B Appl. Biomater. **106**(2), 817–826 (2018)

Su, W.T., Hsu, M.S.: Nanofiber mask fabrication by electrospun and its application. J. Phys. Conf. Ser. **1637**(1), 012102 (2020)

Sultana, T., Amirian, J., Park, C., Lee, S.J., Lee, B.T.: Preparation and characterization of polycaprolactone–polyethylene glycol methyl ether and polycaprolactone–chitosan electrospun mats potential for vascular tissue engineering. J. Biomater. Appl. **32**(5), 648–662 (2017)

Sun, H., Mei, L., Song, C., Cui, X., Wang, P.: The in vivo degradation, absorption and excretion of PCL-based implant. Biomaterials **27**(9), 1735–1740 (2006)

Supraja, P., Singh, V., Vanjari, S.R.K., Singh, S.G.: Electrospun CNT embedded ZnO nanofiber based biosensor for electrochemical detection of Atrazine: a step closure to single molecule detection. Microsyst. Nanoeng. **6**(1), 1–10 (2020)

Suresh, S., Gryshkov, O., Glasmacher, B.: Impact of setup orientation on blend electrospinning of poly-ε-caprolactone-gelatin scaffolds for vascular tissue engineering. Int. J. Artif. Organs **41**(11), 801–810 (2018)

Tammaro, L., Saturnino, C., D'Aniello, S., Vigliotta, G., Vittoria, V.: Polymorphic solidification of Linezolid confined in electrospun PCL fibers for controlled release in topical applications. Int. J. Pharm. **490**(1–2), 32–38 (2015)

Tang, Y., Liu, L., Han, J., Zhang, Z., Yang, S., Li, S., et al.: Fabrication and characterization of multiple herbal extracts-loaded nanofibrous patches for topical treatment of acne vulgaris. Fibers Polym. **22**(2), 323–333 (2021)

Taylor, G.I.: Disintegration of water drops in an electric field. Proc. Roy. Soc. Lond. Ser. A. Math. Phys. Sci. **280**(1382), 383–397 (1964)

Terzioğlu, P.: Electrospun chitosan/gelatin/nano-$CaCO_3$ hybrid nanofibers for potential tissue engineering applications. J. Nat. Fibers 1–10 (2021)

Terzioğlu, P., Öğüt, H., Kalemtaş, A.: Natural calcium phosphates from fish bones and their potential biomedical applications. Mater. Sci. Eng., C **91**, 899–911 (2018)

Toprak, Ö., Topuz, B., Abou Monsef, Y., Oto, Ç., Orhan, K., Karakeçili, A.: BMP-6 carrying metal organic framework-embedded in bioresorbable electrospun fibers for enhanced bone regeneration. Mater. Sci. Eng.: C **120**, 111738 (2021)

Torres-Martínez, E.J., Cornejo Bravo, J.M., Serrano Medina, A., Pérez González, G.L., Villarreal Gómez, L.J.: A summary of electrospun nanofibers as drug delivery system: drugs loaded and biopolymers used as matrices. Curr. Drug Deliv. **15**(10), 1360–1374 (2018)

Tuğcu-Demiröz, F., Saar, S., Tort, S., Acartürk, F.: Electrospun metronidazole-loaded nanofibers for vaginal drug delivery. Drug Dev. Ind. Pharm. **46**(6), 1015–1025 (2020)

Türkkan, S., Atila, D., Akdağ, A., Tezcaner, A.: Fabrication of functionalized citrus pectin/silk fibroin scaffolds for skin tissue engineering. J. Biomed. Mater. Res. B Appl. Biomater. **106**(7), 2625–2635 (2018)

Udangawa, R.N., Mikael, P.E., Mancinelli, C., Chapman, C., Willard, C.F., Simmons, T.J., Linhardt, R.J.: Novel cellulose–halloysite hemostatic nanocomposite fibers with a dramatic reduction in human plasma coagulation time. ACS Appl. Mater. Interfaces. **11**(17), 15447–15456 (2019)

Udomluck, N., Koh, W.G., Lim, D.J., Park, H.: Recent developments in nanofiber fabrication and modification for bone tissue engineering. Int. J. Mol. Sci. **21**(1), 99 (2020)

Vasita, R., Katti, D.S.: Nanofibers and their applications in tissue engineering. Int. J. Nanomed. **1**(1), 15 (2006)

Vega-Cázarez, C.A., Sánchez-Machado, D.I., López-Cervantes, J.: Overview of electrospinned chitosan nanofiber composites for wound dressings. Chitin-Chitosan-Myriad Functionalities Sci. Technol. 157–181 (2018)

Wang, S., Lu, L., Wang, C., Gao, C., Wang, X.: Polymeric biomaterials for tissue engineering applications (2011)

Wang, C., Ma, C., Wu, Z., Liang, H., Yan, P., Song, J., et al.: Enhanced bioavailability and anticancer effect of curcumin-loaded electrospun nanofiber: in vitro and in vivo study. Nanoscale Res. Lett. **10**(1), 1–10 (2015)

Wang, B., Li, H., Yao, Q., Zhang, Y., Zhu, X., Xia, T., ... Ni, S.: Local in vitro delivery of rapamycin from electrospun PEO/PDLLA nanofibers for glioblastoma treatment. Biomed. Pharmacother. **83**, 1345–1352 (2016)

Wei, Q., Xia, X.: Types and processing of structured functional nanofibers: core-shell, aligned, porous and gradient nanofibers. In: Functional Nanofibers and Their Applications, pp. 22–37. Woodhead Publishing (2012)

Wen, H., Jung, H., Li, X.: Drug delivery approaches in addressing clinical pharmacology-related issues: opportunities and challenges. AAPS J. **17**(6), 1327–1340 (2015)

Wenk, E., Merkle, H.P., Meinel, L.: Silk fibroin as a vehicle for drug delivery applications. J. Control. Release **150**(2), 128–141 (2011)

Wongkanya, R., Teeranachaideekul, V., Makarasen, A., Chuysinuan, P., Yingyuad, P., Nooeaid, P., et al.: Electrospun poly (lactic acid) nanofiber mats for controlled transdermal delivery of essential oil from Zingiber cassumunar Roxb. Mater. Res. Exp. **7**(5), 055305 (2020)

Wróblewska-Krepsztul, J., Rydzkowski, T., Michalska-Pożoga, I., Thakur, V.K.: Biopolymers for biomedical and pharmaceutical applications: recent advances and overview of alginate electrospinning. Nanomaterials **9**(3), 404 (2019)

Wu, Y., Qin, Y., Wang, Z., Wang, J., Zhang, C., Li, C., Kong, D.: The regeneration of macro-porous electrospun poly (ε-caprolactone) vascular graft during long-term in situ implantation. J. Biomed. Mater. Res. B Appl. Biomater. **106**(4), 1618–1627 (2018)

Xiang, P., Wang, S.S., He, M., Han, Y.H., Zhou, Z.H., Chen, D.L., et al.: The in vitro and in vivo biocompatibility evaluation of electrospun recombinant spider silk protein/PCL/gelatin for small caliber vascular tissue engineering scaffolds. Colloids Surf., B **163**, 19–28 (2018)

Xing, Y., Gu, Y., Guo, L., Guo, J., Xu, Z., Xiao, Y., et al.: Gelatin coating promotes in situ endothelialization of electrospun polycaprolactone vascular grafts. J. Biomater. Sci. Polym. Ed. (just-accepted) 1–18 (2021)

Xu, W., Shen, R., Yan, Y., Gao, J.: Preparation and characterization of electrospun alginate/PLA nanofibers as tissue engineering material by emulsion eletrospinning. J. Mech. Behav. Biomed. Mater. **65**, 428–438 (2017)

Xu, Y., Zhang, X., Hao, X., Teng, D., Zhao, T., Zeng, Y.: Micro/nanofibrous nonwovens with high filtration performance and radiative heat dissipation property for personal protective face mask. Chem. Eng. J. 130175 (2021)

Xue, C., Zhu, H., Tan, D., Ren, H., Gu, X., Zhao, Y., et al.: Electrospun silk fibroin-based neural scaffold for bridging a long sciatic nerve gap in dogs. J. Tissue Eng. Regen. Med. **12**(2), e1143–e1153 (2018)

Xue, Y., Wang, H., Yu, D., Feng, L., Dai, L., Wang, X., & Lin, T.: Superhydrophobic electrospun POSSPMMA copolymer fibres with highly ordered nanofibrillar and surface structures. Chem. Commun. **42**, 6418–6420 (2009)

Yalcin Enis, I., Gok Sadikoglu, T.: Design parameters for electrospun biodegradable vascular grafts. J. Ind. Text. **47**(8), 2205–2227 (2018)

Yang, L., Jiang, Z., Zhou, L., Zhao, K., Ma, X., Cheng, G.: Hydrophilic cell-derived extracellular matrix as a niche to promote adhesion and differentiation of neural progenitor cells. RSC Adv. **7**(72), 45587–45594 (2017)

Yang, L., Li, X., Wang, D., Mu, S., Lv, W., Hao, Y., et al.: Improved mechanical properties by modifying fibrin scaffold with PCL and its biocompatibility evaluation. J. Biomater. Sci. Polym. Ed. **31**(5), 658–678 (2020)

Ye, K., Liu, D., Kuang, H., Cai, J., Chen, W., Sun, B., et al.: Three-dimensional electrospun nanofibrous scaffolds displaying bone morphogenetic protein-2-derived peptides for the promotion of osteogenic differentiation of stem cells and bone regeneration. J. Colloid Interface Sci. **534**, 625–636 (2019)

Yousefzadeh, M., Ghasemkhah, F. (2018). Design of porous, core-shell, and hollow nanofibers. In: Handbook of Nanofibers; Springer International Publishing: Berlin, Germany, pp. 1–58

Zahid, S., Khalid, H., Ikram, F., Iqbal, H., Samie, M., Shahzadi, L., et al.: Bi-layered α-tocopherol acetate loaded membranes for potential wound healing and skin regeneration. Mater. Sci. Eng., C **101**, 438–447 (2019)

Zahmatkeshan, M., Adel, M., Bahrami, S., Esmaeili, F., Rezayat, S.M., Saeedi, Y., et al.: Polymer based nanofibers: preparation, fabrication, and applications. Handb. Nanofibers 1–47 (2018)

Zamani, F., Amani-Tehran, M., Latifi, M., Shokrgozar, M.A.: The influence of surface nanoroughness of electrospun PLGA nanofibrous scaffold on nerve cell adhesion and proliferation. J. Mater. Sci.—Mater. Med. **24**(6), 1551–1560 (2013)

Zarei, M., Samimi, A., Khorram, M., Abdi, M.M., Golestaneh, S.I.: Fabrication and characterization of conductive polypyrrole/chitosan/collagen electrospun nanofiber scaffold for tissue engineering application. Int. J. Biol. Macromol. **168**, 175–186 (2021)

Zha, F., Chen, W., Hao, L., Wu, C., Lu, M., Zhang, L., Yu, D.: Electrospun cellulose-based conductive polymer nanofibrous mats: composite scaffolds and their influence on cell behavior with electrical stimulation for nerve tissue engineering. Soft Matter **16**(28), 6591–6598 (2020)

Zhang, K., Yin, A., Huang, C., Wang, C., Mo, X., Al-Deyab, S.S., El-Newehy, M.: Degradation of electrospun SF/P (LLA-CL) blended nanofibrous scaffolds in vitro. Polym. Degrad. Stab. **96**(12), 2266–2275 (2011)

Zhao, Y., Gong, J., Niu, C., Wei, Z., Shi, J., Li, G., et al.: A new electrospun graphene-silk fibroin composite scaffolds for guiding Schwann cells. J. Biomater. Sci. Polym. Ed. **28**(18), 2171–2185 (2017)

Zhao, L., Li, X., Yang, L., Sun, L., Mu, S., Zong, H., et al.: Evaluation of remodeling and regeneration of electrospun PCL/fibrin vascular grafts in vivo. Mater. Sci. Eng.: C **118**, 111441 (2021)

Zhou, M., Hou, J., Zhang, G., Luo, C., Zeng, Y., Mou, S., Xiao, P., et al.: Tuning the mechanics of 3D-printed scaffolds by crystal lattice-like structural design for breast tissue engineering. Biofabrication **12**(1), 015023 (2019)

Zhu, Y., Song, F., Ju, Y., Huang, L., Zhang, L., Tang, C., et al.: NAC-loaded electrospun scaffolding system with dual compartments for the osteogenesis of rBMSCs in vitro. Int. J. Nanomed. **14**, 787 (2019)

Zhu, J., Ye, H., Deng, D., Li, J., Wu, Y.: Electrospun metformin-loaded polycaprolactone/chitosan nanofibrous membranes as promoting guided bone regeneration membranes: preparation and

characterization of fibers, drug release, and osteogenic activity in vitro. J. Biomater. Appl. **34**(9), 1282–1293 (2020)

Zhu, T., Gu, H., Zhang, H., Wang, H., Xia, H., Mo, X., Wu, J.: Covalent grafting of PEG and heparin improves biological performance of electrospun vascular grafts for carotid artery replacement. Acta Biomater. **119**, 211–224 (2021)

Zupančič, Š, Preem, L., Kristl, J., Putrinš, M., Tenson, T., Kocbek, P., Kogermann, K.: Impact of PCL nanofiber mat structural properties on hydrophilic drug release and antibacterial activity on periodontal pathogens. Eur. J. Pharm. Sci. **122**, 347–358 (2018)

Preparation of Porous Activated Carbon Materials and Their Application in Supercapacitors

Li Feng, Bing Yan, Changshui Wang, Qian Zhang, Shaohua Jiang, and Shuijian He

Abstract Porous carbon materials (PCMs) possess highly developed pore structure, and their pore size can range from molecular size to nano-size to large pores within micron size. As versatile materials with excellent physical and chemical properties such as large specific surface area, lightweight, high chemical stability, and electrical conductivity, PCMs have shown excellent application prospects in the fields of catalysis, adsorption, hydrogen storage, and energy storage. With the consumption of fossil energy and the rapid development of science and technology, the demands for high-performance supercapacitors are increasing day by day. PCMs are excellent electrode materials for supercapacitors. There are many methods to prepare PCMs, among which activation is the most widely used method. The activation methods can be divided into physical activation, chemical activation, and self-activation according to the activator used. In this chapter, the capacitance performance of PCMs synthesized via the activation process is summarized. The pore structure optimization process and the influence of pore structure on the capacitance performance of PCMs are also discussed. It is expected that this chapter could offer some enlightenments to the researchers' focus on improving the capacitance performance of PCMs.

Keywords Porous carbon · Carbonization · Activation · Supercapacitor

L. Feng · B. Yan · C. Wang · S. Jiang · S. He (✉)
Co-Innovation Center of Efficient Processing and Utilization of Forest Resources, International
Innovation Center for Forest Chemicals and Materials, College of Materials Science and
Engineering, Nanjing Forestry University, Nanjing, China
e-mail: shuijianhe@njfu.edu.cn

S. Jiang
e-mail: shaohua.jiang@njfu.edu.cn

Q. Zhang
College of Science, Nanjing Forestry University, Nanjing, China
e-mail: zhangqian5689@njfu.edu.cn

1 Introduction

Porous carbon materials (PCMs) are important members in the big family of porous materials. PCMs could be prepared from various precursors including synthetic polymers, nature polymers, and carbon-rich small molecules (Borchardt et al. 2017; Gonzalez-Garcia 2018; Wang et al. 2020b). PCMs are widely applied in energy storage and conversion devices, electrocatalysis, water purification, electromagnetic shielding, microwave absorption, and other fields (Zhai et al. 2011; He et al. 2019c; Tian et al. 2020). PCMs show advantages in high yield, low cost, tunable microstructures, high specific surface area (SSA), stability, etc. Tons of PCMs are produced globally every year mainly from low cost biomass. The price of most PCMs could be below 1 $/g. The pore size of PCMs could be adjusted in the range of millimeter to micrometer to nanometer, and the corresponding specific surface area could be varied from a few square meters per gram to thousands square meters per gram. PCMs with pore size in the range of millimeter to sub-micrometer could be obtained from lyophilization/freeze drying, chemical blowing/(gas) foaming, template methods, etc. Usually, pores with the diameter below 100 nm are named nanopores. According to the classification of International Union of Pure and Applied Chemistry (IUPAC), nanopores can be divided into macropores (>50 nm), mesopores (2–50 nm), and micropores (0.2–2 nm). Micropores can be divided into super-micropores (>0.7 nm) and ultra-micropores (0.2–0.7 nm) (Liu et al. 2017). As to PCMs, ultra-micropores are always formed from the release of volatile gas and the condensation of carbon framework. The super-micropores of PCMs could be generated by the physical/chemical activation process (Yin et al. 2020). The formation of mesopores and macropores of PCMs always requires soft/hard templates within nano-size (Nishihara and Kyotani 2012; Zhu et al. 2019; Yan et al. 2021; He et al. 2019b).

Electrochemical double-layer capacitors (EDLCs) are relatively new energy storage devices which store the charge at the electrode/electrolyte interface, via physical ion adsorption/desorption process (He and Chen 2015; Simon et al. 2014). EDLCs possess the merits of high power density, good stability, easy maintenance, wide operating temperature, and low cost (Wang et al. 2016). PCMs are preferred electrode materials for EDLCs attributing to their good conductivity/stability, large specific surface area, tunable pore structure, and low cost (Merlet et al. 2012). The gravimetric specific capacitance of PCMs spans from a few Faraday per gram to hundred Faraday per gram mainly depending on the specific surface area and pore structure. In this chapter, the capacitance performance of PCMs synthesized via the physical/chemical activation process is summarized. The pore structure optimization process and the influence of pore structure on the capacitance performance of PCMs are also discussed. It is expected that this chapter could offer some enlightenments to the researchers' focus on improving the capacitance performance of PCMs.

2 Capacitance Performance of PCMs Synthesized with Activation Agents

PCMs are widely used as electrochemical energy storage devices because of their high SSA, multi-dimensional and tunable pore structure, good electrical conductivity, and low cost. Pore-size distribution and SSA are the main issues that dominate the performance of carbon-based supercapacitors. PCMs with large SSA and controllable pore size are good electrode materials for EDLCs. It is generally believed that microspores can enhance the electric double-layer capacitance of materials, mesopores provide low resistance channel for electrolyte ion transport, and macropores can be used as buffer reservoirs to store electrolyte ions (Wang et al. 2019). Activation is considered as an effective method to increase the SSA of carbon materials and introduce stratified porosity (Ding et al. 2021; He et al. 2013; Wang et al. 2020a).

Porous activated carbon is generally prepared from carbon precursors by the carbonization–activation approach. Activated carbon materials used in supercapacitors must meet the following three requirements: (1) a high SSA, (2) a low internal resistance, and (3) a microstructure conducive to the electrolyte entering the inner surface. High SSA is conducive to high specific capacitance. Low internal resistance determines high power density. Special pore structure is conducive to the formation of electrolyte wetting interface (Li et al. 2020c; Zhu and Xu 2020; Wang et al. 2020c).

The activation methods for preparing porous activated carbon can be divided into three categories: physical activation, chemical activation, and self-activation (Li et al. 2021b; Cao et al. 2021). In addition, it can be subdivided. Usually, the preparation process of porous activated carbon can be divided into one-step or two-step methods. One-step method means carbonization–activation occurs simultaneously. For the two-step method, the first step is carbonization, and the second step is activation that is using activator to further make pores. The different types of activation methods and its mechanisms, and some commonly used activators are described in detail below.

2.1 Physical Activation

Physical activation is usually carried out at high temperature (600–1200 °C) in the presence of oxidizing gases (Li et al. 2021b; Yin et al. 2020). Usually, air (Cai et al. 2020; Leng et al. 2017), carbon dioxide (Ding et al. 2021; Vinayagam et al. 2020; Elmouwahidi et al. 2020; Jin et al. 2016), and steam (Gao et al. 2020a; Qin 2019; Pallarés et al. 2018; Lee et al. 2016) can act as activation agents (Table 1). Most studies consider that activation temperature and activation time are the main factors affecting physical activation. Some studies have also investigated the effect of flow rate on pore structure (Qin 2019). Common physical activation methods are discussed in detail below.

Table 1 Summary of porous carbons produced by physical activation

Carbon source	Activating agent	SSA (m^2 g^{-1})	Mean pore size (nm)	Pore volume (cm^3 g^{-1})	Electrolyte	Specific capacitance	Energy density (Wh kg^{-1})	Power density (W kg^{-1})	Cycle life	References
Paper flower	$ZnCl_2$, CO_2	1801	3.28	1.16	1 M H_2SO_4	118 F g^{-1} (1 A g^{-1})	/	/	97.4% (10,000, 12 A g^{-1})	Veerakumar et al. (2020)
Bea pulp	CO_2	409	2.68	0.27	6 M KOH	106 F g^{-1} (0.25 A g^{-1})	1.7	2.11	93% (20,000, 10 A g^{-1})	Ding et al. (2021)
Spores	CO_2	3035	/	1.43	1 M TEABF$_4$/AN	305 F g^{-1} (1 A g^{-1})	56	60	93.85% (10,000, 2 A g^{-1})	Jin et al. (2016)
Formaldehyde and resorcinol	CO_2	1520	0.66	0.87	1 M H_2SO_4	235 F g^{-1} (0.125 A g^{-1})	5.94	54	100% (12,000, 1 A g^{-1})	Elmouwahidi et al. (2020)
Pine nut shell	Steam	956	2.59	0.62	6 M KOH	128 F g^{-1} (0.5 A g^{-1})	/	/	98% (10,000, 5 A g^{-1})	Qin (2019)
Polymer nanotubes	Steam	852	3.10	0.66	6 M KOH	276 F g^{-1} (1 A g^{-1})	/	/	98% (10,000, 1 A g^{-1})	Gao et al. (2020a)
Pitch-based CF	Steam	3230	/	1.89	1 M ($C_2H_5)_4NBF_4$/propylene carbonate	22.5 F g^{-1}	/	/	91.5% (20)	Lee et al. (2016)

Table 1 (continued)

Carbon source	Activating agent	SSA (m² g⁻¹)	Mean pore size (nm)	Pore volume (cm³ g⁻¹)	Electrolyte	Specific capacitance	Energy density (Wh kg⁻¹)	Power density (W kg⁻¹)	Cycle life	References
Activated hard carbon	Steam	2351	/	1.61	0.5 M Na_2SO_4	71 F g⁻¹ (0.5 A g⁻¹)	/	/	82.8% (5000, 5 A g⁻¹)	Son and Park (2020)
Activated carbon	Steam	2156	1.87	1.01	2 M TEABF₄/C₈H₂₀BF₄N	187.2 F g⁻¹ (0.5 A g⁻¹)	/	/	92% (1000, 1 A g⁻¹)	Li et al. (2017)
Dead pine needles	Air	783	2.55	0.49	1 M H_2SO_4	223 F g⁻¹ (0.5 A g⁻¹)	/	/	98% (10,000, 10 A g⁻¹)	Leng et al. (2017)

2.1.1 Carbon Dioxide Activation

CO_2 is widely distributed on the earth and is rich in content. In those oxidizing gases, CO_2 can be used as an environment-friendly activator of materials, which is not only green but also easy to deal with, and has a good application prospect (Li et al. 2020c). The activation mechanism of CO_2 is shown in Eq. (1) (Navarro et al. 2007). In general, the CO_2 activation degree is mainly affected by the activation temperature, time, and the concentration of CO_2 (Zhu and Xu 2020).

$$C + CO_2 \rightarrow 2CO \qquad (1)$$

Veerakumar et al. studied the capacitance performance of porous carbon nanosheets prepared by the carbonization of paper flower via chemical and physical activation (Veerakumar et al. 2020). The effect of CO_2 activation temperature on the SSA and pore-size distribution of the carbon materials was discussed. The influence on the capacitance performance of paper flower-derived carbon materials was also analyzed. They first activated the carbon material with $ZnCl_2$, followed by CO_2 activation at 700 °C and 800 °C, respectively (Fig. 1). The results show that the sample PFC-800 has the maximum SSA and pore volume, which are 1800 m^2 g^{-1} and 1.16 cm^3 g^{-1}, respectively. In a three-electrode system, the specific capacitances of PFC-800 are 91.2 F g^{-1} at 12 A g^{-1} which is more than twice the value of PFC-700 (44.9 F g^{-1}). The cycle stability of PFC800 is better than that of the activated sample at 700 °C, with a loss of only 3% after 10,000 charge–discharge cycles. They also studied the adsorption capacity of the carbon material to sunset yellow, as shown in the lower right corner of Fig. 1a, and found that PFC-800 had a good adsorption capacity to this pigment (273.6 mg g^{-1}). Elmouwahidi et al. prepared a kind of carbon microsphere and then activated it with CO_2 to investigate the effect of activation time (30, 60, 90, 120 min at 900 °C) on the material's pore structure (Elmouwahidi et al. 2020). Their results indicate that in the process of CO_2 activation, micropores are mainly produced, and the increase of micropores is especially obvious after 30 min, but the rise decreases when the time exceeds 60 min and reaches the peak at 90 min. After activation for 30 min, the formation of ultra-micropores is detected. With the time extension, the pores became wider. When the activation time increases to 90 min, the SSA (1523 m^2 g^{-1}), average pore size (0.95 nm), and pore volume all reach the maximum. Although CO_2 can play an active role in opening and expanding the pores, different activation conditions can produce different pore structures and SSA and influence the capacitance performance of porous carbon.

2.1.2 Steam Activation

As one of the commonly used physical activation methods, steam activation is not only cheap and easy to operate, but also an environmentally friendly activating agent. Steam activation is beneficial to the expansion of micropores, and thus, the activated carbon prepared by this activation method has a lower micropore volume (Zhu and
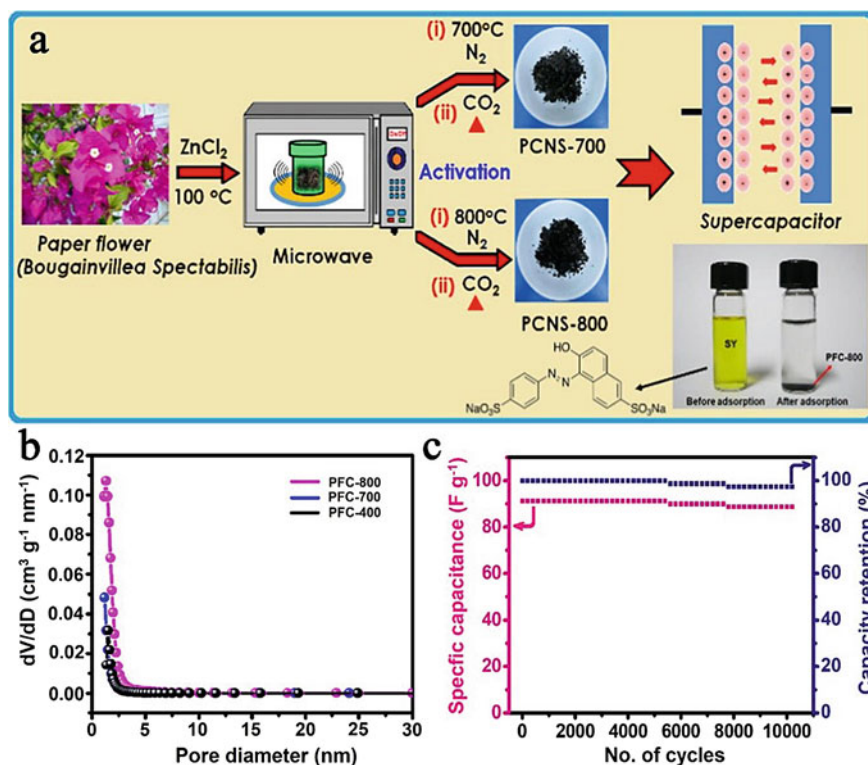
Fig. 1 **a** Preparation schematic of PFC, **b** the pore diameter of PFC samples at different activation temperatures, **c** cyclic performance of PFC-800 (Veerakumar et al. 2020)

Xu 2020; Pallarés et al. 2018). The steam activation mechanism is shown in Eq. (2). First, water vapor is adsorbed on the surface of the carbon, releasing hydrogen and oxygen (Navarro et al. 2007). Then, the presence of hydrogen prevents the continuous reaction of the active site, and the released oxygen further reacts with the carbon monoxide separated from the surface of the carbon to form carbon dioxide and at the same time produces a large number of micro-/mesopores (Sevilla et al. 2021; Li et al. 2020c; Yin et al. 2020).

$$C + H_2O \rightarrow CO + H_2 \tag{2}$$

For the stream activation process, the main factors affecting the pore structure of ACs are the activation temperature, activation time, and steam flow rate (Qin 2019). Lee et al. studied the capacitance performance of pitch-based activated carbon fibers (ACFs) produced by steam activation for different times (Lee et al. 2016). At the fixed activation temperature of 900 °C, the activation time was varied from 10 to 40 min. SSA of the as-prepared porous carbon spans from 1520 to 3230 m^2 g^{-1}, and the pore volume increases from 0.61 cm^3 g^{-1} up to 1.87 cm^3 g^{-1}. The specific capacitance
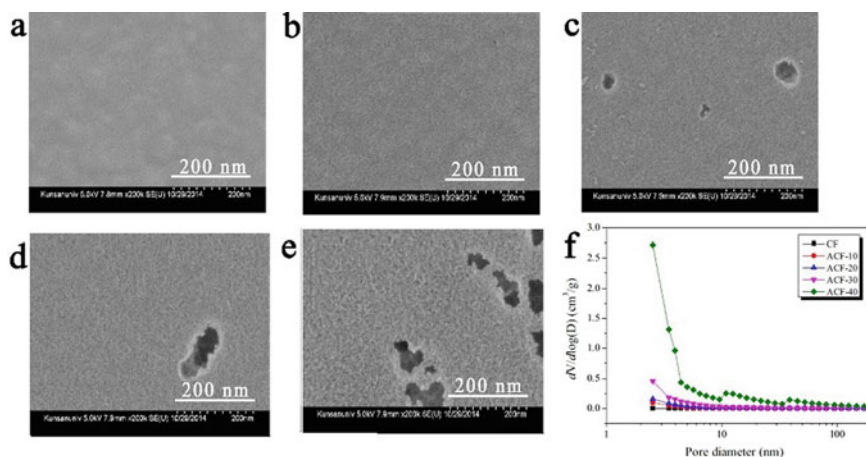
Fig. 2 **a–e** Scanning electron microscopy (SEM) images of activated carbon fiber with different steam activation times: **a** as-received CF, **b** ACF-10, **c** ACF-20, **d** ACF-30, **e** ACF-40, **f** the pore-size distribution curves of different samples (Lee et al. 2016)

increases from 1.1 to 22.5 F g^{-1}. Figure 2 shows that increasing activation time can produce larger pores, which also indicates that steam activation is conducive to mesopore development.

2.1.3 Air Activation

Compared with CO_2 and steam activation, air activation is less used and the activation temperature is lower. However, the redox reaction of oxygen and carbon is a severe exothermic reaction, and the direct use of air to activate carbon may cause excessive combustion of the raw materials and fail to effectively form pores (Li et al. 2020c). Leng et al. successfully synthesized activated carbon by carbonizing dead pine needles (PN) in the air at different temperatures (Leng et al. 2017). The products show pore volume of 0.25–0.49 cm^3 g^{-1} and SSA of 461–783 m^2 g^{-1}. In 1 M H_2SO_4 electrolyte, the PN-1000 exhibits a specific capacitance of 223 F g^{-1} at 0.5 A g^{-1} and maintains 150 F g^{-1} even at 100 A g^{-1}.

2.2 Chemical Activation

Chemical activation is one of the most used methods for the preparation of PCM (Table 2). Unlike physical activation, chemical activation takes place at slightly lower temperatures (i.e., 400–900 °C) and involves the dehydration by certain agents, such as phosphoric acid, zinc chloride, and alkaline hydroxide (Li et al. 2021b; Zeng

Table 2 Summary of porous carbons produced by chemical activation

Carbon source	Activating agent	SSA (m² g⁻¹)	Mean pore size (nm)	Pore volume (cm³ g⁻¹)	Electrolyte	Specific capacitance	Energy density (Wh kg⁻¹)	Power density (W kg⁻¹)	Cycle life	References
Waste coffee grounds	H_3PO_4	763	/	0.47	1 M H_2SO_4	157 F g⁻¹ (1 A g⁻¹)	15	75	82% (10,000, 5 A g⁻¹)	Huang et al. (2013)
Cotton stalk	H_3PO_4	1424	/	1.476	1 M H_2SO_4	341 F g⁻¹ (0.5 A g⁻¹)	/	/	94.3% (10,000, 1 A g⁻¹)	Cheng et al. (2021)
Shiitake mushroom	H_3PO_4, KOH	2988	/	1.76	6 M KOH	306 F g⁻¹ (1 A g⁻¹)	8.2	100	95.7% (15,000, 3 A g⁻¹)	Cheng et al. (2015)
Dry elm samara	KOH	1947	/	1.33	6 M KOH	470 F g⁻¹ (1 A g⁻¹)	25.4 (1 M EMIM BF_4)	15,000	98% (50,000, 10 A g⁻¹)	Chen et al. (2016)
Soybean roots	KOH	2143	/	0.94	6 M KOH	276 F g⁻¹ (0.5 A g⁻¹)	100.5 (1 M EMIM BF_4)	4553	98% (10,000, 5 A g⁻¹)	Guo et al. (2016)
Sorghum stem	KOH	1674	/	1.076	2 M KOH	257.2 F g⁻¹ (1 mV s⁻¹)	/	/	111% (12,000, 10 A g⁻¹)	Kim et al. (2021)
Raw anthracite	KOH	3214	/	1.83	1 M TEABF₄-AN	172 F g⁻¹ (0.5 A g⁻¹)	37.2	303	93% (10,000, 1 A g⁻¹)	Sun et al. (2020)
Butnea monsperma flower pollens	$ZnCl_2$	1422	2.16	0.77	6 M KOH	130 F g⁻¹ (1 mA cm²)	4.53	2070	99% (10,000)	Ahmed et al. (2019)

(continued)

Table 2 (continued)

Carbon source	Activating agent	SSA (m² g⁻¹)	Mean pore size (nm)	Pore volume (cm³ g⁻¹)	Electrolyte	Specific capacitance	Energy density (Wh kg⁻¹)	Power density (W kg⁻¹)	Cycle life	References
Potato waste residue	$ZnCl_2$	1052	2.33	0.61	2 M KOH	255 F g⁻¹ (0.5 A g⁻¹)	/	/	93.7% (5000, 5 A g⁻¹)	Ma et al. (2015)
Bean curd	CH_3COOK	2180	2.17	1.18	1 M H_2SO_4	430 F g⁻¹ (0.1 A g⁻¹)	12 (1 M H_2SO_4)	50	/	Li et al. (2018b)
Bean curd	CH_3COOK	1735	1.10	2.53	1 M H_2SO_4	315 F g⁻¹ (0.1 A g⁻¹)	8.5	50	93.5% (10,000, 1 A g⁻¹)	Li et al. (2019)
Rape pollen	$CuCl_2$	2488	2.65	1.14	6 M KOH	390 F g⁻¹ (0.5 A g⁻¹)	26.8 (1 M Na_2SO_4)	181.4	92.9% (10,000, 20 A g⁻¹)	Liu et al. (2018)
Rice husk	$CuCl_2$	1340	/	0.80	6 M KOH	152 F g⁻¹ (20 A g⁻¹)	/	/	100.1% (10,000)	Tian et al. (2019)
Enzymatic hydrolysis lignin	$CuCl_2$	1083	/	0.52	6 M KOH	736 F g⁻¹ (1 A g⁻¹)	49.3	500	100% (1000, 20 A g⁻¹)	Chen et al. (2021)
Chitin	$CuCl_2$	1535	/	0.65	6 M KOH	227 F g⁻¹ (0.5 A g⁻¹)	5.2	/	94.3% (10,000, 10 A g⁻¹)	Chen et al. (2019)
Cornstalk	NaCl KCl	1588	/	1.018	1 M H_2SO_4	407 F g⁻¹ (0.5 A g⁻¹)	14.35	123.9	96.2% (20,000, 5 A g⁻¹)	Wang et al. (2018)
Java kapok tree shell	NaCl KCl	1260	1.24	0.439	6 M KOH	169 F g⁻¹ (1 A g⁻¹)	12.5	1900	97% (10,000, 1 A g⁻¹)	Thileep Kumar et al. (2018)

Table 2 (continued)

Carbon source	Activating agent	SSA (m² g⁻¹)	Mean pore size (nm)	Pore volume (cm³ g⁻¹)	Electrolyte	Specific capacitance	Energy density (Wh kg⁻¹)	Power density (W kg⁻¹)	Cycle life	References
Cork	$KMnO_4$	1199	/	1.17	6 M KOH	290 F g⁻¹ (0.2 A g⁻¹)	14.7 (1 M Na_2SO_4)	395	95.2% (10,000, 5 A g⁻¹)	Qiu et al. (2019a)
Foxtail grass seeds	$NaHCO_3$ $KHCO_3$	1428	2.30	0.821	6 M KOH	358 F g⁻¹ (0.5 A g⁻¹)	18.2 (1 M Na_2SO_4)	/	95.8% (10,000, 200 mV s⁻¹)	Liang et al. (2021)
α-D-Glucose	$KHCO_3$	2230	/	1.05	1 M H_2SO_4	246 F g⁻¹ (0.1 A g⁻¹)	3.6	17,000	98% (5000, 5 A g⁻¹)	Sevilla and Fuertes (2016)
Gelatin	$NaNO_3$	2872	/	1.618	1 M $EMIBF_4$	166 F g⁻¹ (0.5 A g⁻¹)	92	1000	92.2% (10,000, 5 A g⁻¹)	Li et al. (2018a)
Soluble starch	$NaNO_3$	1864	/	2.22	6 M KOH	385 F g⁻¹ (1 A g⁻¹)	11.6	101	97.4% (8000, 2 A g⁻¹)	Huo et al. (2020)
Albizia procera leaves	$NaHCO_3$ $ZnCl_2$	910	2.80	/	1 M H_2SO_4	231 F g⁻¹ (1 A g⁻¹)	32	625	97.3% (1000, 20 A g⁻¹)	Mohamedkhair et al. (2020)
Chitosan	$FeCl_3$	807	/	0.93	1 M H_2SO_4	393 F g⁻¹ (0.5 A g⁻¹)	19.1	400	103% (8000)	Qiu et al. (2019c)
Mushroom	$FeCl_3$	1374	2.7	0.95	1 M H_2SO_4	307 F g⁻¹ (1 A g⁻¹)	6.6	1500	97.4% (8000, 2 A g⁻¹)	Hou et al. (2018)

et al. 2014). Compared with physical activation, chemically activated porous carbon shows higher porosity development with porous network combining micropores and mesopores. Moreover, its selectivity is more extensive. At present, there are many kinds of chemical activators that have been used to prepare PCMs. The most used ones are KOH and $ZnCl_2$. Chemical activators can be divided into three main groups: acids, alkalis, and salts. The commonly used chemical activation methods are discussed below.

2.2.1 Acid Activation

Common acid activating agents include H_3PO_4 (Cheng et al. 2015, 2021; Budinova et al. 2006), H_2SO_4 (Kigozi et al. 2020), HNO_3 (Li et al. 2016; Pourhosseini et al. 2017; Zhu et al. 2017; Bo et al. 2018), etc. Phosphoric acid is used more often in those acidic activating agents. H_3PO_4 activation is related to its ability to promote bond cleavage and cross-linking formation. It can form phosphate bonds with the carbon precursors, resulting in a cross-linked structure. The activation process is roughly divided into six aspects as shown in Eqs. (3)–(8) (Myglovets et al. 2014; Olivares-Marín et al. 2006; Shi et al. 2019; Zhang et al. 2020):

$$nH_3PO_4 \xrightarrow{100\,°C\sim400\,°C} H_{n+2}P_nO_{3n+1} + (n-1)H_2O \tag{3}$$

$$2H_3PO_4 \rightarrow P_2O_5 + 3H_2O \tag{4}$$

$$2H_3PO_4 \xrightarrow{>500\,°C} H_2P_2O_7^{2-} + H_2O + 2H^+ \tag{5}$$

$$2H_2P_2O_7^{2-} \rightarrow P_4 + 6O_2 + 2H_2O \tag{6}$$

$$2P_2O_5 + 5C \rightarrow P_4 + 5CO_2 \tag{7}$$

$$P_2O_5(liquid) \rightarrow P_2O_5(gas) \tag{8}$$
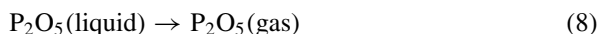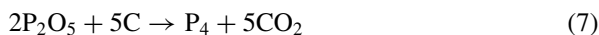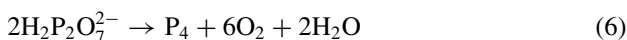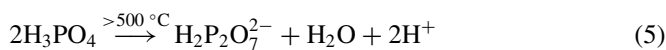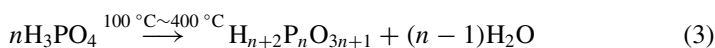
Cheng et al. first activated shiitake mushrooms with H_3PO_4 at 500 °C and then activated them with KOH for a second time (Cheng et al. 2015). The surface area of the activated sample (PAC-500) in the first step is 1341 $m^2\ g^{-1}$, and the pore volume is 2.02 $cm^3\ g^{-1}$. The size of pores formed is mainly between 2 and 5 nm, and considering that phosphoric acid reacts with carbon above 500 °C to form phosphate bond (Myglovets et al. 2014), so those nanopores are mainly due to the dehydration effect. After the activation of H_3PO_4, the rich channels are more conducive for the entry of KOH electrolyte into the interior, and the contact surface is larger to achieve a better effect. Finally, after two steps of activation and carbonization, the shiitake mushroom-derived carbon showed an interconnected hierarchical porous network.

The obtained hierarchical pores exhibited a high specific capacitance of 306 F g^{-1} at 1 A g^{-1} in KOH electrolyte; even when the current density rises to 30 A g^{-1}, the capacitance retention is 78.4%.

Unlike H_3PO_4, H_2SO_4 and HNO_3 activations mainly rely on their strong oxidizing property, not only can react with carbon atoms to produce some gas, which can achieve pore-forming, but also can enhance the surface wettability of the active porous carbon (Li et al. 2016; Zhu et al. 2017; Kigozi et al. 2020). Thus, enhance the capacitance performance of the carbon material.

2.2.2   Alkali Activation

Alkali activation is the most widely used activation method in chemical activation. The carbon materials are often activated by KOH to make pores to enhance the capacitive performance (Wang and Kaskel 2012). It was found that the KOH activation could inhibit the generation of tar, reduce the activation temperature, and accelerate the reaction rate. KOH activation also shows the advantages of high yield, low reaction temperature, high SSA, and micropore development (Kumar et al. 2020; Sun et al. 2020; Li et al. 2020c). Chemical activation mechanism of KOH is suggested as Eqs. (9)–(13) (Li et al. 2021b; Lozano-Castelló et al. 2007; Yin et al. 2020). KOH dehydration to form K_2O (Eq. 9) and then at about 400 °C is converted into K_2CO_3 (Eq. 10). At 600 °C, KOH is completely consumed. When the temperature rises to above 700 °C, K_2CO_3 and K_2O are reduced to metallic potassium (Eqs. 12–13). In the process of activation, CO_2, H_2O, CO, H_2, and other gaseous substances are released, which play the role of physical activation (Gao et al. 2020b; Sun et al. 2020; Wang et al. 2019; Li et al. 2020c; Yin et al. 2020).

$$2KOH \rightarrow K_2O + H_2O \tag{9}$$

$$K_2O + CO_2 \rightarrow K_2CO_3 \tag{10}$$

$$K_2CO_3 \rightarrow K_2O + CO_2 \tag{11}$$

$$K_2CO_3 + 2C \rightarrow 2K + 3CO \tag{12}$$

$$K_2O + C \rightarrow 2K + CO \tag{13}$$

The activation temperature (Guo et al. 2016; Kim et al. 2021; Sun et al. 2020; Li et al. 2020b), immersion time (Yakaboylu et al. 2021), concentration of KOH (Chen et al. 2016), and the mass ratio of carbon precursors to KOH (Guo et al. 2016; Lv et al. 2019; Mo et al. 2020; Yu et al. 2019) will affect the pore-size distribution, porosity, and SSA of the carbon materials. Guo et al. studied the influence of KOH/carbon source mass ratio and activation temperature on capacitive performance of soybean
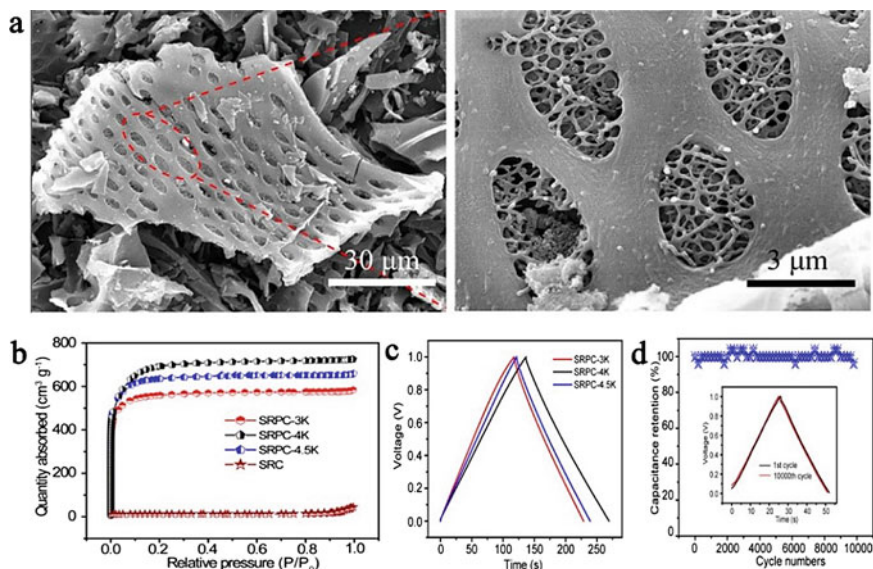
Fig. 3 **a** SEM images of SRPC-4K, **b** N_2 physisorption isotherms, **c** charge/discharge curves at 1 A g^{-1}, **d** cyclic stability at 5 A g^{-1} for 10,000 cycles of SRPC-4K (inset: charge/discharge curves of the 1st and 10,000th cycles) (Guo et al. 2016)

root-derived hierarchical porous carbon (SRPC) (Fig. 3) (Guo et al. 2016). When the mass ratio of KOH to soybean root is 4:1 and the activation temperature is 800 °C, the porous carbon obtained has the largest SSA ($2143 \text{ m}^2 \text{ g}^{-1}$) and the largest proportion of micropore SSA ($1772 \text{ m}^2 \text{ g}^{-1}$). The mesopore volume of SRPC-4K is $0.13 \text{ cm}^3 \text{ g}^{-1}$, and the micropore volume is $0.81 \text{ cm}^3 \text{ g}^{-1}$. It has the richest hierarchical micro-/mesoporous structure. The high microporosity is conducive to the accumulation of charge, and the mesopores can transport abundant electrolyte into the micropores, thus enhancing the capacitive performance of porous carbon. When used as electrodes of SC, SRPC-4K displays a high specific capacitance of 276 F g^{-1} at 0.5 A g^{-1} and 98% capacitance retention after 10,000 cycles at 5 A g^{-1} (Fig. 3d) in a two-electrode configuration in 6 M KOH electrolyte. In conclusion, although KOH activation is used for pore-forming, appropriate activation conditions are needed to achieve the best capacitance performance for different carbon sources.

2.2.3 Salt Activation

In addition to acid and alkali activation, there is a class of salt-activating agents. Those reagents include some metal chlorides, decomposable salts, and oxidizing salts.

Metal Chlorides

In the preparation of porous carbon, metal chlorides, such as $ZnCl_2$ (Ahmed et al. 2019; Li et al. 2021a; Ma et al. 2015), $FeCl_3$ (Bedia et al. 2018; Hou et al. 2018; Li et al. 2020a), NaCl (Wang et al. 2018; Zong et al. 2020; Thileep Kumar et al. 2018), KCl (Wang et al. 2018; Thileep Kumar et al. 2018), and $CuCl_2$ (Liu et al. 2018; Chen et al. 2019, 2021; Tian et al. 2019), are often used as activators.

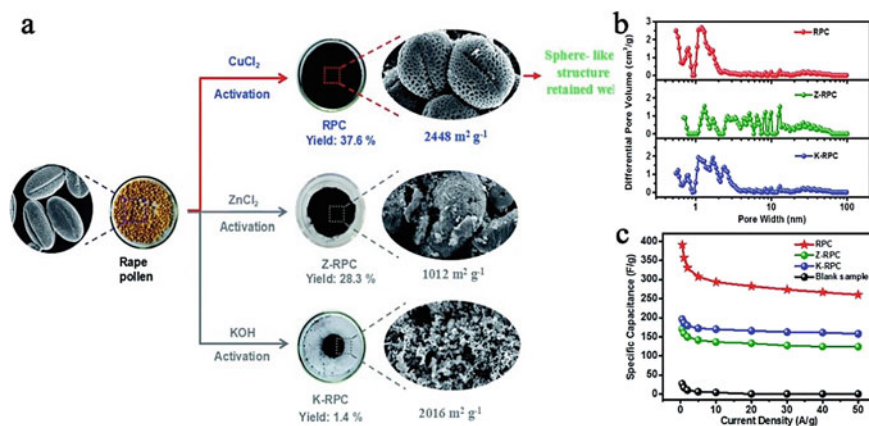$ZnCl_2$ is mainly acted as a dehydrating agent and can be deoxidized in the form of water (Zhu and Xu 2020). Beyond that, $ZnCl_2$ can also converted to ZnO (Eq. 14), which further etches carbon and be reduced to Zn (Eq. 15) (Kim et al. 2007; Wang et al. 2019). Better porous structure and higher carbon yield can be obtained. The activation temperature of $ZnCl_2$ is usually between 600 and 1000 °C. When the temperature is above 700 °C, $ZnCl_2$ volatilizes without post-treatment. The factors affecting the pore formation of $ZnCl_2$ are close to those of KOH, but the activation temperature and impregnation ratio are more important. Ahmed et al. used pollen as a carbon source, and they investigated the effect of impregnation ratio with zinc chloride on the pore structure of porous carbon (Ahmed et al. 2019). The optimum mesopore ratio can be obtained by the appropriate impregnation ratio. If the impregnation ratio is too large, $ZnCl_2$ will destroy the walls between adjacent micropores. It is confirmed that when the mass ratio of carbon source $ZnCl_2$ is 1:2, the SSA of the resulting porous carbon is 1422.66 m^2 g^{-1}, the total pore volume is 0.77 cm^3 g^{-1}, the micropore volume is 0.33 cm^3 g^{-1}, and the mesopore volume is 0.44 cm^3 g^{-1}. Using ionic liquid electrolyte, the activated carbons achieved large magnitudes of energy density (~42 Wh kg^{-1}) and power density (~19 kW kg^{-1}).

$$ZnCl_2 + 1/2O_2 \rightarrow ZnOCl + 1/2Cl_2 \qquad (14)$$

$$2ZnO + C \rightarrow 2Zn + CO_2 \qquad (15)$$
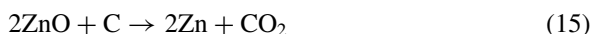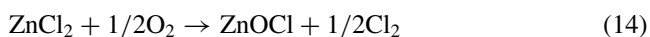
In recent years, some metal chlorides have also acted as molten salts, reacting with carbon at high temperatures to produce porous structures, which is so-called molten salt etching method. Wang et al. adopted non-toxic NaCl and KCl mixed salt as reaction media to regulate the activation process of corn straw (Wang et al. 2018). Hierarchical porous carbon sheets (HPCSs) with good capacitive properties were successfully prepared. They found that when the temperature is higher than 800 °C, Cl^- etched the carbon skeleton to form micro- and mesopores. The hierarchical porous carbon obtained by this strategy has a SSA of 1588 m^2 g^{-1} and a high specific capacitance of 407 F g^{-1} at 1 A g^{-1} in the three-electrode system.

$CuCl_2$ is another molten salt that can be used as an activation agent. The mechanisms of $CuCl_2$ porogen are described as Eqs. (16–17) (Liu et al. 2018)

$$3CuCl_2 + C + 2H_2O \rightarrow Cu + 2CuCl + CO_2 + 4HCl \qquad (16)$$

$$4CuCl + C + 2H_2O \rightarrow 4Cu + CO_2 + 4HCl \qquad (17)$$

Fig. 4 **a** Schematic illustration of the preparation of RPC, **b** pore-size distribution (PSD) curves of RPC, Z-RPC, and K-RPC, **c** specific capacitances of RPC, Z-RPC, K-RPC, and the blank sample at different current densities (Liu et al. 2018)

The porous carbon can maintain the spherical shape (Fig. 4a) of the original carbon precursor, with the pores distributed below 2 nm and pore-size distribution centered at 1.2 nm. As is shown in Fig. 4b, under the same conditions, compared with the activation of $ZnCl_2$ (Z-RPC) and KOH (K-RPC), the pore-size distribution of the former is wide (1–60 nm), while that of the latter is mainly below 3 nm. Moreover, the porous carbon obtained by the activation of $CuCl_2$ shows a high SSA of 2488 $m^2\,g^{-1}$ and presents an outstanding gravimetric capacitance of 390 F g^{-1} at 0.5 A g^{-1} in 6 M KOH electrolyte (Fig. 4c). There is no doubt that molten salt etching is milder than acid/base activation, but it is more expensive and unsuitable for practical production.

Decomposable Salts

There are various salts that can be decomposed to produce gases, which can etch carbon to produce pores, such as carbonates (Mao et al. 2020; Ma et al. 2019; Tang et al. 2018), acetates (Li et al. 2018b, 2019), bicarbonates (Liang et al. 2021; Sevilla and Fuertes 2016), nitrates (Li et al. 2018a; Huo et al. 2020; Wang et al. 2017), and so on. Li et al. produced a macro- and mesoporous carbon material by using the decomposable and water-removable $NaNO_3$ as the porogen (Li et al. 2018a). Above 600 °C, $NaNO_3$ begins to decompose, generating N_2, O_2, and NO, which is conducive to the formation of mesopores (Eqs. 18 and 19) (Li et al. 2018a). The pore size of the material is affected by the dosage of $NaNO_3$. The modified carbon material showed small mesopores of 2–4 nm and larger mesopores of 5–50 nm, with a SSA of 2872.2 $m^2\,g^{-1}$. Due to the synergistic effect of suitable macro-mesoporous ion-diffusion channels and continuous conductive network, the porous carbon material exhibits a high power density. Huo et al. used $NaNO_3$ and KOH to activate soluble
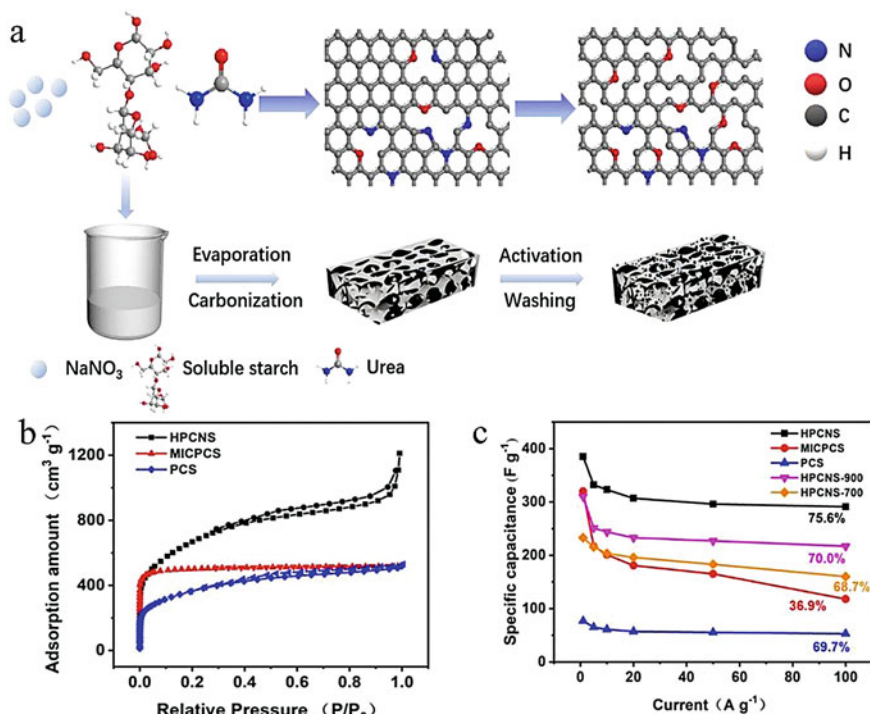
Fig. 5 **a** Schematic illustration of the synthesis of HPCNS, **b** N_2-adsorption/desorption isotherms, **c** specific capacitance as a function of the current densities (Huo et al. 2020)

starch to produce interconnected layered porous carbon networks (Fig. 5a) (Huo et al. 2020). As can be seen from Fig. 5b, the PCMs prepared by $NaNO_3$ and KOH activation (HPCNS) possess micropores, mesopores, and macropores at the same time. However, the materials prepared only with KOH (MICPCS) have no obvious mesoporous and macroporous characteristics. The results showed that the HPCN prepared at 800 °C had a maximum specific surface area of 1864 m^2 g^{-1} and a total pore volume of 2.22 cm^3 g^{-1}. In a three-electrode system with 6 M KOH electrolyte, it shows good capacitance performance. The specific capacitance reaches 385 F g^{-1} at 1 A g^{-1}. Even when the current density is up to 100 A g^{-1}, HPCNs can achieve a capacitance retention of 75.6% (Fig. 5c).

$$12NaNO_3 \rightarrow 6Na_2O + N_2 + 10O_2 + 10NO \tag{18}$$

$$2Na_2O + C \rightarrow 4Na + CO_2 \tag{19}$$
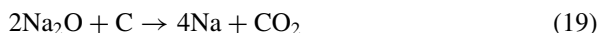
Some oxidizing salts are also used in the preparation of porous activated carbon. For example, $KMnO_4$ gradually decomposes into oxygen, water-soluble potassium salt, and non-water-soluble manganese salt in the process of continuous pyrolysis,

which are beneficial to the formation of hierarchical pores (Qiu et al. 2019a, b; Yi et al. 2020). In addition, KNO_3 (Leng et al. 2020; Wang et al. 2017) can also be used as an oxidizing salt for the activation of porous carbon.

2.3 Self-activation

Although the above-mentioned activation methods and activation reagents have been widely used in the preparation of PCMs, they inevitably have some disadvantages, such as corrosive reagents, complex activation operation, post-treatment, and secondary pollution. Self-activation can simplify the activating process without the need for additional activation reagents and reducing the cost. Its pore generation mechanisms include three aspects: (1) chemical activation (it contains some inorganic salts, organic salts, and some special components, which can be used for activation), (2) physical activation (utilization of CO_2 and H_2O produced by pyrolysis), and (3) removal of inorganic nanoparticles in carbon source (Sevilla et al. 2021). The main influencing factors of self-activation are carbonization temperature and time (Wang et al. 2021; Gao et al. 2021; He et al. 2019a; Bhat et al. 2021). Niu et al. fabricated mesopore-dominant porous carbon as electrode materials by direct pyrolysis (600, 850, 900, 1000, 1100, 1200 °C) of cattle bones in an Ar atmosphere (Niu et al. 2017). With the increase of temperature, the surface of carbon changes from nonporous to porous. The porous carbon obtained at 1100 °C presented a hierarchical porous structure with a large SSA of 2096 m^2 g^{-1}. The mesopore volume is 1.83 cm^3 g^{-1}, and the conductivity reached 5141 S m^{-1}. PC-1100 displayed a high specific capacitance of 258 F g^{-1} at a current density of 5 A g^{-1} in a symmetrical supercapacitor. Even at 100 A g^{-1}, a high capacitance of 176 F g^{-1} was maintained.

3 Summary and Perspectives

PCMs are promising electrode materials for supercapacitors attributing to their rich precursors, low cost, high specific surface area, tunable pore structure, and good stability. PCMs could be prepared from various precursors including biomass, natural polymers, synthetic macromolecules, and carbon-rich small molecules by pyrolysis at high temperature. However, the carbonaceous products obtained from directly carbonization of precursors often show porous-less or even nonporous feature with limited SSA. It is necessary to improve the SSA and adjust the pore structure of carbon materials to enhance their capacitance performance. Physical/chemical activation methods are proved to be effective approaches.

Nowadays, PCMs have produced tons of kilograms annually through carbonization–activation way. However, there are some issues still unsolved which block the production and application of PCMs. As to the physical activation, steam and CO_2

are the commonly used activation agents which are low corrosive to the production facilities and more favorable for practical application. But physical activation always results in PCMs with narrowly distributed micropores, and the particle and microdomain sizes are reduced. Physical activation also shows the shortage in product yield, tap density, and SSA. As to chemical activation, corrosive reagents like $ZnCl_2$, KOH, NaOH, H_2SO_4, HNO_3, and K_2CO_3 are the traditional activation agents. Compared with physical activation, chemical activation shows advantages in relatively low activation temperature, high yield, large SSA, and high mesopore ratios. However, chemical activation often requires high mass ratio of corrosive activation agents to carbon sources and generates great amounts of contaminants. Hence, tradition chemical activation method is only limit to laboratory-scale research.

In recently years, great efforts have been investigated on the exploration of much less corrosive chemical activation agents and molten salts (KCl, NaCl, $CuCl_2$, $FeCl_3$, $NiCl_2$, etc.), decomposable salts (nitrates, carbonates, bicarbonates, acetates, oxalates, etc.), and oxidative salts ($KMnO_4$, $KClO_4$, $(NH_4)_2S_2O_8$, H_2O_2, etc.) are proved to be better choices. Among these new chemical activation agents, potassium salts and sodium salts are more preferred owing to their water solvable nature which are benefit for post-treatment. Moreover, potassium salts and sodium salts could be served as templates to generate hierarchical pores. Ammonium salts are also good choices attributing to their fully decomposable nature which could act as chemical blowing/foaming agents generating lots of macropores. Besides, ammonium salts could be used as nitrogen sources to introduce nitrogen species to contribute pseudocapacitance and modify the surface feature of carbon materials.

The pore structure optimization process is complicated and sometimes uncontrollable. It is very hard to obtain PCMs with idea pore structure from only one method within one-step experiments. As to application in supercapacitors, the ratio among macropores, mesopores, and micropores of PCMs should be well adjusted to keep a balance on specific capacitance, rate performance, stability, and tap density. From a production point of view, it is more favorable to synthesize PCMs from one-step carbonization and activation process with multifunctional agents (e.g., KCl, NaCl, NH_4NO_3). It is necessary to combine activation with other methods including template, chemical vapor deposition, electrospinning, hydrothermal/solvothermal method to design PCMs with finely tuned pore structures, and good capacitive performance.

References

Ahmed, S., Ahmed, A., Rafat, M.: Investigation on activated carbon derived from biomass Butnea monosperma and its application as a high performance supercapacitor electrode. J. Energy Storage **26** (2019). https://doi.org/10.1016/j.est.2019.100988

Bedia, J., Belver, C., Ponce, S., Rodriguez, J., Rodriguez, J.J.: Adsorption of antipyrine by activated carbons from $FeCl_3$-activation of Tara gum. Chem. Eng. J. **333**, 58–65 (2018). https://doi.org/10.1016/j.cej.2017.09.161

Bhat, V.S., Krishnan, S.G., Jayeoye, T.J., Rujiralai, T., Sirimahachai, U., Viswanatha, R., Khalid, M., Hegde, G.: Self-activated 'green' carbon nanoparticles for symmetric solid-state supercapacitors. J. Mater. Sci. (2021). https://doi.org/10.1007/s10853-021-06154-z

Bo, Y., Zhao, Y., Cai, Z., Bahi, A., Liu, C., Ko, F.: Facile synthesis of flexible electrode based on cotton/polypyrrole/multi-walled carbon nanotube composite for supercapacitors. Cellulose **25**(7), 4079–4091 (2018). https://doi.org/10.1007/s10570-018-1845-9

Borchardt, L., Zhu, Q.-L., Casco, M.E., Berger, R., Zhuang, X., Kaskel, S., Feng, X., Xu, Q.: Toward a molecular design of porous carbon materials. Mater. Today **20**(10), 592–610 (2017). https://doi.org/10.1016/j.mattod.2017.06.002

Budinova, T., Ekinci, E., Yardim, F., Grimm, A., Björnbom, E., Minkova, V., Goranova, M.: Characterization and application of activated carbon produced by H_3PO_4 and water vapor activation. Fuel Process. Technol. **87**(10), 899–905 (2006). https://doi.org/10.1016/j.fuproc.2006.06.005

Cai, R., Si, Y., You, B., Chen, M., Wu, L.: Yolk-shell carbon nanospheres with controlled structure and composition by self-activation and air activation. ACS Appl. Mater. Interfaces **12**(25), 28738–28749 (2020). https://doi.org/10.1021/acsami.0c02980

Cao, L., Li, H., Xu, Z., Gao, R., Wang, S., Zhang, G., Jiang, S., Xu, W., Hou, H.: Camellia pollen-derived carbon with controllable N content for high-performance supercapacitors by ammonium chloride activation and dual N-doping. ChemNanoMat **7**(1), 34–43 (2021). https://doi.org/10.1002/cnma.202000531

Chen, C., Yu, D., Zhao, G., Du, B., Tang, W., Sun, L., Sun, Y., Besenbacher, F., Yu, M.: Three-dimensional scaffolding framework of porous carbon nanosheets derived from plant wastes for high-performance supercapacitors. Nano Energy **27**, 377–389 (2016). https://doi.org/10.1016/j.nanoen.2016.07.020

Chen, W., Luo, M., Wang, X., Yang, K., Zhou, X.: Rapid synthesis of chitin-based porous carbons with high yield, high nitrogen retention, and low cost for high-rate supercapacitors. Int. J. Energy Res. **44**(2), 1167–1178 (2019). https://doi.org/10.1002/er.5008

Chen, W., Luo, M., Yang, K., Zhang, D., Zhou, X.: A clean and industrially applicable approach for the production of copper-doped and core-shell structured porous carbon microspheres as supercapacitor electrode materials. J. Cleaner Prod. **282** (2021). https://doi.org/10.1016/j.jclepro.2020.124534

Cheng, P., Gao, S., Zang, P., Yang, X., Bai, Y., Xu, H., Liu, Z., Lei, Z.: Hierarchically porous carbon by activation of shiitake mushroom for capacitive energy storage. Carbon **93**, 315–324 (2015). https://doi.org/10.1016/j.carbon.2015.05.056

Cheng, J., Hu, S.-C., Sun, G.-T., Kang, K., Zhu, M.-Q., Geng, Z.-C.: Comparison of activated carbons prepared by one-step and two-step chemical activation process based on cotton stalk for supercapacitors application. Energy **215** (2021). https://doi.org/10.1016/j.energy.2020.119144

Ding, Y., Li, Y., Dai, Y., Han, X., Xing, B., Zhu, L., Qiu, K., Wang, S.: A novel approach for preparing in-situ nitrogen doped carbon via pyrolysis of bean pulp for supercapacitors. Energy **216** (2021). https://doi.org/10.1016/j.energy.2020.119227

Elmouwahidi, A., Bailón-García, E., Pérez-Cadenas, A.F., Celzard, A., Fierro, V., Carrasco-Marín, F.: Carbon microspheres with tailored texture and surface chemistry as electrode materials for supercapacitors. ACS Sustain. Chem. Eng. **9**(1), 541–551 (2020). https://doi.org/10.1021/acssuschemeng.0c08024

Gao, Y., Tang, Y., Liu, W., Liu, L., Zeng, X.: Porous bamboo-like CNTs prepared by a simple and low-cost steam activation for supercapacitors. Int. J. Energy Res. **44**(13), 10946–10952 (2020a). https://doi.org/10.1002/er.5672

Gao, Y., Yue, Q., Gao, B., Li, A.: Insight into activated carbon from different kinds of chemical activating agents: a review. Sci. Total Environ. **746**, 141094 (2020b). https://doi.org/10.1016/j.scitotenv.2020.141094

Gao, Y., Sun, R., Li, A., Ji, G.: In-situ self-activation strategy toward highly porous biochar for supercapacitors: direct carbonization of marine algae. J. Electroanal. Chem. **882** (2021). https://doi.org/10.1016/j.jelechem.2021.114986

Gonzalez-Garcia, P.: Activated carbon from lingocellulosics precursors: a review of the synthesis methods, characterization techniques and applications. Renew. Sustain. Energy Rev. **82**, 1393–1414 (2018). https://doi.org/10.1016/j.rser.2017.04.117

Guo, N., Li, M., Wang, Y., Sun, X., Wang, F., Yang, R.: Soybean root-derived hierarchical porous carbon as electrode material for high-performance supercapacitors in ionic liquids. ACS Appl. Mater. Interfaces **8**(49), 33626–33634 (2016). https://doi.org/10.1021/acsami.6b11162

He, S., Chen, W.: 3D graphene nanomaterials for binder-free supercapacitors: scientific design for enhanced performance. Nanoscale **7**(16), 6957–6990 (2015). https://doi.org/10.1039/c4nr05895j

He, S., Chen, L., Xie, C., Hu, H., Chen, S., Hanif, M., Hou, H.: Supercapacitors based on 3D network of activated carbon nanowhiskers wrapped-on graphitized electrospun nanofibers. J. Power Sources **243**, 880–886 (2013). https://doi.org/10.1016/j.jpowsour.2013.06.104

He, J., Zhang, D., Han, M., Liu, X., Wang, Y., Li, Y., Zhang, X., Wang, K., Feng, H., Wang, Y.: One-step large-scale fabrication of nitrogen doped microporous carbon by self-activation of biomass for supercapacitors application. J. Energy Storage **21**, 94–104 (2019a). https://doi.org/10.1016/j.est.2018.11.015

He, S., Zhang, C., Du, C., Cheng, C., Chen, W.: High rate-performance supercapacitor based on nitrogen-doped hollow hexagonal carbon nanoprism arrays with ultrathin wall thickness in situ fabricated on carbon cloth. J. Power Sources **434**, 226701 (2019b). https://doi.org/10.1016/j.jpowsour.2019.226701

He, Y., Zhuang, X., Lei, C., Lei, L., Hou, Y., Mai, Y., Feng, X.: Porous carbon nanosheets: synthetic strategies and electrochemical energy related applications. Nano Today **24**, 103–119 (2019c). https://doi.org/10.1016/j.nantod.2018.12.004

Hou, L., Chen, Z., Zhao, Z., Sun, X., Zhang, J., Yuan, C.: Universal FeCl$_3$-activating strategy for green and scalable fabrication of sustainable biomass-derived hierarchical porous nitrogen-doped carbons for electrochemical supercapacitors. ACS Appl. Energy Mater. **2**(1), 548–557 (2018). https://doi.org/10.1021/acsaem.8b01589

Huang, C., Sun, T., Hulicova-Jurcakova, D.: Wide electrochemical window of supercapacitors from coffee bean-derived phosphorus-rich carbons. ChemSusChem **6**(12), 2330–2339 (2013). https://doi.org/10.1002/cssc.201300457

Huo, S., Zhang, X., Liang, B., Zhao, Y., Li, K.: Synthesis of interconnected hierarchically porous carbon networks with excellent diffusion ability based on NaNO$_3$ crystal-assisted strategy for high performance supercapacitors. J. Power Sources **450** (2020). https://doi.org/10.1016/j.jpowsour.2019.227612

Jin, Y., Tian, K., Wei, L., Zhang, X., Guo, X.: Hierarchical porous microspheres of activated carbon with a high surface area from spores for electrochemical double-layer capacitors. J. Mater. Chem. A **4**(41), 15968–15979 (2016). https://doi.org/10.1039/c6ta05872h

Kigozi, M., Kali, R., Bello, A., Padya, B., Kalu-Uka, G.M., Wasswa, J., Jain, P.K., Onwualu, P.A., Dzade, N.Y.: Modified activation process for supercapacitor electrode materials from African Maize Cob. Mater. **13**(23) (2020). https://doi.org/10.3390/ma13235412

Kim, C., Ngoc, B.T.N., Yang, K.S., Kojima, M., Kim, Y.A., Kim, Y.J., Endo, M., Yang, S.C.: Self-sustained thin webs consisting of porous carbon nanofibers for supercapacitors via the electro-spinning of polyacrylonitrile solutions containing zinc chloride. Adv. Mater. **19**(17), 2341–2346 (2007). https://doi.org/10.1002/adma.200602184

Kim, M., Lim, H., Xu, X., Hossain, M.S.A., Na, J., Awaludin, N.N., Shah, J., Shrestha, L.K., Ariga, K., Nanjundan, A.K., Martin, D.J., Shapter, J.G., Yamauchi, Y.: Sorghum biomass-derived porous carbon electrodes for capacitive deionization and energy storage. Microporous Mesoporous Mater. **312** (2021). https://doi.org/10.1016/j.micromeso.2020.110757

Kumar, T.R., Senthil, R.A., Pan, Z., Pan, J., Sun, Y.: A tubular-like porous carbon derived from waste American poplar fruit as advanced electrode material for high-performance supercapacitor. J. Energy Storage **32** (2020). https://doi.org/10.1016/j.est.2020.101903

Lee, H.-M., Kwac, L.-K., An, K.-H., Park, S.-J., Kim, B.-J.: Electrochemical behavior of pitch-based activated carbon fibers for electrochemical capacitors. Energy Convers. Manage. **125**, 347–352 (2016). https://doi.org/10.1016/j.enconman.2016.06.006

Leng, C., Sun, K., Li, J., Jiang, J.: From dead pine needles to O, N codoped activated carbons by a one-step carbonization for high rate performance supercapacitors. ACS Sustain. Chem. Eng. **5**(11), 10474–10482 (2017). https://doi.org/10.1021/acssuschemeng.7b02481

Leng, C., Zhao, Z., Song, Y., Sun, L., Fan, Z., Yang, Y., Liu, X., Wang, X., Qiu, J.: 3D carbon frameworks for ultrafast charge/discharge rate supercapacitors with high energy-power density. Nano-Micro Lett. **13**(1) (2020). https://doi.org/10.1007/s40820-020-00535-w

Li, Y.-J., Ni, X.-Y., Shen, J., Liu, D., Liu, N.-P., Zhou, X.-W.: Preparation and performance of polypyrrole/nitric acid activated carbon aerogel nanocomposite materials for supercapacitors. Acta Phys. Chim. Sin. **32**(2), 493–502 (2016). https://doi.org/10.3866/pku.Whxb201511131

Li, Z.-Y., Akhtar, M.S., Kwak, D.-H., Yang, O.B.: Improvement in the surface properties of activated carbon via steam pretreatment for high performance supercapacitors. Appl. Surf. Sci. **404**, 88–93 (2017). https://doi.org/10.1016/j.apsusc.2017.01.238

Li, J., Wang, N., Tian, J., Qian, W., Chu, W.: Cross-coupled macro-mesoporous carbon network toward record high energy-power density supercapacitor at 4 V. Adv. Funct. Mater. **28**(51) (2018a). https://doi.org/10.1002/adfm.201806153

Li, Q., Wu, X., Zhao, Y., Miao, Z., Xing, L., Zhou, J., Zhao, J., Zhuo, S.: Nitrogen-doped hierarchical porous carbon through one-step activation of bean curd for high-performance supercapacitor electrode. ChemElectroChem **5**(12), 1606–1614 (2018b). https://doi.org/10.1002/celc.201800230

Li, Q., Mu, J., Zhou, J., Zhao, Y., Zhuo, S.: Avoiding the use of corrosive activator to produce nitrogen-doped hierarchical porous carbon materials for high-performance supercapacitor electrode. J. Electroanal. Chem. **832**, 284–292 (2019). https://doi.org/10.1016/j.jelechem.2018.11.013

Li, B., Xiong, H., Xiao, Y., Hu, J., Zhang, X., Li, L., Wang, R.: Efficient toluene adsorption on metal salt-activated porous carbons derived from low-cost biomass: a discussion of mechanism. ACS Omega **5**(22), 13196–13206 (2020a). https://doi.org/10.1021/acsomega.0c01230

Li, H., Cao, L., Wang, F., Duan, G., Xu, W., Mei, C., Zhang, G., Liu, K., Yang, M., Jiang, S.: *Fatsia japonica*-derived hierarchical porous carbon for supercapacitors with high energy density and long cycle life. Front. Chem. **8**, 89 (2020b). https://doi.org/10.3389/fchem.2020.00089

Li, Z., Guo, D., Liu, Y., Wang, H., Wang, L.: Recent advances and challenges in biomass-derived porous carbon nanomaterials for supercapacitors. Chem. Eng. J. **397** (2020c). https://doi.org/10.1016/j.cej.2020.125418

Li, P., Feng, C.-N., Li, H.-P., Zhang, X.-L., Zheng, X.-C.: Facile fabrication of carbon materials with hierarchical porous structure for high-performance supercapacitors. J. Alloys Compd. **851** (2021a). https://doi.org/10.1016/j.jallcom.2020.156922

Li, Y., Pu, Z., Sun, Q., Pan, N.: A review on novel activation strategy on carbonaceous materials with special morphology/texture for electrochemical storage. J. Energy Chem. **60**, 572–590 (2021b). https://doi.org/10.1016/j.jechem.2021.01.017

Liang, X., Liu, R., Wu, X.: Biomass waste derived functionalized hierarchical porous carbon with high gravimetric and volumetric capacitances for supercapacitors. Microporous Mesoporous Mater. **310** (2021). https://doi.org/10.1016/j.micromeso.2020.110659

Liu, T., Zhang, F., Song, Y., Li, Y.: Revitalizing carbon supercapacitor electrodes with hierarchical porous structures. J. Mater. Chem. A **5**(34), 17705–17733 (2017). https://doi.org/10.1039/c7ta05646j

Liu, S., Liang, Y., Zhou, W., Hu, W., Dong, H., Zheng, M., Hu, H., Lei, B., Xiao, Y., Liu, Y.: Large-scale synthesis of porous carbon via one-step $CuCl_2$ activation of rape pollen for high-performance supercapacitors. J. Mater. Chem. A **6**(25), 12046–12055 (2018). https://doi.org/10.1039/c8ta02838a

Lozano-Castelló, D., Calo, J.M., Cazorla-Amorós, D., Linares-Solano, A.: Carbon activation with KOH as explored by temperature programmed techniques, and the effects of hydrogen. Carbon **45**(13), 2529–2536 (2007). https://doi.org/10.1016/j.carbon.2007.08.021

Lv, Z., Li, X., Chen, X., Li, X., Wu, M., Li, Z.: One-step site-specific activation approach for preparation of hierarchical porous carbon materials with high electrochemical performance. ACS Appl. Energy Mater. **2**(12), 8767–8782 (2019). https://doi.org/10.1021/acsaem.9b01729

Ma, G., Yang, Q., Sun, K., Peng, H., Ran, F., Zhao, X., Lei, Z.: Nitrogen-doped porous carbon derived from biomass waste for high-performance supercapacitor. Biores. Technol. **197**, 137–142 (2015). https://doi.org/10.1016/j.biortech.2015.07.100

Ma, L., Liu, J., Lv, S., Zhou, Q., Shen, X., Mo, S., Tong, H.: Scalable one-step synthesis of N, S co-doped graphene-enhanced hierarchical porous carbon foam for high-performance solid-state supercapacitors. J. Mater. Chem. A **7**(13), 7591–7603 (2019). https://doi.org/10.1039/c9ta00038k

Mao, Y., Xie, H., Chen, X., Zhao, Y., Qu, J., Song, Q., Ning, Z., Xing, P., Yin, H.: A combined leaching and electrochemical activation approach to converting coal to capacitive carbon in molten carbonates. J. Cleaner Prod. **248** (2020). https://doi.org/10.1016/j.jclepro.2019.119218

Merlet, C., Rotenberg, B., Madden, P.A., Taberna, P.L., Simon, P., Gogotsi, Y., Salanne, M.: On the molecular origin of supercapacitance in nanoporous carbon electrodes. Nat. Mater. **11**(4), 306–310 (2012). https://doi.org/10.1038/nmat3260

Mo, C., Zhang, J., Zhang, G.: Hierarchical porous carbon with three dimensional nanonetwork from water hyacinth leaves for energy storage. J. Energy Storage **32** (2020). https://doi.org/10.1016/j.est.2020.101848

Mohamedkhair, A.K., Aziz, M.A., Shah, S.S., Shaikh, M.N., Jamil, A.K., Qasem, M.A.A., Buliyaminu, I.A., Yamani, Z.H.: Effect of an activating agent on the physicochemical properties and supercapacitor performance of naturally nitrogen-enriched carbon derived from *Albizia procera* leaves. Arab. J. Chem. **13**(7), 6161–6173 (2020). https://doi.org/10.1016/j.arabjc.2020.05.017

Myglovets, M., Poddubnaya, O.I., Sevastyanova, O., Lindström, M.E., Gawdzik, B., Sobiesiak, M., Tsyba, M.M., Sapsay, V.I., Klymchuk, D.O., Puziy, A.M.: Preparation of carbon adsorbents from lignosulfonate by phosphoric acid activation for the adsorption of metal ions. Carbon **80**, 771–783 (2014). https://doi.org/10.1016/j.carbon.2014.09.032

Navarro, R.M., Peña, M.A., Fierro, J.L.G.: Hydrogen production reactions from carbon feedstocks: fossil fuels and biomass. Chem. Rev. **107**(10), 3952–3991 (2007). https://doi.org/10.1021/cr0501994

Nishihara, H., Kyotani, T.: Templated nanocarbons for energy storage. Adv. Mater. **24**(33), 4473–4498 (2012). https://doi.org/10.1002/adma.201201715

Niu, J., Shao, R., Liang, J., Dou, M., Li, Z., Huang, Y., Wang, F.: Biomass-derived mesopore-dominant porous carbons with large specific surface area and high defect density as high performance electrode materials for Li-ion batteries and supercapacitors. Nano Energy **36**, 322–330 (2017). https://doi.org/10.1016/j.nanoen.2017.04.042

Olivares-Marín, M., Fernández-González, C., Macías-García, A., Gómez-Serrano, V.: Thermal behaviour of lignocellulosic material in the presence of phosphoric acid. Influence of the acid content in the initial solution. Carbon **44**(11), 2347–2350 (2006). https://doi.org/10.1016/j.carbon.2006.04.004

Pallarés, J., González-Cencerrado, A., Arauzo, I.: Production and characterization of activated carbon from barley straw by physical activation with carbon dioxide and steam. Biomass Bioenerg. **115**, 64–73 (2018). https://doi.org/10.1016/j.biombioe.2018.04.015

Pourhosseini, S.E.M., Norouzi, O., Naderi, H.R.: Study of micro/macro ordered porous carbon with olive-shaped structure derived from *Cladophora glomerata* macroalgae as efficient working electrodes of supercapacitors. Biomass Bioenerg. **107**, 287–298 (2017). https://doi.org/10.1016/j.biombioe.2017.10.025

Qin, L.: Porous carbon derived from pine nut shell prepared by steam activation for supercapacitor electrode material. Int. J. Electrochem. Sci. 8907–8918 (2019). https://doi.org/10.20964/2019.09.20

Qiu, D., Guo, N., Gao, A., Zheng, L., Xu, W., Li, M., Wang, F., Yang, R.: Preparation of oxygen-enriched hierarchically porous carbon by $KMnO_4$ one-pot oxidation and activation: mechanism

and capacitive energy storage. Electrochim. Acta **294**, 398–405 (2019a). https://doi.org/10.1016/j.electacta.2018.10.049

Qiu, D., Kang, C., Gao, A., Xie, Z., Li, Y., Li, M., Wang, F., Yang, R.: Sustainable low-temperature activation to customize pore structure and heteroatoms of biomass-derived carbon enabling unprecedented durable supercapacitors. ACS Sustain. Chem. Eng. **7**(17), 14629–14638 (2019b). https://doi.org/10.1021/acssuschemeng.9b02425

Qiu, S., Chen, Z., Zhuo, H., Hu, Y., Liu, Q., Peng, X., Zhong, L.: Using $FeCl_3$ as a solvent, template, and activator to prepare B, N Co-doping porous carbon with excellent supercapacitance. ACS Sustain. Chem. Eng. **7**(19), 15983–15994 (2019c). https://doi.org/10.1021/acssuschemeng.9b02431

Sevilla, M., Fuertes, A.B.: A green approach to high-performance supercapacitor electrodes: the chemical activation of hydrochar with potassium bicarbonate. ChemSusChem **9**(14), 1880–1888 (2016). https://doi.org/10.1002/cssc.201600426

Sevilla, M., Diez, N., Fuertes, A.B.: More sustainable chemical activation strategies for the production of porous carbons. ChemSusChem **14**(1), 94–117 (2021). https://doi.org/10.1002/cssc.202001838

Shi, Y., Liu, G., Wang, L., Zhang, H.: Heteroatom-doped porous carbons from sucrose and phytic acid for adsorptive desulfurization and sulfamethoxazole removal: a comparison between aqueous and non-aqueous adsorption. J. Colloid Interface Sci. **557**, 336–348 (2019). https://doi.org/10.1016/j.jcis.2019.09.032

Simon, P., Gogotsi, Y., Dunn, B.: Where do batteries end and supercapacitors begin? Science **343**(6176), 1210–1211 (2014). https://doi.org/10.1126/science.1249625

Son, Y.-R., Park, S.-J.: Preparation and characterization of mesoporous activated carbons from nonporous hard carbon via enhanced steam activation strategy. Mater. Chem. Phys. **242** (2020). https://doi.org/10.1016/j.matchemphys.2019.122454

Sun, F., Wu, D., Gao, J., Pei, T., Chen, Y., Wang, K., Yang, H., Zhao, G.: Graphitic porous carbon with multiple structural merits for high-performance organic supercapacitor. J. Power Sources **477** (2020). https://doi.org/10.1016/j.jpowsour.2020.228759

Tang, D., Luo, Y., Lei, W., Xiang, Q., Ren, W., Song, W., Chen, K., Sun, J.: Hierarchical porous carbon materials derived from waste *Lentinus edodes* by a hybrid hydrothermal and molten salt process for supercapacitor applications. Appl. Surf. Sci. **462**, 862–871 (2018). https://doi.org/10.1016/j.apsusc.2018.08.153

Thileep Kumar, K., Sivagaami Sundari, G., Senthil Kumar, E., Ashwini, A., Ramya, M., Varsha, P., Kalaivani, R., Shanmugaraj Andikkadu, M., Kumaran, V., Gnanamuthu, R., Karazhanov, S.Z., Raghu, S.: Synthesis of nanoporous carbon with new activating agent for high-performance supercapacitor. Mater. Lett. **218**, 181–184 (2018). https://doi.org/10.1016/j.matlet.2018.02.017

Tian, Y., Xiao, C., Yin, J., Zhang, W., Bao, J., Lin, H., Lu, H.: Hierarchical porous carbon prepared through sustainable $CuCl_2$ activation of rice husk for high-performance supercapacitors. ChemistrySelect **4**(8), 2314–2319 (2019). https://doi.org/10.1002/slct.201804002

Tian, W., Zhang, H., Duan, X., Sun, H., Shao, G., Wang, S.: Porous carbons: structure-oriented design and versatile applications. Adv. Func. Mater. **30**(17), 1909265 (2020). https://doi.org/10.1002/adfm.201909265

Veerakumar, P., Maiyalagan, T., Raj, B.G.S., Guruprasad, K., Jiang, Z., Lin, K.-C.: Paper flower-derived porous carbons with high-capacitance by chemical and physical activation for sustainable applications. Arab. J. Chem. **13**(1), 2995–3007 (2020). https://doi.org/10.1016/j.arabjc.2018.08.009

Vinayagam, M., Suresh Babu, R., Sivasamy, A., Ferreira de Barros, A.L.: Biomass-derived porous activated carbon from *Syzygium cumini* fruit shells and *Chrysopogon zizanioides* roots for high-energy density symmetric supercapacitors. Biomass Bioenergy **143** (2020). https://doi.org/10.1016/j.biombioe.2020.105838

Wang, J., Kaskel, S.: KOH activation of carbon-based materials for energy storage. J. Mater. Chem. **22**(45), 23710 (2012). https://doi.org/10.1039/c2jm34066f

Wang, Y., Song, Y., Xia, Y.: Electrochemical capacitors: mechanism, materials, systems, characterization and applications. Chem. Soc. Rev. **45**(21), 5925–5950 (2016). https://doi.org/10.1039/c5cs00580a

Wang, D., Liu, S., Jiao, L., Fang, G., Geng, G., Ma, J.: Unconventional mesopore carbon nanomesh prepared through explosion–assisted activation approach: a robust electrode material for ultrafast organic electrolyte supercapacitors. Carbon **119**, 30–39 (2017). https://doi.org/10.1016/j.carbon.2017.03.102

Wang, C., Wu, D., Wang, H., Gao, Z., Xu, F., Jiang, K.: A green and scalable route to yield porous carbon sheets from biomass for supercapacitors with high capacity. J. Mater. Chem. A **6**(3), 1244–1254 (2018). https://doi.org/10.1039/c7ta07579k

Wang, Y., Qu, Q., Gao, S., Tang, G., Liu, K., He, S., Huang, C.: Biomass derived carbon as binder-free electrode materials for supercapacitors. Carbon **155**, 706–726 (2019). https://doi.org/10.1016/j.carbon.2019.09.018

Wang, F., Chen, L., Li, H., Duan, G., He, S., Zhang, L., Zhang, G., Zhou, Z., Jiang, S.: N-doped honeycomb-like porous carbon towards high-performance supercapacitor. Chin. Chem. Lett. **31**(7), 1986–1990 (2020a). https://doi.org/10.1016/j.cclet.2020.02.020

Wang, H., Shao, Y., Mei, S., Lu, Y., Zhang, M., Sun, J.K., Matyjaszewski, K., Antonietti, M., Yuan, J.: Polymer-derived heteroatom-doped porous carbon materials. Chem. Rev. **120**(17), 9363–9419 (2020b). https://doi.org/10.1021/acs.chemrev.0c00080

Wang, Y., Zhang, L., Hou, H., Xu, W., Duan, G., He, S., Liu, K., Jiang, S.: Recent progress in carbon-based materials for supercapacitor electrodes: a review. J. Mater. Sci. **56**(1), 173–200 (2020c). https://doi.org/10.1007/s10853-020-05157-6

Wang, A., Sun, K., Xu, R., Sun, Y., Jiang, J.: Cleanly synthesizing rotten potato-based activated carbon for supercapacitor by self-catalytic activation. J. Cleaner Prod. **283** (2021). https://doi.org/10.1016/j.jclepro.2020.125385

Yakaboylu, G.A., Jiang, C., Yumak, T., Zondlo, J.W., Wang, J., Sabolsky, E.M.: Engineered hierarchical porous carbons for supercapacitor applications through chemical pretreatment and activation of biomass precursors. Renew. Energy **163**, 276–287 (2021). https://doi.org/10.1016/j.renene.2020.08.092

Yan, B., Zheng, J., Wang, F., Zhao, L., Zhang, Q., Xu, W., He, S.: Review on porous carbon materials engineered by ZnO templates: design, synthesis and capacitance performance. Mater. Design **201**, 109518 (2021)

Yi, S., Qin, X., Liang, C., Li, J., Rajagopalan, R., Zhang, Z., Song, J., Tang, Y., Cheng, F., Wang, H., Shao, M.: Insights into KMnO₄ etched N-rich carbon nanotubes as advanced electrocatalysts for Zn-air batteries. Appl. Catal. B Environ. **264** (2020). https://doi.org/10.1016/j.apcatb.2019.118537

Yin, J., Zhang, W., Alhebshi, N.A., Salah, N., Alshareef, H.N.: Synthesis strategies of porous carbon for supercapacitor applications. Small Methods **4**(3) (2020). https://doi.org/10.1002/smtd.201900853

Yu, D., Ma, Y., Chen, M., Dong, X.: KOH activation of wax gourd-derived carbon materials with high porosity and heteroatom content for aqueous or all-solid-state supercapacitors. J. Colloid Interface Sci. **537**, 569–578 (2019). https://doi.org/10.1016/j.jcis.2018.11.070

Zeng, F., Kuang, Y., Zhang, N., Huang, Z., Pan, Y., Hou, Z., Zhou, H., Yan, C., Schmidt, O.G.: Multilayer super-short carbon nanotube/reduced graphene oxide architecture for enhanced supercapacitor properties. J. Power Sources **247**, 396–401 (2014). https://doi.org/10.1016/j.jpowsour.2013.08.122

Zhai, Y., Dou, Y., Zhao, D., Fulvio, P.F., Mayes, R.T., Dai, S.: Carbon materials for chemical capacitive energy storage. Adv. Mater. **23**(42), 4828–4850 (2011). https://doi.org/10.1002/adma.201100984

Zhang, Z., Lei, Y., Li, D., Zhao, J., Wang, Y., Zhou, G., Yan, C., He, Q.: Sudden heating of H₃PO₄-loaded coconut shell in CO₂ flow to produce super activated carbon and its application for benzene adsorption. Renew. Energy **153**, 1091–1099 (2020). https://doi.org/10.1016/j.renene.2020.02.059

Zhu, Z., Xu, Z.: The rational design of biomass-derived carbon materials towards next-generation energy storage: a review. Renew. Sustain. Energy Rev. **134** (2020). https://doi.org/10.1016/j.rser.2020.110308

Zhu, K., Wang, Y., Tang, J.A., Guo, S., Gao, Z., Wei, Y., Chen, G., Gao, Y.: A high-performance supercapacitor based on activated carbon fibers with an optimized pore structure and oxygen-containing functional groups. Mater. Chem. Front. **1**(5), 958–966 (2017). https://doi.org/10.1039/c6qm00196c

Zhu, S., Zhao, N., Li, J., Deng, X., Sha, J., He, C.: Hard-template synthesis of three-dimensional interconnected carbon networks: rational design, hybridization and energy-related applications. Nano Today **29**, 100796 (2019). https://doi.org/10.1016/j.nantod.2019.100796

Zong, S., Zhang, Y., Xaba, M.S., Liu, X., Chen, A.: N-doped porous carbon nanotubes derived from polypyrrole for supercapacitors with high performance. J. Anal. Appl. Pyrol **152** (2020). https://doi.org/10.1016/j.jaap.2020.104925

Porous Ionic Liquid Derived Materials for CO₂ Emissions Mitigation

Raquel V. Barrulas, Marcileia Zanatta, and Marta C. Corvo

Abstract The purpose of this chapter is to demonstrate alternative porous IL-grafted materials for CO_2 capture and reuse. ILs are known for their affinity and selectivity towards CO_2, however, their liquid nature restrains the scope of applications. The effort to gather IL features within porous materials has therefore widened their functionalities. Since the choice of support is essential to achieve the adequate porosity, the chapter is organized according to the nature of support, namely organic, inorganic and hybrid or crystalline frameworks materials. The discussion is mainly based on organic supports since the desired functionality with modulated properties can be introduced into the porous materials by using PIL-based materials. In addition, in all sections, the methodologies and support trends are highlighted to facilitate the development of future tailored materials.

Abbreviations

Cations

[AEMIM]⁺	1-Aminoethyl-3-methylimidazolium
[AIM]⁺	Allylimidazolium
[APy]⁺	Aminopyridinium
[BMIM]⁺	1-Butyl-3-methylimidazolium
[BMPyrr]⁺	1-Butyl-1-methylpyrrolidinium
[BPhIM]⁺	3-Butyl-2-phenylimidazolium
[BVBzIM]⁺	1,3-Bis(4-vinylbenzyl)imidazolium
[BzBIM]⁺	1-Benzyl-3-butylimidazolium
[BzCOOHPIM]⁺	1-Benzyl-3-carboxypropylimidazolium
[BzDPhIM]⁺	Bis-phenylimidazolium

R. V. Barrulas · M. Zanatta · M. C. Corvo (✉)
Department of Materials Science (DCM), NOVA School of Science and Technology (FCT NOVA), i3N|Cenimat, NOVA University Lisbon, 2829-516 Caparica, Portugal
e-mail: marta.corvo@fct.unl.pt

[BzEIM]+	1-Benzyl-3-ethylimidazolium
[BzHexadecIM]+	1-Benzyl-3-hexadecylimidazolium
[BzHOEIM]+	1-Benzyl-3-hydroxyethylimidazolium
[BzIMBz]+	1,3-Dibenzylimidazolium
[BzPhIM]+	3-Benzyl-2-phenylimidazolium
[CEIM]+	3-(2-Carboxyl-ethyl)-1-(3-amino-propyl)imidazolium
[CEMIM]+	1-Carboxyethyl-3-methylimidazolium
[DHPIM]+	1-(2,3-Di-hydroxyl-propyl)-imidazolium
[DVIM]+	1,4-Butanediyl-3,3'-bis-1-vinylimidazolium
[EMIM]+	1-Ethyl-3-methylimidazolium
[Et$_4$N]+	Tetraethylammonium
[GIBIM]+	1-Glycidyl-butylimidazolium
[HEIM]+	1-(2-Hydroxyl-ethyl)-imidazolium
[HEMIM]+	1-Hydroxyethyl-3-methylimidazolium
[HMIM]+	1-Hexyl-3-methylimidazolium
[MACEMIM]+	Methylacetamido-3-methylimidazolium
[MACEMIBzM]+	Methylacetamido-3-methylbenzimidazolium
[MBMIM]+	Isopentylmethylimidazolium
[MIM]+	Methylimidazolium
[SPMIM]+	Triethoxy-[3-(3-methylimidazolium)propyl]silane
[VMOEIM]+	1-Vinyl-3-methoxyethylimidazolium
P[VEIM]+	Poly(1-vinyl-3-ethylimidazolium)
[CbzMIM]+	4-Carboxybenzyl)methylimidazolium
[N(n-Bu)$_3$]+	Trybutylammonium
[P(n-Bu)$_3$]+	Trybutylphosphonium

Anions

[BF$_4$]−	Tetrafluoroborate
Br−	Bromide
Cl−	Chloride
[EtSO$_4$]−	Ethyl sulphate
[Gly]−	Glycinate
I−	Iodide
[MSO$_3$]−	Methanesulfonate
[NTf$_2$]−	Bis(trifluoromethylsulfonyl)imide
[OAc]−	Acetate
[Sal]−	Salicylate
[SO$_3$CF$_3$]−	Trifluoromethanesulfonate

General Abbreviation

AE	Anion exchange
BET	Brunauer–Emmett–Teller
Bmz	Benzimidazole
BuBr	1-Bromobutane
BuCl	1-Chlorobutane
BuI	1-Iodobutane
CHT	Chitosan
COFs	Covalent organic frameworks
CTAB	Hexadecyltrimethylammonium bromide
CUS	Coordinatively unsaturated metal sites
DB	Dimidium bromide
DBX	α,α'-Dibromo-p-xylene
DCX	α,α'-Dichloro-p-xylene
DFT	Density-functional theory
DS	Direct synthesis
DVB	Divinylbenzene
EtBr	1-Bromoethane
FRP	Free-radical polymerization
HCPs	Hyper-cross-linked polymers
HEBr	2-Bromoethanol
HexBr	1-Bromohexane
HPILs	Hyper-cross-linked PILs
HT	Hard templating
ILs	Ionic liquids
Imi	Imidazole
IPOP	Ionic porous organic polymers
IxHCP	Imidazolium-functionalized HCPs
MIP	Molecularly imprinted polymer
mlc-SILP	Multi-layered covalently supported IL phases
MOFs	Metal-organic frameworks
NH_2-Py	Aminopyridine
NIP	Non-imprinted polymer
OctBr	1-Bromooctane
OPICs	Ordered porous PILs crystallines
Pa	P-Phenylenediamine
PCPs	Porous coordination polymers
PeC	Polyelectrolyte complexation
PIL	Poly(ionic liquid)
PM	Post-modification
PMq	Post-modification with quaternization reactions
POPs	Porous organic polymers
PQA	Polymerized quaternary ammonium salt

PS	Polystyrene
PSIL	Polymer-supported imidazole-based ILs
Py	Pyridine
RAFT	Reversible addition–fragmentation chain transfer
S_{BET}	Specific surface area
SCD	Supercritical CO_2 drying
SEM	Scanning electron microscopy
SILP	Supported IL phase
ST	Soft templating
SX	Silica xerogel
TBAB	Tetrabutylammonium bromide
TBPB	Tetrabutylphosphonium bromide
TEA	Triethylamine
TEM	Transmission electron microscopy
THAB	Tetrahexylammonium bromide
TMA	Trimethylamine
TOA	Triethanolamine
TOF	CO_2 turnover frequency
TON	Turnover number
Tp	1,3,5-Triformylphloroglucinol
TSIL	Task-specific IL
VIM	1-Vinylimidazole
ZIF	Zeolitic imidazolate framework

1   Introduction

The greenhouse effect all over the world is regarded as one of the main challenges for humans in this century. CO_2 is considered one of the most common greenhouse gases, consequently, to reduce the emissions, capture and reuse of this gas are an urgent need. Conventional CO_2 capture is based on chemical absorption with aqueous amine solvents. Despite the high absorption capacity, these methodologies have shortcomings such as solvent loss through evaporation, formation of corrosive by-products and high energy consumption during regeneration, which reduce the energy efficiency and increase the process cost (Azapagic and Cue 2015; Singh et al. 2020; Spigarelli and Kawatra 2013; Zhou et al. 2019).

Solid porous materials offer a solution for CO_2 capture with high energy-efficiency, fast adsorption/desorption rate and low cost. Porous materials are mainly empty space framed by a structure, which gives them a high surface area, ideal for interacting with atoms, ions, or molecules. To develop advanced functional materials, it is imperative to create more specific and highly effective solutions for industrial and technological applications—gas sorption, treatment of water, separation, electrochemical, energy storage, sensors, catalysis, proton conduction, biomedicine and

optoelectronics (Peh et al. 2019; Wu et al. 2019). Despite the increasing interest in this area, to achieve control over porous architectures and their functionalization is still a challenge.

The combination of porous materials with ionic liquids (ILs) has been studied to create tailored materials for gas storage and separation, catalysis (Ding et al. 2019), water purification (Cunha et al. 2019), energy conversion and storage (Azcune et al. 2014; Xu et al. 2018) and sensors (Yin et al. 2018). ILs are organic salts generally constituted of organic cations and organic or inorganic anions that have melting points below 100 °C. The prospect of the multitude of cation/anion IL combinations generates unique properties that can be tailored according to the application (Bui et al. 2018; Filippov et al. 2019). The choice of the anion in ILs is of the utmost importance, especially regarding basicity, for the establishment of intermolecular interactions (Lopes et al. 2019). Meanwhile, cation's structure in ILs is responsible for the presence of certain functional groups that can also favour intermolecular interactions, such as hydrogen bonds, π–π stacking and C–H–π interaction. The cation structure can also influence porosity depending on the length of the side chain, or on the presence of benzyl groups since they can bend towards imidazolium ring forming clusters (Barrulas et al. 2019; Shimomura et al. 2011).

Several methods to immobilize ILs non-covalently and covalently have been demonstrated since the first report of IL–polymer gel preparation (Carlin and Fuller 1997). The advantages of heterogeneous catalytic systems based on a supported IL phase (SILP), when compared to the homogeneous analogous, include easier separation from the reaction media, recyclability and the possibility of using them in fixed bed reactors. The non-covalent methodology is mainly based on intermolecular forces between the ILs and the supports, including van der Waals forces, π-stacking interactions, hydrogen bonding and Coulomb forces. The preparation of this type of material is relatively simple, although it presents inherent drawbacks, such as IL leaching and poor recyclability. To overcome this, the IL phase can be grafted onto the surface of porous solid supports, to form novel hybrid sorbents for CO_2 separation. Moreover, the covalent linkage of ILs on the support helps to avoid leaching, minimizing the IL amount and improving stability (Xin and Hao 2014). A complete review regarding the use of IL heterogeneous catalysis for CO_2 cycloaddition has recently been published (Wang et al. 2019a).

In the case of grafting of ILs, different linkers must be specifically designed and used according to different support materials or surface modification. Consequently, many different heterogeneous IL-modified solid materials have been obtained by introducing imidazolium-based IL moieties onto (Fig. 1): (i)*inorganic supports* as: silica, metal oxides, zeolites and carbon materials; (ii)*organic supports:* chitosan, cellulose, polyhedral oligomeric silsesquioxanes, porous coordination polymers (PCPs), poly(ionic liquid)s (PILs), porous organic polymers (POPs); and (iii)*hybrid or crystalline framework materials:* as zeolitic imidazolate frameworks (ZIFs), metal–organic frameworks (MOFs) and covalent organic frameworks (COFs) (Ramos et al. 2020). This chapter presents a short review on ILs covalently bonded onto porous materials, organized by these three main classes, mainly applied to CO_2 emission mitigation.
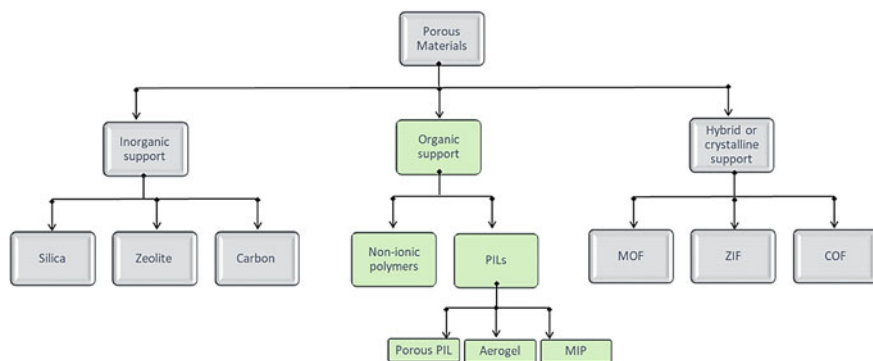
Fig. 1 Classification of porous support materials focused on this chapter

To obtain ILs supported on traditional inorganic porous materials, the support must have surface-functionalized groups (hydroxyl, carboxyl, amino). This type of material can be efficient in carbon capture and utilization processes, despite the limited tailoring, since they are generally obtained from commercial supports (Olajire 2017; Ramos et al. 2020; Xie et al. 2020).

The development of inorganic–organic hybrid materials with crystalline structure including ZIFs, MOFs and more recently COFs provides the possibility of promoting CO_2 adsorption and successive catalytic conversion (Pal et al. 2020).

The emergence of organic functional materials reflects a significant development of covalent chemistry, offering the possibility to synthesize materials with the required functional groups. In principle, any desired functionality can be introduced into the porous materials through atomic-level control over the structures and compositions. In this context, PILs represent a class of organic polymer with easily modulated properties (Barrulas et al. 2021; Luo et al. 2020; Xu et al. 2018).

2 Organic Porous Materials

It is well known that there are two main catalysis methodologies to reuse the CO_2, by using homogeneous or heterogeneous catalysts. The homogeneous (metal complexes, quaternary ammonium or phosphine salts, organic bases, ILs, among others) have the problem of catalyst-product separation. The heterogeneous (metal oxides, porous inorganic materials, MOFs, COFs, POPs, among others) are advantageous in product separation and catalyst recycling. Additionally, IL-based heterogeneous catalysts lead to a decrease in the amount of ILs used, together with the efficient recovery of the catalyst. As a strategy for the fabrication of stable and reusable heterogeneous catalysts, the use of polymer materials as support for ILs has been demonstrated by chemical grafting (Luo et al. 2020; Watile et al. 2012). The organic features of the support enable material synthesis with the required functional groups

for grafting the IL and for activating the CO_2. An even more advanced strategy to tailor the material properties is the preparation of polymeric ILs. The great challenge in this topic is to create controlled and adequate porosity into the support. Recently, two promising methodologies have been reported, the preparation of aerogels and the use of molecular imprinting techniques for the synthesis of molecularly imprinted polymers (MIPs) (Barrulas et al. 2021). This section presents the two possibilities of organic supports: (i) non-ionic polymer with grafted ILs; and (ii) ionic polymeric supports (PILs) (Fig. 2). In addition, promising strategies to improve the support porosity are demonstrated (MIP and aerogel).
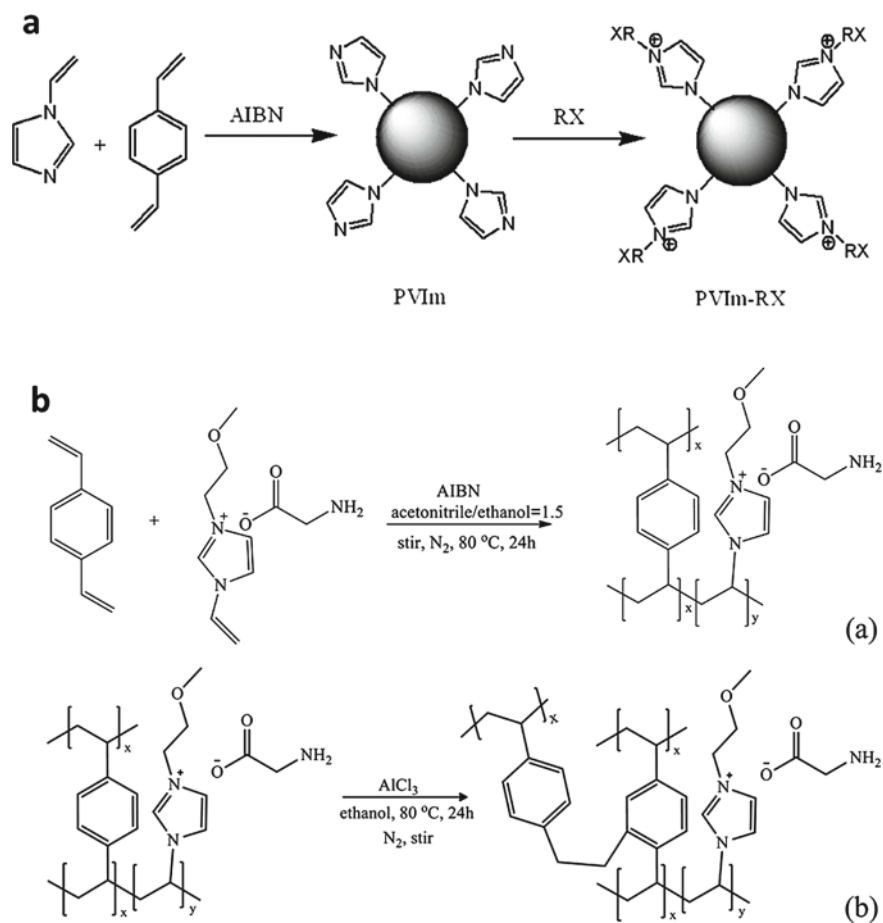
Fig. 2 Examples of organic supports applied to CO_2 emission mitigation: **a** IL grafted on polymeric support, reproduced from reference (Han et al. 2011) with permission. **b** PIL, reproduced from reference (Sun et al. 2020) with permission

2.1   IL Grafted in Polymeric Supports

The combination of CO_2-philic moieties, as the ones presented in ILs, with tailored porous structures is of paramount importance for carbon capture and utilization. This design provides the incorporation of ionic moieties into the polymer backbone, and also the interaction controls through the functional groups in the materials (Luo et al. 2020).

In 2009, Sun et al. reported a polymer-supported IL catalyst for cycloaddition of epoxide with CO_2. [HEIM]-based ILs ([HEIM]X, X = Cl, Br, I) were covalently linked into a highly cross-linked polystyrene (PS) resin with divinylbenzene (DVB). This cross-linking, besides enhancing the activity, prevented the catalyst dissolution. Through SEM images it was seen that the supported-IL catalyst had a rough surface, however, no structural parameters were presented. The catalytic activity is dependent both on the anion nucleophilicity (PS-[HEIM]I ~ PS-[HEIM]Br > PS-[HEIM]Cl), and the presence of the hydroxyl group in IL cation that accelerates the reactions, besides having a synergetic effect with the anions. In the end, 98% propylene oxide conversion and > 99% selectivity were obtained using PS-[HEIM]Br as catalyst (25 bar, 393 K, 4 h). The catalyst was also recycled for six runs without loss of catalytic activity (Sun et al. 2009).

In 2012, Zhang et al. described a similar approach, in which [CEIM]Br was grafted onto a cross-linked DVB polymer (PDVB-[CEIM]Br). Through SEM images it was seen that the surface of PDVB-IM is smooth and with the IL grafting becomes rough, however, no structural parameters were presented. Under optimal conditions (20 bar, 413 K, 4 h), propylene carbonate was obtained with > 99% selectivity and 96% yield. Additionally, the catalyst is stable and can be reused for five runs without activity loss. The authors suggested that there was a synergetic effect among the -COOH, the Br^- and the support that promotes the coupling reaction (Zhang et al. 2012).

Also in 2012, Watile et al. reported polymer-supported diol functionalized ILs. Imidazolium-based ILs with diol functionality and different anions (Br^-, Cl^-) were used, being covalently linked to PS (PS-[DFIL]X, X = Br, Cl). Polymer-supported [DHPIM]Br (PS-[DHPIM]Br) exhibited the best catalytic activity, under solvent-free conditions, towards propylene carbonate synthesis with 99% selectivity (20 bar, 403 K, 3 h). In addition, it was possible to reuse the catalyst for five recycles without any significant loss in its activity. No SEM images or structural parameters were presented. The authors explained that the vicinal hydroxyl group in the structure and the nucleophilicity of the anions led to the highest catalytic activity (Watile et al. 2012).

Sun et al., in 2012, also reported an IL-supported catalyst, but instead of PS resin the authors used chitosan (CHT), a biopolymer support. CHT was functionalized with [EMIM] halides (CHT-[EMIM]X, X = Cl, Br). Once again, no SEM images or structural parameters were presented. The catalytic activity was evaluated through the synthesis of propylene carbonate (20 bar, 393 K, 4 h), and CHT-[EMIM]Br had a high yield of 96% in opposition with CHT-[EMIM]Cl (74%). Moreover, the catalyst was reused for five times without any significant loss in its activity

. The authors explained that this higher activity is related to the leaving ability and nucleophilicity of the anion, as well as, the hydroxyl groups of CHT provided efficient synergetic sites, accelerating the ring-opening of epoxide (Sun et al. 2012).

In 2011, Han et al. reported porous polymer bead-supported ILs to be applied in CO_2 catalysis. Cross-linked porous poly(N-vinylimidazole-co-DVB) beads (P[VIM]) were synthesized by suspension polymerization, and then the surface of the beads was modified with alkyl halides (1-bromoethane—EtBr, 1-bromohexane—HexBr, 1-bromooctane—OctBr, 1-bromobutane—BuBr, 1-chlorobutane—BuCl, 1-iodobutane—BuI, 2-bromoethanol—HEBr) in toluene, that were covalently linked, to obtain IL-grafted porous polymer beads (P[VIM]-RX). SEM images revealed that the cross section of the beads is rough with several permanent pores, persistent after the grafting. The structural parameters of the polymer matrix are presented in Table 1, entries 1–4. As it is possible to see, they all have high surface areas and large pore sizes with some variations. This combination makes them promising for CO_2 conversion since the diffusion through the material is easier. The authors verified that grafted ILs with more nucleophilic anions, bulkier alkyl chains, or hydroxyl groups have improved reactivity. Also, the presence of small amounts of water or ethanol contributes to higher reactivity. Better catalytic activity for the conversion of allyl glycidyl ether was obtained with P[VIM]-2-BuBr (18.2 bar, 383 K, 6 h), with 98% conversion and > 99% selectivity. Furthermore, five recycles were performed for the catalyst, and no significant loss in its catalytic activity was observed (Han et al. 2011).

More recently, in 2017, Wang et al. reported polymer-supported imidazole-based ILs (PSIL) for CO_2 conversion. The materials were obtained from two different routes: (1) solvothermal copolymerization of [BVBzIM]Cl and DVB (PSIL-[BVBzIM]Cl-1); (2) copolymerization of 1-(chloromethyl)-4-vinylbenzene with DVB, followed by cross-linking with imidazole (PSIL-[BVBzIM]Cl-2). Trimethylamine-based (PSIL-[TMA]), triethylamine-based (PSIL-[TEA]) and triethanolamine-based (PSIL-[TOA]) PSILs were obtained through the substitution of imidazole with trimethylamine, triethylamine and triethanolamine. SEM and TEM images revealed that all PSILs have a dense structure. Additionally, aggregated particles were observed in PSIL-[TMA] probably due to the presence of water during the synthesis that changed for suspension polymerization. The structural parameters of PSILs are presented in Table 1, entries 5–9. For the PSILs catalytic activity evaluation, the reaction of cycloaddition of CO_2 with propylene oxide was carried out at 20 bar, 403 K for 5 h. PSIL-[BVBzIM]Cl-1 exhibited the highest yield of propylene carbonate of > 99%. The authors explained this regarding the high nitrogen content (3.7 wt.%). Also, PSIL-[BVBzIM]Cl-1 was stable after continuous flow reaction for 130 h (Wang et al. 2017).

As can be seen in these examples, there is only an analysis of the results with respect to the CO_2 catalysis and not from CO_2 capture data. Moreover, either there is no control over the 3D structure of the final material and the only concern is the evaluation of the application regarding the chemical functionalities in the starting materials, or, in the cases where there is a greater concern with the textural properties, the fine-tuning of porosity is still to be achieved. To accomplish a successful

Table 1 Structural parameters of polymer matrix P[VIM] and PSILs

| Entry	Samples	Molar ratio (DVB/N-vinylimidazole)	S_{BET} (m^2 g^{-1})	Pore volume (cm^3 g^{-1})	Pore size (nm)	IL amount (mmol g^{-1})	References
1	P[VIM]-1	2:3	905.0	n.d.[b]	5.41	0.90	Han et al. (2011)
2	P[VIM]-2	3:3	952.0	n.d.[b]	7.55	0.92	
3	P[VIM]-3	3:2	1009.0	n.d.[b]	7.10	0.78	
4	P[VIM]-4[a]	3:3	< 0.1	n.d.[b]	n.d.[b]	0.14	
5	PSIL-[BVBzIM]Cl-1	n.d.[b]	82.2	0.10	n.d.[b]	n.d.[b]	Wang et al. (2017)
6	PSIL-[BVBzIM]Cl-2	n.d.[b]	98.9	0.08	n.d.[b]	n.d.[b]	
7	PSIL-[TMA]	n.d.[b]	75.8	0.15	n.d.[b]	n.d.[b]	
8	PSIL-[TEA]	n.d.[b]	95.0	0.06	n.d.[b]	n.d.[b]	
9	PSIL-[TOA]	n.d.[b]	73.2	0.12	n.d.[b]	n.d.[b]	

[a] Absence of porogen. [b] n.d.: no data

CO_2 adsorption and catalysis, besides the tailoring of chemical functionalities, the optimization of the material's morphology is necessary to potentiate all the active sites (Barrulas et al. 2021).

2.2 IPOP (Ionic Porous Organic Polymers)

New strategies have been used for the development of differentiated materials such as porous ionic polymers (Lin et al. 2020; Xu et al. 2018), MIPs (Viveiros et al. 2018) and aerogels (Zhao et al. 2018). Ionic porous organic polymers (IPOPs) (also called porous ILs) are functionalized materials that result from the integration of ILs into polymers and porous materials (Dani et al. 2018; Liu and Han 2019; Zhang et al. 2015c). IPOP materials combine the spatial architecture of polymers with the chemical diversity of ILs. PILs are essentially non-porous, as such, obtaining porous PILs upgrades both their relevance and applications. The combination of PILs with porosity may result in materials with enhanced efficiency and selectivity applied in several areas (electrochemistry, analytical chemistry, biosciences, catalysis, sensors, magnetism, energy and environment) (Xu et al. 2018). In this section, recent advances and challenges regarding IPOPs for carbon capture and utilization applications are highlighted.

PILs show enhanced features, namely mechanical stability, processability, durability and control over meso- to nanostructures (Einloft et al. 2018; Qian et al. 2017; Yuan and Antonietti 2011; Zulfiqar et al. 2015). Furthermore, their physicochemical properties can be changed easily through counterion exchange (Zhang et al. 2015c). According to the location of the polymerizable units, PILs can be classified in: cationic (polymerizable unit on a cation—imidazolium, pyridinium, viologen, quaternary phosphonium); anionic (polymerizable unit on an anion—tetrakis(phenyl)borate, tris(catecholate)phosphate (V)); and zwitterionic (cations and anions in the backbone) (Kuzmina 2018; Liu and Han 2019; Zhang et al. 2018). Designing IPOP materials requires a balance of porosity and PILs functionalities.

The properties and applications of polymers, such as water purification, gas storage and separation, energy conversion and storage, catalysis (Azcune et al. 2014; Xu et al. 2018), and sensors (Yin et al. 2018), depend on their Brunauer–Emmett–Teller specific surface area (S_{BET}), the pore size distribution and the pore volume. According to the pore size, nanoporous materials can be classified as: microporous (< 2 nm), mesoporous (2–50 nm) and macroporous (> 50 nm) (Azcune et al. 2014; Dani et al. 2018; Nasrollahzadeh et al. 2019; Yang et al. 2017). The porosity can be related to polymer synthesis methodology that can be divided into two main approaches: (a) template-free and (b) templating, as previously reviewed by us (Barrulas et al. 2021). In turn, these methodologies are subdivided into several strategies (Fig. 3) (Dani et al. 2018; Zhang et al. 2015c):
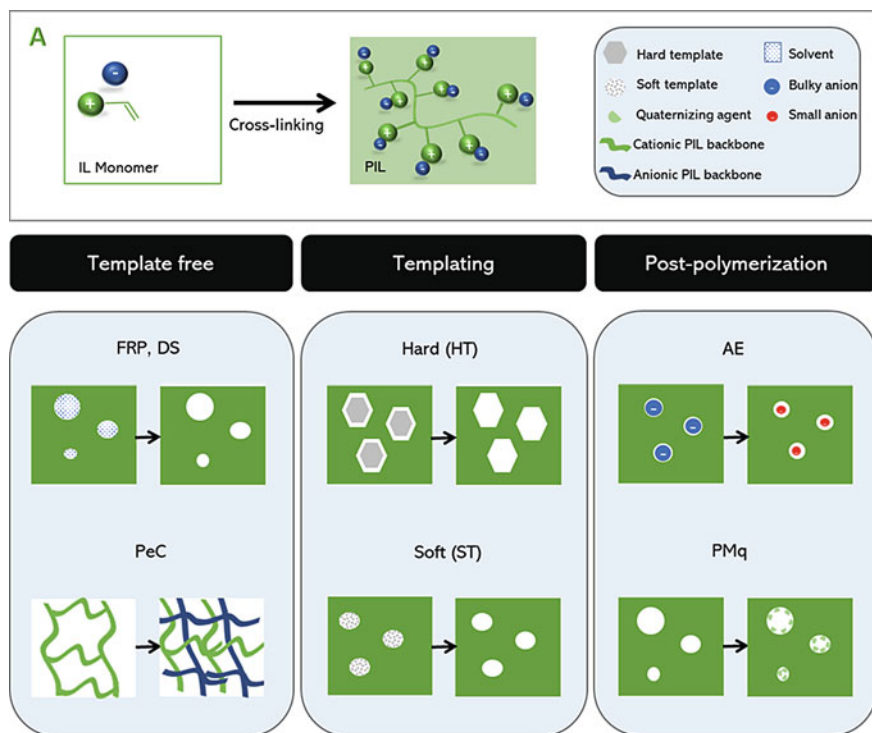
Fig. 3 Representation of common synthetic methodologies to prepare IPOPs (A). Reproduced from reference (Barrulas et al. 2021) with permission

(a) ***Template-Free Synthesis***

(I) *Free-radical polymerization (FRP):* in this method, polymers are obtained from consecutive additions of free-radical building blocks, commonly using vinyl-based IL monomers. The solvent used for the reaction can also function as a porogenic agent (which can also be classified as a type of templating, but without a definite form associated). Polymers with different pore sizes are formed (Dani et al. 2018).

(II) *Direct synthesis (DS)*: this strategy leads to a porous network through C–C coupling methods, for example, condensation polymerization. The polymer network can be formed through Yamamoto-type Ullman cross-coupling, Sonogashira–Hagihara cross-coupling, Schiff base reaction, Friedel–Crafts reaction, Debus–Radziszewski imidazolium synthesis or click-based Debus–Radziszewski imidazolium synthesis. This method leads to microporous structures with high S_{BET} as well as ordered crystalline networks (Dani et al. 2018).

(III) *Polyelectrolyte complexation (PeC)*: this method consists in an electrostatic cross-link between PILs and oppositely charged polyelectrolytes, which

control pore size tuning. This strategy results on macroporous and mesoporous materials (Dani et al. 2018).

(b) **Templating Synthesis**

(I) *Hard templating (HT)*: Is a direct method where porosity is obtained using a pre-existing template structure during polymerization, normally, a solid-state material with a particular structure and morphology, such as silica, for example. This methodology produces meso- or macroporous materials with well-defined pore size (Dani et al. 2018; Zhang et al. 2015c).

(II) *Soft templating (ST)*: Is an indirect methodology where porous ILs are produced by in-situ IL monomers polymerization, resulting in mesoporous structures with defined architecture (Dani et al. 2018). The soft template is in a fluid-like state, such as a supramolecular self-assembly. Inside of these categories, there is another technique called solvothermal/ionothermal that uses, respectively, non-aqueous organic solvents or ILs as templates (Qin et al. 2017).

Despite the efficiency in generating porosity, some drawbacks are associated with this methodology due to the requirement of sacrificial compounds, namely: being energy and time-consuming, producing small surface areas and the need for an additional step for template removal through solvent extraction or etching (Zhang et al. 2015c). In consequence, other strategies appeared that do not involve the use of templates, with the advantage of reducing costs and make the all process simpler (Zhang et al. 2015c). Some examples are the so-called *post-polymerization strategies* that can be divided into:

- *Anion exchange (AE)*—The exchange of bulky anions for smaller ones generates space, creating pores (Qin et al. 2017).
- *Post-modification (PM)*—Is a methodology of changing the polymer structure, commonly with quaternization reactions (PMq) (Qin et al. 2017) or carbonization processes. In these last process, PILs enable the preservation of pore, the impregnation of inorganic nanoparticles and heteroatom doping (Balach et al. 2013; Lin et al. 2020).

Understanding the influence of porosity on the selectivity of guest molecules is imperative to create and optimize adequate porosity. The chemical composition has to be wisely thought out, particularly, in respect to the monomer/template control, besides several synthetic parameters (Liu and Han 2019; Yang et al. 2017). Some examples of porous ILs are discussed below.

In 2014, Azcune et al. described a new synthesis of a nanoporous PIL-based material through radical polymerization of bis-vinyl-ended IL ([DVIM][NTf$_2$]$_2$), in the presence of porogenic solvent, in this case, a non-polymerizable IL ([BMIM][NTf$_2$]). This strategy is template-free, so the authors needed to understand the effect of the weight ratio of monomer/porogen (M:P) on S$_{BET}$, pore size and total porosity (Azcune et al. 2014). With this objective, several ratios were studied in order to access the effect of concentration on porous PIL synthesis, as specified in Table 2.

**Table 2** List of PILs with the M:P weight ratio, surface area and pore diameter (Azcune et al. 2014)

Entry	PIL$_{M:P\ ratio}$	S_{BET} (m^2 g^{-1})	Pore diameter (nm)
1	P([DVIM][NTf$_2$]$_2$)$_{1:0}$	0.00	n.d.[a]
2	P([DVIM][NTf$_2$]$_2$)$_{1:0.5}$	0.08	n.d.[a]
3	P([DVIM][NTf$_2$]$_2$)$_{1:1}$	86.20	8.50–6.80
4	P([DVIM][NTf$_2$]$_2$)$_{1:2}$	20.10	7.30–4.00
5	P([DVIM][NTf$_2$]$_2$)$_{1:3}$	0.00	n.d.[a]
6	P([DVIM][NTf$_2$]$_2$)$_{1:5}$	0.06	n.d.[a]
7	P([DVIM][NTf$_2$]$_2$)$_{1:10}$	0.11	n.d.[a]

[a]n.d.: no data

As it is possible to observe, only M:P ratios of 1:1 and 1:2 allowed the synthesis of PILs (Table 2, entries 3–4). The unsuccessful attempts were attributed to a higher porogen mass fraction. The obtained mesoporous PILs were tested for CO_2 sorption (Table 7, entries 1–2). It was concluded that CO_2 sorption was not only associated with S_{BET}, but also to the absorption in the polymer matrix. So, by modifying the IL monomer's chemical structure it is possible to tune the affinity towards CO_2. Although this method is simple, scalable and atom-efficient, fine-tuning the porous properties and reproducibility remained drawbacks (Azcune et al. 2014; Dani et al. 2018).

Qin et al. reported in 2017, a new methodology for synthesizing porous PILs via AE (Fig. 4a). The anion salicylate was exchanged from poly(bisvinylimidazolium-base disalicylate) (P[DVIM][Sal]$_2$) and its dimers or clusters by smaller anions like chloride or bromide. Theoretically, the exchange of bulky anions of PILs with smaller ones can release space and produce porous structures. The influence of AE on the final porosity was accessed through the S_{BET} and pore. In Table 3, the synthesized porous PILs are described with the values of S_{BET}, and the pore size distribution intervals. Analysing the data in Table 3, entries 1–7, it is possible to conclude that the synthesis via AE increases S_{BET}, creating a hierarchical porous structure. Despite this, some problems may appear derived from the fact that the polymeric network needs to have strict requirements and reaction control in order to assure reproducibility of results (Dani et al. 2018). In the end, structurally stable hierarchical porous PILs with high S_{BET} were obtained to be applied in catalysis—in N-heterocyclic carbomethoxy-lation reaction and cycloaddition of CO_2 with epoxides. For CO_2 reuse reaction, higher S_{BET} of the polymers promoted an effective contact with substrates due to increased accessibility of active sites. For the N-heterocyclic carbomethoxylation, porous and non-porous PILs exhibited different behaviours, with higher catalytic activities obtained for porous materials (89% against than 68%). No CO_2 absorption values were reported (Qin et al. 2017).

Following an earlier work by Sun et al., Song et al. reported, in 2020, the synthesis of porous frameworks with pyridine moieties with and without amine substitution. The authors used a FRP of vinyl functionalized monomers, inducing hierarchical
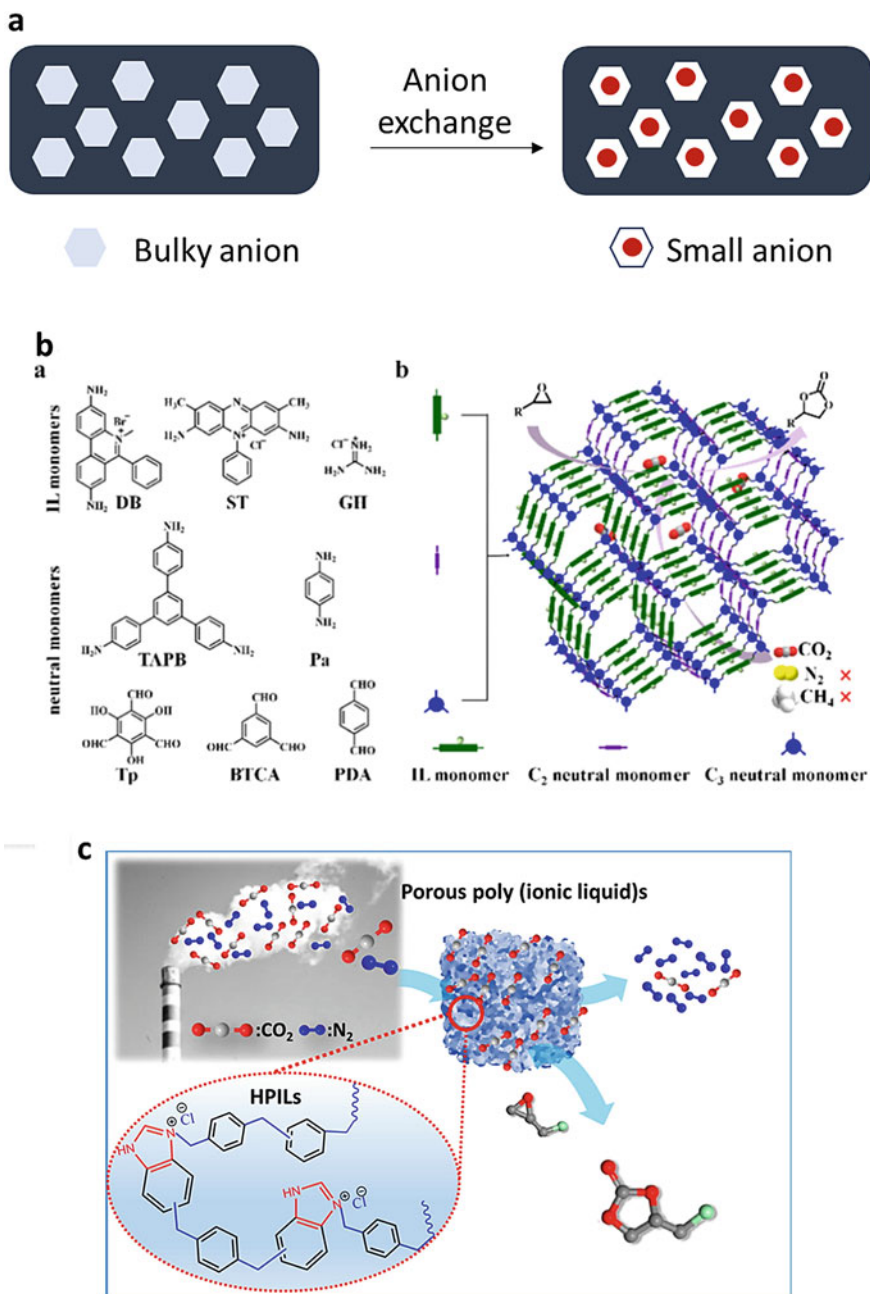
Fig. 4 **a** Synthesis of porous PILs by anion exchange (Qin et al. 2017). **b** Synthesis of OPICs. Reproduced from reference (Cao et al. 2019a) with permission. **c** Benzimidazolium-based HPILs. Reproduced from reference (Sang and Huang 2020) with permission

Table 3 List of the obtained PILs and their structural parameters (Qin et al. 2017)

Entry	PILs	S_{BET} (m^2 g^{-1})	Pore volume (cm^3 g^{-1})	Pore size (nm) and pore type	Polymerization type
1	P[DVIM][Sal]$_2$	15.10	0.03	No micropores some 10–20 nm mesopores	FRP
2	AE-P[DVIM]Cl$_2$	227.50	0.20	0.6–1.0 nm micropores; 2–10 nm mesopores	AE
3	AE-P[DVIM]Br$_2$	180.60	0.20		
4	AE-P[DVIM][OAc]$_2$	129.20	0.14		
5	DS-P[DVIM]Cl$_2$	25.60	0.03	No micropores; few 10–20 nm mesopores	Direct Polymerization
6	DS-P[DVIM]Br$_2$	18.20	0.03		
7	DS-P[DVIM][OAc]$_2$	17.90	0.02		

porosity in the resulting polymers—micro- and mesopores. Then, a quaternization reaction with methyl iodide introduced ion-exchange sites on the pyridine groups, generating the IPOP of polymerized quaternary ammonium (PQA) salt. In Table 4, a summary of the POPs synthesized and their corresponding PQA salts with their values of S_{BET}, as well as total pore volume, when data is provided, are presented. The authors explained that PQA salt formation decreases S_{BET} after the functionality addition because of the increased mass resulting from the process. Hence, it can be concluded that fine-tuning the porosity is harder with this multiple-step methodology (Dani et al. 2018). Usually, amine groups in a material favour CO$_2$ activation (Table 7, entry 5). In this work, the catalytic activity increased significantly after the introduction of the amine group on the *ortho* position of the pyridinium moiety. This modification increased the selectivity on the cycloaddition of aziridines to CO$_2$, yielding 5-substituted-2-oxazolidinone under mild conditions (1 bar, 295 K), with very high selectivity (> 99%) and conversion rate. This product can be used as chiral auxiliary and biological active pharmaceutical agent (Song et al. 2020; Sun et al. 2019a).

Table 4 List of POPs and IPOP with surface area and total pore volume

Entry	Porous organic polymers	S_{BET} (m^2 g^{-1})	Pore volume (cm^3 g^{-1})	References
1	POP-Py	979	n.d.[a]	Song et al. (2020)
2	POP-NH$_2$Py	555	n.d.[a]	
3	PQA-POP-Py-I	465	0.645	Sun et al. (2019a)
4	PQA-POP-NH$_2$Py-I	310	n.d.[a]	Song et al. (2020)

[a]n.d.: no data

Porous PILs are characteristically amorphous structures with disordered pores (Cao et al. 2019a). In 2019, Cao et al. obtained ordered porous PILs crystallines (OPICs) with adjustable IL frameworks. The authors used a solvothermally controlled Schiff base condensation of ILs and neutral monomers (Fig. 4b). The following neutral monomers and IL-based salts were used in material preparation: 1,3,5-tris(4-aminophenyl)benzene, terephthalaldehyde, *p*-phenylenediamine (Pa), 1,3,5-benzenetricarboxaldehyde and 1,3,5-triformylphloroglucinol (Tp), guanidine hydrochloride safraninet and dimidium bromide (DB). Ternary monomer mixtures were prepared to evaluate chemical composition *versus* pore configuration. The solvent mixtures used strongly affected the outcome of the reaction. A selection of the obtained OPICs with their values of S_{BET}, pore size distribution as well as total pore volume, and the interlayer distance is listed in Table 5. As it is possible to observe, all OPICs exhibited high S_{BET} and large pore volume. The ionic content could be changed with no effect on porosity. The preparation of a completely ionic material using just DB-Tp (Table 5, entry 5) increased the Coulomb repulsion, due to the concentration of ionic moieties, leading to an enlarged interlayer distance when compared to $DB_{10\%}$-Pa-Tp (Table 5, entry 2), which is a strongly stacked polymer. The authors have proven the possibility to control the atomic stacking, producing a crystalline structure with ordered porosity. Although the procedure is simple, the synthesis is quite long and challenging because of the rigorous conditions of monomers and solvents mixtures (Cao et al. 2019a; Dani et al. 2018). Due to the catalytic function of the ionic moieties, these materials were employed as recyclable heterogeneous organocatalysts for CO_2 fixation. Despite the high CO_2 uptake (Table 7, entry 4), the yield was only 36% in the CO_2 cycloaddition to styrene oxide (Cao et al. 2019a).

Table 5 Selection of OPICs and their surface area, total pore volume, pore size distribution and interlayer distance (Cao et al. 2019a)

Entry	OPICs[a]	S_{BET} ($m^2\ g^{-1}$)	Pore volume ($cm^3\ g^{-1}$)	Pore size (nm)	c (Å)[b]
1	Pa-Tp	781.00	0.59	3.00	3.34
2	$DB_{10\%}$-Pa-Tp	877.00	0.97	4.40	3.05
3	$DB_{25\%}$-Pa-Tp	602.00	0.55	3.60	n.d.[c]
4	$DB_{50\%}$-Pa-Tp	581.00	0.61	4.20	n.d.[c]
5	DB-Tp	916.00	0.99	4.30	3.32

[a]Condensation of ternary monomer mixtures resulting in $X_{x\%} - Y - Z$, where X = ionic monomer, Y = amino neutral monomer, Z = aldehyde neutral monomer, x% is the initial $X/(X + Y)$ molar ratio. [b]Interlayer distance. [c]n.d.: no data

2.2.1 Hyper-Cross-Linked PILs

Generally, hyper-cross-linked polymers (HCPs) have high S_{BET}, stable physico-chemical properties and efficient active sites (Sang and Huang 2020; Xie et al. 2018). Xie et al. (2018) described HCPs with imidazolium moieties synthesized via FRP of monomers with different ionic densities, and dried through super-critical CO_2 drying (SCD). 1,2,3,4,5,6-Hexakis(bromomethyl)benzene, 1,2,4,5-tetrakis(bromomethyl)benzene or 1,3,5-tris(bromomethyl)benzene were used to synthetize the monomers with VIM. For comparison, other drying methods besides SCD were used, vacuum drying and ambient drying. The authors studied S_{BET}, pore size distribution and total pore volume to understand the effect of PILs cross-linking level and how the drying methodology affected the porosity of the final material. In Table 6, entries 1–5, the porous PILs synthesized and their values of S_{BET}, total pore volume as well as pore size distribution are summarized. The ionic density, S_{BET} and pore volume increased with the cross-linking level as the pore size reduced. HCPs with imidazolium moieties presented numerous mesopores, high S_{BET}, CO_2 adsorption and ionic density, as well as catalytic activity through CO_2 cycloaddition with epoxides (Table 7, entry 3), conversion rates between 97 and 100% and selectivity above 99%. The presence of mesopores was an advantage, helping mass and energy transport (Xie et al. 2018).

Sang et al. (2020) presented hyper-cross-linked PILs (HPILs) with benzimi-dazolium (Bmz) moieties synthesized via one-pot $FeCl_3$-catalyzed Friedel–Crafts reaction (Fig. 4c). In Table 6, entries 6–11, the HPILs obtained and their values of S_{BET}, total pore volume as well as their N content, related to the presence of imidazolium cations are summarized. Most of the polymers exhibited a hierarchical meso/macroporous structure, with pore sizes between 0.5 and 1.5 nm,, except for HPILs-Cl-2 (Table 6, entry 8), which had mostly microporosity. The characteristics of these materials, namely the high N content, high S_{BET}, micro/mesoporosity, as well as abundant ionic active sites, make them attractive for CO_2 capture and reuse, being these applications tested by the authors. The porosity of these polymers can be tuned through Bmz proportion. The HPILs (Table 7, entries 6–9) presented good CO_2 uptake and CO_2/N_2 selectivity. HPILs-Cl-2 (Table 7, entry 7), rich in micropores, displayed good catalytic activity for CO_2 cycloaddition, being 99% of propylene oxide effectively converted to cyclic carbonate under mild conditions (Sang and Huang 2020).

Zhang et al. (2020) also reported imidazolium-functionalized HCPs directly synthesized in a $FeCl_3$-catalyzed Friedel–Crafts alkylation process via the copoly-merization of Bmz salts as IL monomers and cross-linkers [α,α′-dichloro-p-xylene (DCX) and α,α′-dibromo-p-xylene (DBX)]. Several imidazolium salts were used, including [BzEIM]Br, [BzBIM]Br, [BzHexadecIM]Br, [BzHOEIM]Br, [BzCOOHPIM]Br, [BzIMBz]Br. Nonetheless, the influence of initial monomer composition, cross-linker and catalyst amount was evaluated on the hyper-cross-linkage with [BzEIM]Br. The results for the HCPs obtained with the best cross-linker, DCX, are presented in Table 6, entries 12–17, since the results with this were better than with DBX. All these polymers presented abundant micro/mesoporosity.

Table 6 Compilation of porous PILs obtained from literature and their surface area, total pore volume, pore size distribution and N content

Entry	HPILs (composition)	S_{BET} (m^2 g^{-1})	Pore volume (cm^3 g^{-1})	Pore size (nm)	N content (%)	References
1	P[VIM-6-SCD][b]	797.70	2.05	9.64	n.d.[a]	Xie et al. (2018)
2	P[VIM-4-SCD][b]	484.50	1.75	13.93	n.d.[a]	
3	P[VIM-3-SCD][b]	270.20	1.05	16.80	n.d.[a]	
4	P[VIM-6-VD][b]	191.50	0.57	8.40	n.d.[a]	
5	P[VIM-6-AD][b]	n.d.[a]	n.d.[a]	n.d.[a]	n.d.[a]	
6	HCP-Cl[c] (DCX/FeCl$_3$—10/20)	1063.00	1.03	n.d.[a]	0.00	Sang and Huang (2020)
7	HPILs-Cl-1[c] (Bmz/DCX/FeCl$_3$—5/5/20)	780.00	0.77	n.d.[a]	1.61	
8	HPILs-Cl-2[c] (Bmz/DCX/FeCl$_3$—5/3/20)	500.00	0.40	n.d.[a]	2.47	
9	HCP-Br[d] (DBX/FeCl$_3$—10/20)	672.00	0.90	n.d.[a]	0.00	
10	HPILs-Br-1[d] (Bmz/DBX/FeCl$_3$—5/5/20)	570.00	0.40	n.d.[a]	1.29	
11	HPILs-Br-2[d] (Bmz/DBX/FeCl$_3$—5/3/20)	485.00	0.40	n.d.[a]	2.01	
12	Ic$_2$HCP-1[e] (IL/DCX/FeCl$_3$—1/1/2)	518.00	0.34	n.d.[a]	2.72	Zhang et al. (2020)
13	Ic$_2$HCP-5[e] (IL/DCX/FeCl$_3$—1/5/10)	712.00	0.69	n.d.[a]	2.42	
14	Ic$_2$HCP-10[e] (IL/DCX/FeCl$_3$—1/10/20)	877.00	0.94	n.d.[a]	1.70	
15	Ic$_2$HCP-5a[e] (IL/DCX/FeCl$_3$—1/5/5)	963.00	1.02	n.d.[a]	2.04	
16	Ic$_2$HCP-5b[e] (IL/DCX/FeCl$_3$—1/5/6)	1017.00	1.63	n.d.[a]	2.25	
17	Ic$_2$HCP-5c[e] (IL/DCX/FeCl$_3$—1/5/15)	615.00	0.61	n.d.[a]	2.55	
18	HP(0.6DVB-[VMOEIM][Gly])	508.00	0.90	8.60	n.d.[a]	Sun et al. (2020)
19	HP-[BPhIM]Br-Co-Tol-1	604.00	0.44	2.91	0.34	Song et al. (2021)
20	HP-[BPhIM]Br-Co-Tol-2	512.00	0.29	2.97	0.42	
21	HP-[BPhIM]Br-DCX-1	1264.00	1.98	6.27	1.20	

(continued)

Table 6 (continued)

Entry	HPILs (composition)	S_{BET} ($m^2\ g^{-1}$)	Pore volume ($cm^3\ g^{-1}$)	Pore size (nm)	N content (%)	References
22	HP-[BPhIM]Br-DCX-2	1285.00	1.92	5.97	1.18	
23	HP-[BzPhIM]Cl-Co-Tol-1	405.00	0.29	2.83	0.96	
24	HP-[BzPhIM]Cl-Co-Tol-2	366.00	0.27	2.91	1.24	
25	HP-[BzPhIM]Cl-DCX-1	763.00	1.08	5.64	2.05	
26	HP-[BzPhIM]Cl-DCX-2	263.00	0.27	4.17	2.53	
27	HP-DCX	1282.00	1.66	5.18	n.d.[a]	
28	HP-Co-Tol	736.00	0.68	3.67	n.d.[a]	

Tol Toluene. [a]n.d.: no data. [b]VIM-η: η = cross-linking degree (η = 6, 4, 3). *AD* ambient drying. *VD* vacuum drying. [c]Synthesized with DCX as cross-linker. [d]Synthesized with DBX as cross-linker. [e]I$_x$HCP: x = imidazolium cation functional group

Table 7 Comparison of CO_2 sorption capacity and S_{BET} of PIL sorbents at low pressure

Entry	Sorbent	Synthetic Method	$S_{BET}(m^2 \, g^{-1})$	CO_2 uptake (original values)	CO_2 uptake $(mg \, g^{-1})$	$T(K)^a$	References
1	P([DVIM][NTf$_2$]$_2$)$_{1:1}$	FRP	86.2	0.098 mol Kg^{-1}	4.3	293	Azcune et al. (2014)
2	P([DVIM][NTf$_2$]$_2$)$_{1:2}$		20.1	0.100 mol Kg^{-1}	4.4	293	
3	P[VIM-6-SCD]		797.7	3.600 mmol g^{-1}	158.4	273	Xie et al. (2018)
4	DB$_{10\%}$-Pa-Tp	Schiff base reaction	877.0	4.830 mmol g^{-1}	212.6	273	Cao et al. (2019a)
5	PQA-POP-NH$_2$Py-Br	FRP	310.0	36.500 cm^3 g^{-1}	71.3	273	Song et al. (2020)
6	HPILs-Cl-1	Friedel–Crafts reaction	780.0	143.0 mg g^{-1}		273	Sang and Huang (2020)
7	HPILs-Cl-2		500.0	79.0 mg g^{-1}			
8	HPILs-Br-1		570.0	101.0 mg g^{-1}			
9	HPILs-Br-2		485.0	83.0 mg g^{-1}			
10	I$_{C2}$HCP-5b		1017.0	3.050 mmol g^{-1}	134.2	273	Zhang et al. (2020)
11	HP(0.6DVB-[VMOEIM][Gly])		508.0	64.5 mg g^{-1}		298	Sun et al. (2020)
12	HP-[BzPhIM]Cl-DCX-1		763.0	1.470 mmol g^{-1}	64.7	273	Song et al. (2021)

^{a}Conditions: T = temperature, Pressure = 1 bar

Moreover, evaluating other methodological parameter, the authors concluded that a higher temperature and extended reaction time cause a slight modification of porosity and chemical composition. The CO_2 uptake is related to the surface area, having I_{C2}HCP-5b the highest S_{BET}, abundant microporosity and consequently the highest CO_2 uptake (Table 7, entry 10). This polymer displayed high efficiency in the synthesis of cyclic carbonates from the coupling of several epoxides giving yields between 85–96% and 99% selectivity (Zhang et al. 2020).

Also in 2020, Sun et al. reported HCPs synthesized first via copolymerization using [VMOEIM][Gly] as monomer and DVB as cross-linker in different molar ratios, and then through $AlCl_3$-catalyzed Friedel–Crafts reaction. SEM and TEM images revealed that HP(nDVB-[VMOEIM][Gly]) had higher porosity, more meso-pores and micropores compared to the parent copolymers, and that the molar ratio of 0.6 of DVB to [VMOEIM][Gly] had a looser structure. This ratio is important for the intended final porous structure. HP(0.6DVB-[VMOEIM][Gly]) presented the best textural properties (Table 6, entry 18) and achieved the highest CO_2 uptake due to the functional groups and porous structure (Table 7, entry 11). This polymer was efficient for catalysis, being the yield of 4-(chloromethyl)-1,3-dioxolan-2-one 94%, with 4 wt.% of HP(*0.6*DVB-[VMOEIm][Gly]) (based on the epichlorohydrin) as catalyst at 403 K for 10 h under ambient pressure and without co-catalyst (Sun et al. 2020).

In 2021, Song et al. reported HPILs synthesized via $FeCl_3$-catalyzed Friedel–Crafts reaction with phenylimidazolium salt monomers with one ([BPhIM]Br), two ([BzPhIM]Cl) or four ([BzDPhIM]Cl_2) benzene rings and DCX or formaldehyde dimethyl acetal as cross-linkers. In formaldehyde dimethyl acetal case, toluene was used as co-cross-linker. All samples were composed of hierarchical micro-mesoporous structures. The final morphology, structure and IL moiety could be tuned by adjusting the IL type, the cross-linker, and the ratio IL/cross-linker, being the textural properties of the best cases presented in Table 6, entries 19–26. The porous HCPs without IL were synthesized similarly and are also presented in Table 6, entries 27–28. Besides the large porosities and S_{BET}, the high positive charge density of the polymers promotes CO_2 affinity. Therefore, all these factors need to be balanced in the end. HP-[BzPhIM]Cl-DCX-1 showed a good CO_2 uptake capacity (Table 7, entry 12), and in the CO_2 cycloaddition reaction with epichlorohydrin at 353 K for 24 h under 1 bar CO_2 pressure, the yield was equal to 98.9% (Song et al. 2021).

Table 7 presents a summary of the porous PIL-based materials applied to carbon capture and utilization, and the respective synthetic paths according to the techniques reviewed above.

CO_2 capture data need to be standardized because some discrepancies appear in the literature. Even so, pore size or pore volume and S_{BET} seem to be really more important for catalysis applications. Evaluating the data available, it appears that for a compound to be effective in CO_2 capture it should have a pore size up to 10 nm, a pore volume ranging from 0.4 to 2.1 $cm^3\ g^{-1}$ and S_{BET} above 20.1 $m^2\ g^{-1}$. Moreover, there is no linear relation among these data and the CO_2 uptake values,

since apparently an effective material must have an ideal balance between porosity and cation/anion interactions with CO_2.

Methodologies for porosity manipulation are evolving, nonetheless more studies need to be made regarding the fine-tuning and scalability of the material. More recently, two innovative strategies emerged as alternatives for templating and post-polymerization, resulting in materials known as MIPs and aerogels.

2.3 Material Trends (MIP and Aerogel)

2.3.1 PIL-Based Molecularly Imprinted Polymers

Briefly, molecular imprinting is a methodology that uses target molecules to create template-shaped cavities in the polymer matrixes and, consequently, induces molecular recognition properties in the polymers (Fig. 5) (Viveiros et al. 2018, 2017; Zhao et al. 2012).

This method has been applied in solid-phase extraction, CO_2 capture, chemical sensors and artificial antibodies (Chen et al. 2011; Chen and Huang 2017; Dai et al. 2020; Ding et al. 2016; Fan et al. 2013; Guo et al. 2011; Hanak and Manovic 2018; Keçili et al. 2019; Liu et al. 2016, 2018, 2021; Lu et al. 2018, 2020; Ma and Row 2018; Nabavi et al. 2017a, b; Pichon et al. 2020; Sarpong et al. 2019; Sun et al. 2019b; Tashakkori et al. 2017; Viveiros et al. 2018; Wang et al. 2021; Wei et al. 2020,2019; Yang et al. 2020; Zhang et al. 2021; Zhao et al. 2014, 2012; Zhu et al. 2020, 2019, 2018). Synthetic methodologies of MIPs include the use of the template, cross-linker, functional monomer, porogen (solvent) and initiator. Several methodologies can be used to polymerize, as: bulk polymerization, precipitation polymerization, iniferter polymerization and reversible addition–fragmentation chain transfer (RAFT) polymerization, suspension or bead polymerization and emulsion polymerization (Barrulas et al. 2021; Keçili et al. 2019; Sarpong et al. 2019; Wu et al. 2018).
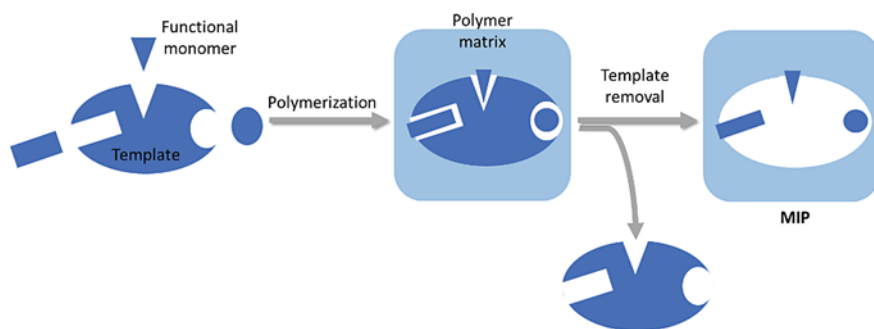
**Fig. 5** General scheme of the molecular imprinting method (Chen et al. 2017)

To the best of our knowledge, PIL-based MIPs have not yet been studied for CO_2 capture and conversion. However, due to the characteristics of the methodology and PILs CO_2-philicity, we envision that these are very promising materials for this application.

2.3.2   PIL-Based Aerogels

Aerogels are 3D-porous materials characterized by low density, mechanical and thermal stability, high S_{BET} and porosity, good sorption properties and tuneable surface functionality. They can be obtained from inorganic (silica, alumina, titania, among others) or organic sources (resorcin-formaldehyde, melamin-formaldehyde, polysaccharides—cellulose, chitin, chitosan, starch, lignin, alginate, agarose, agar, pectin or proteins) (Ganesan et al. 2018; Miao et al. 2020; Qian et al. 2019; Zhao et al. 2018). The methodology consists of replacing solvent trapped in the gel structure, with gas, for example, air or CO_2, generating a mesoporous structure with around 95–99% of empty space (Fig. 6) (Ganesan et al. 2018; Soorbaghi et al. 2019; Wang et al. 2019b).

Aerogels materials have already been used for biomedicine, nutrition and food industry, pharmaceutical applications, air filtration, thermal insulation, metal-ion sorption, oil–water separation, dye adsorption, CO_2 capture, catalysis, electrochemistry, among other applications (Chang et al. 2008; Druel et al. 2018; Ganesan et al. 2018; García-González et al. 2019; Jiang et al. 2020; Miao et al. 2020; Nissilä et al. 2018; Qian et al. 2019; Rodríguez-Dorado et al. 2019; Sun et al. 2021; Wang et al. 2019b; Zhao et al. 2018).

So far, there are only few reported PIL-based aerogels that are being applied for protein separation (Qian et al. 2019) and solid-phase extraction (Sun et al. 2021). PIL-based aerogels are not being developed so far for CO_2 capture and conversion, however, due to their characteristics they are envisioned as promising materials for
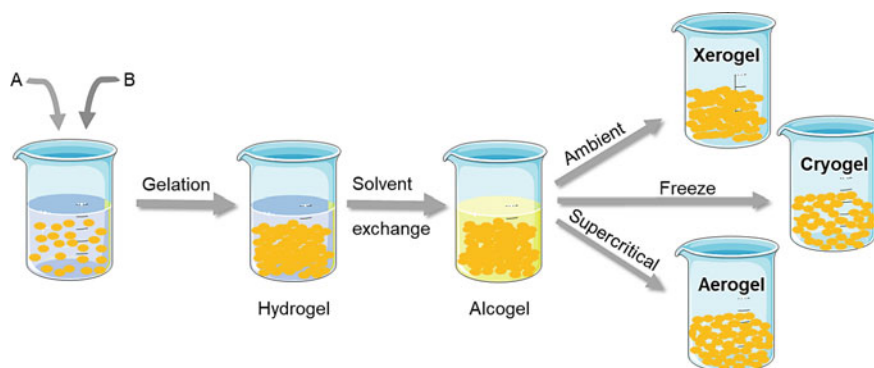
Fig. 6   General scheme of the synthesis of biopolymer aerogels (Soorbaghi et al. 2019)

CO_2 mitigation in association with the well-known action of PILs towards CO_2 (Barrulas et al. 2021).

3 Hybrid or Crystalline Frameworks

Hybrid materials combine both properties of organic and inorganic compounds. MOFs are a new class of crystalline porous materials that finds major applications in energy and environment, such as gas storage, separation, conductivity, nonlinear optics, luminescence, sensors and catalysis. The major features of MOFs are accessible pore volumes, ordered pores, high internal surface area, high adsorption capacity and the existence of diverse means of functionalization. The control of linker length and the coordination enable the regulation of pore size and favour the establishment of interesting host–guest interactions (Stock and Biswas 2012).

ZIFs are MOFs with a tetrahedral network structure, bearing transition metals (Zn and Cu) linked by imidazolate ligands (Wang and Wang 2016). ZIFs resemble zeolites, with Zn^{2+} in the role of silicon, and the imidazolate anions that form bridges mimicking the role of oxygen. ZIFs exhibit permanent porosity and high thermal and chemical stabilities that make them interesting for CO_2 adsorption, separation and conversion, as well as industrial adsorption applications, in general. ZIFs have been shown to display high affinity towards CO_2 and, in some cases, a completely reversible CO_2 adsorption–desorption behaviour. Moreover, the imidazolate motifs influence CO_2 adsorption abilities, through the functionalization groups polarizability and symmetry (Morris et al. 2010). However, the relatively complicated synthesis protocol of ZIFs may still disfavour their general use for CO_2 adsorption in practical scale.

The incorporation of ILs into MOFs has been explored as a strategy to enhance CO_2 capture capabilities, adding recyclability and catalytic activity features.

The regularity, the balance of rigidity and flexibility, and the structural tunability of MOFs and ZIFs have granted a place among the materials for carbon capture and utilization, however, the chemical, thermal and water stability still remain a challenge (Li et al. 2012). In the last years, an emerging class of porous crystalline polymers named COFs has been developing. COFs are composed of organic building blocks, with pre-designed geometries connected by stable covalent linkages, forming an extended network with an ordered π-structure, which makes them highly porous, with high surface areas, low densities and thermal and chemical stability (Cao et al. 2019b) (see Fig. 7).

3.1 Metal-Organic Frameworks (MOFs)

An amino-functionalized imidazolium-based IL was grafted in a single step into the porous MOF, MIL-101-SO$_3$H. The grafting employed a self-assemble method that
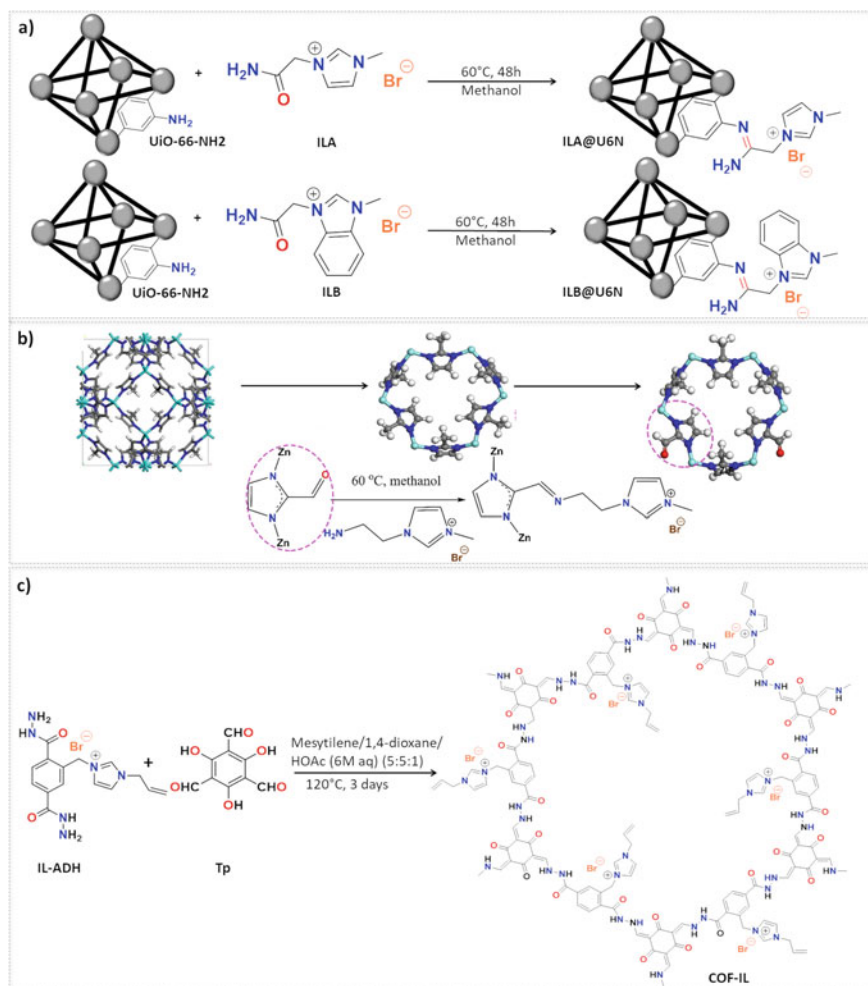
Fig. 7 Examples of IL grafting into hybrid or crystalline supports applied to CO$_2$ emission mitigation: **a** MOF derived from UiO-66-NH$_2$, adapted from reference (Kurisingal et al. 2019) with permission, **b** ZIF, reproduced from reference (Xiang et al. 2021) with permission, **c** COF derived from IL-ADH reaction with triformylphloroglucinol (Tp), adapted from reference (Ding et al. 2019) with permission

consisted of an acid–base attraction between the positively charged IL ammonium groups of [AEMIM]Br, and the negatively charged sulfonate groups from the MOF. The heterogeneous catalyst was tested in the cycloaddition of CO$_2$ to epichlorohydrin, to prepare chloropropene carbonate. The IL@MOF was very efficient and stable, with easy separation from the products and able to be reused multiple times. Although the IL@MOF revealed a lowering in S$_{BET}$ from 1458 m^2 g^{-1} down to 1049 m^2 g^{-1}, with increasing amount of IL, the pore occupation was only partial, and an improvement

of CO_2 capture yield was observed for MOFs with higher IL loading without the addition of a co-catalyst (Sun et al. 2018).

Recently, Jian and co-workers reported a post-synthetical modification of MIL-101 with a PIL, producing PILs@MIL-101 that could efficiently perform the cycloaddition reaction between CO_2 and epoxide. The confinement of imidazolium-based PILs into the MOF MIL-101, via in-situ polymerization of encapsulated monomers, allowed the obtention of composite PILs@MIL-101 with a hierarchical pore structure, and although the lower surface area compared to MIL-101, these materials denoted higher CO_2 sorption capacities, probably due to the generation of additional small pores (< 0.8 nm) upon loading PILs. These features promoted the catalytic cycloaddition at sub-atmospheric pressure, in the absence of any co-catalyst. The significantly enhanced activity of PILs@MIL-101, compared to either MIL-101 or PILs, was attributed to the synergetic effect among the good CO_2 enrichment capacity, the Lewis acid sites in the MOF, as well as the Lewis base sites in the PILs (Ding and Jiang 2018). In another report, two MOFs derived from quaternary phosphorus IL functionalized coordinatively unsaturated metal sites (CUS) and quaternary ammonium salts, MIL-101-N-(n-Bu)$_3$Br and MIL-101-P(n-Bu)$_3$Br, were obtained by a post-synthesis modification method. The synergetic role of dual functional sites, namely Lewis acid sites in the MOF framework, and bromide ions in the IL, justified the high catalytic activity for the cycloaddition of CO_2 to epoxides under mild and co-catalyst-free conditions, outperforming other benchmark MOF catalysts (Ma et al. 2015).

A novel heterogeneous catalyst constituted of MOF, MIL–101(Cr) and a new "task-specific" IL was synthesized (MIL–101(Cr)–TSIL) and used as catalyst in CO_2 cycloaddition reaction with epoxides, without the need for a co-catalyst or a solvent. The excellent performance of the catalyst was attributed to three effective factors: (1) carboxylic acid group, (2) imidazolium cation and (3) mesoporous framework. The combination of these factors result in a notable increase in catalytic activity in comparison with pure MIL–101(Cr). Several cyclic carbonates were obtained with high yield and selectivity. Good thermal stability was observed for MIL–101(Cr)–TSIL catalyst, enabling its recycle after simple separation, without a significant loss in catalytic activity. These good results reported for MIL–101(Cr)–TSIL catalyst can be associated with synergetic effect of the hydrogen bond from the carboxylic acid group through the stabilization of the intermediate, the activation of the C–O bond in the epoxy ring, and the high concentration of CO_2 around the TSIL arisen from the mesoporous framework (Bahadori et al. 2019).

Park's group reported the synthesis of two new IL-tethered Zr-based UiO-66-NH$_2$ heterogeneous catalysts by a post-impregnation method, wherein the ILs were incorporated into MOFs after their preparation. Imidazolium ILs were incorporated into UiO-66-NH$_2$ to form bifunctional heterogeneous catalysts, that were used for the cycloaddition of epoxides to CO_2. Condensation of methylimidazolium and methylbenzimidazolium-based IL units (ILA and ILB, respectively) into the pore walls of UiO-66-NH$_2$ framework, generated ILA@U6N and ILB@U6N catalysts, respectively. The resultant heterogeneous catalysts, especially ILA@U6N, exhibited

excellent CO_2 adsorption capability, proving them effective for cycloaddition reactions towards cyclic carbonates under mild reaction conditions, in the absence of any co-catalyst or solvent. DFT analysis allowed the proposal of a mechanism where the effectiveness of ILA@U6N is justified by the synergetic cooperation between the coordinately unsaturated Lewis acid Zr^{4+} centres, and the bromide ions in the bifunctional heterogeneous catalysts. The influence of the ILs size on epoxide/CO_2 coupling was also studied (Kurisingal et al. 2019).

Using similar porous scaffolds, several bifunctional porous imidazolium-functionalized Zr-MOFs were produced (Ding et al. 2017; Liang et al. 2017). These materials were highly stable exhibiting a hierarchical porous structure that was selective for CO_2 capture, and catalyzed the cycloaddition to epoxides at ambient pressure, without a co-catalyst, under mild conditions.

The textural properties and IL moieties used in the MOFs highlighted in the text are presented in Table 8, entries 1–8.

3.2 Zeolitic Imidazolate Frameworks (ZIFs)

One of the first reports on IL functionalization of ZIFs with excellent CO_2 transforming capabilities also came from Park's group in 2016 (Tharun et al. 2016). A novel heterogeneous one-component catalyst was developed, by the covalent post-functionalization of ZIF-90 with a pyridinium-based IL to generate IL-supported ZIF-90 (IL-ZIF-90). The catalyst was employed in the cycloaddition of CO_2 to epoxides, yielding cyclic carbonates, under mild reaction conditions and in the absence of solvent. A mechanism for the IL-ZIF-90 catalyzed propylene oxide–CO_2 cycloaddition has been proposed based on DFT calculations, that involved the epoxide activation by the Lewis acidic centre (Zn), a nucleophilic attack by the halide ion, and a ring-opening followed by ring closure yielding the cyclic carbonate.

IL immobilized ZIF catalysts (IL-ZIF-8) were obtained by a post-synthetic modification, through grafting on a dual-ligand ZIF. The IL, [AEMIM]Br, was anchored to the hybrid ZIF-8 framework by a coupling reaction between C=O groups of ZIF and NH_2 groups of the IL (Xiang et al. 2021). The resulting IL-ZIF exhibited coordinately unsaturated Zn centres as Lewis acid sites, and nucleophilic bromide ions as Lewis base sites. Variation of the content of mixed linkers in the framework, and/or IL loadings allowed tuning the density of Lewis acid/base sites. All samples presented microporous characteristics. The catalytic activity of the bifunctional IL-ZIF was tested on the cycloaddition of CO_2 to propylene oxide, exhibiting excellent performance under mild conditions. Relying on DFT calculations, a catalytic mechanism for propylene oxide-CO_2 cycloaddition was proposed, where the synergetic interaction of the exposed Lewis acid sites from the ZIF and Lewis base sites (Br^-) from the IL reduced notoriously the energy barrier of propylene oxide ring-opening, promoting the CO_2 cycloaddition reaction. The IL-ZIF-8(0.3) obtained a yield of 97% with good stability and reusability, in the absence of co-catalysts and solvent.

Table 8 List of hybrid-IL porous material obtained in the literature

Entry	Material	S_{BET} (m^2 g^{-1})	Pore volume (cm^3 g^{-1})	Pore size (nm)	IL or IL moiety	References
1	MIL–101(Cr) MIL–101(Cr)–TSIL	1458 1499	0.7530 0.5725	n.d.[a]	[AEMIM][Br]	Sun et al. (2018)
2	MIL-101 PILs-MIL-101	3603 2462	1.83 1.26	n.d.[a]	P[VEIM][Br]	Ding and Jiang (2018)
3	MIL–101(Cr) MIL–101(Cr)–TSIL	2729.0 577.6	1.358 0.325	n.d.[a]	[CbzMIM][Br]	Bahadori et al. (2019)
4	MIL-101-NH2 MIL-101-Br MIL-101- N(n-Bu)3Br MIL-101-P(n-Bu)3Br	1100 890 660 601	0.782 0.586 0.538 0.476	n.d.[a]	[N(n-Bu)$_3$][Br] [P(n-Bu)$_3$][Br]	Ma et al. (2015)
5	UiO-66-NH2 ILA@U6N ILB@U6N	721 304 237	0.37 0.29 0.17	n.d.[a]	[MACEMIM][Br] [MACEMIBzM][Br]	Kurisingal et al. (2019)
6	UiO-66 Im–UiO-66 IL-UiO-66	803 528 328	0.62 1.11 0.88	0.6–1.5 0.7–1.3 0.6–1.1	[MIM]$^+$	Liang et al. (2017)
7	UiO-67 IL-UiO-67	2113 846	n.d.[a]	n.d.[a]	[AIM]$^+$	Ding et al. (2017)
8	n-ZIF-90 IL-ZIF-90	1261 153	0.45 0.05	n.d.[a]	[APy][I]	Tharun et al. (2016)

Table 8 (continued)

Entry	Material	S_{BET} (m^2 g^{-1})	Pore volume (cm^3 g^{-1})	Pore size (nm)	IL or IL moiety	References
9	ZIF-8	1769	0.84	0.70	[AEMIM][Br]	Xiang et al. (2021)
	ZIF-8 (0.15)	1811	0.78	0.68		
	ZIF-8 (0.30)	1473	0.79	0.57		
	ZIF-8 (0.50)	1451	0.72	0.49		
	IL–ZIF-8 (0.15)	1305	0.49	0.46		
	IL–ZIF-8 (0.30)	577	0.26	0.24		
	IL–ZIF-8 (0.50)	314	0.18	0.11		

[a]n.d.: no data

The textural properties and the IL moieties used in the MOFs highlighted in the text are presented in Table 8, entry 9.

The interest in combining the size and shape selectivity of porous domains with the fluidity of liquids has motivated another important progress to the ILs community. Thus, one expeditious approach to obtain ILs with permanent porosity has been the incorporation of empty cavities into liquid phases. This strategy adds novel functionalities to conventional fluids, opening new perspectives for applications such as separations, catalysis and drug delivery. Porous liquids can be classified in three categories—neat fluids composed by molecular entities with empty cavities are denominated type I porous liquids; type II consists of a molecular entity dissolved in sterically hindered solvents; and type III concerns the dispersion and stabilization of solid porous materials in hindered solvents, where the solvents are larger than the solid pores (O'Reilly et al. 2007; Zhang et al. 2015a).

Type II porous liquids were prepared from dispersions of 2–5% ZIF-8 in a phosphonium-based IL. Density measurements provided evidence for the free volume presence in the successful MOF@IL suspensions that were capable of absorbing reversibly up to 63% more CO_2, 150% more nitrogen and 100% more methane than the pure IL (Costa Gomes et al. 2018).

Another example of the porous liquid approach comes from Bennett and Nitschke group that developed IL, porous, tetrahedral coordination cages that behave as a liquid in the neat state and can bind gaseous compounds as chlorofluorocarbons. The liquid coordination cages were obtained by incorporating poly(ethylene glycol)–imidazolium chains into the periphery of the parent Zn_4L_4 tetrahedron. The affinity of these materials was shown to increase with the respective size (Ma et al. 2020).

3.3 Material Trends (COF)

COFs exhibit periodic architectures, low densities and high porosity that make them ideal candidates for various applications in catalysis, gas storage and separation, and optoelectronics. However, the availability of 3D scaffolds is still limited, and their synthesis is mostly confined to the high-temperature solvothermal method.

The IL [Et_4N]Br was immobilized in mesoporous imine-linked pyrene COFs scaffolds through a post-synthetic methodology, producing [Et_4N]Br50%-Py-COF. This material afforded a high CO_2 adsorption capacity of 164.6 mg g^{-1} (1 bar, 273 K) and was a highly efficient heterogeneous catalyst for the transformation of CO_2 into value-added formamides under ambient conditions (Dong et al. 2016). A new synthetic strategy for COF materials has been described by Fang and co-workers. A fast and ambient temperature and pressure ionothermal synthesis of a series of 3D-IL-COFs was described. The subsequent COFs exhibited a high crystallinity and S_{BET} between 500 and 600 m^2 g^{-1}. The IL-COFs contained 8–12% IL in their pores and were tested for gas adsorption, exhibiting a selectivity increase between 3 and 4 times higher for CO_2/N_2 and CO_2/CH_4 than the original COF (Guan et al. 2018). An interesting approach combined COFs with polymers and oligomers.

A novel COF–CHT composite aerogel (COF-IL@CHT) was fabricated by chemical cross-linking of an allylimidazolium IL-decorated COF (COF-IL) with a thiol-attached CHT (CHT–SH) binder via a photoinduced thiol–ene reaction. The aerogel presented a crystalline structure and was highly selective for CO_2 adsorption and catalytic conversion features. This COF-IL@CHT aerogel was shaped into a simplified fixed bed reactor model via a facile templated freeze-drying procedure, and a scaled-up recyclable CO_2 cycloaddition reaction to styrene oxide was performed (Ding et al. 2019).
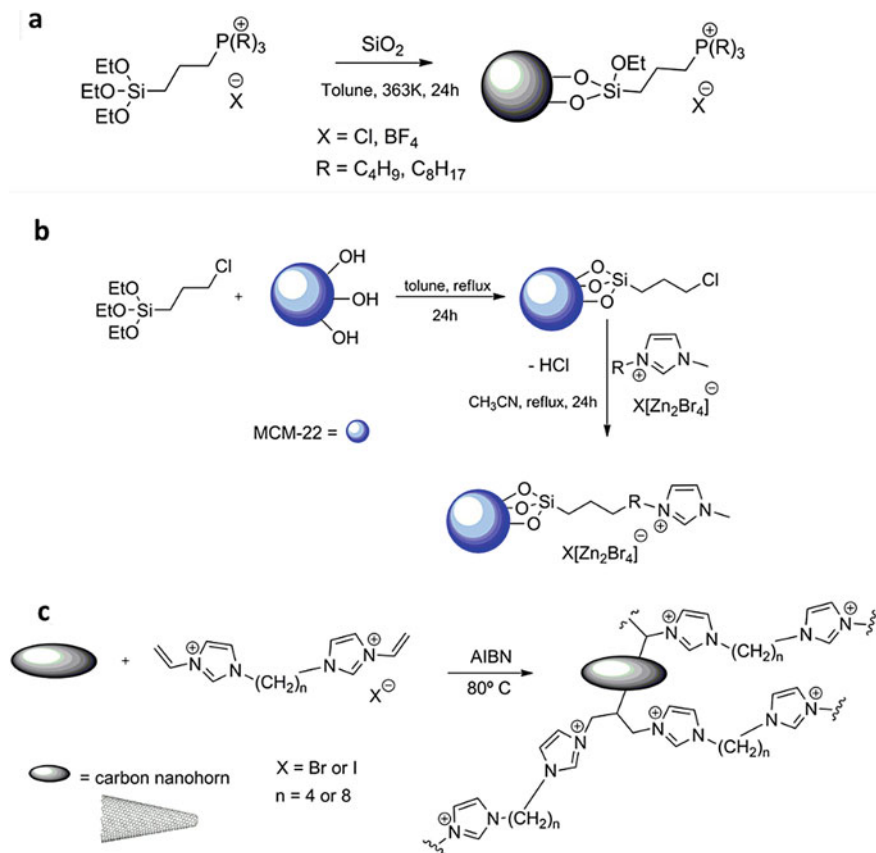
4 Inorganic Supports

Inorganic compounds as silica and zeolite are the most traditional supports used due to their high thermal stability. Recently, carbon porous materials have emerged as one alternative inorganic support. This material is generally classified as inorganic because it has already been carbonized and presents inorganic features. A brief review of these three types of supports is discussed here (see Fig. 8).

4.1 Silica

Silica-based materials are widely used as supports for ILs. Particularly, mesoporous silicas possess large surface areas and ordered pore structures that allow chemical modifications (Ramos et al. 2020). The most common grafting methodologies used for carbon capture and utilization materials are covalent-binding strategy or cross-linking methods.

One example of covalent-binding of glycidyl-group-containing ILs on organic and inorganic supports with functional surfaces was published by Xi et al., in 2010. The authors used supports based on polymer spheres functionalized with NH_2 and COOH groups, and silica (SBA15 and silica gel) functionalized with NH_2 groups. The IL [GIBIM]Cl was grafted onto various supports, and all materials were investigated as catalyst of CO_2 cycloaddition reactions with epoxides. Under conditions of 60 bar of CO_2 and 403 K, the NH_2-functionalized polymer present higher TOF (1693 h^{-1}) compared to the silica-based material (TOF < 29 h^{-1}). The authors attributed this result to synergetic effects between the support and the IL, able to promote the coupling reaction of CO_2 with propylene oxide. No porosity data was reported (Xie et al. 2010).

Similar methodology was demonstrated by Zhu et al., in 2014. A phosphonium-based IL ($P_{8883}BF_4$) was covalently grafted onto the porous silica surface via wet impregnation method to be used for CO_2 capture. Adsorption/desorption tests were performed at 298, 313 and 333 K under 2 bar of CO_2, using a gravimetric method. The grafting of ILs on SiO_2 surface generated a loss of microporosity and consequently a

Fig. 8 Examples of IL grafting into inorganic support applied to CO_2 emission mitigation: **a** silica, adapted from reference (Zhu et al. 2014). **b** zeolite (Guo et al. 2018). **c** carbon (Calabrese et al. 2017)

small decrease in CO_2 adsorption capacity (Table 9, entry 1). However, the grafting method provided good recyclability capacity (Zhu et al. 2014).

In 2011, Aprile et al. have prepared inorganic–organic composite catalysts, called multi-layered covalently supported IL phases (mlc-SILP). Reaction between bisvinylimidazolium salts and mercaptopropyl-modified silicas (amorphous or ordered SBA-15) or cross-linked PS using free-radical "click" process were performed. The organic and inorganic materials were used as catalyst for the synthesis of cyclic carbonates performed under supercritical CO_2. The material containing bis-imidazolium bromide salt at the SBA-15 surface was identified as the most efficient catalyst. The good performance was attributed to the formation of covalent bonds with SBA-15, leading to a multi-layered ionic phase anchored to the support. In addition, this catalyst was easily recovered and recycled in five consecutive catalytic runs without loss of activity. The morphological properties of the mlc-SILP materials were

Table 9 List of inorganic-IL porous material obtained in the literature

Entry	Support	S_{BET} (m^2 g^{-1})	Pore volume (cm^3 g^{-1})	Pore size (nm) and pore type	References
1	SiO$_2$ SiO$_2$–Si SiO$_2$–Si–P$_{8883}$BF$_4$	313.1 139.4 253.7	0.1132 0.0471 0.0781	n.d.[a]	Zhu et al. (2014)
2	SiO$_2$ SiO$_2$–Cl–A SiO$_2$–Br–A SiO$_2$–Br–B SBA-15 SBA-15-Cl-A SBA-15-Cl-B SBA-15-Br-B	750 112 126 124 735 73 62 45	0.68 0.11 0.14 0.13 0.71 0.07 0.07 0.06	n.d.[a]	Aprile et al. (2011)
3	XEROGEL SILTF2NX20[b] SILTF2NX40	9 4 1	0.016 0.008 0.002	7.1 7.5 4.9	Aquino et al. (2019)
4	SX SX–[BMIM]Cl SX–[EMIM][MSO$_3$] SX–TBAB SX–TBPB SX–[BMPyrr]Cl SX–[EMIM][SO$_3$CF$_3$] SX–CTAB SX–THAB SX–[EMIM][NTf$_2$] SX–[BMIM][NTf$_2$] SX–[MBMIM][NTf$_2$]	595 116 180 223 388 100 282 141 278 546 343 378	0.24 0.10 0.16 0.13 0.25 0.07 0.19 0.11 0.22 0.33 0.24 0.26	1.18 1.63 1.83 1.24 1.27 1.33 1.32 1.50 1.58 1.20 1.41 1.35	Aquino et al. (2015), Rodrigues et al. (2020), dos Santos et al. (2020)
5	MCM-41 Cl-MCM-41 MCM-41-Imi MCM-41-Imi/Br	1115 585 302 130	0.92 0.55 0.30 0.18	2.3 2.3 1.3 1.2	Appaturi and Adam (2013)
6	H-ZSM-5 zeolites	362.7	0.304	n.d.[a]	Li et al. (2019)
7	AC AC oxidized AC reduced [HMIM][NTf$_2$] physical SILP [SPMIM][NTf$_2$] grafted SILP [EMIM][OAc] physical SILP [SPMIM][OAc] grafted SILP	1193.8 983.5 461.1 23.95 24.62 13.96 78.80	n.d.[a]	n.d.[a]	Karousos et al. (2016)

AC activated carbon. [a]n.d.: no data. [b]SILTF2NX20=Silica xerogel with 20% of 1–(trimethoxysilylpropyl)–3–methylimidazolium trifluoromethylsulfonyl)imide

determined by N_2 adsorption/desorption measurements. Comparing the amorphous silica and the ordered mesoporous SBA-15 before and after IL grafting, a significantly decrease on the surface areas and pore volume after grafting was observed (Table 9, entry 2). The activity of the catalyst having SBA-15 as support is slightly higher than amorphous SiO_2 support. According to the author, this demonstrates that a high S_{BET} is the crucial feature to achieve a multi-layered supported IL phase with a high catalytic activity (Aprile et al. 2011).

Other common methodology of covalent grafting is the *in-situ* polymerization via sol–gel process. In this methodology, the IL is used as a templating agent for the synthesis of silica xerogels due to its surfactant character and the low surface tension. The sol–gel process allows the control of the silica particle size, gelation time, structure and morphology. Generally, an alkoxide precursor is hydrolyzed leading to the formation of Si–OH bonds that generate an inorganic 3D network. The final material is then obtained after drying, resulting in xerogel or aerogel. This methodology has been used by Einloft group to produce IL derived materials for CO_2 capture (Aquino et al. 2019; dos Santos et al. 2020) and reuse to convert in cyclic carbonate (Rodrigues et al. 2020). The group has demonstrated the synergetic effect of combining the well-known affinity between pure ILs and CO_2 adsorbents (Aquino et al. 2015). The complete porous characterization of material can be observed in Table 9, entries 3–4. In general, they concluded that there is a maximum amount of IL that can be used in the synthesis of silica xerogel (SX)-IL. Increasing the amount of IL immobilized in the xerogel, decreases the adsorption and conversion capacity, due to a blocking of the solid's pores by the IL and/or IL trapped without accessibility or free volume to adsorb CO_2 (Aquino et al. 2015, 2019). They also demonstrated that the success in CO_2 uptake relies on a compromise between S_{BET}, pore volume and IL type (dos Santos et al. 2020).

4.2   Zeolites

Zeolites are crystalline aluminosilicates with periodic arrangement of cages and channels which were found to have extensive industrial use as catalysts, adsorbents and ion exchangers. Zeolites have attracted huge attention due to their highly microporous structure that could be used for diverse specific applications in gas storage, separations and catalysis. Herein, we present some examples of the use of these types of materials in carbon capture and utilization. The methodologies to graft IL into zeolites are similar to those applied to silica.

An important progress into catalytic conversion of CO_2 using a continuous fixed bed reactor was reported by Guo et al. in 2018. The authors prepared IL composites, namely [HEMIM]Cl/$(ZnBr_2)_2$, [CEMIM]Cl/ $(ZnBr_2)_2$ and [AEMIM][Zn_2Br_5], covalently immobilized on a molecular sieve support (MCM-22), with the help of a silane coupling agent, 3-chloropropyltriethoxysilane. These composites were applied as heterogeneous catalysts in cycloaddition of CO_2, to prepare propylene carbonate. Despite no data from porosity was reported, an excellent

catalytic performance in the fixed bed reactor was observed. In addition, the authors presumed that hydroxyl, carboxyl and amino groups of functionalized ILX/(ZnBr$_2$)$_2$ had removed a hydrogen atom in the immobilization process. Thus, a Lewis acid zinc bromide of ILX/(ZnBr$_2$)$_2$ was generated in the catalyst and promoted the catalytic activity (Guo et al. 2018), and this effect is similar to the one described using organic support (Zhang et al. 2012).

Similar procedure was employed previously by Appaturi and Adam. They prepared immobilized IL into zeolite MCM-41, by reacting dibromoethane with imidazole (Imi), generating a catalyst material via sol–gel technique. The catalyst was used in the solventless synthesis of styrene carbonate from CO$_2$ and styrene oxide, under ambient conditions with a maximum selectivity of 99.1% (Appaturi and Adam 2013). Similar to other articles, a reduction in S$_{BET}$ was observed due to the immobilization of organic moieties (Table 9, entry 5).

Differently of sol–gel technique, in 2019, Li et al. developed a new efficient strategy for the liquefaction of H-form zeolites by the hydrogen bonding interaction between the alkyl chains of branched IL (with NTf$_2^-$, BF$_4^-$, EtSO$_4^-$ anions) and Brønsted H-form zeolites sites (Table 9, entry 6). The authors demonstrated the formation of porous liquid zeolites, which significantly improved the CO$_2$ gas sorption performance and sorption–desorption capacity due to the preserved permanent porosity (Li et al. 2019). This work opens new possibilities on the use of liquid zeolite materials.

4.3 Material Trends (Carbon)

The carbon-based materials present large S$_{BET}$ and pore size, good thermal stability and hydrophobicity. Due to these features, carbon materials have recently been reported as promising for nanotechnological applications such as gas storage, biosensors, drug delivery systems and catalysis (Wang et al. 2019a; Xie et al. 2020; Zhang et al. 2015b, d). In addition, the use of ILs as carbon precursors opens a new direction in the synthesis of porous carbon materials, since ILs are suitable for preparing customized carbon with specific morphology, pore structure and heteroatom doping. However, problems of high cost and low sustainability in practical application limit the development of carbon synthesis from direct carbonized IL (Xie et al. 2020). Despite the several reports using IL as template for carbonization or self-carbonization, (Gong et al. 2017; Mahurin et al. 2014) rare examples of IL grafting in carbonized species or activated carbon can be found. Here a few significative examples of IL grafting in activated carbon were selected to highlight the possibility of the use of this material in carbon capture and utilization.

SILPs absorbents on commercial microporous activated carbon were prepared and tested for gas separation in SO$_2$/CO$_2$/O$_2$/N$_2$ mixtures. Physically and chemically grafting were performed using [HMIM][NTf$_2$], [EMIM][OAc] and [SPMIM] (Table 9, entry 7). The results showed that the SILPs with acetate IL were highly effective, although they present poor regeneration capacity. Nevertheless, SILPs prepared with

the physisorption of IL exhibited remarkable stability accompanied by satisfactory performance (Karousos et al. 2016).

Carbon nanotubes present unique properties making them ideal support candidates for IL. They have been used as heterogeneous catalysts of cycloaddition reaction with epoxides (Han et al. 2012), or carbamates synthesis from halides, amines and CO_2 (Krawczyk et al. 2016). Pristine nanocarbon is commonly used as a material that presents a good thermal stability, micro- and mesoporosity, internal pore accessibility and semiconducting properties. Calabrese et al. reported the preparation of pristine carbon nanohorns materials, composed with highly cross-linked imidazolium salts using a one-step radical oligomerization of bis-vinylimidazolium salts in the presence of pristine carbon nanohorns. The porous materials were tested as catalysts for carbon capture and utilization, converting epoxides into cyclic carbonate, presenting excellent TON (> 3226 h^{-1}) and productivity (>95%). The catalysts containing an octyl linker and Br^- or I^- as anions of IL showed good capacity of reuse, yielding no loss in activity after three cycles. To study the nature of the catalytic behaviour after recycling, mercury porosimetry was performed. The measurements of differential intrusion *versus* pore diameter, performed in fresh and reused catalyst presented a similar pore size. No data regarding N_2 porosity was reported (Calabrese et al. 2017).

From the table and the results demonstrated in the articles related to grafting of ILs onto inorganic supports, it is possible to observe a significant improvement the recyclability compared to supported ILs. However, a loss of porosity is generally associated that could lead to a reduced efficiency in CO_2 capture and reuse applications. Thus, to achieve a desired and adequate porosity is still a challenge for inorganic supports.

5 Conclusions and Outlook

The importance of porous materials has risen considerably across all fields of science. In this context, the nature of the support plays an important role in the design of suitable porosity. This chapter focused on porous carbon capture and utilization materials with (P)IL functionalities, since the possibility to tailor the properties according to the cation and anion of the IL moiety has added another layer of designability. The ideal material for carbon capture and utilization should have proper porosity, and a balance between acidic or basic sites and CO_2-philic features. Several classes of compounds from organic, to hybrid and inorganic were highlighted.

Inorganic compounds have been the most traditional porous supports, with routine industrial use for quite some time. In this field, silica, zeolites and oxides are the most classical materials. Meanwhile, carbon-based materials have recently emerged as an alternative. This success can be related to the fact that besides presenting thermal stability and high porosity, they exhibit a high conductivity, resulting in perfect candidates for electrocatalysis of CO_2. The grafting of ILs onto inorganic supports improves the recyclability, however, there is generally a loss of porosity. Crystalline materials such as MOFs and ZIFs exhibit a high control over the

porosity, and the inclusion of IL moieties can enhance selectivity towards CO_2, but the versatility of synthetic procedures as well as the chemical, thermal and water stability are still a concern. COFs are promising new scaffolds with porous channels that can have adjustable internal environments, granting them a high performance towards carbon capture and utilization. Ionic organic porous supports can be obtained from several approaches. Using mainly FRP and post-polymerization modifications, the production of these materials leads to porous PILs, MIPs and aerogels. In general, the porosity in PIL supports is influenced by the ratio of IL monomer/cross-linker/solvent, besides the processing methods. Imidazolium-based PILs are the most explored structures, a trend that is also seen in ILs. Nevertheless, PILs from other cationic families still need to be studied such as ammonium, pyridinium, pyrrolidinium, phosphonium or sulfonium.

Comparing to traditional PILs, porous PILs exhibit increased pore sizes, however, the homogeneity is yet to be accomplished. An interesting alternative that improves the recognition of target molecules, by producing more selective and specific materials, is the introduction of templates that are imprinted during polymerization (MIP). However, regarding CO_2, the ideal conditions for imprinting are still a challenge, particularly, the ratio of template/functional monomer/cross-linker. Another alternative is the production of aerogel materials that allow the creation of porosity after the polymerization. The low density of PIL-functionalized aerogels, their high porosity associated with the presence of charged moieties, make aerogels eligible candidates for carbon capture and utilization.

In general, materials with hierarchically porous structures present advantages, since the macropores facilitate the accessibility and the diffusion of guest molecules to the active sites. Micro- and mesopores provide not only the size, but also the shape selectivity (Yang et al. 2017). Organic supports offer numerous possibilities to tailor both the porosity, the acid/basic sites and CO_2-philic features. Moreover, compared to non-ionic polymers, ionic organic supports add the possibility of non-covalent and covalent intermolecular interactions, and the possibility to establish interactions between ionic moieties and CO_2, metallic ions, or any other guests (Liu and Han 2019; Yin et al. 2018; Zhang et al. 2018). The optimization of porosity with increasing adsorption can be attained with counter-ion exchange (Nayebi et al. 2019). In polymeric materials, a higher capillary pressure is experienced by smaller pores. This effect creates unstable pores and materials that easily collapse. Polymer chains that are more rigid or highly cross-linked can retain the microporous structure and minimize swelling when vapour or solvent molecules are adsorbed. This can be an advantage over commonly cross-linked polymers that are susceptible to pore swelling when in contact with gases or solvents (Sun et al. 2016). Porous PILs are easily processable into thin films, membranes, particles and fibres, which is an advantage in comparison with other porous materials such as MOFs, COFs and zeolites. Although the synthetic procedures are more diverse than for the other classes of materials considered, the exact modulation of pore size, shape and surface functionalities at multiple length scales, and micropores in particular, are still lacking (Zhang et al. 2018). Nevertheless, some materials are effective for carbon capture and utilization,

so we can conclude that although the porosity should be controlled, this is not a determining factor.

Overall, many challenges still exist on the path to controlled porous PILs. Improvements on synthetic procedures need to be made to induce adequate porosity, with control and uniformity, that is suited for the material's application. In addition, for porous PILs to be applicable at industrial scale future studies should include theoretical/computational research on chemical, thermal and water stability, porosity control and scaling up.

References

Appaturi, J.N., Adam, F.: A facile and efficient synthesis of styrene carbonate via cycloaddition of CO2 to styrene oxide over ordered mesoporous MCM-41-Imi/Br catalyst. Appl. Catal. B Environ. **136–137**, 150–159 (2013). https://doi.org/10.1016/j.apcatb.2013.01.049

Aprile, C., Giacalone, F., Agrigento, P., Liotta, L.F., Martens, J.A., Pescarmona, P.P., Gruttadauria, M.: Multilayered supported ionic liquids as catalysts for chemical fixation of carbon dioxide: A high-throughput study in supercritical conditions. Chemsuschem **4**, 1830–1837 (2011). https://doi.org/10.1002/cssc.201100446

Aquino, A.S., Bernard, F.L., Borges, J.V., Mafra, L., Vecchia, F.D., Vieira, M.O., Ligabue, R., Seferin, M., Chaban, V.V., Cabrita, E.J., Einloft, S.: Rationalizing the role of the anion in CO2 capture and conversion using imidazolium-based ionic liquid modified mesoporous silica. RSC Adv. **5**, 64220–64227 (2015). https://doi.org/10.1039/c5ra07561k

Aquino, A.S., Vieira, M.O., Ferreira, A.S.D., Cabrita, E.J., Einloft, S., de Souza, M.O.: Hybrid ionic liquid-silica xerogels applied in CO$_2$ capture. Appl. Sci. **9**, 2614 (2019). https://doi.org/10.3390/app9132614

Azapagic, A., Cue, R.M.: Carbon capture, storage and utilisation technologies: a critical analysis and comparison of their life cycle environmental impacts. J. CO2 Util. **9**, 82–102 (2015). https://doi.org/10.1016/j.jcou.2014.12.001

Azcune, I., García, I., Carrasco, P.M., Genua, A., Tanczyk, M., Jaschik, M., Warmuzinski, K., Cabañero, G., Odriozola, I.: Facile and scalable synthesis of nanoporous materials based on poly(ionic liquid)s. Chemsuschem **7**, 3407–3412 (2014). https://doi.org/10.1002/cssc.201402593

Bahadori, M., Tangestaninejad, S., Bertmer, M., Moghadam, M., Mirkhani, V., Mohammadpoor−Baltork, I., Kardanpour, R., Zadehahmadi, F.: Task-specific ionic liquid functionalized–MIL–101(Cr) as a heterogeneous and efficient catalyst for the cycloaddition of CO2 with epoxides under solvent free conditions. ACS Sustain. Chem. Eng. **7**, 3962–3973 (2019). https://doi.org/10.1021/acssuschemeng.8b05226

Balach, J., Wu, H., Polzer, F., Kirmse, H., Zhao, Q., Wei, Z., Yuan, J.: Poly(ionic liquid)-derived nitrogen-doped hollow carbon spheres: Synthesis and loading with Fe2O3 for high-performance lithium ion batteries. RSC Adv. **3**, 7979–7986 (2013). https://doi.org/10.1039/c3ra41229f

Barrulas, R.V., Paiva, T.G., Corvo, M.C.: NMR methodology for a rational selection of ionic liquids: extracting polyphenols. Sep. Purif. Technol. **221**, 29–37 (2019). https://doi.org/10.1016/j.seppur.2019.03.077

Barrulas, R.V., Zanatta, M., Casimiro, T., Corvo, M.C.: Advanced porous materials from poly(ionic liquid)s: challenges, applications and opportunities (2021)

Bui, M., Adjiman, C.S., Bardow, A., Anthony, E.J., Boston, A., Brown, S., Fennell, P.S., Fuss, S., Galindo, A., Hackett, L.A., Hallett, J.P., Herzog, H.J., Jackson, G., Kemper, J., Krevor, S., Maitland, G.C., Matuszewski, M., Metcalfe, I.S., Petit, C., Puxty, G., Reimer, J., Reiner, D.M., Rubin, E.S., Scott, S.A., Shah, N., Smit, B., Trusler, J.P.M., Webley, P., Wilcox, J., Mac Dowell, N.: Carbon capture and storage (CCS): the way forward. Energy Environ. Sci. **11**, 1062–1176 (2018). https://doi.org/10.1039/C7EE02342A

Calabrese, C., Liotta, L.F., Carbonell, E., Giacalone, F., Gruttadauria, M., Aprile, C.: Imidazolium-functionalized carbon nanohorns for the conversion of carbon dioxide: unprecedented increase of catalytic activity after recycling. Chemsuschem **10**, 1202–1209 (2017). https://doi.org/10.1002/cssc.201601427

Cao, J., Shan, W., Wang, Q., Ling, X., Li, G., Lyu, Y., Zhou, Y., Wang, J.: Ordered porous poly(ionic liquid) crystallines: spacing confined ionic surface enhancing selective CO_2 capture and fixation. ACS Appl. Mater. Interfaces. **11**, 6031–6041 (2019a). https://doi.org/10.1021/acsami.8b19420

Cao, S., Li, B., Zhu, R., Pang, H.: Design and synthesis of covalent organic frameworks towards energy and environment fields (2019b)

Carlin, R.T., Fuller, J.: Ionic liquid-polymer gel catalytic membrane. Chem. Commun. 1345–1346 (1997). https://doi.org/10.1039/a702195j

Chang, X., Chen, D., Jiap, X.: Chitosan-based aerogels with high adsorption performance. J. Phys. Chem. b. **112**, 7721–7725 (2008). https://doi.org/10.1021/jp8011359

Chen, L., Huang, X.: Preparation and application of poly(ionic liquids)-based molercularly imprinted polymer for multiple monolithic fiber solid-phase microextraction of phenolic acids in fruit juice and beer samples. Analyst **142**, 4039–4047 (2017). https://doi.org/10.1039/C7AN01186E

Chen, L., Xu, S., Li, J.: Recent advances in molecular imprinting technology: current status, challenges and highlighted applications. Chem. Soc. Rev. **40**, 2922–2942 (2011). https://doi.org/10.1039/c0cs00084a

Chen, L., Muhammad, T., Yakup, B., Piletsky, S.A.: New immobilisation protocol for the template used in solid-phase synthesis of MIP nanoparticles. Appl. Surf. Sci. **406**, 115–121 (2017). https://doi.org/10.1016/j.apsusc.2017.02.105

Costa Gomes, M., Pison, L., Červinka, C., Padua, A.: Porous ionic liquids or liquid metal-organic frameworks? Angew. Chemie Int. Ed. **57**, 11909–11912 (2018). https://doi.org/10.1002/anie.201805495

Cunha, B.S., Bataglioli, R.A., Taketa, T.B., Lopes, L.M., Beppu, M.M.: Ionic liquid functionalization of chitosan beads for improving thermal stability and copper ions uptake from aqueous solution. J. Environ. Chem. Eng. **7**, 1–9 (2019). https://doi.org/10.1016/j.jece.2019.103181

Dai, H., Deng, Z., Zeng, Y., Zhang, J., Yang, Y., Ma, Q., Hu, W., Guo, L., Li, L., Wan, S., Liu, H.: Highly sensitive determination of 4-nitrophenol with coumarin-based fluorescent molecularly imprinted poly (ionic liquid). J. Hazard. Mater. **398**, 122854 (2020). https://doi.org/10.1016/j.jhazmat.2020.122854

Dani, A., Crocellà, V., Latini, G., Bordiga, S.: Porous ionic liquid materials. In: Eftekhari, A. (ed.) Polymerized ionic liquids, pp. 23–82. Royal Society of Chemistry, Cambridge (2018)

Ding, M., Jiang, H.-L.: Incorporation of imidazolium-based poly(ionic liquid)s into a metal-organic framework for CO2 capture and conversion. ACS Catal. **8**, 3194–3201 (2018). https://doi.org/10.1021/acscatal.7b03404

Ding, H., Chen, R., Liu, M., Huang, R., Du, Y., Huang, C., Yu, X., Feng, X., Liu, F.: Preparation and characterization of biocompatible molecularly imprinted poly(ionic liquid) films on the surface of multi-walled carbon nanotubes. RSC Adv. **6**, 43526–43538 (2016). https://doi.org/10.1039/c6ra08782e

Ding, L.G., Yao, B.J., Jiang, W.L., Li, J.T., Fu, Q.J., Li, Y.A., Liu, Z.H., Ma, J.P., Dong, Y.: Bin: bifunctional imidazolium-based ionic liquid decorated UiO-67 type MOF for selective CO2 adsorption and catalytic property for CO2 cycloaddition with epoxides. Inorg. Chem. **56**, 2337–2344 (2017). https://doi.org/10.1021/acs.inorgchem.6b03169

Ding, L.G., Yao, B.J., Li, F., Shi, S.C., Huang, N., Yin, H.B., Guan, Q., Dong, Y.: Bin: Ionic liquid-decorated COF and its covalent composite aerogel for selective CO_2 adsorption and catalytic conversion. J. Mater. Chem. a. **7**, 4689–4698 (2019). https://doi.org/10.1039/c8ta12046c

dos Santos, L.M., Bernard, F.L., Polesso, B.B., Pinto, I.S., Frankenberg, C.C., Corvo, M.C., Almeida, P.L., Cabrita, E., Einloft, S.: Designing silica xerogels containing RTIL for CO2 capture and CO2/CH4 separation: influence of ILs anion, cation and cation side alkyl chain length and ramification. J. Environ. Manage. **268**, 110340 (2020). https://doi.org/10.1016/j.jenvman.2020.110340

Dong, B., Wang, L., Zhao, S., Ge, R., Song, X., Wang, Y., Gao, Y.: Immobilization of ionic liquids to covalent organic frameworks for catalyzing the formylation of amines with CO2 and phenylsilane. Chem. Commun. **52**, 7082–7085 (2016). https://doi.org/10.1039/c6cc03058k

Druel, L., Niemeyer, P., Milow, B., Budtova, T.: Rheology of cellulose-[DBNH][CO2Et] solutions and shaping into aerogel beads. Green Chem. **20**, 3993–4002 (2018). https://doi.org/10.1039/C8GC01189C

Einloft, S., Bernard, F.L., Dalla Vecchia, F.: Capturing CO2 with Poly(Ionic Liquid)s. In: Eftekhari, A. (ed.) Polymerized ionic liquids, pp. 489–514. Royal Society of Chemistry, Cambridge (2018)

Fan, J.P., Tian, Z.Y., Tong, S., Zhang, X.H., Xie, Y.L., Xu, R., Qin, Y., Li, L., Zhu, J.H., Ouyang, X.K.: A novel molecularly imprinted polymer of the specific ionic liquid monomer for selective separation of synephrine from methanol-water media. Food Chem. **141**, 3578–3585 (2013). https://doi.org/10.1016/j.foodchem.2013.06.040

Filippov, A., Bhattacharyya, S., Shah, F.U.: CO2 absorption and ion mobility in aqueous choline-based ionic liquids. J. Mol. Liq. **276**, 748–752 (2019). https://doi.org/10.1016/j.molliq.2018.12.045

Ganesan, K., Budtova, T., Ratke, L., Gurikov, P., Baudron, V., Preibisch, I., Niemeyer, P., Smirnova, I., Milow, B.: Review on the production of polysaccharide aerogel particles. Materials (basel). **11**, 1–37 (2018). https://doi.org/10.3390/ma11112144

García-González, C.A., Budtova, T., Durães, L., Erkey, C., Del Gaudio, P., Gurikov, P., Koebel, M., Liebner, F., Neagu, M., Smirnova, I.: An opinion paper on aerogels for biomedical and environmental applications. Molecules **24**, 1815 (2019). https://doi.org/10.3390/molecules24091815

Gong, J., Lin, H., Grygiel, K., Yuan, J.: Main-chain poly(ionic liquid)-derived nitrogen-doped micro/mesoporous carbons for CO2 capture and selective aerobic oxidation of alcohols. Appl. Mater. Today. **7**, 159–168 (2017). https://doi.org/10.1016/j.apmt.2017.02.009

Guan, X., Ma, Y., Li, H., Yusran, Y., Xue, M., Fang, Q., Yan, Y., Valtchev, V., Qiu, S.: Fast, ambient temperature and pressure ionothermal synthesis of three-dimensional covalent organic frameworks. J. Am. Chem. Soc. **140**, 4494–4498 (2018). https://doi.org/10.1021/jacs.8b01320

Guo, L., Deng, Q., Fang, G., Gao, W., Wang, S.: Preparation and evaluation of molecularly imprinted ionic liquids polymer as sorbent for on-line solid-phase extraction of chlorsulfuron in environmental water samples. J. Chromatogr. A. **1218**, 6271–6277 (2011). https://doi.org/10.1016/j.chroma.2011.07.016

Guo, L., Deng, L., Jin, X., Wang, Y., Wang, H.: Catalytic conversion of CO2 into propylene carbonate in a continuous fixed bed reactor by immobilized ionic liquids. RSC Adv. **8**, 26554–26562 (2018). https://doi.org/10.1039/c8ra03952f

Han, L., Choi, H.J., Kim, D.K., Park, S.W., Liu, B., Park, D.W.: Porous polymer bead-supported ionic liquids for the synthesis of cyclic carbonate from CO2 and epoxide. J. Mol. Catal. A Chem. **338**, 58–64 (2011). https://doi.org/10.1016/j.molcata.2011.02.001

Han, L., Li, H., Choi, S.J., Park, M.S., Lee, S.M., Kim, Y.J., Park, D.W.: Ionic liquids grafted on carbon nanotubes as highly efficient heterogeneous catalysts for the synthesis of cyclic carbonates. Appl. Catal. A Gen. **429–430**, 67–72 (2012). https://doi.org/10.1016/j.apcata.2012.04.008

Hanak, D.P., Manovic, V.: Techno-economic feasibility assessment of CO2 capture from coal-fired power plants using molecularly imprinted polymer. Fuel **214**, 512–520 (2018). https://doi.org/10.1016/j.fuel.2017.10.107

Jiang, X., Kong, Y., Zhao, Z., Shen, X.: Spherical amine grafted silica aerogels for CO2 capture. RSC Adv. **10**, 25911–25917 (2020). https://doi.org/10.1039/d0ra04497k

Karousos, D.S., Vangeli, O.C., Athanasekou, C.P., Sapalidis, A.A., Kouvelos, E.P., Romanos, G.E., Kanellopoulos, N.K.: Physically bound and chemically grafted activated carbon supported 1-hexyl-3-methylimidazolium bis(trifluoromethylsulfonyl)imide and 1-ethyl-3-methylimidazolium acetate ionic liquid absorbents for SO2/CO2 gas separation. Chem. Eng. J. **306**, 146–154 (2016). https://doi.org/10.1016/j.cej.2016.07.040

Keçili, R., Yilmaz, E., Ersöz, A., Say, R.: Imprinted materials: from green chemistry to sustainable engineering. In: Sustainable Nanoscale Engineering: From Materials Design to Chemical Processing. pp. 317–350 (2019)

Krawczyk, T., Jasiak, K., Kokolus, A., Baj, S.: Polymer- and carbon nanotube-supported heterogeneous catalysts for the synthesis of carbamates from halides, amines, and CO2. Catal. Letters. **146**, 1163–1168 (2016). https://doi.org/10.1007/s10562-016-1738-1

Kurisingal, J.F., Rachuri, Y., Pillai, R.S., Gu, Y., Choe, Y., Park, D.: Ionic-liquid-functionalized UiO-66 framework: an experimental and theoretical study on the cycloaddition of CO2 and epoxides. Chemsuschem **12**, 1033–1042 (2019). https://doi.org/10.1002/cssc.201802838

Kuzmina, O.: Cationic and anionic polymerized ionic liquids: properties for applications. In: Eftekhari, A. (ed.) Polymerized ionic liquids, pp. 83–116. Royal Society of Chemistry, Cambridge (2018)

Li, J.R., Sculley, J., Zhou, H.C.: Metal-organic frameworks for separations. https://pubs.acs.org/sharingguidelines (2012)

Li, P., Chen, H., Schott, J.A., Li, B., Zheng, Y., Mahurin, S.M., Jiang, D.E., Cui, G., Hu, X., Wang, Y., Li, L., Dai, S.: Porous liquid zeolites: hydrogen bonding-stabilized H-ZSM-5 in branched ionic liquids. Nanoscale **11**, 1515–1519 (2019). https://doi.org/10.1039/c8nr07337f

Liang, J., Chen, R.P., Wang, X.Y., Liu, T.T., Wang, X.S., Huang, Y.B., Cao, R.: Postsynthetic ionization of an imidazole-containing metal-organic framework for the cycloaddition of carbon dioxide and epoxides. Chem. Sci. **8**, 1570–1575 (2017). https://doi.org/10.1039/c6sc04357g

Lin, H., Zhang, S., Sun, J., Antonietti, M., Yuan, J.: Poly(ionic liquid)s with engineered nanopores for energy and environmental applications. Polymer (Guildf). **202**, 122640 (2020). https://doi.org/10.1016/j.polymer.2020.122640

Liu, Z.W., Han, B.H.: Ionic porous organic polymers for CO2 capture and conversion. Curr. Opin. Green Sustain. Chem. **16**, 20–25 (2019). https://doi.org/10.1016/j.cogsc.2018.11.008

Liu, M., Pi, J., Wang, X., Huang, R., Du, Y., Yu, X., Tan, W., Liu, F., Shea, K.J.: A sol-gel derived pH-responsive bovine serum albumin molecularly imprinted poly(ionic liquids) on the surface of multiwall carbon nanotubes. Anal. Chim. Acta. **932**, 29–40 (2016). https://doi.org/10.1016/j.aca.2016.05.020

Liu, F., Kuang, Y., Wang, S., Chen, S., Fu, W.: Preparation and characterization of molecularly imprinted solid amine adsorbent for CO2 adsorption. New J. Chem. **42**, 10016–10023 (2018). https://doi.org/10.1039/C8NJ00686E

Liu, H., Jin, P., Zhu, F., Nie, L., Qiu, H.: A review on the use of ionic liquids in preparation of molecularly imprinted polymers for applications in solid-phase extraction. TrAC - Trends Anal. Chem. **134**, 116132 (2021). https://doi.org/10.1016/j.trac.2020.116132

Lu, X., Yang, Y., Zeng, Y., Li, L., Wu, X.: Rapid and reliable determination of p-nitroaniline in wastewater by molecularly imprinted fluorescent polymeric ionic liquid microspheres. Biosens. Bioelectron. **99**, 47–55 (2018). https://doi.org/10.1016/j.bios.2017.07.041

Lu, Y., Hu, J., Zeng, Y., Zhu, Y., Wang, H., Lei, X., Huang, S., Guo, L., Li, L.: Electrochemical determination of rutin based on molecularly imprinted poly (ionic liquid) with ionic liquid-graphene as a sensitive element. Sens. Actuat. B Chem. **311**, 1–9 (2020). https://doi.org/10.1016/j.snb.2020.127911

Luo, R., Liu, X., Chen, M., Liu, B., Fang, Y.: Recent advances on imidazolium-functionalized organic cationic polymers for CO2 adsorption and simultaneous conversion into cyclic carbonates (2020)

Lopes, M., Barrulas, R.V., Paiva, G.T., Ferreira, S.D., Zanatta, A.M., Corvo, C.M.: Molecular interactions in ionic liquids: the NMR contribution towards tailored solvents. In: Nuclear Magnetic Resonance, p. 13. IntechOpen (2019)

Ma, D., Li, B., Liu, K., Zhang, X., Zou, W., Yang, Y., Li, G., Shi, Z., Feng, S.: Bifunctional MOF heterogeneous catalysts based on the synergy of dual functional sites for efficient conversion of CO2 under mild and co-catalyst free conditions. J. Mater. Chem. A. **3**, 23136–23142 (2015). https://doi.org/10.1039/c5ta07026k

Ma, W., Row, K.H.: Solid-phase extraction of chlorophenols in seawater using a magnetic ionic liquid molecularly imprinted polymer with incorporated silicon dioxide as a sorbent. J. Chromatogr. A. **1559**, 78–85 (2018). https://doi.org/10.1016/j.chroma.2018.01.013

Ma, L., Haynes, C.J.E., Grommet, A.B., Walczak, A., Parkins, C.C., Doherty, C.M., Longley, L., Tron, A., Stefankiewicz, A.R., Bennett, T.D., Nitschke, J.R.: Coordination cages as permanently porous ionic liquids. Nat. Chem. **12**, 270–275 (2020). https://doi.org/10.1038/s41557-020-0419-2

Mahurin, S.M., Fulvio, P.F., Hillesheim, P.C., Nelson, K.M., Veith, G.M., Dai, S.: Directed synthesis of nanoporous carbons from task-specific ionic liquid precursors for the adsorption of CO_2. Chemsuschem **7**, 3284–3289 (2014). https://doi.org/10.1002/cssc.201402338

Miao, Y., Luo, H., Pudukudy, M., Zhi, Y., Zhao, W., Shan, S., Jia, Q., Ni, Y.: CO2 capture performance and characterization of cellulose aerogels synthesized from old corrugated containers. Carbohydr. Polym. **227**, 1–10 (2020). https://doi.org/10.1016/j.carbpol.2019.115380

Morris, W., Leung, B., Furukawa, H., Yaghi, O.K., He, N., Hayashi, H., Houndonougbo, Y., Asta, M., Laird, B.B., Yaghi, O.M.: A combined experimental-computational investigation of carbon dioxide capture in a series of isoreticular zeolitic imidazolate frameworks. J. Am. Chem. Soc. **132**, 11006–11008 (2010). https://doi.org/10.1021/ja104035j

Nabavi, S.A., Vladisavljević, G.T., Wicaksono, A., Georgiadou, S., Manović, V.: Production of molecularly imprinted polymer particles with amide-decorated cavities for CO2 capture using membrane emulsification/suspension polymerisation. Colloids Surf. A Physicochem. Eng. Asp. **521**, 231–238 (2017a). https://doi.org/10.1016/j.colsurfa.2016.05.033

Nabavi, S.A., Vladisavljević, G.T., Zhu, Y., Manović, V.: Synthesis of size-tunable CO2-Philic imprinted polymeric particles (MIPs) for low-pressure CO2 capture using oil-in-oil suspension polymerization. Environ. Sci. Technol. 51, 11476–11483 (2017b). https://doi.org/10.1021/acs.est.7b03259

Nasrollahzadeh, M., Issaabadi, Z., Sajjadi, M., Sajadi, S.M., Atarod, M.: Types of nanostructures. In: Interface Science and Technology, pp. 29–80. Elsevier Ltd. (2019)

Nayebi, R., Daneshvar Tarigh, G., Shemirani, F.: Porous ionic liquid polymer: a reusable adsorbent with broad operating pH range for speciation of nitrate and nitrite. Sci. Rep. **9**, 11130 (2019). https://doi.org/10.1038/s41598-019-47648-w

Nissilä, T., Karhula, S.S., Saarakkala, S., Oksman, K.: Cellulose nanofiber aerogels impregnated with bio-based epoxy using vacuum infusion: structure, orientation and mechanical properties. Compos. Sci. Technol. **155**, 64–71 (2018). https://doi.org/10.1016/j.compscitech.2017.12.001

O'Reilly, N., Giri, N., James, S.L.: Porous liquids. Chem. A Eur. J. **13**, 3020–3025 (2007). https://doi.org/10.1002/chem.200700090

Olajire, A.A.: Synthesis of bare and functionalized porous adsorbent materials for CO2 capture (2017)

Pal, T.K., De, D., Bharadwaj, P.K.: Metal–organic frameworks for the chemical fixation of CO2 into cyclic carbonates (2020)

Peh, S.B., Wang, Y., Zhao, D.: Scalable and sustainable synthesis of advanced porous materials. ACS Sustain. Chem. Eng. **7**, 3647–3670 (2019). https://doi.org/10.1021/acssuschemeng.8b05463

Pichon, V., Delaunay, N., Combès, A.: Sample preparation using molecularly imprinted polymers. Anal. Chem. **92**, 16–33 (2020). https://doi.org/10.1021/acs.analchem.9b04816

Qian, W., Texter, J., Yan, F.: Frontiers in poly(ionic liquid)s: syntheses and applications. Chem. Soc. Rev. **46**, 1124–1159 (2017). https://doi.org/10.1039/c6cs00620e

Qian, L., Yang, M., Chen, H., Xu, Y., Zhang, S., Zhou, Q., He, B., Bai, Y., Song, W.: Preparation of a poly(ionic liquid)-functionalized cellulose aerogel and its application in protein enrichment and separation. Carbohydr. Polym. **218**, 154–162 (2019). https://doi.org/10.1016/j.carbpol.2019.04.081

Qin, L., Wang, B., Zhang, Y., Chen, L., Gao, G.: Anion exchange: a novel way of preparing hierarchical porous structure in poly(ionic liquid)s. Chem. Commun. **53**, 3785–3788 (2017). https://doi.org/10.1039/C6CC10158E

Ramos, V.C., Han, W., Zhang, X., Zhang, S., Yeung, K.L.: Supported ionic liquids for air purification (2020)

Rodríguez-Dorado, R., López-Iglesias, C., García-González, C.A., Auriemma, G., Aquino, R.P., Del Gaudio, P.: Design of aerogels, cryogels and xerogels of alginate: effect of molecular weight, gelation conditions and drying method on particles' micromeritics. Molecules **24**, 1049 (2019). https://doi.org/10.3390/molecules24061049

Rodrigues, D.M., dos Santos, L.M., Bernard, F.L., Pinto, I.S., Zampiva, R., Kaufmann, G., Einloft, S.: Imidazolium-based ionic liquid silica xerogel as catalyst to transform CO2 into cyclic carbonate. SN Appl. Sci. **2**, 1–11 (2020). https://doi.org/10.1007/s42452-020-03712-z

Sang, Y., Huang, J.: Benzimidazole-based hyper-cross-linked poly(ionic liquid)s for efficient CO2 capture and conversion. Chem. Eng. J. **385**, 123973 (2020). https://doi.org/10.1016/j.cej.2019.123973

Sarpong, K.A., Xu, W., Huang, W., Yang, W.: The development of molecularly imprinted polymers in the clean-up of water pollutants: a review. Am. J. Anal. Chem. **10**, 202–226 (2019). https://doi.org/10.4236/ajac.2019.105017

Shimomura, T., Takamuku, T., Yamaguchi, T.: Clusters of imidazolium-based ionic liquid in benzene solutions. J. Phys. Chem. B. **115**, 8518–8527 (2011). https://doi.org/10.1021/jp203422z

Singh, G., Lee, J., Karakoti, A., Bahadur, R., Yi, J., Zhao, D., AlBahily, K., Vinu, A.: Emerging trends in porous materials for CO2 capture and conversion. Chem. Soc. Rev. **49**, 4360–4404 (2020). https://doi.org/10.1039/D0CS00075B

Song, Y., Sun, Q., Aguila, B., Ma, S.: Optimizing the performance of porous pyridinium frameworks for carbon dioxide transformation. Catal. Today. **356**, 557–562 (2020). https://doi.org/10.1016/j.cattod.2020.01.031

Song, H., Wang, Y., Liu, Y., Chen, L., Feng, B., Jin, X., Zhou, Y., Huang, T., Xiao, M., Huang, F., Gai, H.: Conferring Poly(ionic liquid)s with High Surface Areas for Enhanced Catalytic Activity. ACS Sustain. Chem. Eng. **9**, 2115–2128 (2021). https://doi.org/10.1021/acssuschemeng.0c07399

Soorbaghi, F.P., Isanejad, M., Salatin, S., Ghorbani, M., Jafari, S., Derakhshankhah, H.: Bioaerogels: synthesis approaches, cellular uptake, and the biomedical applications. Biomed. Pharmacother. **111**, 964–975 (2019). https://doi.org/10.1016/j.biopha.2019.01.014

Spigarelli, B.P., Kawatra, S.K.: Opportunities and challenges in carbon dioxide capture. J. CO2 Util. **1**, 69–87 (2013). https://doi.org/10.1016/j.jcou.2013.03.002

Stock, N., Biswas, S.: Synthesis of metal-organic frameworks (MOFs): routes to various MOF topologies, morphologies, and composites. https://pubs.acs.org/sharingguidelines (2012)

Sun, J., Cheng, W., Fan, W., Wang, Y., Meng, Z., Zhang, S.: Reusable and efficient polymer-supported task-specific ionic liquid catalyst for cycloaddition of epoxide with CO2. Catal. Today. **148**, 361–367 (2009). https://doi.org/10.1016/j.cattod.2009.07.070

Sun, J., Wang, J., Cheng, W., Zhang, J., Li, X., Zhang, S., She, Y.: Chitosan functionalized ionic liquid as a recyclable biopolymer-supported catalyst for cycloaddition of CO2. Green Chem. **14**, 654 (2012). https://doi.org/10.1039/c2gc16335g

Sun, J.K., Antonietti, M., Yuan, J.: Nanoporous ionic organic networks: from synthesis to materials applications. Chem. Soc. Rev. **45**, 6627–6656 (2016). https://doi.org/10.1039/c6cs00597g

Sun, Y., Huang, H., Vardhan, H., Aguila, B., Zhong, C., Perman, J.A., Al-Enizi, A.M., Nafady, A., Ma, S.: Facile approach to graft ionic liquid into MOF for improving the efficiency of CO2

chemical fixation. ACS Appl. Mater. Interfaces. **10**, 27124–27130 (2018). https://doi.org/10.1021/acsami.8b08914

Sun, Q., Zhu, L., Aguila, B., Thallapally, P.K., Xu, C., Chen, J., Wang, S., Rogers, D., Ma, S.: Optimizing radionuclide sequestration in anion nanotraps with record pertechnetate sorption. Nat. Commun. **10**, 1–9 (2019a). https://doi.org/10.1038/s41467-019-09630-y

Sun, Y., Feng, X., Hu, J., Bo, S., Zhang, J., Wang, W., Li, S., Yang, Y.: Preparation of hemoglobin (Hb)-imprinted poly(ionic liquid)s via Hb-catalyzed eATRP on gold nanodendrites. Anal. Bioanal. Chem. **412**, 983–991 (2019b). https://doi.org/10.1007/s00216-019-02324-w

Sun, L., Luo, J., Gao, M., Tang, S.: Bi-functionalized ionic liquid porous copolymers for CO2 adsorption and conversion under ambient pressure. React. Funct. Polym. **154**, 104636 (2020). https://doi.org/10.1016/j.reactfunctpolym.2020.104636

Sun, M., Feng, J., Han, S., Ji, X., Li, C., Feng, J., Sun, H., Fan, J.: Poly(ionic liquid)-hybridized silica aerogel for solid-phase microextraction of polycyclic aromatic hydrocarbons prior to gas chromatography-flame ionization detection. Microchim. Acta. **188** (2021). https://doi.org/10.1007/s00604-021-04730-3

Tashakkori, P., Erdem, P., Seyhan Bozkurt, S.: Molecularly imprinted polymer based on magnetic ionic liquid for solid-phase extraction of phenolic acids. J. Liq. Chromatogr. Relat. Technol. **40**, 657–666 (2017). https://doi.org/10.1080/10826076.2017.1343732

Tharun, J., Bhin, K.-M., Roshan, R., Kim, D.W., Kathalikkattil, A.C., Babu, R., Ahn, H.Y., Won, Y.S., Park, D.-W.: Ionic liquid tethered post functionalized ZIF-90 framework for the cycloaddition of propylene oxide and CO2. Green Chem. **18**, 2479–2487 (2016). https://doi.org/10.1039/C5GC02153G

Viveiros, R., Karim, K., Piletsky, S.A., Heggie, W., Casimiro, T.: Development of a molecularly imprinted polymer for a pharmaceutical impurity in supercritical CO2: Rational design using computational approach. J. Clean. Prod. **168**, 1025–1031 (2017). https://doi.org/10.1016/j.jclepro.2017.09.026

Viveiros, R., Rebocho, S., Casimiro, T.: Green strategies for molecularly imprinted polymer development. Polymers (basel). **10**, 1–27 (2018). https://doi.org/10.3390/polym10030306

Wang, S., Wang, X.: Imidazolium ionic liquids, imidazolylidene heterocyclic carbenes, and zeolitic imidazolate frameworks for CO2 capture and photochemical reduction. Angew. Chemie Int. Ed. **55**, 2308–2320 (2016). https://doi.org/10.1002/anie.201507145

Wang, T., Wang, W., Lyu, Y., Chen, X., Li, C., Zhang, Y., Song, X., Ding, Y.: Highly recyclable polymer supported ionic liquids as efficient heterogeneous catalysts for batch and flow conversion of CO2 to cyclic carbonates. RSC Adv. **7**, 2836–2841 (2017). https://doi.org/10.1039/c6ra26780g

Wang, Y., Guo, L., Yin, L.: Progress in the heterogeneous catalytic cyclization of CO2 with epoxides using immobilized ionic liquids. Catal. Letters. **149**, 985–997 (2019a). https://doi.org/10.1007/s10562-019-02669-y

Wang, Y., Su, Y., Wang, W., Fang, Y., Riffat, S.B., Jiang, F.: The advances of polysaccharide-based aerogels: preparation and potential application. Carbohydr. Polym. **226**, 1–13 (2019b). https://doi.org/10.1016/j.carbpol.2019.115242

Wang, L., Chen, J., Li, X., Chen, L., Zhang, K., Wang, X., Zhu, G.: Eco-friendly ionic liquid imprinted polymer based on a green synthesis strategy for highly selective adsorption tylosin in animal muscle samples. Environ. Sci. Pollut. Res. **28**, 16470–16479 (2021). https://doi.org/10.1007/s11356-020-11842-5

Watile, R.A., Deshmukh, K.M., Dhake, K.P., Bhanage, B.M.: Efficient synthesis of cyclic carbonate from carbon dioxide using polymer anchored diol functionalized ionic liquids as a highly active heterogeneous catalyst. Catal. Sci. Technol. **2**, 1051–1055 (2012). https://doi.org/10.1039/c2cy00458e

Wei, X., Wang, Y., Chen, J., Ni, R., Meng, J., Liu, Z., Xu, F., Zhou, Y.: Ionic liquids skeleton typed magnetic core-shell molecularly imprinted polymers for the specific recognition of lysozyme. Anal. Chim. Acta. **1081**, 81–92 (2019). https://doi.org/10.1016/j.aca.2019.07.025

Wei, J., Yuan, X., Zhang, Y., Liu, H., Sun, B.: Ionic liquid-sensitized molecularly imprinted polymers based on heteroatom co-doped quantum dots functionalized graphene for sensitive detection of λ-cyhalothrin. Anal. Chim. Acta. **1136**, 9–18 (2020). https://doi.org/10.1016/j.aca.2020.08.041

Wu, X., Du, J., Li, M., Wu, L., Han, C., Su, F.: Recent advances in green reagents for molecularly imprinted polymers. RSC Adv. **8**, 311–327 (2018). https://doi.org/10.1039/c7ra11047b

Wu, J., Xu, F., Li, S., Ma, P., Zhang, X., Liu, Q., Fu, R., Wu, D.: Porous polymers as multifunctional material platforms toward task-specific applications. Adv. Mater. **31**, 1–45 (2019). https://doi.org/10.1002/adma.201802922

Xiang, W., Shen, C., Lu, Z., Chen, S., Li, X., Zou, R., Zhang, Y., Liu, C.: jun: CO2 cycloaddition over ionic liquid immobilized hybrid zeolitic imidazolate frameworks: Effect of Lewis acid/base sites. Chem. Eng. Sci. **233**, 116429 (2021). https://doi.org/10.1016/j.ces.2020.116429

Xie, L., Jin, Z., Dai, Z., Chang, Y., Jiang, X., Wang, H.: Porous carbons synthesized by templating approach from fluid precursors and their applications in environment and energy storage: a review (2020a)

Xie, Y., Ding, K., Liu, Z., Li, J., An, G., Tao, R., Sun, Z., Yang, Z.: The immobilization of glycidyl-group-containing ionic liquids and its application in CO2 cycloaddition reactions. Chem. - A Eur. J. **16**, 6687–6692 (2010b). https://doi.org/10.1002/chem.201000020

Xie, Y., Liang, J., Fu, Y., Huang, M., Xu, X., Wang, H., Tu, S., Li, J.: Hypercrosslinked mesoporous poly(ionic liquid)s with high ionic density for efficient CO2 capture and conversion into cyclic carbonates. J. Mater. Chem. A. **6**, 6660–6666 (2018). https://doi.org/10.1039/c8ta01346b

Xin, B., Hao, J.: Imidazolium-based ionic liquids grafted on solid surfaces. Chem. Soc. Rev. **43**, 7171–7187 (2014). https://doi.org/10.1039/C4CS00172A

Xu, D., Guo, J., Yan, F.: Porous ionic polymers: design, synthesis, and applications (2018)

Yang, X.Y., Chen, L.H., Li, Y., Rooke, J.C., Sanchez, C., Su, B.L.: Hierarchically porous materials: synthesis strategies and structure design. Chem. Soc. Rev. **46**, 481–558 (2017). https://doi.org/10.1039/c6cs00829a

Yang, Y., Sun, Y., Jin, M., Bai, R., Liu, Y., Wu, Y., Wang, W., Feng, X., Li, S.: Fabrication of superoxide dismutase (SOD) imprinted Poly(ionic liquid)s via eATRP and its application in electrochemical sensor. Electroanalysis **32**, 1772–1779 (2020). https://doi.org/10.1002/elan.201900764

Yin, M.-J., Zhao, Q., Wu, J., Seefeldt, K., Yuan, J.: Precise micropatterning of a porous Poly(ionic liquid) via maskless photolithography for high-performance nonenzymatic H$_2$O$_2$ sensing. ACS Nano **12**, 12551–12557 (2018). https://doi.org/10.1021/acsnano.8b07069

Yuan, J., Antonietti, M.: Poly(ionic liquid)s: polymers expanding classical property profiles. Polymer (guildf). **52**, 1469–1482 (2011). https://doi.org/10.1016/j.polymer.2011.01.043

Zhang, Y., Yin, S., Luo, S., Au, C.T.: Cycloaddition of CO2 to epoxides catalyzed by carboxyl-functionalized imidazolium-based ionic liquid grafted onto cross-linked polymer. Ind. Eng. Chem. Res. **51**, 3951–3957 (2012). https://doi.org/10.1021/ie203001u

Zhang, J., Chai, S.-H., Qiao, Z.-A., Mahurin, S.M., Chen, J., Fang, Y., Wan, S., Nelson, K., Zhang, P., Dai, S.: Porous liquids: a promising class of media for gas separation. Angew. Chemie Int. Ed. **54**, 932–936 (2015a). https://doi.org/10.1002/anie.201409420

Zhang, S., Dokko, K., Watanabe, M.: Carbon materialization of ionic liquids: from solvents to materials (2015b)

Zhang, S., Dokko, K., Watanabe, M.: Porous ionic liquids: synthesis and application (2015c). www.rsc.org/chemicalscience

Zhang, X.Q., Li, W.C., Lu, A.H.: Designed porous carbon materials for efficient CO2 adsorption and separation. Xinxing Tan Cailiao/new Carbon Mater. **30**, 481–501 (2015d). https://doi.org/10.1016/S1872-5805(15)60203-7

Zhang, W., Zhao, Q., Yuan, J.: Porous polyelectrolytes: the interplay of charge and pores for new functionalities. Angew. Chemie - Int. Ed. **57**, 6754–6773 (2018). https://doi.org/10.1002/anie.201710272

Zhang, W., Ma, F., Ma, L., Zhou, Y., Wang, J.: Imidazolium-functionalized Ionic hyper-crosslinked porous polymers for efficient synthesis of cyclic carbonates from simulated flue gas. Chemsuschem **13**, 341–350 (2020). https://doi.org/10.1002/cssc.201902952

Zhang, X., Gao, L., Niu, L., Bi, X.: Microwave-assisted preparation of a molecularly imprinted monolith combining an imidazolium ionic liquid and POSS for enhanced extraction of baicalin-like compounds in Scutellaria baicalensis by means of in-capillary SPME followed by on-line LC and off-l. New J. Chem. **45**, 5195–5205 (2021). https://doi.org/10.1039/d0nj06254e

Zhao, Y., Shen, Y., Bai, L., Hao, R., Dong, L.: Synthesis and CO2 adsorption properties of molecularly imprinted adsorbents. Environ. Sci. Technol. **46**, 1789–1795 (2012). https://doi.org/10.1021/es203580b

Zhao, Y., Shen, Y., Ma, G., Hao, R.: Adsorption separation of carbon dioxide from flue gas by a molecularly imprinted adsorbent. Environ. Sci. Technol. **48**, 1601–1608 (2014). https://doi.org/10.1021/es403871w

Zhao, S., Malfait, W.J., Guerrero-Alburquerque, N., Koebel, M.M., Nyström, G.: Biopolymer aerogels and foams: chemistry, properties, and applications. Angew. Chemie - Int. Ed. **57**, 7580–7608 (2018). https://doi.org/10.1002/anie.201709014

Zhou, X., Weber, J., Yuan, J.: Poly(ionic liquid)s: platform for CO2 capture and catalysis. Curr. Opin. Green Sustain. Chem. **16**, 39–46 (2019). https://doi.org/10.1016/j.cogsc.2018.11.014

Zhu, J., Xin, F., Huang, J., Dong, X., Liu, H.: Adsorption and diffusivity of CO2 in phosphonium ionic liquid modified silica. Chem. Eng. J. **246**, 79–87 (2014). https://doi.org/10.1016/j.cej.2014.02.057

Zhu, X., Zeng, Y., Zhang, Z., Yang, Y., Zhai, Y., Wang, H., Liu, L., Hu, J., Li, L.: A new composite of graphene and molecularly imprinted polymer based on ionic liquids as functional monomer and cross-linker for electrochemical sensing 6-benzylaminopurine. Biosens. Bioelectron. **108**, 38–45 (2018). https://doi.org/10.1016/j.bios.2018.02.032

Zhu, G., Li, W., Wang, L., Wang, P., Shi, D., Wang, J., Fan, J.: Using ionic liquid monomer to improve the selective recognition performance of surface imprinted polymer for sulfamonomethoxine in strong polar medium. J. Chromatogr. A. **1592**, 38–46 (2019). https://doi.org/10.1016/j.chroma.2019.01.053

Zhu, G., Li, W., Wang, P., Cheng, G., Chen, L., Zhang, K., Li, X.: One-step polymerization of hydrophilic ionic liquid imprinted polymer in water for selective separation and detection of levofloxacin from environmental matrices. J. Sep. Sci. **43**, 639–647 (2020). https://doi.org/10.1002/jssc.201900813

Zulfiqar, S., Sarwar, M.I., Mecerreyes, D.: Polymeric ionic liquids for CO2 capture and separation: potential, progress and challenges. Polym. Chem. **6**, 6435–6451 (2015). https://doi.org/10.1039/C5PY00842E

Physical and Mathematical Modelling of Fluid and Heat Transport Phenomena in Porous Media

S. Anitha, Moorthi Pichumani, and Tiju Thomas

Abstract Heat transport finds use in several applications including heat exchangers, marine units, food processing units, oil and gas industries, petroleum industries and so on. By providing a large surface area and irregular motion in flow, made possible by porous media and enhances the thermal efficiency. The addition of a single type of nanosized particles in the base fluid gives rise to nanofluids. It tends to have higher thermal conductivity than the base fluid. However, currently hybrid nanofluids are introduced to overcome the disadvantages associated with nanofluids such as lower chemical stability, lower corrosion-resistant and so on. Hybrid nanofluids consist of dissimilar nanoparticles. Here, the heat transfer performance of nanofluids and hybrid nanofluids which flow through porous media is discussed. In addition, the role of the external magnetic field on the heat transfer performance of nanofluids with porous media is also explored. The relation between important parameters like Darcy number, porosity, Hartmann number, Reynolds number, Biot number and heat transfer performance of fluids with porous media is duly discussed. This chapter focuses on the role of porous media in enhancing heat transfer performance of nanofluids and hybrid nanofluids when flow occurs through different geometries.

Keywords Nanofluid · Hybrid nanofluid · Porous media · Magneto-hydrodynamics · Heat transfer · Darcy and non-Darcy model

S. Anitha · M. Pichumani
Department of Nanoscience and Technology, Sri Ramakrishna Engineering College, Coimbatore, Tamil Nadu, India
e-mail: anithamaths@srec.ac.in

M. Pichumani
e-mail: mpichumani@srec.ac.in

T. Thomas (✉)
Department of Metallurgical and Materials Engineering, Indian Institute of Technology, Chennai, Tamil Nadu, India
e-mail: tijuthomas@iitm.ac.in; tt332@cornell.edu

661

1   Introduction

For nearly two decades, heat transfer performance (HTP) of nanofluids in heat exchangers has been investigated and the outcomes have made their industrial deployment viable today. Several researchers have reported improvements in HTP of heat exchangers with the usage of nanofluids (Angayarkanni et al. 2015; Cho 2020; Elshorbagy et al. 2021; Chamkha 1997; Ali et al. 2020; Ameri et al. 2018). Flow of nanofluids through porous media is quite interesting and offers several possibilities for enhancing HTP.

Porous media is composed of a solid phase with connected voids. It is used in many engineering domains such as environmental, transpiration cooling, and as porous burners in mechanical engineering, petroleum and chemical engineering, geological engineering, etc. Being a heterogeneous medium, this system is made of a solid phase and its voids (pore) are filled with fluids, which are classified as continuum transport systems (see Fig. 1). Such systems exist in nature (rocks, sand beds, wood) or can even be fabricated (pellets, catalytic, wicks, membrane). The size of a pore is classified as small, large and very large. Generally, the voids are distributed non-uniformly. Detailed note on the relation between these specifications and the heat transfer behaviour of the fluid is available in the literature (Adler 1992) and is beyond the scope of this specific chapter.

To describe porous structure in nanofluid flow, the main concept used is that of 'porosity' (ε), which is the fraction between volume of void and the total volume of the porous media (void along with solid phase) (Eq. 1) (Dullien 1992; Kaviany 1992).

$$\varepsilon = \frac{V_{\text{void}}}{V_{\text{total}} \, (V_{\text{void}} + V_{\text{solid}})} \tag{1}$$

For example, the porosity of the soil is between 0.44 and 0.45, whereas it is 0.02–0.12 for coal.

Fig. 1 Structure of porous medium. The porous medium is at least biphasic system and the pore size is not uniform
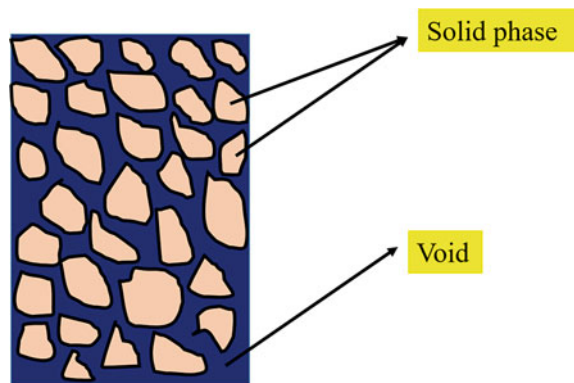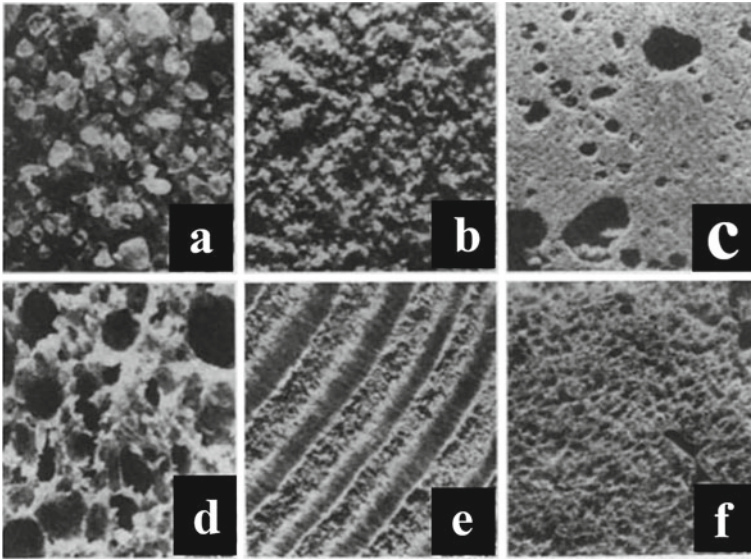
Fig. 2 Examples of porous media **a** beach sand, **b** sandstone, **c** limestone, **d** rye bread, **e** wood and **f** human lung. Reproduced from Dullien (1992) with permission of Elsevier

This porosity is constant for rigid matrices (non-deformable), and it is variable for the deformable matrices, i.e. $\frac{\partial \varepsilon}{\partial p} \neq 0$, where p is the external pressure. Common terms and symbols used in this chapter are explained in the section 'nomenclature and symbols used' (Sect. 7).

In general, three types of pores are defined (a) micro-porous (≤ 2 nm), (b) meso-porous (between 2 and 50 nm) and (c) macro-porous (≥ 50 nm). The former one is named as micro-pores or ultra-micro-pores, whereas the latter is termed as caverns. Earlier reports revealed that the porous media which have a micro-pores possess a higher heat transfer rate (Ewing et al. 2009).

It is very common to encounter porous media in everyday life. For instance, Fig. 2 represents the porous media that are seen in nature (Dullien 1992). The pores (with asymmetric shapes) are randomly distributed inside the porous media, and the distribution of the pores is not uniform.

2 Governing Parameters

The following parameters are used to explain the heat transport phenomena of fluids with porous media. Many of the following parameters are non-dimensional numbers.

2.1 Nusselt Number (Nu)

Nu represents the ratio between heat transfer of a fluid through convection to the transfer that occurs owing to conduction. For a lower *Nu* values, conduction-based heat transfer occurs. Likewise for larger values of *Nu*, convection-based heat transfer dominates. In general, *Nu* is defined as follows:

$$Nu = \frac{\text{Convective heat transfer}}{\text{Conductive heat transfer}}$$
$$Nu = \frac{h\Delta T}{k\frac{(\Delta T)}{L}} = \frac{hL}{k} \tag{2}$$

In Eq. 2, h is the coefficient of heat transfer, L is the length of the geometry, k is the thermal conductivity of the fluid, and ΔT is the temperature difference between the wall and the fluid.

2.2 Rayleigh Number (Ra)

Ra is related to buoyancy force in the case of free or natural convection. The flow is said to be laminar if *Ra* is less than a specific critical number. The flow is said to be turbulent if it is greater than the critical number. The mathematical expression of *Ra* is as follows:

$$Ra = \frac{g\beta d^3 \Delta T}{\alpha \gamma_f} \tag{3}$$

In Eq. 3, g is the acceleration due to gravity, β is the thermal expansion coefficient, ΔT is the temperature difference, α is the thermal diffusivity, and γ_f is the kinematic viscosity of the fluid. Also, below a certain critical value, the mode of heat transfer is by conduction rather than convection.

2.3 Richardson Number (Ri)

Richardson number is a dimensionless number, which expresses the relationship between buoyancy force and flow shear term. A low value of *Ri* denotes the high degree of turbulence. Mathematically, it is termed as

$$Ri = \frac{g\beta(T_h - T_{ref})L}{v^2} \tag{4}$$

In Eq. 4, g is the gravitational force, β is the thermal expansion coefficient, T_h is the hot wall temperature, and T_{ref} denotes the reference temperature. L is the characteristic length of the geometry (based on convective flow direction), and v is the velocity of the fluid.

Also, Richardson number (Ri) is defined as the combination of Grashof number (Gr) and Reynolds number (Re) (both numbers will be defined below). In this context, it can be written as follows:

$$Ri = \frac{Gr}{Re^2}.$$

2.4   Grashof Number (Gr)

In natural convection, Gr is defined to identify whether the flow is laminar or turbulent.

$$Gr = \frac{g\beta_f L^3 (T_h - T_c)}{\gamma_f^2}. \tag{5}$$

In Eq. 5, g, β, L are acceleration due to gravity force, thermal expansion coefficient and characteristic length (in the direction of the flow), respectively. T_h is the hot temperature and T_c is the cold temperature. γ_f is the kinematic viscosity of the fluid. If Gr is greater than 10^9, then the flow is turbulent. Rayleigh number can be expressed in terms of Grashof number (Gr) and Prandtl number (Pr).

i.e. $Ra = Gr.Pr$

Prandtl number is the ratio between momentum diffusivity (γ) and the thermal diffusivity (α) , and it is given as

$$Pr = \frac{\gamma}{\alpha} = \frac{\text{momentum diffusivity}}{\text{thermal diffusivity}} = \frac{\mu/\rho}{k/c_p\rho} = \frac{c_p\mu}{k} \tag{6}$$

Here μ is the dynamic viscosity, ρ is the density, k is the thermal conductivity, c_p is the specific heat at constant pressure. Momentum diffusivity (γ) is also known as kinematic viscosity, and it is the ratio between dynamic viscosity and density of fluid. Thermal diffusivity (α) is a ratio between thermal conductivity and the product of specific heat capacity at constant pressure along with density of fluid.

2.5 Reynolds Number (Re)

Re gives the relationship between inertial and viscous force. In such cases, the impact of viscosity is a crucial phenomenon for the control over the fluid flow pattern.

$$Re = \frac{UL}{\gamma_f} \tag{7}$$

In Eq. 7, U, L are the uniform velocity of the fluid and the characteristic length of the geometry. γ_f is the kinematic viscosity of the fluid. When a fluid flows through a geometry say a pipe, channel, cavity and so on, it can be categorized into two basic flows, namely laminar and turbulent. Compared to laminar flow, turbulent flow increases the heat transfer performance of the fluid and it is due to the increase in Reynolds number. The turbulent effects become a dominant factor over secondary flow at higher Reynolds number. It is to be noted that in general the fluid flow is said to be laminar, if the Reynolds number is lower than 2000. And it is said to be turbulent if the Reynolds number is higher than 2000.

2.6 Hartmann Number (Ha)

Ha provides the relative importance of drag forces resulting from magnetic induction and viscous forces in Hartmann flow. It is the ratio between electromagnetic force and the viscous force. The *Ha* is defined as given below:

$$Ha = BL\sqrt{\frac{\sigma}{\mu}} \tag{8}$$

B is the strength of the magnetic field intensity. L is the characteristic length. σ is the electrical conductivity, and μ is the dynamic viscosity of fluid.

2.7 Darcy Number (Da)

Darcy number is the ratio between the permeability (ability of the fluid to flow) of the porous medium (K) and the characteristic length (L).

$$Da = \frac{K}{L} \tag{9}$$

Permeability is a property of the media which measures the capability of the formation to transit fluid. It is dependent on the size of the pores. It is commonly

used in heat transfer through porous media. (For more information associated with heat transfer performance and Darcy number please refer Sect. 4.)

3   Heat Transfer of Nanofluids with Porous Media

In general, nanofluids (NFs) are applied in many areas and a wide range of applications of NFs are shown in Fig. 3 (Angayarkanni et al. 2015). Nevertheless, nanofluids are used in automobile technologies (as coolants), electronics (cooling of microchips and micro-scale fluidic application), biomedical engineering (nano-drug delivery, cancer therapeutics and nano-cryosurgery) and in chemical engineering (e.g. as nanofluid detergents).

In addition, the flow and HTP of NFs through porous media are an emerging research topic due to its applications in heating and cooling buildings, automobile industry, heat exchanger, etc. The term nanofluid was first termed by Choi et al. in 1998. Dispersion of nanosized particles (1–100 nm) in a base fluid is named nanofluid. The choice of base fluid may be water, bio-fluids, engine oil, non-Newtonian types of fluids and so on. Based on the applications, the following modes of heat transfer can occur: (a) convection, (b) conduction and (c) radiation. The most efficient mode of heat transfer is the convection mode.

Cho (2020) analysed the free convective heat transfer of NFs in the porous cavity which contains wavy walls with a partially heated surface. This physical model has applications in thermal energy storage, biomedical, geothermal and grain storage. Cu/water nanofluid is used, say in a geometry shown in Fig. 4. In this figure, g
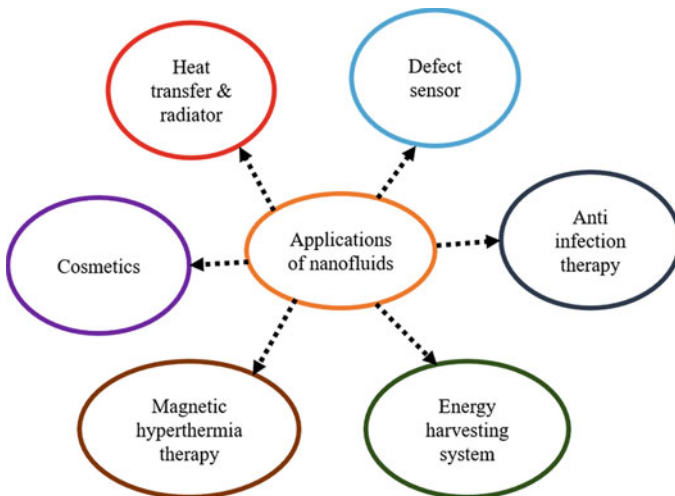
Fig. 3 Applications of nanofluids in various domains **a** radiator, **b** sensor, **c** anti-infection therapy, **d** harvesting system, **e** hyperthermia therapy and **f** cosmetics (Angayarkanni et al. 2015).

Fig. 4 Natural convective heat transfer and entropy generation of system with porous media. Reprinted from Cho (2020).
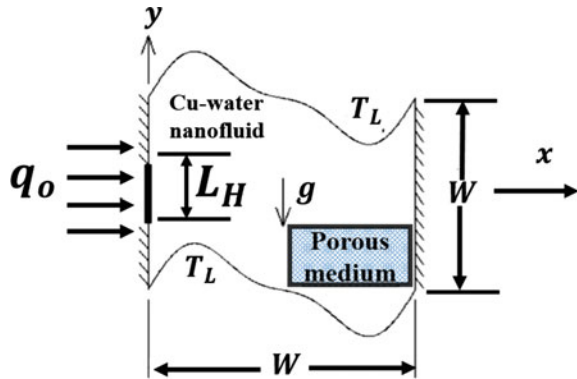
is the gravity, T_L denotes the low temperature and L_H is the length of the wall which is heated partially. W represents the wall, and q_o is the heat flux. The relation between porosity and the HTP of the cavity is discussed and explained; i.e. with an increase in porosity (ε) (refer Eq. 1), the fluid flow through the porous media is enhanced. Consequently, the flow vector increases the circulation of fluid within the cavity. Therefore, the heat transfer between the fluids (in the mode of convection) is increased, thus increasing the Nusselt number.

The relationship between porosity (ε) and the Rayleigh number is as follows (refer Eq. 3). Rayleigh number (Ra) is useful when there is buoyancy-driven flow, and it occurs in the natural convection mode. It is noted that, for smaller values of Ra (refer Eq. 3), the role of porosity on the Nusselt number is very low. It is due to the fact that at lower Ra values, the mode of heat transfer would be conduction, and for higher values, it would be convection. Therefore for $Ra \leq 10^3$, the conductive mode of heat transfer dominates and so the impact on Nu (refer Eq. 2) is not significant (Cho 2020). In general, Ra represents the strength of the buoyancy force. Generally, higher the Ra, larger is the buoyant force. From Fig. 5a, b it is understood that for larger values of Ra and Da (refer Eq. 9) the convection mode of heat transfer is dominant due to the formation of the circular region (see Fig. 5a). This formation is because of the low flow resistance caused by the strong natural convection (produced by strong buoyance force) and the high permeability. Consequently, Nu and HTP of the fluid increase. Likewise lower Ra and Da cause the dominance of conduction mode of heat transfer. Therefore, the Nu and HTP associated with the fluid decrease.

The HTP and mixed convective flow in a trapezoidal channel embedded in porous media (with nanofluid) have attracted attention recently. Solar energy collector is an example that involves trapezoidal enclosure. El-shorbagy et al. (2021) numerically investigated the HTP and NFs flow behaviour in the trapezoidal channel. As seen in Fig. 6, the channel is partially packed with the porous medium, and for two different aspect ratios of the media (0.3 and 0.5), the HTP is analysed numerically.

In general, the momentum equation is derived from Newton's second law $F = ma$. By using this physical principle to the suitable model of the flow, the relevant mathematical equations can be written. F denotes the total forces acting on the fluid.

Fig. 5 Energy flux vectors in partially heated porous wall cavity for **a** $Da = 10^{-6}$ with $Ra = 10^2$ and $Da = 10^{-1}$ with $Ra = 10^6$, **b** $Da = 10^{-1}$ with $Ra = 10^2$ and $Da = 10^{-6}$ with $Ra = 10^6$. For lower values of Ra, no circulation region is created and the conduction heat transfer dominates. Reprinted from Cho (2020)
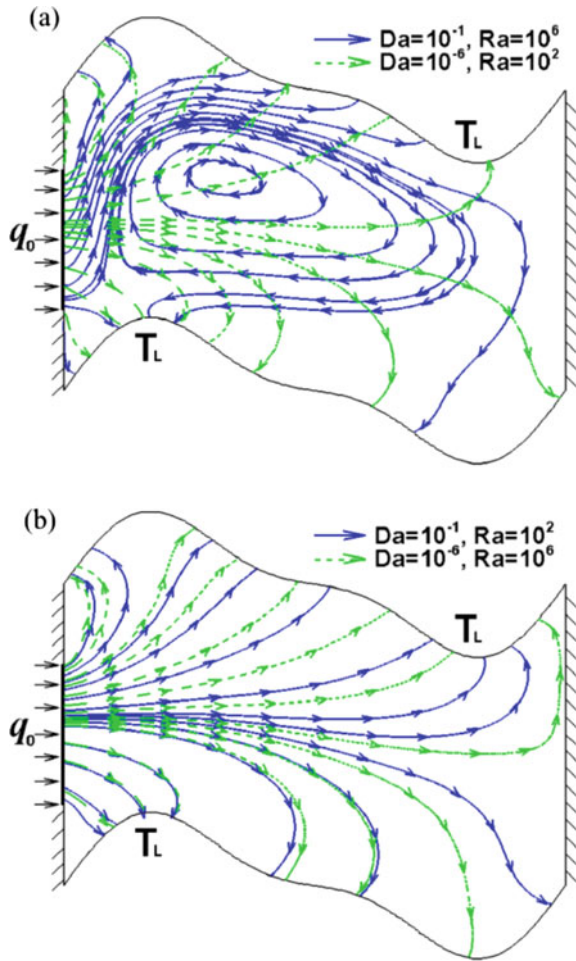
The forces under consideration could be body force or surface force. Gravity (g) and the electromagnetic force (B_o) are some examples of the body forces. Pressure (p) and viscous force (μ) are some of the examples of surface forces.

The momentum equation is derived from the Navier–Stokes equation:

$$\rho \frac{D\vec{V}}{Dt} = -\nabla p + \rho \vec{g} + \mu \nabla^2 \vec{V}. \tag{10}$$

Here $\rho \frac{D\vec{V}}{Dt} = \rho \left[\frac{\partial V}{\partial t} + (V.\nabla)V \right]$

In Eq. 10 $\left(\rho \frac{D\vec{V}}{Dt} \right)$ is the total derivative, and it is the sum of change of velocity with time $\left(\rho \frac{\partial V}{\partial t} \right)$ and the convective term $(\rho(V.\nabla)V)$. ∇p is the pressure gradient. $\vec{g}$

Fig. 6 In the figure, (1) cold wall, (2, 3) adiabatic wall and (4) porous layer. Heat and fluid flow behaviour in a trapezoidal channel with porous medium. For various heights of the porous layer, the heat transfer performance of nanofluid is analysed. The metal foam is used as a porous medium. Reprinted from El-shorbagy et al. (2021)
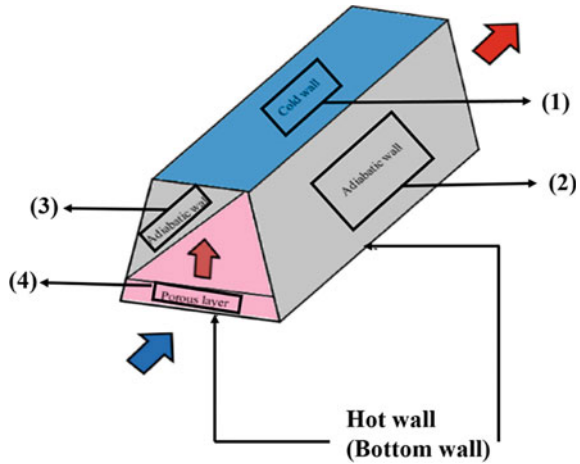
is the body force term. Body force is an external force that acts on the fluid (gravity force or electromagnetic force). $\mu \nabla^2 \vec{V}$ is the diffusion term.

This Eq. 10 can be elaborated in all the velocity directions (say x, y and z).

$$\rho \left[\frac{\partial u}{\partial t} + \frac{\partial u}{\partial x} + \frac{\partial u}{\partial y} + \frac{\partial u}{\partial z} \right] = -\nabla p_x + \mu \left(\frac{\partial^2 u}{\partial x^2} + \frac{\partial^2 u}{\partial y^2} + \frac{\partial^2 u}{\partial z^2} \right) + S_x \quad (10a)$$

$$\rho \left[\frac{\partial v}{\partial t} + \frac{\partial v}{\partial x} + \frac{\partial v}{\partial y} + \frac{\partial v}{\partial z} \right] = -\nabla p_y + \mu \left(\frac{\partial^2 v}{\partial x^2} + \frac{\partial^2 v}{\partial y^2} + \frac{\partial^2 v}{\partial z^2} \right) + S_y \quad (10b)$$

$$\rho \left[\frac{\partial w}{\partial t} + \frac{\partial w}{\partial x} + \frac{\partial w}{\partial y} + \frac{\partial w}{\partial z} \right] = -\nabla p_z + \mu \left(\frac{\partial^2 w}{\partial x^2} + \frac{\partial^2 w}{\partial y^2} + \frac{\partial^2 w}{\partial z^2} \right) + S_z \quad (10c)$$

In these equations, the terms S_x, S_y and S_z are the external force term and it varies dependent on the problem.

On this principal, the momentum equation, which incorporates the influence of body force and the surface forces, is given as (El-shorbagy et al. 2021):

$$\rho_{nf} \left(\frac{\vec{V}}{\varepsilon^2} \right) \nabla \cdot \vec{V} = -\nabla p + \frac{\mu_{nf}}{\varepsilon} \nabla^2 \vec{V} - \frac{\mu_{nf}}{K} \vec{V}$$

$$- \frac{C_F}{\sqrt{k}} \frac{\mu_{nf}}{\varepsilon} \vec{V} \left| \vec{V} \right| - g \rho_{nf} \beta_{nf} (T - T_c) \quad (11)$$

In Eq. 11, p, μ are the pressure force. C_F denotes the Forchheimer coefficient, which is the non-dimensional number that defines the pressure loss which is induced by the friction across porous media. ε stands for the porosity of the medium. $\vec{V}$, K, ρ, γ, β, g, μ and T are the velocity vector, the permeability, density, kinematic viscosity, thermal expansion coefficient of nanofluid, acceleration due to gravity, dynamic

viscosity and the temperature, respectively. The subscript nf denotes the nanofluid. The subscript c denotes cold. The left term of the equation defines the velocity vector in three dimensions, namely x, y and z. The first term $(-\nabla p)$ in the right side denotes the pressure gradient in flow direction and the rate at which pressure increases. The last term $\left(g\rho_{\mathrm{nf}}\beta_{\mathrm{nf}}(T-T_{\mathrm{c}})\right)$ represents the external force (gravity) which acts on the fluid flow. Terms such as $\frac{\mu_{nf}}{\varepsilon}\nabla^2\overrightarrow{V}$, $\frac{\mu_{\mathrm{nf}}}{K}\overrightarrow{V}$, and $\frac{C_F}{\sqrt{k}}\frac{\mu_{\mathrm{nf}}}{\varepsilon}\overrightarrow{V}\left|\overrightarrow{V}\right|$ represent the influence of kinematic viscosity on the porosity and permeability.

Alumina nanofluid is considered a coolant. HTP of the system is analysed by considering Da (10^{-2}, 10^{-3} and 10^{-4}), Ri (refer Eq. 4) (0.1, 1, 10), volume fraction (0–3%). El-shorbagy et al. 2021 adopted the thermal equilibrium model, i.e. temperature gradient between solid and liquid phases is assumed to be negligible. With an increase in the height of the porous medium, the Darcy number increases and so does the Nu; consequently, the HTP of the channel improves as well. Therefore from this investigation, we understand that there exists a relationship between porosity or aspect ratio of the porous medium and the HTP of the system (in which porous medium is embedded). With increase in porosity or aspect ratio of porous media, the heat transfer rate increases. Nevertheless, the pore size distribution significantly influences the HTP of fluid flow through porous media (El-shorbagy et al. 2021).

4 Role of the Magnetic Force on Heat Transfer of Nanofluid with Porous Media

Based on the literature, it is noted that the HTP of any system is highly pronounced with the effect of external magnetic force. This force induces current in the continuum fluid flow, and consequently, an opposite force on the fluid is induced. This force can either increase or decrease the heat transfer performance. For instance, the thermal performance of Fe_2O_3/water and Fe_3O_4/water nanofluids is investigated with the presence and absence of magnetic field (Amar et al. 2015). The volume fraction of the nanoparticles is varied from 0 to 4.8%. Without magnetic field, thermal conductivity of both nanofluids is found to increase. However, in the presence of magnetic field, the thermal conductivity decreases with increase in temperature of the fluid and the detail discussions can be found below. In this section, we will understand the relation between external magnetic field and the HTP of the nanofluid with porous media. Ali J. Chamka 1997 is the first researcher who studied the role of magnetic fields on NFs with porous media. Free convection flow over a flat plate (which is vertical in position) in a porous medium is analysed. Ali included the Darcian and non-Darcian (law) effect along with the Hall current effects (Hall current effect is induced with the presence of magnetic field).

The Darcy law expresses the fluid flow in porous media. It gives the linear relationship between velocity and the pressure gradient.

$$\text{i.e. } u = -\frac{k}{\mu}\nabla p. \tag{12}$$

Here u is the velocity and ∇p is the pressure gradient, k, μ are the thermal conductivity and viscosity of the fluid.

The flow which obeys this law is known as the Darcian flow, and it is observed only for $Re < 10$. However, most industrial applications involve higher velocity flows. In such cases, Eq. 12 is not valid and nonlinear terms must be included, and it is shown in Eq. 13. This kind of flow is known as the non-Darcian flow, and it is defined as:

$$-\nabla p = \frac{\mu}{k}u + \beta\rho u|u| \tag{13}$$

where $\beta = \frac{C_F}{\sqrt{k}}$

β is an inertial resistance coefficient and C_F is the Forchheimer parameter (non-dimensional number). So, the study on the non-Darcian effect/flow for mixed convection/free convection HTP in various geometries has to be explored.

Mixed convection in a trapezoidal enclosure with a rotating cylinder is evaluated numerically, and the geometry is shown in Fig. 7 (Ali et al. 2020). This system is used in solidification processes and food processing units. The nanofluids are saturated with porous media. The influence of Darcy number and Richardson number (Ri) is evaluated by varying volume fraction of nanoparticles. Darcy number is varied from 10^{-5} to 10^{-1}, and the maximum heat transfer attained is at 10^{-1}. However, Darcy number is varied from 10^{-4} to 10^{-2} by El-shorbagy et al. (2021) and the maximum HTP is attained at 10^{-2}. The precise Darcy number at which heat transfer becomes maximum is dependent on the geometry. Also, the thermal efficiency is reported with

Fig. 7 Schematic of the trapezoidal enclosure. Effect of external magnetic field (B) on the heat transfer performance of nanofluid is analysed. Reprinted from Ali et al. (2020).
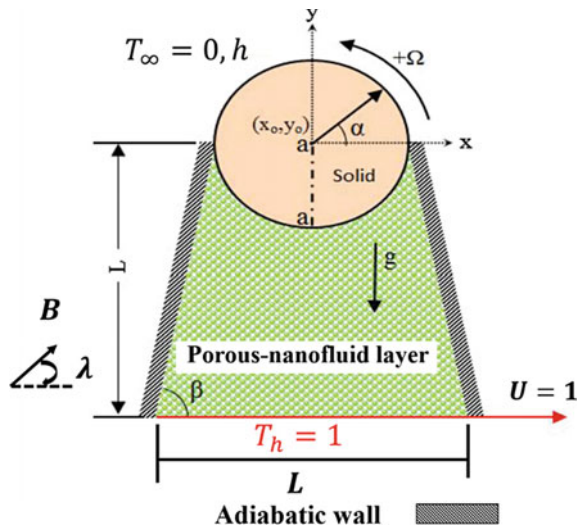
the variations in Hartmann number (Ha) and it is shown that, the external magnetic force significantly influences the fluid flow and HTP inside the enclosure. From these studies, it can be seen that efficiency of the HTP of the system is influenced by porosity, Darcy number and the external force which is applied on the fluid flow.

Heat transport through porous media with applied magnetic field have been examined for various engineering applications. For example, recently HTP between the 'novel flat plate collector' and 'rival flat plate collector' is studied experimentally (Ameri et al. 2018). The flat plate collector (FPC) which contains NF and porous media along with constant magnetic field is the 'novel flat plate collector' in this study. The rival flat plate collector uses NF in porous media without magnetic field. Exergy analysis and thermal assessments of this nanofluid in FPC are numerically evaluated. Exergy is a form of energy or in another word, and it is a measure of the work potential. The weight concentrations of the nanofluid are 1 and 2%. The porosity (ε) of this medium is 0.8. The model experimental setup of novel FPC is given in Fig. 8. Interestingly, the Nu of Novel FPC is 1.36 times higher. Also, the exergy efficiency is higher for novel system rather than rival system, and this is due to the presence of magnetic field in rival system. The external magnetic field induces a synergistic effect between the nanoparticles and the base fluid, and consequently, the exergy efficiency is increased (Anitha et al. 2020). This in fact opens up the possibility of usage of porous media for heat transfer in industrial applications.

The thermal performance of lid-driven porous cavity is analysed numerically with the effect of magnetic field (Sheikholeslami 2018), and the geometry is shown in Fig. 9. CuO/water nanofluid is used as a coolant. In this case, two different Darcy numbers 10^{-2} and 10^{2} are considered. Brownian motion and the influence of various shape factors of nanoparticles are examined. As discussed earlier, the increase in permeability (porosity and the pore structure) enhances the temperature gradient of the fluid. In this work, it is noted that with Darcy number of 10^{2}, the HTP of the system is higher and it is also due to the wavy walls (Sheikholeslami 2018). In general, the

Fig. 8 Porous structure used in the experimental setup of novel and rival Flat plate collector. Reprinted from Ameri et al. (2018)

Fig. 9 Geometry and the boundary conditions of the lid-driven porous cavity (Sheikholeslami 2018)
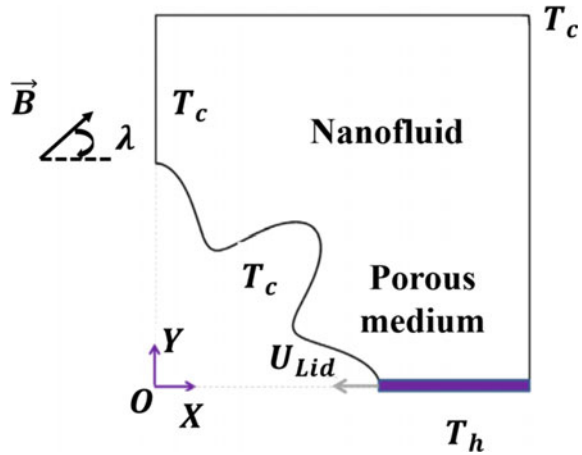

wavy walls help to increase the contact area between two different mediums which are of different temperature.

Unlike the above studies (which consider the normal convective heat transfer), forced convective heat transfer (which mimics industrial processes) has been analysed (Servati et al. 2014). Alumina nanofluid is used as a coolant in this case. Here, the HTP of the system is evaluated with partially filled porous media. The streamlines of the flow of the fluid through the porous media are shown in Fig. 10. It is shown that with an increase in volume fraction of nanoparticles (NPs), the HTP of the nanofluid also increases. With increase in volume fraction of NPs, the velocity of the fluid rises, and consequently, the Nusselt number of the system is increased. Therefore, akin to porosity and Darcy number, volume fraction of NPs is one of the important phenomena that influence the HTP of the system.

Triple convection heat transfer, namely free, forced and Marangoni connective flow of micropolar nanofluids, is numerically investigated in an open closure with

Fig. 10 Streamlines of the fluid flow in porous media. The considered channel is partially filled with porous medium. Reprinted from Servati et al. (2014)
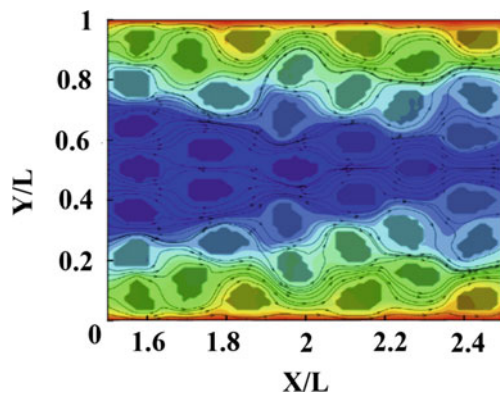
Fig. 11 Open enclosure partially filled with porous media with boundary conditions is shown. The lower wall is partially heated (red region). Reproduced from Mansour et al. (2020)
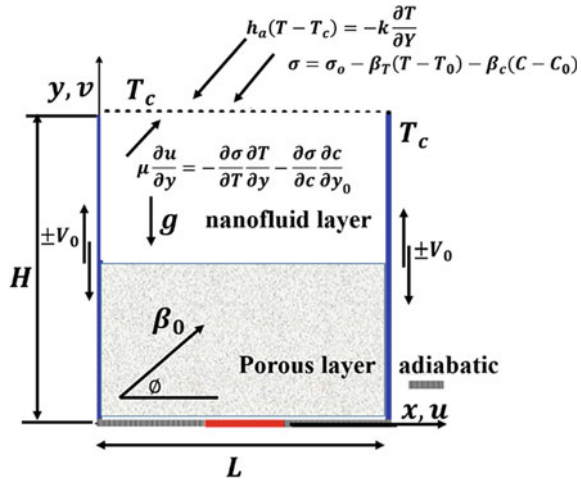
partially filled porous media. The geometry is shown in Fig. 11 (Mansour et al. 2020). A fluid that contains rotating micro-components is known as a micropolar fluids. It is a combination of the macroscopic velocity of the fluid and the rotational motion of the particles. The momentum equation can be derived in three dimensions. The x-direction momentum equation can be written as below by elaborating Eq. 10a (Mansour et al. 2020):

$$\frac{1}{\varepsilon^2}\left(u\frac{\partial u}{\partial x} + v\frac{\partial u}{\partial y}\right) = \frac{-1}{\rho_f}\frac{\partial p}{\partial x} + \frac{1}{\varepsilon}\left(\gamma_f + \frac{k}{\rho_f}\right)\nabla^2 u$$
$$+ \frac{k}{\rho_f}\frac{\partial n}{\partial y} - \frac{\gamma_f}{K}u + \frac{\sigma_f B_o^2}{\rho_f}\left(\gamma\sin\emptyset\cos\emptyset - u\sin^2\emptyset\right) \quad (14)$$

In Eq. 14, ε is the porosity of the medium, k is the thermal conductivity of the fluid. K is the permeability. B_o denotes the external magnetic field, u, v are the velocity components in x- and y-directions, respectively. γ is the kinematic viscosity. $\emptyset$ is the inclination angle (see Fig. 16). σ_f is the surface tension at the free surface due to nanofluid and n is the angular velocity. ρ_f is the density of the fluid. The above equation incorporates the effect of external magnetic effect on the fluid flow. We request our reader to refer Sect. 7 (nomenclature and symbols used) for common terminologies/terms. The heat transfer performance is calculated in terms of different governing parameters like Gr, Pr (refer Eq. 6), Ha, Da and so on. Left side $\left(\frac{1}{\varepsilon^2}\left(u\frac{\partial u}{\partial x} + v\frac{\partial u}{\partial y}\right)\right)$ of the equation describes the convective derivative term which is the rate of change due to the movement of the fluid element from one location to another. The last term $\left(\frac{\sigma_f B_o^2}{\rho_f}\left(\gamma\sin\emptyset\cos\emptyset - u\sin^2\emptyset\right)\right)$ in right-hand side denotes the influence of external force (magnetic force) towards the fluid flow. Ferro fluids and blood flows are some of

the examples of micropolar nanofluids. By varying Hartmann numbers, the convective HTP of the micropolar system is analysed. *Da* is varied from 10^{-2} to 10^{-5}. By decreasing the Darcy number, streamlines are reduced (Table 1).

This is due to the fact that at lower Darcy number, porous media resist the fluid to flow through the porous media. Therefore, it reduces the thermal performance of the coolant. For most of the analysis, Darcy number is fixed as 10^{-3}, and by varying *Ha* (refer Eq. 8) from 0 to 50, the numerical analysis is carried out. It is concluded that, the average Nusselt number increases with an increase in *Re*, *Da* and a decrease in *Ha*. The variations in *Nu* with the increase in *Ha* are given in Table 2 for fixed

Table 1 Key investigations on the heat transfer performance of nanofluids and hybrid nanofluids with porous media in different geometries

References	Nanofluid	Geometry with porous media	Darcy number (Da) or porosity (ε)	Volume fraction of nanofluid
Cho (2020)	Cu/water	Porous cavity with wavy walls	Da = 10^{-6} to 10^{-2}	2%
El-shorbagy et al. (2021)	Al$_2$O$_3$/water	Trapezoidal channel	Aspect ratio = 0.3 and 0.5	0–3%
Ali et al. (2020)	Cu/water	Trapezoidal enclosure	Da = 10^{-5} to 10^{-1}	0–0.1%
Ameri et al. (2018)	Fe$_3$O$_4$/water	Flat plate collector	$\varepsilon = 0.8$	1 and 2%
Sheikholeslami (2018)	CuO/water	Porous cavity	Da = 10^{-2} to 10^{2}	0–4%
Servati et al. (2014)	Al$_2$O$_3$/water	Channel	$\varepsilon = 0.74$	0–7%
Mansour et al. (2020)	Micro-nanofluid	Open enclosure	Da = 10^{-2} to 10^{-5}	–
Agrawal et al. (2021)	$\gamma - $ Al$_2$O$_3$ nanofluid	Stretching sheet	$\varepsilon = -0.5, 0, 0.5$	0.1–0.2%
Cimpean et al. (2020)	Cu-Al$_2$O$_3$/water	Trapezoidal chamber	Da = 10^{-2} to 10^{-4}	0–0.04%
Kadhim et al. (2020)	Cu-Al$_2$O$_3$/water	Wavy walls	Da = 10^{-2} to 10^{-5}	0–0.2%
Moghadasi et al. (2020)	Al$_2$O$_3$-CuO/water	U-bend pipe	Da = 10^{-4} to 10^{-1}	0–5%
Mehryan et al. (2020)	Ag-MgO/water	Square cavity with porous enclosure	$\varepsilon = 0.1$–0.9	0–2%
Jakeer et al. (2021)	Cu-Al$_2$O$_3$/water	Square porous cavity	Da = 10^{-2} to 10^{-6}	–

By varying Darcy number, porosity and width of porous media, significant tuning of the heat transfer performance is possible

Table 2 Variations in *Nu* for different values of *Ha* (Mansour et al. 2020)

| Hartmann number	Nusselt number
10	10.361
50	10.314
100	10.311

$Gr = 10^5$ (refer Eq. 5). With the increase in *Ha*, the *Nu* value is decreased. This is due to the existence of thermal plume inside the channel. The presence of magnetic field induces thermal plume in the channel and makes the isotherm parallel to each other due to the domination of conduction mode of heat transfer. Consequently, *Nu* value decreases. Ata A Servati et al. have discussed more about the influence of base fluid on the heat transfer performance of coolant, and the associated discussions are beyond the scope of this chapter.

Magneto-Marangoni flow on the stretching surface that is embedded in porous media is numerically analysed (Agrawal et al. 2021). The magneto-Marangoni convection of fluids can be defined as interfacial electrically conducting nanofluid flow driven by the surface tension gradient under the influence of magnetic field. HTP of two different nanofluids made of H_2O (water) and $C_2H_6O_2$ (ethylene glycol) as base fluids but with a common dispersoid ($\gamma - Al_2O_3$ nanoparticles) is compared. The porosity values chosen in this study are 0.5, 1 and 1.5. With the variations in porosity values, the corresponding velocity profiles of the nanofluids are calculated. With an increase in permeability parameter (K), the velocity profile of the fluid flow in porous media decreases. This is due to the relation between permeability parameter (K) and the thermal conductivity (k) of the fluid; that is, $K \propto \frac{1}{k}$ (Agrawal et al. 2021).

5 Heat Transfer of Hybrid Nanofluids with Porous Media

Even though nanofluids enhance the thermal conductivity, there are some experimental limitations such as potential clogging in the flow pattern, corrosion, lower chemical and thermal stability. It is demonstrated that hybrid nanofluids (HYNFs) have higher chemical stability and corrosion-resistant with respect to the appropriate choices of nanoparticles. Furthermore, significant improvement in thermal performance is noted (Anitha et al. 2019; Vinoth et al. 2021; Vidhya et al. 2020; Waini et al. 2020). The properties of hybrid nanofluids depend on both the physical and chemical behaviours of all the constituent nanoparticles (more than one type in this case). The advantages of hybrid nanofluids are shown in Fig. 12. The commonly used nanoparticles for heat transfer applications are (a) metal nanoparticles (Al, Au, Fe, Ag, Cu, Mn, Ni, Ti and Zn), (b) metal oxide nanoparticles (Al_2O_3, Fe_3O_4, CuO, TiO_2 and ZnO) and (c) elongated structures (CNTs, SWCNTs, MWCNTs).

In hybrid nanofluids, the drawback associated with the use of just one type of nanoparticle can be overcome by using different types of nanoparticles as well. The
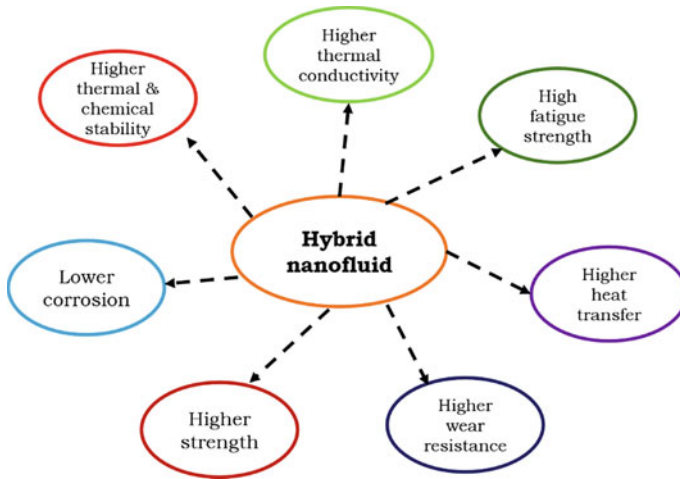
Fig. 12 Advantages of hybrid nanofluids

usage of alumina and copper nanoparticles in a base fluid (Al_2O_3–Cu/water hybrid nanofluid) can be a suitable example. Alumina nanoparticles possess lower thermal conductivity and higher chemical stability when compared to copper nanoparticles. The drawbacks of one of the nanoparticles, however, can be overcome by use of the other nanoparticles in appropriate volume proportion and fraction.

The thermal performance of hybrid nanofluids is being explored for different engineering applications like heat exchangers, solar systems and plate collectors.

Thermal performance analysis of single pass shell and tube heat exchanger is carried out numerically with Al_2O_3–Cu/water HYNF as the coolant (Anitha et al. 2019). Alumina nanoparticles have lower thermal conductivity but higher chemical stability, whereas copper nanoparticles have higher thermal conductivity and lower chemical stability (Anitha et al. 2019). So, with the appropriate volume proportion of these nanoparticles, the HTP of the heat exchanger can be improved. However, the thermal conductivity associated with copper and alumina nanoparticles is approximately 400 and 40 W/mK, respectively. Thus, the thermal performance of heat exchanger is primarily influenced by copper nanoparticles.

HTP of hybrid nanofluids in porous media has become an important research topic. and it has gained significant attention owing to its industrial applications like thermal insulation engineering, heat pipes, filtration process and drying processes. In recent years, notable improvements in thermal efficiency (42%) have been accomplished (Alhajaj et al. 2020; Cimpean et al. 2020; Kadhim et al. 2020; Moghadasi et al. 2020).

For instance, forced convective heat transfer of HYNF in different numbers of porous channels (say two, three and four channels) is analysed numerically and experimentally, and the geometry is shown in Fig. 13 (Alhajaj et al. 2020). Each porous channel has a porosity of 91%, and the pore density is 40 pores per inch. It is equivalent to the permeability of 3.36×10^{-8} m^2. Alhajaj et al. stated that HYNF

Fig. 13 Different number of channels have been used in an experimental setup. Hybrid nanofluid increases the heat transfer performance than nanofluids. Reprinted from Alhajaj et al. (2020)

(a) Two channels   (b) Three channels
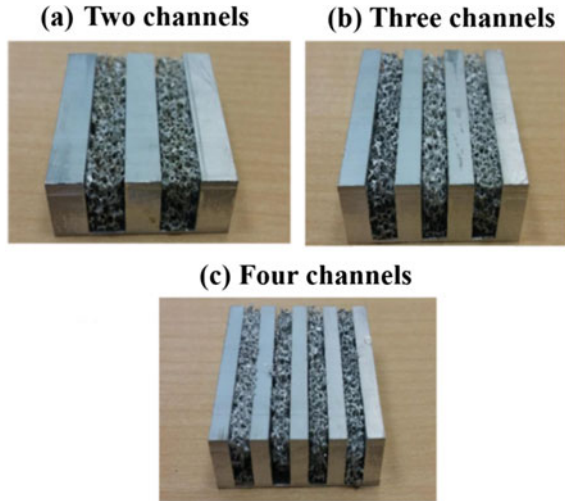
(c) Four channels

enhances the heat transfer efficiency but a higher pressure drop is noted with the usage of HYNF. Role of volume fractions of NPs on the HTP of these channels has been studied.

It is shown that after an optimal volume fraction, no further changes in heat transfer are observed. Nevertheless, by increasing the number of channels, the cooling performance is enhanced. By comparing two-channel and three-channel configurations with the same temperature difference, it is found that the rate of cooling is higher in the latter configuration. In the three-channel case due to the relative increase in the solid–liquid interface, improved HTP is observed.

The mixed convective heat transfer of $Cu–Al_2O_3$/water HYNF in a porous trapezoidal chamber is studied numerically, and the geometry is given in Fig. 14 (Cimpean et al. 2020). One of the basic problems which relate to the relationship between porous media and energy transport has to do with mixed convective flow in trapezoidal

Fig. 14 Mixed convective hybrid nanofluid flow through the trapezoidal chamber. The upper wall of the chamber is moving with uniform velocity. The walls (side) of the chamber are adiabatic (in which the heat cannot be transferred or enter). Reprinted from Cimpean et al. (2020)
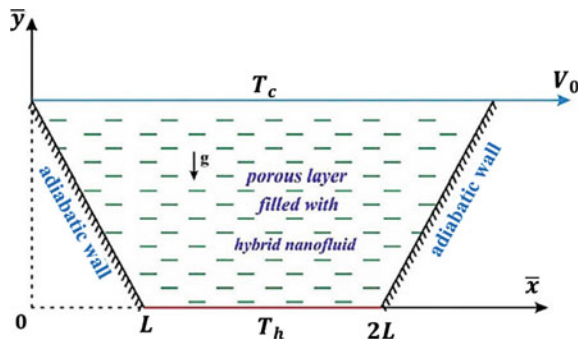
chamber. Cu–Al$_2$O$_3$/water HYNF is used as a coolant. Based on the Brinkman–Darcy model, the momentum equation in x-direction is given as below by elaborating Eq. 10a (Cimpean et al. 2020):

$$\rho_{hnf}\left(\frac{1}{\varepsilon}\frac{\partial u}{\partial t} + \frac{u}{\varepsilon^2}\frac{\partial u}{\partial x} + \frac{v}{\varepsilon^2}\frac{\partial u}{\partial y}\right)$$
$$= -\frac{\partial p}{\partial x} + \frac{\mu_{hnf}}{\varepsilon}\left(\frac{\partial^2 u}{\partial x^2} + \frac{\partial^2 u}{\partial y^2}\right) - \frac{\mu_{hnf}}{k}u \tag{15}$$

In this Eq. 15, ρ_{hnf} and μ_{hnf} are the density and viscosity of the hybrid nanofluid. ε is the porosity value and k is the thermal conductivity. p is the pressure force acting on the fluid. We request our reader to refer Sect. 7 (nomenclature and symbols used) for common terminologies/terms. The left side $\left(\rho_{hnf}\left(\frac{1}{\varepsilon}\frac{\partial u}{\partial t} + \frac{u}{\varepsilon^2}\frac{\partial u}{\partial x} + \frac{v}{\varepsilon^2}\frac{\partial u}{\partial y}\right)\right)$ denotes the local derivative term which is said to be the time rate of change of velocity at a fixed point. The second $\left(-\frac{\partial p}{\partial x}\right)$ and third terms $\left(\frac{\mu_{hnf}}{\varepsilon}\left(\frac{\partial^2 u}{\partial x^2} + \frac{\partial^2 u}{\partial y^2}\right)\right)$ represent convective derivatives, and its' physical significance comes from discussions on Eqs. 11 and 14 given above. In general, the right side of the equation represents the total forces acting on the fluid flow. In this case, the external forces are pressure and viscous forces. The right side of the equation is formulated accordingly.

The effect of isothermal, streamlines, Reynolds number and Darcy number is investigated by varying volume fractions of nanoparticles (0–0.04%) in a single-phase model. The desired HTP can be obtained by tuning the Darcy number. In this case, the Darcy number is varied from 10^{-2} to 10^{-4}. By increasing Darcy number from 10^{-4} to 10^{-2}, the parallel flow of the streamlines is changed and vortices are created. This directly leads to an increase in the thermal performance of the fluid in the porous chamber. In addition, for $Da \leq 10^{-3}$, the conduction mode dominates, whereas for $Da \geq 10^{-2}$, the heat convection mode dominates the HTP in porous chamber. At higher Da value, thermal plume is developed inside the cavity due to the stronger convective motion of the fluid and this is helpful for improvement in HTP (Cimpean et al. 2020). Nevertheless, it is shown that the trapezoidal chamber gives more effective performance than the square chamber.

Four different values of Re (say 50, 100, 200 and 400) and the associated HTPs of the chamber are analysed. For higher values of Re, the convective circulation of the streamlines is observed and it is shown in Fig. 15. It is observed that there is a development of a counterclock-wise vortex motion to the left side (clearly seen in Fig. 15a, b) at lower Reynolds numbers ($Re = 50$ and 100). For Reynolds numbers ($Re = 200$ and 400) (Fig. 15c, d), the formation of the vortices in the right side (see Fig. 15d) is observed. This is due to the variations in convective heat transfer mode from normal convection to forced convection.

Normal convection of HYNF flow in the enclosure which is layered by porous medium is numerically analysed, and it is shown in Fig. 16 (Kadhim et al. 2020). In addition, at a different inclination angle of the porous media, the heat transfer has been analysed. The inclination angle is considered between 0 and 90°. The inclination

Fig. 15 Streamlines inside the trapezoidal chamber for **a** $Re = 50$, **b** $Re = 100$, **c** $Re = 200$ and **d** $Re = 400$ for $Da = 10^{-3}$, and volume fraction of nanoparticles are 0.02 (where ψ is the stream function). When Reynolds number is increased, formation of vortices in the right side of the trapezoidal cavity is observed. Reproduced from Cimpean et al. (2020)
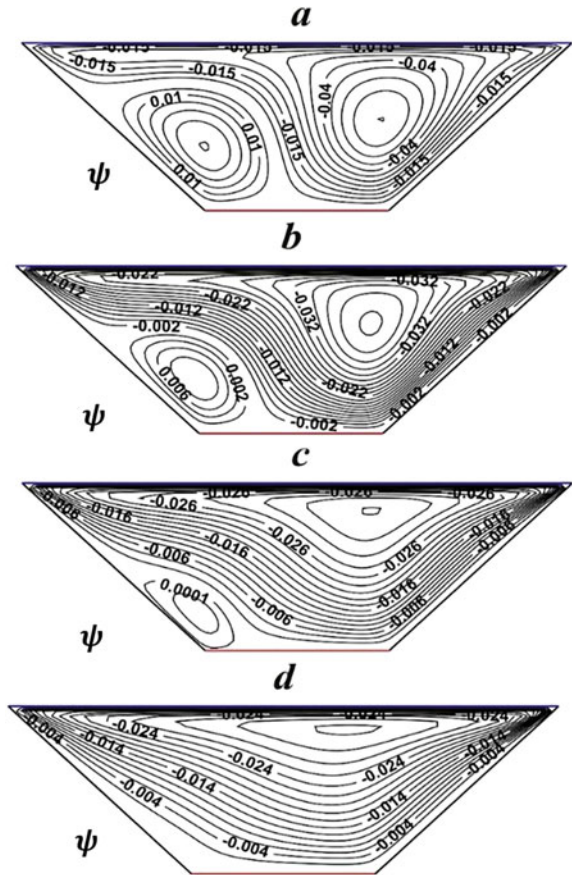
angle of the enclosure significantly influences the HTP of hybrid nanofluid. Table 3 displays the variations in Nu with the inclination angle for different Darcy numbers. It is noted that Nu significantly increases with increasing Da value due to the increase in permeability of the porous media. In addition, higher Nu is noted at 30°; this would evidently be useful to design these types of enclosure for the practical applications.

Hakim et al. have used Galerkin finite element method with semi-implicit pressure-linked algorithm to solve the algebraic equations.

Six different parameters, namely Rayleigh number, Darcy number, porous width, volume fraction, number of undulation and the angle of inclination, are studied. The Darcy number is varied from 10^{-5} to 10^{-2}. The porous layer width (W_p) is varied from 0.2 to 0.8. It is found that, the HTP of HYNF is mainly dependent on the Darcy number (Da). By increasing Da, the intensity of the streamlines increases which improves the motion of the hybrid nanofluid inside the enclosure. It is also observed that, Nusselt number predominantly depends on the inclination angle of the porous media rather than on the porous width (Kadhim et al. 2020). Primarily,

Fig. 16 Natural convection in an enclosure with an opposing wavy wall with porous medium. The lower and upper walls of the system are adiabatic. Reprinted from Kadhim et al. (2020)
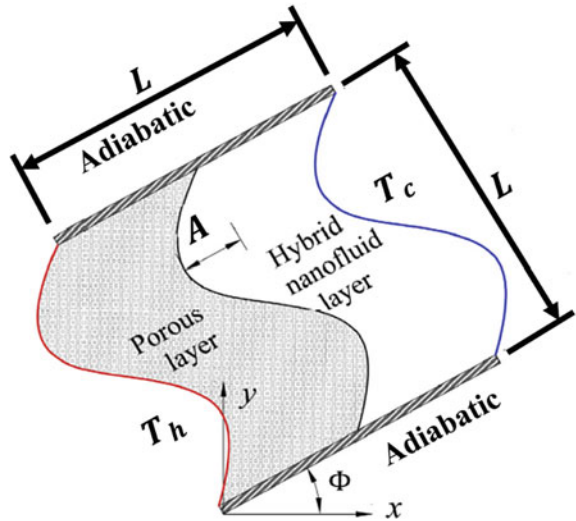
Table 3 Nusselt number variations in terms of different inclination angle of the porous media with $Ra = 10^6$ and $\varphi = 0.2$. At 30°, the Nu value is highly notable

Inclination angle	Darcy number			
	10^{-5}	10^{-4}	10^{-3}	10^{-2}
0	1.88	4.24	7.91	9.12
30	2.94	4.94	11.61	14.39
60	2.86	4.21	9.99	12.09
90	2.88	4.84	10.94	12.97

two inferences can be obtained from this discussion (a) at higher Da value, the HTP of fluids is higher, and (b) at lower porous width (e.g. $W_p = 0.2$), higher HTP of hybrid nanofluid is observed (Agrawal et al. 2021; Anitha et al. 2019; Alhajaj et al. 2020; Cimpean et al. 2020; Kadhim et al. 2020).

HTP of U-bend pipe with porous medium is studied numerically (Moghadasi et al. 2020). Laminar convective forced convection of Al_2O_3-CuO/water HYNF is simulated in three dimensions. Important parameters such as volume fraction of nanoparticles (0–5%), Darcy number, porous thickness, Nusselt number, performance evaluation criteria are calculated. The Darcy number is varied from 10^{-4} to 10^{-1}. The momentum equation in x-direction is given as by elaborating Eq. 10a (Moghadasi et al. 2020):

$$
\frac{1}{\varepsilon^2}\left(u\frac{\partial u}{\partial x} + v\frac{\partial u}{\partial y} + w\frac{\partial u}{\partial z}\right)
$$
$$
= \frac{-1}{\rho_{nf}}\frac{\partial p}{\partial x} + \frac{\gamma_{nf}}{\varepsilon}\left(\nabla^2 u\right) - \frac{\gamma_{nf}}{K}u - \frac{\gamma_{nf}C_d|u|}{\sqrt{K}}u \tag{16}
$$

Here ε, p, ρ, γ, K and C_d are the porosity of the porous media, pressure acting on the fluid, density of the fluid, kinematic viscosity, permeability of the porous medium and the inertia coefficient of the porous media. The inertia coefficient of porous media is defined as $C_d = \frac{1.75}{\sqrt{150\varepsilon^{\frac{3}{2}}}}$.

Equation 16 represents the 3D steady-state flow. The left side $\left(\frac{1}{\varepsilon^2}\left(u\frac{\partial u}{\partial x} + v\frac{\partial u}{\partial y} + w\frac{\partial u}{\partial z}\right)\right)$ denotes the convective heat transfer of fluid flow in three dimensions. The first term on right of the equation $\left(\frac{-1}{\rho_{nf}}\frac{\partial p}{\partial x}\right)$ denotes the pressure gradient, and the physical significance comes from discussions on Eqs. 10 and 13 given above. The right side of the equation always represents the total net force acting on the fluid flow. Here in this work, the influence of pressure force and the viscous force is given in terms of porosity and the permeability on the fluid flow. We request our reader to refer Sect. 7 (nomenclature and symbols used) for common terminologies/terms. Terms associated with gravity are considered negligible. Furthermore, heat transfer through radiation is considered as negligible in this study.

Also based on the porous thickness ratio (r_p), the HTP of the U-bend pipe is calculated. By increasing porous thickness ratio (r_p) from 0 to 1, and Da from 10^{-3} to 1, the Nusselt number and the HTP are found to be increase due to the increment in heat transfer coefficient of the fluid flow. With the increase in porous thickness ratio, the averaged Nusselt number is increased (Fig. 17). Heat transfer coefficient (Eq. 16) is the ratio between heat flux (q) and the temperature difference (ΔT) (from solid surface temperature to surrounding fluid temperature). It is written as: $h = \frac{q}{\Delta T}$. In general, heat flux (q) is the rate of heat energy that passes through a surface.

Natural convective HTP of Ag-MgO/water HYNF in a porous inclusion is numerically evaluated by using Galerkin finite element method (Mehryan et al. 2020). Two different porous systems are used in this work (a) glass ball and (b) aluminium foam. The geometry chosen is given in Fig. 18. In general, there are two models for
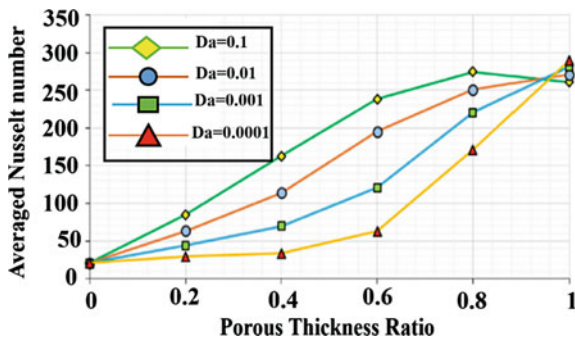
Fig. 17 Effect of porous thickness ratio on Nusselt number for different Darcy numbers. It is observed that with the increase in porous thickness ratio, the Nusselt number of the system is increased. This study analyses two cases, namely porosity (1) at the wall (2) at the centre of the U-bend. Reprinted from Moghadasi et al. (2020)

Fig. 18 Free convection of Ag-MgO/water HYNF flow in a porous enclosure. T_h and T_c denote the hot wall and cold wall temperature. The lower and upper walls are adiabatic. Reprinted from Mehryan et al. (2020)
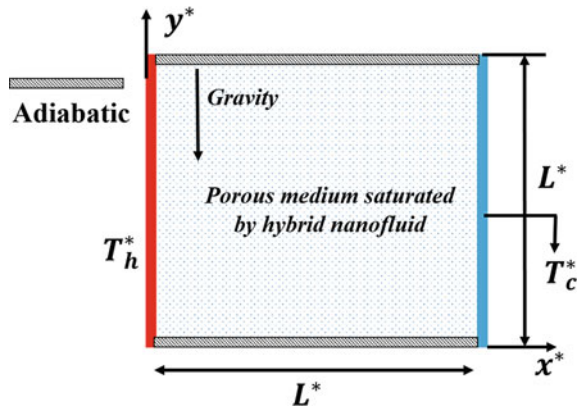
analysing the HTP of porous media. One is local thermal equilibrium (LTE) model, and the second is the local thermal non-equilibrium model (LTNE). In the first model, temperature gradient between solid and liquid phases is negligible. In second model, the temperature gradient between solid and liquid phases is considered. This study uses the first model to analyse the HTP of HYNF in the porous medium. The LTE model is valid when the solid and fluid phases do not locally exchange heat, or when the thermal conductivities of two phases are similar, resulting in equal local temperature of two phases. However, LTNE model is used when solid and fluid temperature fields are assumed to be distinct.

Three important parameters such as volume fraction, porosity and *Ra* are measured concerning the HTP of hybrid nanofluid. Range of porosity is varied from 0.1 to 0.9. This study reports that by increasing porosity from 0.1 to 0.9, the HTP improves. With an improvement in porosity, the circulation size and the strength of the vortices are enhanced. In fact, this leads to the movement of hybrid nanofluids which are helpful in enhancing the HTP. Recent research results on HTP of nanofluids and hybrid nanofluids flowing through porous media are listed in Table 1.

Magneto-Cu-Al$_2$O$_3$/water HYNF (non-Darcy flow) is numerically investigated in a porous cavity with a heated obstacle (Mehryan et al. 2020). Different positions of the heated obstacle are compared for analysing the HTP. Six important parameters, namely Richardson number, Hartmann number, height and width of the heated surface, *Re* and *Da*, are varied. Darcy number is varied from 10^{-2} to 10^{-6}. Like earlier reports, the HTP of HYNF is higher than that observed in nanofluid. Also, it is noted that by increasing *Da*, the *Nu* is also increased. With increase in Darcy number and porosity, the velocity of the fluid flow increases. Velocity variations are seen in the streamlines (these lines circulate in the clockwise direction) of the fluid flow inside the cavity. Therefore, HTP of the fluid is increased.

6 Conclusions and Outlook

Several efforts have been made towards improving the thermal efficiency of heat transfer systems. Convective heat transfer of fluids through porous media is an emerging research area due to its applications that range from biological systems to lubricant industries. The flow-through porous media augments the streamlines of the flow. This along with the higher surface area afforded by the pores enables the enhancement of the heat transfer performance.

Darcy, non-Darcy, Darcy–Brinkman–Forchheimer models are widely used for studying heat transfer applications in porous media. Also, nanoparticles (for nanofluids) greatly influence the thermal performance of porous media. It is noted that by increasing the Darcy number, porous width and porosity, HTP of the system is increased.

From several reports that have been studied; friction factor, surface tension and the flow of the nanofluid/hybrid nanofluid through porous media are found to be the key factors which influence the sedimentation of nanoparticles. However, studies on these key factors are rather sparse. Most of the studies consider nanofluid flow through porous media as single-phase flow, whereas two-phase flow-through porous media is increasingly investigated. Importantly, experimental research on transport phenomena of fluids through porous media is very limited. Many studies have focused on the laminar flow; however, the impact of turbulent fluid flow through porous media could be considered as well (in particular, to enable further applications for industrial deployment).

Finally, there are several open-ended problems that remain, that are amenable to further investigations. These pertain to influence of pore size and the selection of geometry (such as through selection among trapezoidal or square chamber, closed or open cavity with wavy walls, stretching sheet and flat plate). Nonetheless, role of parameters such as pore size and its distributions in determining HTP of nanofluids in porous media are yet to be explored. The impact of volume fraction and the shape of nanoparticles on HTP of nanofluid in porous media are yet to be explored in detail.

When the pore geometries are being considered in ultra-low dimensions (10^{-4} to 10^{-9} m), it is indeed required to tailor the size and the volume fraction of nanoparticles (for constituting nanofluids or hybrid nanofluids). Also, it is possible that nanoscale and quantum effects become prominent below certain length scales. These too can be considered duly to further this area of research.

7 Nomenclature and Symbols Used

B	Magnetic field strength
C_F	Forchheimer coefficient
C_d	Inertia coefficient of the porous media
d	Diameter

Da	Darcy number
f	Friction factor
FEM	Finite volume method
Gr	Grashof number
g	Gravity force
h	Heat transfer coefficient
HTP	Heat transfer performance
Ha	Hartmann number
k	Thermal conductivity
K	Permeability of porous media
L	Characteristic length
MHD	Magneto-hydrodynamics
n	Angular velocity
Nu	Nusselt number
p	Pressure
PEC	Performance evaluation criteria
Ra	Rayleigh number
Ri	Richardson number
Re	Reynolds number
S_x, S_y, S_z	External force
T	Temperature
U	Uniform velocity
V	Volume
v	Velocity
U	Uniform velocity
q	Heat flux
x, y, z	Direction components
ΔT	Temperature difference
∇p	Pressure gradient

Greek symbol

ε	Porosity
β	Thermal expansion coefficient
$\varnothing$	Inclination angle
α	Thermal diffusivity
σ	Electrical conductivity
ρ	Density
γ	Kinematic viscosity
μ	Dynamic viscosity

Subscript

h	Hot
w	Wall

c	Cold
ref	Reference
hnf	Hybrid nanofluid
nf	Nanofluid
L	Low temperature
H	Hot surface
f	Base fluid

References

Adler, P.M.: Porous Media: Geometry and Transports. Butterworth-Heinemann, A Division of Reed Publishing (USA) Inc. (1992)

Agrawal, P., Kumar, P., Jat, R.N., Nisar, S., Bohra, M., Dutt, S.: Magneto Marangoni flow of $\gamma-Al_2O_3$ nanofluids with thermal radiation and heat source/sink effects over a stretching surface embedded in porous medium. Case Stud. Therm. Eng. **23**, 100802 (2021)

Alhajaj, Z., Bayomy, A.M., Saghir, M.Z., Rahman, M.M.: Flow of nano fluid and hybrid fluid in porous channels: experimental and numerical approach. Int. J. Thermo Fluids **2**, 100016 (2020)

Ali, F.H., Hamzah, H.K., Kadhim, A., Jabbar, M.Y., Talebizadehsardari, P.: MHD mixed convection due to a rotating circular cylinder in a trapezoidal enclosure filled with a nanofluid saturated with a porous media. Int. J. Mech. Sci. **181**, 105688 (2020)

Ameri, M., Eshaghi, M.S.: Exergy and thermal assessment of a novel system utilizing flat plate collector with the application of nano fluid in porous media at a constant magnetic field. Therm. Sci. Eng. Prog. **8**, 223–235 (2018)

Angayarkanni, S.A., Pilip, J.: Review on thermal properties of nanofluids: recent developments. Adv. Colloid Interface Sci. **225**, 146–176 (2015)

Anitha, S., Thomas, T., Parthiban, V., Pichumani, M.: What dominates heat transfer performance of hybrid nanofluid in single pass shell and tube heat exchanger? Adv. Powder Technol. **30**, 3107–3117 (2019)

Anitha, S., Loganathan, K., Pichumani, M.: Approaches for modelling of industrial energy systems: correlation of heat transfer characteristics between magnetohydrodynamics hybrid nanofluids and performance analysis of industrial length-scale heat exchanger. J. Therm. Anal. Calorim. **144**, 1783–1798 (2020)

Chamkha, A.J.: MHD-free convection from a vertical plate embedded in a thermally stratified porous medium with Hall effects. Appl. Math. Model. **21**, 603–609 (1997)

Cho, C.-C.: Effects of porous medium and wavy surface on heat transfer and entropy generation of Cu-water nanofluid natural convection in square cavity containing partially-heated surface. Int. Commun. Heat Mass Transf. **119**, 104925 (2020)

Cimpean, D.S., Sheremet, M.A., Pop, I.: Mixed convection of hybrid nanofluid in a porous trapezoidal chamber. Int. Commun. Heat Mass Transf. **116**, 104627 (2020)

Dullien, F.A.L.: Porous Media: Fluid Transport and Pore Structure. Academic Press Inc. (1992)

El-shorbagy, M.A., Eslami, F., Ibrahim, M., Barnoon, P., Xia, W., Toghraie, D.: Numerical investigation of mixed convection of nanofluid flow in a trapezoidal channel with different aspect ratios in the presence of porous medium. Case Stud. Therm. Eng. **25**, 100977 (2021)

Ewing, D., Ching, C.Y.: The effect of pore size on the heat transfer between a heated finned surface and a saturated. J. Heat Transfer **131**, 1–7 (2009)

Jakeer, S., Reddy, P.B., Rashad, A.M., Nabwey, H.A.: Impact of heated obstacle position on magneto-hybrid nanofluid flow in a lid-driven porous cavity with Cattaneo-Christov heat flux pattern. Alexandria Eng. J. **60**, 821–835 (2021)

Kadhim, H.T., Jabbar, F.A., Rona, A.: Cu-Al$_2$O$_3$ hybrid nanofluid natural convection in an inclined enclosure with wavy walls partially layered by porous medium. Int. J. Mech. Sci. **186**, 105889 (2020)

Karimi, A., Goharkhah, M., Ashjaee, M., Shafii, M.B.: Thermal conductivity of Fe$_2$O$_3$ and Fe$_3$O$_4$ magnetic nanofluids under the influence of magnetic field. Int. J. Thermophys. **36**, 2720–2739 (2015)

Kaviany, M.: Principles of Heat Transfer in Porous Media. Springer, New York (1992)

Mansour, M.A., Ahmed, S.E., Aly, A.M., Raizah, Z.A.S., Morsy, Z.: Triple convective flow of micropolar nanofluids in double lid-driven enclosures partially filled with LTNE porous layer under effects of an inclined magnetic field. Chinese J. Phys. **68**, 387–405 (2020)

Mehryan, S.A.M., Ghalambaz, M., Chamkha, A.J., Izadi, M.: Numerical study on natural convection of Ag–MgO hybrid/water nano fluid inside a porous enclosure: a local thermal non-equilibrium model. Powder Technol. **367**, 443–455 (2020)

Moghadasi, H., Aminian, E., Saffari, H., Mahjoorghani, M., Emamifar, A.: Numerical analysis on laminar forced convection improvement of hybrid nanofluid within a U-bend pipe in porous media. Int. J. Mech. Sci. **179**, 105659 (2020)

Servati, A.A., Javaherdeh, V.K., Ashorynejad, H.R.: Magnetic field effects on force convection flow of a nanofluid in a channel partially filled with porous media using Lattice Boltzmann Method. Adv. Powder Technol. **25**, 666–675 (2014)

Sheikholeslami, M.: CuO-water nano fluid flow due to magnetic field inside a porous media considering Brownian motion. J. Mol. Liq. **149**, 921–929 (2018)

Vidhya, R., Balakrishnan, T., Kumar, B.S.: Investigation on thermophysical properties and heat transfer performance of heat pipe charged with binary mixture based ZnO-MgO hybrid nanofluids. Mater. Today Proc. **37**, 3423–3433 (2020)

Vinoth, R., Sachuthananthan, B.: Flow and heat transfer behavior of hybrid nanofluid through microchannel with two different channels. Int. Commun. Heat Mass. **123**, 105194 (2021)

Waini, I., Ishak, A., Pop, I.: Flow and heat transfer of a hybrid nanofluid past a permeable moving surface. Chinese J. Phys. **66**, 606–619 (2020)